AEROSOL IMPACTS ON DEEP CONVECTIVE CLOUDS

William R. Cotton
Colorado State University
Dept. of Atmospheric Science
Fort Collins, CO

1. INTRODUCTION

Recent modeling studies and inferences from field measurements suggest that aerosols acting as cloud condensation nuclei (CCN) can significantly impact the dynamics and precipitation processes in deep convective clouds. Some of these studies indicate increases in precipitation while others indicate decreases in precipitation. Likewise, several modeling studies have suggested that aerosols acting as CCN can even reduce the likelihood of tornado damage and can affect the intensity of tropical cyclones.

In this paper I will overview the previous work on this topic including research in my group. Some of the material I refer to was extracted from the IAPSAG report (Levin and Cotton, 2008). I will discuss possible sources for discrepancies between the previous studies on aerosol impacts on deep convective clouds, tropical cyclones.

2.0 CCN IMPACTS ON PRECIPITATION IN DEEP CONVECTIVE CLOUDS

Early studies by Mather (1991) indicated an increase in radar-estimated precipitation from mixed-phase deep convective clouds downwind of paper mills in South Africa. It was hypothesized that paper mill effluent was rich in giant CCN concentrations and these accelerated the warm cloud precipitation process and consequently accelerated the glaciation of the clouds. This observation led to a large field experiment for rain enhancement using hygroscopic particles.

Airborne and ground observations of cloud and precipitation development in the Amazon region by Andreae et al. (2004) indicated that "Smoky Clouds" exhibited high concentrations of CCN from smoke emitted from older fires. The authors reported that the high CCN concentrations produced high concentrations of cloud droplets, hence smaller sizes and narrower size distributions, thus reducing the efficiency for growth by collection. Therefore, these clouds were surmised to reach high altitudes and cold temperatures where ice could form. Since these clouds were deep, they could produce lightning, hail and heavy rain.

Using MODIS and TRMM satellite data, Lin et al. (2006) analyzed the effects of forest fires on precipitation in the dry season in the Amazon region. They report on increases in cloud heights and in precipitation with increases in aerosol optical depth. The increase cloud height led to enhanced growth of ice crystals, which culminated in heavier precipitation. However, in spite of the good correlation between these variables, the authors could not unequivocally establish causal links between aerosols and the observed changes in cloud height or with precipitation increases.

Modeling studies by Seifert and Beheng (2006) showed that the effect of changes in CCN on mixed phase convective clouds is quite dependent on cloud type. They found that for small convective storms, an increase in CCN decreases precipitation

Corresponding author: William R. Cotton, Dept. of Atmospheric Science, Colorado State University, Fort Collins CO 80523, USA; e-mail: cotton@atmos.colostate.edu

and the maximum updraft velocities. For multicellular storms, the increase in CCN has the opposite effect – namely, promoting secondary convection, and increasing maximum updrafts and total precipitation. Supercell storms were the least sensitive to CCN. Their study also showed that the most important pathway for feedbacks from microphysics to dynamics is via the release of latent heat of freezing. Likewise, Lynn et al., 2005a) performed mesoscale simulations with bin-resolving microphysics for Florida deep convective clouds and found that for shallow clouds, high concentrations of CCN delayed the formation of precipitation in initial clouds relative to clean clouds. Thus clouds in a maritime airmass precipitated sooner than clouds forming in a continental airmass but this led to weaker secondary clouds than those formed in the continental airmass. As a consequence clouds that formed in the continental airmass exhibited stronger updrafts, higher cloud tops, greater peak rainwater amounts and heavier precipitation rates.

When the environment can support deeper convective clouds, cloud modeling studies with bin-resolving microphysics by Khain et al. (2004) found that pollution-induced smaller cloud droplets reduce the production of drizzle drops. When these droplets froze, the associated latent heat release resulted in more vigorous convection. In contrast to a clean cloud, drizzle depleted the cloud liquid water so that less latent heat was released when the cloud glaciated, resulting in less vigorous convection. Thus, they found that a squall line developed under continental aerosol conditions and produced more precipitation after two hours whereas this did not happen with clean aerosol conditions. Zhang et al. (2005) came to similar conclusions in their model simulations for different three-week periods over the ARM site in Oklahoma.

Similarly, mesoscale simulations of deep convection over Florida Lynn et al (2005b) showed that higher CCN concentrations delayed the onset of precipitation but led to more intense convective storms with higher peak precipitation rates. However, the accumulated precipitation was largest for the cleaner atmosphere.

Likewise, mesoscale simulations of entrainment of Saharan dust into Florida thunderstorms with bin-emulating bulk microphysics by van den Heever et al. (2006) showed that dust not only impacts cloud microphysical processes but also the dynamical characteristics of convective storms. Dust may serve as CCN, GCCN, and IN. They found the updrafts are consistently stronger and more numerous when Saharan dust is present compared with a clean airmass. Like Seifert and Beheng (2006) they found that dust results in enhanced glaciation of convective clouds, which then leads to dynamical invigoration of the clouds, larger amounts of processed water, and thereby enhanced rainfall at the ground. However, rainfall was enhanced by dust ingestion only during the first two hours of the formation of deep convective cells, but it was reduced later in the day. Thus the clean aerosol simulations produced the largest surface rain volume at the end of the day. This is a result of complex dynamical responses of clouds to aerosol changes associated with subcloud evaporation of rain in which low-level cold pools influence storm propagation and to scavenging of dust, so that few GCCN and IN remained late in the day.

In another study van den Heever and Cotton (2007) examined the impacts of urban-enhanced aerosol concentrations on convective storm development and precipitation over and downwind of St. Louis, MO. In that study RAMS was set up as a cloud-resolving, mesoscale model with both sophisticated urban land-use processes and aerosol microphysics using a bin-model emulation approach. The results indicate that urban land-use forced convergence downwind of the city, rather than the presence of greater aerosol concentrations, is the dominant control on the locations and amounts of precipitation in the vicinity of an urban complex. Once convection is initiated, urban-enhanced aerosols can exert a significant effect on the dynamics, microphysics and precipitation produced by these storms. The model results indicate, however, that the response to urban-enhanced aerosol depends on the background concentrations of aerosols; a weaker response occurs with increasing background aerosol concentrations.

Like in the sea breeze study, urban pollution enhanced updrafts initially, and downdrafts developed more quickly. The larger amounts of supercooled liquid water available, together with the stronger updrafts, led to the generation of greater ice mixing ratios earlier in the storm development. Greater amounts of surface precipitation were also produced during the first 1.25-1.5h of convective storm formation. However, the greater and more rapid production of surface precipitation generates stronger downdrafts and more intense cold pools earlier in the storm lifecycle than in the clean control simulation. As a result the polluted storms die earlier than the clean storms as the polluted storms become decoupled from the urban heat island driven convergence and total area wide precipitation is less at the end of the day. We now believe that essentially the same thing happened in the Florida dust simulations wherein the intensified earlier storms in the dusty atmosphere became decoupled from their parent sea-breeze convergence fields.

3.0 SEVERE CONVECTIVE STORMS

It is becoming increasingly apparent that tornadogenesis within supercell storms is closely related to the characteristics of the rear flank downdraft (RFD) (e.g., Burgess et al. 1977; Davies-Jones 1982a,b, Markowski et al., 2002). Markowski et al. (2002) found that air parcels within RFDs of tornadic supercells tended to be warmer and thus more buoyant than those within RFDs associated with nontornadic supercells. In a related study, idealized simulations by Markowski et al. (2003) revealed that tornado-like vortices increased in both intensity and longevity as the buoyancy of the downdraft parcels increased owing to the thermodynamic characteristics of the precipitation-filled downdraft. Modeling studies by van den Heever and Cotton (2004) and Snook and Xue (2008) found that larger hailstones and/or raindrops, as compared to those that favored smaller sizes, resulted in warmer cold pools and stronger, longer-lived tornadoes (Snook and Xue, 2008).

In collaboration with Dr. Brian Gaudet of The Pennsylvania State University, numerical simulations of an idealized supercell thunderstorm were performed using RAMS and a nested grid set up to assess possible effects dust or pollution aerosol would have on storm severity.

Preliminary results of the analysis of the simulation of tornadic supercell storms by David Lerach suggests that increasing CCN produces larger hailstones and raindrops which van den Heever and Cotton (2004) and Snook and Xue (2008) suggests leads to RFD cold pools which are less stable(not as cold). As suggested by Snook and Xue (2008), the importance of stability may be related to the tilt of the updrafts such that warmer cold pools result in slower motion of a gust front and therefore vorticies forming along the gust front are better able to couple with the main mesocyclone aloft. With colder cold pools, the near-surface vorticies are less likely to be drawn into the mesocyclone where they are stretched and intensified. Thus dust or other aerosol pollution sources may increase the likelihood of tornadoes for a given dynamic and thermodynamic environment.

4.0 AEROSOL INDIRECT EFFECTS ON TROPICAL CYCLONES

Two recent papers have examined the potential influence of hygroscopic aerosols on hurricanes. Rosenfeld et al. (2007) turned off the warm rain parameterization in the outer rainbands in a simulation of hurricane Katrina with WRF. Their simulations suggested that insertion of hygroscopic CCN in the outer rainbands of a storm like Katrina would decrease the area covered by hurricane force winds. Zhang et al. (2007) examined the influence of Saharan dust acting as CCN on simulations of an idealized tropical cyclone using RAMS. Increasing the background CCN concentration from 100 to 1000 and 2000 cm-3 in a layer between 1 and 5 km influenced the TC development by inducing changes in the hydrometeor properties, modifying the storm diabatic heating distribution and thermodynamic structure, and ultimately influencing the TC intensity through complex dynamical responses. The difference in the total precipitation between simulations was less than 5% even though significant differences in horizontal distributions were seen. The impact of CCN on storm intensity was also found to be sensitive to the background GCNN vertical profile and presumably other environmental profiles.

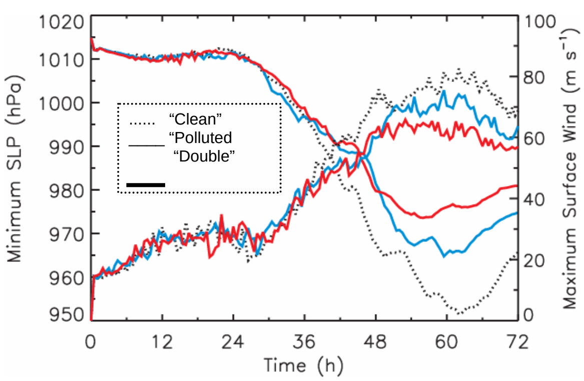

Fig. 1. Temporal evolution of the MSLP and maximum surface wind for "Clean," (dotted line), "Polluted" (thin solid line) and "Double" (thick solid line). From Zhang et al. (2007).

The results of that work so excited me that I authored a paper (Cotton et al., 2007) proposing that seeding hurricanes with small hygroscopic particles would decrease storm intensity under certain conditions. Further simulations by Zhang (personal communication) with CCN concentrations introduced into the boundaries in the storms with a broad range of concentrations and at different stages of the lifecycle of the storm revealed that the storm response to CCN is far more complicated than I originally envisioned. This work shows that the response to increasing CCN concentrations is not monotonic with increasing CCN concentrations as the lowest minimum sea level pressure (SLP) occurs with a CCN concentration of 1500/cc. Moreover when dust, serving as CCN, was introduced at 36h, the response was weaker and again not monotonic. Introducing CCN at 60h when the storm was more balanced and mature, resulted in very weak response to CCN. Clearly the simulated response of hurricanes to ingestion of CCN is quite complex and nonlinear even for these idealized simulations. In nature, the aerosol and TC interaction occurs in a much more complex environment. The ultimate influence of CCN on a TC could be very case sensitive to the details of the storm environment and the maturity of the storm.

5.0 SUMMARY

We now see that simulations and observations, to some extent, suggest that increasing CCN concentrations results in a suppression of collision and coalescence in deep convective clouds. In some storms (where CAPE is large), this results in greater amounts of supercooled water being thrust into the upper levels of the clouds where freezing of the larger amounts of water increases the buoyancy of the clouds and intensifies updrafts.

The impacts of CCN on precipitation on the ground, however, are far more difficult to understand owing to the nonlinear response of clouds to precipitation anomalies. Depending on stability, shear, interactions with mesoscale circulations and so forth, such invigorated storms by ingesting higher CCN concentrations may increase or decrease precipitation.

There is some suggestion that even supercell tornadic storms may be responsive to ingesting pollutants and dust, with the limited simulations to date suggesting that enhanced CCN concentrations will increase the size of hailstones and raindrops, resulting in cold pools of reduced strength, and increase the likelihood of tornado formation, *other things being the same!*

The simulations of hurricanes to date display mixed responses to pollution aerosols and dust with the weakest response being for mature intense storms.

5.0 ACKNOWLEDGEMENTS:

Much of the background material came from the extensive literature review in the IAPSAG report: Aerosol Pollution Impacts on Precipitation: A Scientific Review; (Levin and Cotton, 2008). That report was supported by WMO and IUGG. This material is also based upon work supported by the National Science Foundation under Grant No. ATM-0526600. Any opinions, findings, and conclusions or recommendations expressed in this material are those of the author(s) and do not necessarily reflect the views of the National Science Foundation. The research cited in collaboration with Susan van den Heever was supported under NSF Grant No. ATM-0451439. The work of Henian Zhang and Greg McFarquar was also supported by the National Aeronautics and Space Administration under grants NAG5-11507 and NNG04GG44G.

The research cited by Henian Zhang under the supervision of Greg McFarquhar was supported by NASA Earth System Science (ESS) Fellowship grant number NNG04GQ99H and Tropical Cloud Systems and Processes (TCSP) mission grant number NNG05GR61G.

6.0 REFERENCES

Andreae, M.O., D. Rosenfeld, P. Artaxo, A. Costa, G.P. Frank, K.M. Longo, and M.A.F. Silva-Dias, 2004: Smoking rain clouds over the Amazon. *Science*, **303**, 1337-1342.

Burgess, D. W., R. A. Brown, L. R. Lemon, and C. R. Safford, 1977: Evolution of a tornadic thunderstorm. Preprints, *10th Conf. On Severe Local Storms,* Omaha, NE, Amer. Meteor. Soc., 84–89.

Cotton, W.R., H. Zhang, G.M. McFarquhar, and S.M. Saleeby, 2007: Should we consider polluting hurricanes to reduce their intensity? *J. Wea. Mod*., **39**, 70-73.

Davies-Jones, R. P., 1982a: A new look at the vorticity equation with application to tornadogenesis. Preprints, *12th Conf. on Severe Local Storms,* San Antonio, TX, Amer. Meteor. Soc., 249–252.

Davies-Jones, R. P., 1982b: Observational and theoretical aspects of tornadogenesis. *Intense Atmospheric Vortices,* L. Bengtsson and J. Lighthill, Eds., Springer-Verlag, 175–189.

Khain, A., A. Pokrovsky, M. Pinsky, A. Seifert, and V. Phillips, 2004: Simulation of effects of atmospheric aerosols on deep turbulent convective clouds using a spectral microphysics mixed-phase cumulus cloud model. Part I: Model description and possible applications. *J. Atmos. Sci*., **61**, 2963-2982.

Levin, Z. and W. R. Cotton, 2008: Aerosol pollution impact on precipitation: A scientific review. Report from the WMO/IUGG International Aerosol Precipitation Science Assessment Group (IAPSAG), World Meteorological Organization, Geneva, Switzerland, 482 pp.

Lin, J. C., T. Matsui, R. A. Pielke Sr. and C. Kummerow, 2006: Effects of biomass-burning-derived aerosols on precipitation and clouds in the Amazon Basin: a satellite-based empirical study. *J. Geophys. Res*., **111**, D19204, doi:10.1029/2005JD006884.

Lynn, B., A. Khain, J. Dudhia, D. Rosenfeld, A. Pokrovsky, and A. Seifert, 2005a: Spectral (bin) microphysics coupled with a mesoscale model (MM5). Part 1: Model description and first results. *Mon. Wea. Rev*., **133**, 44-58, 2005a.

Lynn, B., A. Khain, J. Dudhia, D. Rosenfeld, A. Pokrovsky, and A. Seifert, 2005b: Spectral (bin) microphysics coupled with a mesoscale model (MM5). Part 2: Simulation of a CaPe rain event with squall line. *Mon. Wea. Rev.*, **133**, 59-71.

Markowski, P. M., J. M. Straka, and E. N. Rasmussen, 2002: Direct surface thermodynamic observations within the rear-flank downdrafts of nontornadic and tornadic supercells. *Mon. Wea. Rev.,* **130,** 1692– 1721.

Markowski, P. M., J. M. Straka, and E. N. Rasmussen, 2003: Tornadogenesis resulting from the transport of circulation by a downdraft: Idealized numerical simulations. *J. Atmos. Sci*., **60**, 795-823.

Mather, G.K., 1991: Coalescence enhancement in large multicell storms caused by the emissions from a Kraft paper mill. *J. Appl. Meteor.,* **30***,* 1134–1146.

Rosenfeld, D., A. Khain, B. Lynn, and W.L. Woodley, 2007: Simulation of hurricane response to suppression of warm rain by sub-micron aerosols*. Atmos. Chem. Phys.*, **7**, 3411-3424.

Seifert, A. and K.D. Beheng, 2006: A two-moment cloud microphysics parameterization for mixed-phase clouds. Part II: Maritime vs. continental deep convective storms, *Meteorol. and Atmos. Phys.*, **92**, 67-82.

Snook, N. and M. Xue, 2008: Sensitivity of Tornadic Thunderstorms and Tornadogenesis in Very-high resolution Numerical Simulations to Variations in Model Microphysical Parameters. *J. Atmos. Sci*., submitted.

van den Heever, S.C., and W.R. Cotton, 2004: The impact of hail size on simulated supercell storms. *J. Atmos. Sci*., **61**, 1596-1609.

van den Heever, S., and W. R. Cotton, 2007: Urban aerosol impacts on downwind convective storms. *J. Appl. Met.,* **46**, 828-850.

van den Heever, S.C., G.G. Carrió, W.R. Cotton, P.J. DeMott, and A.J. Prenni, 2006: Impacts of nucleating aerosol on Florida storms. Part I: Mesoscale Simulations. *J. Atmos. Sci.,* **63**, 1752-1775.

Zhang, J., U. Lohmann, and P. Stier, 2005: A microphysical parameterization for convective clouds in the ECHAM5 Climate Model: 1. Single column model results evaluated at the Oklahoma RM site. *J. Geophys. Res*., **110**, D15S07, doi:10.1029/2004JD005128..

Zhang H., G. M. McFarquhar, S. M. Saleeby, W. R. Cotton, 2007: Impacts of Saharan dust as CCN on the evolution of an idealized tropical cyclone. *Geophys. Res. Lett*., **34**, L14812, doi:10.1029/2007 GL029876.

ENTRAINMENT AND MIXING IN WARM CONVECTIVE CLOUDS: EFFECTS ON DROPLET SPECTRA AND ON THE ONSET OF PRECIPITATION

F. Burnet and J.-L. Brenguier

Météo-France/CNRS, CNRM/GAME, Toulouse, France

1. INTRODUCTION

The Small Cumulus Microphysics Study (SCMS) experiment, that took place in Florida during the summer 1995, was focused on the onset of precipitation in shallow convective clouds. On August 10, the Meteo-France Merlin-IV research aircraft sampled the top of three convective clouds, following the cells from their initial stage of young vigorous ascending turrets up to their decaying stage. These data are investigated here to document the evolution of cloud microphysical properties along the life cycle of the convective cells.

2. DATA ANALYSIS

Fig 1 shows the flight track during the sampling of the three cells referred to as A, B and C, with the cloud penetrations indicated by thick arrows. Notice the drift in the horizontal location of the cloud traverses, that reflects horizontal advection of the cloud along the mean wind that is blowing from west-northwest with a mean speed of 3.3 ± 1.1 m.s^{-1}.

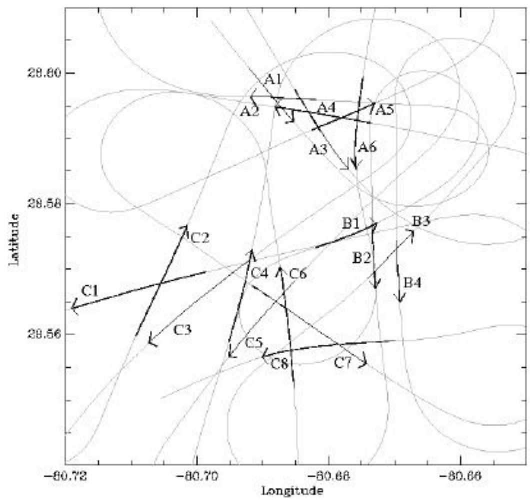

Fig. 1: Flight track of the Merlin-IV with the sampled cloud sections for the three selected cells.

Six penetrations were made in cell A from 15:26:48 (UTC) to 15:34:07, four in cell B from 15:35:31 to 15:40:01 and eight in cell C from 15:42:11 to 15:54:17. The mean altitude of each cloud traverse is reported as a function of time in Fig 2 that also shows, from top to bottom, the vertical velocity (w) , the air temperature (T) and potential virtual temperature (θ_v). For each cloud traverse, the frequency distribution of the 10 Hz values is derived and it is represented by its mean and 10% percentiles. The temperature measured with a Rosemount probe is corrected from wetting by cloud liquid water (Burnet and Brenguier, 2007). The θ_v values of the environment (black dots) are averaged over a distance of about 1 to 2 km on each side of the cloud. This figure illustrates the thermodynamical evolution of the three sampled cells during their life cycle.

Much warmer than its environment, cell A (~500 m wide) rises rapidly (up to 8 m.s^{-1}) at 2170 m. As the cell ascents the buoyancy progressively decreases, indicating intense cooling, the vertical velocity becomes negative at 2420 m and the cell finally collapses during the 6th penetration at 2340 m.

At this level, cell B (~700 m wide) shows a well defined updraft and θ_v greater than θ_{ve} by up to 2°C. Nevertheless, this cell also collapses 5 minutes latter at 2420 m with an overall negative vertical velocity and a virtual temperature ~1 °C colder than the environment.

Cell C (~1.2 km wide) also exhibits features of a young active turret with a strong updraft associated with a large buoyancy. The updraft observed during the 2nd traverse is weaker, likely because the aircraft missed the main cloud core, but during the third traverse the peak vertical velocity again exceeds 6 m.s^{-1}. The cell continues its ascent despite a strong cooling, comparable to cell A, but it reaches 2750 m, with a virtual temperature still greater than the environment. The two last traverses at this level reveal heavy showers in that cell that rose at much higher altitudes.

Figure 3 shows the time evolution of the microphysical parameters derived from Fast-FSSP measurements of the cloud droplet size distribution in the diameter range 5.5-44 µm (Brenguier et al., 1998, Burnet and Brenguier, 2002). The adiabatic values of

Corresponding author's address: Frédéric Burnet, Météo-France, CNRM/GMEI/MNPCA, 42 av. Coriolis, 31 057 Toulouse Cedex 01, France.
E-Mail: frederic.burnet@ meteo.fr

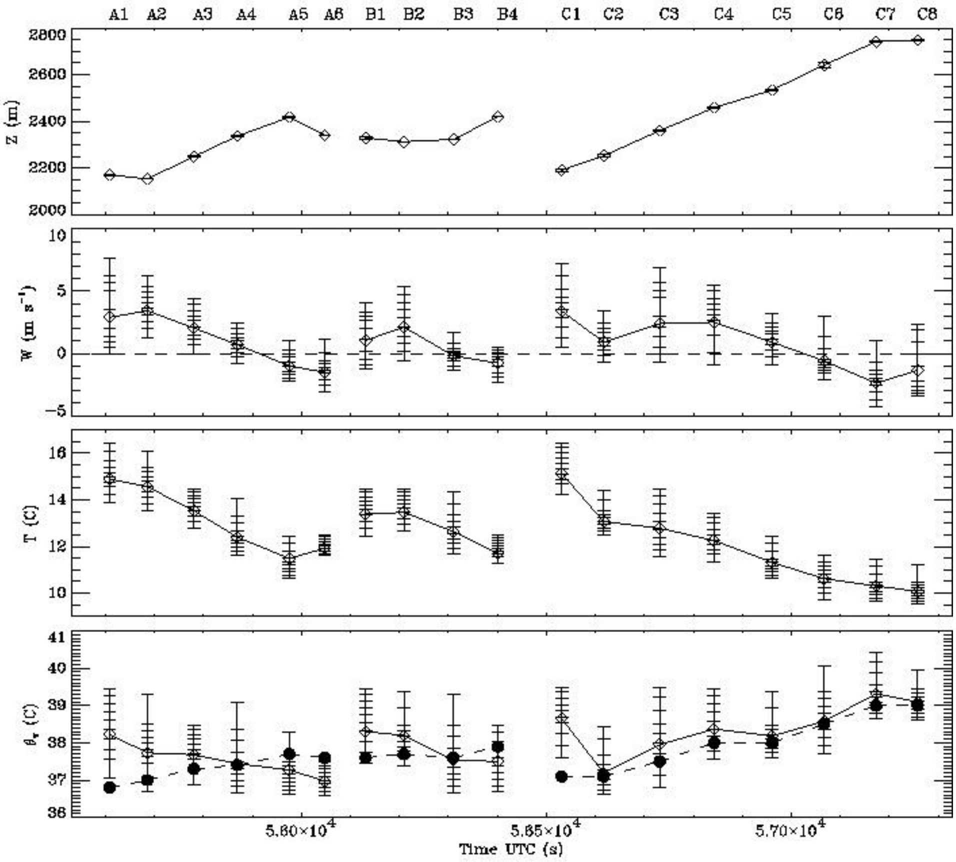

Fig 2: Time evolution of the three cloud cells. From top to bottom: altitude, vertical velocity, temperature and virtual potential temperature θ_v. Statistics of the parameters for each cloud traverse are represented by the mean (diamond) and the 10% percentiles. On the lower panel, black dots are the θ_v values of the environment.

liquid water content (LWC) are derived from cloud base height and temperature values of 942 hPa and 22.7 C, respectively.

The evolutions of the cloud droplet number concentration (CDNC) and LWC are consistent with the thermodynamics. When the convective cell is young, CDNC is maximum and LWC is close to the adiabatic value. As a result, more than 20% of the cloudy samples in cell A, and more than 60% in cell C, have LWC values > 3 g m^{-3}, i.e. ~85% of the adiabatic value. This is remarkable at this level ~1500 m above cloud base. Both CDNC and LWC further continuously decrease as the cell evolve. The cloud cells become cooler than their environment, implying an intense evaporation of the liquid water.
The mean volume diameter D_v of the cloud droplet size distribution (DSD), decreases only very slightly from ~28.5 µm to 25.5 µm and 26.5 µm on average for cells A and B respectively. This feature, apparently typical of inhomogeneous mixing, results in fact from the entrainment of very humid air (Burnet and Brenguier, 2007). Because of higher CDNC values, D_v is ~2.5 µm lower in Cell C, but unlike in cells A and B, it continuously increases, up to the last traverse.

Statistics of the 95% percentile of the DSD in the third panel follows the same trend. It exceeds 30 µm in almost all samples indicating the presence of droplets greater than 40 µm in diameter, which is considered as the threshold for coalescence (Klett and Davis, 1973). This is confirmed by the statistics of these biggest droplet relative concentration displayed in the bottom panel of Fig. 3. Note that this parameter also decreases in cell A and B, but not in cell C.

The Merlin-IV was also equipped with an OAP200X (1D-C) and an OAP230Y (1D-P) for measurements of drops in the diameter range 15-315 µm (drizzle drops) and 200-6000 µm (rain drops), respectively. The cells evolution of the drizzle and rain parameters derived from these 5 Hz data are reported in Fig. 4, with the concentration and water content derived from the 1D-C (upper panels) and from 1D-P (lower panels). Comparison with the FFSSP measurements confirm the significant uncertainty of the 1D-C first bin (15-35 µm) that is therefore not accounted for in the calculation of the drizzle drop concentration and water content.

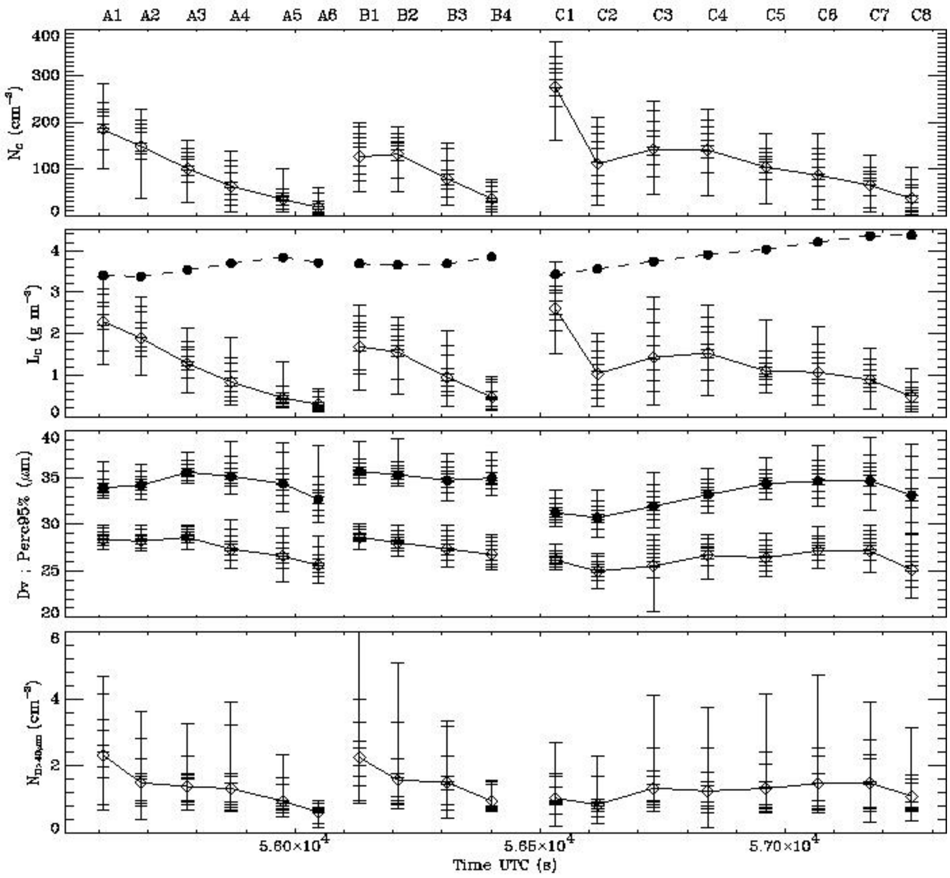

Fig. 3: Microphysical parameters evolution of the three cloud cells represented by the mean and 10 % percentiles of the frequency distributions of, from top to bottom: total droplet number concentration (N_C); cloud (open diamond) and adiabatic (black dot) liquid water content (L_c); mean volume diameter (open diamond) and 95th droplet size distribution percentile (black dot); and relative concentration of droplets with diameter > 40 μm.

The 1D-P data reveal a rapid development of the precipitation in cell C. Indeed both the rain drop concentration and water content, that are fairly constant at ~0.2 L^{-1} and ~0.02 g m^{-3}, respectively, until section C5, increase by a factor of 100 in 5 minutes. The transition between sections C5 and C6 is sharper in water content, with 20% of the samples above 0.1 g m^{-3} in section C6, a value that cell A, nor B never reach.

The transition is less pronounced for the drizzle drops that show similar values as in cell A and B until section C7 for the whole range of drizzle sizes and for parameters derived from the bin2 only (35-45 μm), represented in grey. Theses observations then do not reveal any significant increase of the relative concentration of droplets < 50 μm in diameter before the onset of precipitation occurring in section C6.

Examination of the 1D-P rain drop concentration bigger than 800 μm in diameter (grey symbols on Fig.4-b) reveals that such large drops exist in almost all sections with a substantial concentration ranging from 0.03 to 0.1 L^{-1}. The corresponding water content dominates the total LWC, and is thus not plotted for clarity. These concentration values increase in section C6, but also does the number of samples with such drops. As a result this number has doubled in C6, compared to sections C1 to C5, and corresponds to 55.1% of the cloud width. These observations suggest that while large drizzle drops (> 200 μm) are present in almost all the cloud traverses, the onset of precipitation is more reflected by an increase of the fraction of samples with large drops (>800 μm).

4. SUMMARY

Thermodynamical and microphysical measurements collected at the top of three marine cumulus clouds have been examined to document their life cycle. Turrets that emerge at cloud top have a strong updraft associated with a buoyant core and a significant fraction with LWC content values larger than 85 % of the adiabatic. These three cells contain a concentration of big droplets (> 40 μm in diameter) large enough (> 1 cm^{-3}) to trigger the coalescence process and they show concentrations of big drops (> 800 μm in diameter) of the order of ~0.05-0.1 L^{-1}.

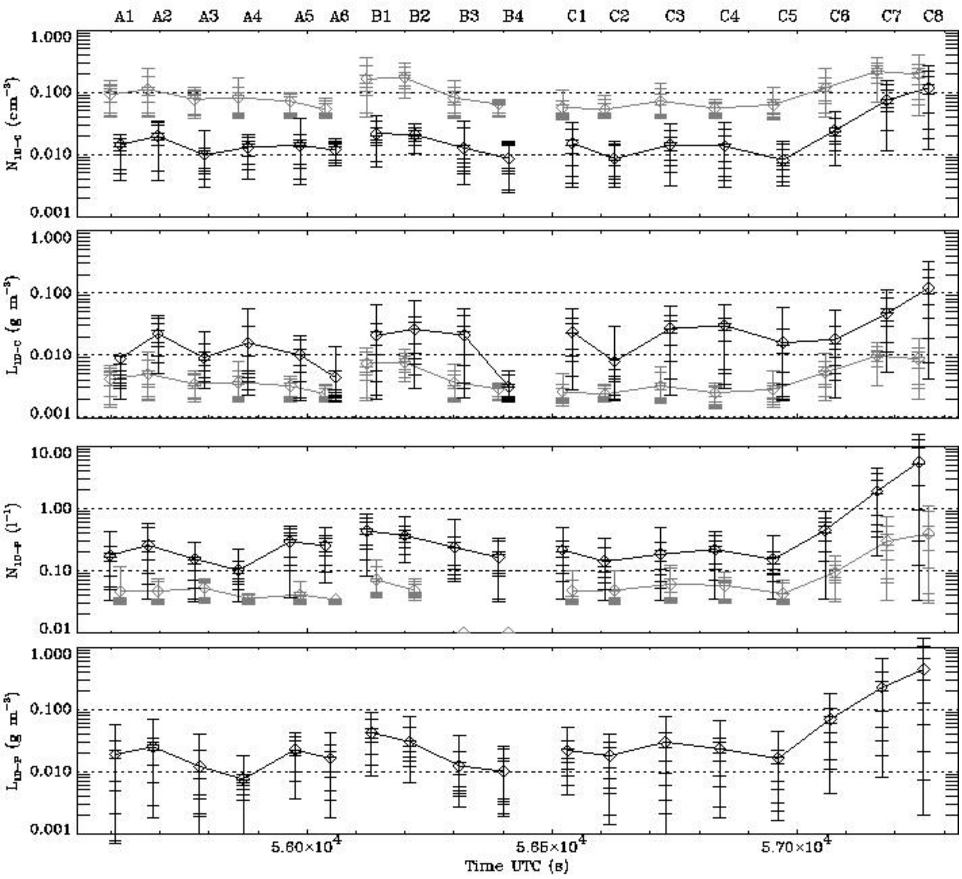

Fig. 4: Microphysical parameters evolution of the three cloud cells from the 1D-C and 1D-P data. From top to bottom: drop concentration from 1D-C (bin2 [35-45 µm] only in grey, drops > 45 µm in black), corresponding water content, drop concentration from 1D-P (all bins in black, drops > 800 µm only in grey), corresponding water content.

There is however a noticeable difference between cells A and B on the one hand, and cell C on the other hand. The virtual temperature in cells A and B decreases rapidly below the one of the environment and the cells collapse, while in cell C, it remains slightly greater or at least equal to the virtual temperature of the environment and cell C rises to much higher levels and produce a significant amount of precipitation. Cell C produces rain with a concentration of drops bigger than 200 µm in diameter that exceed 10 L^{-1} in less than 5 minutes. The onset of precipitation is reflected by a sharp increase of the number of samples with drops > 800 µm in diameter that contribute mainly to the observed increase of the precipitating water content. More surprising is the fact that before the concentration of precipitation drops increases, there is no noticeable increase of drops in the range 40-200 µm, the so called precipitation embryos.

These observations suggest that in these three cases, the rainfall production is driven by the competition between the coalescence process, that is effectively triggered when droplets are large enough, and the mixing that reduces the efficiency of the drop collection by removing the available water.

5. ACKNOWLEGMENTS

The authors acknowledge the contributions of the SCMS participants, and the support of Météo-France and CNRS/INSU/PATOM.

6. REFERENCE

Brenguier, J. L., T. Bourrianne, A. Coelho, J. Isbert, R. Peytavi, D. Trevarin, and P. Wechsler, 1998: Improvements of the droplet size distribution measurements with the Fast FSSP., *J. Atmos. Sci.*, **15**, 1077-1090.

Burnet F., and J. L. Brenguier, 2007: Observational Study of the Entrainment-Mixing Process in Warm Convective Clouds. *J. Atmos. Sci.*, **64**, 1995-2011

Burnet F., and J. L. Brenguier, 2002: Comparison between standard and modified Forward Scattering Spectrometer Probes during the Small Cumulus Microphysics Study., *J. Atmos. Oceanic Technol.*, **19**, 1516-1531.

Klett J. D., and D. H. Davis, 1973: Theoretical collision efficiencies of cloud droplets at small Reynolds number. *J. Atmos. Sci.*, **30**, 107-117

UNDERSTANDING ICE SUPERSATURATION, PARTICLE GROWTH, AND NUMBER CONCENTRATION IN CIRRUS CLOUDS

Jennifer M. Comstock[1], Ruei-Fong Lin[2], David O'C. Starr[3]

1 - Pacific Northwest National Laboratory, Richland, Washington, USA
2 - Goddard Earth Sciences and Technology Center, University of Maryland, Baltimore County, Baltimore, Maryland, USA
3 - Laboratory for Atmospheres, NASA Goddard Space Flight Center, Greenbelt, Maryland, USA

1. INTRODUCTION

Many factors control the ice supersaturation and microphysical properties in cirrus clouds. We explore the effects of dynamic forcing, ice nucleation mechanism, and ice crystal growth rate on the evolution and distribution of water vapor and cloud properties in cirrus clouds using a detailed microphysical model and remote sensing measurements obtained at the Department of Energy's Atmospheric Radiation Measurement (ARM; www.arm.gov) Climate Research Facility located at the Southern Great Plains (SGP) site near Lamont, OK, USA (36° 36.30'N, 97° 29.10'W).

2. MODEL DESCRIPTION

We use the one-dimensional (1D) time-dependent cirrus model with size resolved microphysics described in Lin et al. (2005). In this version of the model, the prognostic variables are the dry static energy, $s = C_p T + gz$, the water vapor mixing ratio, q_v, and the number concentration of aerosols and ice crystals per unit mass of air for each bin, N_k. The model is also coupled with large-scale forcing data derived using the constrained variational analysis approach (Zhang and Lin, 1997; Zhang et al. 2001). The model takes into account the horizontal advection of s and q_v, but neglects advection of condensate, as in a single column model.

Homogeneous nucleation of sulfuric acid droplets is simulated following Sassen and Dodd (1988) and Heymsfield and Miloshevich (1993). We also include the classical theory heterogeneous nucleation scheme for immersion freezing and deposition (Khvorostyanov and Curry 2000, 2004) to compare with empirical representations (e.g. Meyers et al. 1992). The diffusional growth of ice crystals follows the analytical expression including both kinetic and ventilation effects (e.g. Pruppacher and Klett 1997) and treats the direct radiative effect on the growth of ice crystals.

3. MEASUREMENTS

We compare model simulations with lidar and radar measurements from the ARM SGP site. The ARM Raman lidar (RL) transmits a laser pulse at 355 nm using a Nd:YAG laser and detects Raman shifted photons at 387 nm and 408 nm due to the rotational-vibrational Raman scattering off nitrogen and water vapor molecules, respectively (Goldsmith et al. 1998). The extinction at 355 nm and water vapor mixing ratio can be derived directly from these measurements. The ARM RL also measures the depolarization ratio at 355 nm, enabling the distinction between aerosols and cloud phase (ice/liquid) in the atmosphere. We use the ARM RL water vapor profile along with radiosonde temperature measurements to initialize the model simulations.

In addition to the RL extinction (α_e), we use radar reflectivity (Z_e) measurements from the 35 GHz millimeter cloud radar (MMCR) for model evaluation. Note that simulated α_e and Z_e are computed directly from the predicted ice crystal size distributions. The ice water content (IWC) and effective radius (r_{eff}; assuming hexagonal columns) are computed from measured α_e and Z_e using the radar-lidar retrieval algorithm of Wang and Sassen (2002), which are also compared with model results.

In addition to Z_e, the MMCR measures the Doppler velocity (V_D), from which we compute the mesoscale vertical velocity using a method similar to that of Orr and Kropfli (1999). To summarize, we use a conditional averaging approach where V_D is binned then averaged according to Z_e and altitude. If a particular altitude-Z_e bin has insufficient samples, we interpolate between bins with sufficient samples. Each altitude-Z_e bin should represent volumes that contain similar PSDs and thus similar fall speeds (V_f). This method assumes that if the samples of V_D in each altitude-Z_e bin are averaged, then the random turbulent motions are removed, and the mean V_D then represents the crystal fall speed for that population of ice crystals. We then compute the cloud mesoscale velocity (V_m) by subtracting V_f and the large-scale velocity (V_{LS}) from the observed V_D ($V_m = V_D - V_f - V_{LS}$). We then compute the mean "in-cloud" mesoscale velocity between cloud base and top and force the model with these values, which are updated every 5 sec in the simulations. The value of V_{LS}~2 cm s^{-1} for this case is derived from the variational analysis produced by the ARM program (Zhang and Lin 1997; Zhang et al. 2001).

4. SIMULATIONS USING LARGE-SCALE FORCING AND MESOSCALE WAVES

Table 1: Explanation of simulation parameters.

Run	Vertical Velocity Forcing	Nucleation Mechanism
LS-0	Large-Scale	HOM
LS-2	Large-Scale +2 cm s^{-1}	HOM
LS-4	Large-Scale +4 cm s^{-1}	HOM
MS-HOM	Meso-Scale	HOM
MS-KC	Meso-Scale	HET-KC + HOM
MS-M92	Meso-Scale	HET-M92+ HOM

We simulate a cirrus cloud observed at the ARM SGP site on 7 December 1999. The cloud top temperature is -53°C and the peak RHI is ~130% in the initial profile. The baseline large-scale vertical velocity is ~2 cm s^{-1}.

First, we compare time series of simulated bulk properties with observations to understand how well simulations capture

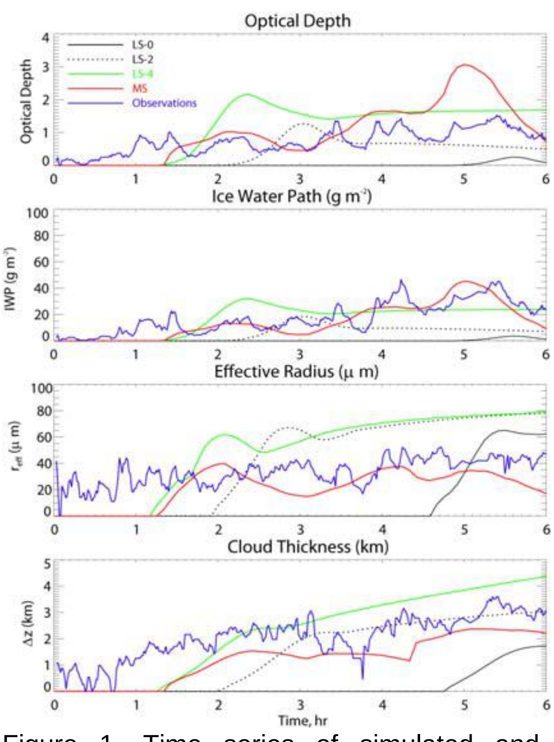

Figure 1. Time series of simulated and observed bulk cloud properties. These simulations depict variations due to velocity forcing.

the evolution of the cloud structure. Figure 1 compares large-scale and mesoscale forcing simulations (see Table 1 for an explanation of simulation specifics and nomenclature). The simulation using the baseline large-scale forcing (LS-0) grossly underestimates the bulk properties and delays cloud initiation until ~5 hr. Next, we uniformly increase the LS forcing by ~2 cm s^{-1} (LS-2) and then ~4 cm s^{-1} (LS-4). Although simulations are improved, the timing of cloud initiation is still delayed for both LS-2 and LS-4. The optical depth (τ), is somewhat underestimated (overestimated) for LS-2 (LS-4). IWP is generally underestimated for both LS-2 and LS-4, although LS-4 tends to overestimate IWP at the beginning of the simulation. r_{eff} is grossly overestimated for both LS-2 and LS-4, although cloud thickness (Δz) is somewhat reasonable. Forcing the simulation using the mean mesoscale air velocity (MS-HOM) derived from the radar Doppler velocity measurements appears to overall improve the simulation, although Δz is smaller than observed and τ is larger than observed at the end of the simulation. The timing of cloud initiation is still delayed until ~1.3 hr. Note that for MS-HOM the mean V_m is added to the background large-scale velocity, which is ~2 cm s^{-1}.

Next, we compare the Probability Density Function (PDF) of measured and modeled "in-cloud" relative humidity with respect to ice (RHI), r_{eff}, IWC, Z_e, and α_e to understand if the distribution of simulated quantities is similar to measurements. Although measurements of ice crystal number concentration (N_i) are not available for this case, we include N_i in the PDF plots to better understand what a reasonable order of magnitude is for this quantity. Our approach in evaluating the PDF figures are 1) a "good" simulation is one that captures both the location of the mode and the width of the distribution, and 2) if both Z_e and α_e are simulated well, then we infer that N_i is likely correct. The latter condition is rendered using the knowledge that radar

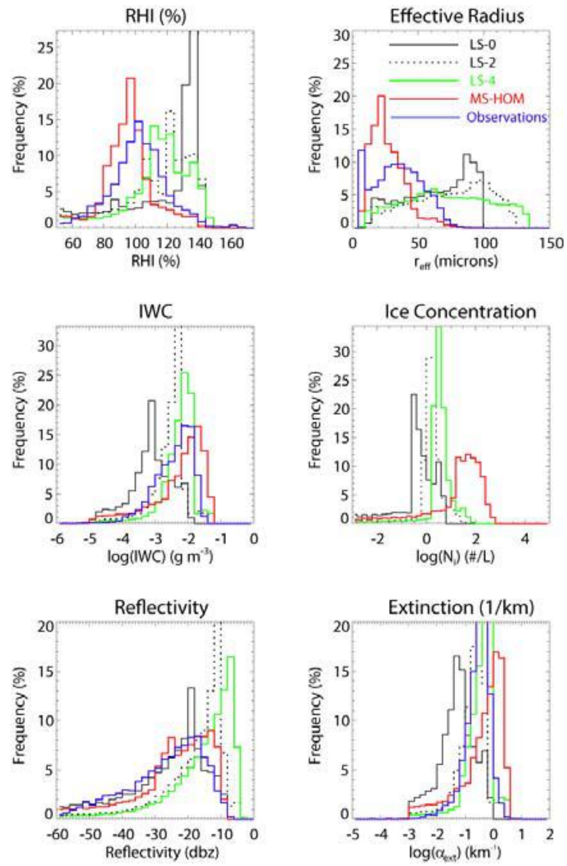

Figure 2. Frequency of occurrence (in %) of RHI, r_{eff}, IWC, N_i, Z_e, and α_e comparing model simulations depicted in Fig. 1 with observations. All data are screened to include only "in cloud" points over the duration of the simulation and simulated quantities are removed that are below the instrument sensitivity level.

wavelengths are sensitive to the large particle mode, whereas lidar wavelengths are sensitive to the small particle mode.

All runs using large-scale forcing (LS-0, LS-2, LS-4) have a higher frequency of large RHI and r_{eff} compared with observations (Fig. 2). This is caused by the small number of ice crystals nucleated, which grow quickly to large sizes. Since the particles are primarily large, the Z_e comparison is reasonable (although somewhat larger for LS-2 and LS-4). The distribution of α_e for LS-0 is much smaller than observed. As the large-scale vertical velocity increases (LS-2 and LS-4), the

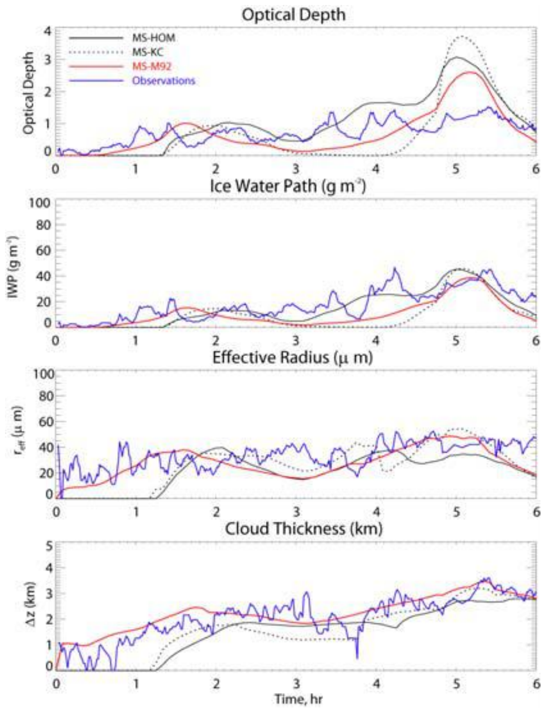

Figure 3. Same as in Fig. 1 but comparing the effects of nucleation mechanism.

number of ice crystals nucleated increases, and thus the total surface area available for uptake of water vapor increases. This causes the RHI to be drawn down (relative to LS-0). Note that for LS-2 and LS-4 the frequency of r_{eff}>50 μm is still much larger than observed, and thus the PDF of Z_e is skewed to large values. On the other hand, the mode value of α_e is much closer to observations, implying that the number concentration of small crystals is comparable; however, LS-2 and LS-4 underestimate the frequency of small r_{eff} compared with observations. The mesoscale forced simulation (MS-HOM) produces the largest N_i and largest frequency of small ice crystals, which shifts the mode α_e toward larger values than observed. This is somewhat inconsistent with the results in Fig. 1. It is possible that the observed τ is underestimated due to attenuation of the lidar beam, which could account for an overestimation of r_{eff}.

5.0 NUCLEATION MECHANISM

All simulations in Sec. 4 were performed assuming homogeneous nucleation. It was shown that using MS forcing greatly improves the evolution of the cloud development (Fig. 1); however there remains some issues in the PDF comparisons. Next we examine the effects of allowing heterogeneous as well as homogenous nucleation to occur in the MS simulations. Figure 3 depicts the evolution of the bulk properties (as in Fig. 1) assuming homogeneous nucleation only (MS-HOM), using the Khvorostyanov and Curry (2000; 2004) approach (MS-KC), and the Meyers et al. (1992) parameterization (MS-M92). Note that in the latter two simulations, homogeneous nucleation is allowed to occur if the critical supersaturation is reached. Only the MS-KC run achieves RHI large enough for this to occur. The RHI for MS-M92 remains below 140%, which is below the 145-150% required to form crystals homogeneously in this case.

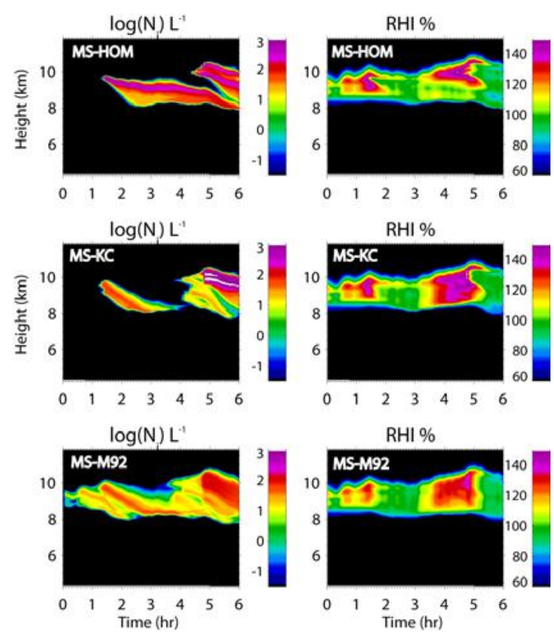

Figure 4. Time evolution of the vertical profile of log(N_i) (left panels in L^{-1}) and RHI (right panels in %). Simulations use mesoscale forcing and vary with nucleation mechanism (MS-HOM on top, MS-KC in the middle and MS-M92 on the bottom).

The MS-M92 run improves the timing of cloud formation and the magnitude of all bulk properties compares favorably with observations, with the exception of the 3-4 hr time period when τ and IWP decrease significantly, which is also seen in MS-KC (Fig.3). This is related to the fact that ~10 times fewer ice crystals are nucleated in MS-M92 and MS-KC as compared to MS-HOM during the initial pulse that begins at ~1 hr (see Fig. 4), and these crystals are generally larger and fall out quicker than in MS-HOM. It is also notable that τ is overestimated in all MS runs (Fig. 3) compared to observations. The lidar is somewhat attenuation limited for a short time period near 0500 UTC, which causes an underestimation of τ. Since large particles tend to dominate the IWP, we don't see a significant difference between model simulations and observations during that same time period.

We also compare the PDFs for these simulations (Fig. 5). Although the variation between PDFs in Fig. 5 is smaller than in Fig. 2, there are some differences worth noting. First, the MS-KC RHI has a secondary peak near 130% (Fig. 5). This occurs because nearly all the ice crystals generated during the first cloud pulse sublimate before the last cloud pulse initiates (MS-KC; Fig. 4). During this time period (~3.5-5 hr) the RHI increases substantially until the homogeneous nucleation threshold is reached (just before ~5 hr; MS-KC RHI in Fig. 4).

The second notable difference in the PDFs (Fig. 5) is that the MS-KC N_i has a secondary peak as well. This is caused by a strong pulse that occurs at ~5 hrs due to homogeneous nucleation. This pulse generates ~10 times more crystals in the MS-KC run than in the MS-HOM run at that same time step.

Finally, it is notable that in each of the MS-HOM simulations, the Z_e is simulated well, and the α_e is only slightly overestimated compared with observations

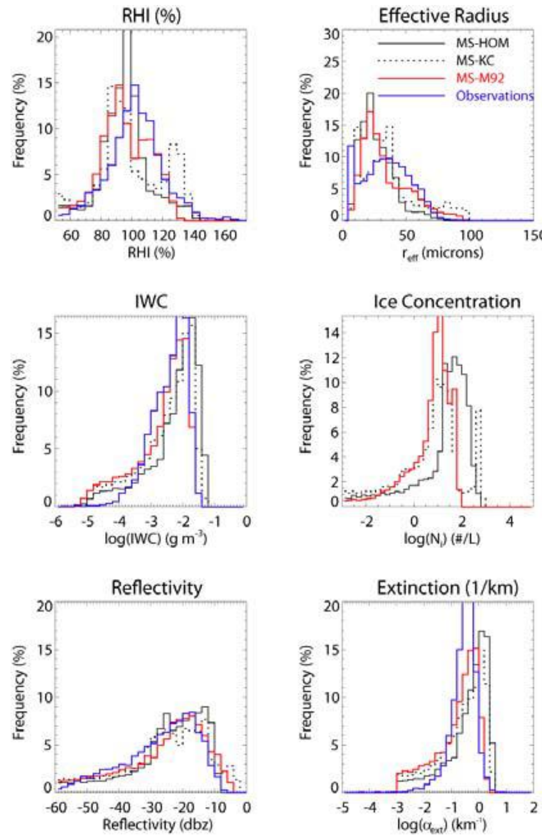

Figure 5. As in Fig. 2 but for simulations comparing the effects of nucleation mechanism.

(Fig. 5). This results implies that the N_i is reasonable and has peak values ranging between 10 and 100 L^{-1}, which is much less than the 10^4 L^{-1} reported in some aircraft measurements.

6.0 DISCUSSION

We have presented simulations analyzing the effects of dynamic forcing and nucleation mechanism on cirrus formation and evolution. All simulations performed and displayed here assume a deposition coefficient (α_D) of 1.0, which causes ice crystals to grow quickly. We have also performed a similar set of simulations assuming α_D=0.006, which effectively causes ice crystals to grow much more slowly, increasing the number concentration of small ice crystals by a factor of 10-100. Interestingly, we found that the sensitivity to the growth assumption (α_D=1 vs α_D=0.006) are affected by the characteristics of the vertical velocity forcing. When mesoscale forcing was used, the increase in N_i was dampened somewhat.

In summary, the simulations that are the most consistent with ground based observations of cirrus clouds are those that include the mesoscale variability. This result is consistent with previous results of Kärcher and Ström (2003) and Jensen et al. (2005). We also find that the Meyers et al. (1992) parameterization for deposition nucleation performs slightly better than other nucleation mechanisms for nearly all parameters. These results emphasize the need to better understand and parameterize nucleation and the effect of subgrid variability within global climate models. We have demonstrated the potential for using radar Doppler velocity measurements to improve cirrus simulations. We plan to further exploit the V_D measurements to characterize and parameterize cirrus variability on the scale of a GCM grid box.

7.0 BIBLIOGRAPHY

Goldsmith, J. E. M., F. H. Blair, S. E. Bisson and D. D. Turner, Turn-key Raman lidar for profiling atmospheric water vapor, clouds, and aerosols, *Appl. Opt., 37*, 4979-4990, 1998.

Heymsfield, A.J., and L.M. Miloshevich (1993), Homogeneous ice nucleation and supercooled liquid water in orographic wave clouds, *J. Atmos. Sci.*, *50*, 2335–2353.

Jensen and coauthors, 2005: Formation of tropopause cirrus layer observed over Florida during CRYSTAL-FACE. *J. Geophys. Res.*, 110, doi:10.1029/2004JD004671.

Kärcher, B. and J. Ström, The roles of dynamical variability and aerosols in cirrus cloud formation, *Atmos. Chem. Phy., 3*, 823-838, 2003.

Khvorostyanov, V. I., and J. A. Curry, 2000: A new theory of heterogeneous ice nucleation for application in cloud and climate models. *Geophys. Res. Lett., 27*, 4081-4084.

Khvorostyanov, V. I., and J. A. Curry, 2004: The theory of ice nucleation by heterogeneous freezing of deliquescent mixed CCN. Part I: Critical radius, energy, and nucleation rate. *J. Atmos. Sci., 61*, 2676-2691.

Lin, R. F., D. O. Starr, J. Reichardt and P. J. Demott, Nucleation in synoptically forced cirrostratus, *J. Geophys.Res., 110*, 2005.

Meyers, M. P., P. J. DeMott, and W. R. Cotton, 1992: New primary ice-nucleation parameterizations in an explicit cloud model. J. Appl. Meteor., 31, 708-721.

Orr, B. W. and R. A. Kropfli, A method for estimating particle fall velocities from vertically pointing Doppler radar, *J. Atmos. Ocean. Tech., 16*, 29-37, 1999.

Pruppacher, H. R., and J. D. Klett (1997), *Microphysics of Clouds and Precipitation*, 2nd ed., 954 pp., Springer, New York.

Sassen, K. and G. C. Dodd, Homogeneous Nucleation Rate for Highly Supercooled Cirrus Cloud Droplets, *J. Atmos. Sci., 45*, 1357-1369, 1988.

Wang, Z. and K. Sassen, Cirrus cloud microphysical property retrieval using lidar and radar measurements. Part I: Algorithm description and comparison with in situ data, *J. Appl. Meteor., 41*, 218-229, 2002.

Zhang, M. H. and J. L. Lin, Constrained variational analysis of sounding data based on column-integrated budgets of mass, heat, moisture, and momentum: Approach and application to ARM measurements, *J. Atmos. Sci. 54*, 1503-1524, 1997.

Zhang, M. H., J. L. Lin, R. T. Cederwall, J. J. Yio and S. C. Xie, Objective analysis of ARM IOP data: Method and sensitivity, *Mon. Wea. Rev., 129*, 295-311, 2001.

ENHANCEMENT OF COALESCENCE DUE TO DROPLET INERTIA IN TURBULENT CLOUDS

Steven K. Krueger,[1*] Jaekyoon Oh,[1] and Alan R. Kerstein[2]
[1]University of Utah, Salt Lake City, Utah, USA
[2] Sandia National Laboratories, Livermore, California, USA

1. INTRODUCTION

The EMPM (Explicit Mixing Parcel Model) predicts the evolving in-cloud variability of temperature and water vapor mixing ratio due to entrainment and finite-rate turbulent mixing using a 1D representation of a rising cloudy parcel (Krueger et al. 1997). The 1D formulation allows the model to resolve fine-scale variability down to the smallest turbulent scales (about 1 mm). The EMPM calculates the growth of thousands of individual cloud droplets based on each droplet's local environment (Su et al. 1998).

In the EMPM, turbulent advection of fluid is implemented by rearranging the fluid cells. Each permutation represents an individual turbulent eddy, and is called a "triplet map." (See Kerstein, 1991 for an illustration and motivational discussion). The triplet map takes a fluid segment $[x_0, x_0 + l]$, shrinks it to a third of its original length, and then places three copies ("images") on the original domain. The middle copy is reversed, which maintains the continuity of advected fields and introduces the rotational folding effect of turbulent eddy motion. Property fields outside the size l segment are unaffected.

This implementation of the triplet map captures flow processes as small as the smallest turbulent eddy (Kolmogorov microscale, η), but the response of small droplets to turbulence has important features at scales as small as the droplet radius. Namely, droplet motion relative to the fluid at scales less than the Kolmogorov microscale induces droplet clustering that is estimated to increase droplet collision rates significantly. We have developed (Kerstein and Krueger 2006), implemented, and tested a 3D triplet map for droplets that captures this clustering effect. We have also implemented a collision detection algorithm so that we can simulate collisions and coalescence between finite-inertia particles. Once the 3D droplet triplet map, along with stochastic collision and coalescence, are implemented in the EMPM, we will be able to investigate the relative roles that entrainment and mixing, droplet inertial effects, and ultragiant nuclei play in warm rain initiation in cumulus clouds.

*Corresponding author address: Department of Meteorology, University of Utah, Salt Lake City, UT 84112. E-mail: steve.krueger@utah.edu

3. 3D TRIPLET MAP FOR DROPLETS

In contrast to the original EMPM, each droplet now has a 3D spatial location that evolves with time. Droplet displacements due to turbulence are based on the triplet map applied at that instant to the fluid cells, but with the following modification. Droplets are displaced by amounts $(1+S)D$, where D is the displacement in x, y, or z due to the (continuum) fluid triplet map, and the additional displacement SD represents droplet slip (motion relative to the the fluid). Here S is analogous to the droplet Stokes number St. The triplet map is applied to only one coordinate direction (x, y, or z) at a time. The coordinate is randomly selected for each map.

Each droplet contained within a triplet map is randomly assigned, with equal probability and independently of the assignments of the other droplets, to one of three images. (See Appendix A for details.) With this assumption, both the dispersive (extensional) and the compressive eects of eddy strain are repre- sented. Displacements to a given image are compressive in nature, i.e., they reduce droplet pair separations, while displacements to dierent images are the model representation of dispersion. The analysis of map-induced cluster- ing of finite-inertia droplets in Kerstein and Krueger (2006) indicates that this representation has quantitative as well as qualitative validity.

Despite the simplicity, and consequent computational efficiency, of this representation of droplet slip compared to the low-St droplet momentum equation, it captures a key feature of droplet motions. To define this feature, consider two droplet size categories, 1 and 2. Analysis and simulations have demonstrated that the probability $p(r)$ of finding a type-2 droplet at a location a distance $r \ll \eta$ from a given type-1 droplet obeys $p(r) \sim r^{-c\mathrm{St}_1\mathrm{St}_2}$, where c is an empirical coefficient and $\mathrm{St}_j \ll 1$ are droplet Stokes numbers for $j = 1$ and 2. The droplet Stokes number is defined as the droplet response time times the mean velocity gradient. This increasing probability with decreasing r is the signature of droplet clustering.

Kerstein and Krueger (2006) proved mathematically that the stated model obeys $p(r) \sim r^{-c' S_1 S_2}$ to leading order in $S_j \ll 1$, where S_j denotes assigned values of S for a given droplet pair, $j = 1$ and 2, and the constant c' is determined from the analysis. This implies a proportionality between S_j and St_j that recovers the known result, expressed in terms of St_j. This result is an advance in the theoretical understanding of droplet clustering as well as a demonstration of the practical utility of the model.

To use the 3D triplet map to calculate the effects of turbulence on droplet motions, we must first relate the triplet map parameters S, l (map size), and λ_p (map frequency at a point), to the physical parameters of the droplets and turbulence. Because the largest turbulent strain rates occur at the smallest turbulence scales, it is justified to consider just a single map size l that corresponds to the smallest turbulent eddy size.

Specifically, we must relate: (1) the ratio of droplet displacement to fluid displacement (S) for each map to the particle Stokes number (St), (2) the triplet map's size l to the Kolmogorov length scale, and (3) the interval between maps, $1/\lambda_p$, to the Kolmogorov time scale.

The first two relationships were determined by comparing the radial distribution function for inertial bidisperse particles produced by our model to the DNS (direct numerical simulation) results of Chun et al. (2005). We determined that $S \approx$ 0.5 St, where

$$\mathrm{St} = t_d \gamma$$

is the droplet Stokes number,

$$t_d = \frac{m_p}{6\pi r \mu} = \frac{2\rho_p r^2}{9\mu}$$

is the droplet response time, m_p is the droplet mass, ρ_p the droplet density, r the droplet radius, and μ the dynamic viscosity, and

$$\gamma = (\epsilon/\nu)^{1/2} = 1/\tau_K$$

is a global measure of strain, ϵ is the dissipation rate of turbulence kinetic energy, ν is the kinematic viscosity, and τ_K is the Kolmogorov time scale. We also determined that $l \approx 20\ \eta$, where

$$\eta = (\nu^3/\epsilon)^{1/4}.$$

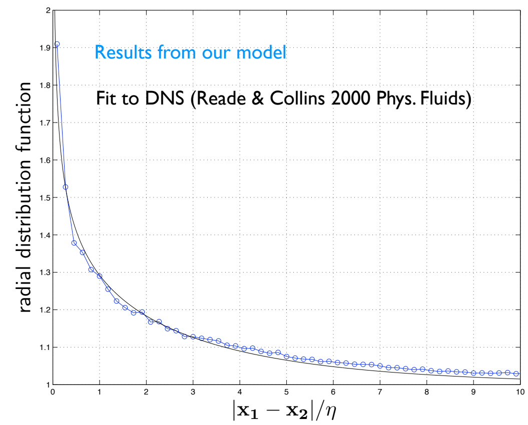

Figure 1: Average 3D radial distribution function (blue) from LEM for S =0.08. Reade-Collins fit to DNS results (black) for St=0.136, η/l =0.055. The abscissa is the particle separation normalized by the Kolmogorov microscale.

After establishing these two relationships based on the results of Chun et al. (2005), we made an independent comparison to DNS results obtained by Reade and Collins (2000). Figure 1 illustrates the excellent agreement between our results using the 3D triplet map and DNS results obtained by Reade and Collins (2000).

The third relationship was determined by comparing the number of collisions per triplet map to the collision rate for zero-inertia monodisperse particles in turbulence (Saffman and Turner 1956; Wang, Wexler, and Zhou 1998), as explained in Appendix B. We obtain

$$\lambda_p = 0.464\gamma.$$

Therefore the average interval between triplet maps events at a point is $\Delta t = 1/\lambda_p = 2.16\tau_K$.

In order to perform a simulation of 3D droplet motions due to turbulence using the droplet triplet map, we also need the 3D domain dimensions (X, Y, and Z) and droplet size distribution (radius and number for a monodispersion). The complete procedure for specifying the required parameters involves the following steps.

1. Calculate Kolmogorov scales (η and τ_K) from ϵ and ν.
2. Calculate t_d from r and μ.
3. Calculate St from t_d and $\gamma = 1/\tau_K$.
4. Obtain S, l, and λ_p from the parameters above using the derived relationships.
5. Specify X, Y, and Z to be integer multiples of l.
6. Specify droplet concentration.
7. Specify initial droplet locations.

The initial droplet locations are immaterial because the turbulence rapidly disperses the droplets.

3. DROPLET SEDIMENTATION, COLLISIONS, AND COALESCENCE

Sedimentation due to gravity is included by moving each droplet at its terminal velocity in the direction of gravity during the time intervals between triplet maps. Collisions between droplets are detected after each triplet map by finding newly overlapped pairs, and during sedimentation by calculating collision times based on the droplet locations and terminal velocities after each triplet map. Overlap and collision detection use an efficient cell indexing method and linked lists (Allen and Tildesley 1987).

Coalescence may occur when two droplets collide. The probablilty of coalescence (the collision efficiency) is assumed to be the same as that used in the Hall kernel (Hall 1980).

For sedimenting droplets with St < 1, there is fairly good agreement with the DNS results (collision kernels and radial distribution functions) obtained by Franklin et al. (2005, 2007) and by Ayala (2005).

ACKNOWLEDGMENTS. This material is based upon work supported by the National Science Foundation under Grant No. ATM-0346854, and by the Division of Chemical Sciences, Geosciences, and Biosciences, Office of Basic Energy Sciences, United States Department of Energy. Sandia National Laboratories is a multi-program laboratory operated by Sandia Corporation, a Lockheed Martin Company, for the United States Department of Energy under contract DE-AC04-94-AL85000.

APPENDIX A

DROPLET TRIPLET MAP

Kerstein and Krueger (2006) idealized particle motion due to turbulence as a sequence of instantaneous displacements based on representations of fluid displacements and particle response. In 1D, the kth fluid displacement is defined as a transformation $x \rightarrow x'(x) = x + d_k(x)$ of the spatial coordinate x. To represent incompressible flow, this transformation must be measure preserving, i.e. $\int_{\sigma'} dx' = \int_{\sigma} dx$ for any subset σ of x, where σ' is the image of the subset σ after displacement k. The displacement rule adopted,

$$d_k(x) = \begin{cases} \frac{2}{3}(x_k - x) & \text{if } x_k \leq x'(x) \leq x_k + \frac{1}{3}l, \\ \frac{2}{3}(2x_k - 2x + l) & \text{if } x_k + \frac{l}{3}l \leq x'(x) \leq x_k + \frac{2}{3}l, \\ \frac{2}{3}(x_k - x + l) & \text{if } x_k + \frac{2}{3}l \leq x'(x) \leq x_k + l, \\ 0 & \text{otherwise,} \end{cases} \tag{1}$$

obeys this property. In (1), x_k is a random variable that is uniformly sampled within a 1D domain. The parameter l is a random variable sampled for given k from a specified probability density function (PDF) $f(l)$. The "triplet map" d_k is a triple-valued function of x in $[x_k, x_k + l]$. Namely, the first three lines of (1) define "images" $j = 1$, 2, and 3 of $[x_k, x_k + l]$, but the pre-image x of fluid displaced to location x' is unique. (In this context, σ' in the incompressibility condition is the union of the images of σ.) Therefore the inverse $x(x')$ is uniquely defined. It obeys the continuity relation $|x(x'_1)-x(x'_2)| \leq 3|x'_1-x'_2|$. (Here, subscripts denote particular values of x' rather than particular displacements.) This assures that the displacement operation does not introduce spatial discontinuities into a continuous function. In addition to their formal connection to multi-dimensional fluid motion, measure preservation and continuity as defined here have direct bearing on the particle-clustering properties of present interest.

APPENDIX B

ZERO-INERTIA PHENOMENA: SHEAR-INDUCED COLLISIONS

Collisions between zero-inertia droplets are considered under the assumption that the droplets pass through each other without affecting their trajectories, i.e. they are 'ghosts.' In this case, collisions do not introduce correlations among droplet locations, so droplet locations are independent of each other. It is also assumed that droplets are uniformly distributed in 3D space.

Under model assumptions, zero-inertia droplets are displaced by triplet maps but are otherwise immobile. A collision is deemed to occur when a triplet map causes two droplets to overlap spatially, i.e., their centers are separated by a distance less than twice the droplet radius r, here assumed to be the same for all droplets. If they overlapped by this definition prior to the triplet map, then this is not deemed to be a collision event.

The ODT analog of the Saffman-Turner analysis of collisions between zero-inertia droplets is considered. Because mappings of zero-inertia droplets do not induce clustering or other deviations from spatial independence, it suffices to consider the probability that a given droplet displaced by a triplet map is brought into contact (i.e., overlap configuration) with some other droplet, conditioned on non-overlap of the pair prior to the triplet map.

A displaced droplet may be brought into contact with another droplet mapped to the same image, a droplet mapped to a different image, or a droplet outside the triplet map. The latter two scenarios require the final droplet location to be less than a distance $2a$ from an endpoint of the image into which it is mapped. The fraction of mapped droplets that obey this condition is of order r/l_0, where l_0 is the size of the smallest allowed triplet map. The physical regime of interest is the limit in which this ratio approaches zero, so only the first scenario need be considered.

In the present context, a triplet map is applied to a rectangular volume of space. Consider a map oriented in the z-direction, although orientation is immaterial to the present analysis. Droplets in contact with a given droplet after a triplet map are those whose centers are within a distance $2r$ of center of the given droplet. Prior to the triplet map, the centers of those droplets were contained in an ellipse whose z axis is of length $6a$ and whose x and y axis lengths are $2r$. The volume of this ellipse is $32\pi r^3$, which is three times the volume of a sphere of radius $2r$.

Let $\bar{n}$ be the droplet mean number density. Then the mean number of droplets in the specified ellipse with the given droplet at its center is $32\pi r^3 \bar{n}$. However, the droplets initially (pre-map) in contact with the given droplet do not contribute to collision events, so the volume containing droplets that collide with the given droplet is $\frac{64\pi}{3} r^3$. Because only $\frac{1}{3}$ of these droplets are mapped to the same image as the given droplet, the number density of the colliding droplets is $\bar{n}/3$. Therefore, the mean number of droplets colliding with the given droplet is $\frac{64\pi}{9} r^3 \bar{n}$.

To obtain the number of collisions per unit volume within a triplet map, this quantity is multiplied by the number of test droplets per unit volume, $\bar{n}$, divided by 2 because each droplet has now been counted as both a test droplet and a collision partner, giving $\frac{32\pi}{9} r^3 \bar{n}^2$. To obtain the number of collisions per unit volume per unit time, denoted $\dot{N}_c$, this is multiplied by the frequency λ_p that a given point is contained within a triplet map to obtain

$$\dot{N}_c = \frac{32\pi}{9} \lambda_p a^3 \bar{n}^2. \tag{2}$$

Comparison to the Saffman-Turner (1956) result for a monodispersion,

$$\dot{N}_c = \left(\frac{8\pi}{15}\right)^{1/2} \gamma (2r)^3 \frac{\bar{n}^2}{2}, \tag{3}$$

where

$$\gamma \equiv (\epsilon/\nu)^{1/2} \tag{4}$$

is a global measure of strain, implies the relationship

$$\lambda_p = \frac{3}{2}\left(\frac{3}{10\pi}\right)^{1/2} \gamma = 0.464\gamma. \tag{5}$$

This establishes a direct relationship between the total rate λ_p of eddy events of all types (summed over all three orientations) affecting a given point and a global turbulence property.

REFERENCES

Allen, M. P., and D. J. Tildesley, 1987: *Computer Simulation of Liquids.* Oxford University Press, 385 pp.

Ayala, O., 2005: Effects of Turbulence on the Collision Rate of Cloud Droplets. Ph.D. dissertation, University of Delaware, 207 pp.

Chun, J., D. L. Koch, S. L. Rani, A. Ahluwalia, and L. R. Collins, 2005: Clustering of aerosol particles in isotropic turbulence. *J. Fluid Mech.,* **536,** 219–251.

Franklin C. N., P. A. Vaillancourt, M. K. Yau, and P. Bartello, 2005: Collision rates of cloud droplets in turbulent flow. *J. Atmos. Sci.,* **62,** 2451–2466.

Franklin C. N., P. A. Vaillancourt, and P. Bartello, 2007: Statistics and parameterizations of the effect of turbulence on the geometric collision kernel of cloud droplets. *J. Atmos. Sci.,* **64,** 938-954.

Hall, W. D., 1980: A detailed microphysical model within a twodimensional dynamic framework: Model description and preliminary results. *J. Atmos. Sci.,* **37,** 2486–2507.

Kerstein, A. R., 1991: Linear-eddy modeling of turbulent transport. Part 6. Microstructure of diffusive scalar mixing fields. *J. Fluid Mech.,* **231,** 361–394. *J. Fluid Mech.,* **447,** 85–109.

Kerstein, A. R., and S. K. Krueger, 2006: Clustering of randomly advected low-inertia particles: A solvable model. *Phys. Rev. E,* **73,** 025302.

Krueger, S. K., C.-W. Su, and P. A. McMurtry, 1997: Modeling entrainment and fine-scale mixing in cumulus clouds. *J. Atmos. Sci.,* **54,** 2697–2712.

Reade, W. G., and L. R. Collins, 2000: Effect of preferential concentration on turbulent collision rates. *Phys. Fluids,* **12**, 2530–2540.

Saffman, P. G., and J. S. Turner, 1956: On the collision of drops in turbulent clouds. *J. Fluid Mech.,* **1,** 16–30.

Su, C.-W., S. K. Krueger, P. A. McMurtry, and P. H. Austin, 1998: Linear eddy modeling of droplet spectral evolution during entrainment and mixing in cumulus clouds. *Atmos. Res.,* **47–48,** 41–58.

Wang, L.-P., A. S. Wexler, and Y. Zhou, 1998: On the collision rate of small particles in isotropic turbulence. Part I: Zero-inertia case. *Phys. Fluids,* **10,** 266–276.

ENHANCEMENT OF COALESCENCE DUE TO DROPLET INERTIA IN TURBULENT CLOUDS

Steven K. Krueger,[1*] Jaekyoon Oh,[1] and Alan R. Kerstein[2]
[1]University of Utah, Salt Lake City, Utah, USA
[2] Sandia National Laboratories, Livermore, California, USA

1. INTRODUCTION

The EMPM (Explicit Mixing Parcel Model) predicts the evolving in-cloud variability of temperature and water vapor mixing ratio due to entrainment and finite-rate turbulent mixing using a 1D representation of a rising cloudy parcel (Krueger et al. 1997). The 1D formulation allows the model to resolve fine-scale variability down to the smallest turbulent scales (about 1 mm). The EMPM calculates the growth of thousands of individual cloud droplets based on each droplet's local environment (Su et al. 1998).

In the EMPM, turbulent advection of fluid is implemented by rearranging the fluid cells. Each permutation represents an individual turbulent eddy, and is called a "triplet map." This implementation of the triplet map captures flow processes as small as the smallest turbulent eddy (Kolmogorov microscale), but the response of small droplets to turbulence has important features at scales as small as the droplet radius. Namely, droplet motion relative to the fluid at scales less than the Kolmogorov microscale induces droplet clustering that is estimated to increase droplet collision rates significantly. We have developed (Kerstein and Krueger 2006), implemented, and tested a 3D triplet map for droplets that captures this clustering effect. We have also implemented a collision detection algorithm so that we can simulate collisions and coalescence between finite-inertia particles. Once the 3D droplet triplet map, along with stochastic collision and coalescence, are implemented in the EMPM, we will be able to investigate the relative roles that entrainment and mixing, droplet inertial effects, and ultragiant nuclei play in warm rain initiation in cumulus clouds.

[*] *Corresponding author address:* Department of Meteorology, University of Utah, Salt Lake City, UT 84112. E-mail: steve.krueger@utah.edu

2. 3D TRIPLET MAP FOR DROPLETS

In contrast to the original EMPM, each droplet now has a 3D spatial location that evolves with time. Droplet displacements are based on the triplet map applied at that instant to the fluid cells, but with the following modification. Droplets are displaced by amounts $(1 + S)D$, where D is the displacement in x, y, or z due to the (continuum) fluid triplet map, and the additional displacement SD represents droplet slip (motion relative to the the fluid). Here S is analogous to the droplet Stokes number St. The triplet map is applied to only one coordinate direction (x, y, or z) at time. The coordinate is randomly selected for each map.

Despite the simplicity, and consequent computational efficiency, of this representation of droplet slip compared to the low-St droplet momentum equation, it captures a key feature of droplet motions. To define this feature, consider two droplet size categories, 1 and 2. Analysis and simulations have demonstrated that the probability $p(r)$ of finding a type-2 droplet at a location a distance $r \ll \eta$ from a given type-1 droplet obeys $p(r) \sim r^{-c\mathrm{St}_1\mathrm{St}_2}$, where c is an empirical coefficient and $\mathrm{St}_j \ll 1$ are droplet Stokes numbers for $j = 1$ and 2. The droplet Stokes number is defined as the droplet response time times the mean velocity gradient. This increasing probability with decreasing r is the signature of droplet clustering.

Kerstein and Krueger (2006) proved mathematically that the stated model obeys $p(r) \sim r^{-c' S_1 S_2}$ to leading order in $S_j \ll 1$, where S_j denotes assigned values of S for a given droplet pair, $j = 1$ and 2, and the constant c' is determined from the analysis. This implies a proportionality between S_j and St_j that recovers the known result, expressed in terms of St_j. This result is an advance in the theoretical understanding of droplet clustering as well as a demonstration of the practical

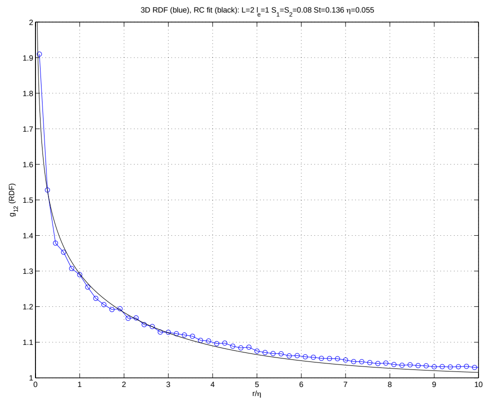

Figure 1: Average 3D RDF (blue) from LEM for $S_1 = S_2 =$0.08. Reade-Collins fit to DNS results (black) for St=0.136, $\eta/L =$0.055.

utility of the model.

Figure 1 illustrates the excellent agreement between our results using the 3D triplet map and DNS (direct numerical simulation) results obtained by Reade and Collins (2000). There is also good agreement with the DNS results obtained by Franklin et al. (2005, 2007) who included droplet sedimentation due to gravity.

ACKNOWLEDGMENTS. This material is based upon work supported by the National Science Foundation under Grant No. ATM-0346854.

REFERENCES

Franklin C. N., P. A. Vaillancourt, M. K. Yau, and P. Bartello, 2005: Collision rates of cloud droplets in turbulent flow. *J. Atmos. Sci.,* **62,** 2451–2466.

Franklin C. N., P. A. Vaillancourt, and P. Bartello, 2007: Statistics and parameterizations of the effect of turbulence on the geometric collision kernel of cloud droplets. *J. Atmos. Sci.,* **64,** 938-954.

Kerstein, A. R., and S. K. Krueger, 2006: Clustering of randomly advected low-inertia particles: A solvable model. *Phys. Rev. E,* **73,** 025302.

Krueger, S. K., C.-W. Su, and P. A. McMurtry, 1997: Modeling entrainment and fine-scale mixing in cumulus clouds. *J. Atmos. Sci.,* **54,** 2697–2712.

Reade, W. G., and L. R. Collins, 2000: Effect of preferential concentration on turbulent collision rates. *Phys. Fluids,* **12**, 2530–2540.

Su, C.-W., S. K. Krueger, P. A. McMurtry, and P. H. Austin, 1998: Linear eddy modeling of droplet spectral evolution during entrainment and mixing in cumulus clouds. *Atmos. Res.,* **47–48,** 41–58.

TURBULENT MIXING OF CLOUD WITH THE ENVIRONMENT: TWO-PHASE EVAPORATING FLOW AS SEEN BY PARTICLE IMAGING VELOCIMETRY

Szymon P. Malinowski[1] Piotr Korczyk[2], Tomasz A. Kowalewski[2]
[1]Institute of Geophysics, University of Warsaw, Poland
[2]Institute of Fundamental Technological Research, Polish Academy of Sciences, Warsaw, Poland.

1. INTRODUCTION

We present new experimental results that demonstrate influence of evaporative cooling and buoyancy fluctuations on the anisotropy of small-scale turbulence in clouds (c.f. (Andrejczuk et al., 2004), (Andrejczuk et al., 2006), (Korczyk et al., 2006), (Malinowski et al., 2008)). In these papers results of the numerical and laboratory experiments with small-scale turbulent mixing of cloud with unsaturated environmental air are discussed. The key findings indicate importance of small-scale fluctuations of buoyancy. These fluctuations are caused by evaporation of droplets mixing and from droplet sedimentation. Effecting buoyancy forces influence small-scale turbulence in clouds, making it anisotropic and more vigorous than expected.

The set-up of the experiments described here is designed to mimic basic aspects of small-scale turbulent mixing of a cloudy air with unsaturated environment. Thermodynamic conditions reconstructed in the chamber are, however, slightly different from those typical for clouds due to requirements of the visualization technique. Nevertheless, we believe that documented small-scale anisotropy of turbulent motions calls for the experiment investigating its role in natural conditions.

2. EXPERIMENTAL SETUP

The experimental setup is based on experiences gathered in earlier attempts (Malinowski et al., 1998), (Jaczewski and Malinowski 2005), (Korczyk et al., 2006). In the laboratory mixing takes place inside a cloud chamber of dimensions of 1.0 m ×1.0 m×1.8 m, (Figs 1 and 2 , for the detailed description consult (Korczyk et al., 2006) and (Korczyk 2008)).

Saturated and negatively buoyant cloudy plume (containing droplets of ~10 µm diameter) enters the chamber through the round opening in the ceiling. The initial velocity of the plume is about 20cm/s at the inlet, and it increases to about 30 cm/s in the middle of the chamber in response to the buoyancy forces. LWC in the plume is typically more than 10 g/kg --- somewhat higher than in natural clouds. The plume's temperature is about 25°C, close to the temperature of the unsaturated chamber air. Relative humidity of the clear air inside the chamber varies from 20% to 65% for different experiments. The plume descends through the chamber while mixing with the environment, creating complicated continuously evolving structures (eddies, filaments, etc.).

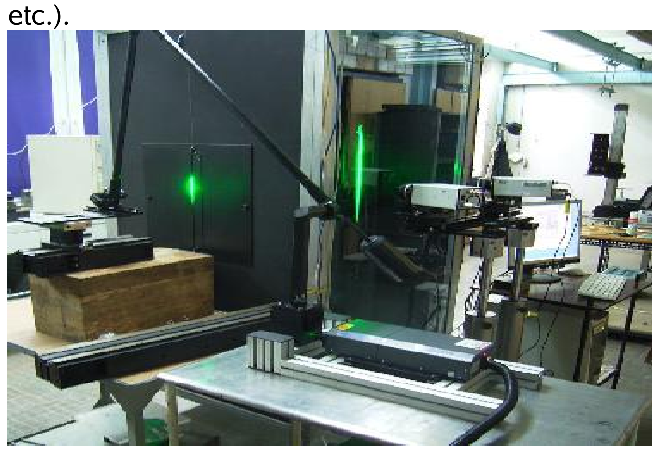

Fig.1 Cloud chamber with the laser producing planar sheet of light and CCD cameras.

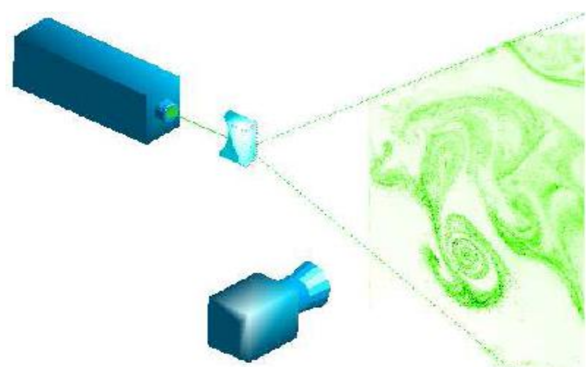

Fig.2. The principle of the visualization technique. A pulsed laser with the suitable optical system produces planar sheet of light. Light scattered by cloud droplets is imaged with the CCD camera.

Droplet spectra at the inlet to the cloud chamber have been measured by a microscopic technique: droplets were collected on a glass plate covered with the silicone oil and imaged with the microscope. The data were processed with the algorithm allowing for determination of droplet diameters. Results, presented in Fig. 3 indicate that initial droplet spectrum is not atypical for natural clouds.

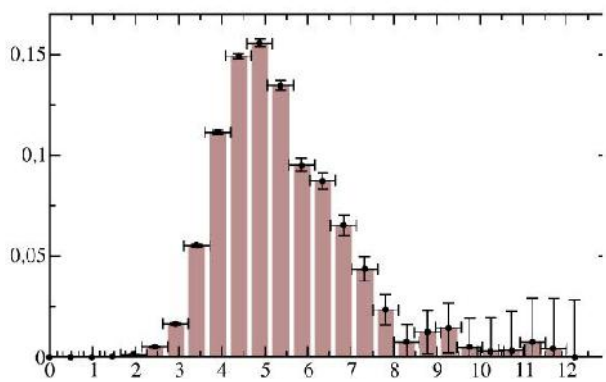

Fig.3 Initial droplet spectrum. Vertical axis: relative mass, horizontal axis – droplet radius [μm]

Illuminating the chamber interior with 1.2 mm thick sheet of laser light enables imaging in a planar cross section through the scene with a high-resolution CCD camera. An example image from the experiment, covering an area of 9×6 cm^2, is presented in Fig 4.

Fig 4: The negative of the image from the experimental chamber showing small-scale structures created in a process of cloud-clear air mixing. Imaged area corresponds to 9×6 cm^2 in physical space.

The image reveals fine structures created in the process of turbulent mixing of the cloud with its unsaturated environment. One pixel corresponds to 1.2 mm deep volume with about 69×69 μm^2 area in the plane of the laser-light sheet. Such elementary volumes occupied by droplets are represented by dark pixels; bright pixels correspond to volumes void of droplets.

Pattern recognition in two consecutive images separated by a known time interval allows to retrieve two velocity components in the image plane. This technique, referred to as Particle Image Velocimetry (PIV) (Raffel 1998), is widely adopted in experimental fluid mechanics. An original, accurate multi-scale PIV algorithm was developed for this experiment (Korczyk et al., 2006), (Korczyk 2008). First, it identifies motions of large structures, and then analyzes the displacements within the structures. Application of the algorithm allows estimating the two components of velocity vector with spatial resolution of about 0.07 mm; i.e., an order of magnitude smaller than the Kolmogorov length scale, the value of which was estimated from the measurements at approximately 0.76 mm. Fig. 5 shows an example pattern of droplets superimposed on the retrieved velocity vectors.

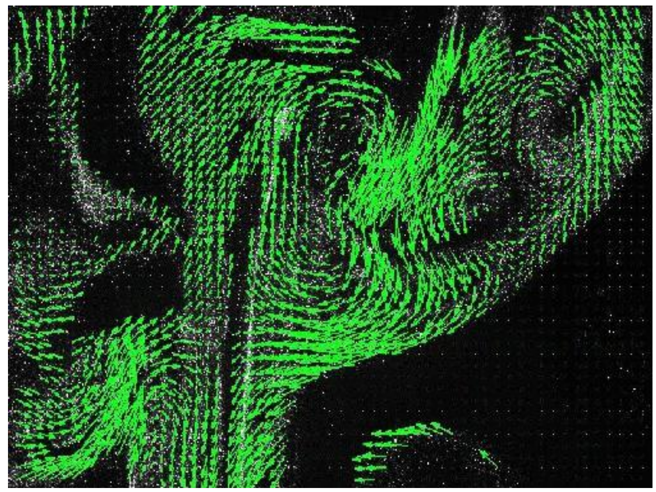

Fig. 5. Two components of velocity field retrieved by means of PIV technique.

3. RESULTS

The data were collected in a series consisting of 50 experiments, each subject to slightly different thermodynamic conditions inside the chamber. For each experiment, at least 100 pairs of frames (tens of thousands of velocity vectors in each frame) were analyzed, in order to retrieve statistical properties of velocity fluctuations.

3.1. Anisotropy of turbulent velocity fluctuations

Experimental probability distribution functions (PDF) of the velocity fluctuations in horizontal (u') and vertical (w') directions are summarized in Table 1. It follows, that PDF of w' is wider than the PDF of u'. The derived kurtosis and skewness indicate that both distributions are close to Gaussian. The ratio of velocity variances $\langle u'^2\rangle/\langle w'^2\rangle=0.46\pm0.07$ (a mean over all 50 experiments) is consistent with the numerical simulations, discussed in (Malinowski et al., 2008). Mean Taylor microscales, estimated independently for horizontal (λ_1) and vertical (λ_3) velocity components, are 7.5±0.4 mm and 9.2±0.6 mm, respectively. These values, obtained from measurements resolving smallest scales of the flow, also indicate anisotropy in agreement with results of numerical simulations ((Malinowski et al., 2008) and references therein).

***Table 1**. Distribution of horizontal (u') and vertical (w') turbulent velocity fluctuations. Average from 50 experiments.*

	Standard deviation [cm/s]	Skewness	Kurtosis
u'	5.4	-0.01	3.2
w'	8.0	-0.2	3.1

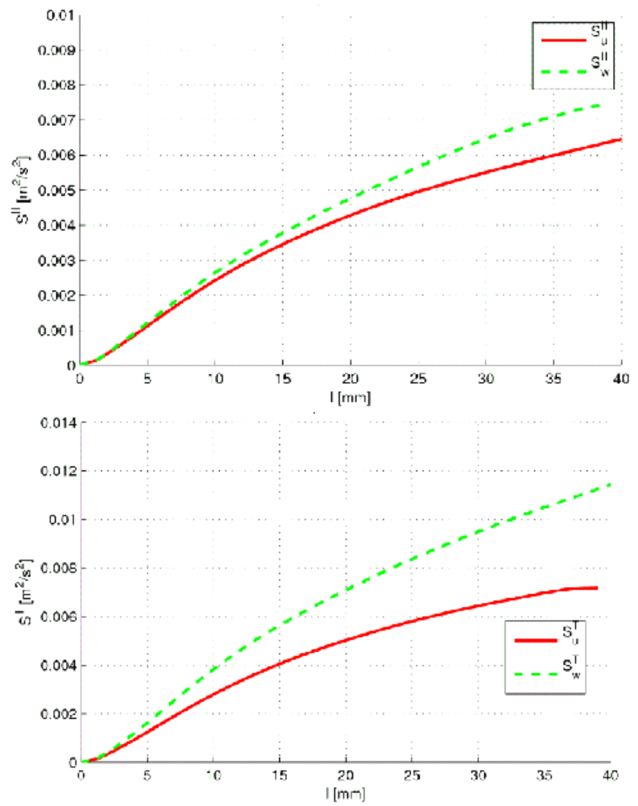

Fig.6 Longitudinal (upper panel) and transversal (lower panel) 2nd order structure functions of horizontal (red) and vertical (green, dashed) turbulent velocity fluctuations evaluated from PIV measurements 70 cm from the inlet to the cloud chamber.

More on anisotropy can be inferred from presented in Fig. 6 structure functions of turbulent velocity fluctuations calculated according to the formulas:

$$S_u^{//}(l)=\langle[u(x+l,z)-u(x,z)]^2\rangle,$$
$$S_w^{//}(l)=\langle[w(x,z+l)-w(x,z)]^2\rangle.$$

$$S_u^{\perp}(l)=\langle[u(x,z+l)-u(x,z)]^2\rangle,$$
$$S_w^{\perp}(l)=\langle[w(x+l,z)-w(x,z)]^2\rangle.$$

Here superscripts *II* and $\perp$ denote longitudinal and transversal directions, respectively; *u* and *w* are horizontal and vertical turbulent velocity fluctuations in the plane of the image; *x* and *z* are horizontal and vertical coordinates in the image; <> means averaging over many scenes. We see a considerable differences between the structures along and across the flow. In the whole range of scales investigated the most variable are the horizontal differences of the vertical velocity.

3.2. Effects of evaporative cooling and liquid phase load.

Anisotropy of small-scale turbulence in the laboratory experiments is most likely the result of evaporative cooling at the cloud-clear air interface, but the impact of the other buoyancy effects cannot be ruled out. This is corroborated by additional experiments using the same laboratory setup but with non-evaporating oil (DEHS) droplets replacing cloud water (Korczyk 2008) of spectrum presented Fig. 7. The observed $\langle u'^2\rangle/\langle w'^2\rangle$ ratio in these experiments was 0.86±0.02, suggesting non-negligible impact of the buoyancy oscillations, due to weight of oil droplets in "oil cloud" filaments, on the observed small-scale anisotropy.

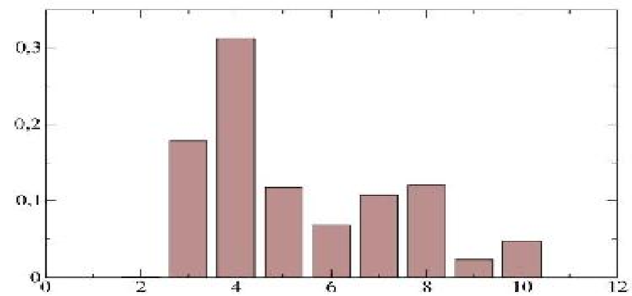

Fig.7 Spectrum of DEHS droplets. Vertical axis: relative mass, horizontal axis – droplet radius.

In order to analyze the role of evaporative cooling of water droplets at the cloud-clear air interface on the buoyancy fluctuations consider mixing diagrams of cloudy air entering the chamber with the clear air of various relative humidities (RH, Fig. 8).

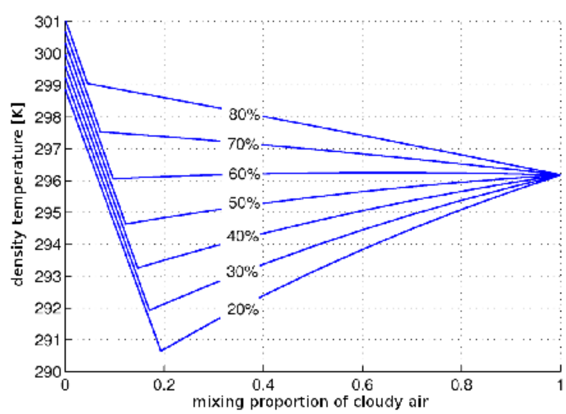

Fig. 8. Mixing diagrams (vertical axis: density temperature, horizontal axis – mixing proportion of cloudy air) for conditions in the cloud chamber.

The TKE dissipation rate ε is estimated with use of PIV measurements from the relation:

$$\varepsilon \approx \nu \left\langle 2\left(\frac{\partial u}{\partial x}\right)^2 + 4\left(\frac{\partial u}{\partial z}\right)^2 + 2\left(\frac{\partial w}{\partial x}\right)^2 + \left(\frac{\partial w}{\partial z}\right)^2 \right\rangle;$$

where ν is kinematic viscosity of the air.

The amplitude between the maximum and the minimum density temperature at given RH of the environmental air indicates the potential for buoyancy oscillations due to both effects: evaporative cooling and liquid water load. It follows, that for the conditions in the chamber the maximum buoyancy fluctuations are at low relative humidities, at which evaporative cooling (at high liquid water loads in the chamber) is most efficient. In such a case a systematic relation between the relative humidity (in the range 20%-50% at which potential for buoyancy fluctuations changes) and some parameters of turbulence should be measurable. Fig. 9 documents such systematic relation. The dependence of the TKE dissipation rate on the relative humidity of the environmental air is evident.

Another result documenting effect of evaporative cooling on the intensity of the small-scale turbulence is shown in Fig. 10. It presents 2nd order structure function of horizontal velocity fluctuations for experiments with different relative humidities of the environmental air. At low RH, at which contribution of evaporative cooling to buoyancy fluctuations has its maximum, structure function indicates large velocity differences. These differences decrease with increasing RH.

CONCLUSIONS

Results presented here confirm that small scale buoyancy fluctuations cause anisotropy of small scale turbulence. Two effects which contribute to these fluctuations are identified: evaporative cooling and uneven spatial distribution of droplets in cloud and clear air filaments (uneven distribution of liquid phase load).

Effect of evaporative cooling depends on the thermodynamical properties of cloud and clear air. Mixing diagram of shows the possible range of buoyancy fluctuations due to evaporative cooling. Increased range of buoyancy fluctuations results in more intense turbulence.

Effect of mass load, documented in experiments with non evaporating droplets, requires more investigations.

Third effect, additional transport of liquid water due to sedimentation of droplets (Andrejczuk et al., 2006) may contribute to first two: evaporative cooling and mass load. All effects combined cause, that small-scale turbulence in non-uniform cloud is anisotropic with the privileged direction in vertical.

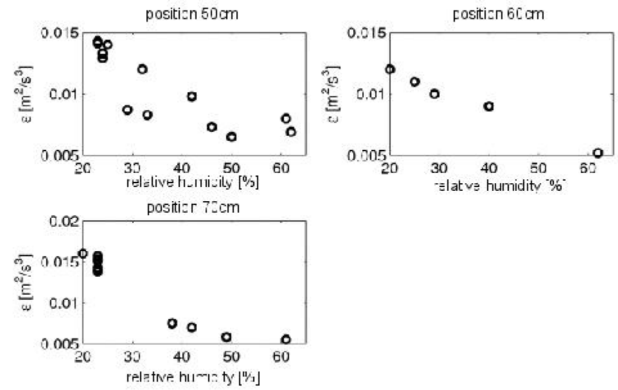

Fig.9 Dependence of the relative humidity (horizontal axis) in the cloud chamber on the TKE dissipation rate estimated from PIV measurements. Consecutive plots show results of measurements at 50cm, 60cm and 70cm from the inlet to the cloud chamber.

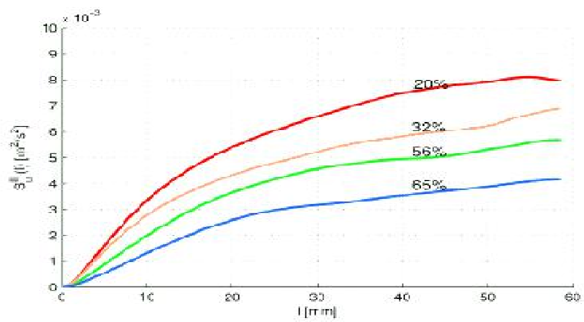

Fig. 10. Longitudinal 2nd order structure function of u for varying relative humidities of the environmental air, measured 30 cm from the inlet

References:

Andrejczuk, M., W.W. Grabowski, S.P. Malinowski and P.K. Smolarkiewicz, 2004: Numerical simulation of cloud-clear air interfacial mixing. *J. Atmos. Sci.*, **61**, 1726-1739.

Andrejczuk, M., W.W. Grabowski, S.P. Malinowski and P.K. Smolarkiewicz, 2006: Numerical Simulation of Cloud-Clear Air Interfacial Mixing: Effects on cloud- microphysics. *J. Atmos. Sci.*, **63**, 3204-3225.

Korczyk, P.M., S.P. Malinowski and T.A. Kowalewski,2006: Mixing of cloud and clear air in centimeter scales observed in laboratory by means of particle image velocimetry. *Atmos. Res.*, **82**, 173-182.

Korczyk. P., 2008: Effect of cloud water on small-scale turbulence - laboratory model (in Polish), PhD thesis, IPPT, Polish Academy of Sciences.

Jaczewski. A. and S.P. Malinowski, 2005: Spatial distribution of cloud droplets investigated in a turbulent cloud chamber. *Q. J. Roy. Meteorol. Soc,.* **131**, 2047-2062.

Malinowski. S.P., M. Andrejczuk, W.W. Grabowski, P.K. Korczyk, T.A. Kowalewski and P.K. Smolarkiewicz,2008: Laboratory and modeling studies of cloud-clear air interfacial mixing: anisotropy of small-scale turbulence due to evaporative cooling. *New J. of Physics*, accepted..

Malinowski, S.P., I. Zawadzki and P. Banat, 1998: Laboratory observations of cloud-clear air mixing in small scales. *J. Atmos. Oceanic. Technol.*, **15**, 1060-1065.

Raffel, M., Ch.E. Willert and J. Kompenhans, 1998: Particle image velocimetry: a practical guide. Springer.

FALL-SPEED MEASUREMENTS OF RAINDROPS NEAR THE GROUND DURING PRECIPITATION EVENTS IN MEXICO CITY

G. Montero-Martínez [1,2], R. Shaw [3], A. Kostinski [3] and F. García-García [1,2]

[1] *Posgrado en Ciencias de la Tierra, Universidad Nacional Autónoma de México*
[2] *Centro de Ciencias de la Atmósfera, Universidad Nacional Autónoma de México*
[3] *Physics Department, Michigan Technological University*

1. INTRODUCTION*

During the formation and development of rain, a falling drop may interact with other cloud and precipitation particles. Because larger raindrops have larger terminal velocities, as they fall they catch-up and collide with smaller drops in their paths. The outcome of raindrop collision events may result in bouncing, coalescence or breakup, and the knowledge of the probability of occurrence of each of these is essential for predicting the evolution of drop size distributions (DSD).

Several studies have identified some of the key factors for these processes to occur (see, for example, Testik and Barros, 2007). The differential response of drops to gravitational force is considered to be the main cause of raindrop collisions. However, this is not the only factor to be taken into account to quantify the collision, coalescence and breakup efficiencies. These quantities have been determined in laboratory experiments with drop pairs falling at terminal velocities (Low and List, 1982; Ochs *et al.*, 1995; Beard and Ochs, 1995). In addition, drop falling speeds are used for the calculation of the collision kinetic energy [CKE] involved in a interacting drop pair system. This parameter, along with the surface energy [SE], allows one to establish criteria to determine whether colliding drops would coalesce or break up. The laboratory evidence has shown that, if sufficient energy is supplied during the early drop collision stage, the process tends to result in a breakup.

In the present study, raindrop fall-speed measurements were made during summer precipitation events that occurred in Mexico City over several years. The aim is to observe the occurrence of a possible, anomalous behavior of the measured drops fall-speeds and its effects in the evolution of DSD.

2. INSTRUMENTATION AND METHODOLOGY

A number of instrumental techniques using optical devices are available for measuring drop fall velocities during natural rain events (Baumgardner *et al.*, 2002; García and Montero, 2004). In the present study, two optical array spectrometer probes (OAPs, by Particle Measuring Systems – Knollenberg, 1981) were used. The nominal drop diameter sizing-ranges for each instrument are 20 to 640 μm and 200 to 6400 μm, respectively. Briefly, an OAP uses a photodiode array and associated photodetection electronics to achieve 2D information of particles passing through a laser beam at the sampling region. By operating the OAP fixed at the ground in a vertical orientation, the drop size is determined from the maximum width across the array. Thus, its fall velocity is calculated by dividing the minor axis (corresponding to the drop shape deformation – Green, 1975) by the time it takes to cross the array. The latter is determined, in turn, by the number of slices and the sampling frequency of the probe. In this way, fall-speed data for individual raindrops near the ground were obtained during rain events under mostly calm

*Corresponding author's address:
Guillermo Montero-Martínez.
Centro de Ciencias de la Atmósfera,
Universidad Nacional Autónoma de México.
Circuito de la Investigación Científica,
Ciudad Universitaria. Del. Coyoacán.
04510 México, D.F. México.
e-mail: **gmontero@atmosfera.unam.mx**

wind conditions (maximum horizontal wind velocity less than 3 m s^{-1}). Data were classified in terms of constant rainfall intensity periods, usually lasting between 2 and 4 minutes.

The measurements were performed at the Centro de Ciencias de la Atmósfera in the Mexico City campus of the National University (UNAM) during the 2002, 2004 and 2006 rainy seasons. Environmental conditions were monitored and recorded with a weather station located besides the OAPs, and rainfall rates were derived from the raingauge installed. Temperatures recorded during the field observations ranged from 15 to 25℃.

The image data were analyzed with a software routine specifically developed for the particular sampling conditions (Álvarez and Torreblanca, 1992). The reconstruction algorithm uses a center-in technique and is capable of taking into account the slanting of the images. Various probe resolutions were used depending on the sampling season (Table 1), thus limiting the peak detection threshold accordingly. The maximum size for peak detection for the 2D-C was 770 µm in 2002 and 2004, and 890 µm in 2006; whereas the minimum for the 2D-P was 360 µm during all sampling seasons.

Table 1. Probes resolutions (in µm) used during each sampling season.

Probe / Year	2002	2004	2006
2D-C	25	25	35
2D-P	200	200	200

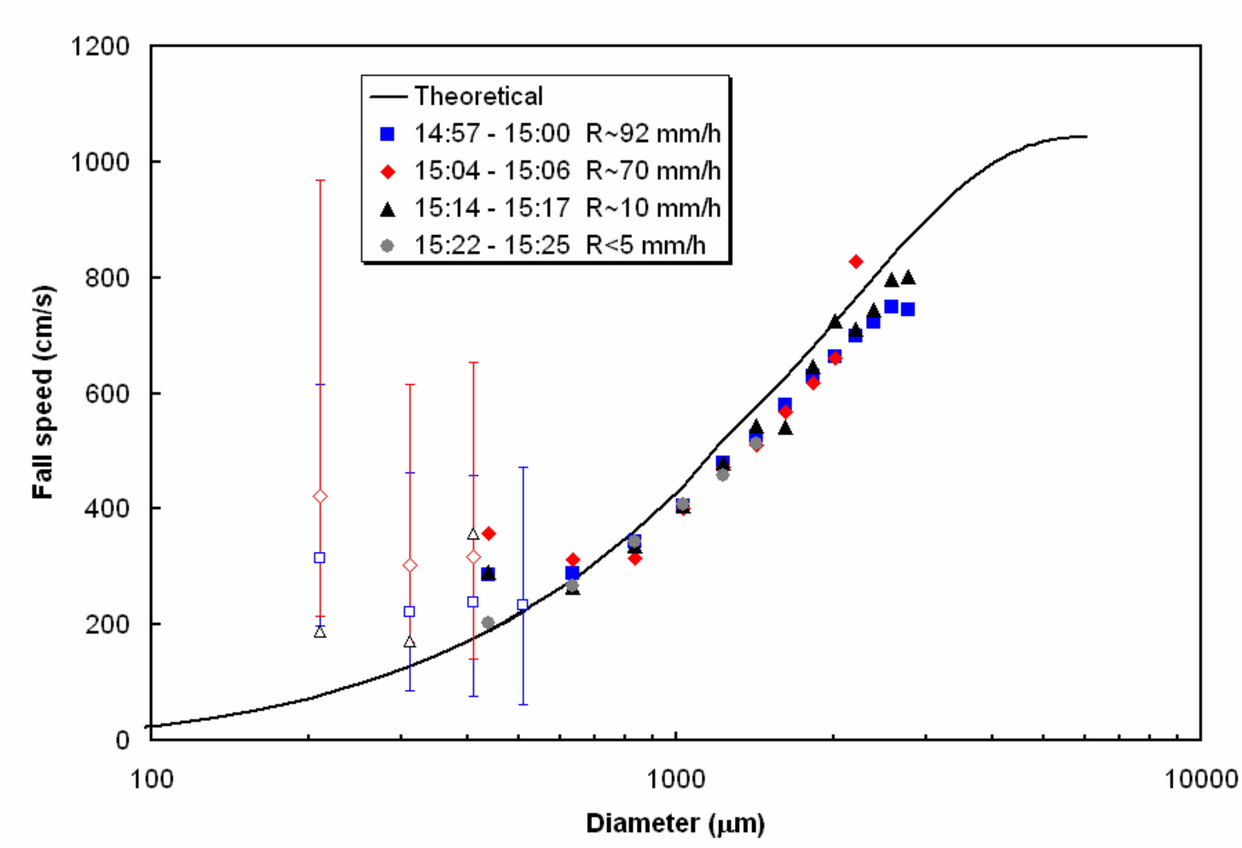

Figure 1. Averaged raindrop vertical fall-speed as a function of drop-size during a rain event occurring on 3 June 2004. Solid symbols refer to 2DP data whereas the open ones represent 2DC measurements. The solid line depicts the theoretical prediction by Beard (1976) for the particular surface atmospheric pressure and air temperature over Mexico City. Horizontal winds during the event were less than 2 m s^{-1} for the first time-period and less than 1 m s^{-1} for the others. Error bars in 2DC data correspond to 30 and 70 percentiles.

3. RESULTS AND DISCUSSION

Figure 1 shows fall-speed data averaged over drop size, obtained with the 2DC and 2DP spectrometers for four different time intervals during a rain event occurring on 3 June 2004. It is readily evident that there are some deviations from the average fall-speed for certain drop-sizes, in particular those with diameters less than 500 μm, with respect to the values predicted by Beard (1976). These deviations become larger as the rainfall intensity increases. Even though the 2DC resolution is quite different from that of the 2DP, measurements with both instruments reveal similar fall-speed values in their overlapping sizing ranges.

The observed fall-speed deviations from their predicted, theoretical values can be illustrated with the case of the 440-μm diameter raindrops. Both optical probes observe particles in this size range, although in the case of the 2DC the drops counted by three contiguous "bins" have been grouped together. In this way, the number of data points increases, thus improving the statistical significance of the measurements. It has to be remembered that, in the case of the 2DP probe, a resolution of 200 μm is used. Thus, the "bin" corresponding to sizes of about 440 μm actually detects drops in the range between 320 and 550 μm. In other words, the diameter of the larger drop detected within this "bin" is almost twice that of the lower sizing threshold. It has been already mentioned that drop fall-speed is calculated as a function of time that the particle takes to cross through the sampling area and the number of diodes covered. In this way, the 2D image obtained from the 2DP probe, with a measuring frequency of 50 kHz, for a 440-μm raindrop should have twelve slices, if the drop is falling with a speed value similar to the predicted one. If the drop is falling faster, the number of slices in the image is less than twelve, depending on its speed. In the cases for drops within the sizing threshold, the image obtained by the same instrument is exactly the same, although their expected fall speed values are quite different, as shown in Table 2 (in the V_∞ column). From this table, drop fall-speed for the three mentioned sizes can be calculated using the number of slices in the 2D image. Based on these calculations, the difference in fall-speed between two drops with the same size, but detected with one slice difference from the "expected" value, is close to 24%. By considering a variation of two slices, the value increases only to 25%, which means that deviations smaller than this may be considered as instrumental errors.

Table 2. Estimated fall-speeds for raindrops sized within the 2DP "bin" corresponding to a 440-μm central diameter. V_∞ is the theoretical terminal velocity, according to Beard (1976), at typical atmospheric conditions in Mexico City.

D_0 (μm)	V_∞ (cm s^{-1})	Number of slices				
		10	**11**	**12**	**13**	**14**
320	132	160	145	133	123	114
438	188	218	199	182	168	156
549	242	273	248	227	210	195

Figure 2 shows the percentage of 440-μm individual drops with fall-speed deviations smaller than 20% from their theoretical values, as a function of the rainfall rate. As it can be appreciated, the percentage of drops falling at speeds larger than the predicted value increases with rain intensity. Thus, during periods with rainfall rates less than 10 mm h^{-1}, at least 70% of the 440-μm drops fall at speeds close to the theoretical value predicted by Beard (1976). On the other hand, during rain events with rainfall rates larger than 10 mm h^{-1}, only half the drops within the same size range fall at speeds similar to the expected value.

Fall-speed anomalies for individual drops with diameters within a given size-range can be displayed using frequency diagrams for the ratio of the measured to the theoretical speed, v/v_t. These were obtained for the whole data set and then classified according to rainfall intensity. An example is presented in Figure 3, which shows the frequency distribution diagram obtained for the v/v_t ratio of 440-μm drops (more than 15,000 in the 2DP case) for all precipitation periods classified by rainfall rate, *R*, less and larger than 5 mm h^{-1}. Based on this, it can be appreciated that almost 75% of the 440 μm-diameter drops reach the ground at their predicted speeds during light rain periods. On the other hand, this proportion decreases to 55% when the rest of the whole data set (*R* larger than 5 mm h^{-1}) is considered. It should be noticed that there are no drops falling "slowly", that is, drops only attain higher speeds than their theoretical values. Data with v/v_t values larger than 4.5 are not statistically significant or even physically meaningful because of the drop size they represent.

Comparisons of fall-speed measurements between the two probes in their overlapping sizing range were carried out in an attempt to rule out instrumental biasing. To do this, drop counts in three contiguous "bins" in the 2DC probe (range between 360 and 460 μm) were added together to have a similar drop-size category than that of the 2DP probe and larger statistical significance. Figure 3 shows the v/v_t frequency distribution obtained from the 2DC during rain events with rain intensities larger than 50 mm h^{-1}, and using the theoretical terminal speed of a 410 μm-drop. It can be noticed that the shape of this distribution is very similar to those presented for 2DP data.

The striking feature of the distributions in Figure 3 is the extended, positively skewed tail corresponding to droplet falling with a higher speed than expected from theoretical and laboratory measurements. There also are hints of drops tending to fall with certain ranges of fall-speed, although sampling statistics do not allow this to be conclusive. The faster than expected fall speeds may have, at least, two possible explanations:

1) the drop is falling down near a larger drop (within a distance less than one or two diameters of the large drop - the so-called "wake effect"); or
2) the detected drop is the result of the breakup of a larger, parental drop that was falling at its proportionally higher equilibrium fall speed.

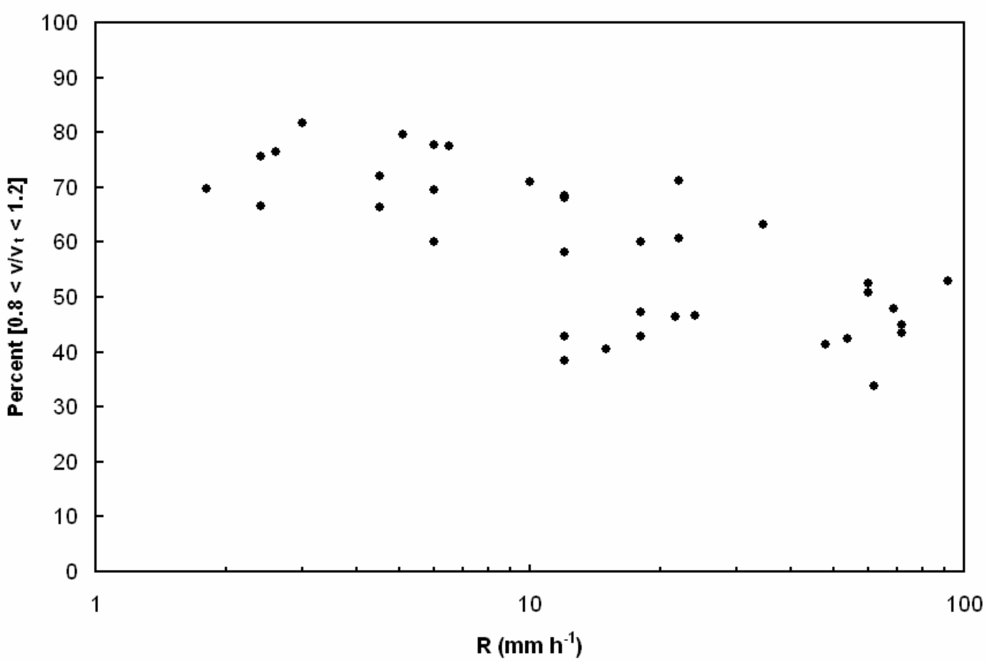

Figure 2. Percentage of individual 440-μm diameter drops, as detected with 2DP probe, with fall-speeds within 20% of their expected, theoretical value, as a function of rainfall rate.

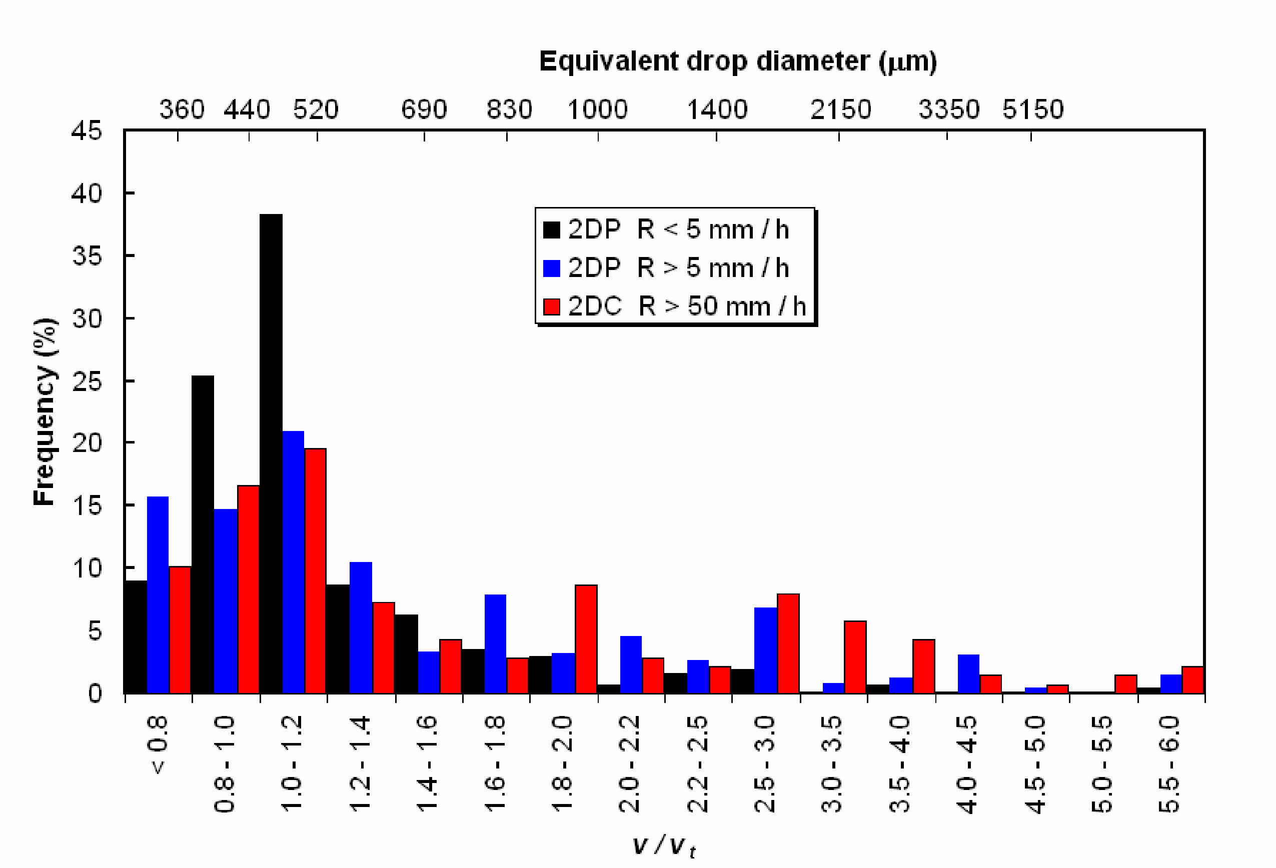

Figure 3. Frequency distribution of the v/v_t ratio for 400-µm diameter drop bins, as detected by the 2DP, for rainfall periods with *R* smaller and larger than 5 mm h^{-1}. For the 2DC case, data are shown only for periods with rainfall intensities larger than 50 mm h^{-1}. The numbers in the top axis are indicative of the diameter of a drop with a fall-speed corresponding to the velocity ratio of the x-axis.

When a large drop breaks up, the resulting fragments will fall down at a velocity similar to that of the parent drop, at least for a short period before they relax to their terminal speeds by effect of the drag force. Should one of these fragments be detected just after the breakup, it is possible to estimate the size of the parental drop through the fall-speed of the fragment. The time required for a drop with a diameter around 440-µm to reduce its fall-speed from 1,000 cm s^{-1} to its terminal speed (of about 190 cm s^{-1}) is estimated to be in the range of 0.3 to 0.5 seconds. This time corresponds to a distance of about 3 to 5 meters. In this way, the modes in the v/v_t frequency distributions can be considered as indicative of the parental drop. In this sense, by considering the 2DC and 2DP (R > 5 mm h^{-1}) data, it is feasible to assume that some of these 'fall-speed enhanced' drops are dropping within speed value ranges centered at 380 and 560 cm s^{-1} (which are equivalent to v/v_t values of 2 and 3 in Figure 3). These quantities correspond to the terminal speed of raindrops with equivalent diameter sizes of about 850- and 1,400-µm, respectively. In the 2DP case for the 4.5 and 6 modes, these values should correspond to vertical fall-speeds of drops with diameters around 2,600 and 5,500 µm, respectively. It should be noticed that the peaks for the larger v/v_t values become more prominent as the larger rainfall rates (*R* > 5 mm h^{-1}) are considered. This is an expected result given the presence of larger, milimeter-sized raindrops during events with heavy rain.

Table 3. Percentage of drop counts in the overlapping sizing range of the probes (~ 440 µm-center "bin" diameter) falling at different speeds.

Probe	Percentage of counts			
	v_t	$v/v_t = 2$	$v/v_t = 3$	$v/v_t = 4$
2DC	58	14.6	10	7.3
2DP	55	16.5	8.9	5.8

Besides the similitude in the shape of the distribution, the relative heights of the peaks are important too. Table 3 shows the relative frequencies measured with each of the probes, over their overlapping sizing ranges, during the periods of largest rainfall intensity. The similarities in the measurements of 2DP and 2DC probes are to be stressed because, although both of them have similar optical and electronic components, each instrument has a different, independent clock for controlling the sampling frequencies.

Coalescence efficiency should change depending on differences in impact velocities. The impact energy of a colliding drop pair can be calculated from their masses and impact velocities ($\Delta V = V - v$) and it can be characterized by the Weber number. Figure 4 shows the changes in Weber number (collision energy) produced when a 440-µm drop, falling with an enhanced fall-speed, interacts with a larger drop falling at its terminal speed. It can be observed that impact energy significantly changes from the estimated values when drops fall at their theoretical terminal speeds. From Figure 4 it can be argued that the result of a drop pair collision event (coalescence or breakup) may be modified by considering that, if the drop collision energy decreases, then the breakup efficiency is also reduced. However, the conclusion on how these observations would impact the overall outcome on the processes involved in warm rain is not straightforwad since, as it has been pointed out, they depend on the relative number of drops falling with enhanced speeds and on the time they spend with these increased velocities.

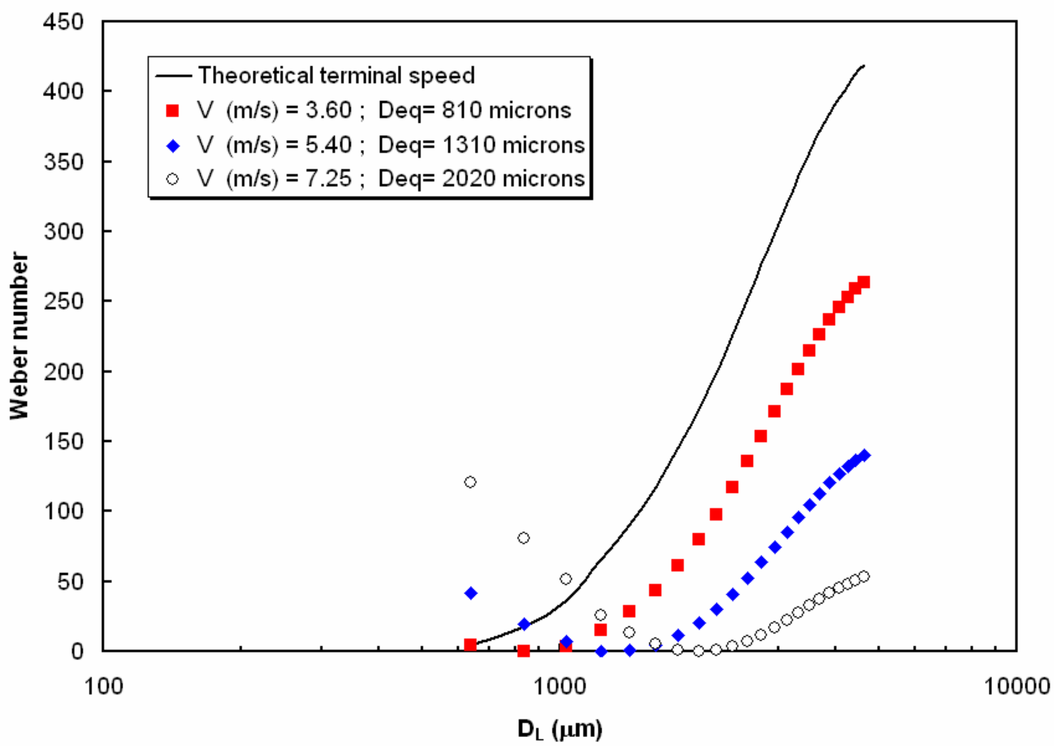

Figure 4. Weber number calculations for the collision between a large raindrop (*x*-axis) falling at terminal speed, and a 440-µm diameter (small-sized drop) with various fall-speeds. Colored symbols correspond to 440-µm drops falling with a 'preferred' enhanced fall-speed.

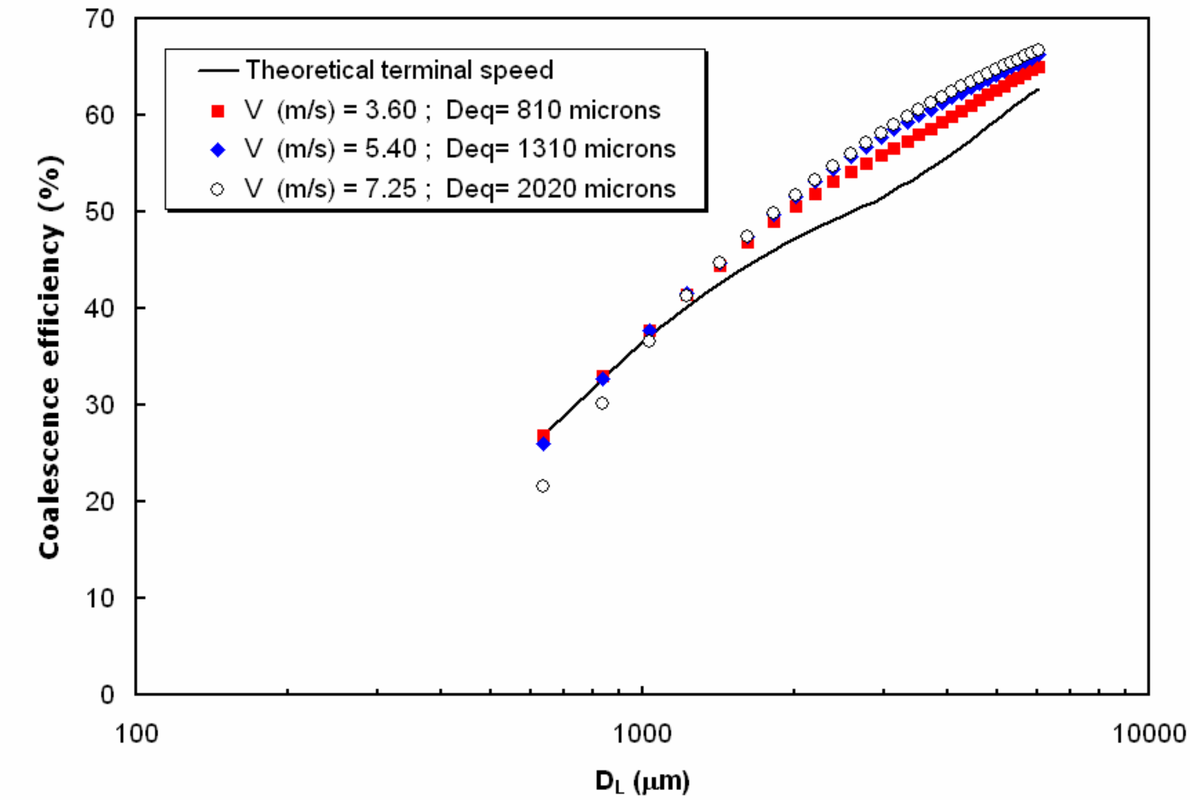

Figure 5. Estimates of the coalescence efficiency for large raindrops, D_L, colliding with 440-µm diameter, small drop. The solid line represents the coalescence efficiency as calculated from Low and List's (1982) parameterizations. See text for details.

To illustrate this, and based on the parameterizations by Low and List (1982), coalescence efficiencies of 440 µm-drops colliding with drops of all larger size-categories were estimated using the observed, enhanced fall-speeds at typical conditions in Mexico City. These estimates are shown in Figure 5. It has to be pointed out that changes in the coalescence efficiency are expected to be considerable if the process occurred when the small drop falls with a larger velocity than its terminal fall-speed. Due to the presence of raindrops falling at larger speeds than the theoretical one, an increase in the coalescence efficiency is observed for the cases where the diameter of the large drop is larger than 1,000-µm. This is due to the fact that the fall speed difference of the drop pair decreases in comparison with the situation where the two drops are falling at their theoretical terminal speeds. On the other hand, for the cases when the diameter of the collector drop is less than 1,000-µm, the coalescence efficiency may decrease. Besides these considerations, the collection kernel itself is of course directly influenced by the decrease in differential fall speed (cf. Fig. 1).

4. SUMMARY AND CONCLUSIONS

Measurements of raindrop fall-speeds near the ground were carried out in Mexico City with two optical array probes. Deviations from the theoretical values were observed for drops with diameters smaller than 500 µm. A careful analysis of the data indicates that a significant amount of raindrops fall at speeds larger than those predicted by theoretical calculations. In addition, their fractional number concentration and fall-speed deviations become larger as the rainfall rate increases. Frequency diagrams show that raindrops falling with enhanced speeds may do so with certain “preferred” values. Although our results are only based on the fall-speed observations of ~440-μm drops, it is expected from data in Figure 1 that smaller drops will show a similar fall-speed behavior. This may be an indication of the mechanisms that lead to the observed enhanced fall speeds. By assuming that these faster-falling particles are the product of the collision and breakup of larger raindrops, information on their fall-speeds can be used to infer the sizes of the original, breaking drops.

Furthermore, these observations may produce a significant change in the calculated breakup kinetic energy used, for example, in erosion effects studies. Regarding the collision-coalescence-breakup processes and collection kernels, the effects of these measurements are not straightforward since different factors, such as the fraction number of drops falling with enhanced speeds and the time they spend with that behavior, have to be considered. Further studies are currently under way in this direction.

Acknowledgments. The authors appreciate the continuous technical support provided by Messrs. J. Escalante, W. Gutiérrez, M.A Meneses, A. Rodríguez and V. Zarraluqui.

References

Álvarez P., J.M., and J. Torreblanca B., 1992: *Desarrollo de un Sistema de Software para Interpretación y Análisis de Datos de Espectrómetros de Gotas*. Tesis de Licenciatura (Ingeniero en Computación). Facultad de Ingeniería, Universidad Nacional Autónoma de México. 150 pp.

Baumgardner, D., G. Kok, W. Dawson, D. O'Connor and R. Newton, 2002: A new grounded precipitation spectrometer: the Meteorological Particle Sensor (MPS). *Proc 11th Conf. Cloud Phys., Ogden, Utah*. Amer. Meteor. Soc. [Boston, Mass, USA] CD-ROM, Paper P8.6, 4pp.

Beard, K.V., 1976. Terminal velocity and shape of cloud and precipitation drops aloft. *J. Atmos. Sci.*, **33**, 851-864.

Beard, K.V., and H. T. Ochs III, 1995: Collisions between small precipitation drops. Part II: Formulas for coalescence, temporary coalescence, and satellites. *J. Atmos. Sci.*, **52**, 3977-3996.

García-García, F., and G. Montero-Martínez, 2004: On the measurement of raindrops fall speeds at the ground using optical array probes. *Proc. 14th Intern. Conf. Clouds Precip.*, *Bologna, Italy*. IAMAP/ICCP, **2**, 1085-1088.

Green, A.W., 1975. An approximation for the shapes of large raindrops. *J. Appl. Meteor.*, **14**, 1578-1583.

Knollenberg, R.G., 1981: Techniques for probing cloud microphysics. In *Clouds: Their Formation, Optical Properties, and Effects.* P.V. Hobbs and A. Deepak (Eds), Academic Press, 15-91.

Low, T.B., and R. List, 1982: Collision, coalescence and breakup of raindrops. Part I: Experimentally established coalescence efficiencies and fragment size distributions in breakup. *J. Atmos. Sci.*, **39**, 1591-1606.

Ochs III, H.T., K.V. Beard, R.R. Czys, N.F. Laird, D.E. Schaufelberger and D.J. Holdridge, 1995: Collisions between small precipitation drops. Part I: Laboratory measurements of bounce, coalescence, and temporary coalescence. *J. Atmos. Sci.*, **52**, 2258-2275.

Testik, F.Y., and A.P. Barros, 2007: Toward elucidating the microstructure of warm rainfall: A survey. *Rev. Geophys.*, **45**, RG2003, *doi:10.1029/2005RG000182*.

A NOVEL APPROACH FOR REPRESENTING ICE MICROPHYSICS IN MODELS: DESCRIPTION AND TESTS USING A KINEMATIC FRAMEWORK

Hugh Morrison* and Wojciech Grabowski

National Center for Atmospheric Research, Boulder, Colorado

1. INTRODUCTION

The representation of ice microphysics in models has a significant impact on quantitative precipitation forecasts, radiative transfer through clouds, and cloud-dynamical interactions (e.g., Rangno and Hobbs 1984; Lord et al. 1984). The one-moment bulk approach was first applied by Kessler (1969) to warm (ice-free) clouds based on the natural separation between cloud droplets and drizzle/rain. Thus, mixing ratio was separately predicted for each category (cloud droplets and drizzle/rain drops), with parameterized conversion rates (autoconversion and accretion) transferring the cloud water to drizzle/rain. The bulk approach was extended to the ice phase using a similar separation between cloud ice and large precipitating ice (e.g., Lin et al. 1983; Rutledge and Hobbs 1984). This separation was required since the empirical particle fallspeed-size relationships used in these schemes apply to only a limited size range (thus requiring separation of small and large ice particles). This approach also represents a legacy of the Kessler-type warm-rain scheme. However, the distinction between small and large particle modes is less clear for ice than liquid because large precipitating ice particles can be produced by both accretional and vapor depositional growth; rain is produced by accretional growth only. Precipitation ice is often further subdivided into different predefined categories (e.g., snow, aggregates, graupel, hail). The parameters needed for calculating microphysical process rates are specified a priori for each predefined ice category.

A key point is that in nature the boundaries between different ice categories (cloud ice, snow, graupel, hail) are difficult to define and transitions between various categories happen gradually. For instance, as ice crystals grow by diffusion of water vapor and aggregation, their mass and terminal velocities gradually increase, and they gradually move from the “cloud ice” into the “snow” category. The same is true for the growth by riming, where ice particles gradually increase their mass and rimed mass fraction, and move from the “snow” to the “graupel” category. In traditional schemes, there are no transitional regimes between various ice categories and conversion of ice from one category to another occurs in a single discrete step. For example, some schemes produce graupel immediately after a minimum riming rate or mixing ratio is reached. More detailed models prognose the particle density to more accurately determine the threshold for conversion to graupel (e.g., Ferrier 1994). However, none of these schemes treat the transitional regimes that represent the growth of a small ice particle into a large ice crystal or an aggregate (i.e., the snowflake), or growth of a rimed crystal into a graupel particle. This has the potential to produce undesirable thresholding behavior, i.e., model solutions may diverge depending whether a particular threshold (e.g., the cloud ice mixing ratio or the riming rate) is reached or not. Thus, significant sensitivity of the simulated clouds and precipitation to these thresholds has been noted (e.g., Rangno and Hobbs 1984; Thompson et al. 2004); these thresholds must therefore be tuned to produce desirable results.

In this paper, we propose a novel approach for parameterizing ice microphysics that shifts away from the traditional approach of predefined ice categories. Our approach allows the crystal habit and associated microphysical parameters to evolve during the simulation as a function of particle size and rimed mass fraction.The history of the rimed mass fraction is retained by predicting two ice mixing ratio variables: i) the mixing ratio due to vapor deposition and ii) the mixing ratio due to riming. It follows that the rimed mass fraction is derived locally from the ratio of the riming and total (riming plus deposition) mixing ratios. This approach allows the mass-dimension (m-D) and projected area-dimension (A-D) relationships to evolve according to the predicted rimed mass fraction and particle dimension. All relevant microphysical parameters in the scheme are based on these m-D and A-D relationships for self-consistency. This approach removes the need for arbitrary thresholds for conversions of small ice to snow during vapor deposition and/or aggregation, and conversion of crys-

* *Corresponding author address*: Dr. Hugh Morrison, NCAR, PO Box 3000, Boulder, CO 80307; e-mail: morrison@ucar.edu.

tals to graupel during riming. The goal is to provide a physically-based treatment of the ice microphysics that accounts for the transitional regimes and avoids thresholding behavior while retaining a relatively simple and flexible framework.

2. DESCRIPTION OF THE NEW SCHEME

The two-moment bulk warm rain scheme of Morrison and Grabowski (2006; hereafter MG06) has been extended to the ice phase using the novel approach outlined in the Introduction. The new ice scheme is described in detail in Morrison and Grabowski (2008), and outlined here.

All ice microphysical processes and parameters are calculated consistently in terms of the particle mass-dimension (m-D) and projected area-dimension (A-D) relationships. These relationships are obtained across the whole range of particle sizes using observationally-based relations for different types of ice particles (available in the literature) and the rimed mass fraction predicted by the model. The history of rimed mass fraction is retained by predicting separately the mixing ratios of ice due to the vapor deposition, q_{dep}, and due to riming, q_{rim}. The change in ice mixing ratio due to water vapor deposition and initiation of ice by deposition/condensation freezing and freezing of cloud droplets contributes to q_{dep}. The change in ice mixing ratio due to collisions between ice particles and cloud droplets/rain (in subfreezing conditions) and ice initiation due to freezing of raindrop contributes to q_{rim}. Sublimation and melting (including melting due to rain-ice collisions above freezing) are applied to both q_{dep} and q_{rim}. Since we also predict the ice number concentration N, there are a total of three prognostic variables for ice in the scheme.

Similarly to the liquid species (cloud droplets and rain) described in MG06a, the ice particle size distribution follows a generalized gamma distribution:

$$N(D) = N_o D^{\mu} e^{-\lambda D}, \tag{1}$$

where D is the particle dimension (hereafter dimension refers to length of the major axis), N_0 is the "intercept" parameter, λ is the slope parameter, and $\mu = 1/\eta^2 - 1$ is the spectral shape parameter (η is the relative radius dispersion, the ratio between the standard deviation and the mean radius). These size distribution parameters are needed for calculation of the various microphysical process rates.

Parameters N_0 and λ can be found by relating the PSD to the predicted number concentration N and mixing ratio q (note that for ice, $q = q_{dep} + q_{rim}$):

$$N = \int_0^{\infty} N(D)dD, \tag{2}$$

$$q = \int_0^{\infty} m(D)N(D)dD, \tag{3}$$

where $m(D)$ is the particle mass and $N(D)$ is given by (1). A solution for the size distribution parameters N_0 and λ in terms of μ, N, and q using (1) - (3) requires specification of the m-D relationship across the PSD. Note that although the A-D relationship is not used to derive the size distribution parameters using (1) - (3), it is needed, along with the size distribution parameters and m-D relationship, for calculation of several of the process rate (e.g., collection of cloud water and rain by ice particles).

For the ice phase, a complication arises because the m-D and A-D relationships vary as a function of crystal habit, degree of riming, and particle size. Thus, by predicting both q_{dep} and q_{rim} and retaining the history of bulk rimed mass fraction F_r [defined as $F_r \equiv q_{rim}/(q_{rim}+q_{dep})$], we seek to provide a physical basis for the evolution of m-D and A-D relations across a wide range of conditions. The m-D and A-D relationships as a function of crystal habit, rimed mass fraction, and particle size are detailed in Morrison and Grabowski (2008). The evolution of m-D and A-D as a function of rimed mass fraction follows from the conceptual model of Heymsfield (1982). Based on this model, rime accumulation in the crystal interstices increases the particle mass *but not the particle dimension D*, and such a picture is valid up to the point of a complete "filling-in" of crystal interstices. From this point the particle becomes a graupel and further rimimg increases both particle size and mass. Prior to the complete "filling-in" of the interstices, the rimed mass fraction of an individual crystal is assumed equal to the bulk rimed fraction F_r and the particle dimension D is determined by the crystal mass grown by diffusion of water vapor and aggregation.

3. DESCRIPTION OF THE KINEMATIC FRAMEWORK AND CASE STUDY

The bulk model with the new ice microphysics scheme was implemented in a 2D kinematic modeling framework similar to that presented by Szumowski et al. (1998). The kinematic framework employs a specified flow field, which allows for testing of the microphysics scheme in a framework that includes advective transport and particle sedimentation, while at the same time avoiding complications due to feedbacks between the dynamics and microphysics. In addition to the equations describing conservation of the mixing ratios and number concentrations of ice, cloud droplets, and rain, the kinematic model solves equations for the potential temperature and water vapor mixing ratio. These equations include advective transport and sinks/sources due to condensation/evaporation and latent heating. Transport in physical space is calculated using the 2D version of the MPDATA scheme

(Smolarkiewicz and Margolin 1998). The vertical and horizontal grid spacing is 50 m over a domain that is 9 km wide and 3 km deep. The model time step is 0.5 sec.

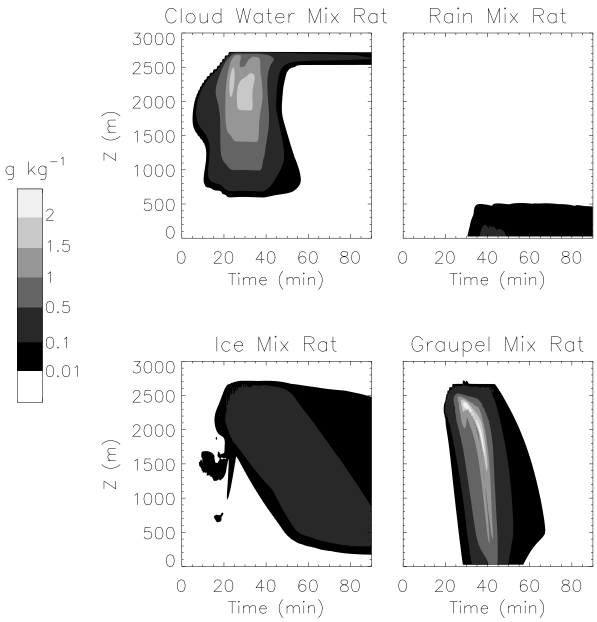

Figure 1: Time evolution of horizontal maxima of cloud water mixing ratio, rain mixing ratio, ice/snow mixing ratio, and graupel mixing ratio at each vertical level using the traditional scheme.

The specified flow field varies in time, representing the evolution of an idealized shallow convective plume. The flow pattern consists of low-level convergence, upper-level divergence, and a narrow updraft at the center of the domain. Two flow configurations are tested, corresponding with a maximum updraft speed of 8 m s^{-1}. The updraft speed is held constant at 1 m s^{-1} for the first 15 min, intensifies to a peak value of 8 m s^{-1} at 25 min, and decays to zero after 40 min. The simulated time period is from $t = 0$ to 90 min. The cloud-top temperature is about 258 K, with temperatures above freezing in the lowest 500 m.

To test the new approach for ice microphysics (hereafter referred to as the "new scheme"), we have also developed a version of the scheme that uses the traditional approach for conversion of ice/snow to graupel following Rutledge and Hobbs (1984; hereafter RH84); hereafter, this version is referred to as the "traditional scheme". In this scheme there are four prognostic ice variables: ice/snow mixing ratio and number concentration, and graupel mixing ratio and number concentration. This scheme requires threshold rain/snow/cloud droplet mixing ratios for the conversion of snow to graupel during riming. The sensitivity of the traditional scheme to these threshold mixing ratios is described in the next section.

4. RESULTS

Model results are generally similar when using either the traditional or new scheme, but there are significant differences. Time-height plots of the maximum cloud droplet, rain, ice/snow, and graupel mixing ratios in the horizontal at a given level are shown in Figs. 1 and 2 for the traditional and new schemes, respectively. Cloud water is produced in both simulations as the updraft increases in strength between $t = 0$ and 25 min. Significant amounts of ice are produced by the time of the maximum updraft ($t = 25$ min) through deposition/condensation-freezing nucleation as well as droplet freezing.

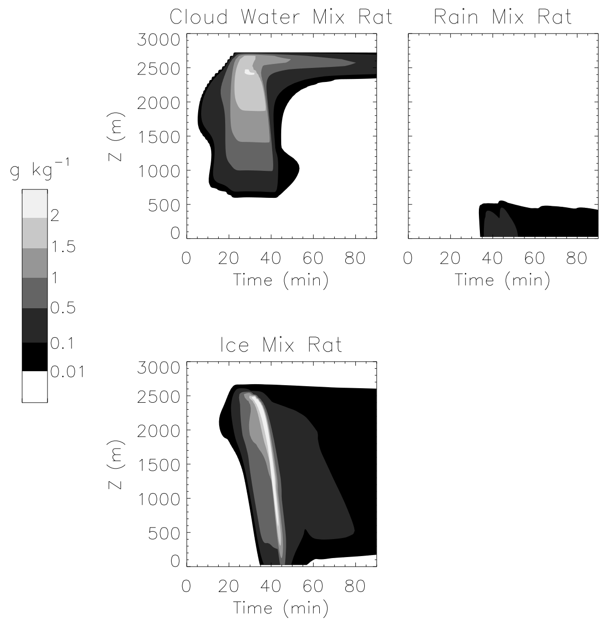

Figure 2: Time evolution of horizontal maxima of cloud water mixing ratio, rain mixing ratio, and ice mixing ratio at each vertical level using the new scheme.

The noisy pattern seen in the ice and graupel mixing ratios using the traditional scheme in Fig. 1 likely reflects the thresholding behavior of graupel conversion. As the updraft weakens after $t = 25$ min, a shaft of ice precipitation develops and partially melts near the surface. The cloud water is rapidly glaciated throughout most of the cloud layer, except near cloud top due to limited amounts of ice in this region. The separation of ice/snow and graupel into different categories using the traditional approach produces two shafts of ice precipitation and associated maxima of surface precipitation rate consisting of either graupel or ice/snow (see Figs. 1).

Since the traditional approach converts ice/snow to graupel in a single step, rapid conversion to graupel occurs once the threshold conditions are met, and this shaft of graupel precipitates rapidly to the surface with mean fallspeeds greater than 1.5 m s^{-1}. Significant surface precipitation (consisting of both graupel and rain) begins at t = 30 min in this run and produces a sharp peak in the precipitation rate at $t = 40$ min (Fig. 3). A secondary peak in the surface precipitation rate occurs at about t = 80 min associated with the weaker shaft of ice precipitation consisting of ice/snow. Because of the much slower particle fallspeeds associated with the ice/snow category (about 0.5 - 1 m s^{-1}) relative to graupel, much of this shaft does not reach the surface by the end of the simulation at $t = 90$ min (see Fig. 1).

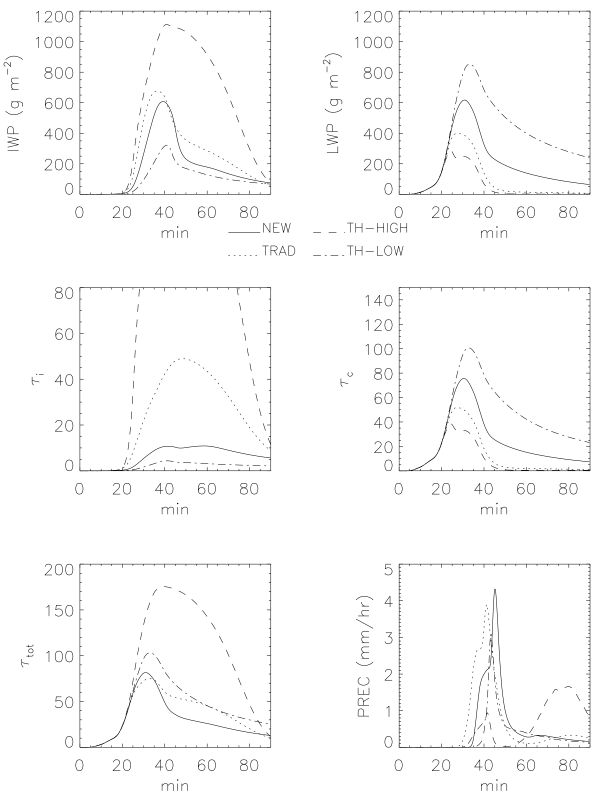

Figure 3: Time evolution of domain-average cloud liquid water path (LWP), ice water path (IWP), droplet optical depth (τ_c), ice optical depth (τ_i), total cloud optical depth (τ_{tot}), and surface precipitation rate (PREC). NEW and TRAD refer to simulations using the new and traditional ice microphysics schemes, respectively. TH-HIGH and TH-LOW refere to sensitivity tests using the traditional scheme but the threshold ice/snow and droplet mixing ratios for graupel production increased or decreased, respectively.

In contrast, the new scheme produces a single shaft of ice precipitation; its formation is also slightly delayed relative to the main precipitation shaft produced by the traditional scheme (see Fig. 2 and 3). Similarly to the traditional scheme, weak surface precipitation continues up to the end of the simulation, but in contrast there is not a distinct second peak in precipitation rate. Ice mixing ratio is primarily grown by vapor deposition initially; rimed mass fraction exceeding 90% occurs 10-20 min after the first appearance of the ice (see Fig. 4).

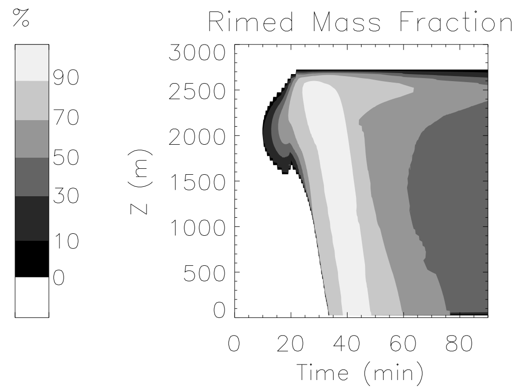

Figure 4: Time evolution of the rimed mass fraction at the location of the horizontal maximum ice mixing ratio at each vertical level using the new scheme.

Rimed mass fraction steadily decreases after about $t = 45$ min corresponding to the reduction of droplet mixing ratio and hence decrease in the riming rate and accumulated rime mass. Since the shaft of ice precipitation consists of a mixture of partially-rimed crystals and graupel, the mean particle fallspeed is slightly less than that for a population consisting solely of graupel. Thus, this shaft of precipitation falls slower than the graupel shaft in the simulation using the traditional scheme, and significant precipitation does not reach the surface until about t = 35 min, a delay of about 5 min compared to the run with the traditional scheme (see Fig. 3). The peak surface precipitation rate is similarly delayed by about 5 min. Moreover, the new scheme produces significantly more cloud liquid water than the traditional scheme, especially after $t = 45$ min. These differences are also evident for the time- and domain-average values of LWP, optical depths, and surface precipitation rate (not shown). For ice optical depth, the difference is more significant, even though the ice water path is only somewhat smaller using the new scheme. This appears to reflect the fact that dense, heavily-rimed crystals in the new scheme have a relatively large ratio of mass to projected area (i.e., larger effective radius) compared to the unrimed crystals in the traditional scheme. Similar differences are apparent for the simulations with maximum updraft velocity of 2 m s^{-1}.

Simulations using the traditional scheme exhibit strong sensitivity to the assumed ice/snow and cloud water threshold mixing ratios required for conversion to graupel during riming of snow. Two tests demonstrate this sensitivity. In the first test, conversion to graupel during collection of droplets is allowed only when both the ice/snow and droplet mixing ratios exceed 1 g/kg, compared to thresholds of 0.1 and 0.5 g/kg for ice/snow and droplets, respectively, for the baseline run using the traditional scheme (as well as in RH84). In the second test, conversion to graupel during collection of droplets occurs when any ice/snow and droplet mixing ratio is present (i.e., thresholds are set to zero). Note that results are not sensitive to the mixing ratio thresholds for conversion to graupel during rain-snow collisions because the formation of graupel is dominated by collisions between ice/snow and cloud droplets. A similar result was noted by RH84 in simulations of cold-frontal rainbands.

As expected, increasing the threshold ice/snow and droplet mixing ratios to 1 g/kg decreases the amount of graupel. Since particles fallspeeds for ice/snow are much slower than they are for graupel, ice mass is removed relatively slowly from the cloud. This leads to much larger values of IWP and rapid depletion of cloud liquid water through droplet collection and the diffusional growth of the ice field (see Fig. 3). It also leads to a smaller initial peak in the surface precipitation rate (at about $t = 41$ min) and much larger second peak (at $t = 80$ min) relative to the baseline run using the traditional scheme. Not surprisingly, reducing the threshold mixing ratios for graupel production leads to an increase in the LWP and decrease in the IWP relative to baseline due to faster removal of cloud ice. Despite large changes in the ice and liquid water paths, the total cloud optical depth is similar to baseline. Thus, the traditional approach produces a larger total cloud optical depth than the new scheme regardless of values specified for the threshold mixing ratios for graupel production. This suggests that simple tuning of the threshold mixing ratios in the traditional approach will not be able to reproduce results using the new scheme; even if such tuning were possible, it would likely be case-dependent.

5. SUMMARY AND CONCLUSIONS

This paper documents a novel approach for representing the ice-phase microphysics in numerical models. It includes only a single species of ice but retains the history of rimed mass fraction, in contrast to the traditional approach of separating ice into several distinct categories (e.g., cloud ice, snow, graupel). The new approach allows for a physically-based representation of the conversion of cloud ice into snow due to diffusional growth and aggregation, and the conversion of cloud ice and snow into graupel due to riming. The conceptual model of Heymsfield (1982) is applied for the latter. The history of rimed mass fraction in the new scheme is retained by predicting two ice mixing ratio variables: the mixing ratio acquired through water vapor deposition and the mixing ratio acquired through riming. The scheme was applied in a 2D kinematic modeling framework mimicking a mixed-phase shallow cumulus. The new scheme was compared against a version that included the traditional approach for graupel conversion processes following RH84. Significant differences were apparent between the new and traditional approaches, especially in terms of precipitation at the surface and the cloud radiative properties. In the traditional approach, threshold mixing ratios must be reached before graupel production is allowed during riming. The values specified for these thresholds are arbitrary and have little physical basis. Results using the traditional scheme exhibited strong sensitivity to these thresholds.

Future work will focus on testing the scheme within a 3D dynamic framework over a range of different conditions (e.g., deep convection, synoptic cirrus, mixed-phase stratocumulus), including comparison with observations, as well as looking at the impact of ice microphysics on the cloud dynamics. Application of the new approach to a detailed bin ice microphysics model is also currently under development.

BIBLIOGRAPHY

Ferrier, B., 1994: A double-moment multiple-phase four-class bulk ice scheme. Part I: Description. *J. Atmos. Sci.*, **51**, 249-280.

Heymsfield, A. J., 1982: A comparative study of the rates of development of potential graupel and hail embryos in high plains storms. *J. Atmos. Sci.*, **39**, 2867-2897.

Kessler, E., 1969: *On the Distribution and Continuity of Water Substance in Atmospheric Circulations. Meteor. Monogr.,*, No. 32, Amer. Meteor. Soc., 84 pp.

Lin, Y.-L., R. D. Farley, and H. D. Orville, 1983: Bulk parameterization of the snow field in a clouds model. *J. Climate Appl. Meteor.*, **22**, 1065-1092.

Lord, S. J., H. E. Willoughby, and J. M. Piotrowicz, 1984: Role of a parameterized ice-phase microphysics in an exisymmetric tropical cyclone model. *J. Atmos. Sci.*, **41**, 2836-2848.

Morrison, H., and W. W. Grabowski, 2007: Comparison of bulk and bin warm rain microphysics models using a kinematic framework. *J. Atmos. Sci.* **64**, 2839-2861.

Morrison, H., and W. W. Grabowski, 2008: A novel approach for representing ice microphysics in models: Description and tests using a kinematic framework. *J. Atmos. Sci.* (in press)

Rutledge, S. A., and P. V. Hobbs, 1984: The mesoscale and microscale structure of organization of clouds and precipitation in midlatitude cyclones. XII: A diagnostic modeling study of precipitation development in narrow cold-frontal rainbands. *J. Atmos. Sci.*, **41**, 2949-2972.

Smolarkiewicz, P. K. and L. G. Margolin, 1998: MPDATA: A finite-difference solver for geophysical flows. *J. Comput. Phys.*, **140**, 459-480.

Szumowski, M. J., W. W. Grabowski, H. T. Ochs III, 1998: Simple two-dimensional kinematic framewsork designed to test warm rain micorphysics models. *Atmos. Res.*, **45**, 299-326.

Acknowledgments.
This work was partially supported by the NOAA Grant NA05OAR4310107 and the NSF Science and Technology Center for Multi-Scale Modeling of Atmospheric Processes (CMMAP), managed by Colorado State University under cooperative agreement ATM-0425247. The National Center for Atmospheric Research is operated by the University Corporation for Atmospheric Research under sponsorship of the National Science Foundation.

DISTINCT CLOUD DROPLET NUCLEATION KINETICS ABOVE THE MARINE BOUNDARY LAYER ALONG THE CALIFORNIA COAST

Chris Ruehl[1], Patrick Chuang[1], and Athanasios Nenes[2,3]
[1]University of California, Santa Cruz, Earth and Planetary Sciences Dept.
[2]Georgia Institute of Technology, Earth and Atmospheric Sciences Dept.
[3]Georgia Institute of Technology, Chemical and Biomolecular Engineering Dept.

1. INTRODUCTION

Traditional Köhler theory predicts the ability of an atmospheric particle of known size and composition to act as a cloud condensation nucleus (CCN) at equilibrium. However, it is not known to what extent particles exist in the atmosphere that may be prevented from acting as CCN by kinetic limitations. We measured the rate of cloud droplet formation at a high-elevation site near the California coast that is typically above the marine boundary layer by sampling ambient particles, exposing them to a known supersaturation (S) for durations of 20 to 35 s, and measuring the diameters (D) of the resulting droplets. We then used a fully-coupled numerical model to estimate the mass accommodation coefficient (α) distribution of CCN that would best match the observed D distributions.

2. RESULTS

We observed two or more modes in roughly 50% of all D spectra, typically at night. These two modes persisted when S was varied by several tenths of a percent (Fig. 1), and therefore cannot be caused by a difference in the critical supersaturations of the modes. Instead, kinetic effects must be incorporated into Köhler theory to explain these observations.

Figure 1. Typical D_d histrograms as a functionof S during field campaign

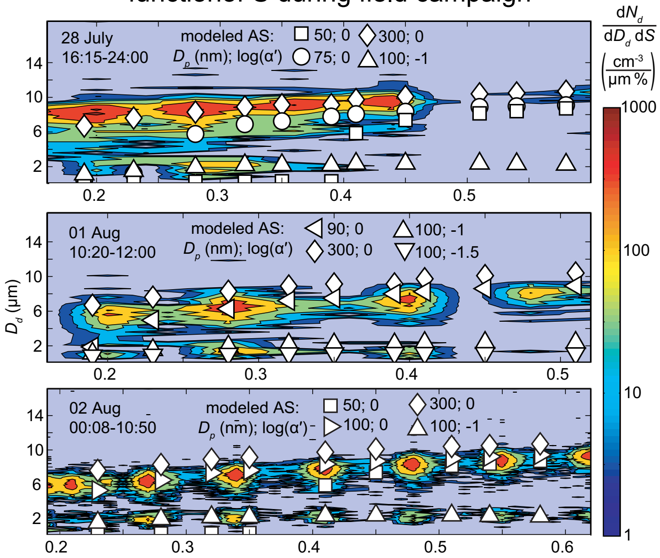

Figure 2. Example α histrograms

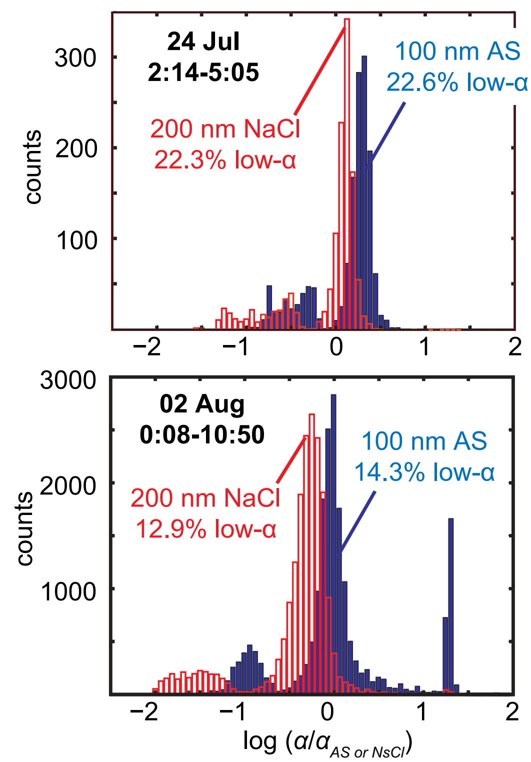

To calculate a value of α that best fits a D measurement, an assumption of starting (dry) CCN size and composition is required. We calculated α spectra assuming both ammonium sulfate (D=100 nm) and sodium chloride (D=200 nm) (Fig. 2). In both cases, approximately 10-25% of activated CCN had α roughly 10-15× lower than that observed for the larger, "high-α" mode. This high-α mode grew at a similar rate to ammonium sulfate and sodium chloride particles generated in the lab.

3. CONCLUSIONS

A distinct and persistent slowly-growing mode was observed representing 10-25% of all CCN, with α 10-15× lower than the rest of the CCN.

NUMERICAL INVESTIGATION OF COLLISION-INDUCED BREAKUP OF RAINDROPS. PART I: METHODOLOGY AS WELL AS DEPENDENCIES ON COLLISION ENERGY AND EXCENTRICITY

J. Schlottke[1] , W. Straub[2] , K. D. Beheng[2] and B. Weigand[1]

[1] Institut für Thermodynamik der Luft- und Raumfahrt (ITLR), Universität Stuttgart, Pfaffenwaldring 31, 70569 Stuttgart, Germany, e-mail: jan.schlottke@itlr.uni-stuttgart.de

[2] Institut für Metereologie und Klimaforschung, Universität Karlsruhe/Forschungszentrum Karlsruhe, Hermann-von-Helmholz-Platz 1, 76344 Eggenstein-Leopoldshafen, Germany, e-mail: winfried.straub@imk.fzk.de

Numerical investigations of binary raindrop collisions, comprising the drop pairs of Low and List (1982a), have been performed using a DNS tool based on the Volume-of-Fluid method. Looking at the coalescence efficiencies as well as the number and sizes of the fragment droplets, both agreement and discrepancies between the numerical simulations and the experimental data of Low and List (1982a) are observed. The results show that the size distribution of fragments is dependent on the collision energy and is shifted to smaller fragments for higher energies. In the second part of this paper, Straub et al. (2008) present new parameterizations of coalescence efficiencies and fragment size distributions based on the results obtained.

1 INTRODUCTION

Collision-induced breakup resulting from binary collisions of large raindrops is considered to be the principal mechanism limiting the size of raindrops (Pruppacher and Klett 1997). During this process, two raindrops that are moving at different velocities temporarily coalesce into one larger drop. The final outcome can be a single large raindrop or remnants of the original raindrops with a number of secondary droplets of different sizes. Comprehensive experimental investigations habe been presented in the past by Low and List (1982a) who, however, concentrated on very few drop pairs. Consequently the data base from which parameterizations have been derived is rather small and incomplete. Furthermore, the parameters relevant to this process like droplet velocity, droplet size, and most notably collision excentricity could not be determined with high accuracy. To overcome these deficiencies Beheng et al. (2006) have performed numerical experiments by computational simulations of binary collisions for same drop pairs as Low and List (1982a) and for some more drop pairs. The present study is a further extension of the work of Beheng et al. (2006) by again increasing the range of drop pair combinations and by additionally investigating the influence of excentricity and impact energy. To this end, the DNS-CFD code FS3D (Free Surface 3D) which has been developed at ITLR is applied. It solves the incompressible Navier-Stokes equations and employs the Volume of Fluid (VOF) method to account for multiple phases. The free surface is reconstructed using the PLIC method and the convective transport is based on this reconstruction.

2 FORMULATION AND NUMERICAL METHOD

The applied code FS3D has been used for numerous investigations of drop dynamics in the past and is well validated. Gotaas et al. (2007) for example studied the effect of viscosity on binary droplet collisions, Rieber and Frohn (1999) simulated the process of drops splashing onto a liquid film.

2.1 Governing Equations

The representation of different phases is based on the Volume of Fluid (VOF) method by Hirt and Nichols (1981). In order to distinguish between the liquid and the gaseous phase, the additional field variable f is introduced. f is defined as

$$f(\mathbf{x},t) = \begin{cases} 0 & \text{in the gaseous phase} \\ 0 < f < 1 & \text{in cells containing a part of the interface} \\ 1 & \text{in the liquid phase} \end{cases} \tag{1}$$

and is transported by

$$\frac{\partial f}{\partial t} + \nabla \cdot (f\mathbf{u}) = 0. \tag{2}$$

In order to maintain a sharp interface, the convective transport of f is performed based on the reconstructed interface using the Piecewise Linear Interface Calculation (PLIC) method by Rider and Kothe (1998), thus minimizing numerical diffusion.

The governing balance equations for momentum read

$$\begin{aligned}\frac{\partial(\rho\mathbf{u})}{\partial t}+\nabla\cdot(\rho\mathbf{u})\otimes\mathbf{u} &= -\nabla p+\rho\mathbf{k}\\ &+\nabla\cdot\left[\mu\left(\nabla\mathbf{u}+(\nabla\mathbf{u})^T\right)\right]+\mathbf{f}_\gamma \quad (3)\end{aligned}$$

where $\mathbf{k}$ represents an external body force (e.g. gravity). The surface tension is included by the volume force $\mathbf{f}_\gamma$.

The continuity equation for the considered incompressible flow is given by

$$\nabla\cdot\mathbf{u}=0. \quad (4)$$

The local fluid properties are obtained by applying the *one-field* formulation. Viscosity and density are hence calculated by

$$\mu(\mathbf{x},t) = \mu_l f(\mathbf{x},t)+(1-f(\mathbf{x},t))\mu_g, \quad (5)$$
$$\rho(\mathbf{x},t) = \rho_l f(\mathbf{x},t)+(1-f(\mathbf{x},t))\rho_g. \quad (6)$$

2.2 Spatial and Temporal Discretization

The spatial discretization of the equations is done using the Finite Volume method on a staggered grid and is of second order accuracy. The temporal integration is performed using the Crank-Nicholson method. A fast and robust multigrid solver is used for the projection of the velocity field onto one fulfilling eq. (4).

3 NUMERICAL SETUP AND SIMULATION PROCEDURE

All presented simulations were performed using a 3D computational domain with free-slip condition on the lateral walls and periodic boundary conditions on the bottom and top walls. This setup permits a numerically justifiable effort for the large number of conducted simulations as the collision process can be observed for a rather long time period using a limited computational grid. The spatial resolution was chosen to be 100 µm for all cases except investigations on grid dependency where a spatial resolution of 50 µm has been applied. According to the drops' sizes, different grids were employed, resulting in approx. 16×10^6 cells for the largest one (2.56^3 cm^3) used for standard calculations and nearly 135×10^6 cells for grid dependency investigations.

For the initial placement and velocities v of the drops, terminal fall velocities have been calculated following Beard (1976). The vertical distance between the drops was set to $\Delta y = v\Delta t$ with Δt=0.5ms, allowing for an interaction of the drops with their surrounding flow field to some extent. The nonspherical shape of large drops was

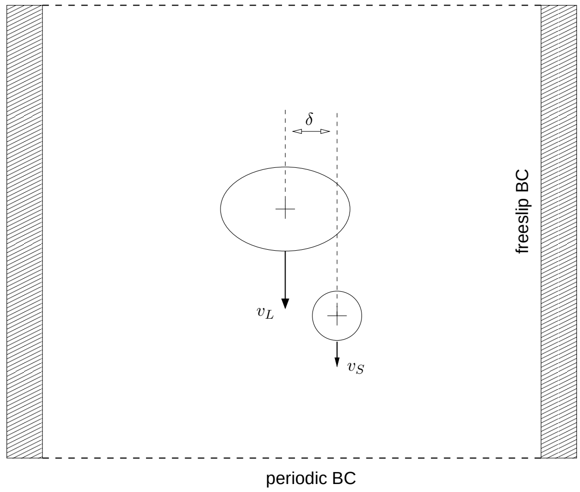

Figure 1: Numerical setup

considered by initializing them as ellipsoids with the ratio of the equatorial radii to the polar radius according to Beard and Chuang (1987). The excentricity of the droplet collisions, defined as the ratio of the distance of the drops' centers δ to the arithmetic mean of their diameters d (with subscripts L and S for the large and the small drop, respectively)

$$\epsilon=\frac{2\delta}{d_L+d_S} \quad (7)$$

has been varied from 0.05 to 0.95 with six different excentricities (ϵ=0.05, 0.2, 0.4, 0.6, 0.8, 0.95). The initial setup is sketched on a plane through the drops' centers in figure 1. Material properties for water and air were chosen at 20° C with a surface tension of σ=73×10^{-3} N/m.

The simulations were performed until a stable outcome of the collision process was reached. This condition was assumed to be fulfilled by a visual assessment of the results especially with the number of fragments becoming stationary. The number and size of the fragments were then determined by the use of a region growing approach. Mass conservation was satisfied for all cases. In order to compare to data from literature, the obtained results for different excentricities have been weighted according to their probability.

4 RESULTS

Overall, 32 drop pairs were investigated. Details of the drop diameters, the collision and surface energy and the resulting Weber number are given in table 1, an overview of the drop pairs considered is shown by figure 2. The 10 drop pairs investigated by Low and List (1982a) are included and listed as numbers 1-10 in table 1, those additionally simulated by Beheng et al. (2006) as 11-18; the remaining drop pairs (19-32) are considered to cover the pairs' matrix as complete as

No.	d_L	d_S	CKE	S_c	We	No.	d_L	d_S	CKE	S_c	We
1	0.18	0.04	0.33	0.75	0.44	17	0.32	0.04	0.73	2.35	0.31
2	0.4	0.04	0.86	3.67	0.23	18	0.41	0.14	9.6	3.96	2.43
3	0.44	0.04	0.9	4.44	0.2	19	0.24	0.06	1.29	1.33	0.97
4	0.18	0.07	0.92	0.77	1.19	20	0.3	0.07	2.43	2.08	1.17
5	0.18	0.1	0.99	0.83	1.2	21	0.36	0.07	2.97	2.99	0.99
6	0.3	0.1	4.18	2.11	1.98	22	0.45	0.07	3.43	4.66	0.74
7	0.36	0.1	5.46	3.01	1.81	23	0.12	0.1	0.07	0.45	0.15
8	0.46	0.1	6.62	4.89	1.35	24	0.41	0.1	6.18	3.89	1.59
9	0.36	0.18	8.55	3.21	2.66	25	0.25	0.12	3.14	1.54	2.04
10	0.46	0.18	12.53	5.04	2.48	26	0.3	0.12	5.04	2.15	2.34
11	0.06	0.04	0.01	0.09	0.12	27	0.36	0.12	6.93	3.05	2.28
12	0.12	0.04	0.12	0.34	0.35	28	0.46	0.12	8.7	4.91	1.77
13	0.12	0.06	0.24	0.36	0.68	29	0.36	0.14	8.07	3.09	2.61
14	0.25	0.04	0.55	1.44	0.38	30	0.18	0.16	0.13	1.06	0.12
15	0.24	0.09	2.36	1.37	1.73	31	0.41	0.16	10.62	4.01	2.65
16	0.27	0.15	3.93	1.86	2.11	32	0.25	0.18	1.88	1.77	1.06

Table 1: Investigated drop pairs, d_L and d_S in [cm], CKE and S_c in [µJ]

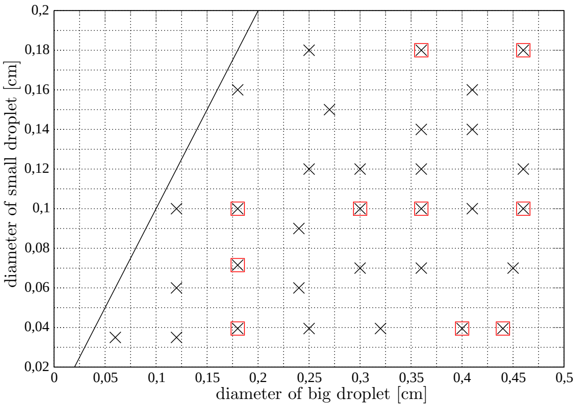

Figure 2: Investigated drop pairs; red squares indicate the pairs studied by Low and List (1982a).

possible.

The collision energy of the drop pairs CKE is calculated by (ρ_l = bulk density of water)

$$CKE = \frac{\pi}{12}\rho_l \frac{d_L^3 d_S^3}{d_L^3 + d_S^3}\left(v_L - v_S\right)^2, \qquad (8)$$

the surface energy S_c of the coalesced system is given by

$$S_c = \pi\sigma\left(d_L^3 + d_S^3\right)^{2/3}. \qquad (9)$$

The Weber number We is the ratio of the aforementioned energies

$$We = \frac{CKE}{S_c}. \qquad (10)$$

4.1 Collision Outcomes

Results are shown exemplarily in figures 3 and 4 for two different drop pairs with 5 collision excentricities, respectively. The two pairs of drops chosen for this comparison have high (Pair 10, CKE=12.53 µJ) and low (Pair 16, CKE=3.93 µJ) collision energies.

For Pair 10 shown in figure 3 the dependency of the breakup mode on excentricity is evident. As it can be expected for the considered collision energy, there is disc breakup for ϵ=0.05 and ϵ=0.2, resulting in numerous small droplets of different sizes after the collision process. For ϵ=0.4 and ϵ=0.6, the breakup mode is sheet breakup and the size distribution of the secondary droplets is more homogeneous. For ϵ=0.8 and ϵ=0.95 (not shown), finally, there is filament breakup, the initial drops persist after the collision process with almost no change in drop size. Moreover some additional, very small droplets are produced. An overview on the mentioned dependency is also shown in figure 9 for the discussed droplet pair and two supplemental pairs with lower collision energies.

The collision outcomes for Pair 16 are shown in figure 4. For ϵ=0.05 and ϵ=0.2 the two drops form a single larger permanent drop after collison. For the other excentricities, there is filament breakup with no additional droplets for ϵ=0.4 and ϵ=0.8; some small secondary droplets are produced for ϵ=0.6.

4.2 Budget of Energy

To get a picture of the evolution of energies during a collision process, the temporal development

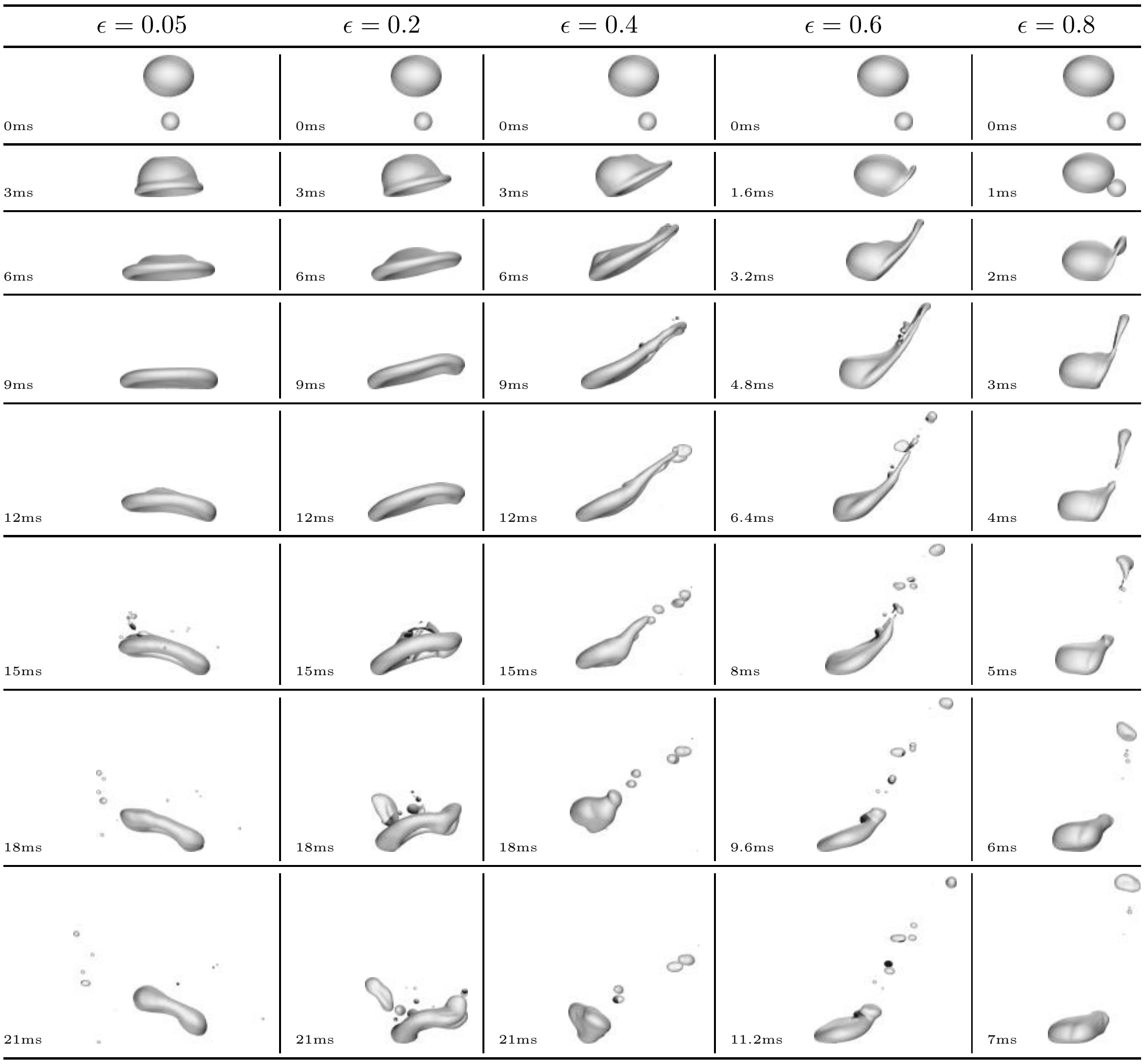

Figure 3: Snapshots of droplet collisions at different times, Pair 10 (CKE=12.53µJ)

of the kinetic energy of the fluid contained in the system, the surface energy and the surface area is depicted for Pair 26, ϵ=0.6, in figure 5. Gravity was set to zero for this consideration. The appropriate images of the collision process are presented in figure 6. The surface energy is obtained as the product of surface area and surface tension. For convenience, both the initial surface energy and the initial kinetic energy are plotted starting from zero.

Looking at the surface area and energy, there is a sudden drop as the drops coalesce. This area reduction is caused by the contact of the two drops and the merging of their surfaces. Subsequently, the relative velocity leads to a strong deformation of the generated larger drop whereas the surface area is increased by about 50 %. That is followed by the separation into one large drop and several smaller droplets where the drops attain a roughly spherical shape and oscillate.

The kinetic energy decreases at first during the aggregation phase of the drops. Then it increases again and reaches a momentary maximum as the liquid disintegrates and surface energy gets transformed. Subsequently, the kinetic energy is continuously reduced, presumably caused by viscous dissipation due to the inner flowfield of the drops and interaction with the surrounding gas.

4.3 Coalescence Efficiency

The coalescence efficiency E_c is defined as the propability of coalescence for a binary collision process with a single drop resulting. For an experimental study consisting of numerous repetitions for one drop pair, E_c is obtained by dividing the number of collisions leading to coalescence c_c by

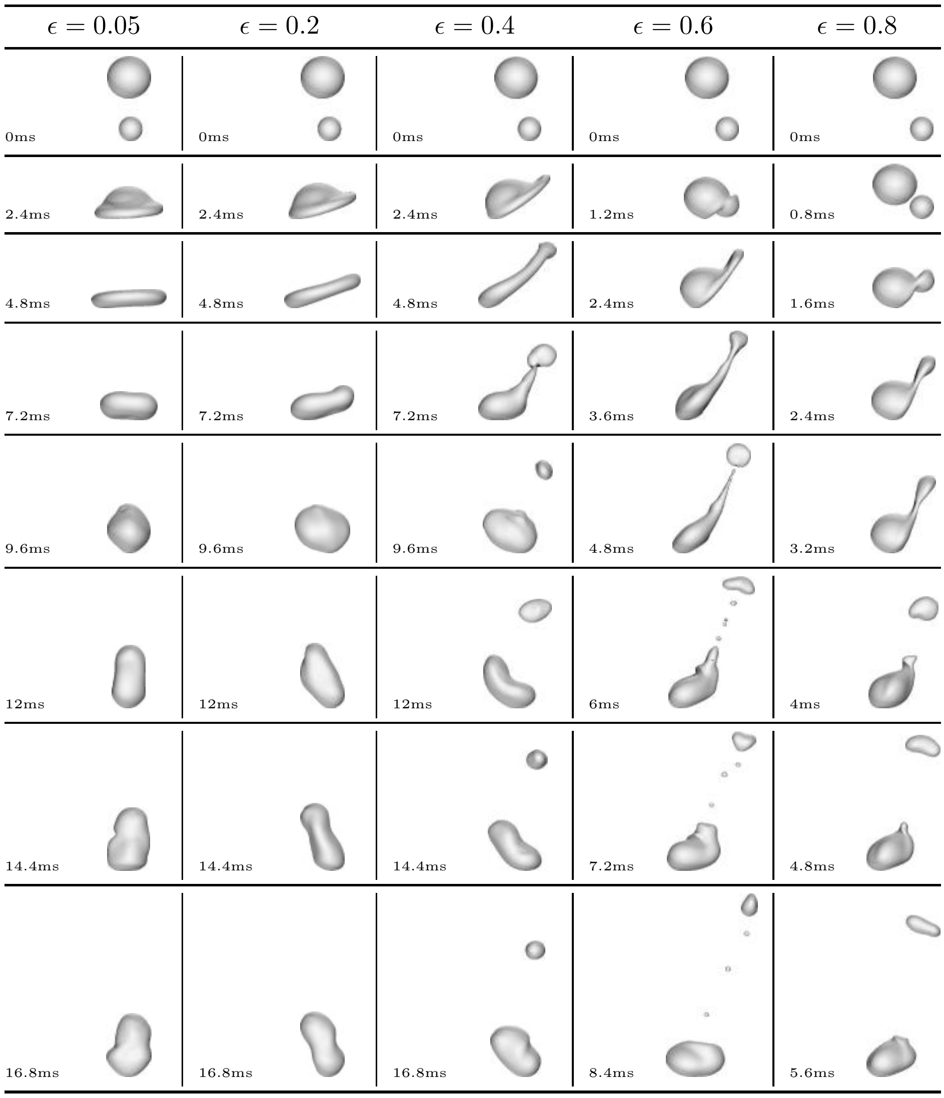

Figure 4: same as figure 3 but for Pair 16 (CKE=3.93µJ)

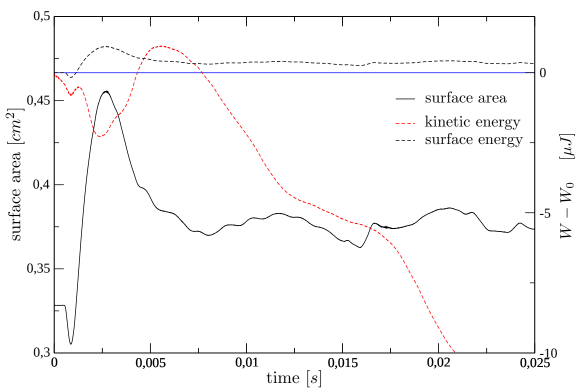

Figure 5: Temporal evolution of kinetic energy, surface energy and surface area for drop pair 26, ϵ=0.6; left ordinate: surface area, right ordinate: energies

the total number of collisions c:

$$E_c = c_c/c. \tag{11}$$

It should be mentioned that an equipartition of collisions over the collision cross section (collision excentricities) is assumed for this approach. Keeping in mind the strong dependency of collision outcomes on excentricity, experimental results for E_c seem to be quite sensitive to systematic errors influencing the aforementioned equipartition.

On the other hand, collisions with six different excentricities per drop pair were investigated numerically for the present study. Here, each collision is representing all collisions taking place in the according annulus of the projected collision cross section (circle with radius $r_L + r_S$). The result for one excentricity ϵ_i is weighted with the area of the corresponding annulus (δ_i = separa-

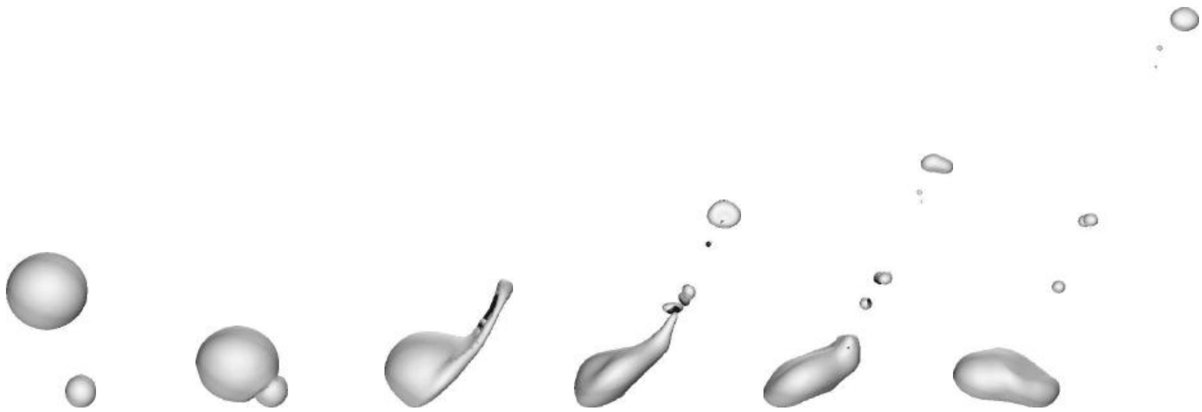

Figure 6: Collision process of Pair 26, ϵ=0.6

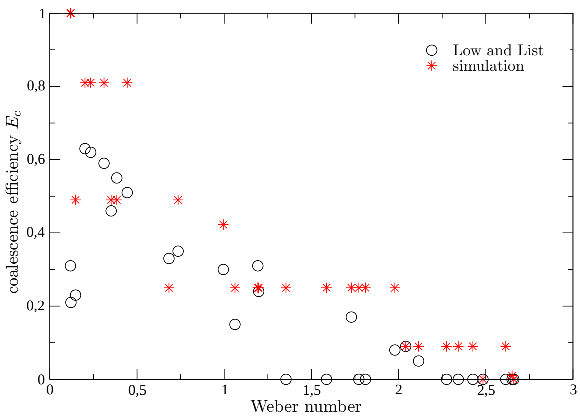

Figure 7: Coalescence efficiency vs. Weber number for all drop pairs. Numerically obtained results (stars) and values from the parameterization by Low and List (1982b) (circles)

tion distance, cf. figure 1)

$$A_{\circledcirc,i} = 2\pi\delta_i\Delta\delta_i = 2\pi\left(r_L + r_S\right)^2 \epsilon_i\Delta\epsilon_i. \qquad (12)$$

Hence the coalescence efficiency is calculated by

$$\begin{aligned} E_c &= \sum_{ic} A_{\circledcirc,ic} / \sum_i A_{\circledcirc,i} \\ &= \sum_{ic} \epsilon_{ic}\Delta\epsilon_{ic} / \sum_i \epsilon_i\Delta\epsilon_i \qquad (13) \end{aligned}$$

where ic identifies excentricities for which coalescence occurs.

The results for the investigated drop pairs are plotted in figure 7 as function of the Weber number. Values obtained by the parameterization of Low and List (1982b) are shown additionally. Here, the agreement is quite good. Looking at the experimental values, there are several outliers with E_c=0 that do not seem physical; they are not reproduced by the numerical results. For small Weber numbers, the deviation between numerical and experimental values is increasing. Whereas the coalescence efficiency of the simulations is approaching 1, the efficiency given by the Low and List parameterization is dropping to values of approximately 0.3. This behaviour can be explained by the illegitimate application of the parameterization to the region of very low collision energies which has not been investigated by Low and List. For the numerical results on the other hand, the bouncing process taking place for very low relative velocities can not be simulated due to the employed numerical method, thus leading to values of E_c which are too large.

4.4 Number of Fragments and Fragment Size Distribution

The mean number of fragments $\overline{n}$ is calculated analogously to the coalescence efficiency E_c:

$$\overline{n} = \sum_i n_i\epsilon_i\Delta\epsilon_i / \sum_i \epsilon_i\Delta\epsilon_i. \qquad (14)$$

The spectral number $\overline{p_j}(D_j)$, representing the number of fragments in the diameter interval $D_j \pm \Delta D_j/2$, is given by

$$\overline{p_j} = \frac{\sum_i n_{j,i}\epsilon_i\Delta\epsilon_i / \sum_i \epsilon_i\Delta\epsilon_i}{\Delta D_j} \qquad (15)$$

where $n_{j,i}$ is the number of fragments for excentricity i encountered in the according diameter interval.

The mean number of fragments obtained for all investigated drop pairs is depicted in figure 8 together with values calculated by the Low and List parameterization. The development is very similar for both cases. However, the numerically obtained values are slightly smaller than those from the experiments, mainly for high collision energies. This is, amongst other reasons, due to an insufficient spatial resolution of the computational domain. As shown below in section 4.6, the numerical results are not grid independent with respect to the generation of very small fragment

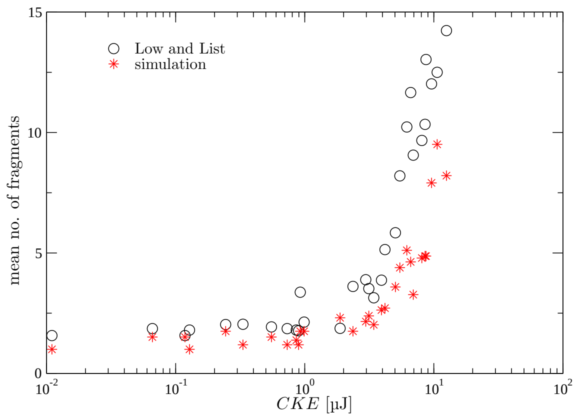

Figure 8: Mean number of fragments vs. collision energy found from the numerical simulations (stars) and from the experiments of Low and List (1982a)

droplets which appear numerously for high collision energies.

Fragment size distributions in spectral resolution are shown for all investigated drop pairs in appendix A. The comparison to the Low and List parameterization shows both agreement as well as discrepancies. Whereas the agreement between numerical and experimental results is good for emerging larger fragments, large deviations can be observed especially for very small fragments. This finding can be explained by the already mentioned grid dependency. On the other hand, the experimental results may have been influenced by systematic errors which is particularly important if one takes into account the strong dependency on excentricity as it is shown in the following section.

4.5 Influence of Excentricity

The number of fragments versus excentricity is plotted exemplarily in figure 9 for 3 pairs with different CKE.

As already stated, there is a strong influence of the collision parameter excentricity on the collision outcome. However, this statement is not unambiguous. Looking at high collision energies, a disc mode breakup occurs for low excentricities and multiple small fragments are produced. Increasing excentricity leads to a decreasing number of secondary droplets until the initial drops persist for a grazing collision.

On the other hand, the behaviour in case of medium and low collision energies is contrary. While the two drops coalesce for almost central collisions and persist for grazing collisions, a number of fragment droplets is produced in between.

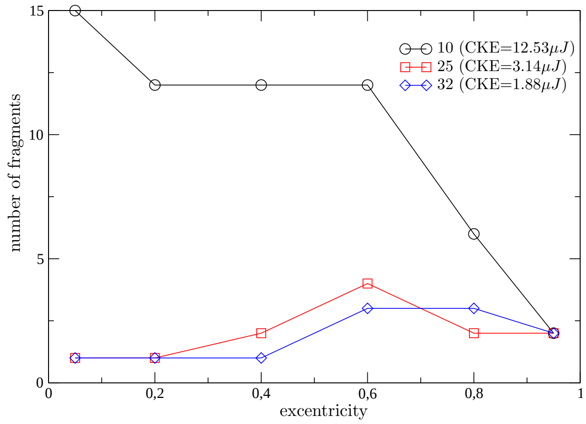

Figure 9: Fragment number vs. excentricity for pairs of different CKE as indicated

4.6 Assessment of Results

Assessing the obtained numerical results, various factors have to be considered. The most relevant ones seem to be both the spatial resolution and the boundary conditions.

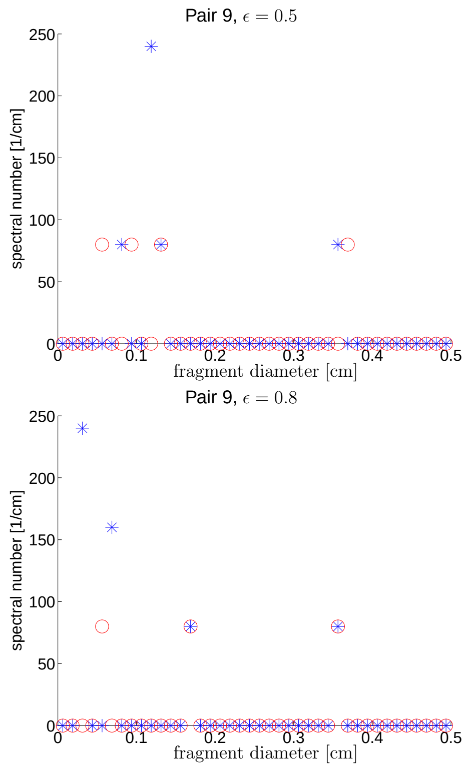

Figure 10: Influence of spatial resolution for pair 9, $\epsilon = 0.5$ and $\epsilon = 0.8$. $\Delta x = 100$µm (red circles) and $\Delta x = 50$µm (blue stars).

In order to elucidate the grid dependency of the results, particular cases have been simulated with doubled spatial resolution, resulting in $\approx 135 \times 10^6$ control volumes. The results for the standard resolution (Δx=100µm) and the fine resolution (Δx=50µm) are shown in figure 10 for Pair 9, ϵ=0.5 and ϵ=0.8. It is well known that the ability of the Volume of Fluid method which is employed for tracking the interface to correctly reproduce the physical behaviour of small ligaments is quite sensitive to the spatial resolution of the grid. This fact is reflected by the presented results. For both excentricities, there is a higher number of small fragments in case of finer grid resolution. For larger fragments, however, it is important to point out that there is only a minor discrepancy of results applying either a fine or a coarse grid. From a physical point of view it seems feasible to apply a lower radius limit of fragment droplets to be considered as very small droplets may evaporate quickly and thus do not contribute to the coalescence-collision process.

As for the boundary conditions, the drawback of the presented approach with periodic boundary conditions is that the drops are falling in their own wake which is of major importance to large droplets where the aerodynamic influence of the oncoming flow plays an important role for the deformation and the breakup process. Future investigations will therefore be performed with a moving frame of reference, thus facilitating a natural flow approaching the drops.

5 CONCLUSION, PERSPECTIVE

The collision process of different pairs of raindrops has been investigated numerically. The drop pairs studied by Low and List (1982a) are amongst the considered pairs. Comparing to their experimental results, there are both agreement as well as discrepancies.

Future investigations will focus on the use of a moving frame of reference with a specific inflow boundary condition. Thus, more realistic simulations are expected. Clearly the according simulations will significantly increase the numerical efforts.

The results presented in this paper are used by Straub et al. (2008) to create a new parameterization of coalescence efficiencies and fragment size distributions.

ACKNOWLEDGEMENT

The simulations were performed on the national super computer NEC SX-8 at the High Performance Computing Center Stuttgart (HLRS) under the grant number FS3D/11142. The authors also gratefully acknowledge support by the German Research Foundation (DFG) under grants BE 2081/7-1 and WE 2549/17-1 in the framework of the priority program Quantitative Precipitation Prediction.

NOMENCLATURE

CKE	collision energy	J
c_c	no. of coll. leading to coalescence	-
c	total number of collisions	-
d	(volume equivalent) diameter	m
D	fragment diameter	m
E_c	coalescence efficiency	-
f	VOF variable	-
$\mathbf{f}_\gamma$	surface tension term	N/m^3
$\mathbf{k}$	body force (gravity)	m/s^2
m	mass	kg
n	number of fragments	-
$\overline{n}$	mean number of fragments	-
p	pressure	Pa
$\overline{p_j}$	spectral number	1/m
r	radius	m
S_c	surface energy	J
t	time	s
$\mathbf{u}$	velocity	m/s
v	vertical velocity	m/s
W	energy	J
$\mathbf{x}$	position	m
Δx	grid resolution	m

Greek

δ	distance	m
ϵ	excentricity	-
μ	viscosity	kgm/s
ρ	density	kg/m^3
σ	surface tension	N/m

Dimensionless quantities

We	Weber number	$(= CKE/S_c)$

Subscripts

0	initial
g	gas
i, j	indices
l	liquid
L	large droplet
S	small droplet

REFERENCES

K. V. Beard. Terminal velocity and shape of cloud and precipitation drops aloft. *J. Atmos. Sci.*, 33:851–864, 1976.

K. V. Beard and C. Chuang. A new model for the equilibrium shape of raindrops. *J. Atmos. Sci.*, 44:1509–1511, 1987.

K. D. Beheng, K. Jellinghaus, W. Sander, N. Roth, and B. Weigand. Investigation of collision-induced breakup of raindrops by numerical simulations: First results. *Geophys. Res. Lett.*, 33, 2006.

C. Gotaas, P. Havelka, H. Jakobsen, H. Svendsen, M. Hase, N. Roth, and B. Weigand. Effect of viscosity on droplet-droplet collision outcome: Experimental study and numerical comparison. *Phys. Fluids*, 19, 2007.

C.W. Hirt and B.D. Nichols. Volume of fluid (VOF) method for the dynamics of free boundaries. *J. Comput. Phys.*, 39:201–225, 1981.

T. B. Low and R. List. Collision, coalescence and breakup of raindrops: Part i: Experimentally established coalescence efficiencies and fragment size distribution in breakup. *J. Atmos. Sci.*, 39:1591–1606, 1982a.

T. B. Low and R. List. Collision, coalescence and breakup of raindrops: Part ii: Parameterization of fragment size distributions. *J. Atmos. Sci.*, 39:1607–1618, 1982b.

H. R. Pruppacher and J. D. Klett. *Microphysics of Clouds and Precipitation*. Springer, New York, 1997.

W.J. Rider and D.B. Kothe. Reconstructing volume tracking. *J. Comput. Phys.*, 141:112–152, 1998.

M. Rieber and A. Frohn. A numerical study on the mechanism of splashing. *Int. J. Heat Fluid Flow*, 20:455–461, 1999.

W. Straub, J. Schlottke, K. D. Beheng, and B. Weigand. Numerical investigation of collision-induced breakup of raindrops. part ii: Parameterizations of coalescence efficiencies and fragment size distributions. In *ICCP*, 2008.

A Spectral numbers

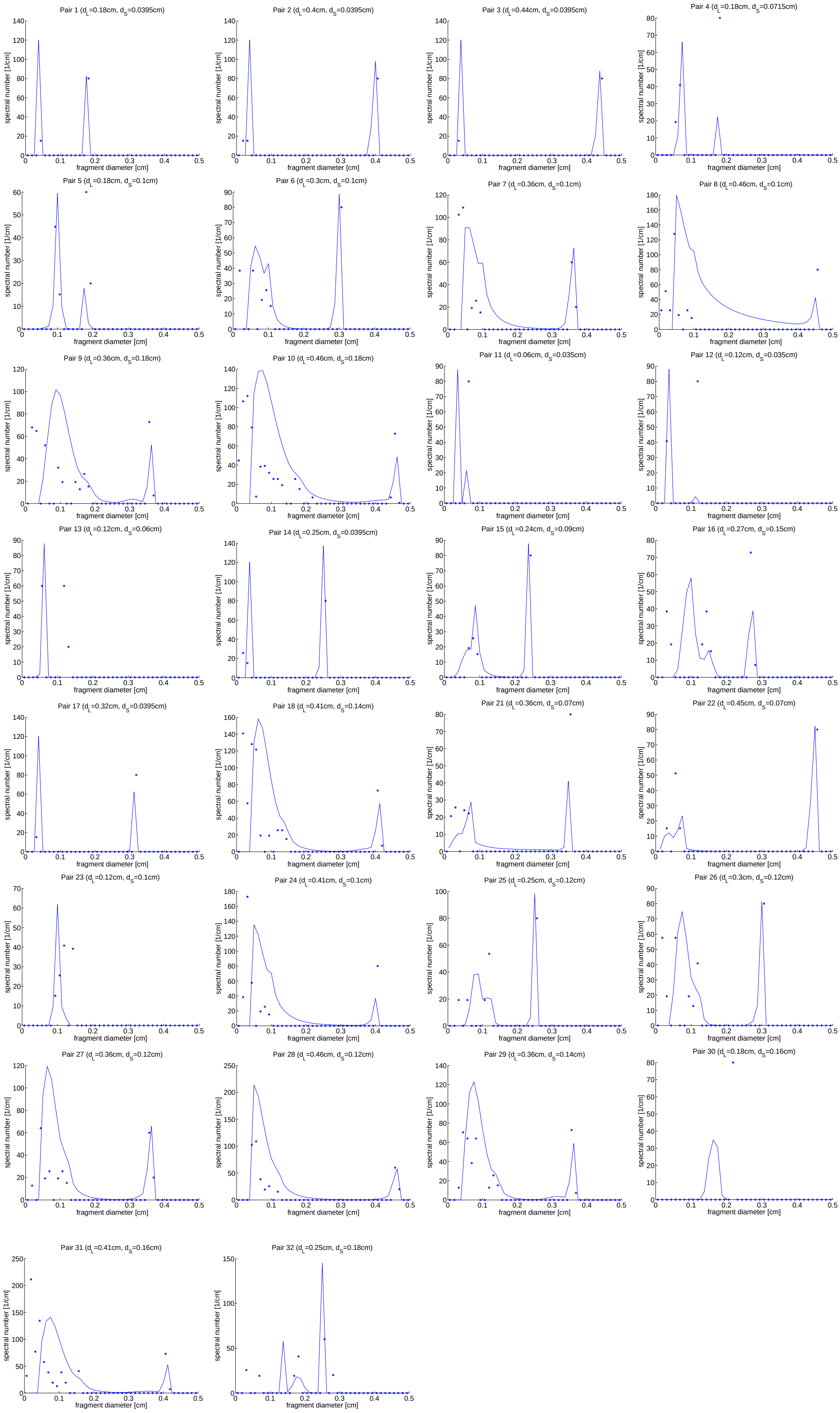

Figure 11: Spectral numbers of fragments as function of fragment diameter for d$_L$ and d$_S$ as indicated. Stars denote present results, lines those according to the parameterization of Low and List (1982b).

VERTICAL SUPERCOOLED CLOUD TUNNEL STUDIES ON THE GROWTH OF DENDRITIC SNOW CRYSTALS

Tsuneya Takahashi[1], Norihiko Fukuta[2] and Takayuki Hashimoto[3]

[1] Hokkaido Univ. of Education, Sapporo, 002-8501, Japan
[2] Univ. of Utah, Salt Lake City, Utah 84112-0110, USA
[3] New Peak Film Inc., Sapporo, 062-0901, Japan

1. INTRODUCTION

Snow crystals grow by vapor diffusion while falling in the atmosphere. This process is known to play important roles in various weather phenomena.

Laboratory studies of snow crystal habits have been carried out in a static cloud chamber, in which ice crystals have been grown on a hair or a fiber (Nakaya, 1954; Hallett and Mason, 1958; Kobayashi, 1961). These studies revealed that a crystal habit is determined mainly by temperature and that the complicated secondary features depend on the supersaturation of water vapor in air; however, information regarding the free-fall behavior of a snow crystal during its growth could not be obtained. On the other hand, simulation experiments of ice crystal growth under free-fall conditions have been carried out by many researchers (Fukuta 1969; Ryan et al. 1974, 1976; Michaeli and Gallily 1976; Song and Lamb 1994a). Unfortunately, these experiments were carried out for a time period of less than 4 min; experimental studies carried out over much longer growth periods are required to better understand the growth of snow crystals.

Corresponding author address:
Tsuneya Takahashi, Hokkaido Univ. of Education, Sapporo 002-8501, JAPAN

For simulating the growth of a snow crystal in the atmosphere, vertical supercooled cloud tunnels were developed with the second author as the central figure (Fukuta 1980; Fukuta et al. 1982, 1984; Takahashi and Fukuta 1988; Takahashi et al. 1991; Fukuta and Takahashi 1999). The tunnel was distinguished by the Lagrangian way; that is, a single snow crystal could be suspended continuously in front of an experimenter. In these tunnels, the growth of an isolated snow crystal under free-fall conditions was studied for up to 30 min of growth.

In this paper, we show the results of a 30-min dendritic snow crystal growth on a high-definition-television (HDTV) film. With respect to the growth of dendritic snow crystals, Takahashi and Endoh (2000) pointed out that growth enhancement by the cloud droplets that coexist with a snow crystal was essential in addition to the ventilation effect. In order to discuss the growth enhancement, research has been carried out to make up for the data deficiency by continuing and extending the work. In this study, we have also addressed the conditions of temperature and liquid water content necessary for the dendritic growth.

2. EXPERIMENTS

The present study was carried out in a

vertical wind tunnel at Sapporo, Japan, in which a snow crystal could be suspended freely and grown in a vertical stream of artificially generated supercooled cloud by applying aerodynamical mechanisms for horizontal stability. A convergent configuration of the working/observation section provides excellent horizontal stability for the crystal suspension; vertical stability is not suitable because the upward wind velocity increases from the bottom to the top. Therefore, the upward wind velocity at the holding position is ceaselessly adjusted to the terminal fall velocity of the floating snow crystal by constantly manipulating the velocity control valves. The snow crystal fluctuates vertically because of the repeated and slight overshooting of the holding position of the snow crystal. Here, a video of a dendritic snow crystal grown in the tunnel for 30 min was taken using a HDTV camera by the third author who is a professional TV cameraman.

Further, for investigating the characteristics of the dendritic crystal growth in a cloud, experiments were carried out for 10 min under isothermal and water-saturated conditions from –12°C to –16.5°C with constant liquid water contents between 0 and 1.2 g m^{-3}. The concentration of fog was controlled by adjusting impressed voltage to an ultrasonic atomizer. The liquid water content was calculated from the air temperature, and the dew point of air was obtained by evaporating the cloud. The air temperature and the dew point were continuously monitored by a thermistor thermometer and a quartz dew point hygrometer, respectively. The vapor pressure corresponding to the dew point was calibrated at ice saturation. In this case, the acceleration of the falling crystal was zero: a condition was achieved by lowering the impressed voltage provided to the atomizer in the course of the experiment. The cloud droplet size distri-

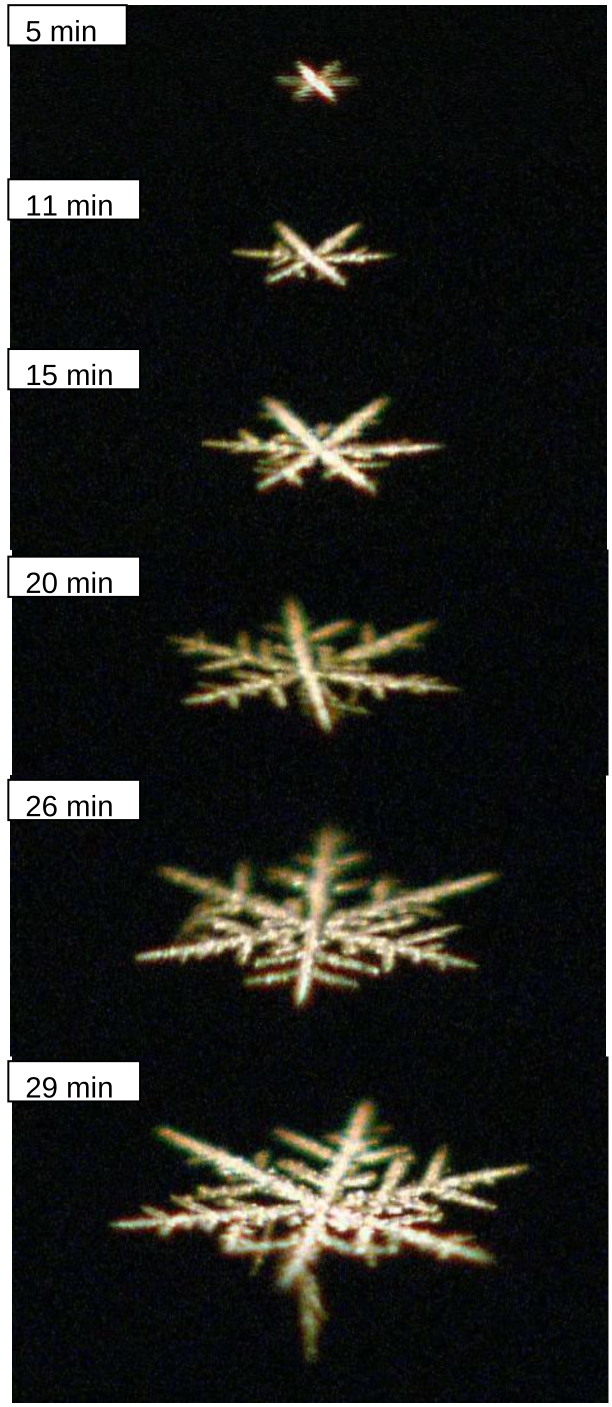

Fig. 1. The growth of a dendritic snow crystal with time up to 30 min at –15.0°C. The crystal was suspended in a vertical stream of supercooled cloud. The growth time is shown for each stage. The stills were extracted from a video taken using a HDTV camera.

Fig. 2. Spatial dendritic branch grown downward. The crystal is the same as that shown in Fig. 1. The growth time is 29 min.

butions were measured by an impaction method. The diameters of more than 60% of the droplets ranged from 5 to 10 µm, and the average diameter was approximately 8 µm; these conditions varied little with the changes in the liquid water content.

3. RESULTS AND DISCUSSION

The HDTV video of a snow crystal grown in the tunnel at –15.0°C for 30 min was analyzed. Figure 1 shows the growth of a dendritic snow crystal with time. The secondary branches started growing at 10 min and were well developed at 20 min. After about 20 min, a spatial branch also grew downward as shown in Fig. 2. Looking at the crystal from above, it was observed that the crystal rotated clockwise before 16 min of growth and anticlockwise after 18 min; from 16 min to 18 min, the rotation stopped. The rotation rate varied: for example, 1.9 times per minute at 15 min of growth and 23 times per minute at 30 min of growth. The rotation appeared to be caused by the asymmetry of the crystal-shaped pattern around the c-axis or around the vertical air streamline.

Figure 3 shows the variation in crystal dimension along the a-axis with the growth

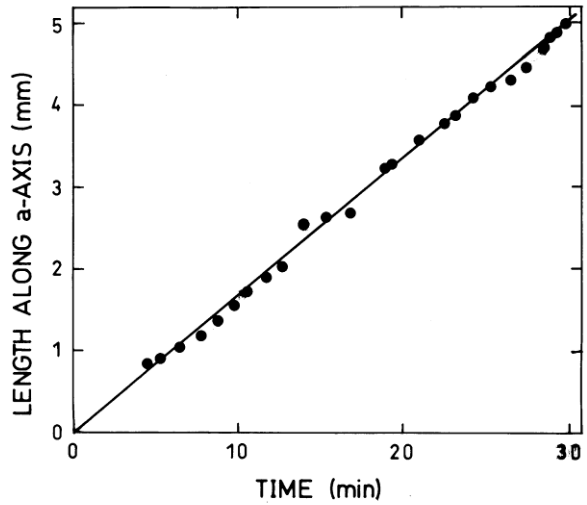

Fig. 3. Variation in dimension of the snow crystal as shown in Fig. 1 along the a-axis with increasing growth time.

time. The dimension of the crystal was approximately proportional to time, and the crystal reached a diameter of 5 mm after 30 min of growth; this size is almost equal to the maximum size of natural dendritic snow crystals.

The variation in the crystal fall velocity with time is shown in Fig. 4. There were velocity fluctuations within 1.5 cm s^{-1} because of the vertical instability, as mentioned in the previous section. The variation was expressed by a curve that was convex upward

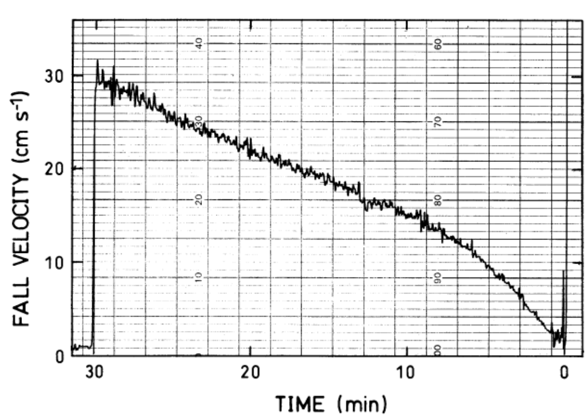

Fig. 4. Variation in fall velocity of the snow crystal as shown in Fig.1 with time.

up to about 7 min of growth and thereafter a straight line. This was probably because the drag increased due to the change in the shape of the crystal from a plate to a dendrite in the first stage, and a dendrite continued to grow in the second stage, as pointed out by Takahashi et al. (1991). Contrary to the observations of Nakaya and Terada (1935), the fall velocity did not become constant when the dendrite grew large.

The variation in crystal shapes formed at different temperatures between –12°C and –16.5°C and the liquid water contents between 0 to 1.2 g m^{-3} after 10 min of growth are summarized in Fig. 5. The crystal shape depended on the liquid water content in the temperature range of –12.3°C and –13.8°C. The crystal shape shifted from a sector to a broad branch between –12.3°C and –13.2°C, and a broad branch to a dendrite between –13.2°C and –13.8°C with increasing liquid water content: examples of snow crystals are shown in Fig. 6. Further, sectors and plates grew above the temperature of –12.3°C. The lowest temperature limit for the growth of a dendrite was observed to be –15.8°C. Broad branches and sectors grew at temperatures between –15.8°C and –16.2°C and at those below –16.2°C, respectively. Around –16°C, a shift in the shape of the snow crystal with increasing liquid water content was not observed.

Dendritic crystals (dendrites and broad branches) were observed at temperatures ranging from –12.3°C to –16.2°C; this range coincides with the results obtained using a static chamber (Hallett and Mason 1958; Kobayashi 1961). Takahashi et al. (1991) pointed out that the dendritic crystal growth at water saturation between –14°C and –16°C was ascribed to the ventilation effect. It was shown that dendritic crystals grew from –

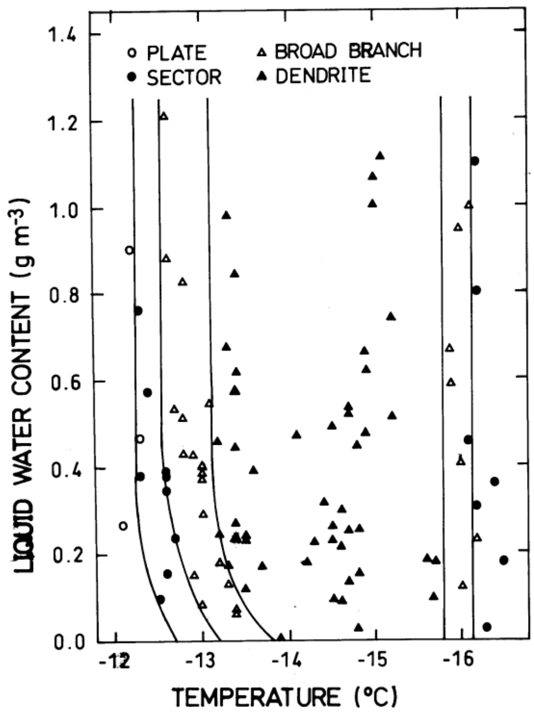

Fig. 5. Shape of a snow crystal as a function of temperature and liquid water content for a growth time of 10 min.

12.3°C to –13.8°C owing to the effect of the existence of supercooled cloud droplets around the crystals in addition to the ventilation effect.

Figure 7 shows the changes in crystal di-

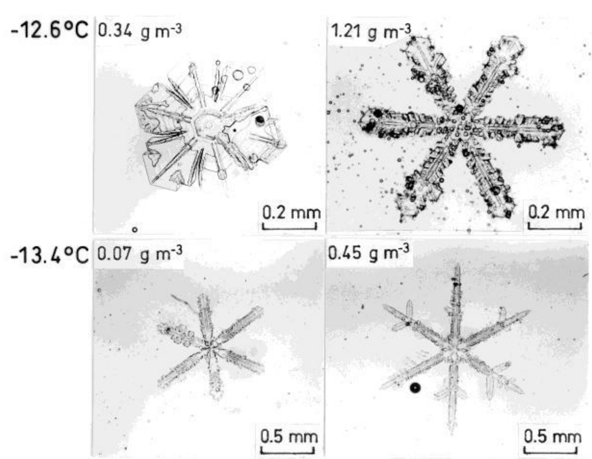

Fig. 6. Snow crystals grown for 10 min at –temperatures of −12.6°C and –13.4°C and different liquid water contents.

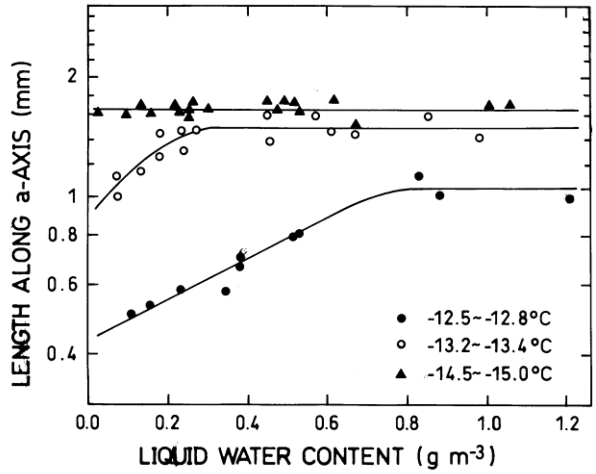

Fig. 7. Changes in crystal dimensions along the a-axis with changes in the liquid water content at various temperatures after 10 min of growth.

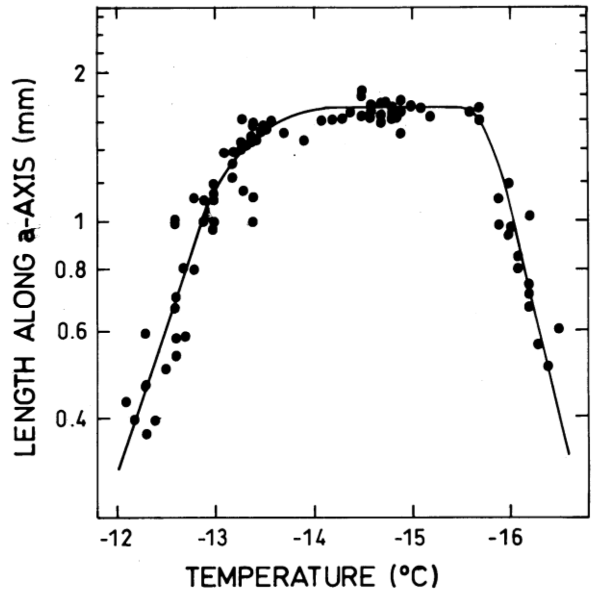

Fig. 8. Variation in crystal dimensions along the a-axis with decreasing temperature at the growth of 10 min.

mension along the a-axis with changes in liquid water content at temperatures ranging from –12.5°C to –12.8°C, from –13.2°C to –13.4°C, and from –14.5°C to –15.0°C after 10 min of growth. The lengths of the snow crystals increased as the cloud became denser up to a liquid water content of about 0.8 g m^{-3} in the first case and about 0.3 g m^{-3} in the second case. However, the length of a dendrite grown between –14.5°C and –15.0°C was independent of the liquid water content. Figure 8 shows the variation in crystal dimensions along the a-axis with a change in temperature at the growth of 10 min. The dimensions of dendrites grown between –14°C and –15.7°C were almost constant, i.e., 1.7 mm for a 10-min growth. Between –12°C and –13.5°C, the data was scattered at constant temperatures because the crystal shape changed with changes in the liquid water content.

4. CONCLUSIONS

The dendritic snow crystal growth was studied by a vertical wind tunnel to simulate the growth of an isolated snow crystal under free fall conditions in a supercooled cloud environment.

A video of a snow crystal grown at –15.0°C for 30 min in the tunnel was taken using a HDTV camera. The dimension of the dendritic crystal grown was approximately proportional to time, and the crystal finally reached a diameter of 5 mm. The crystal rotated. Secondary branches were well developed, and a spatial branch was grown downward. The variation of the fall velocity with time was expressed by a curve that was convex upward up to about 7 min of growth and thereafter a straight line.

Moreover, for investigating the characteristics of the dendritic crystal growth in a cloud, experiments were carried out for 10 min under isothermal and constant water saturation conditions with liquid water contents between 0 and 1.2 g m^{-3} and temperatures between –12°C and –16.5°C. Dendritic crystals appeared between –12.3°C and –16.2°C. With increases in the liquid water content, the crystal shapes changed from a sector to a broad branch between –12.3°C and –13.2°C and from a broad branch to a dendrite between –13.2°C and –13.8°C. In response to the shape enhancements, the crystal dimensions increased as the liquid water content increased; however, the dimensions of the dendrite grown between –14°C and –15.7°C were almost constant regardless of the liquid water contents, i.e., 1.7 mm for a 10-min growth. Takahashi et al. (1991) pointed out that the dendrites grew at water saturation due to the ventilation effect. It was shown that dendritic crystals grew at temperatures ranging from –12.5°C to –14°C owing to the effect of the existence of supercooled cloud droplets around the crystals in addition to the ventilation effect.

REFERENCES

Fukuta, N., 1969: Experimental studies on the growth of small ice crystals. *J. Atmos. Sci.*, **26**, 522-531.

___, 1980: Development of fast falling ice crystals in clouds at –10°C and its consequence in ice phase processes. *Proc. 8th Intl. Conf. on Cloud Phys.*, Clermont-Ferrand, 97-100.

___, N., M. H. Kowa and N. H. Gong, 1982: Determination of ice crystal growth parameters in a new supercooled cloud tunnel. *Preprints Conf. on Cloud Phys*., Chicago, IL, 325-328.

___, A.-S. Wang, 1984: The mechanism development in diffusional ice crystal growth. *Proc. 9th Intl. Conf. on Cloud Phys*., Tallinn, 159-162.

Hallett, J. and B.J. Mason, 1958: The influence of temperature and supersaturation on the habit of ice crystals grown from the vapour. *Proc. Roy. Soc. London*, **A247**, 440-453.

Kobayashi, T., 1961: The growth of snow crystals at low supersaturations. *Phil. Mag.*, **6**, 1363-1370.

Michaeli, G. and I. Gallily, 1976: Growth rates of freely falling ice crystals. *Nature*, **259**, 110.

Nakaya, U., 1954: *Snow crystals*. Harvard Univ. Press, 510 pp.

Ryan, B.F., E.R. Wishart and E.W. Holroyd, 1974: The densities and growth rates of ice crystals between –5°C and –9°C. *J. Atmos. Sci.*, **31**, 2136-2141.

___, ___ and D.E. Shaw, 1976: The densities of ice crystals between –3°C and –21°C. *J. Atmos. Sci.*, **33**, 842-850.

Song, N., and D. Lamb, 1994: Experimental investigations of ice in supercooled cloud. Part I: System description and growth of ice by vapor deposition. *J. Atmos. Sci.*, **51**, 91-103.

Takahashi, T. and T. Endoh, 2000: Experimental studies on the dendritic growth of a snow crystal in a water cloud. *Proc. 13th Intl. Conf. on Clouds and Precipitation*, Reno, NV, 677-680.

Takahashi, T., T. Endoh, G. Wakahama and N. Fukuta, 1991: Vapor diffusional growth of free-falling snow crystals. *J. Meteor. Soc. Japan*, **69**, 15-30.

Takahashi, T. and N. Fukuta, 1988: Supercooled cloud tunnel studies on the growth of snow crystals between –4°C and –20°C. *J. Meteor. Soc. Japan*, **66**, 841-855.

SURFACE SOURCE OF ICE PARTICLES IN MOUNTAIN CLOUDS

Gabor Vali, Bart Geerts, David Leon and Jefferson R. Snider.
Department of Atmospheric Science, University of Wyoming
Laramie, WY USA. <vali@uwyo.edu>

1. BACKGROUND

This paper focuses on wintertime orographic clouds not associated with major synoptic disturbances, but formed by strong winds across major barriers. Such clouds constitute a major source of precipitation in many regions of the world and are frequent targets of cloud seeding activities aimed at increasing the mountain snowpack. For these reasons such clouds have been extensively observed and modelled. However, these systems are no exception to the general difficulty of predicting the concentrations of ice particles that form in them at different temperatures. The most frequently made assumption is that ice particle concentrations follow ice nucleus concentrations, which in turn are assumed to be an exponential function of temperature. This assumption is justified by the absence of processes of secondary ice generation and the relatively simple dynamics of these clouds. Yet, it is known that the observed ice concentrations vary over large ranges and are not well predicted by available models.

2. OBSERVATIONS OF SURFACE SOURCES OF ICE

The data to be here presented provide one explanation for unexpected ice concentrations. With the help of the Wyoming Cloud Radar (WCR) carried on the Wyoming King Air (WKA) aircraft, observations have been obtained that provide direct evidence for significant input to ice concentrations from surface sources.

The WCR operates at a wavelength of 3 mm, has a 0.7° beam angle and 15...45-m rangegate spacing. Data used in this paper was collected using antennas pointed upward and downward from the aircraft so that a vertical cross-section is obtained in a plane containing the flight track. The downward pointing beam provides data right to the surface; data that cannot be obtained by other observational systems with comparable resolution.

The minimum detectable signal is about -25 dBZ (at 1 km range). Because of small droplet sizes and low liquid water contents in the sampled clouds, the radar echoes are due almost entirely to scattering by ice crystals and regions with only liquid and no ice particles are not detected.

Flights were carried out over the Medicine Bow Range (41°N; 106° W) in southeast Wyoming during Jan-Feb 2006. The mountain range has a dominant N-S axis, but contains additional minor peaks. The highest point of the range is about 1500 m above the valley to the West from where the dominant windflow is.

The first example, shown in Fig. 1, has two cloud layers. The lower one had its base, estimated from the upwind sounding, at 2.9 km and echo top that increased from about 4 to 5 km as the mountain slope rose. The upper cloud appears to be a wave that dips down into the lower cloud just downwind of the mountain crest. The aircraft at its 4260 m flight level was out of cloud until just a kilometer W of the crest. Beyond that point, the in situ data indicated ice concentrations up to 50 L^{-1} over 7 km of flight and max. 0.1 g m^{-3} of LWC over a 1 km stretch. Temperature and wind information are included in the figure. Wind direction was within 15° of the plane depicted in the figure.

The radar echo reveals the main message: there is a deepening layer of echo hugging the surface right up to the crest. Beyond the crest, the upper and lower echoes merge. A notable feature of the echo in the surface layer is that the highest values tend to be found near the ground and reflectivities decrease with height.

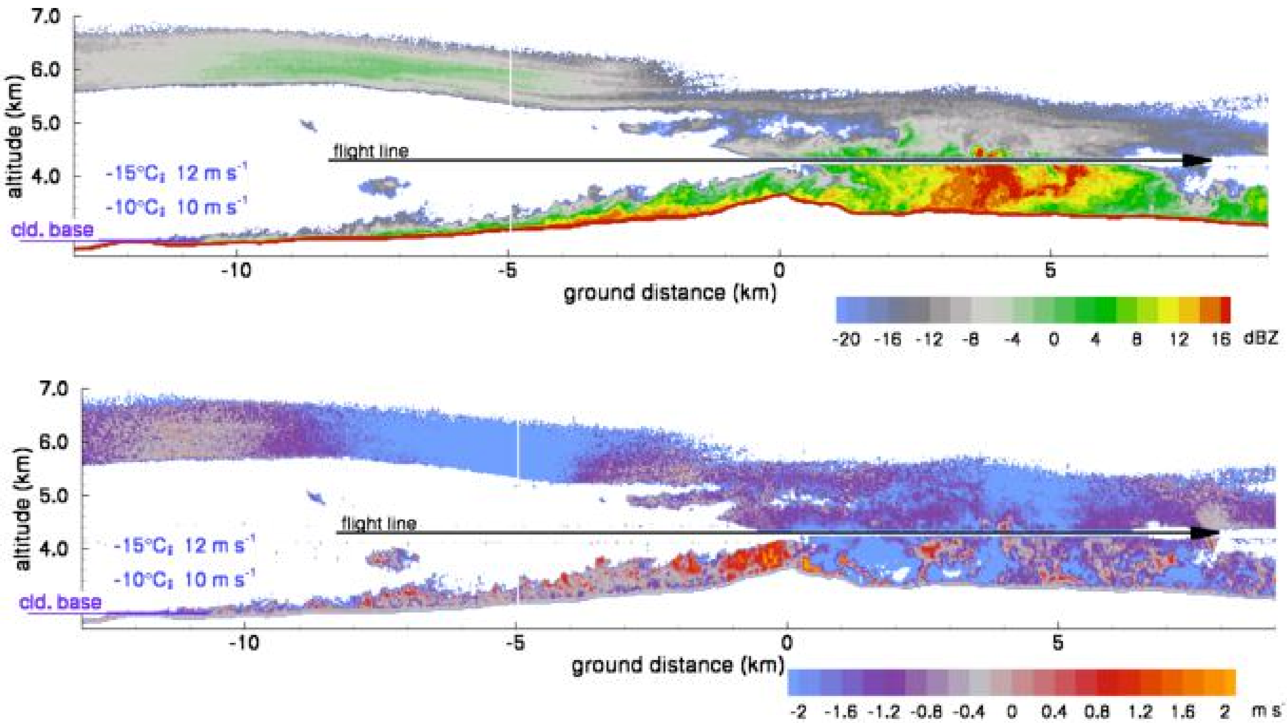

Fig.1. Reflectivity (upper panel) and vertical Doppler velocity (lower panel) for a vertical section across the mountain range from pass at 22:22 – 22:31 on Jan 27, 2006. Images are shown with 1:1 axis proportions. Wavy line at the bottom of the images delineates the ground.

The large-scale pattern in the vertical velocity data reflect the wave motion of the upper layer and the orographic forcing in the lower cloud. Superimposed on that one can see a considerable degree of turbulence in the boundary layer. The measured Doppler velocity is a sum of the air velocity and the fall velocity of the scatterers. For small ice crystals the fall velocity is 0.5...1 m s-1; so that areas with the grey to the warm colors represent likely upward air velocities. Large patches of significant upward velocities are apparent in the surface layer upwind of the peak, and again downwind. Just upwind of the ridge the upward velocities approach 2 m s^{-1}.

In looking at the images in Fig. 1. it should not be forgotten that the area below flight level down to the surface is mostly filled with cloud even though the reflectivity is below the minimum detectable signal. The cloud is visible on the video images from the cockpit. The frame shown here was taken from about the -14 km position; the leading edge of the cloud is seen, as well as trees, and the snow covered ground

in the clrearcut patches.

Right upon cloud entry, the detected crystals were (from the 2D-C imaging probe) irregular in shape and roughly 150 to 200 µm in size:

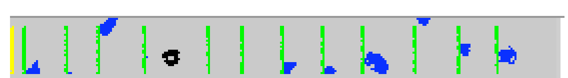

In this image, the vertical dimension of the strip is 800 µm.

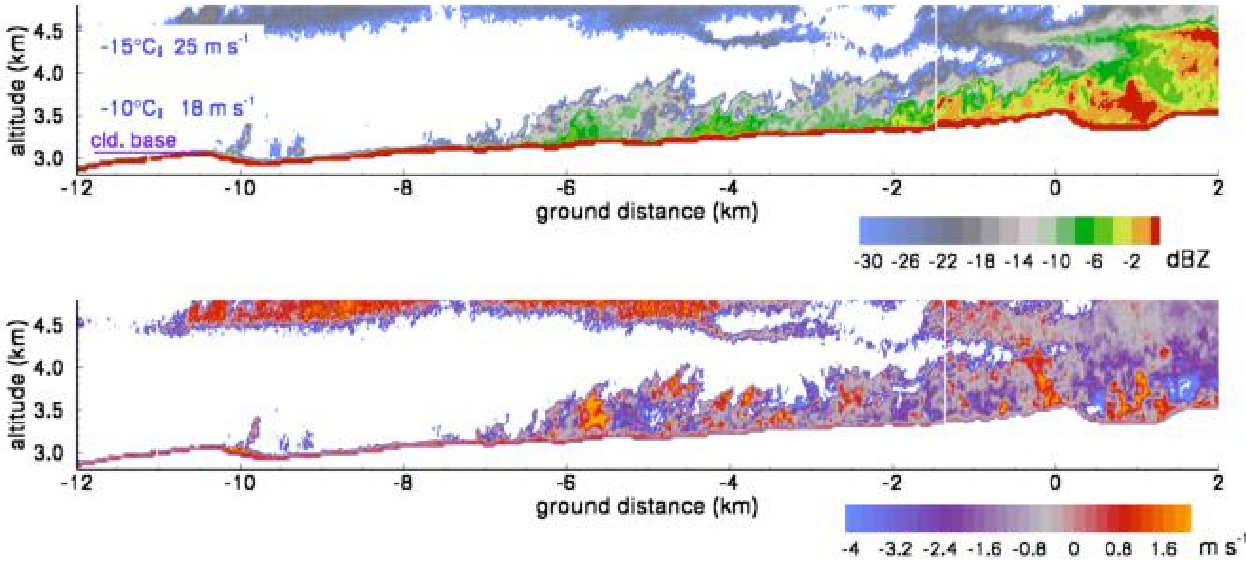

Fig. 2. Similar to Fig. 1 but for Jan. 18, 2006, 22:09-22:22 pass. Upper panel shows reflectivity (dBZ) and the lower panel the vertical Doppler velocity (m s^{-1}). The flight altitude was 4.8 km, and the images shown are from the nadir pointing antenna.

Fig. 3. Upwind and downwind views of the cloud sampled during the pass depicted in Fig. 2.

A second example of radar echoes hugging the mountain surface is shown in Figs. 2 and 3. Wind speeds were higher on this day than for the case shown in Fig. 1; cloud base height and temperatures were not much different. Both the sounding and the photographic evidence point to somewhat more instability and the development of convection. The surface echo also exhibits more plume-like appearance. However, the main characteristics are the same: more intense echoes near the surface and upward air motion coincident with reflectivity plumes. Probably because of the higher wind velocities and shear, another important aspect is apparent in this example, namely that the plumes have convex curvatures (slopes decreasing with height). That pattern, for wind that increases with altitude, is consistent only with a rising plume; a fall-trail would have concave curvature as is seen for cirrus trails and other precipitation shafts in wind shear.

At flight level, LWC of about 0.2 gm^{-3} was encountered, together with 1...5 L^{-1} of small (<200 μm) irregular ice crystals, over the stretch between -11 and 3 km ground distance (0 km marks the ridge). That was followed within about a kilometer by a transition to ice concentrations of about 20 L^{-1} with sizes up to a millimeter. That transition corresponds to the merging of the echo near the surface and the upper level echo.

3. WHAT GOES ON?

The evidence is strong that radar echoes are generated near the surface. The radar's sensitivity to ice, the decreasing reflectivity with altitude, and the inhomogeneity of the echo, argue against the possibility that the echoes are due to liquid cloud condensing. We also know from other cases that droplet clouds are not detected by the radar along the mountain slope due to the low LWC that develops. Thus, it seems certain that the surface echoes are due to ice particles.

There is support for the conclusion of the preceding paragraph in the observations reported by Rogers and Vali (1987; RV87). Ice concentrations measured at the Elk Mountain Observatory when the Observatory was inside mountain clouds (cap clouds) were about two orders of magnitude larger than those measured about 1 km above the Observatory during aircraft passes through the same clouds. That difference was evident at temperatures ranging from -5ºC to -25ºC, with a slight indication that stronger winds are accompanied by higher concentrations.

The vertical gradient of reflectivity, the association with upward motions, and the curvatures of the plumes provide strong support for the assumption that the origin of the ice is at the surface and that an upward transport of this ice is involved.

Given those characteristics, the most ready explanation for the echoes would seem to be that snow is being lofted from the surface. Blowing snow is a well-known phenomenon and has extensive literature documenting its characteristics. There is broad agreement that the mass concentration of blowing snow decreases exponentially with height above the surface and that the size distributions shift toward smaller and smaller particles with increasing height. Using data from the few studies that report size distributions of blowing snow (Schmidt, 1972, 1982; Nishimura and Nemoto, 2005; Nishimura, private communication) we estimate the radar reflectivity during blowing snow conditions at 10 m altitude (the maximum for which such data are available) to be between -20 and -10 dBZ. Extrapolating to altitudes consistent with the observed echoes in Figs. 1 and 2 would yield -30 to -20 dBZ at 100 m, and -35 to -25 dBZ at 300 m. These are lower than the observed values. However, the comparison is really not satisfactory since the blowing snow observations are taken under conditions when the lofted snow rapidly sublimates, whereas the conditions of our observations are with a supercooled cloud present. The presence of the cloud no doubt assures that snow particles can survive and grow, subject only to the limitation imposed by fallout. We have no good basis to estimate what to expect under such conditions.

There is one factor that casts somewhat of a doubt on the viability of the blowing snow explanation: no surface echoes have been observed where the mountain surface is below cloud base, not even in the range (to the extent that we can determine that from available data) where ice supersaturation can be expected.

None of the other possible explanations suggested in RV87 can be confirmed or discounted by the new observations. These include rime shedding from trees, generation of new ice crystals during riming, or the activation of ice nuclei in regions of high temperature and vapor pressure gradients.

The main novelty from the current observations is the definitiveness of the diagnosis of ice crystal lofting from or near the surface into clouds. The radar evidence indicates that the surface sources are not uniform, but show some relation to surface features such as small local ridges and increased slope; the echo layer is definitely within a turbulent boundary layer. The echoes also show that many of the ice particles fall back to the surface. Apart from the smaller-scale turbulence, there is a monotonic increase in the depth and intensity of the surface echo with distance along the mountain slope. This could be an indication that (i) the boundary layer is deepening, though there is no strong reason to think that that should happen, (ii) that the process of ice generation somehow depends on the sizes of cloud droplets, (iii) that rime intensity on trees is a factor, (iv) that the amount, or state of the snow on the surface is important, or (v) something less evident.

4. IMPLICATIONS

The findings here presented demonstrate the phenomenon of surface origin of ice crystals only in a qualitative sense and without delineating the range of conditions under which it is operative.

The most evident consequence of the findings is that models, and predictions, of ice crystal concentrations for clouds that are in contact with mountain surfaces have to take into account the surface source as well. Since, the quantitative aspects of this phenomenon are not yet known, a large uncertainty is introduced. It can be expected that the process alters the quantity and distribution of snow over a mountain barrier. The cases shown in this paper indicate spreading of the surface generated ice into the main part of the cloud at points downwind of the ridge. Other cases suggest, albeit less clearly, that even the upwind portions of the cloud can ingest plumes of ice from the surface.

For cloud seeding projects which aim at increasing snowpack from mountain clouds, the surface source represents a competition with the artificial ice nuclei introduced into the cloud. Supercooled liquid is depleted, or is prevented from forming by the increased concentrations of ice crystals. It is premature to estimate the potential magnitude of this effect.

Acknowledgements:

Flight operations were directed by B. Geerts, D. Leon, and J.R. Snider; analyses are by G. Vali. Members of the University of Wyoming flight facility are thanked for making these flight observations possible. This work was funded by grants ATM 0094956 and ATM 0650609 from the National Science Foundation, and by NASA-EPSCoRE grant #3412.

5. REFERENCES

Nishimura, K. and M. Nemoto, 2005: Blowing snow at Mizuho station, Antarctica. *Phil. Trans. Roy. Soc. – Math. Phys. Eng. Sci.*, **363,** 1647-1662

Rogers, D. C. and G. Vali: Ice crystal production by mountain surfaces. *J. Clim. Appl. Meteorol.*, **26,** 1152-1168, 1987

Schmidt Jr, R. A., 1972: Sublimation of wind-transported snow - A model. *USDA Forest Service Research Paper RM-90***,** 1-24

Schmidt, R. A., 1982: Vertical profiles of wind-speed, snow concentration, and humidity in blowing snow. *Bound. Lay. Meteor.*, **23,** 223-246

TURBULENT COLLISION-COALESCENCE OF CLOUD DROPLETS AND ITS IMPACT ON WARM RAIN INITIATION

Lian-Ping Wang,[1*] Bogdan Rosa,[1] and Wojciech W. Grabowski[2]
[1]*Department of Mechanical Engineering, University of Delaware, Newark, Delaware 19716, U.S.A.*
[2]*Mesoscale and Microscale Meteorology Division, National Center for Atmospheric Research, PO Box 3000, Boulder, Colorado 80307-3000, USA*

1. INTRODUCTION

In recent years, there is a renewed interest in studying the effects of air turbulence on the collision-coalescence growth of cloud droplets [1–6]. This is motivated by the need to resolve an open issue in cloud physics concerning the growth of cloud droplets in the size range from 10 to 50 μm in radius (i.e., the so-called size gap), for which neither the condensation nor the gravitational collision-coalescence mechanism is effective [5, 7]. Observations of radar reflectivity in tropical regions suggest that rain could form in cumulus clouds by warm rain process in approximately 15 to 20 minutes [8, 9]. Theoretical predictions based on the gravitational-coalescence mechanism alone, however, would require a time interval on the order of an hour for droplets to grow from 20 μm to 100 μm in radius (the actual time depends on the cloud water content, initial droplet size spectrum, updraft speed, *etc.*, see Pruppacher and Klett [7]). Therefore, there appears to be a factor of 2 or more difference between the predicted growth time and the observed growth time. The onset of drizzle-size ($\sim 100\mu m$ in radius) raindrops is still poorly understood in many precipitating cloud systems.

It has long been speculated that the effect of air turbulence could play an important role in closing the size gap [10], although several other alternative explanations have also been proposed, including growth by ultragiant particles, entrainment-induced spectral broadening, and effects of preexisting clouds [7, 11]. Resolving this open issue quantitatively is crucial in view of the fact that warm rain accounts for 31% of the total rain fall and 72% of the total rain area in the tropics [12].

Here we shall focus on the effects of air turbulence on droplet growth by collision-coalescence. The central issue is the magnitude of the enhancement of the gravitational collection kernel due to the air turbulence, and whether the enhancement can significantly impact rain initiation. The collection kernel is defined as the number of collisions per unit time between droplets of two different sizes, divided by the corresponding number of pairs involved. We will show that, despite the complexity of the problem, recent quantitative studies begin to address these long-standing issues with confidence.

2. TURBULENT COLLISION-COALESCENCE

During the last 10 years, studies have emerged in both engineering and atmospheric literature concerning the collision rate of particles in turbulent flow. These studies suggest that the collection kernel of cloud droplets can be enhanced by several effects of air turbulence: (1) the enhanced relative motion due to differential acceleration and shear effects [1, 13–16, 34]; (2) the enhanced average pair density due to local clustering ("preferential concentration") of droplets [14–17]; (3) the enhanced settling rate [18–20], and (4) the enhanced collision efficiency [21, 22]. The enhancement depends, in a complex manner, on the size of droplets (which in turn determines the response time and terminal velocity) and the strength of air turbulence (*i.e.*, the dissipation rate, flow Reynolds number, *etc.*).

For cloud droplets, the two key physical parameters are the droplet inertial response time τ_p and the still-fluid droplet terminal velocity v_T. For the background air turbulence, the dissipation-range motions are characterized by the Kolmogorov time τ_k and the Kolmogorov velocity v_k. The Stokes number St, the ratio τ_p/τ_k, emphasized in early studies of particle-laden flows, is not the only parameter governing the interaction of droplets with air turbulence. The nondimensional settling velocity, $S_v \equiv v_T/v_k$, is the second key parameter, typically one order of magnitude larger than St [23, 24]. This implies that the gravitational sedimentation determines the interaction time between the cloud droplet and the small-scale flow structures. Most of the published results on droplet clustering and collision rate from numerical simulations and theoretical studies assume no sedimentation and, as such, are not directly applicable to cloud droplets. For the case of strong sedimentation, a new governing parameter $F_p \equiv \tau_p v_T^2/\Gamma$ (where Γ is the circulation of vortical structures) has been found to better characterize the interaction of droplets with small-scale vortical structures and its effect on the mean settling rate [19, 25].

Recent systematic studies of the collection kernel for cloud droplets have been undertaken through either direct numerical simulation [22, 25–28] or a kinematic/stochastic representation of turbulence [21, 29, 30]. These studies provide not only quantitative data on the turbulent collision kernel, but also a better understanding of interaction between cloud droplets and air turbulence. An important observation emerging from these studies is that the enhancement factor, defined as the ratio of turbulent collision rate to the gravitational collision rate in still-air, is typically between one and five. Since the level of enhancement is moderate and the differences between various approaches are often comparable to the enhancement itself, quantification becomes extremely important.

*Corresponding author: Department of Mechanical Engineering, 126 Spencer Laboratory, University of Delaware, Newark, Delaware 19716-3140. Phone: (302) 831-8160; Fax: (302) 831-3619; Electronic mail: LWANG@ME.UDEL.EDU

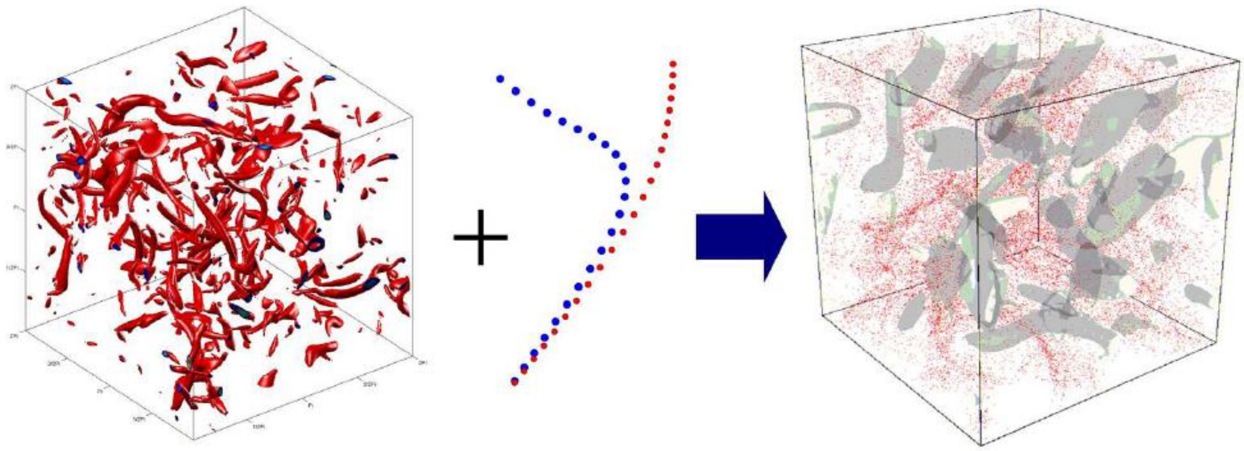

FIG. 1: Visualizations from the hybrid simulation approach [31]. The droplets are much smaller than the dissipation-range eddies of the background air turbulence so the disturbance flows due to droplets are represented analytically by Stokes flow solutions. The background air turbulence is solved numerically by integrating the Navier-Stokes equations. The left panel shows vortical structures of the background air turbulence; the center panel shows relative trajectories at the scale of droplets in the turbulent flow; and the right panel is a snapshot of flow vorticity surfaces and the locations of droplets in a subdomain of the computational region.

3. HYBRID DNS AND TURBULENT ENHANCEMENT

Motivated by the issues explained above, we have developed a consistent and rigorous simulation approach to the problem of turbulent collisions of cloud droplets [22, 31]. The basic idea of the approach is to combine direct numerical simulation (DNS) of the background air turbulence with an analytical representation of the disturbance flow introduced by droplets (Fig. 1). The approach takes advantage of the fact that the disturbance flow due to droplets is localized in space and there is a sufficient length-scale separation between the droplet size and the Kolmogorov scale of the background turbulent flow. This hybrid approach provides, for the first time, a quantitative tool for studying the combined effects of air turbulence and aerodynamic interactions on the motion and collisional interactions of cloud droplets. The disturbance flow is coupled with the background air turbulence through the approximate implementation of the no-slip boundary conditions on each droplet. Dynamical features in three dimensions and on spatial scales ranging from a few tens of centimeters down to 10 μm are captured. Both the near-field and the far-field droplet-droplet aerodynamic interactions could be incorporated [32], with possible systematic improvements of their accuracy.

The most important aspect of the approach is that dynamic collision events are detected, along with the direct and consistent calculations of all kinematic pair statistics related to the collision rate [15, 16, 22]. These unique capabilities allow application of the following general kinematic formulation of the collection kernel K_{12} [14, 15, 22]

$$K_{12} = 2\pi R^2 \langle |w_r(r=R)| \rangle g_{12}(r=R), \tag{1}$$

where the geometric collision radius R is defined as $R = a_1 + a_2$, with a_1 and a_2 being the radii of the two colliding droplets, w_r is the radial relative velocity at contact which combines the differential sedimentation and turbulent transport, and g_{12} is the radial distribution function (RDF) that quantifies the effect of droplet-pair clustering on the collision rate. This formulation is applicable to aerodynamically interacting droplets in a turbulent background flow, showing that the total enhancement factor η_T of the collision rate is a product of the enhancement of the geometric collision, η_G, and the enhancement of the collision efficiency, η_E, [22].

We found that the net enhancement factor $\eta_T = \eta_E \eta_G$ is typically in the range of one to five [28]. It tends to be larger when the droplets are rather different in size or of nearly equal in size (Fig. 2). In the first limiting case, the gravitational hydrodynamic kernel is small due to small differential sedimentation. In the second limiting case, the gravitational hydrodynamic kernel may also be small due to small collision efficiency. Therefore, air turbulence plays an important role in enhancing the collision kernel in both limiting cases. The values of η_E and η_G from our HDNS have been tabulated in [25, 28].

4. IMPACT ON RAIN INITIATION

We next consider the question of how the above turbulent enhancements on the collection kernel alter the size evolution of cloud droplets. An analytical model has been developed for the geometric collision rate of cloud droplets based on the results from the hybrid simulation approach [33]. The model consists of a parameterization of the radial relative velocity $\langle w_r \rangle$ similar to [34] for sedimenting particles, and a parameterization of the RDF g_{12} following the work reported in [35]. Of significance is the fact that the above parameterizations for both $\langle w_r \rangle$ and g_{12} consider the effects of flow Reynolds number which cannot be fully represented by the hybrid simulations. For example, the parameterization for $\langle w_r \rangle$ makes use of velocity correlations that are valid for both the dissipation subrange and the energy-containing subrange of turbulence [17]. The intermittency of small-scale turbulent fluctuations can be incorporated into the model for RDF [35]. Therefore, our parameterization of the collection kernel, while

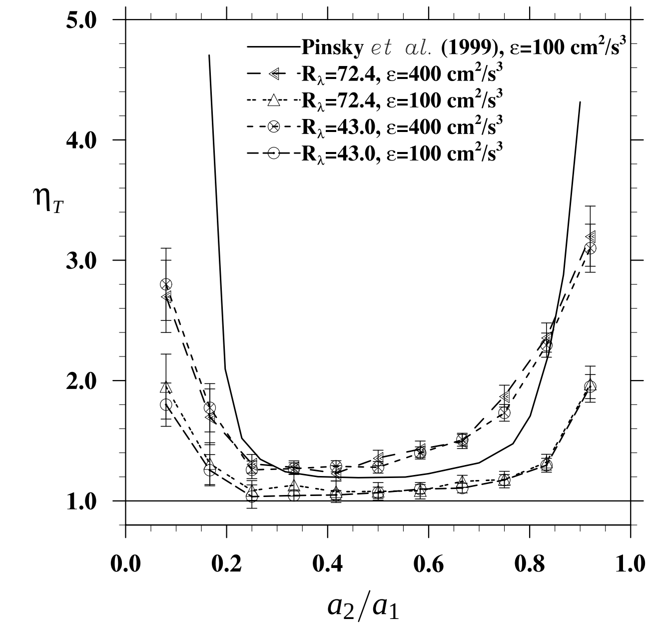

FIG. 2: The net enhancement factor, the ratio of the turbulent collection kernel and the hydrodynamic-gravitational collection kernel, as a function of a_2/a_1 for $a_1 = 30$ μm. The largest enhancements occur at small size ratio or for nearly equal-size pairs, in qualitative (but not quantitative) agreement with the results in [21]. In the legend, ε is the flow viscous dissipation rate and R_λ is the Taylor microscale Reynolds number of the simulated background turbulent air flow. The overall enhancements reported in [29, 30] appear to be quantitatively similar to the results shown here.

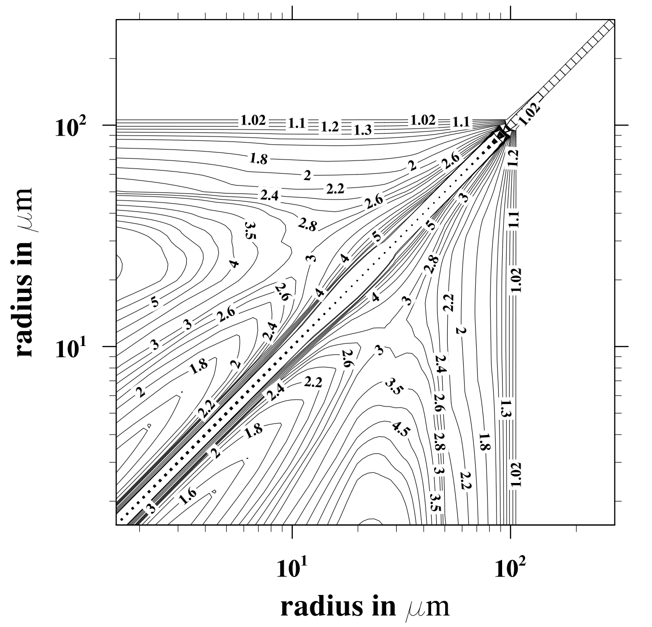

FIG. 3: The ratio of a typical turbulent collection kernel to the Hall kernel. The Hall kernel [36] is a hydrodynamical gravitational kernel in still air. The ratio on the 45^o degree line is undefined due to the zero value of the Hall kernel. The ratio is essentially one when droplets are above 100 μm. The flow dissipation rate is 400 cm^2/s^3 and rms velocity is 202 cm/s.

guided by the results from the hybrid simulations, extends the capabilities of the simulations concerning the flow Reynolds number effect. Moreover, we include the effect of η_E by interpolating the tabulated simulation results of η_E from [28]. The ratio (η_T) of the resulting turbulent collection kernel to the Hall kernel [36] is shown in Fig. 3 for a typical condition of cloud turbulence. The Hall kernel [36], a hydrodynamical gravitational kernel independent of air turbulence, is used as a base to compare the relative impact of turbulence.

Several important inferences can be made from Fig. 3. First, a noticeable enhancement occurs for droplets less than 100 μm. Second, the overall enhancement is moderate with a value ranging from 1.0 to 4.0 for most regions or an average value of about 2 for droplets in the bottleneck range. The magnitudes are one to two orders of magnitude smaller than assumed in [3] for reasons given herein and also in [24]. An important fact is that the enhancement factors shown in Fig. 3 are similar to those reported recently in [29, 30], where dramatically different approaches were employed. Third, the enhancement is more uniform for droplets less than 60 μm than other unrealistic turbulent kernels [3]. In general, it is the average enhancement over the bottleneck range that determines the overall impact of turbulence on the warm rain initiation [6].

The above turbulent collection kernel is then used in the kinetic collection equation to solve for droplet size distributions at different times, starting from the initial number density distribution

$$n(x,t=0) = \frac{L_0}{X_0^2}\exp\left(-\frac{x}{X_0}\right), \tag{2}$$

where x is the droplet mass, L_0 is the liquid water content and is set to 1 g/m^3, and X_0 is the initial average mass of the cloud droplets and is assumed to be 3.3×10^{-9} g which corresponds to a mean radius of 9.3 μm. The kinetic collection equation is solved by an accurate method [37] which combines the advantages of flux-based methods [38] and spectral moment-based methods [39]. A small bin mass ratio of $2^{0.25}$ ensures that the numerical solutions are free from numerical diffusion and dispersion errors. The mass distribution $g(\ln r,t) \equiv 3x^2 n(x,t)$ is usually plotted at different times in order to examine growth processes [40]. In Fig. 4, we instead plot the local rate of change, $\partial g/\partial t$, as a function of radius for times from 0 to 60 min every 1 min. We compare the results using the turbulent kernel to those using the Hall kernel. The plots naturally reveal the three growth phases first described qualitatively in [40]: (1) *the autoconversion phase* in which self-collections of small cloud droplets near the peak of the initial size distribution slowly shift the initial peak of the distribution toward larger sizes; (2) *the accretion phase* in which the accretion mode dominates over the autoconversion mode and serves to quickly transfer mass from the initial peak to the newly formed secondary peak at drizzle sizes; and (3) *the large hydrometeor self-collection phase* in which the

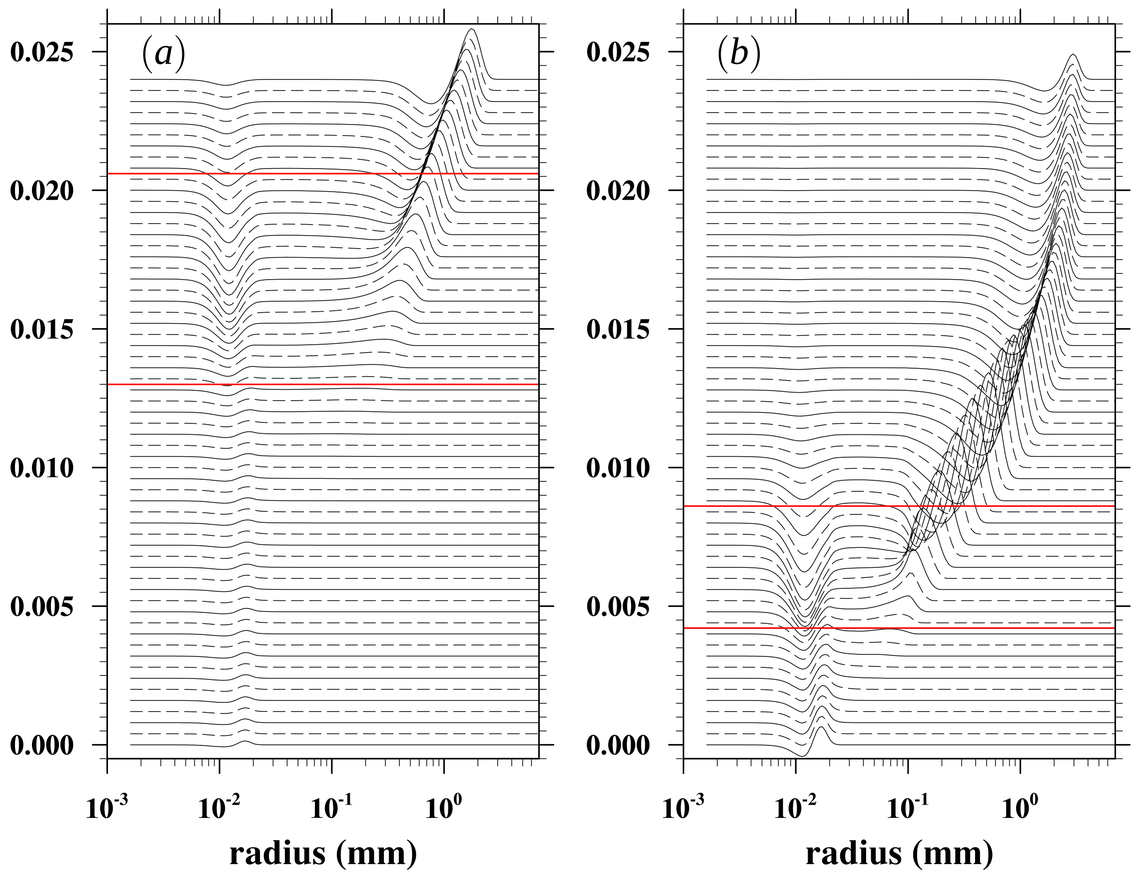

FIG. 4: The rate of change ($\partial g/\partial t$, $g\ m^{-3}\ s^{-1}$) of droplet mass density in each numerical bin as a function of droplet radius: (a) solutions using the Hall kernel; (b) solutions using a turbulent kernel at flow dissipation rate of 400 cm^2/s^3 and rms fluctuation velocity of 2.0 m/s. There are 61 curves in each plot, representing $t = 0$ to $t = 60$ min with a time increment of 1 min. The curves for $t > 0$ is shifted upwards by a constant in order to distinguish them. The value of $\partial g/\partial t$ can be either positive or negative, with the total integral over the whole size range equal to zero due to the mass conservation. At any given time, a positive $\partial g/\partial t$ for a given size bin implies that the mass density for that size bin is increasing. The two red lines mark the begin and the end of the accretion phase. The figure shows that air turbulence can shorten the growth time by a factor of about two.

self-collections of drizzle droplets near the second peak dominate over the accretion mode; the initial peak diminishes and the second peak gains strength and shifts toward the raindrop sizes (a few millimeters). By examining the locations corresponding to the maximum and minimum $\partial g/\partial t$, one can unambiguously identify the time intervals of the three phases [6]. In Fig. 4, we indicate in each plot the beginning and end of the accretion phase by two red horizontal lines.

Figure 4 highlights striking differences between the two collection kernels. The intensity of the autoconversion is significantly increased by the turbulent effects as shown by the magnitude of $\partial g/\partial t$ at early times (Fig. 4b) when compared to the base case (Fig. 4a). The time interval for the autoconversion phase *is reduced from about 32.5 min (Hall kernel) to only 10.5 min (the turbulent kernel)*. This demonstrates that turbulence has a strong impact on the autoconversion phase, which is typically the longest phase of warm rain initiation. The time interval for the accretion phase is also significantly reduced and smaller drizzle drops ($\sim$ 100 to 300 μm) are produced during this phase.

If a radar reflectivity factor of 20 dBZ (or the mass-weighted mean droplet radius of 200 μm) is used as an indicator for the drizzle precipitation, the time needed to reach such a reflectivity (or mean droplet radius) changes from about 2450 s (or 2470 s) for the Hall kernel to 1230 s (or 1250 s) for the turbulent kernel. This two-fold reduction factor increases with either the dissipation rate or rms turbulent fluctuation velocity [6].

5. SUMMARY AND ON-GOING WORK

Studies during the last 10 years have significantly advanced our understanding of the effects of cloud turbulence on the collision-coalescence of cloud droplets. Since the moderate enhancements by air turbulence occur within the bottleneck range and since the autoconversion is the longest phase of the initiation process, there is now convincing evidence showing that turbulence plays a definite role in promoting rain formation. The level of reduction in rain initiation time by turbulence appears to be at the level needed to resolve the discrepancy between the observed time and the time predicted based on the gravitational mechanism alone.

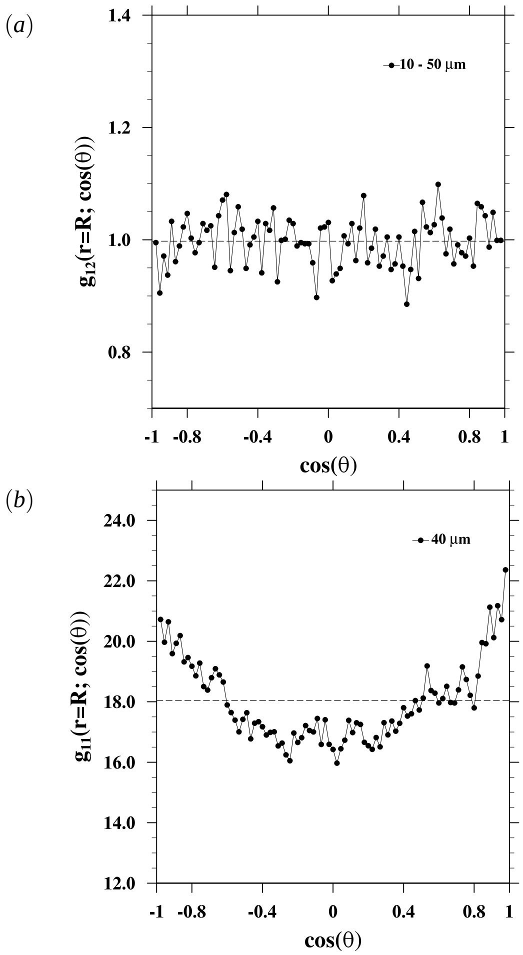

FIG. 5: Dependence of pair density on the orientation angle as shown by the angle-depdnent radial distribution function. The horizontal line is the usual orientation-averaged radial distribution function. Droplets are assumed to be ghost particles. The data were from 128^3 simualtions at $R_\lambda = 100$. (a) 10 μm $-$ 50 μm cross-size pairs, (b) 40 μm $-$ 40 μm same-size pairs.

The parameterization of the radial distribution function discussed in [33] is far from satisfactory. To obtain a better understanding, we are investigating if the droplet sedimentation introduces an orientation dependence. Prelimary results are shown in Fig. 5. For cross-size geometric collision between 10 μm and 50 μm droplets, there is essentially no orientation dependence. However, for the same-size collision between 40 μm droplets, it is more likely to find pairs approaching each other in the vertical direction than in the horizontal direction.

The hybrid DNS results on dropelt collision statistics we have obtained to date were based on OpenMP implemtation at 128^3 grid resolution or less. The relatively low flow Reynolds number in DNS implies that only a very limited range of scales of flow motion was explicitly represented in DNS. The relative motion and pair statistics of larger cloud droplets may be affected by larger-scale fluid motion not included in our DNS flow. Currently, we are implementing MPI into our simulation code in order to embark on simulations containing a large cloud volume. This allows us to increase the DNS flow

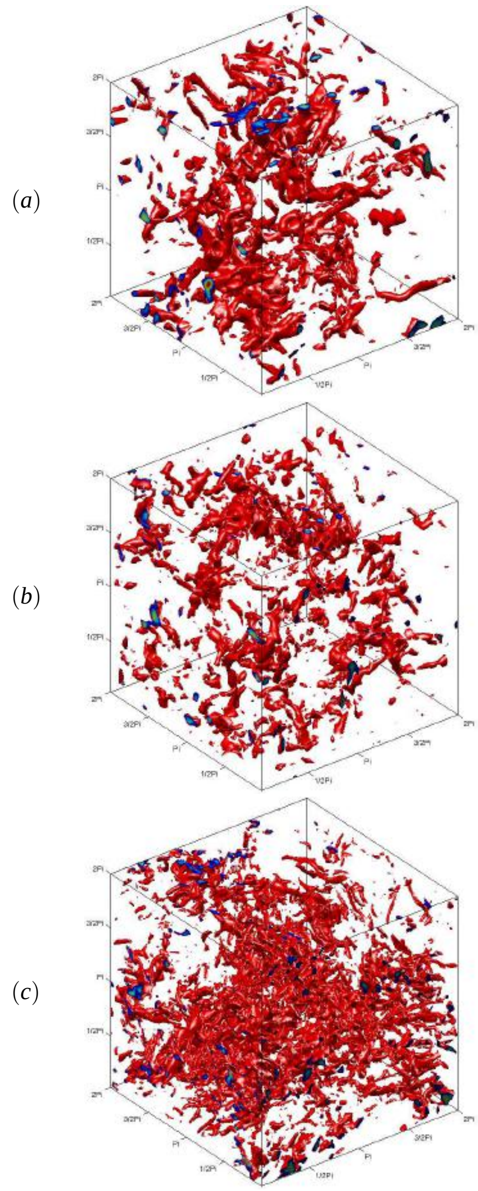

FIG. 6: Vorticity contours from flow simulations at three higher grid resolutions: (a) 256^3 and $R_\lambda = 145$, (b) 512^3 and $R_\lambda = 168$, (c) 1024^3 and $R_\lambda = 241$. The contour level for all visualizations was set to twice the field-mean vorticity magnitude.

Reynolds number and the number of droplets followed in the simulation. Visualizations from preliminary flow simulations up to 1024^3 are shown in Figure 4. These high-resolution simulations allows a direct representation of the interaction of large cloud droplets with air turbulence.

Short-range scaling law of the radial distribution function is also being studied to extract the scaling exponent, which may be important for modeling the at-contact radial distribution function. For the case of same-size (i.e., monodisperse) interactions, the power-law scaling appears to remain valid for sedimenting droplets (Fig. 7). The power-law exponent for g_{11} is plotted as a function of droplet radius in Fig. 8 for two different grid resolutions, with $\varepsilon = 400\ cm^2/s^3$. A Stokes

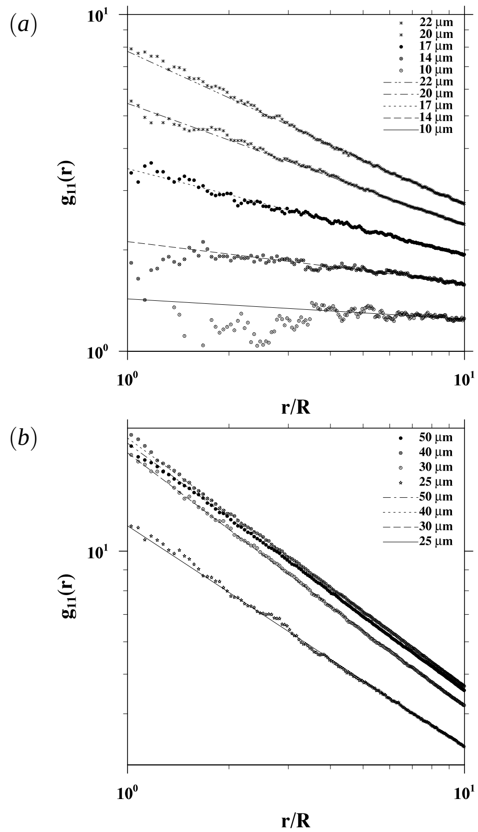

FIG. 7: The short-range power-law scaling of monodisperse radial distribution function for sedimenting droplets.

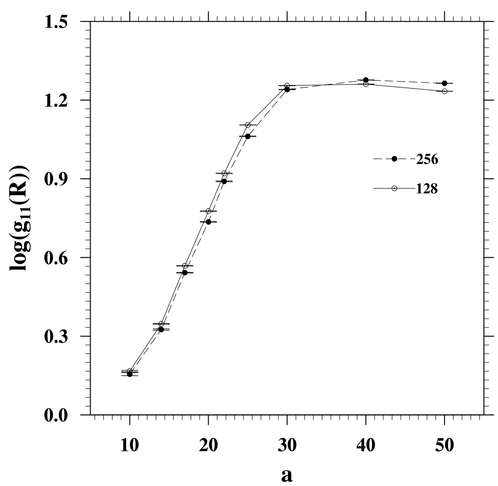

FIG. 8: The power-law exponent for g_{11} as a function of droplet radius.

number of one corresponds to $a = 40\ \mu m$ [25]. The power-law exponent increases quickly with droplet radius and then levels off at around $a = 30\ \mu m$. The similar results between the two grid resolutions implies that most of the interactions of droplets with the air turbulence are captured in our simulations, for the size range considered in Fig. 8.

The initial impact study discussed above and in [6] is also being extended to a detailed microphysics parcel model where condensational growth and collision-coalescence growth are considered together. In the parcel model, the changing environment (e.g., pressure and temperature) and parcel rising velocity can also be incorporated.

Acknowledgments

This study has been supported by the National Science Foundation through grants ATM-0114100 and ATM-0527140, and by the National Center for Atmospheric Research (NCAR).

[1] M. Pinsky, A. Khain, M. Shapiro, *J. Aero. Sci.* **28**, 1177 (1997).

[2] G. Falkovich, *Nature* **419**, 151 (2002).

[3] N. Riemer, A.S. Wexler, *J. Atmos. Sci.* **62**, 1962 (2005).

[4] S. Ghosh, J. Davila, J.C.R. Hunt, A. Srdic, H.J.S. Fernando, P. Jonas, *Proc. Roy. Soc. A* **461**, 3059 (2005).

[5] L. P. Wang, Y. Xue, O. Ayala, W. W. Grabowski, *Atmos. Res.* **82**, 416 (2006).

[6] Y. Xue, L.-P. Wang, W.W. Grabowski, *J. Atmos. Sci.*, 65, 331-356 (2008).

[7] H.R. Pruppacher, J.D. Klett, *Microphysics of clouds and pre-*

cipitation. Kluwer Academic Publishers, 954 pages (1997).
[8] M.J. Szumowski, R. M. Rauber, H.T. Ochs, L.J. Miller, *J Atmos. Sci.* **54**, 369 (1997).
[9] C. A. Knight, J. Vivekanandan, S.G. Lasher-Trapp, *J Atmos Sci.* **59**, 1454 (2002).
[10] D. Arenberg, *Bull. Amer. Meteor. Soc.* **20**, 444 (1939).
[11] K.V. Beard, H.T. Ochs, *J. Appl. Meteorol.* **32**, 608 (1993).
[12] K.M. Lau, H.-T. Wu, *Geophys. Res. Lett.* **30**, 2290 (2003).
[13] F.E. Kruis, K. A. Kusters, *Chem. Eng. Comm.* **158**, 201 (1997).
[14] S. Sundaram, L.R. Collins, *J. Fluid Mech.* **335**, 75 (1997).
[15] L.-P. Wang, A. S. Wexler, and Y. Zhou, *J. Fluid Mech.* **415**, 117 (2000).
[16] Y. Zhou, A.S. Wexler, L.-P. Wang, *J. Fluid Mech.* **433**, 77 (2001).
[17] L.I. Zaichik, O. Simonin, V.M. Alipchenkov, *Phys. Fluids* **15**, 2995 (2003).
[18] L.-P. Wang, M.R. Maxey, *J. Fluid Mech.* **256**, 27 (1993).
[19] J. Davila, J.C.R. Hunt, *J. Fluid Mech.* **440**, 117 (2001).
[20] S. Ghosh, P.R. Jonas, *Geop. Res. Let.* **28**, 3883 (2001).
[21] M.B. Pinsky, A.P. Khain, M. Shapiro, *J. Atmos. Sci.* **56**, 2585 (1999).
[22] L.-P. Wang, O. Ayala, S.E. Kasprzak, W. W. Grabowski, *J. Atmos. Sci.* **62**, 2433 (2005).
[23] W. W. Grabowski, P. Vaillancourt, *J. Atmos. Sci.* **56**, 1433 (1999).
[24] L.-P. Wang, O. Ayala, Y. Xue, W. W. Grabowski, *J. Atmos. Sci.* **63**, 2397 (2006).
[25] O. Ayala, B. Rosa, L.-P. Wang, and W. W. Grabowski, Effects of Turbulence on the Geometric Collision Rate of Sedimenting Droplets: Part 1. Results from direct numerical simulation, *New J. Physics*, in press.
[26] C.N. Franklin, P.A. Vaillancourt, M.K. Yau, P. Bartello, *J. Atmos. Sci.* **62**, 2451 (2005).
[27] L.-P. Wang, C.N. Franklin, O. Ayala, W.W. Grabowski, *J. Atmos. Sci.* **63**, 881 (2006).
[28] L.-P. Wang, O. Ayala, B. Rosa, and W. W. Grabowski, Turbulent Collision Effi ciency of Cloud Droplets, *New J. Physics*, in press.
[29] M.B. Pinsky, A.P. Khain, *J. Atmos. Sci.* **61**, 1926 (2004).
[30] M.B. Pinsky, A.P. Khain, B. Grits, M. Shapiro, *J. Atmos. Sci.* **63**, 2123 (2006).
[31] O. Ayala, L.-P. Wang, W.W. Grabowski, *J. Comput. Phys.*, **225**, 51-73 (2007).
[32] L.-P. Wang, O. Ayala, W.W. Grabowski, *J. Turbulence*, **8.1**, 1-23, DOI: 10.1080/14685240701233426 (2007).
[33] O. Ayala, B. Rosa, and L.-P. Wang, Effects of Turbulence on the Geometric Collision Rate of Sedimenting Droplets: Part 2. Theory and parameterization, *New J. Physics* (Focus Issue on Cloud Physics), in review.
[34] Z. Dodin, T. Elperin, Phys. Fluids **14**, 2921 (2002).
[35] J. Chun, D. Koch, S.L. Rani, A. Ahluwalia, L.R. Collins, *J. Fluid Mech.* **536**, 219 (2005).
[36] W.D. Hall, *J. Atmos. Sci.* **37**, 2486 (1980).
[37] L.-P. Wang, Y. Xue, W.W. Grabowski, *J. Comp.Phys.*, 226, 59-88 (2007).
[38] A. Bott, *J. Atmos. Sci.* **55**, 2284 (1998).
[39] I.M. Enukashvily, *J. Atmos. Sci.* **37**, 2521 (1980);
[40] E.X. Berry, R.I. Reinhardt, *J. Atmos. Sci.* **31**, 1814 (1974).

ON THE CONTRIBUTION OF AITKEN MODE PARTICLES TO CLOUD DROPLET POPULATIONS AT CLEAN CONTINENTAL AREAS – A PARAMETRIC SENSIVITY STUDY

T. Anttila and V.-M. Kerminen

Finnish Meteorological Institute, Research and Development, P.O. Box 503, 00101 Finland

1. INTRODUCTION

Atmospheric aerosol particles act as nuclei onto which cloud droplets are formed, but the connection between the microphysical properties of aerosols and those of clouds is far from being completely understood. The associated uncertainties are closely tied to our incomplete knowledge of how different aerosol properties affect their cloud droplet nucleating ability (Lohmann and Feichter, 2005; McFiggans et al., 2006). What is known, however, is that aerosol particles need to contain sufficient amounts of water-soluble material in order to form cloud droplets in the atmosphere. The minimum particle diameter required for this varies typically between 50 and 100 nm in the lower troposphere (Seinfeld and Pandis, 1998). This size range is also characteristic for the Aitken mode particles which often make dominant contribution to the total particle number concentration in this size range >50 nm in continental areas (Tunved et al., 2003). Therefore it is important to understand the impact of the Aitken mode particles to the cloud microphysics in these areas. These effects can be quantified using large-scale atmospheric models. Due to the various spatial scales involved, however, relevant microphysical processes have to be described in a computationally efficient way in such models. In order to make an optimal compromise between computational efficiency and accuracy, we aim to give an answer to the following question: "which physico-chemical properties of Aitken mode particles are most important regarding their contribution to cloud droplet number concentrations?". We have approached the problem using the sensitivity analysis method proposed by Tatang et al. (1997).

2. METHODS

The present study attempts to identify and rank the physicochemical properties of Aitken mode particles that determine the cloud-nucleating ability of these particles in continental background areas. The approach is based on performing calculations with an adiabatic air parcel model (AAPM) and analyzing the model output with the probabilistic collocation method (PCM). Briefly, PCM is a sensitivity analysis technique for numerical models that is "global" in a sense that the sensitivity of model output with respect to a varied parameter is quantified over the entire parameter space. Also, the net effects of simultaneously varying input parameters are accounted for. PCM is based on approximating the considered model output by polynomials called as polynomial chaos expansions (PCEs), the terms of which are functions of the varied input parameters. Once the PCEs have been generated, the required statistical properties of the model output can be readily calculated. The parameters towards which the model output displays the highest sensitivity are the parameters whose variation mainly regulates the impact of Aitken mode particles to cloud formation, and thereby the method allows for ranking quantitatively the importance of the varied parameters. Detailed description of PCM can be found from the literature (Tatang et al., 1997).

Here the considered model output is the number concentration of cloud droplets formed on Aitken mode particles, CD_2, as a function of the updraft velocity. The varied input parameters were those describing the modal and chemical properties of the Aitken mode particles, including their total number concentration, size and water solubility of their chemical constituents (see Table 1 for a complete list). The values of other model parameters were kept constant and they reflect conditions typical for the investigated atmospheric environment.

A proper choice of the value ranges of the varied parameters is problematic due to aerosol-phase organics that are not completely characterized at the present. Therefore it was decided to make several sensitivity studies where different value ranges were adopted for the most poorly-constrained parameters. The first scenario does not fully account the potential variability in the aerosol chemical composition. We term this scenario as "BASE". Since this scenario may underestimate the importance of the particle chemical composition, we performed two additional sets of sensitivity studies, called "MACRO" and "FILM". In these scenarios, we adopted larger value ranges (highlighted in Table 1) for the most uncertain parameters.

The validity of our approach was evaluated as follows. For each PCE generated, we performed 750 additional cloud simulations in which the considered input parameters were varied randomly according to their probability distributions. The results were compared with the corresponding predictions based on the generated PCEs.

3. RESULTS

The cloud droplet concentrations predicted by the original model and by the PCEs displayed good agreement, the R^2 values being 0.77 at minimum. In general, the agreement increased with increasing updraft velocity. Moreover, the PCEs can used to calculate the expected value and variance of CD_2 and hence we compared also these quantities with the corresponding ones describing the output of the original model. The comparison showed also good agreement: errors in the expected value and variance were 15% at maximum and below 10% in most cases. From these results we conclude that the agreement is sufficient to warrant the conclusions based on the sensitivity analysis, of which main results are discussed next.

The varied input parameters can be divided into into two groups: those related to the modal properties (first three parameters in Table 1) and those related to the chemical composition (last six parameters in Table 1). Here we call these parameters as physics- and chemistry-related parameters,

Table 1. Investigated parameters, their abbreviations and ranges over which their values were varied. All the parameters refer to Aitken mode particles and not to the whole particle population. The value ranges of which are changed compared to "BASE" scenario are highlighted using the bold font.

Parameter	Abbrev.	"BASE"	"MACRO"	"FILM"
Geometric standard deviation	σ_g	1.3-1.9	1.3-1.9	1.3-1.9
Total particle concentration (cm^{-3})	CN	10-10 000	10-10 000	10-10 000
Particle mean diameter (nm)	D_m	50-100	50-100	50-100
Average molecular weight (g mol^{-1})	MW_{avg}	60-250	**60-600**	60-250
Water-soluble mass fraction	ε	0.25–1.0	0.25–1.0	0.25-1.0
Particle dry density (g cm^{-3})	ρ	1.0–2.0	1.0–2.0	1.0-2.0
"Effective" Van't Hoff factor	$\nu\Phi$	1-3	**1-5**	1-3
Particle surface tension (N m^{-1})	σ_s	0.05–0.072	**0.02–0.072**	0.05-0.072
Mass accommodation coefficient	α	10^{-2}-1	10^{-2}-1	**10^{-3}-1**

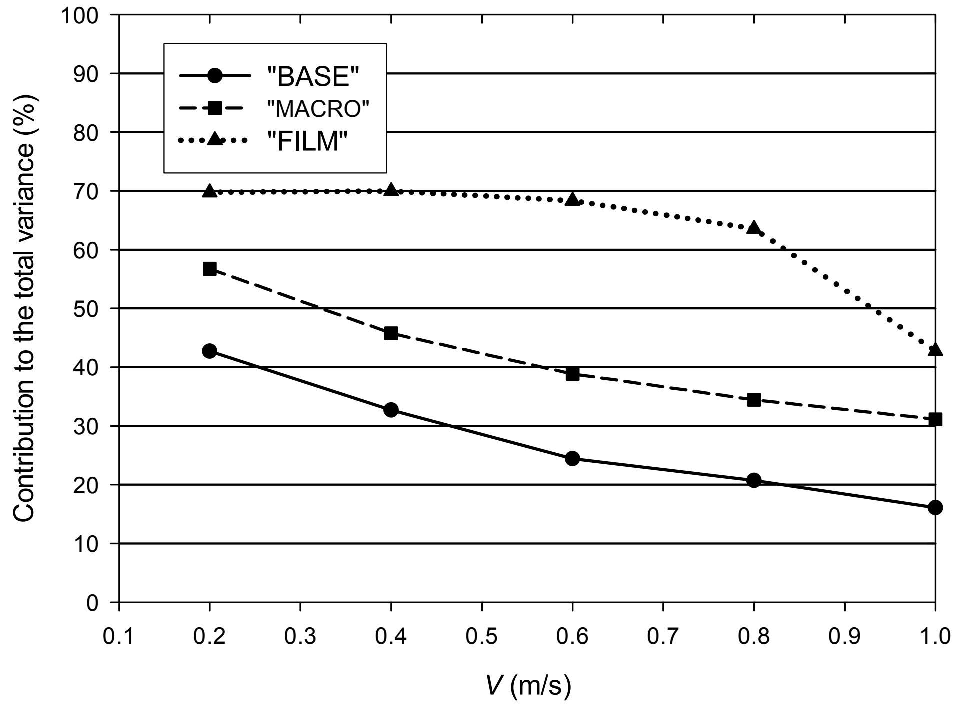

Figure 1. The net contribution of chemistry-related parameters to the total variance of the model output as a function of the updraft velocity, V. The scenario is indicated in the legend.

respectively. With an aim to find out which of them cause most of the variation to the model output, Figure 1 shows the relative importance of the particle size distribution versus the particle chemical composition for all three scenarios. The importance of the particle chemical composition is seen to decrease consistently as *V* increases. Also, the net contribution of the physics-related parameters to the total variance becomes larger than that of the chemistry-related parameters at updraft velocities of around 0.3 and 0.9 m/s in the "MACRO" and "FILM" scenarios, respectively. In the "BASE" scenario, the physics-related parameters dominate consistently the total variance of the model output. The larger roles of the chemical composition in the "MACRO" and "FILM" are mainly due to larger value ranges adopted for the surface tension and mass accommodation coefficient, respectively (Table 1). The results thus suggest that the chemical composition can be even more important as the physical properties what it comes to the cloud-nucleating ability of Aitken mode particles in the continental background areas.

4. DISCUSSION AND CONCLUSIONS

The relative roles played by the particle size distribution and chemical composition in determining the cloud-nucleating ability of atmospheric particles is a subject of intense research at the present (Dusek et al., 2006), and the results of our study have also implications on this issue. First, unless the particle surface tension or mass accommodation coefficient of water is strongly reduced due to the presence of surface-active organics, the parameters describing the size distribution are generally more important than the particle chemical composition. In the absence of such compounds, the chemical composition may have roughly an equal importance with the size distribution only at low updraft velocities characterized by maximum supersaturations <0.1%. Furthermore, a closer look to the results revealed that the largest source of variance in the model output is generally the particle number concentration, followed by the particle size. Another interesting result is that the shape of the particle mode, described by the geometric standard deviation (GSD), can be as important as mode size at low updraft velocities. This suggests that using a prescribed value for the GSD (e.g. Vignati et al., 2004) might cause errors to the predicted effect of sub-100 nm sized particles on the cloud droplet number concentrations. Finally, the performed sensitivity analysis revealed that the variability of the particle chemical composition may dominate the total variance of CD_2 if: 1) the value of varies three orders of magnitude or more, or 2) the particle surface tension varies more than roughly 30% under conditions close to reaching saturation.

5. BIBLIOGRAPHY

Dusek, U., Frank, G. P., Hildebrandt, L., Curtius, J., Schneider, J., Walter, S., Chand, D., Drewnick, F., Hings, S., Jung, D., Borrmann, S., and Andreae, M. O.: Size matters more than chemistry for cloud-nucleating ability of aerosol particles, Science, 312, 1375–1378, 2006.

Lohmann, U. and Feichter, J.: Global indirect aerosol effects: a review, Atmos. Chem. Phys., 5, 715–737, 2005.

McFiggans, G., Artaxo, P., Baltensperger, U., Coe, H., Facchini, M. C., Feingold, G., Fuzzi, S., Gysel, M., Laaksonen, A., Lohmann, U., Mentel, T. F., Murphy, D. M., O'Dowd, C. D., Snider, J. R., and Weingartner, E.: The effect of physical and chemical aerosol properties on warm cloud droplet activation, Atmos. Chem. Phys., 6, 2593–2649, 2006.

Seinfeld, J. H. and Pandis, S. N.: Atmospheric chemistry and physics: From air pollution to climate change, John Wiley, New York, United States of America, 1998.

Tatang, M., Pan, W., Prinn, R., and McRae, G.: An efficient method for parametric uncertainty analysis of numerical geophysical models, J. Geophys. Res., 102, 21 925–21 932, 1997

Tunved, P., Hansson, H.-C., Kulmala, M., Aalto, P., Viisanen, Y., Karlsson, H., Kristensson, A., Swietlicki, E., Dal Maso, M.,Ström, J., and Komppula, M.: One year boundary layer aerosol size distribution data from five Nordic background stations, Atmos. Chem. Phys., 3, 2183–2205, 2003.

Vignati, E., Wilson, J., and Stier, P.: M7: An efficient size-resolved aerosol microphysics module for large-scale aerosol transport models, J. Geophys. Res., 109, D22202, doi: 10.1029/2003JD004485, 2004.

Acknowledgements

The work has been supported by the Academy of Finland and European Union (project 018332). One of the authors (T.A.) acknowledges financial support from the Emil Aaltonen Foundation and Vaisala Foundation.

DRIZZLE FORMATION IN STRATIFORM CLOUDS: LUCKY PARCELS

L. Magaritz, M. Pinsky and A. Khain
Department of Atmospheric Sciences, The Hebrew University of Jerusalem, Israel
Email: khain@vms.huji.ac.il

ABSTRACT

A novel trajectory ensemble model of a cloud-topped boundary layer containing 1340 Largangian parcels moving with the turbulent like flow with observed statistical properties was applied to investigate the formation of the microphysical structure of stratocumulus clouds (Sc) in a non-mixing limit (when turbulent mixing between the parcels is not taken into account). Sc observed in two research flights during the DYCOMS-II field experiment RF01 (no drizzle) and RF07 (weak drizzle) are simulated. The mechanisms leading to high variability of droplet size distributions (DSD) with different spectrum width and dispersion are discussed. Drizzle formation was investigated using the Z-LWC and $LWC - r_{eff}$ diagrams simulated by the model in the non-drizzle and drizzle cases. It is shown that in the RF07 case large cloud droplets which trigger drop collisions and drizzle formation form only in a small fraction (a few %) of parcels (which will be referred to as lucky parcels), in which LWC exceeds ~1.5 gm^{-3}. This threshold exceeds the horizontally averaged LWC maximum value of 0.8 gm^{-3} by 2 to 3 standard deviations, indicating a small amount of lucky parcels. In a non-drizzling cloud simulation the LWC actually does not exceed this threshold. It shows that for the formation of drizzling clouds the threshold value should be exceeded in a few percent of the cloudy parcels. The dependence of the threshold value of LWC on aerosol concentration is discussed. The lucky parcels (at least in the non-mixing limit) start their updraft in the vicinity to the surface, where water vapor mixing ratio is maximum, and ascend to the highest levels close to the cloud top. It is shown that the lucky parcel tracks are related to the large eddies in the BL, which indicates a substantial role of the large eddies in drizzle formation.

1. INTRODUCTION

The precipitating, radiative and reflectivity properties of warm stratiform clouds strongly depend on the shape of droplet size distributions (DSD), which can vary substantially at the scales of several tens of meters (Korolev and Mazin, 1993; Korolev 1994, 1995). Especially strong changes of radiative cloud properties are related to drizzle formation (e.g., Stevens et al 1998a; vanZanten et al, 2005; Petters et al 2006). The microphysical properties of stratocumulus clouds have been measured and simulated in a great number of observational and numerical studies (see references in Pinsky et al 2008, hereafter Pt1). Typical vertical profiles of horizontally averaged droplet concentration, liquid water content (LWC), drizzle flux etc. in non-drizzling and drizzling clouds have been measured (e.g., Wood 2005). It was found from observations that intense drizzle formation starts when the effective radius of droplets exceeds about 10 μm to 15 μm (Gerber 1996; Yum and Hudson 2002; VanZanten et al, 2005; Twohy et al 2005). Dependence of droplet concentration and droplet size on aerosol concentration was widely discussed in literature (e.g. Twomey 1977; Martin et al, 1994). Based on observations, drizzle parameterizations were formulated for general circulation models (e.g. Pawlowska and Brenguier

2003), dependences of drizzle fluxes on the mean cloud depth and droplet concentration have been proposed (e.g. Gerber 1996; Brenguier et al 2000b). At the same time many fundamental questions concerning the mechanisms of drizzle formation remain unanswered.

Large eddy simulation (LES) models have emerged as a powerful tool to simulate the microphysical properties of stratocumulus clouds (e.g., Kogan et al, 1994, 1995; Feingold et al, 1994, 1998a,b; Stevens et al, 1996, 1999; 2005a; Moeng et al 1996; Khairoutdinov and Kogan, 1999; Khairoutdinov and Randall 2003). We suppose, however, that the Lagrangian approach used in the trajectory ensemble models (TEM) (e.g., Stevens et al 1996; Feingold et al, 1998b; Harrington et al 2000; Erlick et al, 2005) has some advantages over the Eulerian approach used in the LES models as regards the investigation of microphysical processes because it allows one to follow the DSD evolution along air trajectories and to compare histories of different air parcels forming within the cloud. However, the state-of the art TEMs does not take into account droplet collisions and sedimentation and cannot be used for investigation of drizzle formation.

In Pt1 a new TEM is described and successively applied for reproduction of microphysical properties of stratocumulus clouds observed during research flights RF01 (negligible drizzle fluxes) and RF07 (weak drizzle) in the DYCOMS-II field experiment. The specific feature of the model is that a great number of Lagrangian air parcels with linear size of about 40 m cover the entire BL area. The parcels are advected by a time dependent turbulent-like flow generated by a statistical model which reproduces the velocity field with statistical properties derived from observations. A great improvement of the approach as compared to that used in the state-of-the art TEMs, was that the new model took into account collisions between droplets in each parcel and droplet sedimentation. These improvements allow simulation of drizzle formation and of the change of drizzle flux during drizzle fall within and below cloud base.

The present study is the continuation of Pt1 as regards the investigation of the physical mechanisms of droplet size distribution (DSD) and drizzle formation. We address here the following questions:

a) What are the mechanisms determining a significant horizontal variability of the DSD shapes and the integral parameters (e.g., LWC, droplet concentration, DSD dispersion) at spatial distances as small as several tens of meters (e.g., Korolev 1995)?
b) What are the main microphysical parameters determining the drizzle triggering in stratocumulus clouds?
c) Why are drizzle fluxes strongly non-uniform in the horizontal direction and cover a comparatively small area fraction of stratocumulus clouds which seem to be visibly uniform? Why the minimum characteristic distances between neighboring zones of drizzle are about 1 km or a few of kilometers (Wood 2005; VanZanten et al 2005)

It is clear that it is impossible to give exhausted answers to these fundamental questions related to the drizzle formation mechanisms within one paper. Moreover, in order to identify the main physical mechanisms, the analysis will be performed first under the simplified conditions, namely in the non-mixing limit, i.e. in neglecting turbulent mixing between Lagrangian parcels. It was shown in Pt1 that the many microphysical cloud properties of non-drizzling and drizzling clouds can be realistically simulated even under such simplification.

2. A BRIEF MODEL DESCRIPTION

The model is described in Pt1 in detail, hence, only a short description is presented below. The velocity field is represented as the sum of a great number of harmonics with random amplitude and characteristic time scales. The velocity field obeys turbulent laws. The parameters of the model are calculated to obey the correlation properties of the measured velocity field.

A great number of Largangian parcels with linear scales of about 40 m are advected by this velocity field. At t=0 the volumes of the air parcels were assumed equal, and parcels are distributed uniformly over the whole area of the BL. At t=0 the BL is assumed to be cloud free, so that parcels contain non-activated aerosol particles (AP) only. In ascending parcels crossing the lifting condensation level some fraction of aerosols activate and gives rise to droplet formation. Thus, non-activated aerosols and droplets can exist in each cloud parcel. In the course of parcel motion supersaturation in parcels can increase, which may lead to the nucleation of new droplets and to the formation of bimodal and multimodal DSD. In case the supersaturation in a parcel is replaced by undersaturation droplets evaporate partially or totally. In the latter case the cloud parcel turns out to be a droplet-free containing only wet aerosol particles, including those remaining after drop evaporation. Motion of parcels accompanied by condensation/evaporation lead to the formation of realistic horizontally averaged vertical profiles of temperature, moisture and microphysical characteristics in the cloud topped BL (CTBL). We do not take into account the effects of microphysics on the dynamical (turbulent) structure explicitly. Instead, we generate a turbulent-like dynamical structure that corresponds to that observed in the CTBL. In nature this dynamical structure is formed under the combined effect of many factors: latent heat release, radiation, thermal instability, wind shear, surface heat and moisture fluxes, etc. Assimilating the real dynamics, we implicitly take into account all factors affecting the CTBL dynamics. Simulation of turbulent-like flows corresponding to different thermodynamic situations in the CTBL makes it possible to investigate the effects of the BL dynamics, thermodynamics and aerosol properties on the microphysical structure of stratocumulus clouds.

The microphysics of a single Largangian parcel (see Pinsky and Khain 2002 and Pt1 for detail) includes the diffusion growth/evaporation equation used for aerosols and water droplets, the equation for supersaturation S and the stochastic collision equation describing collisions between droplets. The mass of aerosols within droplets is calculated as well. The size distribution of cloud particles (both non-activated nuclei and droplets) is calculated on the mass grid containing 500 bins within the 0.01 μm to 1000 μm radius range. The mass of each bin changes with time (height) in each parcel according to the equation for diffusion growth. A small 0.01 s time step is used to simulate adequately the growth of the smallest APs, so that the separation between non-activated nuclei attaining equilibrium (haze particles) and the growing droplets is simulated explicitly (without any parameterization). The precise method proposed by Bott (1998) is used to solve the stochastic collision equation. The collision droplet growth was calculated using a collision efficiency table with a high 1 μm- resolution in droplet radii (Pinsky et al. 2001). Drop collisions are calculated with one second time interval. The AP budget is calculated in the model. The APs exist in two "states": a) non-activated wet AP (haze particles) and b) AP dissolved within droplets. The mass of AP in droplets does not change during condensation/evaporation process. Each act of drop collisions leads to an increase of the dissolved AP mass in the drop-collectors. The droplet evaporation leads to the formation of wet AP. Thus, drop collisions can change the AP size distribution during parcel recirculation within the BL.

The specific feature of the model is the accounting for droplet sedimentation (see for detail Pt1). The algorithm of sedimentation actually represents an extension of the widely used flux method (e.g. Bryan 1966; Bott 1989) to describe the advection and sedimentation in the Eulerian models with irregular finite difference grids to the irregular grid formed by the centers of the parcels. In this sense, the model can be referred to as the hybrid Lagrangian-Eulerian model. Main dynamical and microphysical parameters of the model are presented in **Table 1.**

Table 1. The main parameters used in preliminary simulations of cloud formation.

Dynamic parameters		**Microphysical and thermodynamical parameters**	
Characteristic size of air parcels	~ 40 m	Number of mass bins	500
Number of parcels	1344	Range of cloud particles, μm	0.01-1000
Length of the area L, m	2550	Time step of diffusion growth, s	0.01
Height of the area H, m	850	Time step for collisions, s	1.0
Number of harmonics M=N	50	Time step for sedimentation, s	1.0
Maximum r.m.s vertical velocity fluctuation, m/s	0.7	Chemical composition of aerosols	NaCl
Life time of harmonics, s	30-1000	Surface temperature, K	291.5 (RF01) 291.6 (RF07)
Time period of velocity field updating (eq. 2), s	0.1		
Turbulent dissipation rate, cm^2/s^3	10		

3. DESIGN OF NUMERICAL EXPERIMENTS AND DATA ASSIMILATION

For analysis of DSD formation mechanisms in both non-drizzle and drizzle stratocumulus clouds, we simulated stratocumulus clouds observed during two research flights conducted as part of the DYCOMS-II field experiment, RF01 (negligible drizzle at the surface) and RF07 (a weakly drizzling cloud). The investigation of the Sc observed in these flights makes it possible to determine the necessary conditions (demarcation) for drizzle formation. The corresponding numerical simulations are referenced to as the *RF01*-run and the *RF07*-run, respectively. In both cases the cloud top height was about 850 m (Stevens et al., 2003a,b; 2005a). The ridged upper boundary is identified with the temperature inversion at this level. To reproduce the statistical properties of the velocity field which were similar in both flights the structure function measured by Lothon et al (2004) for the conditions of flight RF01 was applied for both simulations. Amplitudes of the harmonics were calculated to reproduce the observed profile of turbulent vertical velocity variation $\left\langle W'^2 \right\rangle$ (Stevens et al, 2005a). Harmonics of the largest scales represent large eddies, which usually exist in the cloudy and cloud-free BL (e.g., LeMone 1973; Ivanov and Khain 1975, 1976, Stevens et al, 1996). In order to perform simulations both dynamical and thermodynamical parameters were adopted as it was discussed in detail in Pt1 of the study. The specific feature of the flights under consideration was that many parameters such as the droplet concentrations, the sea surface temperatures, the cloud top heights, etc. were quite similar. Observed and simulated parameters of the clouds are presented in **Table 2**.

Table 2. Comparison of calculated values with those measured in flights RF01 and RF07.

	Flight RF01	No Drizzle case	Flight RF07	Drizzle case
Cloud base [a]	585 m	530m- 600m	310 m	350-450 m
$\overline{q}_t$	9 g/kg	9 g/kg	10 g/kg	10 g/kg
LWC_{max}	0.5 g/kg	0.6 g/kg	0.8 g/kg	0.8 g/kg
Drizzle flux [b]	Below Detection level	Below detection level	0.6 (±0.18) mm/day	0.5 mm/day
Droplet Concentration	~150 cm^{-3}	~190 cm^{-3}	~150 cm^{-3}	~160 cm^{-3}
The range of effective radii at 820 m		8-12 μm	10-14 μm	10-14 μm
Mean effective radius of DSD near the surface		75 μm	100 μm	100 μm
Maximum effective radius near the surface		100 μm	160 μm	200 μm
Maximum radar reflectivity	-12 dBZ	-12 dBz	4-5 dBz	4-5 dBz

The main difference between the conditions was the difference in the mean specific humidity: $9\ g/kg$ in RF01 versus 10 g/kg in RF07, which determined the difference in the cloud base height: 585 m in the RF01 and 310 m in the RF07. As it was mentioned above, the purpose of the simulation was to form clouds in the initially non-cloudy BL by vertical mixing of air parcels. Correspondingly, at t=0 the relative humidity (RH) in all parcels was set less than 100%. Hence, we could not use the vertical temperature and humidity profiles observed in the cloudy BL as the initial ones. In contrast, the model had to generate by itself the profiles close to the observed ones as a result of the BL mixing. Since amount of total water content (water vapor + liquid water) conserves in the BL in the process of vertical mixing and condensation, the initial mixing ratio profiles were chosen to have mean values of $9\ g/kg$ and 10

g/kg to simulate clouds in the RF01 and the RF07, respectively. Similar considerations were applied for the choice of initial temperature profiles. The most important in such choice was to get the RH within the BL and cloud base heights close to observations. Supplemental simulations indicate that the sensitivity of the temperature profile after model 'spin-up" to the choice of the initial temperature gradient is weak, because vertical BL mixing leads to dry adiabatic temperature gradient below cloud base and nudges the temperature gradient to the moist adiabatic aloft. The initial profiles of the mixing ratio and liquid water static energy temperature used in the model as well as the changes of these profiles with time are shown in Pt 1. At t=0 the aerosol size distributions in all parcels were assumed similar (Pt1). These distributions were taken from in-situ measurements.

4. FORMATION OF THE CLOUD MICROIPHYSICAL STRUCTURE

4.1 SPATIAL INHOMOGENEITY OF THE INTEGRAL PARAMETERS

As it was shown in Pt 1, the model reproduces well the vertical profiles of specific humidity, LWC, drizzle size, averaged drizzle fluxes, as well as the radar reflectivity. As an example, we present **Figure 1** which compares the measured and simulated vertical profiles of the horizontally averaged LWC. Simulated profiles are plotted with increment of 5 min. One can see that the mean LWC in the RF07 case exceeds that in the RF01 case both in observations and simulations. The model reproduces the observed LWC profiles quite well. The model tends to slightly overestimate the maximal values of LWC measured by the Gerber and King probes (especially in the *RF01*-run), which can be attributed to the lack of the turbulent mixing between the parcels.

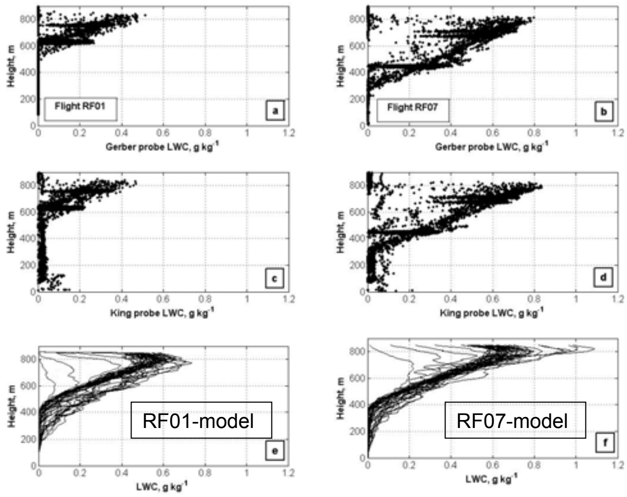

*Figure 1: **V**ertical profiles of the horizontally averaged values of the LWC measured (upper and middle panels) and simulated (lower panels) in the RF01 case (left panels) and the RF07 case (right panels). Simulated profiles are plotted with increment of 5 min.*

Figure 2 shows the spatial dependencies of the LWC, droplet concentration, the DSD width and DSD dispersion (ratio of the DSD width and mean radius) at z= 800m in the *RF07* and *RF01* runs, respectively. One can see high variability of all parameters with significant changes at distances of a few tens of meters. Such variability was found to be a typical feature of stratocumulus clouds (Korolev 1995). The spatial variability in the non-drizzling *RF01* run is even stronger because non-cloudy parcels cover larger areas above the geometric cloud base in this run (see below).

Figure 3 shows the normalized horizontal correlation functions $B(x)$ of LWC, droplet concentration, vertical velocity and radar reflectivity calculated at the levels of 500m, 650m and 800 m in both *RF01* (left panels) and *RF07* (right panels) runs. The values of the integral spatial scale determined as

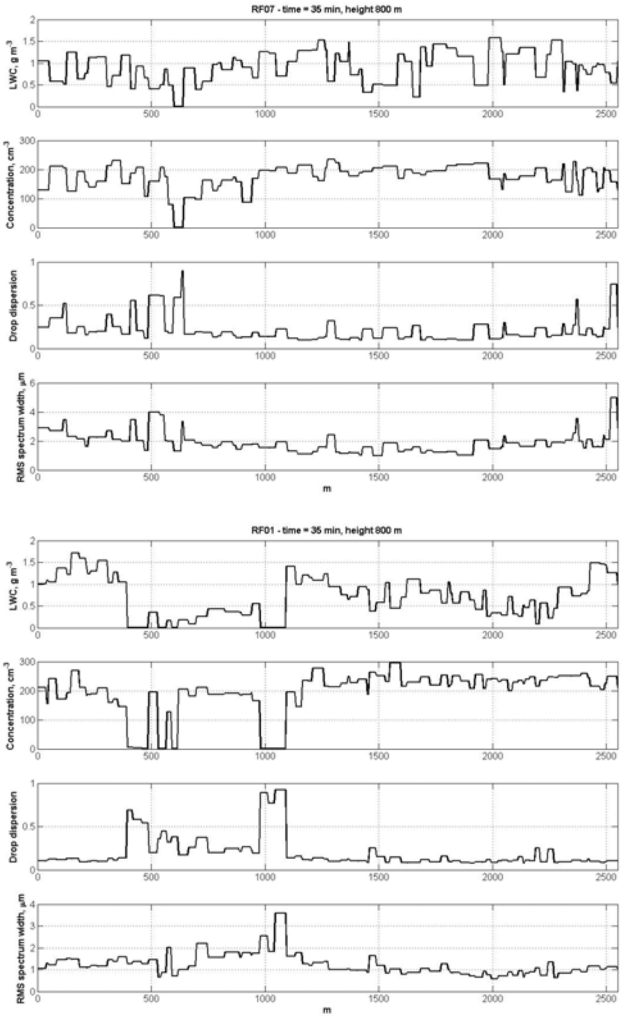

Figure 2. *Upper panels: The horizontal cross-sections of the LWC and droplet concentration, the DSD width and the DSD dispersion at z=800m in simulation RF07 at t=35 min. Lower panel: the same as in the upper panel, but for the RF01 run.*

$L_o = \dfrac{1}{B(0)}\int\limits_0^{\infty}\left|B(x)\right|dx$ is presented in the figure as well. One can see the droplet concentration has the minimum L_o (ranged from 60 m to 75m), while the radar reflectivity has maximal L_o (ranged from 120 m to 217 m). Near the cloud base the LWC has the same L_o as the drop concentration. However, in the

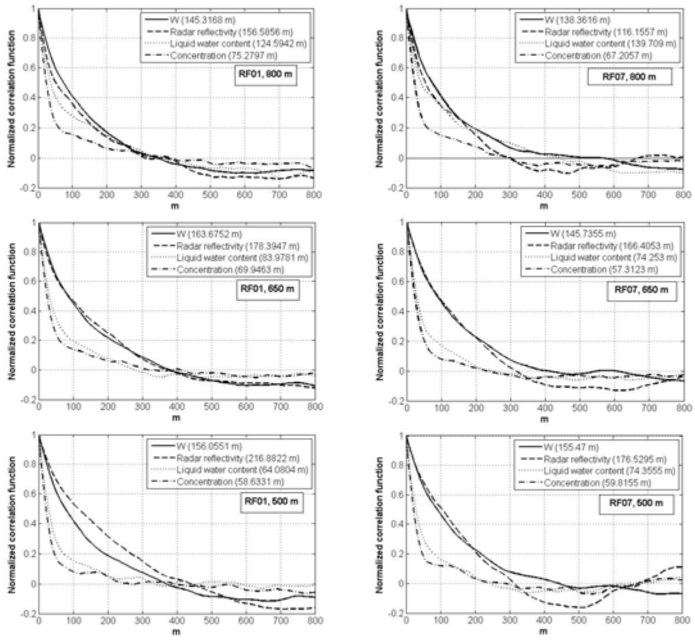

Figure 3. *The correlation functions of LWC, droplet concentration, vertical velocity and radar reflectivity calculated at the levels of 500m, 650m and 800 m in both RF01 (left panel) and RF07 (right panels). Values of the integral scale (correlation radius) are presented in the panels as well.*

vicinity of the cloud top the integral scale of the LWC increases. We attribute the differences in the integral scales of these quantities to the following. Droplet concentration is the zero moment of the DSD, any vertical shift of parcels can lead to nucleation or evaporation of small droplets which can affect droplet concentration, but may not affect LWC significantly. The LWC is the third moment of the DSD, which is a more "inertial" parameter as compared to the droplet concentration. The characteristic time of condensation determining variation of the LWC is larger than that of nucleation. The vertical velocity fluctuations decrease toward cloud top. It can be one of the reasons of increase in the integral scales of concentration and, especially LWC with height (in more detail this mechanism is discussed in section 4.4). The radar reflectivity (the sixth moment of DSD) reflects the existence of largest drops. The characteristic time of formation of radar reflectivity includes also the time for collisions and exceeds the characteristic time of the condensation. The reflectivity has the integral scale, which is quite close to that of the vertical velocity. This large integral scale reflects the fact that the fluctuations of radar reflectivity are caused by the fluctuations of the most energetic velocity harmonic of the large scale (large eddies) (see below). Note that the integral spatial scale of the turbulent velocity field was taken as 158 m (Lothon et al 2004).

The variability of the LWC and concentration is often attributed to non-adiabatic processes, such as parcel mixing or the dilution by dry air penetrated through the cloud top and drizzle loss (Stevens 1998; Wood 2005). Note that in the *RF01*-run all parcels are close to adiabatic (very weak droplet sedimentation and no turbulent mixing with the neighboring parcels). Nevertheless, the DSD dispersion in the RF01 case is actually similar to that in the RF07. Thus, the non-adiabatic processes do not play a dominating role in the formation of DSD and its variability. The mechanisms responsible for the DSD formation will be discussed in the next section.

4.2. THE DSD FORMATION

As can be seen in **Figures 2 and 4**, the averaged value of the DSD dispersion is about 0.2-0.3, and droplet spectrum widths is about 2 μm which is in a good agreement with the observations in stratocumulus clouds (e.g. Martin et al. 1994; Pawlowska et al 2006).

At the same time the dispersion actually varies in simulations within a wide range from 0.1 to about 1.0 **(Figure 5)**. There were many attempts to explain the DSD broadening within the frame of the stochastic condensation theory (see review in Khain et al, 2000). The simplified equation for diffusion/evaporation in which "curvature" and "chemical" terms are neglected implies that the DSD in ascending and in descending branches of parcel trajectory should be similar at the same height level.

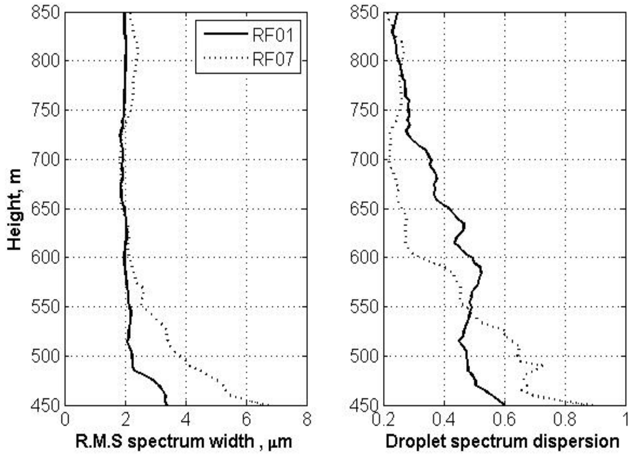

Figure 4*. Vertical profiles of the horizontally averaged droplet spectrum width and the droplet spectrum dispersion at t = 100 min in RF01 and RF07 runs.*

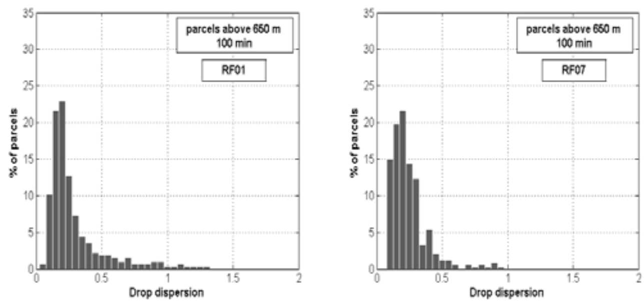

Figure 5. *Histograms of droplet spectra dispersion in clouds simulated in the RF01 (left) and RF07 (right) runs at the levels located above z=650 m at 100 min.*

This creates problems with the explanation of the horizontal variability of the DSD parameters observed in situ. Korolev (2005) showed that the accounting for these terms in the equation of the diffusion growth introduces some asymmetry in the diffusion growth and evaporation processes and to the DSD broadening. However, the asymmetry becomes visible after a great number of successive updrafts and downdrafts of a parcel within the cloud layer. Hence, this mechanism is not efficient. Another mechanism leading to a DSD broadening is the secondary drop nucleation (Korolev and Mazin, 1993, Korolev 1994, Pinsky and Khain 2002; Segal et al, 2003), when supersaturation in an ascending parcel exceeds that at the lifting condensation level (hereafter, LCL). It is clear that in case the secondary droplet nucleation takes place, the DSDs in the ascending and descending branches of parcel trajectory differ.

We will discuss here two other mechanisms leading to a dramatic difference in DSD parameters in the ascending and descending branches of parcel trajectory in a Sc.As a first example, we take a parcel beginning its ascent below the geometric cloud base, which trajectory is shown in **Figure 6.** The DSD in this parcel at different points along the trajectory are shown as well. The lifting condensation level (LCL) of this parcel is ~300 m and the parcel rapidly ascends to the upper levels (800 m).

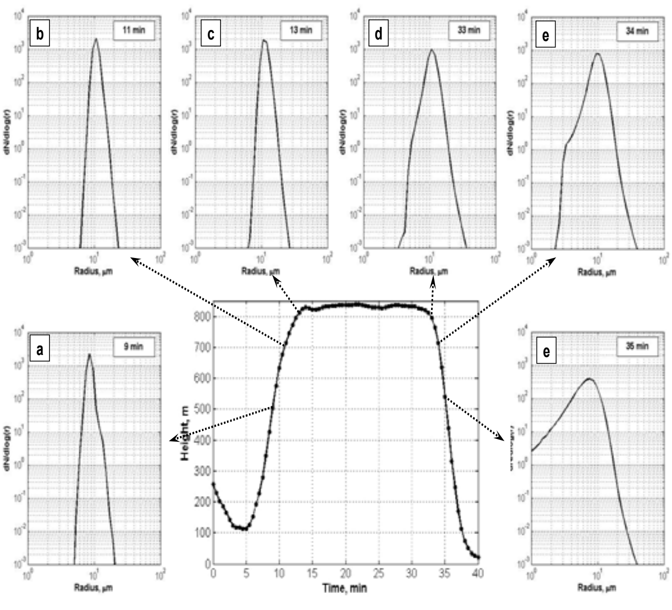

Figure 6. *Trajectory of one of the parcels in the RF07 run. DSDs are presented in several points along the trajectory.*

One can see that DSD dispersion is small at the ascending branch of parcel trajectory. The DSD at the panel (d) indicates the formation of larger droplets by collisions. Descending of the parcel leads to negative supersaturarion and to the formation of small drops. At the same time the size of large droplets decreases to a smaller extent. As a result a significant increase in the DSD dispersion takes place. The DSDs at the same levels turned out to be quite different. Above 300m the DSD dispersion first rapidly decreases to 0.07 in agreement with the equation of the diffusion growth and then slightly increases by appearance of the smallest droplets with the increase in supersaturation and droplet sedimentation from above. The parcel is located near the cloud top for about 20 min. During this horizontal motion the DSD changes, and larger drops (up to radius of 20 μm) form by droplet collisions. As it was shown by Pinsky and Khain (2002) droplet collisions (even not efficient) play a very important role at the stage which is usually referred to as the diffusion growth stage, leading to the formation of drops of the size larger then it could be obtained by only diffusion growth. Further parcel descending leads to a dramatic growth of the DSD dispersion in the parcel, because of a significant decrease in the size of small droplets due to evaporation, while the size of largest droplets decreases to much less extent. As a result, DSDs as well as all their characteristics (including the DSD dispersion) turn out to be different at the same levels within parcel updraft and downdraft branches. Thus, existing of collisions between droplets and succeeding evaporation make DSD in updraft and downdrafts significantly different, increasing the averaged DSD width and dispersion. The existence of small droplets with radii below ~5 μm in Sc at significant distances above the cloud base is a well established observational fact (Nicholls, 1984; Khairoutdinov, and Kogan, 1999). Both the secondary droplet nucleation and partial droplet evaporation in the downdrafts can be the mechanisms explaining this effect. Analysis shows that the DSD dispersion in ascending parcels is as a rule smaller than in the descending ones. One of the reasons of this is the effect of collisions.

Figure 7 presents another example of an air parcel.

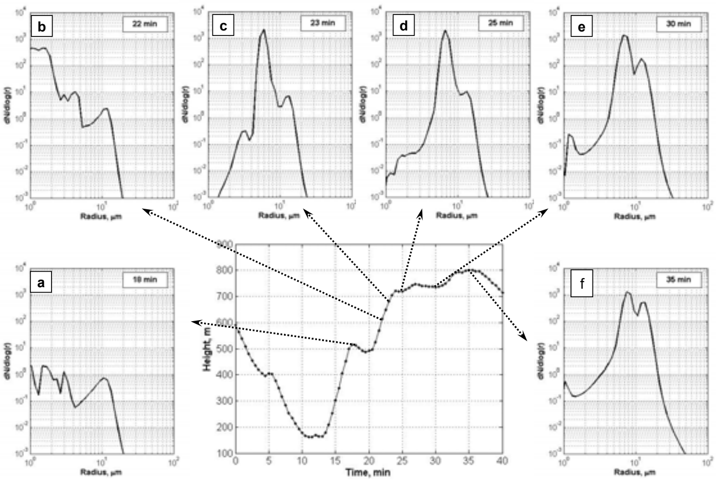

Figure 7. *Trajectory of a parcel which starts moving above the geometric cloud base. Panels (a) and (b) show that particles exceeding 1 μm in radius represent non-activated wet aerosols. Droplet nucleation takes place at t=22 min at z= 600 m. Panels (c) and (d) indicate the dominating role of diffusion growth. In panel (e) one can see that collisions contribute to increase in the concentration of the largest droplets in the DSD. The DSD dispersion decreases during the diffusion growth, remaining, however larger than 0.1. Collisions and new nucleation increase the DSD width.*

Initially the parcel was located in the upper half of the BL it was initially a non-cloudy one. The parcel first moves down and then ascends. Below LCL the size distribution is formed by haze particles (non-activated aerosols). The largest radius of the wet particles exceeds 10 μm, which corresponds to the largest size of dry aerosols of 2 μm in the aerosol spectrum. Since the mean radius is very small, the dispersion of the spectrum of the wet aerosols is large (0.96). The parcel crosses its LCL in the upper half of the BL (slightly above 600m), indicating the formation of new cloudy parcels within the cloud layer. Since the mean droplet radius is small just above LCL, the DSD dispersion is large (0.4). Then the dispersion decreases to 0.1 due to diffusion growth and starts increasing again by collisions and new drop nucleation.

The histograms of LCL of the parcels in the RF07 run are shown in **Figure 8**. The existence of parcels with low LCL is determined by high air humidity preset in all parcels at t=0. The number of parcels with low LCL decreases with time. At the same time the number of parcels with LCL above the geometrical cloud base (450 m) remains significant.

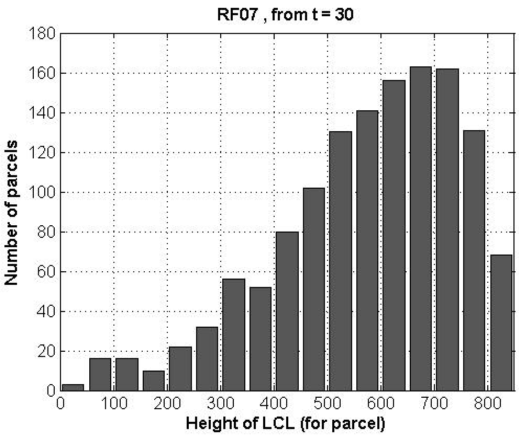

Figure 8. *The histograms of lifting condensation level heights of parcels in the RF07 run at t>30 min.*

Droplet sedimentation and collisions lead to the fact that the LCL of a parcel does not coincide with the level of total droplet evaporation in downdrafts. It means that the DSD will be different at the same height level. Thus, the secondary droplet nucleation, droplet collisions, the formation and disappearance of cloudy parcels at different heights within the cloud layer lead to a high spatial inhomogeneity of cloud parameters, as well as to the high values of the mean DSD dispersion.

4.3 LUCKY PARCELS AND THEIR PARAMETERS

High inhomogeneity of DSD parameters in a Sc shows that drizzle cannot form in all parcels at the same time. Moreover, many parcels cannot produce drizzle during their short residential time in the cloud, and all (or most) droplets evaporate in these parcels in downdrafts not reaching the size needed for collision triggering. This statement agrees with the observations showing that drizzle covers as a rule a comparatively small area of stratiform clouds (e.g. Stevens et al, 2003a,b, 2005; Wood 2005). It is especially valid for lightly drizzling Sc (such Sc in the RF07). The latter suggests the existence of parcels, in which large droplets exceed some critical size and trigger droplet collisions leading to the drizzle formation. The largest drops fall down and collect smaller ones in parcels located below. The parcels in which intense droplet collisions is first triggered will be referred here to as "lucky" parcels. To simplify the analysis of lucky parcels a supplemental simulation *RF07_no_sed* has been carried out, in which no droplet sedimentation was included. We assume that parcels, in which large droplets and drizzle form first, are lucky ones. Since we are looking for parcels in which intense collisions have just started, the droplet sedimentation should not be an important factor at this stage.

Figure 9 shows the radar reflectivity-LWC (hereafter, Z –LWC) diagrams at t=25 min, t=30 min, t=35 min and t=40 min in the *RF07_no_sed* run.

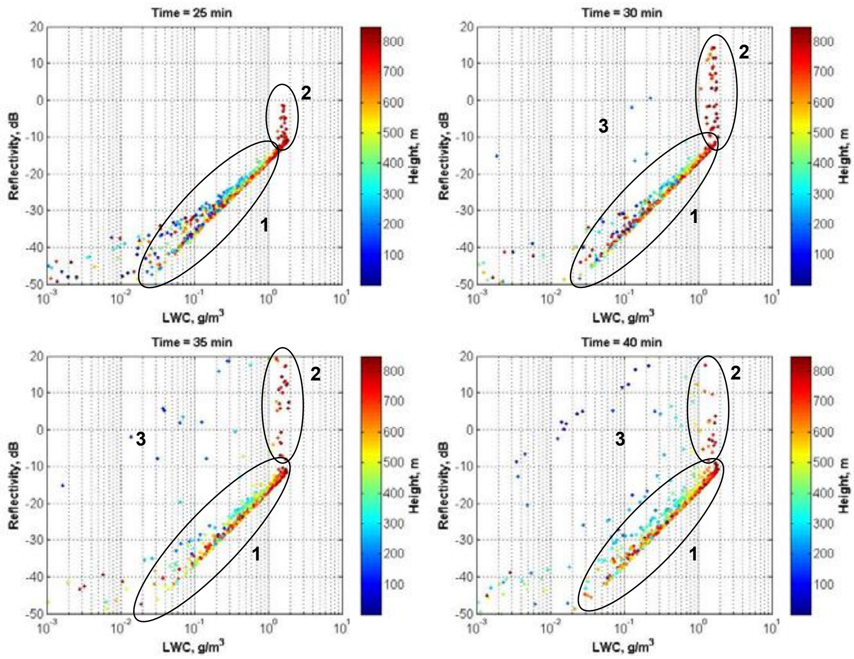

Figure 9. *The Z –LWC diagrams at t=25 min and t=30 min, t=35 min and 40 min in the RF07_no_sed run. Colors denote the height of parcel location. Numbers in the figures denote zones corresponding to different microphysical processes: zone 1 represents the diffusion growth, in parcels belonging to zone 2 intense collisions and drizzle formation takes place. Zone 3 is formed by descending parcels in which LWC decreases by evaporation. One can see that drizzle formation begins in parcels with LWC exceeding ~1.5* gm^{-3}. *These parcels are located near cloud top.*

One can distinguish three main zones on this diagram. The first zone corresponds to the stage of the diffusion growth, when Z is small (less than -10 DBZ) and the LWC growth leads to the growth of Z (zone 1 in the figure). The second zone with Z>-10 DBz corresponds to the beginning of intense collisions and drizzle formation. In this zone the sharp growth of Z takes place under the nearly constant LWC (zone 2 in the figure). Zone 3 is formed by descending parcels, in some of which intense collisions are accompanied by partial drop evaporation (i.e. by decrease in LWC). One can see that intense collisions start in parcels with LWC exceeding about 1.5 gm^{-3}. These parcels are located near the cloud top. One can see also that the radar reflectivity of -10 DBz can serve as a threshold separating Sc in which drizzle is produced from those in which drizzle does not form.

To show at which effective radii the intense collisions are triggered, we present **Figure 10** where the relationship $LWC - r_{eff}$ in the *RF07_no_sed* is shown at time 35 min. The arrows in the Figure show the shift of corresponding parcels on $LWC - r_{eff}$ diagram during the previous 5 min period. In Figure 10 one can identify the same zones that were seen in Figure 9. In parcels forming zone 1 the diffusion growth dominates, zone 2 is formed by parcels in which intense collisions are triggered and drizzle is forming. Zone 3 is formed by descending parcels, in which small droplets evaporate, which results in rapid increase in r_{eff}. During the diffusion growth the effective radius increases with LWC monotonically. Beginning of intense collisions is seen by the increase in r_{eff} under the nearly the same LWC. One can see that intense collisions start when LWC exceeds ~1.5 gm^{-3} and r_{eff} exceeds about 12 μm. These values of r_{eff} are in good agreement with observations (Gerber, 1996; VanZanten et al, 2005; Twohy et al 2005), as well as with results of detailed numerical simulations of the DSD formation in an ascending cloud parcel (Pinsky and Khain 2002). Decrease in the LWC and strong increase in r_{eff} that is seen in zone 3 is related to descending of corresponding parcels, which is accompanied by evaporation of smallest droplets in the DSD.

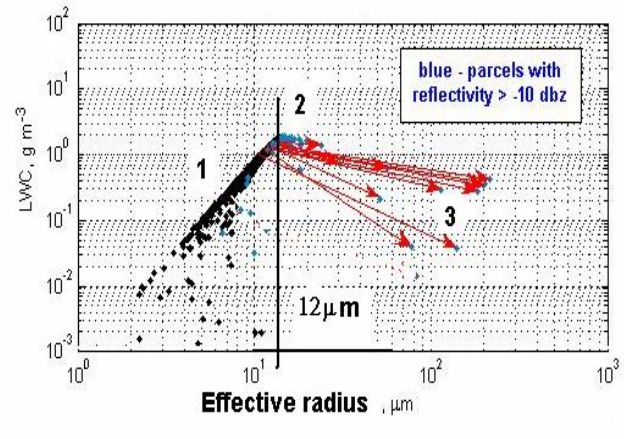

Figure 10. *The LWC-r_{eff} scattering diagrams in the RF07_no_sed run at t=35 min. Numbers denote the same zones as in Figure 9. One can see that triggering of intense collisions begins when LWC exceeds 1.5 gm^{-3} and effective radius exceeds 12 μm.*

Figure 11 shows the LWC–drizzle drop concentration relationships along the trajectories of several parcels in the *RF07_no_sed* run. One can see that very small amount of large droplets form even at comparatively small LWC. However, at small LWC these droplets cannot trigger intense drizzle formation, and the increase in the mean and effective radius is related to the diffusion growth (see Pinsky and Khain 2002 for detail). In most parcels LWC does not reach the values necessary for the collision triggering. When these parcels start descending, both LWC and the large drop concentration decreases. The line of red arrows illustrates changes in the LWC and the concentration of large droplets each 5 min in one of the lucky parcels. Triggering of the formation of large droplets takes place when the LWC exceeds 1.5 gm^{-3} (right panel).

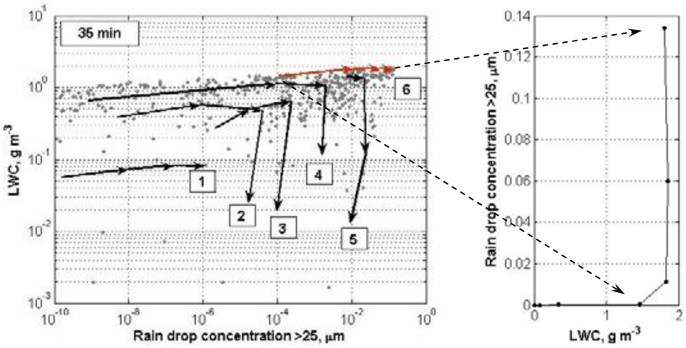

Figure 11. *The LWC–drizzle drop concentration along tracks of six different parcels in the RF07_no_sed run during the first t=35 min. Arrows indicate the changes in the parcel location on the diagram for the previous 15 minutes. The line of red arrows (marked by number 6) illustrates changes in the LWC and the concentration of large droplets in one of the lucky parcels. Significant concentration of large droplets is reached when the LWC exceeds 1.5* gm^{-3} *(see the right panel).*

Figures 9 -11 indicate that the rapid formation of large drops (drizzle) by collisions takes place when LWC exceeds about 1.5 gm^{-3}. It should be noted that such large values of LWC in the RF07 run are reached only in a small fraction of cloud parcels. The maximum value of the horizontally averaged LWC in the *RF07*-run is 0.8 gm^{-3} (Figure 1). The formation of lucky parcel corresponds to the fluctuations of LWC that can exceed two LWC standard deviations. **Figure 12** shows the LWC histograms in (a) the non-drizzling (*RF01*) and (b) the drizzling (*RF07*) runs plotted for all parcels located above 600 m in the entire simulation. Note first that there is a significant amount of non-cloudy parcels with negligible LWC above the 600 m level. The existence of such parcels (non-cloudy volumes) within the stratocumulus layer and their role in the formation of mean DSD parameters were discussed in section 4.2. One can see also that the fraction of parcels with LWC> 1.5 gm^{-3} is about 1% in the weakly drizzling cloud and about 0.36 % in non-drizzling clouds. We consider the value of LWC~ 1.5 gm^{-3} as a threshold value that should be exceeded for drizzle formation (for the aerosol conditions of the RF01 and RF07). The Sc observed in the RF07 is a weak drizzle cloud. So, the fraction of lucky parcels in Sc producing light drizzle can be evaluated as ~1%. On the one hand, this result shows that drizzle in Sc is triggered by a small number of lucky parcels. On the other hand, we assume that in order to produce heavy drizzle, Sc cloud should have the fraction of lucky parcels higher than 1%.

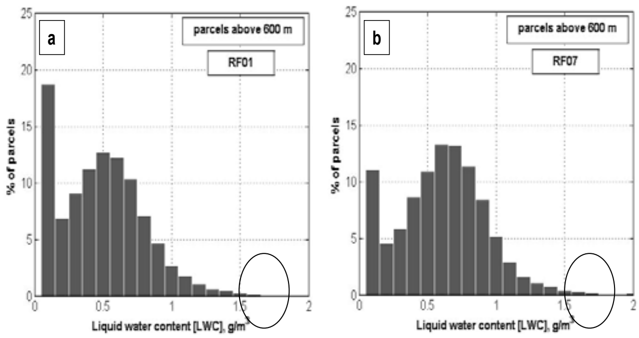

Figure 12. *The LWC histograms in (a) the non-drizzling (RF01) and (b) the drizzling (RF07) runs plotted for all parcels above 600 m in the entire simulation. The fraction of parcels with LWC > 1.5* gm^{-3} *is about 1% of cloud parcels in the drizzling cloud and about 0.3 % in non-drizzling clouds.*

Note in this connection the difficulties which arise in simulation of the drizzle formation in the 1-D models of CTBL, which use horizontally averaged values of the parameters (see also the comments by Stevens et al., 1998b). According to our results, drizzle hardly can form under the LWC equal to the horizontally averaged values in a drizzling stratocumulus clouds.

The question arises: "what are the specific features of parcels in which LWC can exceed 1.5 gm^{-3} in the *RF07*-case?" Note first, that the LWC in parcels increases with height during their ascent. So, the LWC can exceed 1.5 gm^{-3} only in the parcels reaching the cloud top, as was shown in Figure 9. However, as can be seen in Figure 2, the LWC near cloud top also varies with space and time. So, additional factors exist, e.g., the specific initial parcel location in which the mixing ratio is high. In our simulations parcels with the maximum values of mixing ratio were located near the surface (which is a quite typical feature of the BL). **Figure 13** supports the assumption concerning an important specific feature of the lucky parcels: namely they are initially located near the surface.

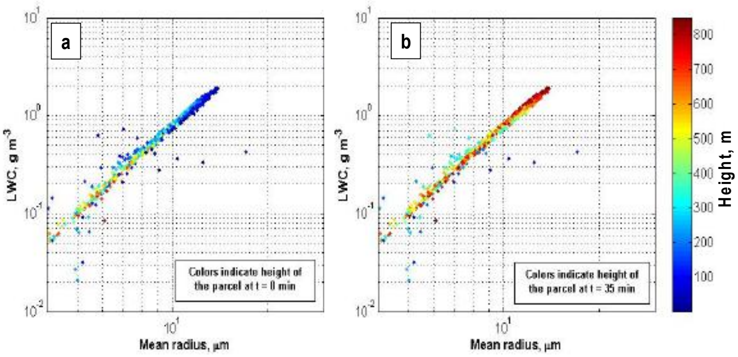

Figure 13. *LWC – mean radius diagram in the RF07_no_sed run at t=35min in panel (a) the colors indicate the parcel's initial height (at t=0). In panel (b) color indicates the height of the parcel at t=35 min. The parcels with large LWC (lucky parcels) start at t=0 near the surface where mixing ratio was maximum and reach the top levels of the cloud.*

Besides, high value of LWC should exist in a parcel for certain period of time needed for collisions to form large drops (Pinsky and Khain 2002). An increase in the residential time (determined here as the time during which supersaturation in a parcel is positive) favors the formation of the largest drops in the DSD, i.e. fosters the collision triggering (Feingold et al 1996). Analysis shows that parcels with the largest LWC and the largest effective radii have as a rule longer residence time. While the residence time for most particles is about 10 min, the parcels in which LWC exceeds 1.5 gm^{-3} have residence time of 15 min to 25 min. Such correlation between large LWC and the long residential time can be attributed to the following. Parcels with large LWC values are parcels that reach high levels near the cloud top where vertical velocities are small. So, parcels reaching the high levels (where small positive supersaturation takes place) tend to remain at these high levels longer. In parcels which do not reach higher levels positive supersaturation is replaced by negative one with the change of the vertical velocity sign. We assume that the increase in the spatial radius of correlation with height for LWC seen in Figure 3 can be related to this effect. Thus, it seems that the condition LWC> 1.5 gm^{-3} in most cases can serve as a sufficient condition for triggering the drizzle formation (under thermodynamic and aerosol conditions of RF01 and RF07).

The scheme presented in **Figure 14** summarizes the results concerning specific features of the lucky parcels. Most parcels starting from lower levels do not reach the highest levels of the cloud and instead start descending which leads to a decrease in the LWC and the drop concentration. The fraction of parcels with larger LWC and low residential time (which start descending just after reaching the cloud top) is comparatively small. A great number of parcels starting at higher levels have low initial mixing ratio, which is not enough to produce large LWC. Only a small amount of parcels can become lucky and produce drizzle.

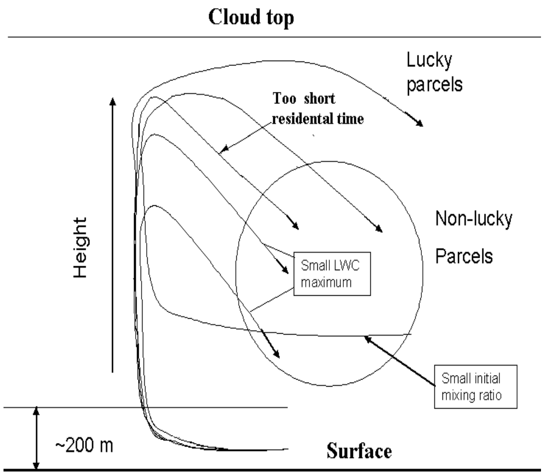

Figure 14. Conceptual scheme of parcel tracks separating lucky and non-lucky parcels in non-mixing limit. Lucky parcels start ascending near the sea surface and reach heights close to the cloud top. Lucky parcels have significant residential time with high LWC.

4.4 DRIZZLE FLUXES

After drizzle formation near cloud top the evolution of the DSD continues according to several mechanisms (see Khain et at., 2007, and Pt1). According to the first mechanism, drizzle falls from the parcels-donors down and can collect small droplets within parcel acceptors. As a result, radar reflectivity in parcels having low LWC sharply increases. At the same time parcel-donors loose part of their large drops, so that radar reflectivity in these parcels decreases together with the decrease in LWC. As a result of all of these processes, in the lower part of the BL a zone forms in which large values of Z are accompanied by comparatively small values of LWC. This zone is denoted as zone 3 in the Z-LWC diagram (**Figure 15)**.

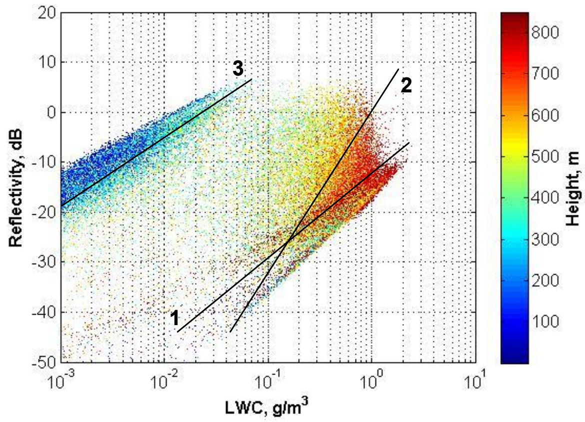

Figure 15. The Z-LWC diagram for simulation RF07. Each point indicates cloud parcel. The location of parcels in the diagram are indicated each 5 min. Colors denote the height of parcel location in the BL. Lines indicate approximate dependencies Z(LWC) for three regimes: (1)- the diffusion growth; (2) collision triggering; and (3) the regime of the developed drizzle (see Pt 1 for detail)

In Khain et al (2008) this zone is associated to "drizzle" stage of the Sc evolution. The detailed analysis of drizzle evolution using the Z-LWC diagrams is presented by Khain (2008) and in Pt1. Here we will be interested in the relationship between drizzle fluxes and the velocity field. As it was shown in the section 4.3 the lucky parcels start their ascent in the vicinity of the surface and ascend to the upper levels close to the cloud top. Such updrafts are, supposedly, related to large eddies in the BL. This makes the role of large eddies in the BL of high importance for drizzle formation. The characteristic size of the large eddies is about one km, i.e. of the scale of the BL depth. Taken into account the characteristic aspect ratios of large eddies (2-3), the distance of 1-2 km should be close to the minimum intermittent distance between the neighboring zones of significant drizzle fluxes. It seems that this conclusion is supported by observations of Sc (Wood 2005, vanZanten et al 2005). **Figure 16** shows the changes in the horizontal direction of a) drizzle flux at z=400 m and 600m, and the vertical velocity at z=400 m in the *RF07*-run at t=100 min when the maximum drizzle flux took place. One can see that the zones of strong drizzle flux (determined as $F_{driz} = -\int_{1\mu m}^{\infty} N(r)m(r)\left[W - V_t(r)\right]dr$, where $N(r)$, $m(r)$ and $V_t(r)$ are the concentration, mass and sedimentation velocity of drop with radius r, W is the air vertical velocity) coincide with zones of strong downdrafts caused by the most powerful harmonic representing large eddies.

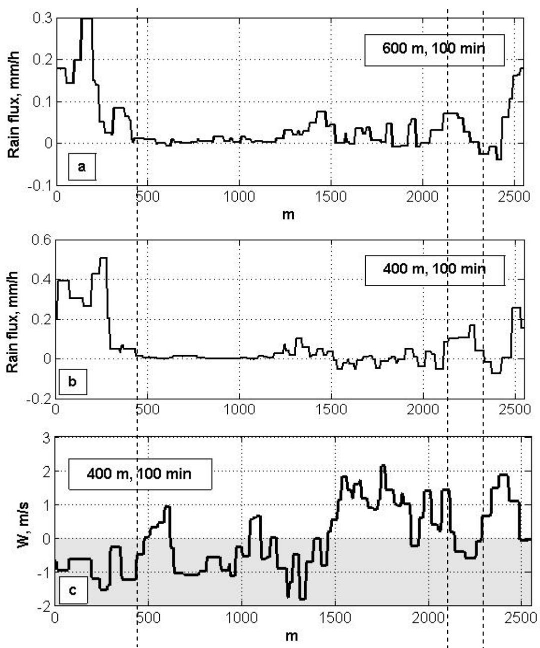

Figure 16. *Horizontal cross sections of a) drizzle flux at z=600m, b) drizzle flux at z= 400 m and c) vertical velocity at z=400 m in the RF07 run at t= 100 min when the maximum drizzle flux takes place. Vertical dashed lines are plotted to stress the relationship between drizzle flux and vertical velocity structure determined by large eddies.*

This result agrees well with the fact that the correlation radii of vertical velocity and radar reflectivity are very close (Figure 3). This result also supports the scheme of drizzle formation plotted in Figure 14. It seems that trajectories of lucky parcels are determined by the outermost streamlines of the large eddies. Drizzle is triggered near cloud top in zones close to downdrafts related to large eddies, so that large drops fall largely within zone of cloud downdrafts. Smaller droplets have low sedimentation velocity and can descend only within downdrafts. As was discussed above, drizzle is triggered near the cloud top. Further growth of the drizzle flux depends on the liquid water pass in the cloud, and consequently, on the cloud depth (because LWC is the linear function of height above the cloud base, Figure 1).

During the period of developed drizzle the maximum drizzle flux is reached near the cloud base. The rate of the increase of drizzle flux agrees well with the observations in Sc clouds (Woods 2005). The fluxes decrease below the cloud due to evaporation. The drizzle flux at the surface depends on the balance between drizzle flux growth within the cloud and drizzle evaporation. In the *RF01*-run at cloud base there is a very small amount of drizzle and it fully evaporates below the cloud, so no drizzle reaches the surface. In the *RF07*-run the decrease of drizzle flux by evaporation can reach 40 to 50% which agrees with evaluations presented in VanZanten et al. (2005) for drizzling clouds measured during DYCOMS-II

5. DISCUSSION AND CONCLUSIONS

In Pt 1 of the study a novel trajectory ensemble model (TEM) of a cloud-topped boundary layer was presented in which a great number of Largangian parcels move with the turbulent like flow with observed statistical properties. The model was applied to the simulation of stratocumulus clouds observed in two research flights

RF01 (no drizzle) and RF07 (weak drizzle) conducted during the field experiment DYCOMS-II. It was shown that the model reproduced well the vertical profiles of horizontally averaged quantities such as absolute air humidity, the droplet concentration, LWC, as well as drizzle size and drizzle flux.

The present study is a continuation of Part 1. It is dedicated to the investigation of the formation of the microphysical structure of stratocumulus clouds in a non-mixing limit (when no turbulent mixing between Largangian parcels is taken into account). The following questions have been addressed: a) what are the factors leading to a significant spatial variability of LWC, droplet concentration, DSD width, etc. in stratocumulus clouds? b) What mechanisms of DSD formation lead to realistic DSD width and dispersion in the non-mixing limit? c) How does drizzle form in stratiform clouds and what are the specific conditions (thresholds) leading to the drizzle triggering? d) what is relationship between drizzle flux and large eddies in the BL.

It is shown that spatial variability of microphysical parameters is determined by several mechanisms: the secondary droplet nucleation above the lifting condensation level, droplet collisions and formation/disappearance of cloudy parcels within the cloud layer. These factors lead to a dramatic difference in the DSDs parameters in ascending and descending branches of the parcel motion. These mechanisms lead to high spatial variability of DSD parameters, and to mean DSD width and dispersions similar to those observed in-situ.

It is clear that small scale turbulent mixing should also influence the DSD shape. This problem will be addressed in the next study.

Drizzle formation was investigated using the Z-LWC and $LWC - r_{eff}$ diagrams calculated by the model in non-drizzle and drizzle cases (including the simulation in which drop sedimentation was switched off). The analysis showed that

a) Collisions are triggered when LWC in the parcels exceeds a threshold value $LWC_{theshold}$ which in the RF07 case turned out to be 1.5 gm^{-3} .

b) The threshold value of LWC exceeds the maximum horizontally averaged LWC (of 0.8 g/kg) by ~2 standard deviation values. The latter shows that the number of the parcels with LWC> $LWC_{theshold}$ (referred here as lucky parcels) in clouds with light drizzle is quite small, about one percent of the total number of cloudy parcels. Smaller amount of lucky parcels in the *RF01* case (0.36%) was not enough to induce drizzle flux. We assume that for formation of heavy drizzling clouds the fraction of lucky parcels should be larger than 1%.

c) The lucky parcels start their motion near surface and reach cloud top, where remain for a comparatively long period of time. Their tracks are closely related to the outermost stream lines of the large eddies. Large droplets form first in the lucky parcels near the cloud top. This result following from the numerical analysis can be derived also from the observed data presented by Wood (2005) and VanZanten et al (2005) (see Fig. 2 in that paper).

d) Rapid drizzle formation starts in the parcels when effective radius exceeds 12-14 μm, which is in agreement with observational (Gerber 1996; Yum and Hudson 2002; VanZanten et al, 2005; Twohy et al 2005) and numerical (Pinsky and Khain 2002) results.

e) Minimum radar reflectivity in parcels producing drizzle was found to be -10 Dbz, this value can be used to separate drizzling and non-drizzling clouds. These evaluations agree well with observations. For instance, Figure 2 in depicting the radar reflectivity in the RF01 shows that a) large drops form first near cloud top, and b) maximum values of Z in this flight were -12 to -10 Dbz, so no large drizzle drops were formed in that case.

As follows from the results of the present study, the lucky parcel tracks are related to the large eddies in the BL. It seems that large eddies determine the minimum distance between neighboring maxima of the drizzle fluxes. Such structure of the drizzle fluxes is clearly seen in Fig. 2 in the study by VanZanten et al (2005) where minimum distance between the neighboring maxima of radar reflectivity is a few km, which corresponds to the size of large eddies. The close relationship between the drizzle formation and the dynamical structure (actually large eddies) was shown in observations (e.g., Stevens et al, 2005b, Petters et al 2006).

Further drizzle development in a Sc is closely related to the process of the drizzle drop sedimentation and collisions with droplets in parcels with lower LWC located below. As a result, a drizzling regime arises, in which large radar reflectivities and large effective radii are observed in parcels with relatively low LWC. This regime is clearly seen in the Z-LWC diagrams. The drizzle flux increases from cloud top down to the cloud base and then decreases below due to the drop evaporation. The resulting drizzle rate at the surface depends on cloud depth and humidity below cloud base. In non-drizzling RF01 cloud the drizzle flux at the cloud base is fully evaporated below cloud base. In the drizzling RF07 case the evaporation decreases the drizzle flux by 40-50 %, which agrees well with the observations.

The question arises: to what extent is the threshold value of the LWC of 1.5 gm^{-3} found in the simulations general? We would like to stress that the threshold value of LWC found in the simulations is related to the aerosol conditions observed during the RF01 and RF07, which lead to the droplet concentration of 150-200 cm^{-3}. It is reasonable to assume that the threshold value of LWC should increase with the increase in the aerosol concentration. In general, the drizzle formation should be determined by the following condition that maximum of LWC determined by environmental conditions such as the mixing ratio and temperature near the surface, etc. should exceed $LWC_{theshold}$ which determines by the aerosol concentration. The thermodynamic conditions (in our case the mixing ratio near surface) did not allow LWC in the RF01 to exceed the threshold value of 1.5 gm^{-3} which should be similar to that in the RF07 because droplet concentrations were nearly similar in these cases. The doubling of the aerosol concentration in a supplemental run led to increase in the $LWC_{theshold}$ so that drizzle did not form under the RF07 thermodynamic conditions in that run. The conceptual scheme of the drizzle formation in Sc under effects of thermo dynamical conditions and aerosols is shown in **Figure 17**. The increase in the mixing ratio near the surface (and some other thermodynamic conditions) increases the maximum value of LWC that can be reached in ascending parcels. It is clear, however, that the maximum value cannot reach large values typical of convective clouds. An increase in the aerosol concentration increases $LWC_{theshold}$. As follows from observations (e.g. Rosenfeld 2000; Andreae et al 2002) and numerical studies (e.g., Khain et al 2004) aerosols with concentrations of a few thousand per cm^{-3} can suppress warm rain from cumulus clouds with LWC max of several gm^{-3}. Because of comparatively small LWC, the drizzle formation can be suppressed by a substantially smaller aerosol concentrations. This determines a high sensitivity of Sc drizzle fluxes to aerosols (e.g. Albrecht, 1989). The condition separating drizzle formation from that of no drizzle is schematically plotted in Figure 17 by a straight line corresponding to the condition $LWC_{\max}$ = $LWC_{theshold}$. We suppose that performing a set of simulations using the model will make it possible to represent the drizzle flux as a function of thermodynamic conditions and aerosol loading.

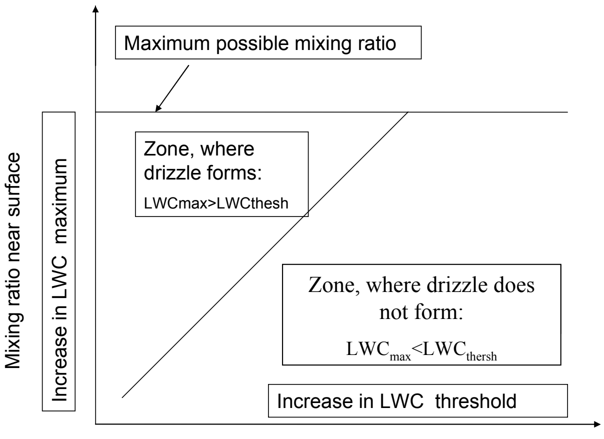

Figure 17. *A conceptual scheme showing the condition of drizzle formation in Sc. Drizzle arises when the LWC maximum determined by environmental conditions exceeds a threshold value determined by aerosol concentration. At high aerosol concentrations no environment conditions can produce the value of the LWC maximum high enough to exceed the threshold. In this case the drizzle formation will be suppressed.*

It should be mentioned that number of lucky parcels is small and can vary depending on structure of large eddies and some other factors. Thus, the number of lucky parcels necessary to trigger drizzle formation can be reached at different time instances or in different places in a cloud. It is possible that the number of the lucky parcels will not exceed a threshold value and drizzle will not form. This indicates that the drizzle formation is of random nature.

Note that a good agreement with observations found in many aspects of microphysical and geometrical cloud structure was obtained in neglecting turbulent mixing between parcels, i.e. in the non-mixing limit. The detailed investigation of role of the turbulent mixing will be presented in the further study.

Acknowledgements

The study has been conducted under support of the Israel Science Foundation (grant 950/07). The authors express their gratitude to Prof. B. Stevens for the interest to this study and useful advice.

REFERENCES

Albrecht, B.A., 1989: Aerosols, cloud microphysics, and fractional cloudiness, *Science.,***24**5, 1227-1230.

Albrecht, B.A., C.S. Bretherton, D. Johnson, W. Schubert, A.S. Frish, 1995: The Atlantic stratocumulus transition experiment, ASTEX. Bull. Am. Meteor.Soc., 76, 889-904.

Andreae, M.O., D. Rosenfeld, P. Artaxo, A.A. Costa. G.P. Frank, K.M. Longlo, and M.A.F. Silva-Dias, 2004: Smoking rain clouds over the Amazon. Science, 303, 1337-1342.

Bott A., 1989: A positive definite advection scheme obtained by nonlinear renormalization of the advective fluxes. *Mon. Wea. Rev*., 117, 1006-1015.

Bott, A., 1998: A flux method for the numerical solution of the stochastic collection equation *J. Atmos. Sci.,* 55, 2284-2293.

Bryan K, 1966. A scheme for numerical integration of the equations of motion on an irregular grid free of nonlinear instability. Mon. Wea. Rev, 94.N 1.

Brenguier J.-L., H. Pawlowska, L. Schuller, R. Preusker, and J. Fischer, 2000b: Radiative properties of boundary layer clouds: droplet effective radius versus number concentration. J. Atmos. Sci., 57, 803-821.

Erlick C., A. Khain, M. Pinsky and Y. Segal, 2005:The effect of wind velocity fluctuations on drop spectrum broadening in stratocumulus clouds*. Atmos. Res.* 75, 15-45.

Feingold, G, B. Stevens, W.R. Cotton, and R.L. Walko, 1994: An explicit cloud microphysical/LES model designed to simulate the Twomey effect. Atmos. Res. 33, 207-233.

Feingold G, B., Stevens, W.R. Cotton, and A.S. Frisch, 1996: The relationship between drop in-cloud residence time and drizzle production in numerically simulated stratocumulus cloud. *J. Atmos. Sci.*, 53, 1108-1121.

Feingold, G., R.L. Walko, B. Stevens, and W.R. Cotton, 1998a: Simulation of marine stratocumulus using a new microphysical parameterization scheme. *Atmos. Res.,* 47-48, 505-528.

Feingold G., S.M. Kreidenweis and Y. Zhang 1998b: Stratocumulus processing of gases and cloud condensation nuclei. 1. Trajectory ensemble model. *J. Geophys. Res.,* 103, D16, 19,527-19,542.

Gerber H., 1996: Microphysics of marine stratocumulus clouds with two drizzle modes. *J. Atmos. Sci*. **53,** 1649–1662.

Harrington, J. Y., G. Feingold, and W.R. Cotton, 2000: Radiative impacts on the growth of a population of drops within simulated summertime arctic stratus. *J. Atmos. Sci.,* 57, 766-785.

Ivanov, V. N. and A. P. Khain, 1975: On dry and moist cellular convection in the atmosphere, *Atmospheric and Oceanic Physics*, 11, 1211-1219.

Ivanov,V. N. and A. P. Khain, 1976: On characteristic values of Rayleigh numbers during the development of cellular convection in turbulent atmosphere, *Atmospheric and Oceanic Physics,* 12, 23-28.

Khain, A. P., M. Ovtchinnikov, M. Pinsky, A. Pokrovsky, and H. Krugliak, 2000: Notes on the state-of-the-art numerical modeling of cloud microphysics. *Atmos. Res.* 55, 159-224.

Khain A., A. Pokrovsky and M. Pinsky, A. Seifert, and V. Phillips, 2004: Effects of atmospheric aerosols on deep convective clouds as seen from simulations using a spectral microphysics mixed-phase cumulus cloud model Part 1: Model description. *J. Atmos. Sci 61, 2963-2982.*

Khain A., M. Pinsky, L.Magaritz, O. Krasnov and H. W. J. Russchenberg, 2008: Combined observational and model investigations of Z-LWC relationship in stratocumulus clouds. *J. Appl. Meteorol.* (in press).

Khairoutdinov M.F., and Y.L. Kogan, 1999: A large eddy simulation model with explicit microphysics: validation against observations of a stratocumulus-topped boundary layer. J. Atmos. Sci., 56, 2115-2131.

Khairoutdinov ,M., and Y. Kogan, 2000: A new cloud physics parameterization in a large-eddy simulation model of maritime stratocumulus. Mon. Wea. Rev. 128, 229-243.

Khairoutdinov, M ., and D. A. Randall, 2003: Cloud resolving modeling of the ARM summer 1997IOP: Model formulation, results, uncertainties and sensitivities. J. Atmos. Sci. 60, 607-625.

Kogan Y, L., M.P. Khairoutdinov, D.K. Lilly, Z.N. Kogan and Q. Liu, 1995: Modeling of stratocumulus cloud layers in a large eddy simulation model with explicit microphysics. *J. Atmos. Sci.,* 52, 2923-2940.

Kogan Y. L., D.K. Lilly, Z.N. Kogan, and V.V. Filyushkin, 1994: The effect of CNN regeneration on the evolution of stratocumulus cloud layers. Atmos. Res., 33, 137-150.

Korolev, A.V., and I.P. Mazin, 1993: Zones of increased and decreased droplet concentration in stratiform clouds. *J. Appl. Meteor.,* 32, 760-773.

Korolev, A.V., 1994: A study of bimodal droplet size distributions in stratiform clouds. Atmos. Research, 32,143-170.

Korolev, A.V., 1995: The influence of suresaturation fluctuations on droplet size spectra formation. *J. Atmos. Sci.*, 52, 3620-3634.

LeMone, M. A., 1973: The structure and dynamics of horizontal roll vortices in the planetary boundary layer. *J. Atmos. Sci*., **30**, p. 1077-1091

Lothon M, D. H. Lenschow, D. Leon, and G. Vali, 2004: Turbulence measurements in marine stratocumulus with airborne Doppler radar. *Quart. J. Roy. Met. Soc.* 999, 1-19.

Martin G.M., D. W. Johnson and A. Spice, 1994: The measurements and parameterization of effective radius of droplets in warm stratocumulus clouds. *J. Atmos. Sci., 51*, 1823-1842.

Mazin, I. P., A. Kh. Khrgian, and I. M. Imyanitov, 1989: Handbook *of Clouds and Cloudy atmosphere*. Gidrometeoizdat, 647p.

Moeng, and Coathors, 1996: Simulation of a stratocumulus-topped PBL: Intercomparison among different

numerical codes. *Bull. Amer. Meteor. Soc.*, 77, 261-278.
Nicholls S. 1984: The dynamics of stratocumulus: aircraft observations and comparisons with a mixed layer model. Quart. J. Roy. Met. Soc., **110**, 783-820.
Pawlowska H., and J.L. Brenguier, 2003: An observational study of drizzle formation in stratocumulus clouds for general circulation model (GCM) parameterizations. J. Geophys. Res. 108,8630, doi:10.1029/2002JD002679.
Pawlowska H, W.W. Grabowski and J._L. Brenguier, 2006: Observations of the width of cloud droplet spectra in stratocumulus. G. Res. Lett. 33, L19810, doi: 10.1029/2006GL026841.
Petters M.D., J. R. Snider, B. Stevens, G. Vali, I. Faloona and L. Russel, 2006: Accumulation mode aerosol, pockets of open cells, and particle nucleation in the remote subtropical Pacific marine boundary layer, *J. Geophys. Res., 111,*D02206,doi:10.1029/2004JD005694.
Pinsky, M., A. P. Khain, and M. Shapiro 2001: Collision efficiency of drops in a wide range of Reynolds numbers: Effects of pressure on spectrum evolution. *J. Atmos. Sci.* 58, 742-764.
Pinsky, M., and A. Khain, 2002: Effects of in-cloud nucleation and turbulence on droplet spectrum formation. *Quart. J. Roy. Meteor. Soc.*, 128, 501-533.
Pinsky M.,, L. Magaritz,, A. Khain, O.Krasnov and A. Sterkin, 2008: Investigation of droplet size distributions and drizzle formation using a new trajectory ensemble model. Part 1: model description and first results in a non-mixing limit. *J. Atmos. Sci.* (in press)
Rosenfeld D., 2000: Suppression of Rain and Snow by Urban and Industrial Air Pollution. *Science*, 287 (5459), 1793-1796.
Segal Y., M. Pinsky, A. Khain and C. Erlick, 2003: Thermodynamic factors influencing bimodal spectrum formation in cumulus clouds. Atmos. Res. 66, 43-64.
Stevens, B., G. Feingold, W. R. Cotton, and R. L. Walko, 1996: Elements of the microphysical structure of the numerically simulated nonprecipitating stratocumulus. *J. Atmos. Sci.,* **53**, 980-1006.
Stevens, B, W.R. Cotton, G. Feingold, and C. Moeng, 1998a: Large eddy simulations of strongly precipitating, shallow, stratocumulus-topped boundary layers. J. Atmos. Sci. 55, 3616-3638.
Stevens, B., W. R. Cotton, and G. Feingold, 1998b: A critique of one and two-dimensional models of marine boundary layer clouds with detailed representations of droplet microphysics. Atmos. Res., 47--48, 529-553.
Stevens, B, C.H. Moeng and P.P. Sullivan 1999: Large-eddy simulations of radaitively driven convection: Sensitivities to the representation of small scales. J. Atmos. Sci. 56, 3963-3984.
Stevens, B, and Coauthors, 2003a: Dynamics and Chemistry of maritime stratocumulus-DYCOMS-II. Bull. Amer. Meteorol. Soc. 84, 579-593.
Stevens, B, and Coauthors, 2003b, On entrainment rates in nocturnal maritime stratocumulus. Quart. J. Roy. Meteorol. Soc. 129, 3469-3492.
Stevens, B, G and COAUTHORS, 2005a: Evaluation of large-eddy simulations via observations of nocturnal marine stratocumulus. Mon. Wea. Rev., 133, 1443-1455.
Stevens, B, G. Vali, K. Comstock, R. Wood, M.C. vanZanten; P.H. Austin, C. S. Bretherton, and D.H. Lenshow, 2005b: Pockets of open cells (POCs) and drizzle in marine stratocumulus. *Bull. Amer. Meteorol. Soc., 86*, 51-57.
Twohy, C.H, M.D Petters, J. R. Snider, B. Stevens, W. Tahnk, M. Wetzel, L. Russell, and F. Burnet, 2005, J. Geophys. Res 110, D08203, doi: 10.1029/2004JD005116
Twomey S., 1977: The influence of pollution on the shortwave albedo of clouds. *Journal of Atmospheric Sciences*, **34**, 1149-1154.
VanZanten M. C., B. Stevens, G. Vali, D. H. Lenschow, 2005: Observations in nocturnal marine stratocumulus. *J. Atmos. Sci.*, **62**, 88-106.
Wood R. 2005: Drizzle in Stratiform Boundary Layer Clouds. Part I: Vertical and Horizontal Structure. J. Atmos. Sci. 62, 3011-3033.
Yum, S.S. and J.G. Hudson (2002): Maritime/continental microphysical contrasts in stratus. Tellus, Se. B, 54, 61-73.

AS SNOW CHANGES TO RAIN: UNDERSTANDING THE VICISSITUDES OF ELECTROMAGNETIC SCATTERING THROUGH THE MELTING LAYER (FROM ABOVE AND BELOW)

Kenneth Sassen
Geophysical Institute, University of Alaska Fairbanks
Fairbanks, Alaska 99775
Email: ksassen@gi.alaska.edu

1. INTRODUCTION

An unexpected consequence of the transformation of hydrometeors undergoing the phase change in the melting layer is what World War II microwave radar operators called the bright band. Literally, a bright signal band sometimes appeared on the radar set oscilloscope displays of their time during rainfall. It was soon recognized by the new breed of post-war radar meteorologists that this phenomenon was attributable to certain characteristics of melting snowflakes, which briefly enhanced radar returns. Relatively simple models that treated the changes in hydrometeor size, fallspeed (and thus concentration), and ice/water content were able to reproduce the salient features of the radar bright band (Battan 1973; Dennis and Hitchfield 1990; Fabry and Zawadski 1995). Because of the large increase in the dielectric constant (and hence Rayleigh backscattering) between ice and water particles, the influence of the melt water was considered to be a major factor, along with the gradual decrease in particle concentrations as snowflakes changed to faster-falling raindrops. Doppler radar vertical velocity profiles through the melting layer soon confirmed this basic conception. Laboratory and field studies of the composition of the melting layer were also spurred by attempts to better understand bright bands (e.g., Stewart et al. 1984; Mitra et al. 1990; Oraltay and Hallett 2005).

At least this was the early view when predominantly centimeter-wavelength weather radars were used to probe precipitation. Since the 1950s, however, new research tools have discovered new electromagnetic scattering features associated with the melting region. For example:

2. LIDAR ANALOGS

Early lidar studies detected a bright band analog (i.e., a relatively narrow signal spike) under some melting layer conditions that was attributed to strong optical backscattering *and* overwhelming attenuation in the larger snowflakes- this is simply a particle density effect, not a dielectric one (Sassen 1977a). Like polarization radars, lidars found variations in depolarization in the melting layer due to special nonspherical particle scattering effects (Sassen 1975). Lidars later discovered a pronounced dark band near the bottom of the melting layer (Sassen and Chen 1995), apparently a result of the backscattering behavior of mixed-phase raindrops with ice blocking the central retro-reflected internal ray path (Sassen 1977b). (Wet lidars were something to be avoided, previously!)

3. MILLIMETER-WAVE RADAR DARK AND BRIGHT BANDS

The situation at millimeter radar wavelengths is, in comparison to weather radars, chaotic. Measurements of rain at K-band (~10-mm) radar only occasionally show a bright band, while those at W-band (3.2 mm) may never and sometimes even detect a weak dark band at the top of the melting layer (Sassen et al. 2005). Clearly, non-Rayleigh scattering effects at these wavelengths are coming into play in a major way because snowflakes (and many raindrops) are too large to behave as Rayleigh scatterers. Theories to explain the still-debated W-band radar dark band can be divided into two distinct groups. The first believes that the well-known Mie theory backscattering oscillations for particles with sizes of about the incident wavelength (due to scattering resonance effects) cause depressions in radar reflectivity from growing snowflakes of just the right size (Lhermitte 2002; Kollias and Albrecht 2005). A related W-band radar *dim band* was attributed to a combination of this effect with a specified snowflake density-versus-size relationship that strongly limited radar reflectivities in the Mie regime (Heymsfield et al. 2008), although this affect is not directly tied to the melting layer. The other approach to account for the W-band radar dark band involves treating barely-wet snowflakes as concentric water-coated ice spheres, with the backscattering reductions coming from the reverse dielectric effect predicted by Mie theory (Sassen et al. 2005).

4. THE VIEW FROM SPACE

With the advent of spaceborne radar observations of precipitation (TRMM, Simpson et al. 1996) and clouds (CloudSat, Stephens et al. 2003), melting layer effects are being examined from the top-down. Although conventional TRMM radar bright bands are commonly observed, surprisingly so are apparent CloudSat W-band radar bright bands, but only in observations from above (Sassen et al. 2007). Analogous to the lidar bright band, this feature has been attributed to increasing microwave backscatter followed by strong extinction, not in the snow above, but the rain below in this case (Matrosov 2007).

5. CONCLUSIONS

These findings at several radar/lidar wavelengths have put new constraints on melting layer microphysical and scattering theories, which will be discussed to see if our current understanding of the bright and dark bands are consistent with the microphysics of precipitation (and vice versa), particularly with regard to the evolution of the particle size distribution. We suggest that an additional tool that should be applied to completing our understanding of melting layer microphysics and scattering are scanning polarization lidar measurements (Roy and Bissonnette 2001), which will reveal through backscattering anisotropy further details of the evolution of hydrometeor shape and orientation in the melting region.

Acknowledgements. This research is supported by NSF grant ATM-0630506.

REFERENCES

Battan, L. J., 1973: *Radar Observation of the Atmosphere*, University of Chicago Press, 324 pp.

Dennis, A. S., and W. Hitchfield, 1990: Advances in precipitation physics following the advent of weather radar. *Radar in Meteorology,* D. Atlas, Ed., Amer. Meteor. Soc., 98-108.

Fabry, F., and I. Zawadski, 1995: Long-term radar observations in the melting layer of precipitation and their interpretation. *J. Atmos. Sci*., **52**, 838-851.

Heymsfield, A. J., A. Bansemer, S. Matrosov, and L. Tian, 2008: The 94-GHz radar dim band: Relevance to ice cloud properties and CloudSat. *Geophys. Res. Lett*., 35, L03802, doi:10.1029/2007GL031361.

Kollias, P., and B. Albrecht, 2005: Why the melting layer radar reflectivity is not bright at 94 GHz*,* *Geophys. Res. Lett*., *32,* L24818, doi:10.1029/2005GL024074.

Lhermitte, R., 2002: *Centimeter and Millimeter Wavelength Radars in Meteorology*. Lhermitte Productions, Miami.

Matrosov, S. Y., 2007 Potential for attenuation-based estimations of rainfall rate from CloudSat. *Geophys. Res. Lett*., *34*, L05817, doi:10.1029/2006GL029161.

Mitra, S. K., O. Vohl, M. Ahr, and H. R. Pruppacher, 1990: A wind tunnel and theoretical study of the melting layer behavior of atmospheric ice particles. VI: Experiment and theory for snow flakes, *J. Atmos. Sci., 47*, 584-591.

Oraltay, R. G., and J. Hallett, 2005: The melting layer: A laboratory investigation of ice particle melt and evaporation near 0°C. *J. Appl. Meteor*., **44**, 206-220.

Roy, G., and L. R. Bissonnette, 2001: Strong dependence of rain-induced lidar depolarization on the illumination angle: experimental evidence and geometrical-optics interpretation. *Appl. Opt*., **40**, 4770-4780.

Sassen, K., 1975: Laser depolarization "bright band" from melting snowflakes. *Nature*, **225**, 316-318.

Sassen, K., 1977a: Lidar observations of high plains thunderstorm precipitation. *J. Atmos. Sci*., **34**, 1444-1457.

Sassen, K., 1977b: Optical backscattering from near-spherical water, ice and mixed phase drops. *Appl. Opt*., **16**, 1332-1341.

Sassen, K., and T. Chen, 1995: The lidar dark band: An oddity of the radar bright band analogy, *Geophys. Res. Lett.,* 22, 3505-3508.

Sassen, K., J. R. Campbell, J. Zhu, P. Kollias, M. Shupe, and C. Williams, 2005: Lidar and triple-wavelength Doppler radar measurements of the melting layer: A revised model for dark and bright band phenomena, *J. Appl. Meteor.*, **44**, 301-312.

Sassen, K., S. Matrosov, and J. Campbell, 2007: CloudSat spaceborne 94 GHz radar bright bands in the melting layer: An attenuation-driven upside-down lidar analog. *Geophys. Res. Lett.,* **34**, L16818, doi:10.1029/2007GL030291.

Simpson, J., C. Kummerow, W. K. Tao, and R. F. Adler, 1996: On the Tropical Rainfall Measuring Mission (TRMM). *Meteor. Atmos. Phys.*, **60**, 19-36.

Stephens, G. L., D. G. Vane, R. Boain, G. G. Mace, K. Sassen, Z. Wang, A. Illingworth, E. O'Conner, W. B. Rossow, S. L. Durden, S. Miller, R. Austin, A. Benedetti, and C. Mitrescu, 2003: The CloudSat mission and the A-train: A new dimension of space-based observations of clouds and precipitation. *Bull. Amer. Meteor. Soc*., **83**, 1771-1790.

Stewart, R. E., J. D. Marwitz, J. C. Pace, and R. E. Carbone, 1984: Characteristics through the melting layer of stratiform clouds. *J. Atmos. Sci*., **41**, 3227-3237.

THE SMALL-SCALE STRUCTURE OF TURBULENCE IN MARINE STRATOCUMULUS

Holger Siebert and Raymond A. Shaw

Leibniz-Institute for Tropospheric Research, Leipzig, Germany

1 INTRODUCTION

The statistics of small-scale turbulence in clouds is an important issue when dealing with mixing and coalescence processes. Many of these turbulent processes take place on small scales down to the distances between the cloud droplets themselves, which also corresponds to the energy dissipation scale ($\sim$ mm for atmospheric conditions). However, whereas measurements of small-scale turbulence under cloud-free conditions have been successfully performed for many decades, measurements under cloudy conditions with sub-meter resolution are still an experimental challenge and are quite rarely presented. The main reason for the lack of high-resolution turbulence data in clouds might be based on the typically high true air speed (TAS) of research aircraft and, therefore, the high sampling frequency needed to resolve sub-meter structures of the flow field. On the other hand, sensors typically used in laboratory or atmospheric (but ground/tower-based) experiments such as hot-wire anemometers are fragile and only a few airborne turbulence measurements (e.g., Lenschow et al., 1978) and especially in two-phase flows are presented (Merceret, 1970, 1976; Sheih et al., 1971; Andreas et al., 1981).

In this work we present high-resolution turbulence data based on hot-wire anemometry measured in marine stratocumulus. Based on the experience from laboratory experiments (Siebert et al., 2007) we are convinced that hot-wire anemeometers can be useful for experiments in a two-phase flow under certain conditions, e.g., comparable low TAS and low droplet concentration. The low TAS could be realized by using the helicopter-borne measurement payload ACTOS (Airborne Cloud Turbulence Observation System) where the hot-wire anemeometer is attached among other turbulence and cloud probes (Siebert et al., 2006a). Comparable low droplet concentrations ($\sim 100\,\mathrm{cm}^{-3}$) can be found in clean environments such as marine clouds.

The aim of this work is to investigate the intermittent character of small-scale turbulence even under calm conditions as typically found in stratocumulus clouds. The motivating question is if turbulence has the potential to significantly influences the collision process even under such conditions where the average energy dissipation rate is low and corresponding turbulence induced acceleration of air parcels is low compared with gravitational acceleration.

The article is organized in the following way: first an introduction of the experimental setup is given followed by an overview of the data analysis with special emphasis on the use of the how-wire anemometer and spike removal due to drop impaction. The small-scale features are investigated by means of velocity increments, their probability density functions (PDF), and structure functions. Local estimates of the energy dissipation rate together with its probability density function (PDF) are presented with a spatial resolution of 10 m. Finally, the results are summarized and discussed.

2 EXPERIMENTAL

The helicopter-borne payload ACTOS was used to perform high-resolution measurements of turbulence and cloud microphyisical parameters in stratocumulus clouds at the coast of the Baltic Sea around Kiel, Germany. ACTOS is an autonomous measurement system which is attached to a helicopter with a 140 m long tether and carried with a true airspeed (TAS) of 15 - 20 $\mathrm{m\,s}^{-1}$ which is much lower compared with typical research air-

Corresponding author's address: Holger Siebert, Institute for Tropospheric Research, Germany
Permoser Straße 15, 04318 Leipzig
siebert@tropos.de

craft yielding higher spatial resolution. A picture of ACTOS during a measurement flight shortly before diving into a cloud field is shown in Fig. 1 and a general introduction of the experimental setup is presented in Siebert et al. (2006a).
In addition to the standard equipment, a one-dimensional hot-wire anemometer was installed on ACTOS. The general use of a hot-wire in (primarily artificial) clouds for turbulence measurements was discussed in Siebert et al. (2007). In contrast to that work, where a more complex de-spike algorithm is presented, here the spikes are removed by a more simple running median filter. A typical spike due to droplet impaction lasts about 2 ms, that is, about four samples (sampling frequency 2 kHz). A running median filter with a rank of 10 and final block averages over 10 samples remove the spikes and reduces the resolution from 2 kHz to 200 Hz which yields (with a TAS = 16 $\mathrm{m\,s^{-1}}$) a spatial resolution of 8 cm. The hot-wire data were corrected for temperature drift and calibrated with an ultrasonic anemometer.

Figure 1: A picture of ACTOS during a measurement flight shortly before diving into a cloud field. The picture is taken from the helicopter 140 m above ACTOS. All turbulence sensors are attached to an outrigger (right part of ACTOS in the picture) to minimze flow distortions due to the solid body of ACTOS. The flags which are attached to the tether (see left part in the picture) are used to increase visibility for other aircraft.

3 DATA ANALYSIS

3.1 Overview and Cloud Structure

Before investigating the small scale structure of cloud turbulence a brief overview of the large scale cloud structure is presented. Data were sampled in a field of dissipating stratocumulus clouds about 15 km off the coast. The analyzed flight leg was performed along the mean wind direction. From vertical profiling (data not shown here) cloud top was observed in 1120 m above sea level and the vertical thickness of the cloud layer was about 200 m. The 6 km long (6 minutes) leg which is analyzed in detail was flown against the mean wind at a height of 1090 m, about 30 m below cloud top. The mean temperature was slightly below the freezing level.
Figure 2a presents a time series of the liquid water content (LWC, measured with a Particle Volume Monitor, PVM-100A, see Gerber et al. (1994) for more details). The LWC was slightly increasing from 0.4 to 0.5 $\mathrm{g\,m^{-3}}$ with increasing distance from the coast. The vertical velocity w (Fig. 2b) shows limiting values of ± 1.3 $\mathrm{m\,s^{-1}}$ with a mean

value close to zero. The horizontal wind velocity U (Fig. 2c) was quite calm inside the cloud layer and ranges from 0 to 2.5 $\mathrm{m\,s^{-1}}$. The vertical and horizontal wind velocities which are shown here were derived from the ultrasonic anemeometer and were corrected for attitude and platform motion. The stratocumulus layer was capped by a strong temperature inversion with significantly increasing wind speeds.

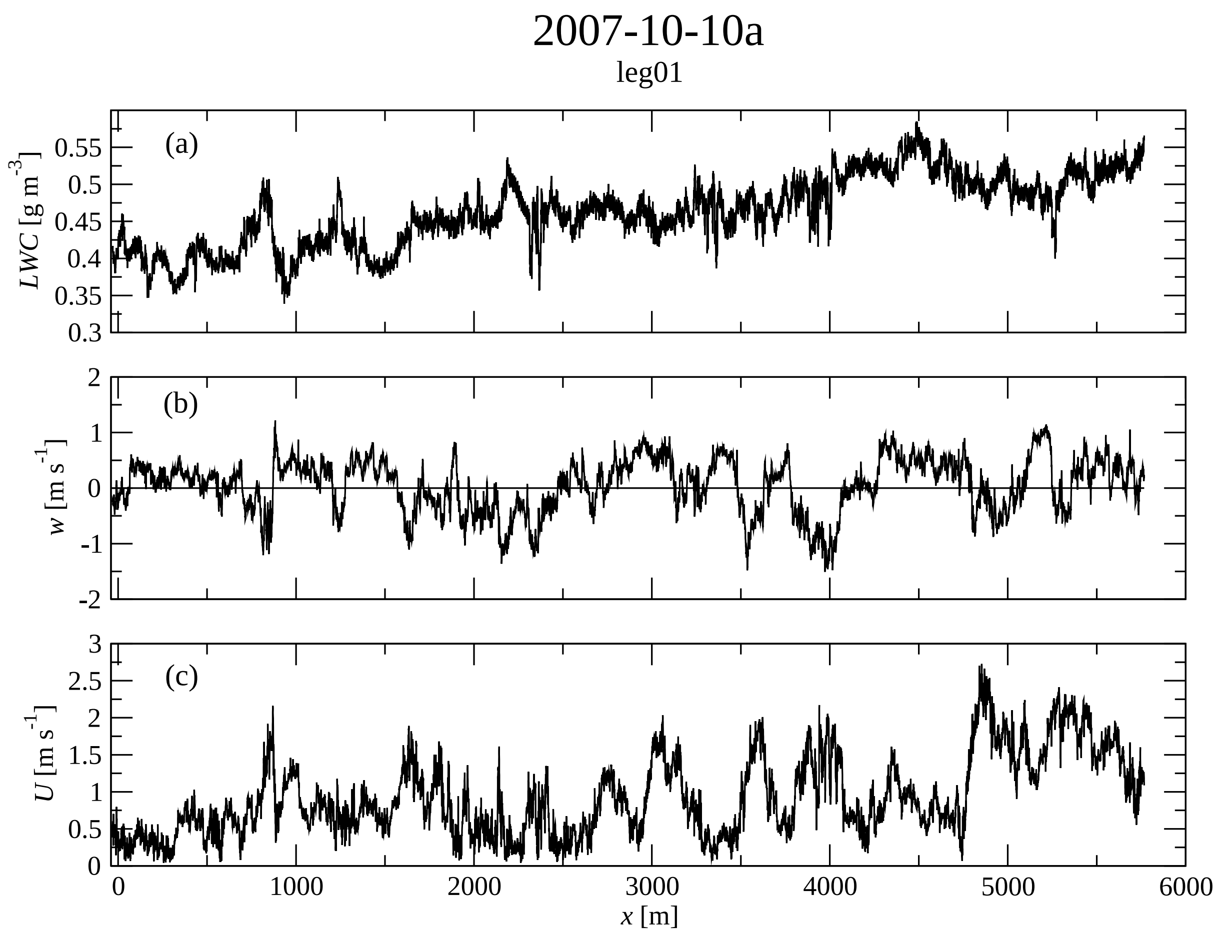

Figure 2: Time series of (a) Liquid Water Content (LWC), (b) vertical velocity component w, and (c) horizontal wind velocity U of a 6 km long ($\sim$ 6 min) leg in a stratocumulus layer. The data was sampled in a nearly constant height of 1090 m (a slow variation of the measurement height of $\pm$10 m was due to technical reasons).

3.2 Hot-Wire Data

For the same leg as shown in Fig. 2, the velocity fluctuations $u'(x)$ (high-pass filtered at 0.1 Hz corresponding to a length scale of 160 m) and the velocity increments $\Delta u'(x) = u'(x+r) - u'(x)$ are shown with $r = 7.5$ cm (distance between two subsequent measurement points). The data are derived from the hot-wire anemometer and processed as described in Sec. 2. The intermittent character of these data (see Fig. 3) is obvious, regions with high fluctuations and regions with comparable low fluctuation can be found close to each other. The standard deviation is $\sigma_{u'} \approx 0.13\,\mathrm{m\,s^{-1}}$ and $\sigma_{\Delta u'} \approx 0.03\,\mathrm{m\,s^{-1}}$, respectively.
Using classical Kolmogorov scaling one can esti-

mate the mean energy dissipation rate $\varepsilon \sim \sigma_{u'}^3/l$, with l is a typical length scale. Since the measurements are performed close to cloud top and the cloud thickness is about 200, l is assumed to be in the order of a few tens of meters which yields $\varepsilon \sim 10^{-4}\,\mathrm{m\,s^{-3}}$, a typical mean value for stratocumulus clouds.

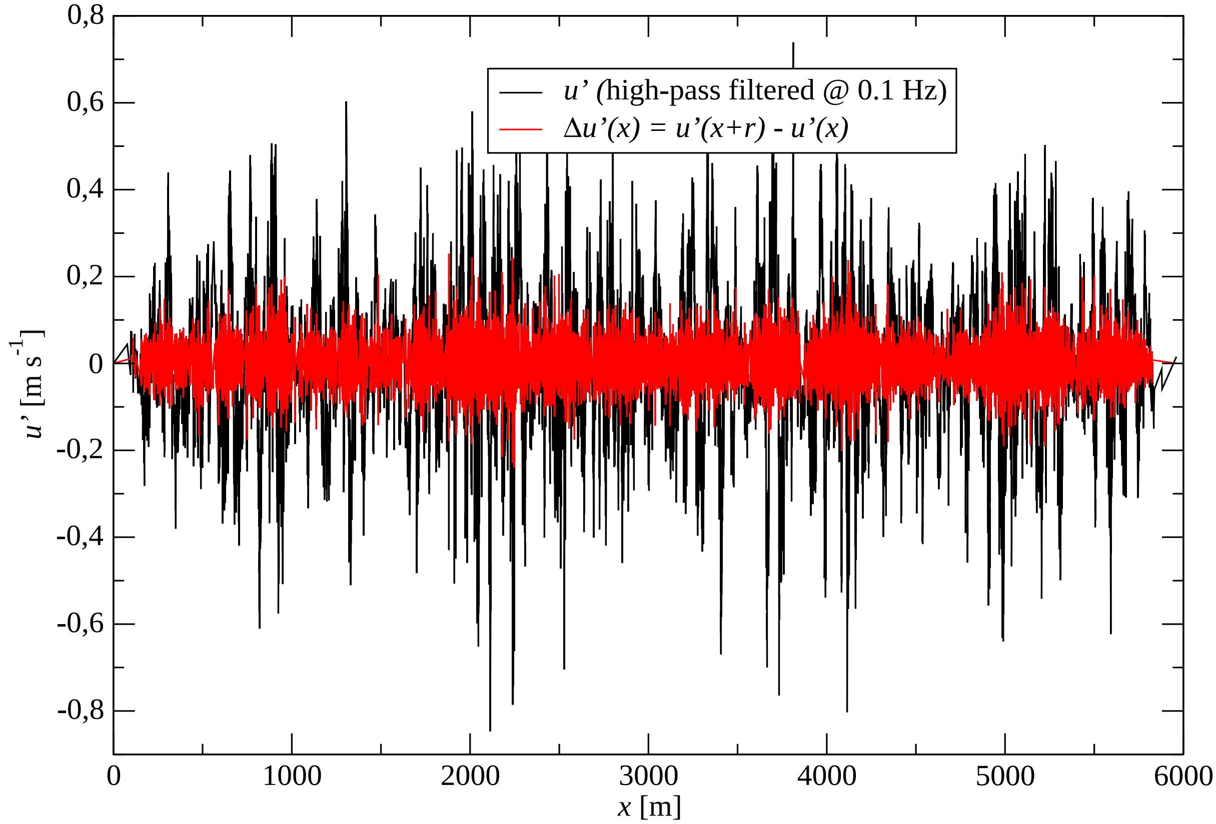

Figure 3: Time series of velocity fluctuations u' and increments $\Delta u(x) = u'(x+r) - u'(x)$ (with fixed $r = 7.5$ cm) derived from hot-wire data. The data is from the same record as for Fig. 2.

Next, we investigate the statistics of u' and $\Delta u'$ by means of probability density functions (PDFs). From basic considerations one would expect the fluctuations to be nearly Gaussian distributed since u' is the result of many randomly distributed vorticies along the flight path. On the other hand, the velocity increments depend on the direct neighborhood and the velocity at two points close together should be highly correlated and, therefore, the PDF($\Delta u'$) is highly non-Gaussian (see discussions about velocity and increment PDFs in Frisch (1995) and Davidson (2004) for example). In Fig. 4 the normalized PDFs of u' (Fig. 4a) and $\Delta u'$ (Fig. 4b) are plotted. The PDF(u') could be sufficiently approximated with a Gaussian fit, whereas the tails of PDF($\Delta u'$) are more exponential ($\sim e^{-x/\sigma_{\Delta u}}$).

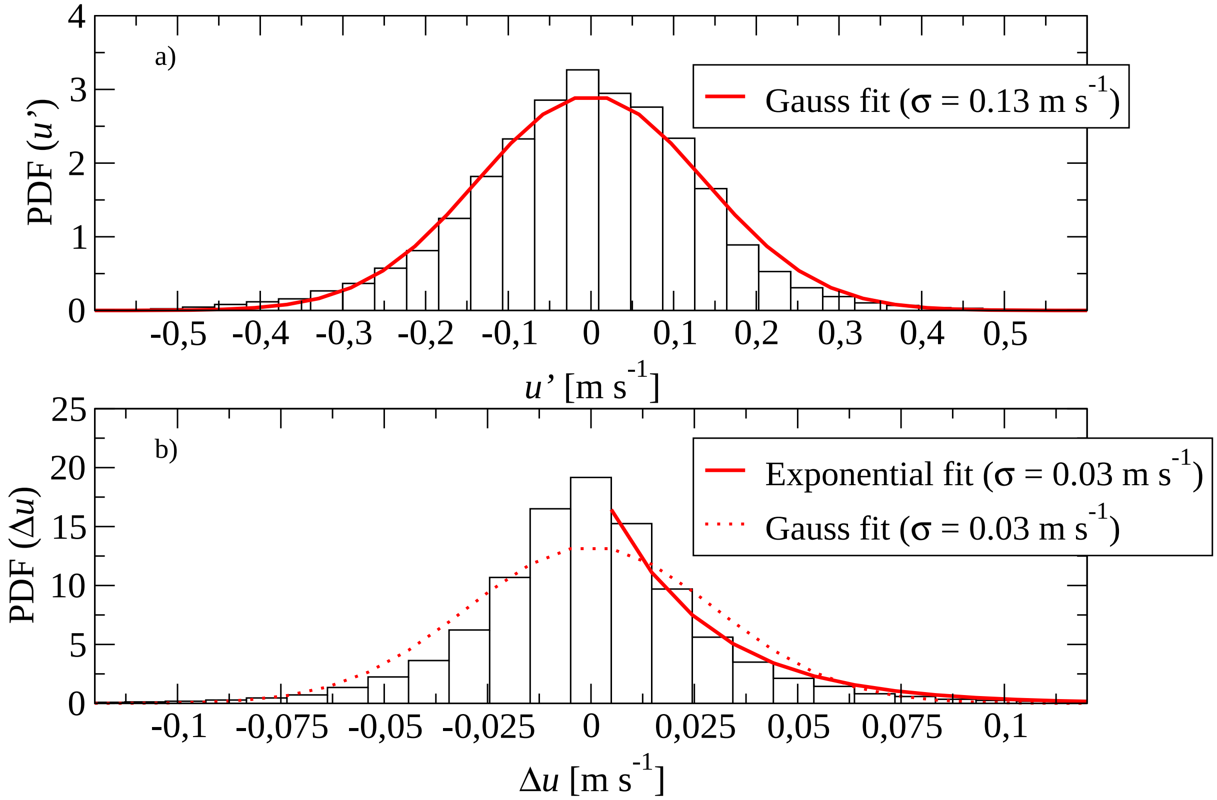

Figure 4: Probability density functions (PDFs) of the velocity fluctuations u' and increments $\Delta u'$ as shown in Fig. 3.

Another way to investigate the small-scale statistics of velocity increments is the scaling behavior of so-called "nth-order structure function $D^{(n)}$":

$$D^{(n)}(r) = \langle \Delta u(r)^n \rangle = C_n(\varepsilon r)^{\zeta}, \qquad (1)$$

with a constant C_n and the scaling exponent $\zeta = n/3$ for classical Kolmogorov scaling in the inertial subrange. For intermittent turbulence, this scaling exponent was modified in Kolmogorov's refined similarity theory (Kolmogorov, 1962) which leads to $D^{(n)} \sim (\varepsilon r)^{(n/3-\mu n(n-3)/18)}$ with the intermittency constant $\mu \approx 0.25$ (Davidson, 2004)

Before estimating $D^{(n)}$, the velocity data were transferred from time to space domain by a applying local Taylor hypothesis ($u'(t_i) \rightarrow u'(x_i = t_i \cdot u_i)$). Due to the pendulum motion of ACTOS using a constant TAS would lead to misinterpretation. In the space domain, the data were interpolated and re-sampled with a constant spatial resolution of 7.5 cm. From this equidistant data $D^{(n)}$ were calculated for $n = 2$ and 4 and plotted in Fig. 5a together with a classical $r^{n/3}$-fit function and the modified model which takes intermittency into account.

The second-order structure function shows nicely a 2/3 slope indicating inertial subrange scaling; only for scales smaller $\sim$ 1 m $D^{(2)}$ drops significantly off - probably due to a low-pass filter which was set at 200 Hz (corresponding to 7.5 cm). The difference between classical 2/3 scaling and the intermittency correction is negligible for low-order structure functions. The fourth-order structure function shows a steeper slope compared with classical $r^{4/3}$ scaling for $r < 4$ m but agrees much better with the intermittency model. For $r > 8$ m, $D^{(4)}$ starts to flatten which is obviously due to the short distance of the measurement height to cloud top which might violate the assumption of isotropy.

In the lower panel (Fig. 5b) the compensated 2nd-order structure function $\left[1/2\, D^{(2)}(r)\right]^{1/\zeta}/r$ is plotted with $\zeta = 2/3$ (K41 scaling) and $\zeta = 2/3 - \mu\, 2(2-3)/18$. Following Eq. 1 (with the Kolmogorov constant $C_2 = 2$) the compensated structure function equals the energy dissipation rate $\varepsilon \approx 1.6 \cdot 10^{-4}\,\mathrm{m}^2\,\mathrm{s}^{-3}$ which agrees well with the estimate at the beginning of this subsection. It is obvious that the scaling exponent which accounts for the intermittent character of the turbulence results in a more flattened curve compared with K41-scaling.

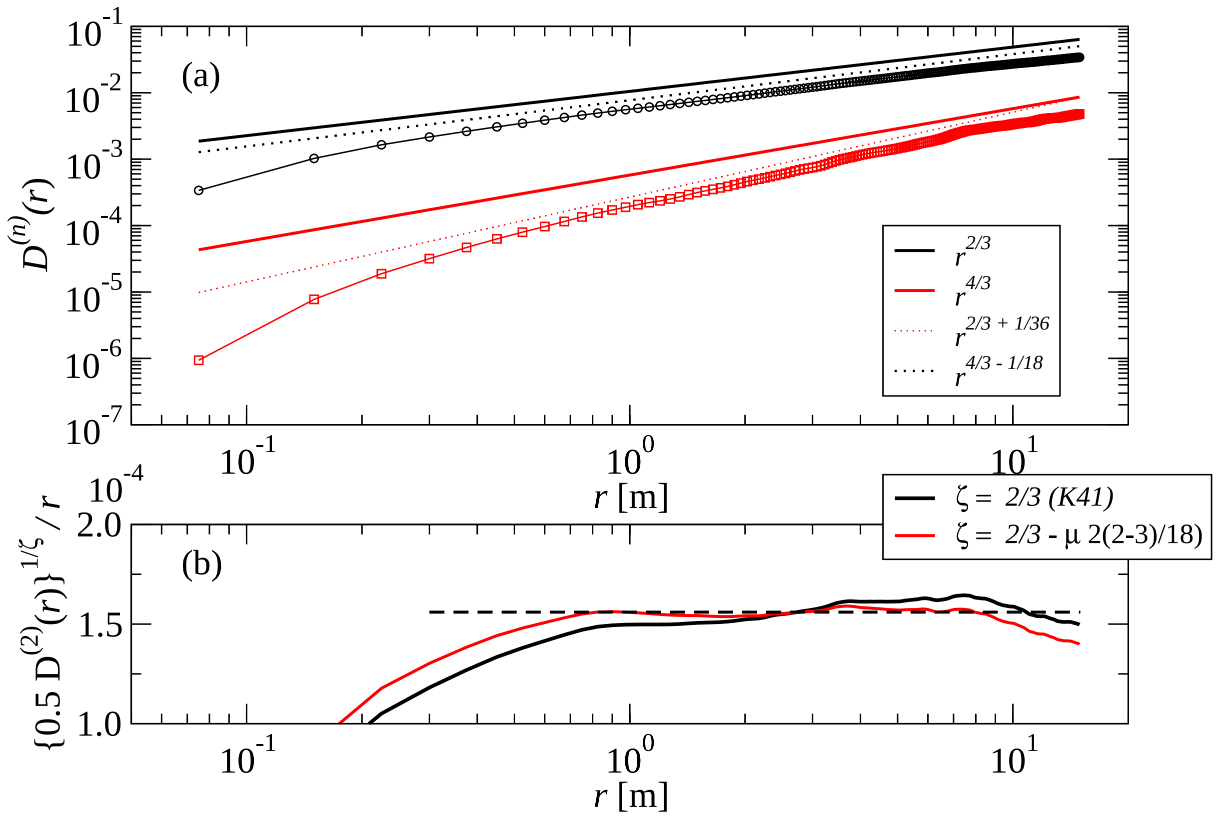

Figure 5: a) nth-order structure functions $D^{(n)}$ of the data presented in Fig. 3. b) Compensated structure function $\left[1/2D^{(2)}(r)\right]^{1/\zeta} = \varepsilon$

3.3 Local Energy Dissipation Rates

Instead of using an average value of the energy dissipation rate ε, intermittent turbulence is better described by a local value ε_τ integrated over the time τ. This concept (Kolmogorov, 1962) is based on the assumption that ε_τ is an independent variable. The high temporal resolution of the hot-wire allows us to estimate ε_τ from 2nd-order structure functions calculated from 0.5 s long subrecords (see Siebert et al., 2006b, for a more detailed discussion). In Fig. 6 the time series of $\log_{10}\varepsilon_\tau$ is shown together with its PDF. From peak-to-peak, ε_τ covers a range of three orders of magnitude and regions with ε_τ values more than one order of magnitude higher than the average value occur quite frequently. The PDF of $\log_{10}\varepsilon_\tau$ is shown in Fig. 6b and can be well approximated with a Gaussian fit which means a log-normal distribution of ε_τ. All these findings agree well with the classical picture of intermittent turbulence.

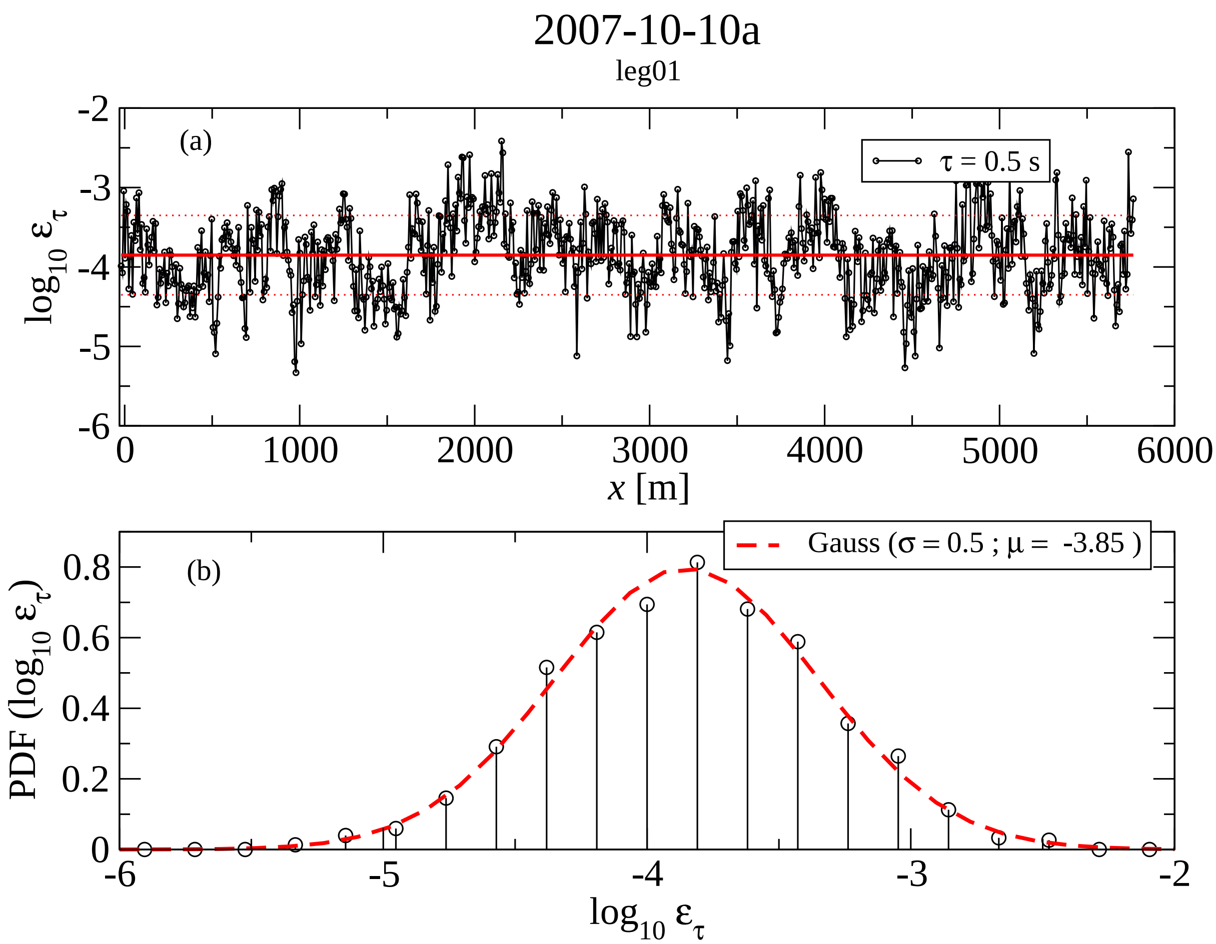

Figure 6: Time series of the logarithm of the local energy dissipation rate ($\log_{10} \varepsilon_\tau$) derived from one-dimensional hot-wire data. ε_τ values are derived from 2nd-order structure functions averaged over $\tau = 0.5$ s (e.g., 100 samples). The horizontal red lines mark the average values and the standard deviation $\pm\sigma_{\varepsilon_\tau}$. A PDF of $\log_{10} \varepsilon_\tau$ is shown together with a Gaussian fit in the lower panel (log-normal distribution of ε_τ)

4 SUMMARY AND DISCUSSION

A case study of turbulence in a field of stratocumulus clouds is presented. The measurements were performed close to cloud top of a 200 m thick cloud layer; the flight path is 6 km long. The average degree of turbulence in terms of energy dissipation is comparable low ($< \varepsilon > \sim 10^{-4}\,\mathrm{m^2\,s^{-3}}$). The statistics of velocity fluctuations and increments are analyzed. The results indicate a classical picture of intermittent turbulence with a highly variable local energy dissipation field. We wish to point out that in the two proceeding ICCP conferences, both the 2000 conference in Reno and the 2004 conference in Bologna, comments were made by prominent members of the cloud physics community questioning whether "Kolmogorov turbulence" is a realistic picture of turbulence in clouds. Admittedly such statements are vague and can be addressed in many ways, but one conclusion we draw from the analysis presented here is that the turbulence in these stratocumulus clouds is strikingly representative of any classical, single-fluid, statistically-homogeneous, isotropic turbulent flow. Intermittency corrections that have been developed in well characterized water and air flows, mostly in carefully controlled laboratory experiments, match the cloud data very well. This is perhaps even somewhat surprising given that we know the stratocumulus cloud is not isotropic on the largest scales — nevertheless, the revised Kolmogorov concept of the energy cascade hold remarkably well.

A second conclusion that can be drawn from this work is that in order to evaluate the influence of turbulence on cloud processes it will be necessary to go beyond the simple use of average turbulence quantities such as energy dissipation rate and instead to find methods for representing the statistical distribution of highly intermittent events. Even in these weakly-turbulent stratocumulus clouds we observe that the broad regions of mild turbulence are punctuated by rare bursts of intense energy dissipation. The intermittent nature of cloud turbulence is likely to influence many cloud processes, ranging from mixing to droplet coalescence. These data support, for example, the development of collision kernels which take the intermittent character of the turbulent velocity field on small scales into account.

Finally, we note that because the scale of our ε_τ measurements (~ 10 m) is still four orders of magnitude greater than the dissipation scale (~ 1 mm), one would expect on smaller scales locally much higher values of ε_τ than we estimated. As is discussed in an accompanying abstract this is likely to result in local acceleration of air parcels comparable to gravitational acceleration.

5 ACKNOWLEDGMENTS

We acknowledge Rolf Maser and Dieter Schell from the enviscope GmbH (Frankfurt/M, Germany) for technical support and the two pilots Alwin Vollmer and Oliver Schubert from the rotorflug GmbH (Friedrichsdorf, Germany) for great helicopter flights. RAS acknowledges support from the Alexander von Humboldt Society during the period in which this research was carried out.

References

Andreas, E. L., R. M. Williams, and C. A. Paulson: 1981, 'Observations of condensate profiles over Arctic leads with a hot-film anemeometer'. *Q. J. R. Meteorol. Soc.* **107**, 437 – 460.

Davidson, P. A.: 2004, *Turbulence.* Oxford University Press, 657 p.

Frisch, U.: 1995, *Turbulence - The legacy of A. N. Kolmogorov.* Cambridge University Press, Cambridge, England, 296 pp.

Gerber, H., B. G. Arends, and A. S. Ackerman: 1994, 'New microphysics sensor for aircraft use.'. *Atmos. Res.* **31**, 235–252.

Kolmogorov, A. N.: 1962, 'A refinement of previous hyotheses concerning the local structure of turbulence in a viscous incompressible fluid at high Reynolds number'. *J. Fluid Mech.* **13**, 82–85.

Lenschow, D. H., C. A. Friehe, and J. C. Larue: 1978, 'The development of an airborne hot-wire anemometer system'. In: *Symposium on Meteorological Observations and Instrumentation, 4th, Denver, Colo., April 10-14, 1978, Preprints. (A79-21901 07-35) Boston, Mass., American Meteorological Society.* pp. 463–466.

Merceret, F. J.: 1970, 'On the use of hot-film anemometry to measure turbulence in the presence of heavy rain'. *J. Appl. Meteor.* **9**, 191–193.

Merceret, F. J.: 1976, 'Measuring atmospheric turbulence with airborne hot-film anemometers'. *J. Appl. Meteor.* **15**, 482 – 490.

Sheih, C. M., H. Tennekes, and J. L. Lumley: 1971, 'Airborne hot-wire measurements of the small-scale structure of atmospheric turbulence'. *Phys. Fluids* **14**, 201–215.

Siebert, H., H. Franke, K. Lehmann, R. Maser, E. W. Saw, R. A. Shaw, D. Schell, and M. Wendisch: 2006a, 'Probing Fine-Scale Dynamics and Microphysics of Clouds with Helicopter-Borne Measurements'. *Bull. Am. Meteor. Soc.* **87**, 1727 – 1738.

Siebert, H., K. Lehmann, and R. Shaw: 2007, 'On the use of a hot-wire anemometer for turbulence measurements in clouds'. *J. Atmos. Oceanic Technol.* **24**, 980 – 993.

Siebert, H., K. Lehmann, and M. Wendisch: 2006b, 'Observations of small scale turbulence and energy dissipation rates in the cloudy boundary layer.'. *J. Atmos. Sci.* **63**, 1451 – 1466.

GLOBAL STATISTICS OF THE LIQUID WATER PATH AND DRIZZLE OCCURRENCE IN LOW LEVEL LIQUID WATER CLOUDS DERIVED FROM CLOUDSAT USING THE ATTENUATION OF THE OCEAN RETURN

L. D. H. Smith and A. J. Illingworth
Department of Meteorology, University of Reading, Reading RG6 6BB, UK

1. INTRODUCTION

Low level liquid water clouds have a strong radiative impact and make a large contribution to uncertainty in climate modelling (e.g. Bony and Dufresne, 2006), yet such clouds are poorly represented in current numerical climate and weather prediction models, and in intercomparison studies, large variations in liquid water path (LWP) are observed between models (e.g. Wyant *et al.* 2006). The numerous, as yet poorly understood feedbacks in such clouds present a serious modelling challenge. Drizzle can have a strong influence on these processes, yet observations are currently limited to isolated ground stations or localised campaigns.

Global observations of LWP are currently available from methods which utilise passive microwave radiometers over the ocean, and optical techniques which infer water path from optical depth and cloud top effective radius in daytime. The Aqua satellite in the A-Train provides LWP by both methods, using the Advanced Microwave Scanning Radiometer – EOS (AMSR-E) and Moderate Resolution Imaging Spectrometer (MODIS) respectively. Whilst these methods are consistent for low level water clouds (Horvath and Davies, 2007), optical methods require daylight, may suffer shadowing effects in broken clouds, and require that the liquid cloud top is not obscured by ice above. Passive microwave methods are limited to resolutions of ~12km, and operation over the ocean.

The CloudSat cloud profiling radar (CPR) is the first cloud radar in space and provides vertical profiles of clouds globally. However, because of the low reflectivity of liquid cloud droplets, many liquid clouds fall below the sensitivity of the CPR (-31 dBZ).

We present a method to retrieve liquid water path from the attenuation of the ocean surface radar return which can be applied day and night, at the radar resolution of ~1km, even where the liquid cloud layer is overlaid by thin ice cloud, and does not require droplet size distribution assumptions. We correct for the effects of undersampling in the range gates (~1.5dB), surface scattering changes as a function of surface temperature (SST) and near surface wind (~10dB), and water vapour attenuation, up to ~7dB in the tropics. Attenuation of 1dB corresponds to an LWP of ~70-100gm^{-2} at 94GHz, and we aim to correct the surface return to 0.5dB, to give LWP accurate to ~50gm^{-2}, which may be better than passive methods.

This method is extended to take advantage of CloudSat's ability to observe drizzle globally for the first time. We will present statistics of liquid water path, drizzle occurrence, and estimates of drizzle rates, and examine how these statistics compare with their representation within operational forecast models.

2. METHOD

The algorithm we present uses the attenuation of the CloudSat radar ocean surface backscatter, σ_0 to derive liquid water path. It takes advantage of the complementarity of observations available from the range of instruments on CloudSat, CALIPSO and Aqua in the A-Train.

The CloudSat radar operates at 94 GHz. At this frequency, clear sky attenuation is dominated by water vapour, with a smaller and less variable contribution from oxygen. In clouds, liquid water significantly attenuates the radar signal, whereas attenuation due to ice is negligible. The ocean surface provides a relatively homogenous background reference against which attenuation can be measured. Corrections can be made for the undersampling of the surface echo, attenuation due to water vapour, and natural variation in the surface echo due to near surface winds and SSTs.

In this study, we use data from 8 July 2006, when good collocation between the radar and CALIPSO lidar, to within 0.6km, was achieved, following the repointing of the radar at nadir, to 31 July 2006. We use lidar data regridded to correspond to the CloudSat along track resolution, retaining its native vertical resolution. AMSR-E, on Aqua, provides ocean surface products including SSTs at 38 km resolution, and near surface winds and water vapour path at 21 km resolution, on a 10 km grid. Triangle based linear interpolation was used to map the AMSR-E data on to the CloudSat path.

2.1 SURFACE GATE UNDERSAMPLING

The CloudSat CPR, unlike wind scatterometers, is not optimised for retrieving the ocean surface backscatter to high accuracy. The vertical resolution of ~500m, oversampled to 242m, means that ocean surface pulse echo is spread over 4-5 of the near surface gates, but the echo power in any one gate depends on the height of that gate relative to the surface. As the satellite – surface distance changes during orbit, the gate heights vary. Periodically, the range to the gates is shifted in steps to correct for this effect. This results in an oscillation in the echo power measured by each individual near surface gate, superposed with the actual changes in σ_0.

In Release 4 of the CloudSat data, an estimate of the sub-bin scale position of the surface is used to derive a 'surface clutter' estimate, so that the surface echo can be removed from the lowest gates, which also yields the surface echo as a product. However, in the current data release this is only applied intermittently, so we apply a correction based on the method of Caylor and Heymsfeld (1997). The difference in echo power received at the peak echo gate, and the adjacent gate further from the satellite can be expressed as:

$$d = P(r_s) - P(r_{s+1}) \qquad (1)$$

where P is the received power, r_i is the range to the ith gate, and r_s indicates the gate containing the peak surface echo.

Because of the regular vertical profile of the surface pulse, the difference in power between adjacent near surface gates is simply a function of their distance from the surface. Each gate is equally affected by changes in the ocean surface characteristics and attenuation, so taking their difference cancels these terms.

Using the lidar to identify clear periods to reduce the noise, a look-up table of $P(r_s)$ as a function of d was compiled, and is shown in *Fig 1*.

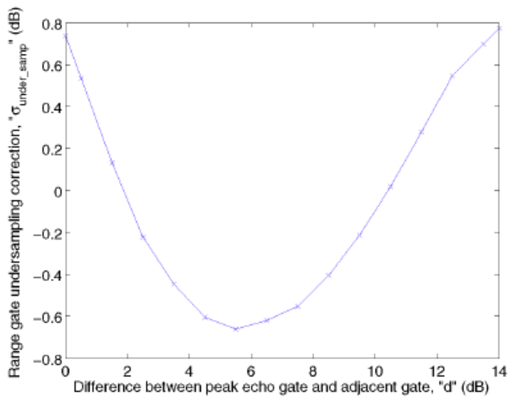

Figure 1: Look-up table used to correct for undersampling of surface echo, with the correction as a function of d.

Interpolation of the values in this table is used to calculate the true peak value of the received echo power, σ_{0s}.

2.2 VAPOUR CORRECTION

A correction for water vapour attenuation, *VAP_CORR*, is given by:

$$VAP\_CORR = k_{vap} WVP \qquad (2)$$

where k_{vap} is the temperature dependent 2-way attenuation coefficient, and WVP is the water vapour path from AMSR-E. Using the Liebe (1985) line by line model, a look-up table of the attenuation coefficient as a function of temperature was compiled, shown in *Fig 2.*

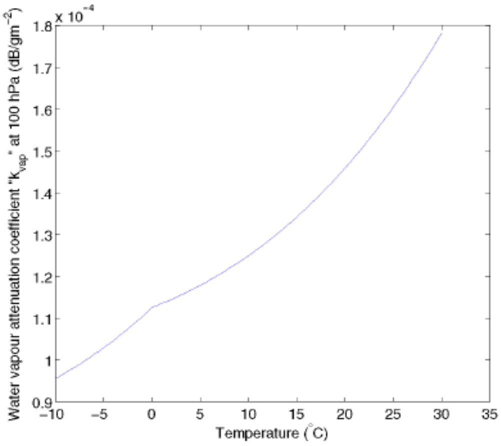

Figure 2: Water vapour attenuation coefficient as a function of temperature at 100hPa.

As the majority of the water vapour in an atmospheric column will be within a few kilometres of the surface, the temperature of the vapour distribution is approximated by subtracting 6^0C from the AMSR-E SST, or EMCWF model SST where an AMSR-E retrieval is unavailable. Although this does not capture changes in the temperature distribution, sensitivity tests show that this effect is small, particularly as changes in vapour attenuation are important rather than the absolute value. The surface echo corrected for vapour attenuation is given by:

$$\sigma_{0vap} = \sigma_{0s} + VAP\_CORR \qquad (3)$$

2.3 CORRECTION FOR EFFECT OF NEAR SURFACE WIND AND SST

It has been found that the variation of the vapour corrected ocean surface backscatter, σ_{0vap}, can be well characterised by the near surface wind, *u*, which controls the surface roughness, and the sea surface temperature (SST).

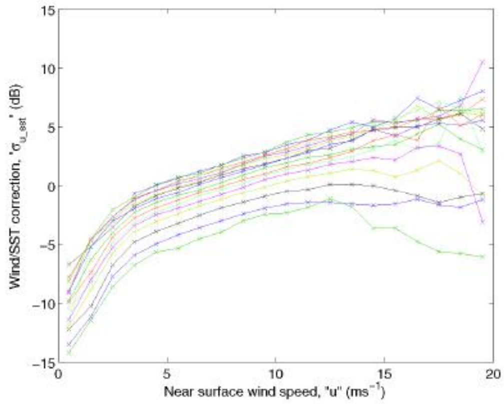

Figure 3: Look-up table correction for effect of near surface wind speed and SST variation. The coloured lines represent SSTs ranging from 0^0C to 32^0C in 2^0 intervals, with higher SSTs giving more negative corrections.

Using all clear sky data from 8 – 31 July 2006, a 2D look-up table of σ_{0vap} as a function of *u* and SST from AMSR-E was compiled. *Fig 3.* shows the strong relationship between σ_{0vap} and the SST and *u.* A correction for this variation, *U_SST_CORR* is applied using this look up table, excluding wind speeds outside the range $5 < u < 15$ ms^{-1} which are less well characterised. The fully corrected surface echo, σ_{0corr} is given by:

$$\sigma_{0corr} = \sigma_{0vap} + U\_SST\_CORR \qquad (4)$$

To check the performance of the correction algorithm, statistics of the constancy of σ_{0corr} as a function of path length deemed to be clear by the lidar were produced and are shown in *Fig. 4.* Even for path lengths in the range 100-200km, the accuracy of the fully corrected signal is good to 0.5dB.

(a) (b)

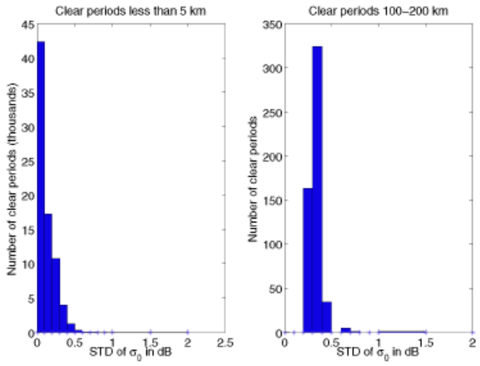

Figure 4: Bar charts showing the distribution of the standard deviations of σ_{0corr} in clear sky for the month July 2006, for (a) clear path lengths <5km and (b) clear path lengths from 100 to 200km.

2.4 CALCULATION OF LWP FROM ATTENUATION

A useful advantage of this method is that as LWP is proportional to attenuation, the accuracy of the absolute value of σ_0 is not important. Therefore, by identifying clear sky using the lidar, a local clear sky reference, σ_{0clear} can be obtained. The difference between this clear sky reference and the corrected σ_{0corr} observed in a cloud will be largely due to liquid water, that is, liquid cloud droplets and precipitation. As rain drops are much larger than cloud droplets, in precipitation the measured reflectivity, Z, from the cloud which will be much stronger. We flag precipitation with a Z threshold of 10dBZ. This precipitation flag when spread over the resolution of the AMSR-E products excludes unreliable retrievals.

Cloud droplets are in the Rayleigh scattering regime for CloudSat, such that the attenuation due to liquid clouds droplets is directly proportional to liquid water path. The attenuation coefficient is purely a function of temperature.

In cloudy periods, the liquid water path, *LWP* is then given by:

$$LWP = k_{liq}\,(\sigma_{0clear} - \sigma_{0corr}) \qquad (5)$$

where k_{liq} is the temperature dependent 2-way attenuation coefficient for liquid water. This coefficient is calculated using the Liebe (1985) model and cloud temperature taken from the ECMWF model temperature at the lidar determined cloud top.

A limitation to the precision of this method is the resolution difference between AMSR-E and CloudSat. However, in general, SST, wind and vapour fields vary over large scales, of the order of the AMSR-E resolution, such that the surface echo can still be well characterised. Another issue is that attenuation due to vapour is also temperature dependent, and therefore the vapour attenuation will depend to some extent on the vertical distribution of vapour. However, using a clear sky reference improves the accuracy of the method, particularly for regions of broken cloud, where individual clouds have short along-track length. The corrections for vapour attenuation and the effect of variations in *u* and SSTs are of particular benefit for stratiform cloud, where a local clear sky reference is not available. The effect of these corrections over extended paths is shown in *Fig 5.*, which shows the surface echo corrected only for undersampling, $\sigma_{0s,}$ which varies by 6 dB, and the fully corrected signal, σ_{0corr}, which is correct to 0.5dB apart from negative excursions due to liquid cloud, over a 400km stretch of ocean.

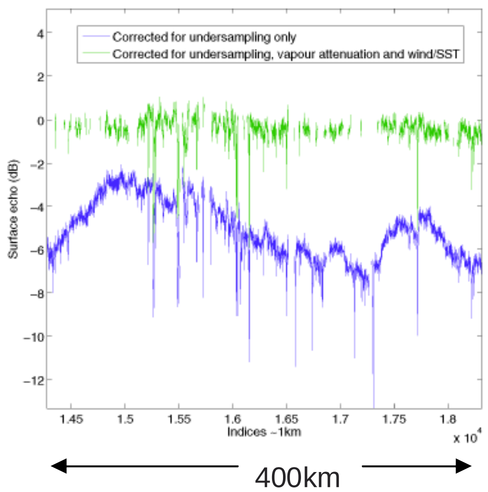

Figure 5: Time series of σ_{0s} in blue and σ_{0corr} in green, over a 400km stretch of ocean with patches of broken cloud, giving negative excursions in the trace.

2.5 DRIZZLE

We extend this method to provide estimates of drizzle rates. A difficulty in the interpretation of Z from cloud radars is distinguishing which hydrometeor dominates the reflectivity. First, a distinction must be made between ice and liquid phase, which may be inferred from model temperatures, but a greater problem is the sixth power dependence of Z on droplet size. Fox and Illingworth (1997) have shown that occasionally drizzle droplets can dominate Z, whilst contributing little to the liquid water content. *Fig 6.* demonstrates this. For example a drizzle free cloud of LWC 0.2 gm^{-2} would have a Z of around -25 dBZ. However, the same reflectivity would be observed from a cloud with much lower water content but with a few drizzle drops present. Our retrieval of LWP, however, is independent of droplet size, assuming the absence of larger Mie scattering rain drops.

For low level water clouds, to a good approximation, LWC scales linearly with height within the cloud. Therefore, by assuming an adiabatic cloud, an LWC profile can be

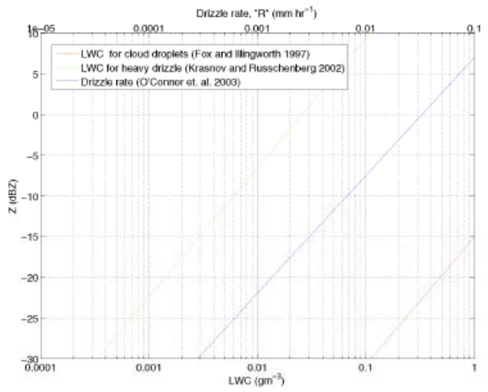

Figure 6: Reflectivity as a function of cloud liquid water content and drizzle rate, for three empirical relationships. The red line is a Z-LWC relationship for drizzle-free clouds, the green line a Z-LWC relationship for 'heavy' drizzle, and the blue line is a Z-R relationship for drizzle.

simulated using the LWP, cloud top height, and cloud top temperature.

Using the empirical Z-LWC relation of Fox and Illingworth (1997);

$$Z \text{ (mm6 m23)} = 0.031 \, LWC^{1.56} \qquad (6)$$

the reflectivity attributable to cloud droplets, Z_{cloud} can be derived from the simulated LWC profile. The reflectivity attributable to drizzle is then given by;

$$Z_{drizzle} = Z_{obs} - Z_{cloud} \qquad (7)$$

where Z_{obs} is the observed reflectivity.

Using the empirical Z - $LWF_{drizzle}$ relation of O'Connor *et. al.* (2005), the drizzle liquid water flux can be estimated by;

$$LWF_{drizzle} = 9.3 \times 10^6 \, Z^{0.69} \qquad (8)$$

3. RESULTS

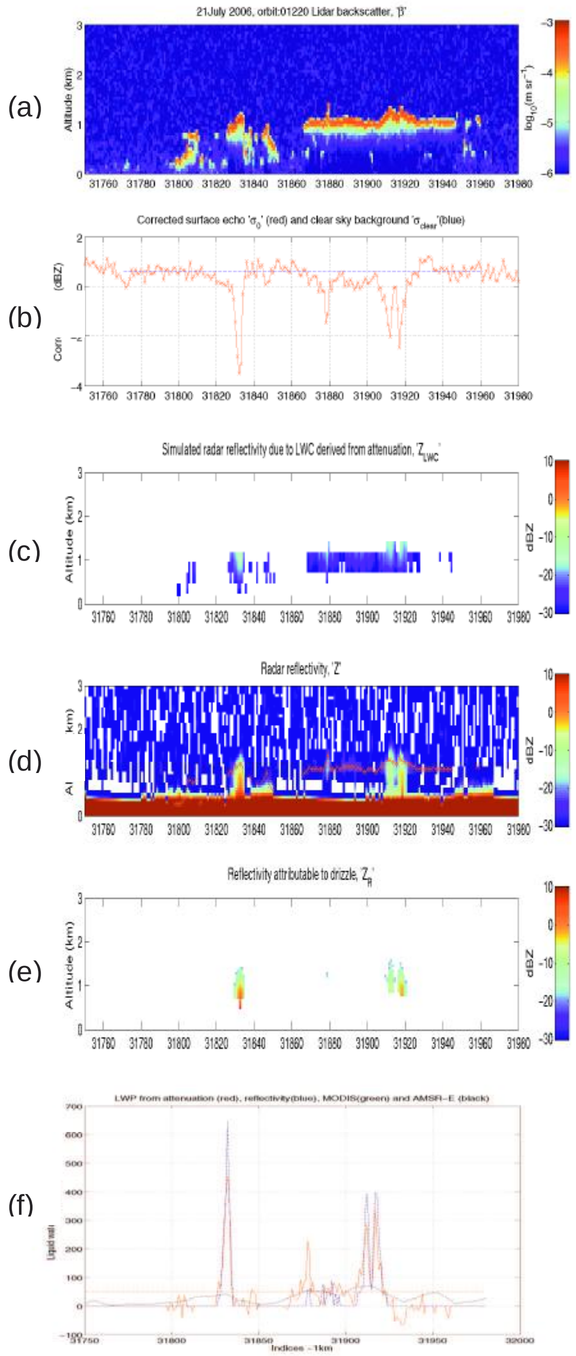

Figure 7: Case study from 21 July 2006. (a) Lidar backscatter in the lowest 3km of the atmosphere, with cloud top marked in red (b) Time series of σ_{0corr} and σ_{0clear} indicating the attenuation from which LWP is derived (c) Z from the simulated LWC profile, Z_{cloud} (d) Observed reflectivity, Z_{obs} (e) Z attributable to drizzle (f) Comparison of LWP calculated from attenuation (red), reflectivity (blue) and AMSR-E (blue). Note that the dashed line indicates that Z_{obs} was above -15 dBZ and is deemed unreliable.

Fig. 7 shows a case study highlighting how the technique works in individual clouds. In this case there is a patches of cloud from index 31800-31850, and a more prolonged cloud from 31870-31950. The indices here refer to individual cloud profiles and correspond to ~1.1km. As this is a night time case no MODIS retrieval of LWP is available. The radar profile shows two sections of high reflectivity, around 31830 and 31915, however, although the attenuation method indicates greater liquid content in this region, the simulated LWC profile shows a much lower reflectivity than is observed. Therefore, this much higher reflectivity is due to the presence of drizzle droplets, the drizzle rate is estimated at 0.15 mm hr^{-1} using equation (8).

We will present global statistics of liquid water path, drizzle occurrence, and estimates of drizzle rates, and comparisons with operational forecast models in the conference paper.

4. BIBLIOGRAPHY

Bony, S. and J-L Dufresne, 2005: Marine boundary layer clouds at the heart of tropical cloud feedback uncertainties in climate models, *Geo. Res. Lett.* **32** L20806, doi:10.1029/2005GL023851.

Caylor, I. J. and G. M. Heymsfield, 1997: Correction of Sampling Errors in Ocean Surface Cross-Sectional Nadir-Looking Weather Radar, *J. Atmos. Oc. Tech.* **14** 203-210.

Fox, N. I., and A. J. Illingworth, 1997: The retrieval of stratocumulus cloud properties by ground-based cloud radar *J. Appl. Meteorol.* **36(5),** 485-492.

Krasnov, O. A., and H. W. J. Russchenberg, 2002: The relation between the radar to lidar ratio and the effective radius of droplets in water clouds: An analysis of statistical models and observed drop size distributions. Preprints, *11th Conf. on Cloud Physics,* Ogden, UT, Amer. Meteor. Soc., P2.18.

Liebe H. J., 1985: An updated model for millimeter wave propagation in moist air. *Radio Sci.*, **20**, 1069–1089.

O'Connor, E. J., R. J. Hogan and A. J. Illingworth, 2005: Retrieving stratocumulus drizzle parameters using Doppler radar and lidar. *J. Appl. Meteorol.,* **44**, 14-27.

Wyant, M.C., C.S. Bretherton, A. Chlond, B.M. Griffin, H. Kitagawa, C.-L. Lappen, V.E. Larson, A. Lock, S. Park, S.R. de Roose, J. Uchida, M. Zhao, and A.S. Ackerman, 2007: A single-column model intercomparison of a heavily drizzling stratocumulus-topped boundary layer. *J. Geophys. Res.*, **112**, D24204, doi:10.1029/2007JD008536.

ACKNOWLEDGEMENTS

We would like to thank Julien Delanoë for assistance with collocation of the lidar and radar data. This work was funded NERC and the Met Office.

MODELING AEROSOL EFFECTS ON THE FORMATION OF POCKETS OF OPEN CELLS IN MARINE STRATOCUMULUS USING WRF MODEL

Hailong Wang[1, 2], Graham Feingold[2] and Huiwen Xue[3]

[1]CIRES, University of Colorado, Boulder, CO, USA
[2]NOAA Earth System Research Laboratory, Boulder, CO, USA
[3]Department of Atmospheric Sciences, Peking University, Beijing, China

1. INTRODUCTION

Satellite imagery (e.g., Figure 1) shows the recurrence of striking images of cellular structures exhibiting both closed- and open-cell patterns in marine stratocumulus (Sc) cloud fields. The broad region of open cells may have a very different large-scale environment from the region of closed cells (e.g., Atkinson and Zhang 1996). The embedded open cells in otherwise unbroken Sc are referred to as pockets of open cells (POCs) (Stevens et al. 2005) or rifts (Sharon et al. 2006). They manifest themselves as optically thin open regions with dimensions of tens of kilometers, ringed by more reflective clouds. In contrast to the broader region of open cells, POC regions have similar large-scale environment and thermodynamic profiles to adjacent closed-cell or more stratiform cloud fields (e.g., Stevens et al. 2005; Sharon et al. 2006).

Marine Sc clouds undoubtedly play a prominent role in climate system by affecting earth's radiation, heat and water budgets. Large variances in regional planetary albedo caused by the cellular structure of Sc have significant and complicated impacts on the local radiation budget. However, there are considerable difficulties and uncertainties in representing Sc clouds in large-scale models because of the myriad small-scale, coupled processes involved, such as aerosol-cloud-precipitation interactions. Using a process model Ackerman et al. (1993) found that depletion of cloud condensation nuclei (CCN) by drop collection can dissipate marine Sc by shutting off cloud-top radiative cooling. Precipitation not only depletes CCN in clouds but also alters cloud dynamics through evaporative cooling. Previous observational and modeling studies (e.g., Bretherton et al. 2004; Stevens et al. 2005; Xue et al. 2008; Savic-Jovcic and Stevens 2008) have suggested that POCs appear to be initiated by precipitation, thus representing a powerful mechanism via which aerosol, through its effect on precipitation, can modify the planetary albedo and hydrological cycle.

Corresponding author address: Hailong Wang, 325 Broadway, Boulder, CO 80305, USA.
Email: Hailong.Wang@noaa.gov

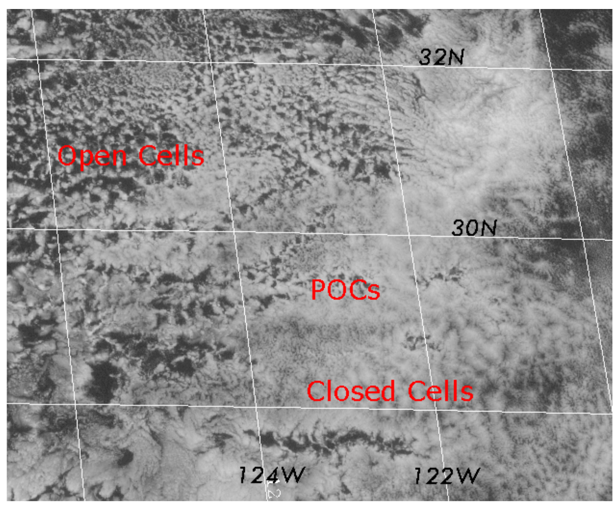

Figure 1: GOES-10 visible imagery of cellular patterns over the Northeast Pacific on 11 July 2001 (4:45pm PDT). (Source: NCAR/JOSS EOL data server)

In this study, aerosol-cloud-precipitation-dynamical feedbacks are investigated within a numerical modeling framework to study the evolution of marine Sc and the formation of POCs, and to examine how depletion of CCN by drop collection and sedimentation impacts these processes.

2. NUMERICAL EXPERIMENTS

2.1 MODEL DESCRIPTION

We perform simulations of marine Sc using an LES version of the Weather Research and Forecasting (WRF) model with treatment of aerosol-cloud interactions in a large domain. The state-of-the-art Advanced Research WRF (ARW) model is suitable for use in a broad spectrum of applications across scales ranging from meters to hundreds of kilometers. A detailed description of the governing equations, numerical methods and physics of ARW is documented by Skamarock et al. (2005).

A double-moment warm-rain microphysical scheme initially developed by Feingold et al. (1998) has been modified and incorporated in WRF V3.0. This scheme uses lognormal basis functions to represent aerosol, cloud droplet and drizzle drop spectra. Supersaturation is calculated in a similar fashion to the bin method. Look-up tables are generated *a priori* for drop collection using a stochastic collection bin model. Cloud and rain drop sedimentation is also size-dependent and based on the bin method. This allows drops in each bin to fall at the appropriate velocity. This double-moment scheme captures the main features of precipitating marine Sc when compared with a detailed bin microphysical scheme in the same modeling framework (Feingold et al. 1998). Moreover, the enhanced computational efficiency enables performing three-dimensional simulations over much larger domains or much longer timescales than is possible with bin microphysics.

2.2 CASE DESCRIPTION

POCs were extensively measured during the second Dynamics and Chemistry of Marine Stratocumulus (DYCOMS-II) field campaign (Stevens et al. 2003; Stevens et al. 2005). In this study, initialization of model simulations is mostly based on nocturnal measurements made during the research flight RF02 of DYCOMS-II (Ackerman et al. 2008), which occurred on the same day shown in Fig. 1. The initial inversion base is at about 800 m. Total water mixing ratio (q_t) decreases from 9.45 g kg^{-1} in the boundary layer to about 5 g kg^{-1} near the inversion top, and potential temperature (θ) increases from 288.3 to 296.7 K across the inversion. No wind shear is assumed in the initial profile, which is different from that in LES studies by Ackerman et al (2008) and Savic-Jovcic and Stevens (2008), because observational studies (Atkinson and Zhang 1996, and references therein) showed that three-dimensional cloud cells tend to form in conditions of little or no wind shear. As boundary conditions, the upward surface sensible and latent heat fluxes are fixed at measured values of 16 and 93 W m^{-2}, respectively, and the surface friction velocity is fixed at 0.25 m s^{-1}. Radiative forcing is taken into account by using online simple spectral-band column schemes. No other large-scale forcing is assumed.

The double-moment microphysical scheme assumes a lognormal size distribution for CCN, cloud droplets and rain drops with a prescribed geometric standard deviation of 1.5, 1.2 and 1.2, respectively. The CCN spectrum has a median radius of 0.1 μm. Number concentration of total available CCN in clean and polluted environment is assumed as 65 and 300 cm^{-3}, respectively. The cutoff radius between cloud and drizzle drops is 25 μm.

Three numerical experiments (N65v, N65c and N300v) with different CCN are conducted in a 60 x 60 km^2 domain with a uniform grid spacing of 300 m in the horizontal and ~30 m in the vertical for 16 hours starting from 00UTC (5pm PDT). The model depth is 1.5 km with a sponge layer at the upper 250 m. In experiment N65v and N300v, initial CCN concentration of 65 and 300 cm^{-3}, respectively, decreases with time due to continuous depletion but with no replenishing source. The experiment N65c with constant CCN of 65 cm^{-3} is designed to simulate the case with idealized sources to counteract the CCN depletion.

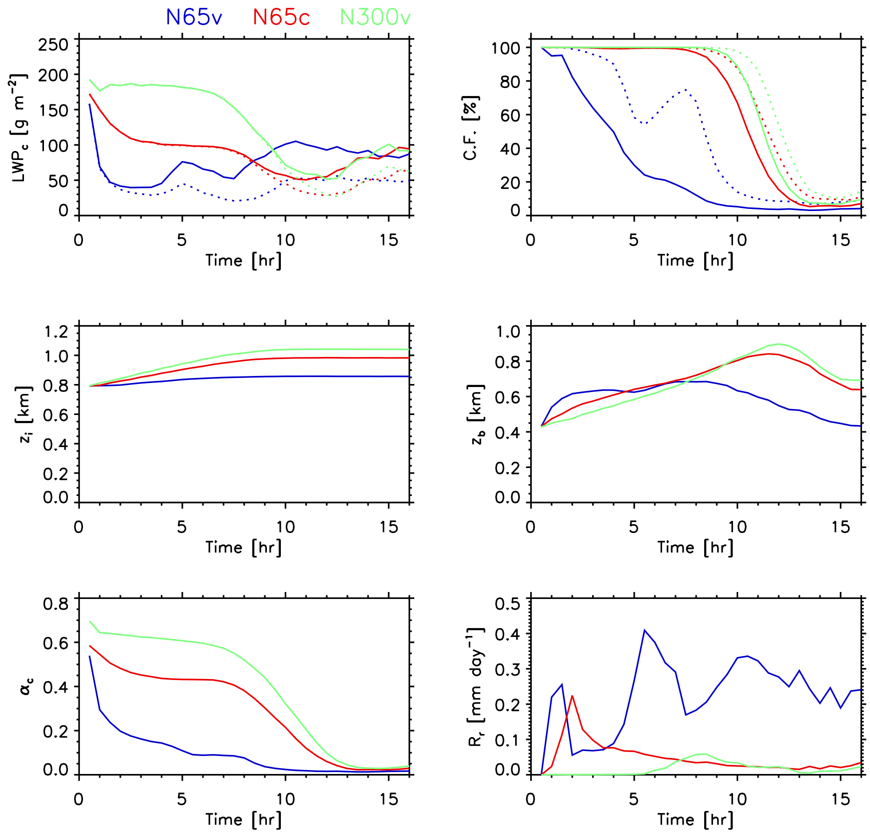

Figure 2: Time evolution of cloud-average liquid water path (LWP_c), cloud fraction (C.F.), domain-average inversion base height (z_i), mean cloud base height (z_b), domain- average cloud albedo (α_c) and domain-average surface rain rate (R_r) for the three experiments as indicated by different colors. In the top two panels, cloudy columns are defined by an optical depth threshold of 2 (solid lines) and 0.5 (dotted lines).

3. RESULTS AND DISCUSSIONS

Time series of cloud properties, boundary layer depth and drizzle rate are presented in Figure 2. In the clean case N65v, the cloud-average LWP drops about 100 g m^{-2} within one hour mainly due to precipitation. Cloud fraction drops quickly from 100%, indicating the fast breakup of an overcast Sc deck. In the case N65c, where CCN concentration is maintained by constant sources, the decrease in LWP and cloud fraction is significantly slowed down. In the polluted case N300v, even though no source complements the CCN loss, the initial concentration is high enough to support significant drop concentrations, suppression of drizzle, thus further delaying the breakup of the Sc deck. The thinning and breakup of the Sc deck can be illustrated by comparing the two sets of lines defined by different optical depth threshold values (2.0, solid lines; and 0.5, dotted lines) in the top two panels of Fig. 2. The departure point of solid and dotted lines is a good indicator of the start time of breakup of the Sc deck.

Smaller drops in polluted clouds delay the onset of surface drizzle by 5 hours and significantly lower the rain rate. The mean rain rate in N65v, N65c and N300v is 0.22, 0.05 and 0.02 mm day^{-1}, respectively, where the rate of 0.22 mm day^{-1} is very close to the ensemble mean reported by Ackerman et al. (2008), but smaller than the measured mean rain rate of 0.35 mm day^{-1}. The boundary layer is deepening with time, more so in the polluted than in the clean case because cloud top entrainment is weaker in clean case where drizzle is stronger and cloud top radiative cooling is weaker. Drizzle thins the cloud layer by eroding the base. The mean cloud base height increases more when surface drizzle is stronger in the N65v case. After the Sc deck has completely broken up, the mean cloud base decreases and LWP increases in all cases because small cumuli form in the moistened air underneath the patchy Sc.

The time variation of albedo is highly correlated with LWP and cloud fraction. The domain average cloud albedo is significantly lower in the N65v case than in the N65c and N300v cases. The temporal average value is 0.09, 0.28 and 0.39, respectively. Although cloud albedo in the polluted case N300v is high (up to 0.7) initially, it drops to as low as 0.04 when the Sc deck has broken up. A planar view of cloud albedo fields at different times is shown in Figure 3 to visualize the evolution of the Sc deck and the formation of POCs in both the N65v and N300v cases. At the end of the 3rd hour, a closed-cell structure is well formed in a solid Sc deck for both cases. After 2 further hours in the clean case, the Sc deck has clearly broken up and bright spots along the edges of the dissipating closed cells tend to organize as rings. About 4 hours later, thin clouds in the center of the rings disappear but the bright spots remain (see e.g., GOES images in Xue et al. 2008). These bright spots organize as a wall of POCs. The wall is by no means stationary but tends to expand with time.

The closed-cell structure lasts longer in the polluted case. Closed cells keep growing with the broadening of in-cloud circulations, and their size increases to about 15 km in 8 hours. After growing up to their maximum size, they start to thin from the edges and are clearly broken after 4 hours mostly due to entrainment. At the end of the 16th hour, bright cells in the polluted case also tend to form POC-like structures, but they are not as organized as in the clean case.

CCN are continuously depleted in the cloud layer, down to less than 30 (150) cm^{-3} at the open-cell stage in the N65v (N300v) case. CCN in the mixed layer are also depleted indirectly through vertical mixing.

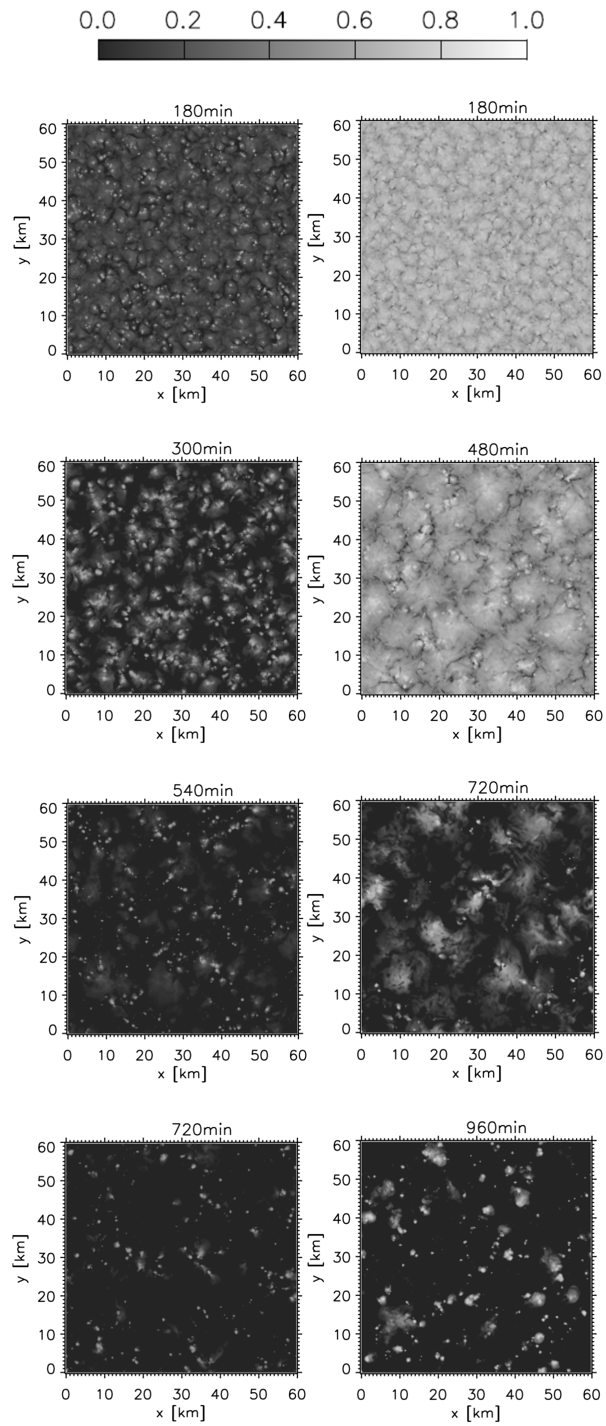

Figure 3: Cloud albedo fields at different stages during the life cycle of Sc deck in experiment N65v (left column) and N300v (right column).

Although cloud-top entrainment has brought CCN into clouds from above, it is minimal. The depletion of CCN in the case N65v has largely contributed to the continuous relatively strong drizzle, compared to that in the N65c and N300v cases, as shown in Fig. 2.

4. SUMMARY

In this study, aerosol effects on the formation of open cells in marine stratocumulus sheets over the Northeast Pacific are simulated using a three-dimensional LES model with a double-moment microphysical scheme that is based on bin-by-bin collection and sedimentation. Three simulations with different aerosol number concentrations are performed in a 60x60 km^2 domain, which allows closed cells to grow up to the size of about 15 km in weak precipitating cases. The simulation time of 16 hours is even long enough for the Sc sheet to break up in the relatively polluted environment.

Simulation results support the hypothesis that drizzle plays a critical role in the lifecycle of Sc. Without an aerosol source in a clean environment, depletion of CCN due to drop collection and sedimentation ensures continuous and relatively strong drizzle. This at least accelerated, if not triggered, the thinning of solid Sc deck and the transition from closed-cell to open-cell structure. Continuous CCN sources added to the clean boundary layer can significantly delay the breakup of Sc deck.

Simulation results also suggest that low CCN concentration and significant precipitation are not absolutely necessary for the breakup of a Sc deck. In the polluted case, the Sc thinning process was largely slowed down, but the ultimate breakup of Sc did happen, which may be mostly attributed to the continual cloud-top entrainment. Our ongoing and future studies focus on examining other factors that are important to marine boundary layer cloud processes and how they interact with aerosol effects through dynamical feedbacks. We will take full advantage of the two-way nesting ability and the integrated aerosol chemistry of the WRF model to simulate real cases.

5. ACKNOWLEDGEMENTS

We acknowledge support from NOAA's Climate Goal. Hailong Wang is supported by the Cooperative Institute for Research in Environmental Sciences (CIRES) Post-doctoral Fellowship. We thank Hongli Jiang, Adrian Hill, Georg Grell, Jian-wen Bao, Si-Wan Kim, Bill Skamarock, Chin-Hoh Moeng and Mary Barth for thoughtful discussions. We also thank the WRF development team for technical help and the NOAA ESRL High Performance Computing Systems team for computational and technical support.

6. REFERENCES

Ackerman, A. S., O. B. Toon, and P. V. Hobbs, 1993: Dissipation of marine stratiform clouds and collapse of the marine boundary layer due to the depletion of cloud condensation nuclei by clouds. *Science*, **262**, 226–229.

Ackerman, A. S., and coauthors, 2008: Large-eddy simulations of a drizzling, stratocumulus-topped marine boundary layer. *Mon. Wea. Rev.*, submitted.

Atkinson, B. W., and J. W. Zhang, 1996: Mesoscale shallow convection in the atmosphere. *Rev. Geophys.*, **34**, 403–431.

Bretherton, C. S., T. Uttal, C. W. Fairall, S. Yuter, R. Weller, D. Baumgardner, K. Comstock, R. Wood, and G. Raga, 2004: The epic 2001 stratocumulus study. *Bull. Amer. Meteor. Soc.*, **85**, 967–977.

Feingold, G., R. L. Walko, B. Stevens, and W. R. Cotton, 1998: Simulations of marine stratocumulus using a new microphysical parameterization scheme. *Atmos. Res.,* **47–48,** 505–528.

Savic-Jovcic, V., and B. Stevens, 2008: The structure and mesoscale organization of precipitating stratocumulus. *J. Atmos. Sci.,* in press.

Sharon, T. M., B. A. Albrecht, H. H. Jonsson, P. Minnis, M. M. Khaiyer, T. M. van Reken, J. Seinfeld, and R. Flagan, 2006: Aerosol and cloud microphysical characteristics of rifts and gradients in maritime stratocumulus clouds. *J. Atmos. Sci.*, **63**, 983–997.

Skamarock W. C., J. B. Klemp, J. Dudhia, D. O. Gill, D. M. Barker, W. Wang, and J. G.

Powers, 2005: A description of the advanced research WRF version 2. NCAR Tech. Note NCAR/TN-468+STR, 88 pp.

Stevens, B., and coauthors, 2003: Dynamics and chemistry of marine stratocumulus – DYCOMS-II. *Bull. Amer. Meteor. Soc.*, **84**, 579–593.

Stevens, B., G. Vali, K. Comstock, M. C. vanZanten, P. H. Austin, C. S. Bretherton, and D. Lenschow, 2005: Pockets of open cells (POCs) and drizzle in marine stratocumulus. *Bull. Amer. Meteor. Soc.*, **86**, 51–57.

Tzivion, S., G. Feingold, and Z. Levin, 1987: An efficient numerical solution to the stochastic collection equation. *J. Atmos. Sci.*, **44**, 3139–3149.

Xue, H., G. Feingold, and B. Stevens, 2007: Aerosol effects on clouds, precipitation, and the organization of shallow cumulus convection. *J. Atmos. Sci.*, **65**, 392-406.

MICROPHYSICAL CHARACTERISTICS OF ARTIC STRATUS OBSERVED DURING ASTAR2 – A COMPARISON OF OBSERVATIONS WITH DETAILED MICROPHYSICAL MODELING

Wolfram Wobrock, Jean-François Gayet, Guillaume Mioche, Alfons Schwarzenböck and Andrea.I. Flossmann

Laboratoire de Météorologie-Physique, Université Blaise Pascal
Clermont-Ferrand, France

W.Wobrock@opgc.univ-bpclermont.fr

1. INTRODUCTION

During 2-16 April 2007 the second campaign of the Artic Study of Aerosols, Clouds and Radiation (ASTAR) took place west of Spitzbergen in latitudes between 75°-80°N. Airborne measurements were performed onboard the AWI Polar 2 aircraft focusing on the detailed in situ characterization of the microphysical and optical properties of Arctic mixed phase clouds.

In the present study we discuss at first the microphysical and optical measurements. By means of a 3D cloud model with bin resolved microphysics for aerosols, droplet and ice crystal also an attempt was made to understand the microphysical mechanisms of this arctic stratocumulus.

2. INSTRUMENTATION

The observational results discussed in this study are obtained from measurements with a FSSP100, a Polar Nephelometer, and a Cloud Particle Imager (CPI) on board the German research aircraft Polar 2 of the Alfred Wegener Institut, Bremerhaven. The flight discussed took place on 7 April 2007 along a track in southeastern and northwestern directions in between latitudes of 77.1- 78.6°N and longitudes of 6-13°E. Between 9 to 11 UTC the aircraft flew 8 soundings in a precipitating stratocumulus layer ranging from 100 to 2000 m which will be the focus of our analysis.

Spectra of hydrometeors in the range from 2 to 32 µm were performed by a PMS FSSP probe (Baumgardner, 1983). Information on drops and crystals of larger sizes were obtained from CPI measurements. The Cloud Particle Imager measures cloud particles by taking images of the particles on a one-million pixel CCD camera by freezing the motion of the particle using a 40 ns pulsed, high-power laser diode (Lawson et al., 2001). The CPI images were preprocessed using a newly developed technique (Lefevre, 2007), which provides additional information about the ice-particle morphology that is not available from the original CPIview software (Lawson et al., 2001; Baker and Lawson, 2006). Microphysical and optical parameters retrieved from CPI data are number concentration, ice and water contents, effective diameter, shape classification, extinction coefficient and size distribution of cloud particles in the size range from 10 µm to 2.3 mm.

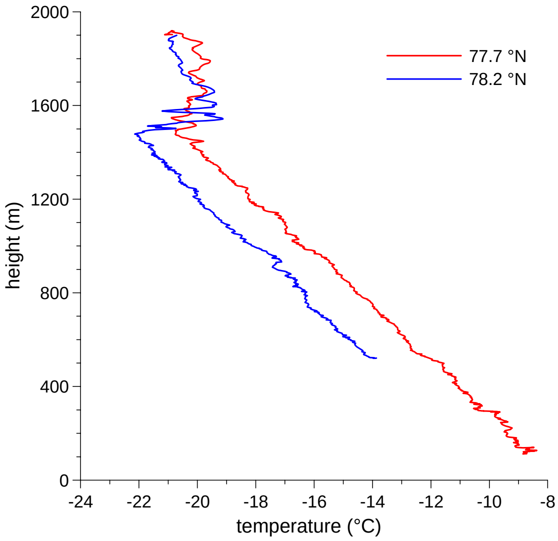

Fig.1: Temperature profiles in the strato-cumulus layer for two different locations

The Polar Nephelometer (Gayet et al., 1997) measures the scattering phase function of an ensemble of cloud particles with sizes from a few to about 800 µm in diameter, which intersect a collimated laser beam near the focal point of a parabolic mirror. The light scattered at polar angles from ±3.5° to ±169° is

reflected onto a circular array of 56 photodiodes. The sampling volume is determined by the sampling surface (10-mm long and 5-mm diameter beam) multiplied by the aircraft speed (Polar-2 aircraft cruise speed of approximately 80 m/s during ASTAR 2007), that is, 400 cm^3 for an acquisition frequency of 10 Hz.
The direct measurement of the scattering phase function allows particle types (water droplets or ice crystals) to be distinguished and calculation of the optical parameters to be derived (extinction coefficient and asymmetry parameter, Gayet et al., 2002). All observations are available with a time resolution of 1 s.

3. OBSERVATIONAL RESULTS

In the morning of 7 April a northern flow with wind speeds between 6 to 14 m/s prevailed transporting cold air from the arctic ice shelf. These variation of the wind speed mainly occurred in horizontal scales of 50-70 km but the vertical shear was significantly weaker. Fig.1 displays the vertical profiles of the temperature for two locations 55 km apart from each other and thus illustrating the cold air advection from the north.
Cloud base was found in levels between 600 to 800 m. The studied stratocumulus had an average depth of 800m which was sufficient for precipitation formation. As expected due to the low temperatures precipitation occurred through graupel or

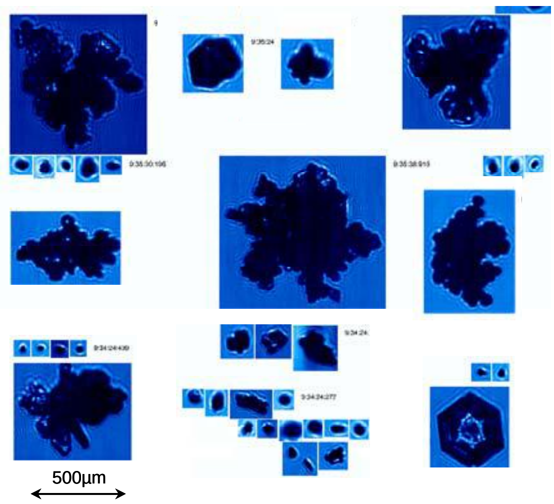

Fig.2a: CPI images of cloud particles close to cloud base (500 – 700 m) at 9.34 - 9.35 UTC

snow particles. The presence of ice crystals over the entire cloud layer is well documented by the CPI measurements. Fig.2a shows individual ice crystals and small drops next to or just below cloud base.

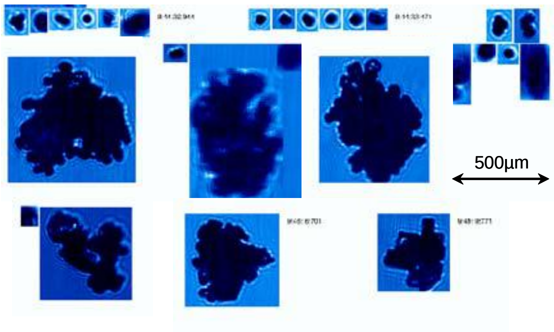

Fig.2b: CPI images at the cloud top around 1500 m from 9.44 - 9.45 UTC

The larger particles are in most cases irregularly shaped and indicate that riming with small cloud droplets took place. Most particles below sizes of 100 µm have a spherical form supposing to be liquid drops.
Fig.2a shows ice crystals and small drops next to the cloud top in altitudes between 1450 to 1550m. Also in the Sc top cloud droplets and large ice crystals prevail, however, their spectral number distribution shows some differences. Fig.3 depicts the spectra measured by means of FSSP and CPI. We only selected those observations performed near cloud base (500-800m) and near cloud top (1400-1700m).

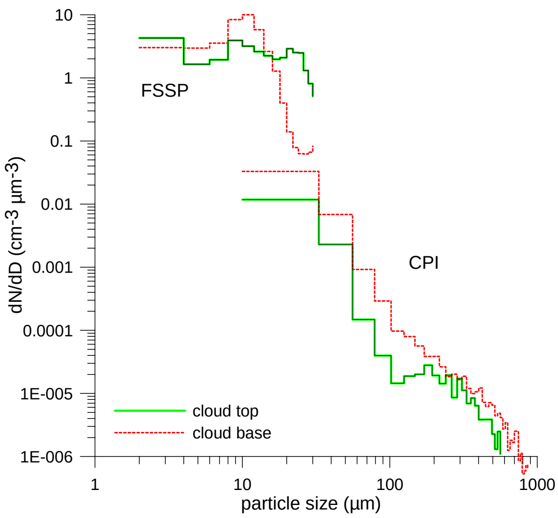

Fig.3: Mean number distribution observed with FSSP and CPI at cloud base and cloud top

From the 8 flight profiles about 400 CPI spectra were available for cloud base however only 100 for cloud top. In the case of the FSSP spectra the numbers were about the same but inversed: about 80 for cloud base and 370 for cloud top.

The graphs illustrated in Fig. 3 are the corresponding mean spectra. It is obvious from this illustration that more and larger precipitation particles (sizes > 100 µm) were present at the cloud base. The FSSP spectra show that the small cloud particles (< 30µm) do not differ significantly in their number concentration (77 cm^{-3} for cloud base and 68 cm^{-3} for cloud top) but in their size. While at cloud base the mean diameter is about 9 µm the one for the cloud top reaches 14 µm.

The effect of the presence of larger cloud droplets and a lower concentration of precipitation size particles at cloud top becomes most pronounced in the results of the asymmetry parameter measured by the Polar Nephelometer.

Fig.4 illustrates the asymmetry parameter as function of height. All flight data (about 2800 observation points) between 100 to 2000 m were analyzed. The black points indicate the asymmetry parameter when the FSSP counts more than 5 particles per cm^3. The red points are plotted when the CPI number concentration for particles larger 100 µm exceeds 20 particles per liter.

Only two different groups for the asymmetry value become visible: 0.79 for most levels below 800 m and 0.84 for levels above 1200 m. Values close to 0.84 indicate that the scattering phase function is predominantly determined by the presence of liquid cloud droplets, while a shift to lower values indicate the influence of irregular shaped ice particles (Gayet et al., 2006, Garrett et al., 2003).

From Figs. 2 and 3 we have seen that irregularly shaped ice crystals are present over the entire stratocumulus layer. Fig. 4 however demonstrates that an influence of the ice phase on the optical cloud properties only occurs when significant numbers of large irregularly shaped particles prevail. Furthermore Fig.4 makes evident that the upper part of this arctic stratocumulus deck is dominated by liquid water despite the prevailing low temperatures of -18 to -22°C. In contrast to that the presence of large ice crystals characterizes the microphysics of the lower and warmer part of cloud and thus also controls the precipitation mechanism. In the intermediate range of the cloud layer from 800 to 1200 m both phases can occur.

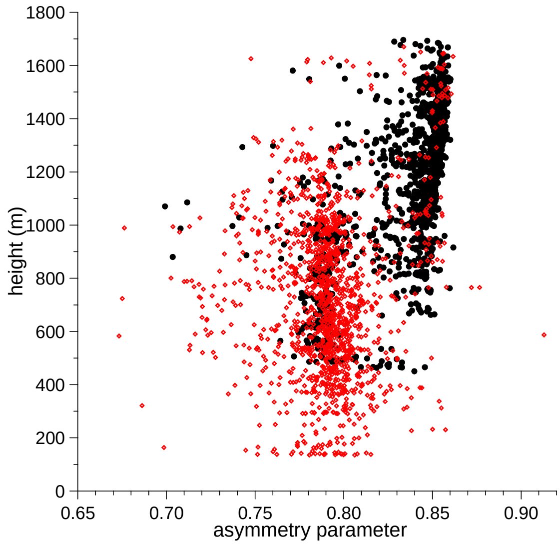

Fig.4: Asymmetry parameter calculated from nephelometer measurements as a function of altitude. The red diamonds indicate data points when CPI measurements count more than 20 particles per liter.

4. MODELING WITH DETAILED MICRO-PHYSICS

4.1. MODEL DESCRIPTION AND SETUP

The 3D model with detailed (bin) microphysics used herein couples the 3D non-hydrostatic model of Clark and Hall (1991) with the Detailed Scavenging Model DESCAM (Flossmann et al., 1985) A detailed description of the microphysical package, including sensitivity studies of DESCAM under mixed phase conditions can be found in Leroy et al. (2007).

Below only a brief summary of the essential features is given. The microphysical model employs five distribution functions: three number density distributions functions respectively for the wet aerosol particles (AP), the drops and the ice crystals and two mass density distributions of aerosol particles inside drops and ice particles. The five functions are discretized over 39 bins that cover a range of radius from 1 nm to 6 µm for the wet AP and from 1 µm to 6 mm for the liquid or solid hydrometeors. All together, the detailed microphysics introduces 195 supplementary prognostic variables to the initial code.

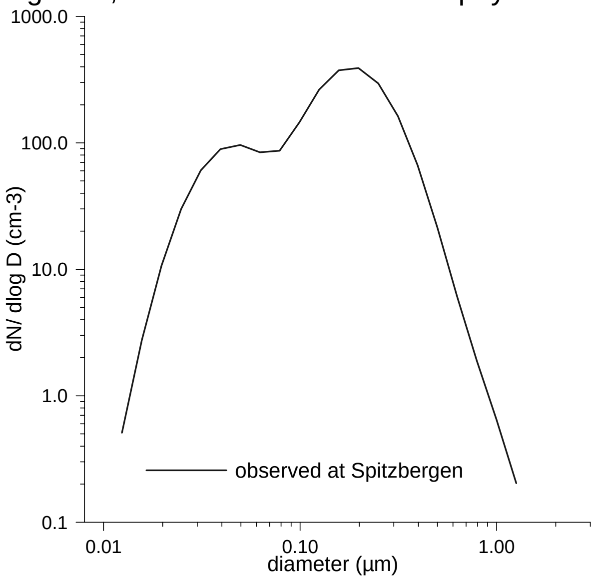

Fig. 5: Aerosol particle number distributions used for the numerical simulations

The microphysical processes that are considered in the model are: condensational growth and activation/ deactivation of AP, condensation and evaporation of droplets, coalescence, homogeneous and heterogeneous nucleation, vapour deposition on ice crystals and riming. Droplet nucleation relies on the calculation of the activation radius derived from the Köhler equation (Pruppacher and Klett, 1997), but is also dependent on temperature as described in Leroy et al. (2007). Growth rate of drops and ice crystals are given by Pruppacher and Klett (1997). Homogeneous and heterogeneous nucleation follows respectively the works of Koop et al. (2000) and Meyers et al. (1992). Ice crystals are assumed to be spherical and the density of ice is 0.9 g m^{-3}. Coalescence and riming are treated with the numerical scheme of Bott (1998). The collection kernels for coalescence of drops are calculated with the collection efficiencies of Hall (1980) and the terminal velocities of Pruppacher and Klett (1997). Riming description includes collection of droplets by large ice crystals as well as collection of small ice particles by large drops. The collection kernels for riming are set to be the same as those for coalescence of drops, i.e. we assume that the collection efficiency of a spherical ice crystal is equal to the one of a water drop of the same mass.

Aggregation and secondary production of ice particles during riming is also neglected in the model for the moment.

To initialize the microphysics, aerosol particle spectra as a function of altitude are needed. The total number of aerosol particles in the boundary layer is 219 cm^{-3}. The aerosol particle number distribution was available from ground observations at Mount Zepplin, Spitzbergen as depicted in Fig. 5. Aerosol particles are assumed to be ammonium sulfate, entirely soluble.

For the simulations presented in this study, the model domain is 16.64 km x 16.64 km in the horizontal and 6 km in the vertical. The resolution is 130 m for the horizontal coordinates. For the vertical coordinate a telescopic grid was designed by means of a 5th order polynomial allowing low grid spacing in the lowest 50 m (with Δz ranging from 4-10m) and on stratocumulus top where Δz decrease to 17 m. The dynamical time step is 1 second. The thermodynamical conditions are given from the aircraft sounding at 9 UTC. For simplicity boundary conditions were treated periodic.

4.2 MODEL RESULTS

Due to the high relative humidity between 600 and 1500m the stratocumulus develops rapidly after 20-30 minutes of integration over the observed altitudes. In the following part model results after 100 min of integration will be discussed.

Figs. 6 and 7 illustrate the simulated total droplet and ice crystal number concentration along a vertical cross section in NE direction.

The comparison of both figures makes it obvious that the model describes well the observed features: cloud droplets occur between 600 and 1500 m but ice crystals are present over the entire BL down to the sea surface. From Fig. 6 one cannot detect a variability of droplet number with altitude. Max. number concentrations between 150-180 drops per cm^3 can be found in levels next to the cloud top as well as next to cloud base.

Calculating the domain averages of the model data for 700 m results in 117 droplets per cm^3 and on cloud top 98

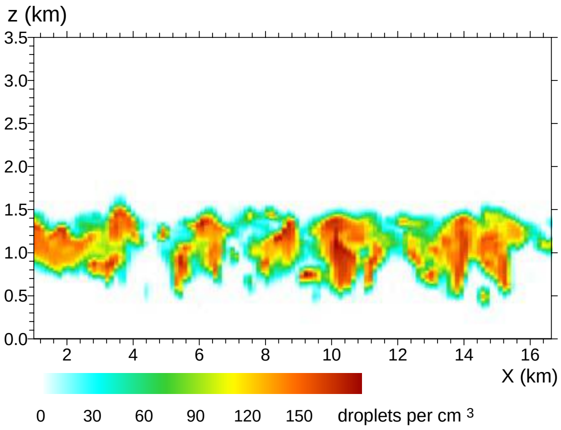

Fig.6: Vertical cross section of the cloud droplet number concentration (cm^{-3}) after 100 min of model time.

droplets per cm^3 are found. The simulation results are thus thus only slightly larger than the FSSP measurements which give 77 cm^{-3} and 68 cm^{-3} particles for cloud base and cloud top respectively.

Simulated drop and ice crystal spectra at cloud base are illustrated in Fig. 8 and those for cloud top in Fig. 9. The red curves for the droplet spectra in both figures demonstrate that the model is capable to well reproduce the differences between cloud base and cloud top spectra.

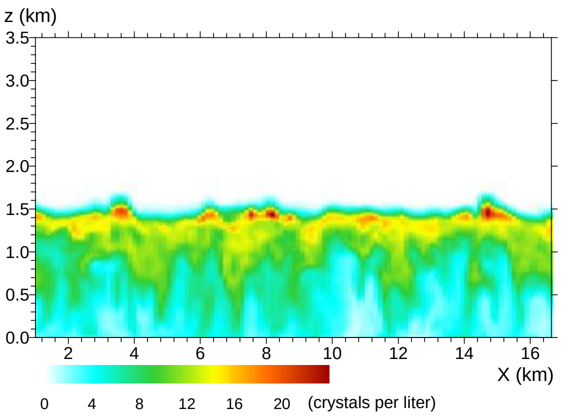

Fig.7: Vertical cross section of the total ice crystal number (cm^{-3}) after 100 min of model time.

In contrast to the droplet number depicted in Fig.6 the vertical cross section for the modeled ice crystal number concentration in Fig.7 shows an increase of the particle number with height. The max concentrations (> 20 crystals per liter) come from freezing of cloud droplets which is most effective on cloud top. As supersaturation prevails over the entire cloud layer supersaturation with respect to ice is highest where lowest temperatures are present (i.e. -22°C at cloud top).

Mean simulated ice crystal number concentrations are 8.3 $liter^{-1}$ at cloud base and 10.6 $liter^{-1}$ at cloud top. Thus, the order of magnitudes agree well with the observations. However, as already shown in Fig.3 observations during ASTAR2 on 7 April 2008 report at cloud base the max number of 15.2 particles $liter^{-1}$ and at cloud top only 7.2 $liter^{-l}$. These values were determined by counting only CPI bins larger than 100 µm in size in order to avoid an overestimation of the crystal concentration. It obvious from Figs.2 and 3 that the smallest CPI bins predominantly count large cloud droplets.

The discrepancies between modeled and observed ice particle numbers become also visible in the presentation of the size number distributions given in Fig. 8 and 9. At cloud base (Fig.8) the simulated crystal numbers only agree with the observations in the size range from 200 to 450 µm. Crystals above 500 µm do not form in the simulation. In addition a clear separation and gap formed in the model spectrum between liquid cloud droplet (< 20 µm) and the precipitating ice (> 150 µm).

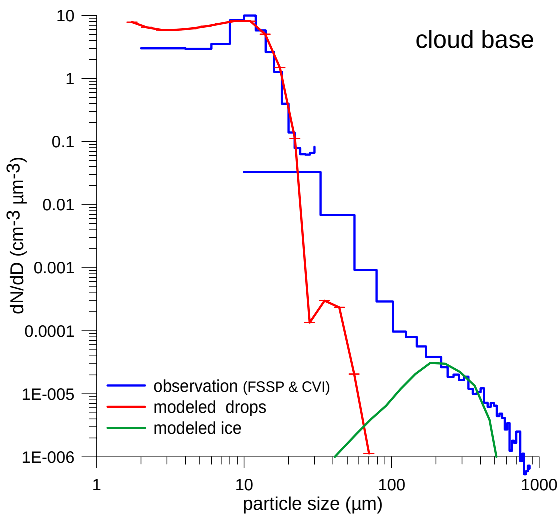

Fig.8: Observed cloud particle spectra versus simulated droplet and ice spectra, both at cloud base.

At cloud top (Fig.9) larger cloud droplets exist and freshly nucleated crystals are present causing for the simulated spectra a continuous transition from cloud to precipitating sizes. The presence of numerous ice crystals with sizes below 100µm comes from the high ice super-saturations at cloud top which cause a significant nucleation rate in the model calculations. On cloud base, however, where temperature is only around -14°C and thus lower RHI prevail, the nucleation mechanism of Meyers et al (1992) used in the model cannot not provide any more new ice crystals. Consequently, in the lower part of the cloud only riming of ice crystals with droplets occurs what it finally responsible for the separation of drop and ice spectrum in Fig.8.

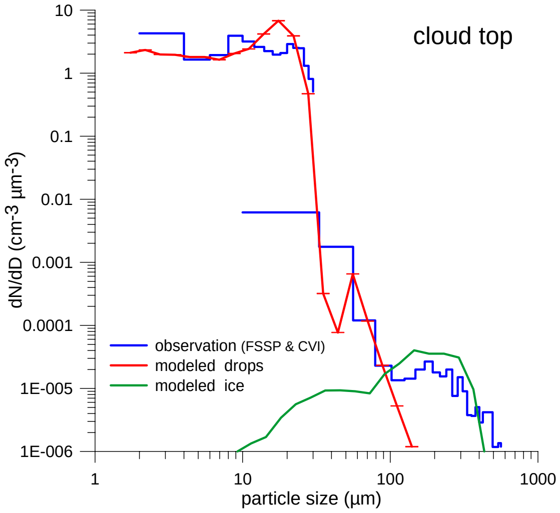

Fig.9: Observed versus simulated droplet and ice spectra at coud top

The strongest discrepancies between observed and simulated spectra thus appear in the transition size range from 30 to 100 µm but also for crystals sizes larger than 400 µm. The underestimation of large ice particles is evident as the model assumes that ice crystals have a spherical form with a density of 0.9 g cm^{-3}. Observed ice particles (Figs. 2 and 3) show irregular shapes and their densities especially for rimed aggregates will significantly deviate from that of pure ice.
The lack of cloud/ice particles ranging from 30 to 100 µm in the lower part of the modeled cloud indicates that other heterogeneous nucleation processes may be important for the formation of ice at temperature around -15°C. By using the approach of Meyers only sorption and condensation freezing are included in the microphysics of the actual model.

5. CONCLUSIONS AND OUTLOOK

The presented results are a first attempt to understand the microphysical mechanisms of the artic stratocumulus cloud during ASTAR. While certain microphysical and dynamical features are well reproduced, others as e.g. the behavior of the ice particles, need further studies. Future investigation need to include the extension of the microphysics to other already identified nucleation mechanisms such as contact and immersion freezing and consider a variable ice density.

6. ACKNOWLEDGEMENTS

The authors want to thank for the support from the *Centre National d'Etudes Spatiales* (CNES) and the *Institut National des Sciences de l''Univers* (INSU/CNRS). Calculations have been done on computer facilities of the *Institut du Développement et des Ressources en Informatique Scientifique* (IDRIS, CNRS) in Orsay (France) and the *Centre Informatique National de l'Enseignement Supérieur* (CINES) in Montpellier (France), under project no.940180. The authors acknowledge with gratitude the hours of computer time and the support provided.

7. REFERENCES

Baker B. and. P. Lawson (2006): Improvement in Determination of Ice Water Content from Two-Dimensional Particle Imagery. Part I: Image-to-Mass Relationships. DOI: 10.1175/JAM2398.1 pp. 1282–1290

Baumgardner, D. (1983), An analysis and comparison of five water droplet measuring instruments, J. Clim. Appl. Meteorol., 22, 891–910.

Bott A., 1998 : A flux method for the numerical solution of the stochastic collection equation. *J. Atmos. Sci.*, **55**, 2284-2293.

Clark T. L., and W. D. Hall, 1991 : Multi-domain simulations of the time dependent Navier-Stokes equations : benchmark error analysis of some nesting procedure, *J. Comp. Phys.*, **92**, 456-481.

Flossmann A. I., W. D. Hall and H. R. Pruppacher, 1985 : A theoretical study of the wet removal of atmospheric pollutants. Part I : The redistribution of aerosol particles captured through nucleation and impaction scavenging by growing cloud drops. *J. Atmos. Sci.*, **42**, 583-606.

Hall W. D., 1980 : A detailed microphysical model within a two-dimensional dynamic framework : Model description and preliminary results. *J. Atmos. Sci.*, **37**, 2486-2506.

Garret T.J., H. Gerber, D.G. Baumgardner, C.H. Twohey and E.M. Weinstock (2003): Small, highly reflective ice crystals in low-latitude cirrus. GRL, Vol. 30, No.31, 2132, doi:10.1029 /2003/GLO18153, 2003.

Gayet, J.-F., O. Crepel, J.-F. Fournol, and S. Oshchepkov (1997), A new airborne polar nephelometer for the measurements of optical and micro-physical cloud properties. Part I: Theoretical design, Ann. Geophys., 15,451–459.

Gayet, J.-F., S. Asano, A. Yamazaki, A. Uchiyama, A. Sinyuk, O. Jourdan, and F. Auriol (2002), Two case studies of winter continental-type water and mixed-phase stratocumuli over the sea: 1. Microphysical and optical properties, J. Geophys. Res., 107(D21), 4569, doi:10.1029/ 2001 JD001106.

Koop T., H. P. Ng, B. Luo, A. Tsias and T. Peter, 2000 : Water activity as the determinant for homogeneous ice nucleation in aqueous solutions. *Nature*, **406**, 611-615.

Lawson, R. P., B. A. Baker, C. G. Schmitt, and T. L. Jensen (2001), An overview of microphysical properties of Arctic clouds observed in May and July 1998 during FIRE ACE, J. Geophys. Res., 106(D14), 14,989–15,014.

Lefevre, R. (2007): Physique de la mesure de la sonde CPI pour la mesure des propriétés des cristaux de glace. Application aux observations réalisées durant la campagne ASTART 2001. *PhD thesis N° 527*,Université Blaise Pascal, UFR Sciences et Technologie, Clermont-Ferrand 187p.

Leroy D., W. Wobrock, and A. I. Flossmann, 2007 : On the influence of the treatment of aerosol particles in different bin microphysical models : a comparison between two different schemes. *Atmos. Res.*, **85**, 269-287. doi : 10.1016/j.atmosres.2007.01.003

Meyers M. P., P. J. Demott and W. R. Cotton, 1992 : New primary ice nucleation parameterizations in an explicit cloud model. *J. Appl. Met.*, **31**, 708-721.

Pruppacher H. R. and J.D. Klett, 1997: *Microphysics of clouds and precipitation*. 2nd ed. Kluwer Academic, 954p.

EVOLUTION OF AEWs AND MCSs OFF WEST AFRICA OBSERVED DURING AMMA SOP-3 IN SEPTEMBER 2006

Joël. Arnault[1] and Frank. Roux[1]
[1]Laboratoire d'Aérologie (Université de Toulouse and CNRS), Toulouse, France

1. INTRODUCTION

Tropical cyclogenesis occurring over the Atlantic off the West African coast during late summer is believed to be driven by scale interaction processes involving the African easterly waves (AEWs), the African easterly jet (AEJ), the west-southerly monsoon flow, the Saharan dry air and the westward propagating mesoscale convective systems (MCSs). It is already known that some Atlantic tropical cyclones have their origin in MCSs propagating over the African continent (Thorncroft and Hodgs 2001). For example, Hill and Lin (2003) related the genesis of Hurricane Alberto (2000) to a MCS initiated over the Ethiopian highlands. Lin et al. (2005) documented this case-study and identified three successive convective genesis and lysis periods before the final cyclogenesis event off the Guinea coast. Berry and Thorncroft (2005) also showed that the MCSs associated with the pre-Alberto disturbance were embedded in an AEW. Scale interactions between the MCSs and this AEW certainly contributed to the cyclogenetic evolution of the pre-Alberto disturbance, although the processes involved are not understood yet. This problem can be further investigated by considering more case-studies of developing and non developing West African disturbances.

Here we propose the case of the so-called "Perturbation D" which is a non-developing West African disturbance observed during the Special Observing Period 3 (SOP-3) of AMMA (African Monsoon Multidisciplinary Analysis) that was conducted from Dakar (Senegal) on 15–29 September 2006. This "Perturbation D" was associated with an AEW. Scale interactions between synoptic and convective processes are investigated on the basis of ECMWF (European Center for Mean Weather Forecast) Operational Analyses and brightness temperatures images from Meteosat-9 water vapour channel n°6 (6.85 – 7.85 µm). Energy conversion terms have been computed in the area of this "Perturbation D" to quantify the growth of the wave associated with the disturbance. Finally some preliminary results with the French non-hydrostatic model Meso-NH are discussed.

2. DATA

The synoptic environment of the "Perturbation D" is deduced from the ECMWF analyses. Air temperature, relative humidity, geopotential, wind components, relative vertical vorticity and horizontal divergence are available on a regular latitude-longitude grid of resolution 0.5°, at 21 pressure levels between 1000 and 1 mb, at 00, 06, 12 and 18 UTC.

The convective activity associated with "Perturbation D" is deduced from the Meteosat-9 brightness temperature images in the water vapour channel available every 15 minutes. The Meteosat-9 raw images have been interpolated on a regular latitude longitude grid of resolution 0.027° and a brightness temperature resolution of 0.5K.

3. SIGNATURE OF WAVE ACTIVITY

AEWs have a maximal intensity south of 15°N at the AEJ level at 600-700 hPa (e.g. Carlson 1969a,b; Burpee 1972). Fig. 1a shows a Hovmöller space-time diagram of the ECMWF-analysed relative vertical vorticity at 700 hPa averaged between 5° and 15°N from 22 to 30 September 2006. The tilted black ellipse shows that "Perturbation D" was associated with a well-defined AEW that started on the 22nd afternoon over Ghana (≈0° longitude) and dissipated on the 28th afternoon near the Cape Verde islands (≈25° W). "Perturbation D" also has a distinct signature in the Meteosat-9 images (Fig. 1b) which let suppose interactions between the synoptic wave and the embedded convective activity.

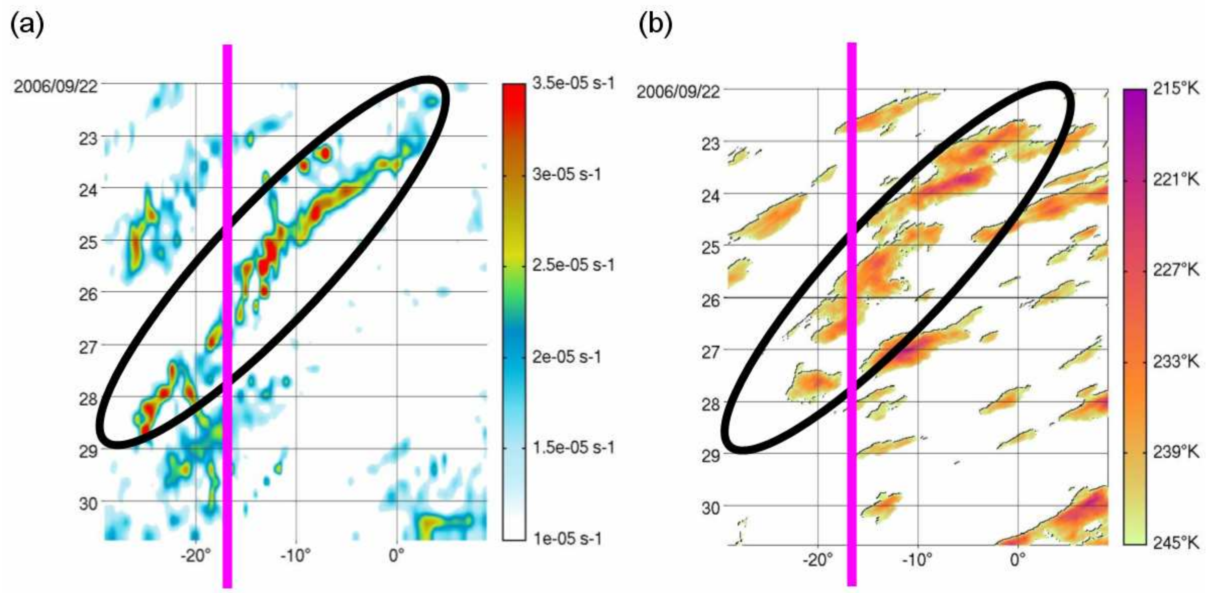

Figure 1 : *(a) Hovmöller space-time diagram of 700 hPa relative vertical vorticity averaged between 5° and 15°N (from ECMWF analyses, colored a bove +10^5 s^{-1}) between 22 and 30 september 2006. The X axis indicates longitude in degrees and the Y axis gives time in days. (b) As in (a) except for Meteosat-9 brightness temperature (colored below 245K). In these two diagrams the purple vertical line indicates the mean position of the West African coast and the tilted black ellipse encloses the "Perturbation D".*

4. SCALE INTERACTIONS

Two types of composite images from ECMWF synoptic fields and Meteosat-9 brightness temperatures reveal scale interaction processes involved in the evolution of "Perturbation D".

The first type of composite images (Fig. 2) shows several horizontal fields : brightness temperatures below -30°C indicate convective activity ; the synoptic environment is characterized at 925 hPa by Saharan dry air from north and monsoon surges from south, and at 700 hPa by easterly wind associated with the AEJ and the AEWs. The trough axes of the AEWs have been computed with the objective method proposed by Berry et al. (2006). The whole set of composite images for the "Perturbation D" on 22-28 September 2006 is too voluminous to be included in this paper and only the period from 25 September 2006 at 06 UTC to 27 September 2006 at 18 UTC when the disturbance crosses the West African coast is shown.

The following evolution of "Perturbation D" was deduced from the whole series of composite images. On the 22nd afternoon, the monsoon flow was well established over Ghana and dry Saharan air remained well to the north. The conditions were therefore favourable for convective developments and the growing MCSs have been carried along by the AEJ to south Mali on the 23rd. Monsoon surges bringing moist air to "Perturbation D" continued during the two following days. The sustained convective activity strengthened cyclonic curvature of the AEW it was embedded in. On the 25th at 18 UTC (Fig. 2b), "Perturbation D" was over southern Senegal and dry Saharan northerly flow coming from northern Mali enhanced the anti-cyclonic curvature of the AEW. This process intensified during the following days with a dry northerly flow extending westward to Mauritania. Consequently the southerly component of the AEJ related to the anti-cyclonic curvature of the AEW moved "Perturbation D" northward, away from the monsoon flow. During the afternoon of the 27th (Fig. 2f), a MCS developed off the Senegal coast. However "Perturbation D"

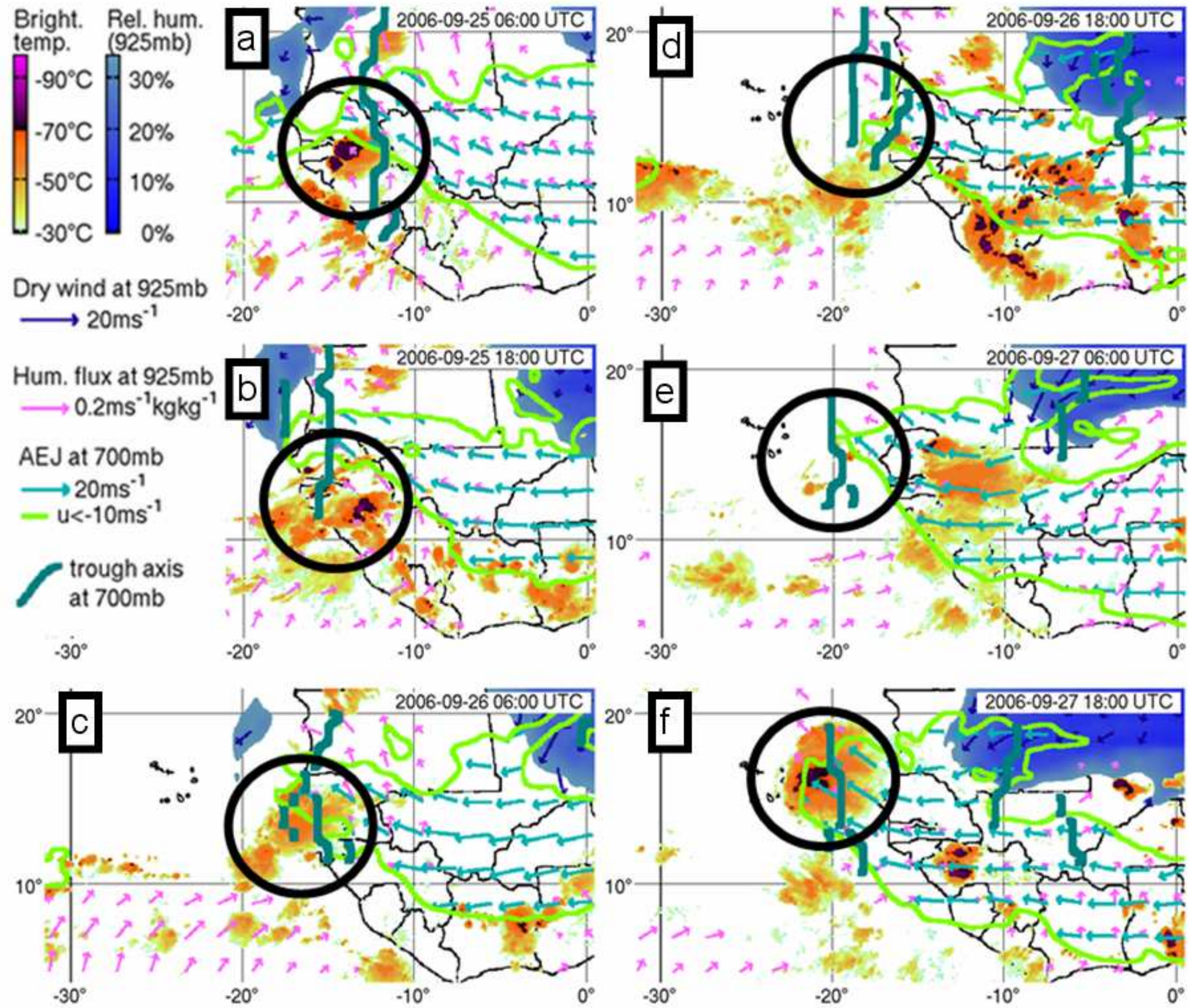

Figure 2 : *Composite images from Meteosat-9 and ECMWF data from (a) 25 September 2006 at 06 UTC till (f) 27 September 2006 at 18 UTC : orange red and black zones show brightness temperature below -30°C, blue areas display relative humidity values less than 30% and northerly wind at 925 hPa, pink arrows represent southerly humidity flux at 925 hPa, bright green lines and blue-green arrows reveal the zonal wind stronger than 10ms^{-1} at 700 hPa, the dark-green lines are the trough axes at 700 hPa computed with the objective method proposed by Berry et al. (2006). The black circles indicate the location of the MCSs associated with "Perturbation D"*

was too far from the monsoon flow, and it finally dissipated during the next day as it interacted with a subtropical trough located near the Canaries islands.

The second kind of composite image focuses more specifically on the interaction between the synoptic wave and the convective activity (Fig. 3). "Perturbation D" can be associated distinctly with a cyclonic maximum of relative vertical vorticity at 700 hPa, or with the trough of the AEW it is embedded in. Fig. 4 displays the evolution of the vertical profile of relative vertical vorticity averaged over the 6°x6° domain enclosing "Perturbation D" (pink squares in Fig. 3). The associated evolution of the cloud area below different temperature thresholds is also shown in Fig. 4. Following Mathon and Laurent (2000) who used brightness temperature thresholds of -60°C, -40°C, -20°C to describe MCS activity in the Sahel region, convection has been quantified here by the evolution of cloudy surfaces with temperatures colder than -70°C, -50°C and

-

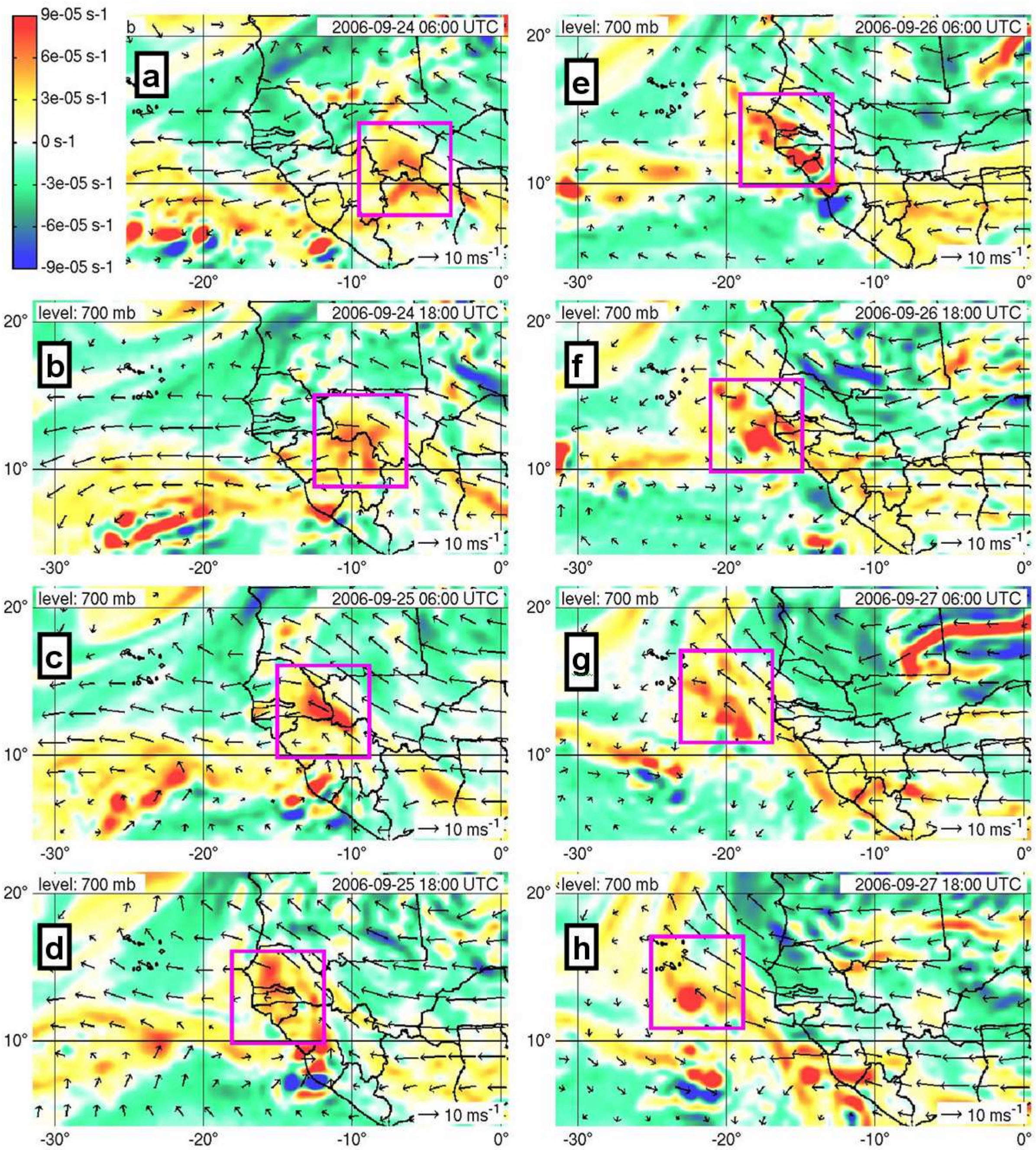

Figure 3 : *Horizontal cross-sections of relative vertical vorticity at 700 hPa derived from the ECMWF analyses for the period from (a) 25 September 2006 at 06 UTC till (h) 27 September at 18 UTC. The 6°x6° pink squares represe nt the domain where average values have been calculated to characterize "Perturbation D".*

30℃. Areas colder than -30℃ give the disturbance's life cycle. The evolution of the area colder than -50℃ focuses on convective activity and the evolution of the area colder than -70℃ is an indicator of phases o intense convection.

Three successive stages have been identified in the evolution of "perturbation D": I : development and propagation over the continent (22-24 September), II : convective re-developments during the crossing of Futa Jallon mountains near the Guinea coast (25-

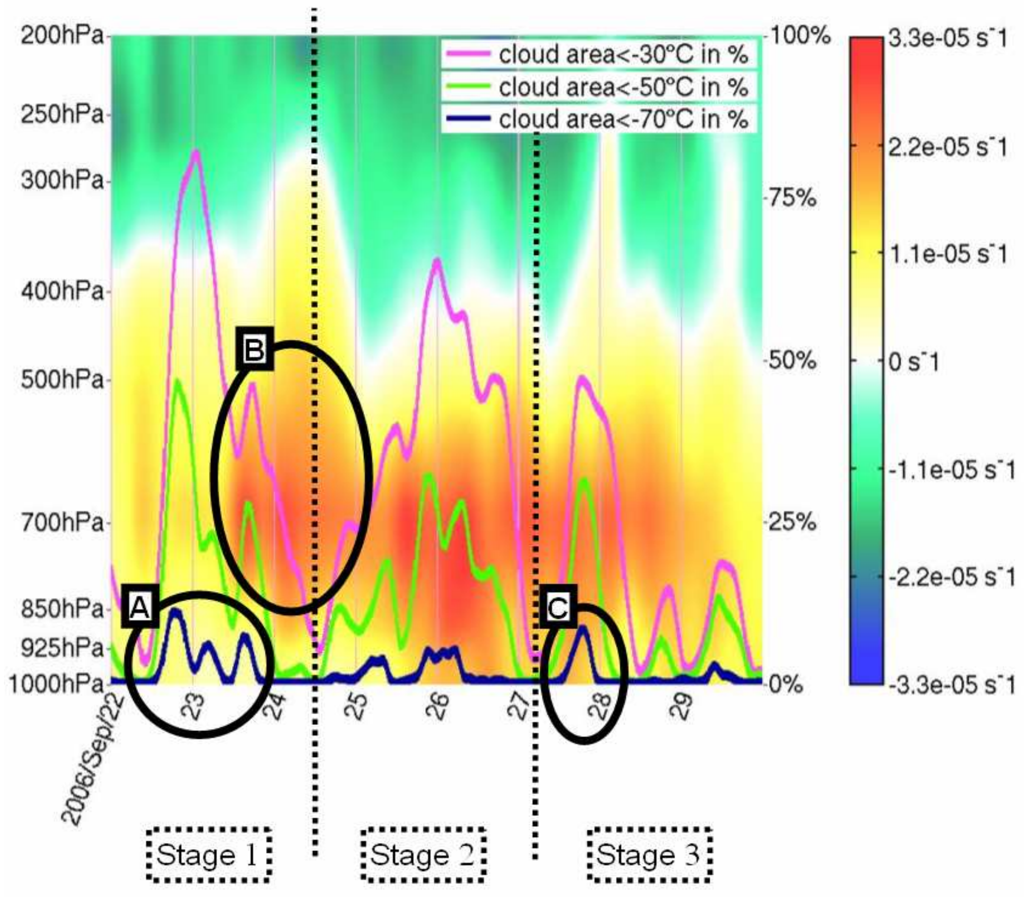

Figure 4 : *Composite image from Meteosat-9 and ECMWF data showing the evolution of several quantities computed in the 6°x6° domain of "Perturbation D" (see pink squares in Fig. 3) between pressure levels 200 and 1000 hPa. The color contours represent the evolution of the vertical profiles of relative vertical vorticity. The pink, green and blue lines denote the evolution of cloud areas colder than -30°C, -50°C and -70°C, respectively. The X axis gives the time in days for the period 22-29 September 2006. The left Y axis corresponds to the pressure levels of the vertical profiles of vertical vorticity, the right Y axis indicates the percentage of the cloudy area in the 6°x6° domain. The colored bar in the ri ght side gives the scale for the relative vertical vorticity. The two vertical dashed black lines delineate the three stages of the "Perturbation D" and the three black ellipses A, B and C enclose features which are discussed in the text.*

26 September), III : decay over the ocean (27-29 September). As seen in Fig. 4, these three stages correspond to oscillations of the cloud area colder than -30°C (pink curve in Fig. 4). The onset of the disturbance and stage I started with surges of intense convection on the evening of 22 and during the 23 September (see black ellipse A in Fig. 4). This was followed by an enhancement of the relative vertical vorticity in the middle atmosphere (see black ellipse B in Fig. 4) which indicates that the growth of the synoptic wave was influenced by convective processes. The deep convective surges actually dissipated on 24 September, but the vorticity disturbance remained visible during the next five days. Stage II is related to the crossing of the mountainous coastal area of Futa Jallon near the Guinea coast. It is characterized by a weaker convective activity and a decreasing altitude of the vorticity disturbance. Actually one weak convective re-development occurred over the Futa Jallon mountains on the 25th

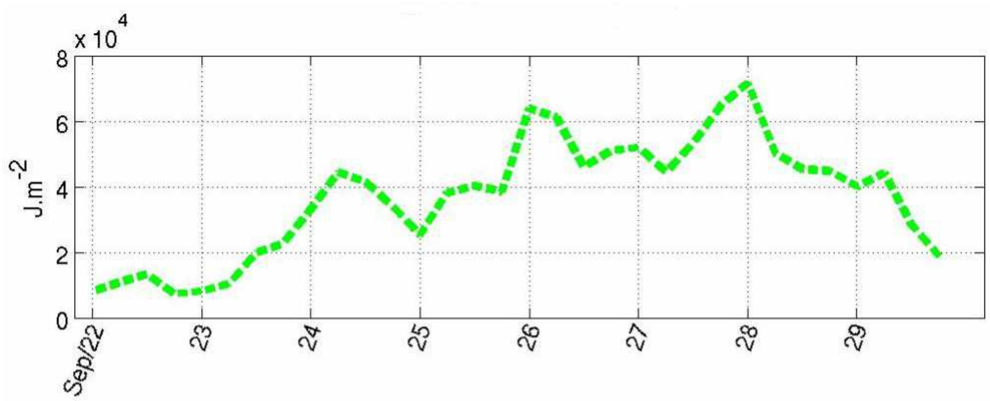

Figure 5 : *Time evolution of K_{eddy} (green dashed line) and A_{eddy} (red dash-dot line) computed in the 6°x6° domain enclosing the "Perturbation D" (see pink squares in Fig 3), between the pressure levels 200 and 1000 hPa, and for the period 22-29 September 2006. The X axis refers to the time in days and the Y axis gives the energy in Jm^{-2}.*

morning, followed by a convective burst over the ocean in the afternoon, which quickly dissipated on the 26th (see Fig. 2a, b and c). "Perturbation D" was dissipating in the beginning of the Stage III when a last MCS rapidly grew up off the Senegal coast on the afternoon of 27th (see black ellipse C in Fig. 4), which probably helped to maintain a mid-tropospheric vorticity maximum.

These two composite analyses help to understand the synoptic and convective processes involved in the evolution of "Perturbation D". Monsoon surges over West Africa lead to the formation of MCSs with several genesis and decay phases. These relatively short-lived systems generated vertical vorticity anomalies in the middle atmosphere which combined at synoptic level in the AEW. This long-lived vorticity disturbance may then have helped to trigger convective re-developments over the Futa Jallon mountains and over the ocean between the West African coast and the Cape Verde Islands. Such oceanic convective re-development sometimes leads to a cyclogenesis event although this was not the case for "Perturbation D". In this case indeed, the dry Saharan air coming from northeast during Stage II and III enhanced the anti-cyclonic curvature of the wave, which moved "Perturbation D" northward. Therefore the oceanic convective re-development observed during Stage III was disconnected from the south-westerly monsoon flow, and no cyclogenesis could happen.

It must be outlined that the ECMWF and Meteosat-9 data used for these composite analyses do not simultaneously resolve the synoptic and convective processes. In consequence the scale interactions between the MCSs and the AEW cannot be studied precisely with the composite analyses presented in this section. Mesoscale numerical modelling is needed to obtain a more precise view of the processes involved in "Perturbation D".

5. GROWTH OF THE WAVE

The AEW associated with the "Perturbation D" is a synoptic process which seems to be partly controlled by convection. In order to complete the preliminary study started in section 4, the growth of the wave is investigated with ECMWF data. The role of convection in the growth of the synoptic wave will however be approximately estimated as the ECMWF model uses parameterized convection. The energy of the AEW is defined as the eddy kinetic energy (K_{eddy}) computed in the 6°x6° domain enclosing the disturbance (see pink squares in Fig. 3) between the pressure levels 200 and 1000 hPa. Fig. 5 shows the evolution of K_{eddy} from 22 to 29 September 2006. It is

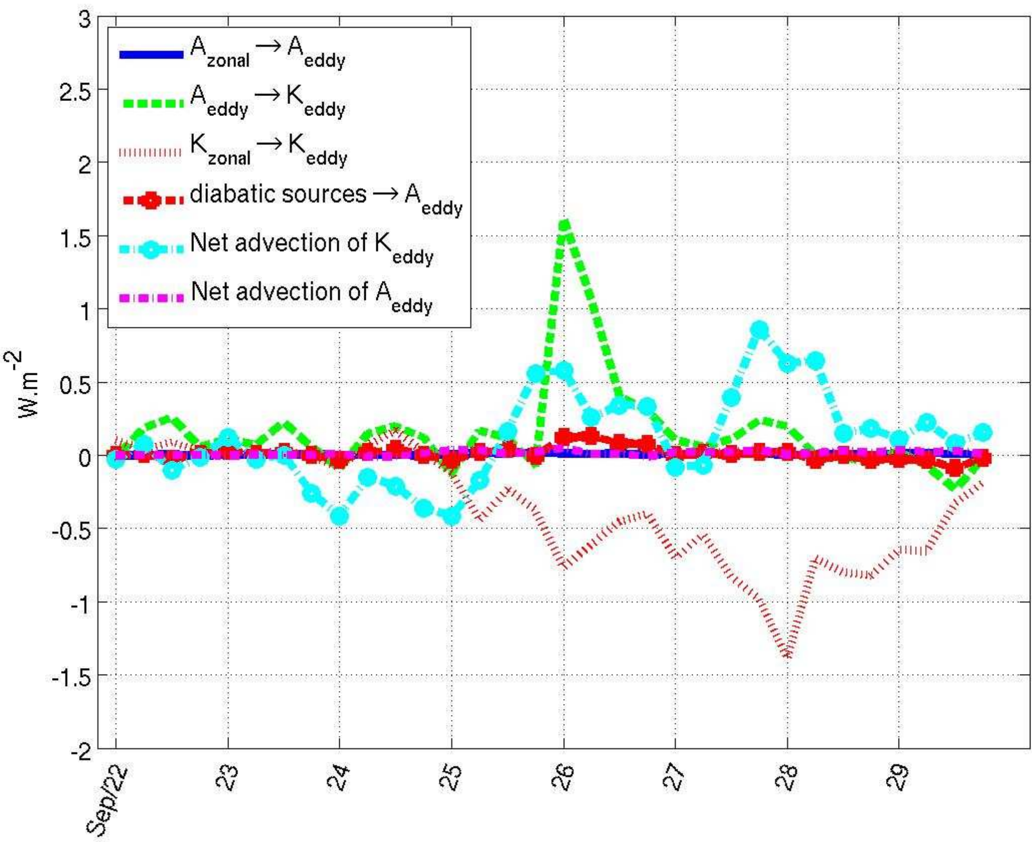

Figure 6 : *Time evolution of the four energy conversion rates ($K_{zonal}\rightarrow K_{eddy}$; $A_{zonal}\rightarrow A_{eddy}$; $A_{eddy}\rightarrow K_{eddy}$; eddy diabatic sources$\rightarrow K_{eddy}$) and of the net advection terms of K_{eddy} and A_{eddy} from ECMWF analyses in the 6°x6° domain enclosing the "Perturbation D" between the pressure levels 200 and 1000 hPa. The X axis refers to the time in days and the Y axis gives the energy tendencies in Wm^{-2}.*

remarkable that K_{eddy} increased by approximately a factor of four (from 1 x10^5 to 4x10^5 Jm^{-2}) during the two first days, which is coherent with the wave intensification on the 23rd deduced from Fig. 4. The wave energy continued to grow until the 27th night, when it reached a maximum value of 7x10^5 Jm^{-2}. This is also the time when the last convective burst of 'Perturbation D" occurred. The fast decrease of K_{eddy} from the 28th morning is in agreement with the dissipation of the disturbance.

There are four possible sources of energy to explain the growth of this wave energy: zonal kinetic energy (K_{zonal}), zonal available potential energy (A_{zonal}), eddy available potential energy (A_{eddy}) and energy released by latent heating in convection. Conversion of K_{zonal} to K_{eddy} is the "barotropic" mechanism. Conversion of A_{zonal} to A_{eddy} followed by conversion of A_{eddy} to K_{eddy} is the "baroclinic" mechanism. It has been hypothesized in the previous section that convection played a significant role in enhancing the wave disturbance, although barotropic and baroclinic mechanisms may also have a non-negligible contribution. The growth of wave energy is usually investigated with the system of equations originally proposed by Lorenz (1955), and firstly applied to AEWs by Norquist et al. (1977). The four energy conversion rates ($K_{zonal}\rightarrow K_{eddy}$; $A_{zonal}\rightarrow A_{eddy}$; $A_{eddy}\rightarrow K_{eddy}$; eddy diabatic energy source$\rightarrow K_{eddy}$) are computed in the 6°x6° domain enclosing "Perturbation D" between pressure levels 200 and 1000 hPa, to quantify the internal processes involved in the wave growth. The analytic expressions of the energy conversion rates can be found in Muench (1965) and Norquist et al. (1977). It must be noted that the energy of the wave can come

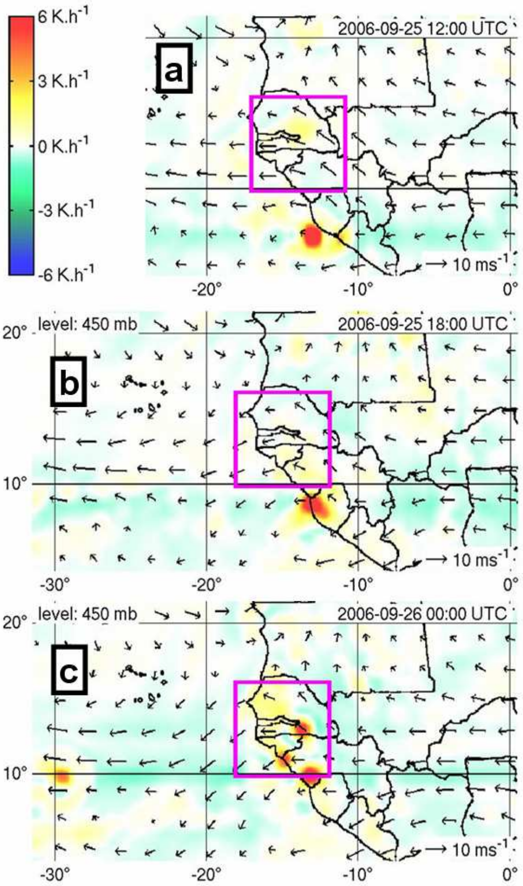

Figure 7 : *Horizontal cross-sections of eddy diabatic heating at 450 hPa derived from ECMWF analyses for the period from (a) 25 September 2006 at 12 UTC till (c) 26 September at 00 UTC. The 6°x6° pink squares corresp ond to the previously defined domain of "Perturbation D"*

from outside the considered domain, which is why we also computed the net advection terms of K_{eddy} and A_{eddy}.

The evolution of these different energy conversion terms is shown in Fig. 6 for the period 22-29 September 2006. The energy budget of Fig. 6 is approximately balanced, which does not allow to study small scale variations but only the main characteristics of the energy conversion and net advection rates. A striking feature in Fig. 6 is the peak of K_{eddy} production by A_{eddy} (dashed green line in Fig. 6) on the 26th when the disturbance crosses the Futa Jallon mountains. This is positively correlated with a smaller peak of A_{eddy} production by the eddy diabatic source of energy (dashed red line marked with plus signs in Fig. 6), which let suppose that convection played a role in the wave's growth at this time.

In order to further understand the processes that occurred in this region, horizontal fields of eddy diabatic heating at 450-hPa have been computed with ECMWF data (Fig. 7). The signature of a convective system growing in the oceanic Inter-Tropical Convergence Zone south of the West African coast is clearly identified on the 25th at 12 UTC (Fig. 7a). This convective system was then carried toward the continent by the south-westerly monsoon flow and it intensified over the Futa Jallon mountains during the afternoon (Fig. 7b). It finally entered the domain of "Perturbation D" on the 26th early morning (Fig. 7c), which explains the peak of A_{eddy} production by eddy diabatic sources observed at this time.
As seen in Fig. 6 (solid blue line), the conversion rate of A_{zonal} to A_{eddy} was negligible, which indicates that the barocline

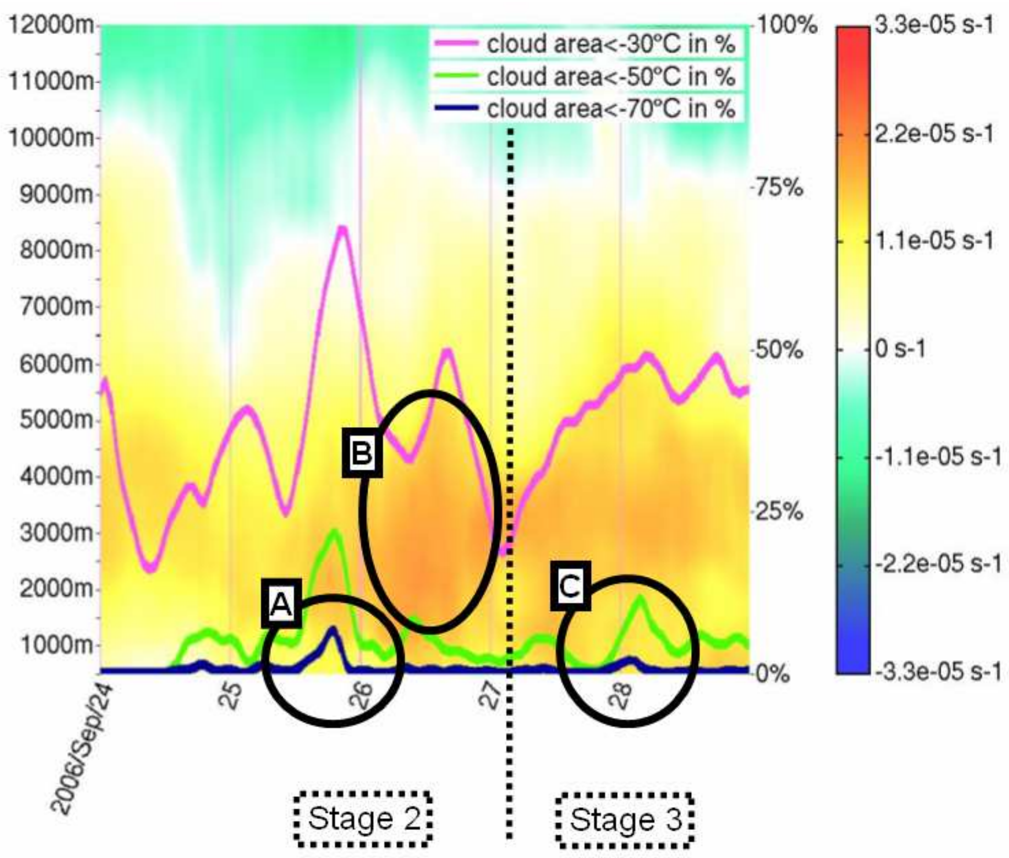

Figure 8 : *As in Fig. 4 except for Meso-NH model 2. The vertical dashed black line delineates the previously defined stages 2 and 3 of "Perturbation D", and the three black ellipses A, B and C enclose features which are discussed in the text.*

mechanism did not play an important role in the growth of the AEW associated with "Perturbation D". The advection of A_{eddy} (dashed magenta line in Fig 6) is also very small compared to the production of A_{eddy} by diabatic processes. Then it is noticeable that the conversion rate of K_{zonal} to K_{eddy} (dotted red line marked in Fig. 6) is negative on the 26^{th} morning, which means that wave energy was converted to zonal energy by an "inverse barotropic" mechanism. However the net advection of K_{eddy} (dash-dot cyan line marked with circles in Fig. 6) was positive on the 26^{th} morning and compensated the barotropic decay of the wave. On the 27^{th} afternoon there was a small peak in the conversion rate of A_{eddy} to K_{eddy}, and the conversion rate of eddy diabatic sources of energy to A_{eddy}, which was associated with the last convective burst of "perturbation D". There was also an intense "inverse barotropic" decay at that time, still compensated by a positive net advection of K_{eddy}. Finally the "inverse barotropic" decay became preponderant on the 28^{th}, with the "Perturbation D" releasing its energy to the mean zonal flow.

6. MESOSCALE MODELLING

The French non-hydrostatic mesoscale model Meso-NH has been used to simulate the evolution of "Perturbation D" at high temporal and spatial resolutions and, eventually, to resolve the interactions between the AEW and the MCSs. The simulation presented here has been conducted with two nested models of horizontal resolution 32 and 8 km for the period 24-29 September 2006. The

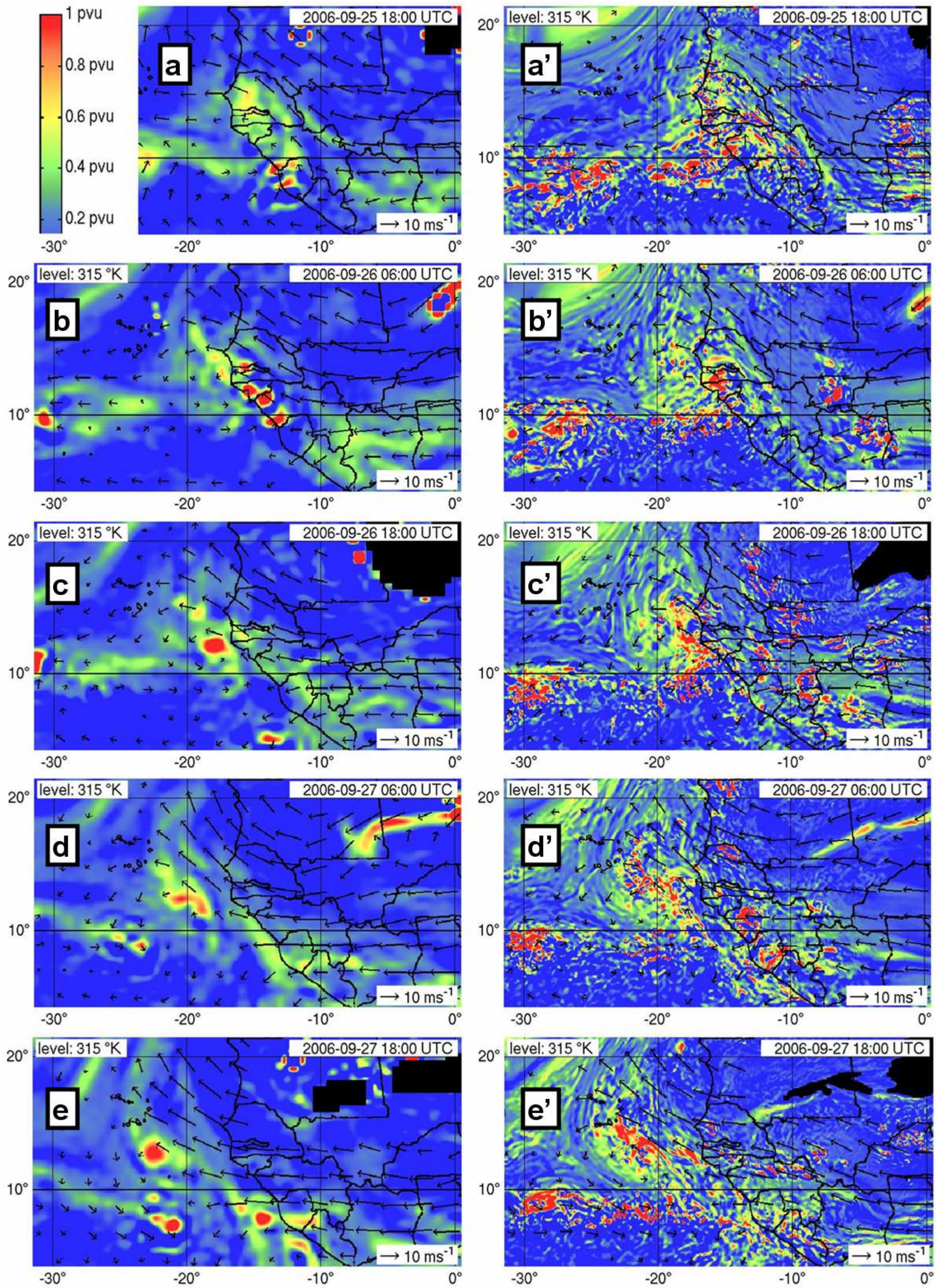

Figure 9 : *Horizontal cross sections of Ertel potential vorticity on the isentropic level 315 K from (a) 25 September 2006 at 18 UTC till (e) 27 September 2006 at 18 UTC. The images in the left column are from ECMWF fields, those on the right are from the Meso-NH model 2.*

outer domain (model 1) has 160 x 160 points and the inner model 2 has 432 x 240 points. The large scale model is coupled with ECMWF operational analyses at 00, 06, 12 and 18 UTC. The model outputs have been saved every hour. Convective parameterization has been activated for both models so that the scale interactions might still not be fully resolved by this numerical approach. It is however expected that the relatively high resolution of model 2 can provide more precise results. A third model with a resolution of 2km and explicit convection will be activated in a future work.

To evaluate the reliability of the numerical simulation, a composite analysis similar to that discussed in section 4 (Fig. 4) has been applied to the fields produced by Meso-NH model 2 (Fig. 8). The brightness temperature in the Meteosat-9 water vapour channel n°6 were calculated from the Meso-NH results using the RTTOV (Radiative Transfer for Tiros Operational Vertical Sounder) code - version 8.7 (Chaboureau *et al.* 2000). As this Meso-NH simulation starts on 24 September 2006 at 00 UTC, the series of initial convective surges and the resulting vorticity enhancement on 23 and 24 September displayed in Fig 4 do not appear in Fig 8. Nevertheless, the simulated area colder than -30°C (pink curve in Fig.8) allows to identify stages II and III of "Perturbation D" relatively similar to those in Fig. 4. In particular, Meso-NH simulates a deep convective event on the 25th afternoon (see the black ellipse A of Fig. 8) which was observed in Meteosat-9 images a few hours later (see Fig. 4). This convective event is then followed by an enhancement of vorticity in the mid-troposphere (see the black ellipse B of Fig. 8) though less intense than in ECMWF data (see Fig. 4). The last convective event on the 27th afternoon (see the black ellipse C of Fig. 4) has been caught by the Meso-NH simulation, though a few hours later and with a weaker intensity (see the black ellipse C of Fig. 8). We can therefore conclude that the Meso-NH simulation is not in contradiction with the observed evolution.

In order to evaluate qualitatively the finer scale structure brought by the Meso-NH model 2 at 8 km horizontal resolution, the Ertel potential vorticity (EPV) on the 315 K isentrope level, where the AEWs have their maximal activity, is displayed. Berry and Thorncroft (2005) also used this quantity to study the pre-Alberto disturbances over the African continent. The accuracy of the EPV to study the scale interaction between convection and the synoptic processes is justified by the fact that this is a conservative quantity for adiabatic processes. However, latent heating associated with convective systems creates EPV which can then be "recycled" by the synoptic AEW. EPV fields at 315 K from ECMWF data and from Meso-NH model 2 are shown in Fig. 9. Whereas the EPV signature of "Perturbation D" in ECMWF data is only a single maximum, Meso-NH model 2 reveals finer scale structures of convective origin. These small vortices are preferentially created during the late afternoon in connexion with the diurnal cycle of convection. This process was particularly intense on the 25th at 18 UTC when "Perturbation D" was over the Futa Jallon mountains (Fig 9a'). These convective and orographically induced small scale vortices partly merged over the ocean, then strengthened the disturbance. These results at higher resolution confirm the role of convection in the growth of the wave although modelling with explicit convection is needed for a more quantitative study.

We also calculated the energy conversion rates and net advection terms in the 6°x6° domain of "Perturbation D" with the fields from Meso-NH model 2 (Fig. 10). A comparison with Fig. 6 allows to more quantitatively evaluate those results. The energy budget of Fig. 10 is approximately balanced, which does not allow to study small scale variations but only the main characteristics of the energy conversion and net advection rates. The most striking feature in Fig. 10 is the positive correlation between the K_{eddy} production by A_{eddy} (dashed green line in Fig. 10) and the A_{eddy} production by the eddy diabatic source of energy (dashed red line in Fig. 10) during all the simulation period, with two maxima on 24th and 25th afternoon. It is also noticeable that peaks of barotropic conversion occur at the same times (see dotted red line in Fig. 10). Then, the evolution of the barotropic term from the 26th shows an "inverse barotropic" decay which becomes preponderant after the 28th, in agreement with previous results from the ECMWF

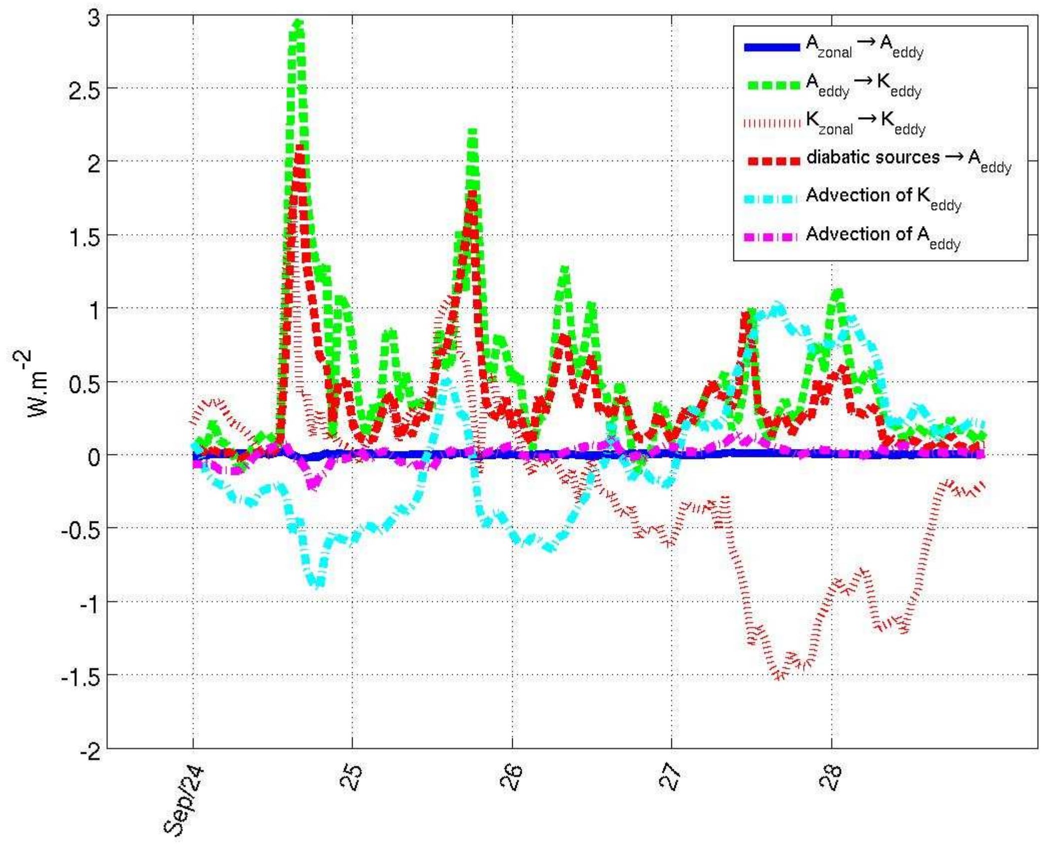

Figure 10: *As in Fig 6 except for the Meso-NH model 2*

.

fields. Three maxima of A_{eddy} production by the eddy diabatic source of energy occur on the 26th morning, the 27th noon and night, the last one corresponding to the final convective burst associated with "Perturbation D" (see green curve in Fig. 8 and dashed red curve in Fig. 10). The shape and intensity of the net advection term of K_{eddy} (dashed green curve in Fig. 10) is comparable with the ECMWF results (see dashed green curve in Fig. 6). The production of A_{eddy} by A_{zonal} (solid blue line in Fig. 10) and the net advection term of A_{eddy} (dashed magenta line in Fig. 10) are also negligible. In conclusion the results from Meso-NH model 2 confirmed the important role played by convection in the growth of the wave associated with "Perturbation D". It also revealed that barotropic mechanism contributed to this growth during the period it crossed the West African coast.

7. PERSPECTIVES

The results derived from Meteosat-9 images, ECMWF analyses and Meso-NH numerical simulations for "Perturbation D" observed during AMMA SOP-3 in September 2006 confirm previous findings on the complex interactions between convection and African Easterly Waves at meso- and synoptic scales (e.g. Berry and Thorncroft 2005). Further information will be obtained on the role played by convection through the analysis of Meso-NH model 3 results at 2 km horizontal resolution. We also plan to compare this situation with those associated with the pre-cyclogenesis phases of Tropical Storm Debby (15-20 August 2006), Hurricane Helen (5-10 September 2006) and Hurricane Dean (5-10 August 2007).

BIBLIOGRAPHY

Berry, G. and C. Thorncroft, 2005: Case study of an intense African easterly wave, *Mon. Wea. Rev.*, **133**, 752-766

——-—, ——-— and T. Hewson; 2006: African easterly waves during 2004 – analysis using objective techniques, *Mon. Wea. Rev.*, **135**, 1251-1267.

Burpee, R. W., 1972: The origin and structure of easterly waves in the lower troposphere of North Africa, *J. Atmos. Sci.*, **29**, 77-90.

Carlson, T. B., 1969a: Synoptic histories of three African disturbances that developed into Atlantic hurricanes, *Mon. Wea. Rev.*, **97**, 256-288.

——-—, 1969b: Some remarks on African disturbances and their progress over the tropical Atlantic, *Mon. Wea. Rev.*, **97**, 716-726.

Chaboureau, J.-P., J.-P. Cammas, P. Mascart, J.-P. Pinty, C. Claud, R. Roca, and J.-J. Morcrette, 2000: Evaluation of a cloud life-cycle simulated by Meso-NH during FASTEX using METEOSAT radiances and TOVS-31 cloud retrievals. *Quart. J. Roy. Meteor. Soc.*, **126**, 1735-1750.

Hill, C., M., and Y.-L. Lin, 2003: Initiation of a mesoscale convective complex over the Ethiopian Highlands preceding the genesis of Hurricane Alberto (2000). *Geophys. Res. Lett*, **30**, 1232, doi:10.1029/2002GL016655.

Lin, Y.-L., K. E. Robertson, and C. M. Hill, 2005: Origin and propagation associated with an African easterly wave as a precursor of hurricane Alberto (2000). *Mon. Wea. Rev*., **133**, 3276-3298.

Lorenz, E. N., 1955: Available potential energy and the maintenance of the general circulation. *Tellus*, **7**, 157-167.

Mathon V., and H. Laurent, 2000: Life cycle of sahelian mesoscale convective cloud systems. *Q. J. Meteorol. Soc.*, **127**, 377-406.

Muench, H. S., 1965: On the dynamic of the wintertime stratospheric circulation, *J. Atmos. Sci.*, **22**, 349-360.

Norquist D. C., E. E. Recker and R. J. Reed, 1977: The energetics of African wave disturbances as observed during phase III of GATE, *Mon. Wea. Rev.*, **105**, 334-342.

Thorncroft, C. D., and K. I. Hodges, 2001: African easterly wave variability and its relationship to Atlantic tropical cyclone activity. *J. Climate*., **14**, 1166-1179.

ACKNOWLEDGEMENTS

The AMMA SOP-3 field campaign was funded by CNES (French space agency). Pilots and technical crews of the Falcon must be thanked for their cooperation and dedication. Numerical simulations were conducted on CNRS / IDRIS computer under grants 070591 and 080591. We thank Didier Gazin and Juan Escobar for the technical support in Meso-NH, Dr. Jean-Pierre Chaboureau for the scientific support in Meso-NH.

PRECIPITATING CONVECTIVE REGIMES IN DARWIN (AUSTRALIA) AND THEIR SIMULATION USING THE WRF MODEL.

Simon Caine[1], Christian Jakob[1], Steven Siems[1], Peter May[2]

[1]Monash University, Melbourne, Australia
[2]Bureau of Meteorology Research Centre, Melbourne, Australia

1. PRECIPITATION REGIMES

A clustering algorithm (Anderberg 1973) was applied to Frequency with Altitude Diagrams (FAD's) (Yuter and Houze 1995) derived from four years of hourly radar data to objectively define four tropical precipitation regimes that occur during the wet season over Darwin, Australia, Figure 1. The order of the panels in this figure is in terms of the relative frequency of occurrence (RFO) of each regime, which is shown in the top left-hand corner of each panel. A fifth regime with no-precipitation also exists but due to its trivial nature is not plotted. However for completeness the RFO of this regime is displayed on the right hand side of each panel.

The precipitation regimes defined are distinguished in terms of convective intensity, presence of stratiform precipitation and precipitation coverage. Regime 1 consists of patchy convection of medium intensity and low area coverage. Regime 2 contains strong convection with relatively small area coverage. Regime 3 is comprised of weak convection with large area coverage and large stratiform regions and regime 4 contains strong convection with large area coverage and large stratiform regions. Analysis of the seasonal cycle, diurnal cycle and regime occurrence as a function of monsoon activity indicate that regimes 1 and 2 are characteristic of continental convection, while regimes 3 and 4 are characteristic of maritime convection.

Further confirmation of the different character of the regimes is derived by evaluating the convective and stratiform contributions to rainfall for each regime. Regime 1 is comprised of 76% convective precipitation, 24% stratiform precipitation and has a total volume coverage (TVC) of 2% (A TVC value of 2% means that 2% of the volume scanned by the radar contains detectable hydrometeors). Regime 2 is comprised of 65% convective precipitation, 35% stratiform precipitation and has a TVC of 10%. Regime 3 is comprised of 36% convection precipitation, 64% stratiform and has a TVC of 18%. Regime 4 is comprised of approximately equal contributions from stratiform and convective precipitation and has a TVC value of 26%.

2. MODEL SIMULATIONS

With the physical nature of each regime clearly established the Weather Researching and Forecasting model (WRF) was employed to determine if the model is able to capture the broad characteristics of the four precipitation regimes. The WRF model was run using a series of nested domains, the inner most domain having a grid spacing of approximately 1.25 km in each horizontal direction.

To compare model simulations directly to the FADS derived from radar, model microphysical data was converted to simulated radar reflectivities. The simulated radar reflectivities were then interpolated to the same vertical levels and averaged horizontally to match the resolution of the radar data (2.5km in each horizontal direction). With the simulated reflectivities in approximately the same format as the radar observations FADS were created for each hour of the model simulation. These FADs were then assigned to one of the precipitation regimes by finding the minimum euclidian distance of the simulated FAD to the observed regime centroids.

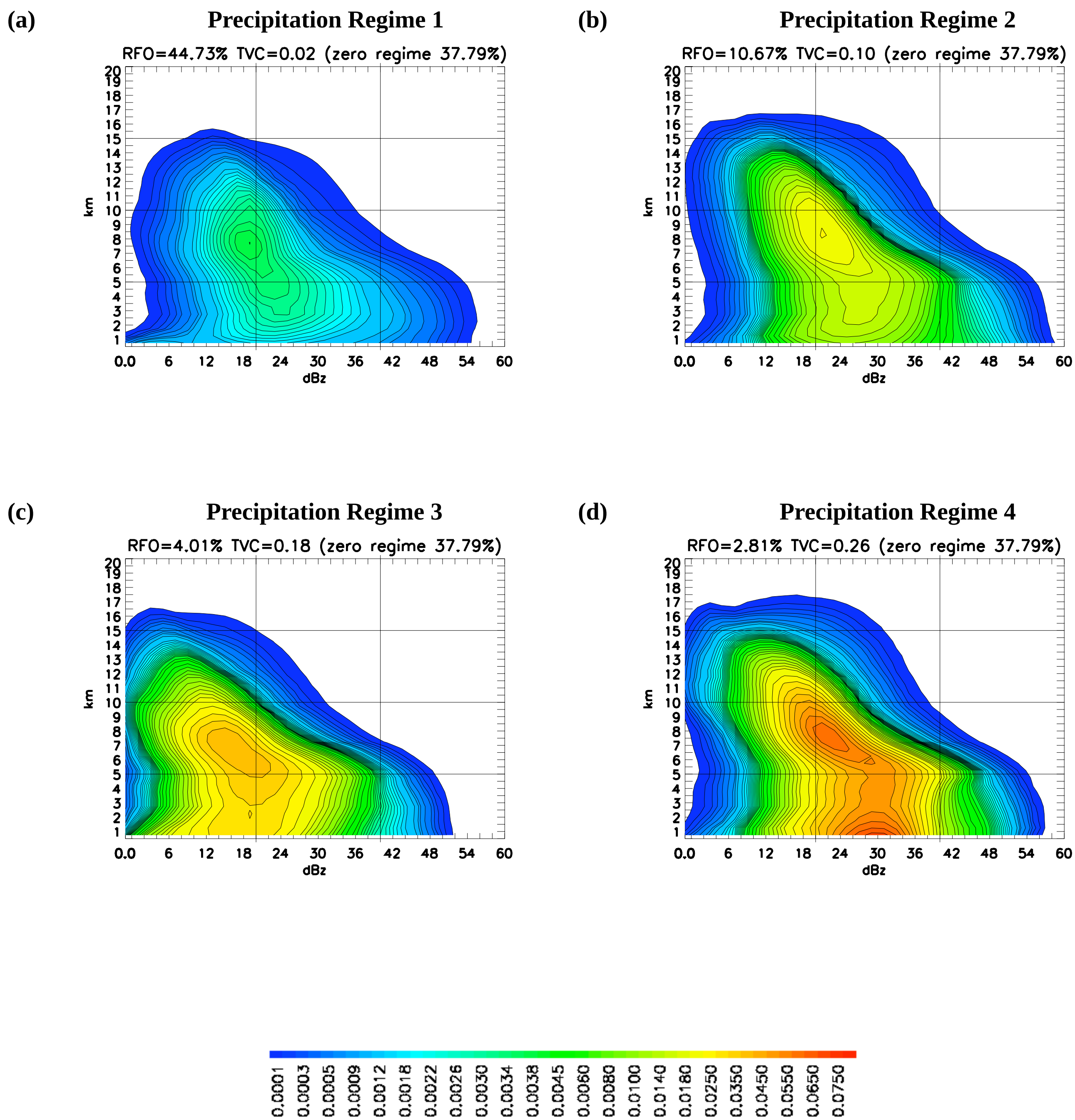

Figure 1: **The four precipitation regimes defined by the K-means algorithm. Regimes are ordered (most to least) by their relative frequency of occurrence (RFO). The RFO of the "zeroth" regime, the regime containing time periods that have no precipitation over the entire radar domain, is shown for completeness.**

To evaluate all four precipitation regimes two case studies were performed to capture the broad range of meteorological conditions encountered in the Darwin region. These case studies were chosen to coincide with the Tropical Warm Pool International Cloud Experiment (TWP-ICE) (May et al. 2008) so that the extensive observational data set could be used for further model evaluation.

Over the course of the TWP-ICE field campaign Darwin experienced a variety of meteorological conditions ranging from monsoon conditions during the early part of the experiment to break conditions during the latter. A six day monsoon simulation starting at 12 UTC on the 24/01/2006 was used to evaluate the WRF's models ability to replicate regimes 3 and 4, and a six day break simulation started at 12 UTC on the 09/02/2006 was used to evaluate the models ability to replicate regimes 1 and 2.

2.1. MONSOON SIMULATION

The WRF model roughly captured the temporal pattern of regime change during the monsoon simulation, Figure 2 (a). The model was not able to capture the high frequency changes between precipitation regimes but was able to roughly capture the low frequency component. When the simulated regimes did not agree with the radar the simulated FADS were generally assigned to a higher precipitation regime. The model was rarely found in regime 1 and stayed in regime 4 longer than the radar. The WRF model may have a problem with suppressing convection once it has been initiated, however at this stage this has not been fully investigated.

2.2. BREAK SIMULATION

The break simulation was unable to capture the change in regimes as seen by the radar. Precipitation was underestimated during the break simulation with the model regimes rarely changing from regime 1. A problem with the break simulation that could lead to the underestimation of precipitation is that the model was unable to simulate a number of squall lines that were seen in the observational data. This is likely due to the fact that the squall lines are not being generated in the outer domains where convective parametizion is required.

(a) **Monsoon Simulation**

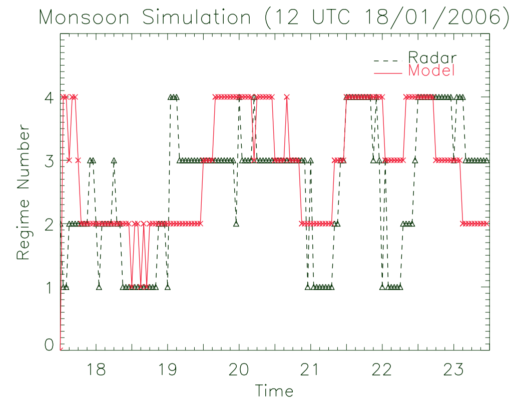

(b) **Break Simulation**

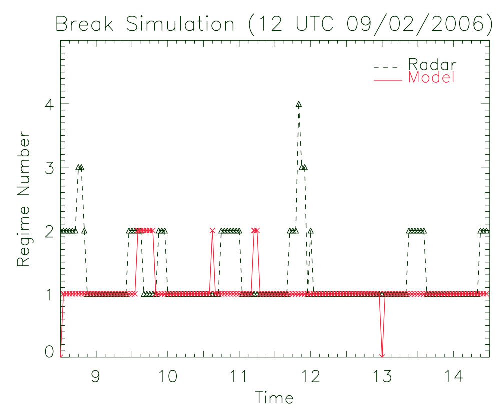

Figure 2: **Temporal evolution of precipitation regimes for both model and radar. (a) Monsoon period. (b) Break period.**

REFERENCES

Anderberg, M. R., 1973: *Cluster Analysis for Applications*. Academic Press, 359 pp.

May, P. T., J. H. Mather, G. Vaughan, C. Jakob, G. M. McFaquhar, K. Bower, and G. G. Mace, 2008: The Tropical Warm Pool International Cloud Experiment (TWP-ICE). *Bull. Amer. Meteor. Soc*, in press.

Yuter, S. E. and R. A. Houze, Jr., 1995: Three-Dimensional Kinematic and Microphysical Evolution of Florida Cumulonimbus. Part II: Frequency Distributions of Vertical Velocity, Reflectivity, and Differential Reflectivity. *Mon. Wea. Rev.*, **123**, 1941–1963.

Field determination of the masses and mass fluxes of ice and liquid water in thunderclouds, from lightning measurements

W. Deierling *[1)], W. A. Petersen [2)] , J. Latham [1)] , S. M. Ellis [1)] and H. J. Christian Jr. [3)]

[1)] National Center for Atmospheric Research, Boulder, Colorado
[2)] Earth System Science Center, University of Alabama, Huntsville, Alabama
[4)] Global Hydrology & Climate Center, NSSTC, Huntsville, Alabama

1. INTRODUCTION

In general a strong updraft in the mixed phase region is needed to produce lightning. This is the region where the non-inductive charging mechanism (Reynolds et al., 1957; Takahashi, 1978; Saunders et al., 1991; Saunders 1993) is generally believed to generate most of the thunderstorm electrification. This mechanism involves rebounding collisions between graupel and ice crystals in the presence of supercooled liquid water. The charge transfer per collision depends on size of the ice crystals and the fall-speed of the graupel pellets, while the sign of the charging depends on temperature and the liquid water content. Significant charging occurs where graupel, ice crystals and supercooled droplets co-exist. This region is referred to as the charging zone. Its vertical extent is limited (Latham et al., 2004), and its boundaries are somewhat diffuse. The upper limit is usually the level above which graupel can no longer be supported by the updraft, typically between the -15°C and -30°C isotherms, and therefore increases with increasing updraft speed, w. Most of the charging that is crucial to lightning production occurs just beneath this upper limit height, principally because the charge transfer per collision increases rapidly with crystal size. The level of the lower boundary is dependent upon the prevailing glaciation mechanism, but can characteristically be taken as a few degrees colder than 0°C.

Based on these ideas, analytical calculations by Blyth et al. (2001), Latham et al. (2004) and Petersen and Rutledge (2001) yielded the prediction that the lightning frequency f was roughly proportional to the product of the downward flux p of solid precipitation (graupel) and the upward mass-flux I of ice crystals, the values of p and I being those existing at the top of the charging zone. Hereafter this will be referred to as the flux hypothesis. The predicted equation valid in the charging zone that describes the flux hypothesis is:

$$f = C \cdot p \cdot I,$$

where C is a constant.

Support for the flux hypothesis was provided by computations made with multiple lightning activity models by Baker et al. (1995) and Baker et al. (1999). These initial investigations show promising results for the predicted relationship between total lighting activity and the product of the upward ice flux and the downward precipitation ice flux. Nevertheless, the predicted relationship is lacking more definite support from field data which will be investigated in this study. Additionally this study investigates observational evidence of the hypothesis that total lightning may be used in conjunction with radar data to indicate the degree to which ice water content contributes to surface rainfall.

To examine the relationship of total lightning activity as a function of precipitation and non precipitation ice mass as well as estimates of their fluxes, polarimetric radar data was used to identify bulk microphysical hydrometeor types (Straka et al. 2000; Vivekanandan et al. 1999), and mass contents of various particles (Straka et al. 2000). It has to be kept in mind that radar measurements are dominated by the largest particles in a given radar volume thus smaller ice crystals in the charging zone will go undetected. To compute flux estimates, three dimensional wind fields were calculated from dual Doppler radar data. In one case radar data from only one radar was available. Here a three dimensional wind field was determined using the National Center for Atmospheric Science's (NCAR's) Variational Doppler Radar Assimilation System (VDRAS) (Sun and Crook, 1997; Sun and Crook, 2001; Crook and Sun, 2004).

To examine if total lightning data can be used to estimate the fractions of liquid water content in convective rainfall that originates from both the cold and the warm rain process, the polarimetric radar data are used to compute rainfall amounts, and to partition ice and liquid water mass on storm scales.

*Corresponding author address: Wiebke Deierling, NCAR/ASP, P.O. Box 3000, Boulder, CO 80301; email: deierlin@ucar.edu

This study uses data from 11 different thunderstorms, which are of different type and originated in two different climate regions of the United States: the High Plains and Northern Alabama. The High Plains data includes data from the Severe Thunderstorm Electrification and Precipitation Study (STEPS) project which took place at the Colorado/Kansas border in the summer of 2000 and from the Stratospheric-Tropospheric Experiment: Radiation, Aerosols and Ozone (STERAO) experiment that took place in the summer of 1996 in Northern Colorado. In Northern Alabama the University of Alabama Huntsville/National Space Science and Technology Center (UAH/NSSTC) ARMOR radar (Petersen et al. 2005) was used with a nearby WSR-88D (Weather Surveillance Radar-1988 Doppler) radar which allows dual Doppler synthesis to be performed under the coverage umbrella of the N. Alabama lightning mapping array (LMA). During STERAO polarimetric radar data were collected from the Colorado State University (CSU)-CHILL radar and total lightning activity was recorded by the Office Nationale d'Etudes et de Recherches Aerospatiales (ONERA) 3-D lightning interferometer as well as cloud-to-ground lightning by the National Lightning Detection Network (NLDN). These data were used to study the lifecycle of a severe storm observed on 10 July 1996 that exhibited multicellular and later in its lifetime supercellular character. During STEPS, polarimetric radar data were collected from the CSU-CHILL radar as well as from the National Center for Atmospheric Research S-band dual-polarimetric Doppler weather radar (S-POL). Total lighting activity was recorded by the New Mexico Institute of Mining and Technology (NMIMT) deployable LMA.

2. METHOD

First the methodology of computing ice masses and their fluxes will be described followed by a description of the computations if liquid water contents and rainfall estimates of the storms that are investigated herein.

To determine bulk hydrometeor types within thunderstorms from polarimetric radar data, the NCAR particle identification algorithm (PID) (Vivekanandan 1999) was applied. It determines bulk hydrometeor types in radar space and is based on a fuzzy logic algorithm which uses nine input variables: the radar reflectivity, the differential reflectivity, the linear depolarization ratio, the correlation coefficient, the specific differential phase, a temperature profile, the standard deviation of velocity, the standard deviation of differential reflectivity and the standard deviation of the differential phase to distinguish between 17 output categories. Those are: cloud droplets, drizzle, light rain, moderate rain, heavy rain, hail, hail/rain mix, graupel/small hail, graupel/small hail/rain mix, dry snow, wet snow, irregular ice crystals, horizontal oriented ice crystals, super cooled liquid drops, insects, second trip, and ground clutter. It can be seen that 14 of these categories are hydrometeor related. To relate the microphysics data to a 3D wind field on a Cartesian grid the PID output, temperature and reflectivity were gridded with the NCAR/EOL software package REORDER using a closest point weighting scheme. Due to microphysical reasons as well as similarities between hydrometeor classifications, two or more particle types were in some cases added together. In this study the hail, hail/rain mix, graupel/small hail and graupel/small hail/rain mix PID categories above the height of the -5°C level were taken to represent precipitation ice in the charging zone over individual radar volumes. The ice crystals are not detected in the updraft region by the radar due to the presence of the larger particles. Therefore as an estimate for non precipitation ice these categories colder than -5°C and with a divergence larger than 0.001 s^{-1} and reflectivity values below 20 dBZ were chosen as a proxy for non precipitation ice mass from the charging zone (Deierling et al. 2007). This non-precipitation ice mass estimate will be referred to as NPIM_DIV in the following.

Using the divergence to identify non precipitation ice coming from the updraft originates from the assumption that the continuity equation is satisfied in the anelastic form:

$$\nabla_H \ \rho_0 V = \partial (w \rho_0) \setminus \partial z,$$

where ρ_0 is the base state density and is a function of height only, w is the vertical velocity and V is the horizontal velocity. One can see that the horizontal mass divergence (left side) is equal to the change of vertical mass flux with height (right side), assuming also that w = 0 m/s at the top of the thunderstorm and at the surface. Thus at a given level, an increase in w with height is expected to be accompanied by horizontal convergence, a decrease in w with height by horizontal divergence. This leads to the assumption of low level mass convergence below the maximum in w and upper level mass divergence above the maximum in w (e.g. Witt and Nelson, 1991; Yuter and Houze, 1995). The assumption here is that the upper level horizontal divergence above a threshold can be used to approximate non precipitation ice out of the updraft. The divergence was calculated using 3D winds from either the dual Doppler synthesis or VDRAS.

Precipitation ice and non precipitation ice mass contents were computed using reflectivity (Z) – mass content (M) relationships of the kind $M = aZ^b$ from the literature that appear to represent adequately different thunderstorm ice types. Note that mass contents using various relationships for an individual particle type were compared and it was found that though values varied in magnitude, computed total mass trends were not modified greatly. The Z-M relationships used for hail, graupel and thunderstorm anvil ice are given in Table 1. The reflectivity factor Z is multiplied by a factor of 5.28 (Sassen, 1987) to account for the lower dielectric constant for ice.

Hydro-meteor categories	**NCAR PID categories**	**Z-M relation-ship [g/m^3]**	**Reference**
Non precip ice	Dry snow, Oriented ice, Irregular ice	$M = 0.017 * Z^{0.529}$	Heymsfield and Palmer, 1986
Graupel	Graupel, Graupel/rain mixture	$M = 0.0052 * Z^{0.5}$	Heymsfield and Miller, 1988
Hail	Hail, Hail/rain mixture	$M = 0.000044 * Z^{0.71}$	Heymsfield and Miller, 1988

Table 1. M-Z relationships for various hydrometeor types .

For each of the PID categories listed in Table 1, ice mass contents for individual grid points were calculated, multiplied by their volume and then summed over the radar volume. The center time of a volume scan was assigned to the volume.

During STEPS the S-Pol and CHILL radars were positioned to allow dual Doppler synthesis. For the Huntsville, Alabama area, the ARMOR radar together with the Hytop WSR-88D radar allow dual Doppler synthesis and for STERAO, VDRAS was used to determine horizontal divergence and three dimensional wind fields. For the dual Doppler synthesis, first radar velocities were unfolded manually using the NCAR software soloii. Contamination such as second trip and ground clutter were removed using the PID information.

For the C-band ARMOR radar, the reflectivity and the differential reflectivity were corrected for attenuation and specific attenuation respectively using locally modified software from the BMRC C-pol radar (developed by V.N. Bringi at CSU and shared by T. Keenan, BMRC) that uses a FIR/adaptive spatial filter approach to compute differential and specific differential phase. Second, the NCAR Reorder software was used to interpolate the radar data from radar space onto a Cartesian grid. A Cressman filter weighting function was used for the conversion. Finally the NCAR Custom Editing and Display of Reduced Information in Cartesian Space (CEDRIC) software was used to determine a three dimensional wind field (u,v as the horizontal wind components and w as the vertical wind component). Vertical wind velocities were determined with three separate methods: integrating the mass continuity equation upward, downward and variationally. The calculations take the hydrometeor terminal fall speeds into account. Thus vertical velocities w were determined as the difference between the measured vertical velocities W from the solution of the mass continuity equation and a bulk estimate of the fall speed of precipitation particles v_t: $w = W - v_t$ (Rogers and Tripp, 1964).

To compute estimates of the non-precipitation ice mass flux *(F_i)*, NPIM_DIV was multiplied by the horizontal divergence in each grid and then summed over the storm volume. Similarly, precipitation ice mass fluxes were calculated at each grid point multiplying the precipitation ice mass with calculated particle fall speeds and computing the sum over the storm volume. Now flux products of non-precipitation and precipitation ice mass fluxes could be computed.

To investigate the relationship between ice mass, liquid water mass, convective rainfall amounts, and total lightning activity the polarimetric radar data were used to first partition ice and liquid water on storm scales using the NCAR PID. Rain rates were computed on the lowest elevation scans using a blended rain rate retrieval algorithm of polarimetric radar variables – rainfall relationships following Bringi and Chandrasekar, 2001 and Dolan and Rutledge, 2007. Similarly a blended algorithm was used to compute liquid water contents from polarimetric radar data following relationships for S and C-band polarimetric radar variables and liquid water mass stated in Bringi and Chandrasekar (2001). Precipitation ice masses were computed as described above.

3. RESULTS

First, in order to test the flux hypothesis, the total mass and mass fluxes of both precipitation and non-precipitation ice within the charging zone were compared with total lightning frequency on an individual storm scale for markedly different convective regimes. Six thunderstorms from the Colorado/Kansas High Plains and five from Northern Alabama were analyzed. Storm types include ordinary single cell, multicell and supercell thunderstorms. Ice mass and ice mass flux estimates were compared to total lightning activity for all investigated thunderstorms together. For all quantified relationships between ice masses and ice mass fluxes and total lightning activity only data points that were accompanied by lightning activity were included in the analysis.

Then, the relationship between ice mass, liquid water mass and rainfall estimates was evaluated.

It is important to note that the radar and lightning measurements have different temporal and spatial resolutions. The lightning measurements used herein have a very high spatial (a few hundred meters) and temporal (order of μs) resolution. Lightning also is a countable discrete quantity. In contrast, radar measurements have a lower spatial (a few hundred meters to kilometers) and temporal resolution (order of several minutes). Radar volume scans are comprised of time integrated spatial “snapshots” from parts of thunderstorms. They give a measure of the “mean” ice mass/ice mass flux over a radar volume time (duration of four to seven minutes). To match the radar and lightning time scales the mean number of total lightning flashes per minute averaged over the radar volume time was computed. This is referred to as mean total lightning in the following.

3.1 CORRELATION BETWEEN ICE MASS FLUX PRODUCT AND TOTAL LIGHTNING

The flux hypothesis predicts a linear relationship between total lightning and ice masses as well as their fluxes. Figure 1 shows a scatter plot of mean total lightning versus the product of precipitation ice mass flux and non-precipitation ice mass flux estimate above the -5°C level with units of $kg^2 \cdot m \cdot s^{-1}$ for individual radar volumes on a logarithmic scale. As predicted in Blyth et al. [2001], the linear fit represents best the relationship between the ice mass flux product and total amount of lightning with a correlation coefficient of 0.96 (see Deierling et al., 2007). This suggests a strong linear relationship between the flux

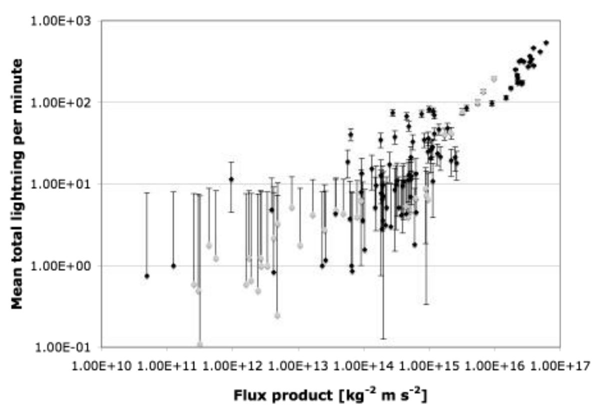

Figure 1. Mean total lightning per minute averaged over the radar volume time versus the product of non-precipitation ice mass flux estimate and precipitation ice mass flux [kg^2 m s^{-1}] above -5°C for individual radar volumes of all eleven thunderstorms. The black dots mark data from the Colorado/Kansas High Plains, whereas the grey dots mark data from Northern Alabama.

product and total lightning in support of the flux hypothesis. Note, that in Figure 1 data are color coded so that the grey points represent data from Northern Alabama and the black points represent data from the Colorado/Kansas High Plains.

3.2 CORRELATION BETWEEN NON PRECIPITATION ICE MASS AND TOTAL LIGHTNING

Non-precipitation ice above the -5°C level and coincident with divergence values larger than 0.001 s^{-1} and reflectivity values below 20 dBZ were used to estimate the non-precipitation ice from the charging zone. Figure 2 shows this non-precipitation ice mass estimate above the -5°C level versus mean total lightning on a logarithmic scale [Latham et al., 2007]. Similar to the flux product, the relationship between NPIM_DIV and mean total lightning is represented best with a linear fit. The correlation of NPIM_DIV and total lightning activity similarly high than the flux product with a correlation coefficient of 0.93. This suggests a strong linear relationship between non-precipitation ice mass and total lightning (Latham et al., 2007).

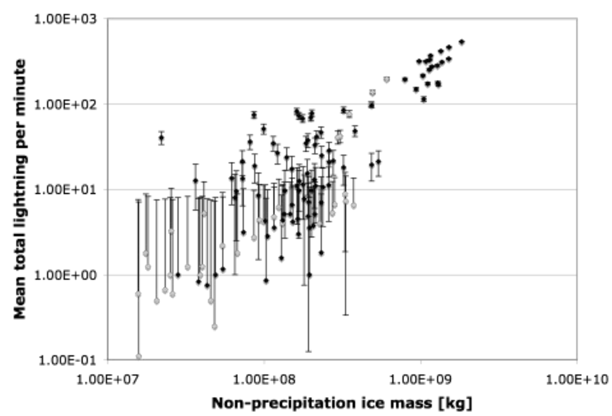

Figure 2. Mean total lightning per minute averaged over the radar volume time versus NPIM_DIV [kg] above the -5°C level for individual radar volumes of all eleven thunderstorms [from Latham et al., 2007]. The black dots mark data from the Colorado/Kansas High Plains, whereas the grey dots mark data from northern Alabama.

3.3 CORRELATION BETWEEN PRECIPITATION ICE AND TOTAL LIGHTNING

Precipitation ice mass above the -5°C level was calculated and compared to mean total lightning activity (Figure 3, from Latham et al. [2007]). Figure 3 implies that precipitation ice is related to total lightning in a close to linear fashion for different types of thunderstorms in different environments on a storm scale with a correlation coefficient of 0.94. These results compliment the findings of Petersen and Rutledge [2001], Petersen et al. [2005a] and Latham et al. [2007] who presented observational evidence for an essentially linear relationship between precipitation ice mass and total lightning for different climate regimes on a global scale.

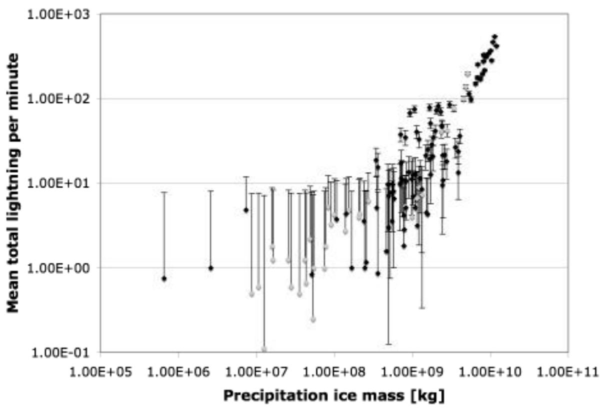

Figure 3. Mean total lightning per minute averaged over the radar volume time versus precipitation ice mass [kg] above the -5°C level for individual radar volumes of all eleven thunderstorms [from Latham et al., 2007]. The black dots mark data from the Colorado/Kansas High Plains, whereas the grey dots mark data from Northern Alabama.

3.4 RELATIONSHIP BETWEEN PRECIPITATION ICE/ LIQUID WATER, CONVECTIVE RAINFALL AND TOTAL LIGHTNING

Precipitation ice mass (P_m) above the -5°C level that was calculated previously was divided by the liquid water mass (LWM) computed from the polarimetric radar data using a blended algorithm for individual storm volumes. Figure 4 shows the ratios of P_m/LWM for all storms. Data from northern Alabama is in red and data from the High Plains is in black. Ratios of P_m/LWM close to one indicate large amounts of the precipitation ice mass would contribute to the LWM through melting – thus indicating that cold rain processes play a larger role in contributing to the LWM and convective rainfall. Conversely, ratios closer to 0 indicate that warm rain processes play a more significant role in producing LWM. It can be seen in Figure 4 that distinctly higher ratios of ice to liquid water mass in rainfall occur in the High Plains storms as compared to those of northern Alabama. This result is consistent with recent studies performed by Petersen

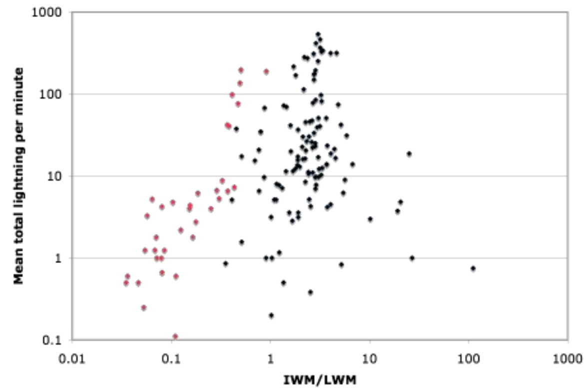

Figure 4. Mean total lightning per minute averaged over the radar volume time and ratios of ice water mass over liquid water mass for individual radar volumes of all eleven thunderstorms. The black dots mark data from the Colorado/Kansas High Plains, whereas the red dots mark data from Northern Alabama.

and Christian (2007) using TRMM satellite data. Figure 5 shows the rain yield (amount of rainfall per total lightning) versus total lightning amounts. It can be seen that, consistent with the P_m/LWM ratios, the amount of rainfall per total lightning is higher for the Northern Alabama storms (red points in Figure 5) than for the High Plains data (black point in Figure 5). Additionally the relationship between total lightning and rainfall amounts has a higher correlation for the High Plains storms than for the Northern Alabama storms suggesting that lightning may be used as an indicator of the degree to which cold rain processes (that are linked to electrification of thunderstorms) contribute to convective rainfall.

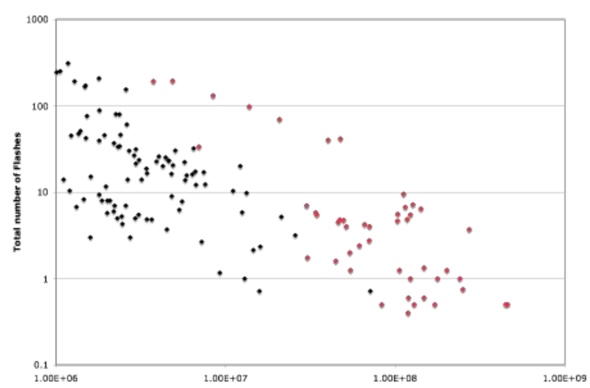

Figure 5. Mean total lightning per minute averaged over the radar volume time and rain yield per flash for individual radar volumes of all eleven thunderstorms.

4. CONCLUSIONS

Overall bulk microphysical trends of precipitation and non precipitation ice mass estimates show a good relationship to total lightning activity for the total of eleven storms of different types and from two different climate regions. Furthermore computing the flux product improves the correlation to total lightning activity, giving observational support for the flux hypothesis.

Preliminary results from the investigation of the relationship between P_m/LWM, convective rainfall and total lightning relationships suggest that it may be possible to use the combination of radar and total lightning data to estimate the portions of liquid water content or convective rainfall that originate from cold rain- versus warm rain processes. This type of partitioning would be useful for climatological and microphysical studies that need quantification of warm and cold rain processes in order to determine their relative roles in precipitation development and the water cycle.

5. REFERENCES

Baker, M.B., H.J. Christian and J. Latham, 1995: A computational study of the relationships linking lightning frequency and other thundercloud parameters. Q. J. R. Meteorol. Soc., **121**, 1525-1548.

Baker, M.B., A.M. Blyth, H.J. Christian, A.M. Gadian, J. Latham and K. Miller, 1999: Relationships between lightning activity and various thundercloud parameters: satellite and modelling studies. Atmos. Res., **51**, 221-236.

P

Blyth, A.M., H.J. Christian, K. Driscoll, A.M. Gadian and J. Latham, 2001: Determination of ice precipitation rates and thunderstorm anvil ice contents from satellite observations of lightning. Atmos. Res., **59-60**, 217-229.

Deierling, W., W. A. Petersen, J. Latham, S. Ellis and H.J. Christian, 2007: The relationship between lightning activity and ice fluxes in thunderstorms. Journal of Geophysical Research, Submitted.

Dolan, B. and S.A. Rutledge, 2007: An integrated display and analysis methodology for multivariable radar data. *J. Appl Meteor*., **46**, 1196-1213.

Crook, N.A. and J. Sun, 2004: Analysis and Forecasting of the Low-Level Wind during the Sydney 2000 Forecast Demonstration Project. Wea. Forecasting, **19**, 151-167.

Heymsfield, A.J., and A.G. Palmer, 1986: Relations for deriving thunderstorm anvil mass of CCOPE storm water budget estimates. J. Climate Appl. Meteor., **25**, 691-702.

Heymsfield, A.J, and K.M. Miller, 1988: Water Vapor and Ice Mass Transported into the Anvils of CCOPE Thunderstorms: Comparison with Storm Influx and Rainout. J. Atmos Sci., **45**, 3501-3514.

Latham, J. A.M. Blyth, H.J. Christian Jr., W. Deierling and A.M. Gadian, 2004: Determination of precipitation rates and yields from lightning measurements. Journal of Hydrology, **288**, 13-19.

Latham, J., W.A. Petersen, W. Deierling and H.J. Christian, 2007: Field Identification of a Unique Globally Dominant Mechanism of Thunderstorm Electrification.Quarterly Journal of the Royal Meteorological Society, 133, 1453-1457.

Petersen, W.A. and S.A. Rutledge, 2001: Regional Variability in Tropical Convection: Observations from TRMM. J. Climate, **14**, 3566-3586.

Petersen, W.A., K. Knupp, J. Walters, W. Deierling, M. Gauthier, B. Dolan, J.P. Dice, D. Satterfield, C. Davis, R. Blakeslee, S. Goodman, S. Podgorny, J. Hall, M. Budge and A. Wooten: The UAH-NSSTC/WHNT ARMOR C-band dual-polarimetric radar: A unique collaboration in research, education and technology transfer. Preprints, AMS 32nd Conference on Radar Meteorology, Albuquerque, New Mexico, 24-29 October 2005.

Petersen, W.A. and H.J. Christian, 2007: Lightning as an Indicator of Liquid and Ice Precipitation Processes in the Tropical Atmosphere. Preprints, 13th International Conference on Atmospheric Electricity. Bejing, China, 13-18 August 2007.

Reynolds, S.E., M. Brook and M.F. Gourley, 1957: Thunderstorm charge separation. J. Atmos. Sci., **14**, 426-436.

Rogers, R.R and B.R. Tripp. 1964: Some Radar Measurements of Turbulence in Snow. J. Appl. Meteor., **3**, 603-610.

Sassen, K., 1987: Ice Cloud Content from Radar Reflectivity. J. of Climate and Appl. Meteor., **26**, 1050-1053.

Saunders, C.P.R., W.D. Keith and R.P. Mitzeva, 1991: The effect of liquid water on thunderstorm charging. J. Geophys. Res., **96**, 11007-11017.

Saunders , C. P. R., 1993 : A Review of Thunderstorm Electrification Processes. J. Appl. Meteor., **32**, 642-655.

Straka J.M., D.S. Zrnic, A.V. Ryshkov, 2000: Bulk hydrometeor classification and quantification using polarimetric radar data: synthesis of relations. J. Appl. Meteor.,**39**, 1341-1372.

Sun,J. and N. A. Crook, 1997: Dynamical and Microphysical Retrieval from Doppler Radar Observations Using a Cloud Model and Its Adjoint. Part I: Model Development and Simulated Data Experiments. J. Atmos. Sci., **55**, 835-852.

Sun,J. and N. A. Crook, 2001: Real-Time Low-Level Wind and Temperature Analysis Using Single WSR-88D Data. Wea. Forecasting, **16**, 117-132.

Takahashi, T., 1978: Riming electrification as a charge generation mechanism in thunderstorms. J. Atmos. Sci., **35**, 1536-1548.

Vivekanandan, J., D.S. Zrnic, S. M. Ellis, R. Oye, A. V. Ryzhkov, and J. Straka, 1999: Cloud microphysics retrieval using S-band dual-polarization radar measurements. Bull. Amer. Meteor. Soc., **80**, 381-388.

Witt. A. and S.P. Nelson, 1991: The Use of Single Doppler Radar for Estimating Maximum Hailstone Size. J. Appl. Meteor., **30**, 425-431.

Yuter, S.E. and R.A. Houze Jr., 1995, Three-Dimensional Kinematic and Microphysical Evolution of Florida Cumulonimbus. Part III: Vertical Mass Transport, Mass Divergence, and Synthesis. Mon. Wea. Rev., **123**, 1964-183.

OBSERVATIONAL AND MODELLING EVIDENCE OF TROPICAL DEEP CONVECTIVE CLOUDS AS A SOURCE OF MID-TROPOSPHERIC ACCUMULATION MODE AEROSOLS

A. Engström[1], A. M. L. Ekman[1], R. Krejci[1], J. Ström[2], M. de Reus[3], C. Wang[4]
[1]Department of Meteorology, Stockholm University, Stockholm, Sweden
[2]Department of Applied Environmental Science, Stockholm University, Stockholm, Sweden
[3]Institut für Physik der Atmosphäre, Universität Mainz, Mainz, Germany
[4]Massachusetts Institute of Technology, Cambridge, Massachusetts, USA

1 INTRODUCTION

The importance of deep convection when considering the redistribution of boundary layer gases and aerosols to the upper troposphere is well known [Chatfield and Crutzen, 1984; Andronache et al., 1999; Wang and Prinn, 2000; Andreae et al., 2001]. Despite its importance, only a limited number of in-situ measurements have focused on processes and links between aerosol properties and deep convection. Therefore, there is still a lack of knowledge regarding the magnitude of the transport, formation and transformation of aerosols within convective clouds. It has previously been established that mid-troposphere aerosols play an important role in the formation of cloud droplets that later freeze to become anvil ice crystals in deep convective clouds [Fridlind et al., 2004]. In addition, the relatively long lifetime of aerosols in the free troposphere compared to the planetary boundary layer could be a critical factor when determining the radiative forcing of aerosols. An accurate description of the aerosol vertical distribution and the life cycle of aerosols in deep convective clouds are therefore crucial to determine the dynamical and microphysical properties of these clouds as well as the magnitude of in-cloud transport of pollutants and aerosols. This is important for improving our understanding of the role of deep convective clouds in the climate system.

The present study is based on observational data gathered during the Indian Ocean Experiment (INDOEX) intensive field phase, which took place during the dry winter monsoon from January to March 1999. During the campaign a large number of measurements within the outflow from South and Southeast Asia were carried out to characterize the chemical composition of the polluted Indo-Asian haze [Ramanathan et al., 2001].

A general increase of aerosols in the accumulation mode (compared to other altitudes in the free troposphere) was noted between 6 - 10 km during airborne observations conducted as a part of INDOEX [de Reus et al., 2001]. The increase was attributed to either direct convective transport of aerosols or evaporation of cloud droplets from previous cloud cycles, as the clouds dissipate. The purpose of this case study is to simulate one of the observed deep convective clouds and to compare simulated aerosol concentrations and size distributions with in-situ gathered observational data, in order to understand the role of deep convective clouds as a source of aerosols to the mid-troposphere (here defined by altitudes between 6 and 10 km).

Noticeably high concentrations ($>$ 500 cm^{-3} STP) of aerosols $>$ 0.12 μm was found within a deep convective cloud in the region above the active core at 7.5 km altitude (see Figure 1). Moreover, layers with increased concentrations were observed as the aircraft circulated around the cloud ($>$ 200 cm^{-3} STP). The presence of larger aerosols within the cloud in the mid-troposphere is noteworthy. Both transport and local evaporation could be possible explanations. However, direct transport of aerosols $>$ 0.12 μm from the boundary layer to the core up-

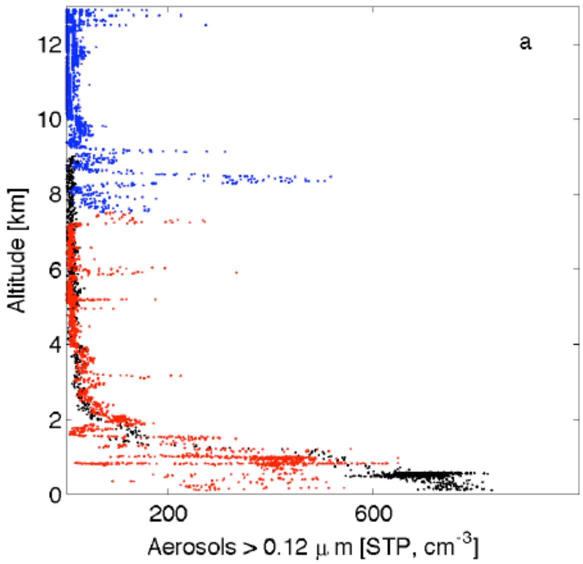

Figure 1: Total number of aerosols with diameter larger than 0.12 μm measured by the instruments onboard the Cessna Citation around, and within, the specific cloud simulated in this study. Black dots represents data not gathered in direct proximity of the cloud, red dots are data gathered around the cloud and blue dots are data gathered within the cloud.

draft region is limited due to cloud droplet formation and scavenging by heavy precipitation. The air around 7.5 km is near saturated with respect to ice and sub-saturated with respect to water. Thus, larger particles released from evaporation above the zero degree isotherm could remain in ambient air without being re-activated. We hypothesize that this is the major reason for the elevated concentrations around 7.5 km, our modeling effort is designed to examine this possibility.

2 METHODS

A three-dimensional, mesoscale, non-hydrostatic cloud-resolving model (CRM) is used for the simulations. The model was originally developed by Wang and Chang [1993]; Wang and Crutzen [1995], with additions according to Ekman et al. [2004], and consists of four main modules; a cloud dynamics module, a chemistry module, a microphysical module, and an aerosol module.

The number of aerosols available as cloud condensation nuclei (CCN) at a certain supersaturation is calculated using the Köhler equation. Four modes are used to describe the aerosol population, namely nucleation mode, Aitken mode, accumulation mode and coarse mode aerosols [Ekman et al., 2004]. Each aerosol mode is represented by a lognormal size distribution. This allows for the population to be described by four parameters; the prognostic variables number concentration (N), mass (M) and median diameter (Dp), and a predefined geometric standard deviation (σ_g). The four aerosol modes are assumed to be completely hygroscopic. 5% of the total aerosol population larger than 0.1 μm is assumed to act as potential IN through heterogeneous freezing of cloud droplets [DeMott et al., 2003; Pruppacher and Klett, 1997]. Release of aerosols through evaporation of cloud droplets, rain drops, ice crystals and graupel was treated in the model by assuming a 1:1 ratio between an evaporated hydrometeor and the residual aerosol. For ice crystals, this assumption is in good agreement with observations [Gayet et al., 2002; Seifert et al., 2003]. For other hydrometeors, the ratio could potentially be different, but the assumption should at least give an approximation of the lower limit of the number of aerosols released. A major part (90%) of the aerosols originating from evaporated hydrometeors are introduced into the accumulation mode assuming growth due to in-cloud processing (CITE). The remaining fraction of the re-suspended aerosols (10%) are introduced into the coarse mode. In this study, two branches of simulations, with and without release of aerosols due to evaporation, was designed. The simulation with release of aerosols (REL) was performed only with 100% hygroscopic aerosols. However, to examine the effect of transport of hydrophobic aerosols on the mid-troposphere aerosol concentration, the branch without release of aerosols include two simulations using 0%, and 50% of externally mixed black carbon in the accumulation mode (NOREL and NOREL-BC50, respectively).

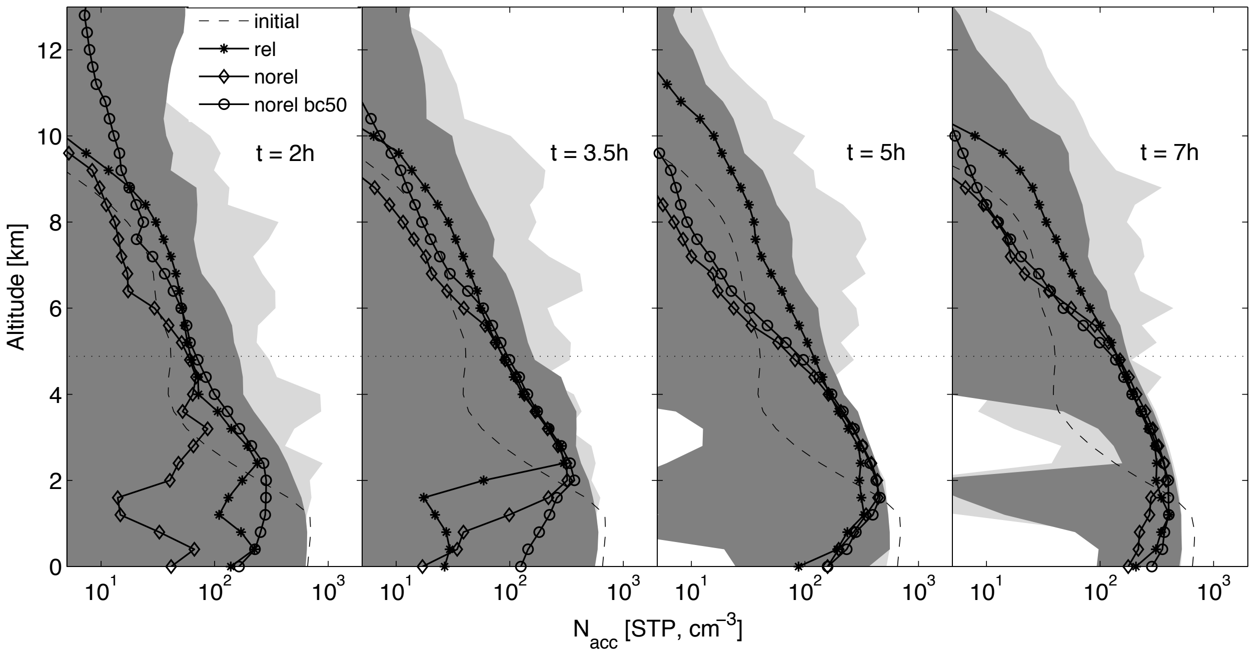

Figure 2: Vertical profiles of accumulation mode aerosols (diameter $> 0.12\mu$m) within the cloud at different stages of cloud development. Dark and light shading represent min. and max. interval of both the NOREL simulations and of the REL simulation, respectively. Also shown is median concentration for NOREL (diamonds) and NOREL BC50 (circles) and REL (stars) as well as initial accumulation mode aerosol concentration (dashed line) and the initial 0°C isoterm (horizontal dotted line). All number concentrations are given at STP.

3 CONCLUSIONS

The model simulations show that direct transport of aerosols cannot explain the high concentration of aerosols within the cloud, even when the aerosols are assumed externally mixed with hydrophobic black carbon (NOREL and NOREL BC50 simulations in Figure 2). We find that significant evaporation of hydrometeors occur at the lateral boundaries of the simulated cloud and at altitudes corresponding to where high concentrations where found in the airborne measurements. The evaporation occurs at altitudes where the, on average, strongest updrafts occur inside the cloud.

Assuming that each evaporated hydrometeor release one aerosol (REL simulation), an increase up to 600 cm-3 is found between altitudes 6 - 10 km (see Figure 2). These high concentrations are comparable to what was measured within the deep convective cloud. There is also a significant mean increase of accumulation mode aerosols in the mid-troposphere inside and around the cloud (~90% increase). The evaporation of hydrometeors begins at early stages of cloud development (around 1h) and coincides with the onset of strong updrafts. This continues throughout the active part of cloud life cycle. The process is not as prominent during the later, less active, stage of the cloud cycle (t $\sim$ 7h). The aerosols released from evaporation are available again to act as CCN and IN, which affect the cloud dynamical and microphysical properties, e.g. maximum updraft, precipitation and hydrometeor number concentration and size. Larger particles within the accumulation and coarse mode are often regarded to be completely scavenged by wet-deposition in deep convective clouds due to the heavy precipitation. This study indicates that large aerosols can be released in the free troposphere and inside the cloud at levels significantly above cloud base. The simulations are based on observations from one particular cloud over the Indian Ocean, but it is reasonable to believe that the process of aerosols release along the cloud core is of general importance. Similar layers of elevated accumulation mode aerosol concentrations have been found at altitudes above 6 km e.g. in measurements gathered during the Large-Scale Biosphere-Atmosphere Experiment in Amazonia (LBA)-Cooperative LBA Airborne Regional Experiment 1998 (CLAIRE 98) over Surinam [Krejci et al., 2003]. A general source of mid-troposphere aerosols through deep convection could potentially have a large impact on long-range transport as well as climate and should thus be considered in general circulation models.

References

Andreae, M. O., P. Artaxo, H. Fischer, S. R. Freitas, J. M. Grégiore, A. Hansel, P. Hoor, R. Kormann, R. Krejci, L. Lange, J. Lelievald, W. Lindinger, K. Longo, W. Peters, M. de Reus, B. Scheeren, M. A. F. S. Dias, J. Ström, P. F. J. van Velthoven, and J. Williams, 2001: Transport of biomass burning smoke to the upper troposphere by deep convection in the equatorial region. *Geophys. Res. Lett.* **28**(6), 951–954.

Andronache, C., L. J. Donner, C. J. Seman, and V. Ramaswamy, 1999: Atmospheric sulfur and deep convective clouds in tropical Pacific: A model study. *J. Geophys. Res.* **104**(D4), 4,005–4,024.

Chatfield, R. B. and P. J. Crutzen, 1984: Sulfur dioxide in remote oceanic air: Cloud transport of reactive precursors. *J. Geophys. Res.* **89**(D5), 7111–7132.

de Reus, M., R. Krejci, J. Williams, H. Fischer, R. Scheele, and J. Ström, 2001: Vertical and horizontal distributions of the aerosol number concentration and size distribution over the northern Indian Ocean. *J. Geophys. Res.* **106**(D22), 28,629–28,641.

DeMott, P. J., D. J. Cziczo, A. J. Prenni, D. M. Murphy, S. M. Kreidenweis, D. S. Thomson, R. Borys, and D. C. Rogers, 2003: Measurements of the concentration and composition of nuclei for cirrus formation. *Proc. Nat. Academy of Sciences of the USA* **100**(25), 14,655–14,660.

Ekman, A. M. L., C. Wang, J. Wilson, and J. Ström, 2004: Explicit simulations of aerosol physics in a cloud-resolving model: A sensitivity study based on an observed convective cloud. *Atmos. Chem. Phys.* **4**, 773–791.

Fridlind, A. M., A. S. Ackerman, E. J. Jensen, A. J. Heymsfield, M. R. Poellot, D. E. Stevens, D. Wang, L. M. Miloshevich, D. Baumgardner, R. P. Lawson, J. C. WIlson, R. C. Flagand, J. H. Seinfeld, H. H. Jonsson, T. M. VanReken, V. Varutbangkul, and T. A. Rissman, 2004: Evidence for the predominance of mid-tropospheric aerosols as subtropical anvil cloud nuclei. *Science* **304**, 718–722.

Gayet, J.-F., F. Auriol, A. Minikin, J. Ström, M. Seifert, R. Krejci, A. Petzold, G. Febvre, and U. Schumann, 2002: Quantitative measurement of the microphyscal and optical properties of cirrus clouds with four different in situ probes: Evidence of small ice crystals. *Geophys. Res. Lett.* **29**(24), 83.

Krejci, R., J. Ström, M. de Reus, P. Hoor, J. Williams, H. Fischer, and H.-C. Hansson, 2003: Evolution of aerosol properties over the rain forest in surinam, South America, observed from aircraft during the LBA-CLAIRE 98 experiment. *J. Geophys. Res.* **108**(D18), 4561.

Pruppacher, H. R. and J. D. Klett, 1997: *Microphysics of Clouds and Precipitation (2 ed.)*. Kluwer Academic Publishers.

Ramanathan, V., P. J. Crutzen, J. Lelieveld, A. P. Mitra, D. Althausen, J. Anderson, M. O. Andreae, W. Cantrell, G. R. Cass, C. E. Chung,

A. D. Clarke, J. A. Coakley, W. D. Collins, W. C. Conant, F. Dulac, J. Heintzenberg, A. J. Heymsfield, B. Holben, S. Howell, J. Hudson, A. Jayaraman, J. T. Kiehl, T. N. Krishnamurti, D. Lubin, G. McFarquhar, T. Novakov, J. A. Ogren, I. A. Podgorny, K. Prather, K. Priestly, J. M. Prospero, P. K. Quinn, K. Rajeev, P. Rasch, S. Rupert, R. Sadourny, S. K. Sateesh, G. Sheridan, and F. P. J. Valero, 2001: Indian Ocean Experiment: An integrated analysis of the climate forcing and effects of the great Indo-Asian haze. *J. Geophys. Res.* **106**(D22), 28,371–28,398.

Seifert, M., J. Ström, R. Krejci, A. Minikin, A. Petzold, J.-F. Gayet, U. Schumann, and J. Ovarlez, 2003: In-situ observations of aerosol particles remaining from evaporated cirrus crystals: Comparing clean and polluted air masses. *Atmos. Chem. Phys.* **3**, 1037–1049.

Wang, C. and J. S. Chang, 1993: A three-dimensional numerical model of cloud dynamics, microphysics, and chemistry. 1: Concepts and formulation. *J. Geophys. Res.* **98**(D8), 14,827–14,844.

Wang, C. and P. J. Crutzen, 1995: Impact of a simulated severe local storm on the redistribution of sulfur-dioxide. *J. Geophys. Res.* **100**(D6), 11,357–11,367.

Wang, C. and R. G. Prinn, 2000: On the roles of deep convective clouds in tropospheric chemistry. *J. Geophys. Res.* **105**(D17), 22,269–22,297.

ON THE REPRESENTATION OF DROPLET COALESCENCE AND AUTOCONVERSION FOR REALISTIC CLOUD SIZE DISTRIBUTIONS

W. C. Hsieh[1], H. Jonsson[2], G. Buzorius[3], R. C. Flagan[4, 5], J. H. Seinfeld[4, 5], and A. Nenes[1, 6]

[1] Earth and Atmospheric Sciences, Georgia Institute of Technology, Atlanta, GA
[2]CIRPAS, Naval Postgraduate School, Monterey, CA
[3]Meteorology, Naval Postgraduate School, Monterey, CA
[4]Environmental Science and Engineering, California Institute of Technology, Pasadena, CA
[5] Chemical Engineering, California Institute of Technology, Pasadena, CA
[6]Chemical and Biomolecular Engineering, Georgia Institute of Technology, Atlanta, GA

1. INTRODUCTION

Studies of anthropogenic climate change have shown that large predictive uncertainty arises from the incomplete representation of cloud microphysical processes, especially autoconversion of cloudwater to rain [e.g., Lohmann and Feichter , 2005].

If the droplet size distribution is known, the autoconversion rate, *A*, can be computed from the Stochastic Collection Equation (SCE) [Pruppacher and Klett, 1997]:

$$A = \int_0^{x_0} \left[\int_{x_0 - x}^{x_0} K(x, x')x' n(x')dx' \right] n(x)dx \quad (1)$$

where $K(x,x')$ is the collection kernel, $n(x)$ is the drop size distribution (DSD). The lack of explicit cloud microphysics in Global Climate Models (GCMs) prohibit the explicit usage of SCE; instead, GCMs use simple parameterizations of the collection process (the rate-limiting step for precipitation formation), and express autoconversion rate in terms of liquid water content (LWC) [Kessler, 1969], cloud droplet number concentration (CDNC) [Manton and Cotton, 1977; Rotstayn, 1997; Khairoutdinov and Kogan, 2000], and dispersion of the droplet size distribution [Beheng, 1994; Cohard and Pinty, 2000; Liu and Daum, 2004].

In this work, we evaluate autoconversion parameterizations against explicit calculations using SCE. Uncertainty in autoconversion rate that arise from neglecting the effects of turbulence and from fitting ambient DSD to a gamma distribution is explored. The DSD used for the evaluations are obtained from in-situ observations of clouds.

2. OBSERVATION DATASETS

Cloud droplet size distributions used in this study were collected aboard the CIRPAS Twin Otter aircraft (http://www.cirpas.org/) during two field campaigns:CRYSTAL-FACE in Key West, FL (July 2002) and CSTRIPE in Monterey, CA (July 2003). Measurements taken during CRYSTAL-FACE were low-level cumuliform clouds [Conant et al., 2004; VanReken et al., 2003], while marine stratocumulus clouds were primarily sampled during CSTRIPE [Meskhidze et al., 2005]. In both campaigns, the binned droplet size distributions were measured with a Cloud and Aerosol Spectrometer (CAS) optical probe and a Forward Scattering Spectrometer Probe (FSSP). The observed DSDs ranged between 1 to 25 μm in radius; haze droplets (less than 1 μm) and their impact on collection is not considered. We used transect-average for SCE calculations; 164 transects are available from CRYSTAL-FACE, and, 52 from CSTRIPE.

3. AUTOCONVERSION PARAMETERIZATIONS USED

The parameterization schemes used in this study include (1) MC, [Manton and Cotton, 1977]; (2) BH [Beheng, 1994]; (3) KK, [Khairoutdinov and Kogan, 2000]; (4) LD4 and (5) LD6, which correspond to the P4 and P6 formulations of Liu and Daum [2004].

4. PARAMETERIZATIONS VS. SCE WITH MEASURED DSD

The comparison of autoconversion rates predicted by parameterizations and SCE calculations for CRYSTAL-FACE DSDs is shown in Figure 1. LD6 systematically overestimates autoconversion, because it provides total coalescence (i.e., total coalescence rate from droplets of all sizes) and not autoconversion (i.e., the rate of production of drizzle droplets). On average, LD6 overpredicts autoconversion by a factor of 47 for CRYSTAL-FACE, and a factor of 4 for CSTRIPE clouds.

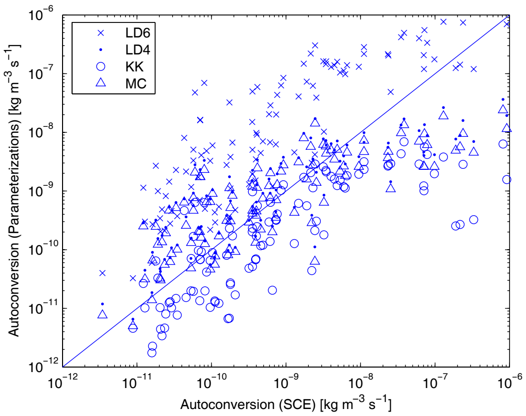

Figure 1. Autoconversion rates predicted by LD6, LD4, KK and MC versus SCE calculations for measured CRYSTAL-FACE DSDs.

The large difference between SCE and parameterizations is also seen when using the DSD from the CSTRIPE stratocumulus dataset (not shown here). Of all parameterizations considered, KK tends to show the least autoconversion bias. The BH parameterization is not included in Figure 1, because the data used in this study are outside its region of applicability.

5. HYDROLOGICALLY IMPORTANT CLOUDS

Conversion rates vary five orders of magnitude in the CRYSTAL-FACE and four orders of magnitude for CSTRIPE datasets. Not all of this dynamic range is ''hydrologically important'', so we focus our parameterization evaluation for clouds closest to a precipitating state. The timescale for forming rain, τ_{rain} = LWC/A, is used for evaluating the probability of precipitation; clouds with τ_{rain} ~ 0.1 h (a typical lifetime of an individual cloud) and 10 h (the lifetime of a stratocumulus layer) are hydrologically important as they can precipitate within their lifetime. For these clouds, errors in autoconversion can difference between a precipitating and non-precipitating cloud.

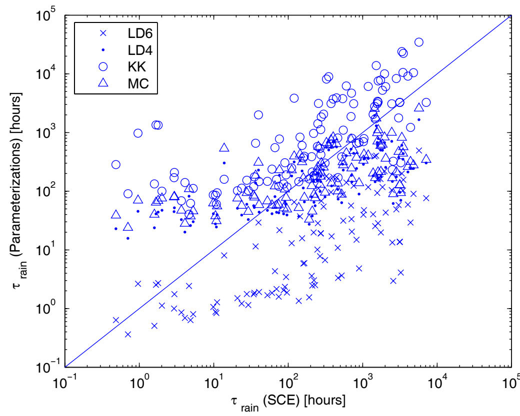

Figure2. τ_{rain} (Parameterizations) versus τ_{rain} (SCE) for CRYSTAL-FACE clouds.

Figure 2 presents τ_{auto}, which ranges from 0.5 to 10^4 h in CRYSTAL-FACE data, and 10 to 10^4 h in the CSTRIPE data. CSTRIPE clouds tend to have larger τ_{auto}, consistent with their lower LWC, weaker dynamical forcing and lower cloud top height.

Compared to SCE, LD6 tends to underestimate τ_{rain} (because autoconversion rate is overestimated) by a factor of 0.36 ± 0.56 and 1.08 ± 0.80 for CRYSTAL-FACE and CSTRIPE, respectively. The remaining parameterizations tend to overestimate τ_{rain} by up to a factor of 100.

6. SCE WITH TURBULENT KERNEL

Turbulence can enhance coalescence rate [Pruppacher and Klett, 1997] and is also important on cloud droplet size distribution evolution [Riemer and Wexler, 2005]. Its impact on autoconversion rates is estimated by using the turbulence kernel of Zhou et al. [2001]. We compare autoconversion rates obtained from SCE integration with gravitational and turbulent kernels. For CRYSTAL-FACE cloud size distributions, the average autoconversion rate with the turbulent kernel is a factor of 1.2 ± 0.6 greater than the average value obtained using the gravitational kernel only. When applied to CSTRIPE clouds, turbulence, compared to gravitation alone, enhances autoconversion by a factor of 1.5 ± 0.4. Our results show that enhancement of turbulence is within the inherent uncertainty of autoconversion parameterizations.

REFERENCES

Beheng, K. D., A parameterization of warm cloud microphysical conversion processes, *Atmos. Res.*, **33**, 193-206, 1994.

Cohard, J., and J. Pinty, A comprehensive two-moment warm microphysical bulk scheme. I: Description and tests, *Q. J. R. Meteorol. Soc.*, **126**, 1815-1842, 2000.

Conant, W., T. Vanreken, T. Rissman, V. Varutbangkul, J. Jimenez, A. Delia, R. Bahreini, G. Roberts, A. Nenes, H. Jonsson, R. C. Flagan, and J. H. Seinfeld, Aerosol-cloud drop concentration closure in warm cumulus, *J. Geophys. Res.*, **109**, D13,204, 2004.

Kessler, E., On the distribution and continuity of water substance in atmospheric circulation, Tech. Rep. 32, Meteor. Monogr., Amer. Meteor. Soc., 1969.

Khairoutdinov, M., and Y. Kogan, A new cloud physics parameterization in a large-eddy simulation model of marine stratocumulus, *J. Atmos. Sci.*, **57**, 229-243, 2000.

Liu, Y., and P. H. Daum, Parameterization of the autoconversion process. Part I: Analytical formulation of the Kessler-Type parameterizations, *J. Atmos. Sci.*, **61**, 1539-1548, 2004.

Lohmann, U., and J. Feichter, Global indirect aerosol effects: a review, *Atmos. Chem. Phys.*, **5**, 715-737, 2005.

Manton, M. J., and W. R. Cotton, Formulation of approximate equations for modeling moist deep convection on the mesoscale, Atmospheric Science Paper. No. 266, Colorado State University, 62 pp, 1977.

Meskhidze, N., A. Nenes, W. C. Conant, and J. H. Seinfeld, Evaluation of a new cloud droplet activation parameterization with in situ data from CRYSTAL-FACE and CSTRIPE, *J. Geophys. Res*., **110**, 10, 2005.

Pruppacher, H. R., and J. D. Klett, Microphysics of Clouds and Precipitation, Kluwer Acad., Norwell, Mass., 1997.

Riemer, N., and A. S. Wexler, Droplets to drops by turbulent coagulation, *J. Atmos. Sci.*, **62**, 1962-1975, 2005.

Rotstayn, L. D., A physically based scheme for the treatment of stratiform clouds and precipitation in large-scale models: I: Description and evaluation of the microphysical processes, *Q. J. R. Meteorol. Soc.*, **123**, 1227-1282, 1997.

VanReken, T. M., T. A. Rissman, G. C. Roberts, V. Varut-bangkul, H. H. Jonsson, R. C. Flagan, and J. H. Seinfeld, Toward aerosol/cloud condensation nuclei (CCN) closure during CRYSTAL-FACE, *J. Geophys. Res.*, **108**, 2003.

Wood, R., and P. N. Blossey, Comments on "Parameterization of the autoconversion process. Part I: Analytical formulation of the Kessler-type parameterizations", *J. Atmos. Sci.*, **62**, 3003-3006, 2005.

Zhou, Y., A. S. Wexler, and L. P. Wang, Modelling turbulent collision of bidisperse inertial particles, *J. Fluid Mech*., **433**, 77-104, 2001.

ACKNOWLEDGMENTS

This research was funded by the Department of Energy, an NSF CAREER award and a graduate teaching assistantship. This work was also funded by the office of Nowel Research under grant N00014-04-1-0118. The authors wish to thank Dr. A. Bott for providing the SCE code. ICCP support for participating in conference is also acknowledged.

P3.40

INVESTIGATION OF THE DEPENDENCE OF SQUALL LINE STRUCTURE AND DYNAMICS ON MICROPHYSICAL PARAMETERIZATION

Kyoko Ikeda*[1], Roy Rasmussen[1], Changhai Liu[1], Greg Thompson[1], and Lulin Xue[2]

[1]*National Center for Atmospheric Research, Boulder, CO, USA*

[2]*Saint Louis University, St. Louis, MO, USA*

1. Introduction

This study examines the sensitivity of squall line structure to various microphysical schemes. The WRF simulations of an idealized two-dimensional squall line were performed at 1-km horizontal resolution using the Weisman et al. (1988) idealized squall line sounding and a retrospective sounding from a squall line case observed on 12 June 2002 during the IHOP (International $H_2$0 Program) field program. Previous studies have shown sensitivity of squall line dynamics to microphysics parameterization (e.g., Yang et al. 1995). A unique aspect of this study is the inclusion of the detailed microphysics schemes of Geresdi et al. (2005) in addition to three more conventional mixed-phase bulk microphysics schemes [Lin, Farley, and Orville (1983); WSM 6-class (Hong et al. 2004); and Thompson et al. (2004)] that are commonly used in the WRF model.

A brief description of the model configuration is given in section 2. Section 3 presents the simulation results. A summary and concluding remarks are given in section 4.

2. Model setups

Two WRF simulations of a two-dimensional squall line were performed. The first simulation was performed using the Weisman et al. (1988) idealized sounding (Fig. 1a). The sounding shows a low-level storm-relative inflow between 0 to 2.3 km and a deep moist layer in the troposphere. The second simulation was initialized with sounding data collected on 12 June 2002 during the IHOP field campaign (Fig. 1b). The IHOP sounding in Fig. 1b was taken from dropsonde data collected just ahead of a dry line in northwestern Oklahoma and rawinsonde data from Norman, OK at ~2100 UTC. The dry line was associated with a squall line that later developed and moved across northern Oklahoma. The presence of a dry layer between 3 and 6 km AGL, capped by a thermal inversion layer, and storm-relative westerly flows in the dry upper levels characterize the atmospheric conditions.

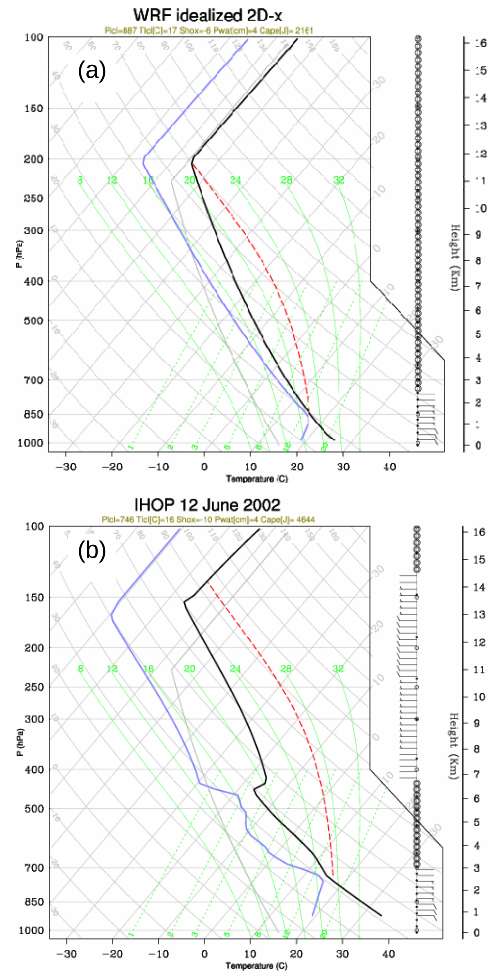

Figure 1: (a) The Weisman et al. (1988), and (b) 12 June 2002 IHOP retrospective soundings used for the 2-D squall line simulations. Full (half) barbs indicate 10 m s^{-1} (5 m s^{-1}).

The model domain had a horizontal dimension of 501 km with a 1-km grid spacing and 81 vertical levels. The simulation times with the Weisman et al. and IHOP soundings were six hours and four hours, respectively, with a time step of four seconds. The convection was initialized with a 3.0 and 1.5^{o}C warm

* Corresponding author address: Kyoko Ikeda, National Center for Atmospheric Research, P.O. Box 3000, Boulder, CO 80301
E-mail: kyoko@ucar.edu

bubble in the Weisman et al. and IHOP sounding simulations, respectively.

The three bulk microphysical schemes examined in this study are: Lin, Farley, and Orville (1983); WSM 6-class (Hong et al. 2004); and Thompson et al. (2004) schemes. In addition, simulations with the detailed microphysics scheme of Geresdi et al. (2005) are compared with those from the three bulk schemes. All of the four schemes involve five hydrometeor categories: cloud water, rain, cloud ice, snow, and graupel.

3. Results

a. Simulation with the Weisman et al. sounding

Figure 2 shows a Hovmuller diagram of rainfall rates simulated with the Weisman et al. sounding. Generally, all of the four microphysics schemes produced a leading squall line with a trailing stratiform region although some differences in the strengths and width of the convective and stratiform regions exist. Vertical cross sections of the system displayed several similarities to the general features of the squall line with trailing stratiform precipitation described in Houze (1993), e.g., the ascending front-to-rear flow, descending rear-to-front flow, precipitation-induced low-level cold pool development, formation of new convective cells in the midlevel on the leading side of the matured intense convective cell, and vertical motions associated with the individual convective cells (Fig. 3).

The simulated system matured rapidly with the Lin et al. and WSM6 schemes developing a maximum rainfall rates in 1.5 hours after the convective initiation (at 0.5 hr) (Fig. 4). The system started its eastward propagation at this model time. The storm development was relatively slower with the detailed and Thompson et al. schemes, requiring ~2.5 hours after the convective initiation for the system to begin its eastward motion due to smaller evaporation rates below the cloud base produced by the two schemes.

b. Simulation with the IHOP retrospective sounding

Rainfall rates simulated with the IHOP sounding are given in Fig. 5. Generally, the system is less organized compared with that of the previous simulation. In this case, the thermal inversion layer capping a relatively dry mid-layer and storm-relative westerly flow in the upper levels in the IHOP sounding (Fig. 1b) affected the storm dynamics. The thermal inversion inhibited the ascending front-to-rear flow to penetrate above ~6 km AGL. Thus, much of the ice and snow that formed in the upper levels of the convective region were advected towards the front of the system (eastward with respect to the storm motion) by the storm-relative westerly flow aloft forming a relatively broader region of overhang instead of a trailing stratiform precipitation (e.g., Fig. 6).

The cooling effects from sublimation, evaporation, and melting of the stratiform precipitation

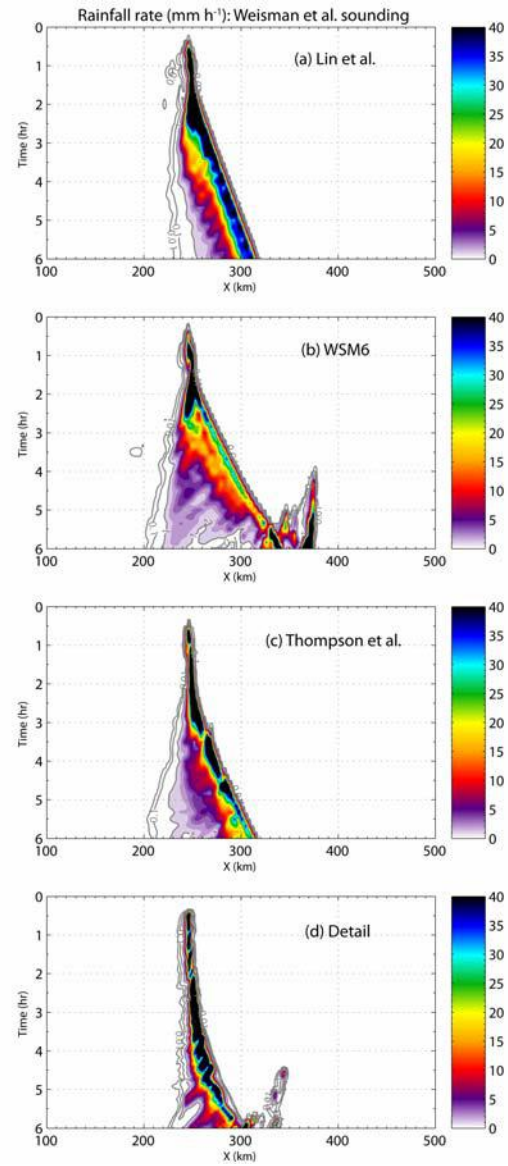

Figure 2: Hovmuller diagrams of rain rate (mm h^{-1}) from a six-hour simulation initialized with the Weisman et al. sounding for (a) Lin et al., (b) WSM6, (c) Thompson et al., and (d) detailed microphysics schemes.

are important to the development of a strong rear inflow jet (Yang et al. 1995) which transports cooler and drier air toward the leading edge of the convective region to form a cold pool (e.g., Houze 1993). In addition, the balance between the strength of the cold pool and low-level wind shear are important factors controlling the strength and longevity of squall lines (e.g., Rutunno et al. 1988; Weisman 1992). For example, in the Weisman et al. sounding simulation, the precipitation-induced rear inflow jet in the stratiform region stayed elevated during the six-hour storm evolution for the four microphysics schemes producing more vigorous convective updrafts at the leading edge of the system as the storm-relative low-level inflow interacted with the cold pool nose.

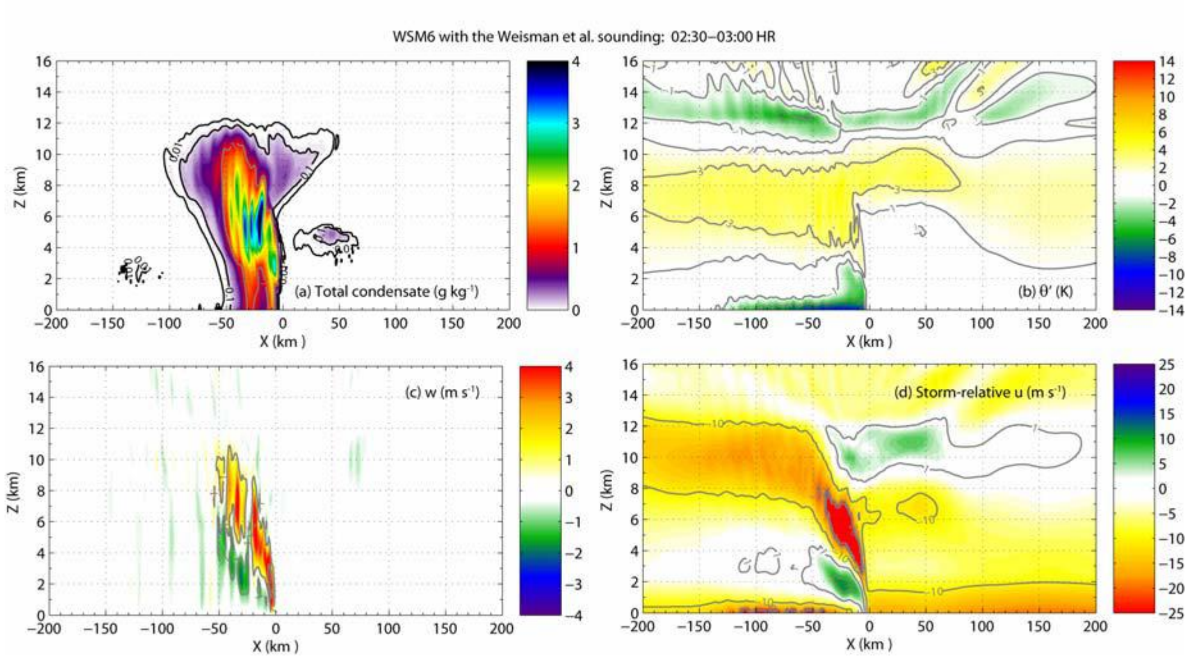

Figure 3: Average vertical cross sections of (a) total condensate (b) perturbation potential temperature, (c) vertical velocity, and (d) storm-relative horizontal velocity simulated by the WSM6 scheme with the Weisman et al. sounding. The cross sections show the average structure between the simulation times 3.5 and 4 hr with respect to the storm motion. Zero km on the abscissa marks the leading edge of the convective region.

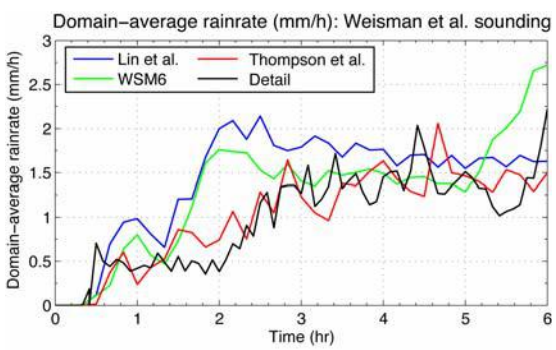

Figure 4: Time history of domain-average rainfall rates (mm h^{-1}) from the Weisman et al. sounding simulation.

Compared with the results from the Weisman et al. sounding, the microphysics parameterization had a significant impact on the storm evolution when the simulation was initiated with the IHOP sounding due to the different cold pool dynamics produced by the various schemes. The Lin et al. and WSM6 schemes initially produced a non-propagating convection (Figs. 5a-b). The gust front from this cell formed new cells on the leading side of the initial convection as in the Weisman et al. sounding simulation, but the system became less organized after ~2.5 hours of the simulation as the rear-inflow jet descended and spread cooler and drier air at the surface ahead of the decaying initial convection (at x ~ -75 km in Fig. 6). Eventually, it broke down into multi-cellular weak convection. In comparison, the systems simulated with the Thompson et al. and detailed schemes were relatively more organized with the initial convection near the leading edge of the system and a narrow trailing stratiform region (Figs. 5c-d). The cold pool nose in these two schemes did not extend too far beyond the initial convection during the simulation time compared with those produced by the Lin et al. and WSM6 schemes (e.g., Fig. 7).

Examination of mixing ratios, sinks, and sources of the five individual hydrometeor types suggested that trailing stratiform precipitation did not form in the Lin et al. and WSM6 schemes because snow formed mainly above the ascending front-to-rear flow (> 6 km AGL; Figs. 8a-b). In these two schemes, the dominant sources for snow were aggregation of ice, which formed in the upper levels by vapor diffusion, and ice-snow coagulation. These hydrometeors were transported ahead of the initial convection by the storm-

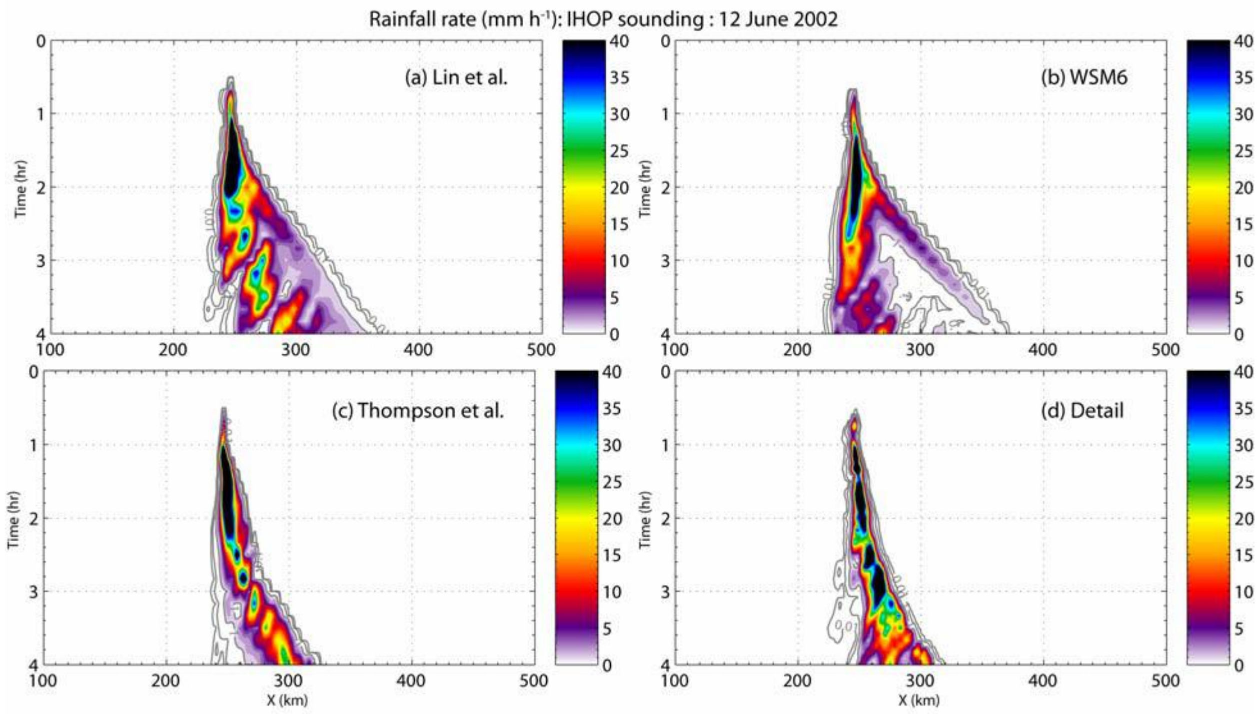

Figure 5: Same as Fig. 2 but for the rainfall rates produced from the IHOP sounding simulation.

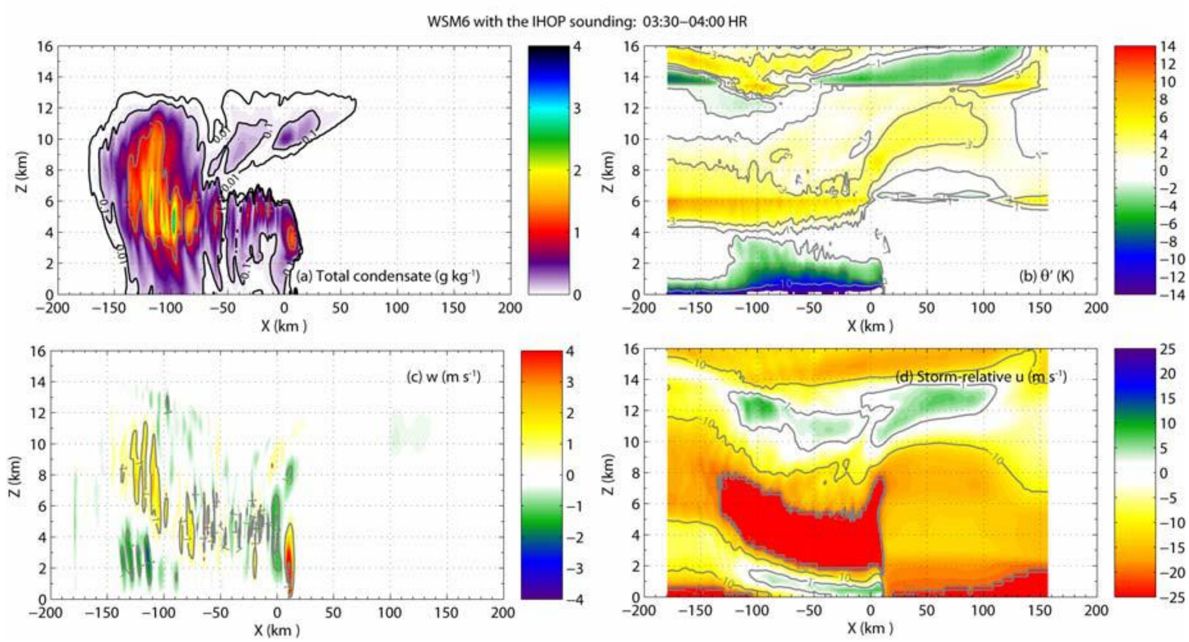

Figure 6: Same as Fig. 3 but for the IHOP sounding simulation with the WSM6 scheme.

relative westerly flow aloft and formed an overhang. On the other hand, some snow formed in the ascending front-to-rear flow in the Thompson et al. and detailed schemes by vapor diffusion and were transported rearward; thereby yielding a narrow trailing stratiform precipitation (Figs. 8c-d). Consequently, the sublimation rate of the snow in the stratiform region was significantly larger compared with that of the Lin et al. and WSM6 schemes, which would impact the formation of a rear inflow-jet and the organization of the system through generation of horizontal vorticity. As in the Lin et al. and WSM6 schemes, snow in the upper levels was carried

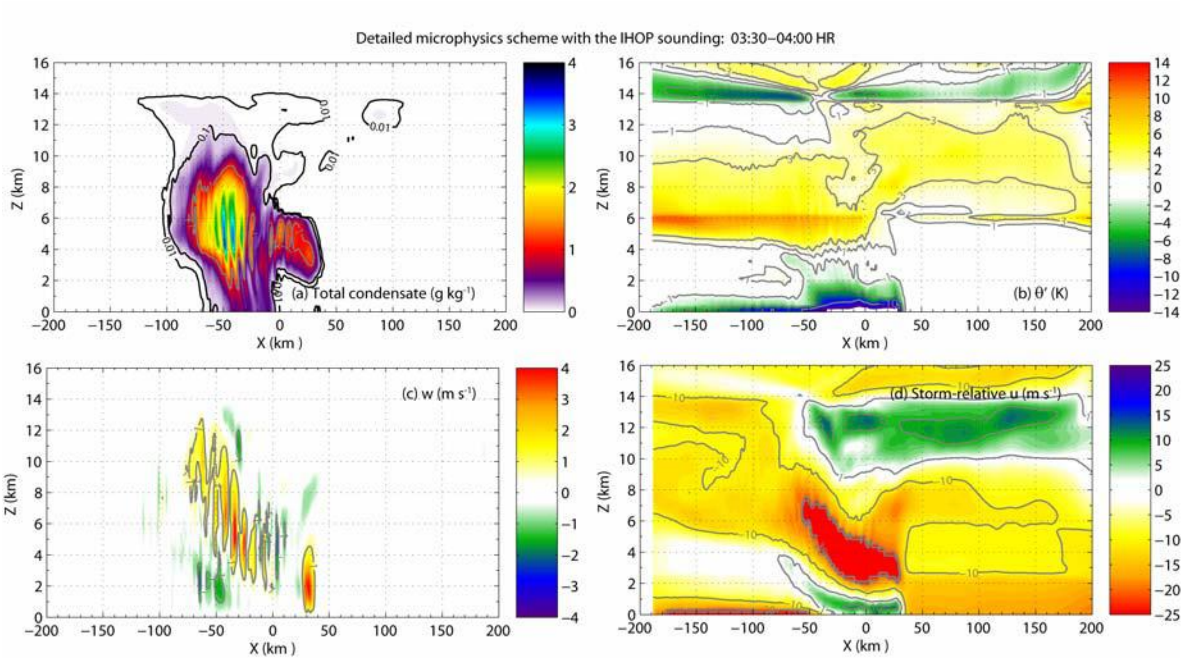

Figure 7: As in Fig. 3 but for the IHOP sounding simulation with the detailed microphysics scheme.

toward the front of the system by the upper level flow in the detailed and Thompson et al. schemes. Vapor diffusion was the most effective process for producing snow in the upper levels in these two schemes. [Very little ice was produced by the Thompson et al. scheme (Fig. 8c).]

The latent cooling of the precipitation behind the new cell also affected the cold pool evolution. In the WSM6 and Lin et al. schemes, graupel formed above the cold pool nose (between x = -50 and 0km in Figs. 8a-b). Evaporation of the melting graupel (explicitly computed by the two schemes) further enhanced evaporative cooling below the cloud deck, and possibly contributed to the rapid break down of the system in these two bulk schemes.

4. Summary and concluding remarks

Two WRF simulations of a two-dimensional squall line system were performed to examine the sensitivity of the system to microphysical parameterization. All four microphysics schemes examined in this study formed a realistic squall line when the simulation was initialized with the Weisman et al. sounding. The microphysical parameterization had a significant impact on the storm evolution with the 12 June 2002 IHOP retrospective squall line case. The Lin et al. and WSM6 schemes produced a non-propagating squall line without trailing stratiform precipitation, and the system rapidly broke down after 2.5 hours. The system formed with the Thompson et al. and detailed microphysics schemes was relatively more organized during the four-hour simulation. The current analysis indicated that (1) whether snow/ice formed in the ascending front-to-rear flow, and (2) latent cooling effects from precipitation forming over the cold pool nose were important in the cold pool dynamics. Further details will be presented at the conference.

Acknowledgement: This research was funded by the Short Term Explicit Prediction program of the National Center for Atmospheric Research.

References

Geresdi, I, and R. Rasmussen, 2005: Freezing drizzle formation in stably stratified layer clouds. Part II: The role of giant nuclei and aerosol particle size distribution and solubility. *J. Atmos. Sci.,* **62**, 2037-2057.

Hong, S.-Y., J. Dudhia, and S.-H. Chen, 2004: A revised approach to ice-microphysical processes for the bulk parameterization of cloud and precipitation. *Mon. Wea. Rev.,* **132**, 103-120.

Houze, R. A, 1993:*Cloud Dynamics.* Academic Press, Inc., 573 pp.

Lin, Y. L., R. Farley, and H. D. Orville, 1983: Bulk parameterization of the snow field in a cloud model. *J. Climate Appl. Meteor.*, **22**, 1065-1092.

Rutunno, R., J. B. Klemp, and M. L. Weisman, 1988: A theory for strong, long-lived squall lines. *J. Atmos. Sci.*, **45**, 463-485.

Thompson, G., R. M. Rasmussen, and K. Manning, 2004: Explicit forecasts of winter precipitation using an improved bulk microphysics scheme. Part I: Description and sensitivity analysis. *Mon. Wea. Rev.*, **132**, 519-542.

Weisman, M. L., 1992: The role of convectively generated rear-in-flow jets in the evolution of long-lived mesoconvective systems. *J. Atmos. Sci.*, **49**, 1826-1847.

Weisman, M. L., J. B. Klemp, and R. Rutunno, 1988: Structure and evolution of numerically simulated squall lines. *J. Atmos. Sci.*, **45**, 1990-2013.

Yang, M.-J. and R. A. Houze 1995: Sensitivity of squall-line rear inflow to ice microphysics and environmental humidity. *Mon. Wea. Rev.*, **123**, 3175-3193.

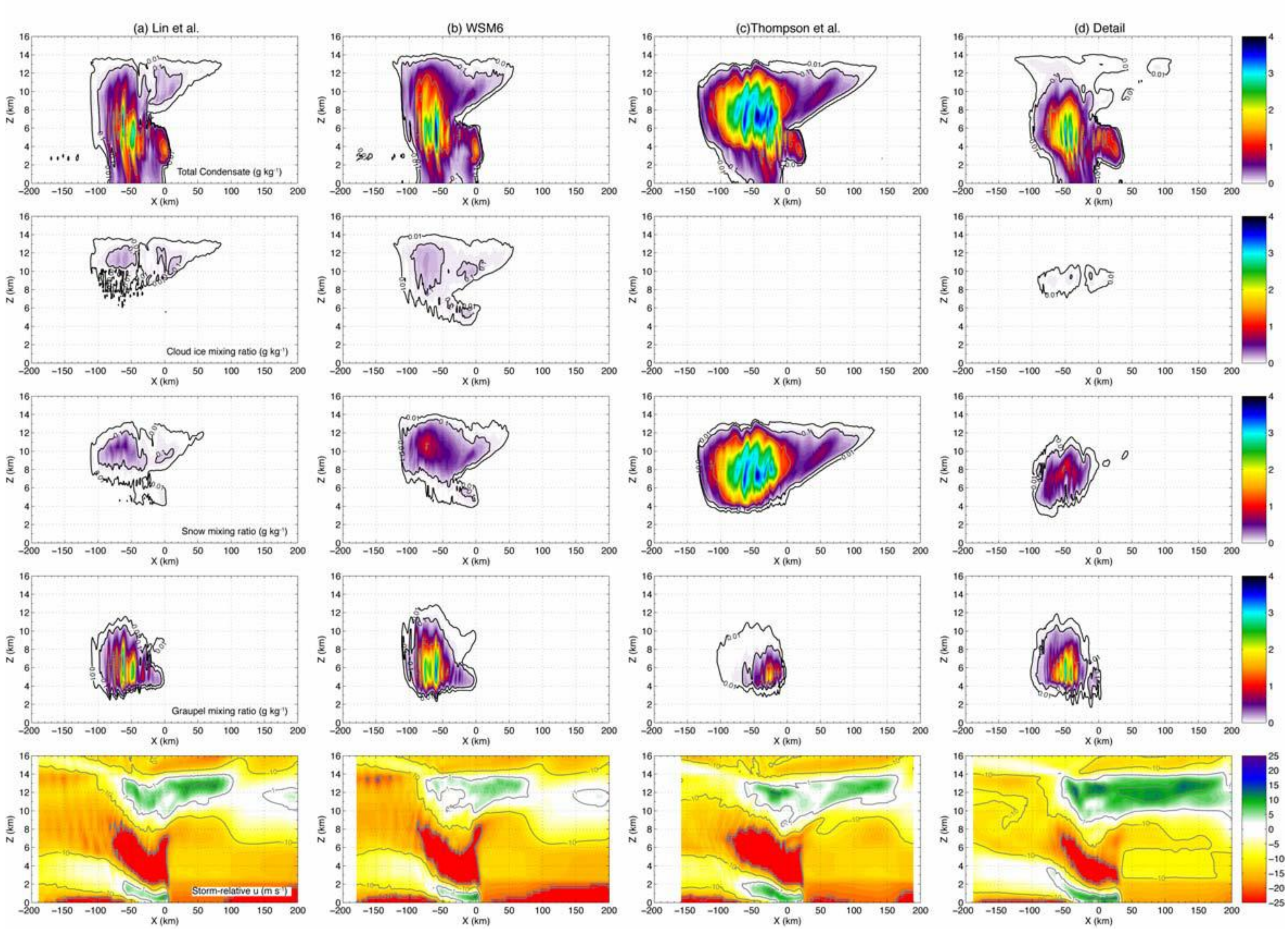

Figure 8: Average vertical cross sections of total condensate, ice, snow, and graupel mixing ratios, and storm-relative horizontal velocity (from top to bottom row) simulated with the (a) Lin et al., (b) WSM6, (c) Thompson et al., and (d) detailed microphysics schemes using the IHOP sounding. The simulation time between 2.5 and 3 h (the onset of the system breakdown period) were averaged in the Lin et al. and WSM6 schemes. For the Thompson et al. and detailed schemes, the simulation times between 3.5 and 4 h were averaged. Color scales for the individual fields are shown on the right.

EFFECTS OF ENTRAINMENT AND MIXING ON DROPLET COALESCENCE IN A SIMULATED WARM CUMULUS CLOUD

Sonia Lasher-Trapp, William A. Cooper* and Alan M. Blyth⁺

Department of Earth and Atmospheric Sciences, Purdue University, West Lafayette, IN, USA
*National Center for Atmospheric Research, Boulder, CO, USA
⁺National Centre for Atmospheric Science, University of Leeds, Leeds, UK

1. INTRODUCTION AND GOAL

Manton (1979) argued that variability in the cloud microphysical structure introduced by entrainment and mixing breaks the otherwise close link between supersaturation and vertical velocity and so can lead to broadening of the size distribution of cloud droplets. Cooper (1989), following this argument, developed a theoretical framework for estimating the broadening of droplet size distributions that can result from variability in the growth histories of cloud droplets. In that study, it was argued that the time integral of the quasi-steady supersaturation could be used to diagnose the variability of growth environments that might be experienced by droplets reaching a single point in the cloud, and that the variable microphysical structure produced by dry-air entrainment might lead to significant broadening of the size distribution of cloud droplets.

Lasher-Trapp et al. (2005) further explored the effects of variability in trajectories in cumulus clouds, using realistic cloud and velocity fields influenced by entrainment and realistic trajectories resulting from turbulent air motions. In that study, a new modeling framework was used, consisting of a large eddy simulation cloud model coupled with a Lagrangian microphysical parcel model. The cloud model represented turbulent cloud dynamics but parameterized microphysical processes such as condensation. The parcel model performed explicit microphysical calculations within the kinematic and thermodynamic constraints established by the cloud model. The Lagrangian parcel calculations made it possible to analyze the droplet trajectories resulting from turbulent entrainment and mixing as well as supersaturation histories of the droplets. The modeling results were able to replicate some important features of observed cloud droplet size distributions, including typical widths, bimodality, and the presence of small droplets high in the clouds. Calculations of droplet coalescence were not included in the parcel model because the modeling framework could not represent drop sedimentation.

Nonetheless, numerous studies (e.g. Latham and Reed 1977; Telford and Chai 1980; Baker et al. 1980) have proposed that entrainment and mixing could be important for enhancing the growth of a few of the largest cloud drops, hence helping to initiate the coalescence process and produce warm rain within the observed time scales. However, the enhanced growth could be moderated due to the activation of new CCN or reactivation of CCN produced by evaporation. In addition, to be effective, the largest cloud drops must enter high liquid water content regions of the cloud in order to grow quickly to drizzle or raindrops.

In this study, we present some new additions to the modeling framework of Lasher-Trapp et al. (2005) that include quasi-stochastic coalescence calculations within the parcel model run along the trajectories before sedimentation becomes important, and subsequent continuous collection calculations that include drop sedimentation. An example of the ability of this new modeling framework to investigate the effects of entrainment and mixing, not only on the initial size distribution of cloud droplets produced by condensation, but also on the production of drizzle and rain are presented and discussed.

Corresponding author's address: Sonia Lasher-Trapp, Dept. of Earth & Atmos. Sciences, Purdue University, West Lafayette, IN, 47907; email: slasher@purdue.edu.

2. THE MODELING FRAMEWORK

The modeling framework consists of three different models, run sequentially.

2.1 General Algorithm

- First, a high-resolution, large-eddy simulation of a cumulus cloud is created to provide 3D, time-evolving fields of the cloud properties (velocities, temperature, pressure, cloud liquid water, etc.). At some altitude within the simulated cloud, a horizontal grid of points at an "averaging level" is selected (Fig. 1). From each point on the grid, 500 backward trajectories are computed using the cloud velocities and small random perturbations to the first appearance of the cloud in the simulation.

- Next, a microphysical parcel model is initialized just below cloud base with a realistic aerosol spectrum, and the model is run forward in time along each trajectory, using the thermodynamic information along each trajectory provided by the cloud model. Activation of CCN, condensation, and quasi-stochastic coalescence are computed, and entrainment is forced in the proportion needed to give parcel characteristics matching the cloud model at each location, but drop sedimentation is not included. The parcel model is run up to the "averaging level", selected so that it is possible to neglect sedimentation of drops in the rising parcels.

- At the averaging level, each of the droplet size distributions (DSDs) from the individual 500 trajectories are averaged together, to represent the DSD expected at this point from contributions from the ensemble of variable trajectories. This new DSD is then grown forward in time (via both condensation and coalescence) to the target level. Thus, the broadening effects found by Lasher-Trapp et al. (2005) are incorporated and the influence of such broadening on the initiation of coalescence is calculated.

- At each point at the target level, droplets greater than 100 μm in diameter move along their own trajectories (determined now by both the cloud velocities and the terminal velocity of the drops) and grow by continuous collection of the cloud water from the cloud simulation. The continuous collection calculations are halted when the drops either fall below the cloud base, or the time at which the simulated cloud (dying, at this point) has mostly evaporated.

- The resulting amounts of drizzle and precipitation can then be quantified.

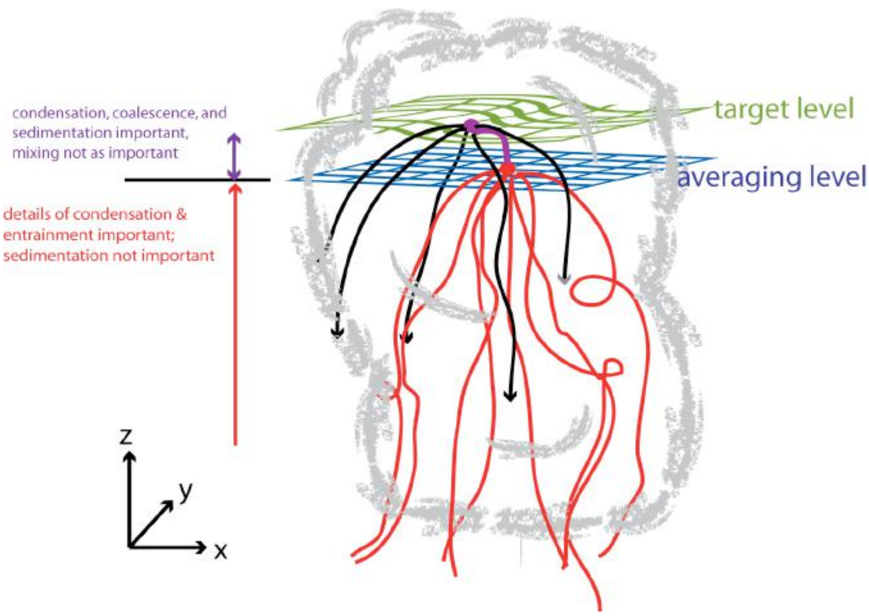

Fig. 1. Sketch of the general model algorithm described above, showing parcel trajectories (red) where entrainment and mixing have an effect on microphysical calculations within different parcels that all later reach the same point in the cloud, the trajectory followed by the DSD averaged at that point for the next 60 s up to the target level (purple), and drizzle trajectories (black) that evolve as the largest drops fall out of the parcel and grow by continuous collection.

2.2 Three-dimensional Cloud Model Simulation and Initial Trajectories

A new simulation of the Florida cumulus cloud studied by Lasher-Trapp et al. (2005) is used here, with a resolution increased to 25 m. The large-eddy simulation model is that of Straka and Anderson (1993) as adapted by Carpenter et al. (1998). The cloud is initiated from a Gaussian heat flux within a boundary layer with superimposed turbulence. The new simulation is an improvement upon that used by Lasher-Trapp et al. (2005) in that the higher resolution allows the explicit representation of smaller eddies, and thus for more explicit variability among droplet trajectories. The base of this cumulus (Fig. 2) is just below 1000 m, and the cloud top ascends for over 800 s to attain a maximum height of 4400 m, approximately 1 km shallower than that used by Lasher-Trapp et al. (2005). The maximum updraft speed in the simulated cloud is 13 m s^{-1} with a maximum liquid water content slightly over 5 g m^{-3}.

Droplet trajectories (sets of 500) are calculated from points at the "averaging level" in the simulated cloud backward in time to below cloud base (also shown in Fig. 2), using the kinematic flow fields from the large eddy simulation. Variability among the trajectories is produced by adding small, random velocity perturbations scaled to the subgrid-scale turbulent kinetic energy predicted by the cloud model at each point along the trajectory, as described by Lasher-Trapp et al. (2005).

2.3 Microphysical Parcel Model

The microphysical model of Cooper et al. (1997) is initiated at each trajectory below cloud base with a full range of aerosol sizes, including giant aerosol as described in Lasher-Trapp et al. (2005), and uses the thermodynamic fields from the large eddy simulation to calculate the supersaturation. Haze droplets are activated according to the calculated supersaturation and droplets grow by condensation as represented by the Fukuta and Walter (1970) growth equation. Quasi-stochastic coalescence among the droplets is also computed at each step using a modified Kovetz-Olund method as described in Cooper et al. (1997).

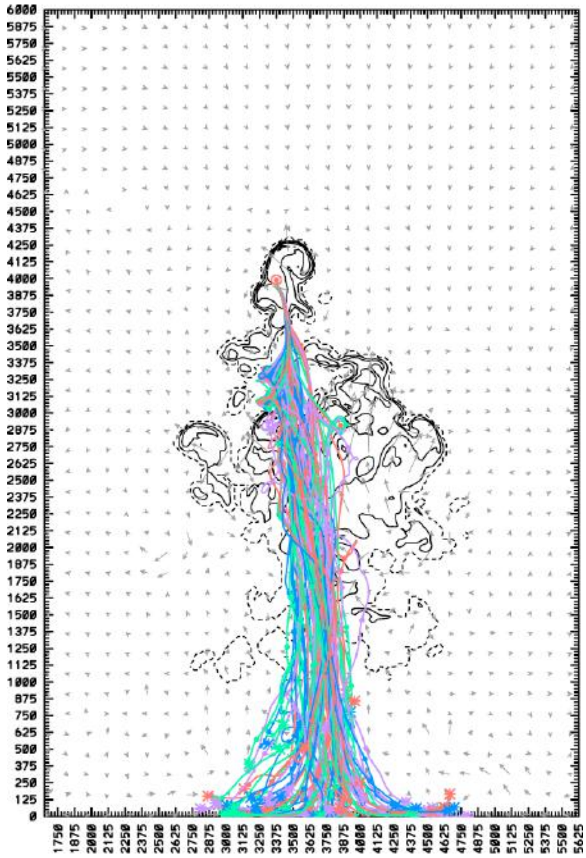

Fig. 2. Vertical cross-section of simulated cloud with contours of liquid water content (contour interval of 1 g m^{-3}, with dashed contour denoting 0.001 g m^{-3}) 12.25 min after first appearance in the simulation. Subset of 500 trajectories starting at asterisks and ending at averaging point (red bulls eye near cloud top) plotted for entire 12.25 min. Trajectories are projected into plane of the cross-section, but are in reality moving in front of and behind this plane as well.

As trajectories move through the cloud, environmental air is entrained into the parcel so that its characteristics match those of the cloud simulation at that location. Environmental CCN are also entrained and then activated if the supersaturation reaches their activation threshold. Options are included to treat the mixing and subsequent evaporation of droplets (i) as homogeneous, leading to uniform evaporation of all drops in the mean subsaturated field produced by entrainment; (ii) as inhomogeneous, leading to complete evaporation of the portion of the drops required to reach saturation and subsequent dilution of the remaining drops without evaporation; or (iii) as a mixture with different fractions of the two preceding processes.

Two changes from Lasher-Trapp et al. (2005) were introduced for this study. First, when evaporation of droplets occurred, the aerosol residue was returned to the CCN population and re-activated if the supersaturation subsequently reached the appropriate value for such activation, and this was allowed to occur repeatedly. This effect was omitted from studies reported earlier with these calculations, including those of Lasher-Trapp et al. (2005). Second, for inhomogeneous mixing, a threshold size was applied beyond which the evaporation step was suppressed. At some size, the evaporation time becomes long compared to the turbulent time scale, and it is not appropriate to apply the inhomogeneous-mixing argument at these largest sizes. Equation (3) from Lasher-Trapp et al. (2005) was used to estimate the integral time scale of the turbulence from the turbulent kinetic energy at each point in the cloud simulation, and when this was less than the evaporation time estimated from Eq. (3) in Cooper (1989), based on the environmental relative humidity, evaporation of such drops was suppressed. This was important for the present study, because otherwise a fraction of the large embryos growing on giant aerosol particles would be unrealistically evaporated and this would underestimate the contribution of such particles to the development of precipitation.

2.4 Continuous Collection Trajectory Model

Up to the grid of target points, sedimentation of the droplets from the parcel is ignored because the majority of drops have small fall velocities up to this level. Once the microphysical parcel model calculations have been run to the target points, sedimentation cannot be ignored. Those drops with diameters greater than 100 μm are initialized into the continuous collection model of Lasher-Trapp et al. (2001). These drops then fall through the cloud as determined by their terminal velocity [that is recomputed as the drops grow using the formulas of Beard (1976)] and the local cloud velocities. The drops grow by collecting cloud water through the 3D cloud simulation as it evolves in time using the collection efficiencies summarized by Rogers and Yau (1989) and collision and coalescence efficiencies reported by Beard and Ochs (1984). As the drops grow by collection, their terminal velocities increase, and the trajectories vary with time as a result (Fig. 3). There is no feedback between these drops and the simulated cloud.

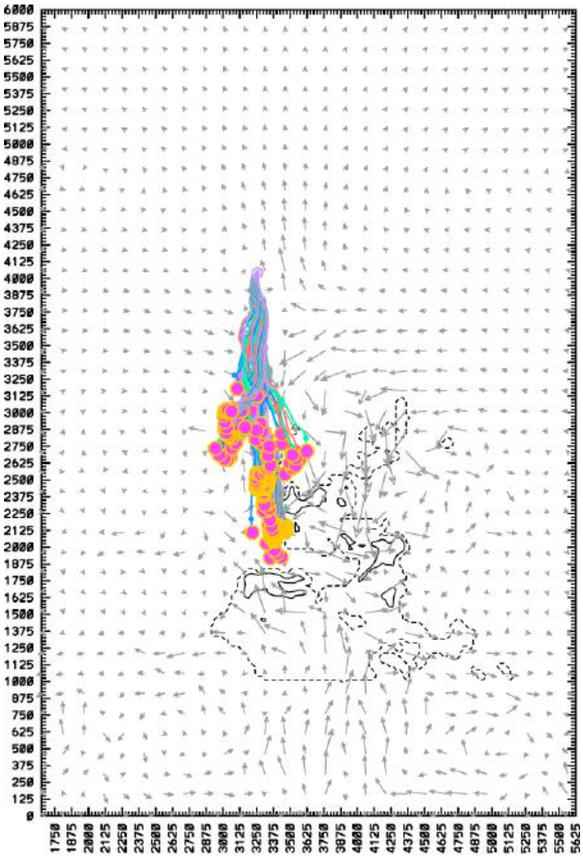

Fig. 3. As in Fig. 2, except cross-section valid 18.5 min after first appearance of cloud in simulation. Trajectories for different drop sizes computed by the continuous collection trajectory model over entire 5.25 min overlaid, starting from purple bulls eye (the target point) and ending at pink dots when the collection model is halted.

3. PRELIMINARY RESULTS

Here we highlight some results from the new modeling framework, selecting a single point at the averaging level (as shown in Fig. 1) and following the trajectories shown in Figs. 2 and 3. This analysis is designed to illustrate not only the capabilities of the new modeling framework, but also to provide an example of the effects of entrainment and mixing on the drop coalescence process.

3.1 Initial Growth to the Averaging Level

The DSD produced by averaging the DSDs among the 500 different trajectories reaching a single point at the averaging level (Fig. 4, top plots) clearly shows the influence of different supersaturation histories among the droplets resulting from entrainment and mixing, as opposed to a single adiabatic parcel traveling up to the same altitude (Fig. 4, bottom). The large-size tail of the distributions resulting from giant aerosol particles is clearly evident in all cases. Inhomogeneous mixing (top right),

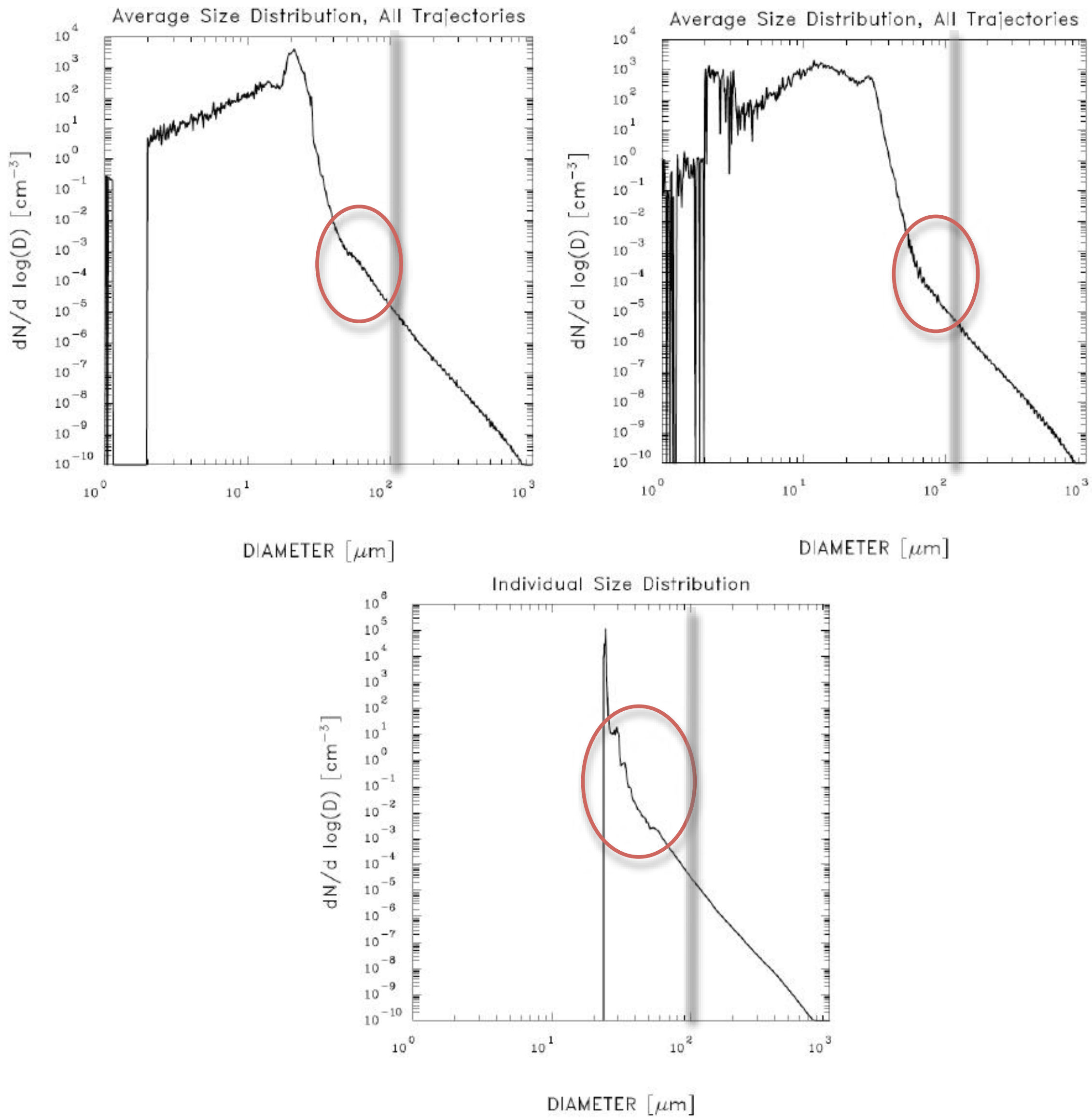

Fig. 4. DSDs produced by averaging the 500 trajectories arriving at the averaging level using homogeneous mixing assumptions (top, left) and using half-inhomogeneous mixing (top, right). DSD produced by adiabatic ascent of a single parcel is also shown (bottom). Liquid water contents for each distribution are 1.6 g m^{-3} (top, left), 1.6 g m^{-3} (top, right) and 4.9 g m^{-3} (bottom). Drop number concentrations are 379 cm^{-3} (top, left), 693 cm^{-3} (top, right), and 663 cm^{-3} (bottom). Shaded gray lines denote drop sizes 100 μm in diameter, and red circles focus on "bumps" in the size distribution produced by coalescence.

even representing just a fraction of the mixing, broadens the droplet size distribution toward smaller sizes because more entrained CCN are activated; this is also reflected in the nearly double drop concentration in the half-inhomogeneous versus the homogeneous mixing run. The peak in the DSD from condensation in the homogeneous mixing run occurs at smaller sizes compared to that for the adiabatic calculation because of the evaporation that has occurred as a result of entrainment and mixing events. The half-inhomogeneous mixing run produces a DSD with multiple peaks: one at the smallest sizes due to newly-activated entrained CCN, a very broad intermediate peak, and a lesser peak at sizes greater than that for the adiabatic distribution. This latter peak is a result of reduced competition among the droplets as a significant fraction are removed (evaporated) after each entrainment and mixing event. These results are in accord with those of Lasher-Trapp et al. (2005), despite the improvements to the inhomogeneous mixing scheme since that study was performed, as noted in Section 2.3.

3.2 Further Drop Growth to the Target Point

From the averaging level, the microphysical parcel model calculations are run forward another 60 s, to see the influence of the averaged (and broadened) DSD on the coalescence process. [In this case the parcel model is descending within the cloud for the majority of that time, as shown in Fig. 5.] The resulting DSDs for homogeneous mixing assumptions (Fig. 6) and half-inhomogeneous mixing (Fig. 6b) show that additional condensation and coalescence growth has occurred compared to their counterparts in Fig. 4, but little difference occurs within this short time in the number of drops greater than 100 μm diameter. A slight "shoulder" due to coalescence is more apparent in the homogeneous mixing case, but the number of the drops greater than 100 μm in diameter in both runs is nearly equivalent (1.1 m^{-3} for the homogeneous mixing case, and 1.6 m^{-3} for the half-inhomogeneous mixing case), because the majority of these drops have formed on the giant aerosol particles.

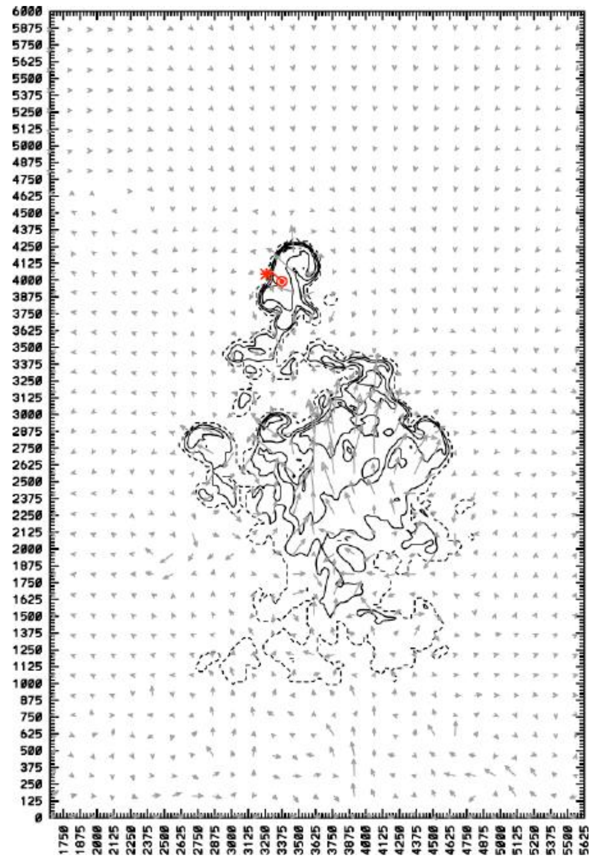

Fig. 5. As in Fig. 2, except shown is the single trajectory for the averaged DSD as it is grown for 60 s after reaching the averaging level to the target point. Asterisk denotes start of trajectory (the averaging level), and bulls eye denotes the end (the target point).

3.3 Results from Continuous Collection Trajectory Model

From the target point shown in Fig. 5, the drops greater than 100 μm diameter (from the DSDs shown in Fig. 6) are then input into the collection-trajectory model, within which they fall through the cloud at a rate determined by their terminal velocities and the local cloud velocities, resulting in a dispersal of trajectories from this point (shown in Fig. 3). The drops grow by continuous collection of cloud water from the simulated cloud during this time, and no longer interact with each other (because they are no longer collocated). The resulting growth of these largest drops (Fig. 7) is not substantial during the

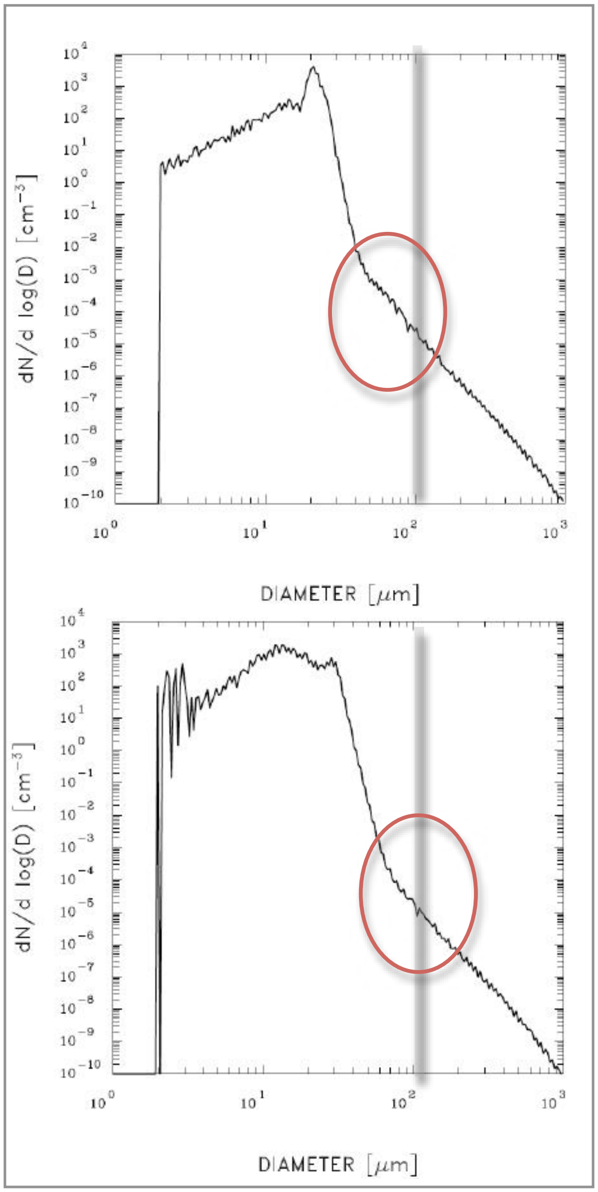

Fig. 6. As in Fig. 4, except for calculations run for 60 s past the averaging point, initialized with the averaged DSDs shown in Fig. 4 for the homogeneous mixing case (top) and half-inhomogeneous mixing case (bottom). Liquid water content for both distributions is 1.7 g m^{-3}. Drop number concentrations are 375 cm^{-3} (top) and 590 cm^{-3}(bottom).

approximately 300 sec that the continuous collection trajectory model is run because the simulated cloud is dying and evaporating. Both runs initiated using the largest drops produced by the

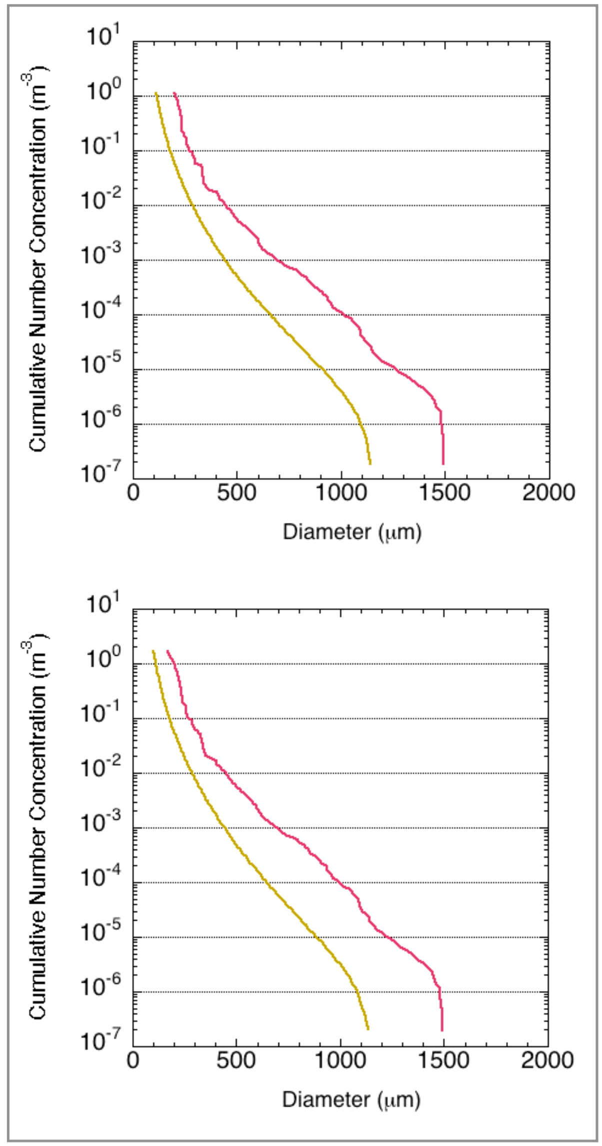

Fig. 7. Initial cumulative DSDs for drops greater than 100 μm at the target point, used to initialize the continuous collection trajectory model (gold), and the final drop sizes produced by the model occurring anywhere in the cloud (red). Top panel is for the largest drops produced by the homogeneous mixing runs, and bottom panel is for the largest drops produced by the half-inhomogeneous mixing runs. Total drizzle/raindrop number concentrations are 1.1 m^{-3} (top) and 1.6 m^{-3} (bottom).

homogeneous or half-inhomogeneous mixing calculations create raindrops over 1.5 mm in diameter, but in very small amounts, because they were primarily formed on the giant aerosol particles.

4. DISCUSSION AND FUTURE WORK

The results presented here show promise that this modeling framework can represent the influence of entrainment and mixing upon droplet size distributions that later initiate coalescence and develop into raindrops, but additional work is required to test the hypothesis that entrainment and mixing will cause an *enhancement* in the growth of the largest cloud drops that could in turn cause drizzle and raindrops to form more rapidly. Only a single point in the simulated cloud has been analyzed here, but a grid of points as shown in Fig. 1, and at different times in the cloud lifetime, will be investigated to understand and quantify the overall effect of these processes within the cloud.

An additional goal of future work, once the effects of entrainment and mixing upon raindrop formation is quantified as described above, is to compare such effects with those from giant aerosol particles. As seen in the point analyzed here, the giant aerosol will always produce a few raindrops, sometimes in very small numbers, and their contribution to the overall rain in the cloud can be compared to that from entrainment and mixing with the new modeling framework.

It is interesting that, for the one point selected here for analysis, it was necessary for the point to be high enough in the cloud to allow time for entrainment and mixing to broaden the DSD, but the time available for further growth by collision and coalescence was then limited by the demise of the simulated cloud. Preliminary experiments with target points lower in the cloud decreased the variability in the trajectories resulting from entrainment and mixing, and thus limited the broadening of the DSD and delayed the onset of coalescence. Other model runs with deeper simulated clouds might produce different results than those presented here, in that more time would be available for growth into raindrops by collision and coalescence.

5. ACKNOWLEDGEMENTS

The authors thank Dr. Jerry Straka for the continued use of his 3D cloud model, and Dr. Rich Carpenter for the use of his adaptations to that model. The cloud simulation and continuous collection calculations were run on computers made available through the Scientific Computing Division at the National Center for Atmospheric Research (NCAR). NCAR is sponsored by the National Science Foundation. The first author was funded by NSF award ATM-0342421.

6. REFERENCES

Beard, K. V., 1976: Terminal velocity and shape of cloud and precipitation drops aloft. *J. Atmos. Sci*., 33, 851-864.

____ and H. T. Ochs III, 1984: Collection and coalescence efficiencies for accretion. *J. Geophys. Res*., 89, 7165-7169.

Baker, M. B., R. G. Corbin and J. Latham, 1980: The influence of entrainment on the evolution of cloud droplet spectra: I. A model of inhomogeneous mixing. *Quart. J. Royal Meteor. Soc*., 106, 581-598.

Carpenter, R. L. Jr., K. K. Droegemeier and A. M. Blyth, 1998: Entrainment and detrainment in numerically simulated cumulus congestus clouds. Part I: General results. *J. Atmos. Sci*., 55, 3417-3432.

Cooper, W. A., 1989: Effects of variable growth histories on droplet size distributions. Part I: Theory. *J. Atmos. Sci*., 46, 1301-1311.

_____, R. T. Bruintjes and G. K. Mather, 1997: Calculations pertaining to hygroscopic seeding with flares. *J. Appl. Meteor*., 36, 1449-1469.

Fukuta, N. and L. A. Walter, 1970: Kinetics of hydrometeor growth from a vapor-spherical model. *J. Atmos. Sci*., 27, 1160-1172.

Kovetz, A. and B. Olund, 1969: The effect of coalescence and condensation on rain formation in a cloud of finite vertical extent. *J. Atmos. Sci*., 26, 1060-1065.

Lasher-Trapp, S. G., C. A. Knight and J. M. Straka, 2001: Early radar echoes from ultragiant aerosol in a cumulus congestus: Modeling and observations. *J. Atmos. Sci*., 58, 3545-3562.

______, W. A. Cooper, and A. M. Blyth, 2005: Broadening of droplet size distributions from entrainment and mixing in a cumulus cloud. *Quart. J. Royal Meteor. Soc*., 131, 195-220.

Latham, J. and R. L. Reed, 1977: Laboratory studies of the effects of mixing on the evolution of cloud droplet spectra. *Quart. J. Royal Meteor. Soc*., 103, 297-306.

Manton, M. J., 1979: On the broadening of a droplet distribution by turbulence neear cloud base. *Quart. J. Royal Meteor. Soc*., 105, 899-914.

Rogers, R. R., and M. K. Yau, 1989: *A Short Course in Cloud Physics.* 3d ed. Pergamon Press, 290 pp.

Straka, J. M. and J. R. Anderson, 1993: Numerical simulations of microburst-producing storms: Some results from storms observed during COHMEX. *J. Atmos. Sci*., 50, 1329-1348.

Telford, J. W. and S. K. Chai, 1980: A new aspect of condensation theory. *Pure Appl. Geophys*., 113, 1067-1084.

Observations of homogeneous and inhomogeneous mixing in cumulus clouds

Katrin Lehmann[1], Raymond Shaw[2], Holger Siebert[2]

[1]Scripps Institution of Oceanography, La Jolla, CA, USA
[2] Leibniz-Institute for Tropospheric Research, Leipzig, Germany

1 INTRODUCTION

The entrainment of dry air into a cloud and the subsequent mixing is of importance for the evolution of the droplet number size distribution (DNSD). Potentially, it can contribute to the broadening of the DNSD and might thus help to bridge the gap between the condensational growth and the growth by collision and coalescence.

The concept of homogeneous and inhomogeneous mixing was introduced in early 80s by Baker et al. (1984), and our current theoretical understanding still closely follows the concepts introduced in that paper. There exist two extreme mixing scenarios, which are determined by the timescales of the two governing processes: the turbulent mixing and the reaction of the microphysical and thermodynamic fields. During the homogeneous scenario, the turbulent mixing is fast compared to the reaction, and all droplets in the mixed cloud volume experience the same subsaturation at once. They all contribute by shrinking towards smaller diameters until the subsaturation is balanced. Therefore, the droplet size distribution (DSD) is shifted towards smaller diameters. In the other case of inhomogeneous mixing, the reaction proceeds faster than the turbulent mixing. In this case, the filaments of cloudy and ambient subsaturated air exist long enough to allow for single droplets at the boundary between cloudy and subsatured air to evaporate completely, while other droplets further inside the filaments don't experience the subsaturation at all. Consequently, the droplet concentration is diminished by dilution and by the complete evaporation of single droplets, while the DSD retains its mode diameter.

Following the concepts given above, the fate of the mixing is determined by the ratio of two timescales, the timescale for turbulent mixing τ_{mix} and the timescale of reaction τ_{react}. This ratio is called Damköhler number Da. For $Da \ll 1$, we expect the mixing to be homogeneous, whereas for $Da \gg 1$, we expect inhomogeneous mixing.

The timescale for an eddy of size l_0 to break down to Kolmogorov microscale l_K is given by (Baker et al., 1984)

$$\tau_{mix} = \left(\frac{l_0^2}{\varepsilon}\right)^{1/3}. \tag{1}$$

Traditionally, τ_{react} is given by the evaporation time for droplets, which for a droplet of diameter D is given by:

$$\tau_e = \frac{D^2\,(F_k + F_d)}{8\,(S-1)}, \tag{2}$$

where F_k and F_d are two thermodynamic terms associated with the heat conduction and water vapor diffusion, respectively (e.g., Rogers and Yau, 1989, pp.102). Strictly speaking, this equation is valid only for a constant subsaturation S.

On the other hand, another timescale exists

Corresponding author's address: Katrin Lehmann,
Scripps Institution of Oceanography
9500 Gilman Drive, La Jolla, CA, 92093-0221, USA
kalehmann@ucsd.edu

that characterizes how fast the subsaturation of the environment reaches its steady-state value. If we neglect source terms for the supersaturation (i.e., rising air motions) and just consider a droplet population within an unsaturated environment, the balance equation for the supersaturation can be written as:

$$\frac{ds}{dt} = -\eta\,(S-1), \tag{3}$$

where η depends on thermodynamic parameters and the integral radius $(1/(4\,n_d\,\overline{D}))$ (e.g., Rogers and Yau, 1989, pp. 110).
After $\tau_p = \eta^{-1}$, the subsaturation has reached 63% of its steady-state value. This timescale is referred to as the phase-relaxation time (Politovich and Cooper, 1988; Cooper, 1989). If $\tau_p \ll \tau_e$, the supersaturation has adjusted before droplets are completely evaporated, which limits the evaporation. In this case τ_p is the proper timescale. However, the prerequisite is that enough condensate exists for S to reach its steady-state value. On the other hand, if droplets evaporate faster than the subsaturation of the environment adjusts, τ_e is the governing timescale. Therefore, both timescale need be evaluated and compared, whereas the smaller of both timescales determines τ_{react} for the calculation of the Damköhler number.
The turbulent mixing timescale, and thus Da, strongly depends on the entrainment length scale. However, there is no clear agreement what length scale is appropriate in this sense. In fact, the situation is much more complex: the classical picture of the turbulent energy cascade, is one of a continuous spectrum of turbulent eddy sizes. For cumulus clouds this ranges from the energy injection scale, typically 100's of meters or more, down to scales at which energy is dissipated by viscosity, typically on the order of millimeters or so, and therefore, a continuous spectrum of turbulent mixing timescales and Damköhler numbers exist. As a result of this continuous range of scales, we alter the question from "what Da is observed?" to "at what scale does mixing make the transition from inhomogeneous to homogeneous?". We refer to that lengthscale as the "transition length scale l_*". For this lengthscale, Da = 1, i.e.,

$$l_* = \varepsilon^{1/2}\,\tau_{react}^{3/2}. \tag{4}$$

If the transition lengthscale lies within the inertial subrange, both homogeneous and inhomogeneous mixing are possible. All eddies of size $l > l_*$ will experience inhomogeneous mixing, whereas smaller filaments will mix homogeneously. Small transition lengthscales indicate a longer time or a higher probabilty for inhomogeneous mixing to occur, whereas a large l_* indicates a higher probability for homogeneous mixing to be observed.

2 EXPERIMENTAL

The helicopter-borne instrument payload ACTOS (Airborne Cloud Turbulence Observation System, Siebert et al. (2006a)) was used in a field campaign performed in Winningen/Koblenz, Germany in 2005.
ACTOS is equipped with high resolution turbulence sensors (e.g., a three-dimensional ultrasonic anemometer) and systems for measuring cloud microphysical properties. Single droplet measurements are performed with the Modified-Fast-Forward Scattering Spectrometer Probe (M-Fast-FSSP, Schmidt et al., 2004), which is an improved version of the Fast-FSSP (Brenguier, 1993; Brenguier et al., 1998). From the measurements of the M-Fast-FSSP, the droplet number size distribution dn_d/dD, the mean volume diameter D_v, the droplet number concentration n_d and the LWC can be inferred. The LWC is measured in addition with a Particle Volume Monitor (PVM, Gerber et al. (1994)). More technical details about ACTOS' instrumentation can be found in Siebert et al. (2003, 2006a).
ACTOS is attached to the helicopter by means of a 140 m long rope, which assures that the measurements are unaffected by the helicopter's downwash. The helicopter is operated at True Air Speeds around 15 m s^{-1}. The measurements were made in shallow warm cumulus clouds. After ascending, horizontal flight

legs in approximately constant altitudes were flown. Horizontal transects through individual cumulus clouds are analyzed with respect to the entrainment/mixing process. During most flights, ACTOS was dipped into the clouds from above while the helicopter remained outside of the clouds. Thus all measurements were made within $\sim$ 100 m from cloud top.
In the following, it will be required to know the saturation deficit of the cloud-free environmental air. Usually, a cloud-free profile was measured before the horizontal cloud legs were flown. However, the terrain was horizontally not homogeneous, and the uncertainty of the ambient saturation ration is therefore estimated to be $\sim 5\%$.

3 METHODS

Local Transition Lengthscale

Following the concepts given in the introduction, we calculate the transition lengthscale using Eq. 4. Thereby, local energy dissipation rates are calculated with a spatial resolution of about 15 m following the methods described in Siebert et al. (2006b). The drop evaporation time is calculated based on the adiabatic droplet diameter D_a and the subsaturation of the ambient air in that altitude, while the phase relaxation time is calculated based on D_a and the adiabatic droplet concentration $n_{d,a}$. The smaller of τ_e and τ_{phase} is chosen to be the reaction timescale in Eq. 4. Therefore, we are able to estimate a local value of l_* with 15 resolution.

Mixing Diagram

Brenguier and Burnet (1996) and Burnet and Brenguier (2006) proposed to study the characteristics of the mixing process by means of a mixing diagram, for which the abscissa is given by the droplet number concentration normalized by its adiabatic value $n_d/n_{d,a}$ and the ordinate is given by the cube of the mean volume diameter normalized by its adiabatic values $(D_v/D_{v,a})^3$. By choosing these coordinates, variations of the cloud base height and the sampling altitude are accounted for by the normalization with the adiabatic value. If the mixing is inhomogeneous, D_v stays constant during dilution while n_d is diminished. Thus, the measured $[n_d/n_{d,a}; (D_v/D_{v,a})^3]$ values will form a horizontal line at $(D_v/D_{v,a})^3 \sim 1$. During homogeneous mixing, the $[n_d/n_{d,a}; (D_v/D_{v,a})^3]$ both decrease with increasing fraction of entrained air and thus scatter around so-called homogeneous mixing lines. The homogeneous mixing lines are obtained by varying the fraction of entrained air and calculating the saturation deficit of the mixture and the corresponding shrinking of the droplets to account for that saturation deficit.
In addition to the thermodynamic parameters of the cloudy and ambient air, the calculation of the homogeneous mixing lines depend on $D_{v,a}$ and $n_{d,a}$.

4 RESULTS

During the field experiment in Winningen, Germany in April 2005, 10 helicopter flights in warm cumulus humilis and mediocris were performed. Out of these 10 flights, one exemplary cloud transects is chosen to illustrate the problem.
Instead of analyzing entire flights or flight legs, individual cloud transects are analyzed within this work, because the cloud fields were not horizontal homogeneous, i.e. the cloud base and height varied significantly as a consequence of the orographic structure.

In Fig. 1, a transect through Cu med cloud measured on April 24, 2005 is shown. During this passage, the flight level was approximately constant at a pressure level of 875 hPa ($\sim$ 1100 m AGL). In order to get an idea about the spatial extension of the analyzed clouds, the approximate distance flown in the respective flight leg is shown on top of the graph. Figure 1a shows the time series of the droplet number concentration, reaching maximum values up to $710\,\mathrm{cm}^{-3}$, while the mean volume diameter ranges between $5.5\,\mu\mathrm{m}$ in more diluted cloud parts where the droplet number concentration is diminished, to $12\,\mu\mathrm{m}$ in regions, where the number concentration is largest (panel b). The vertical wind velocity is shown in panel c. The regions with the highest number concentration at about 37509 - 37519 s (sec of day in UTC) are accompanied by rising air motions with $w \sim 1.7\,\mathrm{m\,s}^{-1}$, whereas descending air with $w \sim -1.3\,\mathrm{m\,s}^{-1}$ can be found in cloud free regions. The local energy dissipation rates displayed in panel d) confirm that the ascending cloud is a region of intense turbulence compared to the surroundings, with ε_τ up to $10^{-2}\,\mathrm{m}^2\,\mathrm{s}^{-3}$ in the updraft region and values between 10^{-4} and $10^{-5}\,\mathrm{m}^2\,\mathrm{s}^{-3}$ in cloud free regions.

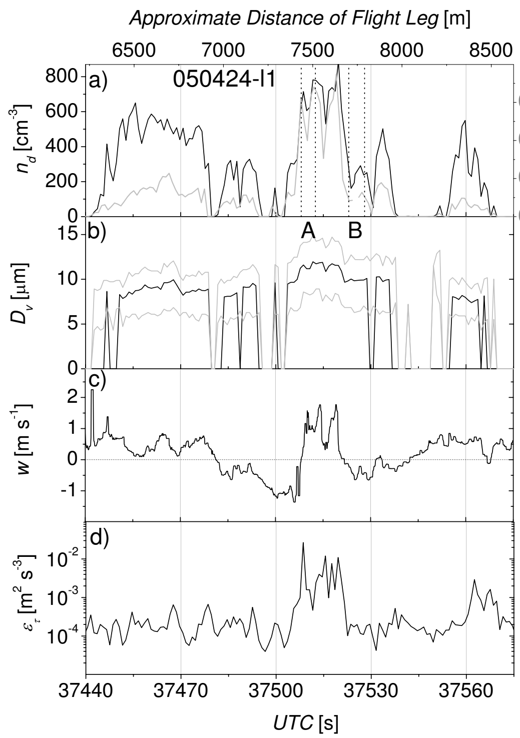

Fig 1: Droplet number density (black line, left scale) and liquid water content (gray line, right scale) with 1 s resolution (a), mean volume diameter with 1 s resolution (including 5% and 95% percentile) (b), vertical wind velocity with 0.1 s resolution (c), and local energy dissipation rates (d) measured during a passage through cumulus clouds on April 24. For regions A and B in panel a, pdfs of the droplet size are calculated and displayed in Fig. 2b.

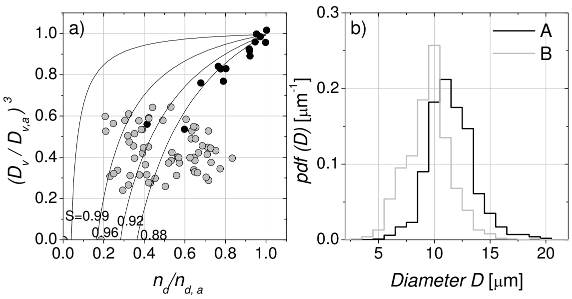

Fig 2: a)Mixing diagram for the time series shown in Fig. 1. The solid lines show values of $n_d/n_{d,max}$ and $(D_v/D_{v,a})^3$ calculated for homogeneous mixing of environmental air with different saturation ratios S following the procedure described above. The black circles correspond to the area that is marked by the black bar in Fig. 3. b): pdf of droplet size averaged over about 75 m for the regions A and B in Fig 1a.

The values of $n_d/n_{d,a}$ and $(D_v/D_{v,a})^3$ are plotted in a mixing diagram in Fig. 2a. All 1 s ($\sim$ 15 m) subsequences for which less than 100 droplets were counted for the calculation of D_v are excluded from the analysis. The subset of $[n_d/n_{d,a}\,;(D_v/D_{v,a})^3]$ marked by solid circles will be closer examined later in this section. The position of the $n_d/n_{d,a}$ and $(D_v/D_{v,a})^3$ values reveals that in some parts of the cloud the mixing is close to the homogeneous scenario as marked by the solid lines. However, for $(D_v/D_{v,n_{d,a}})^3 < 0.6$, the close correlation between the data and the homogeneous mixing lines is lost, and the mixing seems to lie between the homogeneous and the inhomogeneous scenario.

The conclusion that in some regions of the cloud the mixing is close to the homogeneous scenario is corroborated by the pdf of the droplet size is shown in Fig. 2b. The pdf (D) is calculated for the areas labeled A and B in Fig. 1a, where B represents a region which is more diluted compared to region A.

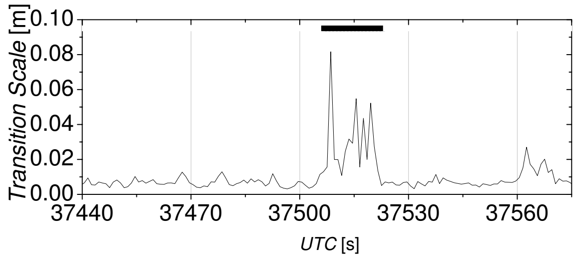

Fig. 3: Timeseries of local transition lengthscales for flight on April 24.

Figures 3 shows the timeseries of the local transition lengthscale (Eq. 4) calculated using local energy dissipation rates. The black bar indicates regions with higher local energy dissipation rate and thus larger transition lengthscales compared to the surroundings. Following the argumentation given in the introduction, homogeneous mixing is more likely to occur in this cloud region. Corresponding to the regions indicated by the black bar are the $[n_d/n_{d,a}\,;(D_v/D_{v,a})^3]$ values marked by black dots in Fig. 2a are very close to the homogeneous mixing lines.

5 SUMMARY AND CONCLUSIONS

We have presented a case study of the entrainment/mixing process made with the helicopter-borne ACTOS. In most parts of the cloud, the values of $n_d/n_{d,a}$ and $(D_v/D_{v,a})^3$ plotted in a mixing diagram indicated mixing between the two extreme cases of homogeneous and inhomogeneous mixing. However, in the cloud core, which was marked by a low degree of dilution and by high values of local energy dissipation rate, the mixing was extreme homogeneous.

We argue that a characterization of the mixing process by a single Damköhler number is not sufficient. Instead, a wide range (one order of magnitude) of Damköhler numbers exists.

In the case study above, the updraft core of the cloud was marked by a higher transition lengthscale than in the surroundings. Consequently, the probability for homogeneous mixing is higher in the turbulent updraft core. In a recent paper, Burnet and Brenguier (2006) suggested that measurements rarely resemble homogeneous mixing because the spatial averaging of the droplet-sizing instrument will bias the measurements towards the inhomogeneous mixing. In contrast to their measurements, we found regions in cumulus clouds, where the microphysical measurements clearly indicate mixing close to the homogeneous scenario. However, these regions are small and seem to be limited to the vigorous cloud core. When analyzing entire flight legs and looking for average characteristics of the mixing process, such regions can easily be missed.

The example shown above is an extreme case. Most of the clouds that we encountered during the campaign showed properties in between the two extreme mixing scenarios. Also, we made observations of extreme inhomogeneous mixing which are not shown here.

References

Baker, M., R. E. Breidenthal, T. W. Choularton, and J. Latham: 1984, 'The effects of turbulent mixing in clouds'. *J. Atmos. Sci.* **41**(2), 299–304.

Brenguier, J.-L.: 1993, 'Observations of cloud microstructure at the centimeter scale'. *J. Appl. Meteor.* **32**, 783–793.

Brenguier, J.-L., T. Bourrianne, A. A. Coelho, J. Isbert, R. Peytavi, D. Trevarin, and P. Weschler: 1998, 'Improvements of droplet size distribution measurements with the fast-FSSP (Forward Scattering Spectrometer Probe)'. *J. Atmos. Oceanic Technol.* **15**, 1077–1090.

Brenguier, J.-L. and F. Burnet: 1996, 'Experimental study of the effect of mixing on droplet spectra'. In: *Preprints 12th International Conference on Clouds and Precipitation.* Zurich, Switzerland.

Burnet, F. and J.-L. Brenguier: 2006, 'Observational study of the entrainment-mixing process in warm convective clouds'. *J. Atmos. Sci.* **64**, 1995–2011.

Cooper, W. A.: 1989, 'Effects of variable droplet growth histories on droplet size distributions. Part I: Theory'. *J. Atmos. Sci.* **46**, 1301–1311.

Gerber, H., B. G. Arends, and A. S. Ackerman: 1994, 'New microphysics sensor for aircraft use.' *Atmos. Res.*, **31**, 235–252.

Politovich, M. K. and W. A. Cooper: 1988, 'Variability of the Supersaturation in cumulus clouds'. *J. Atmos. Sci.* **45**, 1651–1664.

Rogers, R. R. and M. K. Yau: 1989, *A short course in cloud microphysics. Third edition.* Pergamon Press, Oxford, UK, 293 pp.

Schmidt, S., K. Lehmann, and M. Wendisch: 2004, 'Minimizing instrumental broadening of the drop size distribution with the M-Fast-FSSP'. *J. Atmos. Oceanic Technol.* **21**, 1855–1867.

Siebert, H., H. Franke, K. Lehmann, R. Maser, E. Saw, R. Shaw, D.Schell, and M. Wendisch: 2006a, 'Probing Fine-Scale Dynamics and Microphysics of Clouds with Helicopter-Borne Measurements'. *Bull. Am. Meteor. Soc.* **87**, 1727–1738.

Siebert, H., K. Lehmann, and M. Wendisch: 2006b, 'Observations of small-scale turbulence and energy dissipation rates in the cloudy boundary layer'. *J. Atmos. Sci.* **63**, 1451–1466.

Siebert, H., M. Wendisch, T. Conrath, U. Teichmann, and J. Heintzenberg: 2003, 'A new tethered balloon-borne payload for fine-scale observations in the cloudy boundary layer'. *Boundary-Layer Meteorol.* **106**, 461–482.

VARIABILITY OF WARM SEASON CONVECTIVE CLOUDS OVER EUROPE AND THE MEDITERRANEAN

Vincenzo Levizzani[1], Francesca Pinelli[1], Roberto Ginnetti[1], Samantha Melani[2], Massimiliano Pasqui[2], Alberto Ortolani[2], Arlene G. Laing[3], and Richard E. Carbone[3]

[1] CNR-Institute of Atmospheric Sciences and Climate, Bologna, Italy
[2] LaMMA-Institute of Biometeorology (CNR-IBIMet), Firenze, Italy
[3] National Center for Atmospheric Research, Boulder, CO, USA

1. INTRODUCTION

Quantitative precipitation forecasting (QPF) remains one of the greatest challenges in weather forecasting. Warm season precipitation episodes represent an even greater challenge as they may exhibit coherent rainfall patterns, characteristic of propagating events under a broad range of atmospheric conditions. They are frequent under weakly-forced conditions in midsummer and are strongly modulated by diurnal heating. Given the similarity in the properties of MCSs globally (Laing and Fritsch 1997), coherence in propagating characteristics is expected for precipitation all over the globe.

In the United States (US), investigations of the lifecycles of mesoscale convective systems (MCSs) have found that the majority of these systems initiate in the lee of the Rocky Mountains, move towards the east and produce an overnight maximum in precipitation across the central plains, sometimes while undergoing various cycles of regeneration (Maddox 1980, Fritsch et al. 1986; Augustine and Caracena 1994; Anderson and Arritt 1998, Trier et al. 2000). Using the Weather Surveillance Radar-88 Doppler (WSR-88D) data, Carbone et al. (2002) found that clusters of heavy precipitation display coherent patterns of propagation across the continental US with propagation speeds for envelopes of precipitation that exceed the speed of any individual MCS.

Corresponding author address: Vincenzo Levizzani, CNR-ISAC, via Gobetti 101, I-40129 Bologna, Italy, e-mail: v.levizzani@isac.cnr.it

Wang et al. (2003) developed a similar climatology for warm season precipitation in East Asia using infrared brightness temperatures from the Japanese Geostationary Meteorology Satellite (GMS). Their study showed propagation of cold-cloud clusters (or quasi-precipitation episodes) across a zonal span of 3000 km with a duration of 45 h compared with 60h for the precipitation episodes in the US.

A climatology of warm season precipitation episodes over Africa is under study using IR brightness temperatures from EUMETSAT's Meteosat satellite. Laing et al. (2008) have found that in Northern Tropical Africa convective episodes tend to initiate in the lee of high terrain, which is consistent with the principles of thermal forcing from elevated heat sources. They propagate westward under the influence of moderate low to mid-tropospheric shear, which itself varies with the African Easterly Jet migration and the West African monsoon phases. The highest frequency of intense convection occurs close to local shear maxima near high terrain features. The average diurnal frequency maxima results from the superposition of local diurnal maximum with the delayed-phase arrival of systems propagating from the east. For the peak monsoon period and from 10W to 10E, where both easterly waves and convective systems are frequent, about 35% of cold cloud episodes occur east of the easterly wave trough.

Very few observational studies exist on the span and duration of precipitation systems over Europe. Chaboureau and Claud (2003) have observed storm signatures on clouds and precipitation from the TIROS-N Operational Vertical Sounder

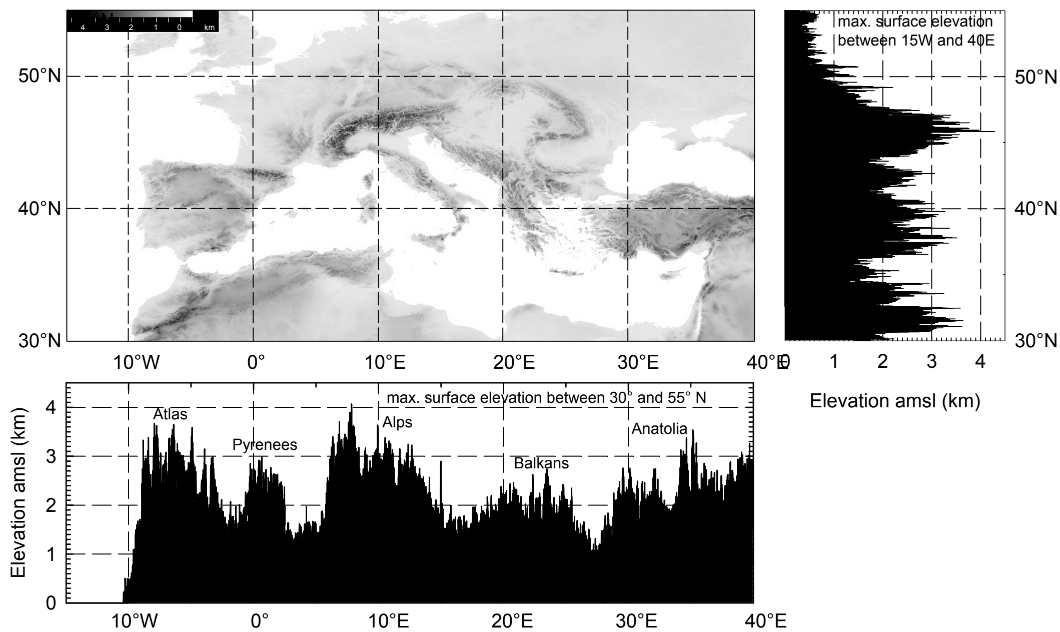

FIGURE 1. *Orography of the selected area with the major mountain chains.*

(TOVS). Chaboureau and Claud (2006) have recently adapted their technique to Mediterranean cyclones, providing a typology of cloud systems for each season, to determine the proportion of lows for which the dynamics is dominated by the upper-level situation and to examine the potential relationship between individual cloud systems and low-frequency variability.

The present study aims to produce a ten-year (1996-2005) climatology of warm season (MJJA) cold cloud systems over Europe using Meteosat IR brightness temperatures. Cold cloud persistence, span and duration of weather systems were determined to derive the zonal propagation speed and daily cycles.

2. DATA AND METHODS

Meteosat Visible and InfraRed Radiometer's (MVIRI) IR spectral band (10.5 – 12.5 μm) radiances were gathered for the 1996-2005 period May to August and brightness temperatures computed using the instrument's calibration. The IR images have a spatial resolution of 5×5 km^2 at the satellite sub-point (0, 0) and are available at 30 min intervals; the resolution at the Southern European latitudes is around 7×8 km^2. A threshold technique is used to

TABLE 1. *Number of total events, events lasting more than 3 h and events spanning more than 1000 km and lasting more than 3 h. The corresponding median phase speeds and the total number of events per each category are also reported.*

	1996	1997	1998	1999	2000	2001	2002	2003	2004	2005	mean	totals
total # of events	2797	2848	2380	2329	2313	2301	2411	2450	2587	2337	2475	24753
# events > 3h	949	1072	808	806	819	812	858	867	941	843	8787	8775
# events > 1000 km > 20 h	78	80	40	48	45	46	53	36	52	60	54	538
median speed all	8.0	8.0	8.4	8.0	8.0	7.8	7.8	8.3	8.0	8.0	8.0	
median speed > 3h	11.4	11.0	12.1	11.8	10.8	10.8	10.5	11.4	11.3	11.0	11.2	
median speed > 1000 km > 3 h	15.3	15.5	15.9	17.1	16.4	15.3	15.2	15.6	15.4	14.8	15.7	

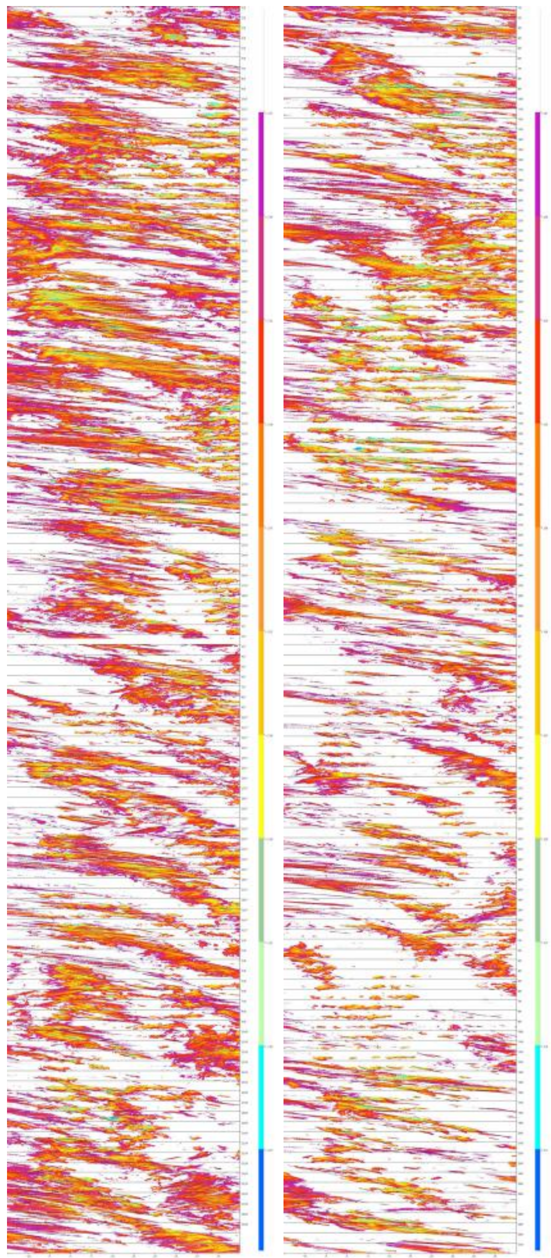

FIGURE 2. *Howmöller diagrams for 1997 (left) and 2005 (right). Time is the vertical and longitude (15 W to 40 E) is the horizontal axis. The temperature threshold for the identification of longitude-time strips*

identify the cold cloud systems that are most likely to be precipitating.

Propagation characteristics were determined using a methodology similar to that employed by Carbone et al. (2002) and Wang et al. (2004). Based on the prevailing low-level flow, the continental boundaries, and tracks of precipitating systems a large domain (30-55 N, 15 W-40 E, Fig. 1) was

TABLE 2. *Mean values in m s^{-1} of exceedance speed, cutoff span / duration ration, and median span / duration ratio for different recurrence frequencies of cold cloud systems.*

	exceedance speed	span / duration	median span / duration
1 per day	22.9	14.1	15.3
1 per 2 days	28.6	15.2	16.3
2 per week	35.2	15.5	16.3
1 per week	46.8	16.2	16.4
2 per month	72.8	16.5	16.1
1 per month	98.7	16.0	15.6

used for the Hovmöller calculations; the latitudinal span towards the north of the domain is bound by the stretching of Meteosat image pixels. Hovmöller strips of 0.05 degree longitude were drawn through the domain. The meridional information is lost while the longitudinal averaging preserves the zonal component of the flow.

3. HOVMÖLLER DIAGRAMS

Monthly Hovmöller diagrams were drawn for the ten warm seasons for a quantitative analysis on duration and span of precipitation systems. The diagrams in Fig. 2 show two examples of strips corresponding to extensive westerly systems for a relatively “wet” (1997) and relatively “dry” (2005) year. The various types of mesoscale systems correspond to strips whose longitudinal span and time duration are characteristic of the phenomenon.

A quantitative analysis was conducted on the Hovmöller strips to draw a statistics on duration, span and zonal propagation speed. The technique used to automatically identify the strips, their length and propagation angle is that proposed by Carbone et al. (2002) who give full account of its mathematical aspects. Here it is sufficient to say that a bounded rectangular autocorrelation function is superimposed to the strips to find their angle, duration and span. The function is uniform in one direction and cosine-weighted in the other.

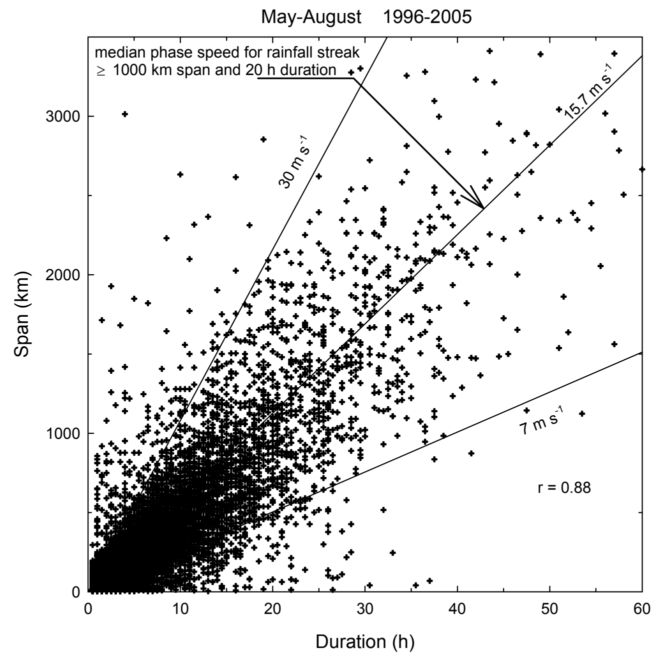

FIGURE 3. *Zonal span – duration of all precipitation system streaks May-August 1996-2005. The external lines represent the phase speeds of 7 and 30 m s^{-1}, respectively, which encompass most streaks extending more than 1000 km and lasting more than 20 h. The central line refer to the median phase speed for such systems.*

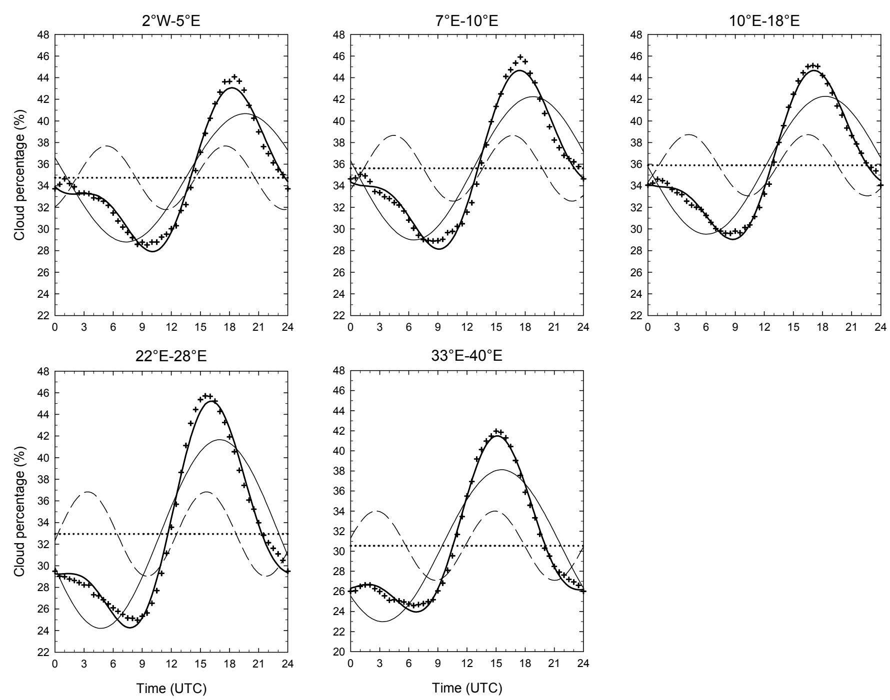

FIGURE 4. *Fourier decomposition (wavenumbers 0-2) of mean diurnal cycle of percentage of IR cloud-top brightness temperature < 241 K for the longitudinal bands where the most relevant mountain chains are located. Dotted, thin solid, dashed and thick solid are wavenumber 0, 1, 2 and their sum, respectively. Crosses represent original data before decomposition.*

Table 1 reports the number of total events, of those lasting more than 3 h and of those spanning more than 1000 km and lasting more than 20 h; the corresponding

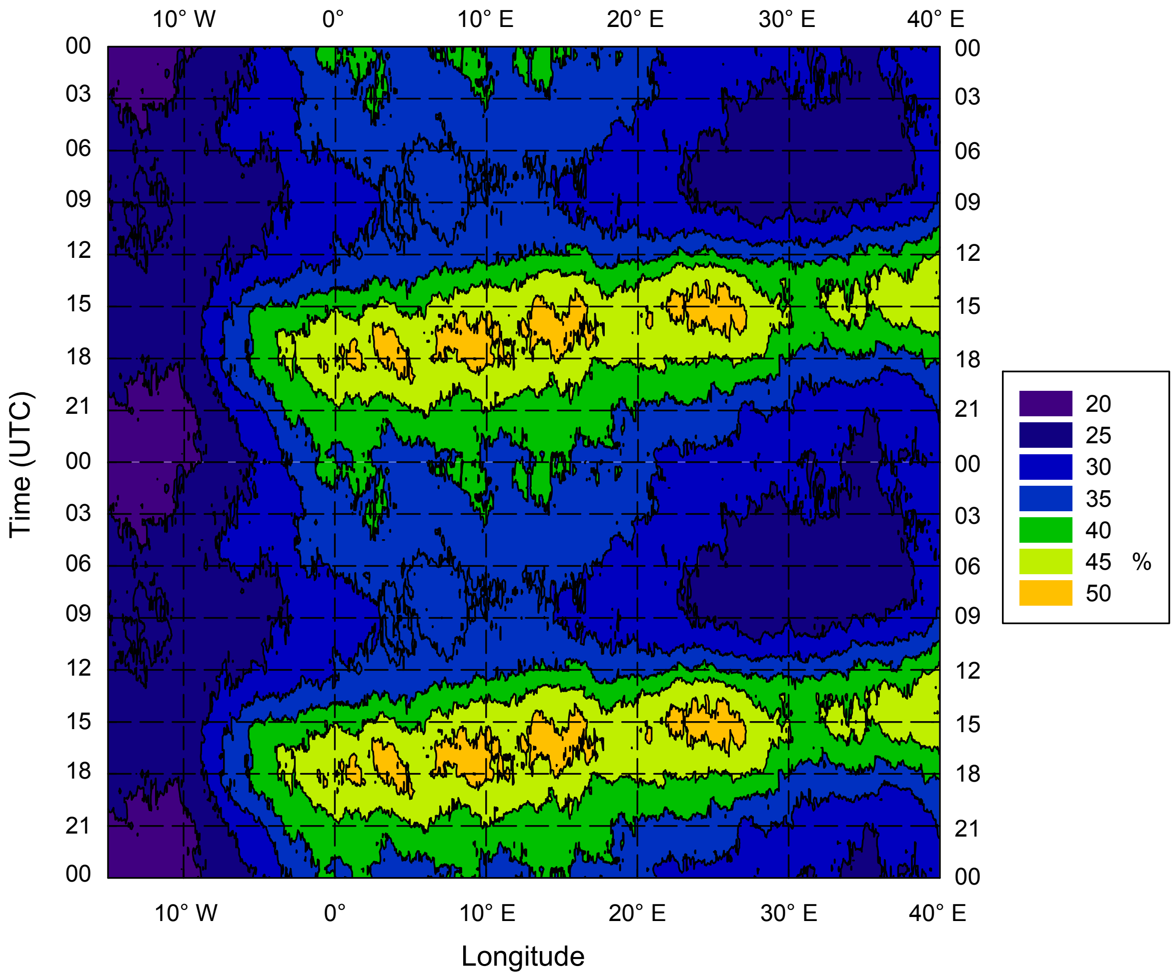

FIGURE 5. *Mean diurnal cycle of the percentage of pixels with IR cloud top brightness temperature < 241 K in the Howmöller (longitude-time) space for the entire period May-August 1996-2005. The cycle is repeated twice for better clarity.*

median phase speeds are also shown. In Table 2 three characteristic phase speeds for a number of categories are listed: a) the exceedance speed that is the span/duration ratios that are exceeded with a particular frequency, b) the cutoff span / duration ratio, and c) the median span/duration ratio.

The coordinates of each point in Fig. 3 represent the zonal span and duration of an individual cloud streak during the period May to August 1996-2005. As for Carbone et al. (2002) and Wang et al. (2004), the vast majority of them has a zonal propagation speed between 7 and 30 m s^{-1}. The median zonal phase speed for all events is 15.7 m s^{-1}.

4. DAILY AND MONTHLY CYCLE

The diurnal signal in five different longitude belts is shown after Fourier decomposition in Fig. 4. A clear maximum in the afternoon is captured shifting earlier in the day while moving towards the East, as clearly expected. As for Wang et al. (2004) the semidiurnal signal shits relatively little.

Figure 5 shows the mean cycle across all years with clearly identified five maxima in correspondence with major orography and low percentage during local night hours.

The distribution of the mean power spectrum of the time series of IR brightness temperature lower than 241 K reported in Fig. 6 shows several interesting features such as the longitudinal distribution of the

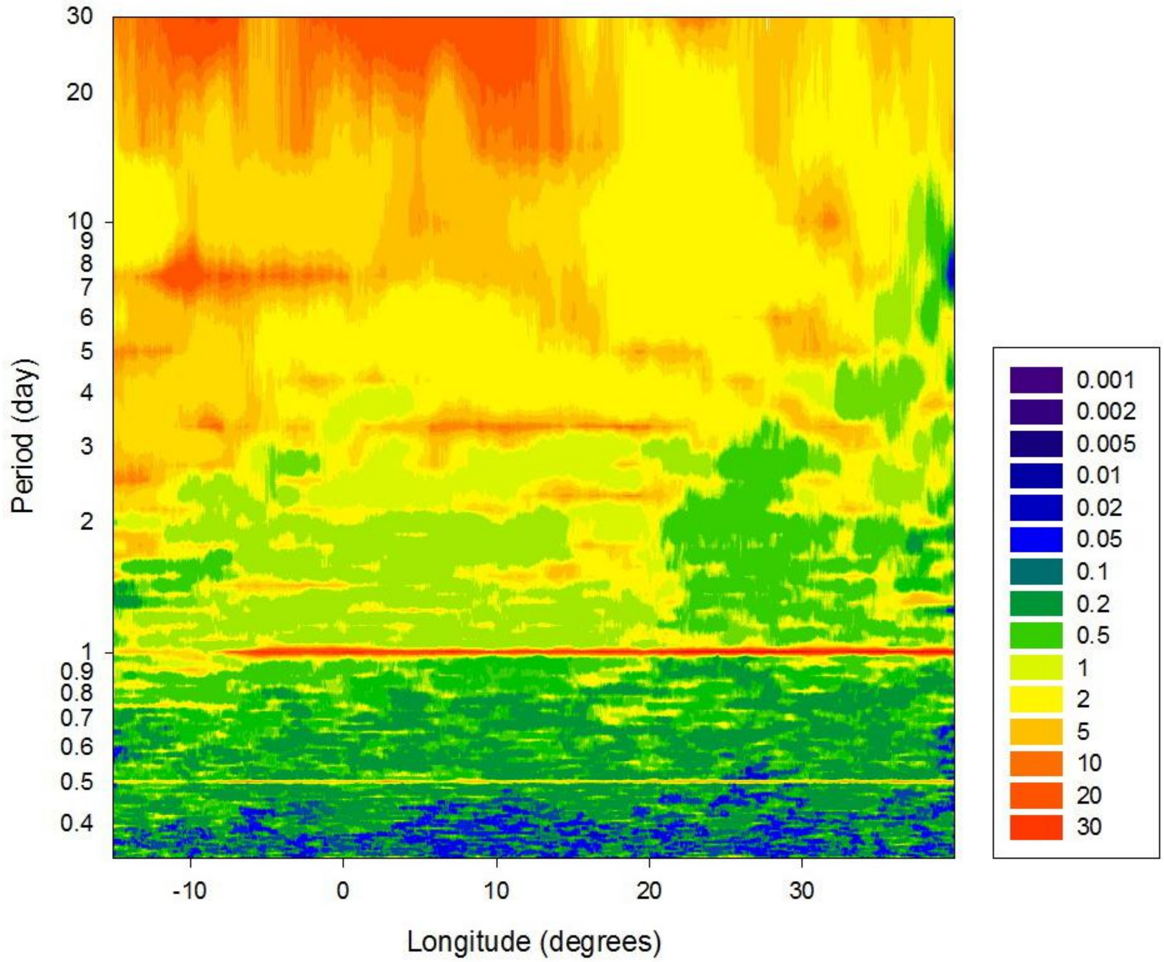

FIGURE 6. *Distribution of mean power spectrum of time series of fraction of IR brightness temperature lower than 241 K in the Howmöller space along each longitude from 15 W to 40 E as a function of the logarithmic period (day) and longitude.*

semi-diurnal and diurnal components that are strongly affected by the orography. Other longer period components are found at 3 days in correspondence with the Alps, at 7 days over the Atlantic and a significant contribution between 15 and 30 days. The analysis is not yet finished and the contribution to the cycles in the various months is to be considered so as to separate the weight of each class of phenomena individually.

5. BIBLIOGRAPHY

Augustine, J. A., and F. Caracena, 1994: Lower-tropospheric precursors to nocturnal MCS development over the Central United States. *Wea. Forecasting*, **9**, 116-135.

Anderson, C., and R. Arritt, 1998: Mesoscale convective complexes and persistent elongated convective systems over the United States during 1992 and 1993. *Mon. Wea. Rev.*, **126,** 578-599.

Carbone, R. E., J. D. Tuttle, D. Ahijevych, and S. B. Trier, 2002: Inferences of predictability associated with warm season precipitation episodes, *J. Atmos. Sci.*, **59**, 2033-2056.

Chaboureau, J.-P., and C. Claud, 2003: Observed variability of North Atlantic oceanic precipitating systems during winter. *J. Geophys. Res.*, **108(D14)**, 4435, doi:10.1029/ 2002JD003,343.

Chaboureau, J.-P., and C. Claud, 2006: Satellite-based climatology of Mediterranean cloud systems and their association with large-scale circulation. *J. Geophys. Res.*, **111**, doi:10.1029/2005JD006460.

Fritsch, J. M., R. J. Kane, and C. H. Chelius, 1986: The contribution of mesoscale convective weather systems to the warm season precipitation in the United States., *J. Climate Appl. Meteor.*, **25**, 1333-1345.

Laing, A. G., and J. M. Fritsch, 1997: The global population of mesoscale convective complexes. *Quart. J. Roy. Meteor. Soc.,* **123**, 389-405.

Laing, A. G., R. E. Carbone, V. Levizzani, and J. D. Tuttle, 2007:

The propagation and diurnal cycle of deep convection in northern tropical Africa. *Quart. J. Roy. Meteor. Soc.*, in press.

Maddox, R. A., 1980: Mesoscale convective complexes. *Bull. Amer. Meteor. Soc.*, **108**, 1374-1387.

Trier, S. B., C. A. Davis, and J. D. Tuttle, 2000: Long-Lived mesoconvective mortices and their environment. Part I: Observations from the Central United States during the 1998 warm season. *Mon. Wea. Rev*., **128**, 3376-3395.

Wang, C.-C., G. T.-J. Chen, and R. E. Carbone, 2004: A climatology of warm-season cloud patterns over East Asia based on GMS infrared brightness temperature observations. *Mon. Wea. Rev*., **132**, 1606-1629.

Wang, C.-C., G. T.-J. Chen ,R. E. Carbone, 2005. Variability of warm-season cloud episodes over East Asia based on GMS infrared brightness temperature observations. *Mon. Wea. Rev.*, **133,** 1478-1500.

ACKNOWLEDGEMENTS

One of the authors (FP) would like to recognize the University of Bologna for the support to her PhD program. Satellite data were kindly made available by the EUMETSAT archives.

THE INITIATION OF DEEP CONVECTION FROM BOUNDARY-LAYER ROLLS

J. H. Marsham[1], K. A. Browning[1], P. A. Clark[2], H. Lean[2], A. M. Blyth[1], D. J. Parker[1], and Q. Huang[1,3]

[1]School of Earth and Environment, University of Leeds, Leeds, LS2 9JT, UK
[2] Met Office Joint Centre for Mesoscale Meteorology, University of Reading, Reading, UK
[3]College of Atmospheric Sciences, Lanzhou University, China, 730000

Abstract

Predicting the precise location and timing of convective storms remains a significant challenge for numerical weather prediction (NWP), but new non-hydrostatic cloud-resolving models are allowing improvements in forecasts. Field campaigns such as the Convective Storm Initiation Project (CSIP) and IHOP_2002 have provided data with which to understand the processes involved in initiating convective storms and to evaluate NWP models.

CSIP took place in southern England in 2005, and IHOP_2002 in the Great Plains of the USA. In almost all cases from CSIP, and at least half the cases from IHOP, storms were initiated from the boundary layer and initiation from boundary-layer rolls was observed in both field campaigns. Observations and modelling of one such case (CSIP IOP 12) are presented. On this day, once the clouds had broken through the initial convective inhibition at the top of the boundary layer, they were stopped by a stable lid at approximately 2 km. The spacing of the cloud streets was observed to approximately double as the clouds broke through this lid. Despite periodic lateral boundary conditions, simulations using a large eddy model show similar behaviour. Initial results from UM simulations, which will be used to investigate the processes controlling the initiation of the deep convection are presented.

1 INTRODUCTION

The advent of high-resolution (grid-spacing $\simeq 1$ km) non-hydrostatic numerical weather prediction (NWP) models has led to a resurgence of interest in attempting to improve forecasts of the initiation of deep convection. Such NWP models do not resolve boundary-layer processes, but can resolve large deep convective systems. Recent field campaigns have also addressed the processes involved in the initiation of convection, in particular, the International H_2O Project 2002 (IHOP_2002), which took place at Southern Great Plains of the United states, the Convective Storm Initiation Project (CSIP) conducted in Southern England in 2005 and the Convective and Orographically-induced Precipitation Study (COPS), which took place in the Black Forest region of Southern Germany and Eastern France in 2007. Convective storms originated from the boundary layer in 94% of cases from CSIP (Browning et al., 2006) , and in at least 50% of cases from IHOP_2002 (Wilson and Roberts, 2006). In such cases, storms are initiated when warm moist updraughts from the boundary layer can overcome the convective inhibition (CIN) and allow deeper moist convection to develop.

Boundary-layer convection can take a variety of forms. Convective rolls have been shown to be common in the boundary layer and there is a substantial literature about them (Etling and Brown, 1993). The initiation of deep convection is often controlled by mesoscale zones of convergence (e.g., Wilson and Schreiber (1986); Bennett et al. (2006); Wilson and Roberts (2006)). However, when such mesoscale forcings are weak the variability within the boundary layer can provide a significant control on convective initiation and storms can be initiated from boundary-layer circulations, such as boundary-layer rolls (Weckwerth, 2000). Where mesoscale forcings are stronger, the intersections of mesoscale convergence lines and rolls have also been observed to provide preferred locations for the initiation of convection (e.g., Wilson et al. (1992); (Crook, 1991); (Atkins et al., 1998); (Xue and Martin, 2006)). It has been noted that the variability induced by boundary-layer rolls can make single radio soundings unrepresentative of the boundary-layer air that contributes to storms, and this can significantly affect the local lifting condensation level, CAPE and CIN (e.g., Weckwerth et al. (1996); Crook (1996)). The importance of rolls for the initiation of deep convection is, however, much less well explored than the factors controlling roll formation (Xue and Martin, 2006).

In this paper we discuss a case (CSIP IOP 12) where deep convection was observed to develop from cloud-topped boundary-layer rolls. Clouds developed through a series of lids and eventually reached the tropopause. Observations from CSIP, LEM simulations and high-resolution simulations using the Unified Model are used to explore the factors that controlled the development of convection on this day.

2 METHOD

The CSIP field campaign took place in southern England in the summer of 2005. Various instruments were deployed in the vicinity of the Chilbolton radar facility. The main steerable radar dish at Chilbolton was used with the CAMRA 3 GHz radar and the ACROBAT 1275 MHz radar. During IOP 12 radiosondes were launched from four locations within 100 km of Chilbolton. These were launched hourly from three of these sites (Reading, Swanage, Preston Farm) and every two hours from the other (Larkhill).

The non-hydrostatic Unified Model (UM, Cullen et al. (1997); Davies et al. (2005)) was run at 1.5 km grid-spacing for CSIP IOP12. This is the grid-spacing of the new operational forecast model that is being developed (currently the highest resolution operational forecast uses a 4 km grid). It was one-way nested inside 4 km, 12.5 km and 60 km grids (see Morcrette et al. (2006) and Lean et al. (2008) for details and discussion of these models). The model uses a rotated latitude/longitude horizontal grid with a terrain following hybrid-height vertical coordinate. The model includes a comprehensive set of parametrisations including those for the surface (Essery et al., 2001), boundary later (Lock et al., 2000), convection (Gregory and Rowntree (1990), with additional downdraught and momentum transport parameterisations) and cloud physics (Wilson and Ballard, 1999), using single moment cloud water, rain and combined ice and snow in the simulations shown here. In addition, simulations were performed using Version 2.4 of the Met Office large eddy model (LEM). This is a non-hydrostatic model with periodic lateral boundary conditions and no orography, and it was run with double moment microphysics. Simulations were performed in a domain oriented across the mean modelled roll orientation with a width of 50km and a length of 25 km, with a grid-spacing of 250 m.

3 RESULTS

3.1 THE OBSERVED DEVELOPMENT OF THE CONVECTION

CSIP IOP 12 (28th of July 2005) was a day of strong winds (and shear) from the south-south-west when boundary-layer convection over land became organised into longitudinal rolls, giving rise to well defined cloud streets in many parts of the CSIP area. The convective clouds were observed to break through lids at approximately 2 km and 4 km (780 and 610 hPa, Figure 1) and reach the tropopause. Deep convection then led to a damaging tornado in Birmingham, but this event was outside the region of the CSIP observational network.

The visible satellite images at 0915, 1000,1115 and 1200 UTC, shown in Figure 2(a,b,c and d), illustrate the increasingly pronounced nature of the associated cloud streets as the morning progressed. The orientation of the cloud streets was from about 194 degrees There is also some evidence of cloud formation occurring preferentially in bands transverse to this direction. This can be seen in Figure 3 to be in a region of slightly higher terrain to the west of the radar at 1000 UTC. However, the transverse banding was only a transitory feature occurring before the convection penetrated above the boundary layer (see later); when penetrative convection occurred, after 1000 UTC, the longitudinal organisation dominated.

A set of four Range-Height-Indicator (RHI) scans from the sensitive Chilbolton radar, at times roughly corresponding to the satellite images in Figs 2(a to d), is shown in Figs 4(a to d). Each of these RHIs is orientated roughly at right angles (within about + or - 20 degrees) to the axes of the convective rolls. RHI scans were made along all the azimuths shown in the overlays in Fig 2 but the specific azimuths of the RHIs shown in Fig 4 have been selected because of the clarity with which they reveal the structure of the boundary-layer convection. Except for some ground clutter mentioned in the caption to Fig 4, most of the echoes were from the clear air owing to Bragg scatter and perhaps some Rayleigh scatter from insects; however, the green and yellow echoes in the last two scans is an indication of developing precipitation.

The columnar echoes in the scans shown in Fig 4 were associated with the convective plumes. They are most likely due to the refractive-index inhomogeneities within the turbulent plumes, supplemented by the developing precipitation in the later stages. In some cases the vertical columns are less well defined or abundant, and the columns are replaced by mantle echoes (see ranges 46 and 58 km in Fig 4(b), for example). These are believed to be due to the refractive-index inhomogeneities at the tops of the convective plumes where they encountered a stable lid near or below 2000 m. Less markedly perturbed parts of the lid are evident in Fig 4(b) in the layer echoes between 1500 and 1700 m at ranges between 20 and 30 km: these perturbations were prob-

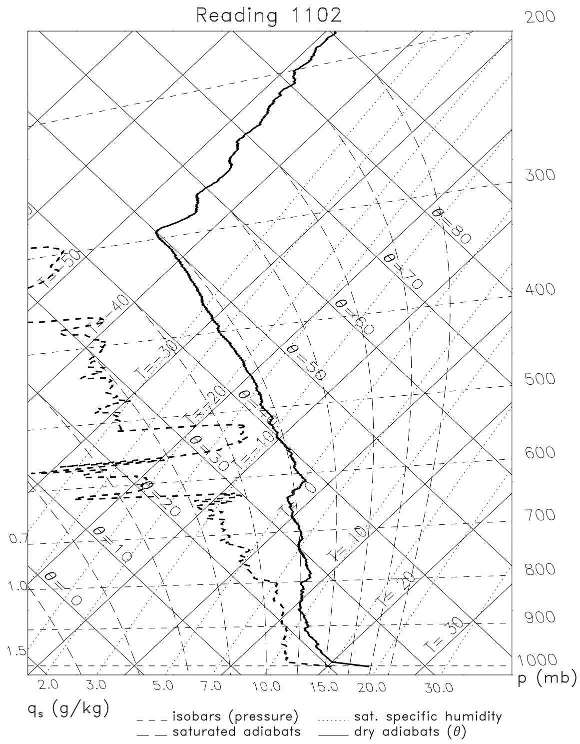

Figure 1: A tephigram from the 1102 UTC radiosonde sounding from Reading (approximately 50 km from the Chilbolton radar, see Figure 2).

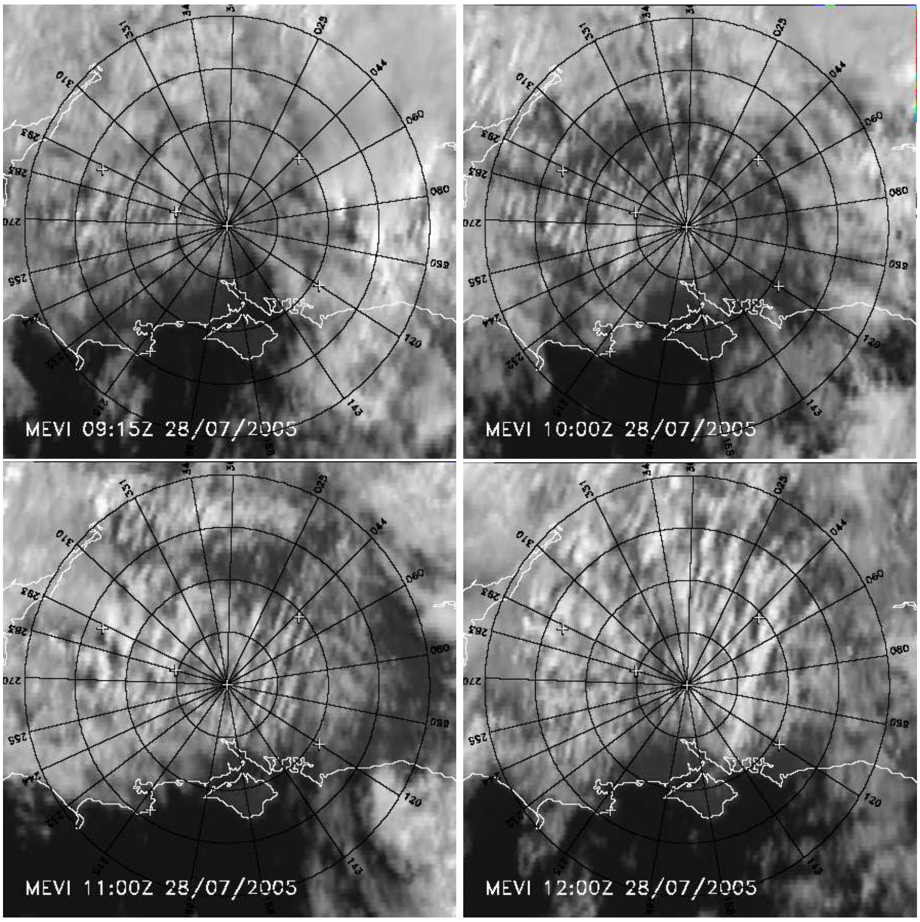

Figure 2: Visible satellite images from Meteosat at (a) 0915 (b) 1000 (c) 1115 and (d) 1200 UTC. Range rings from the Chilbolton radar (25 km spacings) are shown, as well as the directions in which RHI scans were made. Radiosondes were launched from the radar site and locations shown by crosses ("+"). Reading is approximately 50 km north-east of Chilbolton.

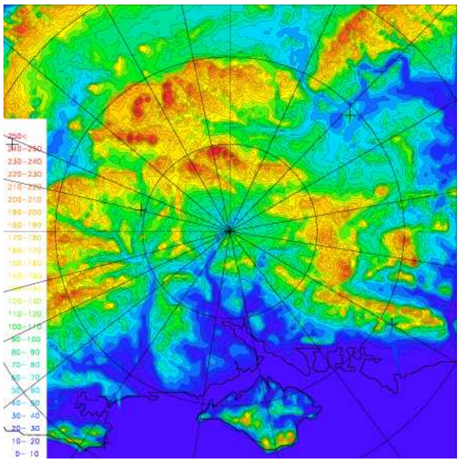

Figure 3: The orography in the vicinity of the Chilbolton radar. Hills reach 300 m above sea level (>250 m are shown in red). Range rings from the Chilbolton radar (25 km spacings) are also shown.

ably due to the lid being impacted by rather weaker convection. Even where the columnar echoes were present there was sometimes evidence of associated mantle echoes. This is seen most clearly in Fig 4(a), at 36 and 42 km ranges, suggesting in this case a crest-to-trough amplitude of the convectively perturbed lid of about 200 m. Forty-two minutes later (Fig 4(b)) the shape of the mantles suggests a crest-to-trough amplitude of the convectively perturbed lid of at least 500 m. At the later times (Figs 4(c and d)) some of the convective tops are seen to have risen up to 3500 m and, although there is no radar evidence of the lid in the immediate vicinity of the deeper convection, a few tens of kilometres closer to the radar the lid can be seen at heights close to 2000 m, suggesting convective penetration of the lid of perhaps in excess of 1000 m.

An intriguing feature of the time period we are examining is the change in spacing of the convective rolls as the convection deepened with time. The increasing spacing is evident not only in the satellite images in Fig 2; it is evident also in the RHIs . Thus, the first RHI, for 0915 UTC (Fig 4(a)), shows radar echoes associated with convective plumes centred at 22, 29, (33), 36, 42, 48, 54 and 62 km, corresponding to a spacing of about 6 km (closer to 5 km when resolved normal to the direction of the convective rolls). As noted above, the convection at this time appeared to be penetrating

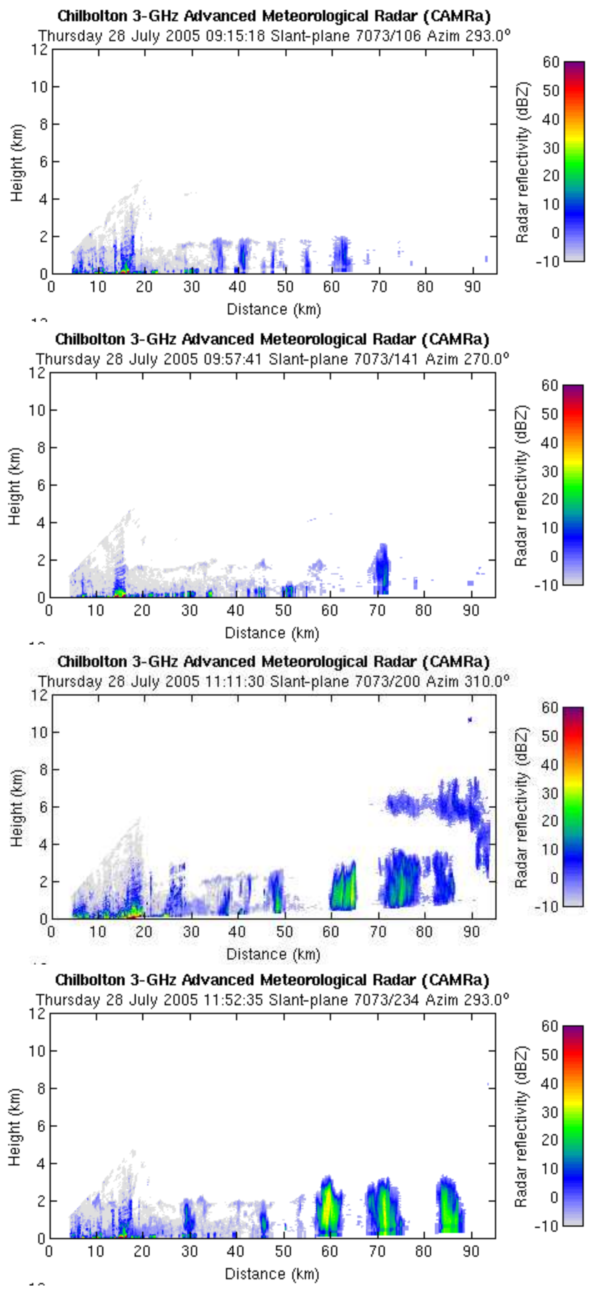

Figure 4: RHI scans from the 10 cm wavelength Chilbolton radar at a sequence of times corresponding roughly to the cloud images in Fig **??**: (a) 0915 UTC along 293°, (b) 0957 UTC along 269° deg, (c) 1111 UTC along 309° and (d) 1152 UTC along 292°. Most of the echoes are clear (or cloudy)-air echoes, but the green and yellow parts of the echoes are due to precipitation. The echo in (c) up to 3000 m between 25 and 28 km range is shown by its Doppler return (not shown) to be due to ground clutter; otherwise ground clutter beyond 20 km range is confined mainly to below 500 m.

about 200 m into a stable lid situated between 1500 and 2000 m.

Figure 4(b) shows that by 0957 UTC the level of the convective tops had risen, mainly to between 1700 and 2200 m, but with one of the tops having risen as high as 3000 m. Although there is a hint of convective features with spacing similar to that in Fig 4(a), (namely those in Fig 4(b) at 35, 39 and 46 km), the principal convective features (at 35, 46,58 and 70 km), were by then more widely spaced. This was the first hint of the rolls with 12-km spacing that came to dominate the field of convection by the end of the morning. As noted earlier, the convection was penetrating the stable lid by at least 500 m by this time.

Figure 4(c) shows that, by 1111 UTC, the tops of the convection had risen to between 2000 and 3800 m. As in Fig 4(b), the spacing of the main tops was about 12 km, these tops being at 37, 49, 62, 74 and 83 km; however, a weak convective feature can also be seen at 41 km perhaps corresponding to a residual convective feature with the narrower spacing. The situation was similar at 1152 UTC (Fig 4(d)): the deep convective plumes are seen to have been spaced at about 13 km but again there is evidence of intermediate convective plumes, giving a spacing of about 6 km, at close ranges where the convection was still relatively shallow.

A summary of the evolving attributes of the convective rolls described above is given in Table 1. The table pertains specifically to the region to the west of Chilbolton; this is because the RHI evidence of roll spacing was clearest in this direction. (Although the rolls were well defined in terms of cloud streets to the north-east of Chilbolton, they were less so when scanned roughly at right-angles to their axes, *i.e.* along 100 or 120 deg from Chilbolton). Table 1 highlights the evidence that the doubling in the spacing of the convective rolls coincided with the convection penetrating significantly (*i.e.* more than 1000 m) above the lid. There is also a suggestion in Figs 4(c and d), at ranges closer than 50 km, that plumes in alternate convective rolls, although still penetrating only a little above the lid, were beginning to intensify as part of the transition from about 6 to 12 km spacing; presumably the intermediate plumes decayed altogether when the convection penetrated far above the lid, leaving just the more widely-spaced convective rolls.

Large eddy model simulations showed cloud-topped boundary layer rolls and gradually deepening moist convection. The cloud streets were not as linear as observed, and sensitivity studies to domain size, orientation and model resolution suggested that this may be due to the periodic boundary conditions allowing the rolls to "wrap around"

	Within 50 km of radar		Beyond 50 km of radar	
Time(UTC)	Max ht (m)	Spacing (km)	Max ht (m)	Spacing (km)
0915	2000	6	2000	6
0957	2100	ill-defined	3000	12
1111	2600	5	3700	10
1152	2300	6	3400	12

Table 1: Summary of attributes (maximum height and horizontal spacing) of the evolving convective rolls to the west of the Chilbolton radar

and interfere with each other. Despite this lack of linearity compared with the observations, spacings and orientations of the cloud streets and boundary-layer rolls could be calculated by Fourier analysis of liquid water path and vertical velocities in the boundary layer. Figure 5 shows that the modelled cloud streets undergo a sudden changes between particular spacings. The initial modelled cloud streets have the same spacing as the boundary layer rolls (approximately 2 km). This then increases to approximately 5 km and then 12 km as the clouds deepen to approximately 3 km. The boundary-layer rolls spacings scales more simply with the boundary-layer depth and reaches a maximum of approximately 3 km. It is interesting that the large eddy simulations produce these sudden jumps in cloud-street spacings, but their lack of linearity compared with the observations suggests a model without periodic boundary conditions should be employed. Figure 6 shows initial results from a simulation using the UM.

Figure 6 shows the UM gives cloud streets west of Chilbolton by 1100 UTC, but none to the east, where they were also observed (Figure 2). Some evidence of the transverse modulation observed (which was perhaps linked to orography) is also apparent in the model at this time. In the model there is no well defined cloud street present downwind of the Isle of Wight (the island shown just off the south coast of England) until 1300 UTC, whereas the satellite observations show that this had formed by 1200 UTC. The pair of cloud streets shown in this region by the UM are, however, similar to those observed, in their position, orientation and spacing.

The initial spacing of the cloud streets observed (6 km) is barely resolved by a model with a 1.5 km grid-spacing and in the model an aliasing of small scale features to larger scales might be expected. An investigation using smaller grid-spacings (500 m and 250 m) will be used to investigate this, the devel-

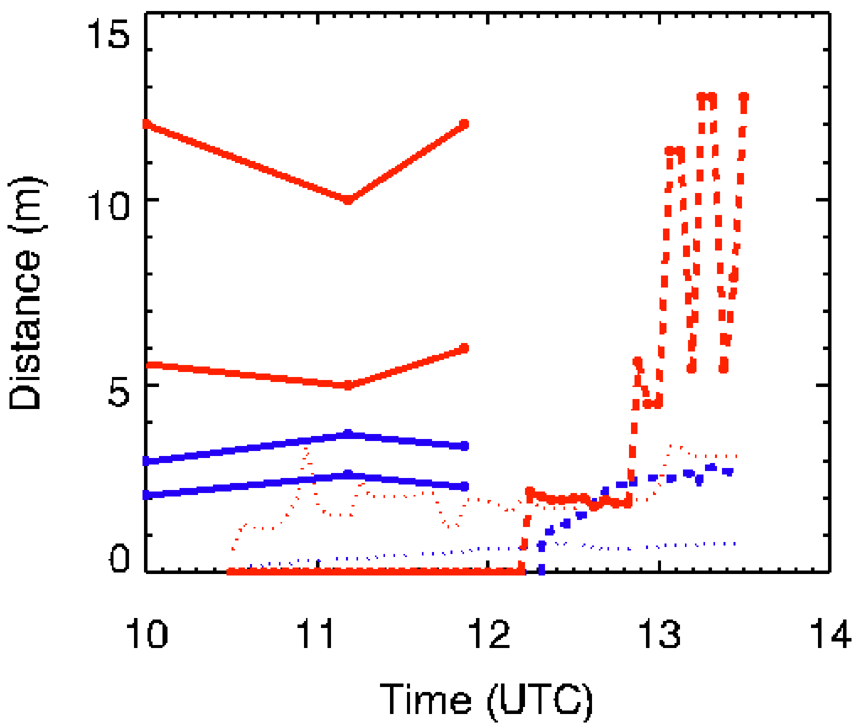

Figure 5: Time-series cloud-street and boundary-layer roll spacings (red) and heights (blue) from observed clouds (solid), clouds in the LEM (dashed) and boundary-layer rolls in the LEM (dotted). The two areas observed are listed in Table 1. Values from the LEM were calculated objectively from Fourier analysis of model fields.

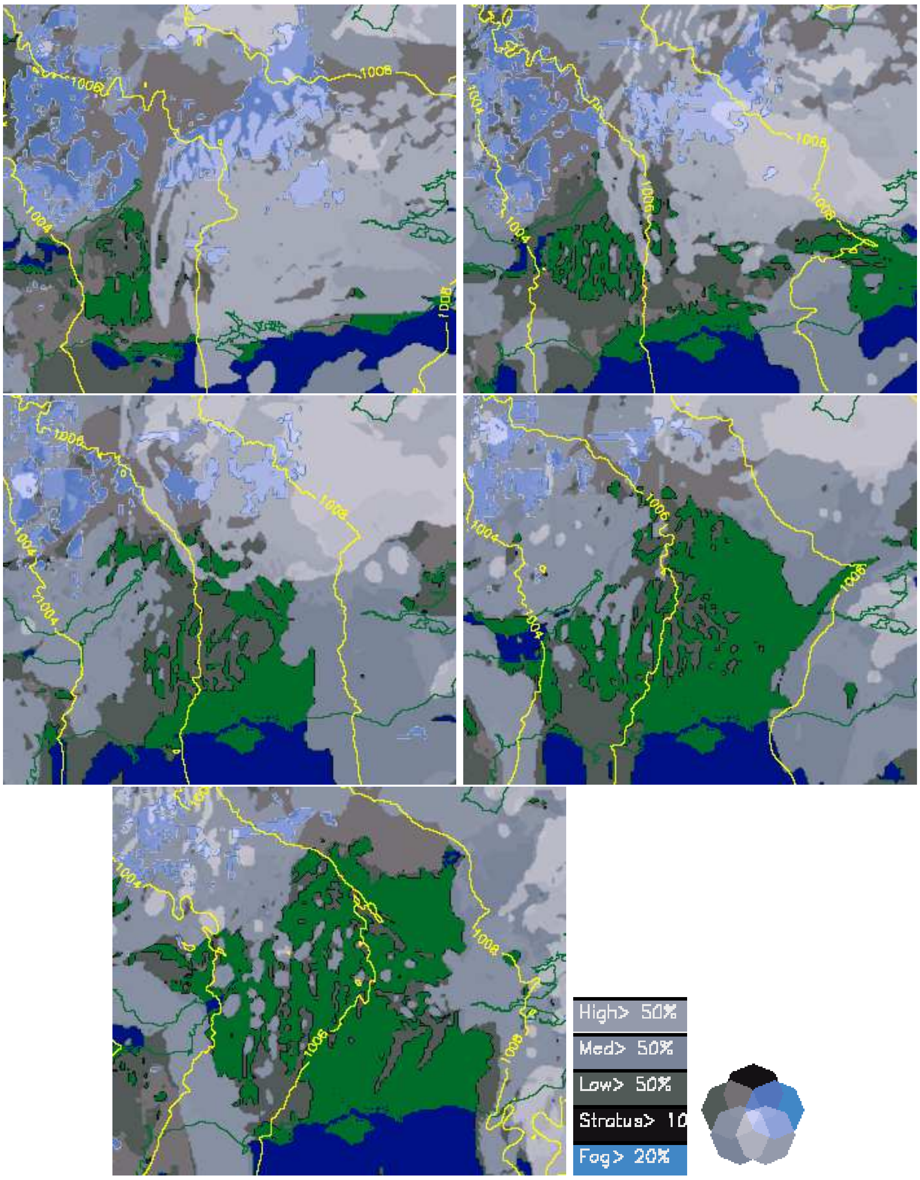

Figure 6: Forecast cloud cover from the Unified Model (UM) running from 9 UTC with a 1.5 km grid-spacing. Contours of pressure at mean sea level are also shown.

opment of the cloud streets and the role of orography and coastal convergence. The study will then focus on the effects of entrainment and mixing in limiting the height of the developing clouds.

4 CONCLUSIONS

CSIP IOP 12 provides a well observed case of deep convection developing from boundary-layer rolls. The deep convection developed through a series of stable lids, which is not unusual for the maritime climate of the UK. Observations suggest that the spacing of the cloud streets approximately doubled as the cloud penetrated a lid at approximately 2 km (*i.e.* convective tops reached 3 km or more), perhaps as a result of alternate streets developing/dissipating. Discrete changes in cloud-street spacings were observed in LEM simulations of this case, but the cloud streets were not as linear as observed. This was probably due to the periodic lateral boundary conditions in the LEM. Initial results from UM simulations using 1.5 km grid-spacings are encouraging, and higher resolution simulations will be used to investigate the processes controlling the development of deep convection in this case.

5 Acknowledgements

The work was supported by NERC grants NER/O/S/2002/00971 and NE/E006124/1". We would like to thank all those involved in the CSIP field campaigns. Meteosat data was obtained form EUMETSAT and observations from Chilbolton were courtesy of the Chilbolton Facility for Atmospheric and Radio Research (CFARR) at the CCLRC Chilbolton Observatory, distributed via the NERC British Atmospheric Data Centre (BADC).

References

Atkins, N. T., Wakimoto, R. M., and Ziegler, C. L.: Observations of finescale structure of a dryline during VORTEX, Mon. Weather Rev., 126, 525–550, 1998.

Bennett, L. J., Browning, K., Blyth, A. M., Parker, D. J., and Clark, P.: A review of the initiation of precipitating convection in the United Kingdom, Quart. J. Roy. Meteor. Soc., 2006.

Browning, K., Morcrette, C., Blyth, A., Bennett, L., Clark, P., Corsmeier, U., et al.: A summary of the Convective Storm Initiation Project Intensive

Observation Periods, Met Office, Forecasting Research Technical Report, 474/JCMM Report No 153, 2006.

Crook, A.: Small-scale moisture variability in the convective boundary layer and its implications for nowcasting, 25th Conf. on Radar Meteor., Paris, France, pp. 67–70, 1991.

Crook, N.: Sensitivity of moist convection forced by boundary layer processes to low-level thermaldynamic fields, Mon. Weather Rev., 124, 1767–1785, 1996.

Cullen, M. J. P., Davies, T., Mawson, M. H., James, J. A., Coulter, S. C., and Malcolm, A.: An overview of numerical methods for the next generation UK NWP and climate model, Numerical methods in atmospheric and oceanic modelling, pp. In The Andre J. Robert memorial volume. Edited by Charles A. Lin, Rene Laprise and Harold Ritchie, Canadian Meteorological and Oceanographic Society, Canada, 425–444, 1997.

Davies, T., Cullen, M. J. P., Malcolm, A. J., Mawson, M. H., A., S., White, A. A., and Wood, N.: A new dynamical core for the Met Office's global and regional modelling of the atmopshere, Quart. J. Roy. Meteor. Soc., 608, 1759–1782, 2005.

Essery, R., Best, M., and Cox, P.: MOSES 2.2 Technical Documentation, Hadley Centre Technical Report No. 30, p. Met Office Hadley Centre, 2001.

Etling, D. and Brown, R. A.: Roll vortices in the planetary boundary layer: A review, Boundary-Layer Meteorol., 65, 215–248, 1993.

Gregory, D. and Rowntree, P. R.: A mass flux convection scheme with representation of cloud ensemble characteristics and stability-dependent closure, Mon. Weather Rev., 118, 1483–1506, 1990.

Lean, H. W., Clark, P. A., Dixon, M., Roberts, N. M., Fitch, A., Forbes, R., and Halliwell, C.: Characteristics of high resolution versions of the Met Ofice Unified Model for forecasting convection over the UK, MWR, pp. In press (http://ams.allenpress.com/perlserv/?request=get–toc–aop&issn=1520–0493% ct=1), 2008.

Lock, A. P., Brown, A. R., Bush, M. R., Martin, G. M. B., and Smith, R. N. B.: A new boundary layer mixing scheme. Part I: Scheme description and single-column model tests, MWR, 128, 3187–3199, 2000.

Morcrette, C. J., Lean, H., Browning, K. A., Nicol, E. G., Clark, P. A., Russell, A., and Blyth, A. M.: Combination of mechanisms for triggering an isolated thunderstorm: observational case study of CSIP IOP 1, Submitted to Mon. Weather Rev., 2006.

Weckwerth, T. M.: The Effect of Small-Scale Moisture Variability on Thunderstorm Initiation, Mon. Weather Rev., 128, 4017–4030, 2000.

Weckwerth, T. M., Wilson, J. W., and Wakimoto, R. M.: Thermodynamic variability within the convective boundary layer due to horizontal convective rolls, Mon. Weather Rev., 124, 769–784, 1996.

Wilson, D. R. and Ballard, S. P.: A microphysically based precipitation scheme for the UK Meteorological Office Unified Model, Quart. J. Roy. Meteor. Soc., 125, 1607–1636, 1999.

Wilson, J. W. and Roberts, R. D.: Summary of Convective Storm Initiation and Evolution during IHOP: Observational and Modeling Perspective, Mon. Weather Rev., 134, 23–47, 2006.

Wilson, J. W. and Schreiber, W. E.: Initiation of Convetive Storm at Radar-Observed Boundary Convergence lines, Mon. Weather Rev., 114, 2516–2536, 1986.

Wilson, J. W., Brant-Foote, G. B., Crook, N. A., Fankhauser, J., Wade, C. G., Tuttle, J. D., Mueller, C. K., and Krueger, S. K.: The role of boundary-layer convergence zones and horizontal rolls in the initiation of thunderstorms: A case study, Mon. Weather Rev., 120, 1785–1815, 1992.

Xue, M. and Martin, W. J.: A high-resolution modeling study of the 24 May 2002 dryline case during IHOP. Part II: Horizontal convective rolls and convective initiation, Mon. Weather Rev., 134, 172–191, 2006.

CHARACTERISTICS OF PRECIPITATION PHYSICS IN THE CONVECTIVE CELLS IN A HUMID ENVIRONMENT

*Mariko Oue, Hiroshi Uyeda, and Yukari Shusse
Hydrospheric Atmospheric Research Center, Nagoya University, Nagoya, Japan

1. INTRODUCTION

Meso-γ-scale convective cells are components of a precipitation system, which sometimes produces heavy rainfalls. A large number of precipitation particles in a convective cell produce a strong rainfall when they reach the ground. Distributions of precipitation particles in the convective cell vary with formation processes. Therefore, it is important to clarify the distribution of precipitation particles in the convective cell for understanding precipitation physics.

Polarimetric radar is available to characterize properties of precipitation particles. Polarimetric variables have information of various properties of precipitation particles which predominate within a sensitive volume of a radar observation. To clarify the distribution of precipitation particles in a convective cell, a direct observation of raindrop size distribution (DSD) is effective in addition to the polarimetric radar observation.

Several studies have been made on precipitation particles in severe convective cells (e.g. Zeng et al., 2001). These convective cells grew above the height of 0°C level (0°C-height) in echo-top of 30 dBZ. However, in a humid environment, as in Okinawa, Japan, during a rainy season, called the "Baiu", from June to July, convective cells have low echo-top heights. Shinoda et al. (2007) represented that convective cells around Okinawa Island during the Baiu period have low altitudes of reflectivity peaks (1.5-2.0 km altitude) and low echo-top heights of 30 dBZ (around 0°C-height) by statistical studies. Shusse et al. (2006) analyzed the characteristics of polarimetric variables in relatively shallow convective cells around Okinawa Island during the Baiu period using a C-band polarimetric radar. They showed that a convective cell embedded in stratiform precipitation area existed with small raindrops below the height of 2 km dominantly.

Convective cells exist not only in a convective rain zone but also in a stratiform rain zone associated with a precipitation system around Okinawa during the Baiu period. Distributions of precipitation particles in the convective cells with low echo-top heights are not revealed. To understand precipitation physics of convective cells developing in the humid environment, it is necessary to clarify distributions of precipitation particles in these convective cells existing in the stratiform rain zone and convective rain zone. We made observations at Okinawa Island during the Baiu period in 2006 using a C-band polarimetric radar and a disdrometer which measures DSD on the ground.

2. OBSERVATION AND DATA

In our observation, the C-band polarimetric radar (COBRA: CRL Okinawa bistatic polarimetric radar) and a Joss-Waldvogel disdrometer of Okinawa Subtropical Environment Remote Sensing Center, National Institute of Information and Communications Technology, Japan, were used. COBRA located at Nago, Okinawa, performed plan position indicator (PPI) scanning of 14 elevations (0.5, 1.1, 1.8, 2.5, 3.3, 4.2, 5.3, 6.5, 8.1, 10.0, 12.3, 14.8, 17.4, and 20.5) and range height indicator (RHI) scanning directed to the disdrometer observation site (Fig. 1). Both scanning were performed every 6 min-

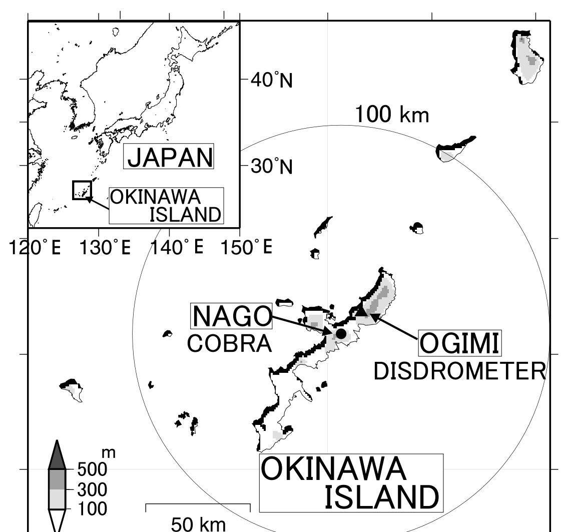

Fig. 1. Locations of each observation site. ● and ▲ show the locations of COBRA and the disdrometer, respectively. The circle shows the radar range of 100 km. Topography is shown with grayscales from 100 m every 200 m.

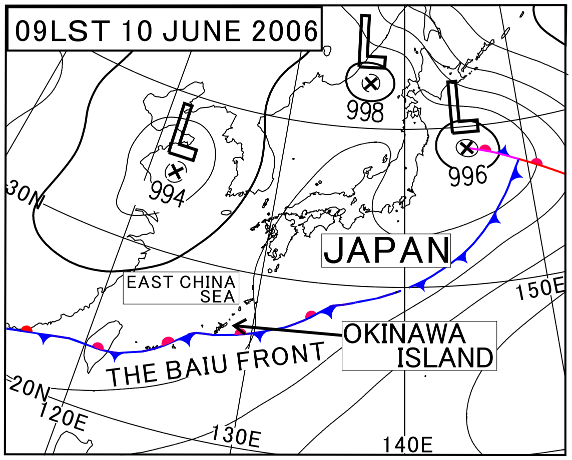

Fig. 2. The surface weather map at 09 LST, on 10 June 2006.

utes. The radar coverage of PPI is 100 km in radius as shown in Fig. 1. Spatial resolution of RHI data is 75 m in range direction and 0.4 degree in elevation direction, and that of PPI data is 300 m in range direction and 1 degree in azimuth direction.

In this study, radar reflectivity (Z_{hh}) was calculated into a constant altitude PPI (CAPPI). The horizontal and vertical grid intervals of the CAPPI were 1 km and 0.25 km respectively. Polarimeteric variables of differential reflectivity (Z_{DR}) and correlation coefficient at zero lag ($\rho_{hv}(0)$) were utilized. Z_{DR} represents a oblateness of precipitation particles predominating within a sensitive volume of a radar observation. In a rain region, a large value of Z_{DR} represents that raindrops having large diameters predominately exist in the sensitive volume (e.g. Bringi and Chandrasekar, 2001). A large (small) value of $\rho_{hv}(0)$ represents that size and category of precipitation particles in a sensitive volume of a radar observation are homogeneous (heterogeneous). A value of $\rho_{hv}(0)$ in a rain region is generally greater than 0.96-0.97 (Doviak and Zrnić, 1993). If snow and raindrops are mixed, $\rho_{hv}(0)$ is small. A value of $\rho_{hv}(0)$ in a melting layer is smaller than 0.95.

The disdrometer was located at Ogimi, Okinawa, and at a distance of 14.8 km from COBRA. The disdrometer measured 1-min-integrated DSDs on the ground every 1 minute.

3. CHARACTERISTICS OF THE BAIU FRONTAL RAINBAND ON 10 JUNE 2006

We selected the Baiu frontal rainband of 10 June 2006 for analyses because many convective cells in the rainband passed over the disdrometer observation site, Ogimi. Sounding data at Ogimi is available on the day. The Baiu front on the surface was analyzed at the south of Okinawa Island (Fig. 2), and that extended from east-northeast to west-southwest. The rainband, which extended along the Baiu front to the north of the Baiu front over East China Sea, moved northeastward and passed over Okinawa Island from 6 LST to 18 LST. Figure 3 shows composite images of horizontal distribution of rainfall intensity by C-band radar network of Japan Meteorological Agency (JMA). The rainband had a convective rain zone along the southern edge of the rainband and a stratiform rain zone to the north of the convective rain zone. In this study, the convective rain zone is defined as a strong rainfall area of 80 km in width along the southern edge of the rainband. The stratiform rain zone is defined as a broadened weak rainfall area to the north of the convective rain zone. Several hours after the passage of the stratiform rain zone over Okinawa Island (Fig. 3a), the convective rain zone passed over Okinawa Island (Fig. 3b).

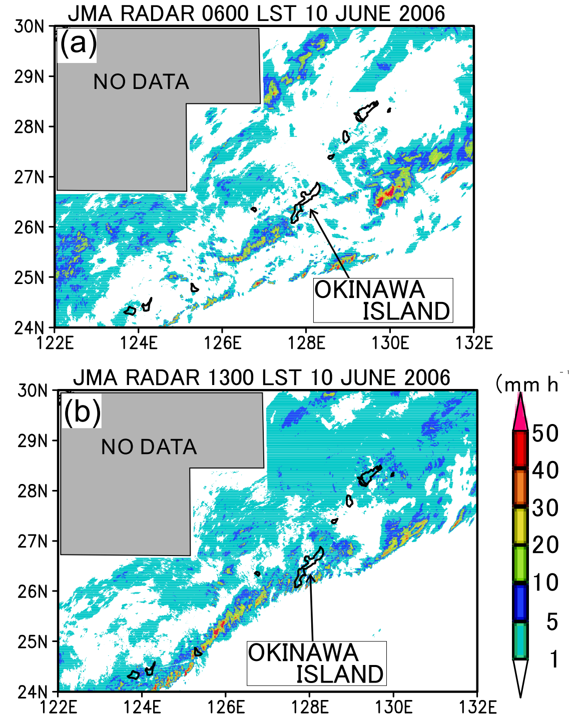

Fig. 3. Composite images of horizontal distribution of rainfall intensity at the 2 km altitude by JMA radar network at (a) 0600 LST and (b) 1300 LST.

Figure 4 shows horizontal radar reflectivity at the height of 2 km in CAPPI around Ogimi. Convective cells (convective echoes exceeding 35 dBZ) in the stratiform rain zone are embedded in the stratiform precipitation area (Fig. 4a) and other convective cells in the convective rain zone are also embedded in stratiform precipitation area formed between convective cells (Fig. 4b). Both types of convective cells passed over the disdrometer observation site.

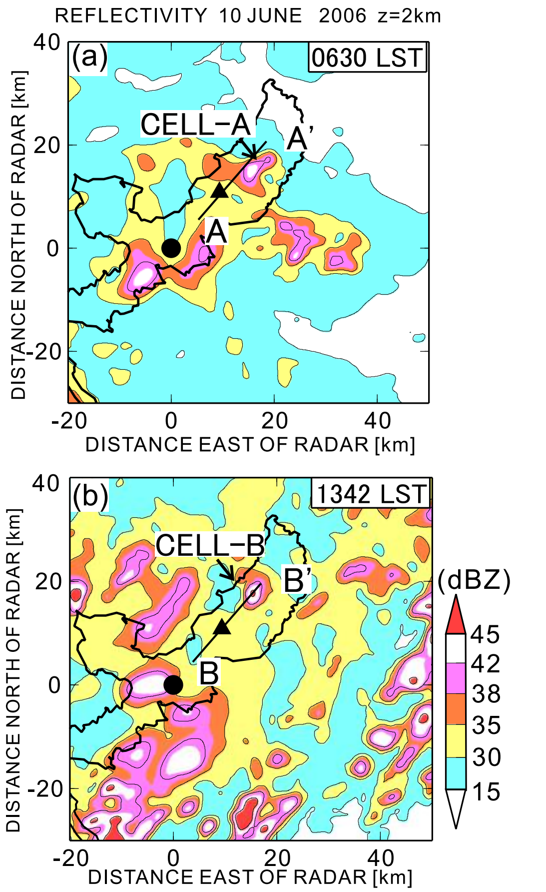

Fig. 4. Horizontal distribution of Z_{hh} in CAPPI at (a) 0630 LST and (b) 1342 LST at the height of 2 km. Cell-A and Cell-B are indicated by arrows in (a) and (b). The symbols ● and ▲ show the locations of COBRA and the disdrometer, respectively.

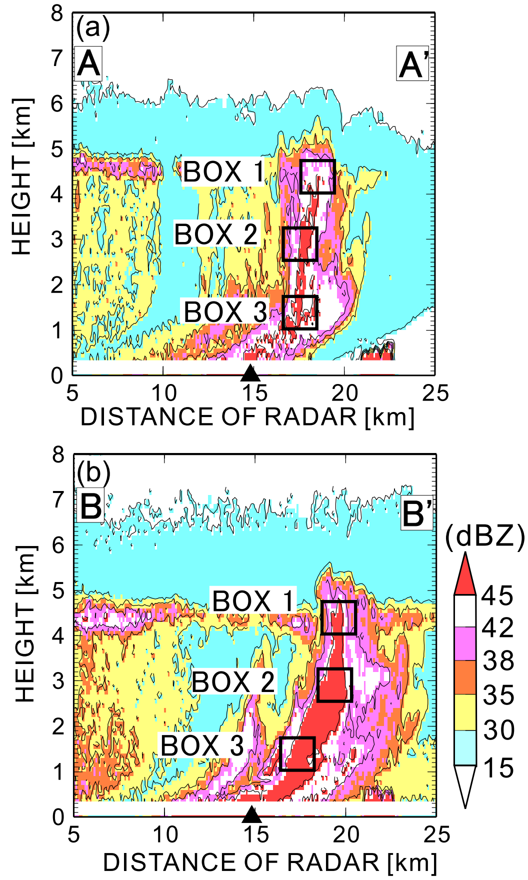

Fig. 5. Vertical distribution of Z_{hh} in RHI along (a) A-A$'$ and (b) B-B$'$ in Fig. 4. Rectangles indicate analyses areas of Z_{hh}, Z_{DR} and $\rho_{hv}(0)$. The symbol ▲ denotes the location of the disdrometer site.

4. DISTRIBUTIONS OF PRECIPITATION PARTICLES IN CONVECTIVE CELLS

A convective cell in the stratiform rain zone and a convective cell in the convective rain zone are selected for detailed analyses using RHI data which have higher spatial resolution than PPI data. The former passed over the disdrometer observation site, at about 0630 LST (Fig. 4a) and is named "Cell-A". The latter passed over the disdrometer site at 1342 LST (Fig. 4b) and is named "Cell-B". Figure 5 shows vertical distributions of Z_{hh} in RHI of Cell-A and Cell-B. Both convective cells passed over the disdrometer site during their mature stages. The disdrometer measured intense rainfall for a short time during the passage of these convective cells over the disdrometer site.

4.1. CONVECTIVE CELL IN STRATIFORM RAIN ZONE

Around Cell-A, a bright band of Z_{hh} is clear at the height of 4-5 km (Fig. 5a). The 0°C-height was 4.8 km from sounding data at Ogimi. The bright band indicates a melting layer because the altitude of the bright band almost corresponded to the 0°C-height. The echo-top height of 30 dBZ was 5.6 km and the maximum reflectivity was 49.6 dBZ at the height of 3.2 km in an RHI scanning. Cell-A had a low echo-top height less than 6.3 km during the mature stage.

Figure 6 shows scatter diagrams of Z_{hh} versus Z_{DR} and $\rho_{hv}(0)$ of Cell-A within rectangle regions in Fig. 5a. At the height of 4-5 km (box-1) corresponding to the 0°C-height, the maximum Z_{DR} is greater than 2.0 dB (Fig. 6a). In the same region, the minimum $\rho_{hv}(0)$ reaches a small value to 0.92 (Fig. 6d). A large Z_{DR} represents that flat particles are dominant in a sensitive volume of a radar observation. At the 0°C-height, $\rho_{hv}(0)$ smaller than 0.98 indicates mixed phase of ice and liquid particles. Therefore, it is considered that Cell-A had a large number of wet snowflakes around the height of 4-5 km. Below the height of 3.5 km (box-2 and box-3), Z_{DR} are smaller than 1.5 dB (Figs. 6b and c), and $\rho_{hv}(0)$ are greater than 0.98 (Figs. 6e and f). The small Z_{DR} and large $\rho_{hv}(0)$ represent that small raindrops were predominant at the low altitudes of Cell-A. The distribution as noted above is similar to that of the con-

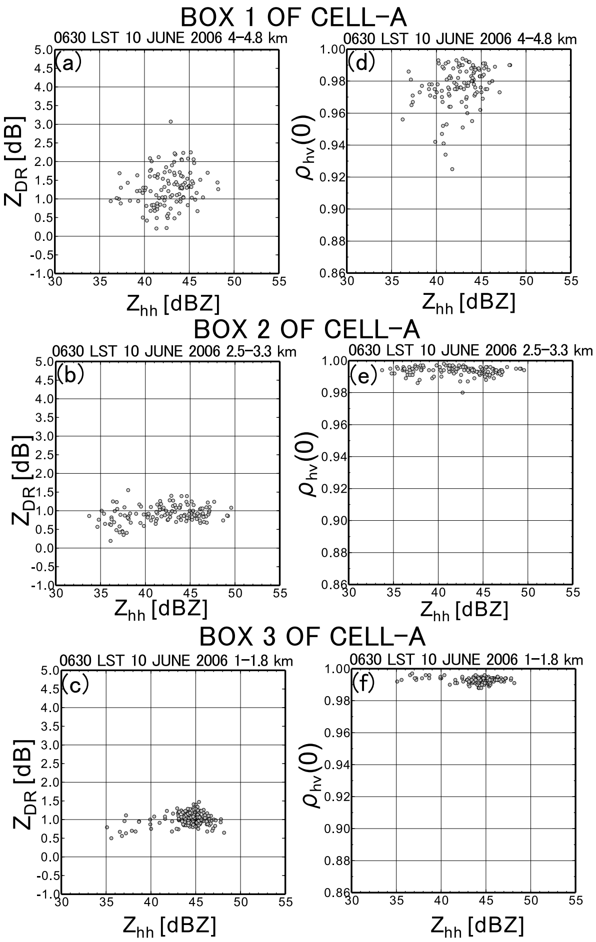

Fig. 6. Scatter diagrams of polarimetric parameters in RHI for Cell-A. The diagrams of the left row is Z_{hh} versus Z_{DR} within the box-1 (a), the box-2 (b) and the box-3 (c) in Fig. 5a. The diagrams of the right row is Z_{hh} versus $\rho_{hv}(0)$ within the box-1 (d), the box-2 (e) and the box-3 (f) in Fig. 5a.

vective cell embedded in stratiform precipitation area of Shusse et al. (2006).

Vertical profiles of averaged Z_{DR} and $\rho_{hv}(0)$ of Cell-A are represented in Figs. 7a and b. Areas of the average are indicated in Fig. 7c. The peak height of averaged Z_{DR} almost corresponds to the height of the minimum of averaged $\rho_{hv}(0)$ (4-4.5 km altitude). Below the height of 3.5 km, averaged Z_{DR} and $\rho_{hv}(0)$ are constant values of 1 dB and greater than 0.99, respectively. The constant values of small Z_{DR} and large $\rho_{hv}(0)$ represent that coalescence processes of raindrops were less in Cell-A.

While Cell-A was passing over the disdrometer, an average rainfall intensity was 18.5 mm h^{-1} and the maximum rainfall intensity was 43.0 mm h^{-1}. DSD during the passage of Cell-A is shown in Fig. 8. The number concentration of raindrops from 1 to 2 mm in diameter is large and few raindrops exceed 3 mm in diameter. Raindrops from 1 to 2 mm in diameter account for 63.3 % of the average rainfall intensity. From the re-

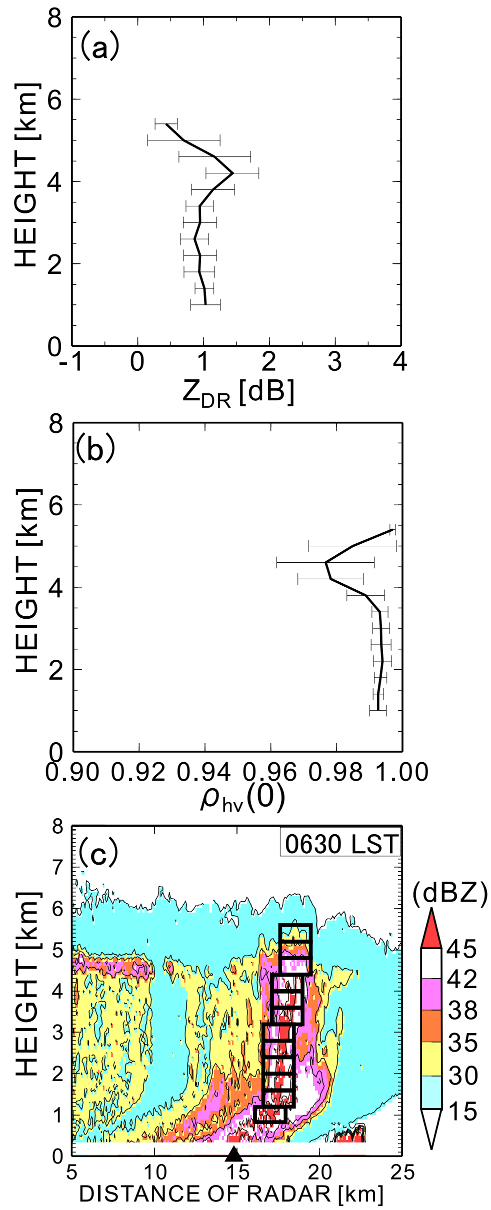

Fig. 7. Vertical profiles of averarged (a) Z_{DR} and (b) $\rho_{hv}(0)$ of Cell-A. Averaging areas are indicated by rectangles in (c). The symbol ▲ in (c) denotes the location of the disdrometer.

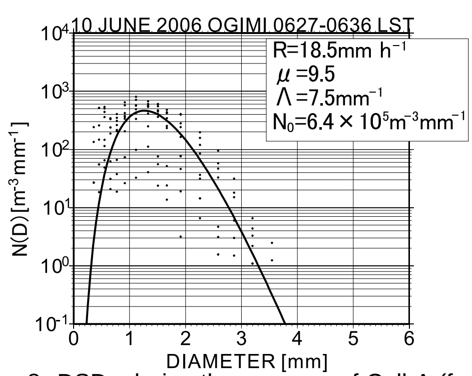

Fig. 8. DSDs during the passage of Cell-A (from 0627 LST to 0636 LST). Dotted markes show DSDs every 1 minute. The solid line shows the DSD fitted to a gamma distribution (Kozu and Nakamura, 1991). Variables right above show averaged rainfall intensity (R) and parameters of gamma distribution (μ, Λ and N_0).

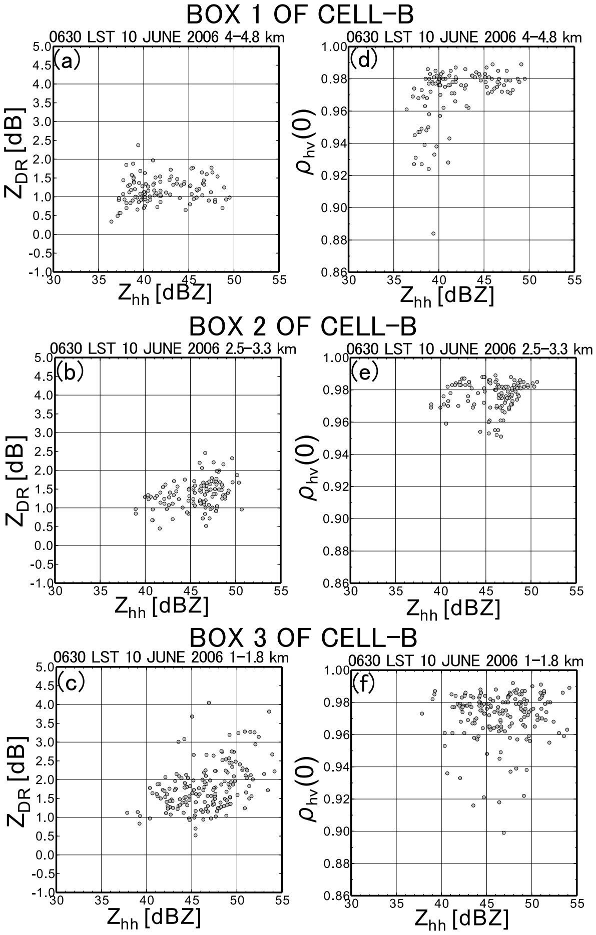

Fig. 9. As Fig. 6 but for Cell-B.

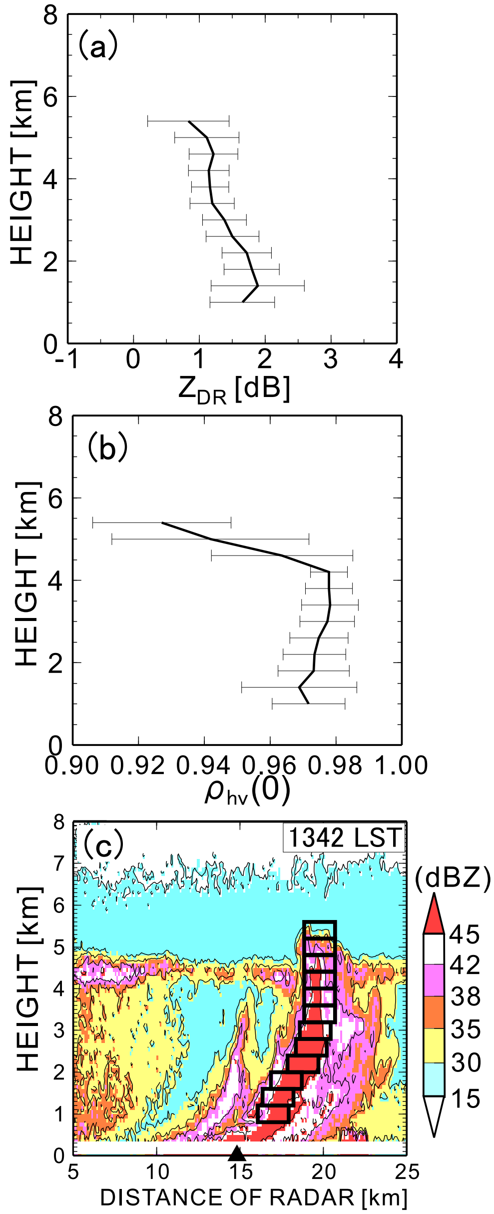

Fig. 10. As Fig. 7 but for Cell-B.

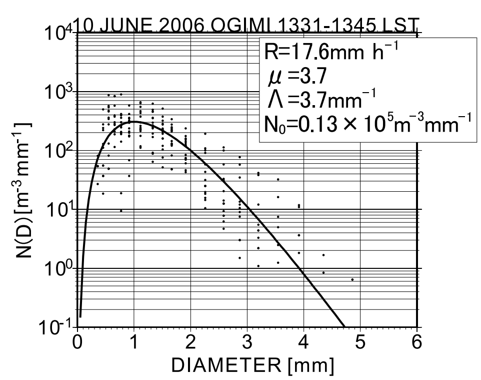

Fig. 11. As Fig. 8 but for Cell-B (from 1331 LST to 1345 LST).

sults of polarimetric variables and DSD on the ground, it is considered that small raindrops having 1-2 mm in diameter predominated near the ground.

4.2. CONVECTIVE CELL IN CONVECTIVE RAIN ZONE

Around Cell-B, a melting layer is also clear such as a bright band of Z_{hh} at the height of 4-5 km (Fig. 5b). The echo-top height was 5.6 km and the maximum reflectivity was 54.2 dBZ at the height of 1.2 km in an RHI scanning. Cell-B also had a low echo-top height less than 5.8 km during the mature stage.

Figure 9 shows scatter diagrams of Z_{hh} versus Z_{DR} and $\rho_{hv}(0)$ of Cell-B within rectangle regions in Fig. 5b. At the height of 4-5 km, Z_{DR} are mostly smaller than 1.5 dB for Z_{hh} greater than 43 dBZ (Fig. 9a). In the same region, $\rho_{hv}(0)$ are greater than 0.97 (Fig. 9d). This represents that there were a large number of small raindrops at the height of 4-5 km in Cell-B. Around the height of 2.5-3.3 km (box-2), Z_{DR} reaches the maximum of 2.5 dB and $\rho_{hv}(0)$ reaches the minimum of 0.95. Below the height of 2 km (box-3), the maximum Z_{DR} is greater than 4 dB and the minimum $\rho_{hv}(0)$ is smaller than 0.90. The small $\rho_{hv}(0)$

below the 0°C-height represents oscillations of large raindrops and broadened DSD from small size to large size. It is considered that large raindrops existed below the 0°C-height in Cell-B.

Figure 10 shows vertical profiles as well as that of Cell-A (Fig. 7). Below the height of 4 km, the averaged Z_{DR} increases with decreasing altitude (Fig. 10a). The averaged $\rho_{hv}(0)$ decreases with decreasing altitude (Fig. 10b). The results represent coalescence processes of raindrops were predominant in Cell-B.

While Cell-B was passing over the disdrometer, the average and maximum rainfall intensity were 17.6 mm h^{-1} and 56.4 mm h^{-1}, respectively. DSD during the passage of Cell-B is shown in Fig. 11. The DSD broaden to large diameter. The number concentration of raindrops from 1 to 2 mm in diameter is smaller than that of Cell-A and a large number of raindrops exceed 3 mm in diameter. Raindrops exceeding 3 mm in diameter account for 19.1 % of the average rainfall intensity. This percentage is grater than that of Cell-A (2.3 %). It is considered that large raindrops in Cell-B had diameters exceeding 3 mm near the ground.

6. SUMMARY AND CONCLUSIONS

In order to clarify distributions of precipitation particles in the convective cells, we analyzed polarimetric variables and DSD in two convective cells associated with the Baiu frontal rainband on 10 June 2006. One convective cell existed in a stratiform rain zone associated with the rainband, the other existed in a convective rain zone associated with the rainband.

The former had a low echo-top height (of 30 dBZ) of about 5-6 km and strong rainfall intensity of about 18 mm h^{-1}. Around the convective cell, the melting layer was clear. Below the height of 3.5 km, Z_{DR} was less than 1.5 dB and $\rho_{hv}(0)$ was greater than 0.98. In the DSD on the ground, the number concentration of raindrops of 1-2 mm in diameter was large and few raindrops exceeded 3 mm in diameter. The results represent a large number of small raindrops of 1-2 mm in diameter existed in the convective cell in the stratiform rain zone.

The latter also had a low echo-top height (of 30 dBZ) of about 5-6 km and strong rainfall intensity of about 18 mm h^{-1}. Around the convective cell, the melting layer was clear. Below the height of 3.5 km, the Z_{DR} indicated greater than 1.5 dB and the $\rho_{hv}(0)$ indicated smaller than 0.98. In this case, the number concentration of 1-2 mm in diameter was smaller than that of the former case and a large number of raindrops exceeded 3 mm in diameter. The results represent large raindrops exceeding 3 mm in diameter were predominant in the convective cell in the convective rain zone.

We show that a convective cell embedded in stratiform precipitation area of the Baiu frontal rainband existed in a convective rain zone associated with the Baiu frontal rainband, as well as in a stratiform rain zone. Distributions of preciptaition particles in the convective cells embedded in stratiform precipitation area in the stratiform rain zone and in the convective rain zone of the Baiu frontal rainband were clarified: small raindrops in the convective cell of the stratiform rain zone and large raindrops in the convective cell of the south convective rain zone of the Baiu frontal rainband. Although these convective cells had common characteristics of the low echo-top height and providing strong rain, distributions of precipitation particles were different. The results show a clue for understanding precipitation physics of convective cells developing in the humid environment.

Acknowledgments: This observation was conducted in collaboration with National Institute of Information and Communications Technology and Hydrospheric Atmospheric Research Center, Nagoya University.

References

Bringi, V. N. and V. Chandrasekar, 2001: Polarimetric Doppler weather radar: Principles and applications. *Cambridge University Press*, 378–533.

Doviak, R. J. and D. S. Zrnić, 1993: Doppler radar and weather observations, 2nd edition. *Academic Press, San Diego, CA*, 562.

Kozu, T. and K. Nakamura, 1991: Rainfall parameter estimation from dual-radar measurements combining reflectivity profile and path-integrated attenuation. *J. Atmos. Ocean. Technol.*, **8**, 259–270.

Shinoda, T., R. Maki, S. Shimizu, K. Tsuboki and H. Uyeda, 2007: Statistical features of precipitation cells observed in East Asia during the Meiyu/Baiu period. *Proc. Conf. on Mesoscale Meteorology and Typhoon in East Asia*, 199–203.

Shusse, Y., K. Nakagawa, N. Takahashi, S. Satoh and T. Iguchi, 2006: Characteristics of polarimetric radar variables and their precipitation type dependence in a highly humid oceanic region. *Proc. 4th European Conf. on Radar in Meteorology. and Hydrology*, 57–60, Barcelona, Spain.

Zeng, Z., S. E. Yuter and R. Houze Jr., 2001: Microphysics of the rapid development of heavy convective precipitation. *Mon. Wea. Rev.*, **129**, 1882–1904.

ON NUMERICAL REALIZABILITY OF THERMAL CONVECTION

Zbigniew P. Piotrowski[1] , Piotr K. Smolarkiewicz[2],
Szymon P. Malinowski[1] and Andrzej A. Wyszogrodzki[2]
[1] Institute of Geophysics, University of Warsaw, Warsaw, Poland
[2] National Center for Atmospheric Research, Boulder, Colorado, USA

1. ABSTRACT

Astounded at the regularity of convective structures observed in simulations of mesoscale flow past realistic topography, we take a deeper look into numerics of a classical problem of flow over a heated plate [1]. We find that solutions are sensitive to viscosity, which is either incorporated a priori or effectively realized in numerical models. In particular, anisotropic viscosity can lead to regular convective structures [2,3,4] that mimic naturally realizable Rayleigh-Benard cells that are, however, unphysical for the specified external parameter range. The details of the viscosity appear to play secondary role; that is, similar structures can occur for prescribed constant viscosities, explicit subgrid-scale turbulence models, ad-hoc numerical filters, or implicit dissipation of numerical schemes. This calls for careful selection of numerical tools suitable for cloud-resolving simulations of atmospheric circulations [5].

2. LINEAR THEORY

Linear model equations that account for anisotropy of the viscosity in Rayleigh-Benard convection can be written as

$$\frac{\partial \mathbf{u}}{\partial t} = -\nabla\phi + g\alpha\theta\nabla z + \nu_h\triangle_h\mathbf{u} + \nu_v\triangle_z\mathbf{u}$$
$$\frac{\partial\theta}{\partial t} = \beta w + \kappa_h\triangle_h\theta + \kappa_v\triangle_z\theta$$
$$\nabla\cdot\mathbf{u} = 0\ .$$

Here $\mathbf{u}$ is velocity vector, and w its vertical component; Φ denotes normalized pressure perturbation; α is the volume expansion coefficient; θ is the potential temperature deviation from a linear profile with adverse gradient β; g is the acceleration of gravity, and subscripts h and v refer to the horizontal and vertical values of viscosity and diffusivity, ν and κ respectively. The resulting marginal stability relation demarcating regime transition is

$$Ra_h = \frac{H^4}{k^2}\left(n\left(\frac{\pi}{\frac{H}{\sqrt{r}}}\right)^2 + k^2\right)^3 \frac{\left(n\left(\frac{\pi}{H}\right)^2 + k^2\right)}{\left(n\left(\frac{\pi}{H}\right)^2 r + k^2\right)}\ .$$

That is, for any given Ra_h all horizontal modes with wave number k such that the rhs of the marginal stability relation exceeds Ra_h are unstable. Ra_h denotes Rayleigh number $Ra = -N^2H^4/\nu\kappa$; $r := \nu_v/\nu_h = \kappa_v/\kappa_h$ is the anisotropy ratio; N denotes the buoyancy frequency (imaginary), and H is the layer depth. The asymptotics of marginal stability relation in Figure 1 indicate that decreasing ν_v at constant ν_h accentuates instability of long horizontal wavelengths, whereas decreasing ν_h at constant ν_v enhances instability of short modes.

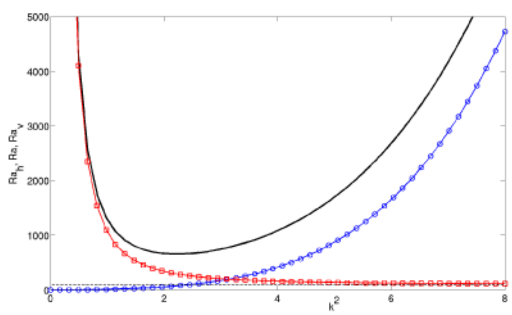

Figure 1. Asymptotic marginal stability relations for a finite Prandtl number and $\nu_h = \nu_v$ *(solid),* $\nu_v = 0$ *(circles) and* $\nu_h = 0$ *(squares). Respective Rayleigh numbers* Ra_h*, Ra and* Ra_v *are shown in function of the squared horizontal wave number. Stability region is below the curves.*

Because the squared aspect ratio of dominant convective cells is predicted as

$$\left(\frac{2H}{\lambda}\right)^2 = \frac{1}{4}\left(\sqrt{8r+1} - 1\right),$$

the simulated convective structures may vary dramatically with the effective anisotropy of viscosity departing from unity.

3. NUMERICAL MODEL

Numerical model Eulag [6] adopted in this study solves thermally forced, viscous, nonhydrostatic anelastic equations of Lipps and Hemler, which can be compactly written as

$$\frac{\mathcal{D}\mathbf{u}}{\mathcal{D}t} = -\mathbf{Grad}\,(\pi') - \mathbf{g}\frac{\theta'}{\theta_b} + \mathcal{D}_m(E, \nabla\mathbf{u})$$
$$\frac{\mathcal{D}\theta'}{\mathcal{D}t} = -\mathbf{u} \bullet \mathbf{Grad}\theta_e + \mathcal{D}_h(E, \nabla\theta)$$
$$\mathbf{Div}(\rho_b\mathbf{u}) = 0$$

Here the operators D/Dt, **Grad** and **Div** symbolize the material derivative, gradient and divergence; $\mathbf{u}$ denotes the velocity vector; θ, ρ, and π denote potential temperature, density, and a density-normalized pressure; and **g** symbolizes the vector of gravitational acceleration. Subscripts $_b$ and $_e$ refer to the basic and ambient states, respectively, and primes denote deviations from the environmental state. The "*D*" terms on the rhs of the momentum and entropy equations symbolize explicit viscous forcings, which depend on the derivatives of dependent variables and, eventually, on the turbulent kinetic energy *E* predicted with subgrid-scale models. The prognostic equations of the model are supplemented with diagnostic anelastic mass continuity constraint, implying the formulation of the elliptic equation for pressure. For integrating the prognostic equations, Eulag uses a second-order-accurate, nonoscillatory forward-in-time MPDATA approach [7]

4. SIMULATION RESULTS

The effects of incorporating effective anisotropic viscosity manifest themselves both in idealized and realistic (numerical) experiments. Figure 2, shows the structure of Rayleigh-Benard convection over a heated plate, after 6h of simulation with horizontal resolution 500 m and constant heat flux 200 W/m^2 imposed at the lower boundary. Cellular structure is apparent for the case with larger horizontal viscosity. In turn, Figure 3 shows the result of simulation of moist convection forming over heated terrain in southern Poland. The routine hydrostatic mesoscale predictions at 17 km resolution, using the Unified Model for Poland Area (UMPL), continuously supplied the initial, boundary, and ambient conditions for high-resolution simulations using EULAG. The EULAG domain of 240×200 km squared, embedded in the UMPL Central European domain (2000×2400 km squared) was covered with 1 km horizontal grid intervals; while keeping the vertical resolution double of UMPL. Similar as in the idealized case, the increase of ν_h in the effective stress tensor manifests as cell broadening, consistent with the linear-theory predictions of section 2.

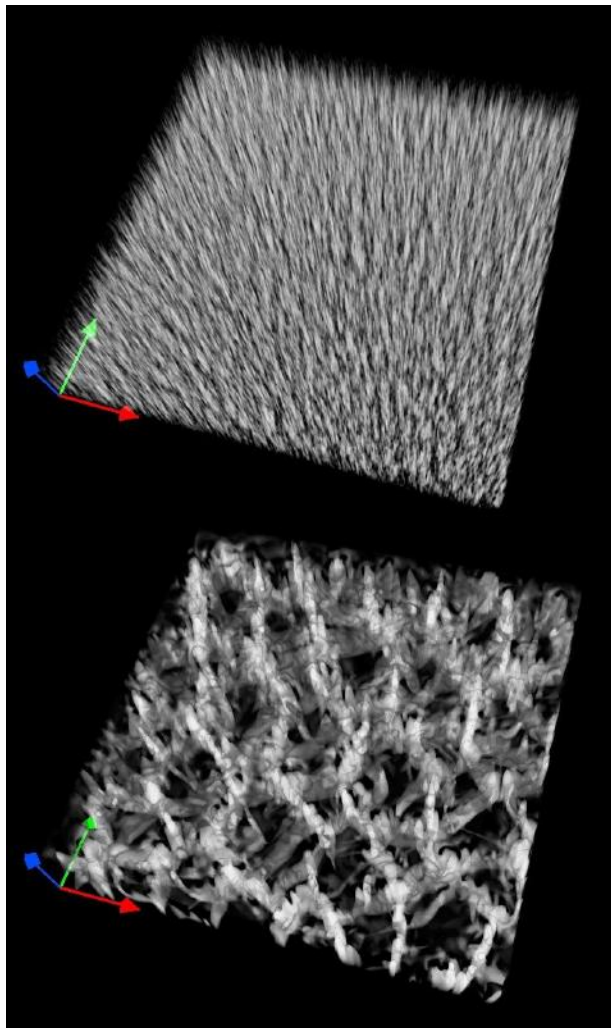

Figure 2. Structure of thermal convection over heated plate. Vertical velocities after 6h of simulated time are shown within the PBL depth. Bright and dark volumes denote updrafts and downdrafts, respectively. The only difference between the two solutions is the value of viscosity in horizontal entries of the stress tensor, ν_h= 2.5 and ν_h= 70 m^2s^{-1}, while constant vertical entry is ν_v= 2.5 m^2s^{-1}

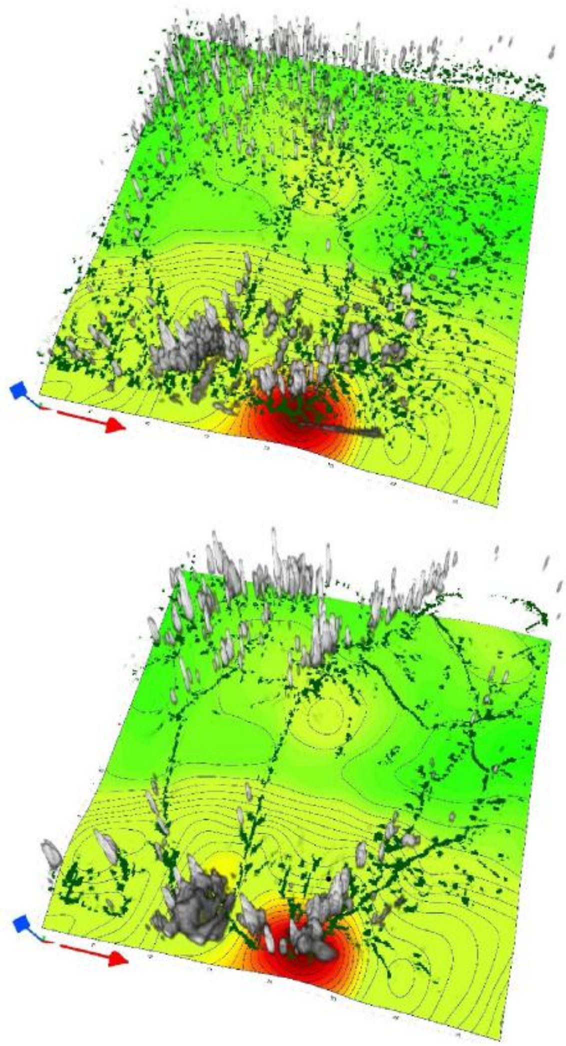

Figure 3. Structure of thermal convection over heated terrain. Vertical velocities after 6h of simulated time are shown within the PBL depth. Grey iso-surfaces represent clouds, and dark green patterns mark updrafts at boundary layer top. Isolines and other colors show the topography. The only difference between the two simulations is the effective viscosity of numerical advection.

5. CONCLUSIONS

We performed a large series of controlled simulations to document the influence of effective viscosity anisotropy on the structure of convection over heated terrain. Here, we show that the differences between realistic cellular convection and the spurious structures resulting from enhanced horizontal viscosity are consistent with linear-theory predictions. Furthermore, we show that enhanced anisotropy of numerical (viz. eddy; either explicit or implicit) viscosity --- typically motivated with arguments of subgrid-scale modeling --- may force convection to group into structures closely resembling Rayleigh-Benard cells observed in the maritime conditions, with geometric characteristics of natural cells, as in Figure 3. Looking forward toward petascale computing, we advocate careful selection of numerical filters for cloud resolving NWP, to avoid a leakage of uncontrolled viscous effects into the models' physics.

6. BIBLIOGRAPHY

[1] Lord Rayleigh, On convection currents in a horizontal layer of fluid, when the higher temperature is on the under side, Phil. Mag 32 (6) (1916) 529–546.

[2] D. Ray, Cellular convection with nonisotropic eddys, Tellus 17 (1965) 434–439.

[3] P. Sheu, E. Agee, J. Tribbia, A numerical study of physical processes affecting convective cellular geometry, J. Meteor. Soc. Japan, 58 (1980) 489–499.

[4] B. Atkinson, J. W. Zhang, Mesoscale shallow convection in the atmosphere, Rev. Geophys. 34 (1996) 403–431.

[5] M. Satoh, T. Matsuno, H. Tomita, H. Miura, T. Nasuno, and S. Iga, Nonhydrostatic icosahedral atmospheric model (NICAM) for global cloud resolving simulations, J. Comput. Phys. 227 (2008) 3486-3514.

[6] J. M. Prusa, P. K. Smolarkiewicz, A. A. Wyszogrodzki, Eulag, a computational model for multiscale flows, Computers & Fluids (2008) in press.

[7] P. K. Smolarkiewicz, Multidimensional positive definite advection transport algorithm: An overview, Int. J. Num. Meth. Fluids 50 (2006) 1123–1144.

7. ACKNOWLEDGEMENTS

The National Center for Atmospheric Research (NCAR) is sponsored by the National Science Foundation. This work was supported in part by the USA Department of Energy CCPP and SciDAC research programs, and by the Polish Ministry of Science and Higher Education grant No. N307059034. Imagery produced by VAPOR www.vapor.ucar.edu

CONVECTIVE SYSTEM STRUCTURE OVER SOUTHEASTERN SOUTH AMERICA FROM TRMM OBSERVATIONS

Paola Salio [(1)], Luciano Vidal [(1)], Edward Zipser [(2)] and Chuntao Liu [(2)]

[(1)] Departamento de Ciencias de la Atmósfera y los Océanos. UBA.
Centro de Investigaciones del Mar y la Atmósfera. CONICET – UBA.
Buenos Aires. Argentina.

[(2)] Department of Meteorology. University of Utah. Salt Lake City.Utah. USA

1. INTRODUCTION

Global and regional characteristics of deep convection over South America have been analyzed by many authors based on different observing tools. Satellite infrared images have been the primary tool since the GOES constellation satellite was launched over the region. These data make it possible to understand the evolution and behavior of convective systems over many regions, especially over large areas without ground-based observations. Based on geostationary satellite information, Machado et al (1998), Velasco and Frisch (1987), among others showed the characteristics and structure of mesoscale convective systems over South America. However, there is an important lack of knowledge of the internal structure of convective systems over the area due to the sparse ground-based radar network.

The Tropical Rainfall Measuring Mission (TRMM) constellation (Kummerow et al., 1998) measures visible and infrared radiances (VIRS), microwave radiance from TRMM Microwave Imager (TMI), radar reflectivity from the Precipitation Radar (PR), and flashes from Lightning Imager Sensor (LIS). This unique dataset provides the opportunity to investigate the internal structure of convection mainly over tropical and subtropical areas and to describe the evolution of its diurnal cycle.

Corresponding Author Address: Dr. Paola Salio. salio@cima.fcen.uba.ar
Departamento de Ciencias de la Atmósfera y los Océanos. UBA. Bs. As. Argentina.

A prime motivation of this study is to generate a climatology and characterize the internal structure of the convection over Southeastern South America (SESA). This paper also describes the diurnal cycle of convection over SESA and the relationship between the internal structure of convection and different synoptic situations dominated by low level jets (LLJs).

2. METHODOLOGY

The University of Utah Version-6 TRMM level 3 dataset spatially and temporal collocate all available sensor information from TRMM constellation during a 9-year period (1998-2006, Liu et al., 2007). Radar Precipitation Features (RPFs) are defined as “a pure precipitation feature” because considering all Precipitation Features (Nesbitt et al., 2003) in the sample, with TRMM 2A25 surface rain rate greater than 0 mm h^{-1}. The characteristics of each feature are summarized from measurements and retrievals from PR, TMI, VIRS and LIS at grouped pixels. Parameters considered in this paper are as follows:

- Stratiform and convective rain area and volume, maximum height of 15, 20 and 40 dBz from algorithm 2A25
- 85 GHz Polarized Corrected Temperature (PCT) from TMI,.
- minimum temperature brightness temperature (T_{B11}) from IR image.
- Number of lightning flashes from LIS.

Synoptic situations associated with LLJ events are detected using GDAS, considering a criterion similar to

Bonner's(1968) already used in Salio et al (2002) and Nicolini et al (2004). Figure 1 shows the low level circulation for each studied event. Situations called Chaco Jet event (CJE) and No Chaco Jet event (NCJE) are known as South American Low Level Jet events (SALLJ), this being a particular categorization aimed at understanding the differences between tropical and subtropical latitudes. Cases associated with an anticyclonic circulation over Argentina are called Low Level Jet Argentina (LLJA) and situation without the presence of a LLJ over the area are called NoLLJ.

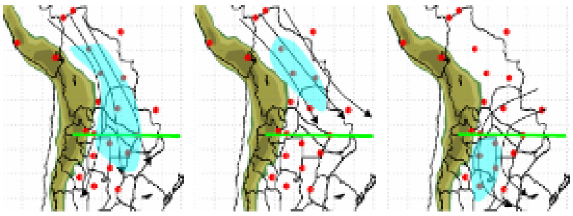

Figure 1: Scheme of the circulation of the wind in low levels under three characteristic low level jet events over Southeast South America. Chaco Jet Event is outlined at the top, on the center No Chaco Jet Event and at the bottom the Low Level Jet Argentina scheme. The area shaded in light blue display the isotach of 12ms^{-1}. The green line indicates the latitude of 25°S.

3. RESULTS
3.1 CONTINENTAL DESCRIPTION

The main dynamic systems that generate precipitation can be identified by the distribution of the RPFs during the four seasons of the year (Figure 2). These include the annual evolution of the Intertropical Convergence Zone, the South Atlantic Convergence Zone during summer, as well as the annual cycle of precipitation over the Altiplano with a maximum in summer and a minimum in winter. It is important to emphasize the maximum south of 30°S, as important as those over the Amazon region, displaying maximum frequency values in summer and spring. Figure 3 shows the frequency of RPFs with T_{B11} values lower than 210 K. This figure shows that the extreme events also tend to

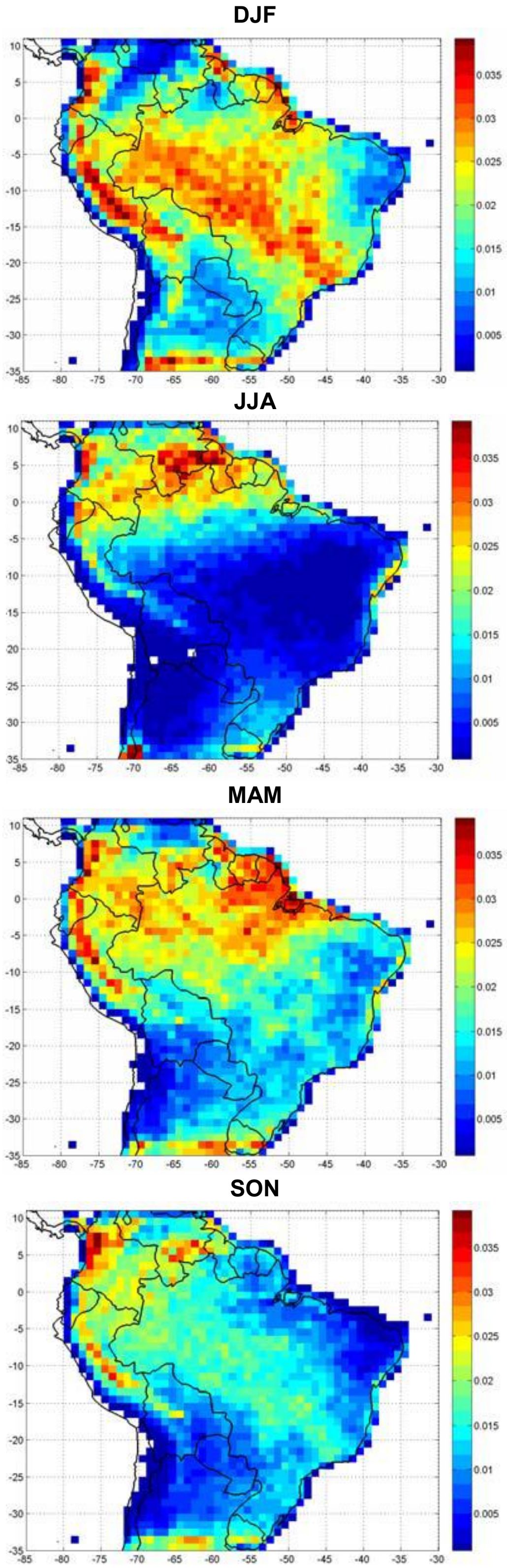

Figure 2: Number of RPFs per km^2 summarized onto a 1x1 degree resolution.

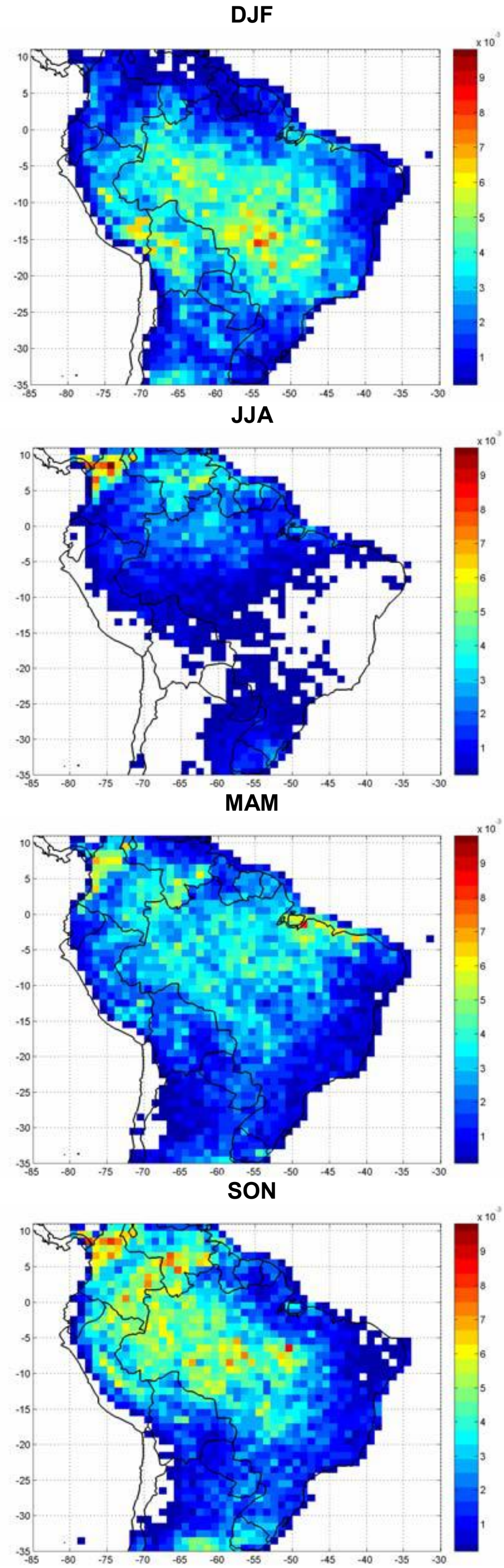

Figure 3: Number of RPFs per km^2 summarized onto a 1x1 degree resolution with T_{B11} lower than 210 K.

be located on the Amazon and SESA regions mainly during summer and spring. Extreme values of 20 dBz heights greater than 5 km indicate the presence of deep convection on the center of Argentina, Uruguay and the Altiplano especially during summer and spring (figure not shown).

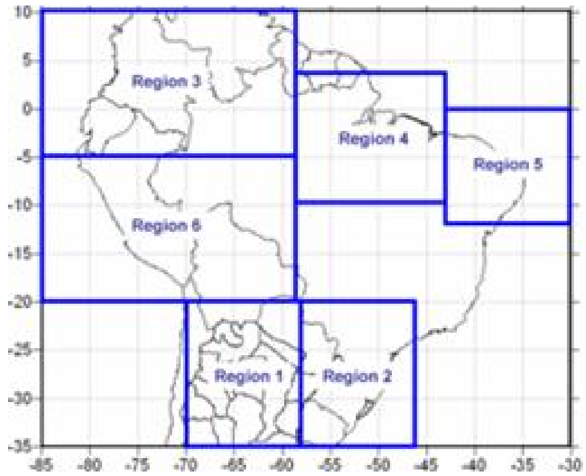

Figure 4: South American area and selected regions mentioned in the text.

Vertical profiles of the relative frequency of the maximum height of the 20 and 40 dBz contours measured from the radar over different selected regions are shown in figure 5. All regions have been indicated in figure 4. One significant finding is that fully 20% of RPFs contain a 40 dBZ radar reflectivity contour attaining an altitude greater than 10 km over SESA, reaching an extreme of 18 km over region 1, while in tropical areas 40 dBZ values are lower than 8 km altitude. Regions 3 to 6, characterized by a tropical behavior, show an important 40 dBZ frequency extreme at 4 km, while the maximum over SESA has the same mean altitude though lower intensity. This fact shows that the convection altitude tends to be higher in the subtropical area than in the tropical, where no cases are detectable up to 10 km. Zipser et al (2006) , Salio et al (2007), among others found that strong deep convective systems tend to occur over SESA during SALLJ situations, extreme results over subtropical area agree with those findings.

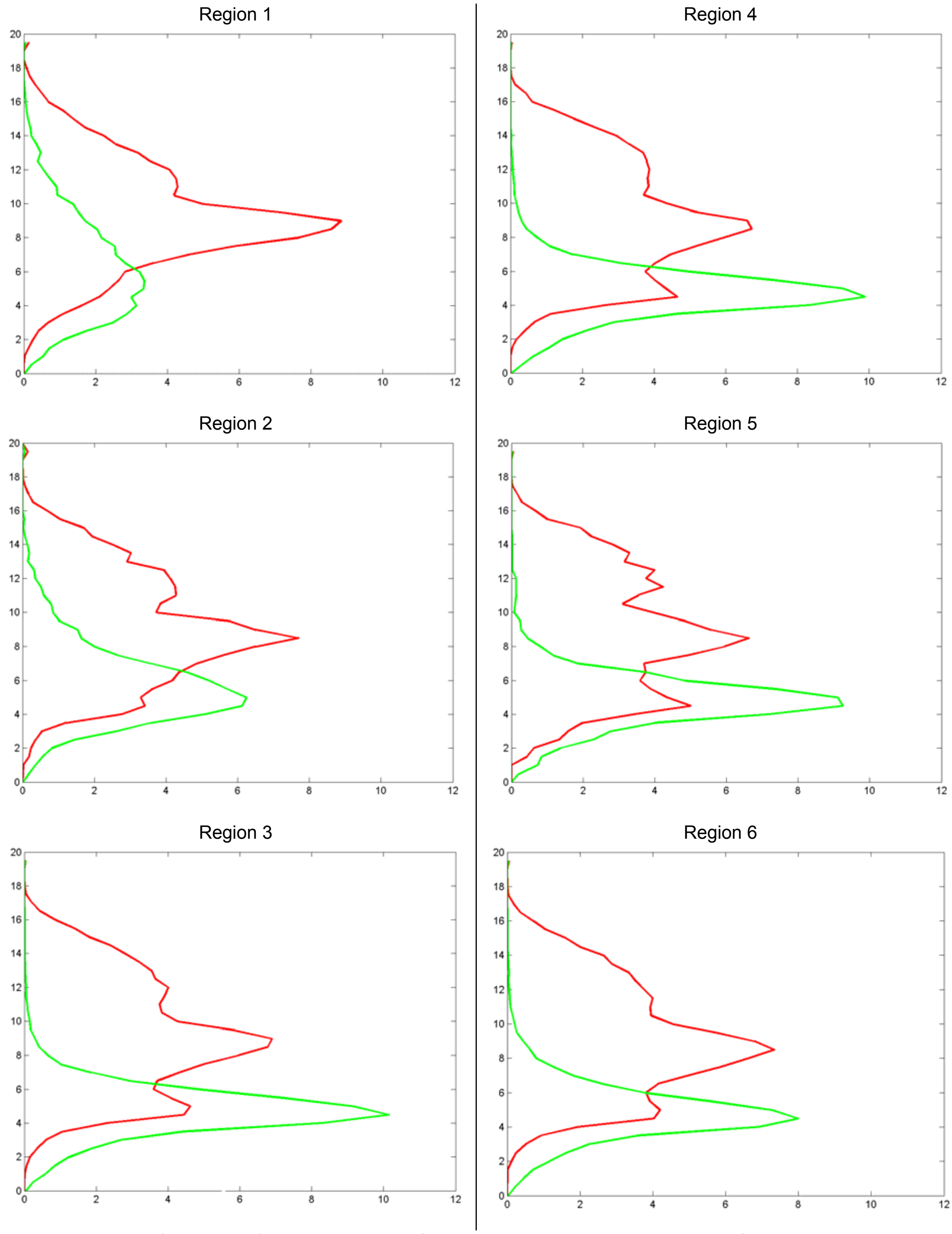

Figure 5: Relative frequency of maximum height of 20 (red line) and 40 (green line) dBZ for all RPFs in the sample, considering all seasons over the different regions showed in Figure 4.

Table 1 shows a number of parameters associated with extreme events. Parameters similar to those in Liuct et al (2007, Table 1 in their paper) have been calculated to compare the behavior of extreme RPF events over SESA. The frequency of occurrence of radar echo tops reaching 15 km shown in that table are 10-times higher than the frequencies in the whole TRMM covered area, where only the 1% of the sample reaches this altitude (Liuct et al 2007). A similar behavior can be depicted from the frequency of PCT lower than 200 K, where values in the studied sample are much higher than in the whole sample.

#	Parameter	West	East
I	$T_{B11} \leq 210$ K (%)	**11.4**	**9.2**
II	MaxH 40 ≥ 10km (%)	**14.1**	**8.5**
III	MaxH 20 ≥ 15km (%)	**10.3**	**8.8**
IV	MaxH 20 ≥ 10km (%)	**58.2**	**57.7**
V	MIN85PCT ≤ 200K (%)	**37.6**	**43.9**
VI	MIN85PCT ≤ 225K (%)	**47.8**	**54.2**
VII	% Convective Area	**27.24**	**19.9**
VIII	Mean Volumetric Rain	**21312.5**	**19901**

Table 1: I) Percentage of RPFs with T_{B11} lower than 210 K. Considering only RPFs with T_{B11} lower than 210 K: II) Percentage of cases with maximum height of 40 dBz higher than 10 km; III) idem II for maximum height of 20 dBz higher than 15 km; IV) idem III for 10 km; V) idem II minimum PCT lower than 200 K; VI) idem V for 225 K; VII) Percentage of convective area of RPF from 2A25 algorithm and VIII) Mean Volumetric rain for all RPFs from 2A25 algorithm.

Some differences between western and eastern area of SESA need to be remarked. While region 1 (western area) tends to show a frequency of RPFs with lower T_{B11} and higher tops, PCT tends to be cooler over region 2 (eastern area). These findings are correlated with the presence of a greater convective area over region 1 and stronger volumetric rain rate.

An extended analysis of the seasonal cycle of extreme values over Region 1 and 2 is summarized in the next section.

3.2 SOUTHEASTERN SOUTH AMERICA CHARACTERISTICS UNDER DIFFERENT LLJ SITUATIONS

The analysis of the vertical profiles of the relative eco top height frequency of different dBz contours (15, 20 and 40) in region 1 and 2 reveals that convective systems are deeper during DJF and SON in the western region, though in a lower degree. The most frequent height ranges from 3 to 5 km for 40 dBZ in both regions. In the case of 15 and 20 dBz, the most frequent height in region 1 is between 5 and 7 km in the DJF period, 4 km in MAM and JJA and 5 km in SON. The eastern region displays values of 5 km in DJF, 4.5 km in MAM, and 4 km in JJA and SON. On the other hand, the 40dBZ curve reaches the ground during MAM and JJA in region 1, though more frequently in fall, which indicates some probability of precipitation on surface (figure not shown).

The relative frequency of top heights of the 15, 20 and 40 dBZ contours of CJE and LLJA cases in region 1 and 2 are shown in figures 6 and 7 respectively. Only the figures of the samples showing significant characteristics are presented. The most interesting feature is the system height during CJE events, mainly in DJF, which reaches values above 8 km in more than 50% of the cases in the western region. In the east, systems are weaker and the nucleus of the maximum 40 dBz height is located at a greater altitude. The 40 dBz contour reaches the surface in both regions, which indicates the possibility of precipitation occurrence. The structure of the NCJEs is quite similar to the CJE cases in both regions, confirming that there is an effect of SALLJ events altogether over SESA (figure not shown). Since maximum frequencies for the 40 dBz contour are located at 3 km and the contours are relatively weak during extreme events, LLJAs tend to be shallower in the seasons shown (DJF and SON) than the systems of CJE events (Figure 7).

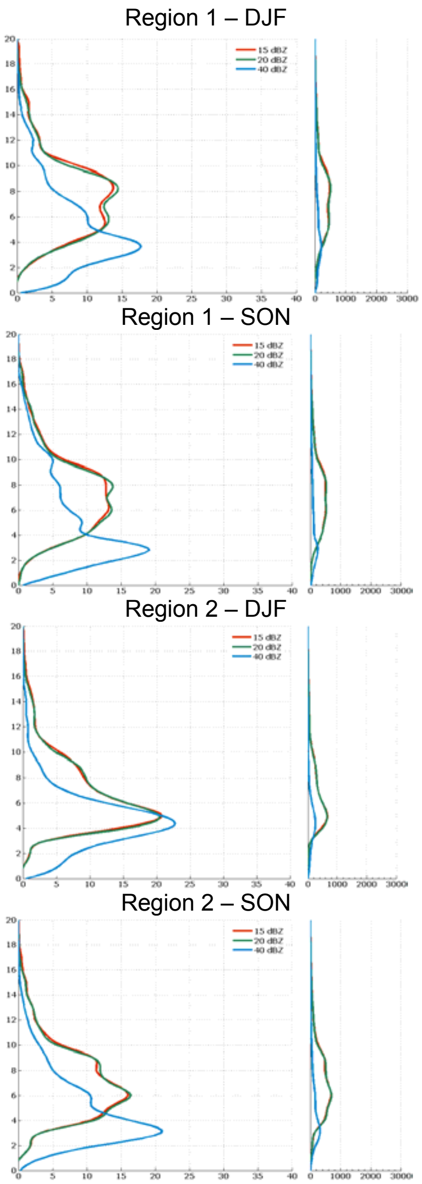

Figure 6: Relative frequency of maximum height of 15 (red), 20 (green) and 40 (blue) dBZ for all RPFs in the sample, considering the regions 1 and 2 showed in Figure 5 for two seasons and CJE situations. Each panel shows the number of RPFs at every level.

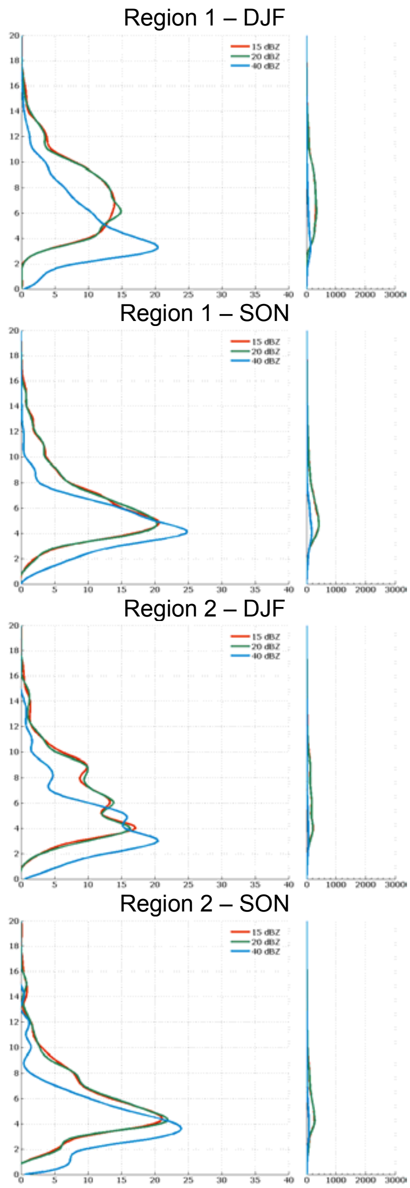

Figure 7: Relative frequency of maximum height of 15 (red), 20 (green) and 40 (blue) dBZ for all RPFs in the sample, considering the regions 1 and 2 showed in Figure 5 for two seasons and LLJA situations. Each panel shows the number of RPFs at every level.

3.3 DIURNAL CYCLE UNDER DIFFERENT LLJ SITUATIONS

In order to study the behavior of extreme convection under different LLJ situations, the diurnal cycle of the frequency of RPFs with volumetric rain higher than 5000 mm is shown in figure 9. The diurnal cycle of the SALLJ-related (CJE and NCJE) RPFs shows a nocturnal peak (06 UTC, 03 LT) in spring in western SESA, whereas the RPFs in eastern SESA have a maximum in phase with radiative heating. An afternoon maximum is extreme during NCJE in summer; on the contrary, a night-time maximum occurs during CJE suggesting a crucial role of the low level jet in CJE events and the radiative heating in NCJE. Previous studies suggest that the SALLJ brings high moisture and instability over SESA (Salio et al., 2007). The figure confirms this evidence given that strong convection over both areas does not occur in other SALLJ-related situations.

ACKNOWLEDGMENTS

This research was supported by UBA grant X266, ANPCyT grant Nº PICT 07 – 14420, PIP 5582.

REFERENCES

Bonner, W. D., 1968: Climatology of the low level jet. *Mon. Wea. Rev.*, **96**, 833-850.

Kummerow, C., W. Barnes, T. Kozu, J. Shiue, and J. Simpson, 1998: The Tropical Rainfall Measuring Mission (TRMM) Sensor Package. *J. Atmos. Oceanic Technol.*, **15**, 809-817.

Liu, C., E. Zipser, and S. W. Nesbitt, 2007: Global distribution of tropical deep convection: Different perspectives using infrared and radar as the primary data source, *J. Climate*, **20**, 489-503.

Liu, C., E. J. Zipser, D. J. Cecil, S. W. Nesbitt, and S. Sherwood, 2008: A cloud and precipitation feature database from 9

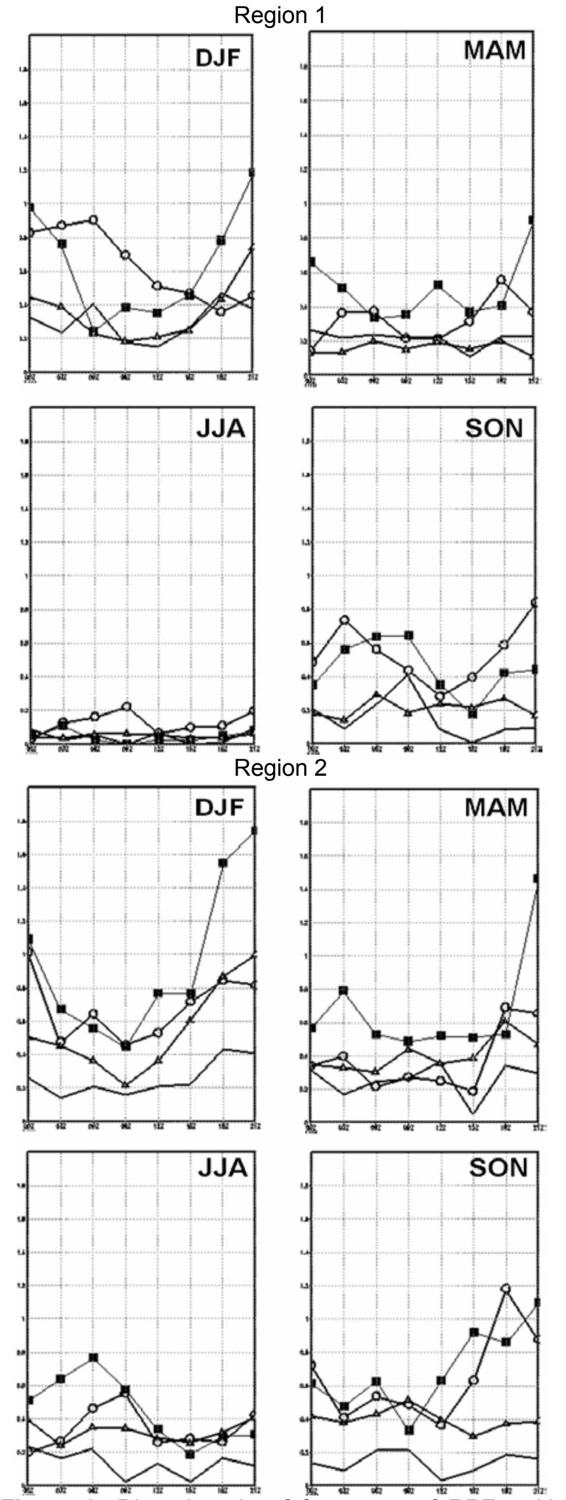

Figure 8: Diurnal cycle of frequency of RPFs with volumetric rain higher than 5000 mm during CJE (open circle), NCJE (bow filled), LLJA (none mark) and NoLLJ (open triangle). All season are presented in each panel.

years of TRMM observations. Submitted to *J. Appl. Meteor*.

Machado, L. A. T., W. B. Rossow, R. L. Guedes, and A. W. Walker, 1998: Life cycle variations of mesoscale convective systems over the Americas. *Mon. Wea. Rev*., **126**, 1630-1654.

Nesbitt, S. W., and E. J. Zipser, 2003: The diurnal cycle of rainfall and convective intensity according to three years of TRMM measurements. *J. Climate.*, **16**, 1456–1475.

Nicolini, M., P. Salio, G. Ulke, J. Marengo, M. Douglas, J. Paegle, and E. Zipser, 2004: South American low level jet diurnal cycle and three dimensional structure. *CLIVAR Exchanges*, No. 9, International CLIVAR Project Office, Southampton, United Kingdom, 6-8.

Salio, P., M. Nicolini, and A. C. Saulo, 2002: Chaco low level jet events characterization during the austral summer season by ERA reanalysis. *J. Geophys. Res.*, **107**, 4816.

Salio, P., M. Nicolini, and E. J. Zipser, 2007: Mesoscale Convective Systems Over Southeastern South America and Their Relationship with the South American Low-Level Jet. *Mon. Wea. Rev.*, **135**, 1290-1309.

Zipser, E. J., D. Cecil, C. Liu, S. Nesbitt, and D. Yorty, 2006: Where are the most intense thunder storms on earth?, *Bull. Amer. Meteor. Soc.*, **87**, 1057-1071.

Velasco, I. Y., and J. M. Fritsch, 1987: Mesoscale convective complexes in the Americas. *J. Geophys. Res.*, **92**, 9591-9613.

THE CHALLENGE OF CONVECTIVE-SCALE QUANTITATIVE PRECIPITATION FORECASTING

AXEL SEIFERT[1], MICHAEL BALDAUF[1],
KLAUS STEPHAN[1], ULRICH BLAHAK[2], KLAUS BEHENG[2]

[1] German Weather Service, Offenbach, Germany
[2] University of Karlsruhe / Research Center Karlsruhe, Karlsruhe, Germany

1. INTRODUCTION

At many operational centers high-resolution convective-scale numerical weather prediction models are currently being developed or already in operation. For example at the German Weather Service (DWD, Deutscher Wetterdienst) a 2.8 km grid-spacing configuration of the COSMO model, named COSMO-DE, is operational since early 2007. These new high-resolution models aim towards the explicit forecasting of weather phenomena on the mesoscale, for example severe convection or downslope windstorms, but a main promise of these models is to improve quantitative precipitation forecasts (QPF). Based on the experience at DWD we will give an overview of the challenges that come with these convective-scale NWP models.

For convective-scale NWP the physical parameterizations of the planetary boundary layer (PBL) and cloud microphysical processes are of great importance. Coming from models with 10 km and larger grid-spacing, the PBL schemes in operational NWP models are often well tuned for a near-neutral boundary layer, but may show some deficiencies for convective PBLs. This can lead to serious problems in a convective-scale NWP model that has to predict the initiation of deep convection explicitly. We will show some long-term sensitivity studies of the effects of certain modifications of the COSMO level 2.5 TKE scheme and discuss the impact on the diurnal cycle of convection and quantitative precipitation forecasts.

The explicit simulation of deep convection poses a special challenge for the microphysical parameterization as the cloud microphysics of convective storms is much more complicated than in stratiform clouds. Therefore the microphysics scheme has to be extended to include at least riming processes (graupel formation). For QPF applications the evaporation of raindrops below cloud base is yet another delicate problem. Due to the complexity of the microphysics of convective clouds it may be reasonable to use multi-moment schemes which have several advantages compared to the simpler and cheaper one-moment parameterizations. In the COSMO model a state-of-the-art two-moment scheme is available that has recently been extended to include hail formation. We will show a comparison of the one-moment scheme and the sophisticated two-moment scheme in operational convective-scale QPF and discuss the benefits gained from the more expensive two-moment parameterization.

Corresponding author's address: Dr. Axel Seifert, Deutscher Wetterdienst, Kaiserleistr. 42, 63067 Offenbach, Germany. E-mail: axel.seifert@dwd.de

2. THE OPERATIONAL COSMO-DE

At DWD a 2.8 km version of the COSMO model, called COSMO-DE (formerly known as LMK), is running operationally since April 2007. With 421×461 grid points the COSMO-

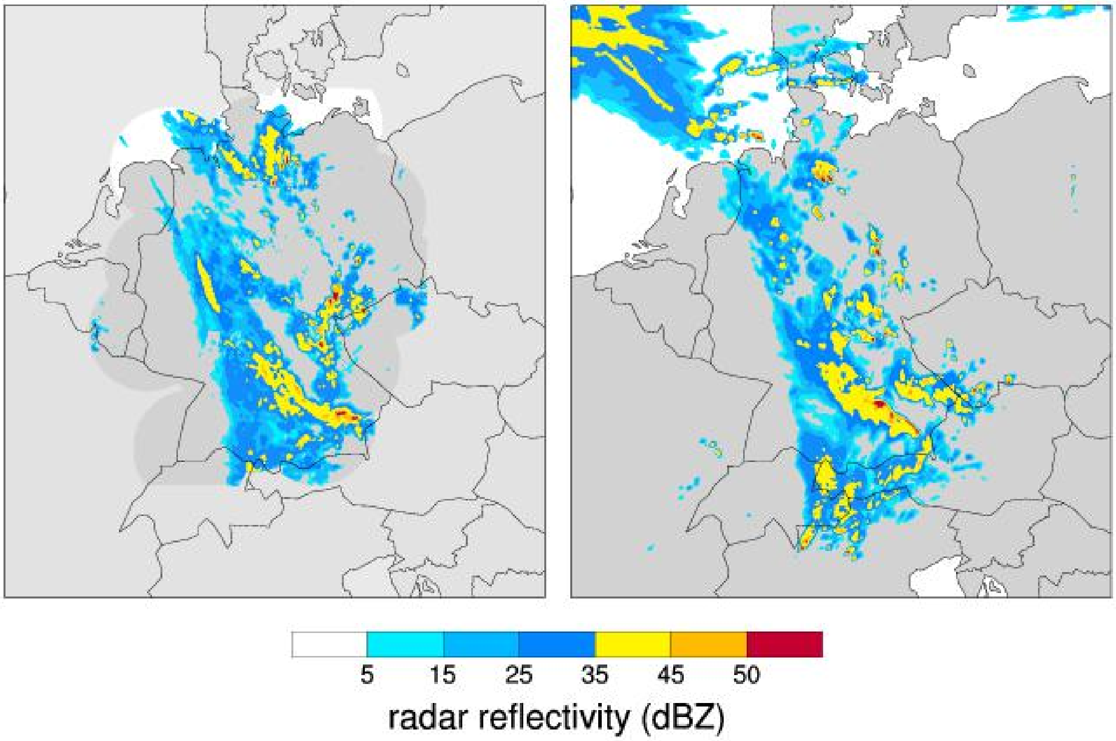

Figure 1: Reflectivity measured by the German radar network (left) and model-derived reflectivity (right) for 15 June 2007 17:30 UTC. Shown is the 00 UTC + 17:30 h COSMO-DE forecast. The domain size is approximately 1200 x 1300 km^2.

DE domain covers about 1200 x 1300 km^2 of central Europe including Germany, Switzerland, Austria, the Netherlands, Belgium, some parts of the neighboring countries and most of the Alps. One aim of the COSMO-DE is to provide shortest-range numerical forecasts of severe weather. Therefore a rapid update cycle of 21 hour forecasts is used with new forecasts every 3 hours. Due to the short cut-off time of 30 min which is used for COSMO-DE it is possible to complete, e.g., the 00 UTC forecast before 01 UTC using 256 IBM Power5 processors. Boundary conditions for COSMO-DE come from a 7 km COSMO model (COSMO-EU) which itself is nested into a global model, the GME (Majewski et al. 2002), which currently runs with 40 km grid spacing.

The COSMO-DE model configuration is based on an efficient Runge-Kutta solver (Wicker and Skamarock 2002), a one-moment cloud microphysics scheme that predicts cloud water, rain water, cloud ice, snow and graupel (Reinhardt and Seifert 2006) and a simple mass-flux parameterization of shallow convection based on the Tiedtke scheme (Doms and Förstner 2004). As for all COSMO model configurations at DWD, the data assimilation system uses a nudging approach which on this scale includes the assimilation of high-resolution radar data by latent heat nudging (Stephan et al. 2007).

During the first year of operational use, the convection-resolving COSMO-DE has proven its ability to forecast deep convection successfully, especially severe convective storms that are associated with frontal systems (forced convection). For example, COSMO-DE has performed quite well for the heavy convection events of 13 May 2007 and 15 June 2007 including the explicit forecasting of supercell storms. As an example, Figure 1 shows the observed vs model-derived radar reflectivities for 15 June 2007 17:30 UTC, depicted is the 00 UTC + 17:30 h forecast. On this day a cold front triggered severe convection along the front, especially in Southern Germany, and also pre-frontal convection occurred. Heavy hail was observed especially in Southern Germany, and overall 4 tornados were reported in Germany including an F2 tornado near the city of Bremen that was probably caused by a pre-frontal supercell. Although the COSMO-DE forecast shown in Fig. 1 is not able to predict individual convective cells in a deterministic sense, it gives a good and sufficient guidance when and where severe convection might occur.

3. BOUNDARY LAYER SENSITIVITIES

Although COSMO-DE has performed quite well for many events, it has also shown some weaknesses. The most prominent problem are the deficiencies in forecasting moist convection in weakly forced situations, e.g. summertime airmass-type convection or small-scale orographically-induced deep convection. These events are often underestimated or completely missing in the COSMO-DE forecasts. A detailed investigation and extensive sensitivity studies have shown that the problem of missing explicit convection is often caused by a too stable or too cold boundary layer.

Although deep convection is partly resolved on the 2.8 km grid, the planetary boundary layer (PBL) has to be described by a sub-grid parameterization in all NWP models. In the COSMO model a one-dimensional turbulence closure is applied using a prognostic equation for the turbulent kinetic energy (TKE). The scheme can be classified as Mellor-Yamada level 2.5 (Mellor and Yamada 1974; Raschendorfer 2007; Mironov 2007), i.e. the stability functions are explicitly predicted. As pointed out by Skamarock and Klemp (2008) and others there are some issues to derive an appropriate PBL scheme for grid sizes between 100 m and 5 km. In this range of grid sizes the two currently available parameterization approaches with a widely accepted theoretical basis, Reynolds-averaging and 'large-eddy simulation' (LES), do not truly apply. In operational NWP an additional problem comes in, since the operational schemes have been developed and 'tuned' over the last decades for considerably larger grid spacings of 7-20 km. At these resolutions the deep convection needs to be parameterized and this - to some extent - decouples the initiation of convection from the actual PBL structure, meaning that a convection parameterization can forecast convection at a certain grid point even if the predicted PBL structure itself would be too stable. A convective-scale model, like COSMO-DE, is not as forgiving as a coarser model when it comes to the representation of the PBL. Without an actual instability in the PBL itself it cannot predict the initiation of deep convection and the subsequent precipitation. This poses a great challenge for operational convective-scale NWP models.

One remarkable sensitivity that we found in the COSMO-DE simulations is that the asymptotic length scale l_∞ in the classic Blackadar-Deardorff formulation of the turbulent mixing length

$$l_{turb} = \frac{\kappa z\, l_\infty}{\kappa z + l_\infty}$$

often determines when and where convection is initiated in the forecast. The standard value used in the COSMO model TKE scheme is $l_\infty = 200$ m, which is not an unusual large value in NWP models, e.g., the ECMWF IFS model uses $l_\infty = 150$ m operationally. Reducing the asymptotic mixing length leads to less vertical mixing, larger vertical gradients and a more unstable PBL which can obviously help to initiate deep convection. This is shown in Fig. 2 for the case of 9 June 2007, a situation when severe convection occurred over the northwestern part of Germany which was probably initiated by a pre-frontal convergence line. In the control run using $l_\infty = 200$ m (Fig. 2b) the pre-frontal convection is missing almost completely while the sensitivity run with the reduced $l_\infty = 60$ m (Fig. 2c) predicts an intense pre-frontal convective system. Although neither of both forecasts would receive

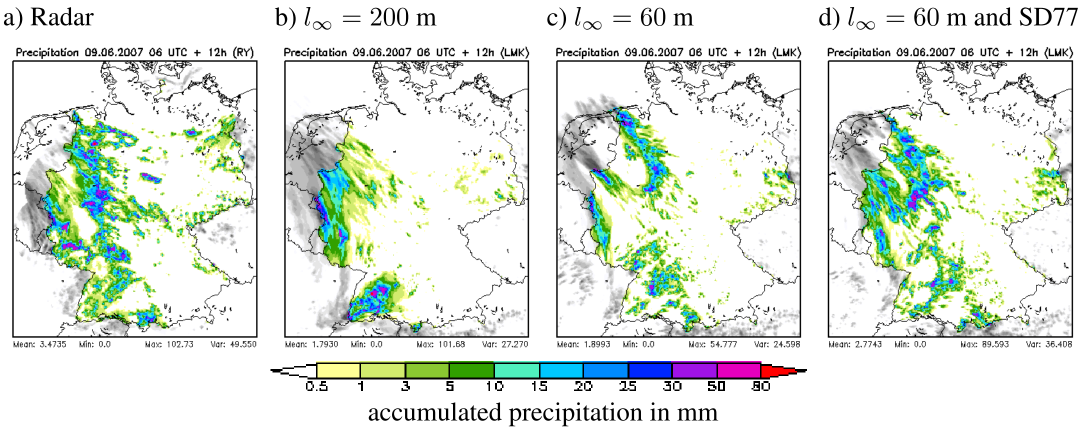

Figure 2: Accumulated surface precipitation for 9 June 2007 6 UTC to 18 UTC. German radar composite (a), 00 UTC + 18 h COSMO-DE forecasts using the operational configuration of the PBL scheme (b), using a reduced mixing length (c), and using the reduced mixing length and the original Sommeria and Deardorff sub-grid cloud scheme (d).

a 'good' on our subjective scale, the reduction of l_∞ clearly fosters the initiation of convection and can help to improve the precipitation forecast.[2]

Another part of the PBL scheme which affects the initiation of convection are the assumptions about sub-grid scale cloudiness which are used to transform from the prognostic model variables temperature T and water vapor mixing ratio q_v to the moist conserved variables liquid water potential temperature θ_l and total water content q_t. To estimate the sub-grid cloud cover and the sub-grid contribution to q_t a statistical cloud scheme is applied (Sommeria and Deardorff 1977, SD77 hereafter). In the operational version the formulation differs slightly from the SD77 formulation, e.g., sub-grid clouds are assumed to form earlier which compares better with satellite observations. In Fig. 2d we used the original SD77 values and for this case this leads to a better initiation and an intensification of the pre-frontal convection. This forecast would actually receive a 'pretty good' on our subjective quality scale. A comparison of the vertical profiles of temperature and moisture with measured soundings also confirms that the combination of $l_\infty = 60$ m with the original SD77 sub-grid cloudiness results in the best forecast for this case.

[2]The namelist parameter `turlen` of the COSMO model differs from l_∞ by a factor $1/\kappa = 2.5$.

4. MICROPHYSICAL SENSITIVITIES

In the following we show some sensitivity studies comparing the operational Lin-type one-moment microphysics scheme with the more sophisticated two-moment scheme of Seifert and Beheng (2006). The two-moment scheme has recently been extended and improved, e.g., it now applies the nucleation/activation parameterization of Segal and Khain (2006) and includes a separate hail category (Blahak 2008). All simulations are initialized by the operational COSMO-DE nudging analysis which applies the one-moment scheme.

In general the 2.8 km resolution COSMO-DE forecasts are quite robust to the microphysical assumptions or the chosen microphysics scheme. Only for a few cases we found a remarkable difference between, e.g., one-moment and two-moment representation of the cloud microphysics or, when using the two-moment scheme, the choice of the assumed aerosol or CCN properties.

One such example is the 20th July 2007 shown in Figure 3. On this day an impressive squall line developed along a cold front extending over almost entire Germany. The operational one-moment scheme was able to simulate at

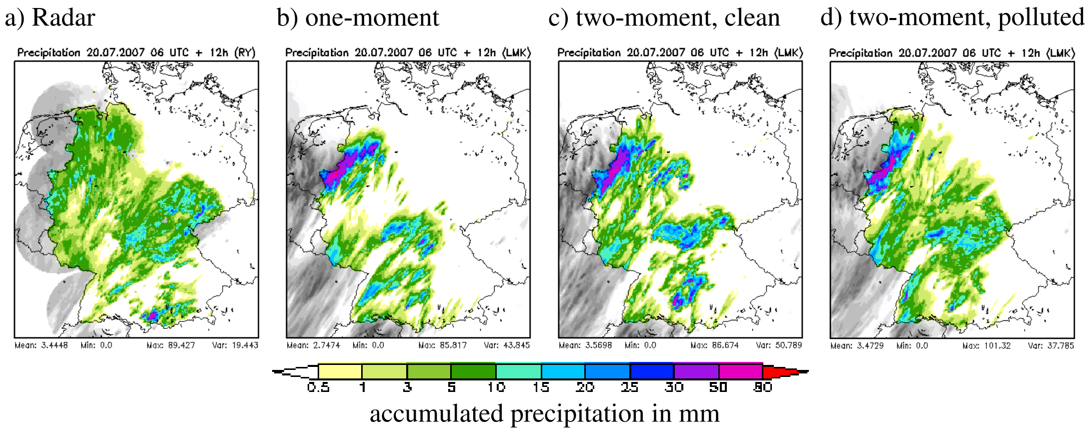

Figure 3: Accumulated surface precipitation for 20 July 2007 6 UTC to 18 UTC. German radar composite (a), 00 UTC + 18 h COSMO-DE forecasts using the one-moment scheme (b), the two-moment scheme assuming clean CCN conditions (c) and the two-moment scheme with polluted CCN conditions (d).

least some parts of the squall line quite successfully, although Fig. 3b shows that the accumulated precipitation is underestimated. This is significantly improved when using the two-moment scheme which seems to be able to describe the organization of the squall line and the development of secondary convection better than the one-moment scheme.

Assuming clean aerosol conditions in the two-moment scheme (Fig. 3c) results in a somewhat more intense squall line compared to the one-moment scheme. Compared to the polluted aerosol assumptions (Fig. 3d) the precipitation pattern is more localized and spotty in the clean case, while the polluted CCN assumptions yield a somewhat smoother precipitation field. This can easily be explained by the fact that assuming clean aerosol conditions favors a rapid rain formation via warm rain processes while polluted conditions lead to smaller particle sizes which slows down the precipitation formation and as a consequence more condensate ends up in the stratiform region of the convective system. In this case the polluted assumption leads to a better agreement with the observations. Note that these results are quite sensitive to the detailed assumptions about activation, entrainment and vertical distribution of aerosols.

An example of a more robust situation is the 11 November 2007 shown in Figure 4 when a winter-time frontal system resulted in a widespread stratiform precipitation over Germany. In this case the typical spatial structures of stratiform orographic precipitation are most obvious, e.g., at the Black Forest mountains in the southwestern part of Germany. Assuming high aerosol concentration leads to a reduction of the orographic precipitation maxima.

5. CONCLUSIONS

We have presented results of the newly operational convective-scale NWP system of the German Weather Service. Based on the 2.8 km grid-spacing COSMO model, the system is able to predict deep convection explicitly. It can therefore provide improved forecast guidance about location, timing and severity of deep convection and improve precipitation forecasts during summertime compared to coarser NWP models that apply a parameterization of convection.

On the convective-scale a good parameterization of the boundary layer is crucial for the success of the forecast, especially for the initiation of deep convection. In the COSMO model parameters like the asymptotic mixing length

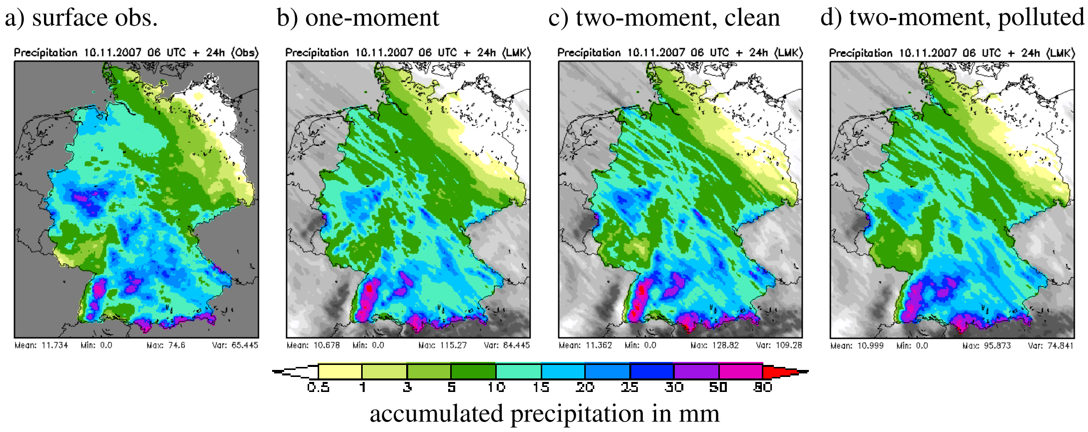

Figure 4: Accumulated surface precipitation for 11 Nov 2007 6 UTC to 12 Dec 6 UTC. Gauge-only 'REGNIE' precipitation estimate (a), COSMO-DE forecasts using the one-moment scheme (b), the two-moment scheme assuming clean CCN conditions (c) and the two-moment scheme with polluted CCN conditions (d).

or the assumptions about sub-grid cloudiness are very important and those parts of the model physics need to be considerably improved during the next years. NWP models that apply a convection parameterization are much less sensitive to those PBL assumptions, since the triggering of deep convection is parameterized within the convection scheme. A convective-scale model needs to do the initiation explicitly which poses a challenge for the boundary layer parameterization.

The cloud microphysics of deep convection is in some sense more complicated than of stratiform clouds and demands a more sophisticated parameterization, maybe even using a multi-moment approach. We have found that for most simulated cases the results, at least quantities like a 12h accumulation of surface precipitation, is quite robust to changes in the cloud microphysics (although individual cells and precipitation structures may differ considerably). Most sensitive to microphysical assumptions are probably cases when secondary convection is triggered by the outflow or cold pools of pre-exiting convective cells. In those cases a more sophisticated parameterization, like the Seifert and Beheng (2006) two-moment scheme for example, seems to be able to improve the forecast.

Although the currently operational version of COSMO-DE shows some systematic deficiencies, our results, and the experience at DWD in general, show that the convective-scale NWP model COSMO-DE is able to forecasts deep convection explicitly and that a so-called hybrid convection scheme is not necessary on this scale. Since individual convective cells are hardly predictable, the COSMO-DE model will be extended to a convective-scale ensemble prediction system in the near future.

References

Blahak, U.: 2008, Towards a better representation of high density ice particles in a state-of-the-art two-moment bulk microphysical scheme. *Proc. 15th Int. Conf. Clouds and Precip.*, Cancun, Mexico.

Doms, G. and J. Förstner, 2004: Development of a kilometer-scale NWP-system: LMK. *COSMO Newsletter*, **4**, 159–167.

Majewski, D., D. Liermann, P. Prohl, B. Ritter, M. Buchhold, T. Hanisch, G. Paul, W. Wergen, and J. Baumgardner, 2002: The operational global icosahedral-hexagonal gridpoint model GME: Description and high-resolution tests. *J. Atmos. Sci.*, **139**, 319–338.

Mellor, G. L. and T. Yamada, 1974: A hierarchy of turbulence closure models for planetary boundary layers. *J. Atmos. Sci.*, **31**, 1791–1806.

Mironov, D.: 2007, Turbulence in the lower troposphere: Second-order closure and mass-flux modelling frameworks. *Interdisciplinary Aspects of Turbulence*, F. Kupka and W. Hillebrandt, eds., Springer, Lecture Notes in Physics, in press.

Raschendorfer, M., 2007: A new TKE-based scheme for vertical diffusion and surface-layer transfer. Technical report, Deutscher Wetterdienst, Offenbach, in preparation.

Reinhardt, T. and A. Seifert, 2006: A three-category ice scheme for LMK. *COSMO Newsletter*, **6**, 115–120.

Segal, Y. and A. Khain, 2006: Dependence of droplet concentration on aerosol conditions in different cloud types: Application to droplet concentration parameterization of aerosol conditions. *J. Geophys. Res.*, **111**.

Seifert, A. and K. Beheng, 2006: A two-moment cloud microphysics parameterization for mixed-phase clouds. Part I: Model description. *Meteorol. Atmos. Phys.*, **92**, 45–66.

Skamarock, W. C. and J. B. Klemp, 2008: A time-split nonhydrostatic atmospheric model for weather research and forecasting applications. *J. Comp. Phys.*, **227**, 3465–3485.

Sommeria, G. and J. Deardorff, 1977: Subgrid-scale condensation in models of nonprecipitating clouds. *J. Atmos. Sci.*, **34**, 344–355.

Stephan, K., S. Klink, and C. Schraff, 2007: Assimilation of radar derived rain rates into the convective scale model COSMO-DE at DWD. *Quart. J. Roy. Met. Soc.*, submitted.

Wicker, L. J. and W. C. Skamarock, 2002: Time-splitting methods for elastic models using forward time schemes. *Mon. Wea. Rev.*, **130**, 2088–2097.

EFFECTIVE RADIUS AND DROPLET SPECTRAL WIDTH FROM RICO OBSERVATIONS

Sylwester Arabas[1], Hanna Pawlowska[1*] and Wojciech W. Grabowski[2]

[1]Institute of Geophysics, University of Warsaw, Warsaw, Poland
[2]National Center for Atmospheric Research, Boulder, Colorado, USA

1 INTRODUCTION

This paper presents a brief discussion of selected cloud microphysical parameters observed by an instrumented aircraft during the RICO (Rain In Cumulus over the Ocean) field experiment (see Rauber et al., 2007). Recent modeling studies (e.g. Chosson et al., 2004, 2007; Grabowski, 2006; Slawinska et al., 2008) show that assumptions concerning microphysical evolution of natural clouds (the homogeneity of cloud-environment mixing in particular) significantly affect the albedo of a field of shallow convective clouds, such as subtropical stratocumulus and trade-wind cumulus. As far as radiative transfer is concerned, the key parameter is the effective radius, the ratio between the third and the second moment of the cloud droplets size distribution. The effective radius is typically slightly larger than the mean volume radius (e.g. Martin et al., 1994; Pawlowska and Brenguier, 2000) and the ratio between the two depends on the width of the droplet spectrum. In a simple parameterization proposed by Martin et al. (1994), the effective radius is proportional to the mean volume radius, and the proportionality coefficient depends on the spectral width.

Motivation for the current analysis comes from two previously published studies. First, Pawlowska et al. (2006) discussed *in-situ* aircraft observations in eight cases of marine stratocumulus investigated during the Second Aerosol Characterization Experiment (ACE-2) in the eastern subtropical Atlantic. For a given flight (i.e., for given characteristics of the cloud condensation nuclei, CCN), local droplet concentration varied considerably, but the standard deviation of the cloud droplet spectra was typically in the range of 1 to $2\,\mu m$. Moreover, the width did not vary systematically between maritime and polluted clouds, and it showed a surprisingly small difference between near-adiabatic and diluted cloud samples. The current study investigates whether the conclusions drawn from stratocumulus observations are equally applicable to shallow cumulus clouds. Second, McFarlane and Grabowski (2007) presented results from ground-based remote sensing of optical properties of tropical shallow convective clouds over the Nauru Atmospheric Radiation Measurement (ARM) site. Remote sensing data suggest that, at a given height, the effective radius shows large spatial variability. The histogram of the effective radius (i.e., the frequency of occurrence) is relatively narrow near the cloud base, but it widens and becomes bimodal at higher elevations, showing a peak at large values representing droplets with radii several micrometers smaller than the adiabatic values, and the peak at small sizes corresponding to droplets not much different than those near the cloud base. However, about 60% of cloudy columns were excluded from the analysis (because of possible drizzle contamination), and it is unclear if this has any effect on the effective radius statistics. Availability of *in-situ* aircraft observations collected during RICO allows comparing remote sensing and *in-situ* data.

**Corresponding author address*: Prof. Hanna Pawlowska, Institute of Geophysics, University of Warsaw, Pasteura 7, 02-093 Warsaw, Poland. E-mail: hanna.pawlowska@igf.fuw.edu.pl.

2 AIRCRAFT OBSERVATIONS DURING RICO

RICO field project (see Rauber et al., 2007) took place in the Antilles in December 2004 and January 2005. The campaign included airborne, ground-based, and shipboard measurements. Current analysis is based on cloud microphysical *in-situ* observations aboard the NSF/NCAR C-130Q research aircraft. Cloud microphysical properties discussed here are derived mainly from measurements performed using the Fast-FSSP optical cloud droplet spectrometer (Brenguier et al., 1998). The NSF/NCAR C-130Q research flights carried out during RICO were composed of several constant-altitude legs and two vertical sounding legs at the beginning and at the end of each flight. Each of the 19 research flights lasted about eight hours, of which about 5 to 10% were spent in clouds. Most of the analyzed data were collected with $10\,Hz$ time-resolution resulting in an about $10\,m$ spatial resolution.

3 EXAMPLE OF RESULTS

Herein, we present results of flight-long statistics for a few selected flights. Such an approach enables one to assess typical properties of an ensemble of clouds of similar origin and preserves day-to-day variability of the cloud field (e.g. the cloud depth), but it averages any differences in cloud microphysics related to a particular stage of the cloud evolution.

Figure 1 summarizes the analysis (for four selected RICO flights) of droplet concentration N and selected droplet spectral parameters: the mean radius $\bar{r}$, its standard deviation σ_r, and its relative dispersion $d = \sigma_r/\bar{r}$. Droplet spectral parameters were derived from the 255-bin description of the 2 to $47\,\mu m$ droplet size-range measured by the Fast-FSSP.

All data are plotted as a function of height above the cloud base (approximated to be constant throughout the day and chosen with $100\,m$ resolution in accordance with the flight crew notes and aided by the analysis of liquid water content profiles). The plots summarize frequency distributions of cloud microphysical properties at different altitudes above cloud base. The considered altitude range ($1500\,m$) is divided into $100\,m$ deep classes. Frequency distributions of considered parameters are constructed for each altitude class. Bin sizes of given parameters have constant width (approximately $20\,cm^{-3}$ for N, $1\,\mu m$ for $\bar{r}$, $0.5\mu m$ for σ_r, and 0.07 for d). Frequency distributions for different altitudes are stacked up creating a two-dimensional sample distribution. Rows representing marginal statistical significance (small number of data-points) are discarded.

The distribution is visualized with frequency isolines (contours) and color-scale (pixel-like colored rectangles representing histogram bins). The contours surround 25%, 50%, and 75% of the most probable cases, while the colored area covers all registered values with color-intensity gradually increasing with the frequency of occurrence.

Analysis covered non-drizzling parts of clouds. An in-cloud data-point is defined using a droplet concentration threshold ($N > 10\,cm^{-3}$) applied to the Fast-FSSP data. A volume of air is considered to contain drizzle when the Optical Array Probe (OAP-2DC) registered concentration above $10\,l^{-3}$ within a two-second time-window. Removal of drizzling areas justifies comparison of the analysis results to a simple condensational growth model.

The four selected cases show that the day-to-day variations of the vertical extent of clouds were significant, ranging from 700 to 1200 meters. In all four flights, 90% of cases were characterized by droplet concentrations lower than $100\,cm^{-3}$ (and even lower than $50\,cm^{-3}$ for the rf07 and rf09). The high-concentration tail (related to about 10% of least frequent cases) observed during the rf06 flight comes from a few clouds with very high concentration of small droplets (in the 5 to $10\,\mu m$ size-range). This feature is also present in the data obtained by the second droplet spectrometer deployed during RICO, the FSSP-100.

The mean radius statistics presented in the second row of plots in Fig. 1 show an increase of droplet size until approximately half of the depth of the cloud field. Above, the increase of $\bar{r}$ is less pronounced. The histograms are quite wide, implying a significant spatial variability of $\bar{r}$, most likely related to entrainment and mixing processes in these clouds. The standard deviation

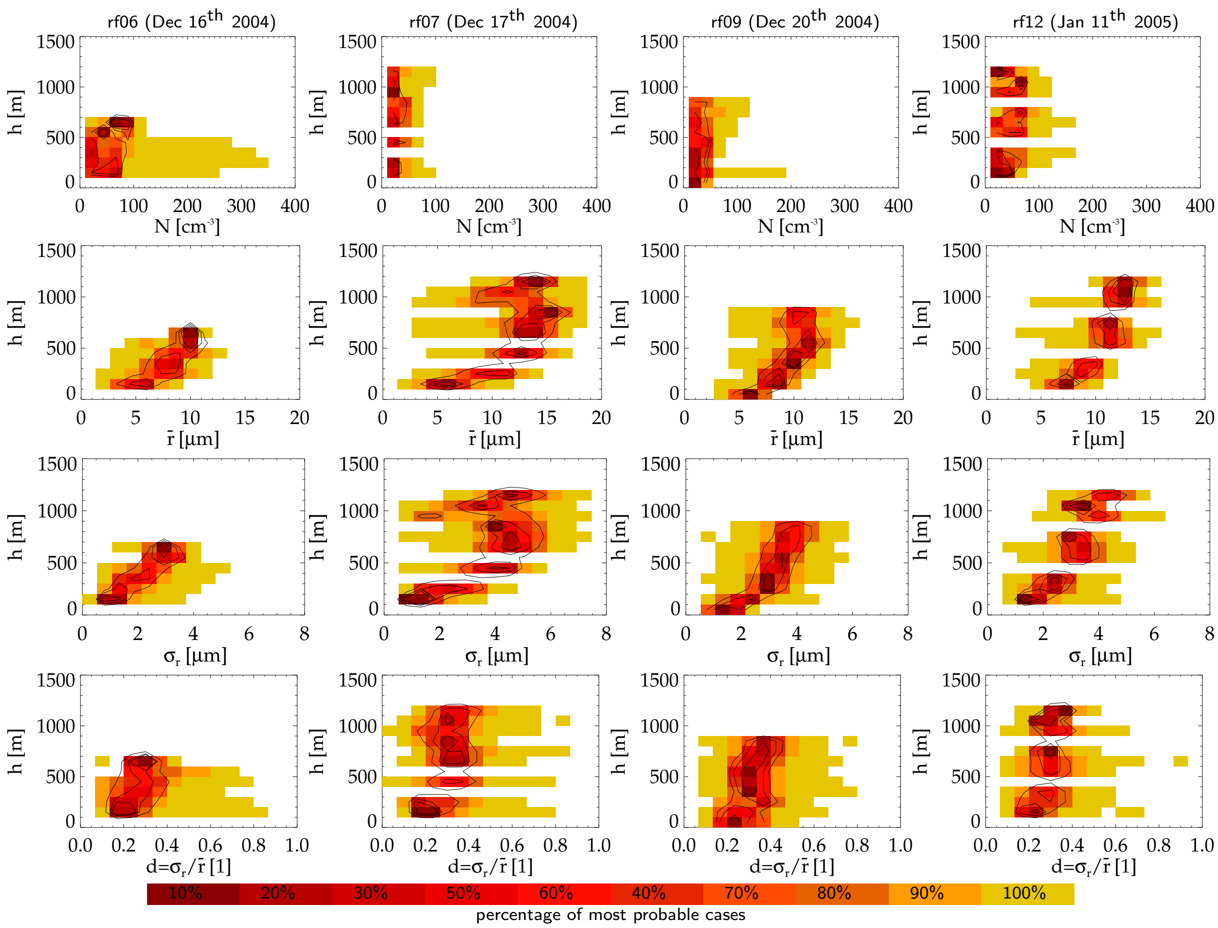

Figure 1: Results of droplet-spectrum and concentration measurements performed during four RICO flights (rf06, rf07, rf09, and rf12). The top-row plots show droplet concentration N, the 2nd, 3rd and 4th rows present the mean radius $\bar{r}$, the standard deviation of radius σ_r, and the relative dispersion $d = \sigma_r/\bar{r}$, respectively. All data plotted as a function of the height above the cloud-base.

of the droplet spectra σ_r (the third row) shows its gradual increase with height, from values in the 1 to $2\,\mu m$ in the lowest couple hundred meters, to values as large as $5\,\mu m$ near the cloud top. The values in the lowest 100–$200\,m$ of the cloud field are similar to those observed in stratocumulus in ACE-2 (see Pawlowska et al., 2006). Large values of σ_r in the middle and upper parts of the cloud field are again most likely related to entrainment and mixing processes, and seem consistent with results presented in Burnet and Brenguier (2007, see their Fig. 9 in particular). The relative dispersion d (the fourth row) is about 0.2 in the lowest couple hundred meters (again consistent with the data from pristine cases in ACE-2; Pawlowska et al., 2006, Fig. 2). It increases slightly at higher levels, with typical values between 0.2 and 0.4. However, the range of values of d observed during the RICO campaign is relatively wide (from 0.1 to 0.8), while the spread of d reported for ACE-2 was significantly smaller (cf. Fig. 2, 3 in Pawlowska et al., 2006).

A closer analysis of the rf07 data suggests that the aircraft probed two separate layers of clouds. On this day, the lower cloud layer was capped by a shallow layer of precipitating stratiform clouds described in the report of the flight crew. This seems to explain the structures suggesting a second cloud base around $900\,m$ in the plots of $\bar{r}$ and σ_r in fig. 1. Such multi-layer situation might be an example of a difficult case for the retrieval procedure applied to the remote-sensing data presented

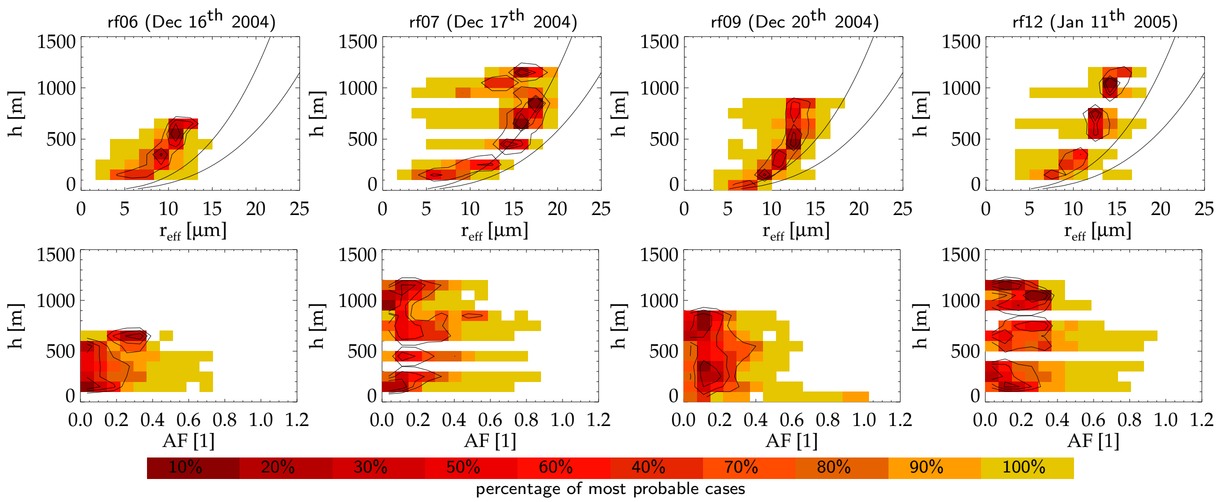

Figure 2: Effective radius r_{eff} and adiabatic fraction AF values, as a function of height above cloud base, derived from the Fast-FSSP measurements during four RICO flights. Effective radius for adiabatic clouds with droplet concentrations of 50 and $100cm^{-3}$ are shown by solid lines (right-hand and left-hand lines respectively).

in McFarlane and Grabowski (2007) where a wide bimodal shape of effective radius frequency distribution was reported at higher parts of the clouds.

Figure 2 presents results of the analysis of the effective radius r_{eff} (top row) and the adiabatic fraction AF (bottom row) in the format similar to Fig. 1 and for the same four flights. As in McFarlane and Grabowski (2007), an adiabatic parcel model was used to obtain the adiabatic liquid water content above the cloud base. The ratio between the observed water content (obtained from the Fast-FSSP measurements) and the adiabatic limit, the adiabatic fraction AF, describes the local dilution of a probed cloud volume. Figure 2 should be compared to Fig. 1 and 2 in McFarlane and Grabowski (2007). In agreement with many previous observations, RICO clouds are significantly diluted by entrainment. However, the dilution is not as strong as in McFarlane and Grabowski (2007). One needs to keep in mind, however, that the values of AF are strongly dependent on the choice of the cloud-base altitude. Since the analysis presented here does not include a precise determination of the cloud-base height, the AF values are characterized by significant uncertainties. The most striking is the difference in the statistics of the effective radius obtained in the current study and those presented in McFarlane and Grabowski (2007). In particular, the distributions here are monomodal (except for the flight rf07 which featured two separate cloud layers as discussed above), with the maximum frequency of values roughly corresponding to the larger r_{eff} values in Fig. 2 in McFarlane and Grabowski (2007).

4 DISCUSSION

This paper discusses results of aircraft data analysis from selected flights in RICO. The goal is to obtain relationships that are needed in cloud model microphysical parameterizations, for instance, in the two-moment bulk microphysics scheme of Morrison and Grabowski (2007, 2008) where the width of the cloud droplet spectrum has to be parameterized. In addition, the width of the spectrum has been shown to affect the relationship between the effective radius and the mean volume radius (Martin et al., 1994; Liu and Daum, 2000). The values of the relative dispersion observed in RICO cumuli are larger than those in ACE-2 and in previous stratocumulus observations (e.g. Martin et al., 1994). This perhaps should not be surprising considering macroscopic (e.g. cloud depth) and dynamical (e.g. entrainment) differences between shallow cumuli and stratocumuli.

As for the frequency distribution of the effective radius, there are significant differences between results presented here and those in McFarlane and Grabowski (2007, Fig. 2 therein). In particular, the aircraft data show much narrower distributions, roughly corresponding to the peak at larger droplet sizes in Fig. 2 of McFarlane and Grabowski (2007), that is, those a few micrometers smaller than the adiabatic size. Arguably, these differences come from the procedure that was used in McFarlane and Grabowski (2007) to avoid columns with drizzle. Arguably, such a procedure removes from the analysis columns that are least diluted (because such columns are most likely to have some drizzle near cloud tops) and thus biases the sample toward columns that are heavily diluted. The adiabatic fraction shown in McFarlane and Grabowski (2007) suggests that the sample used in the analysis consists of columns that are indeed heavily diluted (the mean adiabatic fraction below 0.1, see Fig. 1 therein), and it supports such a conjecture.

ACKNOWLEDGEMENTS

This work was supported by the European Commission's 6. FP IP EUCAARI and Polish MNiSW grant 396/6/PR UE/2007/7 (HP, SA). The National Center for Atmospheric Research is operated by the University Corporation for Atmospheric Research under sponsorship of the National Science Foundation. SA acknowledges the financial support for participation in the ICCP-2008 offered by the organizers.

REFERENCES

Brenguier, J.-L., T. Bourrianne, A. Coelho, J. Isbert, R. Peytavi, D. Trevarin, and P. Weschler, 1998: Improvements of droplet size distribution measurements with the Fast-FSSP (forward scattering spectrometer probe). *J. Atmos. Oceanic Technol.*, **15**, 1077–1090.

Burnet, F., and J.-L. Brenguier, 2007: Observational study of the entrainment-mixing process in warm convective clouds. *J. Atmos. Sci.*, **64**, 1995–2011.

Chosson, F., J.-L. Brenguier, and M. Schröder, 2004: Radiative impact of mixing processes in boundary layer clouds. *Proceedings of the 14th International Conference on Clouds and Precipitation*, Bologna, Italy, 371–374.

Chosson, F., J.-L. Brenguier, and L. Schüller, 2007: Entrainment-mixing and radiative transfer simulation in boundary-layer clouds. *J. Atmos. Sci.*, **54**, 2670–2682.

Grabowski, W. W., 2006: Indirect impact of atmospheric aerosols in idealized simulations of convective-radiative quasi-equilibrium. *J. Climate*, **19**, 4664–4682.

Liu, Y., and P. H. Daum, 2000: Spectral dispersion of cloud droplet size distributions and the parametrization of cloud droplet effective radius. *Geophys. Res. Lett.*, **27**, 1903–1906.

Martin, G. M., D. W. Johnson, and A. Spice, 1994: The measurement and parameterization of effective radius of droplets in warm stratocumulus clouds. *J. Atmos. Sci.*, **51**, 1823–1842.

McFarlane, S. A., and W. W. Grabowski, 2007: Optical properties of shallow tropical cumuli derived from ARM ground-based remote sensing. *Geophys. Res. Lett.*, **34**, L06 808.

Morrison, H., and W. W. Grabowski, 2007: Comparison of bulk and bin warm rain microphysics models using a kinematic framework. *J. Atmos. Sci.*, **64**, 2839–2861.

Morrison, H., and W. W. Grabowski, 2008: Modeling supersaturation and subgrid-scale mixing with two-moment bulk warm microphysics. *J. Atmos. Sci.*, **65**, 792–812.

Pawlowska, H., and J.-L. Brenguier, 2000: Microphysical properties of stratocumulus clouds during ACE-2. *Tellus Series B*, **52**, 868–887.

Pawlowska, H., W. W. Grabowski, and J.-L. Brenguier, 2006: Observations of the width of cloud droplet spectra in stratocumulus. *Geophys. Res. Lett.*, **33**, L19 810.

Rauber, R., and Coauthors, 2007: Rain in shallow cumulus over the ocean – the RICO campaign. *Bull. Amer. Meteor. Soc.*, **88**, 1912–1928.

Slawinska, J., W. W. Grabowski, H. Pawlowska, and A. A. Wyszogrodzki, 2008: Optical properties of shallow convective clouds diagnosed from a bulk-microphysics large-eddy simulation. *J. Climate*, **21**, 1639–1647.

Work presented during the 15th International Conference on Clouds and Precipitation ICCP-2008, Cancún, Mexico

THE PRODUCTION OF WARM RAIN IN SHALLOW CUMULUS CLOUDS.

Jason H. Lowenstein[1], Alan M. Blyth[2], Stewart Davies[1], & Kenneth S. Carslaw[1]
[1] School of Earth and Environment, University of Leeds, UK
[2] National Centre for Atmospheric Science, University of Leeds, UK

1 INTRODUCTION

One of the reasons why the problem of explaining the production of warm rain has remained unsolved for so long is because it is difficult to make observations of the time evolution of individual clouds with aircraft and radar. Here we show that the rate of production of warm rain, as observed in a single, but representative, shallow cumulus cloud during the Rain in Cumulus Over the Ocean (RICO) field campaign (Rauber *et al.*, 2007), can be explained using a 2-D axisymmetric cloud model using only the observed sub-cloud aerosols, including giant and ultra-giant nuclei, that are ingested into cloud base. The agreement between observations and model results is confirmed with parcel model results for more cases.

2 THE FIELD STUDY

The Rain in Cumulus Over the Ocean (RICO) field campaign was different to previous projects (e.g. the Small Cumulus Microphysics Study; Blyth *et al.* (2003)) that were designed to study the development of warm rain in cumulus clouds in two critical ways. Firstly, the aircraft penetrated a large number of clouds at a constant altitude before moving to a different altitude, rather than chasing individual clouds and attempting to sample the growth phase of a single cloud at different altitudes. Secondly, the radar scanned many clouds rapidly at a constant elevation angle during RICO, rather than attempting to coordinate with the aircraft and sample single clouds by varying the elevation angle at several appropriate azimuth angles. This sampling strategy is the key factor that made the difference. It is notoriously difficult to measure an individual cloud with radar and/or aircraft from its early stages through to the onset of precipitation unless the clouds are anchored to particular features, such as a mountain range. However, in RICO many clouds could be tracked with the radar over the critical early stages of their lifetime and DSDs were measured with the aircraft at all altitudes of the clouds at all stages of their development, including near the top of ascending turrets.

RICO took place over the Atlantic Ocean off the Caribbean islands of Antigua and Barbuda, from 15 Nov 2004 through 24 Jan 2005. Several observational platforms were used including: the National Center for Atmospheric Research (NCAR) dual-polarization and dual-wavelength radar SPolKa; the NCAR C-130, University of Wyoming King Air and UK BAe 146 research aircraft; and the Seward Johnson research vessel. The radar scanned clouds in Plan Position Indicator (PPI) mode and was able to complete a full volume scan in 3-4 mins. The aircraft were equipped with sophisticated optical probes to measure the aerosols and cloud droplets. Data gathered with the radar and NCAR C-130 aircraft for one cloud observed on 14 Jan 2005 will be presented in this paper. The temperature at cloud base, the cloud depth and width and the development of this cloud are representative of other clouds sampled during RICO.

3 RESULTS

Giant (1 μm $\leq d_{dry} \leq$ 10 μm) and ultra-giant aerosol particles ($d_{dry} >$ 10 μm) have been shown to be responsible for the onset of the coalescence process, and hence the production of warm rain (e.g. Johnson (1982); Lasher-Trapp *et al.* (2001)). The NCAR

C-130 aircraft typically flew 60-km diameter circles at altitudes below cloud base. During this time, the sub-cloud aerosol size distribution (ASD), measured by the Forward Scattering Spectrometer Probe (FSSP, 3.1 μm $< d <$ 46.5 μm), was averaged over long intervals to maximise the volume sampled. Fig. 1 shows an aerosol size distribution averaged over 750 s at an altitude of 100 m above mean sea level (MSL) on 14 Jan 2005. The sub-cloud particles measured by the FSSP during RICO were deliquesced (Colon-Robles *et al.*, 2006), and hence the raw distribution was converted to the dry sizes to produce the distribution shown in Fig. 1 using the Köhler Equation with the mean values of temperature and relative humidity over the averaging period. The dry sea-salt distributions measured more than fifty years ago with small glass slides at cloud levels in Hawaii (Woodcock, 1953) are overlaid in Fig. 1. There is good agreement with the FSSP distribution when compared at similar low-level horizontal windspeeds. For example, the observed FSSP distribution measured at an average low-level windspeed of 13.5 m s^{-1} lies between Woodcock's measurements made at windspeeds of 10 m s^{-1} and 16 m s^{-1}. The sub-cloud aerosol measurements made by the FSSP during RICO have been shown to be similar to measurements made by a Giant Nuclei Impactor system (Colon-Robles *et al.*, 2006).

The ASD shown in Fig. 1 was used as input in a 2-D, axisymmetric, bin-resolved, dual-moment cloud model (Reisin *et al.*, 1996; Yin *et al.*, 2005). The resolution was 60 m in the horizontal, 120 m in the vertical and the radial and vertical domains were 6 km and 4.8 km, respectively. The liquid-phase microphysical processes included in the model are droplet nucleation (from the ASD), condensation and evaporation, collision and coalescence, and binary breakup. There was no scheme to enhance the collection efficiency due to turbulence (Yin *et al.*, 2005). The sub-cloud ASD was assumed to be composed entirely of ammonium sulphate. For diameters $d \lesssim 3$ μm, the model ASD was defined using a value of C (the number of CCN activated at 1% supersaturation, 144 cm^{-3}) and k (0.57) from the activity distribution, derived from measurements made by the CCN spectrometer onboard the C130 aircraft during flight legs below cloud base (Dr J Hudson personal communication, 2006). For $d \gtrsim 3$ μm, the

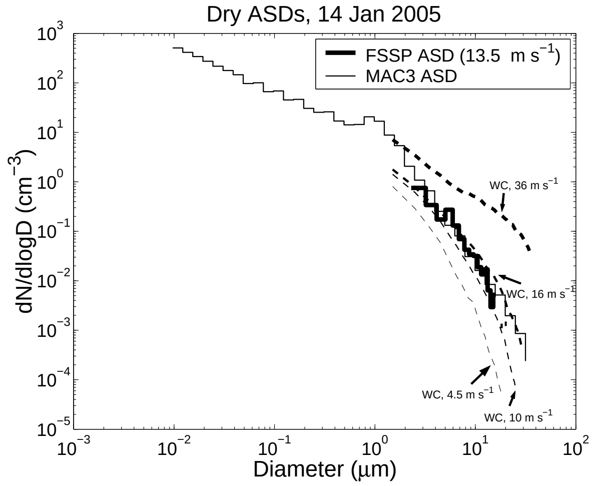

Figure 1: *Aerosol size distributions used in the present study compared with sea-salt distributions measured at cloud levels in Hawaii (Woodcock, 1953). The thick solid line indicates the dry FSSP distribution calculated from measurements made at 100 m above MSL on 14 Jan 2005 (from 16:20:03 to 16:32:31 UTC), while the thin solid line shows the aerosol size distribution used to initialise the 2-D cloud model. Distributions from Woodcock are overlaid as dashed lines, and plotted as a function of four different low-level horizontal wind speeds: 4.5 m s^{-1}, 10 m s^{-1}, 16 m s^{-1} and 36 m s^{-1}.*

model ASD was made to match the observed sub-cloud FSSP distribution. Droplets were activated using a scheme that accounts for the non-equilibrium growth of the largest CCN below cloud base (Yin *et al.*, 2005).

Observations of the time rate of change of radar reflectivity (Z) were made by the SPolKa radar in a cloud tracked from 20:02:10 to 20:52:10 on 14 Jan 2005. The beam width for this radar was 0.91° while range gates were every 150 m. Fig. 2a (at the end of the paper) shows the resulting time-height diagram constructed from the maximum reflectivity values in the cloud during PPI scans. The diagram begins when the radar top is at its minimum altitude. The reflectivity is likely dominated by Bragg scatter for $Z <$ 10 dBZ (Knight and Miller, 1993), so comparisons with model-produced Rayleigh reflectivity cannot be made for times less than about 8 mins. The maximum Rayleigh radar reflectivity increased from 15 dBZ at t = 10 mins, z = 2 km to 30 dBZ at

t = 15 mins, z = 3.2 km, the top of the observed radar echo, i.e. at an average ascent rate of 4 m s^{-1}. The top of the 15 dBZ echo was not measured by the radar. Therefore the ascent rate of the 15 dBZ echo was likely to be slightly greater than 4 m s^{-1}. The maximum rate of increase in radar reflectivity during this time period at 2 km is approximately 15 dBZ to 30 dBZ from one observation point to the next – a time period of about 4.5 mins. The reflectivity subsequently increased to a value of 45 dBZ at 20 mins between about 0.5 and 2 km above MSL.

The time-height diagram of model-produced Rayleigh reflectivity at a radial distance from the axis of the model, R = 420 m is shown in Fig. 2b. The cloud properties reproduced by the model are similar to those observed in clouds penetrated on this day. The maximum observed vertical wind speed measured by the aircraft and produced by the model is about 9 m s^{-1}. At R = 420 m, the maximum model-produced LWC is about 2.4 g kg^{-1} while the maximum observed value is approximately 1.7 g kg^{-1} (derived from the 10-Hz FSSP data).

As shown in Figs. 2a and b, the 2-D model is able to reproduce (i) the general shape of the observed radar reflectivity echo and (ii) the rate of increase of reflectivity in the development stages (15 to 30 dBZ) when raindrops are just beginning to form. Notice that the model 15-dBZ radar reflectivity echo is first produced at $z \approx 2$ km, similar to the observations. The maximum reflectivity is 45 dBZ, which is the same as the observations.

Figs. 2a and b show that the modelled production rate of warm rain compares well with the observations. We emphasise that the observed ASD was used to initialise the model. There was no scheme in the model to enhance the collection efficiency due to turbulence. Furthermore, there is no evidence of entrainment causing an enhancement in the growth of the largest drops. In fact, the DSDs produced by the model indicate that the size of the largest drops in the updraught decreases as the amount of entrainment increases.

The agreement between observations and model results is confirmed by the fact that for all of the cases studied, the growth time required for the tail of the DSDs produced by the parcel model to match the observed DSDs falls within the range of times calculated from cloud-top ascent rates observed by the SPol radar.

In-situ aircraft measurements were made in this cloud (shown in Fig. 2a) between 20:25:18 and 20:25:38, when the cloud was in its decaying stage. Fig. 3 presents a comparison of the largest droplets that contribute to the radar reflectivity between: (i) a 1 Hz droplet size distribution (DSD) measured by a PMS two dimensional optical array cloud probe (2D-C) and a PMS two dimensional optical array precipitation probe (2D-P) during the middle of this penetration through cloud (20:25:27); and (ii) a DSD produced by the cloud model at a similar point in time (23 minutes after 20:02:10), altitude (2 km above MSL) and LWC region (in the centre of the model cloud). This location is indicated by the solid black cross on the observed time-height diagram in Fig. 2a. The model is able to reproduce the large-size tail of the observed DSD from $d \sim 70$ μm all the way to precipitation-sized drops, several mm in diameter. Rayleigh reflectivity calculated from each of these DSDs ($Z \sim 30$ dBZ) compare well with the reflectivity measured by the radar at this point in time and space (Fig. 2a).

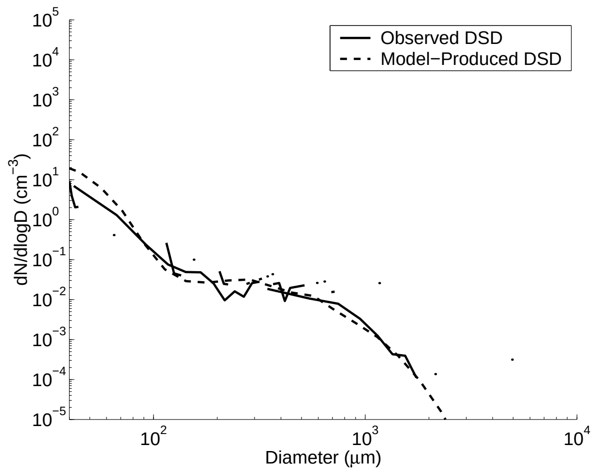

Figure 3: *Comparison of the largest droplets in an observed and model-produced DSD. The solid line represents the large-size tail of the DSD measured on the NCAR C130 aircraft on 14 Jan 2005 at 20:25:27 while the dashed line represents the large-size tail of the 2-D model DSD at a similar point in time (23 minutes after 20:02:10), altitude (2 km above MSL) and LWC region (in the centre of the model cloud).*

4 CONCLUSIONS

The results show that aerosols alone are sufficient to explain the production of warm rain in this shallow maritime cumulus cloud (which was representative of the clouds sampled during the project), as suggested by Woodcock (1953) and Johnson (1982), for example. Thus the warm rain process in this maritime cumulus cloud is a relatively simple process of condensational growth of droplets formed on the sub-cloud aerosols (including giant and ultra-giant aerosols), followed by stochastic collision and coalescence. Comparisons between parcel model results and observed DSDs for other cases suggest that the result applies to several RICO clouds.

References

Blyth A, Lasher-Trapp S, Cooper W, Knight C, Latham J. 2003. The role of giant and ultra-giant nuclei in the formation of early radar echoes in warm cumulus clouds. *J. Atmos. Sci.* **60**: 2557–2572.

Colon-Robles M, Rauber R, Jensen J. 2006. Influence of low-level wind speed on droplet spectra near cloud base in trade wind cumulus. *Geophys. Res. Lett.* **33**: L20 814, doi:10.1029/2006GLO27 487.

Johnson DB. 1982. The role of giant and ultragiant aerosol particles in warm rain initiation. *J. Atmos. Sci.* **39**: 448–460.

Knight C, Miller L. 1993. First radar echoes from cumulus clouds. *Bull. Amer. Meteor. Soc.* **74**: 179–188.

Lasher-Trapp S, Knight C, Straka J. 2001. Early radar echoes from ultragiant aerosol in a cumulus congestus: Modeling and observations. *J. Atmos. Sci.* **58**: 3545–3562.

Rauber RM, Stevens B, Ochs III HT, Knight C, Albrecht BA, Blyth AM, Fairall CW, Jensen JB, Lasher-Trapp SG, Mayol-Bracero OL, Vali G, Anderson JR, Baker BA, Bandy AR, Burnet E, Brenguier JL, Brewer WA, Brown PRA, Chuang P, Cotton WR, Girolamo LD, Geerts B, Gerber H, Gke S, Gomes L, Heikes BG, Hudson JG, Kollias P, Lawson RP, Krueger SK, Lenschow DH, Nuijens L, O'Sullivan DW, Rilling RA, Rogers DC, Siebesma AP, Snodgrass E, Stith JL, Thornton DC, Tucker S, Twohy CH, Zuidema P. 2007. Rain in Shallow Cumulus Over the Ocean. *BAMS* **88**: 1912–1928.

Reisin T, Levin Z, Tzivion S. 1996. Rain production in convective clouds as simulated in an axisymmetric model with detailed microphysics. part i: Description of the model. *J. Atmos. Sci.* **53**: 497–520.

Woodcock A. 1953. Salt nuclei in marine air as a function of altitude and wind force. *J. Atmos. Sci.* **10**: 362–371.

Yin Y, Carslaw K, Feingold G. 2005. Vertical transport and processing of aerosols in a mixed-phase convective cloud and the feedback on cloud development. *Q. J. R. Meteorol. Soc.* **131**: 221–245.

5 ACKNOWLEDGEMENTS

We thank the many people involved in RICO, particularly Drs. Robert Rauber, Bjorn Stevens, Harry Ochs III and Charles Knight for leading the project and all the work involved in making it happen. We are grateful to Al Schanot, David Rogers, Jørgen Jensen and other scientists in EOL and NCAR for assistance with the NCAR C-130 data. We would also like to thank Drs. William Cooper, Jørgen Jensen, Sonia Lasher-Trapp and Justin Peter for providing much insight into the research. The first author would like to acknowledge the financial support provided by the Overseas Research Students Award Scheme (ORSAS). This work was supported by the Natural Environment Research Council under grant number NER/A/S/2003/00360.

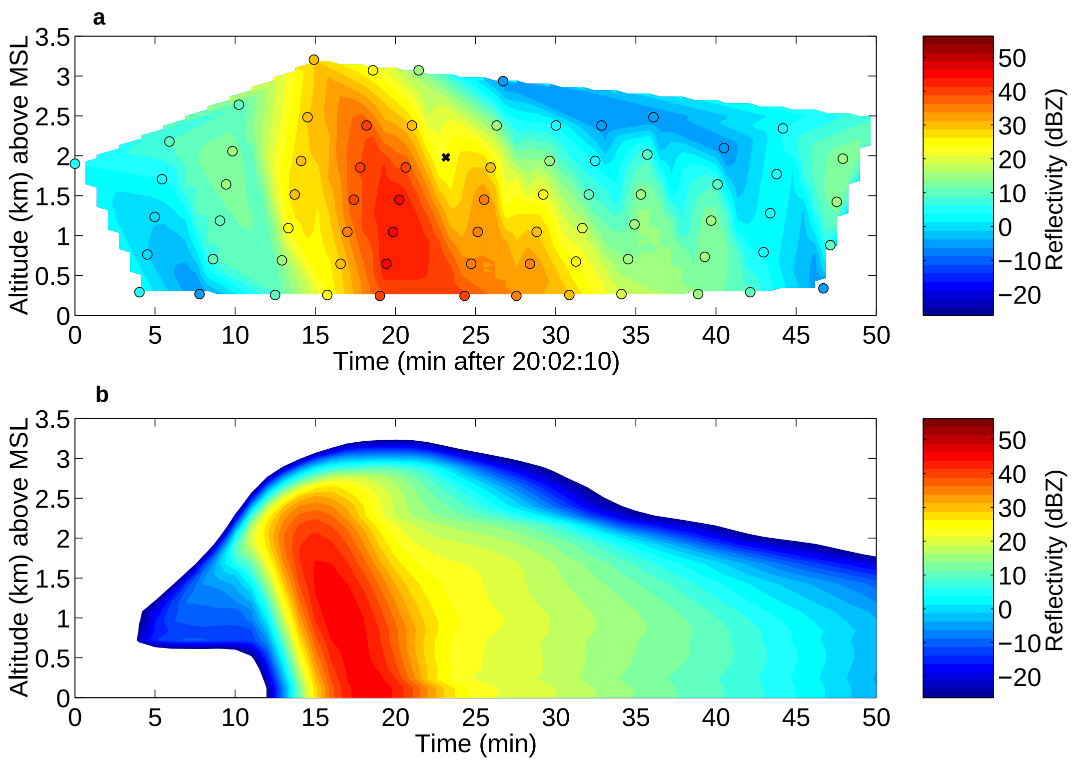

Figure 2: *Time-height diagrams comparing the evolution of maximum reflectivity in a cloud observed on radar and produced by a 2-D axisymmetric cloud model.* ***a,*** *Time-height diagram of observed maximum reflectivity from the SPol radar on 14 Jan 2005. The encircled colours indicate the location in time and space, and also the actual reflectivity where an observation was made. The solid black cross represents the location in space and time where and when the NCAR C130 aircraft penetrated the cloud.* ***b,*** *Same as in* ***a*** *except shows the evolution of reflectivity plotted at a radial distance of 420 m from the centre of the model cloud.*

ENTRAINMENT, MIXING, AND MICROPHYSICS IN TRADE-WIND CUMULUS

Hermann E. Gerber[1], Glendon Frick[1], Jorgen B. Jensen[2], and James G. Hudson[3]

[1] Gerber Scientific Inc., Reston, VA , USA
[2] National Center for Atmospheric Research, Boulder, CO, USA
[3] Desert Research Institute, Reno, NV, USA

1. INTRODUCTION

A study of trade-wind cumulus clouds (Cu) observed during RICO from the NCAR C-130 research aircraft consists of analyzing the entrainment, mixing and microphysics of a conditionally-sampled set of 35 cumuli with active updraft cores penetrated during flight RF12. This study resembles the small-Cu study done by Raga et al (1990); however, the present study differs in that only those Cu are chosen for which the aircraft penetrated the core about 250-m below cloud top. The rationale for sampling in this updraft "bubble" near cloud-top of the Cu comes from the radar observations by Knight and Miller (1998) and Lasher-Trapp et al. (2003) which show that the first radar echo and subsequent precipitation are often observed in this region of actively growing small Cu. The aircraft flew predominately at 5 levels with 7 penetrations of individual clouds at each level chosen for the conditionally-sampled set. The sampling at 5 levels permit estimating the vertical evolution of this part of the Cu under the assumption that this sampling mimicked Lagrangian evolution.

The following summarizes the key findings for these Cu, and reports on the role of giant (GN) and ultra-giant (UGN) nuclei in causing the increasing amount of drizzle as a function of height in the Cu. A quasi-stochastic coalescence model is applied in a parcel model to predict the formation of the drizzle.

2. GENERAL DESCRIPTION OF THE Cu

The set of conditionally-sampled Cu range in height from ~400 m to ~1500 m, and their mean width at the 250-m level below cloud top is ~550 m as determined with the forward-looking digital video aboard the C-130. This relatively small width is similar to the width of the trade-wind Cu studied during BOMEX, but is significantly smaller than the "small" Cu in studies including such as CCOPE, JHWRP, CaPE, and SCMS. The mean value of the vertical velocity in the RICO Cu is ~1.5 m/s, the bulk TKE dissipation rate is 30 cm^2/s^3, the fractional entrainment is 1.3 km^{-1}, with the latter value being identical to the value determined using a different sampling approach by Raga et al (1990) in the Hawaiian rain-band Cu (JHWRP).

The microphysical behavior of the 7 Cu at each of the 5 levels is shown in the following figures: Figure1 shows the liquid water content (LWC; 1-hz data) measured with the PVM and 2D-C probes in all ~200 Cu penetrations on flight RF12. The preferred 5 levels flown by the aircraft are clearly shown. The data show that these Cu are strongly affected by entrainment, and that only a minimum amount of drizzle is observed by the 2D-C probe. The data also includes PVM LWC data (circles) collected at 1000 hz which show maximum LWC values about 25% larger than the 1-hz PVM data.

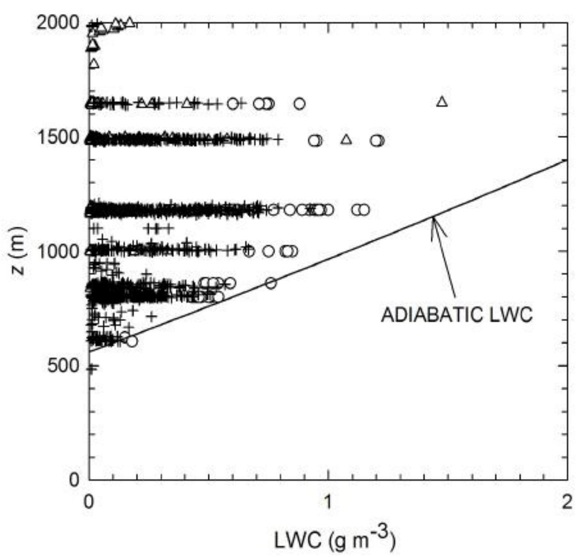

Figure 1 - Liquid water content (LWC) measured at 1 hz for all ~200 Cu passes on RICO flight RF -12, PVM data (crosses), 2D-C data (triangles), 1000-hz PVM data (circles). Adiabatic LWC calculated from cloud base temperature, pressure.

Corresponding Author's Address: Dr. Hermann E. Gerber, GSI,1643 Bentana Way, Reston, VA 20190, USA; Email: hgerber6@comcast.net

Figure 2 shows the average of the mean volume radius r_v for the 7 conditionally-sampled penetrations in individual Cu chosen at each of the 5 aircraft levels above cloud base and ~250 m below cloud top. The calculated adiabatic r_v again illustrates the significant entrainment effect.

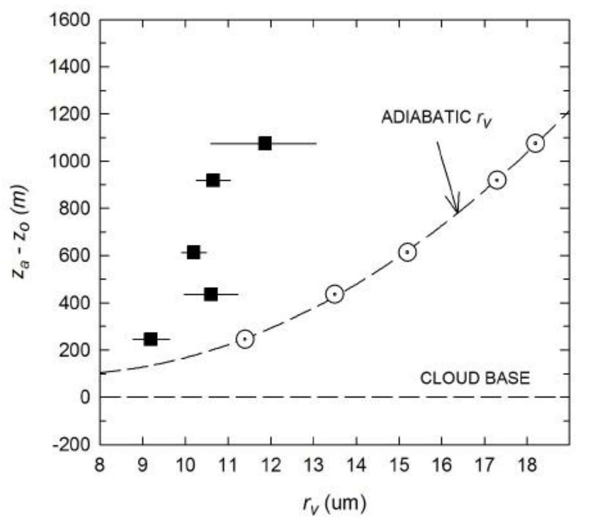

Figure 2 - The average value of mean volume radius r_v (squares) for 7 conditionally-sampled Cu at each of 5 aircraft levels above cloud base (z_a - z_o). Average adiabatic values of r_v calculated from mean measured droplet spectra in the Cu.

Figure 3 shows the mean droplet N and the cloud condensation nuclei CCN (S=1.5%) concentrations for the 7 Cu at the 5 levels above cloud base. Both parameters are approximately constant in the layer containing Cu, and the CCN constancy extends below and above this layer suggesting well-mixed conditions for the aerosol.

3. ENTRAINMENT AND MIXING

The ~10-cm incloud resolution 1000-hz PVM LWC and effective radius (Re) data are used to draw new inferences on the entrainment and mixing processes: The entrainment process involves smaller scales than previously thought; an example of depleted LWC parcels caused by entrained and observed during the aircraft pass into the edge of a Cu is shown in Fig.4. The length of the depleted parcels is lognormally distributed with a geometric mean length of 2.6 m.

The penetration depth of the depleted parcels is only several tens of m into the Cu which is consistent with the "mantle echoes" often observed with radar by Knight and Miller (1998) in small Cu and attributed to sharp gradients in LWC and water vapor. The depleted parcels mix rapidly with the rest of the cloud given the measured TKE dissipation rate. This limits the appearance of "super-adiabatic" drops.

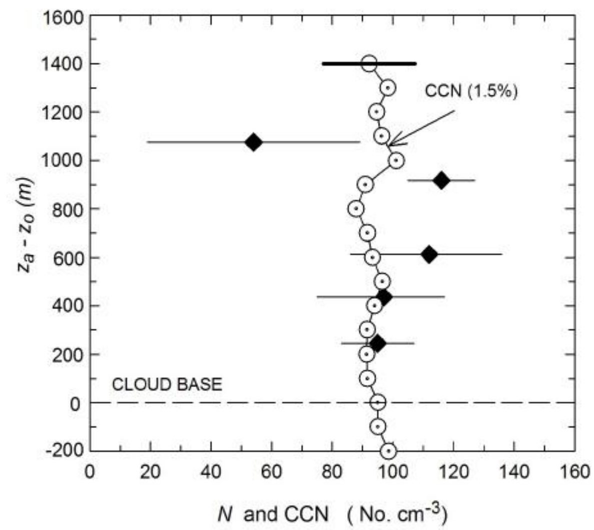

Figure 3 - The average value of mean droplet concentration N for 7 Cu at each of 5 aircraft levels above cloud base (z_a - z_o), and the average condensation nuclei concentration CCN at 1.5% supersaturation from aircraft profiles outside of cloud.

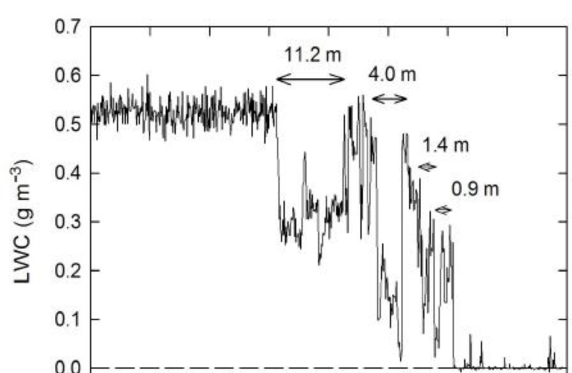

Figure 4 - 10-cm resolution PVM LWC for a horizontal aircraft pass into the edge of a Cu. The location of arrows, defined as entrained parcels, represent the length of depleted LWC parcels with sharp gradients along both edges.

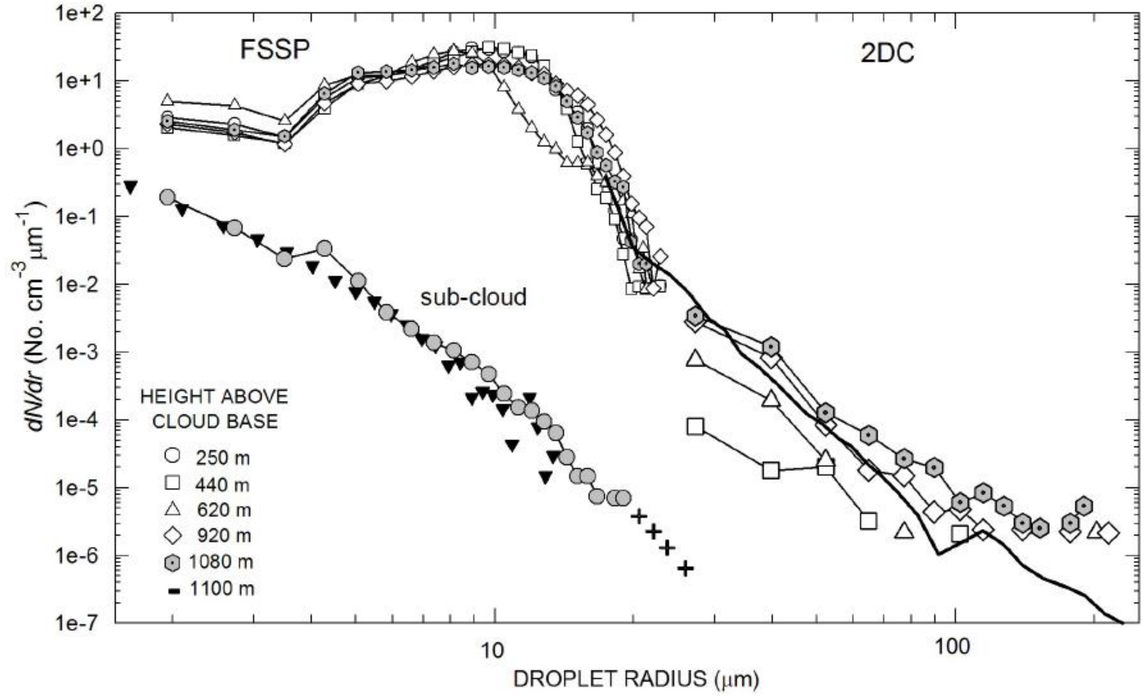

Figure 5 - The average size distribution from 7 conditionally-sampled Cu of incloud droplets measured with the FSSP (small symbols), and incloud drizzle drops measured with the 2D-C probe (large symbols) at each of 5 levels above cloud base. The average subcloud FSSP spectrum (circles) is from the horizontal aircraft leg just below cloud base; and the NCAR GNI (Giant Nuclei Impactor; triangles, unpublished data) spectrum from the GNI dry sea-salt radii adjusted to the ambient RH = 86% in the leg. The solid curve is the parcel-model drizzle prediction for the top level (see text).

The incloud mixing following entrainment can be of three types, inhomogeneous extreme, inhomogeneous, and homogeneous (Jensen at al 1985). The evolution of the droplet spectra with height in the Cu is strongly dependent on which mechanism dominates as illustrated by Lasher-Trapp et al (2003). The 10-cm resolution LWC and Re PVM data show that the dominant mixing mechanism in these trade-wind Cu is either inhomogeneous extreme mixing or homogeneous mixing with entrained air that is near saturation. Both mechanisms cause primarily the dilution of the droplet concentrations without affecting the relative shape of the droplet size spectra, as also noted earlier, e.g., by Blyth and Latham (1990). Deviations from this behavior occur when the LWC in the cloud has been reduced by entrainment/mixing to small values and when new droplets are activated on CCN contained in the entrained air. The latter effect has a high correlation with the fractional entrainment that changes with height above cloud base.

4. EVOLUTION OF DRIZZLE SPECTRA

A principal issue of RICO was to better understand the formation of precipitation in the trade-wind Cu, an issue that has a long unresolved history for warm clouds in general. The conditionally-sampled set of Cu for RF12 are used to address this issue. Figure 5 shows droplet size distributions measured in the Cu set using three probes, the 2D-C for drizzle-sized drops, the FSSP for incloud drops and subcloud particles smaller than ~45-um diameter, and the GNI (Giant Nuclei Impactor; unpublished data provided by Jorgen Jensen) for collecting subcloud sea-salt particles on oil-coated slides exposed to the aircraft airstream. The GNI data is RH-adjusted to the ambient 86% RH of the subcloud aircraft leg to generate the GNI spectrum of salt-solution drops in Fig. 5 which shows reasonable agreement with the FSSP spectrum measured on the same pass. The dry size of the salt-solution drops is calculated using the droplet growth equation and results in spectra that follow Woodcock's (1953) dry sea-salt particle dependence on the Beaufort wind force. The FSSP droplet spectra incloud are averages of the 7 Cu at each level (measured over ~100 m in the center of each Cu) and show a lack of variability with height above cloud base. The 2D-C spectra, on the other hand show a steady increase in drizzle-size drops with height.

The solid curve in Fig.5 is the predicted drizzle spectrum at cloud top resulting from a coalescence parcel model applied to the conditionally sampled set of Cu, using as initial conditions the quasi-steady incloud FSSP spectra as well as the subcloud FSSP sea-salt solution spectrum (for model details see Gerber et al, 2008). The calculations use a bin-less technique to avoid spectral broadening, and the collection efficiency used in the coalescence formulation (no inertial effects) follows the approach used by Cooper et al (1997). Reasonable agreement is found between the model prediction and the measured 2D-C spectrum at cloudtop. We find from the model results that the GN and UGN associated with the subcloud sea-salt solution drops play an essential role in generating the drizzle spectra for these Cu. The exposure of these sea-salt solution drops to saturated conditions in the cloud causes their relatively rapid growth to larger drops that then collect by accretion the smaller drops as measured with the FSSP; see Fig. 6. This behavior is similar to classical coalescence calculations (e.g., Berry and Reinhardt, 1974; Ochs, 1978).

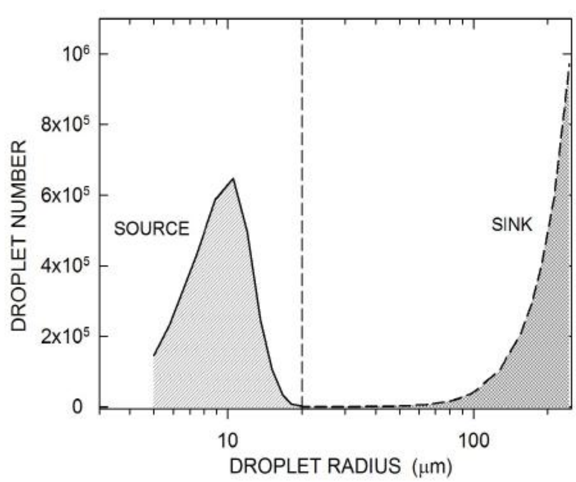

Figure 6 - Predicted number of small drops lost by coalescence (source) to larger drops (sink) as a function of drop size for the 1100-m level above cloud base (see Fig. 5). The vertical dashed line indicates the radius 20 (um) that separates auto-conversion (smaller drops) from the accretion process.

5. FINDINGS

This quasi-Lagrangian study of the RICO trade-wind Cu from flight RF12 finds the entrainment, mixing, and microphysics behavior in the rising bubble of active turrets to be surprisingly uncomplicated. The entrained parcels are quite small, are likely related to the radar "mantle echoes" observed by Knight and Miller (1998), and are quickly mixed with the unaffected cloud preventing the presence of super-adiabatic drops. The mixing mechanism causes essentially only dilution of the droplets, the small droplet spectra remain approximately constant with height above cloud base, and the appearance of drizzle appears to follow the classical coalescence process. The wind generated sea-salt particles follow Woodcock's (1953) wind speed dependence, and their presence is essential in collecting by accretion the small cloud drops to form the observed drizzle.

A surprising result is the approximate self-preserving nature of the small-droplet spectra as a function of height above cloud base. This behavior must represent an approximate balance between the gain of new droplets activating on CCN in entrained air, and losses of droplets by entrainment-dilution and by detrainment and coalescence. It is unknown if this simple behavior can be applied to other small Cu.

ACKNOWLEDGMENTS

Thanks are due Bjorn Stevens, Robert Rauber, Harry Ochs, and Charlie Knight for organizing RICO. Appreciation is expressed to the Research Aviation Facility (RAF) of NCAR for their excellent running of RICO. This work was supported by NSF Grants ATM-0335695 and ATM-0342618.

REFERENCES

Berry, E.X., and R.L. Reinhardt, 1974: An analysis of cloud drop growth by collection. Parts I-IV. *J. Atmos. Sci.*, **31**, 1814-1831.

Blyth, A.M., and J. Latham, 1990: Aircraft studies of altitudinal variability in the microphysical structure of non-precipitating, ice-free, Montana cumuli. *Quart.J. Roy. Meteor. Soc.*, **116**, 1405-1423.

Cooper, W.A., R.T. Bruintjes, and G.K. Mather, 1997: Calculations pertaining to hygroscopic seeding with flares. *J. Appl. Meteor.*, **36**, 1449-1469.

Gerber, H., G. Frick, J.B. Jensen, and J.G. Hudson, 2008: Entrainment, mixing, and microphysics in trade-wind cumuli. *J. Meteor. Soc. Japan*, submitted.

Jensen, J.B., P.H. Austin, M.B. Baker, and A.M. Blyth, 1985: Turbulent mixing, spectral evolution and dynamics in a warm cumulus cloud. *J. Atmos. Sci.*, **42**, 173-192.

Knight, C.A., and R.A. Miller, 2007: Early radar echoes from small, warm cumulus: Bragg and hydrometeor scattering. *J. Atmos. Sci.*, **55**, 2974-2992.

Lasher-Trapp, S.G., W.A. Cooper, and A.M. Blyth, 2005: Broadening of droplet size distributions from entrainment and mixing in a cumulus cloud. *Quart. J. Roy. Meteor. Soc.*, **131**, 195-220.

Ochs, H.T., 1978: Moment-conserving techniques for warm cloud microphysical computations. Part II: Model testing and results. *J. Atmos. Sci.*, **35**,1959-1973.

Raga, G.B., J.B. Jensen, and M.B. Baker, 1990: Characteristics of cumulus band clouds off the coast of Hawaii. *J. Atmos. Sci.*, **47**, 338-355.

Woodcock, A.H., 1953: Salt nuclei in marine ir as a function of altitude and wind force. *J. Meteor.*, **10**, 362-371.

VERTICAL DISTRIBUTION OF ATMOSPHERIC SEA-SALT MIXING RATIO IN THE CARIBBEAN: FLUXES AND IMPLICATIONS FOR THE WARM RAIN PROCESS

J. B. Jensen[1], S. Beaton[1], J. Stith[1], D. C. Rogers[1], Marile Colon-Robles[2] and R. Rauber[2].

[1]National center for Atmospheric Research, Boulder, Colorado, USA.
[2]University of Illinois, Urbana-Champain, Illinois, USA.

1. INTRODUCTION

If warm rain forms as a result of the action of giant sea-salt aerosols (for short called GA, dry radius r_d > 0.5 μm, Woodcock, 1951) and ultra-giant aerosols (UGA, r_d > 5 μm, Johnson, 1982) then one would expect that the warm rain preferentially removes the largest of the GA. In this paper we will for simplicity refer to giant aerosols (GA) covering both giant and ultra-giant aerosols. It is not practically feasible to measure the sizes and concentrations of GA in cloud and precipitation drops. However, measurements of GA in cloud inflow air and in detrained air may be used to determine if transport through a cloud changes the size distribution of the aerosol particles (see e.g. Peter et al, 2006) in such a way that the largest GA particles are preferentially removed.

This paper describes observations of giant sea-salt aerosol particles that were obtained below, outside and above marine trade wind cumuli during the Rain in Cumulus Clouds over the Ocean, RICO (Rauber et al, 2007). The measurements use impaction of salt particles onto microscope glass slides that were exposed outside the aircraft in the free air stream, followed by image analysis using a digital optical microscope in a chamber with high relative humidity. The entire system is referred to as the Giant Nuclei Impacter, GNI.

The impaction system has a very large sample volume, typically 500 times that of common optical laser droplet spectrometers (e.g. PMS FSSP). In addition, as water on the impacted particles is evaporated, thus leaving a dry salt residue, and subsequently deliquesced, the GNI instrument is capable of measuring only salt particles, whereas the optical laser probes may sometimes mistake a cloud drop for a GA particle. The high sample volume rate (about 10 $\ell\, s^{-1}$) ensures that many particles can be sampled, e.g. immediately outside cloud boundaries. The GA concentrations were corrected for impaction efficiency (Ranz and Vong, 1952) for different sized particles by calculating the ambient size at the time of impaction based on the aircraft observed relative humidity and the laboratory-based dry NaCl equivalent radii.

In Section 2 we describe the measurements of GA size distributions; these show lower concentrations and sizes of GA with increasing altitude. Section 3 contains an equillibrium view of aerosol cycling from below cloud base, through cloud and detrainment into the air outside the cumuli, followed by sedimentation down towards the sub-cloud mixed layer. The crux is an evaluation of inferred fluxes through cloud and of the sedimentation fluxes in the clear air outside cumuli as a function of GA size. Section 4 contains a summary and discussion.

2. OBSERVATIONS

The NSF/NCAR C-130 research aircraft flew 19 RICO mission flights during late 2004 and early 2005, generally to the northeast of the island of Antigua in the Caribbean. Typical flight patterns consisted of a 60-km diameter circle at 4.5 km altitude, then a descent to 100 m above sea surface where a second circle was undertaken. This was followed by a third circle at 400 m altitude, after which the aircraft would typically spend a 5-hour period sampling both trade wind cumulus clouds (often 500-2500 m altitude) and the clear air outside clouds. At the end of the flight, three circles at the same altitudes as in the morning would be flown, after which the aircraft returned to Antigua.

The GNI slides were only exposed in the free airstream outside the aircraft during the clear air segments; i.e. intentionally excluding cloud and precipitation segments. The reason is that flight through even small amounts of cloud and precipitation washes off any impacted aerosol particles. Slides were typically exposed for 5 seconds close to sea surface (high aerosol loading) and for up to 15 minutes at 4.5 km altitude (low aerosol loading). On occasion some slides were nevertheless exposed in cloud or rain, and these slides have been removed from further analysis. During a 9-hour flight, up to 80 slides were exposed, although most flights only had exposure of 10-30 slides. A total of 500 slides were exposed during the RICO flights. A small number of these had been modified to have carbon tape attached to the slides. These were separately analyzed by Dr. Jim Anderson for elemental analysis; these slides will also not be included in the following analysis.

The remaining slides have been analyzed in the humidified microscope system. The results are still preliminary as a small humidity correction has not yet been included. We estimate that the actual GA sizes are about 10% larger than those reported in this paper. For each slide we have calculated size distributions of NaCl equivalent particles in 0.2 μm dry radius bins, with the smallest bin being centered at 0.6 μm dry radius. Control slides were handled in the same way as the actual slides, although they were not exposed but only used to examine the amount of contamination in handling. The average control slides size distributions were subtracted from the normal slides, such that we report only the actual added GA from the exposure outside the aircraft.

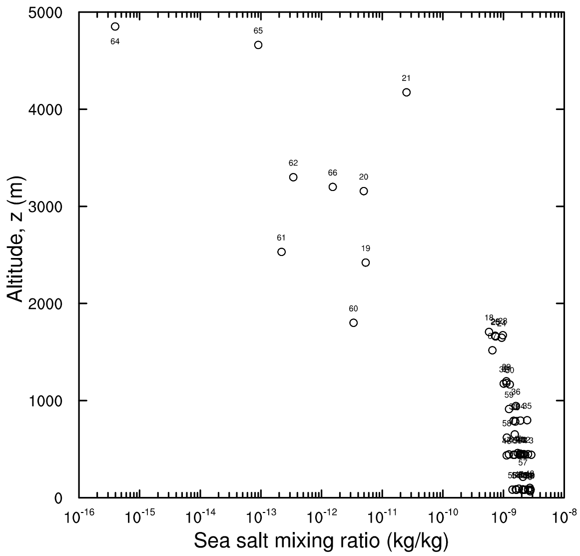

Figure 1. NaCl equivalent seasalt mixing ratio for 59 slides as sampled on RICO RF19, 24 January 2005.

Figure 1 shows the mixing ratio of NaCl equivalent sea salt as a function of altitude for flight RF19 on 24 January 2005. Each slide is shown with a circle, and the slide number is listed above the circle. The figure shows a very narrow distribution in the sub-cloud mixed layer below about 500 m altitude. Here typical values are about 2×10^{-9} kg NaCl equivalent per kg air. Above the mixed-layer the mixing ratio drops off very slowly with altitude, such that it is about a factor 3 lower at 1800 m (apart from one sample). Above 2 km there is a very strong drop-off in mixing ratio, typically by 2 orders of magnitude. The difference below and above 2 km would appear to be related to the trade inversion, with relatively short residence time of the air outside trade wind cumulus clouds, whereas the air above the trade inversion has a very long residence time and a slow descent as part of the Walker circulation. The low concentrations above the trade inversion is the reason for us not considering the slides exposed above 2 km in the following analysis.

For the slides exposed below 2 km, we have created average spectra in vertical bands of 0-500 m, 500-1000 m, etc. These four average spectra will constitute the main data for the following analysis. The four average spectra for RICO RF19 are shown in Figure 2. We are here mainly interested in the relative change in the spectra with altitude; in particular, is there a dramatic drop-off of the concentration of the largest aerosol particles with altitude, presuming the warm rain process becomes more efficient with altitude and thus removes more GA particles? This is difficult to discern from Figure 2. In order to further examine this, the relative spectra are plotted in figure 3. Here we take the mixed-layer spectrum as the reference and show the other spectra as ratios of this mixed-layer spectrum. Thus the mixed-layer spectrum has unit value in all bins.

Figure 3 shows a significant drop-off in the concentration of the largest GA with altitude. This cannot, however, be taken as a clear indication the the largest GA are preferentially removed by the warm rain process (thus possibly being the cause of the warm rain process). It is also possible that these largest GA in the clear air settle so rapidly that their concentration is significantly reduced. In Section 3 we attempt to discern between the removal of the largest GA through warm rain formation in the trade wind cumulus and the removal of the largest GA through faster settling, in comparison to smaller GA particles, in the cloud-free air.

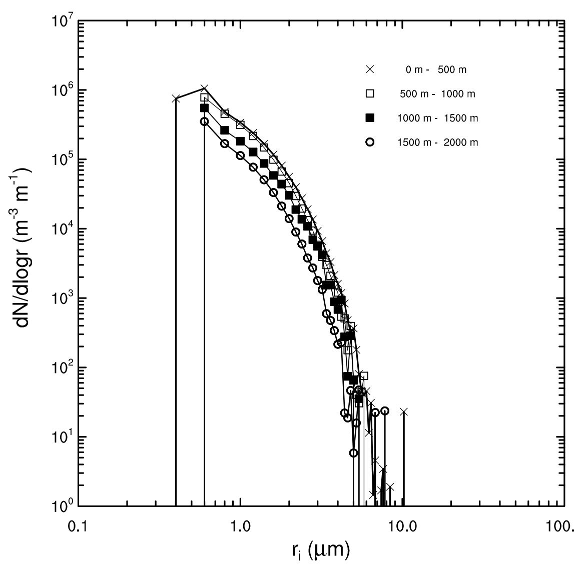

Figure 2. Average giant aerosol spectra for the lowest four 500-m bands for RICO RF19, 24 January 2005.

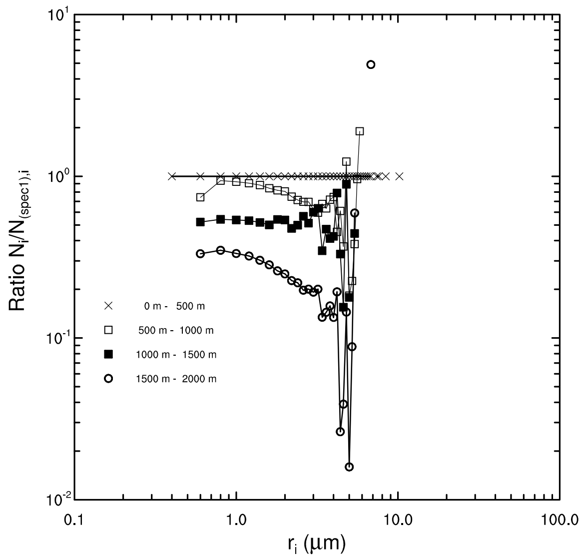

Figure 3. Ratio of average giant aerosol spectra for the lowest four 500-m bands for RICO RF19, 24 January 2005. The spectrum for the lowest 500 m is used as the reference.

There is considerable variation in the vertical profiles of GA from day to day. Figure 4 and 5 shows the vertical GA mixing ratio and relative average size distributions in four altitude intervals, respectively, for RICO RF 13 on 12 January 2005. For RF13, Figure 4 shows a considerably stronger drop-off in the sea-salt mixing ratio with altitude than was shown for RF19 in Figure 1. Figure 4 does not show the marked drop-off above 2 km, suggesting that trade wind cumulus clouds on this day were able to rise to higher altitude than on 24 January (RF19). Figure 5 shows a stronger drop-off in the concentration of the largest GA in comparison to Figure 3; we have here only showed the four composite spectra for the 500-m alatitude bands below 2 km, to make Figures 3 and 5 directly comparable.

3. AEROSOL CYCLING AND THE FLUX-RATIO

The GA observed outside clouds in the trade wind layer is highly likely to be transported up through convection in the trade wind clouds; air outside the cumuli is generally stable with respect to dry adiabatic motions and this impedes vertical mixing. Thus the air observed in the cloud layer (outside clouds) used to be mixed-layer air, with a size distribution as measured in the lowest 500-m layer air, the air between the clouds has almost exclusively been lofted through the clouds. There may also be some

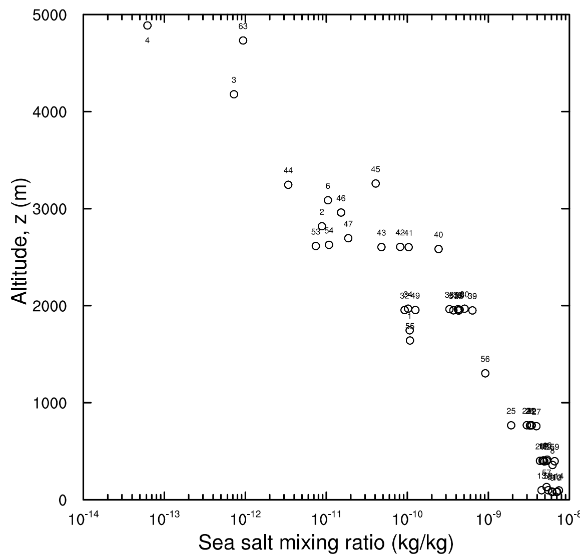

Figure 4. NaCl equivalent seasalt mixing ratio for 50 slides as sampled on RICO RF13, 12 January 2005.

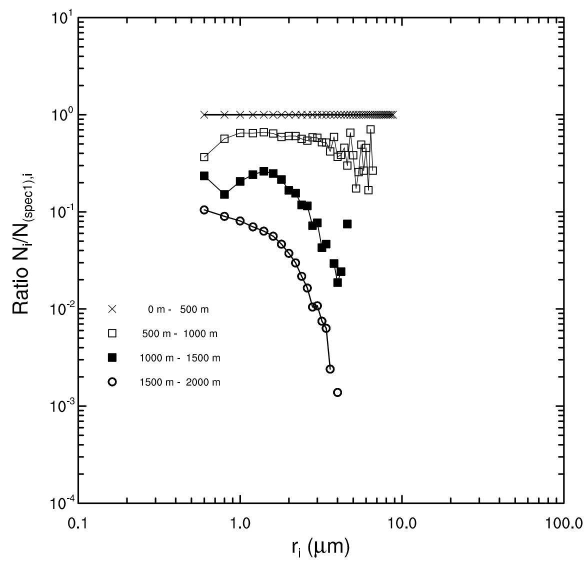

Figure 5. Ratio of average giant aerosol spectra for the lowest four 500-m altitude bands for RICO RF13, 12 January 2005.

amount of mixing down from higher altitudes, but this is likely also a result of the cloud mixing. During passage in the clouds, some GA from the mixed layer may have been removed through precipitation scavenging, and the remainder is at some point detrained into the environment between clouds.

We now make some important assumptions. Firstly, that the sampling using GNI slides yields a statistically significant average size distribution in the cloud-free air. Secondly, that GA reasonably quickly attain their equilibrium size through either condensation or evaporation, such that they can be assumed to sediment with a terminal velocity consistent with their equilibrium size. Thirdly, we assume that a steady-state situation exists, such that there is a balance between the total GA flux through cloud base and the GA flux of detrained air from the cumuli and the sedimentation flux due to gravitational settling of GA solution drops in the cloudfree environment. This conceptual picture may be modified by precipitation removal of GA. We note that we do not make any assumption about the fraction of cloudy and clear air at any altitudes.

We note that, just as the size spectrum of sea-salt particles is defined in i bins, the fluxes of sea-salt particles can also be calculated on a bin basis. We consider four layers, labeled n=1 - 4, each of 500-m altitude depth.

Once the aerosol particles are moved from the mixed layer up through the cumuli and are detrained from the cumuli, then they constitude a source function for GA in the cloud free air. Air in the surroundings of the cloud is assumed to slowly subside, with a velocity linearly increasing from zero at the surface to 2 $\mathrm{mm\,s^{-1}}$ at 1 km altitude. (This is an approximate mean value for RICO as provided by B. Stevens, personal communication). In the clear air environment, the GA thus move downwards with a speed that is the combination of the subsidence velocity and their terminal velocity.

For a pressure of 900 hPa and a temperature of 290K, the terminal velocity of solution drops of unit density and radii of 1, 2, 4 and 8 μm are 0.12, 0.49, 1.9 and 7.8 $\mathrm{mm\,s^{-1}}$, respectively. At 80% relative humidity, the dry aerosol particles have about 60% the radii of those listed above, see Tang et al (1997).

Thus, the ratio, R_1, of the fluxes, F, of two different sized GA particles (say, dry radii of i and j) into the cumulus base is:

$$R_1 = \frac{F_{n=1,i}}{F_{n=1,j}} = \frac{C_{n=1,i}(-w_c + w_{t,i} + w_s)}{C_{n=1,j}(-w_c + w_{t,j} + w_s)}, \qquad (1)$$

where subscript $n = 1$ corresponds to altitude-layer 1 (0-500 m), C_i is the concentration of GA with dry radius r_i, w_c is the cloud updraft speed at cloud base, w_t is the aerosol solution drop terminal velocity, and w_s is the large-scale subsidence velocity. At cloud base, the cumulus updraft is much larger (typically half a meter to several meters) than either w_t and w_s (typically millimeters per second), thus eq. (1) can be approximated as:

$$R_1 = \frac{F_{n=1,i}}{F_{n=1,j}} = \frac{C_{n=1,i}}{C_{n=1,j}}. \qquad (2)$$

Outside the cumulus there is no convective velocity, but simply a small net subsidence velocity and the GA settling. In the air between cumulus at e.g. altitude band 4 (1500 - 2000 m), the the ratio, R_4, of the fluxes of the same two sizes of GA is then given by:

$$R_4 = \frac{F_{n=4,i}}{F_{n=4,j}} = \frac{C_{n=4,i}(w_{t,i} + w_s)}{C_{n=4,j}(w_{t,j} + w_s)}. \qquad (3)$$

In evaluation of eq. (3), we take w_s = 3.5 $\mathrm{mm\,s^{-1}}$ for level 4 (1750 m average height), and we calculate the terminal velocity, w_t, assuming that the sea-salt GA solution drops are in equilibrium with the ambient humidity. For this we use the method of Beard (1976).

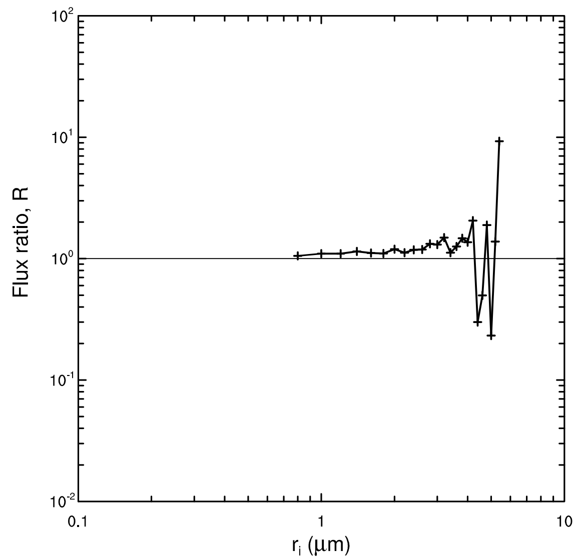

Figure 6. Flux ratio, R, as a function of dry aerosol radius, r_i. The basis for the calculation is r_j=0.6 μm dry radius. R is evaluated for average GA spectral flux out of clouds at altitudes 1500 - 2000 m and related to average GA spectra in the mixed layer below 500 m.

For size i being larger than size j and using the assumptions listed in this section, we evaluate the flux ratio $R = R_4/R_1$. If R < 1, then there has been a preferential removal of the larger GA particles due to precipitation scavenging. The value of R is evaluated by taking j such that r_j=0.6 μm dry radius and i such that r_i covers the entire range of 0.8, 1.0, 1.2 etc. μm dry radius. Figure 5 shows the result for RICO RF19 on 24 January 2005 for a comparison of out-of-cloud aerosols at altitudes between 1500 and 2000 m and for sub-cloud (mixed layer) aerosols at altitudes of 0 - 500 m. For this flight, Figure 6 shows R-values of nearly unity between r_i=0.8 μm and r_i = 4 μm dry radius, and for $r_i >$ 4 μm the results are too noisy due to sampling uncertainty. The implication is that there is no preferential removal of larger GA particles due to precipitation scavenging in the size range of 0.8 to 4 μm on this day.

The situation is very different for RICO flight RF13 on 12 January 2005, see figure 7. Here R shows a dramatic drop-off for r_j increasing from 0.8 to 4 μm. For this flight the implication is that there is a dramatic preferential removal of the largest GA.

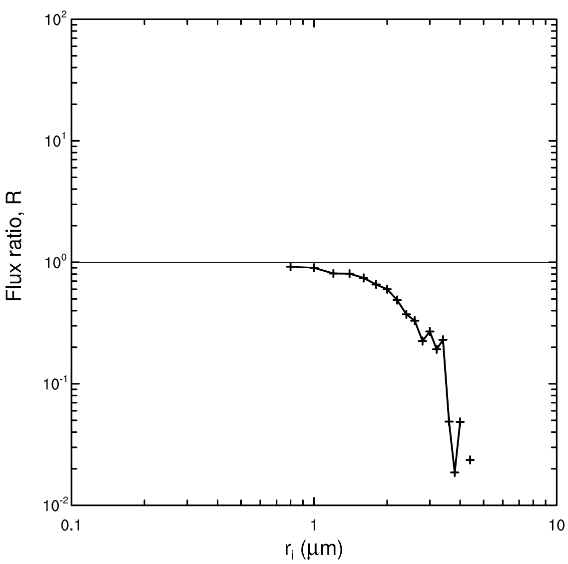

Figure 7. Same as figure 6, but for RF13 on 12 January 2005.

The very different results for RF19 and RF13 is surprising, and there must be a reason for the strong difference. Here we will only make the following statements about the differences between the two days: RF19 was fairly polluted with a PCASP aerosol concentration of 60 cm^{-3} in the mixed layer; in contrast RF13 was much cleaner with a PCASP concentration of only 30 cm^{-3}; i.e. half of the value during RF19. RF13 also had a near-surface wind speed of about twice that of RF19 (11 m s^{-1} and 5.5 m s^{-1}, respectively). As a consequence of the higher wind speed, RF13 had about five times as many GA in the mixed layer in comparison to RF19. Radar observations showed a radar-derived daily rainfall amount of about 2 mm for for 12 January 2005 (RF13) over the ocean northeast of Antigus; in contrast 24 January only had a daily rainfall amount of 0.5 mm.

Although the aerosol size distribution on RF13 was strongly skewed towards clean air and many GA, we nevertheless caution against this as being the only cause for the preferential removal of the largest GA by precipitation. RF13 had also significantly deeper clouds in comparison to RF19, so dynamical effects may also play a role.

4. SUMMARY AND DISCUSSION

One of the core questions for warm rain formations is: Do giant aerosols (GA), in particular the largest of these, lead to the initiation of warm rain?

In this paper we do not answer this question directly, but instead we seek instead to answer the following question: Are the largest GA preferentially removed by the warm rain process? For the trade cumuli studied here it is insufficient to simply compare the size spectra of giant sea-salt aerosols below cloud base and in the detrained air; the reason is that the largest GA in the detrained air settle much faster than the smaller detrained GA.

Hence we examine the fluxes of different sized GA particles in air moving into cloud base and the fluxes of GA particles in air outside the cumulus clouds; i.e. presumably cloud processed air. The method relies on double ratios, and as a consequence it only yields good results for the part of the GA spectrum where counting statistics is good. Fortunately the GNI slide measurements have very large sample volumes for the observed GA spectra, and this allows us to use the size range of 0.8 μm to about 4 μm dry GA radius.

The flux method also relies on a number of assumptions: We assume that the trade cumulus cloud fluxes are in near equilibrium, such that a steady-state can be assumed. We also assume that the sampling of the GA size spectra both below cloud base and in the environment between clouds is done such as to capture average conditions. The air below cloud base has mostly a small variability in GA size spectra, whereas the air between clouds has a much greater variability. Even so, the sea-salt mixing ratio observations (Figs. 1 and 4) for the two days presented have fairly tight variations, implying that the average conditions are likely well observed by the GNI slide measurements. RF13 had 16 slides exposed in the mixed layer and 12 slides exposed in the 1500 - 2000 m layer outside clouds. For RF19, the corresponding number of exposed slides were 32 and 7, respectively. Finally we assume that the subsidence rate is increasing linearly from zero at the surface to 2 $\mathrm{mm\,s^{-1}}$ at 1 km altitude, based on calculations by B. Stevens and co-workers (personal communication). This subsidence rate is comparable to the sedimentation velocity of smaller GA particles.

The results of the double-ratio flux method as applied to two RICO days show very differing results. On one day, RF19, there is no evidence of preferential removal of the larger giant aerosols.

On the other flight, RF13, there is a clear pattern consistent with strong removal of the larger GA. For RF13 we thus conclude that precipitation removal of the largest, well-observed GA was highly likely.

Through sensitivity analysis of the subsidence rate, we have verified that the preferential removal rate could not have been the result of an erroneous subsidence rate for RF13. We conclude that the difference in preferential removal of the largest particles between RF13 and RF19 is real.

RF19 was characterized by a high concentration of smaller aerosols and few GA particles; RF13 had a low concentration of small aerosol particles and many GA particles. RF19 had very little rain (0.5 mm for the day) whereas RF13 had four times more rain for the day. The vertical profiles of sea-salt mixing ratio suggests that the RF19 clouds mainly transports GA particles up to a maximum altitude of 2000 m without much removal; in contrast the RF13 vertical profile of sea-salt mixing ratio shows a much stronger driop-off with altitude, suggesting a strong removal of GA particles. Thus if the clouds during RF19 mainly transports GA particles (without much precipitation removal), then we would expect the flux double ratio, R, to be near to unity as was observed. For stronger raining clouds (RF13) the precipitation preferentially removes the largest GA particles.

Thus the results are consistent with the stronger warm process preferentially removing the largest GA particles; however, the results do not prove that these largest GA particles necedssarily were the cause of the warm rain formation.

BIBLIOGRAPHY

Beard, K. V., 1976: Terminal velocity and shape of cloud and precipitation drops aloft. *J. Atmos. Sci.*, **33**, 851–864.

Johnson, D. B., 1982: The role of giant and ultra giant nuclei in warm rain initiation. *J. Atmos. Sci.*, **39**, 448–460.

Peter, J. R., S. T. Siems, J. B. Jensen, J. L. Gras, Y. Ishizaka and J. Hacker, 2006: Prediction and observation of cloud processing of the aerosol size distribution by a band of cumulus. *Quart. J. Roy. Met. Soc.*, **132**, 835-863.

Ranz, W. E., and J. B. Wong, 1952: Impaction of dust and smoke particles on surface and body collectors. *Indust. and Eng. Chem.*, **44**, 1371-1381.

Rauber, R. M., B. Stevens, H. T. Ochs III, C. Knight, B. A. Albrecht, A. M. Blyth, C. W. Fairall, J. B. Jensen, S. G. Lasher-Trapp, O. L. Mayol-Bracero, G. Vali, J. R. Anderson, B. A. Baker, A. R. Bandy, F. Burnet, J.-L. Brenguier, W. A. Brewer, P. R. A. Brown, P. Chuang, W. R. Cotton, L. di Girolamo, B. Geerts, H. Gerber, S. Goke, L. Gomes, B. G. Heikes, J. G. Hudson, P. Kollias, R. P. Lawson, S. K. Krueger, D. H. Lenschow, L. Nuijens, D. W. O'Sullivan, R. A. Rilling, D. C. Rogers, A. P. Siebesma, E. Snodgrass, J. L. Stith, D. C. Thornton, S. Tucker, C. H. Twohy and P. Zuidema, 2007: Rain in (Shallow) Cumulus Clouds over the Ocean - The RICO Campaign. *B. Amer. Met. Soc.*, **88**, 1912-1928.

Tang, I. N., A. C. Tricdico, and K. M. Fung, 1997: Thermodynamic and optical properties of sea salt aerosols. *J. Geophys. Res.*, **102, D19**, 23,269–23,275.

Woodcock, A. H., 1953: Salt nuclei in marine air as a function of altitude and wind force. *J. Meteor*, **10**, 362-371.

Acknowledgements

The authors gratefully thank Dr. W. A. Cooper for very stimulating discussions. Funding for RICO was provided by the National Science Foundation, Washington, D.C. NCAR is sponsored by the National Science Foundation, Washington, D.C. The GNI system was built using an instrumentation grant from the NCAR Director's Office.

EVALUATION OF AEROSOL-CLOUD-RADIATION-DYNAMICAL INTERACTIONS IN A LARGE-EDDY MODEL

Hongli Jiang[1], Graham Feingold[2], and Adrian Hill[2]

[1]CIRA/NOAA, Earth System Research Laboratory, Boulder, Colorado

[2]NOAA, Earth System Research Laboratory, Boulder, Colorado

April 29, 2008

1 INTRODUCTION

Shallow, warm cumulus clouds are recognized as important to climate because they modify the planetary albedo. The combination of small sizes ($\leq 500m$) and low cloud cover, approximately 15 % in the trade wind regime (*Warren et al.*, 1988) renders cumulus clouds susceptible to entrainment of drier environmental air and turbulent mixing.

The smaller clouds can only be partially resolved by the horizontal resolution of 100 m typically used in the Global Energy and Water Cycle Experiment Cloud System Study (GCSS) cases. Brown (1999) simulated a case based on the BOMEX field experiment using a model resolution of ~ 20 m and showed good agreement with observations (e.g. Nitta, 1975). He showed that the mean cloud radii were on the order of 100 m. Others have studied the sensitivity of LES at much finer resolutions for cumulus under stracocumulus (e.g. Stevens et al., 2002); and stratocumulus (Lewellen and Lewellen, 1998; and Stevens and Bretherton, 1999; and Stevens et al., 1999).

Brown's study is most pertinent to our interest in cumulus clouds as he showed that cloud size distributions are greatly affected by model resolution, while ensemble averaged mean fields are insensitive to resolution changes. Using satellite data, Koren et al. (2008) have shown a doubling of cloud cover in response to changing resolution from 30 m to 1 km in cumulus cloud fields.

Our motivation in this study is to examine the extent to which dynamical and microphysical processes are scale-dependent. To do so, we evaluate how a population of shallow, warm cumulus clouds generated by a LES responds to changes in aerosol concentrations as we progressively increase model resolution.

To address these issues, a number of numerical simulations were performed in a three-dimensional LES. The model is the newest version of the Regional Atmospheric Modeling System v 6.0 with liquid-phase, bin-resolving microphysics (RAMS@NOAA). A thermodynamic sounding taken during the Rain In Cumulus over the Ocean (RICO) field experiment (Rauber et al., 2007) and selected by the GCSS boundary layer working group for intercomparison (http://www.knmi.nl/samenw/rico) is used for all the simulations.

2 EXPERIMENT DESIGN

Three sets of three-dimensional simulations were performed with different model resolutions, as summarized in Table 1. Each set consisted of two simulations with initial aerosol concentration for clean (N_a = 100 cm^{-3}) and polluted (N_a = 1000 cm^{-3}). In all cases we followed the GCSS intercomparison case set up using a simple large-scale forcing and radiation. The surface fluxes are parameterized using a bulk aerodynamical formula based on prescribed sea surface temperature (SST) and other parameters. The simulations were run for 6 h. The domain size was 6.4 km $\times$ 6.4 km $\times$ 4 km. Preliminary results selected from all three sets of simulations will be shown. More results will be presented at the conference.

[1]Corresponding author address: Hongli Jiang, CIRA/NOAA, Earth System Research Laboratory, Boulder, CO 80305, email: hongli.jiang@noaa.gov

Table 1: Description of LES simulations

EXP	$N_{x,y}$	N_z	$\Delta_{x,y}$ m	Δ_z m	N_a (cm^{-3})
dx25-100	256	400	25	10	100
dx50-100	128	200	50	20	100
dx100-100	64	100	100	40	100
dx25-1000	256	400	25	10	1000
dx50-1000	128	200	50	20	1000
dx100-1000	64	100	100	40	1000

$N_{x,y}$ denotes the number of horizontal grid points.
N_z denotes the number of vertical grid points.
$\Delta_{x,y}$ is the horizontal grid spacing;
Δ_z is the vertical grid spacing.

3 SIMULATION RESULTS

Selected variables are time-averaged over 3 hours (4, 5, 6) and plotted as a function of N_a in Figure 1. They are cloud-averaged liquid water path, LWP (averaged only over columns that have liquid water mixing ratio r_l greater than 0.05 g kg^{-3} for at least one grid point in the column), cloud fraction, cf (the fraction of grid points that have cloud optical depth $\tau_c > 0.5$), and cloud optical depth, τ_c (averaged over all cloudy regions with $\tau_c > 0.5$ as the threshold value used in cloud fraction calculation) for all three sets of simulations. These criteria used in identifying cloudy regions are similar to those used by Charlson et al. (2007).

There is about a 10% decrease in the cloud-averaged LWP (Figure 1a) in the finest resolution (blue), approximately constant in the intermediate resolution (green), and about 3% increase in the coarsest resolution (red) as N_a changes from 100 cm^{-3} to 1000 cm^{-3}.

Cloud fraction (Figure 1b) is unaffected by the aerosol in the finest resolution (blue), increases slightly in the intermediate resolution (green) and decreases in the coarsest resolution (red). As expected for a large aerosol increases, cloud optical depth τ_c (Figure 1c) increases from clean to polluted condition in all resolutions without exception.

In response to resolution changes, cloud-averaged LWP behaves slightly differently between clean and polluted conditions. In the clean simulations (N_a = 100 cm^{-3}), LWP remains about the same from dx25-100 (blue) to dx50-100 (green), but increases about 41 % from dx25-100 (blue) to dx100-100 (red). Of interest is that τ_c behaves similarly to the cloud-averaged LWP in response to model resolution changes. In the polluted simulations (N_a = 1000 cm^{-3}), cloud-averaged LWP increases continuously, and produces about 62.6 % increase from the fine (blue) to coarse resolution (red), relative to the fine resolution. Cloud fraction decreases about -23.6 % in the clean and and about -26.1 % in the polluted condition from the fine to coarse resolution relative to the fine resolution. The percentage changes from the finest to the coarsest resolution relative to the finest resolution are summarized in Table 2.

For the coarsest resolution simulations, the response of LWP and cloud fraction to aerosol changes are similar to the studies of Jiang and Feingold (2006) and Xue and Feingold (2006), since both used model resolutions similar to the coarsest resolution applied in this study.

It should be noted that based on the GCSS definition of “precipitation” for this case (> 100 W m^{-2}) no precipitation reaches the surface over the course of 6 hours, even for the clean conditions, at all three resolutions. Thus precipitation is not a big factor for the results shown in Figure 1.

To understand what scale-dependent processes dominate the response of LWP and cloud fraction, vertically integrated TKE_{res} ($\mathrm{TKE_{res}} = \int_0^{z_T} \mathrm{tke\,dz}$, resolved), TKE_{sgs} (subgrid), surface latent heat flux, and the maximum cloud top height $z_{t,max}$ are time-averaged and summarized in Table 3.

The coarsest resolution simulations have the strongest surface latent heat flux, the highest $z_{t,max}$, and the highest total TKE (both resolved and subgrid scale), suggesting more energetic convection and deeper clouds. The highest surface latent heat flux will contribute to stronger convection and deeper cloud cells. The lower cloud fraction is due to the existence of a relatively small number of deeper cells. A progressively more significant part of the vertically-integrated subgrid scale TKE comes from the subgrid model as resolution decreases (for both clean and polluted simulations). The differences due to aerosol changes are small compared to those associated with resolution changes.

3.1 Cloud size distributions

In the coarse resolution simulations, clouds not only grow deeper but also larger. The normalized cloud size distribution for all the simulations are plotted in Figure 2. The cloud size distribution of a cumulus population is defined as the probability of occurrence of clouds for clouds having specified size ranges. As can be seen in Figure 2, the differences are much greater in response to resolution change (similar to Brown, 1999) than to aerosol changes (see figure caption for symbol types). The differences due to aerosol changes occur at the larger clouds where only rare events have occurred.

The cloud size distributions show similar dependence on resolution to that seen by Koren et al. (2008); As more and more smaller clouds are resolved at the finer resolutions, the slopes of the power law fit (not shown) range from -1.25 (in the coarsest resolution) to -1.73 (in the finest resolution), respectively. For comparison, typical slopes in trade cumulus studies are -2.19 (e.g. Zhao and Di Girolamo, 2007 for RICO data), and -1.7 (*Neggers et al.*, 2003 for BOMEX case). A calculation of the distribution with respect to cloud area (rather than width) yields slopes of -1.08 $\pm$ 0.04 compared to -1.3 $\pm$ 0.1 (Koren et al. 2008). There appears to be a scale break at $\sim$ 600 m in the results from all three resolutions. This compares well with the scale break derived by *Neggers et al.* (2003) based on LES of cumulus clouds.

3.2 Subadiabatic factor

The subadiabatic factor β is defined as:

$$\beta = \frac{LWC}{LWC_{ad}} \quad (1)$$

where LWC_{ad} is the height-dependent adiabatic LWC calculated from cloud base conditions for each individual cloud in the cumulus populations. A probability distribution function of β is plotted (Figure 3) from the simulations of the polluted conditions. For the clean conditions (N_a = 100 cm^{-3}), there is no significant difference in response to resolution (not shown). As can be seen in Figure 3, β peaks around $\sim$ 0.1 in all the simulations, but the finer resolution simulations produce a β distribution that is narrower, has fewer occurrences of higher β between 0.3 and 0.5, and has a stronger peak. These results suggest a tendency for the finer resolution simulations to produce clouds that are smaller (Figure 2), more susceptible to dilution, and therefore more subadiabatic.

4 CONCLUDING REMARKS

We have shown some preliminary results of LES of cumulus cloud populations and their sensitivity to changes in aerosol concentration and model resolution. Some of the results are in agreement with the previous studies and some are not. Of note are the following:

1) Cloud fraction is unaffected by the aerosol perturbations applied in this study (1000 cm^{-3} vs 100 cm^{-3};

2) Differences in TKE are driven by resolution with almost no influence by aerosol.

3) Differences in the size distribution of clouds are a strong function of resolution, which has implications for planetary albedo (Koren et al. 2007, 2008; Charlson et al. 2007). Aerosol has relatively little influence on the size distribution of clouds.

4) Smaller clouds generated in the finer resolutions tend to be more subadiabatic.

Table 2. $^{+}$LWP, cloud fraction, and τ_c

DIFF	LWP	cf	τ_c
N_a = 100 cm^{-3}			
$\frac{100-25}{25}$*	40.9%	-23.6%	12.1%
N_a = 1000 cm^{-3}			
$\frac{100-25}{25}$	62.6%	-26.1%	22.3%

* differences are between the coarse and fine, relative to the fine resolution.
τ_c is the cloud optical depth.
$^{+}$ Three hour average over 4, 5, and 6 h of simulations.

Table 3. Time averaged TKE, LHF, and $z_{t,max}$

EXP	TKE_{res}	TKE_{sgs}	LHF	$z_{t,max}$
N_a = 100 cm^{-3}				
dx25	238.0	36.3	159.5	1717
dx50	236.9	51.8	164.9	1737
dx100	325.8	95.1	176.3	1879
N_a = 1000 cm^{-3}				
dx25	234.8	36.4	159.2	1704
dx50	233.7	52.7	165.3	1696
dx100	332.5	93.8	176.3	1882

The results point to the importance of small scale dynamics in establishing cloud macrophysical properties such as LWP, cloud fraction and cloud size. Although these results point to the fact that aerosol perturbations have a minor effect on these cloud macrophysical properties, they do have a strong effect on cloud optical depth (and hence albedo).

Finally, we emphasize that the response of cumulus populations to aerosol changes are very sensitive to the initial thermodynamical state and environment where these cumulus clouds are evolved and developed.

Acknowledgments. This research was funded by NOAA's Climate Goal.

5 REFERENCE

Brown, A, 1999: The sensitivity of large-eddy simulations of shallow cumulus convection to resolution and subgrid model, *Q. J. R. Meteorol. Soc.*, *125*, 469–482.

Charlson, R. J., A. S. Ackerman, F. A-M. Bender, T. L. Anderson, and Z. Liu, 2007: On the climate forcing consequences of the albedo continuum between cloudy and clear air, *Tellus, 59*, 715–727.

Jiang, H. and G. Feingold, 2006: Effect of aerosol on warm convective clouds: Aerosol-cloud-surface flux feedbacks in a new coupled large eddy model. *J. Geophys. Res.*. 111, D01202, doi:10.1029/2005JD006138.

Koren, I, L. L. A. Remer, Y. J. Kaufman, Y. Rudich, and J. V. Martins, 2007: On the twilight zone between clouds and aerosols, *Geophys. Res. Lett., 34*, L08805, doi:10.1029/2007GL029253.

Koren, I, L. Oreopoulos, G. Feingold, L. A. Remer, and O. Altaratz, 2008: How small is a small cloud? *Atmos. Chem. Phys., Disc., 8*, 6380–6407

Lewellen, D. C. and W. S. Lewellen, 1998: Large-eddy boundary layer entrainment, *J. Atmos. Sci., 55*, 2645–2665.

Neggers, R., A., J., H. J. J. Jonker, and A. P. Siebesma, 2003: Size statistics of cumulus cloud populations in Large-Eddy simulations, *J. Atmos. Sci., 60*, 1060–1074.

Nitta, T, 1975: Observational determination of cloud mass flux distributions, *J. Atmos. Sci., 32*, 73–91.

Rauber, R. M., and co-authors, 2007: Rain in shallow cumulus over the ocean, *BAMS, 88*,1912–1928.

Stevens, D. and C. S. Bretherton, 1999: Effects of resolution on the simulation of stratocumulus entrainment, *Q. J. R. Meteorol. Soc., 125*, 425–439.

Stevens, D., A. S. Ackerman, and C. S. Bretherton, 2002: Effects of domain size and numerical resolution on the simulation of shallow cumulus convection, *J. Atmos. Sci., 59*, 3285–3301.

Stevens, B., C-H Moeng, and P. P. Sulliva, 1999: Large-eddy simulations of radiatively driven convection: sensitivities to the representation of small scales. *J. Atmos. Sci., 56*, 3963–3984.

Warren, S. G., C.J.Hahn, J. London, R.M. Chervin,and R. L. Jenne, Global distribution of total cloud cover and cloud type amounts over the ocean, *NCAR/TN-317+STR*, 42 pp. + 170 maps, National Center for Atmos. Res., Boulder, Colo, 1988.

Xue, H, and G. Feingold, Large eddy simulations of trade wind cumuli: investigation of aerosol indirect effects. *J. Atmos. Sci., 63*, 1605–1622, 2006.

Zhao, G. and L. Di Girolamo, Statistics on the macrophysical properties of trade wind cumuli over the tropical western Atlantic. *J. Geophys. Res. 112, D10204*, doi:10.1029/2006JD007371, 2007.

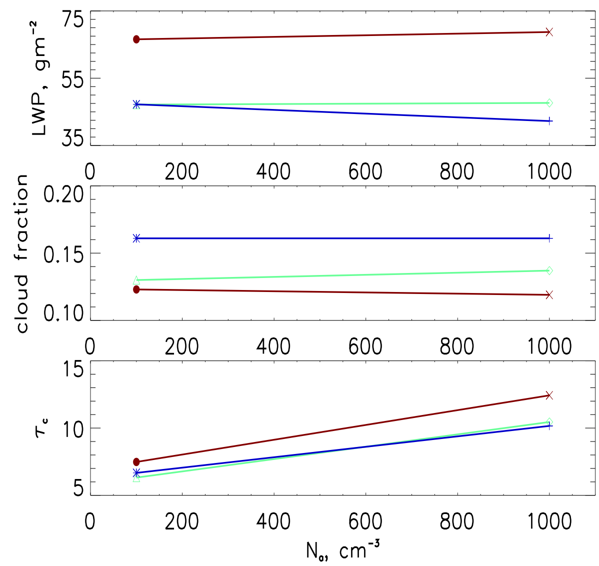

Figure 1: Selected fields averaged over 3 h (hours 4, 5, 6) as a function of aerosol concentration N_a for all the simulations. (a) LWP averaged over cloudy columns, (b) cloud fraction, and (c) cloud optical depth τ_c averaged over regions with $\tau_c > 0.5$. Blue color denotes high resolution (dx25-100 and dx25-1000), green denotes medium resolution (dx50-100 and dx50-1000), and red denotes coarse resolution (dx100-100 and dx100-1000). See Table 1 for details. Note that only the symbols represent the actual model data points. They are connected by lines to facilitate interpretation. Intermediate values of N_a may well generate a different response.

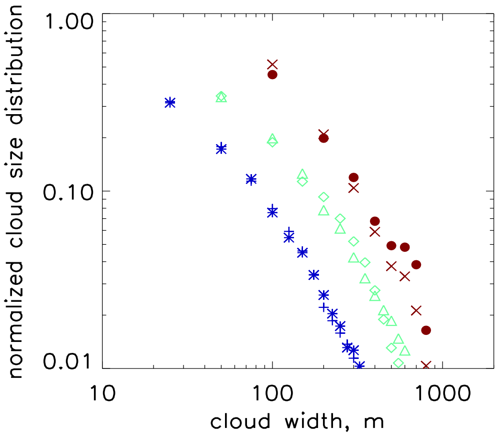

Figure 2: Normalized cloud size distribution ($N(\ell)$) from a sampling of 3 h (hours 4, 5, 6) of model output. Color scheme is the same as in Figure 1. Filled circles (red) denote dx100-n100, crosses (red) denote dx100-n1000, triangles (green) denote dx50-n100, diamonds (green) denote dx50-n1000, stars (blue) denote dx25-n100, and pluses (blue) denote dx25-n1000. The slopes of the power law fits, b (not plotted for clarity, $N(\ell) \sim \ell^b$) range from -1.25 (red), -1.47 (green), to -1.73 (blue), respectively.

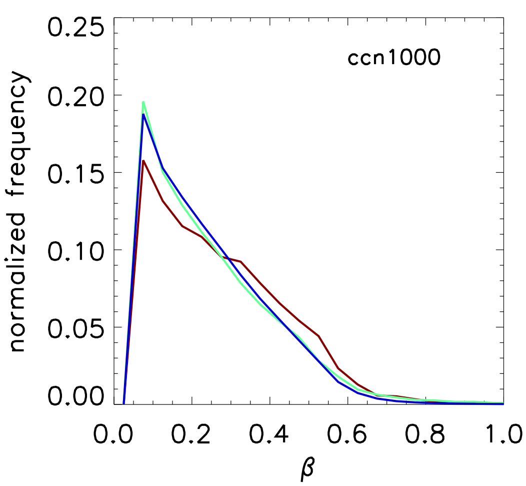

Figure 3: Normalized frequency of occurrence of β from a sampling of 3 h (hours 4, 5, 6) of model output for the polluted conditions (N_a = 1000 cm^{-3}). Color scheme is the same as in Figure 1.

ACTIVATION OF AEROSOL PARTICLES OBSERVED INSIDE CLOUDS AT A MOUNTAIN SITE ON PUERTO RICO DURING THE PUERTO RICO AEROSOL-CLOUD-STUDY (RICO-PRACS)

S. Mertes[1], S. Walter[2], J. Schneider[2], S. Borrmann[2,3], G. Montero[4], M. Krämer[5], A. Gioda[6], O. Mayol-Bracero[6], G. Frank[2,7] and D. Baumgardner[4]

[1] Leibniz-Institute for Tropospheric Research, Leipzig, Germany
[2] Max Planck Institute Mainz, Germany
[3] University of Mainz, Germany
[4] Universidad Nacional Autónoma de México, Mexico
[5] Research Center Juelich, Germany
[6] University of Puerto Rico, Puerto Rico
[7] present affiliation: University of Lund, Sweden

1. INTRODUCTION

The size and chemical composition of atmospheric particles that become activated to drops in different clouds types under different meteorological conditions are important parameters to infer the radiative properties and precipitation capability of clouds. The counterflow virtual impactor [CVI, Ogren et al., 1985] is a drop sampling device that recover particles that served as cloud condensation nuclei (CCN) in the atmosphere as cloud drop residues. Thus, not only the chemical information, just as well inferable from cloud water samplers, but additionally the size information about the CCN can be obtained. This experimental approach has been successfully applied in ground-based observations of mid-latitude stratocumulus [e.g., Hallberg et al., 1994; Mertes et al., 2005a; Schwarzenböck et al., 2000; Targino et al., 2007]. In combination with size distribution measurements of the interstitial aerosol particles, activation diameters $d_{p,50\%}$ between 100 and 200 nm were observed from remote to more polluted regions. Another novel idea is to couple aerosol mass spectrometers (AMS) to a CVI in order to derive in-situ the chemical composition of CCN with regard to the main soluble inorganic ions and organic matter (OM). Before this information was obtained from filter sampling of drop residues, which could be biased by condensation/evaporation of semi-volatile substances (esp. organic gases and ammonia) on/from the filter matrix during collection. These positive and negative artifacts are a priori avoided by using the CVI-AMS coupling as it was carried out in ground-based experiments in mid-latitude continental clouds [Drewnick et al., 2007; Mertes et al., 2007]. Drewnick et al. [2007] concluded from their AMS results of the cloud drop residues that organic and nitrate particles were more efficiently activated than sulfate particles.

The knowledge of the size distribution and chemical composition of actually activated CCN in tropical, marine clouds are still needed to improve our understanding of their formation and microphysical evolution, which determine their radiative properties and precipitation efficiency, especially for trade wind cumuli. Therefore, a ground-based cloud experiment within the Puerto Rico Aerosol-Cloud-Study (RICO-PRACS) was initiated where the CVI drop sampling was combined with an AMS and particle sizing analysis.

2. EXPERIMENTAL

The cloud experiment part of RICO-PRACS was carried out at the East Peak (EP) mountain site (18°18’ N, 65°45’ W, 1050 m asl) located inside a tropical rainforest (El Yunque National Forest) in the north-east of Puerto Rico (Fig.1). The measurements reported here were conducted from the 8th to the 17th of December 2004 within the time frame of the American joint field campaign RICO [Rauber et al., 2007]. During that time the EP site was almost constantly engulfed in clouds fed by trade winds. Due to the steady trade wind conditions, air masses arrived from the Atlantic Ocean slightly changing between north easterly and more easterly wind directions during the measurement period [Allan et al., 2008]. The EP field site was only about 20 km apart from the coast line in this wind direction.

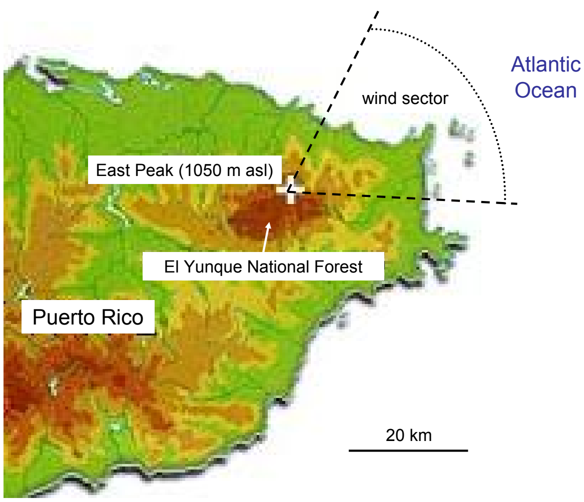

***Fig.1**: Map of the eastern part of Puerto Rico. The East Peak measurement site, the distance to the shoreline and the wind direction sector are indicated.*

In order to characterize the CCN and interstitial particles inside the trade wind cumuli, two complementary samplers were installed side by side on top of the measurement trailer (Fig.2). An interstitial inlet (INT) with an upper cut size of 5 µm and a horizontally oriented counterflow virtual impactor (CVI) with a lower cut size of 5 µm were operated side by side in order to separately collect non-activated interstitial particles and cloud drops [Mertes et al., 2005b]. Inside the CVI, the drops are evaporated releasing dry residual particles that are related to the original CCN.
Particle number size distributions and mass concentration of soluble inorganic ions (sulfate, nitrate, ammonium) and organic matter of residual and interstitial particles with mobility diameters up to about 500 nm were determined by means of a scanning mobility particle sizer (SMPS) and an Aerodyne aerosol mass spectrometer (Q-AMS), respectively, that were periodically switched between both inlets. A condensation particle counter (CPC) and a particle soot absorption photometer (PSAP) at each inlet measured the residual and interstitial particle number N_p and black carbon (BC) mass concentrations simultaneously. The liquid water content (LWC) sampled by the CVI was determined by a Lyman-alpha hygrometer and a dew point mirror.

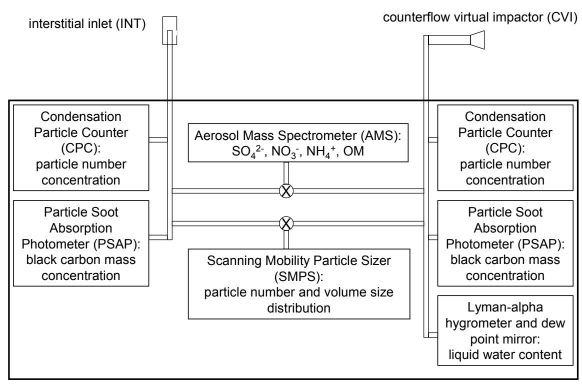

***Fig.2**: Sketch of the interstitial and CVI inlet setup with subsequent analysis of dried non-activated particles and CCN (drop residues after evaporation) inside the measurement trailer.*

A particle volume monitor (PVM) and a forward scattering spectrometer probe (FSSP) were operated in order to derive LWC, effective drop diameter D_{eff}, drop concentration N_D and drop size distribution.
Moreover, cloud water samples were collected using an aluminum version of the single-stage Caltech Active Strand Cloud water Collector 2 (CASCC-2) [Demoz et al., 1996]. The cloud water was analyzed for total ion and insoluble mass [Allan et al., 2008] and specific inorganic ions [Gioda et al., 2008]. For the latter only liquid phase concentration from an ensuing measurement period (January 2005) were available, but are compared to the CVI

results for similar back-trajectories of clean maritime air masses from the Atlantic Ocean.

3. RESULTS

During the measurement period the wind sector and thus the air mass origin changed three times. Air from the east-northeast (ENE) and east-southeast (ESE) was encountered during period A and C and during period B and D, respectively. Whereas the ENE air masses were mostly free of anthropogenic influences, the ESE air masses are found to be moderately influenced by populated islands upwind [Allan et al., 2008].

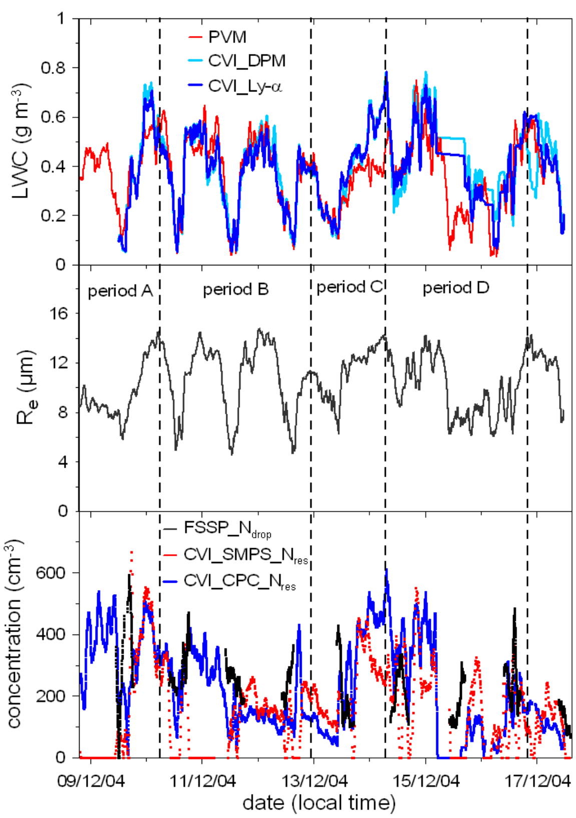

***Fig.3**: Time series of LWC, measured with PVM and CVI, effective drop radius R_e, drop and residual particle number concentration (N_{drop}, N_{res}) for the ENE (periods A, C) and ESE (periods B, D) air masses.*

Time series of LWC, effective drop radius R_e, drop and residual particle number concentration (N_{drop}, N_{res}) for all four periods are presented in Fig.3. Highest LWC and R_e values were measured during night with values of 0.6 g m^{-3} and 14 µm, respectively. The cloud sometimes dispersed during noon or the cloud base ascent above the EP site for a short time. The good agreement of the PVM and CVI LWC measurements indicates the high CVI drop aspiration efficiency due to its horizontal setup and the steady wind direction. Drop and residual particle number size distributions varied between 200 and 600 cm^{-3}.

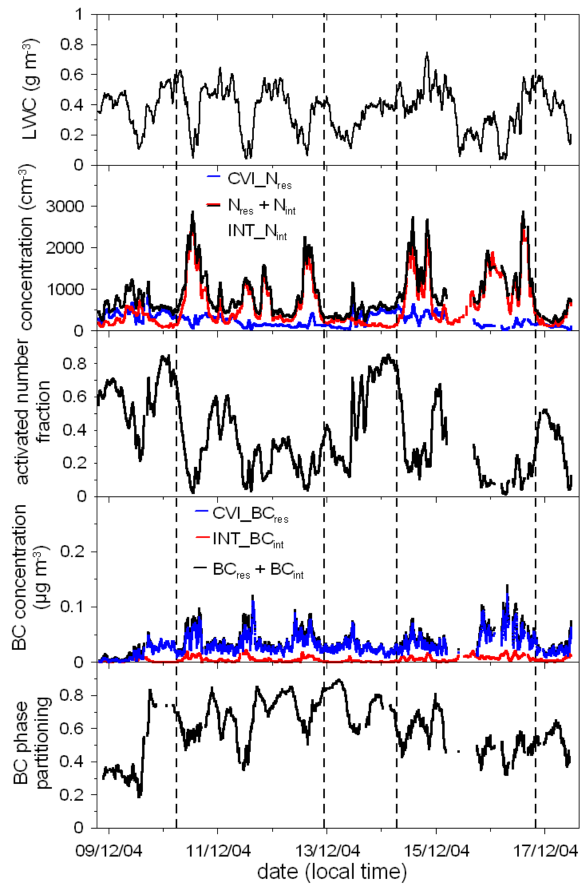

***Fig.4**: Time series of LWC, residual and interstitial particle number concentration (N_{res}, N_{int}) and BC mass concentration (BC_{res}, BC_{int}) for the ENE (periods A, C) and ESE (periods B, D) air masses.*

Fig.4 shows time series of residual and interstitial particle number and BC mass concentration, respectively. Total number and BC mass concentration are derived by adding residual and interstitial results. This values show higher numbers for period B and D supporting the back-trajectory analysis of a slightly anthropogenic influenced air mass. The activated number fraction and the BC phase partitioning, defined in Eq.1, are also plotted in Fig.4.

$$X_f = \frac{X_{CVI}}{X_{CVI} + X_{INT}} \qquad (1)$$

Obviously, the number fraction of activated particles and the BC phase partitioning decreases during the prevalence of the anthropogenic influenced air masses, but both parameters are still significantly higher than for continental stratocumulus clouds.
Mean particle number size distributions of residual and interstitial particles are for all periods are presented in Fig.5 (upper panel).

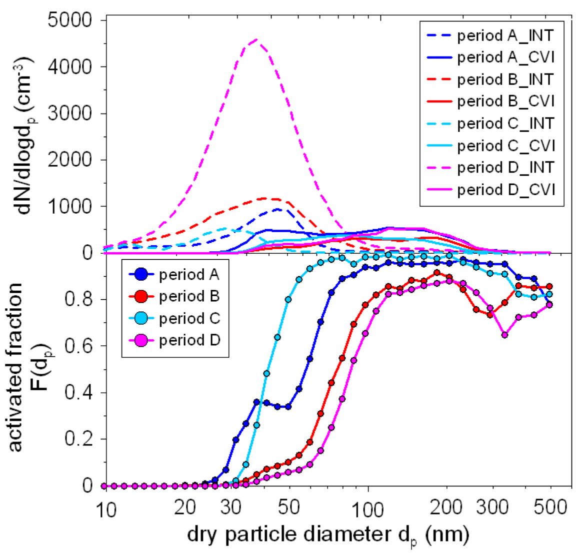

***Fig.5**: Number size distribution of interstitial and residual particles) for the ENE (periods A, C) and ESE (periods B, D) air masses (upper panel) and the respective activated fraction (lower panel).*

The degree of anthropogenic influence is seen by the amount of small interstitial particles whereas the residue number size distributions look quite similar for all periods. From these measurements, the activated particle number fraction F can be inferred as a function of particle size (Fig.5, lower panel) using Eq.2:

$$\mathrm{F}(\mathrm{d_p}) = \frac{\dfrac{dN_{CVI}(d_p)}{d\log d_P}}{\dfrac{dN_{CVI}(d_p)}{d\log d_P} + \dfrac{dN_{INT}(d_p)}{d\log d_P}} \qquad (2)$$

It can be concluded that the activation diameter $d_{p,50}$ (defined for $F(d_p) = 0.5$) increases from 40 to 90 nm with increasing anthropogenic influence on the background aerosol particles. Whereas F reaches a plateau at about 0.96 for the pristine maritime air masses (period A, C), values only around 0.9 are derived for periods B and D. This might indicate the presence of some few larger particles that did not serve as CCN but also the entrainment of sub-saturated air causing a similar effect cannot be ruled [Mertes et al., 2005b]. The step in the activation function for period A implies an external mixture of CCN.
Unfortunately, due to operational problems with the AMS, information about the chemical composition of residual and interstitial particles is only available for period A and the beginning of period B. Ammonium and organic matter were always below the AMS detection limit, so that solely time series of sulfate, nitrate and chloride are shown in Fig.6. Since all these substances are CCN compounds they were never observed in the interstitial reservoir above the AMS noise level. Relating the sulfate and nitrate CCN mass concentration with the measured LWC yields mean liquid phase concentrations of 2.8 and 0.4 mg L^{-1}, which is in the same range of the cloud water analysis for similar air masses [Gioda et al., 2008]. The Cl^- concentration found in the residuals is much lower than for the cloud water sample results, because the letter is dominated by sea-salt, which cannot be vaporized in the AMS. Due to the limited AMS data set no clear differences in the chemical composition of residual and interstitial particles could be observed during the transition from period A to period B.

The sum of soluble ions detected with the AMS in the submicron CCN, which is clearly dominated by sulfate is similar to the total mass derived from the SMPS number distribution assuming spherical particle shape and a particle density of 1.6 g cm^{-3}. This leads to the suggestion that sulfate particles are the main CCN in the size range up to 500 nm in the investigated trade wind cumuli.

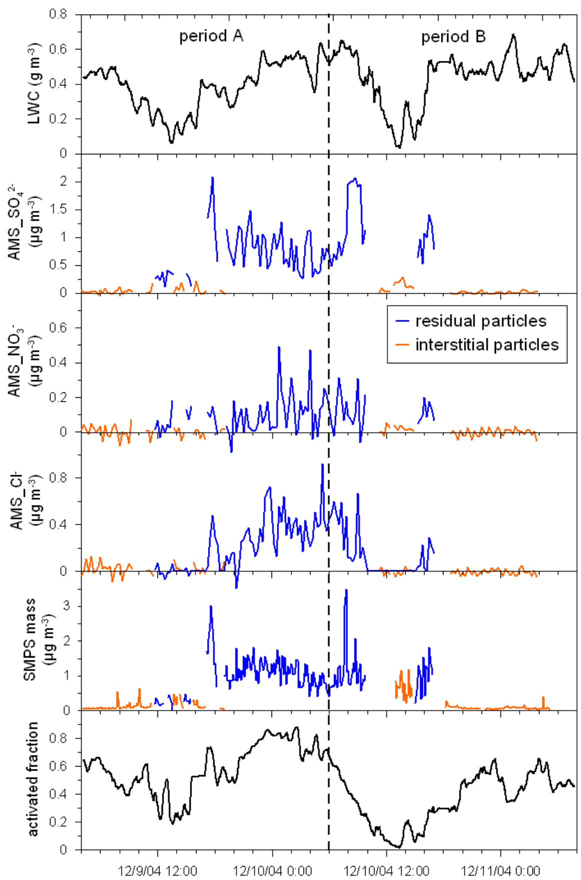

***Fig.6**: Time series of sulfate, nitrate and chloride detected with the AMS and total aerosol mass inferred from the SMPS measurements obtained for residual and interstitial particles.*

This assumption is further supported by the comparison of the sulfate mass size distribution measured with the AMS and the total aerosol mass size distribution derived from the SMPS measurements (Fig.7). For the residual particles both sensors detect a pronounced CCN mode with similar magnitude in a diameter range between 200 and 300 nm. This implies that the SO_4^{2-} is mainly nss-sulfate, because otherwise the SMPS mode should be much higher, due to measured sea salt particles. Thus, the NaCl particles serving as CCN seem to be larger than 500 nm. The interstitial particles contain hardly any soluble compounds. In the SMPS mass size distribution a mode at 50 nm was observed during period B (Fig.7, lower panel) that is most likely due to anthropogenic emissions from the islands upwind.

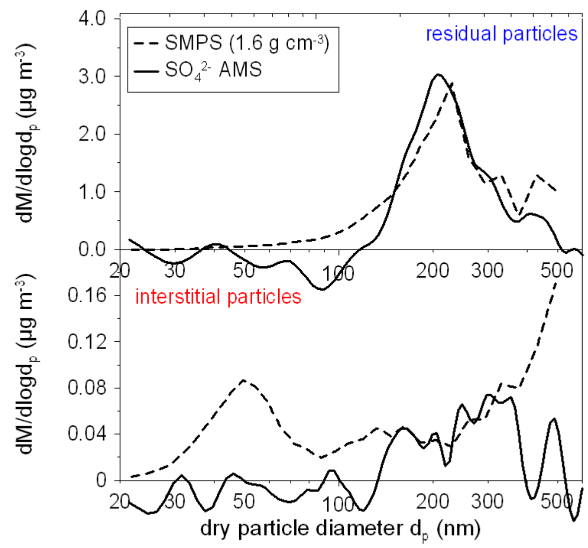

***Fig.7**: Mass size distribution of sulfate and total aerosol for residual and interstitial particles.*

6. ACKNOWLEDGEMENTS

This work was funded by the Max Planck Society, the Mexican Science Foundation (grant #45310) and the National Science Foundation (grant #0342548). The authors would like to thank the Caribbean National Forest and the Federal Aviation Administration for access to the East Peak.

7. REFERENCES

J.D. Allan, D. Baumgardner, G.B. Raga, O.L. Mayol-Bracero, F. Morales-García, F. García-García, G. Montero-Martínez, S. Borrmann, J. Schneider, S. Mertes, S. Walter, M. Gysel, U. Dusek, G.P. Frank and M. Krämer (2008), Clouds and aerosols in Puerto Rico - A new evaluation, *Atmos. Chem. Phys.*, ***8***, 1293-1309.

B.B. Demoz, J.L. Collett Jr. and B.C. Daube Jr. (1996), On the caltech active strand cloudwater collectors, *Atmos. Res.*, ***41***, 47-62.

F. Drewnick, J. Schneider, S. Hings, N. Hock, K.J. Noone, A. Targino, S. Weimer and S. Borrmann (2007), Measurement of ambient, interstitial, and residual aerosol particles on a mountain top site in central Sweden using an aerosol mass spectrometer and a CVI, *J. Atmos. Chem.*, ***56***, 1-20.

A. Gioda, O.L. Mayol-Bracero, F. Morales-Garcia, J. Collett, S. Decesari, M. Emblico, M.C. Facchini, R.J. Morales-De Jesús, S. Mertes, S. Borrmann, S. Walter and J. Schneider (2008), Chemical composition of cloud water in the Puerto Rican tropical trade winds, *Water, Air & Soil Pollution*, submitted.

A. Hallberg, K.J. Noone, J.A. Ogren, I.B. Svenningsson, A. Flossmann, A. Wiedensohler, H.-C. Hansson, J. Heintzenberg, T. Anderson, B. Arends and R. Maser (1994), Phase partitioning of aerosol particles in clouds at Kleiner Feldberg, *J. Atmos. Chem.*, ***19***, 107-127.

S. Mertes, D. Galgon, K. Schwirn, A. Nowak, K. Lehmann, A. Massling, A. Wiedensohler and W. Wieprecht (2005a), Evolution of particle concentration and size distribution observed upwind, inside and downwind hill clouds at connected flow conditions during FEBUKO, *Atmos. Environ.*, ***39***, 4233-4245.

S. Mertes, K. Lehmann, A. Nowak, A. Massling and A. Wiedensohler (2005b), Link between aerosol hygroscopic growth and droplet activation observed for hill-capped clouds at connected flow conditions during FEBUKO, *Atmos. Environ.*, ***39***, 4247-4256.

S. Mertes, B. Verheggen, S. Walter, P. Connolly, M. Ebert, J. Schneider, K.N. Bower, J. Cozic, S. Weinbruch, U. Baltensperger and E. Weingartner (2007), Counterflow virtual impactor based collection of small ice particles in mixed-phase clouds for the physico-chemical characterization of tropospheric ice nuclei: sampler description and first case study, *Aerosol Sci. Technol.*, ***41***, 848-864.

J.A. Ogren, J. Heintzenberg and R.J. Charlson (1985), In-situ sampling of clouds with a droplet to aerosol converter, *Geophys. Res. Lett.*, ***12***, 121-124.

R.M. Rauber, B. Stevens, H.T. Ochs III, C. Knight, B.A. Albrecht, A.M. Blyth, C.W. Fairall, J.B. Jensen, S.G. Lasher-Trapp, O.L. Mayol-Bracero, G. Vali, J.R. Anderson, B.A. Baker, A.R. Bandy, E. Burnet, J.-L. Brenguier, W.A. Brewer, P.R.A. Brown, P. Chuang, W.R. Cotton, L. Di Girolamo, B. Geerts, H. Gerber, S. Göke, L. Gomes, B.G. Heikes, J.G. Hudson, P. Kollias, R.P. Lawson, S.K. Krueger, D.H. Lenschow, L. Nuijens, D.W. O'Sullivan, R.A. Rilling, D.C. Rogers, A.P. Siebesma, E. Snodgrass, J.L. Stith, D.C. Thornton, S. Tucker, C.H. Twohy and P. Zuidema (2007), Rain in shallow cumulus over the ocean: The RICO campaign, *Bull. Amer. Meteor. Soc.*, ***88***, 1912-1928; doi:1910.1175/BAMS-1988-1912-1912.

A. Schwarzenböck, J. Heintzenberg and S. Mertes (2000), Incorporation of aerosol particles between 25 and 850 nanometers into cloud elements: Measurement with a new complementary sampling system, *Atmos. Res.*, ***52***, 241-260.

A. Targino, K.J. Noone, F. Drewnick, J. Schneider, R. Krejci, G. Olivares, S. Hings and S. Borrmann (2007), Microphysical and chemical characteristics of cloud droplet residuals and interstitial particles in continental statocumulus clouds, *Atmos. Res.*, ***86***, 225-240.

NUCLEATION OF CLOUD LIQUID WATER IN A DOUBLE MOMENT BULK MICROPHYSICS SCHEME

Ben J. Shipway, S. J. Abel & C. J. Smith
Met Office, Exeter, UK, ben.shipway@metoffice.gov.uk

1. INTRODUCTION

The rapid onset of rain in shallow warm-rain cumulus clouds is a well-reported, but little understood phenomenon. Several mechanisms for this rapid formation of raindrops have been put forward, however one thing that they all have in common is a need to accurately represent the condensation process, paying particular attention to the size and number of cloud droplets that are formed.

Recent numerical studies (Abel & Shipway 2007) have shown that good agreement between the in-cloud properties of modelled fields and aircraft observations taken during the recent Rain In Cumulus over the Ocean (RICO) field experiment (Rauber et al., 2007). However, in order to obtain this agreement, it was necessary to "tune" some of the model parametrizations (such as fall velocity, autoconversion formulation and most importantly cloud number concentration) to better reflect the conditions during the period of observation.

The microphysics scheme used by Abel Shipway and & Shipway had a single moment representation of cloud liquid water (i.e. representation of cloud mass mixing ratio but not number). In order to better capture the onset and subsequent evolution of rain, a double moment scheme has been incorporated into the model with a view to rerunning the experiments of Abel & Shipway, but with an inherent coupling to an underlying aerosol population (see Abel et al., 2008).

The nucleation process within this double moment scheme is built upon the ideas of Twomey (1959) who provides an analytical method for determining the peak subgrid supersaturation and thence the cloud droplet nucleation rate, based on an approximate equation for humidity evolution. In order to incorporate the dependence upon the underlying dry aerosol distribution and physicochemical properties, we use an approximation to the parametrization developed by Khvorostyanov and Curry (2006).

2. GENERALIZATION OF TWOMEY'S ANALYTICAL APPROACH

It is readily shown (Pruppacher & Klett, 1997, Korolev & Mazin, 2003, Twomey, 1959, Cohard et al., 1998) that the time evolution of the supersaturation, s, of a parcel of air undergoing an ascent at a constant velocity, w, is well approximated by the relation

$$\frac{ds}{dt} = \psi_1(T,p)w - \psi_2(T,p)s\int_0^s \varphi(\sigma)\left[\int_{\tau(\sigma)}^t s dt\right]^{\frac{1}{2}} d\sigma. \tag{1}$$

In this approximation, the first term on the right hand side represents the increase in saturation due to adiabatic cooling of the parcel, while the second term demonstrates the effect of condensation of excess vapour onto droplets and thence the reduction of saturation. Here, $\varphi(\sigma)$ represents the differential activity spectrum of the cloud nuclei present, that is to say a number $\varphi(\sigma)\delta\sigma$ of cloud nuclei are activated in the interval $[\sigma,\, \sigma+\delta\sigma]$. $\tau(\sigma)$ represents the time at which these nuclei become activated and so the inner integral in (1) represents the net supersaturation to which the activated drops are exposed. For details of the thermodynamic functions $\psi_1(T,p)$ and $\psi_2(T,p)$ see Pruppacher & Klett (1997).

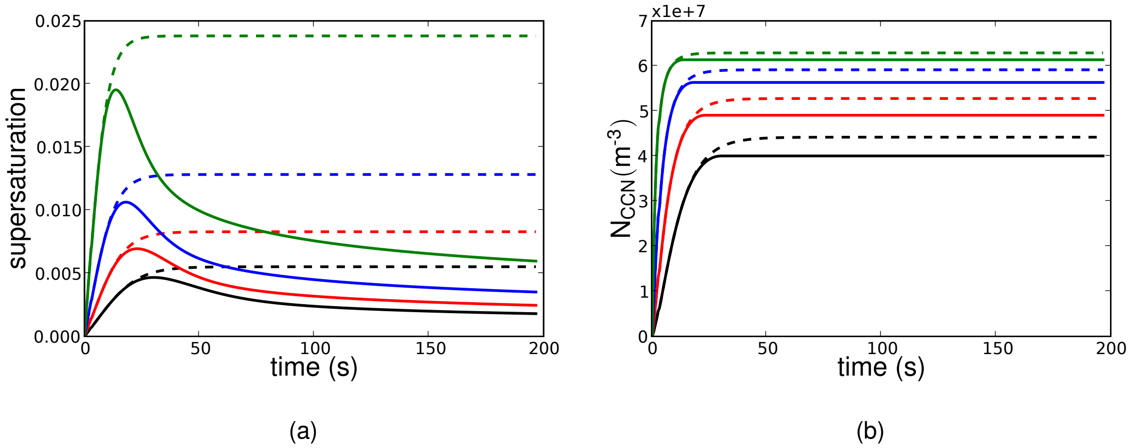

Figure 1: Variation of (a) supersaturation and (b) activation of cloud nuclei with time using a full numerical solution to (1) (solid lines) and the upper bound approximation (2) (dashed lines). The colours correspond to different values of the updraught velocity w: black= 0.5ms^{-1}, red=1ms^{-1}, blue=2ms^{-1}, green=5ms^{-1}.

Twomey (1959) uses geometrical arguments to establish upper and lower bounds on the supersaturation. The lower bound estimate enables us to write the inner integral in (1) as

$$\int\limits_{\tau(\sigma)}^{t} sdt \approx \frac{1}{2\psi_1 w}\left(s^2-\sigma^2\right), \tag{2}$$

which, when used in (1) will result in an upper bound estimate for s. Figure 1 shows the evolution of s and corresponding droplet activation for a given population of aerosol calculated numerically using both the full expression (1) and using the approximation (2).

Within a saturated updraught, aerosol continue to be activated as cloud drops until the peak supersaturation is reached. Setting the left hand side of (1) to zero and applying (2), we see that the maximum supersaturation, s_{max}, is given by

$$\frac{\sqrt{2}\left(\psi_1 w\right)^{3/2}}{\psi_2} = s_{\max}\int\limits_{0}^{s_{\max}} \varphi\left(\sigma\right)\left(s_{\max}^2-\sigma^2\right)^{1/2} d\sigma. \tag{3}$$

If an appropriate form for $\varphi(s)$ is chosen, then (3) can be solved to find s_{max}.

Twomey (1959) used an expression of the form

$$\varphi\left(s\right) = kCs^{k-1}, \tag{4}$$

which when substituted into (3) yields

$$s_{max} = \left(\frac{\left(2\psi_1 w\right)^{3/2}}{kC\psi_2 B\left(\frac{k}{2},\frac{3}{2}\right)}\right)^{1/(k+2)}, \tag{5}$$

where $B(x, y)$ is the complete Beta Function (see Abramowitz & Stegun, 1964).

Although the expression for the differential activity spectrum in (4) allows for an analytical expression for s_{max} to be determined from (3), its is not a particularly realistic representation for larger values of supersaturation as might be seen in convective conditions. Cohard et al.(1998) discuss situations in which use of Twomey's expression might be inappropriate and go on to suggest an alternative form for $\varphi(s)$. Their expression takes the form

$$\varphi\left(s\right) = kCs^{k-1}(1+\eta s^2)^{-\mu}, \tag{6}$$

where now η and μ are additional parameters which modify the asymptotic behaviour for large and small supersaturations. This expression, while more realistic in its representation of activation, also allows for an analytical approach to be taken in the determination of s_{max}. In this case, use of (6) in (3) provides us with an implicit solution for s_{max} of the form

$$s_{max}^{k+2} \cdot {}_2F_1\left(\mu, \frac{k}{2}; \frac{k}{2} + \frac{3}{2}; -\eta s_{max}^2\right) = \frac{(2\psi_1 w)^{3/2}}{kC\psi_2 B\left(\frac{k}{2}, \frac{3}{2}\right)}. \quad (7)$$

Here ${}_pF_q(\mathbf{a}; \mathbf{b}; x)$ is the generalised hypergeometric function (Erdélyi et al., 1953). Equation (7) can be solved to provide a reasonable approximation to s_{max} as long as appropriate values for the parameters (k, C, μ, η) can be determined for the aerosol population of interest.

It will become useful in the next section for us to be able to generalise the expression (6) such that

$$\varphi(s) = kCs^{k-1}(1 + \eta s^{\kappa})^{-\mu}. \quad (8)$$

Here we have introduced a fifth parameter, κ, which replaces the quadratic term in the denominator in (6). While this initially introduces more complexity to our expression for the differential activity spectrum, its use in (3) still allows us to produce an analytical expression for s_{max}, namely

$$s_{max}^{k+2} \cdot {}_{(\kappa/2+1)}F_{(\kappa/2)}\left(\mathbf{a}; \mathbf{b}; -\eta s_{max}^{\kappa}\right) = \frac{(2\psi_1 w)^{3/2}}{kC\psi_2 B\left(\frac{k}{2}, \frac{3}{2}\right)}, \quad (9)$$

where now the tuples $\mathbf{a}$ and $\mathbf{b}$ are given by

$$\mathbf{a} = \left(\mu, \frac{k}{\kappa}, \frac{k+2}{\kappa}, \ldots, \frac{k + (\kappa - 2)}{\kappa}\right)$$

$$\mathbf{b} = \left(\frac{k+3}{\kappa}, \frac{k+5}{\kappa}, \ldots, \frac{k + (\kappa + 1)}{\kappa}\right)$$

and is valid provided κ is an even integer (see Erdélyi et al., 1954 equation 13.1.11, and Norlund, 1955). It can be very simply seen that when $\kappa = 2$, (8) is identical to (6) and (9) reduces to (7). Likewise, when $\eta = 0$ or $\mu = 0$, both (9) and (7) reduce to Twomey's expression (5).

Up until this point, the parameters $(k, C, \mu, \eta, \kappa)$ are all arbitrary and must be chosen to fit some curve inferred from observations which is suitable for our assumed aerosol populations. In the next section, we go on to use results which allow these parameters to be deduced directly from the underlying aerosol distribution and its physicochemical properties.

3. LINKING AEROSOL PROPERTIES TO THE GENERALIZED FORM FOR $\varphi(s)$

From a modelling perspective, the need for an empirical fit to the coefficients for our activation spectrum is undesirable since any evolution in the underlying aerosol population, either in its distribution or its chemical properties, will not feed back onto the parametrization. Khvorostyanov and Curry (2006) have suggested an approach in which the aerosol activation is directly inferred from the dry aerosol distribution and chemistry. This allows coefficients, such as those previously mentioned, to be diagnosed rather than prescribed. The method of Khvorostyanov and Curry assumes an underlying dry aerosol population, $f_d(r_d)$, with a lognormal distribution, such that

$$f_d(r_d) = \frac{N_a}{\sqrt{2\pi}\ln(\sigma_d) r_d} \exp\left(-\frac{\ln^2(r_d/r_{d0})}{2\ln^2 \sigma_d}\right). \quad (10)$$

Here, r_d is the radius of the dry aerosol, N_a is the aerosol number concentration, σ_d and r_{d0} are the dispersion and geometric mean of the distribution respectively.

In order to link the dry aerosol to the wet aerosol and subsequently the activation spectrum, the parameters b and β are introduced in the parametrization

$$B = br_d^{2(1+\beta)}, \quad (11)$$

where B/r^3 represents the effects of solubility in the Köhler equation for supersaturation (see Pruppacher & Klett, 1997 and Khvorostyanov & Curry, 1999). To summarise this parametrization; if $\beta = 0.5$, then the soluble fraction of the aerosol is distributed within the particle volume; if $\beta = 0$ then the mass of soluble fraction is proportional to the surface area of a particle as if in a film or a shell; if

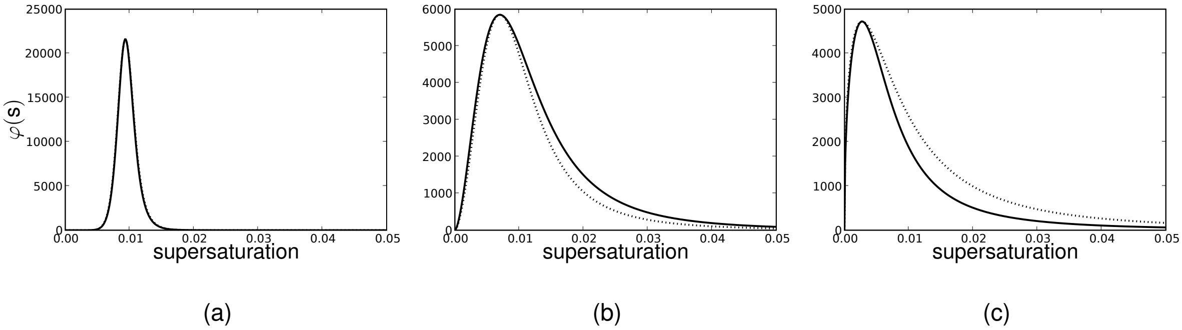

Figure 2: Comparison between differential activity spectra given by expression (15) (solid line) and its approximation in (19). In each case, N_a = 73 cm^{-3}, r_d = .022 μm, b = 0.25 and β = 0.5. In (a) σ_d = 1.1, (b) σ_d = 1.5 and (c) σ_d = 2.12.

$\beta = -1$, then the soluble fraction is independent of the size of the particle. Having established this parametrization, a lognormal differential activity spectrum can be deduced of the form

$$\varphi(s) = \frac{N_a}{\sqrt{2\pi}\ln(\sigma_s)s}\exp\left(-\frac{\ln^2(s/s_0)}{2\ln^2\sigma_s}\right), \quad (12)$$

where now the geometric mean and dispersion of this distribution are given by the relations

$$s_0 = r_{d0}^{-(1+\beta)}\left(\frac{4A_k^3}{27b}\right)^{1/2} \quad (13)$$

and

$$\sigma_s = \sigma_d^{(1+\beta)} \quad (14)$$

respectively. Here A_k is the Kelvin curvature parameter.

The expression (12) now provides us with a form for the activity spectrum with parameters which depend solely on the properties of the underlying dry aerosol. However, this lognormal expression is not of a form that easily allows analytical investigation of equation (3) without further approximation to the inner integral (for example see Fountoukis & Nenes, 2005). Khvorostyanov and Curry (2006) go on to show that (12) can further be well approximated by an algebraic expression of the form

$$\varphi(s) = k_{s0}C_0 s^{k_{s0}-1}(1+\eta_0 s^{k_{s0}})^{-2}, \quad (15)$$

where now

$$k_{s0} = \frac{4}{\sqrt{2\pi}\ln\sigma_s} = \frac{4}{\sqrt{2\pi}(1+\beta)\ln\sigma_d}, \quad (16)$$

$$\eta_0 = s_0^{-k_{s0}} = r_{d0}^{k_{s0}(1+\beta)}\left(\frac{27b}{4A_k^3}\right)^{k_{s0}/2}, \quad (17)$$

$$C_0 = N_a\eta_0. \quad (18)$$

While the definition (15) now matches the generalized form in (8), we are only able to use the relation (9) to determine s_{max} provided k_{s0} is an even integer. In general this will not be the case, and so in order to overcome this, we make a further approximation such that

$$\hat{\varphi}(s) = k_{s0}\hat{C}_0 s^{k_{s0}-1}(1+\hat{\eta}_0 s^{\kappa_{s0}})^{-2k_{so}/\kappa_{s0}}, \quad (19)$$

where now

$$\kappa_{s0} = 2\cdot\mathrm{nint}\left(\frac{k_{s0}}{2}\right) \quad (20)$$

$$\hat{\eta}_0 = \lambda\left(\frac{\eta_0}{\lambda}\right)^{\kappa_{s0}/ks0} \quad (21)$$

$$\hat{C}_0 = C_0\,(1+\lambda)^{2k_{s0}/\kappa_{s0}-2} \quad (22)$$

and $\lambda = (k_{s0}-1)/(k_{s0}+1)$. $\mathrm{nint}(x)$ represents the value of the nearest integer to the real number x. While the definition of κ_{s0} in (19) is chosen so as to facilitate our analytical approach, the definitions for $\hat{\eta}_0$ and $\hat{C}_0$ are chosen so that the peak value of the activation spectrum is maintained and that the modal supersaturation remains the same. The problem with this approximation is that the tail of the distribution may slightly over-predict the activation if $\kappa_{s0} > k_{s0}$ or under-predict the activity if $\kappa_{s0} < k_{s0}$. However, since the large saturations corresponding to these tail values will only be reached in more extreme conditions and represent only a small proportion of the aerosol, this is considered to be an acceptable error. Figure 2 shows the comparison of the activity spectrum as defined through the algebraic distribution of Khvorostyanov and Curry (2006) and the approximation $\hat{\varphi}(s)$ given in (19) for three different aerosol distributions.

4. MULTIMODAL AEROSOL DISTRIBUTIONS

If the dry aerosol size distribution is multimodal, then $\varphi(s)$ can be represented by a sum of terms, each having the form of (19) with the parameters in (16)-(18) calculated using the mean radius and dispersion appropriate for the separate modes of the distribution . Thus, for a dry distribution with N modes we have

$$\varphi(s) = \sum_{i=1}^{N} k_{si}\hat{C}_i s^{k_{si}-1}(1+\hat{\eta}_i s^{\kappa_{si}})^{-2k_{si}/\kappa_{si}}. \tag{23}$$

Substitution in (3) then provides the implicit relation for s_{max}, namely

$$s_{max}^{k+2}\sum_{i=1}^{N} {}_{(\kappa_{si}/2+1)}F_{(\kappa_{si}/2)}\left(\mathbf{a}_i;\mathbf{b}_i;-\eta_i s_{max}^{\kappa_{si}}\right) = \frac{(2\psi_1 w)^{3/2}}{kC\psi_2 B\left(\frac{k}{2},\frac{3}{2}\right)} \tag{24}$$

with

$$\mathbf{a}_i = \left(\frac{2k_{si}}{\kappa_{si}}, \frac{k_{si}}{\kappa_{si}}, \frac{k_{si}+2}{\kappa_{si}}, \ldots, \frac{k_{si}+(\kappa_{si}-2)}{\kappa_{si}}\right) \tag{25}$$

$$\mathbf{b}_i = \left(\frac{k_{si}+3}{\kappa_{si}}, \frac{k_{si}+5}{\kappa_{si}}, \ldots, \frac{k_{si}+(\kappa_{si}+1)}{\kappa_{si}}\right). \tag{26}$$

While the representation of a multimodal distribution allows us to better capture the details of the underlying aerosol distribution, it must be borne in mind that within the double moment scheme, the details of the sizes of the nucleated drops will be lost. For a full treatment of, e.g. ultra-giant aerosols, a more detailed microphysics scheme is needed.

5. ACTIVATION SPECTRUM $N_{CCN}(s)$

The total number of activated particles is obtained by integrating the differential spectrum $\varphi(s)$ over the supersaturation up to the maximum s_{max}, i.e.

$$N_{CCN}(s) = \int_0^{s_{\max}} \varphi(s)ds. \tag{27}$$

While we require $\varphi(s)$ to take the form of (19) in order to facilitate the calculation of s_{max}, we are at liberty to choose a more general form for use in (27). If a differential spectrum of the form (15) is used, then evaluation of (27) yields

$$N_{CCN}(s) = C_0 s^{k_{s0}}(1+\eta_0 s^{k_{s0}})^{-1}. \tag{28}$$

If $\varphi(s)$ takes the log-normal form of (10) then

$$N_{CCN}(s) = \frac{N_a}{2}\left\{1 + erf\left(\frac{\ln(s/s_0)}{\sqrt{2}\ln\sigma_s}\right)\right\}, \tag{29}$$

with $erf(x)$ the error function (Abramowitz & Stegun, 1964). In both (28) and (29) we have

$$\lim_{s\to\infty} N_{CCN}(s) = N_a. \tag{30}$$

That is, if the supersaturation is allowed to get high enough, all the aerosol particles will become active.

If we take (19) as our form for $\varphi(s)$, then

$$N_{CCN}(s) = \hat{C}s_{max}^{k_{s0}} \cdot {}_{\kappa+1}F_{\kappa}\left(\mathbf{c};\mathbf{d};-\hat{\eta}_0 s^{\kappa}\right) \tag{31}$$

with

$$\mathbf{c} = \left(\frac{2k_{s0}}{\kappa_{s0}}, \frac{k_{s0}}{\kappa_{s0}}, \frac{k_{s0}+1}{\kappa_{s0}}, \ldots, \frac{k_{s0}+(\kappa_{s0}-1)}{\kappa_{s0}}\right), \tag{32}$$

$$\mathbf{d} = \left(\frac{k_{s0}+1}{\kappa_{s0}}, \frac{k_{s0}+2}{\kappa_{s0}}, \ldots, \frac{k_{s0}+\kappa_{s0}}{\kappa_{s0}}\right). \tag{33}$$

By exploiting the symmetry in the coefficients of **c** and **d** it is easily shown that the generalized hypergeometric function in (29) can be reduced to Gauss' hypergeometric function, so that

$$N_{CCN}(s) = \hat{C}s_{max}^{k_{s0}} \cdot {}_2F_1\left(\frac{2k_{s0}}{\kappa_{s0}}, \frac{k_{s0}}{\kappa_{s0}}; \frac{k_{s0}}{\kappa_{s0}}+1; -\hat{\eta}_0 s^{\kappa}\right). \tag{34}$$

Furthermore, analysis of (34) shows that

$$\lim_{s\to\infty} N_{CCN}(s) = \tag{35}$$
$$N_a \left(\frac{4k_{s0}^2}{k_{s0}^2-1}\right)^{k_{s0}/\kappa_{s0}-1} \frac{\Gamma\left(\frac{k_{s0}}{\kappa_{s0}}\right)^2}{\Gamma\left(\frac{2k_{s0}}{\kappa_{s0}}\right)}.$$

The fact that (35) does not give an equivalent answer to (30) demonstrates the inaccuracies in the approximation (19). Thus if $k_{s0} > \kappa_{s0}$, the number of activated particles will be overestimated. Conversely, if $k_{s0} < \kappa_{s0}$, the number of activated particles will be underestimated. However, as $k_{s0} \to \infty$, i.e. as $\sigma_d \to 1^+$, $k_{s0}/\kappa_{s0} \to 1$ and $N_{CCN}(s) \to N_a$.

6. RESULTS

Figure 3 shows the activation spectrum obtained using the algebraic expression of Khvorostyanov and Curry (2006) (equation 28) and that obtained using the approximation in (34). The underlying aerosol distribution is chosen so as to fit (34) to the observed subcloud CCN spectra obtained on the 19th January 2005 during RICO. The soluble fraction of the aerosol is chosen to be distributed within the particle volume and consists of ammonium sulfate, i.e., $b = 0.25$ and $\beta = 0.5$. It is apparent from figure 3 that the approximate formulation does not deviate too far from the fitted curve.

Figure 4 shows how the peak supersaturation and activation of droplets vary with aerosol distribution, chemistry and updraught velocity. Of particular interest from these plots is the significant variation seen in the activated CCN with the variation in aerosol solubility at low updraught velocities (figure 4(f)).

Preliminary results regarding the properties of clouds modelled within the Abel & Shipway framework for CRM simulations of RICO are presented in Abel et al.(2008).

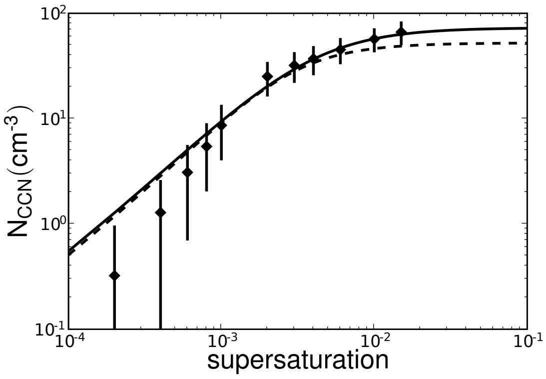

Figure 3: Variation of cloud nuclei with supersaturation. Solid line corresponds to equation (28) and dashed line to the approximation (34), both using a dry aerosol distribution with $N_a = 73$ cm^{-3}, $r_d = .039\mu$m, $\sigma_d = 2.12$, $b = 0.26$ and $\beta = 0.5$. The dots represent observations taken during the RICO campaign with the bars representing on standard deviation.

7. REFERENCES

Abel, S. J. and Shipway, B. J., 2007. A comparison of cloud resolving model simulations of trade wind cumulus with aircraft observation taken during RICO. *Quart. J. Roy. Meteorol. Soc.*, **133**, 781-794.

Abel, S. J., Shipway, B.J and Smith, C.J., 2008. A comparison of cloud resolving model simulations of trade wind cumulus with aircraft observations taken during RICO. 15th International Conference on Clouds and Precipitation, Cancun, 7-11 July.

Abramowitz, M. and Stegun, I.A., 1964. Handbook of mathematical functions, Dover.

Cohard, J.-M., Pinty, J.-P. and Bedos, C., 1998. Extending Twomey's Analytical Estimate of Nucleated Cloud Droplet Concentrations from CCN Spectra. *J. Atmos. Sci.*, **55**, 3348-3357.

Erdélyi A., Magnus, W., Oberhettinger, F. and Tricomi, F.G., 1953. Higher Transendental Functions. Volume II. McGraw-Hill.

Erdélyi A., Magnus, W., Oberhettinger, F. and Tricomi, F.G., 1954. Tables of Integral Transforms. Volume I. McGraw-Hill.

Fountoukis, C. and Nenes, A., 2005. Continued development of a cloud droplet formation parametrization for global climate models. *J. Geophys. Res.*, **110**, D11212, doi10.1029/2004JD005591.

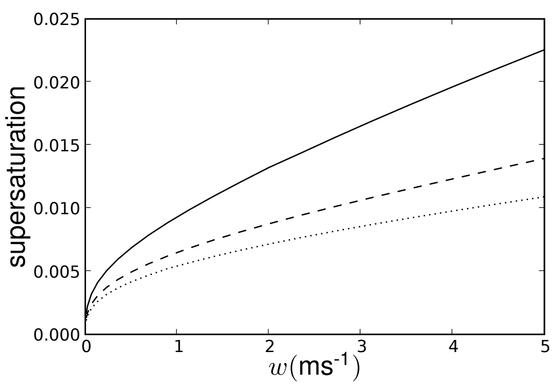

(a) Variation of supersaturation with w. N_a = 73 cm^{-3} (solid line),= 251cm^{-3} (dashed line) and = 500cm^{-3}(dotted line).

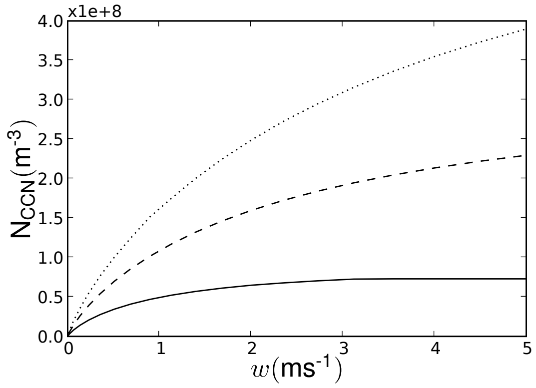

(b) Variation of CCN activation with w. N_a = 73 cm^{-3} (solid line),= 251cm^{-3} (dashed line) and = 500cm^{-3}(dotted line).

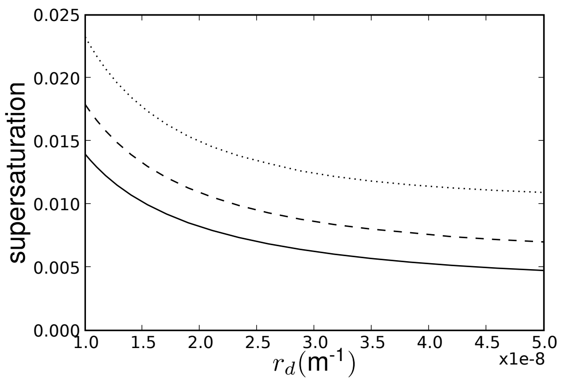

(c) Variation of supersaturation with r_d. $w = .5$ms^{-1} (solid line),= 1ms^{-1} (dashed line) and = 2ms^{-1}(dotted line).

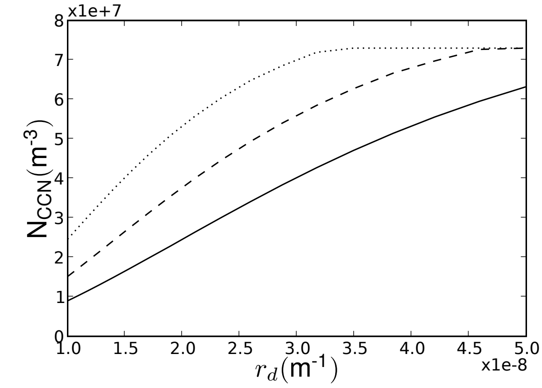

(d) Variation of CCN activation with r_d. $w = .5$ms^{-1} (solid line),= 1ms^{-1} (dashed line) and = 2ms^{-1}(dotted line).

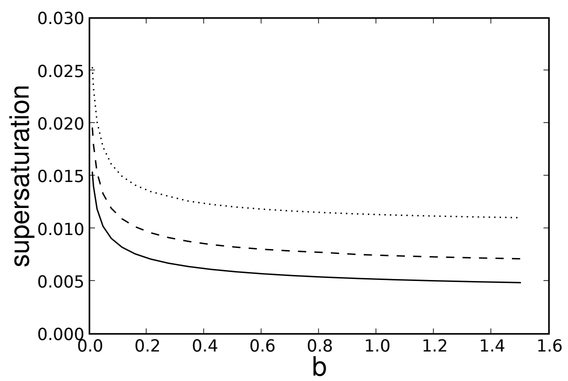

(e) Variation of supersaturation with b. $w = .5$ms^{-1} (solid line),= 1ms^{-1} (dashed line) and = 2ms^{-1}(dotted line).

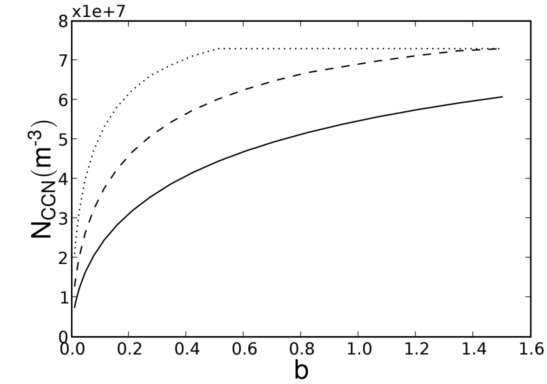

(f) Variation of CCN activation with b. $w = .5$ms^{-1} (solid line),= 1ms^{-1} (dashed line) and = 2ms^{-1}(dotted line).

Figure 4: Variation of supersaturation (a,c,e) and CCN activation (b,d,f) against (a,b) updraught velocity, w, (c,d) geometric mean dry aerosol diameter, r_d and (e,f) aerosol solubility, b calculated using expressions (23) and (34). Unless otherwise stated the dry aerosol distributions have N_a = 73 cm^{-3}, r_d = .026 μm,σ_d = 1.5, b = 0.25 and β = 0.5.

Khvorostyanov, V. I. and Curry, J. A., 1999. A simple analytical model of aerosol properties with account for hygroscopic growth: 1. Equilibrium size spectra and CCN activity spectra, *J. Geophys. Res*, **104**, 2175-2184.

Khvorostyanov, V. I. and Curry, J. A., 2006. Aerosol size spectra and CCN activity spectra: Reconciling the lognormal, algebraic, and power laws. *J. Geophys. Res*, **111**, D12202, doi:10.1029/2005JD006532.

Korolev, A. V. and Mazin, I. P., 2003. Supersaturation of Water Vapour in Clouds. *J. Atmos. Sci.*, **60**, 2957-2974.

Norlund, N. E., 1955. Hypergeometric Functions. *Acta Math*, **94** , 289-349.

Pruppacher, H.R. and Klett, J. D., 1997. Microphysics of Clouds and Precipitation, 2nd ed., 954 pp., Springer, New York.

Rauber, R. M., Stevens, B. et al., 2007. Rain in (shallow) cumulus over the ocean–The RICO campaign. *Bull. of the American Meteorol. Soc.*, **88**, 19121928.

Twomey, S., 1959. The nuclei of natural cloud formation II. The supersaturation in natural clouds and the variation of cloud droplet concentration, *Pure Appl. Geophys.*, **43**, 243-249.

A STUDY OF THE MICROPHYSICAL AND MACROPHYSICAL PROPERTIES OF CIRRUS: AN INTERCOMPARISON BETWEEN CLOUDSAT, IN SITU MEASUREMENTS, A GCM AND AN ICE CRYSTAL MODEL

Anthony J. Baran[1], Clare Lee[2], Richard Cotton[3], Alejandro Bodas-Salcedo[4], Jorge Bornemann[5], Edwin Hirst[6], Richard T. Austin[7], John G. Haynes[8], Graeme L. Stephens[9], and Paul Connolly[10]

[1-5]Met Office, Exeter, UK
[6]University of Hertfordshire, Hatfield, UK
[7-9]Colorado State University, Fort Collins, USA
[10]University of Manchester, UK

1. INTRODUCTION

Cirrus (ice crystal cloud) is now well known to be an important component of the earth-atmosphere radiation balance as well as the hydrological cycle (Liou and Takano 1994; Stephens et al., 2002; Edwards et al. 2007). This balance depends not only on the vertical extent and position of the cloud within the earth's atmosphere but also on its macrophysical and microphysical properties. It is therefore important to characterise cirrus in terms of the vertical distribution of IWC, ice crystal size, shape and how the particle size distribution function (PSD) evolves within the cloud. These characterizations are essential if parameterizations are to be further improved in general circulation models. Moreover, characterizing cirrus is also important in order to test theoretical models of cirrus and space-based measurements of IWC and ice crystal size. Since April 2006 there is now a complete series of space-based instruments (called A-train) able to measure the radiative and hydrological contributions of cirrus to the climate system (Stephens et al., 2007). In this extended abstract we report on a number of field campaigns that attempt to characterise semi-transparent cirrus in terms of its macrophysical and microphysical composition. The in situ measurements of IWC and ice crystal effective dimension are compared against CloudSat retrievals as well as the Met Office Global and Mesoscale operational NWP model products. The in situ measurements are also used to test a theoretical ensemble model of cirrus described in Baran and Labonnote (2007) in terms of its prediction of IWC, ice crystal effective dimension and extinction profiles.

2. THE CAMPAIGNS AND INSTRUMENTATION

During the Winter and Autumn of 2007 the FAAM (Facility for Airborne Atmospheric Measurements) BAE-146 G-LUXE aircraft flew a number of flights as part of the CAESAR (Cirrus and Anvils: European Satellite and Airborne Radiation measurements project) campaign of flying in, above and below cirrus around the United Kingdom located over the sea. The goal of CAESAR is to understand the radiative properties of cirrus over a wide range of wavelengths in combination with airborne in situ measurements of cirrus microphysical properties. Flights observed semi-transparent frontal cirrus co-incident with the CloudSat Aqua-train. In total there were six flights three of which were coincident with CloudSat on the 16th and 25th of January 2007 and on 20th September 2007. For the CloudSat co-incidences the aircraft sampled the cirrus as a series of profiles from cloud-top, which was penetrated in all three cases, to cloud-bottom and as a series of saw-tooth manoeuvres. These manoeuvres were performed in order to obtain a good statistical sample of the macrophysical and microphysical state of the cirrus with which to compare against CloudSat and the Met Office NWP models. The other three

CAESAR flights took place on the 14th November 2005, 1st December 2005 and on the 9th May 2006. These flights are used to test the ensemble model of cirrus briefly mentioned in the introduction. Table 1 summarises each flight in terms of its location and the suite of cloud physics instrumentation that was onboard.

Table1. Flight Summary

Flight No	Date	Lat/Long^o	SID II	2DC	CPI
B258	16/01/07	54.8-56.4N;2-3E	X	X	
B262	25/01/07	56.2-58.3N;-3.5E	X	X	
B327	20/09/07	53.4-55.2N;.8W-3E		X	
B138	14/11/05	49.9-50.8N;8-6W	X	X	X
B143	1/12/05	50.5-51.6N;7.2-5W	X	X	X
B195	9/04/06	49.3-50.8N;8-8.3W	X	X	X

The crosses in the table indicate that the instrument was operational during the flight. Unfortunately, although the 2DP was onboard it was not operational and so ice crystals greater than 800 μm were not measured. Other instrumentation included the new Small Ice particle Detector (SID II) described in Hirst et al. (2001) (although the Hirst et al paper is concerned with SID I its principal of operation is similar to SID II). This instrument can measure the PSD between 3 μm and 100 μm, the particle number concentration, particle phase, and particle size. The SID II instrument given the measurement of ice crystal size can also be used to estimate the IWC by assuming spheres of density 0.92 gcm^{-3}. The error in the SID II estimate of IWC is likely to be ±50% given uncertainties in sampling volume and sizing. The 2D-C overlaps with SID II. The Cloud Particle Imager (CPI) instrument described in Lawson et al. (2001) was available for three of the flights which occurred before the launch of CloudSat. An algorithm developed by Connolly et al. (2007) has been applied to the CPI to correct for over sizing and particle rejection. The 2D-C probe was also used to estimate the IWC and ice crystal effective dimension, D_e. The 2DC IWC was derived assuming the mass-dimensional relationships given in Brown and Francis (1995) and the ice crystal D_e is derived as follows (Foot 1988; Francis et al. 1999);

$$D_e = \frac{3IWC}{2\rho \sum n_j A_j} \qquad (1)$$

where IWC is the ice water content, n_j is the ice crystal number concentration in the j^{th} size bin and A_j is the mean cross-sectional area of the j^{th} bin so $\Sigma n_j A_j$ is the cross-sectional area density of the integrated size distribution function. The density ρ is a reference density assumed to be unity in order to keep the units of Eq. (1) consistent. The definition of D_e used in Eq. (1) was also applied to the CPI. The error in determining the IWC from the 2DC and CPI is likely to be ±50% (Heymsfield et al. 2002). The mean cross-sectional area is likely to be a similar error due to the 2DC being unable to measure ice crystals less than 100 μm in size. This error will be further compounded by shattering on the inlet of the probe (Field et al. 2003). Therefore, given the definition of D_e from Eq. (1) the uncertainty in D_e is likely to be ±70%. The mean cross-sectional area as measured by the CPI is also likely to be a similar error to that of the 2DC due to sampling volume and ice crystal shattering. Therefore, the CPI error in determining D_e will also be of the order ±70%.

From the measured aircraft or CloudSat IWC vertical profile the Ice Water Path (IWP) can be found from;

$$\mathrm{IWP} = \int_{z_1}^{z_2} \mathrm{IWC}(z)dz \qquad (2)$$

where z_1 and z_2 correspond to the aircraft measured cloud-bottom and cloud-top, respectively.

From the IWP given by Eq. (2) and assuming the geometric optics approximation, in which the volume extinction coefficient is just twice the area density, the optical depth of the cloud,τ, is then related to IWP and D_e via;

$$\tau = 3\mathrm{IWP}/\rho D_e \qquad (3)$$

Equations (1), (2), and (3) are used to compare aircraft derived values with those retrieved from CloudSat, predicted by the Met Office NWP models and the ensemble model of cirrus. The D_e derived in the Met Office NWP models is based on cloud temperature relationships described in Edwards et al. (2007).

3. CLOUDSAT RETRIEVALS

The CloudSat retrieved IWC and D_e, based on the 94 GHz radar reflectivities, are obtained from the level 2B radar-only algorithm which is described in Austin et al. (2008) . In this algorithm the IWC is derived from the 1-dvar retrieved particle number density and the geometric mean diameter of ice crystals and by assuming a constant density for ice. Since retrievals are based on a 1-dvar scheme there are uncertainties associated with the retrievals, which are given in the level 2B product. There is an implicit assumption in the radar reflectivities at 94 GHz being dominated by Rayleigh scattering, however, there is a correction for non-Rayleigh scattering which is based on Mie-Lorenz theory. A further point is that there are no retrievals of IWC below a threshold of approximately 2 $\mathrm{mgm^{-3}}$ (determined by the cloud mask algorithm in the 2B-GEOPROF product). The ice crystal effective dimension, D_e, can be related to the retrieved geometric mean diameter via an assumed lognormal size distribution function. The IWP can be derived via Eq. (2) as defined by the aircraft and the D_e related to Eq. (1) via a factor 1.5. Although the definitions of D_e are not exactly the same they are sufficiently close for the purposes of the present study. Moreover, the 2DC probe has not been corrected for ice crystals less than 100 μm in size so that the in situ measurements of D_e are more relatable to the radar-only retrievals of D_e.

4. CLOUDSAT AND NWP MODEL CASE STUDIES

In this section results obtained for B262 are presented in detail, results for the other two cases are similar but are not presented here for reasons of brevity. Results are shown in the form of PDF's for the in situ measurements, CloudSat retrievals and NWP models. For B262 the cloud-top according to the aircraft measured ice particle number concentrations was situated at 10.80 km whilst the cloud-bottom was situated at 6.0 km. Figure 1 (a-c) shows PDF's of the measured in situ IWC obtained from the 2DC and SID II instruments, the corresponding NWP model predictions and the CloudSat retrievals, respectively. The X-axis of Figure 1 is transformed into Log10 (IWC) space so that results for each set are directly comparable.

From Fig. 1 the range of in situ measured binned IWC goes from 0.120 - 126 $\mathrm{mgm^{-3}}$ for the 2DC and between 0.21 - 316 $\mathrm{mgm^{-3}}$ for SID II. This range of measured IWC is not surprising since SID II is biased to smaller ice crystals and the 2DC is biased to the larger ice crystals. Moreover, the SID II estimate of IWC might be considered an overestimate due to the assumption of solid ice spheres in converting size to an IWC. Therefore, SID II gives the upper range of measured IWC whereas the 2DC can be considered as the lower range of IWC. The mean IWC as measured by the 2DC and SID II are18.013 $\mathrm{mgm^{-3}}$ and 35.65 $\mathrm{mgm^{-3}}$, respectively. The mean of the estimated

IWC from the two instruments are within a factor two of each other which is a good result given the uncertainties.

The modes of the two distributions are 9.33– 52.48 mgm^{-3} and 21.88-52.48 mgm^{-3} for the 2DC and SID II instruments, respectively.

The median of the 2DC and SID II IWC distributions are 15.93 mgm^{-3} and 26.32 mgm^{-3}, respectively, and it is around the medians of the two distributions that most of the in situ estimated IWC is concentrated.

(a)

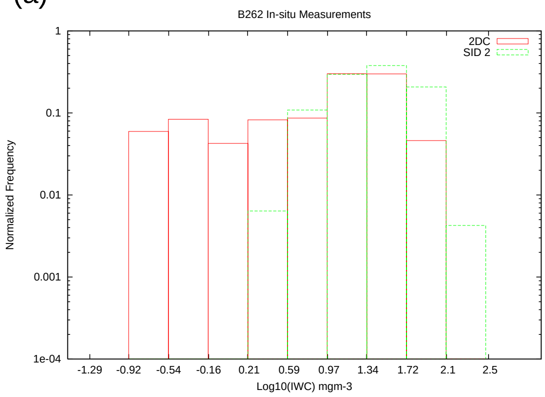

(b)

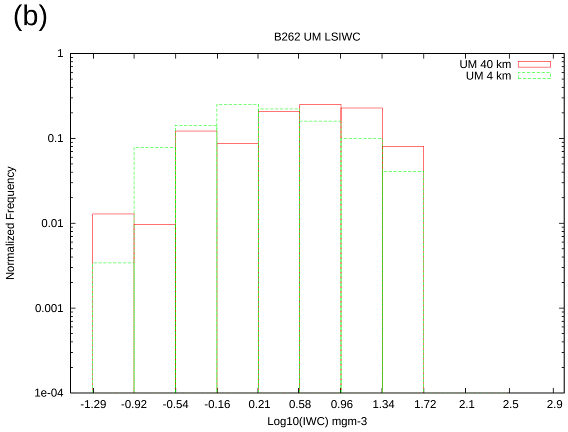

(c)

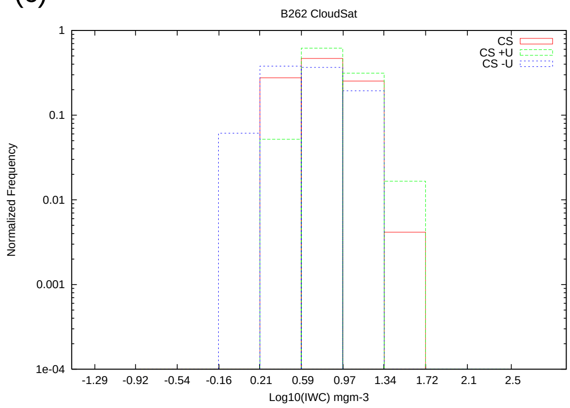

Figure 1. The normalized frequency plotted against Log10 (IWC) for (a) in situ measurements (b) NWP models (40 km and 4 km are the global and mesoscale models, respectively) (c) CloudSat

The NWP distribution of IWC is fairly well distributed in relation to the in situ measurements but IWC's greater than 52.48 mgm^{-3} are not produced by the models. Although both models have the same cloud scheme their distribution of IWC about the cloud is slightly different. This could be due to the models having differing horizontal and/or vertical resolutions. As a result of the models not producing higher IWC's their mean values will be lower than the in situ measured values and so will be biased to the lower end of IWC as indicated by Fig. 1 (b). Indeed, the models produce IWC's lower than it is possible to measure by the in situ probes though this occurrence is about 1% for the Global model and much less than 1% for the Mesoscale model. The mean IWC produced by the Global model is 7.9 mgm^{-3} and 5.0 mgm^{-3} for the Mesoscale model. The mean values for the NWP models are a factor 2-4 less than the in situ mean estimated IWC values. The modal values of the NWP distributions are 3.8-9.12 mgm^{-3} and 0.69-1.62 mgm^{-3} for the Global and Mesoscale models, respectively. There is a tendency for the Mesoscale model to produce less IWC than the Global model. Though, essentially both models underpredict the higher IWC end of the in situ measurements.

The CloudSat results are shown in Figure 1 (c) together with the retrieved uncertainties shown as +U and –U in the figure, respectively. Since CloudSat is a 94 GHz radar it is not expected to estimate IWC less than 2 mgm^{-3} as stated in Section 3. The interesting point to note in Fig. 1 (c) is the lack of retrievals greater than 52.48 mgm^{-3} and the drop off in IWC is sharper than in the NWP models. The mean of the CloudSat distribution is 7.2 mgm^{-3} with the mode centred between 3.8-9.12 mgm^{-3}. These mean results and modal values are not dissimilar from the NWP model results. A possible explanation for the CloudSat behaviour of retrieved IWC is shown in Fig. 2.

Figure 2 shows the vertical distribution of the in situ estimated SID II IWC together with all the CloudSat retrieved vertical IWC uncertainty profiles for B262. SID II is shown in Fig. 2 to highlight the vertical variation of IWC compared to the CloudSat retrievals.

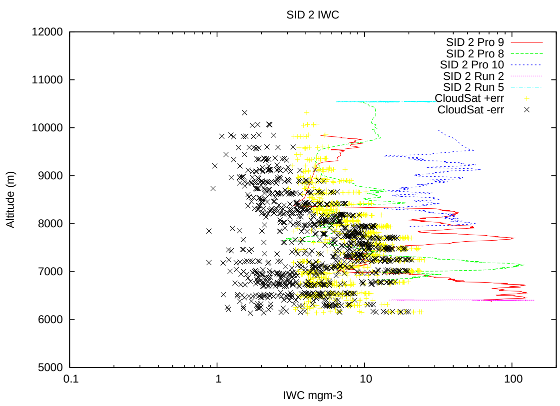

Figure 2. Profiles of retrieved IWC plotted as a function of altitude showing the in situ derived SID II IWC with all the CloudSat retrieved IWC uncertainty profiles for B262.

The SID II Profile 9 (profiles are vertical descents/ascents from cloud-top/bottom to cloud bottom/top) shows a bulge in IWC around the centre of the cloud then a further bulge in IWC towards the cloud-bottom, together with Profile 8. Profile 10 shows consistently high IWC towards cloud-top when compared to profiles 8 and 9. The distance between profiles 8 and 9 towards cloud-top was of the order of 68 km and about 100 km between profiles 8 and 10. Clearly, there are significant variations in IWC both in the vertical and horizontal. The CloudSat vertical profiles also show a bulge in IWC towards the higher regions of IWC shown by Profiles 9 and 8 but the CloudSat retrievals decrease towards cloud-bottom. The reason for this decrease in retrieved CloudSat IWC could be due to much larger volume sampling at cloud-top and bottom compared to the aircraft volume sampling both vertically and horizontally. Moreover, the vertical resolution of CloudSat is of the order of 500 m so towards cloud-bottom CloudSat would be sampling below the cloud as well as within the cloud thus resulting in significantly lower IWC retrievals relative to the aircraft measurements.

Figure 3 shows the distribution of in situ measured 2DC D_e together with the UM predicted D_e based on temperature, and the CloudSat retrieved D_e with the uncertainties associated with those retrievals.

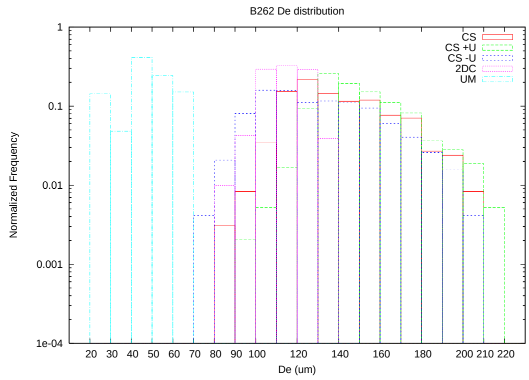

Figure 3. The normalized frequency plotted against D_e for B262 showing the 2DC derived D_e, CloudSat retrieved D_e with its range of uncertainty shown as +U and –U and the NWP model (UM) derived D_e.

Not surprisingly Figure 3 shows distinct differences between the NWP model and in situ measurements as well as the retrievals. As regards D_e agreement is not expected since the NWP model parameterization is biased towards the small particle end of the PSD due to this parameterization being based on Ivanova et al. (2001). The 2DC does not measure ice crystal sizes greater than 800 μm whereas the CloudSat radar-only retrievals will be most sensitive to the largest ice crystals. The mean in situ measured D_e is 114.63 μm compared to 140.32 μm for CloudSat. The modal value of the 2DC measurements is 110-120 μm, this compares to 120-130 μm for CloudSat. Given the uncertainties the mean D_e and modal values between the in situ measurements and CloudSat are in fairly good agreement. The NWP model mean D_e is 47.25 μm, it is not known if this cirrus case was populated by very small ice crystals.

The other two cases B327 and B258 give very similar results to those described above.

Given the differences in retrieved IWC and D_e it is interesting to compare if there are significant differences in the derived IWP and cloud optical depth.

5. COMPARISONS BETWEEN DERIVED IWP AND CLOUD OPTICAL DEPTH FOR THE CASE B262

In this section the IWP is derived using Eq. (2) and from the mean D_e of the vertical profile the optical depth is estimated from Eq. (3). Table 2 shows comparisons between the in situ derived mean IWP, mean D_e and mean τ based on the profiles 8 and 9 shown in Fig. 2, and the NWP model and CloudSat estimates for these quantities.

Table 2. B262 total optical properties

Instrument	IWP gm^{-2}	D_e μm	τ
2DC	31.8±12.4	116.3±2.2	0.82±0.3
SID II	74.4±31.9		
CloudSat	16.0±8.3	137.5±8.6	0.35±0.2
NWP 40	22.72±17	47.32±3	1.41±0.9
NWP 4	16.95±9.0	47.32±3	1.05±0.5

It is instructive to see from Table 2 how NWP models from compensating errors may still predict reasonable solar radiative properties which are within experimental error. This compensating error in models could mean that if the predicted ice crystal size is too small then the clouds would appear brighter than measurements. However, due to the IWC being smaller relative to the measurements this would act to darken the clouds – this competition between too low IWC and ice crystal size might cancel giving reasonable solar cloud brightness when compared against measurements. CloudSat on the other hand would estimate darker clouds relative to the in situ measurements and NWP models due to the very large D_e retrieved relative to the IWP.

6. FURTHER EXAMINATION OF THE CLOUDSAT RETRIEVED IWC

In section 4 it was argued, using Figure 2, that the CloudSat retrievals of IWC could be smaller than in situ measurements due to volume sampling issues and its vertical resolution. In this section evidence is presented which highlights a differing argument recently put forward by Heymsfield et al. (2007). In this paper it was shown that CloudSat could potentially underestimate IWC due to aggregating ice crystals not taken into account in the retrieval algorithm. Such aggregating ice crystals could be sufficiently large enough to violate the Rayleigh assumption. Moreover, the applied Mie-Lorenz correction to take account of this potential violation may further diminish the estimate of IWC. In Heymsfield et. al. (2007) it is concluded that due to ice crystal aggregation and non-Rayleigh scattering the CloudSat retrieval could underestimate IWC by as much as 60%.

For this section the case of B327 is used to illustrate this potential problem. B327 is the deepest of all the cirrus cases and has an estimated in situ solar bulk optical depth of 2.82. Figure 4 shows a comparison between the deepest CloudSat retrieved IWC profile and the deepest in situ 2DC derived IWC profiles. The CloudSat profile shown in Figure 4 also gave the largest IWP of 72.94 gm^{-2}. As indicated in Figure 4 the deepest 2DC IWC profiles were vertically averaged over a distance of about 500 m and for Profiles 8, 9 and 10 the derived IWP values were 69.98, 75.77 and 77.57 gm^{-2}. These in situ derivations of IWP compare reasonably well with the CloudSat derivation.

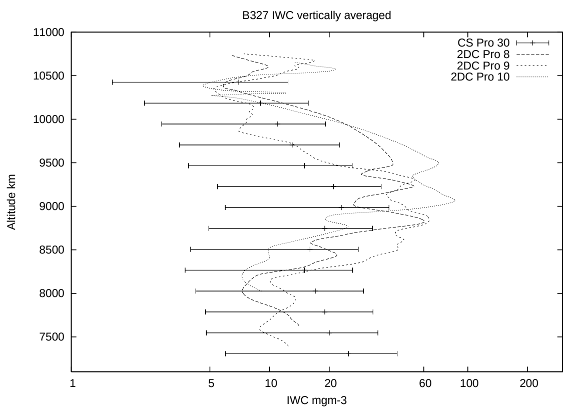

Figure 4. The deepest CloudSat retrieved IWC profile plotted with the deepest 2DC derived IWC profiles as a function of altitude for B327.

From Figure 4 it is interesting to note that towards the cloud-top and cloud-bottom the in situ measurements of IWC are well within the uncertainty of the CloudSat retrieved IWC. However, at about the centre of the cloud the in situ measurements of IWC, even when substantially vertically averaged, can reach nearly 100 mgm^{-3}.

Figure 5 shows the 2DC images that were collected from the region of highest IWC shown in Figure 4.

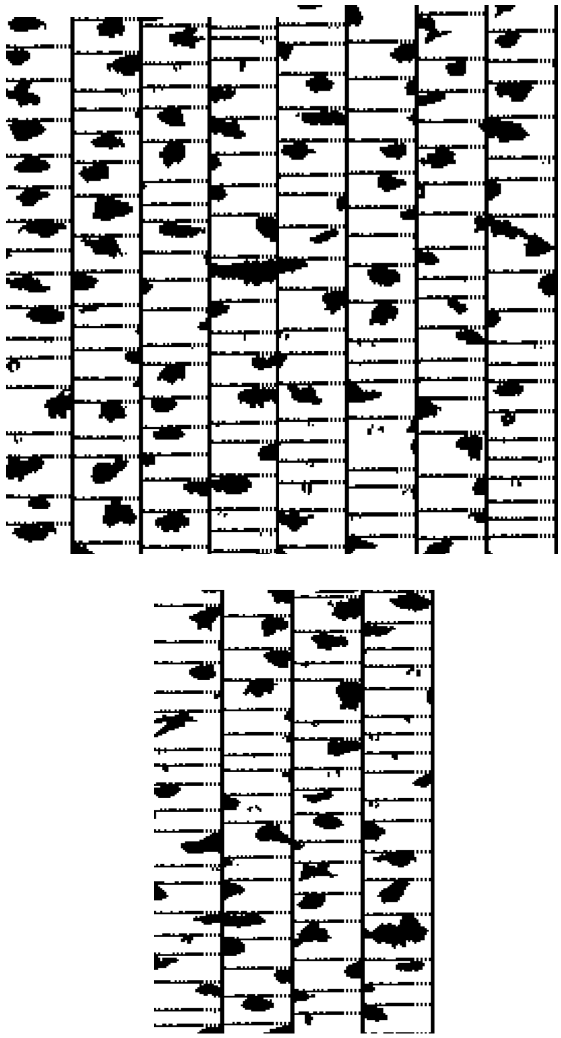

Figure 5. Samples of 2DC images collected in the highest region of IWC for B327.

Figure 5 shows evidence of ice crystals larger than 800 µm since a number of 2DC bins are either full or nearly full; moreover, the figure also shows evidence of ice crystal aggregation in a number of the bins. Given the vertical depth of the cloud being 3.5 km aggregation should certainly be expected. Figure 5 can be contrasted with Figure 6 which shows 2DC images collected near the cloud-bottom.

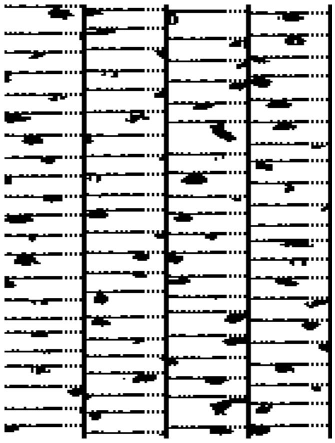

Figure 6. 2DC images collected near cloud-bottom of B327 between an altitude of 7500-8500 m shown in Figure 4.

From Figure 6 it is clear that there are no ice crystals nearly filling the 2DC bins and this image is representative of others near cloud-top and bottom. The reason for the appearance of smaller ice crystals near cloud-bottom is probably due to sublimation.

Given Figure 5 with the evidence of aggregation and the likelihood of the existence of non-Rayleigh scattering then the possibility of CloudSat retrievals being biased towards lower IWC in the central regions of the cloud as demonstrated in Heymsfield et al. (2007) cannot be ruled out for this case.

6. USING CPI DATA TO TEST AN ENSEMBLE MODEL OF CIRRUS

In this section an ensemble model of cirrus described in Baran and Labonnote (2007) is tested against CPI in situ measurements for the other three cases described in Table 1. The ensemble model of cirrus is an attempt to couple cirrus microphysical and macrophysical properties with the radiative properties of the cloud. This requires a prior PSD from which the ensemble model predicts the IWC, volume extinction coefficient and D_e. In the paper by Baran and Labonnote (2007) it was shown that the ensemble model was reasonably able to predict IWC and volume extinction coefficient given the PSD. The PSD was generated from a parameterization of the PSD shape given an IWC and in-cloud temperature (Field et al. 2005; 2007). The Field et al. (2005; 2007) parameterization is independent of particle geometric shape, area density and D_e.

The ensemble model shown in Figure 1 of Baran and Labonnote (2007) consists of six shapes which increase in complexity as a function of maximum dimension. The basic shape of the ensemble model is the hexagonal geometry, which with increasing maximum dimension are aggregated together to form more complex crystals. The smallest ice crystal consists of the hexagonal ice column and the most complex consists of a ten-branched ice aggregate, representing the smallest and largest ice crystal maximum dimension, respectively. From the geometric volume of the ensemble the IWC can be computed by;

$$\mathrm{IWC} = \rho \int V(\boldsymbol{\varepsilon}) n(\boldsymbol{\varepsilon}) d\boldsymbol{\varepsilon} \qquad (4)$$

where in Eq. (4) ρ is the bulk density for ice assumed to be 0.92 gcm^{-3}, V(**ε**) is the geometric volume of the ice crystals. The vector **ε** represents the various sizes and shapes of ice crystals in the size distribution function.

The D_e of the ensemble is defined by Eq. (1) and the volume extinction coefficient has been previously defined in section 2 as twice the area density in the limit of geometric optics.

To test the ensemble model prediction of IWC, volume extinction coefficient and D_e the particle size distribution function is generated from the CPI measured IWC and in-flight cloud temperature profiles using the parameterization due to Field et al. (2005; 2007). The ensemble model is then integrated over the generated particle size distribution function to predict IWC given by Eq. (4). From the ensemble model predicted IWC and volume extinction profiles the IWP can also be predicted from Eq. (2) as well as the cirrus optical depth, given by;

$$\tau = 2\int_{z_1}^{z_2} \sigma(z)dz \qquad (5)$$

where z_1 and z_2 are the cloud-bottom and top defined by the aircraft and $\sigma(z)$ is the volume extinction profile.

In Figure 7 (a) –(c) results are presented for the ensemble model predictions of the vertical profile of IWC, volume extinction coefficient and D_e. The figure shows results for the case B138 profile 3.

(a)

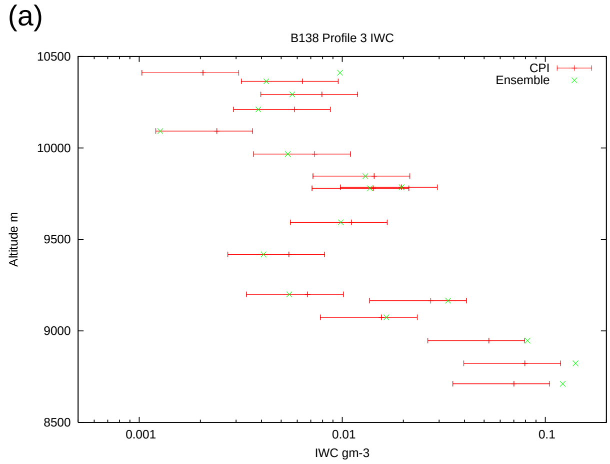

(b)

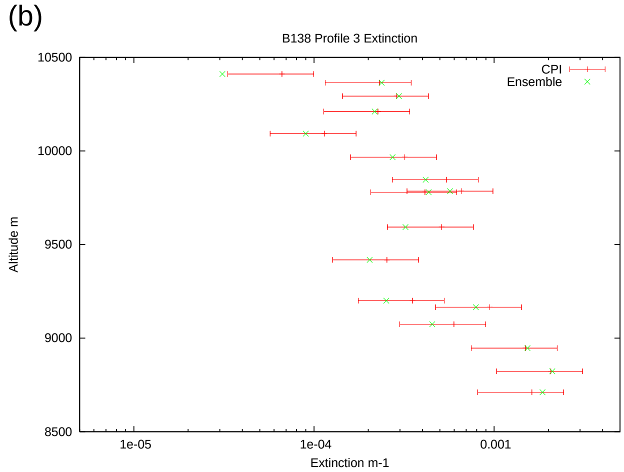

(c)

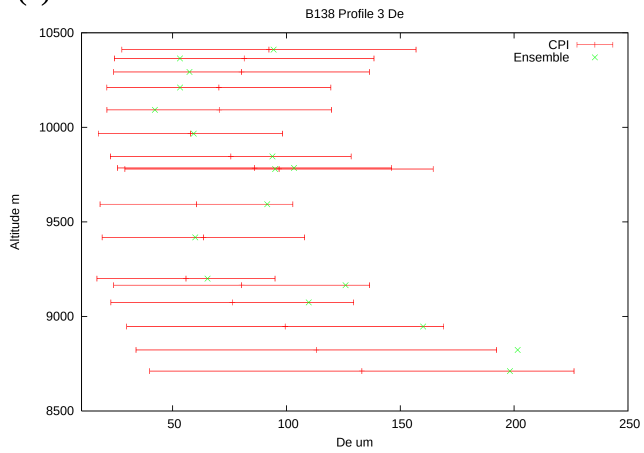

Figure 7. CPI measurements for the case B138 profile 3. (a) Measured IWC, (b) measured volume extinction coefficient and (c) measured D_e shown with ensemble model predictions of the same quantities.

The figure shows that the ensemble model is able to predict the CPI measured IWC, volume extinction and D_e vertical profiles well within experimental uncertainty for this particular case. The measured CPI IWP from Figure 7 is 31.74±15.87 mgm^{-2}, and τ=1.04±0.52. The corresponding ensemble model predictions are 34.95 mgm^{-2} and τ=0.730. The ensemble model predictions of IWP and τ are also well within experimental uncertainty. Results for the other cases also demonstrate that the ensemble model predictions of these quantities are also within experimental uncertainty.

CPI images of the ice crystal shapes for B138 profile 3 are shown in Figure 8.

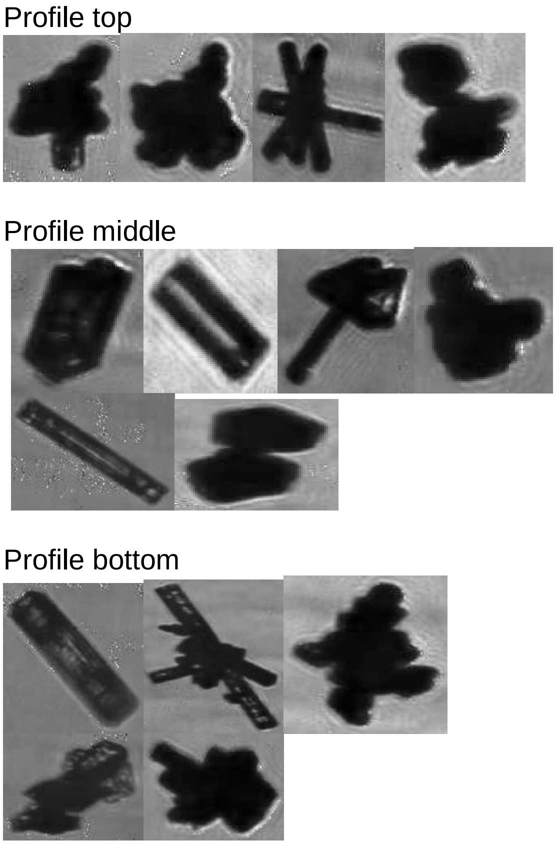

Figure 8. Various CPI images obtained during from B138 of profile 3 from cloud-top, middle and bottom.

Figure 8 shows the variety of ice crystal shapes that were most commonly observed during profile 3. The ice crystals appear to be irregulars with evidence of aggregation as well as rosettes and elongated hexagonal columns. The ensemble model as demonstrated from Figure 7 appears able to predict the fundamental parameters required to compute solar radiative transfer through cirrus to within experimental uncertainty.

7. SUMMARY

In this extended abstract results have been presented from the CAESAR field campaign which took place during the Winter and Autumn 2007. In situ measurements of IWC, D_e, and ice crystal area densities were collected using 2DC, SID II, and CPI probes. Three missions were flown that coincided with CloudSat overpasses and the corresponding Met Office Global and Mesoscale model products were extracted. The in situ measurements were compared to the CloudSat retrievals and NWP predictions of IWC and D_e.

In general it was found that relative to the in situ measurements higher IWC's were not predicted by the NWP models nor retrieved by CloudSat. Though, in the case of the NWP models the distribution of IWC throughout the cloud replicated the measured distribution fairly well. It was noted that in the case of the CloudSat IWC distribution the higher IWC's rapidly decreased after the modal value.

It was hypothesized that this decrease could be due to volume sampling of thin cirrus and the low vertical resolution around the cloud-bottom. However, a further reason, which would add to compound the problem, could be due to very large aggregating ice crystals which would become non-Rayleigh scattering. It was recently reported in the literature that the aggregation of ice crystals could depress CloudSat IWC estimates by as much as 60%. We find that, for a particular case, in the presence of ice aggregation the CloudSat estimates are depressed relative to the in situ 2DC measurements. Moreover, the 2DC measurements could themselves be underestimates as ice crystals greater than 800 μm were not accounted for.

As regards D_e the NWP models prediction were much smaller than either the in situ measurements or CloudSat retrievals. Though this should not be very surprising since the 2DC does not measure ice crystals less than 100 μm in size and CloudSat retrievals of D_e are currently based on the radar-only algorithm.

The Met office NWP model prediction of the solar radiative properties was shown to be consistent with in situ measurements based on the 2DC. Though this was due to the models possibly predicting too small D_e and too low IWC, this compensation may produce solar radiative properties that are consistent with independent measurements.

An ensemble model of cirrus was tested against CPI measurements of IWC, D_e, volume extinction coefficient, IWP and optical depth. The ensemble model was shown to be able to predict these quantities well within the experimental uncertainty for the case shown. Moreover, the ensemble model, which represents, aggregating ice crystals could be used to correct CloudSat retrievals for ice aggregation.

8. BIBLIOGRAPHY

Austin, R. T., A. J. Heymsfield, and G. L. Stephens, "Retrievals of ice cloud microphysical parameters using the CloudSat millimeter-wave radar and temperature", submitted to JGR special issue on CloudSat (2008).

Baran, A. J., and Labonnote, L.-C. A self-consistent scattering model for cirrus. I: The solar region. Q. J. R. Meteorol. Soc. 133, 1899-1912, 2007.

Brown, P. R. A., and Francis, P. N. Improved measurements of the ice water content in cirrus using a total-water evaporator. J. Atmos. Oceanic Technol. 12, 410-414, 1995.

Connolly P. J, Flynn M. J, Ulanowski Z, Choularton, T. W., Gallagher M. W, Bower K. N. Calibration of the cloud particle imager probes using calibration beads and ice crystal analogs: The depth of field. J. Atmos. Oceanic Technol. 24, 1860-1879, 2007.

Edwards, J. M., Havemann, S., Thelen, J.-C., and Baran A. J. A new parametrization for the radiative properties of ice crystals: Comparison with existing schemes and impact in a GCM. Atmos. Res., 83, 19-35, 2007.

Field, P. R., Wood, R, Brown, P. R. A., Kaye, P. H, Hirst, E., Greenaway, R., and Smith, J.A. Ice particle interarrival times measured with a fast FSSP. J. Atmos. Ocean. Tech. 20, 249-261, 2003.

Field, P. R., R. J. Hogan, P. R. A. Brown, A. J. Illingworth, T. W. Choularton, and R. J. Cotton. Parametrization of ice-particle size distribution functions for mid-latitude stratiform cloud, Q. J. R. Meteorol. Soc. 131, 1997-2017, 2005.

Field, P. R., Heymsfield, A. J., and Bansemer, A., 2006: Snow size distribution parameterization for midlatitude and tropical ice cloud. J. Atmos. 64, 4346-4365, 2007.

Foot, J.S. Some observations of the optical properties of clouds. II: Cirrus. Q. J. R. Meteorol. Soc. 114, 141-164,1988.

Francis, P. N., J. S. Foot and A. J. Baran. Aircraft measurements of the solar and infrared radiative properties of cirrus and their dependence on ice crystal shape, J. Geophys. Res., 104, 31685-31695, 1999.

Heymsfield A. J., Lewis S, Bansemer A, Iaquinta J, Miloshevich LM Kajikawa M, Twohy C, Poellot MR. A general approach for deriving the properties of cirrus and stratiform ice cloud particles. J. Atmos. Sci., 59, 3-29. 2002.

Heymsfield, A. J., Bansemer A, Matrosov S, Tian L. The 94-GHz radar dim band: Relevance to ice cloud properties and CloudSat. Geophys. Res. Lett. 35, L03802, 2007.

Hirst, E., Kaye P. H, Greenaway R. S, Field P., Johnson D. W. Discrimination of micrometer-sized ice and super-cooled droplets in mixed phase cloud. Atmos. Environ, 35, 33-47, 2001.

Lawson, R. P., B. A. Baker, C. G. Schmitt and T. L. Jensen. An overview of microphysical properties of Arctic clouds observed in May and July during FIRE.ACE. J. Geophys. Res., 106, 14989-15014, 2001.

Ivanova, D, Mitchell D. L., Arnott W. P., Poellot, M. A GCM parameterization for bimodal size spectra and ice mass removal rates in mid-latitude cirrus clouds. Atmos. Res. 59, 89-113, 2001.

Liou, K. N. and Takano, Y., Light scattering by nonspherical particles: Remote sensing and climatic implications. Atmos. Res., 31, 271-298, 1994.

Stephens G. L., Vane D. G, Boain R. J., Mace G. G., Sassen K., Wang Z. E, Illingworth A. J., O'Connor E. J., Rossow, W. B, Durden S. L., Miller S. D., Austin R. T., Benedetti A., Mitrescu C. The cloudsat mission and the a-train – A new dimension of space-based observations of clouds and precipitation. Bull. Amer. Met. Soc., 83, 1771-1790, 2002.

ACKNOWLEDGEMENTS

We would like to thank FAAM for providing the flights and necessary aircraft data that made this analysis possible. The CloudSat team at CSU for providing the CloudSat products.

ICE CLOUD PROPERTIES FROM SPACE, COMBINIG RADAR, LIDAR AND RADIOMETERS ON THE A-TRAIN

Julien Delanoë and Robin Hogan
Department of Meteorology, University of Reading, UK

1. INTRODUCTION

On 28 April 2006, two satellites, CloudSat (a 94GHz cloud-profiling radar (Stephens et al. (2002)) and CALIPSO (Cloud Aerosol Lidar and Infrared Pathfinder Satellite Observations; Winker et al. (2003)) were launched. They joined Aqua, hosting MODIS (Moderate Resolution Imaging Spectroradiometer) and a large number of radiometers as part of the A-Train of Satellites (Stephens et al. (2002)). The instruments onboard on these satellites can be used separately or combined to improve our understanding of the Earth's climate, specially the role of clouds and aerosols on the radiation balance.
The subject of this paper is the retrieval of ice clouds properties exploiting radar, lidar and infrared radiometer synergy. Almost all existing algorithms use only two instruments so do not take advantage of the full information available, hence the necessity to develop new methodologies to use the combination of radar, lidar and radiometer. In the talk, the Delanoë and Hogan (2008) unified retrieval scheme will be briefly described that uses a variational approach to combine cloud radar, backscatter lidar and infrared radiometer to retrieve the properties ice clouds. The rigorous treatment of observational errors and careful use of additional constraints enables the retrieval to blend smoothly in the vertical between regions where different instruments are sensitive. The unified scheme retrieves an optimum profile of cloud variables that best fits the observations. This scheme has been applied to global observations from the A-Train of satellites.

2. CASE STUDY

As a case study we selected an example of an ice cloud sampled by both CloudSat radar and CALIOP lidar over the Atlantic Ocean (from Iceland toward the Azores). This has been taken from CloudSat granule, 13th October 2006 between 03:52 and 03:58 UTC. The top panel of Fig1 represents the attenuated backscatter coefficient measured by CALIPSO, for this example: CALIPSO can detect the top region of the cloud while CloudSat radar (middle panel) is the only one able to detect cloud base since the lidar starts being attenuated (loss of signal). The central region is simultaneously detected by both radar and lidar.

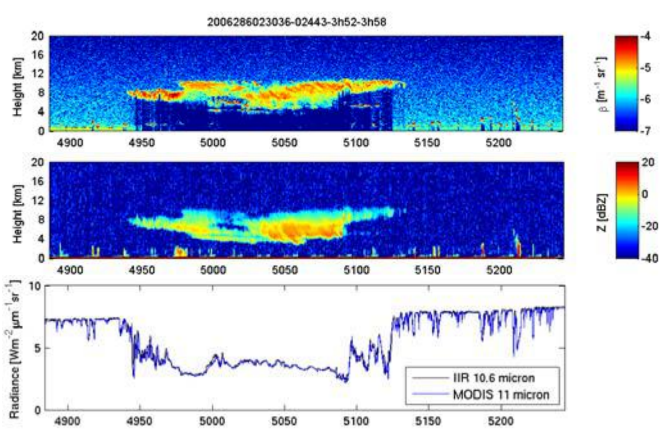

Fig 1: Time height representation of an ice cloud sampled by, CALIOP lidar (upper panel), CloudSat radar (middle panel) and the MODIS and IIR radiometers over Atlantic Ocean (from Iceland toward Azores), 13th October 2006 between 03:52 and 03:58 UTC.

The algorithm proposed by Delanoë and Hogan (2008) is applied to this selected ice cloud. Radar reflectivity, attenuated backscatter and infrared radiance at 11μm (from MODIS) are assimilated to retrieved ice cloud properties (cf, Fig 2) including; visible extinction coefficient, ice water content, effective radius and ice number concentration.

As shown by Fig2, a retrieval is possible between regions of the cloud detected by both radar and lidar and regions detected by just one of these two instruments. Thus, when the lidar signal is unavailable (for reasons such as strong attenuation), the retrieval tends toward an empirical relationship using radar reflectivity factor and temperature (similar to Hogan et al. 2006; Protat et al. 2007), and when the radar signal is unavailable (such as cloud top), accurate retrievals are still possible from the combination of lidar and infrared radiometer (the MODIS channel contain particle size information but are weighted towards the cloud top region similar to Chiriaco et al. 2004). We can see that particle size decreases with height; pristine ice is expected at cloud top while aggregates are likely at cloud base with larger size and smaller concentration.

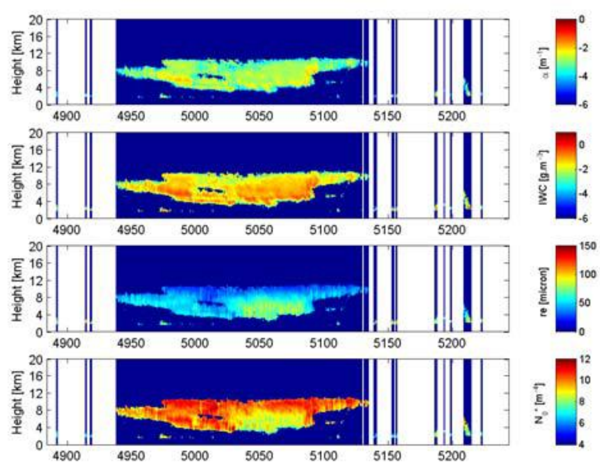

Fig 2: Time-height representation of an ice cloud properties derived from the radar-lidar-infrared radiometer algorithm over the Atlantic Ocean (from the observations shown in Fig 1.

3. ONE MONTH OF GLOBAL ICE CLOUD PROPERTIES

We carried out a one-month study of global ice cloud properties, exploiting radar-lidar synergy from A-Train. Ice cloud properties are derived from the Delanoë and Hogan (2008) algorithm over the globe for July 2006. Fig3 shows the distribution of ice water content as function of temperature (left panel) and visible extinction coefficient as function of temperature (right panel). There is a clear trend: both IWC and extinction increase with temperature but are spread over 2 to 3 orders of magnitude at low temperatures and can reach 5 orders of magnitude close to 0° C. Such information is crucial for global atmospheric modelling.

We are currently using these data to evaluate the clouds in the forecast models of the UK MetOffice and ECMWF.

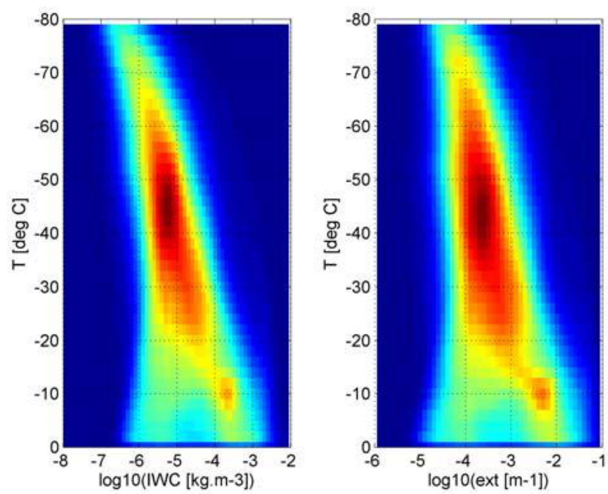

Fig 3: Ice water content and visible extinction coefficient as a function of temperature for July 2006 derived from radar-lidar synergy.

We also derive maps of ice water path (IWP) and ice visible optical depth (τ) for July 2006 as shown by Fig4. As shown by both IWP and τ maps, during the whole month of July, there is a small amount of ice clouds between 0°S and 30°S, in the descending branch of the Hadley circulation but much larger in the Inter Tropical Convergence

Zone (ICTZ). There is a difference between northern and southern middle latitudes; ice visible optical depth is much higher in southern hemisphere since it is the austral winter.

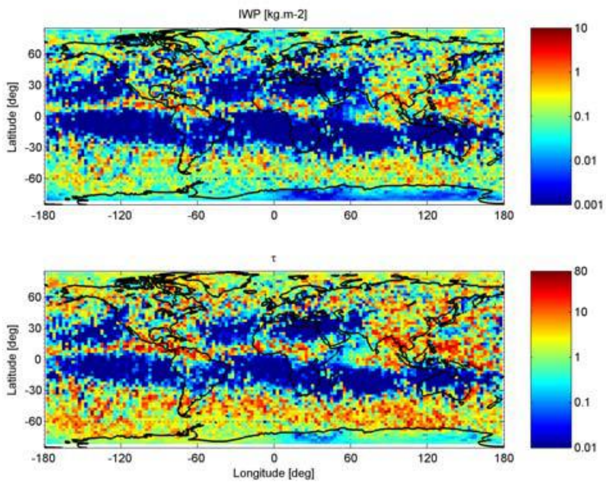

Fig 4: Latitude-longitude maps of ice water path (upper panel) and visible optical depth (lower panel) for July 2006 derived from radar-lidar synergy.

4. BIBLIOGRAPHY

Chiriaco, M., H. Chepfer, V. Noel, A. Delaval, M. Haeffelin, P. Dubuisson, and P. Yang (2004), Improving retrievals of cirrus cloud particle size coupling lidar and three-channel radiometric techniques, Mon. Weather Rev., 132, 1684– 1700.

Delanoë, J., and R. J. Hogan (2008), A variational scheme for retrieving ice cloud properties from combined radar, lidar, and infrared radiometer, J. Geophys. Res., 113, D07204, doi:10.1029/2007JD009000.

Hogan, R. J., M. P. Mittermaier, and A. J. Illingworth (2006b), The retrieval of ice water content from radar reflectivity factor and temperature and its use in the evaluation of a mesoscale model, J. Appl. Meteorol. Climatol., 45, 301– 317.

Protat, A., J. Delanoe¨, D. Bouniol, A. J. Heymsfield, A. Bansemer, and P. R. A. Brown (2007), Evaluation of ice water content retrievals from cloud radar reflectivity and temperature using a large airborne in-situ microphysical database, J. Appl. Meteorol., 46(5), 557–572.

Stephens, G. L., D. G. Vane, R. J. Boain, G. G. Mace, K. Sassen, Z. Wang, A. J. Illingworth, E. J. O'Connor, W. B. Rossow, S. L. Durden, S. D. Miller, R. T. Austin, A. Benedetti, C. Mitrescu, and the CloudSat Science Team (2002), The Cloudsat Mission and the A-Train, Bull. Am. Meteorol. Soc., 83, 1771–1790.

Winker, D. M., J. Pelon, and M. P. McCormick (2003), The CALIPSO mission: Space borne lidar for observation of aerosols and clouds, Proc. SPIE, 4893, 1–11.

Acknowledgements: The radar, lidar and radiometer data were obtained from the NASA Langley Research Center Atmospheric Science Data Center and the NASA CloudSat project. This work was supported by NERC grant NE/C519697/1.

MICROPHYSICAL PROPERTIES OF CIRRUS AND CIRRUS ANVILS BASED ON AIRCRAFT MEASUREMENTS FROM RECENT FIELD CAMPAIGNS

R. Paul Lawson, Bryan Pilson and Qixu Mo

SPEC Incorporated, Boulder, CO

1. INTRODUCTION

It is now well recognized that the size, shape and concentration of ice particles in cirrus and cirrus anvils have a significant impact on the earth's radiation budget, which in turn affects global climate change. For example, Liou (1986) showed that cirrus particles play an important role in the energy balance of the earth-atmosphere system through their interactions with solar and terrestrial radiation. Stephens et al. (1990) concluded that prediction of cirrus cloud feedback on climate is limited by our lack of understanding of the relationship between the size and shape of ice crystals, and the gross radiative properties of cirrus. Labonnote et al. (2000) determined that accurate measurements of the size and shape of cirrus particles were essential to obtain reliable inversion products from remote observations. Kristjánsson et al. (2000) used climate models to show that the treatment of ice particle size and habit may have a significant impact on climate change.

The shape of cirrus ice particles is well resolved using the cloud particle imager (CPI). Lawson et al. (2006a) processed hundreds of thousands of digital images of CPI images in continental mid-latitude cirrus and found that particles with rosette shapes, which include mixed-habit rosettes and plate-like polycrystals, comprise over 50% of the surface area and mass of ice particles > 50 μm in cirrus clouds. Approximately 40% of the remaining mass of ice particles > 50 μm are found in irregular shapes, with a few percent each in columns and spheroidal shapes. Plates account for < 1% of the total mass. However, relatively little data have been reported on the shapes of ice particles in continental anvil cirrus, maritime cirrus and maritime anvil cirrus. Connolly et al. (2005) show limited CPI images from continental and maritime anvil cirrus suggesting that continental anvils contain a higher percentage of aggregates, sometimes forming long chains of small particles. They show laboratory evidence that suggests that the chains of particles are linked due to high electric fields in some continental storms. On the other hand, their data in maritime anvils show that the particles are largely singular and more faceted.

Here we examine particle shapes, sizees and concentrations in maritime anvil cirrus and maritime cirrus formed in situ (i.e., particles that are thought to form at the altitude where the cirrus is observed). In addition to results from previous field campaigns that focused on in situ and anvil cirrus formed over the continental U.S., we present results from two recent field campaigns: the NASA African Monsoon Multidisciplinary Activities (NAMMA) field campaign staged from Cape Verde in August-September 2006, and the NASA Tropical Composition, Cloud, and Climate Coupling (TC^4) experiment that took place near Costa Rica in July-August 2007. The data come from CPI probes and a relatively new imaging instrument, the 2D-S (stereo) probe. The 2D-S is two independent imaging probes, termed the horizontal (H) and vertical (V) channels, contained in a single housing. Each probe has a 128-photodiode array with 10 μm pixel resolution. The 2D-S probe has been evaluated in the laboratory and found capable of imaging an 8 μm diameter optical fiber spinning at 233 m s^{-1}. This is important since the time response of older probes has been shown to be too slow to image particles less than about 100 μm at speeds often encountered by jet aircraft

(Lawson et al. 2006b). The 2D-S also records the arrival time of each particle, which is information used in software processing to eliminate large ice particles that shatter on the probe tips and are seen as spurious small particles. The particle size distributions (PSDs) reported in this paper are from the 2D-S probe, except where other probe data are shown for sake of comparison.

2. DISTINGUISHING ANVIL AND IN SITU CIRRUS

The particle shapes observed in mid-latitude in situ cirrus have been documented in detail by Lawson et al. (2006a). The predominate CPI images observed in mid-latitude cirrus are rosette shapes, as shown in Fig. 1, which has been adapted from Connolly et al. (2005). Rosette shapes are known to form at cold temperatures, generally from about –25 to –55 °C, when a cloud drop or solution drop freezes and forms a polycrystalline structure. Bailey and Hallett (2004) show examples of these rosette shapes grown in the laboratory, which they label as polycrystals. Their laboratory work suggests that "true" bullet rosettes are not observed at temperatures warmer than about –42 ° C. Here we identify crystals with a rosette shape, whether they are true bullet rosettes, platelike polycrystalline shapes, or polycrystals with side plane as rosette shapes, or simply rosettes. The critical point is that the rosette shapes (polycrystals) are not observed to form at temperatures warmer than about –25 ° C.

Figure 1 also shows examples of CPI images of particles found in "fresh" continental and maritime anvils. Here, we use the term "fresh" to designate an anvil that has not appeared to age and spread into regions where nucleation has produced new particle growth. It is apparent from a comparison of typical particle shapes in Fig. 1 that rosette shapes are not commonly observed in fresh convective anvils. This is consistent with the physics of convective storms, where most particles are nucleated in updrafts, or if supercooled drops survive the transport to colder temperatures, they freeze homogeneously near –37 °C and are observed as frozen ice spheres in the anvil region (Heymsfield et al. 2004). Later in Section 4 we show examples of homogeneous freezing in strong convective updrafts from the NASA AMMA (NAMMA) and TC^4 projects. These observations suggest that anvil cirrus can often be distinguished from cirrus that has formed in situ by the presence or absence of ice particles with rosette shapes.

3. CIRRUS FORMED IN SITU

Here we discuss examples of cirrus formed in situ over the Atlantic Ocean Southwest of Cape Verde (NASA NAMMA field campaign) and east of Panama (NASA TC^4 field campaign). In both cases data were collected by the NASA DC-8 research aircraft. The TC^4 example was also coordinated with a CloudSat/CALIPSO satellite overpass. Figure 2 shows CPI and 2D-S images, as well as PSD's from the 2D-S and cloud and aerosol probe spectrometer (CAPS) (Baumgardner et al. 2001). The ice particles are clearly rosette, irregular and columnar shapes, which are the same shapes predominantly found in mid-latitude cirrus (Fig. 1). The region in the CAS portion of CAPS PSD from 0.5 to 50 μm is elevated as a result of large ice particles shattering on the inlet of the probe. Note that suspected shattered particles have been removed from the 2D-S data using arrival times and the technique described by Field et al. (2006).

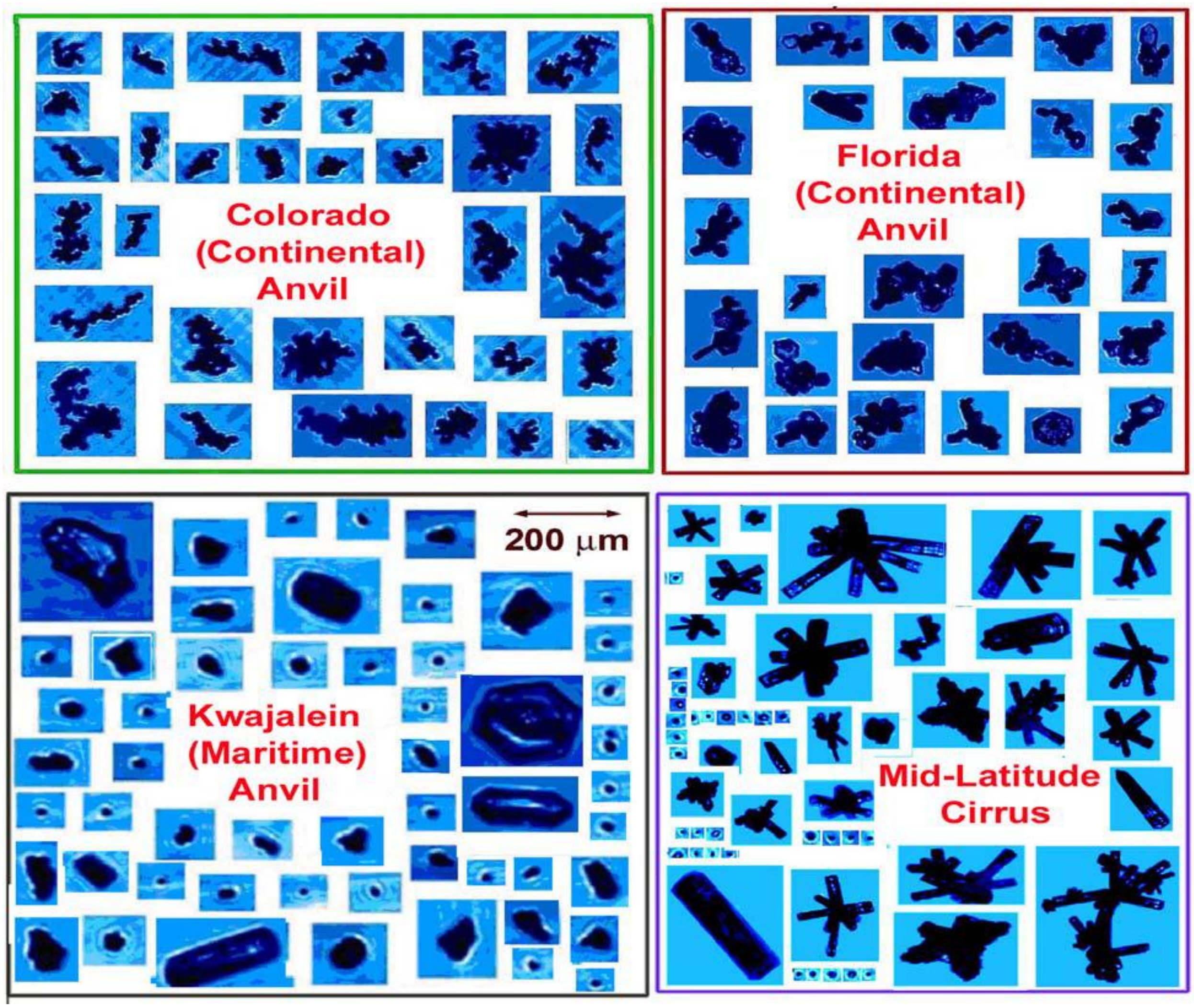

Figure 1. Examples of typical CPI ice crystal images in continental and maritime anvils, and mid-latitude cirrus clouds.

Figure 3 shows examples of 2D-S images, and PSD's from the 2D-S and CAPS during measurements in in situ cirrus from a NAMMA case. The 2D-S images are rosette shapes, irregulars and columns, and are very similar to the 2D-S images seen in the TC^4 example (Fig. 2). Unfortunately, the CPI was mounted on the DC-8 for NAMMA in a location/orientation that prevented larger particles (i.e., rosette shapes) from entering the sample volume. The CAS portion of the CAPS probe, like the TC^4 case, shows the effects of shattering from large ice particles. The concentration of particles in the TC^4 in situ cirrus is higher than the NAMMA case, but the mean particle size in the NAMMA cirrus is slightly larger, so that values of β_{ext}, IWC and τ are of the same order of magnitude. These values are also in close agreement with observations in mid-latitude cirrus in the temperature range from –50 to -63°C, where particles are mostly small and ice crystal shattering is likely to have a minor influence (Lawson et al. 2006a). The 2D-S measurements in TC^4 and NAMMA in cirrus formed in situ are also in good agreement with comparisons of IWC between the 2D-S, a counterflow virtual impactor (Twohy et al. 1996), and derived IWC from a combination of CloudSat, CALIPSO and Aura satellites

(Mace 2008, Personal Communication), as shown in Fig. 4.

The particle images shown in Figs. 2 and 3 and Lawson et al. (2006a) suggest that rosette shapes are the predominate recognizable crystal shape observed in cirrus that is formed in situ, both in mid-latitude continental and tropical maritime clouds. In contrast, as will be seen in the following sections, rosette shapes are rare in anvil cirrus and there are often recognizable differences between particle shapes in continental and maritime anvils.

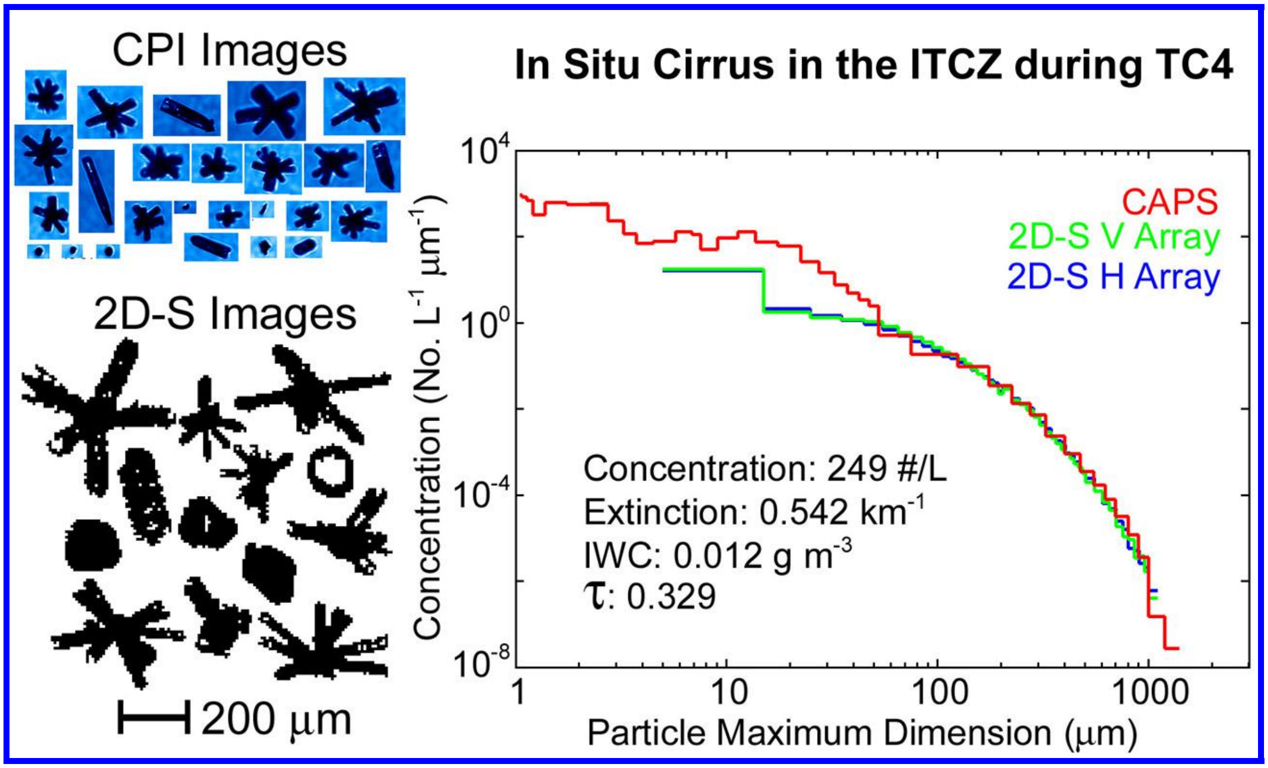

Figure 2. Example from TC^4 project showing (left) CPI and 2D-S images of (mostly rosette shaped) ice particles observed in maritime cirrus formed in situ, and (right) PSD's from the CAPS and 2D-S probes, along with average values of total particle concentration, extinction coefficient, ice water content and optical depth (τ). The relatively high particle concentrations seen by the CAPS are thought to be due to large ice particles shattering on the probe inlet and producing small-particle artifacts.

4. CONTINENTAL AND MARITIME ANVIL CIRRUS

Particle shapes in continental and maritime anvil cirrus are markedly different than observed in cirrus formed in situ. This is understandable since cirrus particles formed in situ are typically nucleated and grow at temperatures < - 30 ° C, while anvil cirrus ice particles are generally nucleated and grow in updrafts and have habits characteristic of warmer temperatures. Even when cloud drops freeze homogeneously at temperatures < -37°C in updrafts, there is seldom subsequent growth, and as we will see in this Section, these particles are injected into the anvil in the form of quasi-spherical ice shapes.

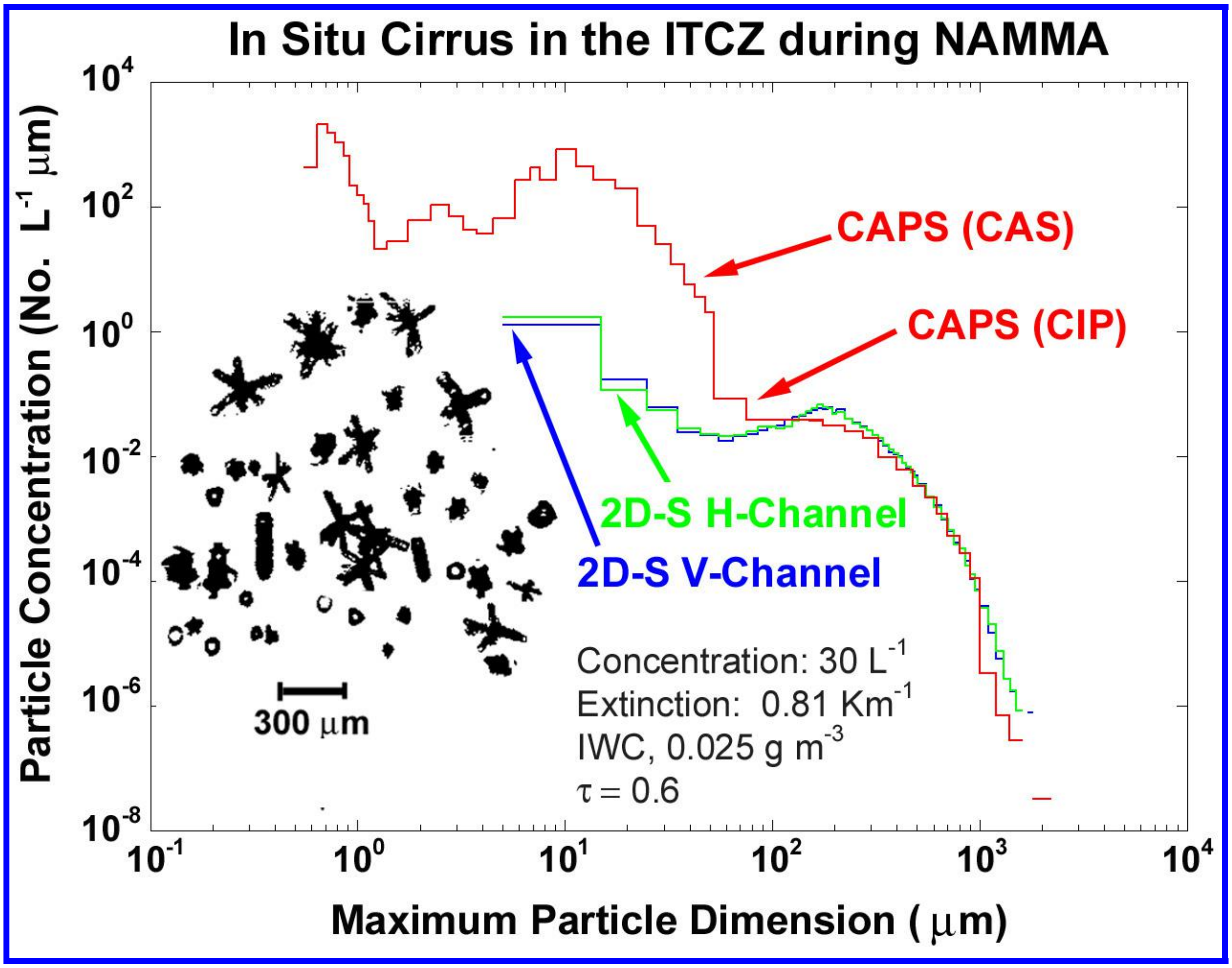

Figure 3. Example from NAMMA project showing (left) 2D-S images of (mostly rosette shaped) ice particles observed in maritime cirrus formed in situ, and (right) PSD's from the CAPS and 2D-S probes, along with average values of total particle concentration, extinction coefficient, ice water content and optical depth (τ). The relatively high particle concentrations seen by the CAPS are thought to be due to large ice particles shattering on the probe inlet and producing small-particle artifacts.

Here we compare microphysical properties of anvil cirrus observed in the Inter Tropical Convergence Zone (ITCZ) off the west coast of Africa during NAMMA, and in the ITCZ west of Costa Rica during TC^4. The measurements are placed into three categories: turrets within anvils that have sustained updrafts that average > 4 m s^{-1}; general (fresh) anvil cirrus that is still part of a cloud system connected to convective turrets; and aged anvil cirrus that is removed from its generating convective turrets. On occasion, ice particles in aged anvil cirrus encounter regions with relatively high ice supersaturation and some start to grow and take on the characteristics of rosette shapes characteristic of in situ cirrus. Otherwise, particles in anvils are not typically rosette shaped and display several different habit types, depending on the temperatures at which they nucleate and grow.

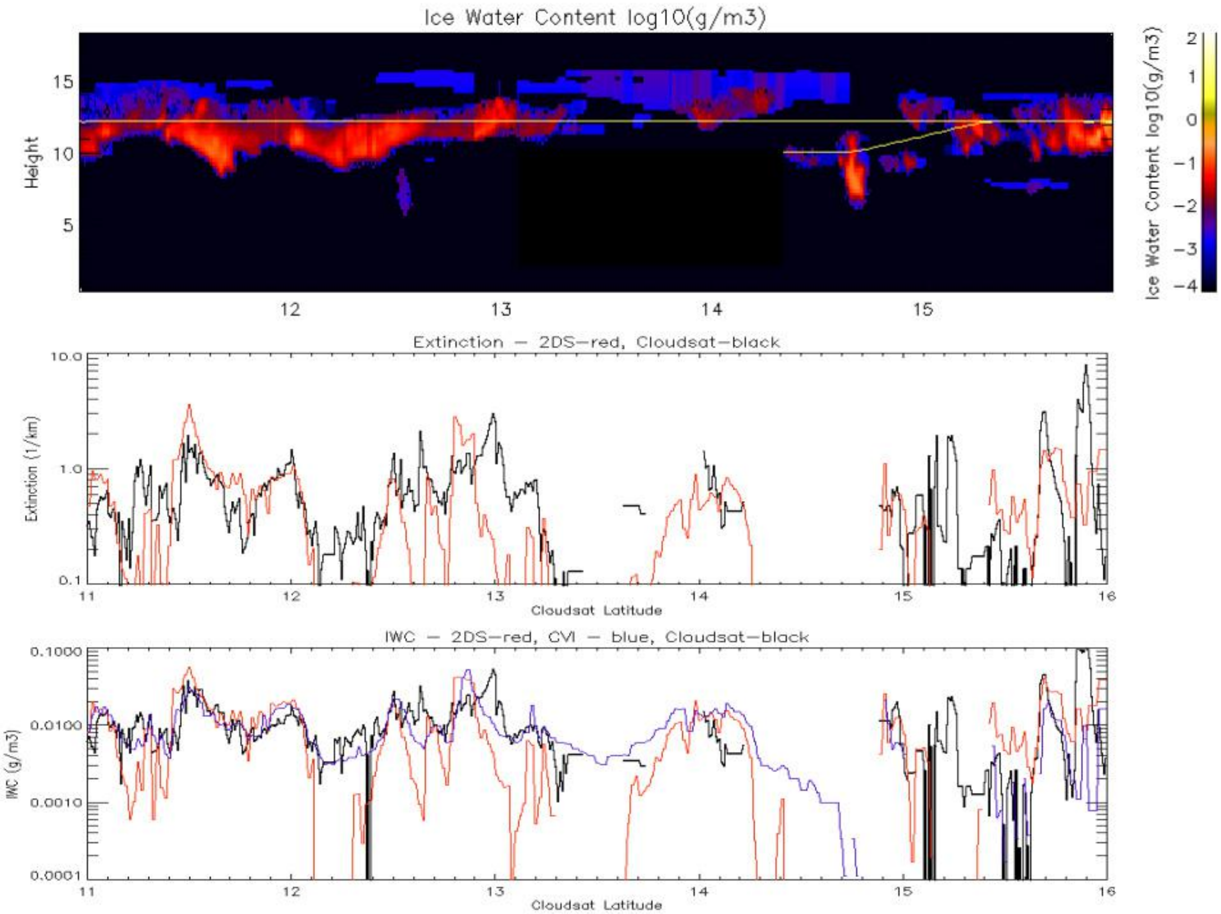

Figure 4. Example showing (top) IWC derived from CloudSat, CALIPSO and Modis and DC-8 flight track (yellow line) on 22 July 2007 during TC^4, (middle) 2D-S measured particle concentration and (bottom) CVI and 2D-S derived IWC (from Mace 2008, Personal Communicaiton).

Figure 5 shows PSD's that are representative of strong convective turrets and a weak convective turret observed during TC^4 and NAMMA. Also shown are PSD's collected in fresh TC^4 anvils near convection, near the edges of anvils that are still attached to convective cells, and aged anvil cirrus that is detached from its original convection. All of the data collected in the convective turrets and anvil cirrus consisted of only ice particles and no supercooled cloud water. The TC^4 turrets were penetrated by the NASA DC-8 at FL400 and a temperature of – 46°C. The PSD's in Fig. 5 show a distinctive trend where the strong convective turrets contain the highest average total particle concentration (~10 cm^{-3}), β_{ext} (69 to 85 km^{-1}) and IWC (~2 g m^{-3}). The weak convective turret has a relatively high average particle concentration (3.3 cm^{-3}), but a much lower IWC (0.1 g m^{-3}), which is due to the lack of large particles in the updraft. It is likely that the larger particles have recently precipitated out of this turret, leaving only small particles. The average particle concentrations, β_{ext} and IWC in the TC^4 anvils, which were investigated near cloud top at FL400, decrease as a function of distance from the convective turrets. This is an expected result and has been observed in other maritime and continental anvils (e.g., Lawson et al. 1998). The decrease in particle concentration in the anvil region far from convection in the size range from about 30 to 300 μm may be due to aggregation (Heymsfield 1986). The aged anvil cirrus has the lowest values of average total particle concentration, β_{ext} and IWC. The aged anvil cirrus has a total particle concentration that is 100 times less than in the turrets, and less than one-tenth the value of the average particle concentration in anvil cirrus close in to the convection. Commensurate decreases are seen in β_{ext} and IWC. Since these strong gradients are often observed over distances of 100's of km or less, it is important to take into account the spatial variability of these clouds remote retrieval algorithms and models of radiative transfer.

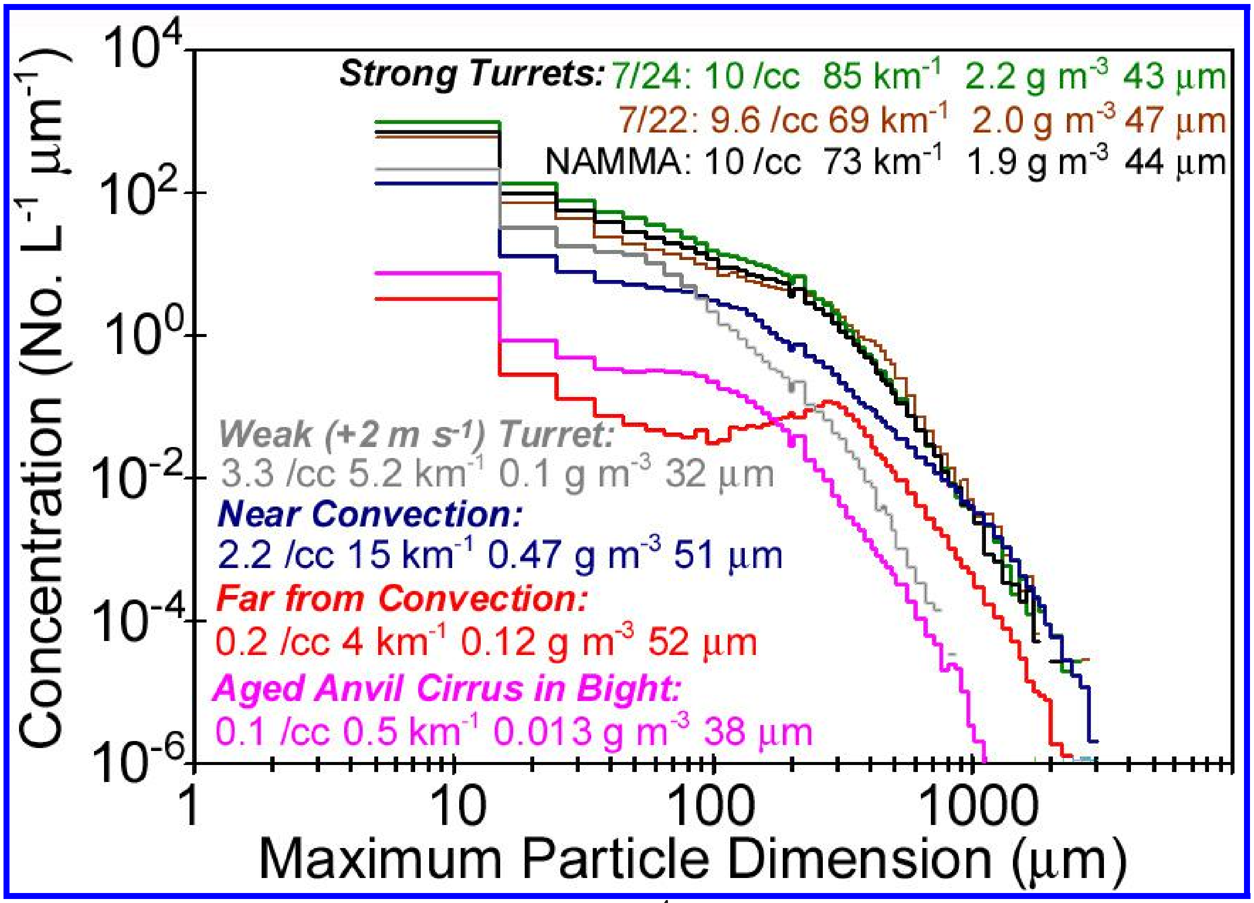

Figure 5. Examples of average PSD's from TC^4 and NAMMA projects in strong convective turrets, a weak turret, anvil cirrus near and far from convective turrets, and detached, aged anvil cirrus. Mean values of total particle concentration (/cc), extinction coefficient (km^{-1}), IWC ($g\ m^{-3}$) and effective particle radius (μm) are shown for the each PSD.

Figure 6 shows examples of 2D-S images of ice particles observed at various altitudes (i.e., Flight Levels, where FL is the altitude in hundreds of feet) and corresponding PSD's in a fresh cirrus anvil observed in the ITCZ off the west coast of Cape Verde during NAMMA. While CPI images were only available for small particles (due to the mounting location of the instrument), the 2D-S images show evidence of columns, capped columns and plates, along with aggregates, especially in the lower regions of the anvil. Average particle concentration is several hundreds per liter and the mean extinction coefficient is 22.8 km^{-1}, which equates to a very high optical depth of about 40. The average IWC in the anvil is 0.8 g m^{-3}, which is substantial and can potentially cause performance degradation (or even temporary failure) of turbofan engines during extended exposure (Lawson et al. 1998).

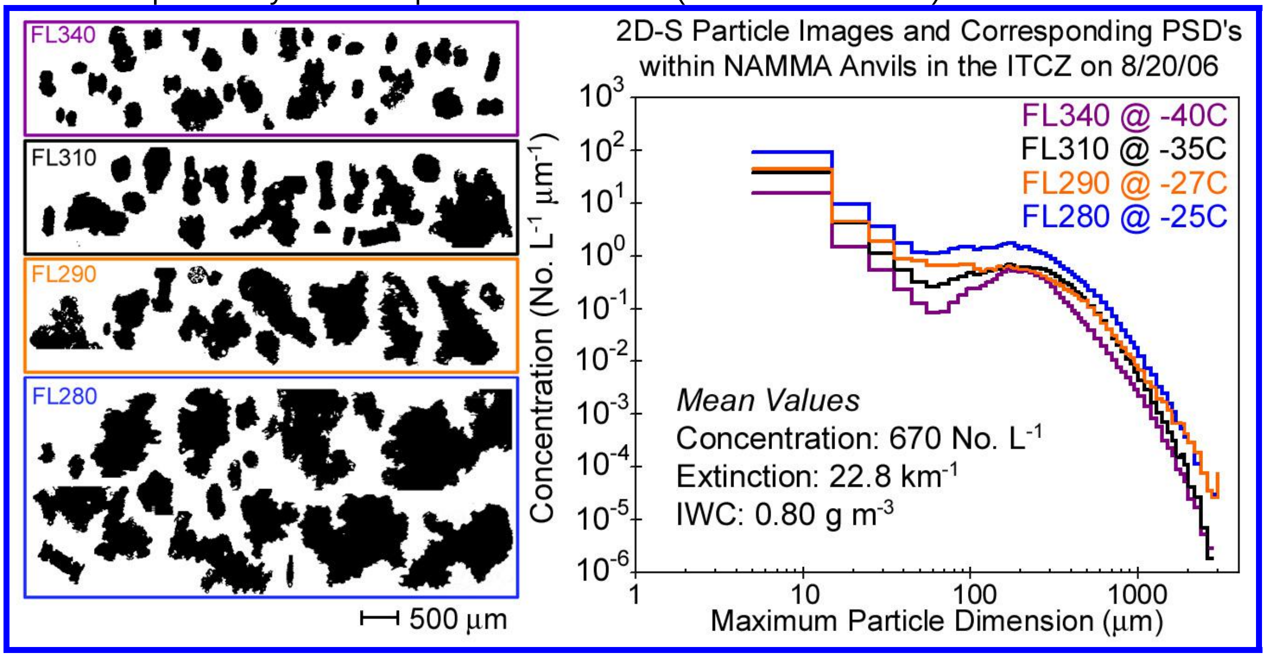

Figure 6. (left) 2D-S images shown as a function of altitude (FL times 100 is altitude in feet) and (right) corresponding PSD's during DC-8 flight in fresh anvil near the ITCZ during NAMMA.

Figure 7 shows a time series of particle concentration, IWC and vertical velocity in two turrets in a TC[4] convective system observed on 24 July 2007 in the ITCZ. Below the time series plot are representative 2D-S images of ice particles. The images at the left show the comparison between the upshear and downshear regions of one turret. The upshear region has more compact particles that appear to be graupel, while the particles in the downshear region appear to be less dense. The turret on the right side of Fig. 7 is exceptionally strong, with a 20 m s^{-1} peak updraft, 2.4 g m^{-3} IWC and peak ice particle concentration of 32 cm^{-3}. Overshooting tops were observed on the forward video of the DC-8 as it flew in and out of cloud at FL400. The 2D-S images in the strong turret (on the right in Fig. 7) are a combination of many small ice particles, likely frozen via homogeneous nucleation, and larger, compact images that appear to be graupel particles. The heights of the overshooting tops were modest, appearing to extend less than 1 km above the general anvil top. The relative shallow depth of the overshooting tops is curious given that a 20 m s^{-1} peak updraft was measured by FL400.

Comparisons between convective turrets and the general anvil region based on DC-8 NAMMA flights in the ITCZ near Cape Verde produced results similar to those observed in the ITCZ in TC[4]; i.e., convective updrafts > 10 m s^{-1}, IWC on the order of 2 g m^{-3}, ice concentrations in turrets of > 5 cm^{-3} and ~1 cm^{-3} in the general anvil region. Figure 8 shows an example of measurements of total particle concentration, β_{ext} and IWC from time series measurements in the general anvil region and in a convective turret. The data show that significantly higher values of all three parameters are observed in the turrets. However, the values in the general anvil region are substantial, with IWC peaks approaching 2 g m^{-3}, peaks in > 2 cm^{-3} and peaks in β_{ext} that exceed 40 km^{-1}. The high

IWC is commensurate with values observed in the anvils of mid-latitude supercell storms and in tropical anvils observed during CEPEX (Lawson et al. 1998). Recently, it has come to public attention that several commercial airliners have experienced engine failures after extended flight in anvil regions with high IWC (Pasztor 2008). As first reported by Lawson et al. (1998), high concentrations of ice crystals melt upon entering the engine, but enough ice melting and evaporating can cause some of the unheated guide vanes internal to the engine to cool below freezing temperatures. Water can then refreeze on the cold guide vanes and distort airflow in the engine, causing the engine to rollback.

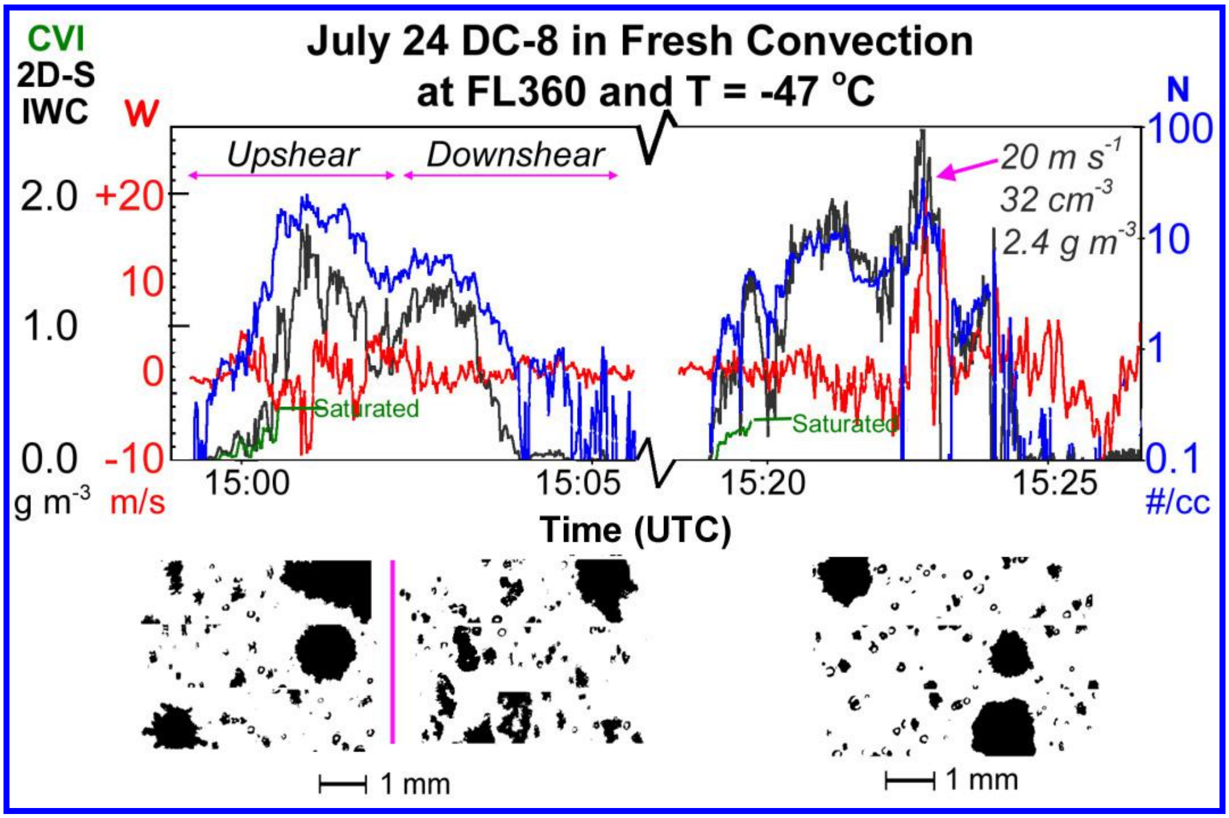

Figure 7. Examples of penetrations of strong convective turrets during TC[4] showing (top) time series of particle concentration (blue trace referenced to right axis) 2D-S derived IWC (black trace), CVI IWC (green trace) and vertical velocity (red trace). Upshear and downshear regions of turret on left are designated and 2D-S images of particles below time series are representative of corresponding regions in the time series.

5. AGED MARITIME ANVIL CIRRUS

Maritime anvil cirrus that has previously detached from its convective source has a composition of particles that are often a combination of anvil and in situ cirrus. Also, total particle concentration, β_{ext}, and IWC are generally substantially less than in fresh anvil cirrus and convective turrets. Since the CPI was not capable of imaging large particles during NAMMA and TC[4], Fig. 9 shows a comparison of CPI images from the DOE TWP-ICE project held near Darwin, Australia in 2005-2006. The images on the left, which are in the transition region where new in situ cirrus particles are growing, show a mixture of anvil shapes and rosette shapes. The particles on the right are farther downwind where most of the anvil particles have precipitated and new in situ cirrus rosette shapes and small irregular shapes are dominant, similar to those seen in mid-latitude cirrus (Lawson et al. 2006a).

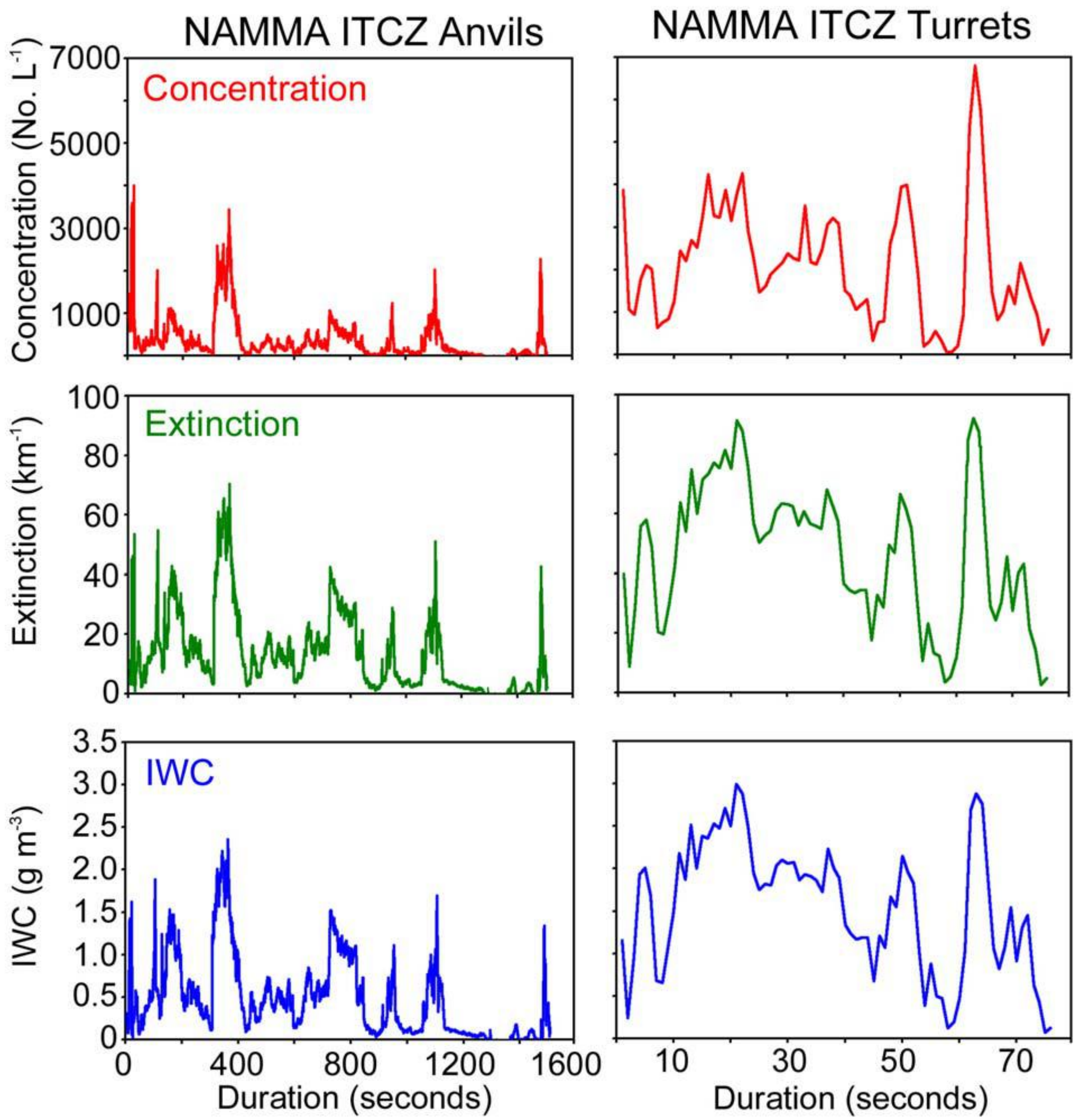

Figure 8. Time series of (top) 2D-S particle concentration, (middle) extinction and (bottom) IWC from DC-8 penetrations of (left) general anvil region and (right) strong turrets in ITCZ during NAMMA.

During TC4 the DC-8 made repeated penetrations through aged cirrus that had detached from its generating convection. Figure 10 shows an example of 2D-S images and PSD's as a function of altitude in aged cirrus from combined data collected by the WB-57 and DC-8 aircraft on 5 August 2007. The sorting of particle sizes from cloud top to cloud bottom is expected as small particles sublimate and larger particles precipitate. This has seldom been observed in the past due to the effects of crystal shattering that produce artificial small particles lower in the cloud.

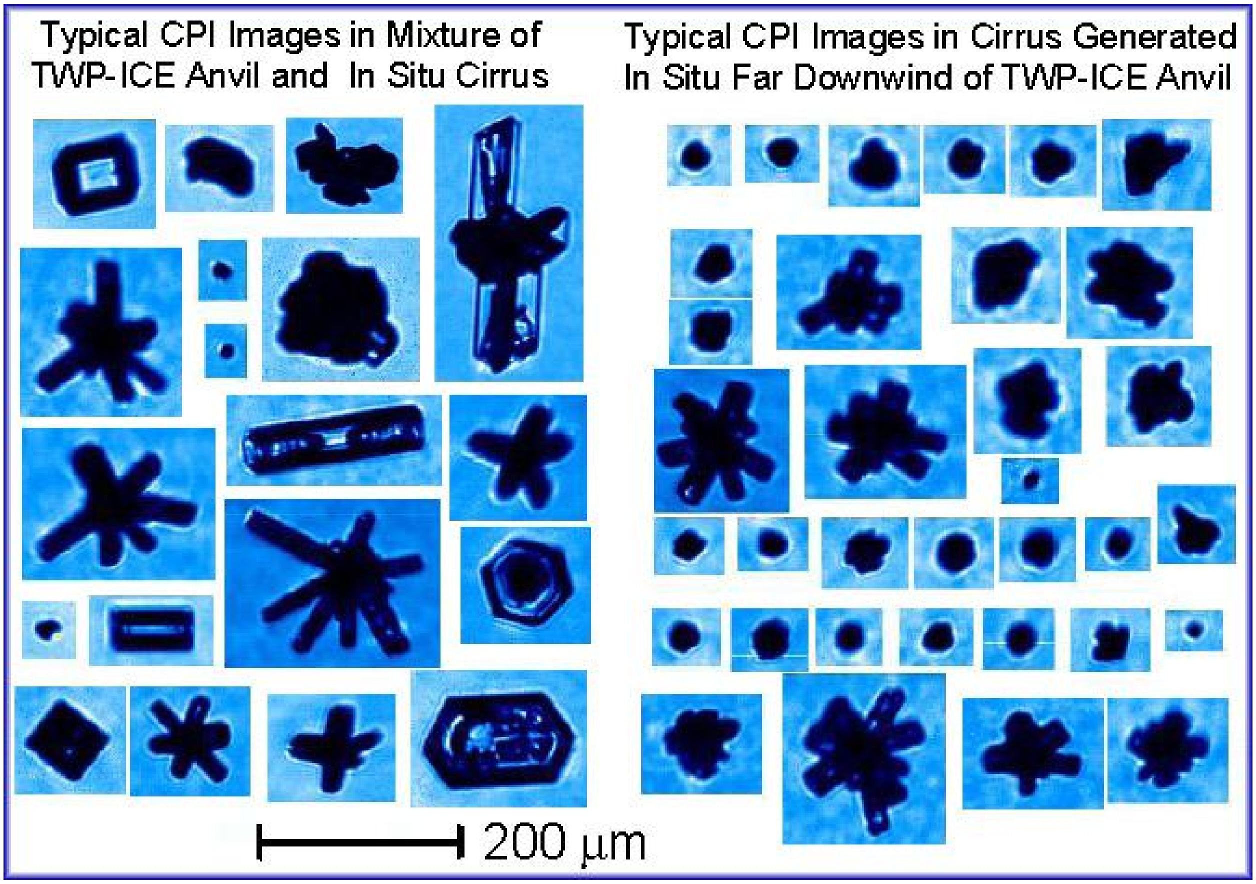

Figure 9. Examples of CPI images collected by DOE Proteus in a detached anvil from TWP-ICE project showing (left) mixture of particles typically found in maritime anvils (i.e., plates and columns) and (right) transition to more rosette shapes typical of cirrus formed in situ. Images on the left were recorded closer to the original convection and images on the right were recorded farther downwind from the original convection.

6. SUMMARY

Data are presented from a various field projects, including Kwajex, CRYSTAL-FACE, TWP-ICE, NAMMA, TC[4] and Learjet studies of anvils in Eastern Colorado. Clouds are distinguished as cirrus formed in situ in continental mid-latitudes and maritime tropical regimes, and anvil cirrus formed in continental and maritime environments. The anvil cirrus is further divided into convective turrets, fresh anvil cirrus and aged anvil cirrus. The data describing particle shape are mostly taken with CPI instruments and particle size distributions are from the 2D-S probe.

Thin cirrus formed in situ at a temperature of around –45°C has particle shapes that are similar in both continental and maritime environments, with rosette configurations being the predominant recognizable shape; substantial concentrations of small spheroids and irregular shapes are also present, along with a minor contribution from columns. Particle concentration in thin (order 1 km thick) cirrus formed in situ is in the range of tens to a few hundreds per liter. Extinction is on the order of 0.5 to 1 km^{-1}, IWC is on the order of 10 to 25 mg m^{-3} and optical depth is about 0.5.

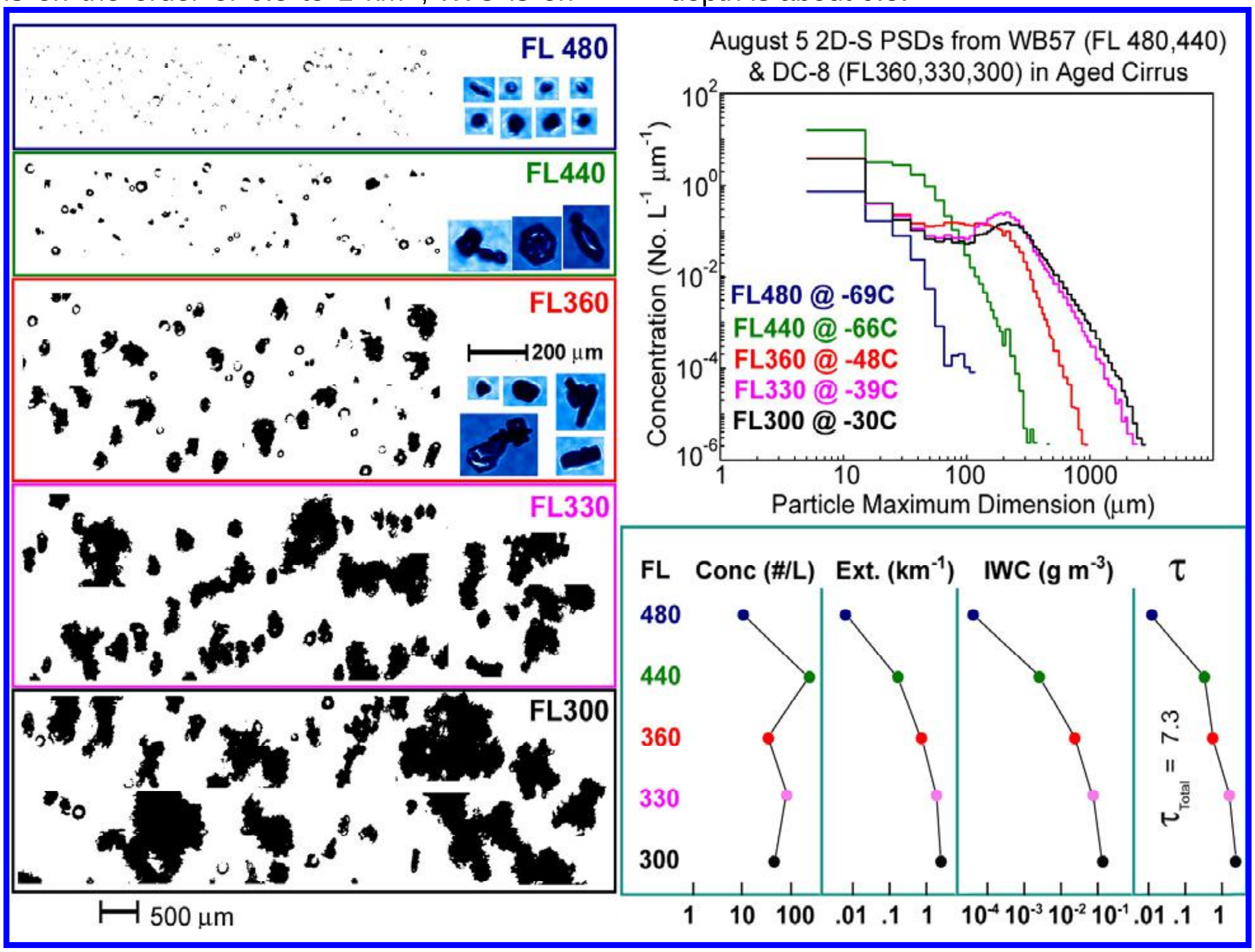

Figure 10. (left) CPI and 2D-S images collected in aged anvil cirrus during TC4 by the NASA WB-57F (FL480 and FL440) and the DC-8 (FL360, FL330 and FL300) showing evolution of particle size with decreasing altitude. (upper right) Average PSD's corresponding to the five Flight Levels and (lower right) microphysical and radiometric quantities derived from 2D-S measurements as a function of height.

Continental cirrus anvils formed in association with strong convection and high electrical activity typically have particle shapes that are mostly aggregates, often forming aggregates of chains of small particles (Connolly et al. 2005). In contrast, maritime cirrus anvils typically display more faceted crystal shapes, including plates, columns and capped columns. Particles in maritime cirrus anvils also form aggregates, but not to the extent seen in continental anvils, and rarely have chains of particles been observed.

Strong convective turrets with high ice particle concentration, extinction and IWC values are observed in both continental and maritime anvils. While maritime anvils do not appear to spawn the extremely strong (i.e., 50 m s^{-1}) updrafts seen in continental supercells, very strong updrafts (i.e., 20 m s^{-1}) were observed in TC^4 turrets at 40,000 ft (12.5 km). A peak ice particle concentration of 30 cm^{-3} was observed in a TC^4 turret at -47°C and 10 cm^{-3} was typical in both TC^4 and NAMMA turrets. Extinction ranged from 50 to 80 km^{-1} and IWC exceeded 2 g m^{-3} in both TC^4 and NAMMA convective turrets. Particle concentrations in fresh maritime cirrus anvil s that were investigated away from active convection averaged about 1 cm^{-3}, extinction is on the order of 10 to 20 km^{-1} and IWC averaged about 0.5 g m^{-3} with peaks of 2 g m^{-3}.

Once maritime anvils detach from the active convection they may (or may not) form cirrus in situ. In regions with high relative humidity the detached anvil cirrus will form rosette shapes identical to cirrus formed in situ. Detached cirrus that formed from maritime convection in the ITCZ, observed in both TC^4 and NAMMA projects, tends to form deep (order 4 to 8 km), aged cirrus with increasing particle size from cloud top to cloud base. Particle concentrations in the deep, aged cirrus are on the order of a few to several hundreds per liter, extinction coefficient increases from a value of 0.01 km^{-1} near cloud top to 0.3 km^{-1} near cloud base, IWC increases from 0.001 g m^{-3} at cloud top to 0.3 g m^{-3} at cloud base and optical depth ranges from about 5 to 10. The observation that particle size systematically increases from cloud top to cloud base is in contrast to some previous findings that suggested that small particles were ubiquitous throughout the depth of cloud, and even more abundant near cloud base. It appears that current measurements that show the stratification of particle size, decreasing from cloud top to cloud base, are possible because errors due to large ice particles shattering on the tips of the 2D-S probe have been minimized by rejecting particles with anomalously short inter-arrival times.

Strong spatial variability in microphysical properties is found in cirrus and cirrus anvils on scales of tens and hundreds of km throughout the ITCZ, both west of Cape Verde and near Costa Rica. For example, small ice particle concentrations can vary over three orders of magnitude and IWC can vary from 0.0001 to 3 g m^{-3}, depending on the distance from convective cores and the age of the cloud. This is a consideration that needs to be taken into account for remote retrievals and numerical models.

Acknowledgements: This research is supported under funding from NASA TC4 Grant No. NASA - NNX07AK81G and NASA NAMMA Grant No. NNX06AC09G.

REFERENCES

Bailey, M and J. Hallet, 2004: Growth rates and habits of ice crystals between -20° and -70°C. *J. of Atmos. Sci.*, **61,** 514-544.

Baumgardner, D., H. Jonsson, W. Dawson, D. O'Connor and R. Newton, 2001: The cloud, aerosol and precipitation spectrometer: a new instrument for cloud investigations. *Atmos. Res.*, **59-60**, 251-264.

Connolly, P.J., C.P.R. Saunders, M. W. Gallagher, K. N. Bower, M. J. Flynn, T. W. Choularton, J. Whiteway, R. P. Lawson, 2005: Aircraft observations of the influence of electric fields on the aggregation of ice crystals, *Quart. J. Roy. Meteor. Soc.,* **18**, 1695-1712.

Field, P.R., A.J. Heymsfield, and A. Bansemer, 2006: Shattering and Particle Interarrival Times Measured by Optical Array Probes in Ice Clouds. *J. Atmos. Oceanic Technol.*, **23**, 1357–1371.

Heymsfield, A.J., 1986: Ice particle evolution in the anvil of a severe thunderstorm during CCOPE. *J. Atmos. Sci.*, **43**, 2463 - 2478.

Heymsfield, A. J., L. M. Miloshevich, C. Schmitt, A. Bansemer, C. Twohy, M. Poellot, A. Fridland, and H. Gerber, 2004: Homogeneous ice nucleation in subtropical and tropical convection and its influence on cirrus anvil microphysics. *J. Atmos. Sci.,* **62***,* 41–64*.*

Kristjánsson, J. E., J. M. Edwards, and D. L. Mitchell, 2000: Impact of a new scheme for optical properties of ice crystals on climates of two GCM's, *J. Geophys. Res.,* **105**, No. D8, 10063 – 10079.

Labonnote, L., G. Brogniez, M. Doutriaux-Boucher, J.-C. Buriez, J.-F. Gayet, and H. Chepfer, 2000: Modeling of light scattering in cirrus clouds with inhomogeneous hexagonal monocrystals. Comparison with in-situ and ADEOS-POLDER measurements. *Geophys. Res. Lett*., **27**, 113–116.

Lawson, R. P., L. J. Angus, A. J. Heymsfield, 1998: Cloud particle measurements in thunderstorm anvils and possible weather threat to aviation. *J. of Aircraft*, **35**, 113-121.

Lawson, R. P., B. A. Baker, B. Pilson, Q. Mo, 2006a: In Situ observations of the microphysical properties of wave, cirrus and anvil clouds. Part II: Cirrus Clouds. *J. Atmos. Sci*., **63**, 3186-3203.

Lawson, R. P., D. O'Connor, P. Zmarzly, K. Weaver, B. A. Baker, Q. Mo, and H. Jonsson, 2006b: The 2D-S (Stereo) Probe: Design and preliminary tests of a new airborne, high speed, high-resolution particle imaging probe. *J. Atmos. Oceanic Technol.*, **23**, 1462-1477.

Liou, K. N., 1986: Influence of cirrus clouds on weather and climate processes: A global perspective. *Mon. Wea. Rev.,* **114**, 1167-1199.

Mace, G., 2008: Personnel Communication

Pastzor, A. Airline Regulators Grapple With Engine-Shutdown Peril. Investigators Find New Icing Threat; FAA Proposes Rules, *The Wall Street Journal,* April 7, 2008, p. A1

Stephens, G. L., Tsay, S-C, Stackhouse, P. W. and Flatau, P. J., 1990: The relevance of the microphysical and radiative properties of cirrus clouds to climate and climatic feedback. *J. Atmos. Sci*., **47**, 1742-1753.

Twohy, C. H., Schanot, A. J. and W.A. Cooper, 1996: Measurement of condensed water content in liquid and ice clouds using an airborne counterflow virtual impactor. *J. Atmos. Oceanic Tech.,* **??Find vol and page number.**

CIRRUS CLOUDS AND ICE SUPERSATURATED REGIONS IN A GLOBAL CLIMATE MODEL

Ulrike Lohmann[1]*, Peter Spichtinger[1], Stephanie Heidt[1], Thomas Peter[1] and Herman Smit[2]

[1] ETH Zurich, Institute for Atmospheric and Climate Science, Switzerland
[2] Forschungszentrum Jülich, Jülich, Germany

1 ABSTRACT

At temperatures below 238 K cirrus clouds can form by homogeneous and heterogeneous ice nucleation mechanisms. A parameterization for homogeneous freezing that includes the effects of aerosol size (Kärcher and Lohmann, 2002) was implemented in the ECHAM5 global climate model (Lohmann et al., 2007). We assume that the soluble/mixed Aitken, accumulation and coarse mode aerosols are available for homogeneous freezing. For the heterogeneous freezing simulations, we consider the immersed dust particles to act as ice nuclei initiating freezing at 130% relative humidity with respect to ice. When changing the mass accommodation coefficient of water vapor on ice crystals from 0.5 in the standard ECHAM5 simulation to 0.005 as suggested by previous laboratory experiments, the number of ice crystals increases by one order of magnitude caused by the delayed relaxation of supersaturation. As the ice water path changes only by 20% in the global annual mean, the ice crystals are much smaller so that the shortwave and longwave cloud forcing at the top-of-the atmosphere change by 12 and 16 W m^{-2}, respectively. The impact of heterogeneous freezing instead of homogeneous freezing is much weaker with changes in the global annual shortwave and longwave cloud forcing of 0.6 and 1.1 W m^{-2}, respectively.

*ulrike.lohmann@env.ethz.ch

2 INTRODUCTION

Cirrus clouds can form by homogeneous and heterogeneous ice nucleation mechanisms at temperatures below 238 K. They cover on average 30% of the Earth surface and thus are important modulators of the radiation budget. Thin cirrus are semi-transparent in the solar radiation spectrum, allowing the majority of the solar radiation to be transmitted to the surface. Because of their cold temperatures, they emit the absorbed infrared radiation at much colder temperatures than the Earth's surface and thus cause a warming of the Earth-atmosphere system (Chen et al., 2000). Only for thick cirrus, the reflected shortwave and emitted longwave radiation are comparable in magnitude.

While homogeneous freezing of supercooled aqueous phase aerosol particles is rather well understood, understanding of heterogeneous ice nucleation is still in its infancy. A change in the number of ice crystals in cirrus clouds could exert a cloud albedo effect in the same way that the cloud albedo effect acts for water clouds. It refers to the change in the radiative forcing at the top-of-the-atmosphere caused by an enhancement in cloud albedo from anthropogenic aerosols that lead to more and smaller cloud droplets for a given cloud water content. In addition, a change in the cloud ice water content could exert a radiative effect in the infrared. The magnitude of these effects in the global mean has not yet been fully established, but the development of physically based parametrization schemes of cirrus formation for use in global models led to significant progress in understanding underlying mechanisms of aerosol-induced cloud modifications (Kärcher and Lohmann, 2002; Liu and Penner, 2005; Kärcher et al., 2006; Liu et al., 2007).

A global climate model study concluded that a cloud albedo effect based solely on ubiquitous homogeneous freezing is small globally (Lohmann and Kärcher, 2002). This is expected to also hold in the presence of heterogeneous IN that cause cloud droplets to freeze at relative humidities over ice close to homogeneous values (above 130-140%) (Kärcher and Lohmann, 2003). Efficient heterogeneous IN, however, would be expected to lower the relative humidity over ice, so that the climate effect may be larger (Liu and Penner, 2005). In situ measurements reveal that organic-containing aerosols are less abundant than sulphate aerosols in ice cloud particles, suggesting that organics do not freeze preferentially (Cziczo et al., 2004). A model study explains this finding by the disparate water uptake of organic aerosols, and suggests that organics are unlikely to significantly modify cirrus formation unless they are present in very high concentrations (compared with sulphate-rich particles) at low temperatures (Kärcher and Koop, 2005). Recent high-altitude aircraft measurements indicated the presence of rather large, thin hexagonal plate ice crystals near the tropical tropopause in very low concentrations that are suggested to result from ice nucleation on effective heterogeneous nuclei at low ice supersaturations (Jensen et al., 2008).

Besides nucleation effects, ice growth impedances were recently found to lead potentially to high supersaturations within cirrus clouds (Peter et al., 2006). The role of physicochemical processes affecting the accommodation coefficient of water vapour on ice and of water vapour on aerosols is presently unclear. These effects could be related to unknown intrinsic properties of the ice substance at the extreme temperatures at high tropical cirrus levels, or due to natural or anthropogenic species on the ice surface (Wood et al., 2001). Magee et al. (2006) suggested that assuming accommodation coefficients between 0.0045 and 0.0075 was necessary to match laboratory data of ice crystal growth at temperatures between -40 and -60°C and variable supersaturations.

The properties and global distributions of ice supersaturated regions (ISSRs) were discovered during the last years, e.g., Spichtinger et al. (2003); Gettelman et al. (2006). ISSRs are potential formation regions of cirrus and persistent contrails. They are rather ubiquitous (Spichtinger et al., 2003) in the upper tropical troposphere, with frequencies of occurrence even exceeding 50% of the time at 150 hPa. Immler et al. (2008) evaluated lidar data over Northern Germany and concluded that 50% of the air at 11-12 km was supersaturated with respect to ice.

In this paper, we discuss the impact of heterogeneous freezing versus homogeneous freezing and of variations in the deposition coefficient on cirrus cloud properties and ice supersaturation.

3 MODEL DESCRIPTION

We use the ECHAM5 general circulation model (GCM) (Roeckner et al., 2003) to estimate the importance of aerosol effects on convective clouds. The version of ECHAM5 used in this study includes the double-moment aerosol scheme ECHAM5-HAM that predicts the aerosol mixing state in addition to the aerosol mass and number concentrations (Stier et al., 2005). The size-distribution is represented by a superposition of log-normal modes including the major global aerosol compounds sulfate, black carbon, organic carbon, sea salt and mineral dust.

The stratiform cloud scheme consists of prognostic equations for the water phases (vapor, liquid, solid), bulk cloud microphysics (Lohmann and Roeckner, 1996), and an empirical cloud cover scheme (Sundqvist et al., 1989). The microphysics scheme includes phase changes between the water components and precipitation processes (autoconversion, accretion, aggregation). Moreover, evaporation of rain and melting of snow are considered, as well as sedimentation of cloud ice. It also includes prognostic equations of the number concentrations of cloud droplets and ice crystals in stratiform and convective clouds and has been coupled to the aerosol scheme ECHAM5-HAM (Lohmann, 2008). In the standard simulation that assumes cirrus cloud formation solely by homogeneous freezing, ECHAM5-hom (Table 1) an accommodation coefficient α for depositional growth of water vapor onto ice crystals of 0.5 is employed (Kärcher and Lohmann, 2002).

The version of the model used here includes a few changes. Ice crystals are now regarded as plates as this is a more realistic shape for ice crystals in clouds within the mixed-phase regime between 0 and -35° C than assuming spherical crystals (Pruppacher and Klett, 1997). This affects the depositional growth equation where the capacitance C now becomes $C = 2r/\pi$ instead of $C = r$, where r is the equivalent crystal radius:

$$Q_{dep} = \left(\frac{\partial q_i}{\partial t}\right)_{dep} = 4\pi C \alpha A_T f_{Re}(S_i - 1)N_i \quad (1)$$

Here q_i is the ice water mixing ratio, f_{Re} is the ventilation factor as a function of the Reynolds number, S_i is the saturation ratio over ice at the beginning of the time step, N_i is the ice crystal number concentration, and A_T is defined as:

$$A_T = \left(\rho\left[\frac{L_s}{k_a T}\left\{\frac{L_s}{R_v\,T} - 1\right\} + \frac{R_v T}{D_v e_{si}}\right]\right)^{-1},$$

Here T is the temperature, L_s is the latent heat of sublimation, k_a is the thermal conductivity of air, R_v is the gas constant of water vapor, D_v is the diffusivity of water vapor in air, and e_{si} is the saturation vapor pressure over a plane ice surface.

Assuming ice crystals to be plates also changes the calculation of the ice crystal effective radius r_i, which is now given as described in Pruppacher and Klett (1997) for a plate of type P1a (in μm):

$$r_i = 0.5 \cdot 10^4 \left(\frac{IWC}{0.0376 N_i}\right)^{0.302} \quad (2)$$

where N_i is the ice crystal number concentration in m^{-3} and IWC is the ice water content in g m^{-3}.

The fall velocity of ice crystals has been changed to one appropriate for monodisperse crystals, that vary their shapes with increasing size following Spichtinger and Gierens (2008). Assuming monodisperse crystals is consistent with the other formulations for microphysical processes in the model and allows us to use the same fall velocity for number and mass.

Also, the critical thickness necessary for the onset of convective precipitation p_c has been changed. While it was set to 150 hPa over oceans and 300 hPa over land in the simulations described in Lohmann (2008), here we use an observed relationship between the depth above cloud base at which precipitation is initiated, p_c in Pa, as a function of the cloud droplet number concentration N_l in cm^{-3} based on data obtained in the Amazon (Freud et al., 2008) and Freud, pers. comm. 2007:

$$p_c = (293 + 2.73 N_l) g \rho \quad (3)$$

where g is the acceleration due to gravity and ρ is the air density.

3.1 Set-up of the simulations

The ECHAM5 simulations have been carried out in T42 horizontal resolution (2.8125° × 2.8125°) and 19 vertical levels with the model top at 10 hPa and a timestep of 30 minutes. All simulations used climatological sea surface temperature (SST) and sea-ice extent. They were simulated for 5 years after an initial spin-up of 3 months using aerosol emissions for the year 2000.

The reference simulation ECHAM5-hom is conducted such that the global annual mean radiation budget is balanced to within 1 W m^{-2} at the top-of-the-atmosphere (TOA) and that the values of the shortwave and longwave cloud

Tab. 1: Sensitivity Simulations

Simulation	Description
ECHAM5-hom	Simulation with ECHAM5-HAM coupled to the double-moment cloud microphysics scheme for stratiform and convective clouds (Lohmann, 2008) assuming that all cirrus cloud form by homogeneous freezing
ECHAM5-het	As ECHAM5-hom, but assuming that all immersed dust particles are available as immersion freezing nuclei initiating freezing at 130% relative humidity with respect to ice
ECHAM5-alpha	As ECHAM5-hom, but decreasing the accommodation coefficient from 0.5 to 0.005

forcings are within the uncertainty of the radiative flux measurements of $\pm$ 5 W m^{-2} as reported by Kiehl and Trenberth (1997). This required changing the critical radius above which aerosols could possible act as CCN from 35 nm to 30 nm for stratiform clouds and from 25 nm to 20 nm for convective clouds.

In the sensitivity experiment ECHAM5-het (Table 1), homogeneous freezing of potentially all supercooled soluble/mixed aerosol particles was replaced by heterogeneous immersion freezing following Kärcher and Lohmann (2003). As there is currently no consensus on the freezing ability of black carbon, e.g. (Möhler et al., 2005; Dymarska et al., 2006), we limit the number of heterogeneous ice nuclei to the number of immersion mode dust particles as described by Hoose et al. (2008). In simulation ECHAM5-alpha, the accommodation coefficient of water vapor on ice crystals has been decreased from 0.5 in simulations ECHAM5-hom and ECHAM5-het to 0.005 as suggested by laboratory experiment (Magee et al., 2006).

4 MODEL EVALUATION

Validation of the coupled aerosol-cloud microphysics scheme in stratiform clouds is described in Lohmann et al. (2007). Here we focus on the validation of ice supersaturated regions (ISSR) and cirrus clouds.

An overview of the global-mean cloud properties is given in Table 2. The most striking difference between ECHAM5-alpha and ECHAM5-hom is the tenfold increase in the number concentration in ice crystals in ECHAM5-alpha. This results from the slower depositional growth that cannot deplete the supersaturation effectively. In fact, the water vapor has increased by 2.7 kg m^{-2} in the global mean. As a result of the slower depletion of supersaturation, more ice crystals are nucleated. These ice crystals do not grow as large thus slowing down the precipitation formation rate and increasing the amount of cloud ice that remains within the atmosphere (cf. Table 2). This reduces the global mean precipitation by 0.39 mm/d in ECHAM5-alpha as compared to ECHAM5-hom. The more numerous and smaller ice crystal scatter more radiation back to space, thus enhancing the shortwave cloud forcing by 11.6 W m^{-2} to -62.7 W m^{-2}. At the same time, more longwave radiation is trapped in the Earth atmosphere system, increasing the longwave cloud forcing by 16.1 W m^{-2} to 41.1 W m^{-2}. Changes in liquid water clouds are much smaller and thus not shown.

The differences between ECHAM5-hom and ECHAM5-het are more modest. Here the ice crystal number concentration decreases by 16%, which reduces the shortwave and longwave cloud forcing by 0.6 and 1.1 W m^{-2}, respectively. The changes are smaller than in the previous version of the ECHAM4 GCM (Lohmann et al., 2004), because there are fewer aerosols in the upper troposphere in ECHAM4 (Lohmann et al., 2007). Thus, limiting heterogeneous freezing by the smaller amount of dust particles in ECHAM4 reduces the ice crystal number concentration more than in ECHAM5-het.

Annual zonal means of the vertically inte-

Tab. 2: Annual global mean cloud properties. Ice water path (IWP) has been derived from ISCCP data (Storelvmo et al., 2008). Water vapor mass (WVM) data stem from MODIS. N_i refers to the vertically integrated ice crystal number concentration. Total precipitation (P_{tot}) is taken from the Global Precipitation Climatology Project (Adler et al., 2003). Total cloud cover (TCC) is obtained from surface observations (Hahn et al., 1994), ISCCP (Rossow and Schiffer, 1999) and MODIS data (King et al., 2003). The shortwave (SCF), longwave (LCF) and net cloud forcing (CF) estimates are taken from Kiehl and Trenberth (1997). In addition estimates of LCF from TOVS retrievals (Susskind et al., 1997; Scott et al., 1999) and SCF retrievals from CERES (Kim and Ramanathan, 2008) are included.

Simulation	ECHAM5-hom	ECHAM5-het	ECHAM5-alpha	OBS
IWP, g m^{-2}	9.4	9.3	11.2	29
N_i, 10^{10} m^{-2}	0.38	0.32	4.2	
WVM, kg m^{-2}	26.1	25.7	28.8	25.1
TCC, %	68.6	66.4	72.5	62-67
P_{tot}, mm d^{-1}	2.95	2.99	2.56	2.74
SCF, W m^{-2}	-51.1	-50.5	-62.7	-46.5 to -50
LCF, W m^{-2}	25.0	23.9	41.1	22-30
CF, W m^{-2}	26.1	26.6	21.6	-19 to -27

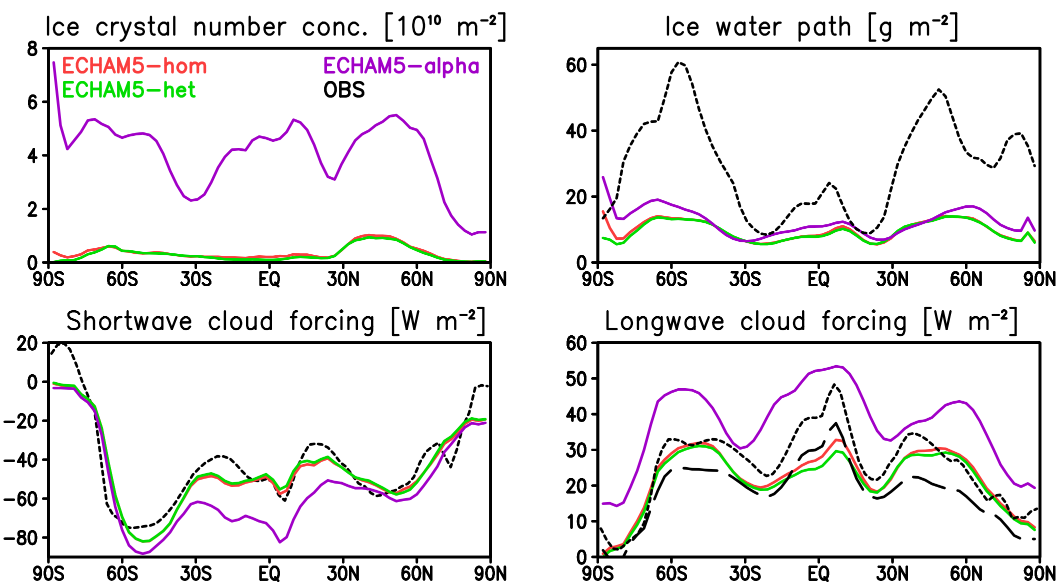

Fig. 1: Annual zonal means of ice water path, vertically integrated ice crystal number concentration, and of the shortwave and longwave cloud forcing from the different model simulations described in Table 1 and from observations described in Table 2. Dotted black lines refer to ISCCP data for IWP (Storelvmo et al., 2008) and to ERBE for the shortwave and longwave cloud forcing. The dashed line refers to TOVS data (Susskind et al., 1997; Scott et al., 1999).

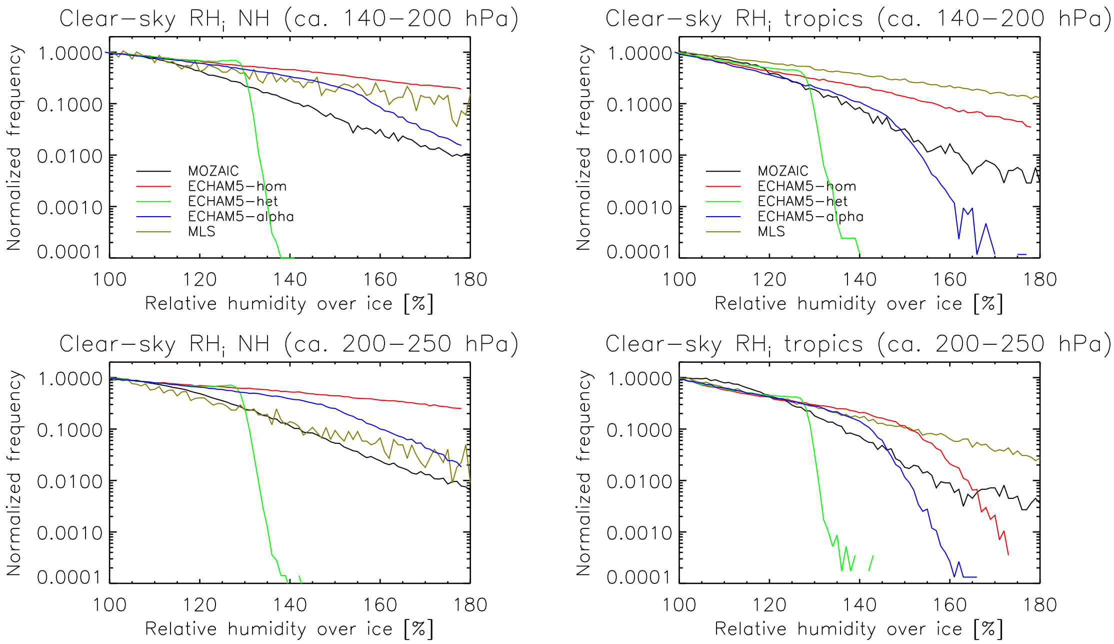

Fig. 2: Frequency of occurrence of relative humidity with respect to ice in the Northern Hemisphere (30°N-90°N) [left panel] and in the tropics (30°S-30°N) [right panel] in two different levels from MOZAIC aircraft data, MLS satellite data and from the simulations ECHAM5-hom, ECHAM5-het and ECHAM5-alpha.

grated ice crystal number concentration, ice water path, shortwave and longwave cloud forcing are shown in figure 1. Most noticeable is the smaller ice water path than observed and than simulated with the previous version of ECHAM5 (Lohmann et al., 2007). This is due to the changes to the model mentioned above. However, one has to bear in mind that the retrieval of the ice water path is very uncertain at this point. The shortwave and longwave cloud forcing of ECHAM5-hom and ECHAM5-het agree well with the observations, except that the longwave cloud forcing is underestimated in the topics. This suggests that the cirrus clouds are either not high enough or not thick enough. Given that the agreement was better in the previous version of ECHAM5 (Lohmann et al., 2007) where the ice water path was higher, the reduced ice water path is the likely cause for this discrepancy. Unfortunately there are no observations of the ice crystal number concentration, thus no conclusions about the right order of magnitude can be drawn.

The frequency of occurrence of different supersaturations with respect to ice in cloud-free regions has been obtained from MOZAIC aircraft data (Helten et al., 1998; Spichtinger et al., 2004) and MLS satellite data (Read et al., 2001; Spichtinger et al., 2003) (Figure 2). Both observational data suggest an exponential decrease for relative humidities with respect to ice (RH$_i$) for RH$_i$ above 100%. They differ in the slope, with the MLS slope being less steep.

In the simulations, we obtained RH$_i$ by restricting the analysis to grid boxes with less than 0.1 mg/kg condensate. In the Northern Hemisphere, the exponential decrease of RH$_i$ in simulation ECHAM5-hom is not as pronounced as suggested in the observations, especially as derived from MOZAIC data. The exponential decrease it better matched in the tropics, where it lies between the observational estimates. In simulation ECHAM5-alpha, the agreement with observations is better for RH$_i$ below 145% in the tropics and generally better than in simulation ECHAM5-hom in the Northern Hemisphere. This could suggest that the ice crystals in ECHAM5-hom sediment out too rapidly so that RH_i cannot be sufficiently depleted. Simulation ECHAM5.5-het does not agree well with observations at RH_i exceeding 130% because by design it depletes higher RH_i, while they are observed rather frequently in observations (Figure 2 and Peter et al. (2006)).

One difference between the MLS and MOZAIC observations is the cloud screening. While MLS is restricted to clear-skies (Spichtinger et al., 2003), MOZAIC detects supersaturation in cirrus clouds as well. Varying the threshold of cloud condensate in the model simulations does not affect the exponential slope significantly (not shown).

5 CONCLUSIONS

The homogeneous freezing scheme for cirrus clouds that was developed and tested in ECHAM4 has been incorporated into ECHAM5 (Lohmann et al., 2007). Here we tested its sensitivity with respect to the accommodation coefficient and with respect to heterogeneous versus homogeneous freezing.

The main findings are:

- If α is decreased from 0.5 to 0.005, then the ice crystal number concentration increases by one order of magnitude, while the impact on ice water content and cloud cover is much smaller.
- This changes the global annual mean shortwave and longwave cloud forcing by 12 and 16 W m^{-2}, respectively.
- The impact of heterogeneous freezing versus homogeneous freezing is much weaker with global annual mean changes of the shortwave and longwave cloud forcing by 0.6 and 1.1 W m^{-2}.

REFERENCES

Adler, R. F., Huffman, G. J., Chang, A., Ferraro, R., Xie, P. P., Janowiak, J., Rudolf, B., Schneider, U., Curtis, S., Bolvin, D., Gruber, A., Susskind, J., Arkin, P., Nelkin, E., 2003. The version-2 global precipitation climatology project (GPCP) monthly precipitation analysis (1979-present). J. Hydrometeor. 4 (6), 1147–1167.

Chen, T., Rossow, W. B., Zhang, Y. C., 2000. Radiative effects of cloud-type variations. J. Climate 13 (1), 264–286.

Cziczo, D. J., DeMott, P. J., Brooks, S. D., Prenni, A. J., Thomson, D. S., Baumgardner, D., Wilson, J. C., Kreidenweis, S. M., Murphy, D. M., 2004. Observations of organic species and atmospheric ice formation. Geophys. Res. Lett. 31, doi: 10.1029/2004GL019822.

Dymarska, M., Murray, B. J., Sun, L. M., Eastwood, M. L., Knopf, D. A., Bertram, A. K., 2006. Deposition ice nucleation on soot at temperatures relevant for the lower troposphere. J. Geophys. Res. 111 (D4).

Freud, E., Rosenfeld, D., Andreae, M. O., Costa, A. A., Artaxo, P., 2008. Robust relations between ccn and the vertical evolution of cloud drop size distribution in deep convective clouds. Atmos. Chem. Phys. 8 (6), 1661–1675.

Gettelman, A., Fetzer, E. J., Eldering, A., Irion, F. W., 2006. The global distribution of supersaturation in the upper troposphere from the atmospheric infrared sounder. J. Climate 19 (23), 6089–6103.

Hahn, C. J., Warren, S. G., London, J., 1994. Climatological data for clouds over the globe from surface observations, 1982-1991: The total cloud edition. Tech. rep., ORNL/CDIAC-72 NDP-026A Oak Ridge National Laboratory, Oak Ridge Tennessee, U.S.A.

Helten, M., Smit, H. G. J., Strater, W., Kley, D., Nedelec, P., Zoger, M., Busen, R., 1998. Calibration and performance of automatic compact instrumentation for the measurement of relative humidity from passenger aircraft. J. Geophys. Res. 103 (D19), 25643–25652.

Hoose, C., Lohmann, U., Erdin, R., Tegen, I., 2008. Global influence of dust mineralogical composition on heterogeneous ice nucleation in mixed-phase clouds. Environ. Res. Lett.In press.

Immler, F., Treffeisen, R., Engelbart, D., Krüger, K., Schrems, O., 2008. Cirrus, contrails, and ice supersaturated regions in high pressure systems at northern mid latitudes. Atmos. Chem. Phys. 8, 1689–1699.

Jensen, E. J., Pfister, L., Bui, T. V., Lawson, P., Baker, B., Mo, Q., Baumgardner, D., Weinstock, E. M., Smith, J. B., Moyer, E. J., Hanisco, T. F., Sayres, D. S., St. Clair, J. M., Alexander, M. J., Toon, O. B., Smith, J. A., 2008. Formation of large ($\sim 100\mu$m) ice crystals near the tropical tropopause. Atmos. Chem. Phys. 8, 1621–1633.

Kärcher, B., Hendricks, J., Lohmann, U., 2006. Physically based parameterization of cirrus cloud formation for use in global atmospheric models. J. Geophys. Res. 111 (D1), doi: 10.1029/2005JD006219, d01205.

Kärcher, B., Koop, T., 2005. The role of organic aerosols in homogeneous ice formation. Atmos. Chem. Phys. 5, 703–714.

Kärcher, B., Lohmann, U., 2002. A parameterization of cirrus cloud formation: Homogeneous freezing of supercooled aerosols. J. Geophys. Res. 107, doi: 10.1029/2001JD000470.

Kärcher, B., Lohmann, U., 2003. A parameterization of cirrus cloud formation: Heterogeneous freezing. J. Geophys. Res. 108, doi: 10.1029/2002JD003220.

Kiehl, J. T., Trenberth, K. E., 1997. Earth's annual global mean energy budget. Bull. Amer. Meteorol. Soc. 78 (2), 197–208.

Kim, D. Y., Ramanathan, V., 2008. Solar radiation budget and radiative forcing due to aerosols and clouds. J. Geophys. Res. 113, doi:10.1029/2007JD008434, d02203.

King, M. D., Menzel, W. P., Kaufman, Y. J., Tanre, D., Gao, B. C., Platnick, S., Ackerman, S. A., Remer, L. A., Pincus, R., Hubanks, P. A., 2003. Cloud and aerosol properties, precipitable water, and profiles of temperature and water vapor from MODIS. IEEE Trans. Geo. Rem. Sens. 41 (2), 442–458.

Liu, X., Penner, J. E., Ghan, S. J., Wang, M., 2007. Inclusion of ice microphysics in the ncar community atmospheric model version 3 (cam3). J. Climate 20, 4526–4547.

Liu, X. H., Penner, J. E., 2005. Ice nucleation parameterization for global models. Meteorol. Z. 14 (4), 499–514.

Lohmann, U., 2008. Global anthropogenic aerosol effects on convective clouds in ECHAM5-HAM. Atmos. Chem. Phys. 8, 2115–2131.

Lohmann, U., Kärcher, B., 2002. First interactive simulations of cirrus clouds formed by homogeneous freezing in the ECHAM GCM. J. Geophys. Res. 107, doi: 10.1029/2001JD000767, d4105.

Lohmann, U., Kärcher, B., Hendricks, J., 2004. Sensitivity studies of cirrus clouds formed by heterogeneous freezing in the echam gcm. J. Geophys. Res 109, 10.1029/2003JD004443, d16204.

Lohmann, U., Roeckner, E., 1996. Design and performance of a new cloud microphysics scheme developed for the ECHAM general circulation model. Clim. Dyn. 12, 557–572.

Lohmann, U., Stier, P., Hoose, C., Ferrachat, S., Kloster, S., Roeckner, E., Zhang, J., 2007. Cloud microphysics and aerosol indirect effects in the global climate model echam5-ham. Atmos. Chem. Phys. 7, 3425–3446.

Magee, N., Moyle, A. M., Lamb, D., 2006. Experimental determination of the deposition coefficient of small cirrus-like ice crystals near-50 degrees c. Geophys. Res. Lett. 33 (17).

Möhler, O. M., Buttner, S., Linke, C., Schnaiter, M., Saathoff, H., Stetzer, O., Wagner, R., Kramer, M., Mangold, A., Ebert, V., Schurath, U., 2005. Effect of sulfuric acid coating on heterogeneous ice nucleation by soot aerosol particles. Journal of Geophysical Research-Atmospheres 110 (D11), d11210.

Peter, T., Marcolli, C., Spichtinger, P., Corti, T., Baker, M. B., Koop, T., 2006. When dry air is too humid. Science 314 (5804), 1399–1401.

Pruppacher, H. R., Klett, J. D., 1997. Microphysics of Clouds and Precipitation. Kluwer Acad., Norwell, Mass.

Read, W. G., Waters, J. W., Wu, D. L., Stone, E. M., Shippony, Z., 2001. UARS Microwave Limb Sounder upper tropospheric humidity measurement: Method and validation. J. Geophys. Res. 106, 32,207–32,258.

Roeckner, E., Bäuml, G., Bonaventura, L., Brokopf, R., Esch, M., Giorgetta, M., Hagemann, S., Kirchner, I., Kornblueh, L., Manzini, E., Rhodin, A., Schlese, U., Schulzweida, U., Tompkins, A., 2003. The atmospheric general circulation model ECHAM5. part i: Model description. Tech. Rep. 349, Max-Planck-Inst. für Meteorol., Hamburg, Germany.

Rossow, W. B., Schiffer, R. A., 1999. Advances in understanding clouds from ISCCP. Bull. Amer. Meteorol. Soc. 80, 2261–2287.

Scott, N. A., Chedin, A., Armante, R., Francis, J., Stubenrauch, C., Chaboureau, J. P., Chevallier, F., Claud, C., Cheruy, F., 1999. Characteristics of the TOVS Pathfinder Path-B dataset. Bull. Amer. Meteorol. Soc. 80 (12), 2679–2701.

Spichtinger, P., Gierens, K., 2008. Modelling of cirrus clouds - Part 1: Model description and validation. Atmos. Chem. Phys. Discuss. 8, 601–686.

Spichtinger, P., Gierens, K., Read, W., 2003. The global distribution of ice-supersaturated regions as seen by the Microwave Limb Sounder. Q. J. R. Meteorol. Soc. 129, 3391–3410.

Spichtinger, P., Gierens, K., Smit, H. G. J., Ovarlez, J., Gayet, J. F., 2004. On the distribution of relative humidity in cirrus clouds. Atmos. Chem. Phys. 4, 639–647.

Stier, P., Feichter, J., Kinne, S., Kloster, S., Vignati, E., Wilson, J., Ganzeveld, L., Tegen, I., Werner, M., Balkanski, Y., Schulz, M., Boucher, O., Minikin, A., Petzold, A., 2005. The aerosol-climate model ECHAM5-HAM. Atmos. Chem. Phys. 5, 1125–1156.

Storelvmo, T., Kristjansson, J.-E., Lohmann, U., 2008. Aerosol influence on mixed-phase clouds in CAM-Oslo. J. Atmos. Sci.In press.

Sundqvist, H., Berge, E., Kristiansson, J. E., 1989. Condensation and cloud parameterization studies with a mesoscale numerical weather prediction model. Mon. Wea. Rev. 117, 1641–1657.

Susskind, J., Piraino, P., Rokke, L., Iredell, T., Mehta, A., 1997. Characteristics of the TOVS Pathfinder Path A dataset. Bull. Amer. Meteorol. Soc. 78 (7), 1449–1472.

Wood, S. E., Baker, M. B., Calhoun, D., 2001. New model for the vapor growth of hexagonal ice crystals in the atmosphere. J. Geophys. Res. 106, 4845–4870.

CONTRIBUTIONS OF SMALL ICE CRYSTALS TO NUMBER, MASS AND EXTINCTION IN TROPICAL CIRRUS: IN-SITU OBSERVATIONS FROM TWP-ICE AND PRIOR CAMPAIGNS

Greg M. McFarquhar[1], Junshik Um[1], Matt Freer[1], Darrel Baumgardner[2], Greg Kok[3] and Gerald Mace[4]

[1]University of Illinois at Urbana-Champaign, Urbana, IL
[2]Universidad Nacional Autonoma de Mexico, Mexico City, Mexico
[3]Droplet Measurement Technologies, Boulder, CO
[4]University of Utah, Salt Lake City, UT

1. INTRODUCTION*

Cirrus covers about 20% of the Earth's surface and is almost exclusively composed of ice crystals. To represent cloud feedbacks in global climate models and to improve predictions of future climate change, the effects of cirrus on longwave and shortwave radiation must be quantified. At a microphysical level, the distributions of crystal sizes and shapes are most important for determining how cirrus impact radiative heating. The Tropical Warm Pool International Cloud Experiment (TWP-ICE), based out of Darwin Australia between 21 January and 14 February 2006, was held to study the interaction of convection with its environment, with an emphasis on the microphysical and radiative properties of anvils generated by convection. Other experiments in the Tropics, including the Central Equatorial Pacific Experiment (CEPEX, McFarquhar and Heymsfield 1996), the Costa Rica Aura Validation Experiment (CR-AVE) and many others, have also measured the microphysical properties of anvils.

One controversial and unsolved problem that impacts our ability to assess cloud feedbacks in the Tropics is quantifying the contributions of small ice crystals (hereafter ice crystals with $D < 50$ μm) to the mass and scattering properties of cirrus. Contradictory conclusions on the importance of small ice crystals have been reached. Both the Cloud and Aerosol Spectrometer (CAS) and Forward Scattering Spectrometer Probe (FSSP) detect particle size from the amount of forward scattered light and have a protruding shroud or inlet near the sample volume to direct airflow. Studies using a CAS or FSSP have shown small ice crystals can make substantial contributions to cirrus mass or extinction (e.g., Knollenberg et al. 1993; Ivanova et al. 2001; Garrett et al. 2003). Although studies using a Video Ice Particle Sampler (McFarquhar and Heymsfield 1996) have also showed number concentrations of small crystals 2 orders of magnitude greater than those with $D > 80$ μm, measured concentrations were less than those from a co-located FSSP. Gardiner and Hallett (1985) found FSSP concentrations a factor of 300 greater than those measured by a formvar replicator in mixed-phase clouds and Gayet et al. (1996) found enhanced FSSP counts in the presence of large ice crystals. The shattering of large ice crystals on protruding components of the FSSP/CAS into several hundred smaller ones (Korolev and Isaac 2005) has been hypothesized as an explanation for the observations of large concentrations of small ice crystals. Field et al. (2003) suggested FSSP concentrations could be overestimated by a factor between 1.05 and 4.

There is a critical need to determine if the shattering of large ice crystals on the protruding shroud of the CAS and the arms and inlet of the FSSP artificially enhance small crystal concentrations. Here, the influence of shattering on small ice crystal concentrations is estimated using data obtained in cirrus during TWP-ICE, CR-AVE and CEPEX.

2. MEASUREMENTS

In-situ measurements of aging anvils, fresh anvils and cirrus of unknown origin were made by the Scaled Composites Proteus aircraft during TWP-ICE based out of Darwin Australia between 21 January and 14 February 2006. The Proteus was equipped with a CAS sizing between 0.5 and 50 μm, a Cloud Droplet Probe (CDP, 2 to 50 μm), and a Cloud Imaging Probe (CIP, 25 to 1550 μm). The Droplet Measurement Technologies CAS and CDP, shown in Figure 1, use a solid angle of 4 to 12^{o} for collecting forward scattered light, the former detecting all forward scattered light, and the later masked with a rectangular slit so that it only detects scattered light from particles within a certain distance of the center of focus.

The same look-up table is used for both instruments to convert scattering intensity to particle size. Thus, any uncertainties in derived size are related to either the refractive index or shape, both of which are identical in each instrument. As seen in Fig. 1, the aerodynamic shape of the two spectrometers differs in that the CAS has an inlet and the CDP has none. The distance from the lip of the CAS inlet to the center of the sample volume is 25.4 cm. The CAS has an inlet with an inner and outer diameter of 0.031 and 0.04 m and a shroud with an inner and outer diameter of 0.16 and 0.21 m. Thus, comparison of the CDP and CAS tests whether CAS concentrations were inflated by shattering. Other data used here include high resolution images of ice crystals between 15 and 1500 μm from the Cloud Particle Imager (CPI), and measurements of liquid water content (LWC) from a Nevzorov probe. The average true air speed for the time of the observations was 130 m s^{-1}.

CR-AVE was conducted during the same time period as TWP-ICE, but based out of San Jose, Costa Rica using the NASA WB-57 aircraft. Identical instruments were used during CR-AVE as during TWP-ICE except no shroud was used on the CAS. Thus, comparisons of

* Corresponding Author: Prof. McFarquhar, University of Illinois, Dept. of Atmospheric Science, 105 S. Gregory Street, Urbana, IL, 61801.

the two datasets can help assess the degree to which the shroud on the CAS may influence the small crystal contributions.

Figure 1: Pictures of the CAS as configured for TWP-ICE and CR-AVE, and of the CDP as configured for both TWP-ICE and CR-AVE.

CEPEX was conducted between 7 March and 5 April 1993 based out of Nadi, Fiji with data collected between 20°S and 2°N latitude and between 165°E and 170°W longitude. The microphysical data were collected by the Aeromet Learjet which was equipped with a Particle Measuring Systems (PMS) two-dimensional cloud probe (2DC), a PMS two-dimensional precipitation probe (2DP), a forward-scattering spectrometer probe model 300 (FSSP-300) and the Video Ice Particle Sampler (VIPS). Based on the VIPS and FSSP data, McFarquhar and Heymsfield (1997) parameterized the ice crystal size distributions from which the contributions of small ice crystals can be computed. Comparison of data from the VIPS, an impactor probe, against data from the FSSP, is valuable for assessing the degree of scattering that might be occurring on the FSSP.

3. RESULTS

Because the CAS and CDP have different and somewhat uncertain lower size thresholds, the threshold of the second channel of the CDP (3 μm) was used as the starting size for comparing concentrations measured by the CAS and CDP during TWP-ICE. Figure 2a shows the number concentration of particles with $3 < D < 50$ μm measured by the CAS, $N_{3\text{-}50,CAS}$, as a function of that measured by the CDP, $N_{3\text{-}50,CDP}$. Data are included from flights on 27 and 29 January and 2 February when all of the CAS, CDP and CIP were operational. Each point represents a 10 s average and is colored according to 4 ranges of $N_{>100}$ measured by the CIP: $N_{>100} = 0$ L^{-1}, $0 < N_{>100} < 0.1$ L^{-1}, $0.1 < N_{>100} < 1$ L^{-1}, and $N_{>100} > 1$ L^{-1}. For points when $N_{3\text{-}50,CDP} < 10^3$ L^{-1} the ratio of $N_{3\text{-}50,CAS}/N_{3\text{-}50,CDP}$ averaged 91±127 whereas it averaged only 0.98±0.69 when $N_{>3\text{-}50,CDP} > 10^3$ L^{-1}. The points with $N_{3\text{-}50,CDP} > 10^3$ L^{-1} were obtained at temperatures near +10°C during spiral descents of the Proteus over Darwin or near -35°C at times when the Nevzorov probe detected water. In these cases, no non-spherical particles were detected by either the CPI or the CIP suggesting little, if any, ice was present.

Points in Fig. 2a with $N_{3\text{-}50,CDP} < 10^3$ L^{-1} were obtained when no liquid water was detected. Thus, the almost 2 orders of magnitude disagreement between $N_{3\text{-}50,CAS}$ and $N_{3\text{-}50,CDP}$ is associated with the presence of ice. There is a strong suggestion that the shattering of large ice crystals is at least partially responsible for this discrepancy because the ratio $N_{3\text{-}50,CAS}/N_{3\text{-}50,CDP}$ gets larger as $N_{>100}$ increases in Fig. 2. However, because $N_{3\text{-}50,CAS}$ was still 20±33 times larger than $N_{3\text{-}50,CDP}$ in ice even when $N_{>100} = 0$, the shattering of ice crystals with $D < 50$ μm may also contribute to enhancing $N_{3\text{-}50,CAS}$. Additional analysis (figures not shown) showed that no single variable, such as the temperature, CAS, CDP or CIP mean diameter could reduce the scatter in the $N_{3\text{-}50,CAS}/N_{3\text{-}50,CDP}$ observed in Fig. 2a.

The sizing of non-spherical ice particles by forward scattering probes is uncertain because sizes derived from Mie theory apply only to spherical particles. Nevertheless, the ratio of $N_{x\text{-}50,CAS}/N_{x\text{-}50,CDP}$, where x denotes the lower limit of the size range, was examined for x of 3, 5, 10 and 25 μm as a function of $N_{>100}$ (figures not shown) to determine the sizes most responsible for differences between the CAS and CDP. The ratio was represented by

$$\frac{N_{x-50,CAS}}{N_{x-50,CDP}} = AN_{>100}^{B} \qquad (1)$$

where A and B are obtained from a regression analysis. A statistically significant relationship between $N_{x\text{-}50,CAS}/N_{x\text{-}50,CDP}$ and $N_{>100}$ exists for x=3, 5 and 10 μm (correlations of 0.387, 0.366, 0.305), but not for x=25 μm (0.036 correlation). The lack of correlation of $N_{25\text{-}50,CAS}/N_{25\text{-}50,CDP}$ with $N_{>100}$ suggests that shattering on the inlet or shroud may be predominantly producing ice crystals with $D < 25$ μm during TWP-ICE. Further, the $N_{x\text{-}50,CAS}/N_{x\text{-}50,CDP}$ ratio was larger for smaller x showing crystals with $D < 25$ μm are most responsible for the difference between $N_{3\text{-}50,CAS}$ and $N_{3\text{-}50,CDP,}$ and hence are those produced by shattering.

CR-AVE data were also examined to assess if shattering might have occurred on the CAS during that experiment. Figure 3 shows the CAS and CDP concentrations in 4 size ranges as a function of IWC estimated assuming spherical particles for TWP-ICE and two CR-AVE cases: in case 1 there was reasonable CIP activity whereas case 2 was in cold thin cirrus with minimal CIP activity. The CAS concentrations from CR-AVE average an order of magnitude less than those from TWP-ICE for the 5-10 and 10-15 μm size ranges. Although lower IWCs were noted during CR-AVE and variations in crystal concentration-IWC relations are expected due to different cloud conditions and geographic locations, the order of magnitude reduced

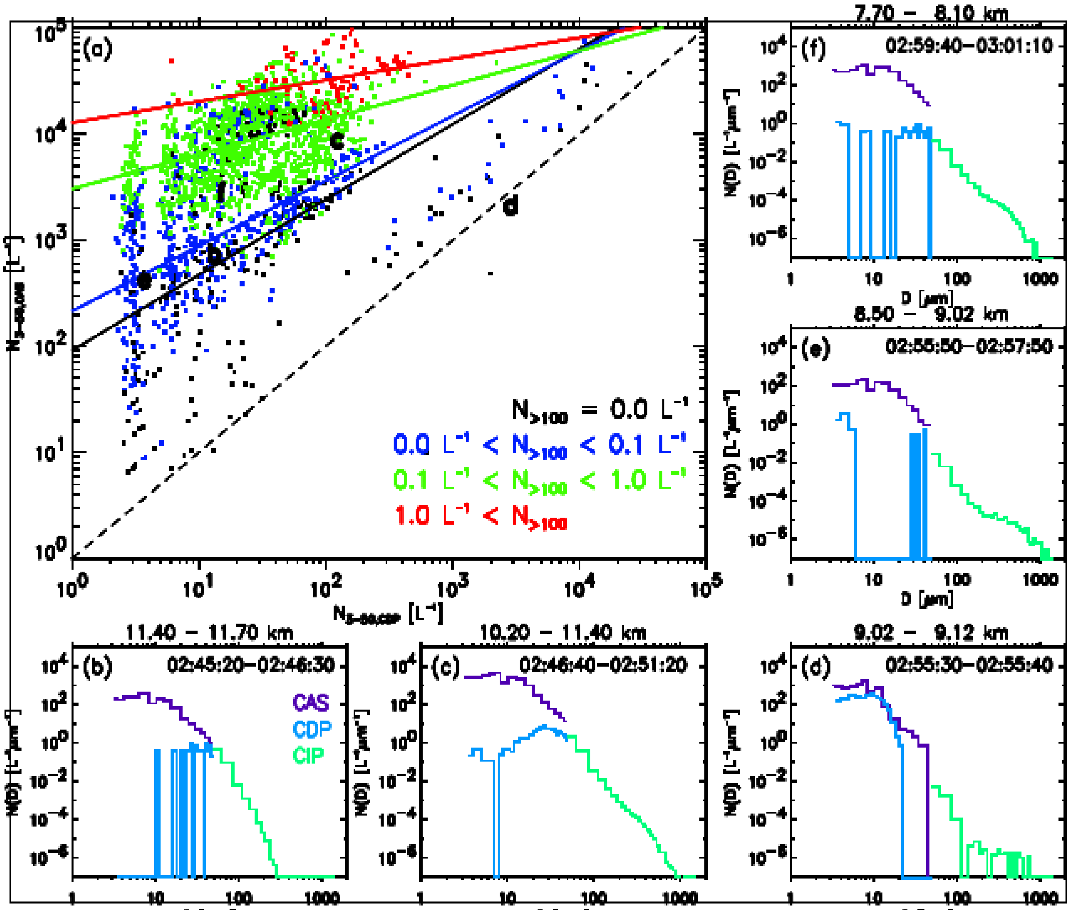

Figure 2: a) $N_{3\text{-}50,CAS}$ as function of $N_{3\text{-}50,CDP}$ for TWP-ICE flights on 27 and 29 January and 2 February (10 s averages). Colors correspond to $N_{>100}$ measured by CIP; lines give best fit to data for given range of $N_{>100}$. Panels b) through f) give N(D) for CAS, CDP and CIP for 5 altitudes during first spiral descent of Proteus on 2 February. Letters b through f indicate these SDs in panel a).

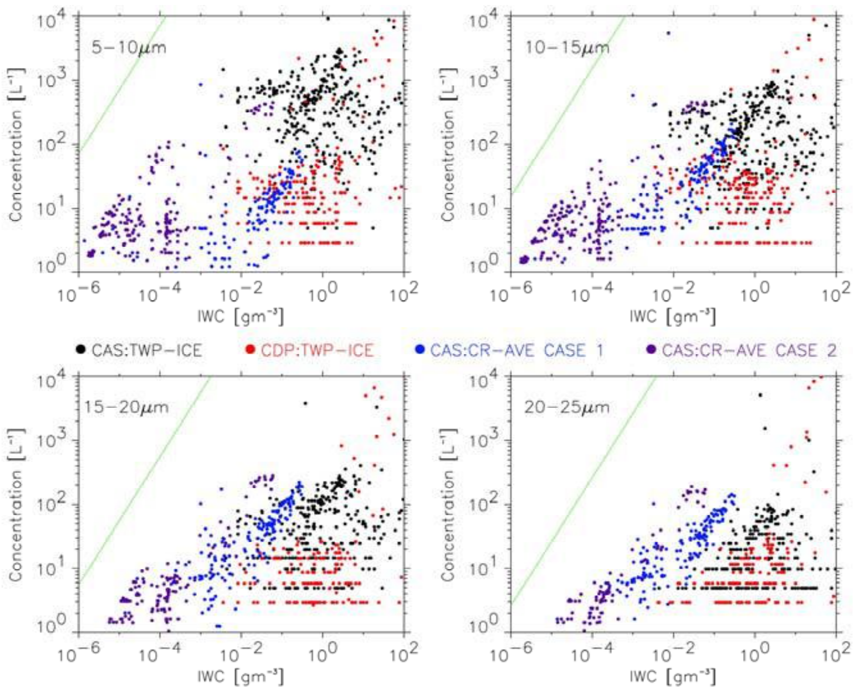

Figure 3: Concentrations measured by CAS and CDP as function of IWC for TWP-ICE and 2 cases during CR-AVE. Green lines correspond to derived relationships assuming maximum shattering on CAS shroud and inlet as explained in text; other symbols indicated in legend.

concentrations between 5 and 15 μm for TWP-ICE compared to CR-AVE suggests that the shattering on the shroud, and not the inlet, is most responsible for amplifying small crystal concentrations. Differences between TWP-ICE and CR-AVE are not as large for 15-20 and 20-25 μm. This is consistent with the TWP-ICE analysis that suggests that smaller ice crystals are predominantly produced by shattering events.

The maximum number of fragments expected from the intercept of particles by the inlet and shroud of the CAS can be estimated. Assuming a true air speed of 130 m s^{-1}, the volume swept out by the inlet and shroud are 65 and 1888 L s^{-1}, respectively. For an IWC of 0.1 g m^{-3}, this corresponds to 0.0065 and 0.189 g s^{-1} of ice which could generate a maximum of 8.8×10^5 and 2.5×10^7 25 μm spherical particles, and 1.4×10^7 and 4.0×10^8 10 μm spherical particles per second for the inlet and shroud respectively assuming the entire ice mass breaks into such sized particles. Modeling calculations show that fragments can arrive in the sample volume for less than only 0.1% of shattering angles, suggesting a maximum of 4.1×10^5 10 μm particles could be artificially produced for TWP-ICE, and 1.4×10^4 for CR-AVE. The green line in Fig. 3, showing concentrations generated by such calculations, has a slope somewhat similar to the N-IWC relationship observed. Vidaurre and Hallett (2006) describe the complex breakup processes for ice particles impacting on surfaces and note that the average number of fragments generated depends on particle diameter, ice habit and impact orientation. Although analysis of TWP-ICE data shows no dependence of the $N_{3\text{-}50,CAS}/N_{3\text{-}50,CDP}$ ratio on crystal impact orientation (i.e., Proteus angle of attack), a future study will examine these data in the context of the energetics of the cloud particle interactions in more detail.

To further assess the role of small crystals, data from the VIPS and FSSP-300 acquired during CEPEX are used. The comparison of the size distributions (McFarquhar and Heymsfield 1996) suggests that the FSSP-300 is overestimating the number of ice crystals smaller than 23 μm, especially in the presence of larger ice crystals detected by the 2DC. In the absence of large crystals measured by the 2DC, the agreement between the FSSP-300 and the VIPS was no worse than that between the VIPS and 2DC. Figure 4 shows the FSSP concentration as a function of the VIPS concentration for particles between 5 and 23 μm in size. The different colors represent different IWCs measured by the 2DC. It can be seen that the ratio of the FSSP concentration to that of the VIPS increases with the IWC, again suggesting that the shattering of large crystals present in higher IWCs may explain the results.

4. TWP-ICE CASE STUDY ANALYSIS

Two case studies from TWP-ICE help understand differences in the response of the CAS and CDP. First, observations from an outflow anvil sampled shortly after its generation on 2 February illustrate time periods with similar and non-similar CAS and CDP $N_{3\text{-}50}$. The anvil was produced by a convective tower that formed over the Tiwi Islands just before the Proteus takeoff. The upper reaches of the convection near 12 km had radar reflectivity of 10 to 15 dBZ as determined from the C-Pol radar and was associated with a 100 km long convective line. The Proteus flew a pair of spiral descents and an ascent in a trailing anvil at 11.6 °S 131.4 °E, the sampling distance behind the core progressively increasing as the tower moved southeast. The anvil rapidly dissipated over the 0241 to 0333 UTC period of the spirals during a period where soundings showed the upper troposphere was dry. To move back into cloud, 2 more ascents and a descent were conducted at 11.4 °S 131.5 °E behind a different cell (0339 to 0448 UTC).

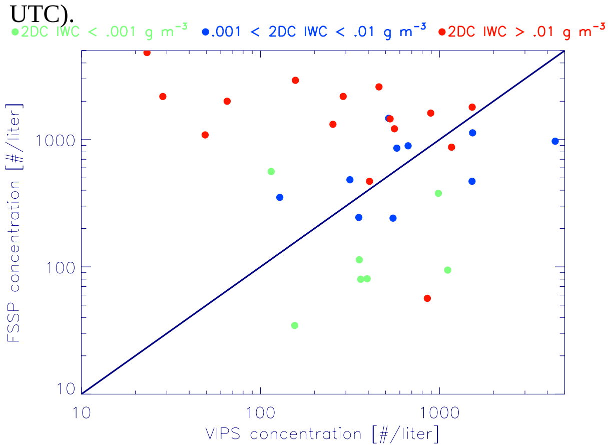

Figure 4: Concentration measured by FSSP for crystals with 5 < D < 23 μm as function of that measured by VIPS for 5 < D < 23 μm in anvils sampled 1 and 4 April 1993 during CEPEX.

Figure 2b through 2f show the number distribution function N(D) for 5 altitudes during the first spiral. The agreement between the CDP and CAS in a thin liquid layer detected by the Nevzorov probe between 9.02 and 9.12 km (Fig. 2d) and the detection of particles with D > 25 μm in an upper cirrus layer by both the CDP and CAS in Fig. 2b and Fig. 2c show the CDP can detect small particles. Many CPI images of particles with D < 50 μm during the 2 February spiral had irregular and elongated shapes that have a more shattered-looking structure compared to quasi-spherical images seen in past cirrus studies. The period in Fig. 2e, when the CDP measured almost no crystals with D < 50 μm, had especially elongated small particles with an average roundness (ratio of particle area to that of circumscribed circle) of 0.75 compared to 0.82 for the times of Fig. 2b and Fig. 2c. The CPI also measured some quasi-spheres in addition to the elongated particles for those times the CDP detected some small ice crystals. Particles with D > 100 μm imaged by the CPI frequently had rounded edges during the spiral suggesting evaporation was occurring; which would have preferentially removed small crystals, explaining their absence.

Observations made during 2 constant altitude legs on 27 January 2006 in aged cirrus bands differ from those on 2 February in that a moister ambient environment was present which might support the presence of small crystals. A leg flown at 15 km in very thin cirrus between 0801 to 0834 UTC (Period 1) and another flown between 13 and 14 km between 0849 and 0914 UTC in thicker cirrus (Period 2) in the presence of generating cells are examined. Figure 5 shows N(D) from the CDP and CIP and from the CAS and CIP. For Period 1, the CIP measured few particles with D > 100 µm and the CDP detected particles, mostly those with D < 25 µm. Both the CAS and CDP recorded few particles with D > 25 µm but the CAS measured significantly more particles with D < 25 µm than the CDP. For Period 2 when more particles with D > 100 µm were measured by the CIP, the CDP detected very few particles whereas the CAS received many counts . Consistent with Fig. 2, the $N_{3\text{-}50,CAS}/N_{3\text{-}50,CDP}$ ratio increased with $N_{>100}$ for Period 2 (figure not shown); no such strong dependence was noted for Period 1 because only 8 10-s periods had any particles with D > 200 µm.

Analysis of the shapes of CPI images with D < 50 µm showed statistically different average roundness for Period 1 (0.94±.09) and Period 2 (0.86±.12). For all sized crystals, quasi-spherical particles contributed 79% to the total number and 19% to the total mass in Period 1, but only 35% to total number and 1.5% to total mass in Period 2. Habits such as bullet rosettes and growing rosettes were seen more frequently in Period 2 than in Period 1. During Period 2, many of the larger ice crystals had rounded edges consistent with sublimation, which may remove the smallest crystals preferentially. Thus, the absence of small crystals in the CDP and the smaller average roundness for Period 2 again suggests that many of the smaller crystals on the CAS are produced by shattering. The presence of small particles in the CDP for Period 1 is consistent with particle growth observed in the generating cells.

To assess whether the presence of these non-spherical particles might have caused the increase in $N_{3\text{-}50,CAS}/N_{3\text{-}50,CDP}$ with increasing $N_{>100}$ for Period 2, laboratory studies at DMT examined the response of the CAS, CDP and a FSSP to glass calibration beads, quartz particles and pollen. Since laser light is polarized and non-spherical particles depolarize light more than spherical particles, these tests with spherical and non-spherical particles determined whether the CDP and CAS optics responded to depolarization differently. No noticeable difference in the CDP and CAS response was seen, further suggesting that shattering on the CAS shroud caused the differences between the CAS and CDP.

5. IMPORTANCE OF CRYSTALS WITH D < 50 µm TO MASS AND RADIATIVE PROPERTIES

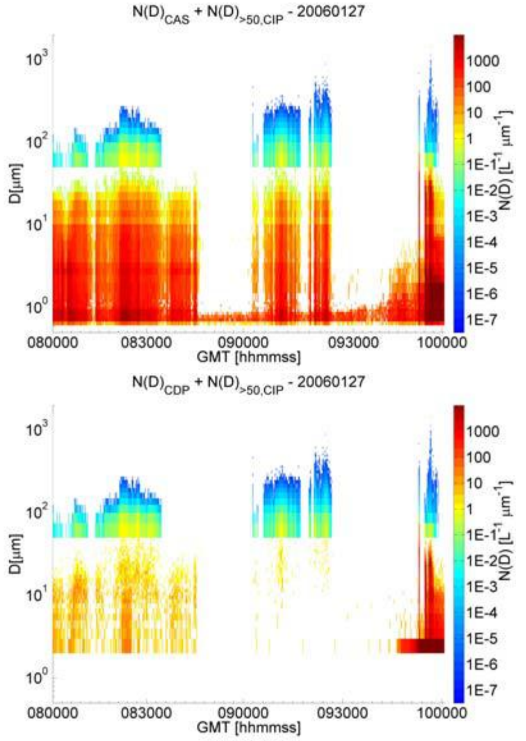

Figure 5: N(D) from (a) CAS and CIP and (b) CDP and CIP as function of D and time for Proteus flight on 27 January 2006 through aged cirrus. Color bar gives scale for N(D).

Differences in the response of probes with the same qualifying detector of forward scattered light are consistent with shattering or bouncing of ice crystals occurring on the CAS inlet and especially on the shroud. This shattering or bouncing artificially enhances total ice crystal concentrations, especially those of crystals with D < 25 µm. The TWP-ICE observations also suggest there may be few small ice crystals even when large ice crystals are present under some conditions.

To understand the ramifications of these findings, the contributions of small ice crystals to cirrus bulk properties are computed using the CAS and CDP TWP-ICE data separately. For 10 s time periods when all of the CAS, CDP and CIP recorded data on the 27 and 29 January and 2 February, ice crystals with 3 < D < 25 µm (3 < D < 50 µm) contributed 95(98)%, 60(75)% and 32(50)% to the total number concentration (N), projected area (A_c), and IWC on average as estimated from the CAS/CIP SDs. The contributions to 3 < D < 25 µm (3 < D < 50 µm) to N, A_c and IWC are only 27(63)%, 7(32)% and 4(20)% when using the CDP/CIP SDs. The differences are substantial as N could be overestimated by 5444%, extinction by 530% and IWC by 151% if shattering or bouncing explains the discrepancies.

McFarquhar and Heymsfield (1996) and McFarquhar and Heymsfield (1997) summarize the contributions of small ice crystals to the number, extinction and mass from the CEPEX data using both the FSSP-300 and VIPS data. Using the FSSP-300 data as a maximum indicator of the contributions of small ice crystals (Fig. 17, McFarquhar and Heymsfield 1996), they found that small crystals contributed about half of the mass for IWCs less than 10^{-3} g m^{-3}, but for IWCs larger than .01 g m^{-3}, the crystals with D < 21 μm contributed less than 20% to the total mass. For analysis with the VIPS, ice crystals with D < 40 μm contributed less than 20% to the total mass except when the IWC was less than 10^{-3} g m^{-3}. For extinction, small crystals contributed up to 40% of the total with contributions of smaller crystals increasing as the total extinction decreased. Consistent with the TWP-ICE and CR-AVE observations, the small crystals dominated the total number concentration.

Thus, model parameterizations based on data from probes with protruding shrouds and inlets may artificially enhance small ice crystal concentrations and in turn lead to overestimates of shortwave reflection by cirrus and errors in estimates of cloud radiative forcing. The findings of this study apply to observations acquired during TWP-ICE and CR-AVE. Observations by the CAS, CDP and other forward scattering probes are needed to determine the robustness of these findings in a variety of cloud types and meteorological conditions. Further, the degree of small crystal amplification reported during TWP-ICE seems greater than in previous studies possibly due to the use of the protruding shroud on the CAS. Thus, more comparisons of the CDP, CAS and FSSP should be performed in additional meteorological conditions to further assess the magnitude of the shattering problem associated with the FSSP and CAS and to assess how frequently significant contributions of small crystals occur in cirrus.

6. ACKNOWLEDGMENTS

Data were obtained from the ARM program archive, sponsored by the U.S. DOE, Office of Science, Office of Biological and Environmental Research (BER), Environmental Sciences Division. This research was supported by the Office of Science (BER), U.S. DOE, Grant Numbers DE-FG02-02ER63337 and DE-FG02-07ER64378. The assistance of R. McCoy, T. Tooman, K. Black, P. Lawson, D. Mitchell, B. Gandrud, and K. Bae was appreciated.

7. REFERENCES

Field, P.R., R. Wood, P.R.A. Brown, P.H. Kaye, E. Hirst, R. Greenaway and J.A. Smith, 2003: Ice particle interarrival times measured with a fast FSSP, *J. Atmos. Ocean. Tech.*, **20**, 249-261.

Gardiner, B.A., and J. Hallett, 1985: Degradation of in-cloud forward scattering spectrometer probe measurements in the presence of ice particles. *J. Atmos. Ocean. Tech.*, **2**, 171-180.

Garrett, T.J., H. Gerber, D.G. Baumgardner, C.H. Twohy and E.M. Weinstock, 2003: Small, highly reflective ice crystals in low-latitude cirrus, *Geophys. Res. Lett.*, **30**, doi: 10.1029/2003GL018153.

Gayet, J.G., G. Febvre and H. Larsen, 1996: The reliability of the PMS FSSP in the presence of small ice crystals, *J. Atmos. Ocean. Tech.*, **13**, 1300-1310.

Ivanova, D.C., D.L. Mitchell, W.P. Arnott and M. Poellot, 2001: A GCM paramterization for bimodal size spectra and ice mass removal rates in mid-latitude cirrus clouds. *Atmos. Res.*, **59**, 89-103.

Knollenberg, R.G., K. Kelly and J.C. Wilson, 1993: Measurements of high number densities of ice crystals in the tops of tropical cumulonimbus, *J. Geophys. Res.*, **98**, 8639-8664.

Korolev, A., and G.A. Isaac, 2005: Shattering during sampling by OAPs and HVPS. Part I: Snow particles, *J. Atmos. Ocean. Tech.*, **22**, 528-543.

McFarquhar, G.M. and A.J. Heymsfield, 1996: Microphysical characteristics of three cirrus anvils sampled during the Central Equatorial Pacific Experiment, *J. Atmos. Sci.*, **53**, 2401-2423.

McFarquhar, G.M., and A.J. Heymsfield, 1997: Parameterization of tropical cirrus ice crystal size distributions and implications for radiative transfer: results from CEPEX. *J. Atmos. Sci.*, **54**, 2187-2200.

Vidaurre, G., and J. Hallett (2006), Energetics of mixed phase cloud particle interactions. 12th Conf. on Cloud Physics, Amer. Meteor. Soc., Madison, WI. Available from http:ams.confex.com/pdfpapers/112624.pdf

Satellite Remote Sensing of Small Ice Crystal Concentrations in Cirrus Clouds

David L. Mitchell[1] and Robert P. d'Entremont[2]

1. Desert Research Institute, Reno, NV
2. Atmospheric and Environmental Research, Inc., Lexington, MA

1. INTRODUCTION

Measurement of small ice crystals (D < 60 μm) remains an unsolved and controversial issue in the atmospheric sciences community. Concentrations of small ice crystals are hard to measure due to shattering of crystals at probe inlets. However, depending on the in situ measurements one uses, these small ice crystals may affect cirrus cloud optical depth by a factor of two (McFarquhar et al. 2007). Through their impact on ice fall speeds, they also may affect the cirrus cloud feedback and surface warming in global climate models (Mitchell et al. 2008; Sanderson et al. 2008).

To facilitate better estimation of small ice crystal concentrations in cirrus clouds, a new satellite remote sensing technique has been used in combination with in situ aircraft measurements. That is, in situ measurements of ice particle size distributions (PSD) are parameterized by temperature and ice water content (IWC), and these PSD schemes in combination with radiances measured from satellite and a treatment of ice cloud optical properties serve as the framework of the retrieval algorithm. The latter is the modified anomalous diffraction approximation (Mitchell 2000, 2002; Mitchell et al. 2006), or MADA, where extinction and absorption are expressed in terms of the size distribution parameters and the measured mass- and projected area-dimension power law relationships for various ice crystal shapes or shape recipes.

2. THEORY

Small ice crystals are evaluated using the properties of photon tunneling or wave resonance. Photon tunneling can be described as the process by which radiation beyond the physical cross-section of a particle is either absorbed or scattered outside the forward diffraction peak (Fig. 1). As shown in Mitchell (2000) and Mitchell et al. (2006), tunneling is strongest when:

- The effective size of the particles and the wavelength of radiation are comparable.
- The particle is spherical or quasi spherical (an attribute of many small ice crystals)
- The real index of refraction is relatively large

Tunneling contributions to the absorption efficiency in the window region can exceed 20% when particle size is less than 60 μm (Fig. 2). Tunneling depends on the real refractive index, which increases substantially for ice between 11 and 12 μm wavelengths.

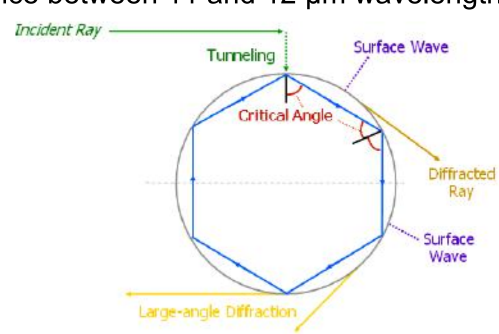

Figure1: Depiction of possible trajectories of an incident grazing ray after tunnelling to the drop surface.

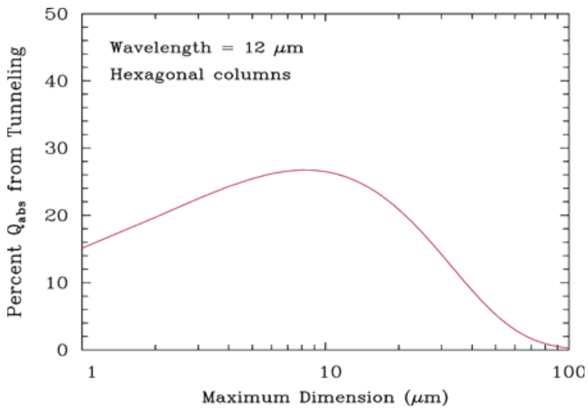

Figure 2. Tunneling contributions to the absorption efficiency for hexagonal columns at 12 μm wavelength based on MADA.

The corresponding emissivity difference at these wavelengths is almost all due to tunneling, making the tunneling signal ideal for inferring the concentrations of small ice crystals. Historically this emissivity difference was attributed to differences in the imaginary refractive index, but for ice clouds, it is the real refractive index that accounts for this difference in emissivity.

Better understanding of remote sensing of small crystals by applying the tunneling technique is shown in Fig. 3. The solid curve shows absorption efficiencies ($\overline{Q}_{abs}$) for a bimodal size distribution (e.g. Fig. 4) of quasi-spheres (droxtals) in the small mode and bullet rosettes in the large mode. The dashed curve is for the large mode, rosettes only. Note that $\overline{Q}_{abs}$ = β_{abs}/P_t, where β_{abs} = absorption coefficient and P_t = PSD projected area. $\overline{Q}_{abs}$ for wavelengths > 11 μm are greater for the complete PSD due to tunneling. Tunneling depends strongly on the real index of refraction, n_r. The reason $\overline{Q}_{abs}$ is greater at 12 μm than 11 μm when the full PSD is used is because n_r has a minimum near 11 μm but is substantial at 12 μm. Since tunneling is a measure of the small mode, and the 12 – 11 μm $\overline{Q}_{abs}$ difference is only from tunneling, this difference serves as a measure of the small mode of the cirrus PSD. These calculations are based on the optical property database given in Yang et al. (2005), but the same result is given by MADA.

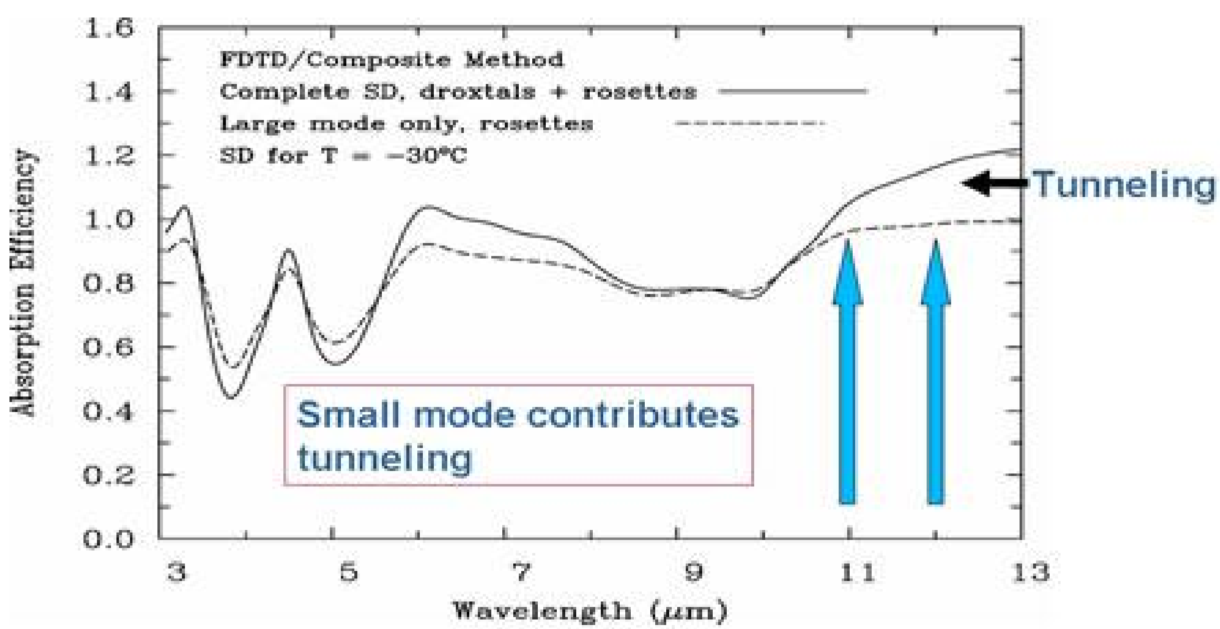

Figure 3: Absorption efficiencies (Q_{abs}) for a bimodal size distribution.

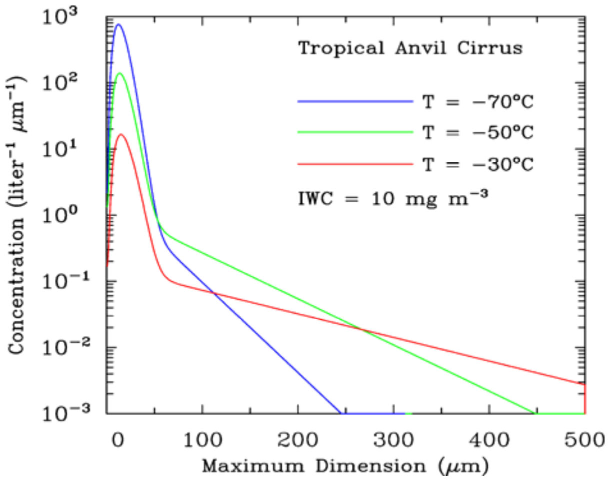

Figure 4. Examples of bimodal size distributions based on measurements from anvil cirrus clouds during CEPEX (Ivanova et al. 2004).

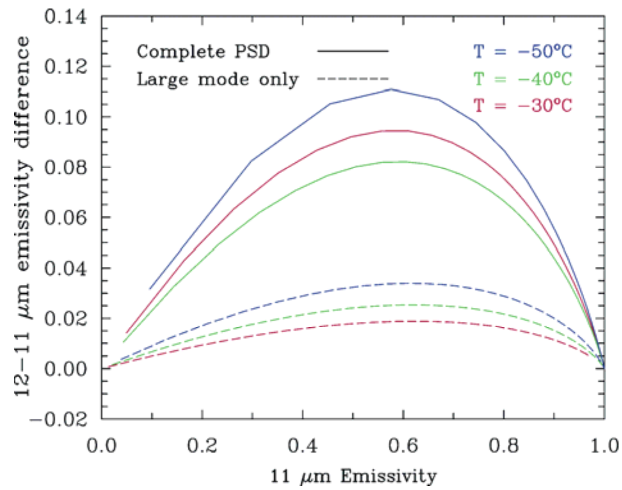

Figure 5. Theoretical curves denoting the large mode (dashed) and the complete PSD (solid) corresponding to 3 temperature-dependent PSD.

3. ESTIMATING SMALL CRYSTAL CONCENTRATIONS

Bimodal PSD examples from anvil cirrus sampled during the Central Equatorial Pacific Experiment (CEPEX) are shown in Fig. 4. The ice crystals associated with the small mode (D < 50 μm) were sampled by the Forward Scattering Spectrometer Probe (FSSP), with the larger particles sampled by the 2DC probe. The key question is whether the small mode is real or an artifact of crystal shattering at the probe inlet (or a little of both). To help answer this, we use satellite radiances at 11 and 12 μm to estimate the number concentration in the small mode. The large mode is first estimated from the PSD parameterization shown in Fig. 4, but can be modified based on the satellite-measured radiances. The small mode ice mass content can be estimated by the "arches" in Fig. 5 and also from the absorption optical depth ratio based on 12 and 11 μm, referred to as β. Several studies have shown that β ≈ 1.08 for synoptic and anvil cirrus (e.g. Inoue 1985, Parol et al. 1991). The higher the small mode ice mass content (or small mode number concentration, N_{sm}), the higher the arches are. This principle is used to determine N_{sm} by matching theory with observations, as described now.

1. The first step is to begin with satellite retrievals of cloud temperature and cloud emissivity (ε) at the 11 and 12 μm wavelength channels. This is described in Section 4.
2. The cloud temperature can then be used to estimate PSD mean size $\bar{D}$ and dispersion for the large and small mode. The difference between the solid and dashed curves above results primarily from differences in the contribution of the small mode to the IWC. This also determines the effective diameter (D_e). The dispersion parameter has little influence on the emissivities or emissivity differences.
3. Locate retrieved Δε (Fig. 5 y-axis) and the 11 μm ε by (1) incrementing the modeled ice water path (IWP) to increase ε(11 μm) and (2) incrementing the small mode contribution to the cirrus IWC, which elevates the curve.
4. If all IWC is in the small mode and retrieved Δε and ε (11 μm) are still not "located", then decrease the small mode $\bar{D}$ to locate them.
5. If retrieved point lies below the "large mode only" curve (e.g. a dashed curve), then systematically increase

$\overline{D}$ for the large mode until a match is obtained. Negative $\Delta\varepsilon$ values correspond to maximum allowed $\overline{D}$ values.

6. This method retrieves IWP, D_e, and the small-to-large mode ice crystal concentration ratio. For a given IWC, it also estimates ice particle number concentration and the complete PSD, even when it is bimodal.

The modified anomalous diffraction approximation (MADA) was used to calculate ice cloud optical properties in this retrieval algorithm since it couples explicitly with the cloud microphysics and its analytical formulation makes it computationally efficient (Mitchell et al. 2006; Mitchell 2000). A temperature dependent ice crystal shape recipe was used based on the observations reported in Lawson et al. (2006). As described in Mitchell et al. (2006), tunneling efficiencies for various ice crystal shapes were determined by comparisons between MADA and finite-difference time-domain (FDTD) calculations, and were parameterized as a function of ice particle shape and large mode $\overline{D}$.

4. SATELLITE RETRIEVAL OF CIRRUS TEMPERATURE AND EMISSIVITY

Cirrus cloud temperature is estimated using radiances measured in four carbon dioxide channels on the MODIS instrument between 13.3 and 14.2 μm. For purposes of explanation the technique can be described considering two of these four bands: we refer to them as channels A & B. The real refractive index, n_r, at 13.3 and 14.2 μm is 1.52 and 1.58 respectively, indicating the absorption contribution from tunneling is almost the same in these channels (Mitchell 2000). The imaginary index n_i is 0.355 and 0.246, respectively, yielding a small mode $Q_{abs} \approx 1.0$ for each wavelength when tunneling is neglected. For these reasons the emissivity in each channel is essentially the same ($\varepsilon_A = \varepsilon_B$), allowing us to solve for the cirrus cloud temperature using the simple non-scattering formulation. For each channel we can say:

$$I_{OBS} = (1 - \varepsilon)\, I_{CLR} - \varepsilon\, B(T_{CLD}) \qquad (1)$$

where I_{OBS} = observed radiance, I_{CLR} = radiance at a nearby clear-sky region, ε = cirrus emissivity and B = Planck function at cirrus temperature T_{CLD}. Equating ε in each CO_2 channel we solve for T_{CLD} as the only unknown:

$$\frac{I_{A,OBS} - I_{A,CLR}}{B_A(T_{CLD}) - I_{A,CLR}} = \frac{I_{B,OBS} - I_{B,CLR}}{B_B(T_{CLD}) - I_{B,CLR}} . \qquad (2)$$

With T_{CLD} retrieved and I_{OBS} and I_{CLR} directly measured, ε is obtained from (1) for the 11 and 12 μm channels as, for example,

$$\varepsilon(11\ \mu m) = \frac{I_{11,OBS} - I_{11,CLR}}{B_{11}(T_{CLD}) - I_{11,CLR}} . \qquad (3)$$

We thus use 3 equations to solve for T_{CLD}, ε(11 μm) and ε(12 μm). To account for the effects of scattering, effective emissivities were used in the retrieval algorithm as described in Parol et al. (1991).

5. TWP-ICE CASE STUDY

During the Department of Energy Atmospheric Radiation and Measurement Program (DOE-ARM) sponsored Tropical Warm Pool International Cloud Experiment (TWP-ICE), in situ microphysical sampling on 2 February 2006 coincided with an Aqua satellite overpass. The MODIS instrument aboard Aqua has a nominal 1 km^2 footprint or spatial resolution at nadir viewing angles and contains the channels used in this retrieval method. Since the Proteus aircraft was measuring cirrus PSD using a variety of probes (McFarquhar et al. 2007), PSD retrieved from MODIS radiances can be compared with temporally and spatially coincident in situ measurements.

MODIS retrievals based on Section 4 are shown below in Fig. 6. The cirrus are

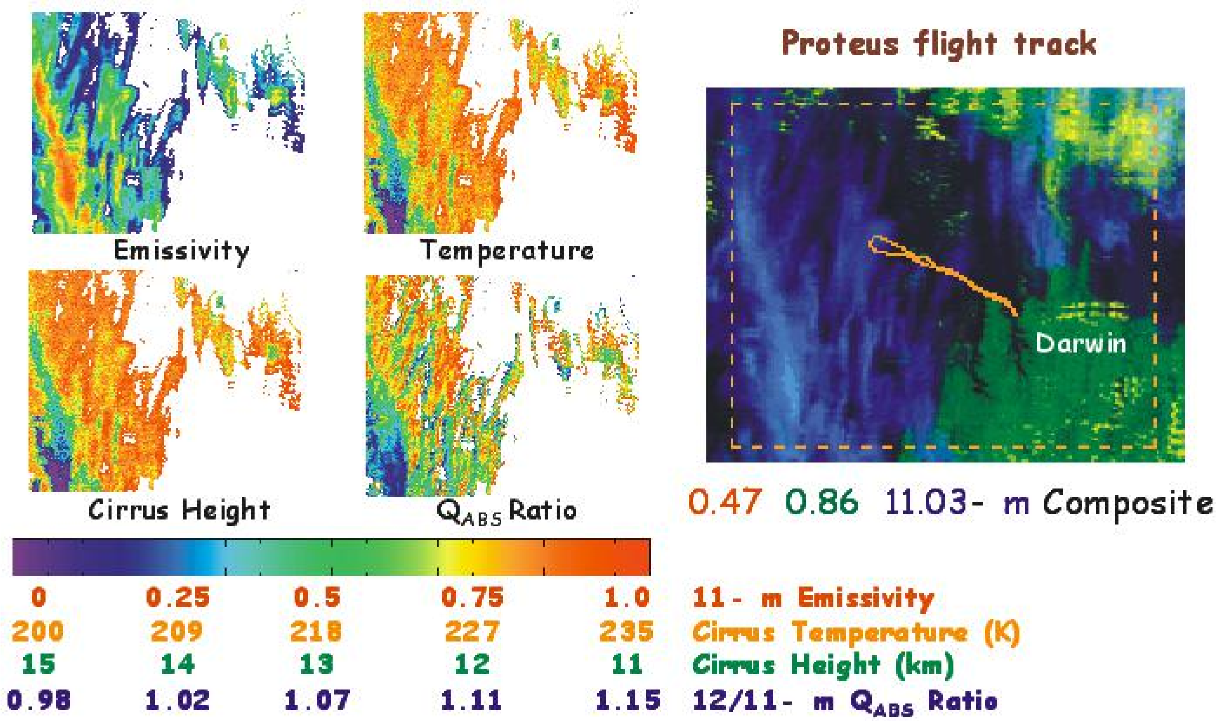

Figure 6. MODIS retrievals during TWP-ICE, 2 February 2006 (5:20 UTC), of cirrus temperature, 11 µm emissivity, height and 12/11 µm absorption efficiency (Q_{abs}) ratio, based on the methodology in Section 4. Also shown is the Aqua satellite image with low clouds in yellow, cirrus clouds in blue (thicker cirrus are lighter blue). The Proteus flight track during the MODIS overpass is shown in orange, and the dashed orange square denotes the spatial extent of the region for which satellite retrievals were performed.

from a rapidly decaying anvil, giving them a detached and broken appearance (McFarquhar et al., 2007). Only ε retrievals satisfying the following theoretical constraints were used in the microphysics algorithm: ε(13 µm) > ε(11 µm), ε(13 µm) > ε(12 µm), ε(12 µm) > ε(11 µm). This removed 18% of the data. In Fig. 6, higher cirrus emissivity and height, and lower cirrus temperature, coincide with the optically thicker cirrus in the MODIS image on the right. The 12/11 µm Q_{abs} ratio or β is also shown, and it helps determine the crystal effective size D_e. When β is near 1.0, D_e is relatively large, with D_e decreasing with increasing β. Near the lower left corner of the image, the Q_{abs} ratio is near 1.0 indicating that the ice particle sizes are relatively large in the thicker cirrus. The retrieved β could also approach 1.0 when the emissivities approach 1.0, but ε(11 µm) is not saturated in most of this region, suggesting the ice particles are larger there.

Streams of cirrus appear to be advected downwind from their source region in Fig. 6 and generally contain higher β and smaller crystals. A possible explanation is that the larger particles sediment out leaving only the smaller crystals behind.

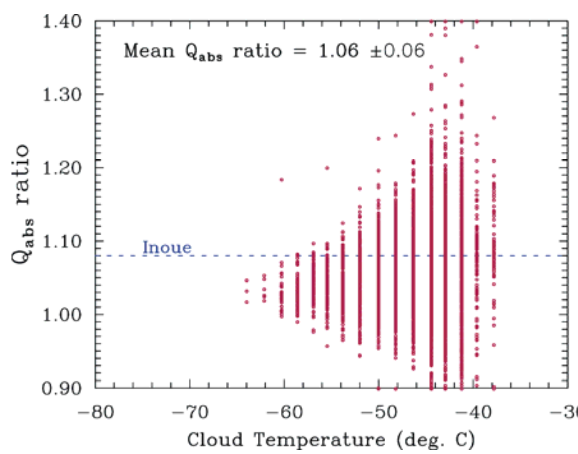

Figure 7. Retrieved β for the MODIS image pixels. The blue dashed line gives the average β found in previous studies.

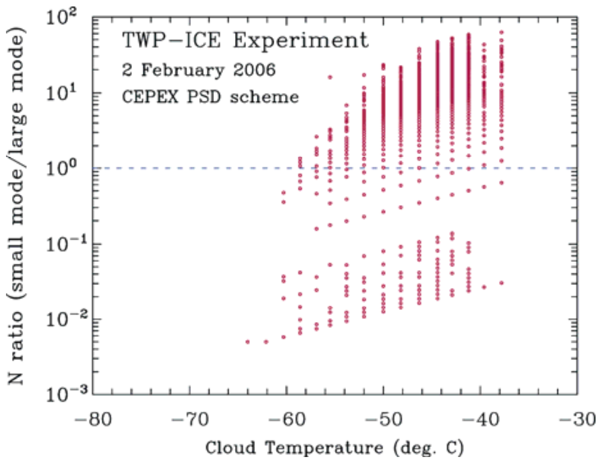

Figure 8. The degree of bimodality of the retrieved PSD, with bimodal spectra above the dashed blue line.

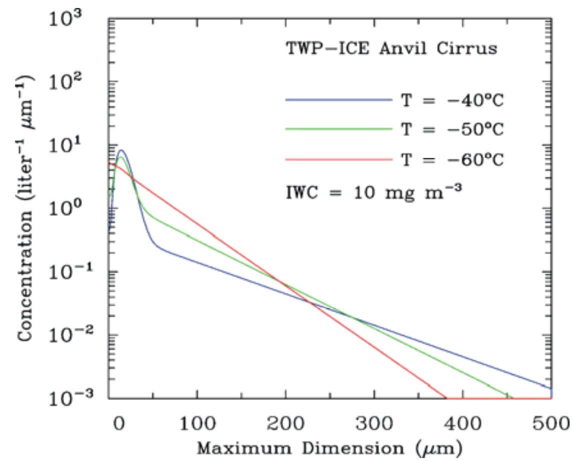

Figure 9. Average PSD for the given IWC and temperatures as predicted by the retrieval scheme.

Several studies (Inoue 1985; Parol et al. 1991; Giraud et al. 1997; 2001) find that for cirrus over the tropics and mid-latitudes, β = 1.08 on average, generally not exceeding 1.14. For this case study, we find that β = 1.06 ± 0.06, as shown in Fig. 7, which is consistent with the earlier findings. On average, β = 1.095, 1.055 and 1.034 for retrieved cirrus temperatures of -40, -50 and -60 ^{o}C. The dashed blue line in Fig. 7 gives the mean β value found by Inoue (1985).

a. PSD bimodality

A unique attribute of this retrieval is the ability to retrieve the ratio of small mode to large mode ice crystal concentration. The degree of bimodality in the retrieved PSD is shown in Fig. 8. Points above the dashed blue line indicate varying degrees of bimodal spectra, while points below the line indicate essentially monomodal PSD. The gap separating the two populations of points is an artifact of the resolution used to increment the small mode IWC (0.2 % of total IWC). Figure 8 shows that retrieved PSD are both monomodal and bimodal, but more commonly bimodal at the warmer temperatures. Figure 9 shows what the retrieved PSD look like, taking the average PSD at the selected temperatures and IWC. It is useful to compare Fig. 9 with Fig. 4, which shows the PSD scheme used in the retrieval initialization. The retrieved PSD were modified based on the 11 and 12 μm radiances, or β. Clearly the retrieved PSD are having much lower small crystal concentrations than the “parent” PSD that are based on in situ measurements from the FSSP and 2DC probes. These results support the argument that ice particle shattering at the probe inlet contributes relatively high concentrations of small crystals to the measured PSD.

The predicted degree of bimodality depends on the PSD scheme used in the retrieval. For example, a steep monomodal PSD can have the same β as a bimodal PSD. Since the radiances used are only sensitive to the smaller crystals, the retrieval is dependent on the accuracy of the temperature dependent PSD scheme describing the larger particles. Since the relationship between mean crystal size and temperature is characterized by considerable scatter (Heymsfield 2003), the retrieval should yield reasonable values most of the time but not all the time, and in some types of cirrus (not considered in the D-T relationship), retrievals could be poor.

The degree of bimodality retrieved also depends on the ice particle shapes assumed, but this dependence is not strong (small mode number concentration may change up to a factor of 2). Note the dependence of radiances to small crystals.

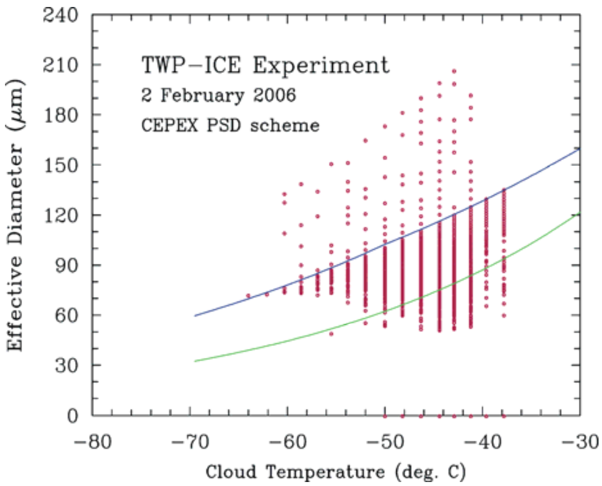

Figure 10. D_e retrievals using our preferred m-D and P-D relationships. The blue curve gives D_e based on only the large mode of our anvil cirrus PSD scheme that is part of the algorithm. The green curve is the mean large mode particle length for this PSD scheme (not an effective diameter).

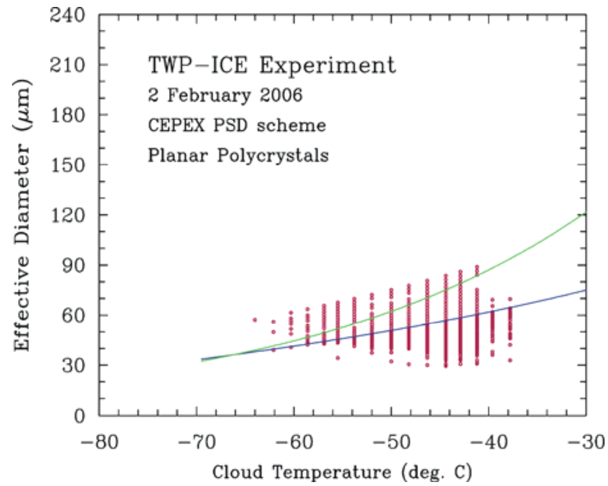

Figure 11. Same as in Fig. 10 except using m-D and P-D expressions for planar crystals, having less mass per unit length than the ice particles in the crystal shape recipe.

b. Effective diameter

The retrieval of effective diameter or D_e using this method depends not only on the radiances but also on assumptions regarding the ice particle mass- and projected area-dimension relationships:

$$m = \alpha D^{\beta} \quad (4)$$

$$P = \delta D^{\sigma} \quad (5)$$

where m and P denote ice particle mass and projected area, and D = maximum dimension. In a radiation sense, these relationships define ice crystal shape. A temperature dependent ice crystal shape recipe was used in this retrieval for the larger particles (D > 80 μm), which is based on Lawson et al. (2006) where particle shape was measured by the Cloud Particle Imager (CPI). "Irregular" crystals at the cirrus temperatures retrieved here comprise between 35% and 60% of the number concentration. Hexagonal columns comprise ~ 8% with the rest being bullet rosettes. Since irregular crystals appear "brick-like", dense and compact, an m-D relationship exhibiting 2.5 times the mass of a bullet rosette at 300 μm was used for irregulars. This contributes to relatively high D_e values. For ice crystals < 80 μm, the following recipe was used, based on CPI measurements in anvil cirrus near Kwajalein: 5% hexagonal columns, 5% bullet rosettes, 5% plates, 42.5% irregulars, and 42.5% quasi-spherical particles (Paul Lawson, personal communication). The P-D expressions for irregulars were based on compact planar polycrystals (Mitchell et al. 1996) and the rosette P-D expression is from Lawson et al. (2006). The universal definition of D_e (for both liquid and ice cloud) is used here (Mitchell 2002).

The temperature dependence of the retrieved D_e is shown in Fig. 10. The blue curve shows the D_e predicted by the anvil (CEPEX) PSD scheme used in the retrieval when only the large mode is used. This describes an approximate upper limit for most of the retrieved D_e. β > 1.04 tends to imply some degree of bimodality which decreases D_e from its large mode value. The D_e lying above the blue curve exhibit β

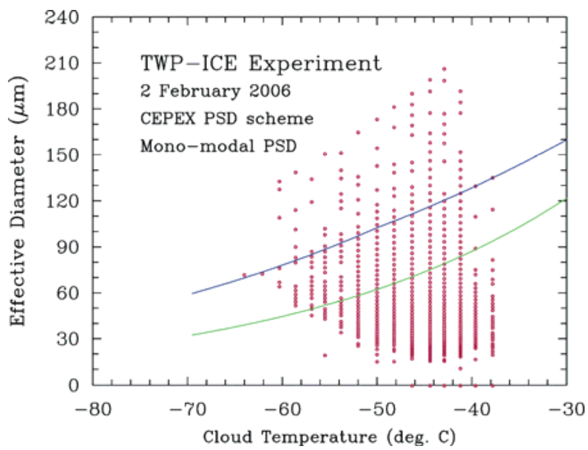

Figure 12. Same as Fig. 10 except mono-modal PSD are assumed in the retrieval algorithm. This may be more consistent with the traditional way of retrieving D_e.

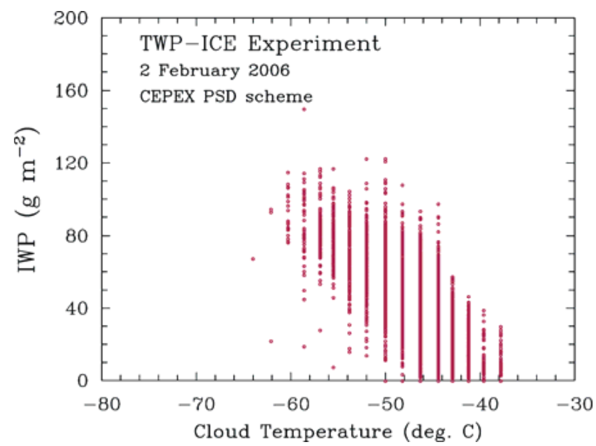

Figure 13. IWP retrievals using our preferred m-D and P-D relationships and the bimodal PSD retrieval method.

lower than predicted by only the large mode, and large mode mean maximum dimension (i.e. length), or $\bar{D}$, was increased to match the predicted β with the observed β. The green curve gives the large mode $\bar{D}$ which does not depend on the m-D and P-D expressions. It thus serves as a reference in this analysis.

Figure 11 is the same as Fig. 10 except the m-D and P-D expressions were changed to conform to planar polycrystals, which have less mass per unit length than the ice crystals noted in the shape recipe. The retrieved D_e values are now lower than before, especially at the warmer temperatures where PSD are broader. Again, the blue curve gives the D_e predicted by the large mode of the PSD scheme used in the retrieval algorithm.

A key principle here is that the difference in radiances defining β are determined by ice particles < 60 μm, as shown in Fig. 2. Thus properties pertaining to the small mode such as the N ratio in Fig. 8 may be accurately retrieved (depending only on radiances), but properties relating to the entire PSD are also subject to assumptions affecting the large mode. For example, as temperature increases, large mode $\bar{D}$ in the PSD scheme becomes larger and ice particle density decreases (less mass per unit length). This widens the difference in D_e retrievals regarding Fig. 10 and 11. So our D_e retrievals are based on the entire PSD, part of which is determined by radiances and part of which is based on a large mode estimated from a PSD scheme developed from in situ measurements. For this reason D_e depends on the m-D and P-D relationships that affect D_e in PSD regions not sensitive to the radiances used.

Figure 12 shows the D_e retrieved when we constrain the PSD to be mono-modal. That is, $\bar{D}$ is incremented when β predicted from the PSD scheme large mode is less than the observed β, and $\bar{D}$ is decreased when the reverse is true. This approach may be similar in concept to split-window D_e retrievals now in use (e.g. Dubuisson et al. 2008). While Fig. 12 shows large variance in D_e, most of the retrievals correspond to D_e much lower than the D_e retrieved based on the bimodal PSD formulation. This appears to be due to the fact that only the smallest ice crystals determine β, and the same β can be produced by either a strongly bimodal PSD with a broad large mode (i.e. large $\bar{D}$) or a mono-modal PSD having a relatively small $\bar{D}$. Since D_e depends on the entire PSD, the two scenarios result in very different D_e retrievals. As for which retrieval is more realistic, that may depend on whether cirrus clouds exhibit predominately bimodal or monomodal PSD. If cirrus PSD in nature are bimodal, then the true D_e may differ substantially from the retrieved D_e based on the monomodal assumption, since the large mode may have a strong influence on D_e and yet the radiances employed are not sensitive to the large mode.

In summary, the accuracy of this D_e retrieval depends on (1) the 11 and 12 μm radiances, (2) the realism of the m-D and P-D expressions employed and (3) how well the algorithm PSD scheme can represent the larger ice particles found in nature.

c. Ice water path

Retrievals of ice water path (IWP) using our standard method (allowing for bimodality and preferred ice crystal shape recipe) are shown in Fig. 13. In Fig. 6 it is seen that the thicker cirrus (i.e. higher ε) correspond to the colder temperatures. Similarly, the higher IWP values coincide with colder temperatures in Fig. 13.

The retrieval of IWP also depends on the m-D and P-D relationships used (i.e. crystal shape) and whether the PSD are constrained to be mono-modal. This dependence is shown in Table 1 for both IWP and D_e. This dependence can be shown analytically for IWP using the equation derived in Mitchell et al. (2006) which assumes no scattering:

$$IWP = \frac{-2\,\rho_i\,D_e\,\ln(1-\varepsilon)\cos\theta}{3\,\bar{Q}_{abs}} \qquad (4)$$

Table 1. Mean values for D_e and IWP and their dependence on retrieval assumptions.

Mean Value	Standard retrieval	Planar polycrystals	Mono-modal PSD
D_e (μm)	102	54	69
IWP (g/m^2)	34	18	23

where $\bar{Q}_{abs}$ is the area-weighted absorption efficiency of the PSD (β_{abs}/P, where β_{abs} is the absorption coefficient and P is the PSD projected area), ρ_i = density of bulk ice (0.917 g cm^{-3}), ε = cirrus emissivity at a non-scattering wavelength, and θ is the satellite viewing angle. Thus, IWP is directly proportional to D_e, which is verified by the results shown in Table 1. Since D_e is sensitive to ice crystal shape and PSD shape assumptions, the same is true for the IWP retrievals.

6. COMPARISONS WITH IN SITU MEASUREMENTS

Microphysical measurements for this same case study are evaluated in McFarquhar et al. (2007). However, the cirrus in that study were sampled about 2.5 hours earlier and were from a different anvil cloud than the cirrus observed in this MODIS overpass at 5:20 UTC. Nonetheless, it may be of interest to know how our consistent our retrieved PSDs are in relation to those sampled in the McFarquhar et al. study. Four of the five PSD shown in McFarquhar et al. (2007) exhibit modest bimodality as measured by the Cloud Imaging Probe (CIP) and the Cloud Droplet Probe (CDP) for D < 100 μm. The open path design of the CDP and CIP (no inlet tube) greatly reduces the problem of ice particle shattering. Therefore a comparison between these in situ measurements and the PSD retrievals in this study is relevant. Peak concentrations for small crystals were about 10^2 times greater than those for the larger crystals near D = 100 μm. This is similar to the blue curve in Fig. 9. The PSD shown in their study that did not exhibit bimodality was nearest cloud top and was similar to the red curve (T = -60 °C) in Fig. 9. So general consistency in PSD shape appears to exist between those in situ measurements and the retrieved PSD described here.

Moreover, the approximate $\bar{D}$ for the large mode in situ measurements was 20, 105, 222 and 128 μm (assuming an exponential large mode), corresponding to mean cloud levels of 11.55, 10.8, 8.76 and 7.9 km. These values are similar to those predicted by the retrieval algorithm for large mode $\overline{D}$, namely

$$\overline{D} = 0.03326 \exp(0.03350\ T)\ , \qquad (5)$$

where T is temperature in degrees C. For example, at -60, -50 and -40 C, $\overline{D}$ is 45, 62 and 87 μm. Earlier it was noted that natural PSDs might not be bimodal if their large mode slope was sufficiently large (i.e. $\overline{D}$ was sufficiently small), but this does not appear to be the case for these observations since observed $\overline{D}$ are generally larger than those predicted. Thus the degree of bimodality reported here appears to be genuine.

Direct comparisons with PSD sampled by the Proteus aircraft during the MODIS overpass with those retrieved here will be available soon.

7. CONCLUDING REMARKS

This study may be the first to use satellite radiances to infer the bimodality of ice particle size spectra, or PSD. The PSD predicted from the retrievals appear consistent with recent PSD measurements based on probes much less vulnerable to ice particle shattering problems than earlier probes (McFarquhar et al. 2007). The retrieved PSD support the argument that earlier in situ measurements of small ice crystals were greatly exaggerated due to the shattering of larger ice particles at the probe inlet. However, the retrievals also suggest that some degree of bimodality in cirrus is common, but this result depends on the realism of the relationship between $\overline{D}$ and temperature.

It is not clear what the best approach would be to retrieving ice cloud properties in the infrared, and more work is needed for algorithm development, determining the optimal interface between observed relationships of temperature, IWP, mean size, D_e, ice crystal shape and the measured radiances. While some investigators indicate that the PSD bimodality is relatively unimportant to retrieval accuracy (Dubuisson et al. 2008), we would argue that it depends on the architecture of the retrieval algorithm. There is a need for analysis of PSD data from the new probes that minimize ice particle shattering and have a means to correct for any shattering artifacts that occur (e.g. using interarrival times). This would hopefully provide guidance on whether a bimodal or monomodal retrieval approach would make the most sense.

It has been shown that when global climate models (GCMs) incorporate more realistic cirrus microphysics, the predicted GCM climatology is sensitive to the representation of the PSD with respect to small ice crystal concentrations. This is largely due to their effect on ice sedimentation rates (Mitchell et al. 2008). Improved characterization of the cirrus PSD through satellite remote sensing may thus contribute to GCM improvements.

The retrieval method described here is limited to cirrus having visible extinction optical depths less than 4.5. Other retrieval methods such as those employing microwaves will be needed for retrieving cloud properties in more optically thick ice clouds.

Acknowledgment: This research was sponsored by the Office of Science (BER), U.S. Dept. of Energy, Grant No. DE-FG02-06ER64201.

REFERENCES

- Dubuisson, P., V. Giraud, J. Pelon, B. Cadet, P. Yang, 2008: Sensitivity of thermal infrared radiation at the top of the atmosphere and the surface to cloud microphysics. *J. Appl. Meteorol. and Clim.*, doi: 10.1175/2008JAMC1805.1

- Giraud, V., J.C. Buriez, Y. Fouquart, and F. Parol, 1997: Large-Scale Analysis of Cirrus Clouds from AVHRR Date: Assessment of Both a Microphysical Index and the Cloud-Top Temperature. *J. Appl. Met.*, **36**, 664-674.

- Giraud, V., O. Thouron, J. Reidi and P. Goloub, 2001: Analysis of direct comparison of cloud top temperature and infrared split window signature against independent retrievals of cloud thermodynamic phase. *Geophys. Res. Lett*., **28**, 983-986.

- Heymsfield, A.J., 2003: Properties of tropical and mid-latitude ice cloud ensembles. Part II: Applications for mesoscale and climate models.

- Inoue, T., 1985: On the temperature and emissivity determination of semitransparent cirrus clouds by bispectral measurements in the 10 µm window region. *J. Meteorol. Soc. Jpn*., **63**, 88-98.

- Ivanova, D., D.L. Mitchell, W.P. Arnott and M. Poellot, 2001: A GCM parameterization for bimodal size spectra and ice mass removal rates in mid-latitude cirrus clouds. Atmos. Res., **59**, 89-113.

- Lawson, R.P., B. Baker, B. Pilson and Q. Mo, 2006: In situ observations of the microphysical properties of wave, cirrus and anvil clouds. Part 2: Cirrus clouds. *J. Atmos. Sci*., **63**, 3186-3203.

- McFarquhar, G.M., J. Um, M. Freer, D. Baumgardner, G. Kok and G. Mace, 2007: The importance of small ice crystals to cirrus properties: Observations from the Tropical Warm Pool International Cloud Experiment (TWP-ICE). Geophys. Res. Lett., 34, L13803,doi:10.1029/2007GL02986, 2007.

- Mitchell, D.L., A. Macke, and Y. Liu, 1996: Modeling cirrus clouds. Part II: Treatment of radiative properties. J. Atmos. Sci., 53, 2967-2988.

- Mitchell, D.L., 2000: Parameterization of the Mie extinction and absorption coefficients for water clouds. J. Atmos. Sci., **57**, 1311-1326.

- Mitchell, D.L., 2002: Effective diameter in radiation transfer: General definition, applications and limitations. J. Atmos. Sci., 59, 2330-2346.

- Mitchell, D.L., A.J. Baran, W.P. Arnott and C. Schmitt, 2006: Testing and comparing the modified anomalous diffraction approximation. *J. Atmos. Sci*., **63**, 2948-2962.

- Mitchell, D.L., R.P. d'Entremont and R.P. Lawson, 2006: Passive thermal retrievals of ice and liquid water path, effective size and optical depth and their dependence on particle and size distribution shape. AMS Conference on Atmospheric Radiation, 10-14 July 2006, Madison, Wisconsin. Paper 12.5 (available on CD).

- Parol, F., J.C. Buriez, G. Brogniez and Y. Fouquart, 1991: Information content of AVHRR channels 4 and 5 with respect to the effective radius of cirrus cloud particles. *J. Appl. Meteorol.*, **30**, 973-984.

- Sanderson, B.M., C. Piani, W.J. Ingram, D.A. Stone, M.R. Allen, 2008: Towards constraining climate sensitivity by linear analysis of feedback patterns in thousands of perturbed physics GCM simulations. Clim. Dyn., 30, 175-190.

- Yang, P., H. Wei, H-L. Huang, B.A. Baum, Y.X. Hu, G.W. Kattawar, M.I. Mishchenko, and Q. Fu, 2005: Scattering and absorption property database for nonspherical ice particles in the near- through far-infrared spectral region. *Appl. Opt*., **44**, 5512–5523.

VERTICAL PROFILES IN FREEZING PRECIPITATION FROM IN-SITU MEASUREMENTS IN WINTER STRATIFORM CLOUDS

Monika E. Bailey, G.A. Isaac, S.G. Cober, A.V. Korolev, J.W. Strapp

Cloud Physics and Severe Weather Research Section, Environment Canada
Toronto, Ontario, Canada

1. INTRODUCTION

Since 1995 during the course of several field campaigns, Environment Canada has collected a large data base of icing related measurements using research aircraft in continental and maritime stratiform cloud environments. A specific goal of each campaign was to characterize aircraft icing environments associated with supercooled large drops (SLD) greater than 50 μm in diameter and with freezing drizzle/rain. The data presented here were extracted as part of a preliminary study of potential icing conditions relevant to northeast Atlantic helicopter operations. Because the effective operational ceilings for helicopters are about 10,000 ft, the icing avoidance strategy of flying up and out is often unavailable. The analysis is focused on characterizing freezing precipitation conditions at elevations below 10,000 ft. This region is also relevant for defining hazardous conditions for aircraft takeoff and landing.

Preliminary results are presented of the analysis of vertical profiles of microphysical parameters determined from measurements collected during aircraft ascent, decent and spiral maneuvers below 10,000 ft along with a statistical comparison of parameters related to icing at elevations above and below this region.

Corresponding Author:
Monika E. Bailey, Environment Canada, 4905 Dufferin St., Toronto, Ontario, Canada M3H 5T4; monika.bailey@ec.gc.ca

2. INSTRUMENTATION

The data used in this study were collected using the National Research Council of Canada (NRC) Convair-580 aircraft during the following four projects: (1) the First Canadian Freezing Drizzle Experiment (CFDE1) flown over Newfoundland and the northeast Atlantic during March 1995 (Cober et al., 1995); (2) the Third Canadian Freezing Drizzle Experiment (CFDE3) flown between December 1997 and February 1998 (Cober et al., 1995, Isaac et al., 1998, Isaac et al., 2001b); (3) the first Alliance Icing Research Project (AIRS1) flown between November 1999 and February 2000 (Isaac et al., 2001a); (4) the Second Alliance Icing Research Project (AIRS2) flown between November 2003 and February 2004 (Isaac et al., 2005). Projects CFDE3, AIRS1 and AIRS2 were flown over southern Ontario and Quebec. Flights were deliberately targeted to observe aircraft icing environments by flying into winter storms for which freezing precipitation with SLD > 50 μm was forecast.

The Convair-580 aircraft was equipped by Environment Canada with a full suite of microphysical sensing instruments for making in-situ measurements. The SLD environment was documented with the following standard instruments: a Rosemount Icing Detector (RID); two Rosemount Temperature Probes; three independent hot wire probes for LWC measurements including two King LWC probes, a Nevzorov LWC probe and a Nevzorov TWC probe (Korolev at al., 1998); two Particle Measuring System (PMS)

Forward Scattering Spectrometer Probes (FSSP); two PMS 2D Cloud Particle Imaging Probes (2D-C and 2D-G) and a PMS 2D Precipitation Particle Imaging Probe (2D-P). The aircraft instrumentation is described in Cober et al. (2001a).

In-cloud	TWC > .005 gm^{-3}
In cold cloud	TWC > .005 gm^{-3}, T <= 0 °C, T > = -40°C
In-icing	TWC > .005 gm^{-3}, T <= 0 °C, T > = -40°C, dmax > 1μm, liquid and mixed phase cases
SLD	super cooled large drops: TWC > .005 gm^{-3}, T <= 0°C, T > = -40°C, dmax > 50μm, ice crystal concentration < 1 L^{-1}, liquid and mixed phase
ZL	(freezing drizzle) TWC > .005 gm^{-3}, T <= 0 °C, T > = -40°C, dmax > 100μm, dmax < 500 μm, ice crystal concentration < 1 L^{-1}, liquid and mixed phase
ZR	(freezing rain) TWC > .005 gm^{-3}, T <= 0 °C, T > = -40°C, dmax > 500μm and dmax < 3000μm, ice crystal concentration < 1 L^{-1}, liquid and mixed phase
dmax	largest drop observed in each 30-s drop spectra
medvd	median volume diameter (50% mass diameter)
80VD	80% mass diameter

Table 1. Definitions of terms used in this paper. Note that freezing drizzle is defined as water drops with dmax between 100 μm and 500μm. Mixed phase is identified when the following conditions hold: "ratio of LWC to TWC between 0.25 and 1.0, fraction of circular 2D images larger than 125 μm is greater than 0.4, FSSP concentrations > 15 cm^{-1}, visual assessment that the 2D images contained ice crystals, RID response > 2 mV s^{-1}" (Cober et al., 2001b). Only mixed-phase records with ice crystal concentrations < 1^{-L} are considered here to minimize errors resulting from misidentifying crystals as drops (Cober et al., 2001b).

The data, acquired at one second intervals, were averaged over 30 second intervals in order to improve the statistical reliability of the particle counts used in classifications. The aircraft speed was ~ 100 m s^{-1} horizontally and on average 5 m s^{-1} during ascent, descent and spiral manoeuvres. Accordingly, a 30-s data record represents ~ 3km of horizontal sampling and ~ 150m vertical sampling. Each 30-s record was classified as liquid, mixed or glaciated phase following Cober et al. (2001a). Drop size spectra were generated for each 30-s liquid or mixed phase record for which the ice crystal concentration was < $1L^{-1}$. The median volume diameter (medvd), 80% volume diameter (m80vd), maximum drop size (dmax) drop concentrations and LWC were obtained for each 30-s record from the drop size spectra for SLD. For each 30-s record, the microphysical parameters identified in Table 1 were identified and analyzed if applicable.

3. DATA SET

The data set comprises over 30,000 km of in-cloud data collected during 84 research flights at altitudes from 0 to 7 km and at temperatures usually colder than 0° C. The goal is to compare microphysics for the maritime and continental environment above and below 10000 ft. For the statistical analysis, data from the CFDE3 and AIRS1 projects (C+A1) (continental environment) are combined, while data from AIRS2 (A2) (also continental) is treated separately because it is the most recent project and some statistical results from it are presented here for the first time. CFDE1 (C1) is treated separately as the only one of the datasets obtained in a maritime environment. Data is divided into high and low altitude sets (above and below 10,000 ft). Most flights were targeted at forecast or observed icing conditions. Within a flight the aircraft could return repeatedly to resample icing in a specific cloud region. Approximately 71% of flight time was below 10,000 ft in the maritime environment (C1), and 59% and 48% respectively for the continental projects (C3+A1 and A1) (Table 2). The number of flights during which 4 or more sequential 30s records of SLD, ZL and ZR were observed are summarized in Table 3. A greater proportion of maritime flights encountered such events.

	CFDE 1	CFDE3+ AIRS1	AIRS2
# of 30 s in-flight Records	6339	22325	7430
% of time below 10kft	71%	59%	48%
% of time above 10kft	29%	41%	52%

Table 2. Distribution of 30s data points above and below 10kft

Project	No of flights	with SLD	with ZL	with ZR
AIRS 1	25	84%	28%	8%
AIRS 2	21	71%	33%	19%
CFDE 1	12	100%	75%	33%
CFDE3	27	81%	59%	2%

Table 3. Occurrence of flights with 4 or more sequential 30s records SLD/ZL/ZR

4. STATISTICAL RESULTS

Tables 4 and 5 summarize statistics for flights times in cold cloud and icing conditions, phase segregation (into liquid, mixed and glaciated phase), icing related parameters (occurrence of SLD, ZL and ZR), formation mechanisms (classical and non-classical), occurrence of the Politovitch criteria for hazardous conditions (Politovich 1989), and the Ashenden and Marwitz criteria for highest performance degradation (Ashenden and Marwitz 1998) categorized by height (above and below 10,000 ft) and geographical environment (maritime and continental). Because of the practice of targeting specific regions and of sometimes resampling the same icing conditions within a flight, the relative values of these numbers are meaningful, but not the absolute values relative to icing-free conditions. It should be noted that different analysis of these data have been reported earlier (Cober et al., 2001b, Cober and Isaac 2006, Korolev and Isaac 2005, Korolev et al., 2007).

A brief summary of the main features of Tables 4 and 5 is as follows:

1) SLD: super cooled large drop conditions were encountered more often below 10,000 ft than above, 95% and 85% of the time for C1 (the maritime project) and C3+A1. However SLD records were observed almost equally above and below 10,000 ft, (54% - 46%) during A2. SLD was observed during 18% of the flight time for C1, and during 13% and 10% of flight time for C3+A1 and A2.
2) Phase: Examining the proportion of liquid, mixed and glaciated phase yields the following:
   a. For the maritime project, there is a strong distinction between high and low altitudes: liquid phase dominates below (48%) glaciated phase dominates above (76%); the proportion of mixed phase records remains approximately the same.
   b. For the continental projects C3 and A1, the contrast is similar but less pronounced, but with significantly more mixed phase at low altitudes than for the maritime case.
   c. The liquid phase is low for project A2, at both high and low altitudes. In fact, the clear distinction that exists between high and low altitudes for the other three projects is absent for A2.
3) Icing parameters: For the maritime environment (C1) 98% of ZL events and 100% of ZR events occurred below 10,000 ft. For continental environments (C3+A1) 87% of ZL and 91% ZR occurred below 10,000 ft. For A2, ZL and ZR were similar (58% ZL and 59% ZR) above and below 10,000 ft.
4) Formation mechanism: an assessment of the formation mechanism as classical (Stewart 1992, Stewart and Crawford 1995) or non classical (Singleton 1960, Bochieri 1980, Huffman and Norman 1988, Strapp et al., 1996; Beard and Ochs 1993) was made for each 30-s interval (Cober et al., 2001b) (Table 5). Classical referred to cloud drops that formed through ice crystals melting in an

above freezing layer while non-classical referred to cloud drops that formed through a condensation and collision-coalescence mechanism. SLD and ZL are formed predominantly by the non-classical mechanism both above and below 10,000 ft. Freezing rain was observed predominantly below 10,000 ft and formed by the classical mechanism. Most of the recorded freezing rain events below 10,000 ft were sampled during six flights; most ZR events observed above 10,000 ft are from two flights during AIRS1 and are formed by the non-classical mechanism. Analysis of formation mechanism for CFDE 1 and CFDE III flights has previously been reported by Cober et al. (2001d).

5) Less than 5% of all in-SLD records exceed the Politovitch criteria while the Ashenden and Marwitz criteria are exceeded in up to 35% of in-SLD records.
6) More than 99% of the observed extreme events, as determined by the Politovich criteria for hazardous conditions and the Ashenden and Marwitz criteria for highest performance degradation, occur below 10000 ft for CFDE1 (maritime) while 69% and 87% of such events occur below 10000 ft for C3-A1. For AIRS2 35% and 52% occur below 10,000 ft. Comparison of the CFDE1 and CFDE3 data to the Politovich and Ashenden and Marzitz criteria has previously been reported by Cober et al. (2001b).
7) Project average and median temperatures are presented in Table 4. The mean temperatures range between -4.0°C to -6.0°C below 10,000 ft and between -10.9°C to -14.3°C above 10,000 ft for CFDE1, CFDE3 and AIRS1. Notably, the mean temperatures above and below 10,000 ft are similar for AIRS2, -8.5°C and -9.3°C respectively. This result is consistent with and may be responsible for the relatively lower proportion of liquid phase records and the similarity of other microphysical parameters at high and low altitudes for AIRS2

	Below 10 kft		Above 10 kft	
	mean T°C	median T°C	mean T°C	median T°C
CFDE1	-4.0	-3.3	-10.9	-7.4
CFDE3	-4.6	-3.8	-11.8	-11.2
AIRS1	-6.0	-6.2	-14.3	-12.1
CFDE3 AIRS1	-5.0	-4.1	-13.1	-11.3
AIRS2	-8.5	-9.0	-9.3	-9.6

Table 4. Average and median temperatures by project.

.

Table 5 Summary of analysis of microphysics measurements made above and below 10,000 ft for maritime and continental environments. The data comprise 30s averages as described and are reported as numbers and percentages.

	MARITIME				CONTINENTAL							
	CFDE 1				CFDE 3 and AIRS 1				AIRS 2			
	Below 10kft		Above 10kft		Below 10kft		Above 10kft		Below 10kft		Above 10kft	
Number of In-Flight Points % of total	4529	71%	1810	29%	13127	59%	9208	41%	3534	48%	3896	52%
% of flight time in:												
cloud (TWC > 0.005 g m-3)	2909	64%	838	46%	9145	70%	4886	53%	2602	74%	2412	62%
cold cloud (T <= 0° C)	2203	49%	765	42%	7740	59%	4206	46%	2172	61%	2083	53%
icing (dmax > 1µm)	1418	31%	179	10%	5745	44%	1376	15%	1335	38%	1158	30%
SLD (dmax > 50µm)	822	18%	43	2%	1779	13%	318	3%	341	10%	401	10%
Freezing drizzle (dmax 100µm to 500µm)	332	7%	6	0.3%	760	6%	111	1%	139	4%	99	3%
Freezing Rain (dmax > 500µm)	94	2%	0	0	210	2%	20	0.2%	19	0.5%	13	0.3%
Summary of Phase Results												
% Liquid phase (of in-cloud cold points)	1049	48%	39	5%	2714	35%	446	11%	279	13%	262	13%
% Mixed Phase (of in-cloud cold points)	369	17%	140	18%	3031	39%	930	22%	1056	49%	896	43%
% Glaciated Phase (of in-cloud cold points)	782	35%	585	76%	1966	25%	2799	66%	834	38%	924	44%
Summary of Icing Parameters												
% SLD (of in-icing points)	822	58%	43	24%	1779	31%	318	23%	341	25%	401	35%
% Freezing drizzle (of in icing points)	332	23%	6	3%	760	13%	111	8%	139	10%	99	8%
% Freezing rain (of in icing points)	94	7%	0	0	210	4%	20	1%	19	1%	13	1%
% of In-SLD classical	168	20%	9	21%	391	22%	7	2%	NA	NA	NA	NA
% of In-SLD non-classical	662	80%	34	79%	1388	78%	311	98%	NA	NA	NA	NA
% of In- Freezing drizzle classical	30	9%	0	0%	108	14%	6	5%	NA	NA	NA	NA
% of In- Freezing drizzle non-classical	302	91%	6	100%	652	86%	105	95%	NA	NA	NA	NA
% of In- Freezing rain classical	86	91%	0	0%	207	99%	0%	0%	NA	NA	NA	NA
% of In- Freezing rain non-classical	8	9%	0	0%	3	1%	20	100%	NA	NA	NA	NA
Politovich Criteria for Hazardous Conditions LWC > 0.2 g m^{-3}, MVD > 30 µm												
% of In-Icing Events	77	5%	3	1.7%	62	1%	27	2%	31	2.3%	36	3%
% of In-SLD Events	44	5%	0	0	46	3%	21	7%	17	5%	31	8%
Ashenden and Marwitz Criteria with Highest Performance Degradation (80VD*LWC > 10 and 80VD*LWC < 100 (g m^{-3} µm)												
% of In-Icing Events	348	24%	4	2.2%	548	9%	73	5%	214	16%	118	10%
% of In-SLD Events	292	35%	1	2.3%	401	22%	62	19%	94	28%	87	22%

5. ZL AND ZR DEPENDENCE ON HEIGHT

Histograms giving the relative likelihood of occurrence, as observed over all four projects, of SLD, ZL, and ZR as a function of altitude are presented in Figures 1a, 1b and 1c. In order to avoid biasing by the unequal sampling of different altitudes by actual flights, these histograms are the observed frequencies divided by the altitude sampling histogram shown in Fig. 1d. The relative probability plotted is the number of records in a given altitude range, divided by the total number of records acquired in that altitude range. The relative frequencies are such that $N_{SLD} > N_{ZL} > N_{ZR}$ at any altitude. The frequencies of all three diminish rapidly in the first 7000 ft, diminishing more slowly (SLD) or not at all (ZL and ZR) between 7000 and 14000 ft. Only SLD persists significantly above about 15000 ft. The following points should be noted: 1) these histograms are not generated from a large number of independent cases; the number of flights is of order 100, 2) these are for a restricted geographic range 3) the low frequencies close to ground level may be an artifact of under sampling very low altitudes under adverse flight conditions 4) the observed bimodality of the distribution of ZR may not be statistically significant, since the upper mode is produced by records from only three flights.

The histograms show that, for the entire data set, the likelihood of icing conditions does not diminish rapidly between 7000 and 14000 ft. At these altitudes therefore, ascending or descending may be equally likely to solve the problem of icing-avoidance which agrees with the recommendation of Korolev et al. (2006)

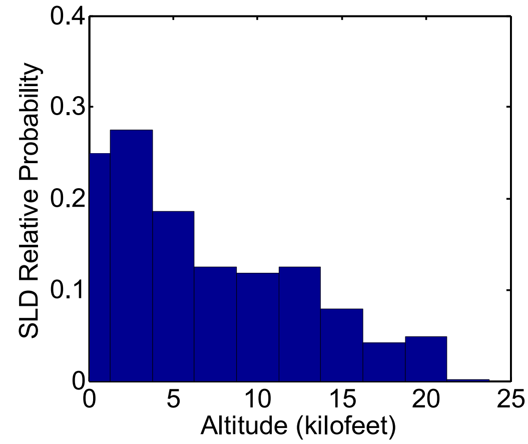

Figure 1a: Relative likelihood of encountering SLD as a function of altitude, over all four projects.

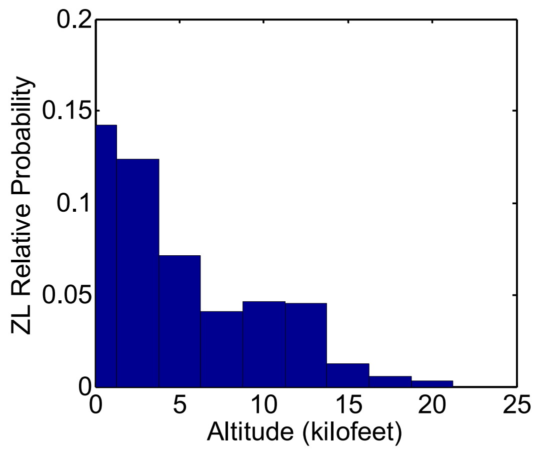

Figure 1b: Relative likelihood of encountering ZL as a function of altitude, over all four projects

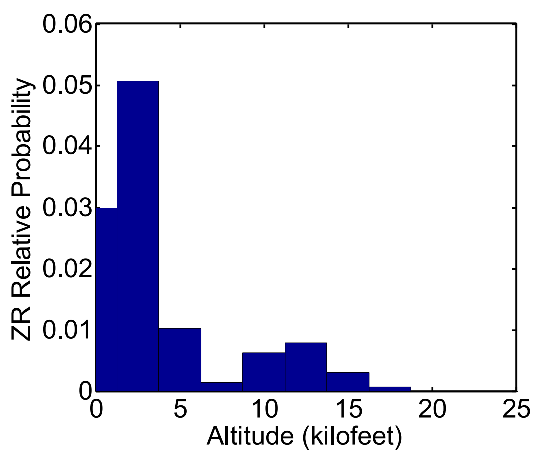

Figure 1c: Relative likelihood of encountering ZR as a function of altitude, over all four projects.

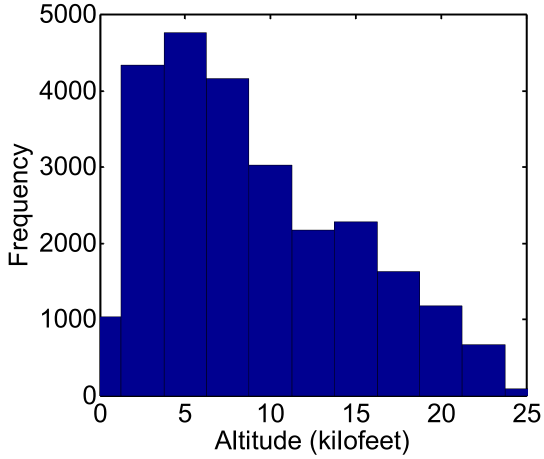

Figure 1d: Number of records obtained at each altitude over all four projects.

6. PROFILES

Time histories of altitude and occurrences of SLD, ZL and ZR were examined for each flight. From these, vertical profiles were selected from periods of continuous aircraft ascent, descent, or Lagrangian spiral, for which at least 300 seconds of uninterrupted data containing segments of ZL were available below 10000 ft. In addition, a strong rate of climb or descent (of the order of 5 m s^{-1} was required to minimize any confounding influence of lateral variations. Vertical profiles of microphysical data from three of the projects have been previously presented without point by point superposition of SLD, ZL, ZR (Korolev and Isaac, 2005). Selected profiles with this added information are presented here. Repeat profiles through the same event have been omitted. All of these profiles extend downward to 2500 ft altitude or below.

Examples of ZL and ZR formed by classical (2a, b, c, d, f) and non-classical mechanisms (2d, 2e) are shown. Most profiles include a temperature inversion or isothermal section as noted in Korolev and Isaac (2005). Figures 2c, e, f show examples of large ZL (>350 μm) and ZR at temperatures < -10°C at the base of the profile, below 500 ft. Further analysis is needed to relate the microphysics to the development of icing conditions and to determine whether characteristic profiles can be identified.

Figures 2a to 2g. show vertical profiles of microphysical parameters measured during periods of continuous or spiral aircraft ascent or descent. The parameters plotted are: temperature (T), liquid water content (LWC), median volume drop size diameter (medvd), maximum drop size diameter (dmax) and total water content (TWC) for liquid and mixed phase records with ice crystal concentrations less than $1L^{-1}$. Superimposed on each profile are occurrences of SLD, ZL, ZR and T ≥ 0°C. Significant features are listed above each profile.

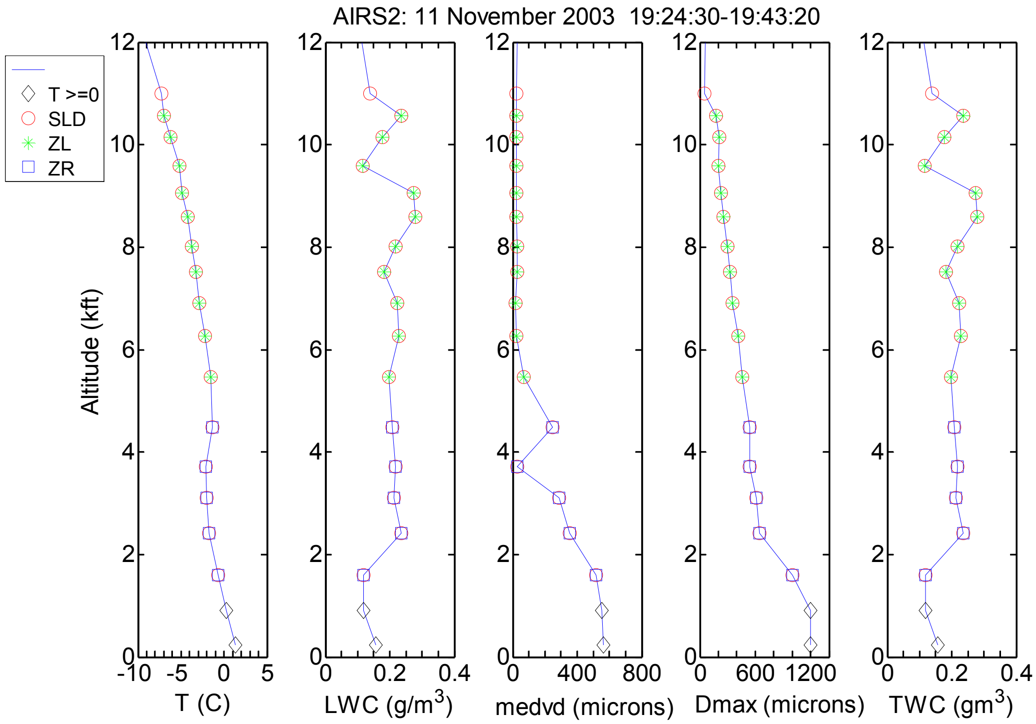

Figure 2a Cold ZL (-7°C) above 10kft, inversion at 4kft, ZR below 4kft, LWC ~uniform with height.

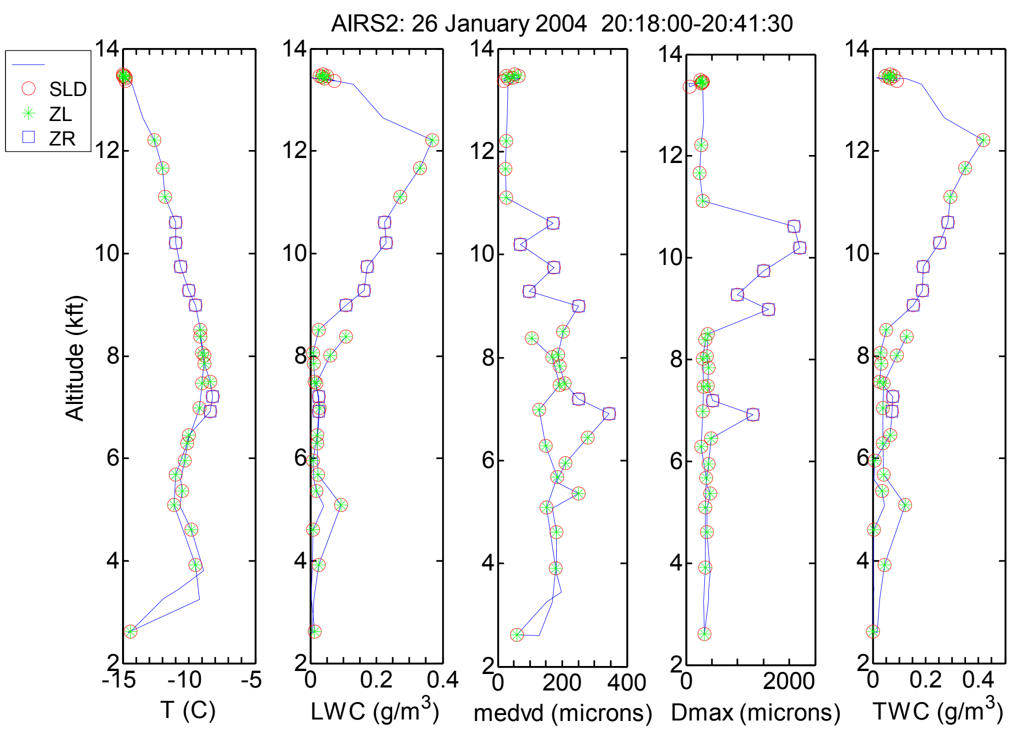

Figure 2b Two layers of cold ZR (-10°C), temperature inversion at lower ZR layer.

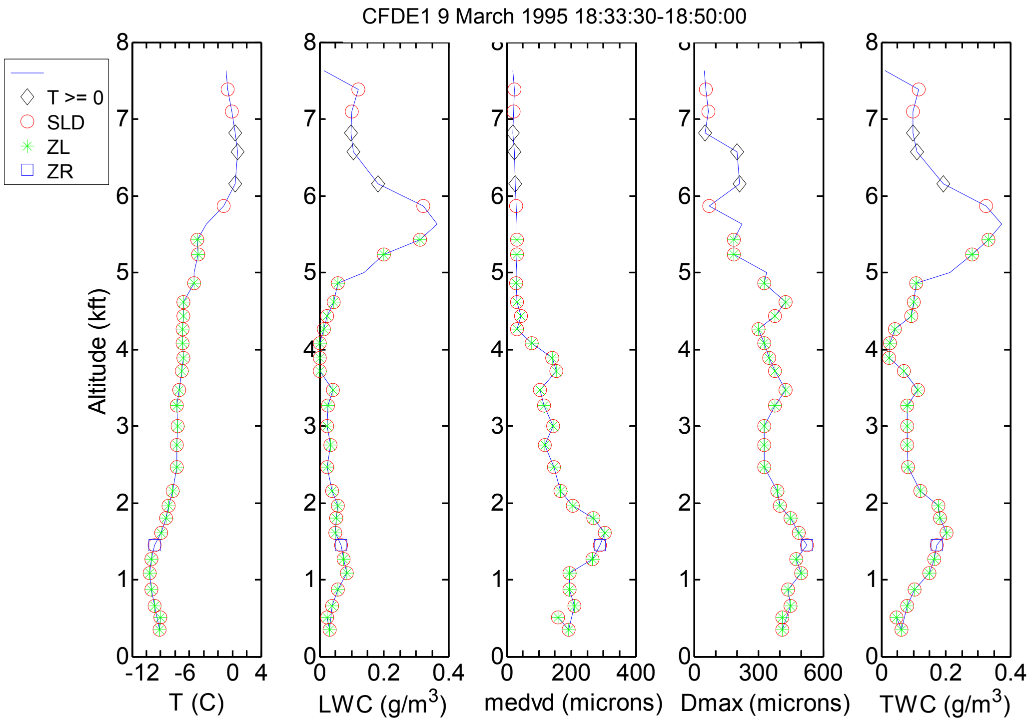

Figure 2c ZR at 1.4kft below deep ZL layer (4kft) and temperature inversion.

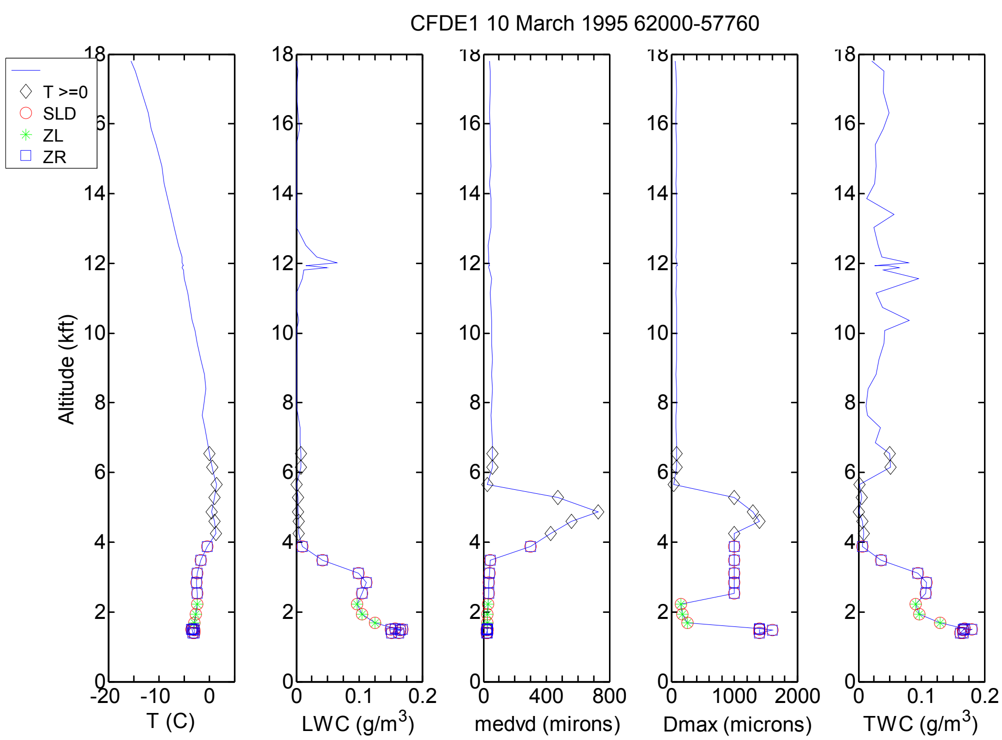

Figure 2d.. Classical formation of ZR below melting layer. Large ice particles were observed above the melting layer.

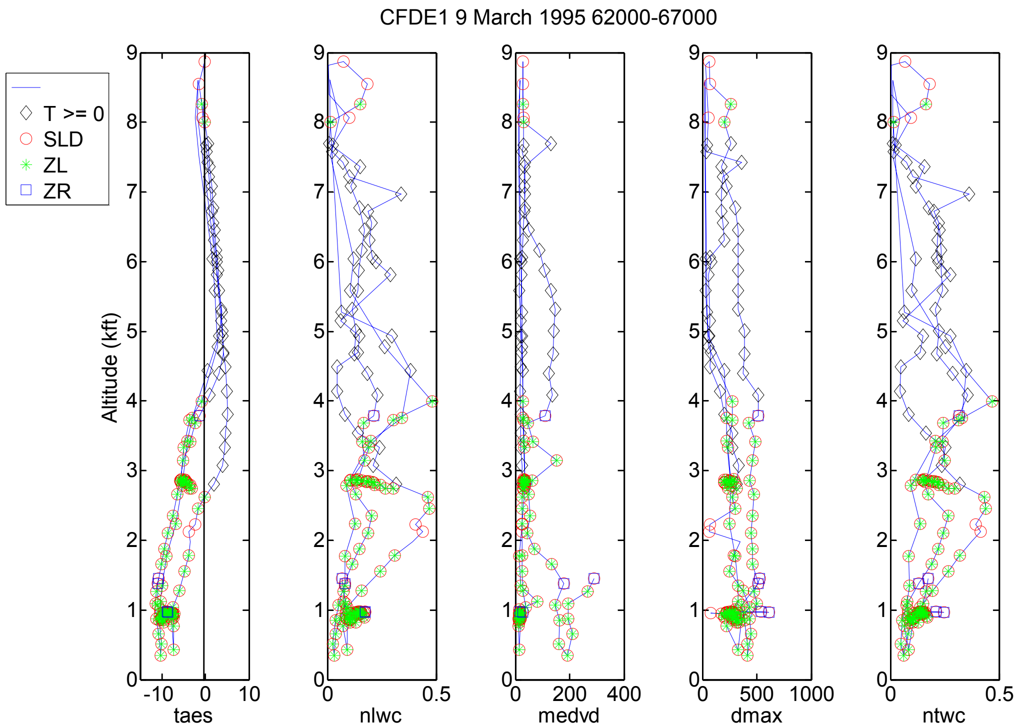

Figure 2e.. Large ZL and ZR, possible example of mixed classical and non-classical formation, temperature inversion, warm layers.

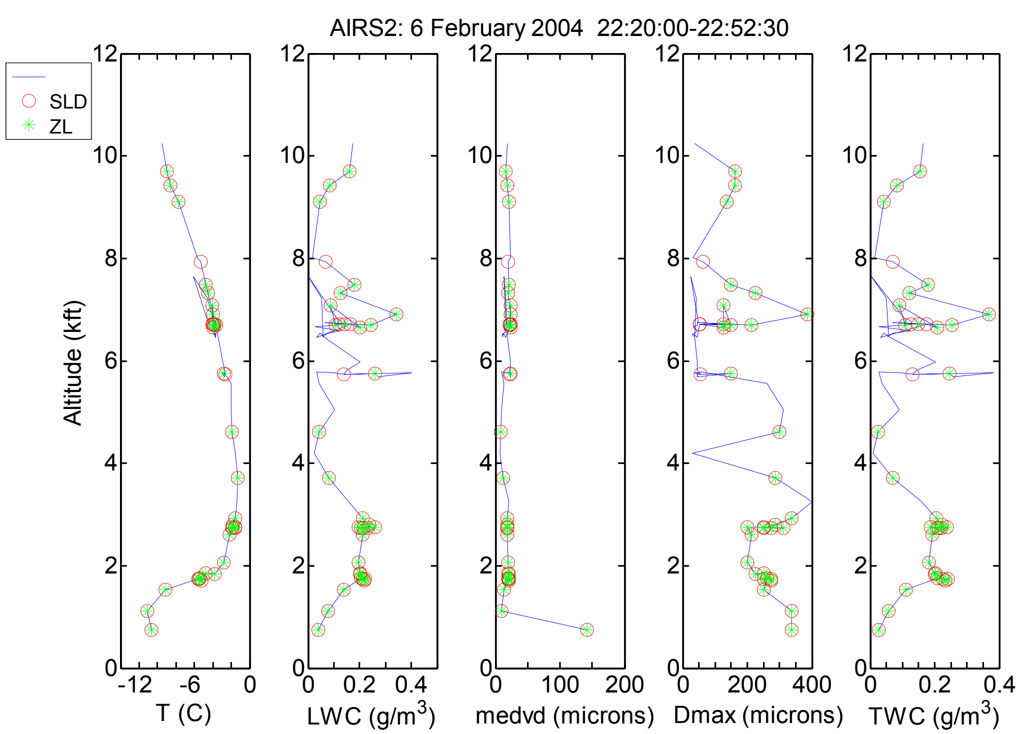

Figure 2f Cold ZL at ground level with dmax ~350μm, temperature inversion below 2kft.

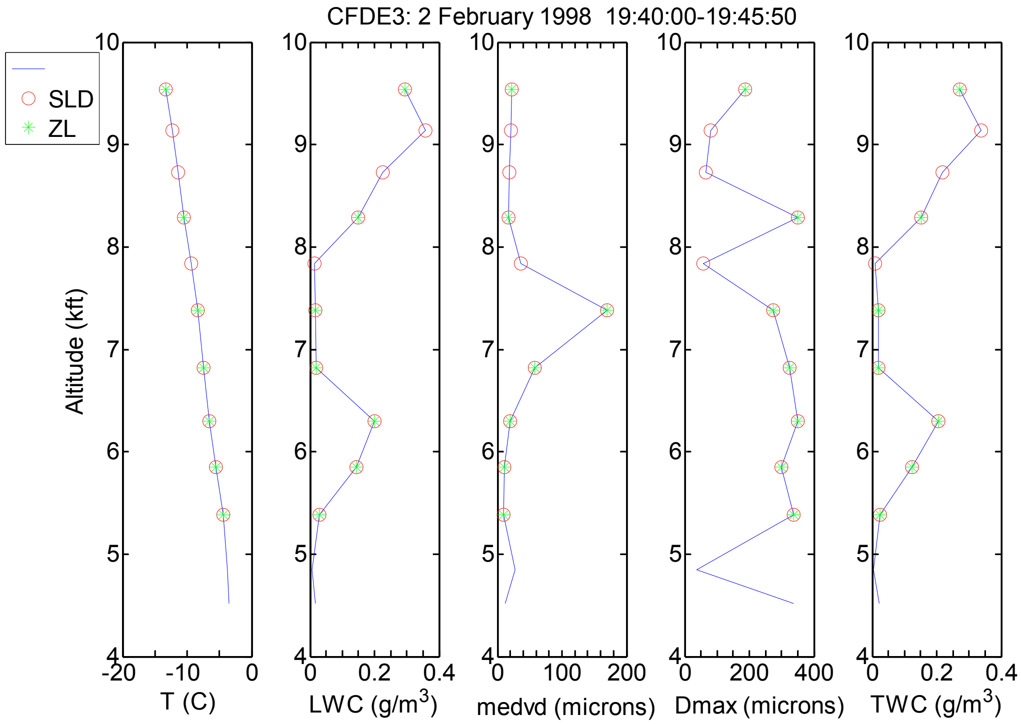

Figure 2g Cold ZL, dmax up to 350µm, pseudo adiabatic temperature gradient.

7. SUMMARY

The main results are:

1) A greater proportion of maritime flights (CFDE1) encountered SLD, ZL, ZR conditions than continental flights (CFDE1, CFDE3 and AIRS1). These conditions were found more often below 10,000 ft.
2) The liquid phase dominates below 10,000 ft (48%) for the maritime project, while the glaciated phase dominates above (76%). The proportion of mixed phase records remains approximately the same above and below 10,000 ft. For the continental projects (CFDE3 and AIRS1) the phase contrast between altitudes is similar but less pronounced and with significantly more mixed phase at low altitudes than for the maritime case. AIRS 2 presents a different scenario, with similar proportions of liquid, mixed and glaciated phases above and below 10,000 ft and with low liquid phase (13%)
3) For the maritime environment, 98% of the observed ZL events and 100% of the observed ZR events occurred below 10,000 ft. For the continental environments, CFDE3+AIRS1, 87% of observed ZL and of observed 91% ZR occurred below 10,000 ft.
4) SLD and ZL are formed predominantly by the non-classical mechanism both above and below 10,000 ft. ZR was observed mostly at lower altitudes and formed mainly by the classical mechanism although several examples of vertical profiles of cold ZR formed by non-classical mechanism are shown.
5) In our dataset, the likelihood of icing conditions did not diminish rapidly with height between 7000 and 14000 ft. At these altitudes, ascending or descending may be equally likely to solve the problem of icing-avoidance.

6) Most (>99%) extreme events (according to the Politovich criteria) occur below 10,000 ft for CFDE1 (maritime) while 69% and 87% of such events occur below 10,000 ft for CFDE3 and AIRS1. Fewer than 5% of all in-SLD records exceed the Politovitch criteria.
7) There are clear differences in the microphysical parameters at high and low altitudes for projects CFDE1, AIRS1 and CFDE3 but not for the AIRS2 project, which encountered significantly lower low-altitude temperatures than the other projects. This highlights the possibility that the above conclusions about rates of occurrence may not be valid in all meteorological conditions or by geographical location. Further analysis to characterize the vertical profiles is on-going.

ACKNOWLEDGEMENTS

Funding for these measurements was provided by Environment Canada, the Canadian Search and Rescue New Initiatives Fund, Transport Canada, the U.S Federal Aviation Administration, NASA and the Boeing Commercial Airplane Group. All the measurements reported in this paper were made using the National Research Council (NRC) Convair-580 and the authors would like to acknowledge their many colleagues at NRC.

REFERENCES

Ashenden, R., and J.D. Marwitz, 1998: Characterizing the supercooled large droplet Environment with corresponding turboprop aircraft response. *J. Aircraft*, **35**, 912-920.

Beard, K. V., and H. T. Ochs, 1993:Warm-rain initiation: An overview of microphysical mechanisms. *J. Appl. Meteor.,* **32,** 608–625

Bocchieri, J. R., 1980: The objective use of upper air soundings to specify precipitation type. *Mon. Wea. Rev.,* **108,** 596–603.

Cober, S.G., G.A. Isaac, and J.W. Strapp, 1995: Aircraft icing measurements in east coast winter storms. *J. Appl. Meteor.*, **34**, 88-100.

Cober, S.G., G.A. Isaac, A.V. Korolev, and J.W. Strapp, 2001a: Assessing cloud-phase conditions. *J. Appl. Meteor.*, **40**, 1967-1983.

Cober, S.G., G.A. Isaac, and J.W. Strapp, 2001b: Characterizations of aircraft icing environments that include supercooled large drops. *J. Appl. Meteor.*, 40, 1984-2002.

Cober, S.G., and G.A. Isaac, 2006: Estimating maximum aircraft icing environments using a large data base of in-situ observations. *AIAA 44th Aerospace Sci. Meeting and Exhibit*, Reno Nevada, 9-12 January 2006, AIAA-2006-266.

Huffman, G. J., and G. A. Norman, 1988: The supercooled warm rain process and the specification of freezing precipitation. *Mon. Wea. Rev.,* **116,** 2172–2182.
Isaac, G. A., S. G. Cober, A. V. Korolev, J. W. Strapp, A. Tremblay, and D. L. Marcotte, 1998: Overview of the Canadian Freezing Drizzle Experiment I, II, and III. Preprints, *Conf. on Cloud Physics,* Everett, WA., Amer. Meteor. Soc., 447–450.

Isaac, G.A., S.G. Cober, J.W. Strapp, D. Hudak, T.P. Ratvasky, D.L. Marcotte, and F. Fabry, 2001a: Preliminary results from the Alliance Icing Research Study (AIRS). Paper AIAA 2001-0393, *39th Aerospace Sci. Meeting and Exhibit*, Reno Nevada, 8-11 January 2001.

Isaac, G.A., S.G. Cober, J.W. Strapp, A.V. Korolev, A. Tremblay, and D.L. Marcotte, 2001b: Recent Canadian research on aircraft in-flight icing. *Canadian Aeronautics and Space Journal*, 47-3, 213-221.

Isaac, G.A., J.K. Ayers, M. Bailey, L. Bissonnette, B.C. Bernstein, S.G. Cober, N. Driedger, W.F.J. Evans, F. Fabry, A. Glazer, I. Gultepe, J. Hallett, D. Hudak, A.V. Korolev, D. Marcotte, P. Minnis, J. Murray,

L. Nguyen, T.P. Ratvasky, A. Reehorst, J. Reid, P. Rodriguez, T. Schneider, B.E. Sheppard, J.W. Strapp, and M. Wolde, 2005: First results from the Alliance Icing Research Study II. *AIAA 43rd Aerospace Sci. Meeting and Exhibit*, Reno Nevada, 11-13 January 2005, AIAA 2005-0252.

Korolev, A. V., J.W. Strapp, and G. A. Isaac, and A. N. Nevzorov, 1998: The Nevzorov airborne hot-wire LWC–TWC probe: Principles of operation and performance characteristics. *J. Atmos. Oceanic Technol.,* **15,** 1495–1510

Korolev, A.V., and G.A. Isaac, 2005: Microphysical characterisation of stratiform layers forming freezing drizzle. *AIAA 43th Aerospace Sciences Meeting*, Reno, Nevada. 11-13 January 2005, AIAA-2005-0858.

Korolev, A.V., G.A. Isaac, and J.W. Strapp, 2006: Aircraft escape strategy from supercooled cloud layers. *AIAA 44th Aerospace Sciences Meeting and Exhibit*, Reno, Nevada. 9-12 January 2006, AIAA-2006-265.

Korolev, A.V., G. Isaac, J.W. Strapp, S.G. Cober, and H. Barker, 2007: In-situ measurements of liquid water content profiles in mid-latitude stratiform clouds. *Quart. J. Roy. Meteorol. Soc.*, 133, 1693-1699.

Politovich, M.K., 1989: Aircraft Icing Caused by Large Supercooled Droplets, *J. Applied. Meteorology*, **28**, 856-868.

Singleton, F., 1960: Aircraft observations of rain and drizzle from layer clouds. *Quart. J. Roy. Meteor. Soc.,* **86,** 195–204.

Strapp, J.W., R.A. Stuart and G.A. Isaac, 1996: Canadian climatology of freezing precipitation, and a detailed study using data from St. John's, Newfoundland. FAA International Conference on Aircraft Inflight Icing, Springfield, Virginia, Volume II, DOT/FAA/AR-96/81, 45-55.

Stewart, R. E., 1992: Precipitation types in the transition region of winter storms. *Bull. Amer. Meteor. Soc.,* **73,** 287–296.

Stewart, R. E., and R. W. Crawford, 1995: Some characteristics of the precipitation formed within winter storms over eastern Newfoundland. *Atmos. Res.,* **36,** 17–37.

AEROSOL IMPACTS ON THE MICROPHYSICS OF MIXED PHASE CLOUDS

K N Bower[1], T W Choularton[1], I Crawford[1], J Crosier[1], J D Allan[1], W Morgan[1], J R Dorsey[1], H Jones[1], M W Gallagher[1], H Coe[1], P Connolly[1], C Deardon[1], A J Illingworth[2] and R Hogan[2]

[1] Centre for Atmospheric Science (CAS), School of Earth, Atmospheric and Environmental Science (SEAES), University of Manchester, Manchester M13 9PL. UK
[2] University of Reading

1. INTRODUCTION

In this paper we investigate the aerosol indirect effect in mixed phase layer clouds, and consider the roles of the aerosol in both droplet and ice crystal nucleation.

The "Aerosol Properties, PRocesses And Influences on the Earth's climate" (or APPRAISE) programme is a UK Natural Environment Research Council (NERC) directed research programme set up to look at the science of aerosols and their effects on climate. One project in particular within APPRAISE is funded to investigate the Aerosol-Cloud Interactions occurring within Mixed Phase Clouds.

2. THE APPRAISE CLOUD PROJECT

Objectives:

- To determine the nucleating ability of specific ice nuclei and the initiation and development of ice in mixed phase clouds.
- To determine how aerosol particles control the cloud microphysics and dynamics in mixed phase clouds
- To determine the type and phase partitioning of absorbing material above below and within clouds and the role of this material in ice nucleation.
- To reduce the uncertainty in the contribution of indirect radiative forcing by better understanding the role of aerosols in the microphysics of mixed phase cloud.

The NERC APPRAISE cloud project consists of a consortium of UK Universities working in collaboration with the Met office and European collaborators. It has the aim of performing, laboratory, modelling and field studies over the UK (and elsewhere*) that address the question of how ice forms in clouds and in particular how this is determined by the properties of the aerosol entering into cloud. Having improved the understanding of these processes, the objective is then to begin to improve the treatment of ice formation in global scale models.

The main thrust of the UK fieldwork involves the use of the UK FAAM (Facility for Airborne Atmospheric Measurement) BAe146 research aircraft flying in the vicinity of a suite radars and lidars operated at the Chilbolton Observatory in Hampshire, southern England (facilities include a scanning 3-GHz Doppler polarization radar, a 94GHz cloud radar, and a suite of lidars and radiation instrumentation). The aim is to make insitu measurements of the microphysical properties of a variety of mixed phase clouds at the same time as these clouds are being investigated remotely by the radars and lidars. The main cloud types to be studied are winter-time stratocumulus, altocumulus, frontal layer clouds, cirrus and convective clouds (should the opportunities arise).

3. METHOD

During winter 2007-2008, flights were made (and during winter 2008-2009 will be made) in the vicinity of Chilbolton, using the FAAM BAe146 research aircraft. This was (will be) equipped with a comprehensive range of instrumentation to measure the ice and liquid phase microphysics of the cloud and the size distribution and size resolved chemical composition of the aerosols entering cloud. The aircraft flew horizontal legs below cloud, in cloud and above cloud top on a radial towards and away from Chilbolton observatory. The vertical separation of in-clouds legs was selected so as to investigate key regions of interest for the cloud microphysics of the system, features which were determined from an initial profile through the cloud system and from the simultaneous observations of the radars and lidars. Passes below cloud base were undertaken in order to investigate the aerosol entering the cloud whilst passes above cloud top were used to investigate any ice crystal seeding that was occurring from above and for the effects of entrainment.

In May 2008 flights were also undertaken in the mid-level orographic wave clouds forming in the air as it flows over the Alps in Switzerland. These were carried out as part of EUCAARI (the European Integrated project on Aerosol Cloud Climate and Air Quality Interactions) and in conjunction with measurements made on the ground at the Jungfraujoch high Alpine research station (which is a GAW site).

4. RESULTS

Results from two flights, B337 and B338, carried out on the mornings of the 15th and the 17th of January 2008, respectively, in the area around and to the west of Chilbolton are presented. On both these occasions,

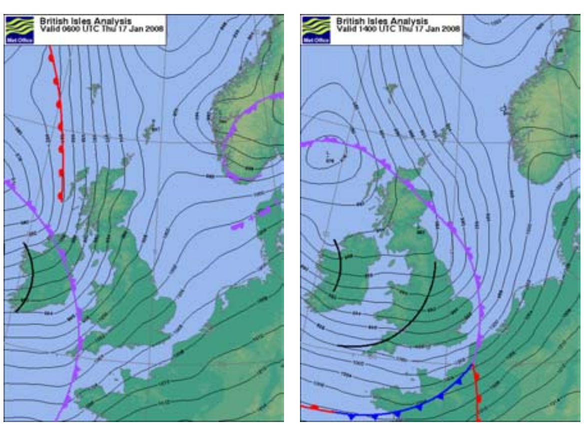

the mid level clouds investigated were associated with the passage of occluded frontal systems through the region (see Figure 1 above for B338).

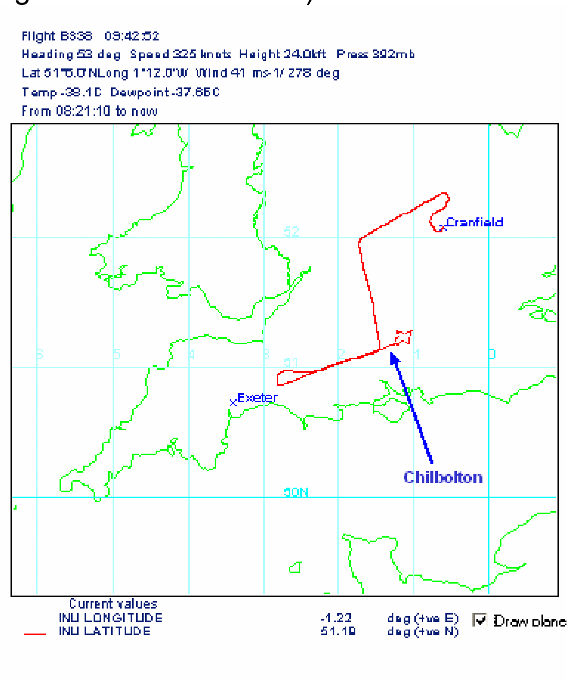

Figure 2 : Track of BAe146 aircraft during flight B338 on 17th January 2008

On each occasion, temperatures at cloud top were significantly colder than -35deg C, and there was evidence that ice crystal formation had occurred following the freezing of haze droplets. Observations using the CPI (Cloud Particle Imager) probe showed the presence of a large concentration of small pristine Bullet Rosette crystals, the preferred habit of ice growing at these ambient temperatures and humidities. Lower in these clouds the CPI showed that these ice crystals had grown to larger sizes and had developed into more complex shapes. This occurs as other crystal habits continue the growth of the crystals from their original pristine form as the ambient temperature and humidity change. At much lower levels (but at still significantly cold temperatures <-15degC) reduced concentrations of much larger crystals were observed. These were generally complex aggregates of the crystal forms seen higher up in the clouds. For these lower regions, aggregation appears to be the dominant method of crystal growth, forming snowflakes which sweep out the smaller crystals as they fall through the cloud.

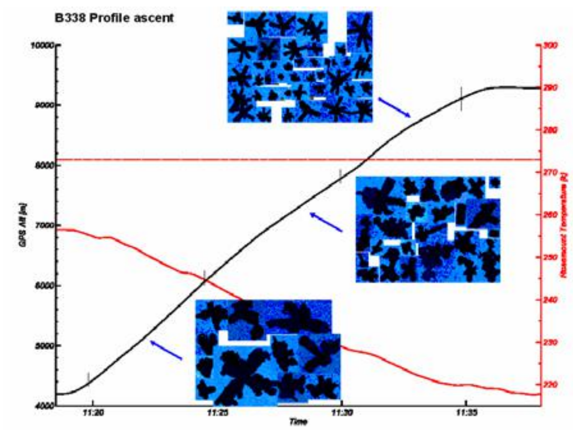

Figure 3 : Change in Ice crystal Habit observed by CPI during profile ascent in flight B338 from 4000 to 9000m

Occasionally, at mid levels in the cloud there was evidence of fragmentation of crystals. These fragments were rounded and aged, which together with their rarity suggests that crystal fragmentation may be taking place as a form of secondary ice formation in certain regions.

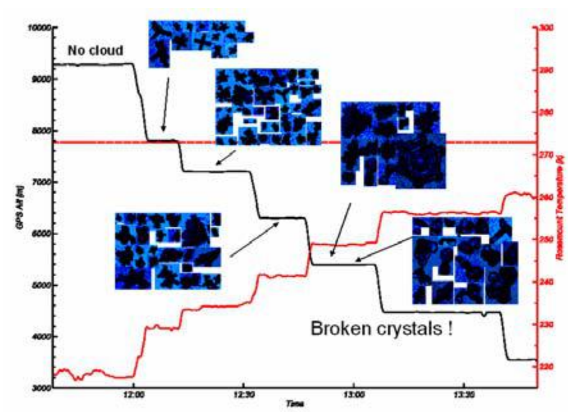

Figure 4 : Observations of a pocket of broken crystals at -24degC (5800m) during flight B338

In lower cloud layers, mixed phase conditions were observed with evidence of HM splinters growing in a narrow region bounded by regions of aggregates from aloft. On both occasions (B337 and B338) at the time of sampling, the lower level mixed phase cloud layers (cloud tops around -6 deg C) were separated completely from the mid/higher cloud levels by a totally cloud free region This is best illustrated by the time history plot of radar reflectivity presented in Figure 5 for January 17th (coinciding with flight B338)

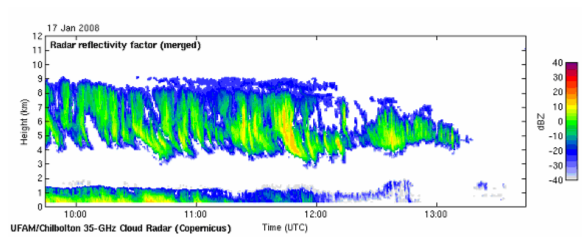

Figure 5 : Merged radar reflectivity times series plot for morning of January 17th - as observed by the 3.5GHz cloud radar at Chilbolton.

5. MODELLING

Detailed modelling of the cloud formation on the aerosols, particularly their ability to produce water droplets and ice crystals, is ongoing to aid interpretation of data. The model used is based on the ADDEM model (Topping 2005) which includes a description of the full range of aerosol chemistry including the effects of organic material. Ice nucleating properties of the aerosols are derived from recent studies at the AIDA environment chamber (eg see Crawford et al., ICCP 2008). A full description of mixed phase cloud microphysics is used including that of secondary ice crystal production and the evolution of precipitation.

Results of this and earlier work indicate that in widespread stratiform rainfall there are often regions of embedded convection, which contain high values of liquid water content. In such regions at temperatures just below freezing many small ice splinters are produced as supercooled liquid drops freeze on collision with larger ice particles by the Hallett-Mossop (HM) mechanism.

These splinters then rise in the cloud and grow rapidly to produce the high concentrations of large ice crystals observed. The HM process was found to be the dominant source of ice crystals in many systems. However, for clouds that lay entirely outside the HM zone primary ice crystal nucleation was important, and the dominant source of ice formation where cloud top temperatures fell below –30degC.

In all cases the glaciation process (and hence the cloud dynamics and precipitation formation) were sensitive to the aerosol population entering the cloud, through both water droplet activation and primary ice nucleation (Choularton et al., ICCP 2008).

In addition to the detailed cloud process modelling described, the WRF mesoscale model is also being used to simulate the dynamics and microphysics of the frontal system clouds that are typically observed over Chilbolton. Over the region of interest (the southern half of the UK), the model grid is nested down to a horizontal resolution of 1km. Output from the model will be validated using a variety of products, including ground-based measurements of reflectivity from the Chilbolton radar, analyses of precipitation rates from the Met Office NIMROD system, and in situ microphysical measurements from the FAAM BAe 146 aircraft (eg on APPRAISE flight B338).

For the B238 case study, initial model simulations have been performed using NCEP analysis data to drive the model. Analysis has focused on the ability of the model to capture the general pattern of weather experienced on the day. Radar reflectivity structure from the Chilbolton radar between 0900 and 1300GMT (Figure 5) reveals the presence of some low level cloud (up to 1.5km), and some colder, thicker cloud aloft, separated by a dry layer between approximately 1.5km and 3.5km deep. The reflectivity structure from the model shows that the model has difficulty in simulating the observed gap in the cloud. However, a tephigram comparison of the NCEP analysis profile over Southern England with a radiosonde ascent from Herstmonceux (both at 1200UTC) reveal that the NCEP analysis is too wet in the upper half of the troposphere, which may be contributing to the deficiencies in the simulation. Given the sensitivity of the model output to initial conditions, repeat simulations will be performed using ECMWF analyses. Also the technique of observation nudging (i.e. gently forcing the model towards the radiosonde data) will be employed in an attempt to achieve the best possible simulation using the default WRF microphysics options.

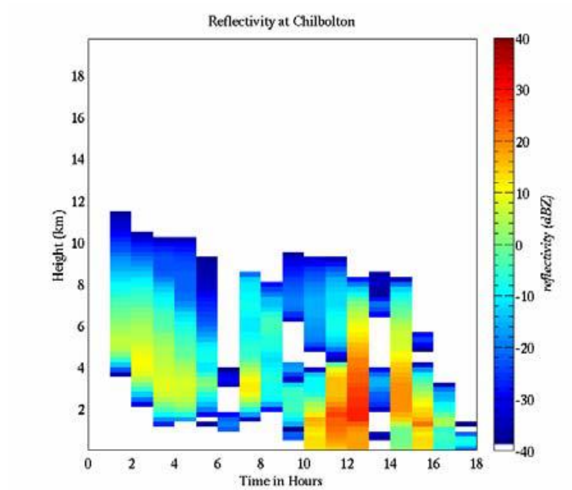

Figure 6 : Simulated radar reflectivity from WRF model at nearest gridpoint to Chilbolton for Jan 17th case study

6. FUTURE WORK

Detailed data interpretation and analyses examining linkages between aerosol and cloud microphysical properties will continue, including work using the detailed process model. Flights in wave clouds over the Alps will proceed in May 2008 to examine further the interaction between aerosols properties and the microphysics and formation of ice in these “natural laboratories”. Flights in the clouds forming over Chilbolton in winter 2008/9 will coincide with a major ground based intensive measurement campaign at the site. Mesoscale model simulations using the WRF model will continue in an attempt to pinpoint deficiencies and improve the simulation of the systems observed during flights but also over a longer period of observations using the radar and lidar facilities.

ACKNOWLEDGEMENTS
This work is supported by funding from the NERC APPRAISE directed research programme. Close collaboration with the MetOffice, FAAM and colleagues at several European sites and facilities is also greatly appreceiated.

ICE INITIATION IN MIXED-PHASE OROGRAPHIC WAVE CLOUDS

Andrew J. Heymsfield, P. R. Field[2], D. C. Rogers[1], J. Stith[1], J. Jensen[1]
Z. Wang[3], J. French[3], S. Haimov[3], P. J. DeMott[4], and C. Twohy[5]

1. NCAR, 3450 Mitchell Lane, Boulder Co. 80301
2. U. K. Met. Office, Devon EX1 3PB United Kingdom
3. Department of Atmospheric Sciences, University of Wyoming, Laramie, WY 82071
4. Department of Atmospheric Science, Colorado State University, Fort Collins, CO 80523
5. College of Oceanic and Atmospheric Sciences, Oregon State University, Corvallis OR 97331

1. INTRODUCTION

More than 50% of the earth's precipitation originates in the ice phase. Ice nucleation, therefore, is one of the most basic processes that lead to precipitation. The poorly understood processes of ice initiation and secondary ice multiplication in clouds result in large uncertainties in the ability to model precipitation production and to predict climate changes. Therefore, progress in modeling precipitation accurately requires a better understanding of ice formation processes.

Recent advances in observational tools, laboratory cloud simulation chambers, numerical models, and computer hardware provide new capabilities to understand and model ice initiation processes. In recognition of these new capabilities, a field program was conducted in November and December 2007 in clouds that are amenable to studying ice nucleation processes. The Ice in Clouds Experiment, referred to as ICE-L, made use of the NCAR C130 to study ice production in lenticular and stratiform layer clouds, focusing on the following scientific goal:

TO SHOW THAT UNDER GIVEN CONDITIONS, DIRECT ICE NUCLEATION MEASUREMENT(S), OR OTHER SPECIFIC MEASURABLE CHARACTERISTICS OF THE AEROSOL, CAN BE USED TO PREDICT THE NUMBER OF ICE PARTICLES FORMING BY NUCLEATION MECHANISMS IN SELECTED CLOUDS.

WITH THESE NEW CAPABILITIES,

WE ATTEMPT TO IMPROVE THE QUANTITATIVE UNDERSTANDING OF THE ROLES OF THERMODYNAMIC PATHWAY, LOCATION WITHIN THE CLOUD, AND TEMPORAL DEPENDENCY ON ICE NUCLEATION PROCESSES.

This article will highlight observations from three of the ICE-L lenticular wave cloud flights. In Section 2, we will provide an overview of the instruments and the flights investigated here. Section 3 will present the observations and Section 4 will provide a summary of the main observations and draw conclusions.

2. FIELD CAMPAIGN

The NCAR C130 was equipped with a wide range of state of the art particle probes, CCN spectrometers, and measurements of IN concentration and composition (Table 1). The completeness of the data set was further enhanced by remote sensing measurements from an upward and downward viewing cloud Doppler radar and an upward viewing lidar.

There were twelve research flights during the six week field campaign. Eight were directed to lenticular clouds and four to stratiform, "upslope" clouds. In-cloud temperatures for the wave cloud studies, the focus of this paper, spanned the range from -7 to -37C. Cloud depths ranged from 100 m to >1 km.

A typical flight pattern involved a series of penetrations along, against, and across the

Table 1
Probes on NCAR C130 during ICE-L

INSTRUMENT	MEASUREMENT	INVESTIGATOR	COMMENTS
-Particle Probes			
• UHSAS	Aerosols 55 nm-1µm	Facility (RAF)	
• FSSP	PSD 3-45 µm	Facility	
• CDP	PSD 3-45 µm	Facility	
• CAS	PSD 3-45 µm	DMT	Part of CAPS Probe
• SID-2	PSD 1-60 µm	Facility	
• FAST FSSP	PSD 3-45 µm	SPEC	Only available for RF06-08
• FAST 2D-C	PSD 50-1000 µm	Facility	
• 2D Grey	PSD 15-1000 µm	DMT	
• 2D-S	PSD 15-1000 µm	SPEC	Only available for RF01-03, 08
-Condensed water			
• CVI	LWC, IWC>0.01g/m^3	Facility	
• King Probe	LWC	Facility	
• RICE	Supercooled LW presence/amount	Facility	
-CCN			
• DRI	CCN-S spectra	Hudson	
• DMT	CCN-S spectra	DMT	
-IN	Ice nucleus conc.	DeMott	
-Mass Spectrometer			
• cToF-AMS	IN composition	Seinfeld	
• A-ATOFMS	IN composition	Prather	
• CVI	CCN/IN composition	Twohy	
-Black Carbon	SP2 spectrometer	DMT	
-Remote Sensing			
• 95 GHz radar	Reflectivity, Doppler particle speed	French/Haimov	Upward and downward viewing
• Lidar	Backscatter, asymmetry param.	Wang	Upward viewing
-Wind/Thermo.			
• 3D winds	U, V, W	Facility	
• T, RH	Temp. RH	Facility	

wind direction to map out the thermodynamic, wind, and microphysical structures in the vertical. The first penetration sampled the upwind thermodynamics and aerosol properties. This leg usually provided data below the visible cloud base to map out the equivalent potential temperature (q_e) and relative humidity (with respect to water, RH_w) structure flowing into the cloud layer. The second leg was usually under cloud base, parallel to the wind, to remotely sense the cloud structure. Successive legs probed the cloud microphysics in-situ.

3. DATA

We present observations from three flights, on 16 December [RF12], 29 November [RF06], and 13 December [RF11]. We highlight the thermodynamic, dynamic and microphysical observations.

Figure 2 shows the track of the C130 during the 11 penetrations of RF12, wave cloud 2. The x axis falls along the mean wind direction 290 +/- 6^o, with the C130 positions derived from a coordinate transformation to that axis. The (0, 0) point of the transformed system is at about the leading cloud edge (x axis) and N-S cloud extent. The region of cloud is approximately 3 km in length along the wind direction, with a temperature close to -22C. Cloud vertical depth is only a few hundred meters. The mean wind direction for these penetrations was and the wind speed was 22.3 +/- 1.7 m/sec. Therefore, the transit time for particles through the cloud is only about 140 sec.

Vertical motions through the cloud layer were strong, exceeding 4 m/sec in places (Fig. 3), with downward motion noted upwind and downwind of these peaks. Parcels would have only ascended about 200 m across the cloud layer, assuming an average 3 m/s updraft across the 2km wide updrafts.

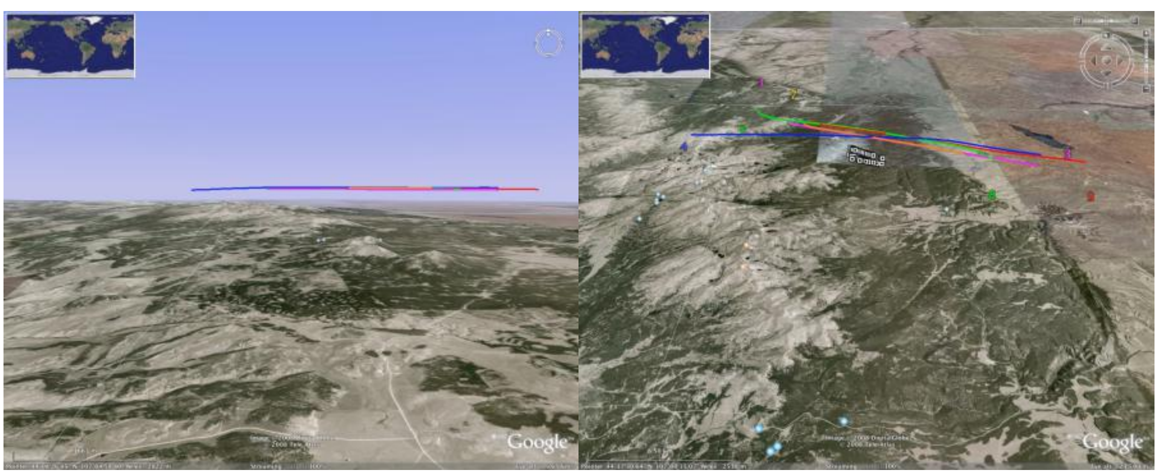

Fig. 1: Track of NCAR C130 aircraft during five penetrations (different colored traces) for RF12 (16 December 2007) during ICE-L. In the right panel, black squares are projection of locations of cloud liquid water noted during the penetrations.

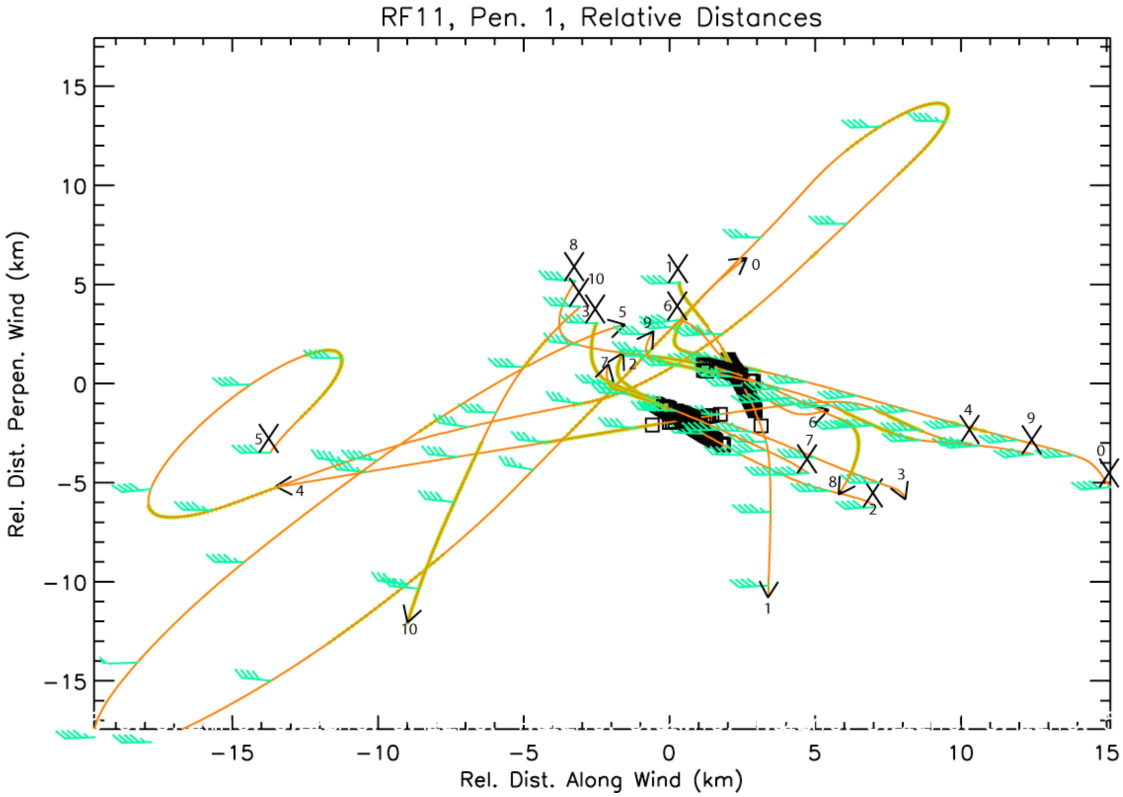

Fig. 2: Track of the C130 during the penetrations for RF12, second cloud sampled. Locations of cloud are shown with black squares.

The emphasis will be placed on Pens. 3, 9, 8, 4, and 7, discussed in that order to reflect increasing height. The tracks of the C130 for these penetrations are shown on the Google Earth maps in Fig. 1. Pens. 3 and 9 just were largely below cloud base and penetrations 8, 4 and 7 were in liquid cloud, profiling from near base to top.

In Figs. 4 and 5, we show the upward and downward viewing 95 GHz radar observations (top panel), and the lidar backscatter and depolarization ratio above the aircraft (middle and lower panels) for Pens. 3 and 8, respectively. Note the arched-shaped cloud base in Pen. 3, (Fig. 4) and the penetration of the ice grown within the wave cloud on the downwind side, which is also evident in the radar observations. Both (and all other) penetrations show the absence of ice upwind of cloud and ice virga streaming downwind of and below the aircraft level. Figure 6 shows some of the microphysical observations for these penetrations, plotted along the x (parcel time) axis, stacked according to increasing penetration height. Orange and blue horizontal bars in the panels in the left two columns show where the vertical velocity is above 0.5 m/s and below -0.5 m/s, respectively. Heights, temperatures, mean aircraft heading (negative into the wind) and winds are shown in the titles for each penetration.

Consider first Pen. 3. There is an absence of condensate (left panel) except the upwind edge (near 0 km), at the upwind cloud edge, and on the downwind side, where the aircraft crossed the ice virga in the downdraft (see Fig. 4). The condensed water contents, in this case all ice (no RICE LW), were less than 0.01 g/m^3, below the detection level of the CVI. Below the panels for this penetration are the concentrations (N) of particles (when detected) from the CDP and FSSP and CPI (>30 μm) and 2D probes (>50 μm). All but the CPI showed N of about 10 L^{-1}. Because drizzle was noted in higher penetrations and cloud droplets extended into the downdrafts (from RICE), we attribute most of these particles to drizzle drops. Particles imaged with the CPI (>30 μm) were all ice, with N~1 L^{-1}.

During Pen. 9, liquid water was detected on the upwind and downwind portions of the cloud, again because the cloud base was arched. (This was noted in the lidar imagery for this penetration, not shown here). Penetration 9 sampled liquid cloud in both the upwind updraft and the downwind downdraft, but the arched cloud base was above the aircraft during part of this penetration. FSSP and CDP concentrations, presumably droplets reached 200 cm^{-3}. Concentrations >30 μm were ~10 L^{-1}, presumably drizzle droplets. The particles sampled by the CPI and fast 2D probe were located on the east side of the cloud, in the downdraft region, in concentrations ~1 L^{-1} or below.

Penetration 8 sampled above cloud base throughout (Figs. 5 and 6). Water contents were only of order several hundredths gram per cubic meter. Drizzle was evidently detected from the FSSP and the CPI and 2D-C suggest N~1 L^{-1}.

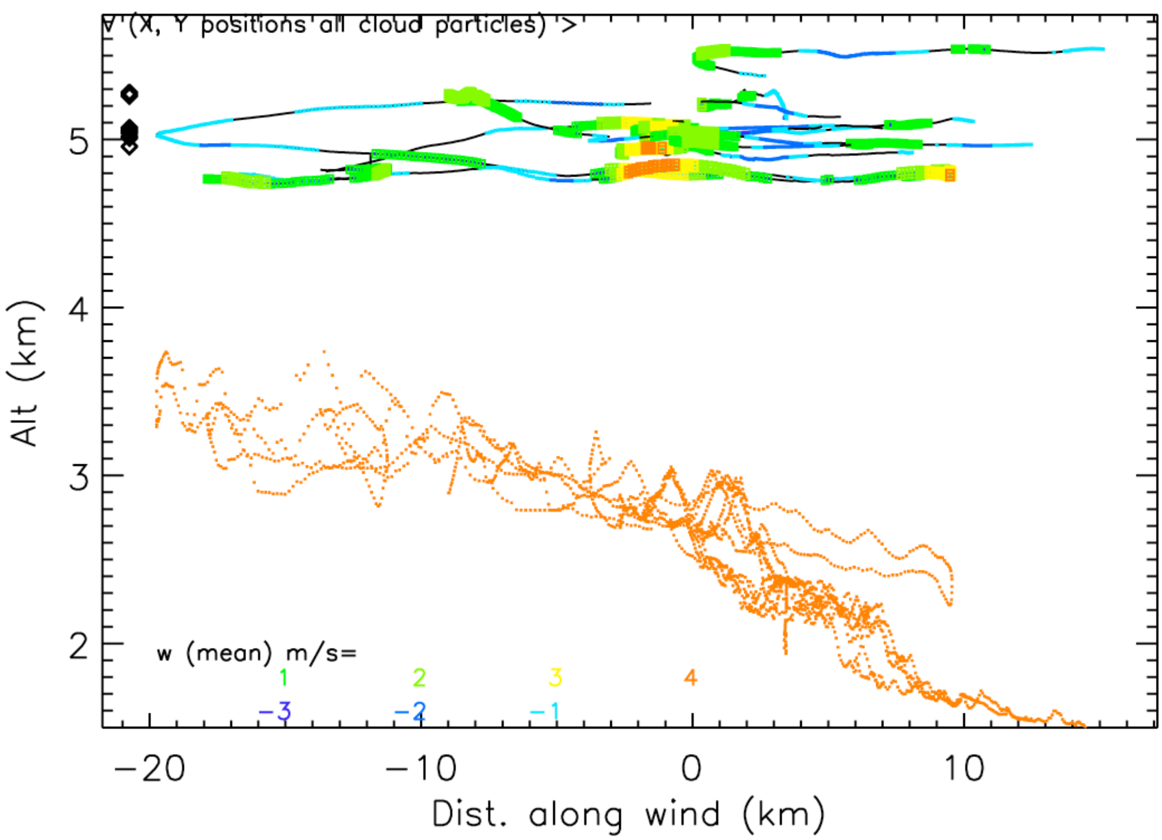

Fig. 3: Profile showing vertical wind speeds along each of the tracks of RF12, with the track numbers shown at the beginning and end of each penetration. Regions of updraft are shown with the thicker lines in green through orange, downdrafts are turquoise through blue. The height of topography at each point below the aircraft are shown.

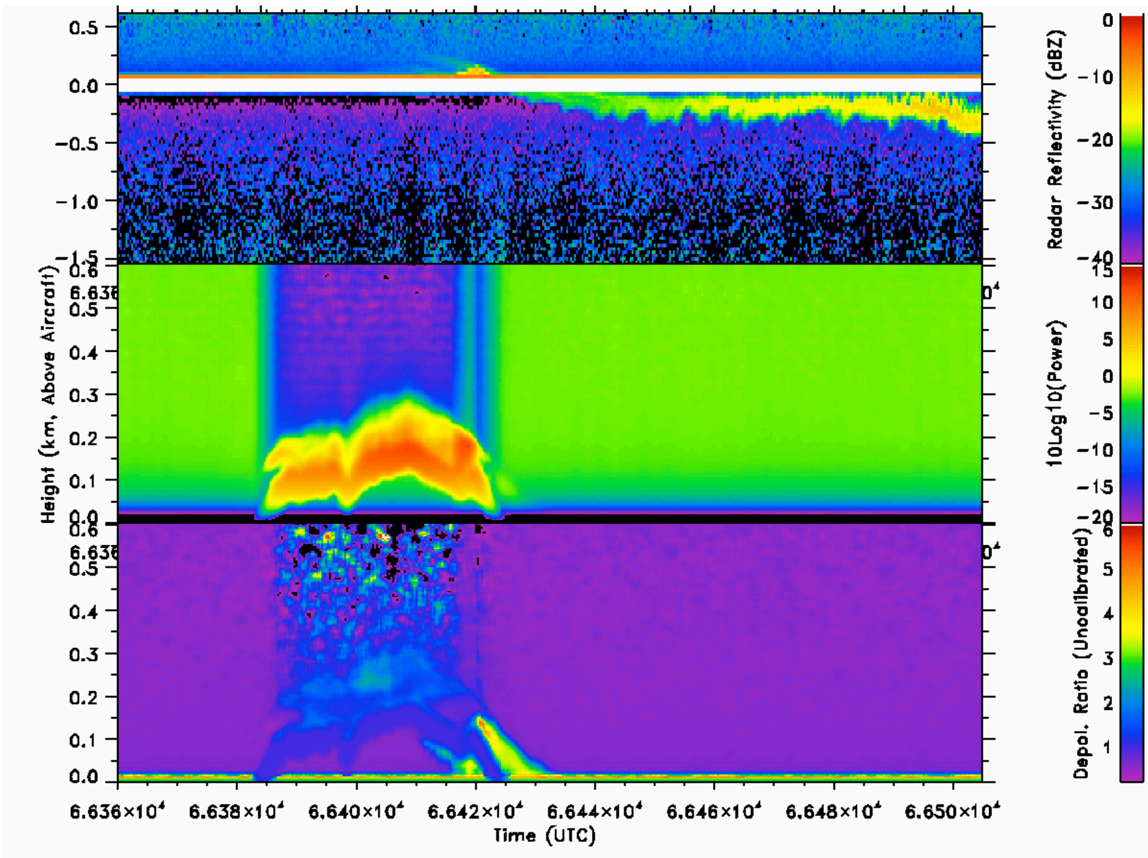

Fig. 4. Remote sensing data acquired from the NCAR C130 across Pen. 3 for RF12. Top panel: Upward and downward viewing 95 GHz radar observations, with the aircraft positioned at a height of 0 km. Middle and lower panels: upward viewing lidar relative backscattered power and depolarization ratio, respectively.

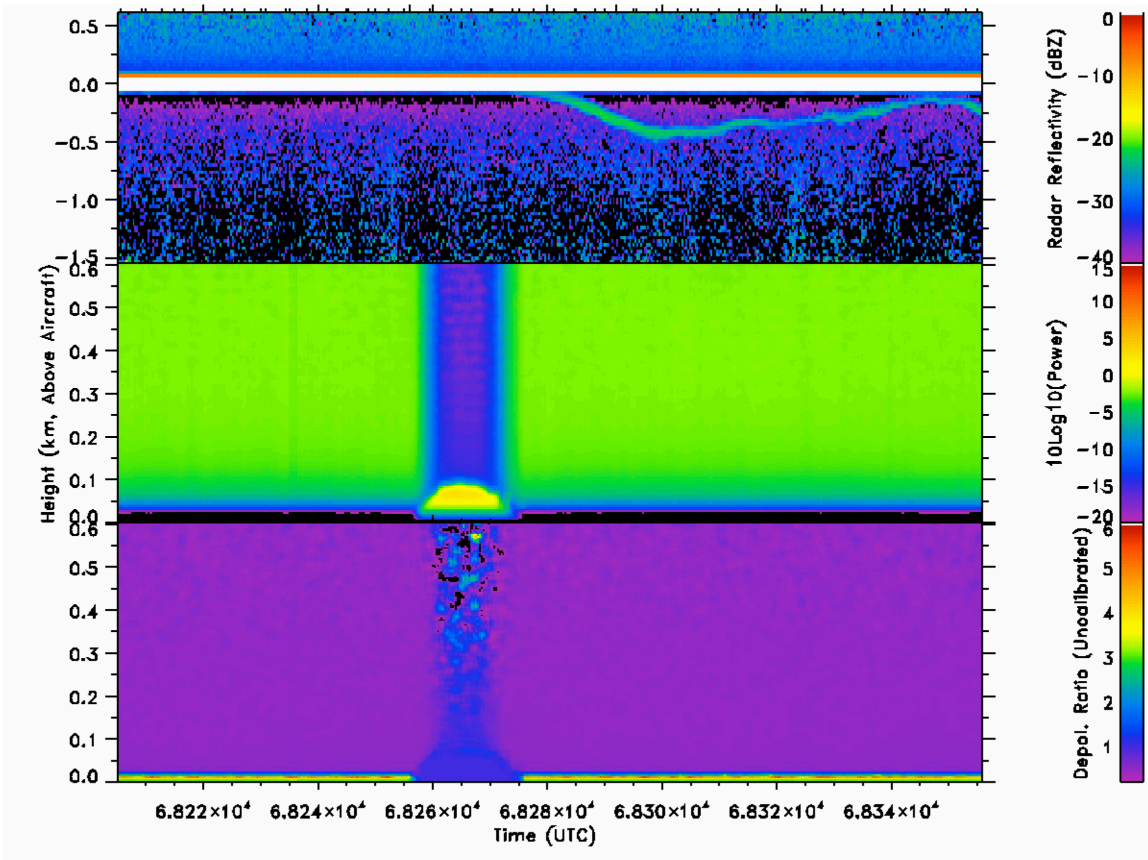

Fig. 5: Same as Fig. 4, except for Penetration 8 for RF12.

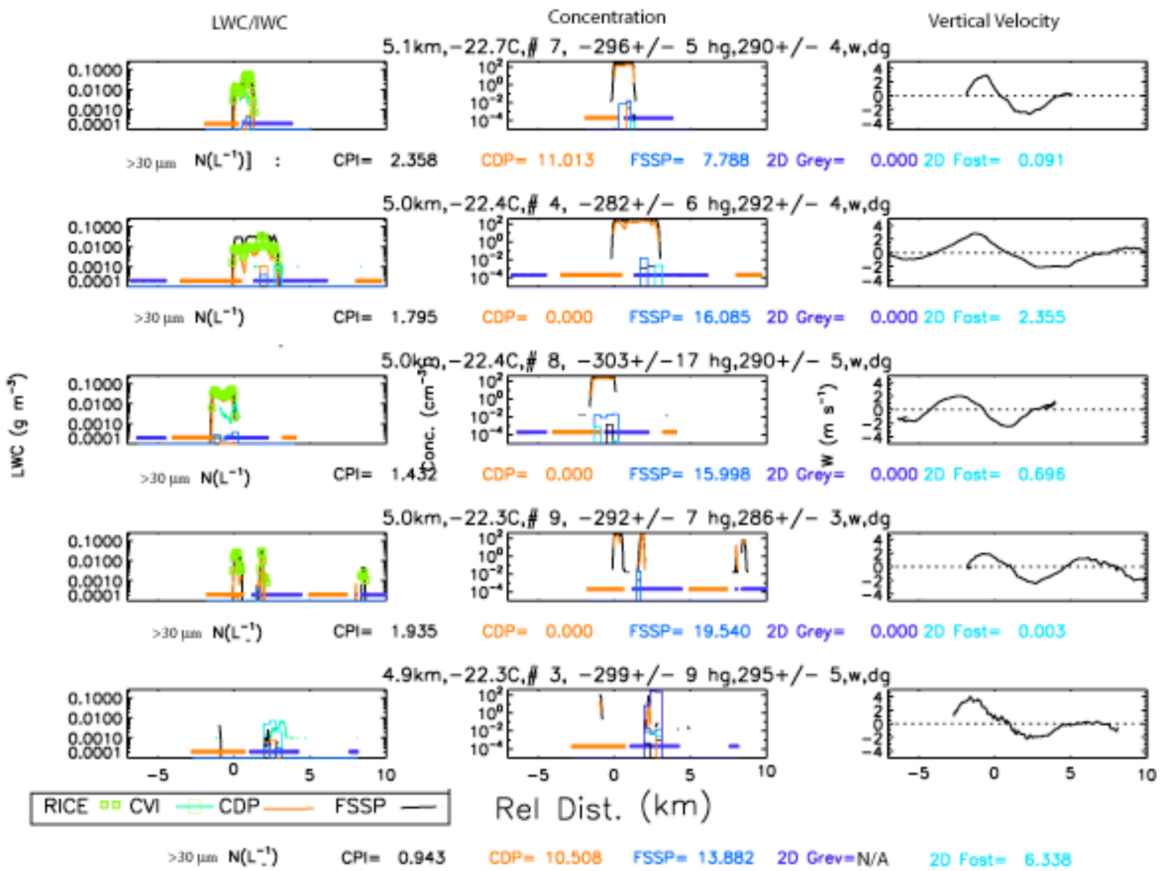

Fig. 6. Microphysical observations obtained during five of the penetrations for RF12. The title for each panel shows the altitude, mean temperature, penetration number, aircraft heading (a minus indicates a penetration into the wind), and the mean wind direction at the flight level. The left panels show the condensed water content, the middle panels the particle concentrations, and the right panels the vertical velocities. The legend for the left and center panels are shown at the bottom of the figure. Average concentrations for ice—taken to be where the diameters are above 30 microns for the FSSP, CDP and CPI, and above 25-50 microns for the 2D probes, are averaged in 5-sec intervals and are plotted and listed between panels.

Penetrations 4 and 7, near cloud top, detected a continuous band of cloud liquid cloud was observed both in the updraft and extending into the downdraft. Concentrations from the CPI and 2D-C were of order 1 L^{-1}.

For the cloud studied during the RF12 penetrations, the CFDC IN concentrations were 0.2-0.3 L^{-1} out of cloud, comparable to those measured here.

On 29 November, the NCAR C130 flew a mission over Wyoming, sampling a wave cloud at heights from 4.6 to 5.6 km and temperatures from -26 to -29C. Vertical velocities were again strong, with a broad and well-defined updraft region approximately 4 km wide (Fig. 7).

The remote sensing data indicates that there was little if any ice generated in the layer nor streaming downwind of the cloud. However, at a height of about 1 km above the C130 flight altitude, corresponding to a temperature of about -35C from earlier C130 sampling, a ice trail streamed downwind of the wave cloud. This height

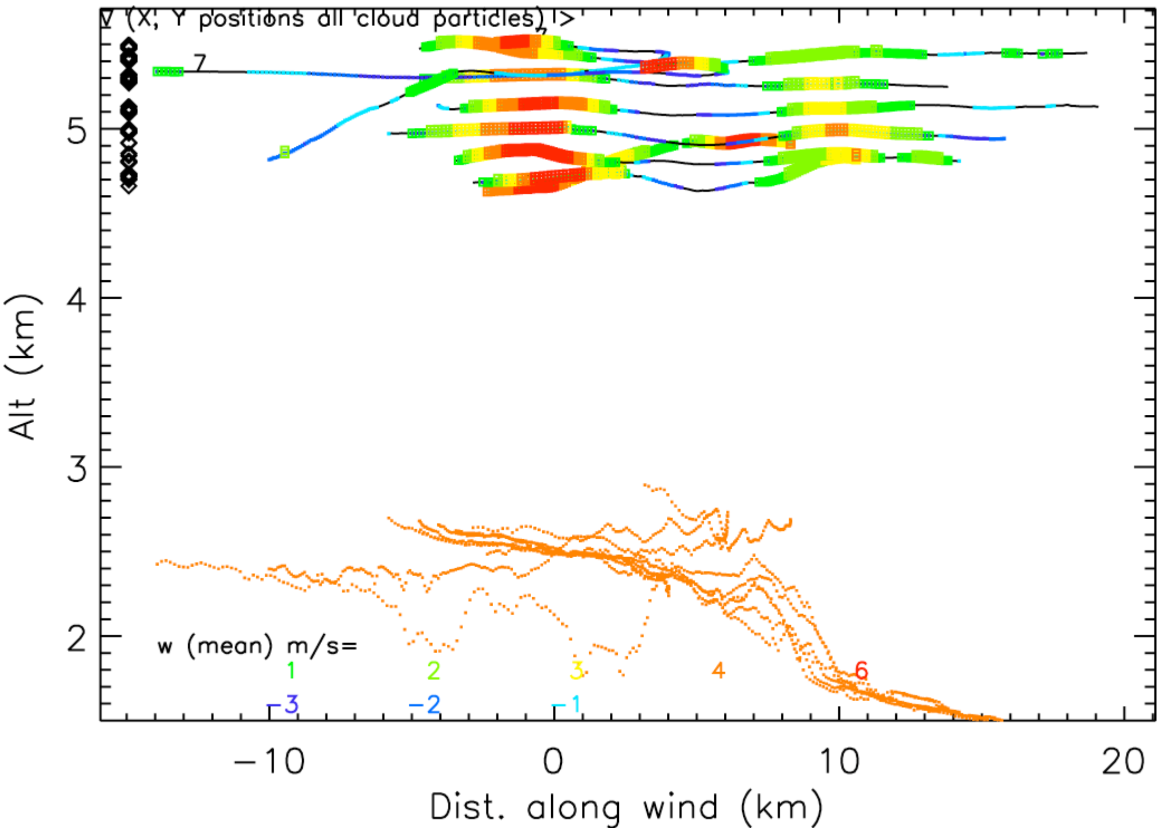

Fig. 7: Same as Fig. 3, except for RF06, 29 November, 2007.

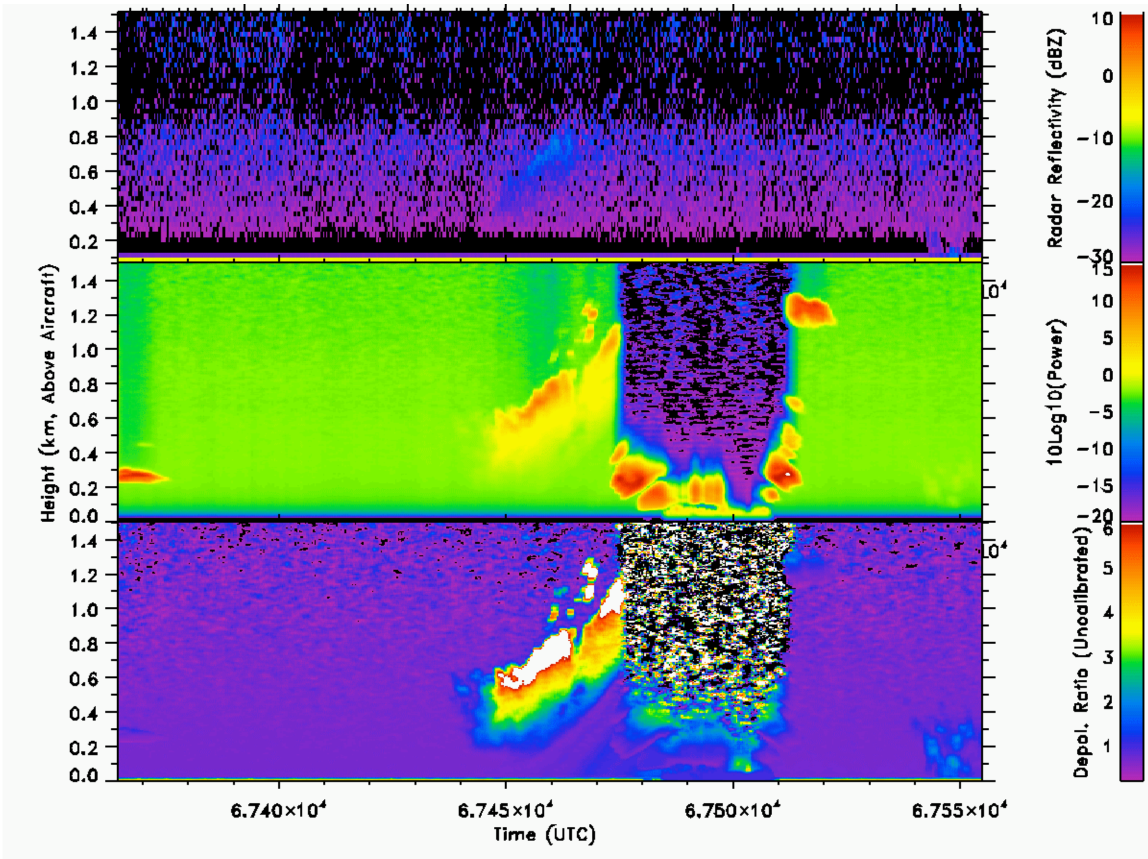

Fig. 8: Same as Fig. 4, except for Penetration 2, RF06. The penetration is from downwind to upwind.

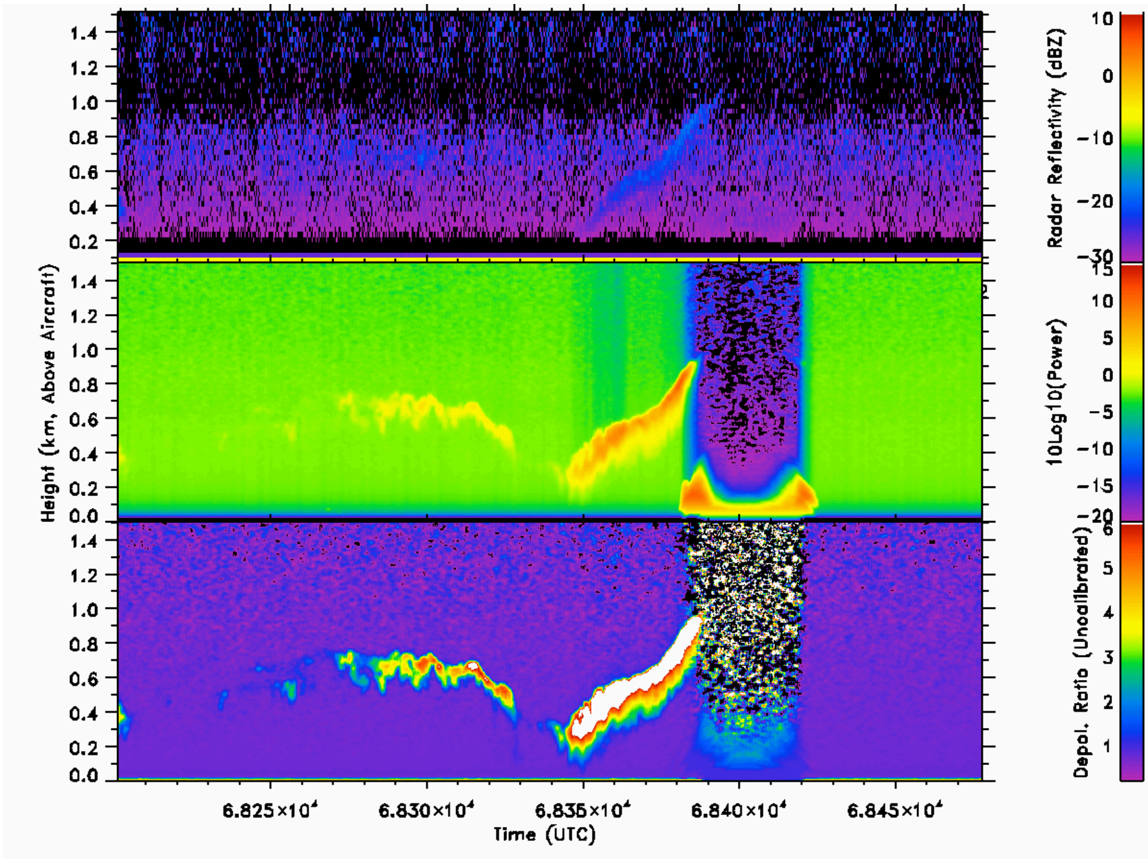

Fig. 9: Same as Fig. 4, except for Pen. 4, RF06. The penetration was from downwind to upwind.

and above is where homogeneous ice nucleation was likely to be operative in the cloud layer.

Just below the wave cloud, an orographic wave cloud developed precipitation and convective elements that we observed to be feeding into the base of the wave cloud. These were noted in the lidar imagery at the base of our cloud (Fig. 9).

Liquid water but significant ice (2D-C and CPI) is noted for the lowest two penetrations (4.6 and 5 km), where the lower cloud layer visually supplied copious ice into the base of the wave cloud. Higher up, the ice was either too small or in concentrations too low for the probes to detect it. The latter is an unlikely explanation because ample growth time would have been available to produce detectable ice as evidenced by the streamers advecting downwind of the cloud in the homogeneous ice nucleation zone. Furthermore, a careful examination of the CPI imagery indicates that there were only a few particles that were ice and these were of sizes of about 150 microns. Copious 20-30 micron drizzle drops were observed on this day.

For RF06 (Fig. 10), there is minimal ice noted in the downwind regions of each of the cloud penetrations, indicating that sufficient time was available for drizzle growth but ice production was suppressed. Therefore, we would conclude on this basis alone that ice nuclei were present in minimal concentrations, even at temperatures close to -30C.

The IN measurements (see later) confirm that ice nuclei were detectable above a sensitive threshold of 0.4 L^{-1} at the cloud pass temperature at this time.

On 13 December 2007, RF11 profiled a cloud centered over Elk Mountain, Wyoming. Two stacked layers of wave clouds were located over and to the east of the mountains (Fig. 11). Vertical motions were strong, with parcels moving upwards at up to 6 m/s. The lower cloud ranged in heights from 4.3 to 4.8 km, with temperatures from -14 to -18C, and the upper one from 5.2 to 5.6 km, with temperatures in the -21 to -23C range.

On the upwind side of the wave cloud, ice is evident in the radar imagery above and below the aircraft (Fig. 12). The cloud is detectable by radar throughout, suggesting that ice particles from upwind are entering cloud. This conjecture is supported by the remote sensing observations. In Fig. 13, the radar data clearly shows Elk Mountain, first going from downwind to upwind, then reciprocally from upwind to downwind. There is clear evidence of detectable wave cloud below the aircraft, over the mountain. It is entirely possible that low concentrations of ice were picked up from the surface (which was covered with snow) and then carried in the winds into the cloud layer.

In Fig. 14, we show that in the wave cloud layer, the concentrations measured by the fast 2D probe were considerably less than

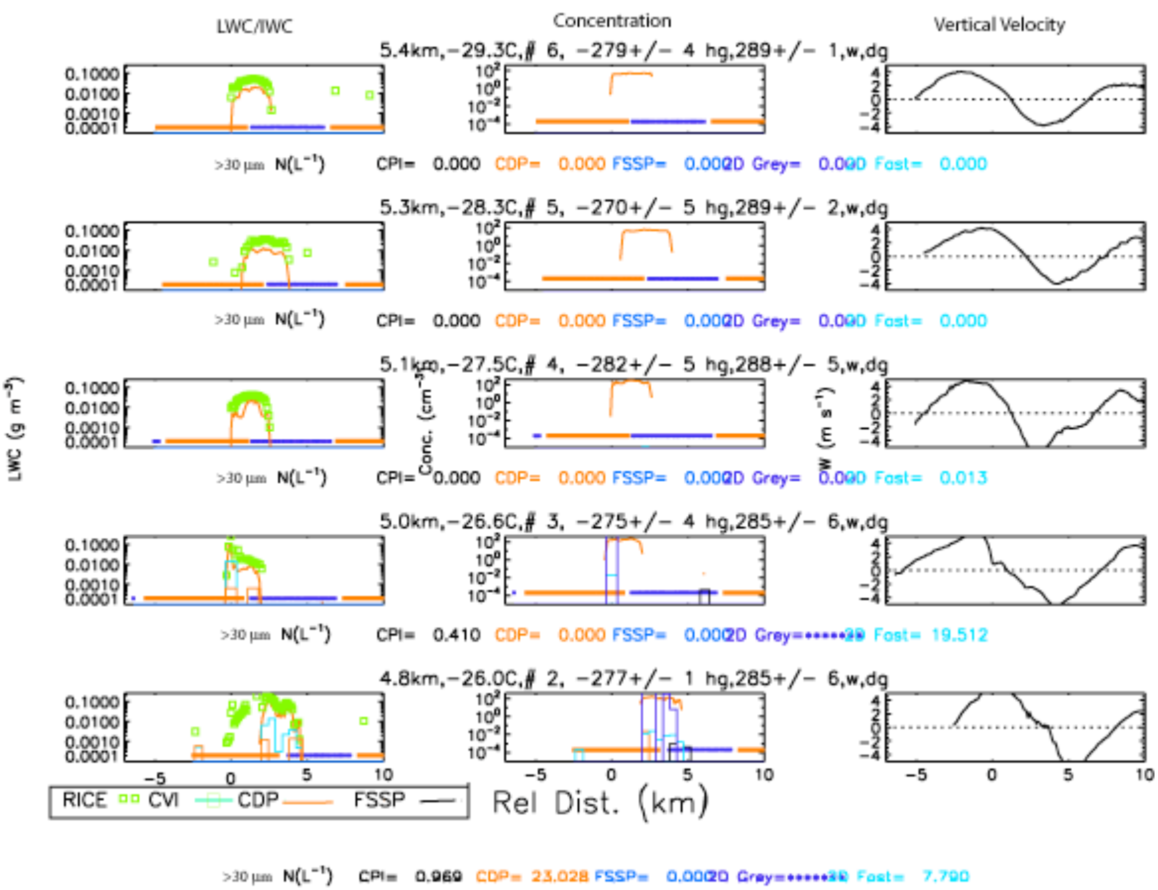

Fig. 10: Same as Fig. 6, but for RF06, 29 November 2007.

observations during the upwind leg (leg 10, 1 L^{-1}. There was obviously a problem with the 2D grey probe at the next to lowest sampling level and the CPI malfunctioned, rendering the concentrations shown as unreliable. In summary, is noted that the concentrations of ice crystals generated in this cloud layer were low.

IN measurements suggest no ice nuclei detectable at a resolution of 1 per liter at this time, although cloud residuals were being processed for water subsaturated conditions at this time to determine deposition nuclei concentrations.

4. SUMMARY AND CONCLUSIONS

This study uses an unprecedented set of in-situ and remote sensing observations to examine whether under given conditions, direct ice nucleation measurement(s), or other specific measurable characteristics of the aerosol, can be used to predict the number of ice particles forming by nucleation mechanisms in selected clouds.

The three wave cloud flights focused on here span the temperature range from about -15 to -30C. The concentrations of ice crystals sampled with many probes in

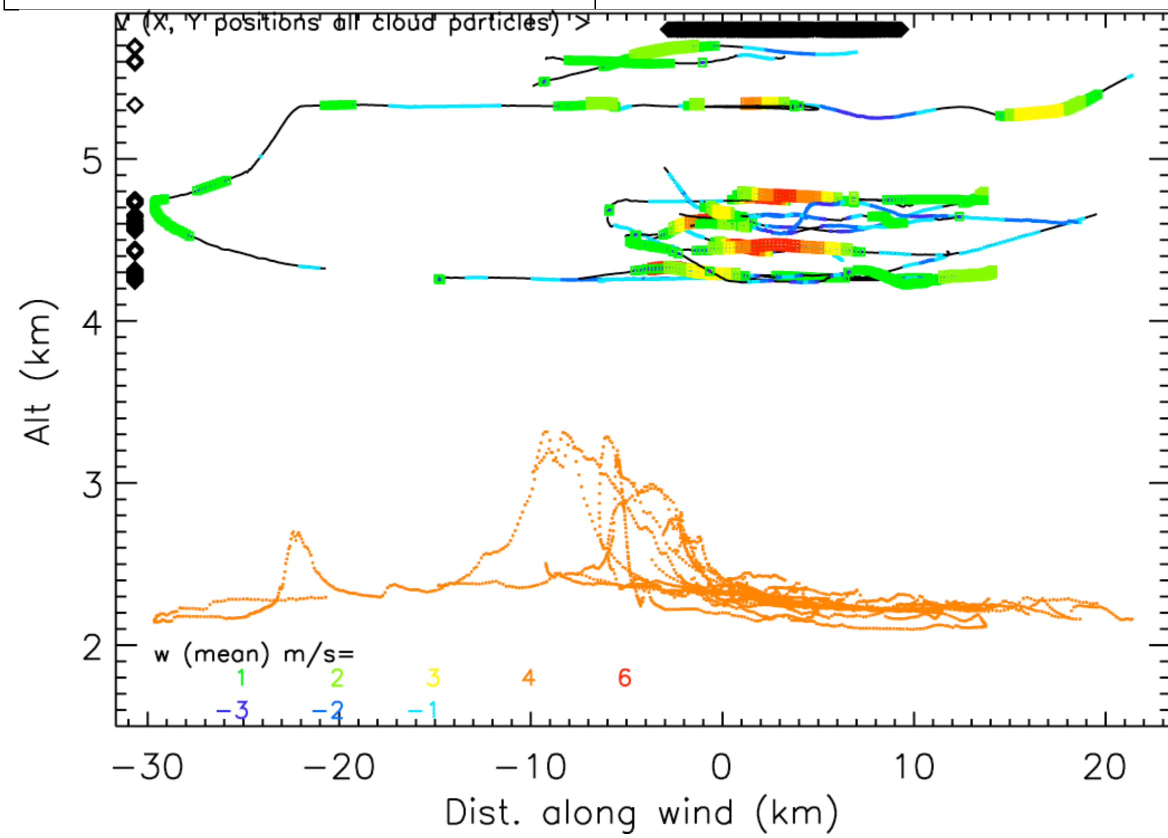

Fig. 11: Same as Fig. 3, except for RF11, 13 December 2007.

the critical size range from about 30 to 200 microns reveals little or no discrepancy with the measurements of ice nuclei concentrations. The following conclusions were also drawn from the observations:

1: *There is no evidence for enhanced ice production in the downdrafts of the wave* studied. This mechanism has been proposed from earlier wave cloud observations.

2: *The concentrations of ice crystals push the limits of the sampling volumes of the various probes.* That is, the scattering-type probes and the 2D imaging probes have insufficient sampling volume to detect the low concentrations of ice observed in the cloud layers.

clouds studied. Such a mechanism that

3. *The remote sensing observations were crucial in unraveling the processes of ice nucleation.* Clear instances of ice streaming from sources upwind that entered the wave clouds could have been construed as the result of deposition nucleation.

Further synthesis of this relatively complete data set, including the observations of the composition of the ice nuclei is ongoing.

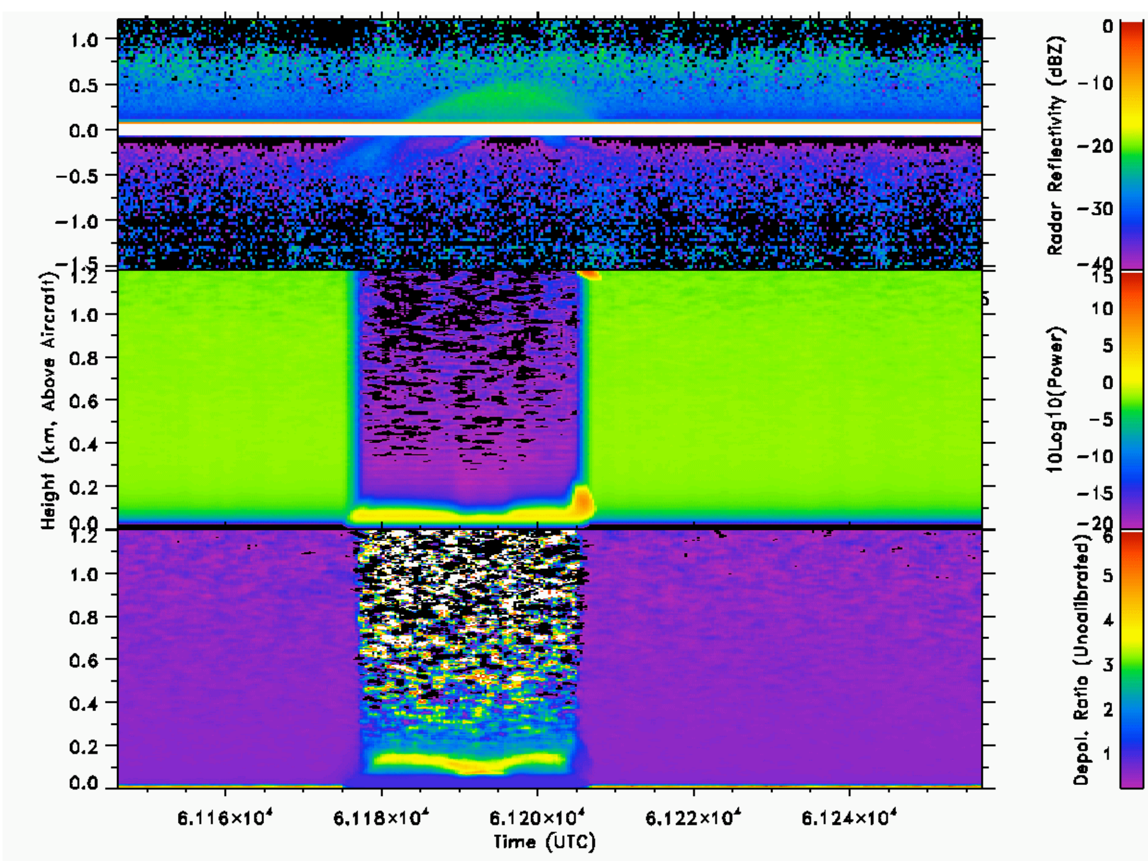

Fig. 12: Same as Fig. 4, except for Pen. 3, RF11, 13 December 2007. Profile shown from downwind to upwind.

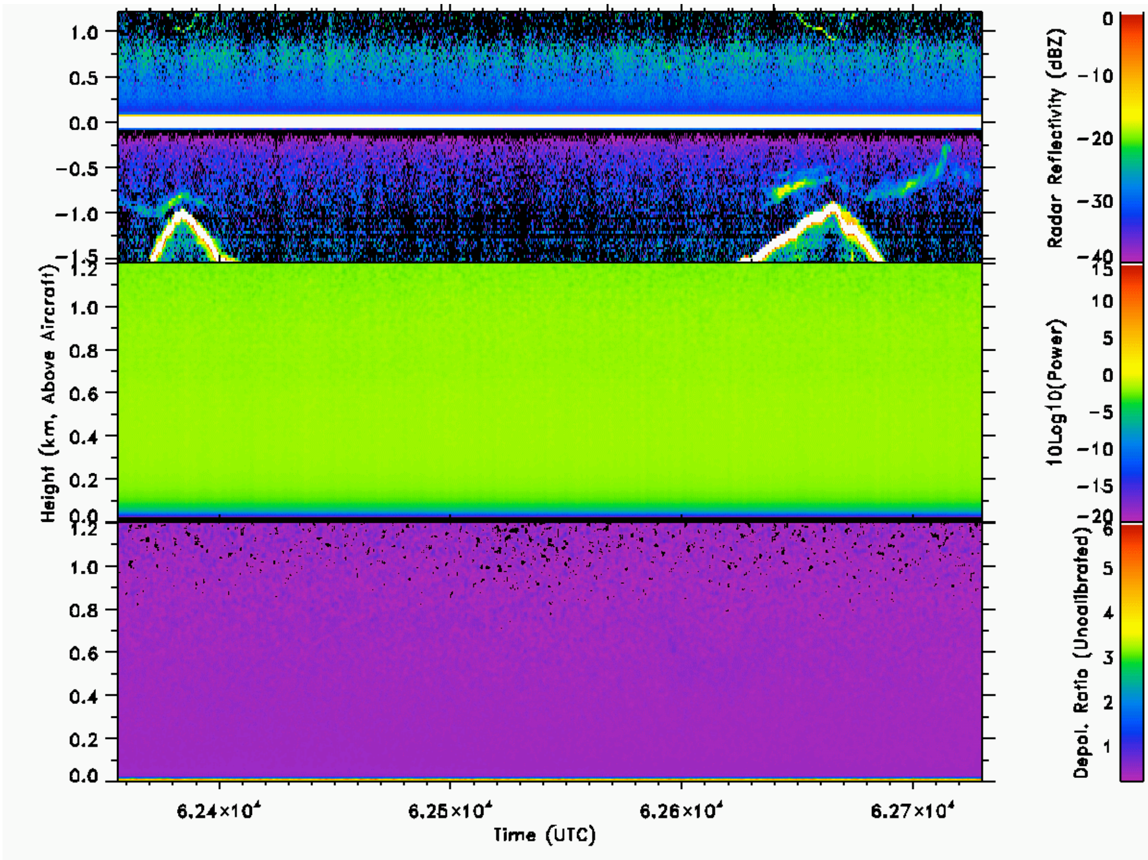

Fig. 13: Same as Fig. 4, except for Pen. 10, RF11, 13 December 2007. The C130 first flew upwind, then turned and sampled downwind to upwind. Elk Mountain is clearly visible, as is cloud overlying it.

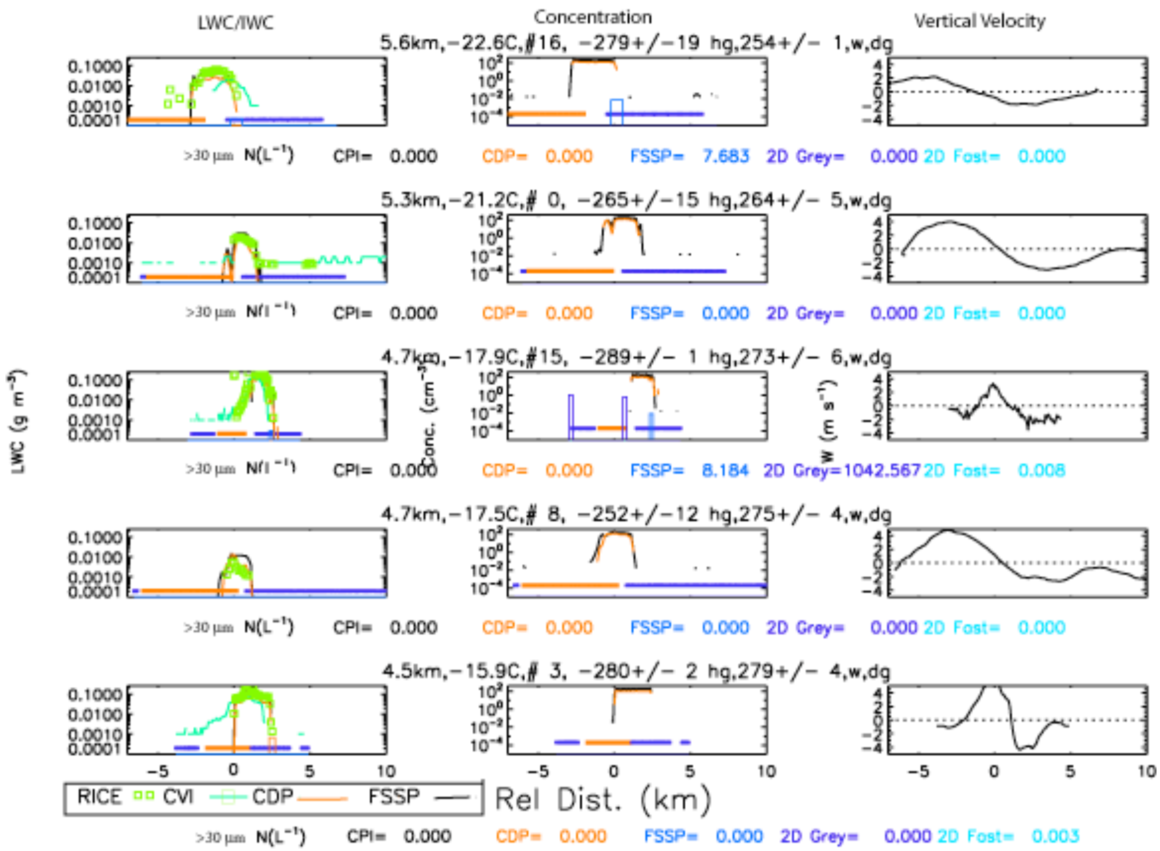

Fig. 13: Same as Fig. 6, except for RF11, 13 December 2007.

ACKNOWLEDGEMENTS

The authors are indebted to the National Science Foundation for funding this project. The National Center for Atmospheric Research contributors are funded by base funding from NCAR[6] . We wish to thank the RAF Aviation Facility, especially Henry Boynton, Ed Ringleman, Bob Olson and Bill Irwin, and to the EOL group including Jim Moore and Steve Williams, for their support of this project. Specific grants from NSF to ICE-L investigators, including DeMott (ATM-0611936), Twohy (ATM-0612605) and Wang (NSF ATM-0645644), contributed substantially to the success of this project. Support for Rogers (NASA NRA-01-OES-02) is also acknowleged.

6. The National Center for Atmospheric Research is sponsored by the National Science Foundation. Any opinions, findings, and conclusions or recommendations expressed in this publication are those of the author(s) and do not necessarily reflect the views of the National Science Foundation.

RATES OF PHASE TRANSFORMATIONS IN MIXED-PHASE CLOUDS

Alexei Korolev
Environment Canada, Toronto, ON, Canada

1. Introduction

This paper presents a theoretical framework describing the thermodynamics and phase transformation of a three phase component system consisting of ice particles, liquid droplets and water vapour. The instant rates of changes of water ($\dot{q}_w$), ice ($\dot{q}_i$) and vapour ($\dot{q}_v$) mixing ratios are described based on the quasi-steady approximation, which assumes that the sizes of cloud particles stay constant (Squires 1952). This assumption allows for the analytical solution of the differential equation for supersaturation in mixed phase clouds (Korolev and Mazin 2003). The local thermodynamical conditions required for the equilibrium of liquid ($\dot{q}_w$=0), ice ($\dot{q}_i$=0) and vapour ($\dot{q}_v$=0) phases are analysed. It is shown that there are four different regimes of the partitioning of water between liquid, ice, and gaseous phases in mixed clouds. The Wegener-Bergeron-Findeisen (WBF) process is identified as being relevant to two of those regimes. The efficiency of the WBF process in characterizing the capability of ice crystals to deplete the water evaporated by liquid droplets is introduced here. It is shown that the WBF process has maximum efficiency at approximately zero vertical velocity. The analysis of the dependences of $\dot{q}_w$, $\dot{q}_i$ and $\dot{q}_v$ on the vertical velocity, temperature, pressure and the integral radii of the cloud particles is presented. It is shown that the maximum rates of ice growth and droplets evaporation does not necessarily occur at T=-12C where the maximum difference between saturation vapour pressure over ice and that over liquid is observed.

Author's address: Alexei Korolev, Environment Canada, 4905 Dufferin Street, Toronto, Ontario, M3H5T4 Canada, e-mail: alexei.korolev@ec.gc.ca

2. Rates of vapour, ice and liquid mass changes in mixed clouds

In the following discussion we consider an idealized adiabatic mixed phase cloud consisting of liquid droplets and ice particles suspended in water vapour. The interaction between ice particles, liquid droplets and water vapour occurs through processes of diffusional growth and/or evaporation. The processes related to particle-to-particle interaction, like riming, aggregation, and coagulation are not considered here. It is assumed that the spatial distribution of ice particles, liquid droplets, water vapour and temperature is uniform. The concentrations of liquid droplets and ice particles stay constant with time and the radiation effects are neglected. It is recognized that this idealization means that some of the quantitative results will not be directly applicable to real cloud systems and this will be addressed in section 7. However, such simplifications allow us to get a good theoretical understanding of mixed-phase phenomenon.

The rate of mass change of an ensemble of liquid droplets can be described as (e.g. Squires 1952, Korolev and Mazin 2003)

$$\frac{dq_w}{dt} = B_w S_w N_w \bar{r}_w \qquad (1)$$

here q_w is the liquid water mixing ratio; $S_w = \frac{e}{E_w} - 1$ is the supersaturation over water; e is water vapour pressure; $E_w(T)$ is saturation water vapour pressure over water at the temperature T; N_w and $\bar{r}_w$ are the concentration and average radius of the droplets, respectively; B_w is a coefficient dependent upon T and P (an explanation of all the variables used in the text is provided in Appendix A).

Similar to the liquid droplets, the rate of mass change of ice particles can be written as

$$\frac{dq_i}{dt} = B_{i0} S_i N_i \overline{r_i c} \qquad (2)$$

Here, $S_i = \frac{e}{E_i} - 1$ is the supersaturation over ice; $E_i(T)$ is saturation water vapour pressure over ice; B_{i0} is a coefficient dependent upon T and P; N_i, is the concentration of ice particles,; r_i is the characteristic size of ice particles; c is a shape factor of ice particles characterizing "capacitance" in the equation of the growth rate. In the following consideration, the size r_i will be defined as a half of a maximum dimension of the ice particle. For this definition of r_i, the shape factor varies in the range $0<c\leq 1$, being equal to 1 for ice spheres. For simplicity in the frame of this study, we assume c=const. This simplification does not disturb the generality of the following consideration. However, for an ensemble of ice particles having different shapes one should consider the average value of the product $\overline{r_i c}$.

The products $N_w \bar{r}_w$ and $N_i \bar{r}_i$ (or the first moments of particle size distributions) will be referred to as the "integral radii" of the droplets and ice particles, respectively.

The supersaturation over ice can be related to the supersaturation over water as

$$S_i = \frac{e - E_i}{E_i} = \xi S_w + \xi - 1, \qquad (3)$$

where $\xi(T) = \frac{E_w(T)}{E_i(T)}$. Then, substituting Eq.3 into Eq.2 yields

$$\frac{dq_i}{dt} = (B_i S_w + B_i^*) N_i \bar{r}_i \qquad (4)$$

Here, $B_i = \xi c B_{i0}$, and $B_i^* = (\xi - 1) c B_{i0}$.

The supersaturation S_w in Eqs. 1 and 4 can be approximated by the quasi-steady supersaturation (Korolev and Mazin, 2003)

$$S_{qsw} = \frac{a_0 u_z - b_i^* N_i \bar{r}_i}{b_w N_w \bar{r}_w + b_i N_i \bar{r}_i} \qquad (5)$$

The remarkable property of the quasi-steady supersaturation is that the actual supersaturation S_w approaches with time to S_{qsw} calculated for current values of N_w, N_i, $\bar{r}_w(t)$, $\bar{r}_i(t)$, $T(t)$ and $P(t)$, i.e.

$$\lim_{t\to\infty} S_w(t) = S_{qsw}(t) \qquad (6)$$

For clouds with typical integral radii $N_w \bar{r}_w$ and $N_i \bar{r}_i$, the difference between S_w and S_{qsw} usually becomes less than 10% within a time period $3\tau_p$, where

$$\tau_p = \frac{1}{a_0 u_z + b_w N_w \bar{r}_w + (b_i + b_i^*) N_i \bar{r}_i} \qquad (7)$$

is the time of phase relaxation (Korolev and Mazin 2003).

In mixed phase clouds τ_p is mainly defined by the integral radius of liquid droplets $N_w \bar{r}_w$, and typically, it does not exceed a few seconds[1]. This time is significantly less than the characteristic lifetime of mixed phase clouds (τ_c), i.e. $\tau_c >> \tau_p$. Therefore, the supersaturation S_w has enough time to relax to S_{qsw}. This justifies the use of S_{qsw} as an approximation of S_w in calculations of the rate of mass changes of ice and liquid.

Thus, substituting Eq.5 into Eq.1 gives the rate of change of liquid water mixing ratio,

$$\dot{q}_w = \frac{\left(a_0 u_z - b_i^* N_i \bar{r}_i\right) B_w N_w \bar{r}_w}{b_w N_w \bar{r}_w + b_i N_i \bar{r}_i} \qquad (8)$$

Similarly, substituting Eq.5 into Eq.4, and taking into account that $B_i^* b_i = b_i^* B_i$ (Appendix A) we obtain the rate of change of ice water mass

$$\dot{q}_i = \frac{\left(a_0 u_z - \frac{1-\xi}{\xi} b_w N_w \bar{r}_w\right) B_i N_i \bar{r}_i}{b_w N_w \bar{r}_w + b_i N_i \bar{r}_i} \qquad (9)$$

The rate of changes of the water vapour mixing ratio ($\dot{q}_v$) can be found from the equation of mass conservation

$$\dot{q}_w + \dot{q}_i + \dot{q}_v = 0 \qquad (10)$$

Substituting Eqs. 8 and 9 into Eq.10 yields

$$\dot{q}_v = \frac{B_w B_i^* (a_1 - a_2) N_w \bar{r}_w N_i \bar{r}_i - a_0 u_z \left(B_w N_w \bar{r}_w + B_i N_i \bar{r}_i\right)}{b_w N_w \bar{r}_w + b_i N_i \bar{r}_i} \qquad (11)$$

The replacement of S_w with its quasi-steady approximation S_{qsw} (Eq.5) raises questions concerning the accuracy of this replacement and the factors limiting the use of Eqs. 8 and 9. The accuracy of the quasi-steady approximation has

---

[1] At the final stage of droplet evaporation, when $N_w \bar{r}_w$ becomes small, the time of phase relaxation will be mainly defined by the integral radii of ice particles $N_i \bar{r}_i$, which eventually results in an increase of τ_p.

been tested by comparing S_w, $\dot{q}_i$ and $\dot{q}_w$ derived from Eqs. 5, 8 and 9, respectively, with that calculated from a parcel model of a vertically moving adiabatic clouds. The parcel model used here is similar to that described in Korolev and Mazin (2003). Figure 1 shows the results of the comparison of S_w, $\dot{q}_i$ and $\dot{q}_w$ for a set of modelled clouds, where the integral radii of droplets and ice particles were changed in the range of $500< N_w\bar{r}_w <5000$μm cm^{-3} and $0.5< N_i\bar{r}_i <500$ μm cm^{-3}, respectively, and the vertical velocity varied in the range $-5<u_z<5$m/s. The initial radius of droplets varied from 2μm to 10μm. The diagrams shown in Fig.1 suggest that Eqs. 5, 8 and 9 reproduce S_w, $\dot{q}_i$ and $\dot{q}_w$ calculated from the parcel model with a good accuracy. These results create a basis for the use of Eqs.8 and 9 in the following analysis.

It was found that at the final stage of glaciation the deviation of S_{qsw} from S_w increases when the droplets begin to rapidly reduce their sizes during evaporation. This deviation occurs because the limiting condition for the quasi-steady approximation (Korolev and Mazin 2003).

$$\frac{2A_w a_0 |u_z|}{b_w^2 \bar{r}_w^4 N_w^2} << 1 \qquad (12)$$

is not satisfied, when the droplets become too small. The limiting condition Eq.12 is also relevant to the initial stage of activation of droplets in the pre-existing ice cloud, when the droplets are yet not big enough. Modelling points, where Eq.12 was not satisfied, were indicated by red triangles in Fig.1. The sizes of the droplets corresponding to the red triangles vary from 0.5 to 3μm, depending on N_w and u_z. Other limiting conditions applied to the rate of changes of P, T, u_z are discussed in detail in (Korolev and Mazin, 2003). It is shown that usually the conditions for P, T, u_z are satisfied in mixed-phase clouds in the troposphere..

Equations 8 and 9 have a simple form and, presumably, they may be implemented in cloud models or used for parameterization in large scale models, with relative ease.

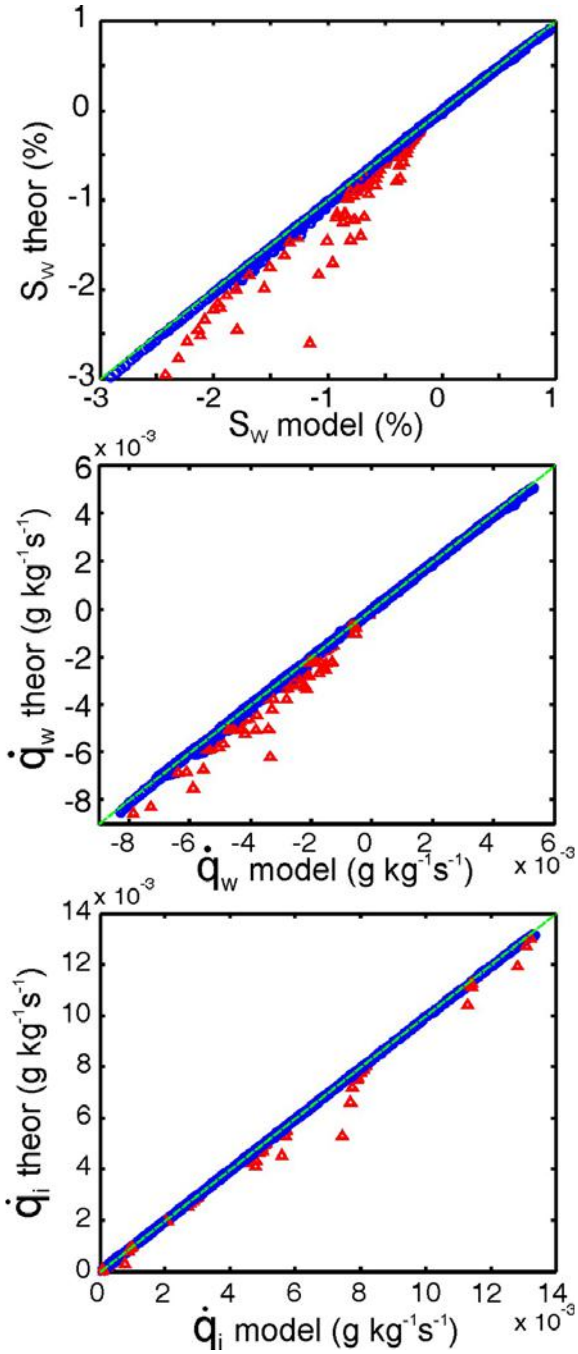

Figure 1. Comparisons of (a) S_w, (b) $\dot{q}_w$ and (c) $\dot{q}_i$ derived from Eqs. 5, 8 and 9, respectively, with that calculated from a parcel model of a vertically moving adiabatic mixed phase cloud. Modelling was conducted for $500< N_w\bar{r}_w <5000$μm cm^{-3}; $0.5< N_i\bar{r}_i <500$ μm cm^{-3}, $-5<u_z<5$m/s; $-40C<T<-5C$; $500mb<P<1000mb$. Blue circles indicate points satisfying Eq.12. Red triangles indicate points outside the envelope of the limiting conditions for the quasi-steady approximation described by Eq. 12.

3. Effect of thermodynamics on $\dot{q}_w$, $\dot{q}_i$ and $\dot{q}_v$

In this section we consider the effect of u_z, T and P on the rates of changes of ice, liquid and water vapour mass under conditions typical for mixed-phase clouds.

Figure 2 shows the growth rate of ice and liquid in mixed phase clouds versus u_z calculated from Eqs. 8 and 9 for $N_w\bar{r}_w$ = 1000µm cm^{-3} and $N_i\bar{r}_i$ =10µm cm^{-3} at three different temperatures; -5C, -15C and -25C. As follows from Eqs. 8 and 9 $\dot{q}_w$ and $\dot{q}_i$ are linearly related to u_z. Figure 2 indicates that $\dot{q}_w$ is significantly more sensitive to changes of u_z as compared to that of $\dot{q}_i$. As seen from Fig.2 $\dot{q}_i$ stays nearly constant, whereas $\dot{q}_w$ changes signs within the range of u_z considered in Fig.2. Formally, the lower sensitivity of $\dot{q}_i$ versus u_z as compared to $\dot{q}_w$ is explained by difference in the coefficients $B_wN_w\bar{r}_w$ and $B_iN_i\bar{r}_i$ in front of u_z in Eqs. 8 and 9, respectively. The difference in coefficients is mainly defined by the difference in values of $N_w\bar{r}_w$ and $N_i\bar{r}_i$. Typically, in mixed-phase clouds $N_w\bar{r}_w >> N_i\bar{r}_i$ and $B_w \approx B_i$.

The physical explanation of the difference in sensitivity of $\dot{q}_i$ and $\dot{q}_w$ to u_z follows from

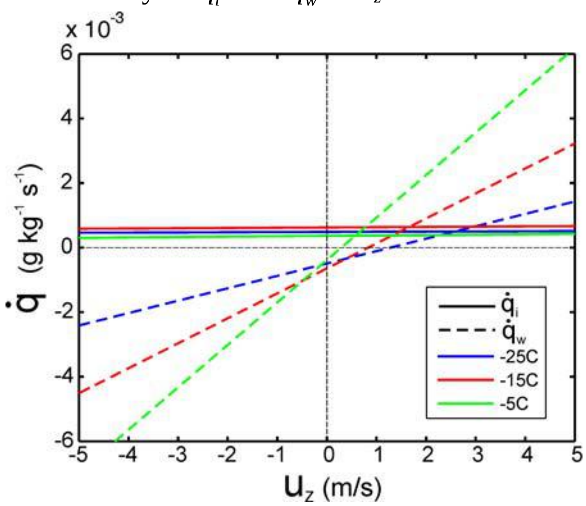

Figure 2. Growth rate of mixing ratio of ice $\dot{q}_w$ (solid line) and liquid $\dot{q}_i$ (dashed line) versus u_z calculated from Eqs. 8 and 9, respectively. Calculations were done for three different temperatures -5C, -15C and -25C, integral radii $N_w\bar{r}_w$ =1000µm cm^{-3}, $N_i\bar{r}_i$ =10µm cm^{-3}, and pressure P=680mb.

the fact that the humidity in mixed phase cloudsis close to saturation with respect to water (Korolev and Mazin 2005, Korolev and Isaac 2006). Therefore, the fluctuations of water supersaturation in mixed-phase clouds generated by fluctuations of vertical velocity with amplitude few meters per second have minor effect on supersaturation over ice, and for practical purposes S_i may be considered approximately constant, i.e. $\Delta S_i << S_i$.

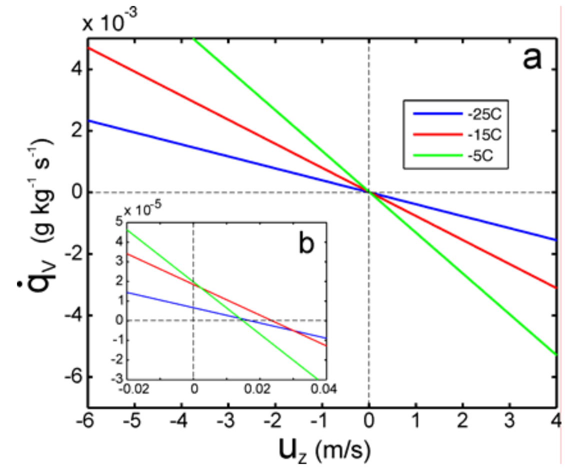

Figure 3. (a) Dependence of $\dot{q}_v$ versus vertical velocity u_z for three temperatures. (b) Zoomed area in the vicinity of the point with u_z=0 and $\dot{q}_v$ =0. The *x*- and *y*-axes in (b) are the same as in (a). Calculations were done for three different temperatures -5C, -15C and -25C, integral radii $N_w\bar{r}_w$ =1000µm cm^{-3}, $N_i\bar{r}_i$ =10µm cm^{-3}, and pressure P=680mb.

Figure 3 shows the dependence of the rate of the water vapour mass $\dot{q}_v$ versus u_z for $N_w\bar{r}_w$ =1000µm cm^{-3}, $N_i\bar{r}_i$ =10 µm cm^{-3} calculated for three temperatures. Equation 11 indicates that $\dot{q}_v$ is also a linear function of u_z. In Fig.3a all $\dot{q}_v$ curves calculated for different T appear to intersect at the same point (0,0). However, a closer look at the region of intersection (Fig.3b) indicates that the $\dot{q}_v$ curves intersect each other at different points.

The rates $\dot{q}_w$, $\dot{q}_i$ and $\dot{q}_v$ depend on T and P through the coefficients a_0, b_w, B_w, b_i, b_i^*, B_i and ξ. Figure 4 shows $\dot{q}_w$, $\dot{q}_i$ and $\dot{q}_v$ versus T for three different pressures P=900mb, 500mb and 300mb and two vertical velocities of u_z =-1m/s and 1m/s.

Figure 4a shows that the growth rate of ice has a maximum ($\dot{q}_{i\max}$) at temperatures below -12C. The temperature corresponding to $\dot{q}_{i\max}$ is decreasing with the decrease of P, and the amplitude of $\dot{q}_{i\max}$ is increasing with the decrease of P. It should be noted, that in mixed phase clouds the temperature corresponding to $\dot{q}_{i\max}$ is not equal to -12C, where the maximum difference is between saturation pressures over ice and liquid, but it may change in the range -40<T<-12C depending on P. For pressure 200<P<1000mb the temperature for $\dot{q}_{i\max}$ varies in the range -19<T<-12C. Cases with P<200mb resulting in T<-19C for $\dot{q}_{i\max}$ have no significance for the mixed phase clouds formed in the troposphere. As seen from Fig.4a, the ice growth rates $\dot{q}_i$ at u_z=-1m/s and u_z=1m/s practically coincide. In other words, u_z has minor effect on $\dot{q}_i$, which is consistent with the above discussion.

Figure 4b shows the dependence of $\dot{q}_w$ versus T and P. Contrary to $\dot{q}_i$, the growth rate of liquid $\dot{q}_w$ has minimum $\dot{q}_{w\min}$, which, depending on P and u_z, may be located anywhere in the range -40<T<0C. Comparisons of Figs 4a and 4b indicate that the temperatures corresponding to the minimum of the growth rate of the liquid phase ($\dot{q}_{w\min}$) and the maximum growth rate of the ice mass ($\dot{q}_{i\max}$) are different.

Figure 4c shows that $\dot{q}_v$ is monotonically increasing for u_z=-1m/s and decreasing for u_z=1m/s. The absolute value $|\dot{q}_v|$ decreases with increase of P. Calculations show that for the considered values of integral radii, $\dot{q}_v$ becomes non-monotonic for low vertical velocities $|u_z|$<0.1m/s.

In some papers it is speculated that the maximum rate of the phase transformation of liquid-to-ice is expected to occur at -12C, where the maximum difference between saturation water vapour pressure between ice and liquid is observed. In fact, the diagrams in Fig. 4 suggest that the extrema of $\dot{q}_w$ and $\dot{q}_i$ varies in a wide range of temperatures depending on P, $N_w\bar{r}_w$, $N_i\bar{r}_i$ and u_z, and that under the same conditions the temperatures corresponding to $\dot{q}_{w\min}$ and $\dot{q}_{i\max}$ are different.

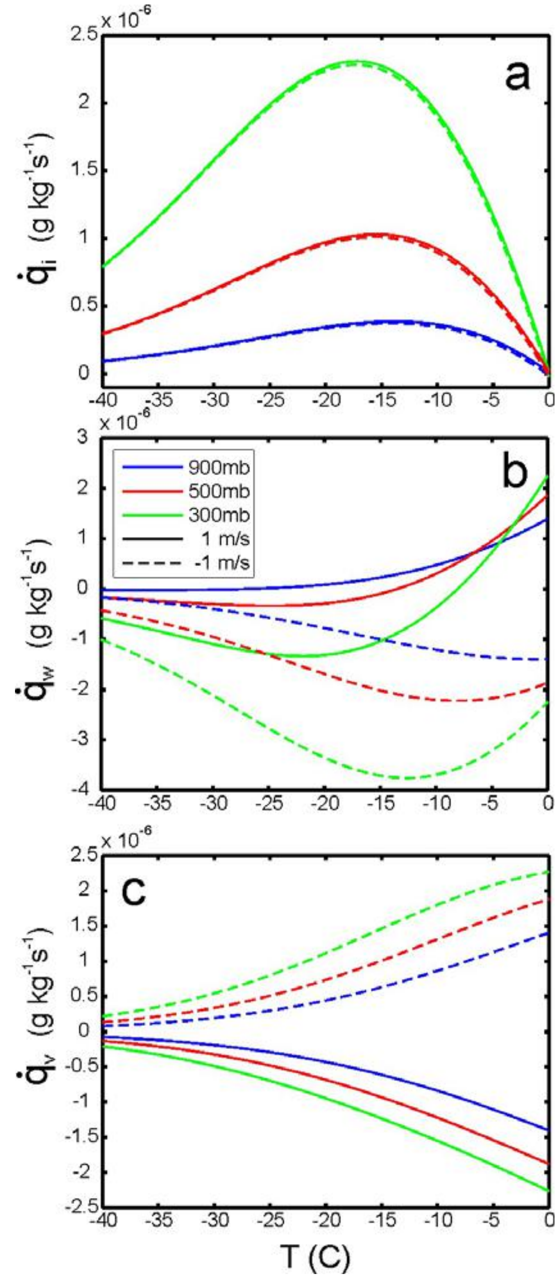

Figure 4. Dependence of the growth rate of (a) ice water mass $\dot{q}_w$, (b) liquid mass $\dot{q}_i$ and (c) water vapour mass $\dot{q}_v$ versus temperature T, for two vertical velocities 1m/s (solid line) and -1m/s (dashed line) and three different pressures 900mb, 500mb and 300mb. Calculations were done for integral radii $N_w\bar{r}_w$ =1000μm cm^{-3}, $N_i\bar{r}_i$ =10μm cm^{-3}.

4. Points of the phase equilibrium in mixed phase clouds

The interaction between solid, liquid and gaseous phases of water in mixed phase clouds is a complex process. The rate and direction of the partitioning of the water between three phases is defined by local thermodynamical (T, P, u_z) and microphysical ($N_w\bar{r}_w$, $N_i\bar{r}_i$) characteristics of the cloud. In this section, we consider thermodynamical conditions required for the equilibrium of each of the three phases, i.e. when (a) $\dot{q}_w=0$ liquid phase is in equilibrium; (b) $\dot{q}_i=0$ ice phase is in equilibrium; (c) $\dot{q}_v=0$ water vapour is in equilibrium.

4.1 Case $\dot{q}_w=0$

As follows from Eq.8 the equilibrium of liquid phase $\dot{q}_w=0$ occurs, when the vertical velocity u_z becomes equal to a threshold velocity,

$$u_z^* = \frac{E_w - E_i}{E_i}\eta N_i\bar{r}_i \qquad (13)$$

here, $\eta = a_2 B_{i0}/a_0$. A similar result was obtained in Korolev and Mazin (2003). The threshold velocity u_z^* separates the regimes of growth and evaporation of liquid droplets in mixed phase clouds, i.e. for $u_z > u_z^*$ liquid droplets grow in the presence of ice, whereas for $u_z < u_z^*$ droplets evaporate. As seen from Eq.13 u_z^* is always positive. Figure 5a shows dependence of u_z^* versus T for different $N_i\bar{r}_i$ and P. As follows from Fig.5a u_z^* increases with the decrease of T. For typical values of $N_i\bar{r}_i$ the magnitude of the threshold velocity u_z^* changes in the range 10^{-2}m/s to 10^{0}m/s in the temperature interval from -5C to -30C (Fig.5a). Such vertical velocities are common in the atmosphere, and they can be generated in clouds by turbulence or convection.

For a general case, including non-adiabatic conditions, the equilibrium of liquid phase in mixed phase clouds occurs when $e=E_w$, which is equivalent to $S_w = 0$.

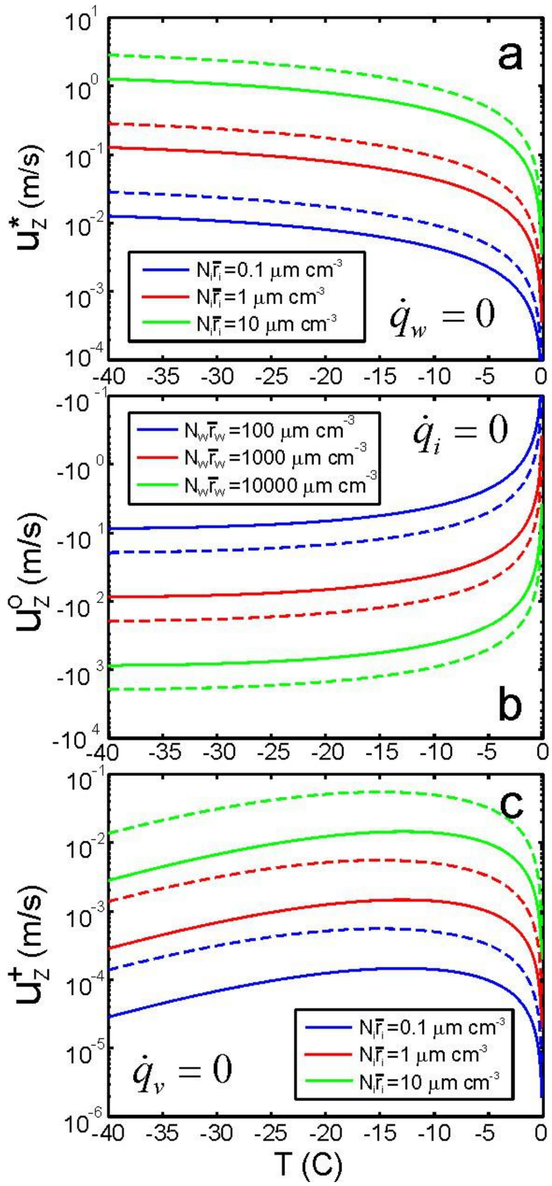

Figure 5. Dependence of the threshold vertical velocities (a) u_z^*, (b) u_z^o, (c) u_z^+, versus temperature for different $N_w\bar{r}_w$ and $N_i\bar{r}_i$. Calculations were conducted for two pressures P=900mb (solid line) and P=400mb (dashed line). The values of u_z^+, were calculated for $N_w\bar{r}_w$=1000μm cm^{-3}.

4.2 Case $\dot{q}_i=0$

Equation 9 yields a vertical velocity u_z^o required for equilibrium of ice phase in a mixed phase cloud

$$u_z^o = \frac{E_i - E_w}{E_w}\chi N_w\bar{r}_w, \qquad (14)$$

here, $\chi = a_1 B_w / a_0$. Similar to u_z^*, the velocity u_z^o separates regimes of growth and evaporation of ice particles in mixed phase clouds, i.e. for $u_z < u_z^o$ ice particles sublimate in the presence of liquid droplets, whereas for $u_z > u_z^o$ ice particles grow. As follows from Eq.14 u_z^o is always negative. Figure 5b shows the dependence of u_z^o versus T for different $N_i \bar{r}_i$ and P. As seen from Fig.5b, u_z^o increases with the increase of T. For typical values of $N_i \bar{r}_i$, the magnitude of the velocity u_z^o changes in the range from -10^0m/s to -10^3m/s in the temperature range -5C to -30C (Fig.5b). Vertical velocities -10<u_z<-1m/s may occur in compensating downdrafts in convective clouds. Downdrafts with a higher velocity are unlikely to be formed in the atmosphere. The diagram in Fig.5b suggests that at temperatures close to 0C, the absolute values of the vertical downdrafts required for reaching ice equilibrium do not exceed -1m/s, and they can be generated by turbulence.

Generally, the equilibrium of ice phase requires $e=E_i$, which is equivalent to the condition $S_w = \xi - 1$ in terms of the supersaturation over water, or $S_i = 0$ in terms of the supersaturation over ice. It should be noted, that for a non-adiabatic case the local equilibrium of ice phase in a mixed phase cloud can be reached during mixing with dry out-of-cloud air.

4.3 Case $\dot{q}_v$ =0

Equation Eq.11 provides a velocity required for the water vapour equilibrium

$$u_z^+ = \frac{(\xi - 1)(B_w b_i - b_w B_i) N_w \bar{r}_w N_i \bar{r}_i}{a_0 \xi (B_w N_w \bar{r}_w + B_i N_i \bar{r}_i)} \qquad (15)$$

For $u_z < u_z^+$, the mass of the water vapour is increasing, i.e. $\dot{q}_v$ >0, whereas for $u_z > u_z^+$ the mass of the water vapour is decreasing, i.e. $\dot{q}_v$ <0. As follows from Eq.15 u_z^+ is always positive. Figure 5c shows the dependence of u_z^+ versus T for different $N_i \bar{r}_i$ calculated for $N_w \bar{r}_w$ =1000μm cm^{-3}. As seen from Fig.5c in mixed phase clouds u_z^+ is close to zero, and for typical $N_i \bar{r}_i$ and $N_w \bar{r}_w$ it is usually of the order of millimetres and centimetres per second.

In a general case, including non-adiabatic conditions the equilibrium of water vapor will be reached when e=E_v, where E_v is the equilibrium vapor pressure,

$$E_v = \left(1 + S_w^{(v)}\right) E_w \qquad (16)$$

Here, $S_w^{(v)}$ is the supersaturation yielding the water vapour equilibrium. In order to find $S_w^{(v)}$ substitute $\dot{q}_v$ =0 in Eq.10, which yields $\dot{q}_w = -\dot{q}_i$. Then, combining Eqs.1, 4, 5 and $\dot{q}_w = -\dot{q}_i$ we obtain

$$S_w^{(v)} = -\frac{B_i^* N_i \bar{r}_i}{B_w N_w \bar{r}_w + B_i N_i \bar{r}_i} \qquad (17)$$

It should be noted that the equilibrium of water vapour in mixed phase clouds has a dynamic nature, i.e. water vapour released by evaporating droplets is depleted by growing ice particles.

5. Different regimes of the phase transformation in mixed phase clouds

Three points of the phase equilibrium $\dot{q}_w = 0$, $\dot{q}_i = 0$, $\dot{q}_i = 0$ and their associated vertical velocities u_z^*, u_z^+, u_z^o, discussed in the previous section, play a fundamental role in the understanding of the phase transformation in mixed phase clouds. The analysis of Eqs. 13, 14, and 15 yields that the inequality

$$u_z^o < u_z^+ < u_z^* \qquad (18)$$

is always satisfied for any $N_i \bar{r}_i$ and $N_w \bar{r}_w$ (Korolev 2008). The inequality in Eq.26 enables separating the phase transformation in mixed clouds into four regimes:

(1) if $u_z < u_z^o$, then $\dot{q}_v$ >0, $\dot{q}_i$ <0 and $\dot{q}_w$ <0. In this case, both ice particles and droplets evaporate, whereas the mass of the vapour increases. In terms of the vapour pressure this case corresponds to the condition, when e<E_i.

(2) if $u_z^o < u_z < u_z^+$, then $\dot{q}_v$ >0, $\dot{q}_i$ >0 and $\dot{q}_w$ <0. Under these conditions ice particles grow, droplets evaporate, and the water vapour

mixing ratio increases. The water vapour pressure in this case changes in the range $E_i<e<E_v$.

(3) if $u_z^+ < u_z < u_z^*$, then $\dot{q}_v$ <0, $\dot{q}_i$ >0 and $\dot{q}_w$ <0. In this case, ice particles grow, droplets evaporate, and the water vapour mass decreases. This case corresponds to the water vapour pressure $E_v<e<E_w$.

(4) if $u_z > u_z^*$, then $\dot{q}_v$ <0, $\dot{q}_i$ >0 and $\dot{q}_w$ >0. In this case, both ice particles and liquid droplets grow, and the water vapour mass decreases. Under this condition the water vapour pressure will be $e>E_w$.

A conceptual diagram in Fig.6 illustrates the four regimes of phase transformation in mixed-phase clouds, based on the analogy between three fluid reservoirs ('liquid', 'vapour' and 'ice') connected with pipes and placed on different levels. The levels of the reservoirs is analogous to the water vapour pressure. Since E_w and E_i are constant, then depending on the vapour pressure *e*, the flow of the water vapour may be directed either from both liquid and ice to the vapour (Fig.6d), or from the vapour to both the liquid and the ice (Fig.6a), or from the liquid to the ice through the vapour (Fig.6b,c).

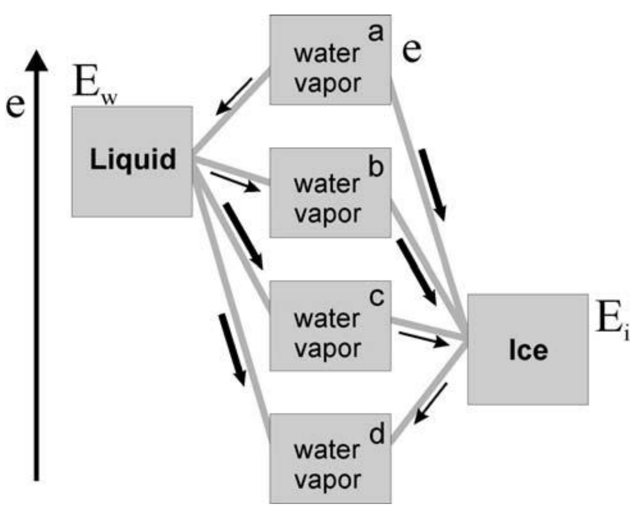

Figure 6. Conceptual diagram of four different scenarios of phase transformation in mixed-phase clouds: (a) $u_z > u_z^*$; (b) $u_z^+ < u_z < u_z^*$; (c) $u_z^o < u_z < u_z^+$; (d) $u_z < u_z^o$. The arrows indicate the direction of the mass transfer. The thickness of the arrows indicates conditional rates of the mass transfer.

6. WBF process

The WBF process is defined as the process, when "*…ice crystals would gain mass by vapour deposition at the expense of the liquid drops that would lose their mass by evaporation*" (Glossary of Meteorology, 2000). The thermodynamical conditions which are a result of the aforementioned condition occur when "*the vapour tension will adjust itself to a value in between the saturation values over ice and over water*" (Wegener, 1911, p.81). Based on the above statements it can be concluded that the WBF process is determined by a set of conditions: $\dot{q}_w$ <0, $\dot{q}_i$ >0 and $E_i<e<E_w$. Thus, of the above four scenarios described in section 5, only cases (2) and (3) suit the definition of the WBF process, i.e. when ice particles are growing at the expense of evaporating liquid droplets. These cases correspond to the velocity range $u_z^o < u_z < u_z^*$.

For the vertical velocities $u_z > u_z^*$, both ice and liquid particles grow simultaneously. Under these conditions the liquid droplets compete with the ice particles for the water vapour. It can be shown, that for $u_z > u_z^*$ liquid droplets slow down the rate of growth of ice particles $\dot{q}_i$ (Korolev 2008). Figure 7 shows the rate of changes of the mixing ratio of ice $\dot{q}_i$ versus $N_w\bar{r}_w$ for different u_z. As seen from Fig. 7, for $u_z > u_z^*$ the increase of $N_w\bar{r}_w$ slows down the ice growth. In other words, when $u_z > u_z^*$, ice crystals grow faster without droplets as compared to when the droplets are present. This type of behaviour of liquid droplets within the presence of ice particles is different from that described by the WBF process, which is when liquid droplets enhance the growth of ice particles by providing them with water vapour through their evaporation (Wegener, 1911, Bergeron 1935, Glossary of meteorology, 2000).

For a case when $u_z < u_z^o$, both ice particles and liquid droplets simultaneously evaporate, which, again, does not match the definition of the WBF process, since ice particle evaporate in presence of liquid droplets (Glossary of Meteorolgy 2000). Figure 7 also shows that liquid droplets slow down the sublimation rate of ice particles when $u_z < u_z^o$, i.e. when both droplets and ice particle evaporate.

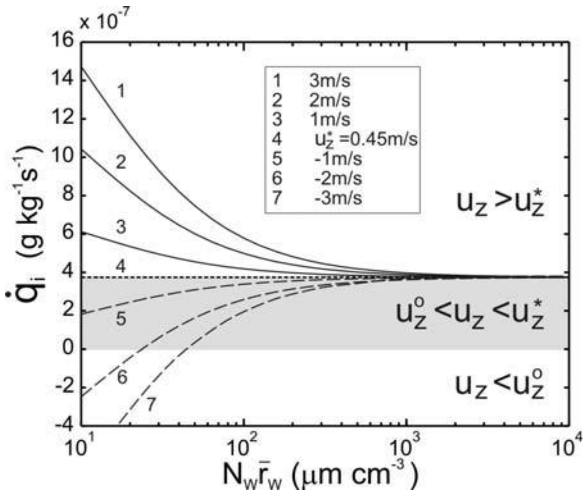

Figure 7. The rates of changes of the mixing ratio of ice $\dot{q}_i$ versus integral radius of cloud droplets $N_w\bar{r}_w$ for different u_z. As seen, for $u_z > u_z^*$ the increase of $N_w\bar{r}_w$ slows down the ice growth (the WBF process is declined), whereas for $u_z^o < u_z < u_z^*$ the increase of $N_w\bar{r}_w$ results in the increase of growth of ice. Grey colour shows the area where the WBF process is enabled. For $u_z < u_z^o$ evaporating droplets slow down the rate of ice sublimation. Calculations were done for $N_i\bar{r}_i$ =10μm cm^{-3}, T=-10C; P=890mb.

Earlier Reisin et al. (1996) came to a conclusion, based on the analysis of results of numerical modelling of convective clouds, that the WBF process "did not play a significant role in the rain formation process" and that in strong updrafts "ice particles grew by deposition, but did not cause the evaporation of the drops". A similar statement can be found in Pruppacher and Klett (1997, p.549). Although it was understood that the WBF process may play a limited role in mixed phase clouds, at that point it was not clear as to what conditions activated the process. In the present section we demarcate three distinctly different regimes of the behaviour of the condensed water in mixed phase clouds and find the conditions for each of them.

For adiabatic parcels, the regimes of growth and evaporation of the droplets and ice particles can be well depicted by the ratio of the growth rates of liquid and ice $\dot{q}_w / \dot{q}_i$. Dividing Eq. 8 by Eq. 9 yields,

$$\frac{\dot{q}_w}{\dot{q}_i} = \frac{\left(a_0 u_z - b_i^* N_i \bar{r}_i\right) B_w N_w \bar{r}_w}{\left(a_0 u_z - \dfrac{1-\xi}{\xi} b_w N_w \bar{r}_w\right) B_i N_i \bar{r}} \qquad (19)$$

Figure 8 shows the dependence of the ratio $\dot{q}_w / \dot{q}_i$ versus the vertical velocity u_z for $N_w\bar{r}_w$ =500μm cm^{-3}, $N_i\bar{r}_i$ =10 μm cm^{-3} at T=-5C. Grey areas in Fig.8 indicated by numbers 1, 2, 3 and 4 correspond to four different regimes as described in section 5. The vertical dashed lines in Fig.8 show the threshold velocities u_z^* (Eq.11), u_z^o (Eq.12) and u_z^+ (Eq.15) separating the four regimes of mixed phase evolution.

For the vertical velocity u_z^*, the growth rate of liquid water $\dot{q}_w$=0 and, therefore, $\dot{q}_w / \dot{q}_i$ =0. For the velocity u_z^o, the growth rate of ice $\dot{q}_i$ =0 and therefore, $\dot{q}_w / \dot{q}_i \to -\infty$. The WBF process is enabled only in the range of vertical velocities $u_z^* > u_z > u_z^o$ (areas 2 and 3 in Fig.8).

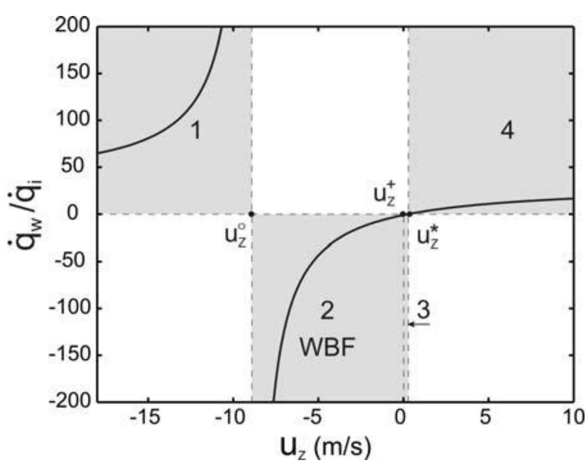

Figure 8. Ratio $\dot{q}_w / \dot{q}_i$ versus vertical velocity u_z in a mixed phase cloud. Grey areas and numbers indicate areas where: (1) $\dot{q}_i$ <0 and $\dot{q}_w$<0, both droplets and ice particles evaporate; (2 and 3) $\dot{q}_i$ >0 and $\dot{q}_w$<0, liquid droplets evaporate, whereas ice particle grow (this condition corresponds to the WBF process); (4) $\dot{q}_i$ >0 and $\dot{q}_w$>0, both droplets and ice particles grow. T=-5C; P=680mb; $N_w\bar{r}_w$ =300μm cm^{-3}; $N_i\bar{r}_i$ =10μm cm^{-3}

During the WBF process the ice particles are growing not only due to the evaporating liquid droplets. The mass of the water vapour deposited on the ice crystals may be partitioned between evaporated and pre-existing liquid droplets within the cloud parcel water vapour. This growth regime corresponds to the condition $-1 < \dot{q}_w / \dot{q}_i < 0$ (area 3 in Fig.8). In other words, in area 3 in Fig.8 when $u_z^+ < u_z < u_z^*$ ice particles consume more water vapour than was evaporated by the liquid droplets. When u_z is approaching to u_z^*, the liquid droplets slow their evaporation down, whereas ice particles increase the growth rate. At $u_z = u_z^*$ liquid droplets reach equilibrium with water vapour and cease growing.

In the case of $-\infty < \dot{q}_w / \dot{q}_i < -1$ (area 2 in Fig.8) only a fraction of water vapour evaporated by liquid droplets will be depleted by growing ice crystals, and another fraction will stay in the gaseous phase. In area 2 in Fig.8, when $u_z^o < u_z < u_z^+$, ice particles uptake less water vapour than that evaporated by the liquid droplets. When u_z is approaching to u_z^o, the liquid droplets evaporate faster, whereas ice particle slow down their growth, and at $u_z = u_z^o$ ice particles stay in equilibrium with the water vapour and stop growing.

The genuine WBF process, when all water evaporated by the droplets is equal to that consumed by the ice particles, occurs when $\dot{q}_w / \dot{q}_i = -1$. Following Eq.10, the condition $\dot{q}_w / \dot{q}_i = -1$ is equivalent to $\dot{q}_v = 0$, which for an adiabatic case is reached when $u_z = u_z^+$ (Eq.15).

In order to characterize the effect of evaporating droplets on the growth of ice particles we introduce the efficiency of the WBF process (ω) The WBF efficiency is defined as the fraction of evaporated liquid water converted into ice ($\omega = \dot{q}_i / |\dot{q}_w|$) for $u_z^o < u_z < u_z^+$. For the velocity range $u_z^+ < u_z < u_z^*$ the growth rate of ice $\dot{q}_i$ becomes larger than that of liquid $|\dot{q}_w|$, since ice grows both due to evaporating droplets and pre-existing water vapour. Therefore, for $u_z^+ < u_z < u_z^*$ the WBF efficiency is defined as the fraction of evaporated liquid to the total water vapour converted into ice, i.e. $\omega = |\dot{q}_w| / \dot{q}_i$. Figure 9 shows the dependence of the WBF efficiency versus u_z. As seen from Fig.9, ω=0, for $u_z = u_z^*$ and $u_z = u_z^o$, and it reaches maximum (ω=1), when $u_z = u_z^+$.

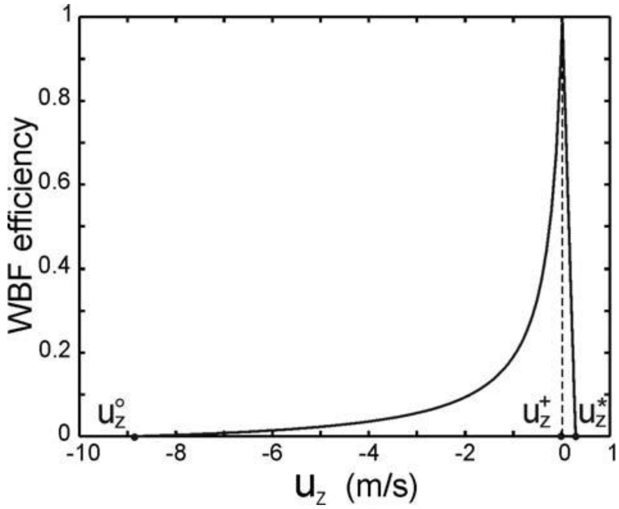

Figure 9. Efficiency of the WBF process versus u_z. The conditions are the same as in Fig.7: T=-5C; P=680mb; $N_w \bar{r}_w$ =300μm cm^{-3}; $N_i \bar{r}_i$ =10μm cm^{-3}

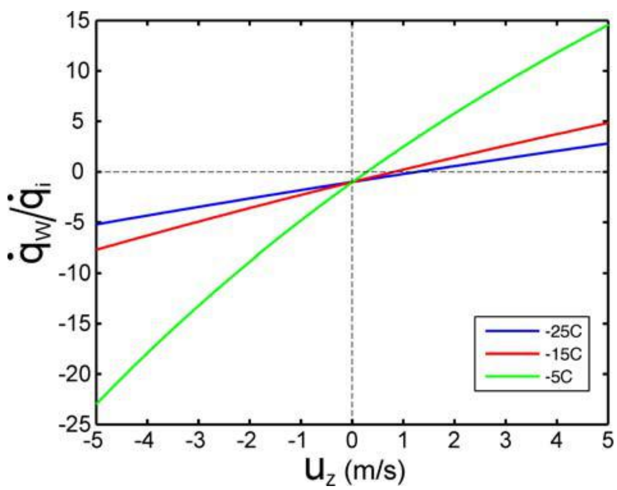

Figure 10. Dependence of the ratio $\dot{q}_w / \dot{q}_i$ versus vertical velocity u_z for three different temperatures. Calculations were done for integral radii $N_w \bar{r}_w$ =1000μm cm^{-3}, $N_i \bar{r}_i$ =10μm cm^{-3}, and pressure P=680mb.

The ratio $\dot{q}_w / \dot{q}_i$ is temperature sensitive. Figure 10 shows the behaviour of $\dot{q}_w / \dot{q}_i$ for the different temperatures in the vicinity of u_z=0. As seen from Fig.10 the dependence of $\dot{q}_w / \dot{q}_i$ on u_z weakening with the decrease of temperature.

At u_z=0 the ratio $\dot{q}_w/\dot{q}_i$ becomes independent of integral radii $N_w\bar{r}_w$ and $N_i\bar{r}_i$, and it is equal to

$$\left(\frac{\dot{q}_w}{\dot{q}_i}\right)_{u_z=0} = -\frac{a_2}{a_1} \qquad (20)$$

The ratio a_2/a_1 is a weak function of T and P, and it changes in the range of $1 < a_2/a_1 < 1.08$, for the changes temperature and pressure in the ranges from $-40<T<0$C to $300<P<1000$mb, respectively. Thus, for practical purposes, it can be considered, with a high degree of accuracy, that $\dot{q}_w / \dot{q}_i \approx -1$ at u_z=0 regardless $N_w\bar{r}_w$, $N_i\bar{r}_i$, T and P. This finding results in the conclusion that the WBF process has a maximum efficiency (ω=1) at $u_z \approx 0$ and to a first approximation it is not dependant on the microphysics of mixed phase clouds, temperature and pressure.

7. Limitations and assumptions

The consideration of an idealized mixed phase cloud as discussed at the beginning of section 2 resulted in the neglecting of some physical processes inherent in real clouds such as: (1) sedimentation; (2) aggregation of ice crystals; (3) riming; (4) nucleation of ice particles; (5) activation and evaporation of liquid droplets; (6) coalescence of droplets; (7) entrainment and mixing; (8) radiation effects.

The above processes affect the rates of phase transformation through the changes of $N_i\bar{r}_i$ (processes #1-4), $N_w\bar{r}_w$ (processes #5, 6), and the humidity and temperature (processes #7, 8). In the present work the instant rates of the phase transformation were considered for the diffusional stage. The characteristic timescale of the diffusional processes is determined by the time of phase relaxation τ_p (Eq.7). Typically, in mixed phase clouds τ_p is of the order of few seconds (Korolev and Mazin 2003). The magnitude of the characteristic timescales of processes related to aggregation, riming, coagulation, sedimentation radiative heating or cooling varies from minutes to hours (Prupacher and Klett, 1997) and it is much larger than τ_p. Due to a naturally low concentration of ice nuclei, secondary ice nucleation in already pre-existing ice or mixed phase clouds is considered to be a relatively slow process, which is not expected to change $N_i\bar{r}_i$ within a few τ_p. Therefore, it is expected that the effect of the processes #1-4, 6, 8 on the instant rates of $\dot{q}_w$, $\dot{q}_i$ and $\dot{q}_v$ will be negligible.

There are two main issues to consider: activation and evaporation of liquid droplets and entrainment and mixing. The entrainment and mixing with the dry out-of-cloud air changes the local relative humidity and temperature. Entrainment and mixing may result in a rapid decrease of the relative humidity followed by the evaporation of cloud particles to compensate for the deficit in humidity. This is an essentially non-equilibrium process, which cannot be described through the quasi-steady approximation. Since at timescales $t \gg \tau_p$ the relative humidity in a cloud parcel relaxes to its quasi-steady value, the mixing is expected to have maximum effect on the steady state $\dot{q}_w$, $\dot{q}_i$ and $\dot{q}_v$ at $t<\tau_p$. Entrainment and mixing is a most common phenomenon in the vicinity of the cloud interfaces, and its effect decreases when moving away from the cloud boundaries deep into the cloud. Therefore, it is expected that the developed theoretical framework may not be applicable to the cloud regions in the vicinity of cloud boundaries with intensive entrainment and mixing.

The activation and evaporation of droplets imposes another limitation on the use of the quasi-steady approximation. During the initial stage of activation or the final stage of evaporation of droplets their sizes become too small, and that they do not satisfy the condition Eq.12 imposing the limitations on the use of the quasi-steady approximation. The activation of the droplets may occur in pre-existing ice clouds when updrafts $u_z > u_z^*$. The evaporation of droplets in a mixed phase cloud may happen during the process of cloud glaciation during ascent or descent, when $u_z < u_z^*$. The examples of the cases which do not satisfy Eq.12 are shown in Fig.3 with red triangles.

It should be noted that Eq.12 was derived in assumption that $N_w\bar{r}_w >> N_i\bar{r}_i$. This condition is typically satisfied in mixed phase clouds. For ice clouds, a limiting condition can be obtained from Eq.12 by simply replacing subscript "*w*" to "*i*".

Despite the limitations discussed above, the quasi-steady approximation provides a relatively accurate estimation of the instant rates of the phase transformation (Fig.1). A more accurate consideration of the phase transformation can be achieved by utilizing the complete set of differential equations describing all processes mentioned at the beginning of this section. Such elaboration may provide more accurate estimations of the threshold velocities u_z^o, u_z^+, u_z^* and the rates $\dot{q}_v$, $\dot{q}_i$ and $\dot{q}_w$.

8. Conclusions

One of the goals of this work is to demonstrate a complexity of interaction of liquid, ice and gaseous phases in mixed phase clouds on a diffusional level. One of the important outcomes of this work is that the interaction between three phases is not limited just by the WBF process, describing a one directional phase transition. In fact, mixed phase has several points of equilibrium and the phase transformation has different regimes and the WBF process is one of them. The direction and the rate of the phase transformation are tightly related to the local thermodynamical and microphysical properties of a mixed phase cloud.

It has been shown that for typical integral radii $N_i\bar{r}_i$, $N_w\bar{r}_w$ the vertical velocities separating different regimes of the phase transformation can be generated by turbulent fluctuations. In other words, during turbulent fluctuations the direction of partitioning of water between ice, liquid, and vapour are constantly changing direction, and occasionally following the WBF process. During turbulent fluctuations cloud parcels are continuously passing through different points of equilibrium, therefore resulting in a continuous change of the rate and direction of partitioning of the mass between ice, liquid and ice phases. Since the integral radii of ice particles and droplets are continuously changing due to the diffusional growth and/or evaporation of droplets and ice particles, the vertical velocities defining the equilibrium between phases are also changing with time.

The following results were obtained within the frame of this study:

1. It is shown that mixed phase clouds have three basic points of phase equilibrium for liquid, ice and vapour phases, which separate the phase transformation in mixed phase clouds into four different regimes.
2. For typical $N_w\bar{r}_w$ and $N_i\bar{r}_i$ the growth rate of ice particles is significantly less sensitive to the vertical velocities in mixed phase clouds in comparison to liquid droplets.
3. The temperature corresponding to the maximum rate of the growth of ice and evaporation of liquid changes depending on P, $N_w\bar{r}_w$, $N_i\bar{r}_i$ and u_z, and it varies within a wide range. This temperature is not necessarily equal to -12C, where the maximum difference between saturation water vapour pressure between ice and liquid is observed.
4. Maximum efficiency of the WBF process, i.e. when all water vapour evaporated by the liquid droplets is deposited on the ice crystals, occurs at $u_z = u_z^+$. It is shown that in mixed phase clouds $u_z^+ \sim 0$.

References

Bergeron, T. 1935: On the physics of clouds and precipitation. *Proces Verbaux de l'Association de Météorologie, International Union of Geodesy and Geophysics*, Paris, 156-178.

Findeisen, W. 1938: Kolloid-meteorologische Vorgänge bei Neiderschlags-bildung. *Meteorologiche Zeitschrift*, **55**, 121-133.

Glossary of Meteorology, Ed. T.S. Glickmann, 2000, American Meteorological Society, Boston, MA, USA, p.855.

Korolev, A. V. and I. P. Mazin, 2003: Supersaturation of water vapor in clouds. *J. Atmos. Sci.*, **60,** 2957-2974

Korolev, A. V., and G. A. Isaac, 2006: Relative humidity in liquid, mixed-phase, and ice clouds. *J. Atmos. Sci*., **63,** 2865-2880

Korolev, A.V., 2007: Limitations of the Wegener-Bergeron-Findeisen Mechanism in the Evolution of Mixed-phase Clouds. *J. Atmos. Sci*., **64**, 3372-3375

Korolev, A.V., 2008: Rates of phase transformations in mixed-phase clouds. *Quart.J.Roy.Meteor.Soc.* **134**, in press.

Pruppacher, H. R. and Klett, J. D. 1997 *Microphysics of Clouds and Precipitation*. Kluwer Academic Publisher, London, 954.

Squires, P., 1952: The growth of cloud drops by condensation. *Aust. J. Sci. Res*., **5**, 66–86.

Reisin, T., Z. Levin, and S. Tzivion, 1996: Rain Production in Convective Clouds as Simulated in an Axisymmetric Model with Detailed Microphysics. Part II: Effects of Varying Drops and Ice Initiation. *J. Atmos. Sci*., **53**, 1815–1837

Wegener, A. 1911: *Thermodynamik der Atmosphäre*. Leipzig, pp.331.

Appendix A
List of Symbols

Symbol	Description	Units
a_0	$\frac{g}{R_a T}\left(\frac{L_w R_a}{c_p R_v T}-1\right)$	m^{-1}
a_1	$\frac{1}{q_v}+\frac{L_w^2}{c_p R_v T^2}$	-
a_2	$\frac{1}{q_v}+\frac{L_w L_i}{c_p R_v T^2}$	-
A_i	$\left(\frac{\rho_i L_i^2}{k R_v T^2}+\frac{\rho_i R_v T}{E_i(T) D}\right)^{-1}$	$m^2 s^{-1}$
A_w	$\left(\frac{\rho_w L_w^2}{k R_v T^2}+\frac{\rho_w R_v T}{E_w(T) D}\right)^{-1}$	$m^2 s^{-1}$
b_w	$a_1 B_w$	$m^2 s^{-1}$
b_i	$a_2 B_i$	$m^2 s^{-1}$
b_{i0}	$a_2 B_{i0}$	$m^2 s^{-1}$
b_i^*	$a_2 B_i^*$	$m^2 s^{-1}$
B_i	$\xi c B_{i0}=\frac{4\pi\rho_i \xi c A_i}{\rho_a}$	$m^2 s^{-1}$
B_{i0}	$\frac{4\pi\rho_i A_i}{\rho_a}$	$m^2 s^{-1}$
B_i^*	$(\xi-1) c B_{i0}=\frac{4\pi}{\rho_a}\rho_i(\xi-1) c A_i$	$m^2 s^{-1}$
B_w	$\frac{4\pi\rho_w A_w}{\rho_a}$	$m^2 s^{-1}$
c	ice particle shape factor characterizing 'capacitance' $0<c\leq 1$ (c=1 for spheres)	-
c_p	specific heat capacity of moist air at constant pressure	$J\ kg^{-1} K^{-1}$

D	coefficient of water vapour diffusion in the air	$m^2 s^{-1}$
e	water vapour pressure	$N m^{-2}$
E_i	saturation vapour pressure above flat surface of ice	$N m^{-2}$
E_v	$\left(1+S_w^{(v)}\right)E_w$ equilibrium water vapour pressure when $\dot{q}_v = 0$ (Eq.16)	$N m^{-2}$
E_w	saturation vapour pressure above flat surface of water	$N m^{-2}$
G	acceleration of gravity	$m s^{-2}$
k	coefficient of air heat conductivity	$J m^{-1} s^{-1} K^{-1}$
L_i	latent heat for ice	$J kg^{-1}$
L_w	latent heat for liquid water	$J kg^{-1}$
M	cloud particle mass	Kg
N_i	concentration of ice particles	m^{-3}
N_w	concentration of liquid droplets	m^{-3}
P	pressure of moist air	$N m^{-2}$
q_i	ice water mixing ratio (mass of ice per 1kg of dry air)	-
q_v	water vapour mixing ratio (mass of water vapour per 1kg of dry air)	-
q_w	liquid water mixing ratio (mass of liquid water per 1kg of dry air)	-
$\dot{q}_i$	rate of change of ice water mixing ratio (Eq.9)	s^{-1}
$\dot{q}_v$	rate of change of water vapour mixing ratio (Eq.11)	s^{-1}
$\dot{q}_w$	rate of change of liquid water mixing ratio (Eq.8)	s^{-1}
$\bar{r}_i$	average of half of a maximum linear dimension of an ice particle	m
$\bar{r}_w$	average liquid droplet radius	m
R_a	specific gas constant of moist air	$J kg^{-1} K^{-1}$
R_v	specific gas constant of water vapour	$J kg^{-1} K^{-1}$
S_{qsw}	quasi-steady supersaturation (Eq.5)	-
S_i	e/E_i-1, supersaturation over ice	-
S_w	e/E_w-1, supersaturation over water	-
$S_w^{(v)}$	supersaturation, when $\dot{q}_v = 0$ (Eq.17)	-
t	time	s
T	temperature	K
u_z	vertical velocity	$m s^{-1}$
u_z^*	vertical velocity, when $\dot{q}_w$ =0 (Eq.13)	$m s^{-1}$
u_z^o	vertical velocity, when $\dot{q}_i$ =0 (Eq.14)	$m s^{-1}$
u_z^+	vertical velocity, when $\dot{q}_v$ =0 (Eq.15)	$m s^{-1}$
Z	altitude	m
η	$a_2 B_{i0}/a_0$	$m^3 s^{-1}$
χ	$a_1 B_w/a_0$	$m^3 s^{-1}$
ξ	E_w / E_i	-
ρ_a	density of the dry air	$kg m^{-3}$
ρ_i	density of an ice particle	$kg m^{-3}$
ρ_w	density of liquid water	$kg m^{-3}$
τ_p	time of phase relaxation (Eq.7)	s
τ_c	characteristic lifetime of a cloud	s
ω	efficiency of the WBF process	s

ON THE EVALUATION OF THE WRF MODEL OVER THE SOUTHERN OCEAN & TASMANIA

Anthony E. Morrison[1], Steven T. Siems[1], Michael J. Manton[1], Alex Nazarov[2]

[1]Monash University, Melbourne, Australia
[2]Hydro Tasmania Ltd. Hobart Australia

1. INTRODUCTION

The Southern Ocean and its accompanying air mass are considered to be one of the most pristine environments on earth. Sporadic research over the last forty years has hinted that many of the frontal cloud bands existing over the southern ocean and south eastern Australia are of mixed phase (often showing significant quantities of supercooled water). Quantitative evidence over the west coast of Tasmania was first recorded during a cloud seeding experiment in 1979 (Ryan and King 1997) where it was not uncommon to find extended regions (5 minute averages) of supercooled water with values $>$0.3g/m^3. Further quantitative evidence by Long and Huggins (1992) studying supercooled liquid water (SCLW) flux over a water catchment area near Melbourne, Victoria found that significant ratios of supercooled water to precipitation were common and that warm cloud-top temperatures of -5°to -10°C were also common relative to similar studies in North America e.g. Rauber and Grant (1986, 1987); Deshler and Reynolds (1990).

This paper has two main aims: Firstly to present observations from a cloud seeding research flight made over the western region of Tasmania and secondly, to evaluate the Weather Research and Forecasting (WRF) NWP model and the Thompson Microphysics package (TMP) (Thompson et al. 2007) regarding the model's ability to simulate these in-situ observations together with selected satellite and ground based observations. The motivation for this research is to ascertain the skill with which WRF is able to predict the temporal and spacial variability of mixed phase conditions, thermodynamic and wind profiles, frontal timing, surface precipitation, radar reflectivities, cloud top temperature and optical depth. Similar studies by Abbs and Jensen (1992), Hong et al. (2001), Hong et al. (2002), Vaillancourt et al. (2003), Morrison and Pinto (2005) and Reisner et al. (1998) have investigated the modeling of mixed phase clouds over south-east Australia, Canada, northern Alaska and North America respectively. The present analysis is a detailed investigation of a single case study, the 4th August 2006 (A06), characterised by large amounts of SCLW, little ice and a relatively small amount of precipitation. The research flight took place in post-frontal conditions and is shown in Figure 1. Cloud top temperature derived from the Moderate Resolution Imaging Spectroradiometer (MODIS) (Justice et al. 1998) instrument on Terra is shown for the A06 case study in Figure 2.

WRF was configured with 5 domains, the outer domain covering the entire of Australia and the finest resolution grid (1km spacing) centered over the western and central regions of Tasmania. The vertical structure is represented using 64 eta levels equally spaced in pressure up to 50mb.

2. THERMODYNAMIC & WIND PROFILES

Figure 3 shows the thermodynamic and wind profiles as measured by the research aircraft and predicted by the model during the A06 case study. The uncertainty in the aircraft measured temperature and dew point is around 1°C. The model predicted ground tem-

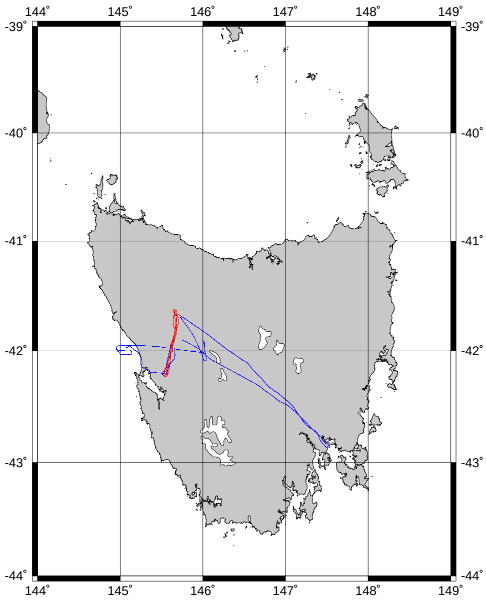

Figure 1: Flight track for the A06 case study. Red indicated regions where the seeding burners were on. The perimeter of the hydro electric catchment area is also shown.

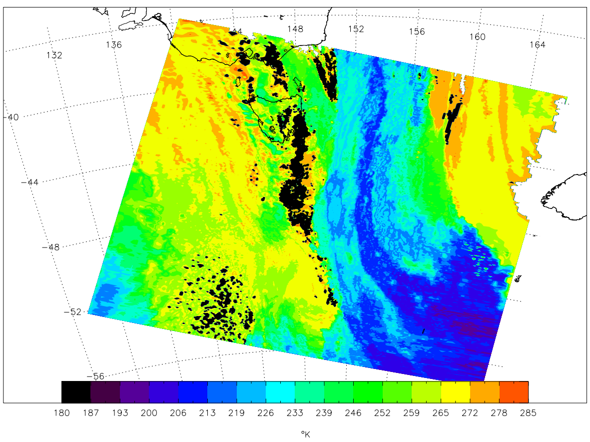

Figure 2: Cloud top temperature (MODIS), 23:50 UTC 08/08/06. The frontal cloud band is observed to the east of Tasmania, the dry slot and post frontal airmass are observed over and to the west of the island. The research aircraft was obtaining in-situ observations at the time of this image.

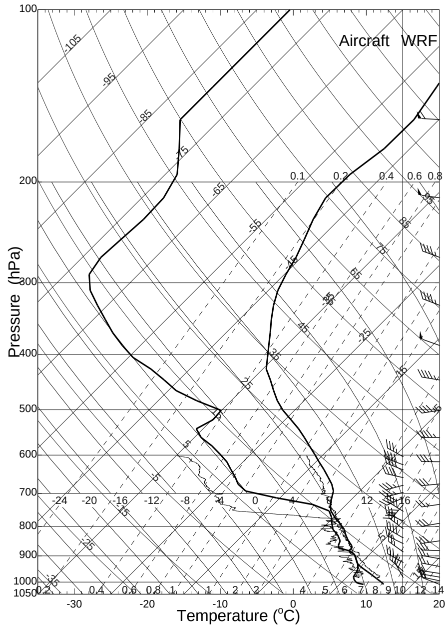

Figure 3: Thermodynamic and wind profile 08/08/06, (-42,145). Aircraft sounding 23:00 UTC (thin line), model sounding 23:00 UTC (thick line).

perature and dew point are within this uncertainty. The model predicts an inversion at approx. 750 hPa, this is not present in the observations. A sizable amount of shear is observed in the mid troposphere, this is not present in the WRF wind field.

3. WATER & ICE

Figure 4 shows the time series of (i) observed and (ii) WRF predicted SCLW measured along the seeding track shown in Figure 1. Figure 5 shows (i) the Cloud Aerosol Spectrometer (CAS) integrated mass of all hydrometeors (0.5-50μm) and (ii) the sum of WRF q_c, q_i & q_s mixing ratios. Observations indicate the relative amounts of water to total cloud particles $\leq 50\mu$m as measured by the hot-wire and CAS is 0.35. The amount of cloud water predicted by WRF relative to the sum of water, ice and snow is 0.52. Comparing these results it is observed that WRF over predicts the fraction of cloud water by at least 50% relative to other hydrometeors. It is observed that WRF tends

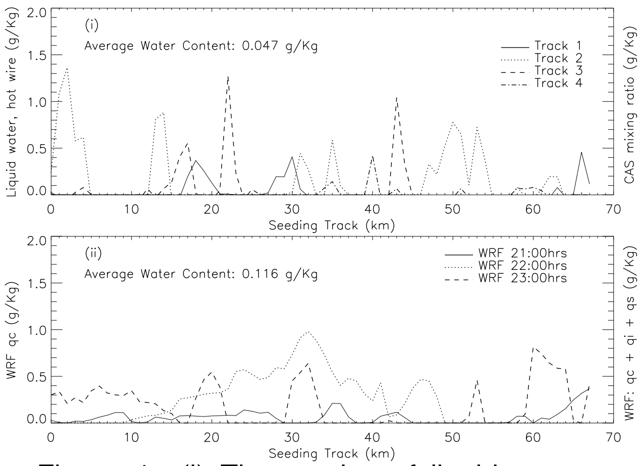

Figure 4: (i) Time series of liquid water as measured by the hot-wire (13s time constant, approx. 1km) for the 4 traverses of the seeding track completed between 21:00 and 22:40 UTC. (ii) Model predicted liquid water content along the simulated flight track for the 3 time periods shown.

to under estimate SCLW in cloud regions containing $<$0.3g/Kg, over estimate medium quantities, 0.3-0.6 g/Kg and under predict regions that have large quantities i.e. between 0.7-1.4 g/Kg (Figure 6). The absolute quantities of both SCLW and CAS measured hydrometeors are 0.047 & 0.131 g/Kg, respectively. WRF predicted values are 0.116 & 0.222 g/Kg indicating that WRF over predicts both quantities by around 100%.

4. CLOUD TOP TEMPERATURE

Figure 7 shows cloud top temperature retrieved using the MODIS instrument on Terra and WRF predicted values. It seems (in this case) that the MODIS algorithm may be assuming parts of the surface to be cloud as some cloud top temperatures are above 280°K. The general structure observed by the MODIS instrument is replicated to some degree by the model i.e. The presence of a lower cloud deck at temperatures around 270°K and the existence of upper level clouds to temperatures well below freezing. It is noted however that the minimum cloud top temperature predicted by the model is considerably higher than is observed.

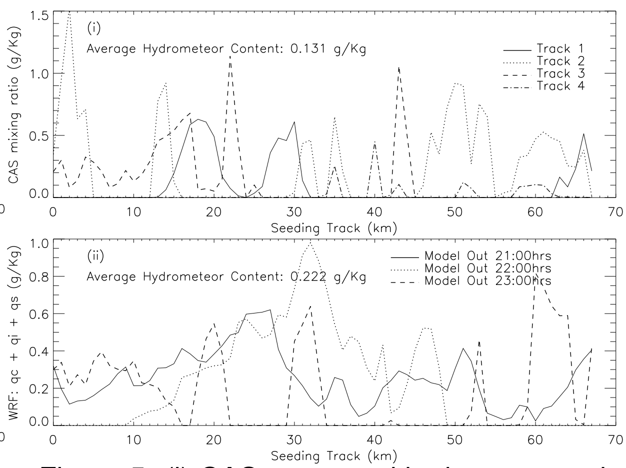

Figure 5: (i) CAS measured hydrometeor mixing ratio (assumed ρ =960Kg/m^3) for each of the 4 traverses of the seeding track completed between 21:00-22:40 UTC. (ii) WRF $qc{+}qi{+}qs$ for the 3 time periods shown.

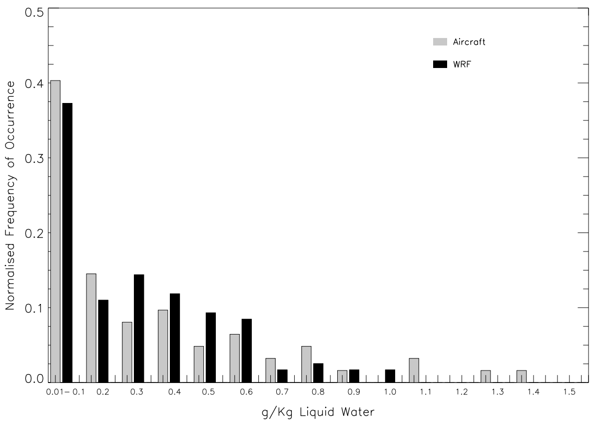

Figure 6: Histogram showing probabilities of encountering specific quantities of liquid water along the aircraft flight track and the model simulated flight track. Data is derived from Figure 4.

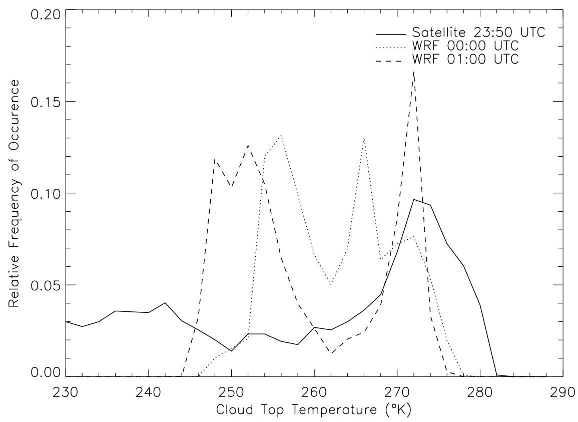

Figure 7: MODIS retrieved and WRF predicted cloud top temperature for the region encompassed by the finest resolution domain.

REFERENCES

Abbs, D. J. and J. B. Jensen, 1992: Numerical modeling of orographically forced post-frontal rain. *Monthly Weather Review*, **121**, 189–206.

Deshler, T. and D. W. Reynolds, 1990: The persistence of seeding effects in a winter orographic cloud seeded with silver iodide burned in acetone. *Journal of Applied Meteorology*, **29**, 477–488.

Hong, G., S. G. Cober, and G. A. Isaac, 2001: Verification of supercooled cloud forecasts with in situ aircraft measurements. *Weather and Forecasting*, **16**, 145–155.

Hong, G., S. G. Cober, G. A. Isaac, A. Tremblay, and A. Methot, 2002: Comparison of three cloud forcaste schemes with in situ aircraft measurements. *Weather and Forecasting*, **17**, 1226–1235.

Justice, C. O., E. Vermote, J. G. Townshend, R. Defries, D. P. Roy, D. K. Hall, P. J. L. Salomonson, V. V., G. Riggs, A. Strahler, W. Lucht, R. B. Myneni, Y. Knyazikhin, S. W. Running, R. R. Nemani, A. R. Zhengming Wan Huete, W. van Leeuwen, R. E. Wolfe, L. Giglio, J. Muller, P. Lewis, and M. J. Barnsley, 1998: The moderate resolution imaging spectroradiometer (modis) land remote sensing for global change research. *IEEE transactions on geoscience and remote sensing*, **36**, 1228–1249.

Long, A. B. and A. W. Huggins, 1992: Australian winter storms experiment 1: Supercooled liquid water and precipitation-enhancement opportunities. *Journal of Applied Meteorology*, **31**, 1041–1055.

Morrison, H. and J. O. Pinto, 2005: Mesoscale modeling of springtime artic mixed-phase stratiform clouds using a new two-moment bulk microphysics scheme. *Journal of Atmospheric Sciences*, **62**, 3683–3704.

Rauber, R. M. and L. O. Grant, 1986: The characteristics and distribution of cloud water over the mountains of northern colorado during wintertime storms. part 1: Temporal variations. *Journal of Applied Meteorology*, **25**, 468–488.

———, 1987: Supercooled liquid water structure of a shallow orographic cloud system in southern utah. *Journal of Applied Meteorology*, **26**, 208–215.

Reisner, R., R. M. Rasmussen, and R. T. Bruintjes, 1998: Explicit forecasting of supercooled liquid water in winter storms using the mm5 mesoscale model. *Quartley Journal of the Royal Meteorological Society*, **124**, 1071–1107.

Ryan, B. F. and W. D. King, 1997: A critical review of the australian experience in cloud seeding. *Bulletin of the American Meteorological Society*, **78**, 239–254.

Thompson, G., P. R. Field, R. M. Rasmussen, and W. D. Hall, 2007: Explicit forecasts of winter precipitation using an improved bulk microphysics scheme. part 2: Implementation of a new snow parameterization. *Submitted to Monthly Weather Review*.

Vaillancourt, P. A., A. Tremblay, S. G. Cober, and G. A. Isaac, 2003: Comparison of aircraft observations with mixed-phase cloud simulations. *Monthly Weather Review*, **131**, 656–671.

HOW DOES ASIAN DUST STORM AFFECT THE MICROPHYSICAL STRUCTURES OF OROGRAPHIC SNOW CLOUDS?

Masataka MURAKAMI[1] and Narihiro ORIKASA[1]

[1]Meteorological Research Institute, Tsukuba, Japan

1. INTRODUCTION

Aerosol particles, which act as ice nuclei, determine ice crystal concentrations and affect precipitation forecast through precipitation efficiency. Also from the viewpoint of climate change study, it is pointed out that ice nuclei as well as cloud condensation nuclei modulate the coverage and life of clouds and precipitation distribution through radiation properties and precipitation efficiency, and affect climate projection 100 years later through consequent modulation of global energy and water cycle.

Studies on ice nuclei have been carried out for more than half a century. However there are many things to remain unsolved because of huge complexity in activation mechanisms of ice nuclei unlike a single process of CCN activation.

Dust particles has been thought to be representative ice nuclei for a long time. Ice nucleation ability of montmorillonite, kaolinite and volcanic ashes as well as dust particles have been investigated. As for dust particles from inland of Chine, Isono et al. (1959) investigate chemical and physical characteristics and ice nucleation ability by using electron microscopic techniques and filter method.

Recently DeMott et al. (2003) measured ice nucleation ability of Saharan dust particles using CFDC IN counter and Sassen et al. (2003) observed clouds in dust storm by using depolarization lidar.

Possibility of internal mixing of dust particles with sea salt particles during their advection is also suggested through electron microscopic analysis of dust particles fallen

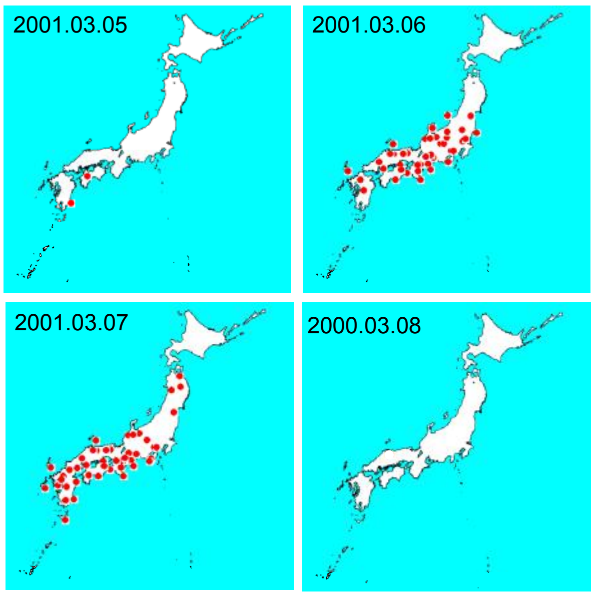

Fig. 1 Observatories of Japan Meteorological Agency where they observed dust storm evens from 5 to 8 Mar., 2000.

Corresponding author's address: Masataka MURAKAMI, Meteorological Research Institute, Tsukuba, Ibaraki 305-0052, Japan; E-Mail: mamuraka@mri-jma.go.jp.

over the western part of Japan.

But there are no in-situ measurements of microphysical structures of clouds during dust storms In this paper, microphysical structures of dust storm and orographic clouds are investigated and the effect of dust storm on orographic snow clouds are evaluated by comparing microphysical structures with and without dust storms.

2. SYNOPTIC FEATURES OF DUST STORMS

The dust storm started to cover the southern parts of Kyushu and Shikoku districts on 5 March 2000, and covered the whole western part of Japan, including Kanto and Hokuriku districts on 6 March and continued to spread out all over the Japan except for the Hokkaido and Okinawa districts on 7 March.

Although on 7 March, around Niigata prefecture seems to be a blank area of dust storm, the intrusion of developed snow storm into inland may have made surface observations difficult to recognize the dust storm (not shown). Indeed the aircraft observation confirmed the existence of the dust storm above snow clouds over the Niigata Prefecture.

Satellite IR imaginary shows that our observation area was partly covered with upper level, thin clouds on 5 and 6 March and was widely covered with developed snow clouds on 7 March.

The difference between the two water vapor channels of GMS, which indicate the dust storm as bright white images, indicated the similar advection of the dust storm

Dust Storm

Dust Storm

Background

Fig. 2 Photos taken just above the tops of orographic clouds on 6 (the first day of the dust storm event), 7 (the second day), and 11 (background) Mar. 2000.

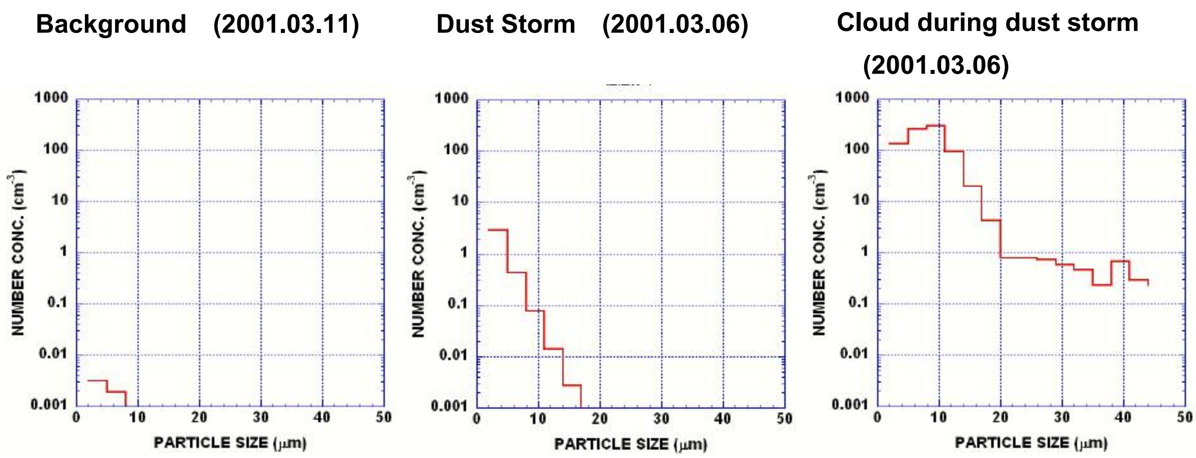

Fig. 3 Size distributions of aerosol particles and cloud droplets larger than 2 microns under typical winter monsoon pressure pattern. Background aerosols, aerosols during dust event and particles in clouds (from left to right).

corresponding to the surface observations mentioned above.

The severe dust storm already covered most of the western parts of Japan, including Hokuriku and Kanto districts.

3. RESULTS OF AIRBORNE IN-SITU MESUREMENTS

3.1 Aircraft Observation

Field campaigns on orographic snow cloud study had been carried out around the Echigo Mountains in the central part of Japan. We had flown an instrumented aircraft for the consequent 6 winter seasons (Feb.-Mar. 1998, Feb.-Mar. 1999, Feb.-Mar. 2000, Feb.-Mar. 2001, Dec. 2001, and Dec. 2002) over the study area.

The instrumented aircraft was equipped with various kinds of cloud microphysics and ordinary meteorological instruments, including three components of wind relative to the ground, on the wing tip pylons and fuselage. Cloud microphysics instruments included FSSP, 2D-C, 2D-P, CAPS, PVM-100 and two KLWC-5 probes.

3.2 Dust Storm

Figure 2 shows photos taken just above the tops of orographic clouds in almost the same location , time and angle of view except for the time of photo taken on 6 Mar., which is about 3 hours earlier than other two photos.

These photos suggest how the dust storm on 6 and 7 March, especially on the first day of the dust storm was severe although the contrast of blue sky and cloud tops may be difficult to evaluate objectively because of its dependency on the elevation angle of the sun, the existence of upper level clouds and the angle of view relative to the position of the sun.

The typical concentration of aerosol particles larger than 2 microns during dust storms is several particles/cm^3 and is 2 to 3

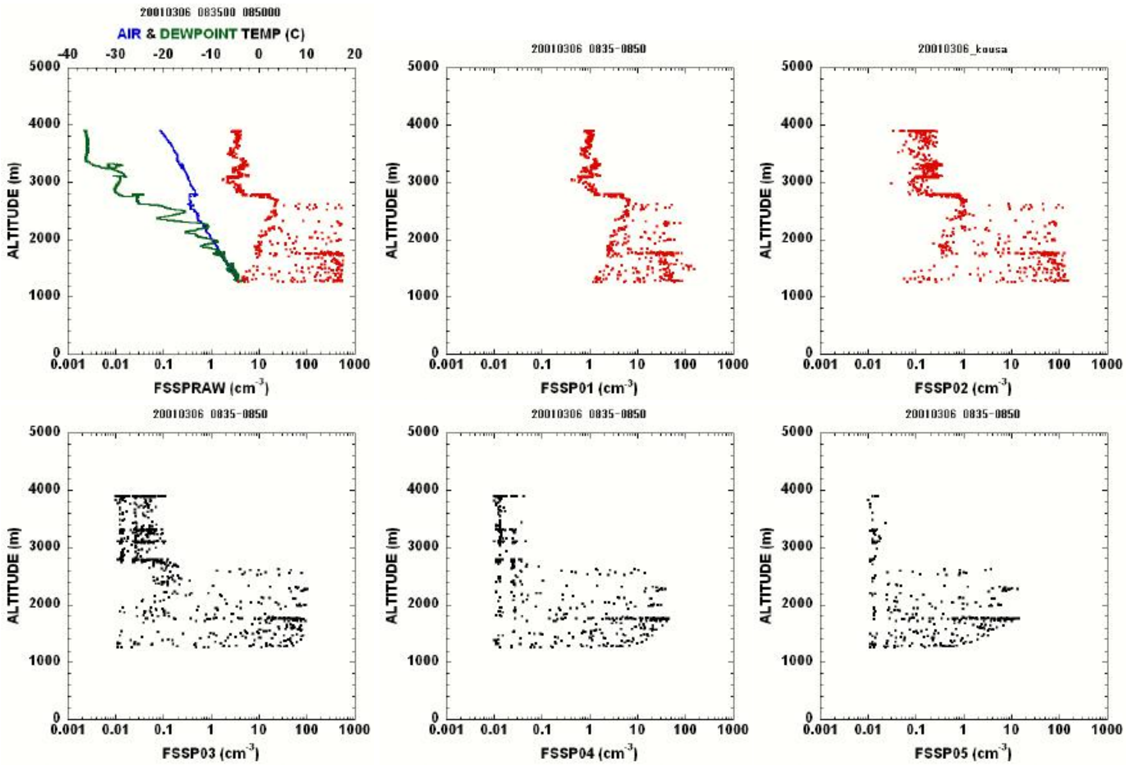

Fig. 4 Vertical change of particle concentrations in each size bin measured with FSSP during vertical profiling flight.

orders of magnitude greater than background concentrations ranging from 0.1 to 0.01 particles/cm^3 (Fig. 3).

The number concentrations of dust particles larger than 2 microns in the air above cloud tops were several particles/cm3 and rather uniform except for the northern part on 6 March while dust particles on 7 March showed low concentrations and a large spatial variation as compared with those on 6 March.

Vertical distributions of particles larger 2 microns in and outside of clouds show that the number concentrations of dust particles gradually decrease with decreasing altitude in the cloud-free or less-cloud atmosphere above the boundary layer and keep almost constant in the boundary layer as shown in the right panel.

On the other hand, in the atmosphere with orographic clouds, concentrations of dust particles gradually decrease with decreasing altitude and rapidly increase just above cloud tops due to swelling up of particles. In the boundary layer (cloudy layer), number concentrations of dust particles decrease with decreasing altitude due to precipitation scavenging.

3.3 Dust and Cloud Interaction

The relative humidity dependency of size distribution of aerosol particles during dust storms are shown in Fig.4.

Remarkable changes of number concentrations due to swelling up at relative humilities close to water saturation were seen

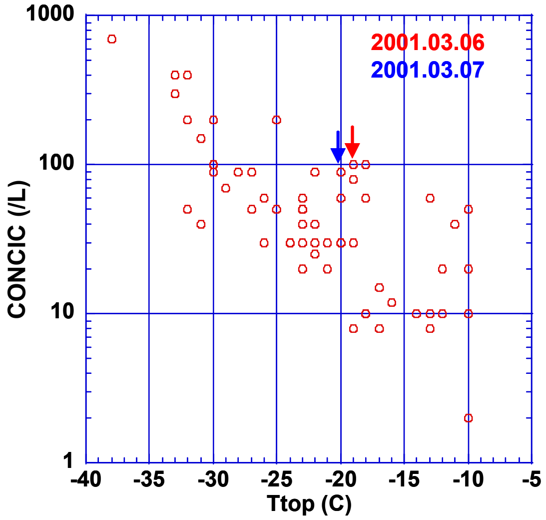

Fig. 5 Relation between the maximum number concentration of ice crystals and cloud top temperature obtained from aircraft observation data for 6 winter seasons from 1998 through 2003.

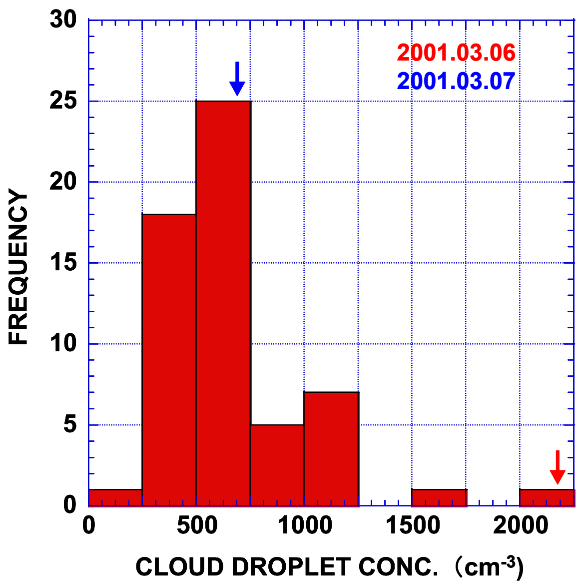

Fig. 6 Appearance frequency of the maximum cloud droplet concentrations obtained from aircraft observation data for 6 winter seasons from 1998 through 2003.

only for particles smaller than 8 microns although slight change in number concentration of particles in the third size bin (8-11 microns) was seen only near the cloud tops. This feature suggests that there remain significant numbers of dust particles un-activated in the clouds, especially near the cloud tops.

The maximum concentrations of ice crystals during heavy dust storms were about 100 particles/L in clouds with top temperature of -20C on the both days, which is half order of magnitude higher than the mean values of those for usual days without dust storm. Although the data points from the both days are located near the upper boundary of scattered data points, there are several data points from clouds without dust storm effects that show number concentrations as high as those on the dust event days (Fig.5).

This observation result suggests that dust particles act as efficient IN, and some particles other than dust particles also act as good IN.

The total concentrations of dust particles may have been at least one to two orders of magnitude higher than the observed concentrations of particles larger than 2 micron according to the past studies on dust particles.

This means that one particle out of 1, 000 to 10,000 particles is activated in orographic clouds during dust storm, which is much less effective as compared with experimental results by DeMott et al. (2003).

Figure 6 shows the appearance frequencyof the maximum cloud droplet concentration. In the most orographic clouds, the number concentrations of cloud droplets ranged from 250 to 750 droplets/cm^3, suggesting that the clouds are already affected by air pollution from domestic industrial activity and/or from east Asian countries.

Even during the same dust storm, we have much difference concentrations of cloud droplets for the first and last half of the dust storm period. On 6 March, the number concentration of the maximum concentration of cloud droplets was 2,100 droplets/cm^3, whereas that on 7 March was about 700 droplets/cm3.

4. DISCUSSION

3-day backward trajectories of air parcels at different pressure levels (red for 850 hPa, blue for 750 hPa and green for 650 hPa) at 00Z on 6 March and at 06Z on 7 March are examined to infer the cause for the difference in cloud droplet concentrations on 6 and 7 March (not shown).

The backward trajectories on 7 March show that air parcels at different levels have a similar history. The air parcel advected at rather high altitudes and did not experience cloud and precipitation processes. Therefore dust particles pumped up to higher altitudes may have had enough time to interact with anthropogenic and sea salt particles lifted up by convection on their way to Japan. On the other hand, air parcel at 850 hPa had much different history from that on 6 March although air parcel at 650 hPa had a similar history to that on 6 March. Air parcel in the boundary layer, which had anthropogenic and sea salt particles, did not experience any significant convection and stayed at lower altitudes and experienced cloud and precipitation processes over the Japan Sea and scavenged before mixing with dust particles.

5. CONCLUSION

Sixty flights were carried out to investigate orographic snow clouds by using an instrumented aircraft for the six consecutive winters starting from 1998.

For two cases (Mar. 6 and 7, 2001), out of 60, we happened to investigate the clouds under the heavy dust storm with dust particle (> 2 micrometers) concentrations greater than several particles/cm^3.

The maximum concentrations of ice crystals during heavy dust storms were about 100 particles/L in clouds with top temperature of -20C on the both days, which is half order of magnitude higher than the mean values of those for usual days without dust storm. This observation result suggests that dust particles act as efficient IN, and some particles other than dust particles also act as good IN.

On the other hand, cloud droplet concentrations were unusually high (2,200 droplets/ cm^3) on the first day of the dust storm and was usual (700 droplets/cm^3) on the second day. Back trajectory analysis suggested that air at lower levels (2000m) had experienced high humidity environment over the Japan Sea on the second day. Anthropogenic hygroscopic aerosol was probably scavenged through cloud and precipitation processes, before being mixed with dust particles and producing internally mixed particles (efficient CCN).

REFERENCES

DeMott P. J., K. Sassen, M. R. Poellot, D. Baumgardner, D. C. Rogers, S. D. Brooks, A. J. Prenni, S. M.Kreidenweis, 2003a: African dust aerosols as atmospheric ice nuclei, *Geophys. Res. Let*t., **30**, 1732,doi: 10.1029/2003GL017410.

Isono, K., M. Komabayasi, and A. Ono, The nature and origin of ice nuclei in the atmosphere, *J. Meteorol. Soc.Japan*, **37**, 211-233, 1959.

Sassen K., P. J. DeMott, J. M. Prospero, M. R. Poellot, 2003: Saharan dust storms and indirect aerosol effects on clouds: CRYSTAL-FACE results. *Geophys. Res. Let*t., **30** (12), 1633, doi: 10.1029/2003GL017371.

LABORATORY EXPERIMENTS OF MIXED- PHASE CLOUD FORMATION

Takuya Tajiri[1*], Katsuya Yamashita[1], Masataka Murakami[1], Narihiro Orikasa[1], Atsushi Saito[1], Tomohiro Nagai[1], Tetsu Sakai[1], and Hiroshi Ishimoto[1]

[1]Meteorological Research Institute, Tsukuba, Japan

1. INTRODUCTION

A new cloud simulation chamber was built in 2005 at Meteorological Research Institute (MRI), Japan Meteorological Agency. Laboratory experiments of ice formation using the MRI chamber has been conducted to identify where ice crystals originate and to quantify their concentrations under various cloud conditions in the troposphere.

Mixed-phase clouds are common features of clouds with top temperatures warmer than -35°C. Mid-latitude precipitating clouds frequently develop as the mixed-phase clouds, which form within preexisting supercooled liquid clouds. Cloud droplets appear first, then ice and snow crystals eventually dominate through ice initiation and subsequent depositional growth at the expense of cloud water until the cloud is completely glaciated. The repartitioning of water (i.e., cloud ice and supercooled cloud water) in such clouds varies throughout the cloud life cycles, and affects cloud radiative properties. In most climate models these treatments are simplified and specified as a function of temperature, although they are essential for proper simulations.

Aerosol particles play an important role as ice nuclei, and then determine the microphysical structures of mixed-phase clouds. However, it is not sufficiently understood how aerosols affect ice nucleation processes and cloud properties. A quantitative description of the relation between physico-chemical properties of aerosol particles and their ice nucleation ability is crucial for an improvement of numerical models.

To investigate ice nucleation processes in the mixed-phase clouds, microphysical instruments used in this study are Cloud Aerosol Spectrometer with Particle by Particle measuring function of forward and backward scattering (CAS-PbP), Cloud Particle Imager probe (CPI) and scattered laser detection system (laser system). Theses devices are potential for sensing the onset of cloud formation and measuring size distributions, shapes and asphericity of aerosol and hydrometeors.

It is expected that the result from this experimental study can be used not only for parameterization in weather prediction, climate and radiative transfer models, but also for development of cloud microphysical retrieval algorithms for remote sensors.

2. OVERVIEW OF THE MRI CHAMBER

MRI chamber was designed to simulate natural processes (adiabatic expansion) in experimental volume (1.4m^3) by synchronously controlling air pressure and wall temperature, after the controlled-expansion type chamber (DeMott and Rogers 1990). The air pressure in the chamber can be decreased down to below 30hPa with a vacuum rate corresponding to updraft velocities of 0 to 30 m/s and the temperature be cooled down to -100°C by circulating the coolant. Sample air, generated aerosol particles and/or natural outdoor air, can be introduced into

* *Corresponding author's address*: TAKUYA TAJIRI, Meteorological Research Institute, 1-1 Nagamine, Tsukuba, Ibaraki 305-0052, Japan; E-mail: ttajiri@mri-jma.go.jp

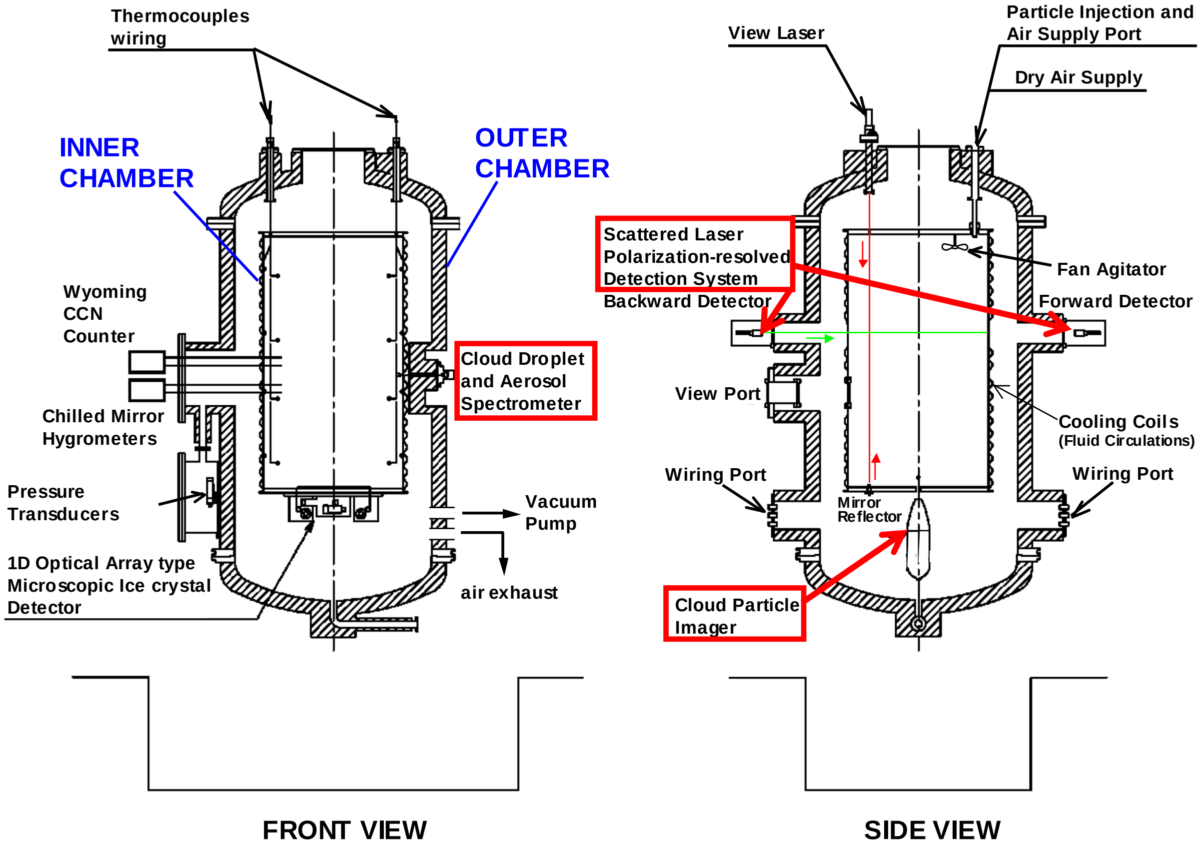

Fig. 1. Schematic cross sections of the MRI cloud simulation chamber. The Ice particle detectors used for the experiments are also indicated (as red line squares).

experimental volume from the particle injection port, which is located at the top of the chamber. A small fan stirs the injected air to achieve homogeneity of aerosol concentration inside the volume. Figure 1 shows a schematic view of the MRI chamber's major technical components and scientific instrumentation used for the experiments. Almost all experimental procedures during the period from pre- to after-expansion are programmed and automatically controlled by the data acquisition system (SEA's M300). More information of the MRI chamber for ice nucleation studies is described in detail by Tajiri et al. (2006).

3. EXPERIMENTAL SETUP AND METHODS

At first, natural outdoor air or test aerosols are introduced into the chamber with air pressure reduced below 30 hPa (i.e., nearly aerosol-free chamber), followed by preconditioning of sample air in terms of temperature and humidity, and then the adiabatic expansions are performed. During the pre-expansion initialization period, the Scanning Mobility Particle Sizer spectrometer (SMPS; MODEL3936, TSI) and the CAS-PbP were used for monitoring aerosol size distributions and number concentrations in the range from 0.01 to several micrometers.

Pre-set parameters such as the initial pressure (1000hPa), temperature (15°C) and adiabatic ascent rate (3m/s) are common to all experiments. It is difficult to continue cloud formations for a long time inside the chamber without sedimentation of the hydrometeors to the bottom of the chamber and condensation of water vapor onto the chamber wall. Thus the exact adiabatic expansions are realized for rather short time. To simulate the mixed-phase clouds appropriately in spite of these limitations, the experimental procedures are devised. Vacuum rate was kept the initial value corresponding to 3m/s until cloud droplets were activated and well-grown. After that, it was increased to the values corresponding to 5m/s (or 10m/s) to pass through the phase transition zones quickly. The initial dewpoint temperature is also adjusted to around 0°C to reach the LCL around -5～-10°C, although clean dry air supply is need to decrease relative humidity. These operations are supposed to help simulate mixed-phase clouds properly.

The dilution ratio of sample air by the addition of dry and/or moist filtered air is estimated from the change in number concentrations of aerosols (CAS data) or water vapor mixing ratios at the beginning of expansions, so that number concentrations of the particles detected by microphysical sensors during expansion experiments can be corrected.

4. ICE PARTICLE MEASUREMENTS

Since ice particles have a variety of shapes under the atmospheric conditions, frozen droplets should eventually change their shape from spherical to aspherical. The chamber is equipped with optical and electrical devices for sensing the ice cloud formation and measuring size distributions, shapes and asphericity of cloud particles

4.1 CAS-PbP

The chamber CAS (DMT) measures both forward (4 – 12°) and backward (168–176°) scattering caused by individual particles that pass through a focused beam from a diode laser and has a Particle by Particle (PbP) function to record the data. Particles can be measured by drawing air from the chamber volume to the CAS at a known flow rate. The minimum detectable concentration is about 0.4 particles/cc, and the size range was adjusted to 0.35 to 30 µm.

4.2 CPI

Cloud particles from the experimental volume are measured at the base of the chamber by using CPI probe (SPEC), which measures two-dimensional digital images of particles larger than 10 µm up to 2 mm in size (Lawson et al. 2001). Individual particle images are identified, sized, categorized, cropped and stored in real time, so that we could yield detailed information on early ice formation; shapes (particle type) and size distributions and concentrations of ice and cloud droplets (> 0.1 particles/cc).

4.3 laser system

Laser radiation (532 nm) is scattered by particles in the centre of the chamber, and depolarization ratios with respect to scattering angles of 176° and 4° are measured by a couple of two independent photomultipliers. We expect that ice particles coexist with supercooled drops was detectable in the chamber by measuring the depolarization ratio of back-scattered laser radiation from the laser system data.

5. RESULTS AND DISCUSSION

An example of chamber experiments to simulate mixed-phase cloud formation is depicted in Figure 2. The initial values of pressure, air temperature and dewpoint temperature were set to 1000 hPa, 15°C and -5°C, respectively. The adiabatic ascent (expansion) was conducted and temperature went down to -40°C (2nd panel). 13 min. after the commencement of expansion, temperature reached -9°C and the chamber air became approximately water-saturated (3rd panel). The results of measurements imply that some of larger aerosol particles commenced to be activated (4th panel), and grew up to cloud droplets (>10µm) before ice crystals were detected by CPI (5th and 6th panels). Below -30°C, ice crystals more than 3 particles/cc were observed and ice formation became very active around -35°C. Figure 3 shows an initial PSD measured by the SMPS and the CAS in this case.

We have carried out more than 10 sensitivity experiments. The initial number concentrations of particles measured by the CAS were roughly a few tens particles/cc in general, even though the initial PSD varied from case to case, depending on weather condition. The maximum concentrations of cloud droplets (10～2000/cc) throughout each expansion tended to increase with increasing ascent rate from 3 to 10m/s and increasing temperature at the LCL from -23 to -5°C. In evaluating the occurrence of ice formation, the CPI sometimes misses tiny ice crystals (D <10μm), and has time lag to detect the onset of ice initiation. Likewise note that, under sparse cloud conditions, microphysical measurements are eliminated due to the sensor's susceptibility to noise. Nevertheless, the temperature zones where ice initiation was frequently observed during the experiments were above -30°C (T1), around -33°C (T2) and below -38°C (T3). Zone T1 ranged from -23 to -29°C, depending on the temperature at the LCL or the initial dewpoint temperature, suggesting that the ice nucleation processes are associated with the presence and evolution of the cloud droplets. Zone T2 appears rather often and occasionally along with T1. Below -30 °C, relatively large cloud droplets (>20μm) are still alive, but turning toward decline in a short time (e.g., Fig.2). The low concentration of large cloud droplets were quickly replaced with high concentrations of ice crystals. For Zone T3, ice crystals were probably produced through homogeneous freezing of tiny droplets.

The peak number concentrations of ice crystals in the mixed-phase region had positive correlation with maximum cloud droplets concentrations, which are affected by ascent rate and the condensation rate of water vapor onto the

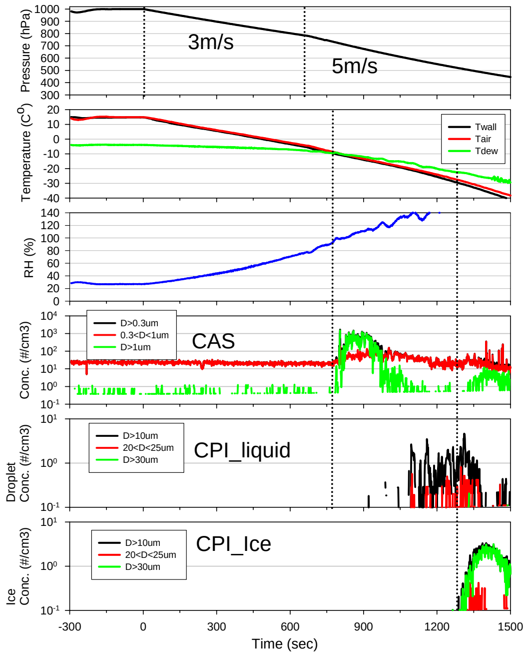

Fig. 2. Ascent profiles (Time versus Pressure, Temperature and Relative Humidity) and the chamber CAS and CPI measurements during an experiment

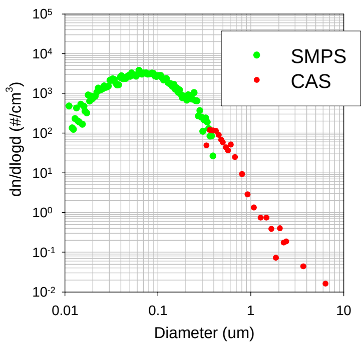

Fig. 3. PSD measured during pre-expansion.

chamber wall. In the cases of low cloud droplet concentrations and/or lower temperatures at the LCL, the peak of ice crystal concentrations in the Zone T1 tends to be ambiguously or be a part of multi-peak distributions with higher ice crystal concentrations.

The ratios of forward and backward scattering intensities measured by CAS-PbP are shown for different temperature ranges (Figure 4). For the mixed-phase and completely glaciated stages, the plotted data corresponding to the regions shown by the rectangles in

Figure 5 are not sufficient. From comparison with the results of theoretical calculation using Finite-difference time domain (FDTD) method (Ishimoto 2006) shown in Fig.5, it can be hard to definitely distinguish between the cloud droplets and the ice crystal in this case. To accumulate such data from many experiments will be necessary for developing a sub-10µm ice detection method using the chamber CAS-PbP.

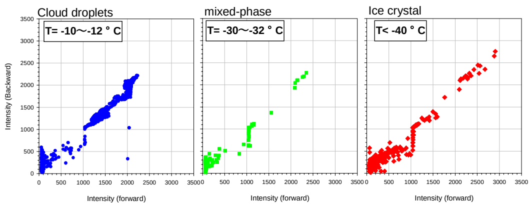

Fig. 4. Scattergrams of the CAS-PbP measurements during the 3 stages of cloud particles formation (see Figure 2).

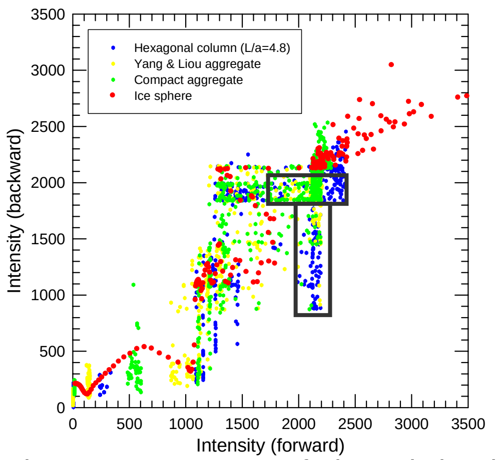

Fig. 5. Scattergram of the relationship between forward and backward light intensity (in arb. unit) scattered by individual particles is evaluated for CAS measurements by using the FDTD method.

The laser system was also operated during all the experiments and measured the forward- and backward scattering intensities. When ice crystal concentrations were less than several particles/cc, due to weak signals in both normal and depolarized component, we could not always calculate the depolarization ratios. For the accurate detection of weak signals, the incident power will need to be sufficiently high to overcome the sensor's intrinsic noise, besides the background noise will be suppressed by improving the optics of system further.

6. SUMMARY

The critical conditions for ice nucleation of natural background aerosol inside boundary layer were investigated at temperatures between about -10°C and -40°C. The ice initiation was achieved in adiabatic expansion experiments simulating ascent rates between 3m/s and 10m/s and the mixed-phase clouds were observed. Specialized microphysical instruments were used to monitor and evaluate the ice initiation processes under realistic atmospheric conditions. According to a tendency of the experimental results, the optimum zone of ice crystal formation was delineated as a double-peak distribution pattern with the maximum ice crystal concentrations above -30°C and around 33°C. It has been suggested these ice nucleation events were caused by different mechanisms. The formation and sedimentation of cloud droplets affect the water vapor budget and subsequent saturation ratio inside the chamber. An adequate method to estimate the supersaturations with respect to ice is required for detailed investigation of ice initiation processes. The microphysical instruments need to be well-calibrated in order to improve the accuracy of water condensate measurements. The optical sensors will need to obtain more precise techniques of particle detection that lead to better understanding of the aerosol effects on cloud microphysics.

REFERENCES

DeMott, P.J., and D. C. Rogers, 1990: Freezing nucleaaggregates by using finite-difference time domain (FDTD) method. *J. Remote. Sensing. Soc. Jpn., 26, 283-295.*

Lawson R. P., B. A. Schmitt, and T. L. Jensen, 2001: An overview of microphysical properties of Arctic cloud observed in May and July 1988 during FIRE ACE. *J. Geophys. Res.*, 106, D14, 14989-15014.

Tajiri T., M. Murakami, N. Orikasa, A. Saito, and K. Kusunoki, 2006: Laboratory experiments of ice formation in cloud simulation chamber. *Proceedings of the 12th Conference on Cloud Physics of the American Meteorological Society*, 10-14 July, 2006, Madison WI. P2.53.

CAUSES OF THE BOSCASTLE EXTREME RAINFALL EVENT IN AUGUST 2004

Brian Golding
Met Office, Exeter, UK

On the afternoon of 16th August 2004 the village of Boscastle on the north coast of Cornwall was severely damaged by flooding. Many people were helped to safety by emergency services but remarkably, there was no loss of life. The rainfall event that caused the flood was well observed by two radars (Cobbacombe to the NE and Predannack to the SW) in the UK network, each being at about 100km range, and by several rain-gauges including a tipping bucket rain gauge (see fig. 1). They show an elongated strip of high rainfall accumulations covering an area of about 100km^2. After correction to match the daily check gauge, the Lesnewth Tipping Bucket raingauge, marked with a daily total of 184.9mm, recorded maximum short period accumulations of 82mm in 1 hour, 148mm in 3 hours, and 183mm in 5 hours. At about 1535 UTC, this gauge recorded an uncorrected peak rate of nearly 300mm.hr^{-1}, implying a true maximum rain rate approaching 400mm/hr.

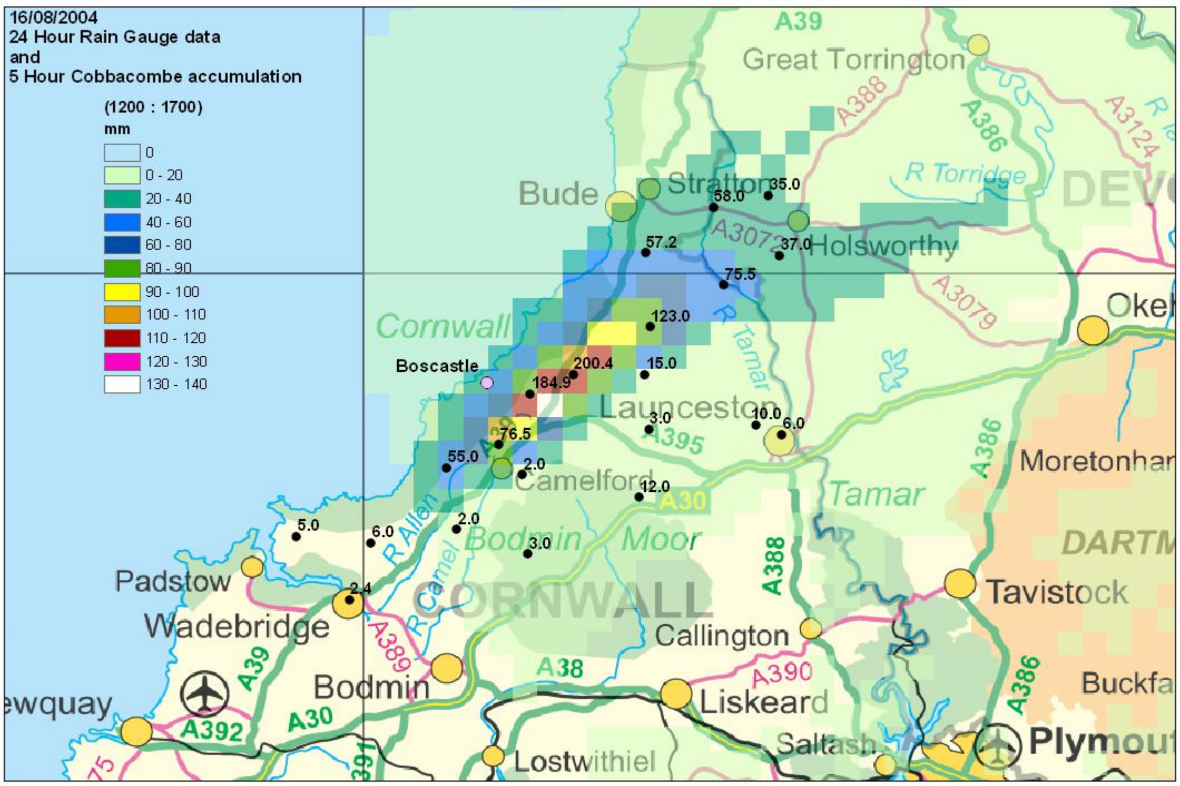

Figure 1 Distribution of accumulated rainfall on 16th August 2004: 5-hour totals (1200-1700 UTC) from 2km corrected Cobbacombe radar data (colours) and 24-hour (0900-0900 UTC) rain gauge totals (spot values)

On 16th August 2004, south-west England was under the left exit region of a jet stream maximum on the south east flank of an upper vortex covering the eastern North Atlantic. The low level flow (figure 2) was dominated by a complex, slow-moving low-pressure area to the west of the UK, with a moist south-westerly gradient over Cornwall. This area had been the graveyard of successive pulses of tropical air, each leaving residual potential vorticity pulses, maintained in the unstable baroclinic environment.

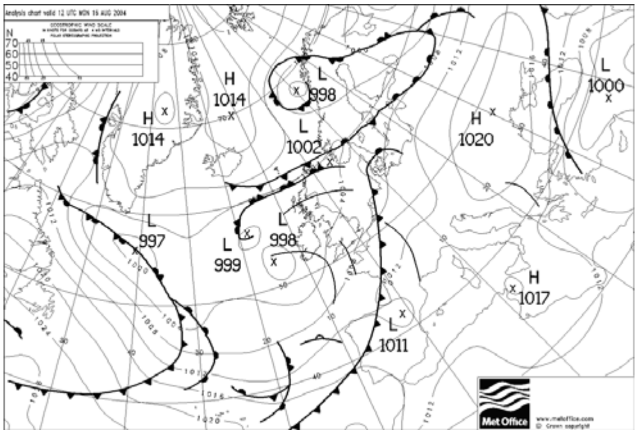

Figure 2 Surface Analysis Chart for 1200 UTC 16th August 2004

Figure 3 shows the radiosonde sounding from Camborne at 1200 UTC. The atmosphere was primed for storm development, with very moist lower layers and no convective inhibition. Above a cloud base at 900m, strong instability would produce a rapidly growing cloud up to an equilibrium level at 450hPa (6.5km), with highest cloud tops at the tropopause at 250hPa (9.7km). Convective Available Potential Energy (CAPE) was about 170 J kg^{-1}, a modest value, indicating maximum updraught velocities in the range 5-10 ms^{-1}. There was 26mm of precipitable water which would yield a 100 mm hr^{-1} rain rate if released over 15 minutes. Observed maximum hourly accumulations of up to 60 mm indicate very high efficiency maintained through multiple cloud lifecycles. The high tropospheric relative humidity (80% or more below 700 hPa) contributed to this high efficiency. The near-surface wind was south-south-westerly, veering to south-westerly 7.5 m s^{-1} at the top of the boundary layer with weak, uni-directional shear from there up to cloud top – the wind speed increasing to 17.5 m s^{-1} at 400hPa. The wind at the middle of the storm layer was southwest 12.5 $m.s^{-1}$ consistent with the observed movement of the storms.

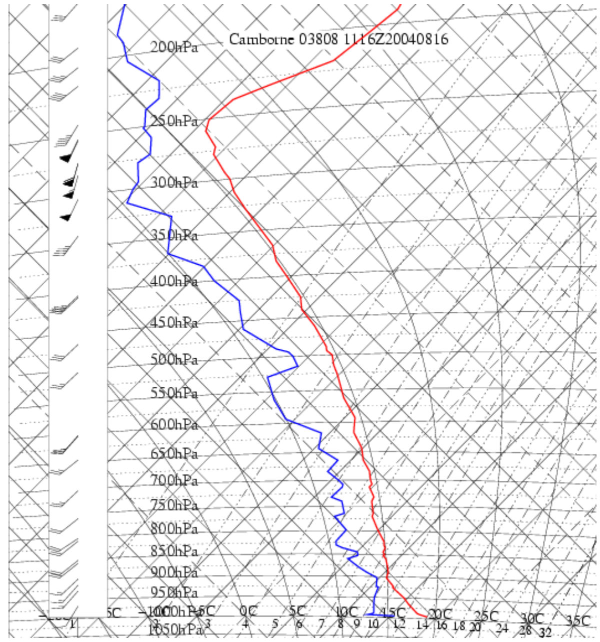

Figure 3 Tephigram showing 1200 UTC radiosonde from Camborne.

Upper level potential vorticity maxima resulting from the complex structure of the upper vortex, can be traced (Roberts, 2000) in the dark, dry bands of the Meteosat-8 upper tropospheric water vapour image (fig. 4) and were associated with the surface troughs identified in figure 2. The first of these is probably associated with 1hPa pressure falls observed in Cornwall during the day, and may have contributed to the storm intensity both by removing convective inhibition and by maintaining high mid-tropospheric humidities.

In order to investigate the mesoscale processes that led to extreme rainfall, the Met Office Unified Model (Davies et al., 2005) was run at high resolution (1 km nested in 4 km nested in the operational 12 km) in a form which allowed individual thunderstorms to form, albeit not well resolved. The model simulated intense precipitation, with maximum accumulations of about 50 mm, similar to radar observations averaged to 5km, the minimum scale realistically represented the model. The accuracy of the location was

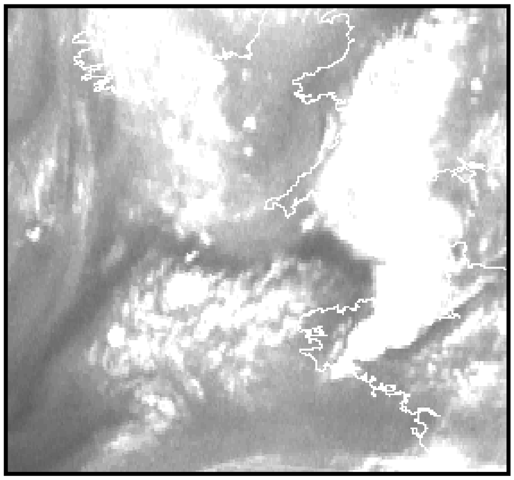

Figure 4 Meteosat-8 image in the upper tropospheric water vapour band at 1230 UTC 16th August 2004.

remarkable, suggesting strong topographic control. In order to clarify the origin of the convergence line, re-runs of the model were performed. The influence of removing variations in the land height was small: the rainfall pattern being smoother and shifted to the north west with the heaviest rainfall in the sea, consistent with the loss of drag from the hills allowing a strengthened offshore wind. Additionally removing the effect of land on the surface fluxes removes both the precipitation peak and the coastal convergence almost entirely. These results indicate that the convergence line was mainly thermally driven with the characteristics of a quasi-stationary sea breeze front.

The extreme rainfall accumulations observed in the Boscastle area resulted from prolonged heavy rain over the four hour period 1200-1600 UTC. The operational rainfall radar data showed that this was produced by a sequence of convective storms that developed along the north coast of Cornwall. Each storm element started as a non-precipitating cumulus. Rapid cloud development started as each cell encountered convergence near the north coast. Figure 5 shows the initiation and subsequent development of precipitating cells along this convergence line between 1100 and 1135 UTC in radar imagery. The mean speed of movement of each cell was close to 10 m s^{-1}, consistent with the mid-level wind, while downstream cell development resulted in an apparent propagation speed closer to 15 m s^{-1}. New cells also formed upstream near the original location, so that each initial shower spread out into a line of storm cells, spaced at intervals of about 5km, appearing as a continuous line on radar imagery. The line was also evident on satellite imagery. This phase of development produced rapid growth to mid-tropospheric depth with cloud tops (based on satellite imagery) in the vicinity of the equilibrium level at 450hPa (6.5km), implying a cloud top temperature of around -15^{o}C to -20^{o}C.

At a later stage, further north east, some individual cells developed further to reach

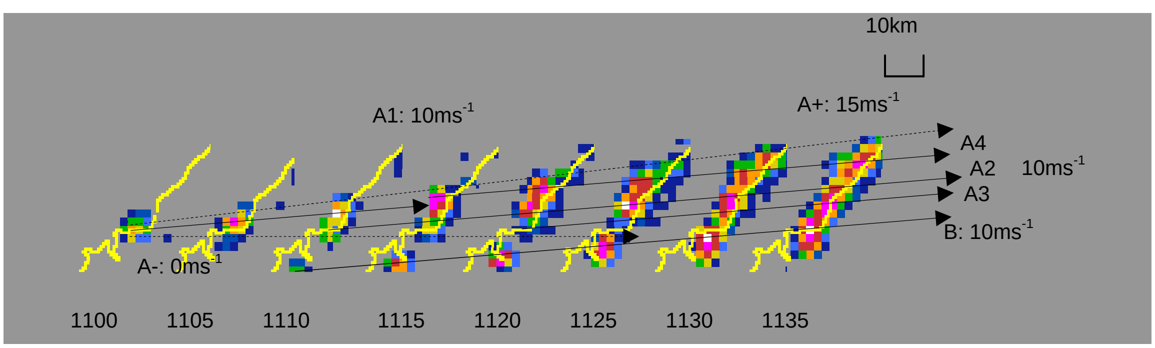

Figure 5 Initial evolution of the 1st & 2nd storm cells, 1100-1135 UTC 16th August 2004. Each time is shifted right by an additional 25km for clarity.

the tropopause at around 250hPa (9.7km) where the temperature was -54^{o}C. These clouds glaciated rapidly. The greater vigour of these storms was reflected in enhanced precipitation and a strong downdraught producing a gust front which caused the convergence line to bow in an eastward arc which then propagated eastward. Accumulations from the resulting squall line were modest due to the short duration of the rain.

With this synoptic and mesoscale context, the microphysical problem is to explain the rainfall intensity, given clouds of very modest depth (~6.5km) and very small horizontal dimension (~5km), with insignificant downdraughts. Satellite imagery confirms that there were no anvils at this stage. Lightning flashes recorded by the Met Office's Arrival Time Difference network indicate that electrical activity was minimal in this phase of storm development. Precipitation was extremely intense, by UK standards, with unusually high efficiency. While ice embryo seeding from prior storms to the south is a possibility, it seems likely that the precipitation was largely formed by in situ warm rain processes operating in remarkably clean maritime air. We postulate that with a substantially higher aerosol load, competition for water would have delayed rain-out, resulting in much reduced accumulations in the Boscastle area.

In summary, the Boscastle flood was generated by a sequence of very small, but very efficient storm cells propagating along a quasi-stationary sea breeze front, in an unstable tropical air mass, under the influence of upper level short waves in the left exit region of a strong Atlantic jet stream. Each of these components contributed to the result and only through integrated multi-scale modelling can the interactions be fully captured.

BIBLIOGRAPHY

Davies T, Cullen, MJP, Malcolm, AJ, Mawson MH, Staniforth A., White, AA, Wood, N. 2005. A new dynamical core for the Met Office's global and regional modelling of the atmosphere. *Quarterly Journal of the Royal Meteorological Soc*iety 608: 1759-1782

Golding, B.W. (Ed), 2005, Boscastle and north Cornwall post flood event study – meteorological analysis of the conditions leading to flooding on 16 August 2004. Forecasting Research Tech. Rep. No. 459, Met Office, UK available from http://www.metoffice.com/research/nwp/publications/papers/technical_reports/2005.html

Roberts, N.M., 2000, A guide to aspects of water vapour imagery interpretation: the significance of dry regions. Met Office NWP Tech Rep No. 294, copy available from National Meteorological Library, FitzRoy Road, Exeter EX1 3PB.

Acknowledgements

The assistance of many colleagues from the Met Office and the Environment Agency is gratefully acknowledged, in particular Malcolm Kitchen, Humphrey Lean, Nigel Roberts.

The work was commissioned by the Environment Agency.

SIMULATIONS OF A SEVERE HAIL STORM USING AN ADVANCED 2-MOMENT CLOUD-MICROPHYSICAL SCHEME

Heike Noppel[†,*], Ulrich Blahak[†], Axel Seifert[‡], and Klaus D. Beheng[†]
† Institut für Meteorologie und Klimaforschung,Universität Karlsruhe/Forschungszentrum Karlsruhe
‡ Deutscher Wetterdienst, Offenbach

1 INTRODUCTION

Recent studies of cloud interactions with particulate air pollution, performed mostly on a conceptual level, suggest that pollution aerosols can invigorate convection into severe storms by slowing down the conversion of cloud drops into precipitation.

In pristine air rain formation is rather fast, invoking early downdrafts and preventing the lifting of much water to the supercooled levels, so that the cloud dies early with a moderate amount of rainfall According to the hypothesis that should be tested within the ANTISTORM project, a high concentration of aerosol acting as cloud condensation nuclei (CCN) slows down rain formation and increases the amount of supercooled water in the mature stage of the cloud. This leads to enhanced riming, the production of hail, high precipitation rates and strong downdrafts.

The objectives of the ANTISTORM project were to test this hypothesis, study the impact of aerosols on convective storms in Europe, and "develop models that should help to improve forecasting and even suggest strategies for mitigating storms before disaster strikes" (http://antistorm.isac.cnr.it/).

The numerical model we used for our studies is the COSMO model, the operational NWP of the German Weather Service and others, combined with the 2-moment bulk microphysical scheme by Seifert and Beheng (2006). Some parameters and process descriptions of the 2-moment scheme have been altered to better represent "hail" particles (Blahak, 2008).

[*] *Corresp. author address:* Heike Noppel, Inst. für Meteorologie und Klimaforschung, Universität / Forschungszentrum Karlsruhe, P.O.Box 3640, D-76021 Karlsruhe, Germany; e-mail: heike.noppel@imk.fzk.de.

In order to test the model and to investigate the impact of CCN, the case study described in the following section was chosen.

2 THE HAILSTORM OF JUNE, 28th 2006

The case that has been chosen by the ANTISTORM consortium is a strong hail storm that hit Villingen-Schwenningen (VS) on 28/06/2006, The small town of VS is situated in South-West Germany between two low mountain ridges, the Black Forest and the Swabian Alb. Due to the storm more than 100 people got injured and one man drowned. Additionally, many crops, cars and buildings were damaged, mainly by hailstones but also by flooding. Fig 1 gives an idea of the amount of hail and the size of the hailstones.

The synoptic situation was characterized by a strong vertical windshear, with northerly to easterly winds at the bottom and a strong wind from West to South-West at levels above 3000 m. According to radio soundings at Nancy and Stuttgart at 12 UTC (not shown), lifting condensation level was at about 800 m amsl and temperature at that level about 14 °C . Air temperature near the ground was about 19 °C with a high relative humidity (86 to 89 %).

Fig. 2 shows radar reflectivities measured at Albis in Switzerland. In the late afternoon several convective cells could be observed in the vicinity of the Black Forest and the adjacent Rhine Valley (not shown). At about 17 UTC one of the cells splits close to the crest of the Black Forest. The right cell moves almost perpendicular to the main wind in south-easterly direction. This right mover intensifies, developing radar reflectivities of more than 65 dBZ, reaches VS at about 17:30 UTC and passes it with the core of the cell situated slightly to the north of the town. At about 18:00 UTC the storm has

Fig. 1: *Some pictures giving an idea of the amount and size of hailstones on 28/06/2006 in Villingen-Schwenningen.*

passed VS and moves further East. After crossing the Swabian Alb it finally weakens about one hour later (not shown).

3 MODEL SETUP

Convection that is not triggered by large scale processes like a convergence zone or a front is difficult to predict because (a) it is quite sensitive to the environment, i.e. stratification, humidity and wind shear, and (b) it can be triggered by rather stochastic processes. Nevertheless, we tried to simulate this hailstorm in a realistic setup.

Full orography was used and the model initial state as well as the boundary values have been adopted from operational COSMO-DE forecasts starting at 12 UTC on 28/06/2006. Integration time was 13 hours and the model domain 291 x 291 x 64 gridpoints with a horizontal resolution of 1 km. The COSMO-DE forecasts provided by the German Weather Service had been performed with the microphysical standard one-moment scheme. The output used as boundary values was available every hour.

For the nested grid, cloud microphysics was paramterized by an extended version of the two-moment scheme by Seifert and Beheng (2006), as mentioned before. Besides the modifications concerning hail by Blahak (2008) a new scheme for cloud droplet nucleation based on look-up tables by Segal and Khain (2006) as well as a shape parameter depending on mean diameter for sedimentation and evaporation of rain drops (Seifert, 2008) have been implemented. The scheme was validated for different CCN conditions by comparison to a spectral bin model (Noppel et al., 2008; Seifert et al., 2006).

Four different CCN concentrations leading to

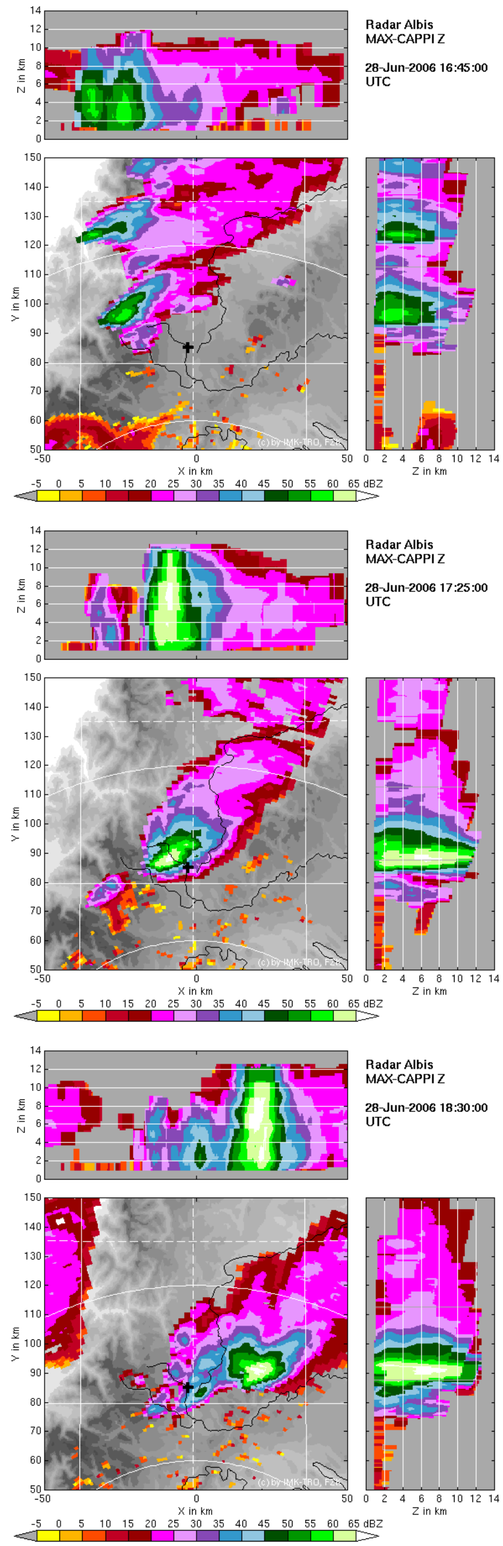

Fig. 2: *Maxcappis of radar reflectivity measured at Albis (near Zurich, Switzerland) on 28/06/2006 at different times. From top to bottom: 16:45, 17:25, 18:30 UTC. The black cross marks the location of Villingen-Schwenningen. Topography in grey shades.*

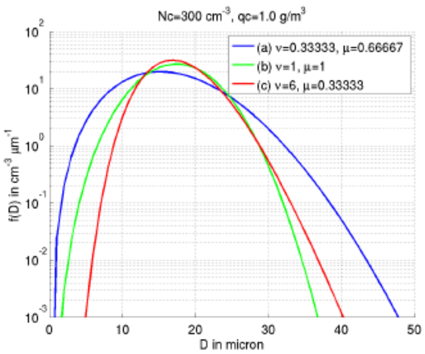

Fig. 3: *Cloud droplet size distributions assumed in the simulations for a bulk number density of 300 cm^{-1} and a mass density of 1 g cm^{-1}.*

different typical maximum cloud droplet concentrations N_{drop} were assumed:

1. low CCN, $N_{drop} =$ 100 cm^{-3}
2. intermediate CCN, N_{drop} =350 cm^{-3}
3. high CCN, $N_{drop} =$ 1200 cm^{-3}
4. very high CCN, $N_{drop} =$ 2100 cm^{-3}

As CCN conditions may also change the size distribution of the nucleated droplets the parameters μ and ν of the assumed generalized gamma-distribution

$$f(x) = Ax^{\nu}\exp\left(\lambda x^{\mu}\right) \quad (1)$$

were also varied (x is particle mass). The two other parameters A and λ can be calculated from the predicted bulk mass and number densities (the 0th and 1st moment of the distribution). Three different cloud droplet size distributions (cdsd) were assumed: (a) ν=1/3, μ=2/3, (b) ν=1, μ=1, (c) ν=6, μ=1/3 (see Fig 3).

4 THE SIMULATED HAILSTORM

In all model runs, no convective cells at all develop in the vicinity of the Black Forest during the afternoon. Only at about 20 UTC first convective cells occur in the southern part of the upper Rhine Valley (West of the Black Forest), the Black Forest and the Swabian Alb. A first weak cell passes VS between 20:30 and 21:00 UTC. It moves with the main wind direction from South-West to North-East and dissipates when reaching the Swabian Alb. The more interesting development starts at about 21:30 UTC at the western edge of the central Black Forest (x=100 km and y=140km). Fig. 4 shows maxcappis of radar reflectivity calculated from model results for the run with intermediate CCN concentration and a rather wide cdsd (cdsd (b), blue curve in Fig. 3). The simulated rightmover occurs several hours late but its development is similar to the observed hail storm, the simulated amount of accumulated precipitation as well in total (up to 55 mm) as for hail only (up to 13 mm) seems to be quite realistic (Fig. 6) and the model produces a significant number of large hailstones (Tab. 2).

5 CCN IMPACT

Fig. 5 to Fig. 9 show accumulated precipitation for different model runs. The tracks of several cells including the rightmover are clearly visible. When comparing the results for the different CCN scenarios it becomes evident that CCN concentration as well as the assumed cdsd do have a significant impact on the intensity, lifetime, and dynamics of a convective storm. For example, for scenario 4a (very high CCN concentration, Fig. 8) the hailstorm is much weaker and passes VS about 15 km further to the North than for scenario 1a (low CCN concentration, Fig. 5). A comparison of Fig. 6 and 9 shows that a variation in cdsd may lead to a significant weakening of one hailstorm and at the same time to an invigoration of another one.

As can bee seen from Tab. 1, higher CCN concentration and narrower cdsd both lead to a lower amount of hail at the ground. Higher CCN concentration also results in lower maximum number concentrations of large hail stones (Tab. 2). Pristine air and a narrow csds with a low number of large droplets but many small droplets produces the most large hailstones.

6 SUMMARY AND CONCLUSIONS

The case study of a hailstorm in South-West Germany showed that the model system COSMO

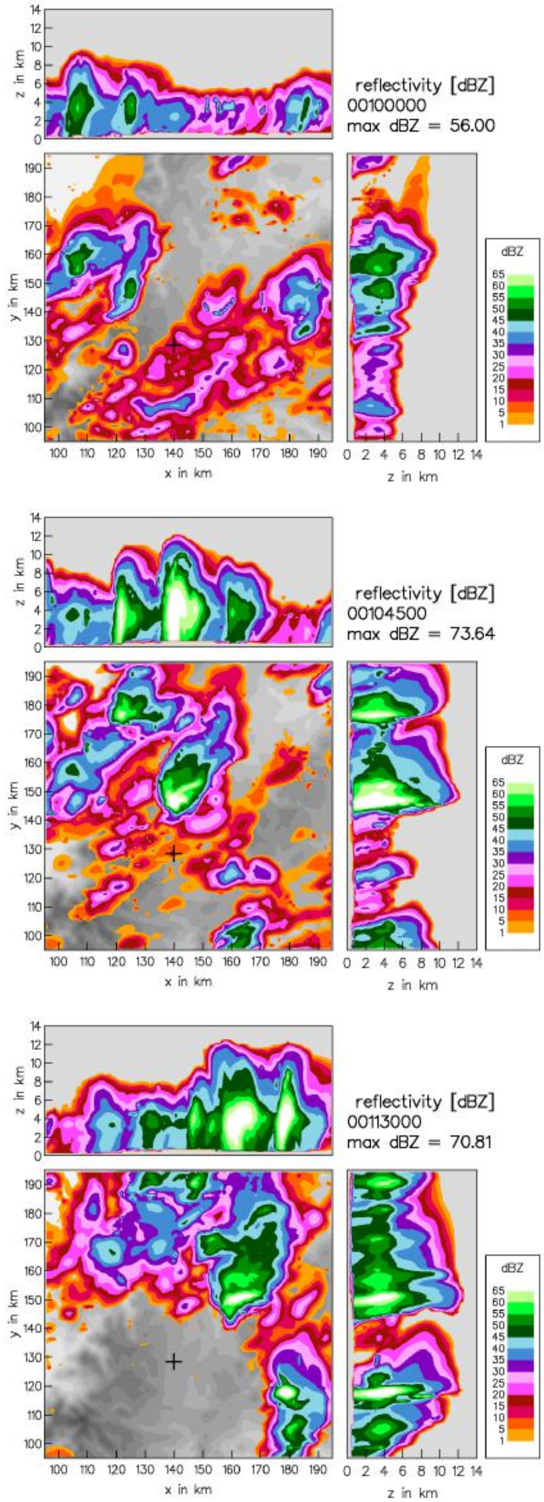

Fig. 4: *Maxcappis of radar reflectivity calculated from model results (CCN scenario 2(a)) for different simulation times. From top to bottom: 22:00 , 22:45, 23:30 UTC. The cutout shows the same domain as Fig. 2 with the black cross marking the location of VS. Topography in grey shades.*

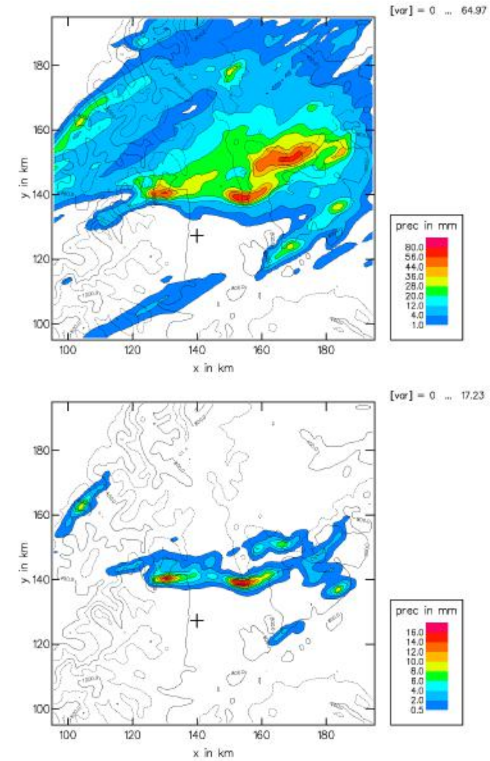

Fig. 5: *Precipitation accumulated after 12 h simulation time for low CCN concentration and a wide cdsd (CCN scenario 1a). Top: total, bottom: by hail.*

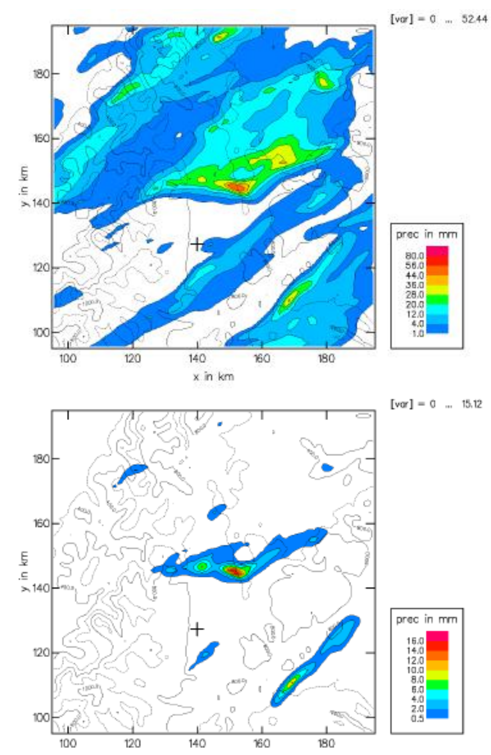

Fig. 6: *Same as Fig. 5 but for intermediate CCN concentration (CCN scenario 2a).*

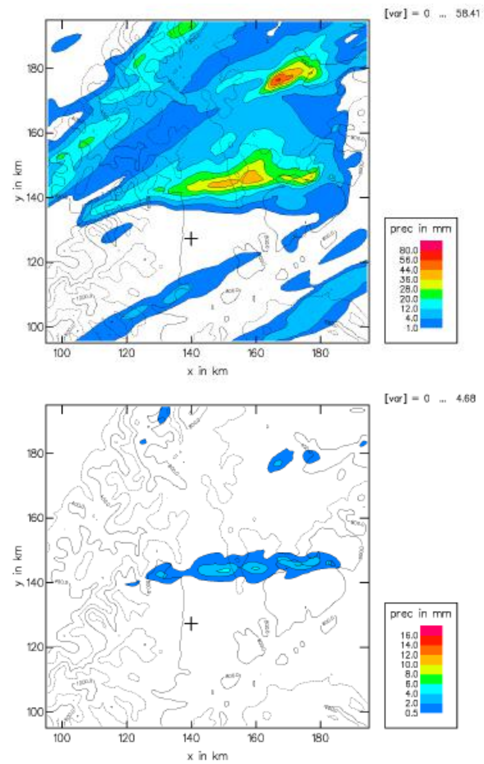

Fig. 7: *Same as Fig. 5 but for high CCN concentration (CCN scenario 3a).*

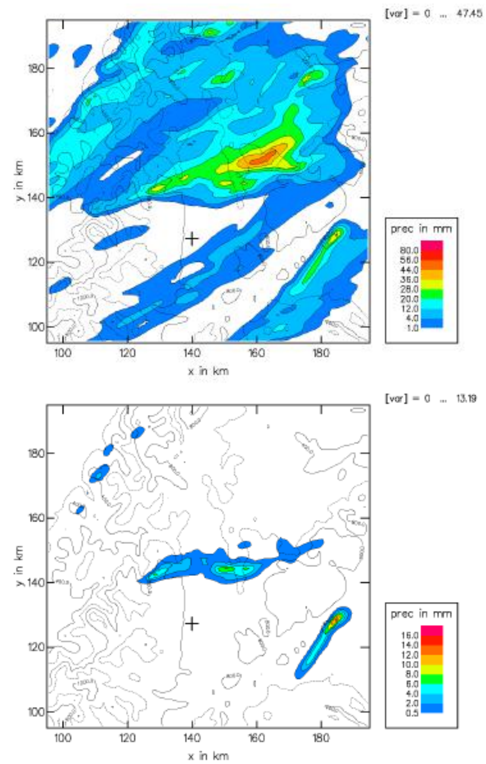

Fig. 9: *Same as Fig. 5 but for cloud droplet size distribution (b) (CCN scenario 2b).*

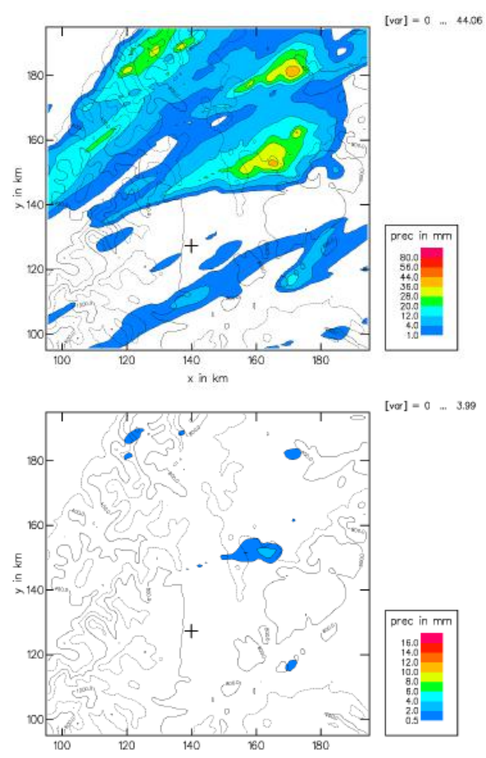

Fig. 8: *Same as Fig. 5 but for very high CCN concentration (CCN scenario 4a).*

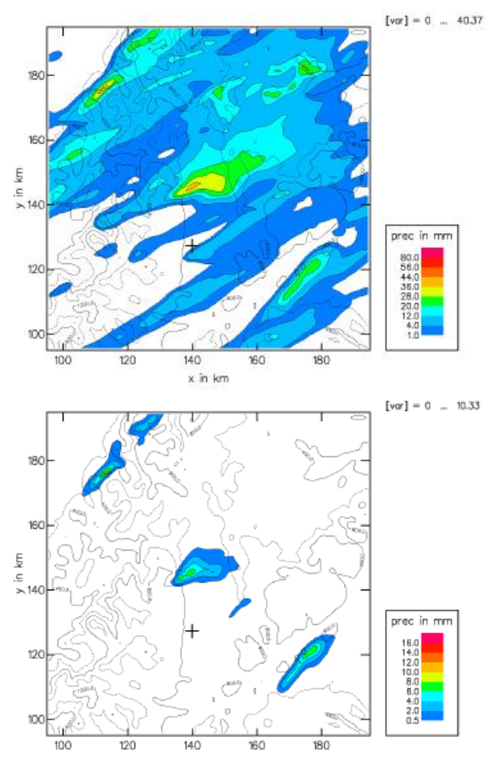

Fig. 10: *Same as Fig. 5 but for cloud droplet size distribution (c) (CCN scenario 2c).*

Table 1: *Maximum accumulated precipitation in mm by hail only, after 12 h simulation time for different model runs.*

	cloud droplet size distribution		
CCN concentr.	a	b	c
low	17.2	12.3	11.4
intermediate	15.2	8.8	8.1
high	4.7	3.8	3.1
very high	4.0	3.3	2.8

Table 2: *Maximum number concentrations of hailstones with $D > 25\,mm$ at output levels $\leq$2 km amsl in 1/1000m^3, estimated from the assumed hailstone size distribution and the predicted moments for the different model runs.*

	cloud droplet size distribution		
CCN concentr.	a	b	c
low	8.5	11.4	5.3
intermediate	5.8	6.5	2.1
high	2.3	0.0	1.8
very high	0.0	0.0	0.0

with the 2-moment scheme for microphysics using a horizontal resolution of 1 km and driven by COSMO-DE output is able to simulate a storm (although appearing some hours late) whose location, development and intensity are very similar to the observed storm. The simulated accumulated precipitation, as well in total as by hail only, are very realistic.

The potential impact of CCN characteristics were studied by varying CCN concentration and independently the shape of the cdsd. The results show that both may have a significant impact on the temporal and spatial development of the storm and as a consequence on the amount and kind (rain or hail) of precipitation. This suggest that the intensity of a hailstorm may be modified by changing CCN characteristics either inadvertently (e.g., by industrial emissions) or intentionally by cloud seeding.

The results also indicate that the correct prediction of the location and intensity of a hailstorm with up to date NWP models using one-moment microphysical schemes is almost a matter of luck and that taking into account CCN properties and using more sophisticated schemes for cloud microphyics would be beneficial.

One shortcoming of the 2-moment scheme is that two parameters of the csds have to be prescribed and, as have been shown, the choice of these parameters may have a significant impact on the results. Unfortunately, the true csds is not known and even with bin microphysics the width of the cdsd depends on the applied parameterizations and on numerical effects, like artifical spectrum broadening.

References

Blahak, U. 2008: Towards a Better Representation of High Density Ice Particles in a State-of-the-Art Two-Moment Bulk Microphysical Scheme. *15th International Conference on Clouds and Precipitation, July 7-11, 2008, Cancun, Mexico*

Noppel, H., Khain, A., Pokrovsky, A., Blahak, U., Beheng, K., 2008: How well can a bulk scheme reproduce the microphysical processes within a convective storm?- Comparisons to a spectral bin model. *15th International Conference on Clouds and Precipitation, July 7-11, 2008, Cancun, Mexico*

Segal, Y. and Khain, A., 2006: Dependence of droplet cocnentration on aerosol condtions in different cloud types: Application to droplet concentration parameterization of aerosol conditions. *J. Geophys. Res.*, **111**, D15240, doi:10.1029/2005JD006561

Seifert, A., 2008: On the paremeterization of evaporation of raindrops as simulated by a one-dimeansional rainshaft model. *J. Atmos. Sci.* (accepted).

Seifert, A. and Beheng, K.D., 2006: A two-moment cloud microphysics parameterization for mixed-phase clouds. Part 1: Model description. *Meteorol. Atmos. Phys.*, **92**, 45–66.

Seifert, A., Khain, A., Pokrovsky, A. and Beheng, K.D., 2006: A comparison of spectral bin and two-moment bulk mixed-phase cloud microphysics. *Atmos. Res.*, **80**, 46–66.

MICROPHYSICAL AND THERMODYNAMIC STRUCTURE AND EVOLUTION OF THE TRAILING STRATIFORM REGIONS OF MESOSCALE CONVECTIVE SYSTEMS DURING BAMEX

Robert M. Rauber[1], Andrea M. Smith[1], Greg M. McFarquhar[1], Joseph A. Grim[1], Michael S. Timlin[1], Brian F. Jewett[1] and David P. Jorgensen[2]

[1]Dept. of Atmospheric Sciences, University of Illinois, Urbana, IL
[2]National Severe Storms Laboratory, NOAA, Norman, OK

1. INTRODUCTION

The kinematic and precipitation structure of summertime midlatitude mesoscale convective systems (MCSs) has been documented in many radar studies (e.g., Smull and Houze 1985, Houze et al. 1990). These studies show that MCSs commonly consist of a *leading convective line*, approximately 10-50 km wide, followed by a more expansive *trailing stratiform region* (TSR), approximately 50-200 km wide. An *enhanced stratiform rain region* of intensified radar reflectivity, which is typically oriented parallel to the convective line, often appears within the TSR. A *transition zone* of mesoscale descent and light precipitation frequently exists between the rear of the convective line and the enhanced stratiform rain region. Two primary flow regimes are usually present within the TSR: a zone of ascending front-to-rear (storm-relative) flow at middle and upper levels, transporting hydrometeors from the convective line rearward to form the enhanced stratiform rain region, and a zone of rear-to-front flow that descends beneath the front to rear flow. This paper focuses on the microphysical structure of the clouds within the TSR and each of the subregions discussed above. The results were compiled from airborne Doppler radar observations, level II WSR-88D radar analyses and aircraft microphysical data from the NOAA P-3 aircraft flown during the Bow Echo and Mesoscale Convective Vortex Experiment (BAMEX) (Davis et al. 2004).

2. CONCEPTUAL FRAMEWORK

McFarquhar et al. (2007, hereafter MF07) provide a detailed description of spiral descent pattern sampling strategy within TSRs behind convective lines. With one exception on 29 June, the locations of microphysical observations were characterized with respect to three trailing stratiform features common to all MCSs examined here: the transition zone/notch region, the enhanced stratiform rain region, and the rear anvil region (Figs. 1 and 2). Data from each spiral descent and horizontal flight leg were classified according to the stage of MCS evolution during which the spiral occurred by tracking each MCS from its initiation to decay using regional composite WSR-88D animations. Twelve of the seventeen spiral descents and numerous horizontal flight legs performed during BAMEX occurred within a typical trailing stratiform MCS. Eleven of the spiral descents and all of the horizontal legs analyzed here were performed at times when a solid band of stratiform rain was readily apparent on plan view tail radar and WSR-88D scans. One spiral, performed on 29 June, was conducted before this time when convective cores were strengthening and beginning to bow. This spiral was conducted within a developing "notch" region of weaker reflectivity (Smull and Houze 1985), which usually intrudes into the back edge of the stratiform precipitation and is often associated with the maximum axis of rear inflow, indicative of dry air inflow or rear inflow descent. MF07 describe the algorithms used to process the data obtained from the in-situ probes to provide estimates of the total number (N_t), total mass content (TMC), observed hydrometeor size distributions, and the calculations of temperature (T), relative humidity with respect to ice (RH_i) and water (RH_w). The only difference from the analysis presented by MF07 is that a 10 s averaging time was used here instead of 60 s to process the microphysical data in order to determine how short time-scale fluctuations in RH and RIJ speed were correlated with fluctuations in the microphysical data. Details of the data processing will be forthcoming in Smith et al. 2008.

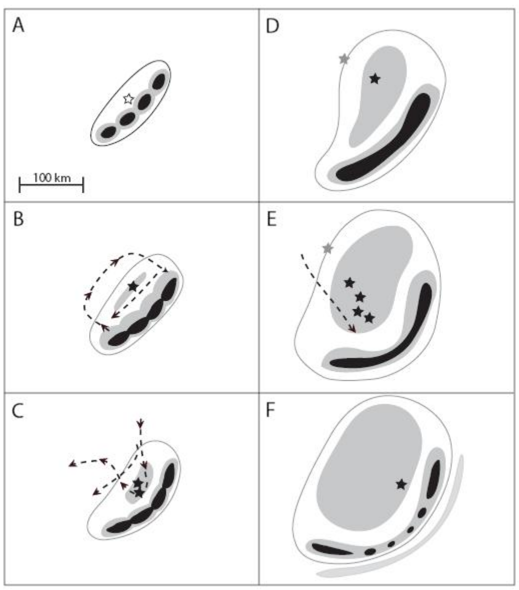

Figure 1: Conceptual radar evolution of a typical summertime midlatitude MCS. Dashed black paths represent the locations and timing of horizontal flight leg tracks while stars represent the locations and timing of microphysical spiral descent patterns flown during BAMEX MCSs. Black shading represents 50 dBZ and above, gray shading represents 35-50 dBZ and the gray outline represents the 0 dBZ echo boundary

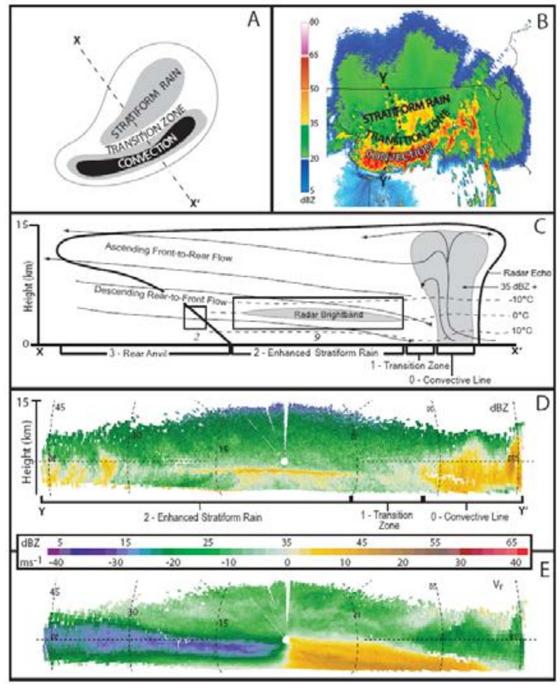

Figure 2: (a) Conceptual plan view of radar reflectivity of a mature, bowing MCS. Black shading represents 50 dBZ and above, gray shading represents 35-50 dBZ and the outline represents the 0 dBZ echo boundary. The dashed black line X-X′ represents the location of the conceptual cross section in panel C (b) Level II WSR-88D 0.5° reflectivity scan of a bowing, mature MCS (4 July 2003). The solid black line (Y-Y′) represents the position of the cross sections in panels D and E. (c) Conceptual cross section of a mature MCS. Squares represent areas in which microphysical spiral descent patterns were flown. Numbers at the bottom of each square denote how many spirals were flown in that region (d) NOAA P-3 tail radar scan of 4 July 2003 MCS radar reflectivity highlighting structural zones denoted in panel C. (e) Same as (d) but for radial velocity.

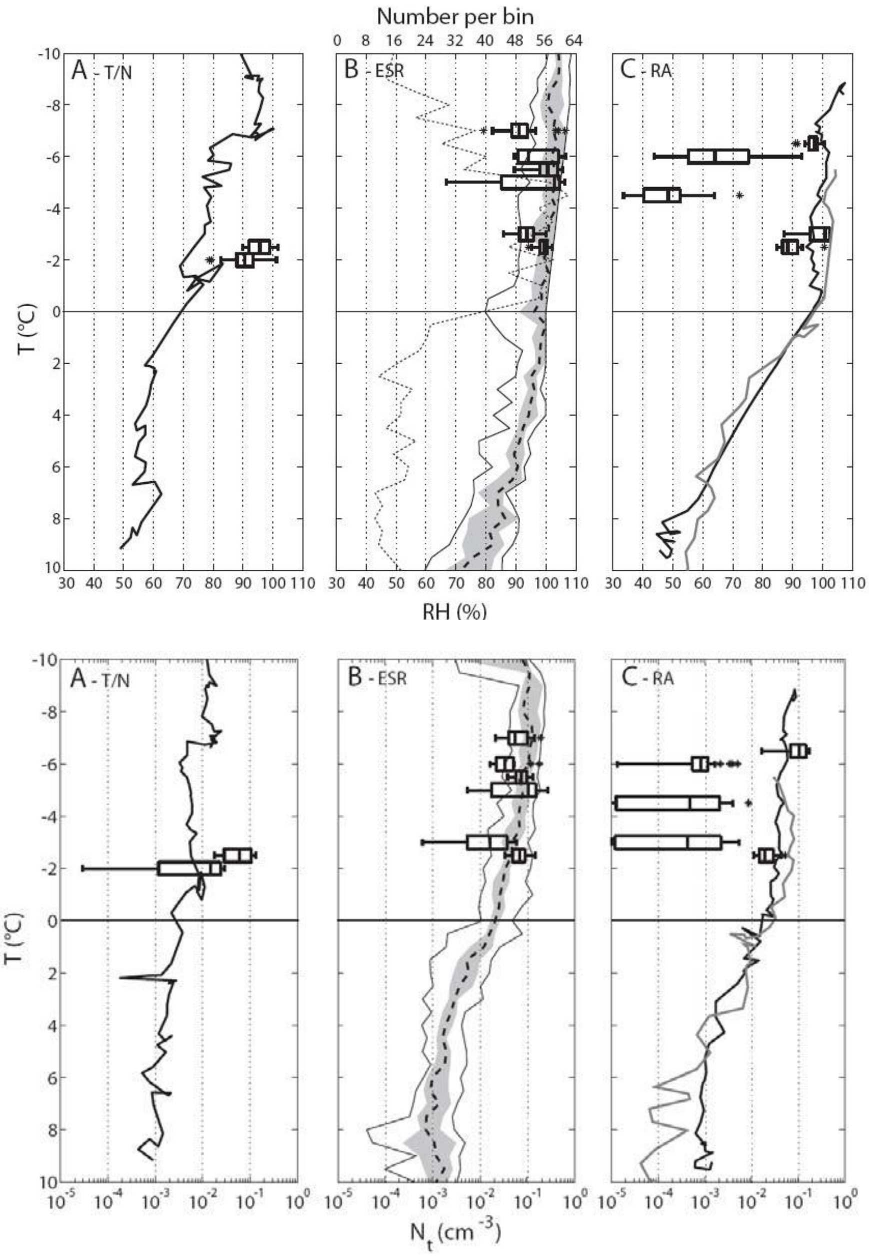

Figure 3: RH (top) and N_t (bottom) as a function of T for spiral descents and horizontal flight legs. For T < 0°C, RH_i is plotted, while RH_w is plotted for T> 0°C for all panels. A) RH (N_t) profile from spiral descent performed in the transition zone on 29 June 2003 (solid black line). Box and whisker plots show RH_i (N_t) for two horizontal legs in which the aircraft was in the transition zone. Solid black line inside of box is the median RH (N_t) value. The area of the boxes contains the 25th through 75th percentiles. Whiskers extend to 1.5 times the interquartile range. Asterisks represent outliers. B) Median (dashed black line), 25th through 75th percentiles (gray shaded regions) and maximum and minimum values (solid black lines) of RH (N_t) for the 9 spiral descents obtained in the enhanced stratiform rain region. Box and whisker plots show RH (N_t) values for horizontal flight legs in the enhanced stratiform rain region. Dotted black line is the number of measurements within each temperature bin. C) RH (N_t) profiles from two spiral descents (solid lines) and horizontal legs (box and whisker plots) obtained in the rear anvil region.

3. Storm Thermodynamic and Microphysical Structure

a. Thermodynamic profiles

As Fig. 1b shows, only one spiral descent was performed early in the lifetime of a MCS (29 June, first spiral). Two horizontal legs, flown on 2 June, sampled the transition zone in a more mature MCS, and are represented by the flight tracks in Fig. 1b. RH values for all sampling conducted within the transition zone are shown in Figure 3a. As noted by MF07, the 29 June vertical profile exhibited RH values well below 100% throughout the duration of the spiral descent. RH_i averaged 85% for T<0°C and RH_w averaged 57% for T>0°C. Such low values throughout the depth of the spiral descent were unique within the BAMEX dataset, and can be attributed to the aircraft's position within downdrafts in a developing and descending RIJ. The RH_i values for the 2 horizontal legs flown in the transition zone are represented by the box and whisker plots in Fig. 3a. The median RH_i of 90% and 96% are also below saturation, but approximately 8% higher than the mean RH_i value for T<0°C found on 29 June.

The RH_i and RH_w values for flight legs conducted within the enhanced stratiform rain region of TSRs of MCSs are summarized in Figure 3b. Here, RH data from 9 spiral descents performed on the following dates are used to derive the median and percentile values for 0.5°C intervals: 2 June (second spiral), 10 June (first and second spirals), 25 June, 2 July, 4 July (first and second spirals) and 6 July (second and third spirals). The average median RH_i for the spirals for T < 0°C was 102%, with a range of 106% to 96%. The median RH_i decreased downward at a rate of 0.33% $°C^{-1}$. The horizontal flight legs conducted in the enhanced stratiform rain region also exhibited RH_i values higher than those in the transition zone, with an average median of 97%. For T > 0°C, the average median RH_w value was 80%, and RH_w values decreased downward more sharply at a rate of 2% $°C^{-1}$. This dichotomy between saturated RH_i values above and subsaturated RH_w values below the melting level occurred in every spiral descent conducted within the enhanced stratiform rain region during BAMEX,. Grim et al. (2008) show that this sharp change in the RH profile develops in response to differential sublimation and evaporation rates due to the rapid increase in hydrometeor fallspeeds from 1 – 2 m s^{-1} for ice to 2 – 11 m s^{-1} for rain. RH values for the rear anvil region are shown in Figure 3c. The 21 June spiral and the first spiral descent on 6 July were conducted within the rear anvil region as the aircraft flew within and eventually underneath the storm rear anvil echo. Five horizontal legs were also conducted within the rear anvil region on 2 June and 10 June.

Consistent with trends observed in the enhanced stratiform rain region, the spiral descent on 21 June shows saturated conditions and on 6 July nearly saturated conditions for most altitudes above the freezing level. However, as the aircraft spiraled down in these cases, it came close to exiting the bottom of the rear anvil echo at T ~ -1 °C and RH_i values began a steady and rapid decrease. This contrasts with the RH_i profiles obtained in the enhanced stratiform rain region, as RH_i values there hovered near saturation until reaching the melting level, usually found near + 1.5°C. The average RH_w for T > 0°C for the rear anvil region spirals was 68%, about 13% lower than the value reported from the enhanced stratiform rain region. Median RH_i values in the rear anvil region decreased downward at a rate of about 0.72% $°C^{-1}$ for T < 0°C, and median RH_w values decreased downward at 4.7% $°C^{-}$

$^{-1}$ for T > 0°C. This rapid decrease in RH_w below the melting level is approximately 3 times greater than that reported for the enhanced stratiform rain region spirals, suggesting that drier environmental air was eroding the back edge of the system in the rear anvil region. Horizontal leg RH_i values varied from 48% to 101% in the rear anvil region, with an average median value of 80%. This wide variation occurred because the aircraft exited the rear anvil echo in some cases, but not others. The horizontal legs at T = -4.5°C and T = -6.0°C (median RH_i of 48% and 64%, respectively) were both conducted between about 20 km and 30 km ahead of the furthest rearward extent of the stratiform anvil echoes but in both instances the aircraft began to sample the echo-free area underneath the anvil. The horizontal legs at T = -2.5°C and T = -6.5°C (median RH_i of 98% and 89%, respectively) were also performed about 20 km ahead of the furthest rearward extent of the stratiform echo, but the aircraft stayed within the precipitation echo for the duration of these legs. In addition, the leg conducted at -2.5°C was in the presence of the remnants of another linear convective system approximately 20 km behind the aircraft, representing another source of moisture. The fifth horizontal leg performed in the rear anvil region had a median RH_i value of 101%, but was performed as the aircraft flew underneath of the anvil echo and exited the rear edge of the system completely. It is unclear how such high RH_i values were maintained in this situation.

b. Microphysical profiles

Vertical and horizontal profiles of N_t and λ were examined in the same manner as the RH profiles. Only the N_t values are presented here. See Smith et al. 2008 for other microphysical analyses. Figure 3a (bottom) shows the profile of N_t from the 29 June spiral, along with box and whisker diagrams for two horizontal legs conducted on 2 June within the transition zone. A linear least squares method was used to calculate the average rate at which $\log_{10}N_t$ varied within the layers T < 0°C and T > 0°C; fractional rates of decrease of N_t were then determined. The average value of N_t for T < 0°C on 29 June was 1.1 x 10^{-2} cm^{-3}, and decreased downward at a rate of 9.4% $°C^{-1}$ in this layer. For T > 0°C, N_t averaged 1.41 × 10^{-3} cm^{-3} and decreased downward at a rate of 9.6% $°C^{-1}$. The two horizontal legs had an average median N_t of 3.8 × 10^{-2} cm^{-3}. Due to the subsaturated conditions present in this zone above the 0°C level, MF07 determined that sublimation and aggregation were causing the decrease in N_t with T.

The N_t values for the enhanced stratiform rain region, shown in Fig. 3b (bottom), were significantly higher than those in the transition zone/notch region. The average median value of N_t from spirals in this zone for T < 0°C was 7.3 × 10^{-2} cm^{-3}, about seven times higher than that from the transition zone/notch region. The overall rate of decrease of N_t for T < 0°C was 25% $°C^{-1}$, nearly 3 times higher than the rate of decrease reported for the transition zone/notch region spiral. The horizontal legs obtained in the enhanced stratiform rain region had an average median N_t of 5.7 x 10^{-2} cm^{-3} and ranged from 1.1 x 10^{-3} to 1.53 x 10^{-2} cm^{-3}. The consistently near-saturated conditions above the melting level in the enhanced stratiform rain region indicate sublimation would not have occurred in this zone. Thus, to the extent that in-cloud heterogeneity did not complicate observed trends, the decreases in N_t found here can be attributed to aggregation (cf., MF07). For T > 0°C, the median N_t averaged 2.2 x 10^{-3} cm^{-3} and decreased at a slightly faster rate than N_t in the T < 0°C layer, at 35% $°C^{-1}$. The evaporation occurring in the drier environment below the melting level is likely the principal cause of this greater rate of decrease in N_t. In the rear anvil region (Fig. 3c, bottom), N_t values for T < 0°C averaged 5.1 x 10^{-2} cm^{-3} during the spiral descents and 2.5 x 10^{-2} cm^{-3} during the horizontal legs. The rate of decrease of N_t at 24% $°C^{-1}$ was comparable to that reported for T < 0°C in the enhanced stratiform rain region. For T > 0°C, N_t averaged 4.5 x 10^{-3} cm^{-3}, approximately twice that of the enhanced stratiform rain region spirals for T > 0°C. The rate of decrease of N_t for T > 0°C was 49% $°C^{-1}$, 13% higher than the enhanced stratiform rain region spirals, and likely a manifestation of increased evaporation in the drier air.

The vertical and horizontal thermodynamic and microphysical profiles provide insight about the structure and microphysical processes occurring in the three zones of MCSs. In general, the results can be summarized as follows: conditions in the transition zone/notch region were subsaturated, especially early in the life cycle as observed during the 29 June spiral. As an MCS matures, the developing stratiform environment is likely moistened from the top by sublimation of particles falling through initially dry air, similar to the moistening described by WH89. Ice saturation is eventually achieved above the melting level within the enhanced stratiform rain regions of well-developed MCSs. Once particles begin to melt, their fallspeeds increase, thereby decreasing observed number concentrations, as noted above. Evaporation rates from more rapidly falling hydrometeors were apparently insufficient to maintain saturation below the melting level. This hypothesis is tested and verified by Grim et al (2008) in a series of model simulations. The effect of more rapidly falling raindrops may be compounded by potentially drier air arriving within an established rear-to-front flow region. In the presentation, we will examine this possibility using thermodynamic and microphysical data analyzed with respect to the front-to-rear and rear-to-front flow regimes.

3. Summary

This study used airborne and ground based radar, and optical array probe data from the NOAA P-3 aircraft, to characterize microphysical and thermodynamic variations in evolving BAMEX MCSs. The findings of MF07 were extended by analyzing the data within the context of key MCS structural features and their evolution. This study represents the first time such analyses have been made across multiple regions of many midlatitude MCSs at varying stages of evolution. Microphysical and thermodynamic data from twelve spiral descents and five horizontal flight legs were categorized according to where they occurred in one of three radar-defined trailing stratiform precipitation zones: the transition zone or notch, the enhanced stratiform rain region and the rear anvil region. These data were also analyzed with respect to whether they were collected within front-to-rear or rear-to-front flow. The main findings of this work are as follows:

1. The 29 June spiral descent was performed before a continuous enhanced stratiform rain region appeared on radar, and exhibited subsaturated conditions both above and below the melting level. N_t values decreased slowly throughout the depth of the spiral and were roughly an order of magnitude lower for this spiral than those performed in other zones. λ remained nearly constant, suggesting that sublimation was occurring in conjunction with aggregation.

2. In all spiral descents performed within the enhanced stratiform rain region, conditions were saturated with respect to ice above the melting level and subsaturated below the melting level. N_t

and λ values decreased steadily from the top of the spirals to the melting level, suggesting that aggregation was the dominant growth mode of ice and that sublimation in this region was insignificant.

3. Spirals conducted within the rear anvil region showed saturation with respect to ice above the base of the anvil (approximately the -1°C level in the cases analyzed), while conditions along some horizontal legs in this zone showed significant subsaturation. Conditions below the melting level were 13% more subsaturated than those for the same layer in the enhanced stratiform rain region. N_t decreased more quickly here than in the enhanced stratiform rain region, suggesting that sublimation was occurring in addition to aggregation.

4. Relative humidity was strongly correlated to storm motion parallel winds (r = 0.79) in spirals performed within the enhanced stratiform rain region, especially to the magnitude of front-to-rear flow (r = 0.87). Relative humidity was less strongly correlated to the magnitude of the rear-to-front flow (r = 0.31), likely a manifestation of compounding factors of drier air below the melting level, downdrafts, and differences in the relative humidity of the surrounding environmental air being transported into the system by the rear inflow jet.

5. Within two single spiral descents in the enhanced trailing stratiform region, minima in storm motion parallel winds (front-to-rear flow) occurred at the same altitudes as maxima in T, T_d, N_t and λ while maxima of rear-to-front flow were observed at the same altitudes as minima of T, T_d, N_t and λ.

Taken together, these findings help to quantify the microphysical and thermodynamic structure of the TSRs of midlatitude MCSs. As the convection merges into a line and broadens, the front-to-rear flow carries hydrometeors rearward where they begin to fall and sublimate in initially dry surroundings. As more hydrometeors arrive, the post-convective environment is moistened from the top down by sublimation. The developing rear-inflow begins to erode the back edge of the system, leading to a notch-like return on radar (see 29 June). As more hydrometeors are carried rearward aloft, the stratiform region expands and saturates with respect to ice downward toward the melting level. Upon reaching the melting level, hydrometeor fallspeeds increase sharply, thereby reducing number concentrations and phase change rates. Thus, saturation is difficult to attain below the melting level. The rear-to-front flow transports potentially drier environmental air toward the convective line, accounting for the subsaturated conditions present above the melting level in the rear anvil region and enhancing sublimation and evaporation.

Acknowledgements. This material is based upon work supported by the National Science Foundation under Award No. NSF-ATM-0413824.

References

Davis et al. 2004: The bow echo and MCV experiment. Bull. Amer. Meteor. Soc., 85, 1075 – 1093.

Grim, J.A., G. M. McFarquhar, R. M. Rauber, A.M. Smith, and B. F. Jewett, 2008:Microphysical and Thermodynamic Structure and Evolution of the Trailing Stratiform Regions of BAMEX MCSs: Part II: Column Model Simulations. Mon. Wea. Rev., in review.

Houze, R.A., B.F. Smull, and P. Dodge, 1990: Mesoscale Organization of Springtime Rainstorms in Oklahoma. *Mon. Wea. Rev.*, **118**, 613–654.

McFarquhar, G. M., M. S. Timlin, R. M. Rauber, B. F. Jewett, J. A. Grim, D.P. Jorgensen, 2007: Observations of the vertical variability of cloud hydrometeors in stratiform regions during the Bow Echo and Mesoscale Convective Vortices Experiment (BAMEX). Mon. Wea. Rev., 135, 3405-1428.

Smith, A. M., G. M. McFarquhar, R. M. Rauber, J. A. Grim, M. S. Timlin, and B. F. Jewett, 2008: Microphysical and thermodynamic structure and evolution of the trailing stratiform regions of mesoscale convective systems during BAMEX. Part I: Observations. *Mon. Wea. Rev.,* (in review)

Smull, B.F., and R.A. Houze, 1985: A Midlatitude Squall Line with a Trailing Region of Stratiform Rain: Radar and Satellite Observations. *Mon. Wea. Rev.*, **113**, 117–133.

ANTHROPOGENIC AEROSOLS INVIGORATING HAIL

D. Rosenfeld and A. Khain

Institute of Earth Sciences, The Hebrew University of Jerusalem, Israel

1. PROJECT ANTISTORM

1.1 The ANTISTORM project summary

Here we report the main results of the ANTISTORM (Anthropogenic Aerosols Triggering and Invigorating Severe Storms) FP6 project that took place for the two years of 2006 and 2007.

According to the ANTISTORM conceptual model, illustrated in Fig. 1, a main cause for the lack of hail in pristine warm base clouds is the depletion of cloud water to rain before reaching the freezing level. The water that does ascend to the supercooled produce many ice precipitation embryos that compete on the remaining cloud water, and hence cannot grow to large hailstones. Suppressing the warm rain up to the supercooled levels requires large amounts of aerosols, which, according to the explicit microphysics model simulation, produce more than 1500 drops cm^{-3} at cloud base. Higher amounts of aerosols can suppress the warm rain to the extent of creating too few ice hydrometeors that would therefore produce less hail, unless significant recirculation of precipitation occurs. Recirculation should produce the largest hailstones, especially in the case of very high aerosol amounts that suppress much of the precipitation in the intense updrafts except when containing re-circulated precipitation particles. In such case all the cloud water would be available for the efficiently growing large hailstones. Therefore, the "optimum" amount of aerosols for warm base clouds should be very high, or even non-existent in certain dynamic circumstances that are prone to significant recirculation.

A shorter distance between cloud base and the freezing level exists in convective clouds with cooler bases, as was observed and simulated. Therefore smaller concentration of aerosols is required for suppressing the early warm rain that would prevent the formation of large hail. On the other hand, large concentrations of aerosols would more easily suppress the warm rain to the extent of scarcity in hail embryos.

Corresponding author's address: Daniel Rosenfeld, Institute of Earth Sciences, The Hebrew University of Jerusalem, Jerusalem 91904, Israel.
E-Mail: daniel.rosenfeld@huji.ac.il

Clouds with very cold base, near 0°C, already form as supercooled clouds with little room for rainout. In such clouds only quite pristine conditions would produce excess of precipitation embryos that would compete on the available cloud water and prevent the formation of hail. Already moderate concentrations of aerosols can suppress the formation of ice precipitation embryos to the extent that hail is substantially reduced.

1.2 The objectives of ANTISTORM project

1. Testing the hypothesis that added pollution aerosols can invigorate convective storms and induce them to produce more hail.
2. Testing the whether this phenomenon can occur within the European region.
3. Providing the basis for improving the numerical weather forecasting of severe convective storms in Europe by merging pollution aerosol prediction with convective storm prediction in a model that contain the physical processes by which these aerosols affect the convective storms.

Much of the effort in the project was concentrated on building 2 moment bulk microphysical model that would provide similar results as the bin microphysics, when run on the same dynamical framework. This objective was not fully achieved. Therefore we report here only on the bin microphysics component of the simulations, without necessarily claiming that it is more correct than the bulk simulations.

1.3 The ANTISTORM consortium

The project was a NEST FP6 consortium, composed of:

1. Daniel Rosenfeld and Alexander Khain, The Hebrew University of Jerusalem, Israel. This partner was responsible for the overall coordination of the project, and for simulations with the Hebrew University Cloud Model with explicit bin microphysics.
2. Meinrat O. Andreae and Jos Lelieveld, Max Planck Institute for Chemistry, Mainz, Germany. This partner was responsible for simulations and observations of CCN aerosols.
3. Klaus Beheng, University of Karlsruhe, Germany. This partner was responsible for simulations with bulk microphysics over domains that are two large for the HUCM simulations.

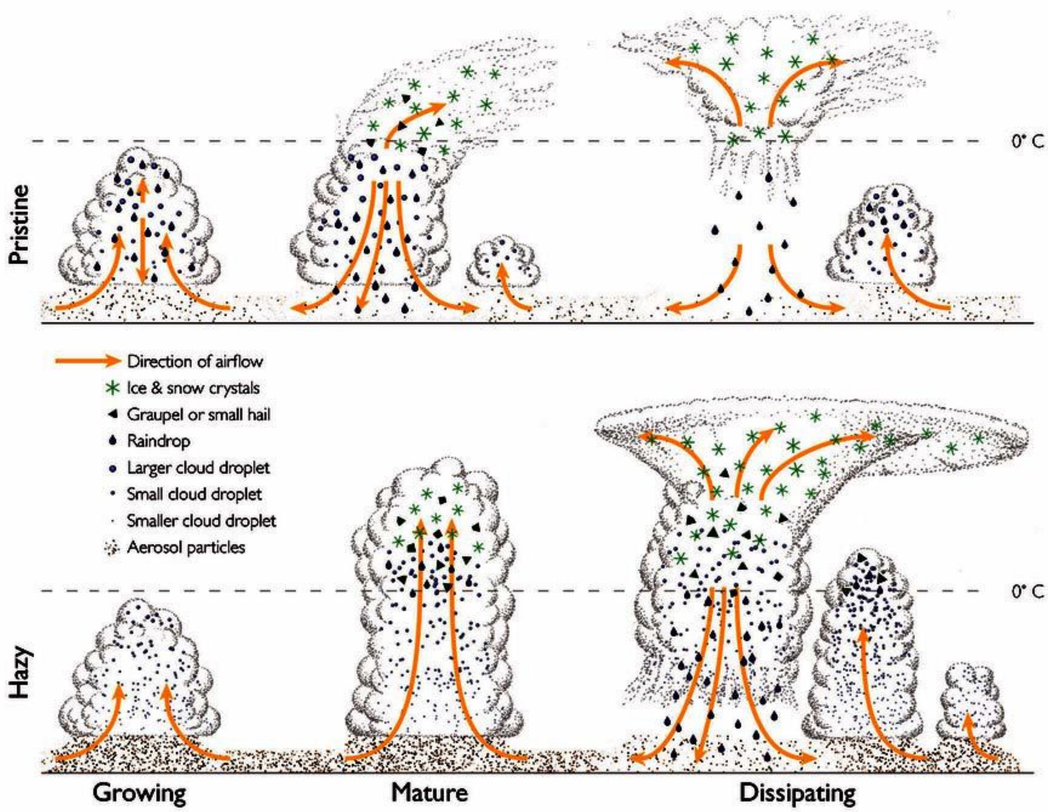

Figure 1: The conceptual model for pollution aerosols invigorating warm-base convective clouds. The early rain formation in the pristine case invokes early downdraft and prevents the lifting of much water to the supercooled levels, so that the cloud dies early with a moderate amount of rainfall. In the hazy case the rain is delayed, so that much supercooled water is accumulated in the mature stage that produces hail, strong precipitation and downdraft in the dissipating stage. The gust front can be sufficiently strong to trigger the next generation of convective clouds and so on, leading to the formation and propagation of a squall line (from Rosenfeld, 2006).

4. Vincenzo Levizzani, Institute of Atmospheric Science and Climate -- CNR, Bologna, Italy. This partner was responsible for satellite remote sensing of the cloud microstructure.

2. THE ANTISTORM CONCEPTUAL MODEL

Impact of manmade pollution aerosols have been widely recognized as affecting the climate system by suppressing drizzle from shallow marine clouds and so extending the cloud cover by preventing their dissipation by raining out, in a mechanism that was recognized only very recently (*Rosenfeld*, 2006). The impact of pollution aerosols on deep cloud has been less obvious, although as important. The suggested climate impact of the aerosols has been summarized by the coordinator of ANTISTORM into a white page paper, which also proposes a way forward. This white page paper was endorsed and announced as a joint IGBP (International Geosphere-Biosphere Programme) – WCRP (World Climate Research Programme) initiative (*Rosenfeld and Silva Dias*, 2008).

The ANTISTORM hypothesis is formulated there in the following language: "In deep convective clouds with warm bases, such as prevail in the tropics and during summer in the midlatitudes, the delayed precipitation due to more and smaller droplets may cause the condensates to ascend to the supercooled levels instead of raining out earlier by processes that do not involve the ice phase. By not raining early, the condensate would then form ice hydrometeors that release the latent heat of freezing aloft and reabsorbing heat at lower levels where they melt. The result would be more upward heat transport for the same amount of surface precipitation. The consumption of more static energy for the same precipitation amount would then be converted to equally greater amount of released kinetic energy that could invigorate the convection and lead to a greater convective overturning, more precipitation and deeper depletion of the static instability. Furthermore atmospheric moisture that is not rained out due to suppression of rainfall by aerosol, may eventually increase the rainfall elsewhere. The enhanced and delayed aerosol-induced release of latent heat may lead to regional scale enhancement and re-distribution of convection, low level moisture convergence and precipitation." The conceptual model is illustrated in Figure 1 (*Rosenfeld*, 2007), and further elaborated on in (*Rosenfeld*, 2006).

3. MODEL SIMULATIONS OF IMPACT OF AEROSOLS ON HAILSTORMS

3.1 <u>The model description</u>

We report here on the results of testing the ANTISTORM hypothesis with a spectral (bin) microphysics (SBM) model. The model is the two-dimensional Hebrew University cloud model (HUCM) with the SBM scheme implemented. The microphysical schemes in the models are described in (*Khain et al.*, 2004; *Khain et al.*, 2005). The model is based on solving a kinetic equations system for size distribution functions for water drops, ice crystals (plate-, columnar- and branch types), aggregates, graupel and hail/frozen drops, as well as atmospheric aerosol particles.

To test the ANTISTORM hypothesis and to simulate mixed-phase microphysics as realistic as possible at the present time, significant activities for model development and update have been carried out. These activities include both further modification of the SBM and other model developments. The modification of the SBM scheme includes:

- The number of mass bins used for the description of all size distribution functions has been increased from 33 to 43. As a result, the maximum diameter of hail stones that can be resolved by the model (as well as melted radii of other hydrometeors) was increased from 1 cm to 6.5 cm. The table of collision efficiencies and kernels has been recalculated accordingly.
- The breakup procedure has been updated (with help of Dr. Seifert) to include larger particles.
- A new approach developed by Dr. Ulrich Blahak for determination of the beginning of wet growth of graupel (which can be interpreted as the formation of hail by graupel riming) has been implemented;
-

A more detailed description of the model and additional improvements beyond the ending of the ANTISTORM project is given in the companion extended abstract (Khain et al., 2008).

3.1 <u>The simulations results</u>

Several important conclusions can be derived from the 2D simulations. The main conclusions can be summarized as follows.

1. Hail intensity, hail kinetic energy at the surface and precipitation are very sensitive to aerosol concentrations. The hail kinetic energy is negligible at low aerosol concentrations (lower than 200-300 cm^{-3}).
2. The dependence of hail kinetic energy and precipitation is non-monotonic. There exist aerosol concentrations under which hail kinetic energy and accumulated rain reach their maximum. These values depend on the environmental conditions. They are small (100-300 cm^{-3}) for very dry or clouds with very cold base temperatures, and very high (exceeding 1500-3000 cm^{-3}) for moist tropical conditions with warm cloud base.
3. The results reported earlier about increase in precipitation in maritime tropical conditions and decrease in precipitation in a very continental unstable conditions (*Khain et al.*, 2001; *Khain and Pokrovsky*, 2004; *Khain et al.*, 2004; *Khain et al.*, 2005) (where only two aerosol concentration were tested) agree well with the results.
4. Under intermediate conditions typical, say, of hail storms in Germany, the CCN concentrations under which hail kinetic energy and precipitation reaches their maximum is about 800 cm^{-3}.
5. It was suggested that one of the main parameters determining the response of hail energy (hail size), as well as precipitation amount is the temperature of cloud base.
6. A special set of simulations with idealized temperatures at cloud base, shown in Fig. 2, supported this hypothesis. Clouds with warm cloud base (20°C) correspond to maritime convective clouds, while clouds with very cold cloud base (0°C) correspond to extremely continental clouds developing in dry atmosphere. Hail storms in Germany develop under intermediate conditions (cloud base around 10°C).

Summarizing the results we can conclude that the results of simulation support the ANTISTORM hypothesis concerning the sensitivity of hail production to aerosol concentration. At the same time, the conditions of the hail formation were investigated in more detail, which allowed us to present a classification of conditions of large hail formation.

To our knowledge, for the first time non-monotonic dependence of hail production and precipitation on aerosol concentration was found. So, the question, whether aerosols increase or decrease hail and precipitation cannot be formulated without mentioning particular meteorological conditions of cloud development (one of the major parameters is the cloud base temperature).

It was found that hail increases precipitation efficiency of clouds with high aerosol concentration.

Note that the results obtained within the frame of the 2 years ANTISTORM project are preliminary to some extent. More 3D simulations are required. In 2D simulations the computational area should be increased to prevent the lost of ice hydrometeors through the boundaries during the computations.

More detailed comparison between the results of 2D and 3D simulations is required.

In course of the project it was found the necessity to improve ice representation in SBM models. It is necessary to implement budget of ice nuclei into the model. High sensitivity to breakup indicates that this process has to be simulated as accurately as possible.

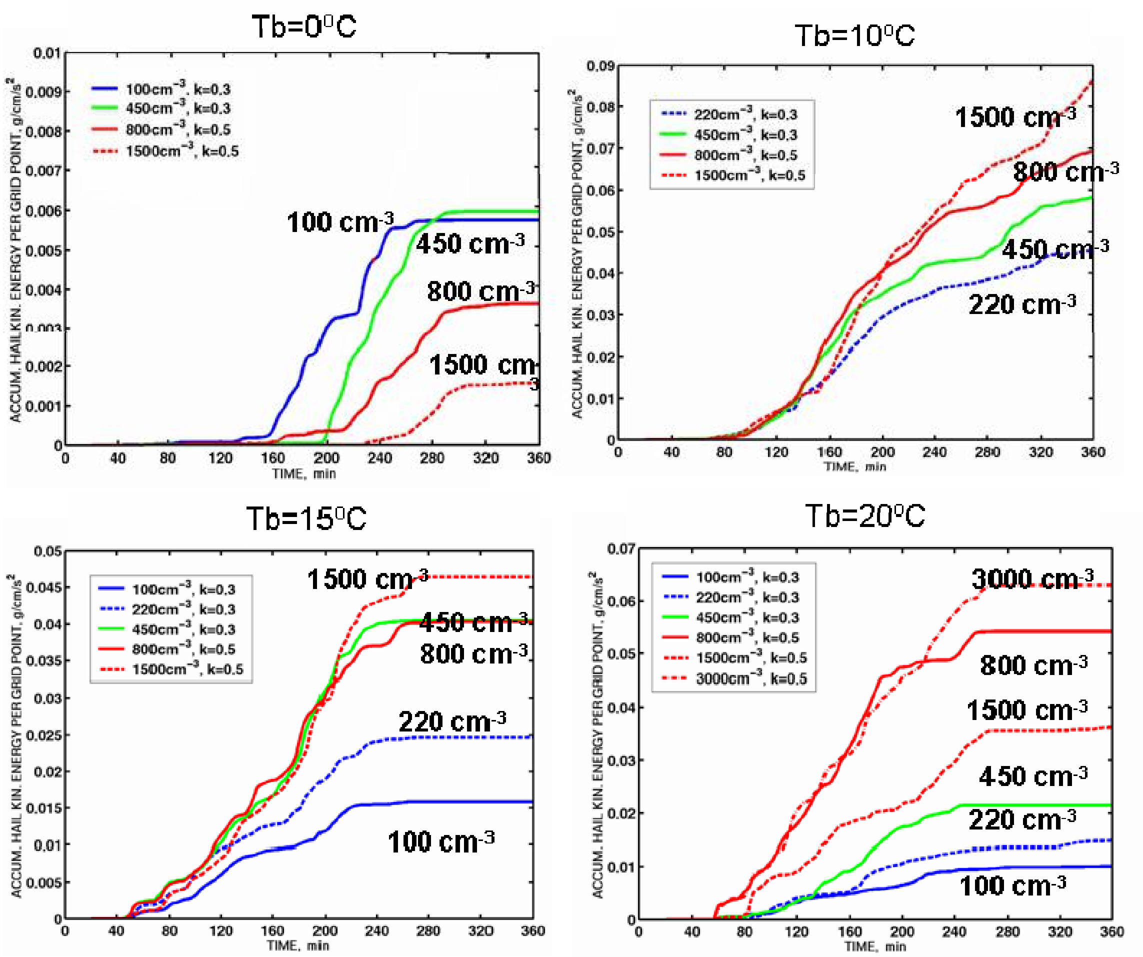

Figure 2: Time dependencies of accumulated hail kinetic energy at the surface in simulations with different cloud base temperatures and aerosol concentrations. The values are exaggerated because shedding of the melting hail is not yet included in these runs.

4. THE REFINED ANTISTORM HYPOTHESIS

According to the conceptual model illustrated in Fig. 1, a main cause for the lack of hail in pristine warm base clouds is the depletion of cloud water to rain before reaching the freezing level. The water that does ascend to the supercooled levels produce many ice precipitation embryos that compete on the remaining cloud water, and hence cannot grow to large hailstones. Suppressing the warm rain up to the supercooled levels requires large amounts of aerosols, which, according to Fig. 3, produce more than 1500 drops cm^{-3} at cloud base. Higher amounts of aerosols can suppress the warm rain to the extent of creating too few ice hydrometeors that would therefore produce less hail, unless significant recirculation of precipitation occurs. Recirculation should produce the largest hailstones, especially in the case of very high aerosol amounts that suppress much of the precipitation in the intense updrafts except when containing re-circulated precipitation particles. In such case all the cloud water would be available for the efficiently growing large hailstones. Therefore, the "optimum" amount of aerosols for warm base clouds should be very high, or even non-existent in certain dynamic circumstances that are prone to significant recirculation.

A shorter distance between cloud base and the freezing level exists in convective clouds with cooler bases, as was observed (see Fig. 3) and simulated. Therefore smaller concentration of aerosols is required for suppressing the early warm rain that would prevent the formation of large hail. On the other hand, large concentrations of aerosols would more easily suppress the warm rain to the extent of scarcity in hail embryos.

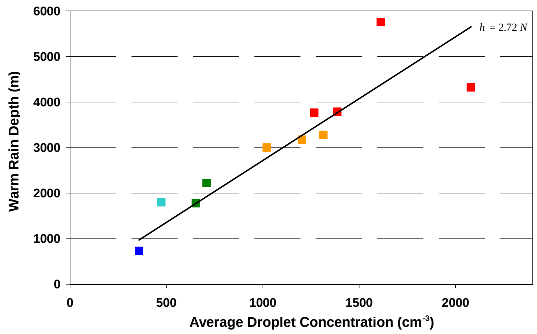

Fig. 3: Relation between cloud base drop concentration and the height for onset of warm rain in young growing convective clouds in the Amazon (*Freud et al.*, 2008). The drop concentration, in turn, depends on the CCN concentrations. Note the increased depth for warm rain with greater number concentration of drops at cloud base and hence of CCN concentration.

According to the refined conceptual model (Fig. 4), clouds with very cold base, near 0°C, already form as supercooled clouds with little room for rainout. In such clouds only quite pristine conditions would produce excess of precipitation embryos that would compete on the available cloud water and prevent the formation of hail. Already moderate concentrations of aerosols can suppress the formation of ice precipitation embryos to the extent that hail is substantially reduced.

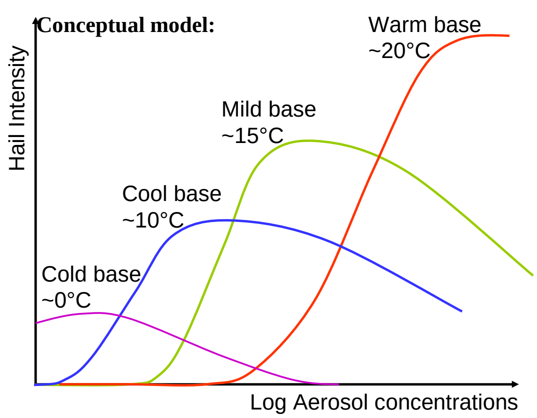

Figure 4: The refined ANTISTORM conceptual model. There is an "optimal" level of amount of aerosols for the most intense hail, which increases with warmer cloud bases. Beyond that optimum the amount of hail and storm intensity starts to decrease, but not to the low level of the pristine storms. The "optimal" storm intensity increases with warmer cloud base, which requires greater amounts of aerosols.

5. CONCLUDING REMARKS

To our knowledge, for the first time non-monotonic dependence of hail production and precipitation on aerosol concentration was recognized. So, the question, whether aerosols increase or decrease hail and precipitation cannot be formulated without mentioning particular meteorological conditions of cloud development (one of the major parameters is the cloud base temperature).

The simulations indicate that hail increases precipitation efficiency of clouds with high aerosol concentration. This feature could not yet unambiguously be captured in the bulk model. Besides different mechanism used in the bin and bulk model to create and grow hail also the different model geometries (2D vs. 3D) may be a source of the differing results (not reported here). Note that the results obtained within the frame of the 2 years ANTISTORM project are preliminary to some extent. More 3D simulations are required. In 2D simulations the computational area should be increased to prevent the lost of ice hydrometeors through the boundaries during the computations.

In course of the project it was found necessary to improve ice representation in SBM models. It is necessary to implement budget of ice nuclei into the model. High sensitivity to breakup indicates that this process has to be simulated as accurately as possible. After the ending of the project additional effort was invested in improvement of the model processes of hailstorms, which are reported in the companion extended abstract (Khain et al., 2008). At the point of conclusion of the project, reported here, we have reached the state where the simulation of hailstorms with a bin model allowed us to gain the insights that led to the refined ANTISTORM conceptual model, shown in Fig. 4.

ANTISTORM did produce a new insight to the way aerosols affect severe convective storms, and opened ways for implementing these insights to a better prediction of severe convective storms. These insights will help in the future also to reduce the risk of these storms if ways will be found to reduce the particulate air pollution during the warm and moist summer days. However, much work remains to foster the results and make them workable in operational forecasting environment.

6. ACKNOWLEDGEMENTS

Funding was provided by the European Commission NEST Insight project ‘‘Anthropogenic Aerosols Triggering and Invigorating Severe Storms’’ (ANTISTORM).

7. REFERENCES

Freud, E., Rosenfeld, D., Andreae, M. O., Costa, A. A., and Artaxo, P., Robust relations between CCN and the vertical evolution of cloud drop size distribution in deep convective clouds: Atmos. Chem. Phys., 8, 1661–1675, 2008.

Khain, A., and Pokrovsky, A., Effects of atmospheric aerosols on deep convective clouds as seen from simulations using a spectral microphysics mixed-phase cumulus cloud model Part 2: Sensitivity study: J. Atmos. Sci, 61, 2983-3001, 2004.

Khain, A., Pokrovsky, A., Pinsky, M., Seifert, A., and V, P., Simulation of effects of atmospheric aerosols on deep turbulent convective clouds using a spectral microphysics mixed-phase cumulus cloud model. Part I: Model description and possible applications: J. Atmos. Sci., 61, 2963-2982, 2004.

Khain, A., Rosenfeld, D., and Pokrovsky, A., Aerosol impact on the dynamics and microphysics of deep convective clouds: Q. J. R. Meterorol. Soc., 131, 2639-2663, 2005.

Khain, A. P., Rosenfeld, D., and Pokrovsky, A., Simulating convective clouds with sustained supercooled liquid water down to -37.5 ºC using a spectral microphysics model: Geophys. Res. Lett., 28, 3887-3890, 2001.

Khain, A. P., Rosenfeld, D., Pokrovsky, A., and Blahak, U., Is the dependence of warm and ice precipitation on the aerosol concentration monotonic? Extended Abstract for the 15th International Conference on Clouds and Precipitation, Cancun, Mexico, 7-11 July 2008.

Rosenfeld, D., Aerosol-cloud interactions control of earth radiation and latent heat release budgets: Space Science Reviews, 125, 149-157, doi:10.1007/s11214-006-9053-6, 2006.

Rosenfeld, D., New insights to cloud seeding for enhancing precipitation and for hail suppression: The Journal of Weather Modification, 39, 61-69, 2007.

Rosenfeld, D., and Silva Dias, M. A. F., Can the slowing of auto-conversion result in increasing precipitation?: iLEAPS Newsletter 5, 30-33, 2008.

NUMERICAL SIMULATIONS OF SEVERE TROPICAL AND CONTINENTAL STORM

V.Spiridonov[1], T.Sampan [2] and M.Curic[3]

[1] Hydrometeorological Service Skopje, Macedonia, [2]Thai Meteorological Department, Bangkok, Thailand and [3]Department of Meteorology, Faculty of Physics, Belgrade Serbia

1. INTRODUCTION

Convective clouds and storms represent one of the most important and challenging problems for forecasters. For this reason, considerable effort has been devoted to studying storm initiation and evolution, as well as the environmental factors governing overall storm structure. A number of three-dimensional cloud models have been developed to simulate the structure, intensity and movement of convective clouds (Cotton and Tripoli, 1978; Klemp and Wihelmson, 1978; Clark, 1979; Tao and Soong, 1986; Wang and Chang 1993; Skamarock et al., 2000; Xue, et. al., 2000; Tao, et. al., 2004; and many others).
Many previous studies using high resolution cloud-resolving models (or convective cloud models) have shown that case-specific simulations are able to represent the storm structure and structure, intensity and movement of convective clouds, radar reflectivity, wind speed and direction, outflow heights. The three-dimensional cloud models developed so far can be classified into two families: one based on anelastic system of equations and the other on the fully compressible system of equations. On the other hand, many previous studies using high resolution cloud-resolving models (or convective cloud models) have shown that case-specific simulations are able to represent the storm structure and kinematics, such as radar reflectivity, wind speed and direction, and outflow heights.

The main motivation of the present study was to understand how the cloud-resolving model behaves when simulating such intensive storms. The model is initialized on two different upper airs sounding representing tropical and continental initial vertical profiles of meteorological data. A 2-d and 3d numerical experiments have been carefully setup in order to simulate storm dynamics, microphysics and heavy precipitation processes. The storm structure is evaluated by comparing the modeled and simulated radar reflectivity through examination of its horizontal and vertical cross sections. The differences in cloud dynamics belongs to difference in potential instability, wind shear and turbulence. Predicted maximum mixing ratios of hydrometeors show differences among cases, as result of different initial moisture content as well as difference in vertical transport of moisture and microphysics production terms. The intercomparison described here also shows differences in rainfall efficiency attributed to differences in the interaction of cloud dynamics and microphysics and precipitation flux processes. The comparative analysis has shown relatively good agreement of selected cases and compare well with observations.

2. DESCRIPTION OF THE MODEL

The present version of the model is a three-dimensional, non-hydrostatic, time-dependant, compressible system with dynamic scheme from Klemp and Wilhelmson (1978), thermodynamics scheme from Orville and Kopp (1977) and bulk microphysics scheme from Lin et al. (1983), with a significant improvement in microphysical parameterization developed by Curic and Janc (1995,1997). The governing equations of the model include conservation equations for momentum, thermodynamics and pressure, four continuity equations for the water substances, and a subgrid scale (SGS) turbulent kinetic energy equation (TKE). More detailed information about the cloud model and the chemistry submodels could be found in studies by Telenta and Aleksic (1988) and Spiridonov and Curic (2003).

2.1 Boundary conditions

Boundary conditions are defined so that the normal component of velocity vanishes along the top and bottom of the model domain. To ensure that a rigid top boundary assumption does not cause vertical oscillations in the numerical simulation, the authors have upgraded the model with a radiative upper boundary condition, as suggested by Klemp and Durran (1983). The lateral boundaries are opened and time-dependent, so those disturbances can pass through with minimal reflection Durran (1981). When the component of velocity normal to the boundary is directed toward the domain (inflow boundary), normal derivatives are set to zero. At outflow boundaries, the normal velocity component is advected out through the boundary with the estimated propagation speed that is averaged in the vertical, and weighted at each level by the approximate local strength of the wave.The pressure boundary conditions are calculated from other boundary values.

2.3 Numerical technique

Model equations are solved on a staggered grid. All velocity components u_i are defined at the edges of the grid, while scalar variables are defined at the mid point of each grid. The horizontal and vertical advection terms are calculated by the centered fourth- and second-order differences, respectively. Since the model equations represent a compressible fluid, a time splitting procedure is applied to achieve numerical efficiency. The scalar prognostic equations, except that for pressure, are stepped from $t-\Delta t$ to $t+\Delta t$ by a single leapfrog step. The terms which are not responsible for sound wave generation in the equations of motion and pressure equation are evaluated at the central time level t.

3. NUMERICAL EXPERIMENTS

3.1. Initial conditions and initializations

The model is initialized on two different upper airs sounding representing continental and tropical initial vertical profiles of meteorological data (Figs. 1,2). For the continental convective cloud simulation, the model is configured to a domain of 120 x 120 x 16 km^3 with 1 km horizontal resolution and 0.5 km vertical resolution.

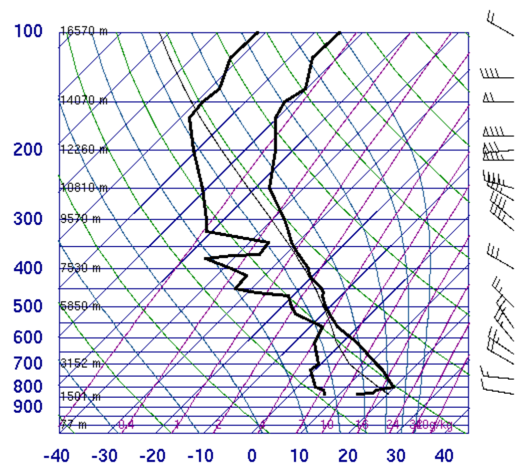

Fig. 1 Upper air sounding for Wyoming on 10July,1996 00 UTC

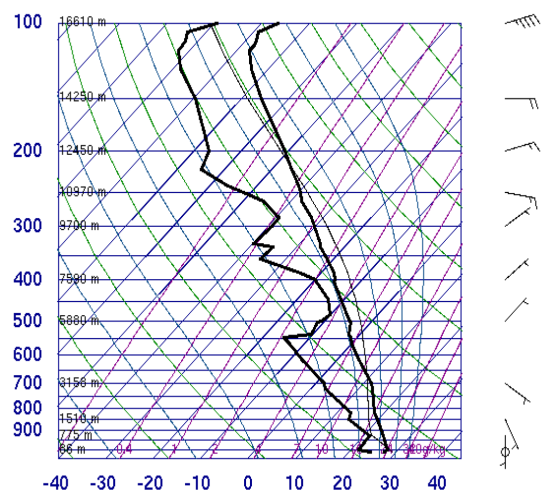

Fig. 2 Upper air sounding for Bangkok, Thailand on 25 July 2007 00 UTC

Initial data and model initialization for a tropical storm are taken from the upper air sounding from Bangkok, Thailand observed on 25 July 2007. A three dimensional simulation for a second case simulation is performed on a smaller domain of 61km x 61km x 16km for a better comparison with the radar maximum range. The horizontal and vertical grid steps are Δx=1km and Δz=0.5km, respectively.

4. RESULTS

Using the same initiation protocol in each of the simulated cases will produce different storm structures and evolution because of the different initial thermodynamics conditions.

4.1. Thermodynamic conditions

The differences in initial vertical atmospheric profiles are obvious. The continental sounding is dry and stable near the surface and unstable and moist with wind shear and strong zonal wind at the middle of the layers. Opposite, the tropical environmental conditions are manifested with low-level moisture, buoyancy air and weak wind veering near surface layers, moisture deficit at 550mb with a weak wind shear, and unstable and moist at the middle part of the atmosphere. The differences in cloud dynamics belongs to difference in potential instability, wind shear and turbulence.

4.2 Microphysical and dynamical parameters of simulated storms

The main characteristics of continental and tropical storm, structural and evolutionary properties are examined by analysis the basic dynamical, microphysical and radar reflectivity parameters. Here, only the dominant dynamical features are illustrated. The maximum calculated updraft has a higher initial value in tropical case relative to continental case and quite similar values in the mature stage of the storm (see Fig. 3). The stronger initial turbulence in tropical case is evident considering time distribution on turbulent diffusion coefficients shown in Fig.4. Opposite, here in the later stage of the simulation time continental storm case shows relatively higher turbulence diffusion versus tropical one. In respect to microphysics we have considered the time evolution of rain water mixing ratios. According to results shown on Fig. 5, we find initial formation and greater values for rainwater mixing ratio in the tropical storm relative to continental storm. Predicted maximum mixing ratios of hydrometeors show differences among cases, as result of different initial moisture content as well as difference in vertical transport of moisture and microphysics production terms. The sensitivity of cloud model simulations to the fine-scale details of the initial conditions raises two distinct multicellural storms with different dynamics, microphysics and rianfall process. Higher convective rainfall efficiency is evidenced in tropical storm relative to continental storm (see Fig. 6). The intercomparison described here also shows differences in rainfall efficiency attributed to differences in the interaction of cloud dynamics and microphysics and precipitation flux processes.The maximum accumulated rainfall at the ground during simulation time in tropical case is 72,1mm, versus 33.5mm in continental case. There is no total accumulated hailfall at the ground in tropical case simulation.

4.3. Comparison of radar reflectivity fields

Comparison of radar reflectivity fields illustrates the capability of convective cloud model to simulate multicellular convection under different (continental and tropical) environments. In both cases, simulated radar reflectivity fileds have a quite good agreement with observed radar echoes. The horizontal cross section of radar reflectivity on continental storm in 90min of the simulation time shown on Fig. 7 is consistent with radar reflectivity recorded by aircraft (see Fig. 8). In tropical case multicell storm in 60 min of the simulation intercomparison clearly illustartes a good coincidence between computed reflectivity and observed by radar.

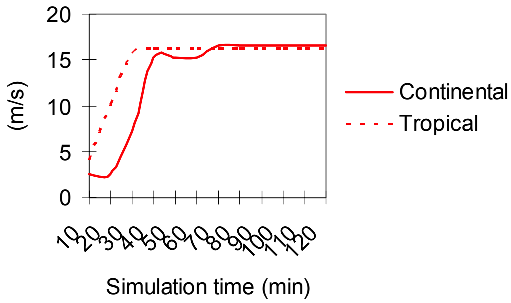

Fig. 3. Time evolution of maximum updraft in (m/s) for continental and tropical storm

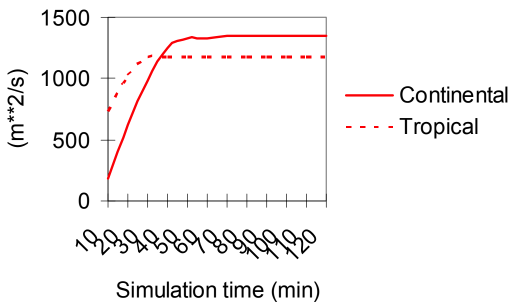

Fig. 4. Time evolution of turbulent diffusion coefficient in (m^2/s) on continental and tropical storm

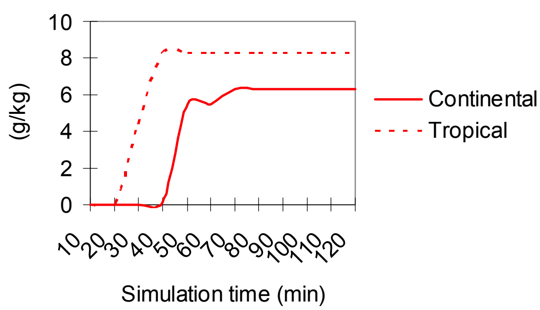

Fig. 5. Time evolution of rainwater mixing ratio in (g/kg) on continental and tropical storm

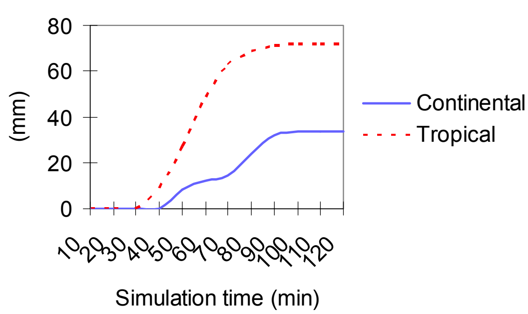

Fig. 6. Time evolution of total accumulated rainfall in (mm) on continental and tropical storm

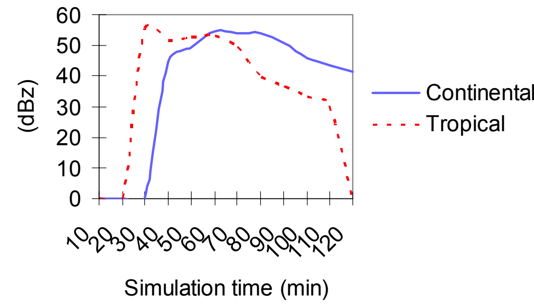

Fig. 7. Time evolution of radar reflectivity in (dBz) on continental and tropical storm

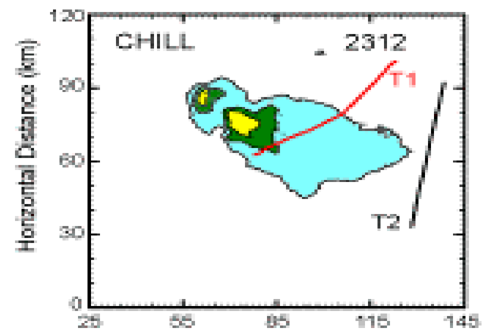

Fig. 8. Observed radar reflectivity in 60 min. (continental storm)

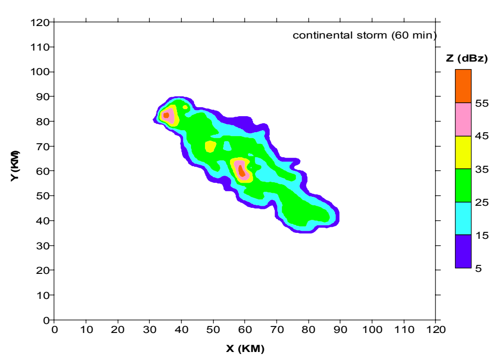

Fig. 9. Horizontal (x-y) cross section of modeled radar reflectivity in 60 min. of the simulation time (continental storm)

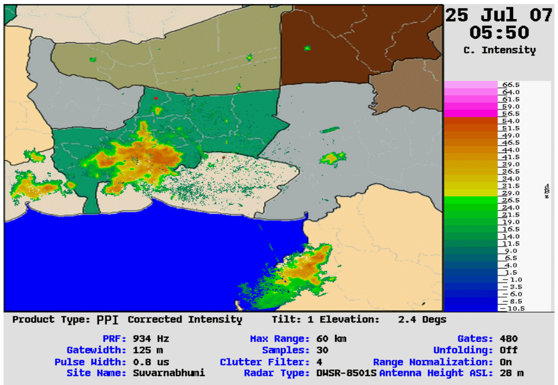

Fig. 9. Observed radar reflectivity (tropical storm)

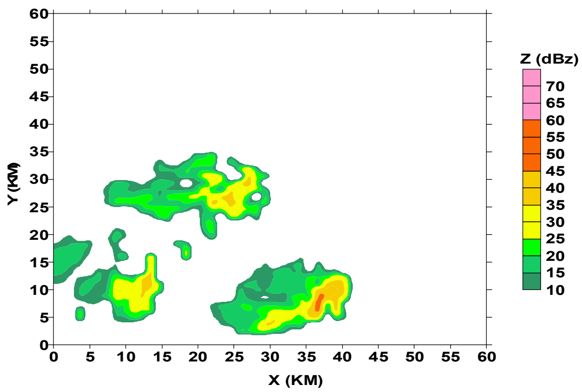

Fig. 10.Horizontal (x-y) cross section of modeled radar reflectivity in 60 min. of the simulation time (tropical).Simulated radar reflectivity (tropical)

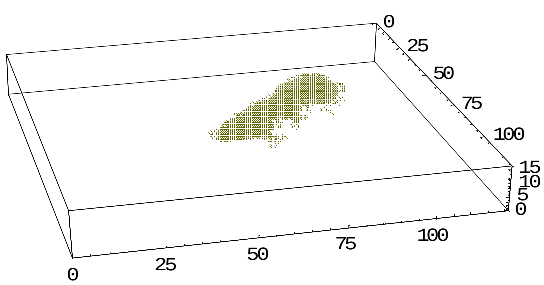

Fig. 12. 3-d view of continental storm in 40 min.

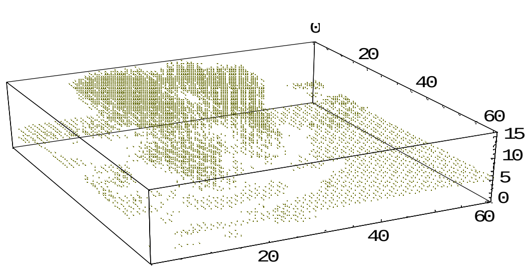

Fig. 12. 3-d view of tropical storm in 40 min

5. Conclusions

The convective cloud model is initialized on two different continental and trpical environments. A 2-d numerical experiments helped in analysing storms dynamics, microphysics and heavy precipitation processes. Tropical storm has shown a more intensive initial convection, associate with strong updrafts, turbulent difusion coefficient and low level moisture relative to continental storm. Continental storm exibits continuos and uniform evolution in the storm mature stage with relatively higher values for turbulence that maintains convection. What is microphysics concern tropical storm has shown an early formation of rainwater with greater mixing ration than in continental storm. The storm structure is evaluated by comparing the modeled and simulated radar reflectivity through examination of its horizontal cross sections. The differences in cloud dynamics belongs to difference in potential instability, wind shear and turbulence. Predicted maximum mixing ratios of hydrometeors show differences among cases, as result of different initial moisture content as well as difference in vertical transport of moisture and microphysics production terms. The intercomparison described here also shows higher rainfall efficiency in tropical case attributed to differences in the interaction of cloud dynamics and microphysics and precipitation flux processes. The comparative analysis has shown relatively good agreement of selected cases and compare well with observations.

References

Cotton, W.R., and G.J. Tripoli, 1978: Cumulus convection in shear flow 3-d numerical experiments. J. Atmos. Sci., 35, 1503-1521.

Clark, T. L., 1979: Numerical simulations with a three-dimensional cloud model: Lateral boundary condition experiments and multicellular severe storm simulations. . *Atmos. Sci.* **36**, 2191–2215

Curic, M. and Janc, D.: On the sensitivity of the continuous accretion rate equation used in bulk-water parameterization schemes. Atmos. Res., 39, 313-332, 1995.

Curic, M. and Janc, D.: On the sensitivity of hail accretion rates in numerical modeling. Tellus, 49A, 100-107, 1997.

Durran, D. R.: The effects of moisture on mountain lee waves. Ph.D. Thesis, Massachusetts Institute of Technology Boston, MA(NTIS PB 82126621),1981.

Klemp, J. B. and Wilhelmson, R. B.: The simulation of three-dimensional convective storm dynamics. J.Atmos.Sci. 35, 1070-1096, 1978.

Klemp, J. B. and Durran, D. R.: An upper boundary condition permitting internal gravity wave radiation in numerical mesoscale models. Mon. Wea. Rev., 11, 430-444, 1983.

Lin, Y. L. Farley, R. D. and Orville, H. D.: Bulk water parameterization in a cloud model. J.Climate Appl. Meteor., 22, 1065-1092, 1983.

Orville, H. D. and Kopp, F. J.: Numerical simulation of the history of a hailstorm. J.Atmos. Sci., 34, 1596-1618, 1977.

Sekhon, R.S. and Srivistava: Snow size spectra and radar reflectivity. J. Atnos. Sci., 27, 299-307, 1970

Skamarock, et. al.:Numerical simulations of the 10 July STERAO/Deep Convection Experiment Convective System: Kinematics and transport, J. Geophys. Res., 105, 19,973-19,990, 2000.

Smith, P.L, G.G. Myers and H.D. Orville: Radar relectivity calculations on numerical cloud models using bulk parameterization of precipitation. J.Appl. Meteor., 14,1975.

Tao, W.-K., D. Johnson, and C.L. Shie, 2004: The atmospheric energy budget and large-scale precipitation efficiency of convective systems during TOGA, COARE, GATE, SCSMEX, and ARM: Cloud-resolving model simulations, *J. Atmos. Sci.*, **61**(20), 2405-2423.

Tripoli, G. J., and W. R. Cotton, 1982: The Colorado State University three-dimensional cloud/mesoscale model: Part I: General theoretical framework and sensitivity experiments J. Rech. Atmos., 16, 185-220, 1982.

Xue, M., K. K. Droegemeier, and V. Wong, 2000: The Advanced Regional Prediction System (ARPS) - A multiscale nonhydrostatic atmospheric simulation and prediction tool. Part I: Model dynamics and verification. *Meteor. Atmos. Physics*,**75,** 161-193.

Wang, C. and Chang, J.: Three-dimensional numerical model of cloud dynamics, microphysics, and chemistry 1. Concepts and formulation, J. Geophys. Res., 98 (D8), 14,827-14,844, 1993a

VIDEOSONDE STUDIES OF ICE CRYSTALS IN TROPICAL CLOUDS AND OF PRECIPITATION PARTICLE EVOLUTION IN RAINBANDS AND SQUALL LINES

Tsutomu Takahashi
Honolulu, Hawaii, USA

1. INTRODUCTION

Videosonde data from East Asian monsoon clouds are used to address two topics. First: between the land and the ocean there are great differences in lightning activity (Christian et al., 2003). This is a consequence of an underlying difference in ice crystal concentrations (Takahashi, 2006). The reason for this difference has been unclear. Secondly: the defining characteristics of long-lasting, heavy rainfall are rainbands and squall lines. However, the microphysical processes are still unknown because of a lack of direct measurements of precipitation particles in high radar echoes. Precipitation particle analysis relevant to these issues is presented.

2. VIDEOSONDE

The primary purpose for the videosonde (Fig.1, Takahashi, 1990, Takahashi et al. 1999) is the measurement of shapes and electric charges on precipitation particles in the cloud with d>0.5mm. An induction ring is used to measure the charges on falling particles (0.1-200 pC). Some of the videosondes also monitor smaller particles collected on transparent, 16 mm film. In the past 12 years more than 200 videosondes have been launched in East Asia (Takahashi, 2006). Fourteen cases have been selected to investigate ice crystal formation. The videosonde results from the "Hector" case have been selected as a study in the evolution of precipitation particles in a squall line in which electric charge information was essential.

3. RESULTS AND DISCUSSIONS

a. Ice Particle Formation

Details of three typical cases are given. As illustrated in Fig. 2, ice crystal evolution was highly varied with different drop sizes and broadening near the melting level. In the U1 case from Ubon on 7 Aug. 1998, the drops were too small, with a modal size, 18 µm, and freezing was considerably delayed (Fig. 4). In the U5 case from Ubon on 10 Aug. 1998 the drops were too large with modal size 48 µm. The drops froze quickly (Fig.5) but failed to grow ice crystals, an effect that had been reported by Nakaya in 1954. For efficient ice crystal production drops should be 20-40 µm in diameter and of moderate modal size as in the B9 case (Figs. 3,6 from Brunei, 3 Dec. 1996). At these sizes the drops freeze at warmer temperatures and through columnar ice particle formation, grow ice crystals and graupel (Fig.7). As shown in Fig. 6

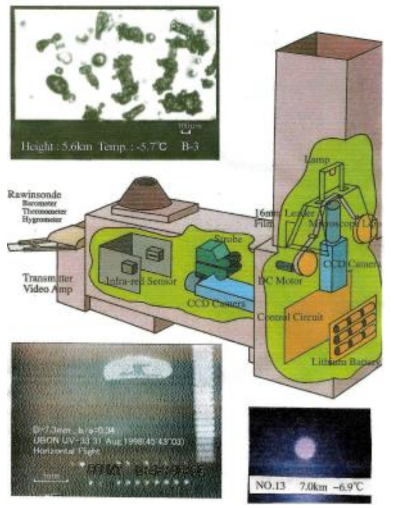

Fig. 1. Videosonde.

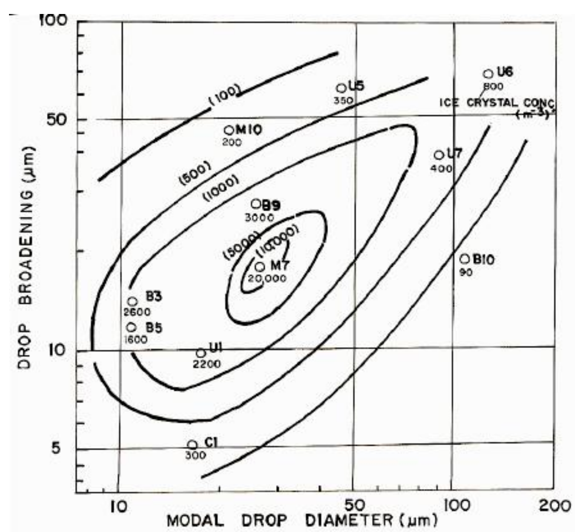

Fig.2. Peak ice crystal concentration, and modal size and broadening of cloud drops near the melting level.

many frozen spherical particles about 100 μm diameter were occasionally observed in the cold temperature layers (around -40- -50℃) above thunderstorm.

Cloud drop size distributions are primarily determined by cloud condensation nuclei (CCN) and they are unique in each air mass. The present work suggests that clouds developing over the ocean with low numbers of CCN will grow large cloud drops. Such drops will freeze quickly but ice crystal growth on them will be delayed and is the primary reason for weak lightning activities (Christian et al., 2003).

In contrast to ocean clouds, clouds developed in continental air masses will contain abundant CCN and produce small drops. Drop freezing is delayed and at higher levels in the cloud collisions of fragile graupel eject ice crystals.

Videosonde data analysis showed that in the East Asian monsoon area, ice crystal formation was primarily determined by the drop size distribution

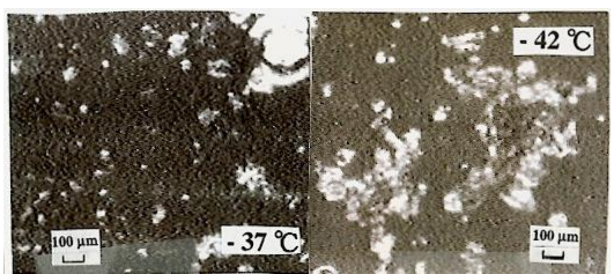

Fig. 4. U1 case. (L) Some supercooled drops. (R) Fragile graupel.

near the melting level. There were two modes of ice crystal formation: at warm temperatures columnar crystal growth on moderately-sized frozen drops in mixed air mass and, at colder temperatures, where drops were too small, fragile graupel formation.

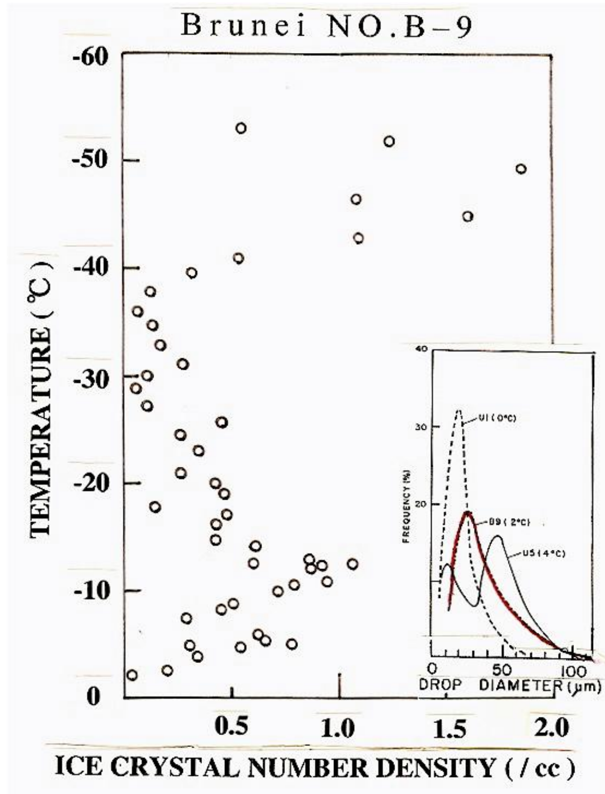

Fig. 3. Ice particle number density with height, and cloud drop size distributions near melting level.

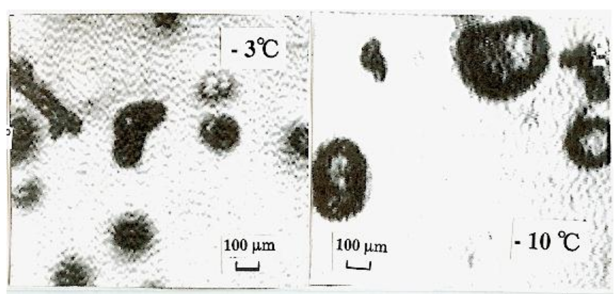

Fig. 5. U5 case. Large frozen drops.

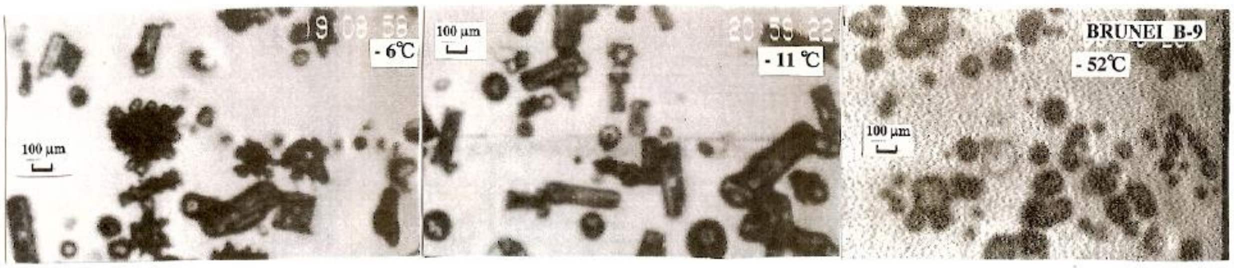

Fig. 6. B9 case. Columnar crystal growth from frozen drops, and spherical frozen drops at high levels.

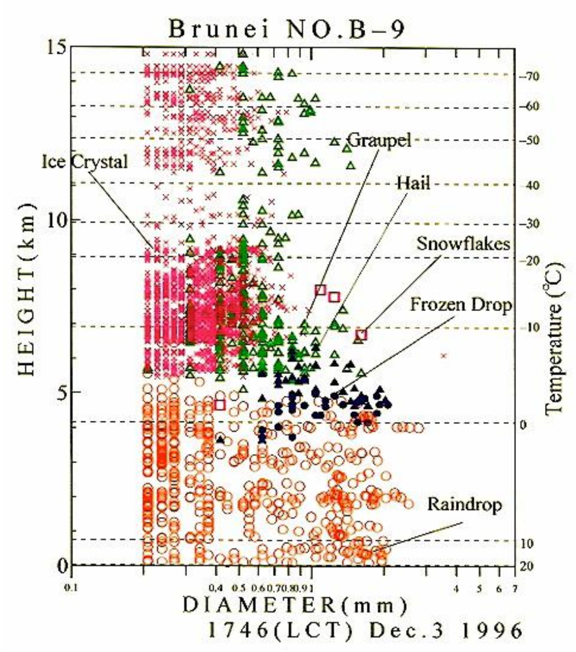

Fig.7. Size and shape distribution of B9.

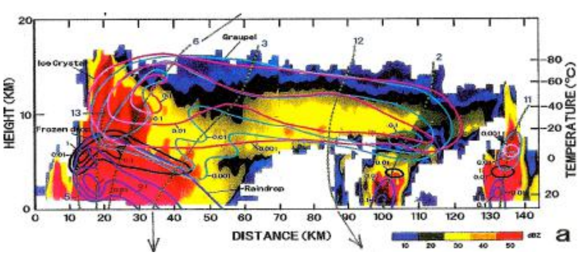

Fig. 8. Mass density distribution of "Hector" squall line.

b. Precipitation Particle Evolution in Squall Line
A "Hector" squall line developed over Melville island, Australia into which seven videosondes

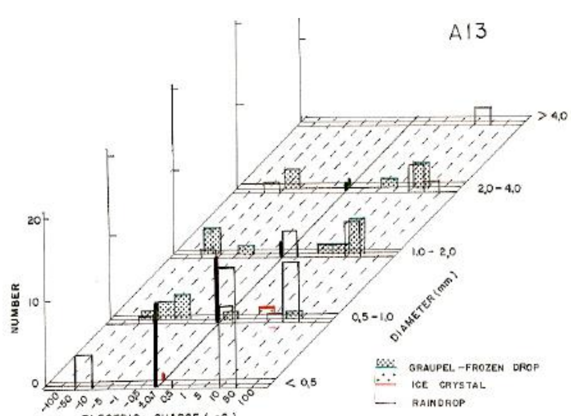

Fig. 9. A-13 from "Hector". Charge and size spectra, forward in the cloud.

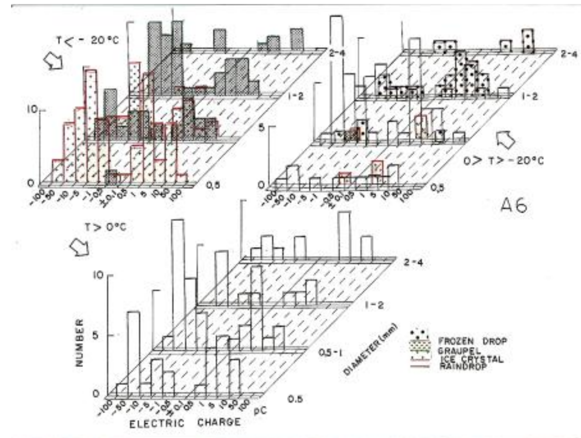

Fig 10. A-6 from "Hector". Charge and size spectra in main convective region.

were successfully launched (Takahashi and Keenan, 2004). With the addition of Doppler radar data, it develops extensive frozen drops at the front at the warmer temperature level, explosive ice crystal and graupel growth in the major precipitation column and many ice crystal in the anvil (Fig. 8).
In this case the analysis was greatly improved by the information on the electrical charges.
(1) Raindrops forward in the cloud were primarily positive, of magnitudes nearly the same, irrespective of size (Fig. 9).
(2) Below -20℃ level in the major convective region there were many supercooled drops (Fig. 10). Although frozen drops were mostly being positively charged, those supercooled drops and raindrops below the melting level were predominantly negative. The amount of charge was similar to that on graupel in the cloud's upper levels. Ice crystals in the upper levels carried charges of both signs.
(3) In the transition layer more ice crystals were positively charged, and graupel and raindrops were predominantly negative.
(4) Ice crystals in the anvil were predominantly positive.
Based on these observations the following scenario may be proposed for the evolution of precipitation particles in a squall line (Fig.11). In the main precipitation region the large raindrops, formed by graupel, are lifted up and forward by a low-level rotor and freeze above 0 ℃ level. Below -10 ℃ level their positive charge increases through collision with ice crystals and

they grow by capturing supercooled drops from warm rain. They fall and melt in the forward updraft. In the different way, small, mostly negatively charged raindrops in the main rainfall area are taken up in the main updraft and freeze as they ascend. These negatively charged drops and negative ice crystals are carried upward where the drops may become embryos for new graupel. Surprisingly, in comparison with charged raindrops and supercooled drops, almost half of the particles falling below 0 ℃ level have been recycled. Recirculation of precipitation particles and the rapid growth of frozen drops through capturing supercooled drops from forward cells must be an efficient precipitation process which may explain the intense rainfall in the leading edge of a squall line.

4. CONCLUSION

The weakness in lightning activity over tropical oceanic areas has been explained by the low numbers of CCNs and the formation of large drops near the melting level. As has been reported in rainbands, frozen drops grow by capturing supercooled drops from warm rain in merging cells and this process also occurs here. However, recirculation of raindrops was extensive and accelerated the accumulation of rain at the leading edge of a squall line.

References

Christian, H., et al., 2003: Global frequency and distribution of lightning as observed from space by the Optical Transient Detector. J. Geophys. Res., 108, (D1), 4005, doi:10.1029/2002JD002347.

Nakaya, U., 1954: Snow Crystals, Natural and Artificial. Harvard University Press., 510 pp.

Takahashi, T., 1990: Near absence of lightning in torrential rainfall producing Micronesian thunderstorms. Geophys. Res. Lett., 17, 2381-2384.

Takahashi, T., 2006: Precipitation mechanisms in East Asian monsoon: Videosonde study. J. Geophys. Res., 111, D09202, doi: 10.1029/2005JD006268.

Takahashi, T., T. Tajiri and Y. Sonoi, 1999: Charges on graupel and snow crystals and electric structure of winter thunderstorms. J. Atmos. Sci., 56, 1561-1578.

Takahashi, T., and T. Keenan, 2004: Hydrometeor mass, number, and space charge distribution in a "Hector" squall line. J.Geophys. Res., D16298, doi:10.1029/2004JD004667.

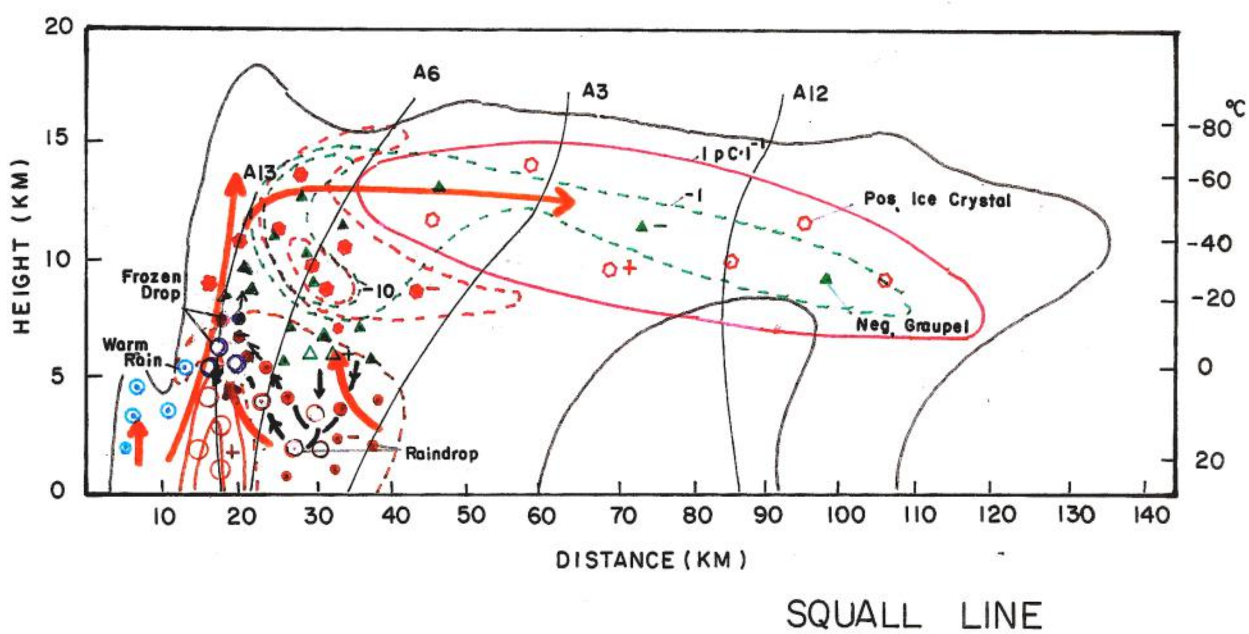

Fig. 11. Model of precipitation particle evolution in squall line.

ENVIRONMENTAL STABILITY CONTROL OF THE PRECIPITATION STRUCTURE AND INTENSITY IN CONVECTIVE SYSTEMS

Tetsuya Takemi *

Disaster Prevention Research Institute, Kyoto University, Uji, Kyoto 611-0011, Japan

1. INTRODUCTION

Organized precipitating convective systems, such as rainbands, squall lines, and other mesoscale convective complexes, develop in various climate regions of the world and induce severe wind and rain storms that harm human lives and social infrastructures. Diagnosing and forecasting the precipitation structure and intensity within those mesoscale convective systems under various environmental conditions are a challenging but an essential task in cloud and precipitation dynamics.

The environment for precipitating convective systems is characterized mainly by the vertical profiles of temperature, moisture, and horizontal wind. As far as squall lines, one of the prominent precipitating systems, are concerned, Previous studies have stressed that the dynamical interaction between the low-level ambient wind shear and evaporatively induced surface cold-air pool controls the structure and intensity of squall lines (e.g., Rotunno et al. 1988; Weisman and Rotunno 2004). It has also been stressed that moisture content not only in the planetary boundary layer but also in the free troposphere has an impact on the squall-line structure and intensity (e.g., Barnes and Sieckman 1984; Lucas et al. 2000). The cold-pool–shear interaction comes to play a more dominant role in determining squall-line characteristics in drier environments (Takemi 2006).

In comparing the characteristics of squall lines in various climate regions, on the other hand, the most controlling factor may be the environmental temperature, that is, static stability. In the Tropics the temperature profile is close to the moist-adiabatic lapse rate, while in the midlatitudes it is rather closer to the dry-adiabatic lapse rate. To put it other way, the stability profile will change in a future global-warming climate even at the same geographic location. Since the stability condition directly affects the development and enhancement of mesoscale convective systems, fundamental understandings of the precipitation structure and intensity associated with the convective systems under various temperature conditions are therefore necessary. Takemi (2007) compared the intensity of squall lines simulated in two contrasting temperature environments characteristic of the Tropics and the midlatitudes under a comparable CAPE condition and found that the midlatitude system is significantly stronger than the tropical one.

In the present study, we investigate the effects of static stability on the precipitation structure and intensity associated with linearly organized convective systems under low-level shear conditions. For this purpose, we conduct a series of numerical experiments with idealized settings and show the relationship between precipitation characteristics and static stability from the large set of simulations. We discuss the dependence of the precipitation intensity on the environmental static stability.

2. MODEL AND EXPERIMENTAL DESIGN

In the present study, we use a compressible, nonhydrostatic cloud model, the Advanced Research Version 2.1.2 of the Weather Research and Forecasting (WRF) Model (Skamarock et al., 2005). The model is configured in a three-dimensional domain having a horizontally homogeneous base state under low-level westerly shear conditions. In order to concentrate on the dynamics of convection, we follow the philosophy of Rotunno et al. (1988) on the model setup and hence configure the model with a minimum but essential set of physics processes. Included parameterized physics are a warm-rain and ice-phase microphysics scheme, and a turbulence mixing scheme that uses a prognostic value of turbulent kinetic energy. The Coriolis effect, surface friction, land-surface processes, and atmospheric radiation processes are neglected.

The model domain has a dimension of 300 km (the east-west, x, direction) $\times$ 60 km (the north-south, y) $\times$ 17.5 km (the vertical, z), with an open condition at the east and west lateral boundaries, the periodic condition at the north and south lateral boundaries, free surface at a constant pressure at the top boundary, and free slip at the bottom boundary. The upper 6-km layer is set to be wave-absorbing for minimizing the effects of reflection at the model top. The domain is discretized with a horizontal grid spacing of 500 m and 70 levels in the vertical.

In order to determine the environmental temperature and moisture, we use the analytic form of temperature and moisture profiles of Weisman and Klemp (1982, hereafter WK82), which originally was intended to represent a typical condition for strong convective storms in midlatitudes. Their analytic function for environmental potential temperature θ_{env} below the tropopause z_{tr} (=12 km) is given as follows:

$$\theta_{env}(z) = \theta_0 + (\theta_{tr} - \theta_0)(z/z_{tr})^{5/4}. \qquad (1)$$

*Corresponding author's address: Dr. Tetsuya Takemi, Disaster Prevention Research Institute, Kyoto University, Gokasho, Uji, Kyoto 611-0011, Japan; takemi@storm.dpri.kyoto-u.ac.jp

Table 1: Thermodynamic parameters for the numerical experiments. θ_{tr} (K), q_{v0} ($\mathrm{g\,kg^{-1}}$), surface relative humidity (RH_{sfc}) (%), convective available potential energy (CAPE) (J kg^{-1}), convective inhibition (CIN) (J kg^{-1}), lifting condensation level (LCL) (m), level of free convection (LFC) (m), level of neutral buoyancy (LNB) (m), and precipitable water content (PWC) (kg m^{-2}), are listed.

Series	Case	θ_{tr}	q_{v0}	RH_{sfc}	CAPE	CIN	LCL	LFC	LNB	PWC
	C37T43	343	16.0	73	3709	21	723	1067	12555	47.6
C17	C17T43	343	13.1	60	1734	62	1116	1791	11390	44.4
	C17T48	348	14.5	66	1767	47	918	1546	11254	47.9
	C17T53	353	16.0	73	1772	31	723	1258	11075	51.3
	C17T58	358	17.7	81	1772	15	521	889	10938	54.7
C10	C10T43	343	12.1	55	1086	88	1268	2215	10303	42.8
	C10T48	348	13.2	60	1061	74	1101	1931	10085	46.2
	C10T53	353	14.5	66	1064	57	918	1704	9921	49.8
	C10T58	358	16.0	73	1081	38	723	1392	9790	53.4
C26	C26T43	343	14.4	66	2634	39	931	1447	12174	46.0
	C26T48	348	16.0	73	2668	25	723	1151	12129	49.4
	C26T53	353	17.7	81	2648	13	521	820	12047	52.5
	C26T58	358	19.0	87	2633	6	377	538	11970	55.2

In WK82 $\theta_{tr} =$ 343 K (at the tropopause) and $\theta_0 = 300$ K (at the surface). We change the value of θ_{tr} as 343, 348, 353 and 358 K. A smaller (larger) θ_{tr} value, that is, a smaller (larger) θ_{env}, means a colder temperature environment, and is regarded as a midlatitude (tropical) environment. Note that the tropopause height is fixed at a constant level irrespective of θ_{tr} in order to exclude the effects of high tropopause in warmer environments (such as on a CAPE value). The tropospheric moisture profile is held fixed for the various $theta_{tr}$ also with the WK82 analytic function, except below the 1.5-km height where water vapor mixing ratio q_{v0} is changed.

A series of numerical experiments are performed by systematically changing the combination of θ_{tr} and q_{v0}. All the experimental cases are listed in Table 1.

As was used in many idealized studies such as in Rotunno et al. (1988), the model is initialized with a linearly y-oriented, elliptical thermal, centered at the model domain, having x radius of 10 km and vertical radius of 1 km having a 1.5-K potential temperature excess (random perturbation added) at the thermal center and decreasing to zero at the edge. The simulations are conducted for four hours. The analyses are conducted for the model outputs at 5 minutes interval.

3. RESULTS

Figure 1 indicates the vertical cross section of the simulated squall lines averaged in the y direction at 4 h. It is seen that as θ_{tr} increases, the across-line width of the system decreases, the volume of surface cold pool decreases, and the degree of the rearward tilt of the system decreases. The precipitation area also diminishes as θ_{tr} increases. This response of the system structure is basically controlled by the strength of the cold pool (Rotunno et al. 1988). It is noted that the response seen in the system structure to θ_{tr} appears more pronounced in the strong-shear cases than in the weak-shear cases.

In order to compare the intensity of the simulated squall lines under the various environmental conditions, the peak values for updraft velocity and precipitation intensity are useful parameters. At every model output time (i.e., 5-min interval), the maximum values of updraft velocity and precipitation intensity are calculated within an analysis domain defined as follows: the domain has a 50 km by 60 km area whose east boundary is at 10 km ahead of the eastward-moving cold-pool front and west boundary is at 40 km behind the cold-pool front. The location of the cold pool front translates with time and thus the analysis domain moves accordingly. This domain is used for the analyses described hereinafter. From the time series of these maxima during 1 to 4 h, means and standard deviations are then calculated. It is noted that the precipitation intensity is defined as the accumulated precipitation for 5 min.

Figure 2 shows the means and standard deviations of the maximum updraft for all the experimental cases. As θ_{tr} increases, the peak updraft unanimously decreases for all the experimental series. It should be emphasized that the environment with an identical amount of CAPE does not lead to a comparable strength of updrafts. On the other hand, with the same θ_{tr} value, updraft strength (and hence system intensity) depends closely on the amount of CAPE, as found in Takemi (2006). The comparison between the results with the weak and the strong shears indicates that the sensitivity to the θ_{tr} value is more significant in the stronger shear cases.

The statistics for the precipitation intensity maxima are shown in Figure 3. In contrast to the features identified in Figure 2, the peak precipitation generally increases as θ_{tr} increases. This feature is more pro-

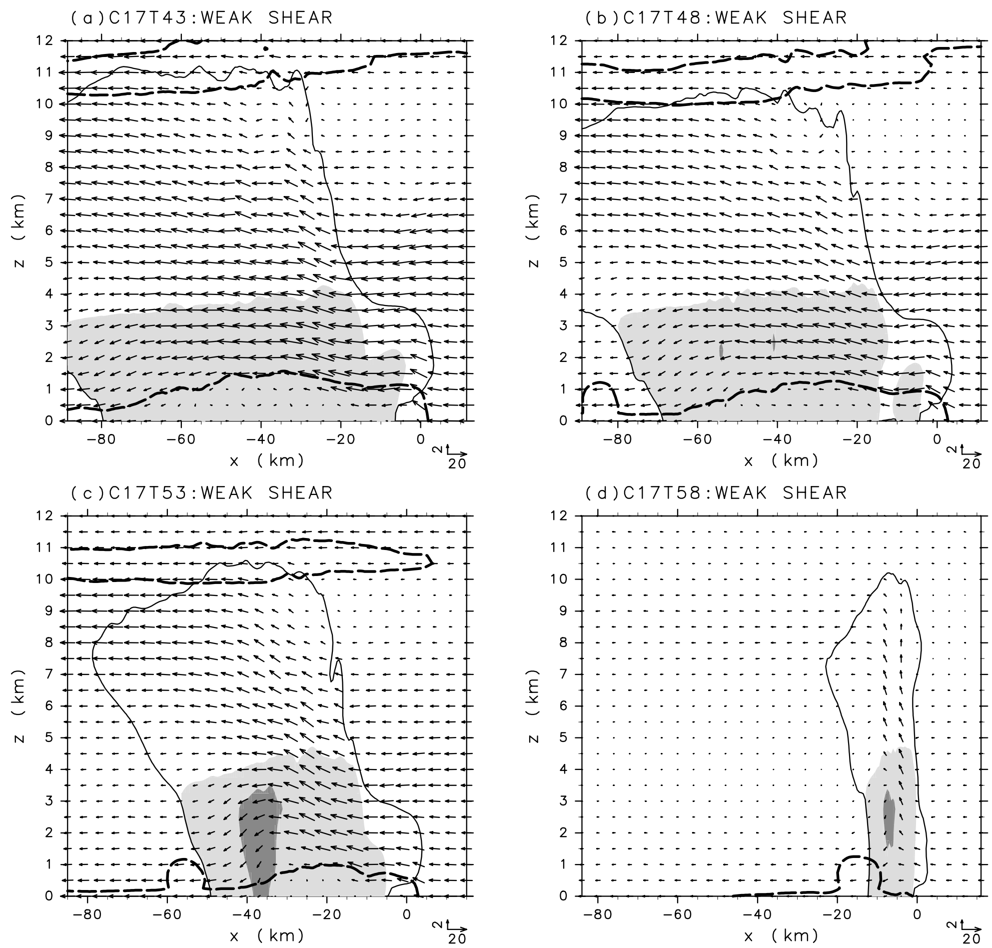

Figure 1: Vertical cross section of system-relative wind vectors, cold-pool boundary (bold dashed line), and rain fields (shading) averaged in the y direction for the weak-shear cases of (a) C17T43, (b) C17T48, (c) C17T53, and (d) C17T58. The unit vector (in $\mathrm{m\,s^{-1}}$) is indicated in the lower right of each panel. Dashed lines indicate potential temperature perturbation of -1 K, and solid lines total water mixing ratio of 0.1 $\mathrm{g\,kg^{-1}}$. The fields of rainwater mixing ratio between 0.1 and 1 $\mathrm{g\,kg^{-1}}$ are lightly shaded, and those greater than 1 $\mathrm{g\,kg^{-1}}$ are darkly shaded. A 100 km by 12 km region is indicated.

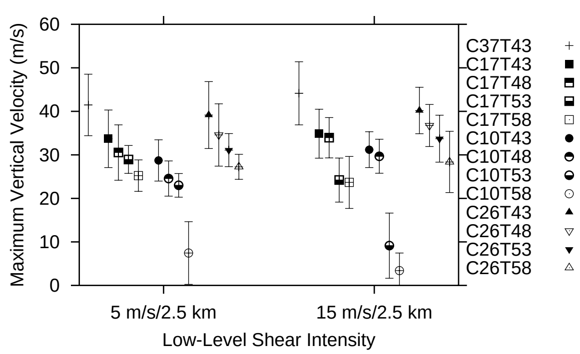

Figure 2: The mean (symbols) and standard deviation (error bars) of the maximum updraft velocity in the analysis domain during 1–4 h for all the cases with the low-level weak and strong shears.

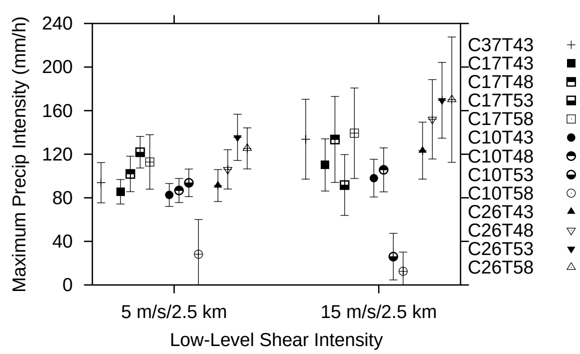

Figure 3: The same as Figure 2, except for the maximum precipitation intensity at the surface.

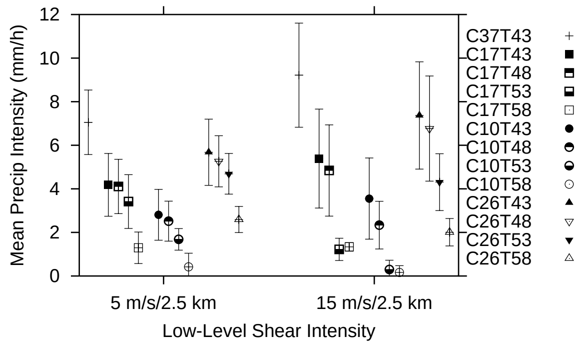

Figure 4: The same as Figure 2, except for the mean precipitation intensity averaged over the analysis area.

nounced in the stronger shear cases, although some cases with higher θ_{tr} values fail to follow the trend because of the absence of an organized squall-line structure. In terms of peak precipitation intensity, the results seem to indicate that the environment with higher θ_{tr} is more favorable. In other words, a warmer temperature environment produces more intense precipitation as long as the environmental CAPE is the same. With the same temperature environment, however, the peak precipitation intensity increases as CAPE becomes larger.

In addition to the peak values, the statistics for precipitation intensity averaged over the analysis area are examined. The mean precipitation intensity is equivalent to the total precipitation produced by the convective system in the area. Therefore, this property is a useful parameter for diagnosing an overall system intensity. Figure 4 shows the means and standard deviations obtained from the time series of the area-averaged precipitation intensity. It is seen that the mean precipitation decreases as θ_{tr} increases under the same CAPE conditions, a trend similar to that seen for the peak updraft. In addition, similar to the peak updraft statistics, the amount of CAPE has a good correlation with the mean precipitation intensity if θ_{tr} is the same.

In order to explain the difference in the intensity of tropical and midlatitude squall lines in terms of an environmental stability index, Takemi (2007) introduced a parameter that represents the stability for convective overturning: temperature lapse rate Γ in a convectively unstable layer that is between the heights of low-level maximum and middle-level minimum equivalent potential temperatures. Temperature lapse rate is referred to as static stability in Takemi (2007) and also in the present study. Figure 5 exhibits the statistics of the area-averaged precipitation intensity for the cases having the three different CAPE values. The mean precipitation intensities under the same CAPE conditions are clearly delineated in terms of Γ for the both shear cases: the condition with lower static stability leads to more precipitation. With Γ being comparable, on the other hand, a larger CAPE condition is favorable for producing a

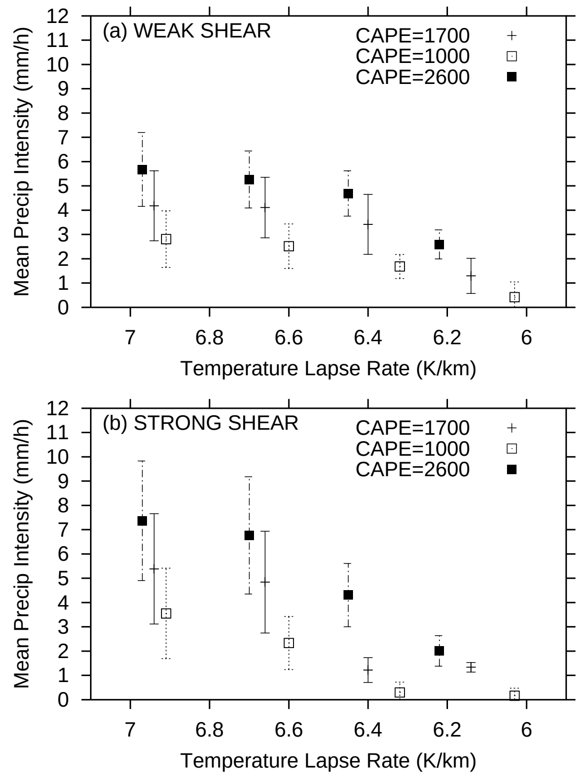

Figure 5: The same as Figure 2, except for the mean precipitation intensity depicted against temperature lapse rate for the C17, C10, and C26 cases with (a) weak shear and (b) strong shear.

larger amount of precipitation. The dependence on Γ looks sharper in the cases with the stronger shear. It is also seen that even with sufficiently large CAPE but higher stability the mean precipitation intensity can be notably smaller than with less CAPE but lower stability (e.g., compare the C26 case with $\Gamma \sim 6.2$ and the C17 case with $\Gamma \sim 6.9$). Therefore, it is suggested that the environmental static stability should be a critical parameter in diagnosing the system intensity. This point will be further discussed in a later section.

4. SUMMARY AND DISCUSSION

The present sensitivity analyses indicated that the precipitation structure and intensity associated with mesoscale convective systems that develop in low-level shears perpendicular to the convective lines is strongly dependent on the environmental temperature profile. This dependence was clearly shown by the experimental series with surface-based CAPE being maintained. The results indicating that wider and stronger updrafts were produced in colder environments are consistent with the previous observational studies (LeMone and Zipser 1980; Lucas et al., 1994) in spite of the idealized modeling setup. According to the parcel theory, the strength of updrafts and hence the precipitation intensity as well as the convective organization are expected to be more or less controlled by the amount of CAPE. However, stronger precipitating systems were simulated with smaller θ_{tr} but with CAPE being unchanged. Moreover, some results showed that a stronger system is generated even with smaller CAPE and lower stability than with larger CAPE and higher stability, irrespective of the magnitude of the low-level shear. In addition to updraft strength and precipitation intensity, stronger cold pools are generated in a less stable environment (which will be discussed shortly). It was shown that stronger cold pools induce wider and stronger updraft cells that lead to the formation of intense convective systems and heavier precipitation. This result is consistent with the sensitivity study of James et al. (2006) who showed that the scale of coherent structures within the squall-line system is closely related to the cold pool strength and stronger cold pools favor larger scales.

One might argue that the different responses of the intensity of precipitating convective systems to environmental profile are caused not only by temperature difference but also by moisture difference. In Takemi (2006), it was shown that a drier condition in the low levels has a more detrimental impact on the squall-line intensity under the same temperature condition. On the other hand, under the present temperature setting a drier low-level condition (i.e., a smaller θ_{tr} case) positively affects the squall-line intensity. Because the influences of moisture profile vary depending on temperature profile, the sensitivity results with CAPE unchanged are considered to be mainly due to the difference in temperature profile.

Comparing the results with the two shear profiles, it is indicated that the simulated squall lines are stronger in the strong shears than in the weak shears if the lapse rate is large, while the squall lines become stronger in the weak shears than in the strong shears if the lapse rate is small. This mechanism can be understood by the theory of Rotunno et al. (1988); in other words, the intensity of the shear-perpendicular squall lines examined here is strongly controlled by the strength of cold pools, which therefore indicates that the precipitation structure and intensity associated with the convective systems are also regulated by the cold-pool intensity.

The analysis of peak precipitation intensity was a seemingly unexpected result that shows that the peak intensity increased as θ_{tr} increased under identical CAPE conditions, which is an opposite sense found in the means of precipitation intensity and updraft. This relationship between peak precipitation intensity and environmental temperature may be due to moister conditions for downdrafts in the warmer environment and hence less evaporation of precipitation. The moist condition is therefore considered to be preferable for producing heavier precipitation in the very short term.

We have shown that the intensity of squall lines is dependent more on the environmental temperature lapse rate in a convectively unstable layer than on CAPE. This leads to a doubt on using parcel theory in diagnosing the activity of deep convection within squall-line systems or the overall intensity of the system. Our previous study (Takemi 2007) showed that among the standard stability indices for diagnosing thunderstorm potential and intensity a parameter that takes into account environmental temperature lapse rate is more suitable than a parameter calculated based on adiabatically lifted parcel. We consider that the reason why the environmental stability in a convective unstable layer well describes the system intensity is due to the fact that updrafts in the layer that is moist absolutely unstable (Bryan and Fritsch 2000) exhibit a slab mode of layer overturning (James et al. 2005). Thus, a simple parcel thinking seems not to be appropriate for the convective overturning within organized convective systems. The present analysis strongly suggests that the magnitude of the static stability controls the intensity of overturning and therefore the precipitation structure and intensity in convective systems.

5. CONCLUDING REMARKS

The results of the present sensitivity simulations reveal that the environmental static stability in a convectively unstable layer of the lower half of the troposphere well delineates the structure and intensity of precipitating convective systems that develop in both weak and strong shears. An environment with a less stable stability is favorable for generating stronger updrafts and also stronger cold pools. The intensity of cold pools significantly affects the scale and strength of convective updrafts, which will lead to the enhancement of tropospheric overturning and hence the development of stronger convective systems.

It has long been argued that CAPE can be a parameter that diagnoses the development and strength of convective storms and systems. The present analysis clearly indicates that the amount of CAPE can only be a good measure for diagnosing the intensity of convective systems so long as the environmental lapse rate is identical.

6. ACKNOWLEDGMENT

This work was supported partly by Grant-in-Aid for Scientific Research 19740287 from Japan Society for the Promotion of Science.

7. REFERENCES

Barnes, G. M., and K. Sieckman, 1984: The environment of fast- and slow-moving tropical mesoscale convective cloud lines. *Mon. Wea. Rev.*, **112**, 1782–1794.

Bryan, G. H., and J. M. Fritsch, 2000: Moist absolute instability: the sixth static stability state. *Bull. Amer. Meteor. Soc.*, **81**, 1207–1230.

James, R. P., J. M. Fritsch, and P. M. Markowski, 2005: Environmental distinction between cellular and slabular convective lines. *Mon. Wea. Rev.*, **133**, 2669–2691.

James, R. P., P. M. Markowski, and J. M. Fritsch, 2006: Bow echo sensitivity to ambient moisture and cold pool strength. *Mon. Wea. Rev.*, **134**, 950–964.

LeMone, M. A., and E. J. Zipser, 1980: Cumulonimbus vertical velocity events in GATE. Part I: Diameter, intensity and mass flux. *J. Atmos. Sci.*, **37**, 2444–2457.

Lucas, C., E. J. Zipser, and M. A. LeMone, 1994: Vertical velocity in oceanic convection off tropical Australia. *J. Atmos. Sci.*, **51**, 3183–3193.

Lucas, C., E. Zipser, and B. S. Ferrier, 2000: Sensitivity of tropical west Pacific oceanic squall lines to tropospheric wind and moisture profiles. *J. Atmos. Sci.*, **57**, 2351–2373.

Rotunno, R., J. B. Klemp, and M. L. Weisman, 1988: A theory for strong, long-lived squall lines. *J. Atmos. Sci.*, **45**, 463-485.

Skamarock, W. C., J. B. Klemp, J. Dudhia, D. O. Gill, D. M. Barker, W. Wang, J. G. Powers, 2005: A description of the Advanced Research WRF Version 2. *NCAR Tech. Note*, NCAR/TN-468+STR, 88 pp.

Takemi, T., 2007: A sensitivity of squall-line intensity to environmental static stability under various shear and moisture conditions. *Atmos. Res.*, **84**, 374–389.

Takemi, T., 2006: Impacts of moisture profile on the evolution and organization of midlatitude squall lines under various shear conditions. *Atmos. Res.*, **82**, 37–54.

Weisman, M. L., and J. B. Klemp, 1982: The dependence of numerically simulated convective storms on vertical wind shear and buoyancy. *Mon. Wea. Rev.*, **110**, 504-520.

Weisman, M. L., and R. Rotunno, 2004: “A theory for strong long-lived squall lines” revisited. *J. Atmos. Sci.*, **61**, 361-382.

PARAMETERIZATION OF CLOUD FROM NWP TO CLIMATE MODEL RESOLUTION

Richard M. Forbes,[1]

European Centre for Medium–Range Weather Forecasts, Reading, UK

1. INTRODUCTION

General Circulation Model (GCM) simulations are performed across a range of resolutions depending on their application, from hundreds of kilometres for decadal climate down to a couple of tens of kilometres for current global operational Numerical Weather Prediction (NWP). Even with the trend in increasing high performance computing power enabling the use of higher and higher resolution, there will still be a need for models with a wide range of grid resolutions for the foreseeable future. The parametrization of cloud is a vital component of models for both climate prediction and NWP, and an effective parametrization is able to represent the effects of sub-grid cloud processes across the scales used in these models. Although GCMs are able to represent a large proportion of the dominant atmospheric motions that lead to cloud generation and dissipation, they may not always be adequately capturing the impacts of smaller scale motions that can significantly affect cloud and precipitation development and evolution. This paper discusses some of the issues for cloud parametrization at different spatial and temporal scales and provides an indication of the behaviour of the cloud scheme in the ECMWF model at resolutions appropriate for short-range and long-term prediction of the atmosphere.

2. ISSUES FOR CLOUD PARAMETRIZATION AT DIFFERENT SPATIAL SCALES

A GCM solves the partial differential equations governing the evolution of the atmospheric state variable after discretizing in time and space with a resolution that is usually determined by the application and available computing resources. The definition of ”resolution” here will cover both spatial (horizontal and vertical) and temporal (timestep) discretization. At any resolution there is a part of the flow along with other physical properties of the atmosphere at scales below the resolution of the model, and it is necessary to find parameters that describe the statistical behaviour of these unresolved processes at the resolved scale of the model. The aim of a parametrization is to represents these average statistical properties as a function of resolved variables of the GCM represented on the model grid. Most GCMs represent cloud with a ”bulk” formulation, predicting the evolution of quantities such as mean grid-box cloud condensate with additional information on sub-grid variability within the grid cell. For the purpose of the discussion here, it is convenient to consider three aspects of the cloud parametrization: (a) choice of variables and formulation of microphysical processes, (b) representation of sub-grid inhomogeneities and their overlap in the vertical, (c) numerical techniques for efficient implementation. These three aspects are discussed briefly below, with reference to the ECWMF model.

(a) Choice and formulation of microphysical processes

As the resolution of the model is increased, the range of spatial and temporal scales of the atmospheric motion that are represented increases. Since it is these atmospheric motions that provide a significant source for cloud formation and dissipation, the microphysical processes in the model need to be representative of the scales of the dynamical forcing. For example, a model with a higher grid resolution will resolve locally higher vertical velocities. The response of the microphysical scheme to the changing forcing will depend on the non-linearity of the processes involved (and many microphysical processes are very non-linear).

Parametrization schemes are based on an assumed break in space and time scales, so that the impact of scales not resolved by the model can be represented diagnostically from the (prognosed) variables at the resolved scale. The diagnostic assumption is equivalent to an assumption of equilibrium within a timestep based on the fact that the timescales of these sub-grid processes are small compared to the timescale associated with typical resolved motions at the grid scale. An example in many GCMs is the diagnostic representation of rain. Diagnosing the profile of rain from the prognosed liquid and ice water contents within a grid

[1]Corresponding author address: Richard Forbes, ECMWF, Shinfi eld Park, Reading, RG2 9AX, UK. E-mail: forbes@ecmwf.int

column is an appropriate assumption as long as the sedimentation timescale is short compared to the advection timescale across the grid box. As the resolution of the model increases, this assumption becomes increasingly invalid and a prognostic representation of rain would be required for a more accurate solution at the smaller time and space scales of the model.

As GCM resolution continues to increase, some of the choices of prognostic vs. diagnostic variables and formulation of non-linear microphysical processes need to be reviewed, and at ECMWF a change from a diagnostic to a prognostic representation of precipitation with corresponding microphysical processes is being investigated.

(b) Representation of sub-grid inhomogeneities

Models that predict only the mean value of cloud properties in each grid cell can be subject to large biases in many process rates (Pincus and Klein, 2000). Therefore the representation of sub-grid inhomogeneities is an important component of the cloud parametrization, as for an area of a typical grid box there is considerable variability in the quantities represented in the model (vertical velocity, humidity, temperature, liquid and ice water content,...) and only part of the grid box may contain cloud. A common approach is to formulate the prognostic equations for the grid box mean liquid/ice water content and corresponding cloud fraction (Tiedtke, 1993; Gregory et al. 2002; Larson 2004) based on assumed probability density functions of total water. An alternative approach is to prognose moments of the underlying probability density function of total water or a related variable (e.g. Tompkins, 2002) and then diagnose the cloud fraction. The latter has the conceptually attractive property of attempting to describe variations in the underlying inhomogeneities in the atmosphere at the sub-grid scale which could be used consistently between different parametrizations within the model. However, both approaches rely on the accurate specification of sinks and sources due to a variety of dynamical and physical processes which are often difficult to represent and in some cases are unknown. The debate is still open as to which of these approaches or indeed whether alternatives are the most appropriate.

Even if we assume that the sub-grid inhomogeneities are represented appropriately in each grid box, there is then also the question of how inhomogeneities are distributed relative to one another in the vertical. This is particularly important for cloud-radiation interactions and precipitation sedimentation (which are both dominated by the vertical component). Atmospheric models which have a sub-grid representation of cloud fraction parametrize how clouds within a grid column overlap in the vertical. The particular choice of assumptions can have a significant impact on the radiation scheme and performance of the model. Traditionally GCMs have used the maximum-random assumption for fractional cloud cover overlap (Geleyn and Hollingsworth, 1979), but more recently, observations (Hogan and Illingworth 2000; Mace and Benson-Troth 2002; Naud et al. 2008) and cloud modelling results (Oreopoulos and Khairoutdinov, 2003) have suggested a more realistic assumption based on increasing randomness in the overlap as the separation between two layers within a cloud increases (referred to here as ”generalised overlap”) with the degree of randomness dependent on wind shear or synoptic regime. A form of the generalised overlap has been applied to both cloud cover and inhomogeneities in cloud condensate in GCM radiation schemes (Räisänen et al. 2004; Morcrette et al. 2007) resulting in a reduced dependence on vertical resolution. Another process in which the vertical overlap assumption can be important is that of precipitation enhancement and evaporation. Jakob and Klein (1999,2000) showed a significant impact of assuming cloud/precipitation overlap on the evaporation of precipitation, but there are other areas of the parametrization such as mixed phase clouds where overlap of ice and liquid inhomogeneities can be crucial and can lead to resolution sensitivity.

(c) Numerical techniques for efficient implementation

A particular problem for GCMs is the combination of high vertical resolution and long timesteps for compuatational efficiency, where the chosen timestep is based primarily on horizontal advection velocities and the horizontal grid resolution. For example, the ECWMF IFS GCM with semi-lagrangian dynamics may use a timestep of 1 hour for a horizontal grid spacing of 125 km. In contrast the vertical resolution in parts of the troposphere may be of the order of 100m. There are thus implications for the sedimentation scheme with hydrometeors falling through many model layers within a timestep. A previous CFL limited explicit sedimentation scheme in the ECMWF model lead to a significant sensitivity to vertical resolution and timestep. A forward-in-time upstream implicit solver is now used for the cloud variables, using a mass flux form for the advection term to ensure conservation, and the sensitivity to resolution is much reduced (Tompkins, pers. comm.).

3. SENSITIVITY OF THE ECMWF CLOUD SCHEME TO MODEL RESOLUTION

A number of sources of resolution sensitivity to cloud parametrization in GCMs have been outlined in the previous section. Here we investigate the sensitivity of aspects of the cloud and precipitation in the ECMWF model (www.ecmwf.int/research) to spatial resolution.

At ECMWF, the IFS (Integrated Forecast System) is used at its highest resolution for global NWP (currently with a spectral truncation of T799 equivalent to a grid spacing of 25 km, 91 levels and a timestep of 12 minutes). A 50 member global ensemble is also run operationally at a lower resolution (T399L62, 50 km grid, 30 minute timestep). Also, the ECMWF seasonal forecasting system currently includes the atmospheric model at T159L62 resolution (125 km grid, 1 hour timestep). All configurations use the same physical parametrizations without tunable resolution dependent parameters, so that the same parametrizations can be used across the range of resolutions.

To assess the extent to which the ECMWF model is successful at different resolutions, the sensitivity of various aspects of the cloud and precipitation to resolution will be evaluated. Clearly, the aim is also to get the model as close to observations as possible for the appropriate scales represented by the model, and one example for global precipitation is highlighted in this section.

As suggested previously, a number of developments of the ECMWF IFS model cloud parametrization over recent years have contributed to an improved simulation of cloud and precipitation and increased consistency across a range of resolutions. These include a modified implicit numerical formulation to give increased robustness for longer timesteps, particularly affecting the sedimentation scheme for ice, and modified vertical overlap of cloud fraction and sub-grid condensate inhomogeneities with a dependence on vertical distance rather than model level.

Although a number of aspects of the cloud and precipitation representation in the ECMWF model will be evaluated, only the impact on global precipitation (convective + large scale) is described here. Figure 1 shows a comparison of global precipitation averaged over a 1 year period from Sep 2000 to Aug 2001 between the ECMWF T159L91 IFS model at version CY32R3 and the precipitation estimate from the Global Precipitation Climatology Project (GPCP, Adler et al., 2003). Although there are identifiable regional differences in the model precipitation compared to the observed estimate and there is still scope for improvement (particularly in the tropics), overall the model is able to capture the global patterns and magnitudes reasonably well at this resolution.

Global average precipitation is calculated from three simulations to look at the sensitivity to horizontal resolution. These simulations have resolutions of T159 (125 km)(as in Fig. 1), T399 (50 km) and T799 (25 km), but the same vertical resolution (91 levels). The respective values of average precipitation for the three models are 2.93 mm/day, 3.03 mm/day and 3.09 mm/day with differences coming primarily from the large-scale cloud scheme rather than the convection parametrization. This is a difference of 0.16 mm/day (5% of the total) between the T159 and T799 resolutions for which the grid spacing differs by a factor of 5 and the grid box area differs by a factor of 25. The estimated mean error of the T159 model compared to the GPCP observations is 0.29 mm/day, so the variation between models is significantly less than the bias compared to GPCP. The large scale spatial pattern of differences is also very similar between models (not shown). This relative insensitivity to resolution is encouraging, but of course there are still possibilities for further improvement, particularly regarding the regional differences from observations. Also, this is just one measure of the robustness of the cloud and precipitation in the model and other characteristics include ice and liquid water content, cloud cover, and humidity, not just averages but other moments of the distributions and sensitivity to timestep and vertical resolution.

4. CONCLUSIONS

Global climate and Numerical Weather Prediction models are currently used across a wide range of scales and require parametrizations that ideally give the correct statistical representation of the sub-grid impacts on the prognostic variables of the model and that are ideally valid across a wide range of model spatial and temporal resolutions. This applies to all parametrizations, but the focus here is on the cloud parametrization scheme.

There are a number of aspects of cloud parametrization formulation that can lead to strong sensitivities to resolution but cloud parametrizations are continously being improved and are increasingly robust to horizontal, vertical and temporal resolution. One particular example of global precipitation in the ECMWF model is highlighted, but there are still further improvements to be made.

One future direction is towards a formulation using physical assumptions that can be applied consistently across the different parametrization schemes in a GCM (e.g. cloud, convection and radiation); for example, microphysical particle characteristics or sub-grid PDFs of condensate, humidity or even vertical velocity. This also ties in with improving the representation of interactions between the microphysics at the particle scale and the small scale dynamics unresolved by the model, which in some situations can be the primary driver of cloud and precipitation processes; for example, the role of in-cloud circulations on sub-grid variability, generating higher super-saturations, activating aerosols and enabling ice particle nucleation, or maintaining layers of supercooled liquid water.

To improve the cloud and precipitation parametrizations for GCMs, we therefore need information about sub-grid inhomogeneities and interaction with cloud-scale dynamics with input from observations, detailed microphysical models and cloud resolving models (CRMs). With active modelling studies (e.g. GCSS, http://www.gewex.org/gcss.html), different approaches to the global parametrization problem (Khairoutdinov et al., 2005), the beginnings of large domain/global near convective-scale resolution models (Tomita et al., 2005) and new global observational data sets such as the A-Train with active profiling radar and lidar sensors (Stephens et al., 2002) to name a few of the recent advances, there is certainly potential to improve cloud parametrization across the wide range of model resolutions required for climate and numerical weather prediction now and into the future.

Acknowledgements Thanks to my colleagues at ECMWF and particularly Adrian Tompkins, Peter Becthold, Jean-Jacques Morcrette, Martin Köhler and Gianpaolo Balsamo who have contributed to recent model developments and model climate diagnostics mentioned in this abstract.

5. BIBLIOGRAPHY

Adler R. F., G. J. Huffman, A. Chang, et al., (2003). The Version-2 Global Precipitation Climatology Project (GPCP) monthly precipitation analysis (1979-present), *J. Hydrometeor.*, **4**, 1147-1167.

Hogan, R. J., and A. J. Illingworth, (2000). Deriving cloud overlap statistics from radar., *Quart. J. Roy. Meteor. Soc.*, **126A**, 2903-2909.

Geleyn, J-F., and A. Hollingsworth, (1979). An economical analytical method for the computation of the interaction between scattering and line absorption of radiation. *Beitr. Phys. Atmos.*, **52**, 1-16.

Gregory, D., D. Wilson, and A. Bushell, (2002). Insights into cloud parametrization provided by a prognostic approach. *Quart. J. Roy. Meteor. Soc.*, **128**, 1485-1504.

Jakob, C. and S. A. Klein (1999). The role of vertically varying cloud fraction in the parametrization of microphysical processes in the ECMWF model. *Quart. J. Roy. Meteor. Soc.*, **125**, 941-965.

Jakob, C. and S. A. Klein (2000). A parametrization of the effects of cloud and precipitation overlap for use in general-circulation models. *Quart. J. Roy. Meteor. Soc.*, **126**, 2525-2544.

Khairoutdinov M. F., D. A. Randall, and C. DeMott, 2005: Simulations of the atmospheric general circulation using a cloud-resolving model as a superparameterization of physical processes. *J. Atmos. Sci.*, **62**, 2136-2154.

Larson, V. E., (2004). Prognostic equations for cloud fraction and liquid water and their relation to filtered density functions. *J. Atmos. Sci.*, **61**, 338-351.

Mace, G. G., and S. Benson-Troth, (2002). Cloud-layer overlap characteristics derived from long-term cloud radar data. *J. Climate*, **15**, 2505-2515.

Morcrette, J.-J, P. Bechtold, A. Beljaars, A. Benedetti, A. Bonet, F. Doblas-Reyes, J. Hague, M. Hamrud, J. Haseler, J.W. Kaiser, M. Leutbecher, G. Mozdzynski, M. Razinger, D. Salmond, S. Serrar, M. Suttie, A. Tompkins, A. Untch and A. Weisheimer, (2007). Recent advances in radiation transfer parametrizations. ECMWF Technical Memorandum No.539, ECMWF, UK.

Naud, C.M., A. Del Genio, G.G. Mace, S. Benson, E.E. Clothiaux, and P. Kollias, (2008). Impact of Dynamics and Atmospheric State on Cloud Vertical Overlap. *J. Climate*, **21**, 1758-1770.

Oreopoulos, L., and M. Khairoutdinov, (2003). Overlap properties of clouds generated by a cloud-resolving model. *J. Geophys. Res.*, **108**, D15, 4479,doi:10.1029/2002JD003329.

Pincus, R., and S. A. Klein, (2000). Unresolved spatial variability and microphysical process rates in large-scale models. *J. Geophys. Res.*, **105**, D22, doi:10.1029/2000JD900504.

Räisänen, P., H. W. Barker, M. F. Khairoutdinov, J. Li, D. A. Randall, (2004). Stochastic generation of subgrid-scale cloudy columns for large-scale models. *Quart. J. Roy. Meteorol. Soc.*, **130**, 2047-2067.

Stephens, G. L., et al., 2002: The CloudSat mission and the A-Train: A new dimension of space-based observations of clouds and precipitation. *Bull. Amer. Meteor. Soc.*, **83**, 1771-1790.

Tiedtke, M. (1993). Representation of clouds in large scale models. *Mon. Wea. Rev.*, **117**, 1779-1800.

Tomita, H., H. Miura, S. Iga, T. Nasuno, and M. Satoh (2005), A global cloud-resolving simulation: Preliminary results from an aqua planet experiment, *Geophys. Res. Lett.*, **32**, L08805, doi:10.1029/2005GL022459.

Tompkins, A. M. (2002). A prognostic parameterization for the subgrid-scale variability of water vapor and clouds in large-scale models and its use to diagnose cloud cover. *J. Atmos. Sci.*, **59**, 1917-1942.

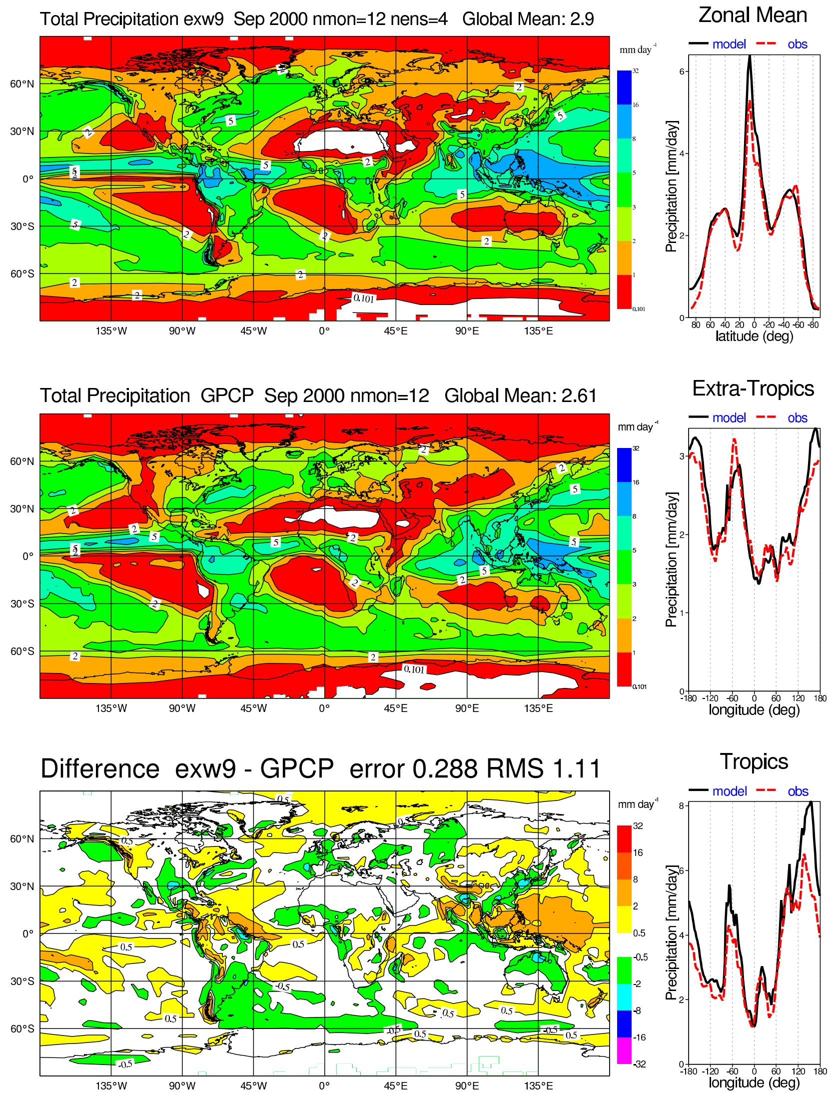

Figure 1: Comparison of global precipitation (mm/day) averaged over a 1year period from Sep 2000 to Aug 2001 between (top panel) the ECMWF T159L92 IFS model at version CY32R3 and (middle panel) the precipitation estimate from the Global Precipitation Climatology Project (GPCP), with the "model minus obs" differences highlighted in the bottom panel. The right hand panels show zonal and meridional means for the model and GPCP precipitation data.

THE INFLUENCE OF AEROSOLS ON CLOUD PROPERTIES AND ALBEDO VARIABILITY IN THE SOUTHEAST PACIFIC

Rhea George[1], Robert Wood[1]
[1]University of Washington

1. INTRODUCTION

Uncertainties in observations and models describing the climate system cause difficulty in predicting the strength of the anthropogenic component to climate change. Aerosol indirect affects contribute strongly to this uncertainty(IPCC 2007), stemming from uncertainties in aerosol emissions and physicochemical processes, uncertainties in how aerosols affect cloud microphysical properties (first indirect effect), and in how clouds respond dynamically to changes in their microphysics(second indirect effect). Observational studies of these effects can be skewed by the particular meteorological conditions and larger scale dynamics and thermodynamics present during the particular time of measurement. Modeling studies can control for the influence of meteorology, but are frequently limited by computing power, either by the need to parameterize small scale processes such as turbulence and cloud microphysical processes in larger scale climate models, or by a lack of generality for high resolution models such as large eddy simulation. There is a need for better observational constraints on regional and global models. This problem necessitates analysis not only of the mean state of cloud properties, but also an understanding of factors controlling cloud variability. To build a better understanding of the influence of aerosols on climate we investigate the relative importance of variability in cloud microphysics and macrophysics on the variability of the climate relevant quantity albedo in the Southeast Pacific. The goal is to compose observational constraints for later modeling studies based on variability.

2. REGION OF STUDY

The albedo of stratocumulus clouds is known to be susceptible to aerosols (Platnick and Twomey 1994) and their homogeneity allows their macrophysical and microphysical properties to be determined reasonably accurately using satellite remote sensing. Marine stratocumulus clouds have been difficult to simulate accurately in general circulation models (Zhang et al. 2005) and these deficiencies render the representation of the aerosol indirect effects in these models highly uncertain (Lohmann and Feichter 2005). The largest and most persistent deck of stratocumulus clouds over subtropical oceans (e.g. Klein and Hartmann 1993) is present in the Southeast Pacific off the coast of South America, where there is a significant source of anthropogenic aerosols that make it a suitable environment for study. A downward branch of the Hadley Cell circulation near 30° S causes a persistent subtropical high throughout the year near 90° W. The Andes effectively block westerly flow, increasing the southeasterly winds associated with the surface high. These strong trade winds cause strong upwelling of cold ocean water near the coast. Hence the Southeast Pacific is a region of strong lower tropospheric stability which results in extensive marine stratocumulus almost all year round (Richter and Mechoso, 2004). Copper smelters near the coasts of Chile and Peru are a major source of oxidized sulfur emissions, which total to about 1.5 TgS yr-1. This is similar to the total sulfur emissions from Mexico or Germany (Benkovitz et al. 1996). Natural emissions from volcanic and biogenic sources and DMS oxidation products from the ocean also contribute to the concentration of cloud concentration nuclei. While the contri-

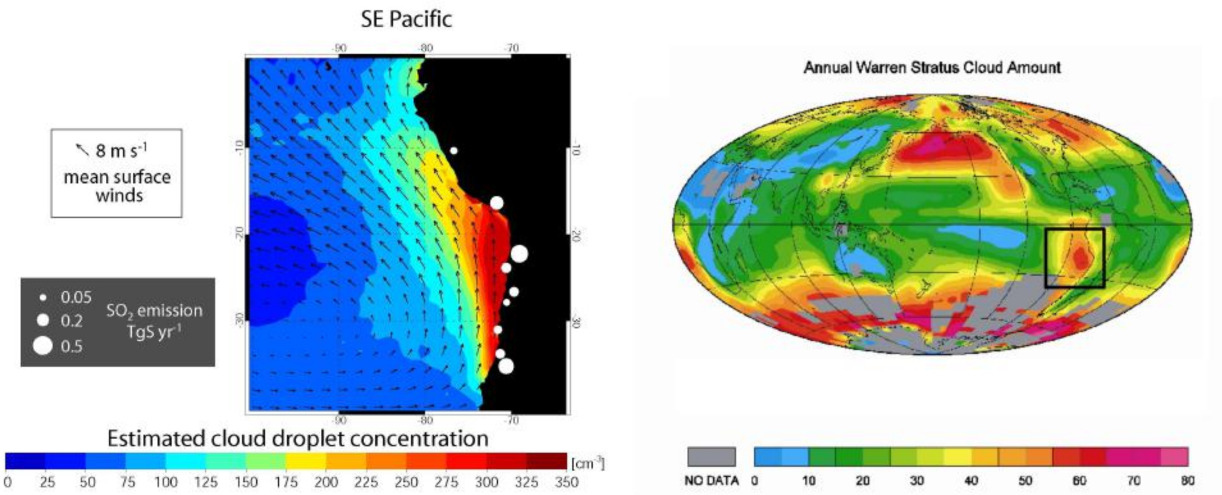

Figure 1: *Top: Annual mean(2001-2004) cloud droplet concentration for overcast (cloud cover $>$ .8) warm clouds. Also shown are the annual mean surface winds from Quickscat(arrows) and annual emissions of SO2 from major sources(filled circles) (Wood 2006).Bottom: Annual mean cloud amount(Hahn,1990)*

bution from the ocean sources is uncertain, it is unlikely to be sufficient to explain the high droplet concentrations observed downwind of the smelters along the coasts of Chile and Peru (Bates et al. 1992). The Andes act as a natural barrier to the dispersion of aerosols and aerosol precursor gases and the relatively steady trade winds reduce the dimensionality of the transport problem in this region.

3. DATA

We use spatially averaged 1x1° daily MODIS data from the NASA Terra satellite for the time period 2000-2006 to compute an estimate of albedo,α,and investigate the dominant sources of variability in a spatial domain of 10-40°S and 100-70° W. In particular, we use cloud droplet effective radius r_e, low cloud fraction (fraction of the sky covered by clouds with cloud top temperature warmer than 273 K), CF, and cloud liquid water path, LWP. When considering meteorological influence, NCEP reanalysis sea level pressure,SLP, data provides us with large-scale information. We consider cloud droplet concentration, N_d, rather than r_e as a measure of the influence of cloud microphysics, as it is not as susceptible to influence by the macrophysical quantity LWP and is more fundamentally related to the underlying aerosol field. N_d was computed from r_e and optical depth,τ, via the relationship:

$$N_d = K\tau^{\frac{1}{2}} r_e^{-\frac{5}{2}} \quad (1)$$

Where K is a thermodynamic constant for an assumed adiabatic cloud (Bennartz, 2007), and τ has been calculated by the relationship:

$$\tau = \frac{9}{5}\frac{LWP}{\rho_w r_e} \quad (2)$$

which uses the observationally supported assumption that liquid water content increases linearly with height within the cloud layer.

4. ALBEDO COMPUTATION

Over the ocean, the average albedo of a region is simply related to the albedo of cloud,α_{cloud}, and cloud fraction by the relationship:

$$\alpha = \alpha_{cloud}CF + (1 - CF)\alpha_{clear} \quad (3)$$

While there are many ways to compute α_{cloud}, sensitivity tests demonstrate that the dominant patterns of variability are not significantly influenced by the particular choice of albedo proxy. Because MODIS data are collected at a local time of roughly 10:30 AM, we consider the albedo due to collimated incident radiation, whereby the incident solar zenith angle θ_s,or the cosine of that angle μ_0, varies in our region of interest with latitude and day of year. While near-infrared absorption by water vapor has the potential to alter the broadband impact of microphysics and macrophysics on albedo, as a first step in understanding variability we restricted the study to the visible region. Most of the incoming solar radiation lies within this spectral range,where absorption is fairly negligible(Slingo,1982) and thus we make a conservative scattering assumption, so that α_{cloud} solely depends on the $\tau_{visible}$ of the cloud and θ_s. The cloud layer is assumed to be plane parallel. Even in relatively uniform stratocumulus clouds the plane parallel assumption can introduce an albedo bias due to horizontally inhomogenous LWP (Cahalan,1994), but for the purpose of investigating dominant sources of variability initially as simply as possible, we do not account for this yet. Based on equation (37) in King and Harshvardhan 1986, cloud plane albedo is calculated using the two-stream approximation via the delta-Eddington method for conservative scattering. This method performed poorly for values of θ_s close to the horizon (King and Harshvardhan,1986), but since data is collected at 10:30 AM, the applicable θ_s's are within the range that the delta-Eddington method is appropriate. Of all the methods compared by King and Harshvardhan, the delta-Eddington method produced results closest to the asymptotic solution for plane albedo calculation, for all values of optical depth, where $\mu_0 > .5$ and conservative scattering is assumed. We approach the variability of albedo with its variance as a measure of dispersion. The clear sky albedo is assumed to be constant at about .1. Over the ocean it has a small variance, and because our region of interest often has a high cloud fraction, the clear sky albedo contribution is relatively small. If we treat (3) as a product of random variables, there is a simple relationship defining the variance of α based on the variance of α_{cloud},of CF, the covariance between the two, and higher order terms(See section 6). The variance of α_{cloud} can also be related, albeit in a more complicated fashion, to the variance of μ_0 and τ, which is controlled by the variance of N_d and LWP. Although these distributions are skewed, we can define each variable as a sum of a mean and perturbation, leading us to results independent of distribution shape. By considering the relative contribution of each variable to the overall σ_α^2, we can define the relative influence of microphysics versus macrophysics and help assess the potential importance of aerosols in contributing to the variance in albedo as a function of location.

5. INFLUENCE OF METEOROLOGY

In the observational data used, microphysical and macrophysical properties affecting the albedo variability may be influenced by large-scale conditions as well. While macrophysical cloud properties such as cloud fractional coverage are modulated, on sub-seasonal timescales, by the strength of the subtropical high (Klein et al. 1995) there is also evidence that that cloud microphysical properties are also modulated by changes to the large scale meteorology over the SE Pacific (e.g. Wood et al. 2007). We use Empirical Orthogonal Function Analysis (EOF) to interpret how sub-seasonal variability in cloud properties relates to the variability in SLP. Values are weighted by the square root of the cosine of the latitude so that equal areas receive equal variance weighting independent of latitude. A running mean of 31 days is removed from the surface pressure at each location to remove the seasonal cycle. In any case, it was found that there is little power between 30 and 90 days, and so the sub-seasonal and sub-monthly variability are both dominated by variability on timescales of less than a month. The dominant mode (first EOF) of sub-seasonal variability in SLP explains 60-70$\%$ of the total sea level pressure variance. The first principal component is significant above the null-hypothesis (a red noise spectrum with the same autocorrelation with a maximum power in periods of 10-20 days). Lag analysis and comparison with a time series of average sea level pressure in a small box around 30° S, 90° W indicates that this dominant mode represents the strengthening and weakening of the subtropical high. Mid-latitude and other types of moving and stationary waves centered to the south of our domain modulate the strength of the subtropical high. Figure 2 shows the dominant mode EOF.

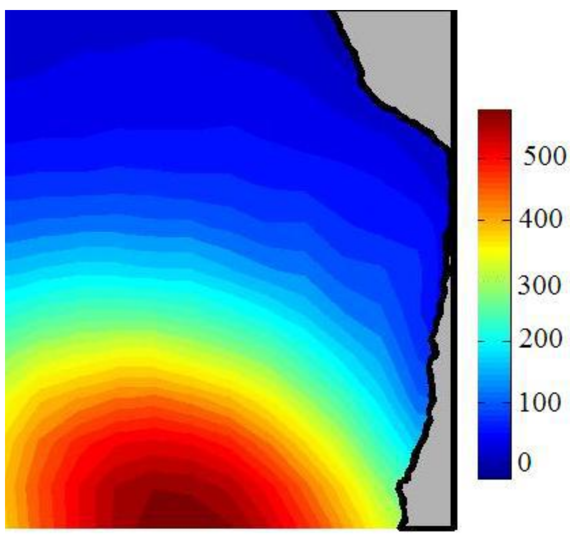

Figure 2: *First EOF of SLP*

Using the principal component time series as an index for the strength of the subtropical high, we can see the covariation of the dominant mode SLP with other variables of interest. Figure 3 shows the patterns of subseasonal variability in CF and r_e(N_d displays a similar pattern) formed by compositing on this index. Composites are generated by differencing the mean fields formed on those days with strong positive and strong negative SLP anomalies (strong indicating that the magnitude of the principal component anomaly is greater than one standard deviation away from zero). The results suggest that to the north of 20° S microphysical variability may be significantly more important at driving cloud albedo variability than it is further to the south where cloud cover variations are more significant.

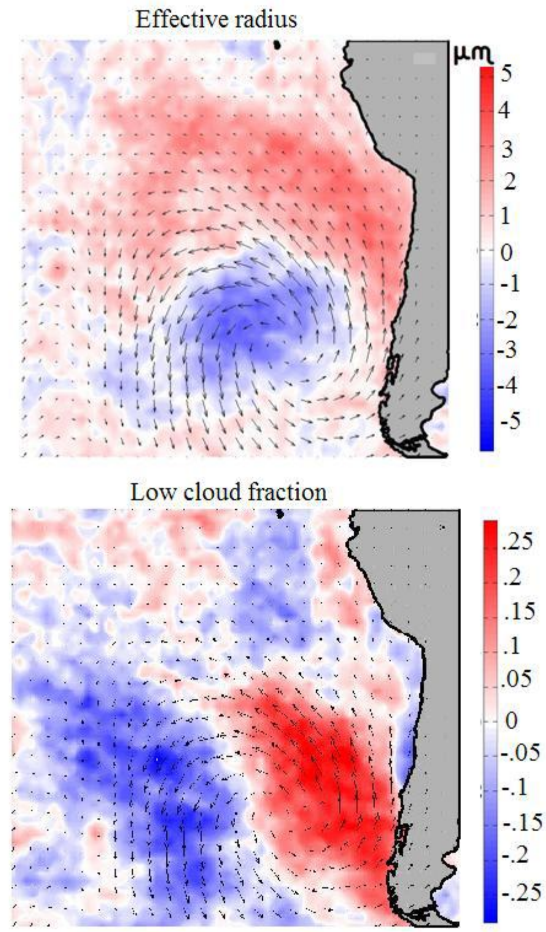

Figure 3: *Composites of r_e and CF on first SLP principal component. The vectors are composite Quickscat surface winds.Max wind anomaly is 1 $\frac{m}{s}$*

6. PRELIMINARY VARIABILITY ANALYSIS

The impact of meteorology will need to be considered. We also investigate the sources of albedo variability directly. The equation for α is a simple product, so the variance can be defined as:

$$\sigma_\alpha^2 = \overline{\alpha'^2} = \overline{(\alpha_{cloud} - \alpha_{clear})CF'} + \overline{\overline{CF}\alpha'_{cloud}} + 2\overline{CF}(\overline{\alpha_{cloud}} - \alpha_{clear})\overline{\alpha'_{cloud}CF'} - \overline{\alpha'^2_{cloud}CF'^2} - (\overline{\alpha'_{cloud}CF'})^2$$

Where for some variable x that is a function of time,$\overline{x}$ is the mean of x, and x' composes the perturbations from that mean. Figure 4 shows the relative contribution of these terms

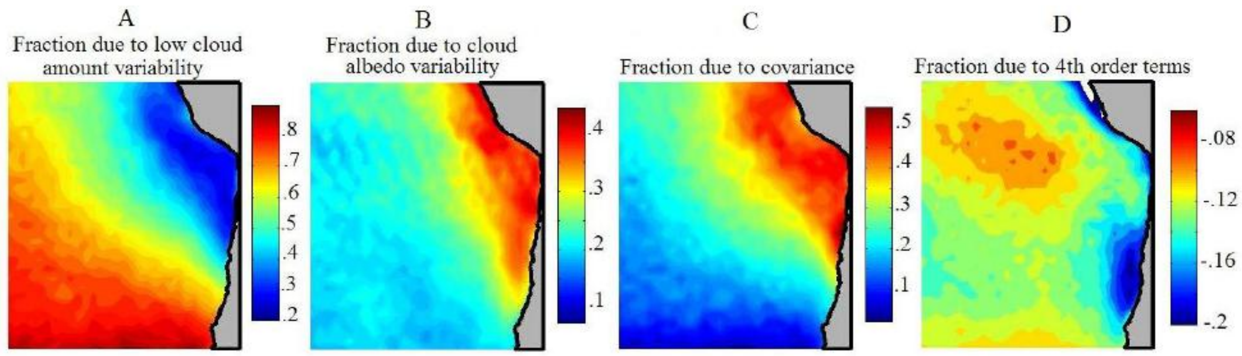

Figure 4: *Fraction of albedo variance attributed to A: variance of CF, B: variance of* α_{cloud}*,C:covariance between* α_{cloud} *and CF, and D: higher order terms in equation of variance*

in our region of interest. The third term is the contribution to the variance by the covariance between low cloud fraction and cloud albedo. The 4th order terms make up for whatever variances is unexplained, and are related to the kurtosis of the distributions. We see that along the coast of Chile and Peru where aerosols concentrations are high, the higher order terms make a non-negligible contribution to the variance, suggesting a relatively higher level of complexity in physical processes. However these terms are small enough that they won't impact whether microphysics or macrophysics dominates α variability. Near the coast where CF tends to be high, the variance explained by CF is substantially lower than in surrounding areas, while α_{cloud} variability and its covariation with CF are more important than further away from the coast. These 4 terms completely explain the variance in albedo, and thus provide a useful tool for distinguishing the impacts of the variances of the defining variables. A similar analysis is applied to $\tau = CN_d^{\frac{1}{3}}LWP^{\frac{5}{6}}$,where C is a constant(Wood,2006), treating τ as a product of the variables $N_d^{\frac{1}{3}}$ and $LWP^{\frac{5}{6}}$. Figure 5 shows the relative contributions of each of these variables, and the preliminary result indicates LWP, or macrophysics dominates τ variability. The minimal contribution by fourth order terms allows us to focus on the two main variables and their covariation. Near the coast the microphysical influence is weaker than in surrounding areas,where high N_d persist(as in Figure 1) and it is the covariation of N_d with LWP that is relatively large compared to surrounding areas.The flip in sign of covariance between N_d and LWP is an interesting feature we will investigate further, though as shown by section 5, it is likely meteorology plays a dominant role in this geographic variability of variance explained.

7. CONCLUSIONS

We have seen that meteorology influences all parameters(not all shown here), and that how it impacts each property varies strongly by geography in the SE Pacific. Meteorology has different impacts on microphysical and macrophysical quantities, and understanding these impacts will help to better understand how aerosols may be influenced by the same meteorology and contribute to these cloud property changes. How the variability in CF and α_{cloud} influence the albedo variability is also strongly tied to geography.More contribution by α_{cloud} near the coast indicates a potential for aerosols to be playing a role. LWP variability appears to dominate τ variability, but the contribution by the covariance with N_d and N_d variance downwind of an anthropogenic aerosol source indicates small scale processes influence on albedo to some extent, necessitating further investigation.

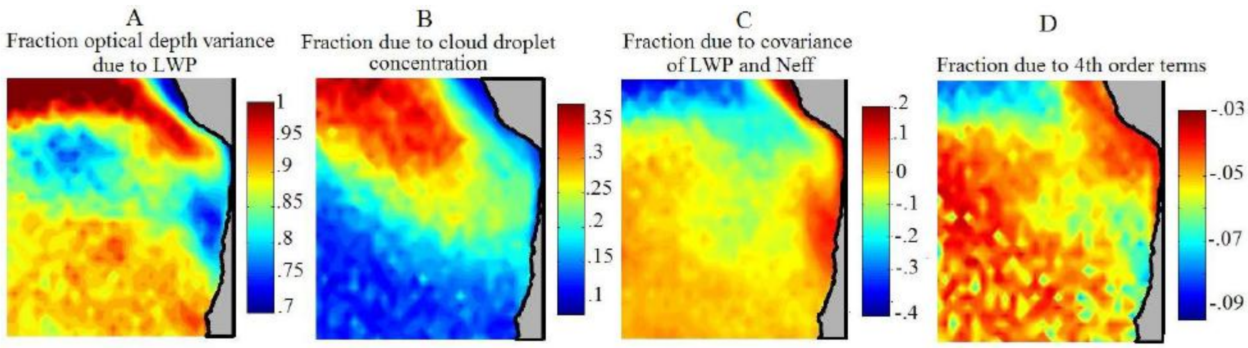

Figure 5: Fraction of τ variance attributed to A: variance of LWP, B: variance of N_d, C:covariance between LWP and N_d, and D: higher order terms in equation of variance

8. FUTURE WORK

The effect of meteorology on the variance analysis will be pursued, and we will extend the analysis in several ways. We expect τ variability to dominate μ_0 variability in α_{cloud} variability, and this will be quantitatively assessed. A running mean will be removed to examine variability on sub-seasonal timescales. Sensitivity tests will be performed, to consider the impacts of our assumptions, for example of negligible near-IR absorption. In the case of non-conservative scattering, the delta-Eddington method performed poorly in King, 1986, and a different method for computing albedo at absorptive wavelengths will need to be used. Analysis will be performed in a lagrangian sense as well, using trajectories to minimize the influence of meteorology. We will form observational metrics of success for model based on variability, and finally build, run, and test a regional model that accurately reproduces mean states and variances of our variables of interest.

9. REFERENCES

[1]Bates, T. S., B. K. Lamb,et al., 1992: Sulfur emissions to the atmosphere from natural sources. J. Atmos. Chem., 14, 315-337.

[2]Benkovitz, C. M., J. Dignon, et.al., 1996: Global inventories of anthropogenic emissions of SO2 and NOx, J. Geophys. Res., 101, 29239-29253.

[3]Bennartz, R., and Harshvardhan,Global assessment of marine boundary layer cloud droplet number conctration from satellite, 2007: J. Geophys. Res.,112,D02201,2007.

[4]Cahalan,R.,Ridgway,W.,etal.,1994:The albedo of fractal stratocumulus clouds, J.Atmos.Sci.,51,(16),2434-55.

[5]Hahn, C.,S.Warren,et. al., 1990: Atlas of simultaneous occurrence of different cloud types over land.

[6]IPCC 2007: Changes in Atmospheric Constituents and in Radiative Forcing,Foster, P.,Ramswamy,V., Cambridge Univ. Press.,Cambridge,U.K.

[7]King, M. D.; Harshvardhan, Comparative accuracy of selected multiple-scattering approximations.1986: J. Atmos. Sci., 43, (8), 784-801.

[8]Klein, S.A., and D.L. Hartmann, 1993: The seasonal cycle of low stratiform clouds. J. Clim., 6, 1587-1606.

[9]Klein, S. A., D. L. Hartmann, et al. 1995: On the Relationships among Low-Cloud Structure, Sea Surface Temperature, and Atmospheric Circulation in the Summertime Northeast Pacific. J.Clim. 8, 1140-1155.

[10]Lohmann,U., and J. Feichter, 2005: Global indirect aerosol effects: a review. Atmos. Chem. Phys. Disc., 5, 715-737.

[11]Platnick, S. and S. Twomey, 1994: Determining the susceptibility of cloud albedo to changes in droplet concentration with the AVHRR. J. Appl. Met.,33,334-347.

[12]Richter, I., and C.R. Mechoso, 2004: Orographic influences on the annual cycle of Namibian stratocumulus clouds. Geophysical Research Letters, 31, L24108.

[13]Slingo, A.; Schrecker, H. M., 1982: On the shortwave radiative properties of stratiform water clouds. Quart. J. R. Met. Soc.,108,(456),407-426.

[14]Wood, R., C.S. Bretherton, B. Hubert, C. R. Mechoso, and R. Weller, 2006: VOCALS Scientific Program Overview, proposal submitted to NSF. Available at $http : \backslash\backslash www.eol.ucar.edu/projects/vocals/science\_planning/VOCALS\_SPO\_rev\_aug06.pdf$.

[15]Wood, R., 2007: Cancellation of aerosol indirect effects in marine stratocumulus through cloud thinning, J. Atmos. Sci., 64(7)

[16]Zhang Y.Y., G.G. Mace, 2006: Retrieval of cirrus microphysical properties with a suite of algorithms for airborne and spaceborne lidar, radar,and radiometer data, J. App. Met. and Clim.,45(12):1665-1689

VERTICAL CLOUD CLIMATOLOGY DURING TC4 DERIVED FROM HIGH-ALTITUDE AIRCRAFT LIDAR+RADAR

Dennis Hlavka[1], Lin Tian[2], William Hart[1], Lihua Li[2], Matthew McGill[3], and Gerald Heymsfield[3]
[1]SSAI, Code 613.1, NASA/Goddard Space Flight Center
[2]UMBC, Code 613.1, NASA/Goddard Space Flight Center
[3]Code 613.1, NASA/Goddard Space Flight Center

1. INTRODUCTION

Accurate knowledge of the vertical distribution of clouds is an important factor in understanding the Earth/atmosphere radiative balance and in improving weather/climate forecast models. Only since nadir pointing lidars and cloud-profiling radars flew together on high-altitude aircraft or satellites have accurate measurements of the locations of all cloud layers in the full atmospheric column been achievable covering large regions. Lidar can detect backscatter from optically thin cirrus layers whose particles are too small for the radar to detect. Radar provides reflectivity profiles through thick cloud layers of larger particles that lidar cannot penetrate. Higher level analysis of the overlap region where both instruments have cloud signals can lead to retrieval estimates of ice particle size.

The first test of combining high-altitude nadir lidar and radar data was achieved during CRYSTAL-FACE in July 2002 using the Cloud Physics Lidar (CPL) and the Cloud Radar System (CRS) on board the NASA ER-2 aircraft. Results from analyzing specific case studies for anvil morphology and radar optical depth sensitivity are shown in McGill (2004). The paper also describes the details for combining the two data sets. A description of the CPL instrument is shown in McGill (2002). Descriptions of the CRS instrument can be found in Li (2004) and Racette (2003). With the launch of the CloudSat and CALIPSO satellites in April 2006, a combined data set using the CALIOP lidar and CPR radar (the 2B-GEOPROF-LIDAR product) has been developed. It is the first with global coverage starting in June 2006 and continues to this day. Details of this combined product are described in Mace (2007).

Three NASA ER-2 aircraft experiments during the summers of 2006 and 2007, with the CPL and CRS on board, have provided the opportunity to formulate new sets of high-quality merged vertical cloud location profiles. In this presentation, we will show results of a cloud statistical analysis for a whole field experiment for the first time. We chose the Tropical Composition, Cloud and Climate Coupling (TC4) experiment in Costa Rica, Central America in July-August 2007 for its high scientific interest and complex tropical cloud formations.

The merged data sets were developed on a per-flight basis and produce cloud and aerosol layer location for every 200 meters (1 second) along track when both the CPL and CRS were operating, with 30 meter vertical resolution. Profiles show where lidar only, radar only, or both signals were observed. The corresponding temperature and pressure profiles, matching the resolution of the combined system, are also recorded. Ground stroke information for both lidar and radar are recorded. Statistics of vertical cloud probability, average number of cloud layers, regional differences, and land verses ocean differences are tabulated. Overall percentage of cloudy pixels and frequency of lidar and radar ground stroke detection are formulated.

2. SAMPLE PRODUCTS FROM MERGE

To better understand the parameters involved in the statistical analysis of clouds during the whole TC4 experiment, it is prudent to show examples of the CPL-CRS merge products. A short segment of the August 8, 2007 flight over the Pacific Ocean is a good example. Figure 1 shows profile products from an optically thick anvil cirrus.

From the type characterization map, the total number of layers and the layer top and bottom heights can be calculated per profile. Vertical cloud frequency profiles can

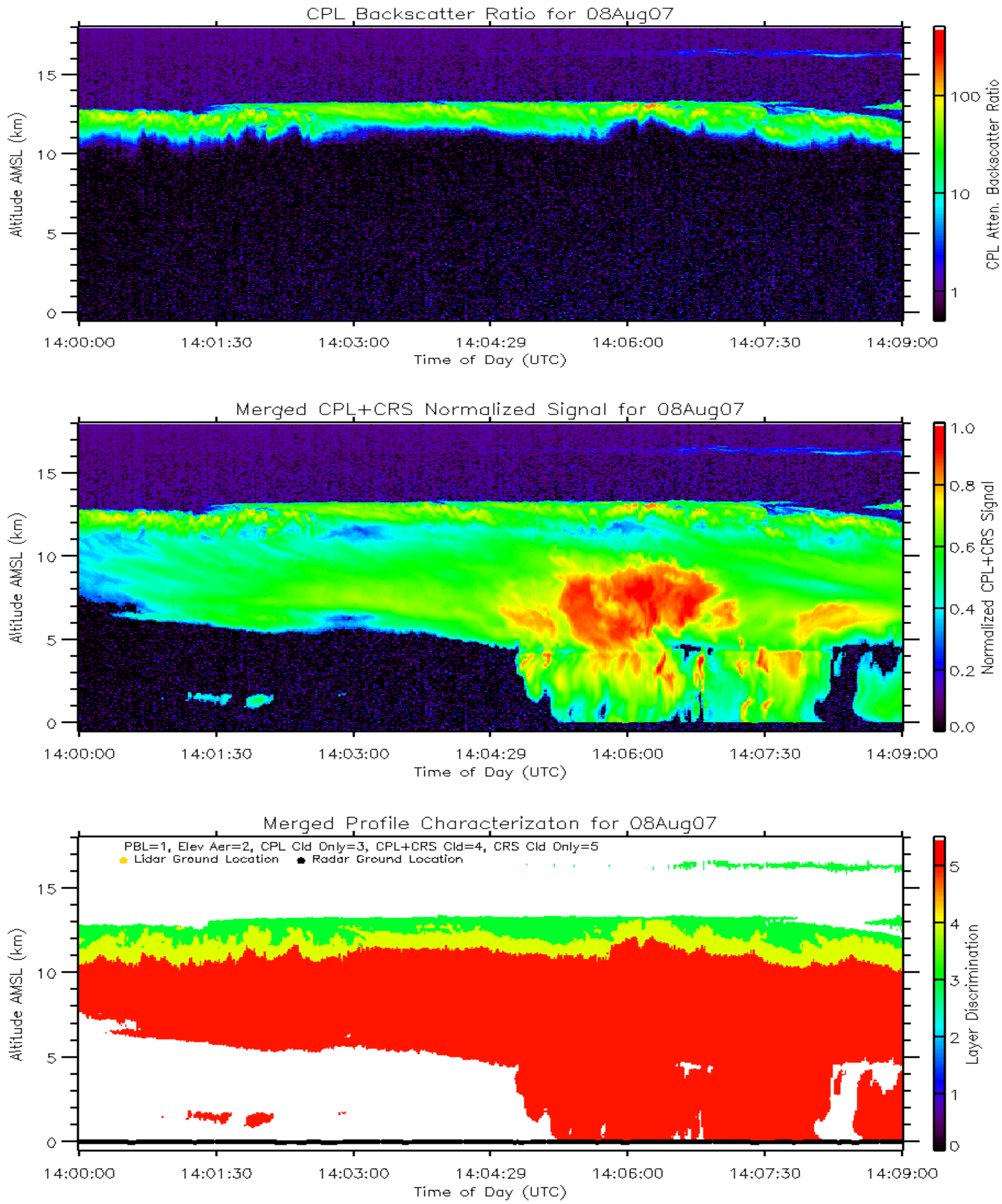

Figure 1: CPL lidar signal only (top), merged CPL lidar-CRS radar signal (middle), and map of signal type characterization (bottom) during a 9 minute segment of the August 8, 2007 ER-2 flight during TC4. The type characterization maps the vertical location of cloud pixels that only CPL detected (green), cloud pixels that only CRS detected (red), and cloud pixels that were detected by both instruments (yellow).

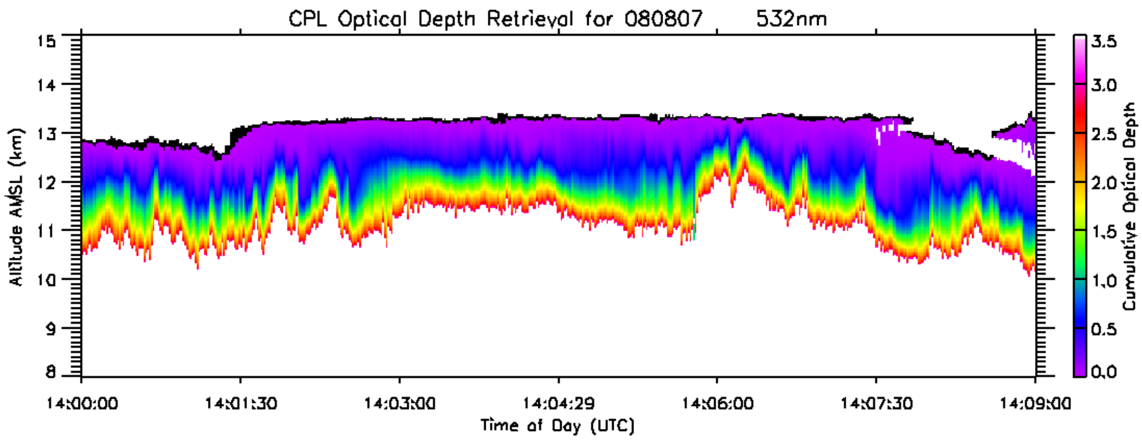

Figure 2: Cumulative optical depth calculations from the CPL lidar portion of the cloud complex in Figure 1. In this case, the lidar signal becomes totally attenuated at an optical depth of ~3.0. Optical depth of 1.0 is just into the green and optical depth of 0.5 is in the middle of the dark blue.

be accumulated when a tally is kept where pixels are populated with clouds. The thick black line at the bottom of the "characterization map" of Figure 1 marks the detected ground stroke location for the CRS radar. The radar signal penetrates to the earth's surface and produces a signal spike when it hits the earth, unless the signal is totally attenuated by moderate to heavy rain. Lack of a radar ground stroke can be used to locate significant rain regions. The map also shows where the detected ground stroke location for the CPL lidar is by a yellow line. However, in this example, all profiles in the time segment have clouds that totally attenuate the lidar signal, so no line is found. The lidar attenuates much sooner than the radar, and in general, attenuates at an optical depth of ~3.

Cumulative optical depth is another product from the merge file, calculated in the area of the cloud where the lidar can retrieve an extinction profile. Figure 2 shows a vertical expansion of the lidar region of the anvil cloud in Figure 1 with cumulative optical depth displayed. From an experiment-wide accumulation of these profiles, the average height of a specific optical depth can be calculated.

3. VERTICAL CLOUD CLIMATOLOGY DURING TC4

Merge data sets were processed for 12 of the 13 flights during TC4. CRS hardware problems caused July 25 data to be missed. The ER-2 was based at San Jose, Costa Rica and executed flights in and around Central America, the Caribbean Sea, and the Pacific Ocean. Cloud statistics were developed for the following five regions: Full TC4 Study Area, San Jose, Panama Bight, Caribbean, and Pacific South. Figure 3 shows the location of these regions on a map of Central America. The regions were formulated by the author based on target areas during the TC4 deployment.

Table 1 displays various cloud statistics calculated during TC4 for the 5 regions. The probability of having a cloud in any 1-second profile is very high in all regions except the Caribbean. The Caribbean had a much different cloud pattern compared to the other regions with a tendency to have only one or two scattered high layers and only a few cumuli. The Pacific South region tended to have more low clouds, especially stratocumulus. The other regions had complex cloud systems at many levels. Inferring from the lidar ground stroke frequency for the full TC4 study area, only about 31 percent of the profiles had total column optical depth below 3.0. The Caribbean region was an exception with 97 percent. The radar ground stroke frequency

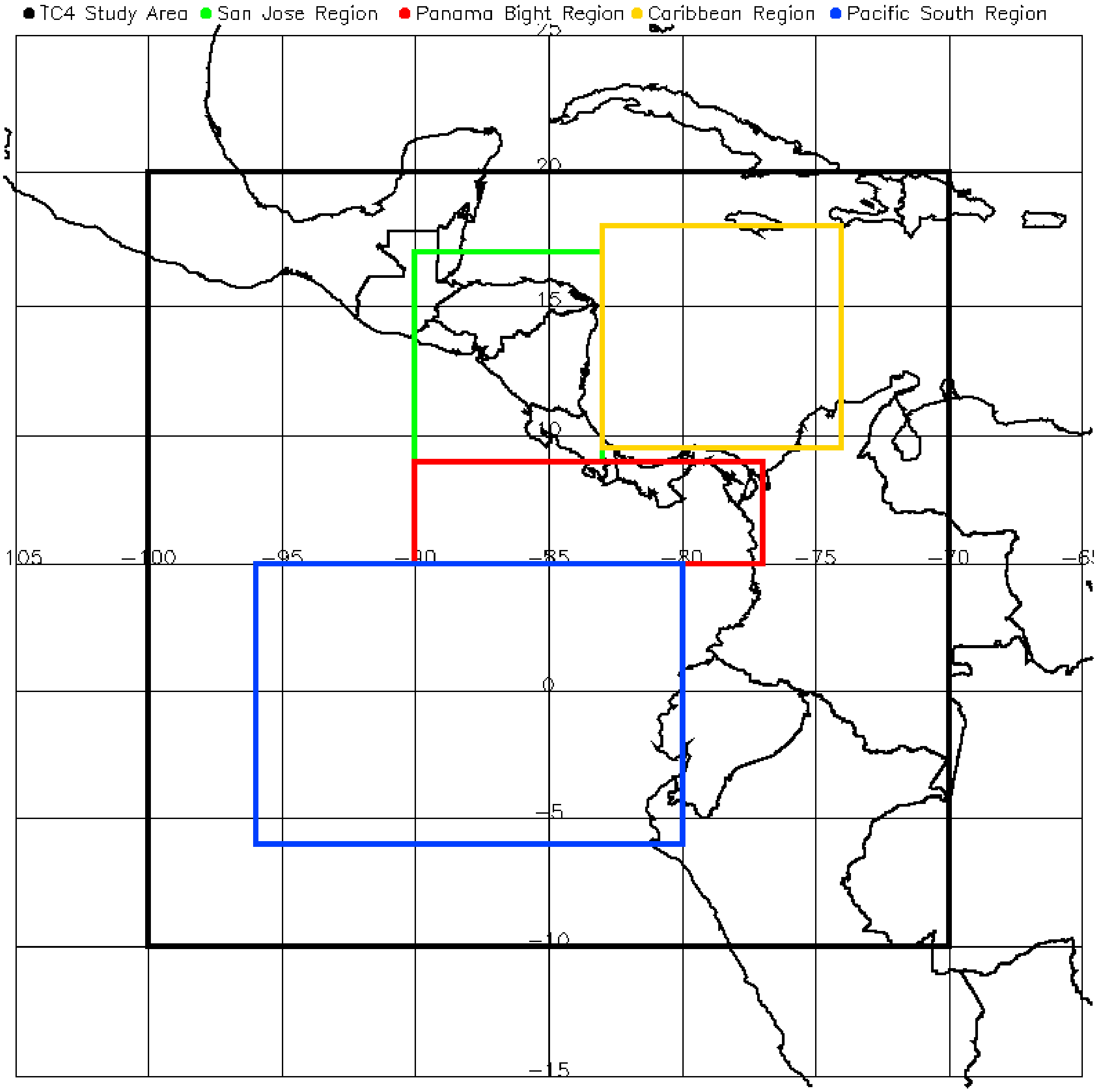

Figure 3: Map of the five regions of the TC4 field experiment conducted July-August, 2007.

was very high, averaging 93.5 percent for the full TC4 study area. This infers the percentage of profiles where moderate or heavy rain obscured the radar reached 6.5 percent. On average for the full study area, the vertical cloud zone ranged from 12.3 km to 4.0 km or 8.3 km thick. The region with the highest average cloud tops was the San Jose region. The cumulative optical depth heights should be interpreted as follows: the lower the height to reach the specific optical depth level, the more transparent the middle and upper troposphere is. If the height is near sea level, this means it did not fully reach the optical depth threshold. For the full study area, the average height of optical depth 1.0 was 6.0 km and optical depth 3.0 was 4.3 km. The Caribbean region easily had the most transparent atmosphere. It should be noted that the cumulative optical depth includes aerosol layers. Only in the Caribbean region were aerosols (Saharan

Statistic	Full TC4 Study Area	San Jose Region	Panama Bight Region	Caribbean Region	Pacific South Region
Cloudy Profile Frequency (%)	94.3	98.7	98.4	44.1	94.4
CPL Lidar Ground Stroke Frequency (%)	30.6	37.8	20.3	97.1	30.1
CRS Radar Ground Stroke Frequency (%)	93.5	89.6	91.2	99.9	99.3
Avg. Ht. (km) of Highest Cloud Top	12.350 (258.4 hPa)	15.087 (144.5 hPa)	13.364 (192.1 hPa)	10.704 (339.0 hPa)	8.709 (460.5 hPa)
Avg. Ht. (km) of Lowest Cloud Bottom	3.994 (700.2 hPa)	5.480 (607.3 hPa)	4.094 (680.5 hPa)	7.338 (516.8 hPa)	2.411 (826.9 hPa)
Avg. Ht. (km) where Cumulative OD Reaches 1.0	5.968 (590.6 hPa)	7.117 (537.3 hPa)	8.044 (453.1 hPa)	0.098 (1002.5 hPa)	2.103 (833.1 hPa)
Avg. Ht. (km) where Cumulative OD Reaches 3.0	4.258 (698.9 hPa)	3.457 (756.6 hPa)	6.470 (552.5 hPa)	0.085 (1003.9 hPa)	1.644 (866.9 hPa)

Table 1: Cloud and Optical Statistics by Geographic Region

dust) prevalent. Be aware also that the Caribbean region had six times fewer profiles than did the region-by-region average, mostly due to the fact only two flights focused on the region and one of those had missing data.

The TC4 cloud analysis was also performed separately for land versus ocean areas. Because water dominates the region and was the preferred destination during most flights, there were six times more water profiles tabulated than for land. Table 2 shows the same parameters as Table 1, only separated by water and land regions. Because the CRS ground stroke height was the parameter used to determine land or water, profiles that did not have a ground stroke were not used and thus the frequency was 100 percent. In this data base, the land recorded the highest average cloud top height, 3.1 km higher than the ocean.

Probably the two most important statistics coming out of this study are the frequency distribution of the number of cloud layers in the total atmospheric column and the vertical distribution of those clouds.

Statistic	Land Region	Ocean Region
Cloudy Profile Frequency (%)	96.2	93.6
CPL Lidar Ground Stroke Frequency (%)	39.8	31.0
CRS Radar Ground Stroke Frequency (%)	100.0	100.0
Avg. Ht. (km) of Highest Cloud Top	14.870 (147.7 hPa)	11.733 (286.3 hPa)
Avg. Ht. (km) of Lowest Cloud Bottom	4.793 (646.1 hPa)	4.018 (700.7 hPa)
Avg. Ht. (km) where Cumulative OD Reaches 1.0	6.283 (567.5 hPa)	5.502 (619.0 hPa)
Avg. Ht. (km) where Cumulative OD Reaches 3.0	3.037 (762.3 hPa)	3.956 (719.3 hPa)

Table 2: Cloud and Optical Statistics by Surface Type

Figure 4 shows the distribution of the number of cloud layers for 1) the full study area, 2) the Pacific South region, which was a region of optically thin cirrus layers and frequent stratocumulus, and 3) the Panama Bight region, which was a region of active thunderstorms and complex cloud formations. Most regions averaged near two layers per profile. The Caribbean and the Pacific South were the exceptions, averaging 0.70 and 1.68 layers, respectively. The Pacific South region layer distribution showed a sharp peak, with one-layer profiles occurring over 40 percent of the time. Note that the 6-layer category is for <u>6-or-more layers</u> for all graphs. Figure 5 shows the vertical frequency distribution of cloudy pixels in the same regions: the full TC4 study area, the Pacific South region, and the Panama Bight region. Each plot has three distributions: 1) the merged CPL/CRS clouds (green), 2) CPL only clouds (blue), and 3) CRS only clouds (red). For the TC4 study area as a whole, the chance of cloud occurrence was highest (just above 40 percent) between 12 and 13 km. The vertical distribution is somewhat bimodal with another frequency peak near 1 km, probably due to scattered cumulus and stratocumulus. The CPL found few clouds between 9 and 2 km because of signal attenuation, but did pick up the low cumulus when the signal was not fully attenuated. The radar retrieved its highest cloud frequency between 8 and 10 km. For the Pacific South region, the highest frequency of clouds (32 percent) occurred below 1 km, influenced by the predominance of stratocumulus. Two other lesser peaks occurred, one at 10 km and one at 15 km. For the Panama Bight region, clouds were frequent at all levels, with the highest frequency (60 percent) at 12-13 km. Because of lidar signal attenuation, the cloud distribution relied on the CRS radar below 8 km.

Comparing land and water regions, the analysis shows that the land had more of a tendency for multiple cloud layers, with an average of 2.35 layers, as opposed to the water, with an average of 1.95. Figure 6 displays the layer frequency distribution for land and water. Figure 7 shows the vertical distribution differences between land and

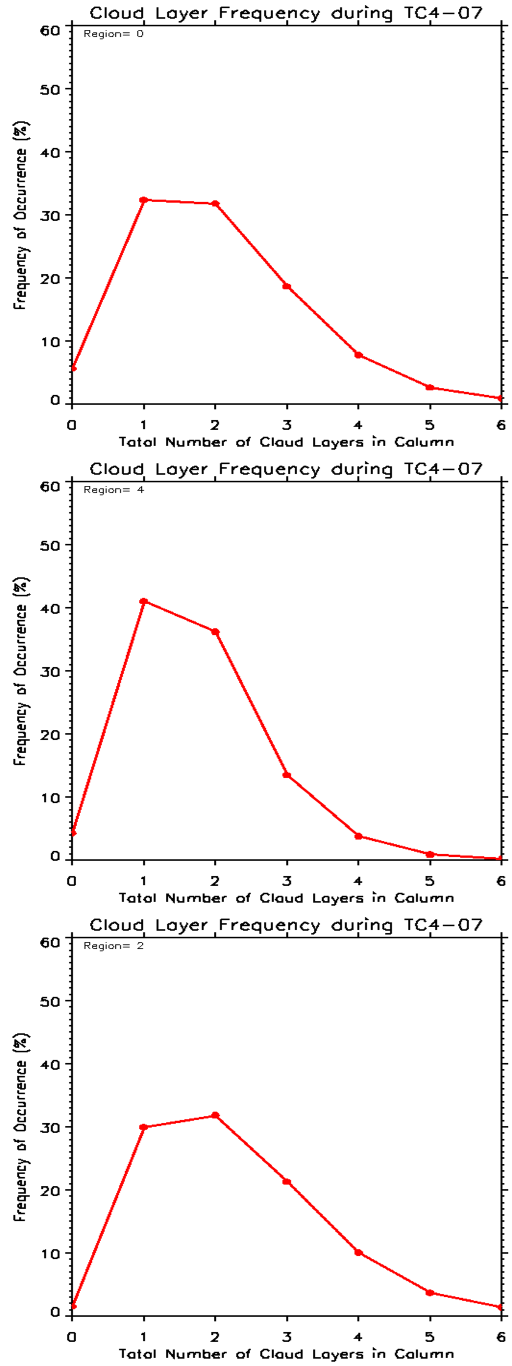

Figure 4: The frequency distribution of total number of cloud layers for Full TC4 region (top), Pacific South Region (middle), and Panama Bight region (bottom). The average number of cloud layers for each region was 2.03, 1.68, and 2.26 respectively. Note that the 6-layer category is for 6-or-more layers for all graphs.

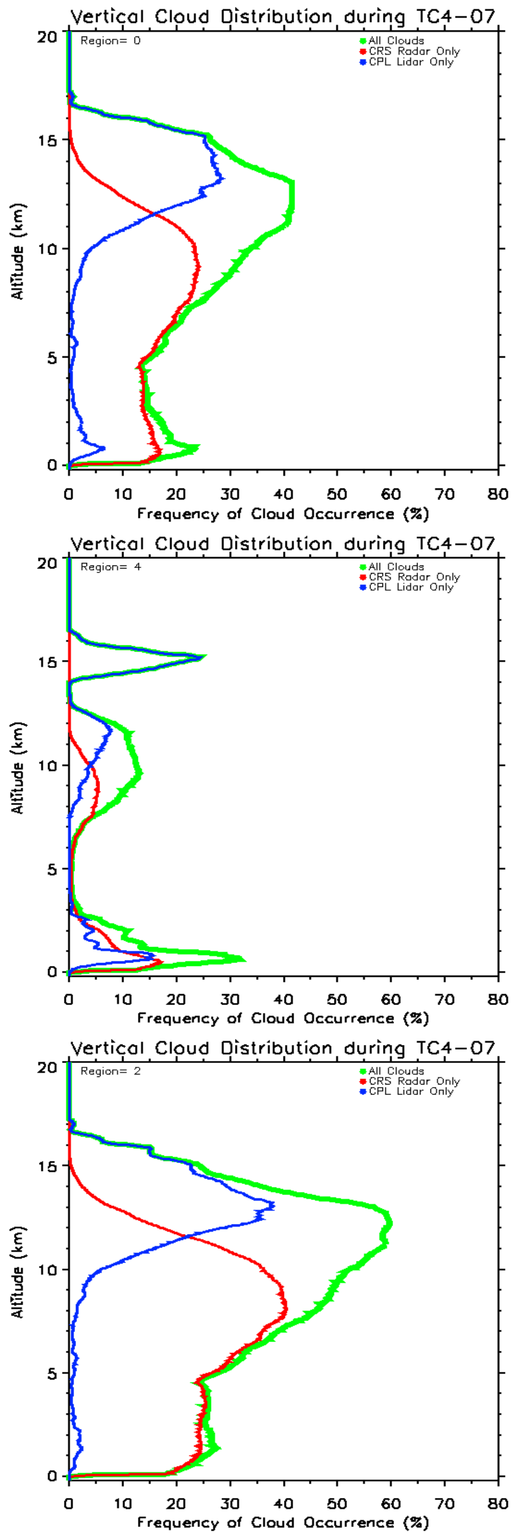

Figure 5: The vertical cloud distribution for Full TC4 region (top), Pacific South region (middle), and Panama Bight region (bottom). The lidar-only cloud frequency is the blue line, the radar-only frequency is the red line, and the merged lidar/radar cloud frequency is the green line.

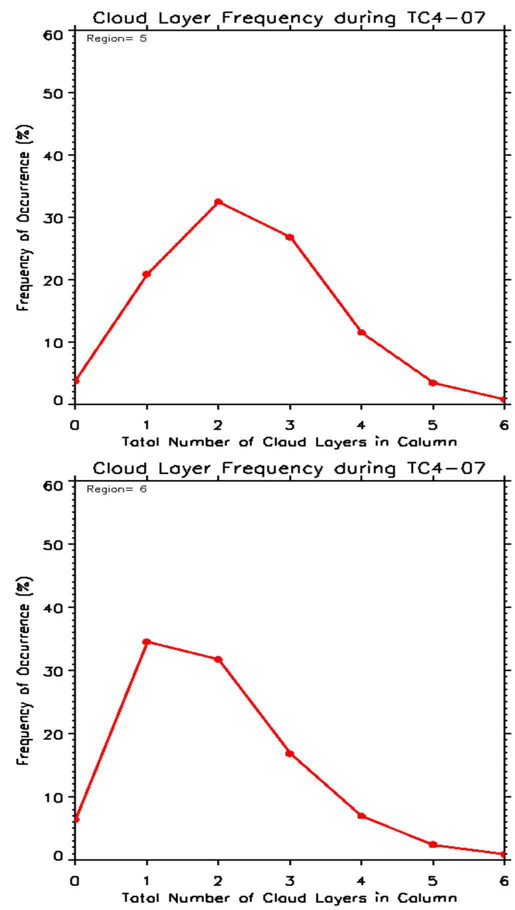

Figure 6: The frequency distribution of total number of cloud layers for Land (top) and Ocean (bottom). The average number of cloud layers for each region was 2.35 and 1.95 respectively. Note that the 6-layer category is for 6-or-more layers for all graphs.

water. The land had a very high frequency (75%) of cloud between 13 and 14 km, but dropped off significantly below that altitude. The ocean region distribution mimics the study area as a whole.

4. SUMMARY

The newly developed CPL lidar and CRS radar merged product is helping to characterize the vertical cloud distributions during the TC4 field experiment. The TC4 Study Area was a very cloudy region, with cloudy profiles occurring 94 percent of the time. One to three cloud layers were common, with the average calculated at 2.03 layers per profile. The average top of the

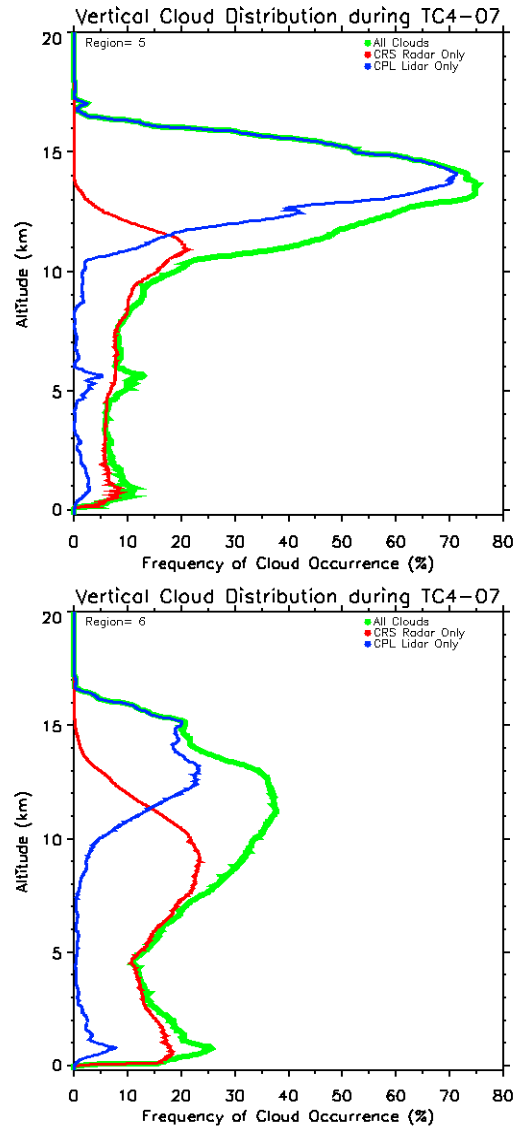

Figure 7: The vertical cloud distribution for Land (top) and Ocean (bottom). The lidar-only cloud frequency is the blue line, the radar-only frequency is the red line, and the merged lidar/radar cloud frequency is the green line.

highest cloud layer reached 12.350 km. From the CPL lidar data, it was determined that the average height where the cumulative optical depth reached 1.0 was located at 5.968 km and where the optical depth reached 3.0 was calculated at 4.258 km. From analysis of the vertical cloud distribution, the upper troposphere had a cloud frequency reaching 42 percent during the study.

5. BIBLIOGRAPHY

McGill, M.J., L. Li, W.D. Hart, G.M. Heymsfield, D.L. Hlavka, P.E. Racette, L. Tian, M.A. Vaughan, and D.M. Winker (2004), Combined lidar-radar remote sensing: Initial results from CRYSTAL-FACE, *Journal of Geophysical Research, 109*, D07203, doi: 10.1029/2003JD004030.

McGill, M.J., D.L. Hlavka, W.D. Hart, J.D. Spinhirne, V.S. Scott, and B. Schmid (2002), The Cloud Physics Lidar: Instrument description and initial measurement results, *Applied Optics, 41*, pg. 3725-3734.

. Li, L., G. M. Heymsfield, P. E. Racette, L. Tian, and E. Zenker, (2004), A 94 GHz cloud radar system on a NASA High-altitude ER-2 aircraft, *J. Atmos. Ocean. Technol., 21,* 1378-1388.

Racette, P. E., G. M. Heymsfield, L. Li, L. Tian, and E. Zenker (2003), The cloud radar system, in *Proceedings of the 31st AMS Conference on Radar Meteorology*, pp. 237-240, Am. Meteorol. Soc., Boston, Mass.

Mace G. G., Q. Zhang, M. Vaughn, R. Marchand, G. Stephens, C. Trepte and D. Winker, (2008), A description of Hydrometeor layer occurrence statistics derived from the first year of merged CloudSat and Calypso data, submitted to *J. Geophys. Res.*

Acknowledgments

The Cloud Physics Lidar and Cloud Radar System are largely supported by NASA's Radiation Sciences Program (Hal Maring, Program Manager). Data shown was collected as part of the Tropical Composition, Cloud and Climate Coupling (TC4) experiment.

IN-SITU CLOUD MEASUREMENTS AND CLIMATE MODELS

by

George A. Isaac, Ismail Gultepe, Alexei V. Korolev,
Faisal S. Boudala and Stewart G. Cober
Cloud Physics and Severe Weather Research Section,
Environment Canada, Toronto, Ontario, M3H 5T4, Canada

1. INTRODUCTION

The ability to measure and characterize cloud parameters has advanced considerably over the past 50 years. In earlier times (e.g. Squires, 1958), cloud drops were captured on a media such as glass slides exposed to the airstream from aircraft platforms and, after suitable corrections, this gave a measure of cloud droplet number concentrations. Those measurements were used to develop the concepts that maritime clouds had droplet concentrations smaller than continental clouds and typical values were assigned to each. That type of characterization still exists today, very often using text book type values of microphysical parameters. However, it is necessary to get away from such simple approaches which use one number characterizations for important variables, ignoring geographic and cloud type differences, and variability on the scale of interest. Only then can progress be made in accurately simulating clouds in climate models.

First, it is necessary to consider the accuracy to which cloud properties must be measured to properly simulate them in numerical model simulations of climate. There have been a few sensitivity studies such as those by Slingo (1990) and Rotstayn (1999).

Slingo (1990) stated:

> "The top of the atmosphere radiative forcing by doubled carbon dioxide concentrations can be balanced by modest relative increases of 15-20% in the amount of low clouds and 20-35% in liquid-water path, and by decreases of ~15-20% in mean drop radius. This indicates that a minimum relative accuracy of ~5% is needed, ….to simulate these quantities in climate models."

Rotstayn (1999) stated:

> "..a 1% increase in cloudiness, a 6% increase in liquid water path, and a 7% decrease in effective radius (r_{eff}) may result in a radiative forcing of about –2.1 W m^{-2} in the heat budget of the atmosphere."

These studies suggest that cloud properties need to be measured, and ultimately simulated in climate models, with significant precision. Slingo suggested a relative accuracy within 5%. This is a very demanding, if not unrealistic goal for in-situ measurements, especially when trying to use those measurements to characterize large scale properties. However, understanding the limitations and using the best possible analysis techniques will help sort out some of these problems. It will provide insights into appropriate methods for developing parameterizations, as well as verifying model simulations. Appropriate use of in-situ measurements also allows remote sensing retrievals of cloud properties (e.g. based on satellite and radar or lidar observations) to be properly validated, thus helping to provide necessary large scale or global data sets.

This paper will discuss some of the issues that need to be addressed. These issues or problems will be illustrated using data and publications from Environment Canada. However, it must be stressed that there exists a large body of data available to modelers which has been obtained by other groups. This is not intended to be a review paper.

2. SCALE EFFECTS

Measurements made using aerosol or cloud microphysical probes often examine particle concentrations in volumes less than one cm^{-3} and in most cases less than a few litres over

Corresponding author's address:
George A. Isaac
Environment Canada
4905 Dufferin Street, Toronto, Ontario, M3H 5T4, Canada. E-Mail: george.isaac@ec.gc.ca

approximately a 100 m scale. Yet these measurements are used in climate models to describe the average properties of clouds on scales reaching 100s of kilometers. It is clear that if you analyze cloud microphysical data over different scales, you can get different answers. Cober et al. (2001) in their paper on icing conditions described this in some detail for cloud liquid water content and droplet concentration (see Figure 1). It is clear that these parameters slowly decrease in value as the scale gets larger. This is partly because more volume with lower concentrations gets added as the scale increases.

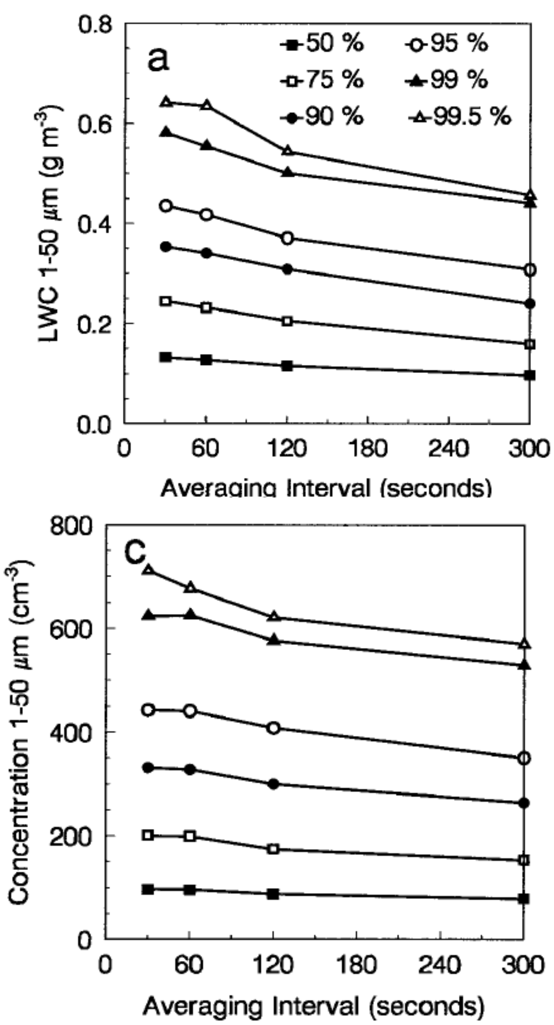

Figure 1: Scale effects of cloud liquid water content and droplet concentration as described by Cober et al. (2001). A 30 and 300 second averaging interval represent 3 km and 30 km scales respectively. The plot shows various percentile values of the distribution.

Figure 2 shows the scale factor used to determine maximum cloud liquid water content for wind tunnel, or numerical icing code, simulations of icing conditions based on the data of Cober and Isaac (2006). Also plotted is the scale factor in the certification envelopes of FAR 25C which is used for the design of all aircraft ice protection systems that are in use today. This curve is based on the work of Lewis and Bergrum (1952).

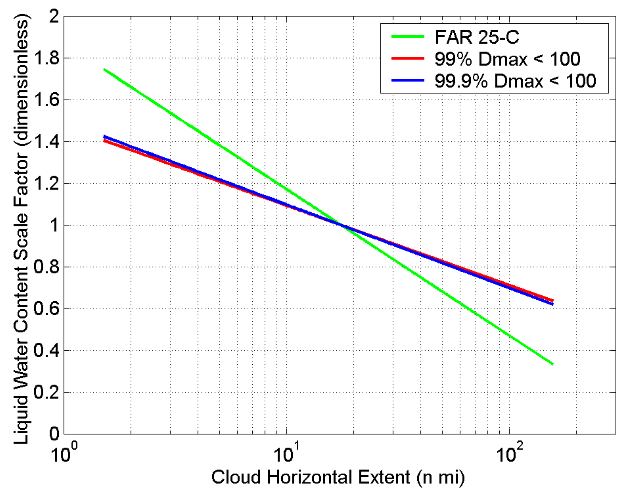

Figure 2: Shows the scale factor used to determined maximum liquid water content for simulating icing conditions. The scale is defined to be one at 17.4 n mi. (From Cober and Isaac, 2006).

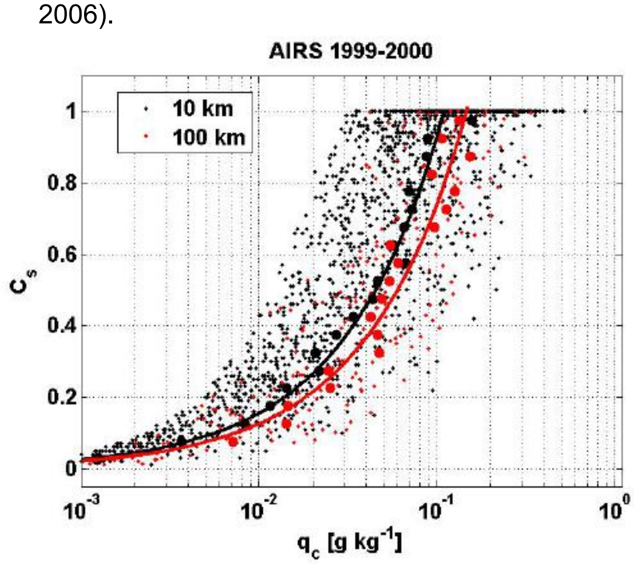

Figure 3: Cloud fraction (C_s) as a function of condensed cloud water (q_c) for scales of 10 and 100 km. (From Gultepe and Isaac, 2007)

Gultepe and Isaac (1999, 2007) showed the scale effect for cloud liquid water, droplet concentration, aerosol number concentration, and parameterizations of cloud fraction. Fig. 3 shows their parameterization for cloud fractions on the 10 and 100 km scales.

3. UNITS OF MEASUREMENT

It is necessary to determine the units to use for reporting measurements. The modeling community tends to use mass units giving the concentrations as a function of a unit mass of air. This has the advantage of being independent of pressure and temperature. Chemists often use such units as well. However, today, most cloud microphysical measurements are reported in volume units. This would not be a problem if the corresponding pressure and temperatures were also reported. However, this is not done routinely. When analyzing measurements from many different days, the altitude and temperature variations are often ignored and the volume unit concentrations are used for averaging.

Isaac et al. (2004) examined this problem and showed the typical type of “errors” that might result. The data were obtained during four different field projects in eastern Canada, central Canada and the Arctic. Table 1 shows the data analyzed in their original volume units at the measurement level and in volume units that were referenced to a standard temperature and pressure (STP) level of 0°C and 1013 mb. The STP data presentation is similar to a mass concentration because a simple multiplication factor would convert the numbers to mass units. However presenting the data in this manner allows a direct comparison of the volume and “mass” measurements. It is clearly shown that there can be a factor of two between the different methods of presenting the data. The rate of change of LWC and TWC with temperature is less when the data are converted into mass units. This is due to the fact that measurements at colder temperatures were usually taken at lower pressure altitudes.

4. PROBABILITY DENSITY FUNCTIONS

Aerosol and cloud microphysical data vary considerably over short distances. It is probably not realistic to represent clouds in climate models with one number for each cloud parameter for grid squares perhaps 10^4 km^2 in size. Table 1 gives the distribution for cloud liquid water content (LWC), cloud total water content (TWC), droplet number concentration (Nd) and ice particle concentration (Ni) in terms of 25%, 50%, 75%, 95% and mean values. Gultepe and Isaac (2004) describe the variations in more detail for droplet number concentration and suggest some probability density functions and Nd-T parameterizations. The modeling community is beginning to recognize that they need to consider the variance of important variables. However, there needs to be more guidance from them to those who are making and analyzing the data.

5. CLOUD TYPE DIFFERENCES

Cloud microphysical properties also depend on geographical location. As mentioned earlier, the distinction between maritime and continental clouds has been well known and documented (see Squires, 1958). Isaac et al. (2001) show clear differences between the frequency distributions of droplet concentrations in stratiform clouds in a maritime (CFDE I) and continental (CFDE III and AIRS) environment (Table 2). However, it is unclear whether the clouds in eastern Canada would be similar to those in other places of the world. Such a study definitely needs to be done. Korolev et al. (2001) did a statistical analysis of cloud properties by cloud type in the former USSR using a large data set. Although the instrumentation and the resulting analysis techniques were different, the data are similar to the stratocumulus and stratus measurements of Tables 1 and 2, at least for LWC.

	1%	25%	50%	75%	99%
Maritime	1154 Points				
Ta (°C)	-21	-5.8	-4.1	-2.0	0.0
Nd (cm^{-3})	1	16	52	108	406
TWC (g m^{-3})	0.01	0.07	0.13	0.20	0.47
MedVD (μm)	10	18	24	34	527
Continental	4759 Points				
T_a (°C)	-25	-9.1	-6.2	-3.2	-0.2
Nd (cm^{-3})	2	55	121	233	643
TWC (g m^{-3})	0.01	0.05	0.11	0.21	0.49
MedVD (μm)	10	13	17	22	643

Table 2: Cloud microphysical summaries, using 3 km averages, for the maritime (CFDE I) and continental cases (CFDE III and AIRS) in terms of static temperature (Ta), Nd, TWC, and median volume diameter (MedVD). For all data points, Ta ≤ 0°C, Ni $\leq$1 litre^{-1} and the TWC $\geq$ 0.005 g m^{-3}. As an example, 25% of the CFDE I Nd were less than 16 cm^{-3}. (From Isaac et al., 2001)

Liquid Water Content (LWC) Versus Temperature (T)

T [°C]	LWC [g m^{-3}]					LWC [g m^{-3}] at STP				
°C	25%	50%	75%	95%	Mean	25%	50%	75%	95%	Mean
-2	0.04	0.11	0.20	0.35	0.13	0.05	0.13	0.23	0.41	0.16
-6	0.04	0.10	0.18	0.34	0.12	0.05	0.11	0.21	0.40	0.14
-10	0.03	0.10	0.20	0.35	0.13	0.04	0.11	0.25	0.46	0.16
-14	0.02	0.06	0.14	0.41	0.11	0.03	0.08	0.18	0.52	0.15
-18	0.01	0.04	0.07	0.15	0.05	0.02	0.05	0.11	0.24	0.08
-22	0.02	0.04	0.07	0.14	0.05	0.03	0.05	0.11	0.29	0.09
-26	0.01	0.01	0.05	0.15	0.04	0.01	0.02	0.09	0.26	0.08

Total Water Content (TWC) Versus Temperature (T)

T [°C]	TWC [g m^{-3}]					TWC [g m^{-3}] at STP				
	25%	50%	75%	95%	Mean	25%	50%	75%	95%	Mean
-2	0.05	0.12	0.20	0.34	0.14	0.06	0.14	0.25	0.41	0.17
-6	0.04	0.09	0.17	0.32	0.12	0.04	0.11	0.20	0.38	0.14
-10	0.02	0.07	0.15	0.31	0.10	0.03	0.09	0.19	0.41	0.13
-14	0.02	0.04	0.09	0.27	0.08	0.02	0.07	0.14	0.40	0.11
-18	0.01	0.02	0.06	0.15	0.04	0.02	0.04	0.10	0.26	0.08
-22	0.01	0.02	0.04	0.12	0.04	0.02	0.03	0.07	0.23	0.07
-26	0.01	0.01	0.03	0.11	0.03	0.01	0.02	0.05	0.22	0.05

Droplet Number Concentration (N_d) Versus Temperature (T)

T [°C]	N_d [cm^{-3}]					N_d [cm^{-3}] at STP				
	25%	50%	75%	95%	Mean	25%	50%	75%	95%	Mean
-2	22	72	151	329	106	25	87	184	371	123
-6	59	121	240	446	165	70	146	286	492	191
-10	43	120	240	568	173	51	143	303	714	214
-14	18	68	142	437	114	27	88	181	520	139
-18	12	28	52	106	45	20	44	70	147	61
-22	14	38	71	87	43	27	63	77	130	59
-26	0	9	38	98	27	0	16	54	142	42

Ice Particle Concentration (N_i) > 100 µm versus Temperature (T)

T [°C]	N_i [L^{-1}]					N_i [L^{-1}] at STP				
	25%	50%	75%	95%	Mean	25%	50%	75%	95%	Mean
-2	3	8	14	27	10	3	9	18	37	13
-6	3	7	13	26	10	3	9	16	34	12
-10	2	4	9	17	6	2	5	12	26	8
-14	2	5	11	23	8	3	8	18	40	13
-18	2	5	10	20	7	3	9	18	38	13
-22	2	6	9	20	7	3	10	17	36	13
-26	2	5	12	23	8	3	8	23	46	15

Table 1: Parameters given here were obtained using volume units from the measurement level and volume units at STP (0°C and 1013mb). The data points are 30 s or 3 km average values representing, 8596 values for LWC, 15,202 values for TWC, 6297 values for Nd and 8298 values for Ni. The volume unit measurements were obtained over a wide range of altitudes. (From Isaac et al., 2004).

Theoretically, if climate models are initialized using aerosols which are then nucleated in updrafts of varying speeds, within an adequate thermodyamical and dynamical framework, the differences in cloud types should be effectively simulated. Analyses of measurements as shown in Tables 1 and 2 could be effective in verifying these simulations.

6. ICE PARTICLE CONCENTRATIONS

Korolev et al. (2000), Gultepe et al. (2001), Field et al. (2005) and Gayet et al. (2006) all showed similar ice particle (> 100 μm) concentrations around the world, in different cloud types. This is a surprising result. These authors also noted that for ice particles (> 100 μm), the concentration appears to be independent of temperature. This can also be shown from the observations reported in Table 1. Boudala and Isaac (2006) also showed that mixed phase clouds contain lower concentrations of ice particles than clouds containing only ice (Figure 4), which suggests that parameterizations of ice particle spectra based on measurements in ice clouds may not be appropriate for mixed phase clouds. Furthermore, these measurements suggest that modelers should not use the ice nucleation curves of Meyers et al. (1992) to predict ice particles in clouds unless all the ice formation mechanisms are also included. Meyers et al would predict higher concentrations with lower temperatures. Perhaps a safer "parameterization" might specify an ice particle concentration that is independent of temperature.

It should be clearly noted that there are many difficulties associated with making ice particle measurements in-cloud, especially for small

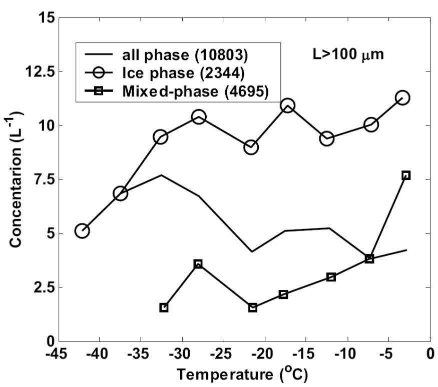

Figure 4: Ice particle concentration (>100 μm) in mixed phase, and all ice clouds, and both phases combined. (From Boudala and Isaac, 2006)

particles less than 100 μm. That is why only ice particle concentrations greater than 100 μm in size are reported in this paper. However, there are also problems associated with shattering off probe tips which could also affect the larger particle size range (Korolev and Isaac, 2005; Isaac et al., 2006).

7. ICE PARTICLE SHAPE

Korolev et al. (1999, 2000) summarize some ice particle shape measurements made by Environment Canada. Most particles tend not to be the pristine shapes (columns, plates, dendrites) that are described in the textbooks, but they are multifaceted crystals with an irregular appearance. However, Korolev and Isaac (2003) found that small ice particles tend to be round, with roundness (R) being defined by the equation

$$R = 4S_{meas}/\pi\ D^2_{max}$$

where S_{meas} is the measured projection area of the particle image and D_{max} is the maximum dimension of the image (Figure 5). This suggests that small ice particles are formed from frozen drops. From observations in the laboratory, Korolev et al. (2004) concluded small frozen drops can retain their spherical shapes for periods of minutes to tens of minutes under conditions close to saturation over water. This helps explain the observation of many spherical ice particles in natural clouds. The radiative properties of clouds clearly depend on the shape of the particles, which is why studies like this are necessary.

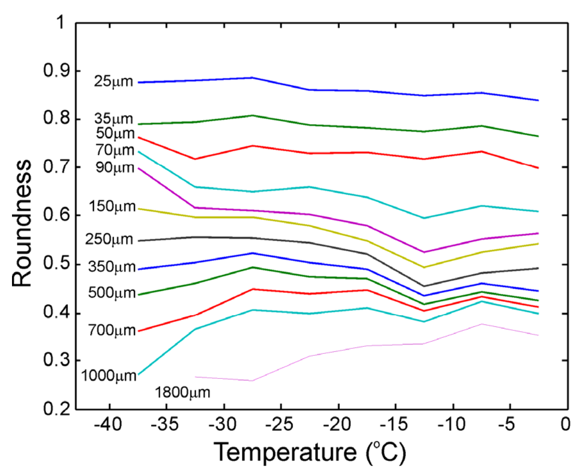

Figure 5: The roundness of ice particles as a function of particle size and temperature (from Korolev and Isaac, 2003).

8. ICE AND LIQUID PARTICLE SIZE DISTRIBUTIONS

Figure 6 shows the ice particle size distributions in all liquid and glaciated stratiform clouds measured in Southern Ontario (see Isaac et al., 2002) as a function of Total Water Content. A straight line has been drawn through the all liquid cloud spectra in the top panel. This shows that simple parameterizations could be developed to describe such distributions which could provide useful guidance for climate models.

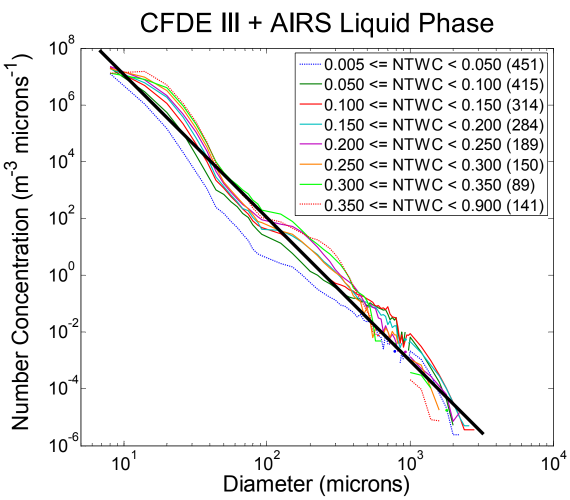

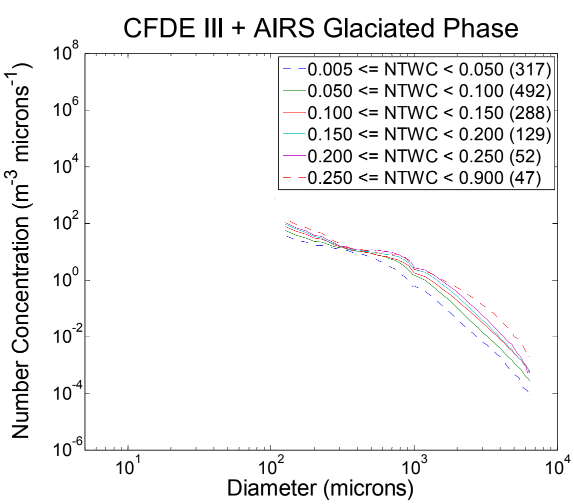

Figure 6: Number concentration spectra obtained in all liquid and glaciated clouds during the Canadian Freezing Drizzle Experiment (CFDE 1) and the Alliance Icing Research Study (AIRS) as described by Isaac et al. (2002). A straight line has been drawn though the data in the top panel.

9. RELATIVE HUMIDITY IN-CLOUD

The theoretical analysis of Korolev and Mazin (2003) and the in-situ observations of Korolev and Isaac (2006) have shown that the vapour pressure in liquid and genuinely mixed clouds is close to saturation with respect to water (Figure 7a).

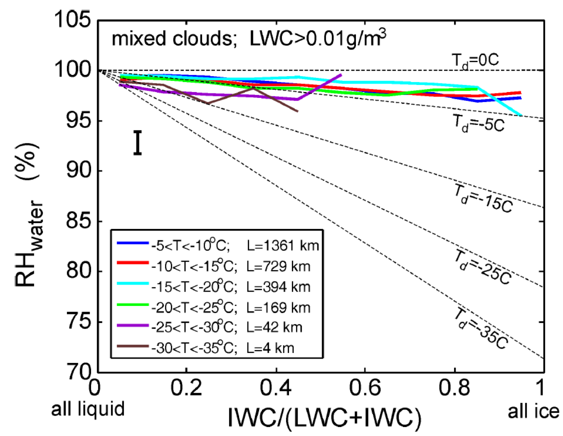

Figure 7a: Dependence of the average humidity RH_w versus ice water fraction IWC/(LWC+IWC) for different temperature intervals measured in mixed phase clouds. Dashed lines correspond to the parameterization $RH_w=100(1 - \mu + \mu RH_{wsi})$ where μ is the ice fraction. Vertical line on the left side represents an error bar.

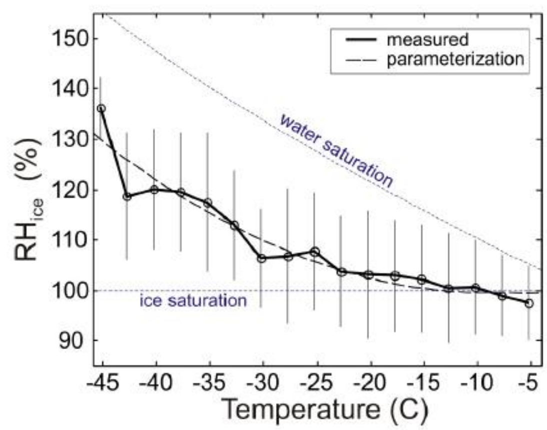

Figure 7b: Average relative humidity with respect to ice $\overline{RH}_i$ versus air temperature measured in ice clouds. Vertical lines indicate standard deviation of RH_i measurements in different clouds. Dashed line is the parameterized humidity in ice clouds.

In ice clouds, Korolev and Isaac (2006) proposed a relationship between RH_{ice} and T as shown in Figure 7b. However, this parameterization is scale dependent as is shown in the paper by Korolev and Isaac (2008) and is probably not suitable for large scale model simulations.

10. MIXED PHASE CLOUDS

Cober et al. (2001), Korolev et al. (2003), and Boudala et al. (2004) showed that mixed phase clouds occur frequently. Most of the precipitation in mid-latitudes, and perhaps globally, falls from such clouds. Boudala et al. (2004) emphasized how the liquid fraction decreases as the temperature gets lower (Figure 8). However, this proposed parameterization only holds for approximately a 1 km scale length. It would be different for other scales. For example, on a very large scale, over 100s of km, probably all sub freezing clouds contain both liquid and ice and thus, on average, could be considered mixed phase. Once again, this suggests that parameterizations for large scale models should consider scale dependence.

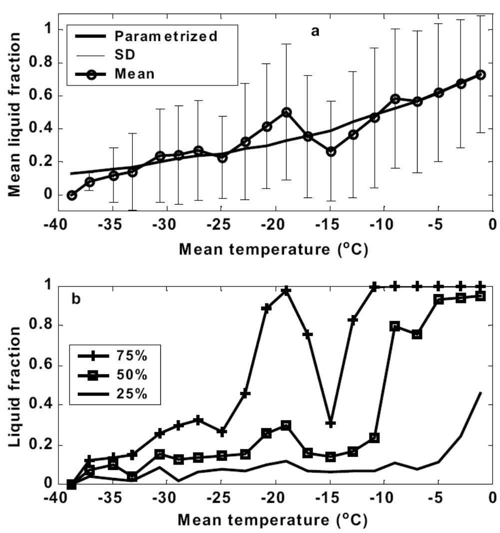

Figure 8: The 1 km averaged liquid fraction for every 2 ^{0}C temperature interval. (a) The mean (circles), standard deviation (bars), and a parameterization. (b) The lines for 75, 50 and 25 percentiles. (From Boudala et al., 2004).

11. SUMMARY

Cloud feedbacks remain the largest source of uncertainty in climate models (IPCC Fourth Assessment Report). As stated in the introduction of this paper, it is necessary to measure and simulate cloud microphysical properties accurately in order to address this problem.

Cloud in-situ measurements are very useful for developing parameterizations that can be used in climate models. These parameterizations will remain necessary until the numerical models can explicitly handle all the complicated processes that occur in the atmosphere. However, too often portions of the climate modeling community attempt to simplify the processes by ignoring such things as scale problems, variability within the grid square, and even the use of proper units.

The same in-situ measurements can be used to verify models that treat important parameters like cloud liquid water content as prognostic variables. However, in such cases, it would be better to first validate remote sensing techniques and then these resulting remote sensing measurements could be used for verification of the model simulations over larger areas.

The ability to measure in-situ properties is rapidly evolving. As mentioned above, there are errors in ice particle concentrations, especially at small sizes (< 100 μm) and the Nevzorov probe which was used extensively by the EC group is now known to underestimate ice mass (see Korolev et al., 2008). This recently discovered error will impact many of the diagrams and tables in this paper (e.g. Figures 3, 7, 8 and Tables 1 and 2). Shattering and splashing off probe tips could also be affecting the measurements and this should be explored more completely. It is essential to further refine and improve our ability to make in-situ measurements.

It is necessary for the modeling and observation communities to talk to each other more often than is presently occurring. This will allow better measurements to be obtained and they will be applied more effectively with an improved understanding of the limitations.

ACKNOWLEDGEMENTS

The authors would like to acknowledge their colleagues at the National Research Council of Canada because all the measurements reported in this paper were made using the NRC Convair-580. Funding for these measurements was also provided by many different agencies such as the Canadian Search and Rescue New Initiatives Fund, Transport Canada, FAA, NASA and the Boeing Commercial Airplane Group.

REFERENCES

Boudala, F., G.A. Isaac, Stewart G. Cober, Qiang Fu , 2004: Liquid fraction in Stratiform Mixed-Phase clouds Using in-Situ Observations. *Quart. J. Roy. Meteorol. Soc*., **130**, 2919-2931.

Boudala, F. S. and G. A. Isaac, 2006: Bulk microphysics parameterization of ice fraction for application in climate models. *Quart. J. Roy. Meteorol. Soc*. **132**, 2377-2392.

Cober, S.G., G.A. Isaac, A.V. Korolev, and J.W. Strapp, 2001: Assessing cloud-phase conditions. *J. Appl. Meteor.*, **40**, 1967-1983.

Cober, S.G., and G.A. Isaac, 2006: Estimating maximum aircraft icing environments using a large data base of in-situ observations. *AIAA 44th Aerospace Sci. Meeting and Exhibit*, Reno Nevada, 9-12 January 2006, AIAA-2006-266.

Field, P.R., R.J. Hogan, P.R.A. Brown, A. Illingworth, T.W. Choularton, and R.J. Cotton, 2005: Parameterization of ice-particle size distributions for mid-latitude stratiform cloud. Q. J. R. Meteorol, Soc., 131, 1997-2017.

Gayet, J.-F., V. Shcherbakov, H. Mannstein, A. Minikin, U. Schumann, J. Strom, A. Petzold, J. Ovarlez, and F. Immler, 2006: Microphysical and optical properties of mid-latitude cirrus clouds observed in the southern hemisphere during INCA. *Quart. J. Roy. Meteorol. Soc*., **132**, 2721–2750.

Gultepe, I, and, G.A. Isaac, 1999: Scale effects on the relationship between cloud droplet and aerosol number concentrations: Observations and models. *J. of Climate*, **12**, 1268-1279.

Gultepe, I., G. A. Isaac, and S. G. Cober, 2001: Ice crystal number concentration versus temperature. International J. of Climate, **21**, 1281-1302.

Gultepe, I., and G.A. Isaac: 2004: Aircraft Observations of Cloud Droplet Number Concentration: Implications for Climate Studies. *Quart. J. Roy. Meteorol. Soc*., **130**, 2377-2390.

Gultepe, I., and G.A. Isaac, 2007: Cloud fraction parameterization as a function of mean cloud water content and its variance using in-situ observations. *Geophys. Res. Lett.*, **34**, L07801, doi:10.1029/2006GL028223.

Isaac, G.A., S.G. Cober, J.W. Strapp, A.V. Korolev, A. Tremblay, and D.L. Marcotte, 2001: Recent Canadian research on aircraft in-flight icing. *Canadian Aeronautics and Space Journal*, **47-3**, 213-221.

Isaac, G.A., S.G. Cober, I. Gultepe, A.V. Korolev, F.S. Boudala and M.E. Bailey, 2002: Particle spectra in stratiform winter clouds. Paper 3.2 in Proceedings of 11th AMS Conference on Cloud Physics, Ogden, Utah, 3-7 June 2002.

Isaac, G.A., I. Gultepe, and S.G. Cober, 2004: Use of mass versus volume units for cloud microphysical parameters. *Proceedings 14th Intl. Conf. on Clouds and Precipitation*, Bologna, 19-23 July 2004, 800-803.

Isaac, G.A., A.V. Korolev, J.W. Strapp, S.G. Cober, F.S. Boudala, D. Marcotte and V.L. Reich, 2006: Assessing the collection efficiency of natural cloud particles impacting the Nevzorov total water content probe. AIAA 44th Aerospace Sciences Meeting and Exhibit, Reno, Nevada. 9-12 January 2006. AIAA-2006-1221.

Korolev, A.V., G.A. Isaac, and J. Hallett, 1999: Ice particle habits in Arctic clouds. *Geoph. Res. Lett*., **26**, 1299-1302

Korolev, A., G.A. Isaac, and J. Hallett, 2000: Ice particle habits in stratiform clouds. *Quart. J. Roy. Meteorol. Soc*., **126**, 2873-2902.

Korolev, A.V., G.A. Isaac, I.P Mazin and H. Barker, 2001: Microphysical properties of continental clouds from in-situ measurements. *Quart. J. Roy. Meteorol. Soc*., **127**, 2117-2151.

Korolev, A.V., G.A. Isaac, S.G. Cober, J.W. Strapp, and J. Hallett, 2003: Observations of the microstructure of mixed phase clouds. *Quart. J. Roy. Meteorol. Soc.*, **129**, 39-65.

Korolev, A.V. and I.P. Mazin, 2003: Supersaturation of water vapor in clouds. *J. Atmos. Sci.,* **60**, 2957-2974

Korolev, A.V. and G.A. Isaac, 2003: Roundness and aspect ratio of particles in ice clouds. *J. Atmos. Sci*., **60**, 1795-1808.

Korolev, A. V., M.P. Bailey, J. Hallett, G.A. Isaac, 2004: Laboratory and In Situ Observation of Deposition Growth of Frozen Drops. *Journal of*

Applied Meteorology, **43**, 612–622.

Korolev, A.V., and G.A. Isaac, 2005: Shattering during sampling by OAPs and HVPS. Part 1: Snow particles. *J. Atmos. Oceanic Tech.*, **22**, 528-542.

Korolev, A.V., and G.A. Isaac, 2006: Relative humidity in liquid, mixed phase, and ice clouds. J. Atmos. Sci., **63**, 2865–2880.

Korolev, A.V. and G.A. Isaac, 2008: The effect of spatial averaging on the relative humidity and phase composition of clouds. *Proceedings 15th Intl. Conf. on Clouds and Precipitation*, Cancun, Mexico.

Korolev, A.V., J.W. Strapp, G.A. Isaac, and E. Emery, 2008: Improved airborne hot-wire measurements of ice water content in clouds. *Proceedings 15th Intl. Conf. on Clouds and Precipitation*, Cancun, Mexico.

Lewis and Bergrum (1952): A probability analysis of the meteorological factors conducive to aircraft icing in the United States. National Advisory Committee for Aeronautics, Technical Note 2738

Meyers, M.P.; P.I. Demott and W.R. Cotton, 1992: New primary ice-nucleation parameterizations in an explicit cloud model. *J Appl. Meteorol*., **31**, 708-721.

Rotstayn, L.D., 1999: Climate sensitivity of the CSIRO GCM: Effect of cloud modelling assumptions. *J. Climate*, **12**, 334-356.

Slingo, A., 1990: Sensitivity of the Earth's Radiation Budget to Changes in Low Clouds. *Nature*, **343**, 49-51.

Squires, P., 1958: The microstructure and colloidal stability of warm clouds. II. The causes of variations in microstructure. *Tellus*, **10**, 262.

Negative Forcing Resulting from Enhancement of CCN Concentrations in Marine Stratocumulus Clouds: Application to Global Warming Mitigation Scheme

Chih-Chieh (Jack) Chen[2], Philip Rasch[2], Laura Kettles[3], Alan Gadian[3], John Latham[1,5,*], Andrew Gettelman[2], Hugh Morrison[1], Keith Bower[5], Tom Choularton[5] & Stephen Salter[4]

1. MMM Division, NCAR, Boulder, P.O. Box 3000, Boulder, Colorado, 80307-3000, USA
2. CGD Division, NCAR, Boulder, P.O. Box 3000, Boulder, Colorado, 80307-3000, USA
3. IAS, School of Earth and Environment, University of Leeds, LS2 9JT, UK
4. School of Engineering & Electronics, University of Edinburgh, EH9 3JL, UK
5. SEAES, University of Manchester, PO Box 88, Manchester M60 1QD, UK

* Corresponding Author. latham@ucar.edu 001-303-497-8182 & 001-303-444-2429

Abstract. *We assess herein the proposal that controlled global cooling sufficient to balance global warming resulting from increasing atmospheric CO_2 concentrations might be achieved by seeding low-level, extensive maritime clouds with seawater particles which act as cloud condensation nuclei, thereby activating new droplets and increasing cloud albedo (and possibly longevity). This paper focuses on scientific and meteorological aspects of the scheme.*

Analytical calculations, cloud modelling and (particularly) GCM computations suggest that if one or two outstanding questions are satisfactorily resolved, the globally averaged negative forcing resulting from deployment of this scheme might balance the positive forcing associated with a doubling of CO_2 concentration: and thus to hold the Earth's temperature constant for many decades.

More work - especially assessments of possible meteorological and climatological ramifications - is required on several components of the scheme, which possesses the advantages that (1), it is ecologically benign – the only raw materials being wind and seawater: (2), the degree of cooling could be controlled: (3), if unforeseen adverse effects occurred the system could be immediately switched off, with the forcing returning to normal within a few days (although the response would take a much longer time).

1. Introduction

Atmospheric clouds exercise a significant influence on climate. They can inhibit the passage through the atmosphere of both incoming, short-wave, solar radiation, some of which is reflected back into space from cloud-tops, and they intercept long-wave radiation flowing outwards from the Earth's surface. The first of these effects produces a global cooling, the second a warming. On balance, the effect of clouds is to produce a cooling effect, corresponding to a globally averaged negative net forcing of about –13 W m^{-2}. (Ramanathan et al., 1989). Since the estimated positive forcing resulting from a doubling of the atmospheric carbon dioxide (CO_2) concentration (from the value – about 275 ppm - existing at the beginning of the industrial period) is about +3.7 W m^{-2}, (Ramaswamy 2001) it is clear that, in principle, deliberate modification of clouds to produce a cooling sufficient to balance global warming resulting from the burning of fossil fuels is feasible.

In this paper we present and assess a proposed scheme for stabilization of the Earth's global mean temperature (in the face of continually increasing atmospheric CO_2 concentrations) by seeding clouds in the marine boundary layer (MBL) with seawater aerosol, in order to increase cloud albedo (and possibly longevity). Changing albedo and lifetime changes the cloud forcing. Altering albedo and cloud lifetime is proposed by increasing the cloud droplet number concentration. This paper focuses attention on the physics and meteorology of the idea.

Section 2 herein outlines the global cooling scheme and some cloud model sensitivity studies designed to determine – for ranges of conditions relevant to this scheme – the sensitivity of cloud albedo enhancement to values of the meteorological and cloud microphysical parameters involved. Section 3 presents some simple calculations designed to illustrate the potential viability of the technique. In section 4 we describe global general circulation (GCM) climate model computations which provide a more rigorous quantitative assessment of our scheme, and display global distributions of the model negative forcing (and other parameters) together with seasonal variations. Technological implications from the results of our cloud modelling and GCM computations are discussed in Section 5. A brief discussion of questions and concerns which would need to be thoroughly and satisfactorily examined before any justification would exist for the operational deployment of the scheme is presented in Section 6. In Section 7 we provide a provisional quantitative assessment of the extent to which global temperature stabilization might be possible with this technique.

2. Outline and Preliminary Assessment of the Idea

Low-level, non-overlapped marine stratiform clouds cover about a quarter of the oceanic surface (Charlson et al., 1987) and characteristically possess albedos, A, in the range 0.3 to 0.7 (Schwartz and Slingo, 1996). They therefore make a significant (cooling) contribution to the radiative balance of the Earth. Latham (1990, 2002) proposed a possible technique for ameliorating global warming by controlled enhancement of the natural droplet number concentrations (N_0) in such clouds, with a corresponding increase ΔA in their albedo (the first indirect, or Twomey effect), and also possibly in their longevity (the second indirect, or Albrecht effect): thus producing a cooling. N_0 values in these clouds range typically from about 20 to 200 cm^{-3}.

The technique involves dissemination - at or close to the ocean surface - of monodisperse seawater (NaCl) droplets of around 1 μm in size, which are sufficiently large always to be activated - as cloud condensation nuclei (CCN) - to form ΔN additional droplets when they rise into the bases of these clouds. The total droplet concentration N is thus equal to (N_0 + ΔN). The central physics behind this scheme - which have been authoritatively treated in a considerable number of studies (e.g. Twomey 1977, 1991; Charlson et al. 1987; Albrecht 1989, Wigley 1989; Slingo 1990, Ackerman et al. 1993, Pincus & Baker, 1994; Rosenfeld, 2000, Brenguier et al. 2000; Peng et al. 2002; Stevens et al., 2005) - is that an increase in droplet concentration N causes the cloud albedo to increase because the overall droplet surface area is enhanced. It can also increase cloud longevity (tantamount to increasing cloudiness) because the growth of cloud droplets by coalescence to form drizzle or raindrops - which often initiates cloud dissipation - is slowed down, since the droplets are smaller and the clouds correspondingly more stable. In some circumstances, increasing N above the natural value N_0 may completely suppress the production of precipitation. (Possibly significant departures from this simple picture are outlined in Section 6.)

Calculations by above-mentioned workers indicate that a doubling of the natural droplet concentration (i.e. to $N = 2N_0$) in all such marine stratiform clouds (which corresponds to an increase ΔA of about 0.06 in their cloud-top albedo) would produce a cooling sufficient roughly to balance the warming associated with CO_2 doubling. Latham (1990, 2002) calculated that for a droplet diameter $d = 0.8$ μm (associated salt-mass $m_s = 10^{-17}$ kg) the total (global) seawater volumetric dissemination rate dV/dt required to produce the required doubling of N in all suitable marine stratocumulus clouds is about 30 $m^3 s^{-1}$, which appears well within the range of modern technology. As indicated earlier, all such particles, on entering the clouds, would be activated to form cloud droplets at lower supersaturations than are required for the great majority of the natural CCN, and thus some of the latter particles may not be activated. It is considered (e.g. Charlson et al. 1987) that most natural CCN over the oceans consist of ammonium sulphate particles formed from dimethylsulphide produced at the ocean surface by planktonic algae. In order to ensure a doubling of N we would need to add at least $2N_0$ particles per unit volume. Their size distribution would be monodisperse, largely in order to avoid the production of ultra-giant nuclei, UGN (Woodcock 1953; Johnson 1982; De Leeuw 1986), which could act to promote drizzle formation and thus cloud dissipation. The monodispersity of the added particles may also make the clouds more colloidally stable, thus inhibiting coalescence and associated drizzle formation.

We point out that ship-tracks are a consequence of inadvertent and uncontrolled albedo increase in such clouds, resulting from the addition of effective CCN in the exhausts from the ships: and that our proposed deliberate generation of efficient sea-salt CCN at the ocean surface, thereby (usually) enhancing N, is of course basically a version of a process that happens naturally, via the catastrophic bursting of air bubbles produced by wave motion. However, except in conditions of high winds or in regions where other aerosol sources are weak, these sea-salt particles constitute only a small fraction of the CCN activated in marine stratocumulus.

A simplified version of the model of marine stratocumulus clouds developed by Bower, Jones and Choularton (1999) was used (Bower et al. (2006)) to examine the sensitivity of albedo-enhancement ΔA to the environmental aerosol characteristics, as well as those of the seawater aerosol of salt-mass m_s and number concentration ΔN deliberately introduced into the clouds. That study used a size resolved microphysical parcel model, focussed upon aerosol drop activation, and neglected those processes leading to drizzle and precipitation. Values of albedo-change ΔA and total droplet number concentration N were calculated for a wide range of values of m_s, ΔN, updraught speed W (assumed constant with altitude), cloud-thickness ΔZ and cloud-base temperature T_B. We review some results from that study in the next few paragraphs to provide the backdrop for the discussion in following sections.

Marine stratocumulus clouds (assumed to be adiabatic, of infinite width and in a steady-state condition) were formed in air whose natural aerosol characteristics were 1 of 3 specified alternatives. Size-spectrum A corresponded to an aerosol size distribution measured in extremely clean southern hemisphere maritime air. Spectrum B corresponded to a relatively typical clean Northern Hemisphere maritime aerosol sample measured on Tenerife during the ACE- 2 experiment in 1997 (Bower *et al.*, 2000). The airmass from which Spectrum C was measured during ACE-2 was classified as being moderately polluted. These clouds could be inoculated with additional NaCl aerosol of prescribed concentration ΔN and constant salt-mass $m_{s,}$ which are added to the original aerosol spectrum. For all scenarios examined calculations were made of the in-cloud vertical distributions of cloud droplet concentration N, liquid-water-content, L, and supersaturation S: as well as the changes, ΔA, in the top-of-cloud albedo resulting from adding the additional aerosol. These calculations were made for: four values of W ranging from 0.05 to 1.0 m s^{-1}, 3 values of T_B ranging from 5 to 25 ^oC; and ΔZ values of 100 and 210 m. The cloud-base height was set to 300m in all model simulations. Values of ΔA were calculated from the droplet number concentrations using the method of Schwartz and Slingo (1996). The natural (unseeded) droplet number concentrations N_0 for the spectra A, B and C were 8, 133 and 453 cm^{-3} respectively for W = 0.2 m s^{-1}: and for spectrum B with W = 1.0 m s^{-1}, N_0 = 301 cm^{-3}. We employed 5 values of ΔN ranging from 10 to 1000 cm^{-3}, and 5 values of m_s ranging from 10^{-18} to 10^{-14} kg.

Our computations showed that for Spectrum B, values of ΔA and N are insensitive to m_s over the range 10^{-17} to 10^{-14} kg. Increasing W from 0.2 to 1.0 m s^{-1} resulted in an increase in N for both seeded and unseeded clouds. For Spectrum A the values of ΔA are insensitive to salt-mass m_s over the range 10^{-18} to 10^{-15} kg; and are typically several times greater (for the same values of ΔN) than those for Spectrum B. For Spectrum C the ΔA values are much lower than those for Spectra A and B. The threshold value of ΔA (= 0.06), mentioned earlier, was achieved for most parameter-value permutations for Spectrum A, a significant fraction for Spectrum B, and scarcely any for Spectrum C.

For all three aerosol spectra, the calculated values of albedo-change ΔA and total droplet concentration N were found to be highly sensitive to the imposed additional aerosol concentrations ΔN, over the range of values employed. This is because, for almost all conditions examined, all the deliberately introduced CCN are activated, with a concomitant significant increase in N and therefore ΔA. The calculated ΔA values were much more sensitive to ΔN than to T_B or ΔZ. The influence of updraught speed W on albedo-change was consistently significantly smaller than that of ΔN.

The relation between ΔN and ΔA was found always to be strongly non-linear (e.g. Twomey, 1991; Pincus & Baker, 1994). For example, for Spectrum B, with W = 1 m s^{-1}

and $m_s = 10^{-17}$ kg, we find that for $\Delta N = 100$ cm^{-3}, $\Delta A = 0.03$: while for $\Delta N = 1000$ cm^{-3}, $\Delta A = 0.13$).

These model computations (summarizing results from Bower et al, 2006) provide provisional quantitative support for the physical viability of the mitigation scheme, as well as offering new insights (see Section 5) into its technological requirements.

3. Spraying Rate, Albedo-Change and Negative Forcing

In this section we present some simple calculations designed to illustrate the relationships between the deliberately imposed increase in cloud droplet number concentration, ΔN, the associated increase in cloud albedo, ΔA, the resultant globally averaged negative forcing ΔF, and the required seawater aerosol volumetric spray production rate dV/dt. These calculations also provide some indication as to whether or not our global temperature stabilization scheme is quantitatively feasible. For the purposes of this discussion we follow Charlson et al. (1987) in assuming that the only clouds deliberately seeded with seawater CCN are non-overlapped marine stratiform clouds. We consider only the first indirect effect, i.e. the increase of albedo resulting from enhancement of the droplet number concentration, N. As discussed in item 4 of section 6, there are still many unknowns in our characterization of aerosol cloud interactions, and aerosol "indirect effects". In the context of those components that we think we understand (the first and s3econd indirect effect), our experience from both theoretical calculations, and global modelling suggests that the first indirect effects dominates. Therefore within this section, we disregard the second indirect effect, whose magnitude – our rough computations suggest - is generally a small fraction of the first one (typically about 10 or 20%), and thus of minor significance in forming a broad view as to whether our technique is quantitatively adequate In this analysis we consider only short-wave radiative effects.

The average solar irradiance F (W m^{-2}) received at the Earth's surface is

$$F = 0.25 F_0 (1 - A_P) \qquad (1)$$

where F_0 (= 1370 W m^{-2}) is the solar flux at the top of the atmosphere and A_P is the planetary albedo. Thus an increase ΔA_P in planetary albedo produces a forcing ΔF of

$$\Delta F = - 340\, \Delta A_P \qquad (2)$$

We define f1 (= 0.7) as the fraction of the Earth's surface covered by ocean, f2 (= 0.25) as the fraction of the oceanic surface covered by non-overlapped marine stratiform clouds and f3 as the fraction of oceanic stratiform cloud cover which is seeded. (In some of the more rigorous and comprehensive global climate modelling studies described in Section 4, other low-level clouds are also seeded). Thus the average change ΔA in cloud albedo associated with a change ΔA_P in planetary albedo is

$$\Delta A = \Delta A_P / (f1.f2.f3) = -\Delta F / 60\, f3 \qquad (3)$$

from which it follows, if f3=1, i.e. if all non-overlapped marine stratiform clouds are seeded, that to produce a globally averaged negative forcing of –3.7 W m^{-2} the required increases in planetary and cloud albedo are 0.011 and 0.062 respectively: the associated percentage changes in albedo being roughly 3.7% and 12%.

The cloud-albedo increase resulting from seeding the clouds with seawater CCN to increase the droplet number concentration from its unseeded value N_0 to N is given (Schwartz & Slingo, 1996) by

$$\Delta A = 0.075 \ln (N/N_0) \qquad (4)$$

and it follows from equations (3) and (4) that

$$-\Delta F = 4.5\ f3.\ln (N/N_0) \qquad (5)$$

which may be rewritten as

$$(N/N_0) = \exp (-\Delta F / 4.5\ f3) \qquad (6)$$

It follows from equation (6) that if f3 = 1 (all suitable clouds seeded) the value of (N/N_0) required to produce a negative forcing of –3.7 W m^{-2} is 2.3, in reasonable agreement with the estimates of Charlson et al. (1987) and Slingo (1990).

Values of globally averaged negative forcing, ΔF (W m^{-2}), derived from equation (5) for a range of values of f3 and N/No show that if the fraction f3 of suitable clouds that are seeded falls below about 0.3 it is not possible, for values of (N/N_0) realistically achievable on a large scale (a rough estimate is $(N/N_0) < 10$) , for our scheme to produce a negative forcing of –3.7 W m^{-2}. They also illustrate the established distinct non-linearity in the relationship between (N/N_0) and ΔF. For example, the negative forcing for $(N/N_0) = 3$ is about half that for $(N/N_0) = 10$.

We now derive a simple equation relating the volumetric spraying rate dV/dt ($m^3\ s^{-1}$) of seawater CCN produced near the ocean surface, and the associated negative forcing ΔF (W m^{-2}) produced as a consequence of albedo-enhancement in the seeded clouds above. We assume that spraying is continuous – as it would have to be, if our temperature stabilization scheme was in operation - and that the seeding is restricted to an areal fraction f3 of suitable clouds. We may write

$$dV/dt = v_d\ dn/dt = (\pi/6)d^3\ dn/dt \qquad (7)$$

where v_d is the volume (m^3) of a seawater droplet of diameter d(m) at creation, and dn/dt (s^{-1}) is the rate of spraying of seawater droplets

We assume that in equilibrium the number of sprayed droplets residing in the atmosphere is constant, i.e. the deliberate creation rate of seawater droplets equals the loss rate. Thus

$$dn/dt = (N - N_0)\ A_E.\ H.\ f1.\ f2.\ f3\ /\ (f4.\ \tau_R)$$

$$= N_0\ (N/\ N_0 - 1)\ A_E.\ H.\ f1.\ f2.\ f3\ /\ (f4.\ \tau_R) \qquad (8)$$

where: A_E (m^2) is the surface area of the earth: H (m) is the height over which the seawater droplets are distributed: f4 is the fraction of the sprayed droplets that are not lost at creation and do not move laterally away from regions of selected cloud cover. τ_R (s) is the average residence time of the seawater aerosol in the atmosphere

Thus, (from 7 & 8),

$$dV/dt = (\pi/6).\ d^3\ A_E.\ H.\ f1.\ f2.\ f3\ (No/f4.\ \tau_R)\ (N/N_0 - 1) \qquad (9)$$

Taking $A_E = 5.1 \times 10^{14}\ m^2$, f1 = 0.7, f2 = 0.25, equation (10) becomes

$$dV/dt = 4.6 \times 10^{13}\ f3.\ d^3\ (H.\ N_0\ /f4.\ \tau_R)\ (N/N_0 - 1) \qquad (10)$$

Finally, substituting for N/No from equation (6), we obtain

$$dV/dt = 4.6 \times 10^{13}\ f3.\ d^3\ (H.N_0\ /f4.\ \tau_R)\ [\{\exp - \Delta F\ /\ 4.5\ f3\}\ -1] \qquad (11)$$

If we assume that: f3 = 1 (i.e. all suitable marine stratiform clouds are seeded): f4 = 0.5: d= 0.8 μm = 8×10^{-7} m: H = 1 km = 1000 m: N_0= 100 cm^{-3} = $10^8\ m^{-3}$: τ_R = 3 days = 2.6×10^5 s: it follows from equation (12) that for a negative forcing $\Delta F = -3.7\ W\ m^{-2}$ the required total volumetric seawater aerosol dissemination rate dV/dt = 23 $m^3\ s^{-1}$. If we keep all the above parameter values the same but seed only half of the suitable clouds (i.e. f3 = 0.5) we find that the value of dV/dt needed to produce $\Delta F = -3.7\ W\ m^{-2}$ is about 37 $m^3\ s^{-1}$.

4. GCM Computations

Global aspects and ramifications of our cloud-albedo enhancement scheme were examined using two separate models.

The first of these was the HadGAM numerical model, which is the atmospheric component of the UK Hadley Centre Global Model, based on UM version 6.1. It is described in Johns et al. (2004) and contains the *New Dynamics Core* (Davies at al 2004). It is run at N96L38 resolution, i.e. 1.25 degrees latitude by 1.875 degrees longitude with 38 vertical levels extending to over 39 km in height. N96 denotes a resolution of 96 two-grid-length waves, i.e 192 grid points in longitude. It has a non-hydrostatic, fully compressible, deep atmosphere formulation and uses a terrain-following, height-based vertical coordinate. It also includes semi-Lagrangian advection of all prognostic variables except density, and employs the two-stream radiation scheme of Edwards and Slingo (1996). The species represented include sulphate, black carbon, biomass smoke and sea-salt. The convection scheme is based on the mass flux scheme of Gregory and Rowntree (1990) (but with major modifications), and the large-scale cloud-scheme is that of Smith (1990).

In our studies, the HadGAM model calculated three-year mean values of cloud-top effective radius r_{eff} (μm), liquid water path LWP (g m^{-2}) and outgoing short-wave radiation flux F_{sw} (W m^{-2}) at the top of the atmosphere (TOA). In the control run (no seeding) the globally averaged cloud droplet number concentration, N, was around 100 cm^{-3}, and the model was then run again with N increased - in all regions of low-level maritime cloud (below approximately 3000m / 700 hPa) - to 375 cm^{-3}. The value of 375 cm^{-3} was chosen because the parameterization of N in the model asymptotes to this value, as a consequence of the field observations of Martin et al. (1994). Such a value of N should be readily achievable technologically, if our global temperature scheme were ever to be operationally deployed.

The computed 3-year mean distributions of layer cloud effective radius r_{eff} (μm) and liquid water path LWP (g m^{-2}) for control and seeded marine low-level clouds indicate that increasing the cloud droplet number concentration N from natural values to the seeded figure of N= 375 cm^{-3} leads to a general decrease in droplet size (the first indirect aerosol effect), and an increase in liquid water path, with consequent decrease in precipitation efficiency (the second indirect effect). The changes in effective radius are clearly evident in the regions of persistent marine stratocumulus off the west coasts of Africa and North & South America, and also over much more extensive regions of the southern oceans. Changes in liquid water path in these same regions are perceptible but less pronounced.

The computations reveal that the imposed increase in N has caused an overall significant negative change ΔF in radiative forcing, indicating a cooling of the earth's climate The largest effects are apparent in the three regions of marine stratocumulus off the west coasts of Africa and North & South America, mentioned earlier, which together cover about 3% of the global surface. Lower but appreciable values of negative forcing are found throughout the much more extensive regions of the southern oceans. The 3-year mean globally averaged TOA negative forcing resulting from the marine low-level cloud seeding, as described, is calculated to be -7.9 ± 0.1 W m^{-2}, more than twice that required to compensate for the 3.7 W m^{-2} warming associated with a doubling of atmospheric CO_2 concentration.

Modifying N only in the above-mentioned three most sensitive areas gave a change in global 5-year mean top-of-atmosphere radiative forcing ΔF of -1.2 ± 0.1 W m^{-2}. When N was increased from 375 to 1000 cm^{-3}, ΔF increased to -2.3 ± 0.1 W m^{-2}.

A similar set of calculations was performed in a developmental version of the NCAR Community Atmosphere Model (CAM). The simulations were performed at 1.9^{o}x2.5^{o} latitude/longitude resolution (26 layers with a top near 40 km) using a newly developed microphysics parameterization (Morrison et al, 2008, Gettelman et al 2008). That parameterization uses a two moment scheme predicting cloud mass and particle number for 4 classes of condensed water (small particle liquid and ice, and precipitation sized rain and snow). Three 5-year simulations were conducted. The first simulation (the control) calculated cloud drop number using the drop activation parameterization of Abdul-Razzak and Ghan (2005) with a functional dependence on aerosol type and concentration, and resolved and turbulent dynamical fields. The other two simulations over-rode the cloud drop number concentrations (Nc) below 850 hPa, prescribing them at 375 and 1000 per cm^3, respectively, wherever clouds were found. The influence of the warm cloud seeding geoengineering strategy is assessed by taking the difference between the geoengineering experiments and the control simulation.

Computations were made of the top of atmosphere shortwave cloud forcing (SWCF) for the NCAR model for the 3 simulations and the difference between SWCF for the control and experiments where the drop number was prescribed to be 375 and 1000 $/cm^3$ below 850hPa. The change in SWCF was about half the amplitude of that seen in the HadGAM model in the marine stratus and trade cumulus regions. The HadGAM simulations prescribed the drop number to about 700 hPa, somewhat higher than the NCAR simulations, but these differences may also result from the many uncertainties in modelling cloud aerosol interactions in global climate models. Unlike the HadGAM simulations, there is also an intriguing response in the mid-latitude storm tracks, and there are some patches of positive ΔSWCF evident in the simulations as well, Some of the areas of positive ΔSWCF in the simulations with more moderate seeding (to $375/cm^3$) (e.g a weakening of the cloud forcing) occur downstream of regions strongly influenced by anthropogenic aerosols (e.g. downstream of China, and the eastern US). In our model producing clouds with 375 $drops/cm^3$ would actually be a reduction in Nc. Those regions are not seen in the simulation where the drop number is increased to $1000/cm^3$.

Because the ΔSWCF field exhibits significant spatial variation, it suggests that some geographic locations are more susceptible to cloud seeding than others. In other words, one may dramatically reduce the cost of the warm cloud seeding geoengineering strategy by selecting the locations where cloud seeding should be applied to achieve the maximum amount of cooling. Therefore, it is important to identify these optimal locations for cloud seeding.

To achieve this goal, we first analyzed the impact of warm cloud seeding geoengineering by ranking the intensity of response (ΔSWCF) in all grid cells over the ocean surface. We considered the amplitude of the forcing change, and the area occupied by each grid cell (varying with the cosine of latitude) in performing the ranking. The accumulated forcing (ΔSWCF) based on the ranked orders of all grid cells over the ocean surface was calculated. Ranking was performed on the monthly mean forcings for each month of the simulation, and the results were composited.

It was found that the December-January-February (DJF) seasonal mean has the strongest response and the June-July-August (JJA) seasonal mean the weakest. The annual average (ANN) falls between the two seasonal means. Since the sun is most intense in the southern hemisphere during DJF we expect most of the important locations for seeding to reside in that hemisphere during that season, with the converse true during JJA. The observed stronger response to seeding during DJF for a given areal extent may be explained by the enhanced susceptibility of the more pristine clouds of the southern hemisphere. In the NCAR model, optimal cloud seeding over 25% of the ocean surface might produce a net cooling close to 3.5/4 W/m^2 in DJF if the cloud drop number concentration was 375/1000 per cm^3. Following this same strategy, weaker cooling is expected in JJA (around 2.5 W/m^2) in both geoengineering experiments.

The corresponding optimal locations based on this ranking were determined for the $Nc=375/cm^3$ experiment for two choices of seeding area. The results indicated that the preferential locations for cloud seeding depend strongly on season. The optimal areas in the summer hemisphere occur first in marine stratus, and shallow trade cumulus regions, and secondarily in mid-latitude storm track regions. Both regions would need to be seeded to reach forcing amplitudes that could balance that associated with a doubling of CO_2.

5. Technological Implications

The calculations and computations presented in Sections 2, 3 & 4 yield some significant implications – outlined below - with respect to technological aspects of our proposed global temperature stabilization technique.

1. The sensitivity studies (Section 2) show that as long as activation of the added CCN occurs, the albedo-changes ΔA are insensitive, over a wide range, to the values of salt-mass m_s. It follows that the choice of disseminated droplet-size can - to a considerable extent - be dictated by technological convenience. These computations also indicate that it would probably be optimum for effective albedo-enhancement to confine our salt-mass value within the range 10^{-17} to 10^{-15} kg, corresponding to seawater droplets in the approximate size-range 0.8 to 4 μm. This is because smaller particles may not be nucleated and larger ones could act as ultra-giant nuclei and thus perhaps promote drizzle onset and concomitant cloud dissipation. In the absence of other considerations it seems sensible to disseminate seawater droplets of diameter about 0.8μm, thus minimising the required volumetric flow-rate dV/dt.

2. Monodispersity of the seawater aerosol – within the size range mentioned in (1) – has little impact on the values of ΔA. However, it is still desirable because it is likely to enhance cloud stability and therefore longevity: thus enhancing the magnitude of the Albrecht effect and the total negative forcing.

3. The GCM studies, cloud modelling and simple calculations presented earlier all indicate that optimal seeding of all suitable maritime clouds can produce values of globally averaged negative forcing ΔF in the range of our yardstick figure of –3.7 W m^{-2}. If this prediction proves to be correct (see discussion of uncertainties in Section 6) the chosen areal fraction of suitable cloud-cover seeded, f3, could be appreciably lower than unity; therefore rendering less daunting the practical problem of achieving adequate geographical dispersal of disseminated seawater CCN.

4. It follows from (3) that there exists, in principle, latitude to: (a) avoid seeding in regions where deleterious effects (such as rainfall reduction over adjacent land) are predicted; (b) seed preferentially in unpolluted regions, where the albedo-changes ΔA for a fixed value of ΔN (and thus spray-rate dV/dt) are a maximum. With reference to (b), however, factors such as the extensiveness of the cloud-cover and ease of access to it could prove to be overriding.

5. The high degree of seasonal variability in the optimal geographical distributions of suitable cloud (Section 4) underlines the desirability of a high degree of mobility in the seawater aerosol dissemination system.

6. Questions requiring further study

In addition to requiring further work on various technological issues concerning our global temperature stabilization scheme, we need to eliminate some limitations in our understanding of important meteorological aspects of it. We also need to make a detailed assessment of possibly adverse ramifications of the deployment of the technique, for which there would be no justification unless these effects were found to be acceptable. A number of these issues were addressed by Latham (2002) and Bower et al. (2006) and so will not be examined herein. They were concerned with topics such as: competition between the natural and deliberately added CCN; the possible influence of the additional CCN on higher-level clouds which may contain ice; the importance of ultra-giant nuclei in precipitation formation; and the influence of wind-speed on the droplet-number enhancement. Useful papers in assessing these issues included ones by: Blyth and Latham (1990), De Leeuw (1986), Exton et al. (1985), Ghan et al. (1998), Illingworth, (1988), Johnson (1982), Latham and Smith (1990), O'Dowd et al. (1999a,b,c) and Woodcock (1953). In the following paragraphs we address further points considered to be of importance.

1. It was assumed in the foregoing specimen calculations (Section 3) that about half of the seawater droplets disseminated at or near the ocean surface would be transported upwards by turbulent air motions to enter suitable clouds and be activated to form additional cloud droplets: i.e. f4 = 0.5. In actuality the value of f4 will probably vary considerably, according to the meteorological situation and other factors. Thus we need to obtain reliable estimates of f4 for all situations of interest. Airborne measurements (Smith et al. 1993) together with estimates (Blanchard 1969) based on the reported global rate of creation of NaCl CCN at the ocean surface by bubble-bursting (about 10^{28} per year), both suggest that f4 is greater than 0.1. Lenschow and (separately) Smith (private communications) suggest that the fraction will be close to 0.5. Fortunately, the volumetric spraying rates dV/dt calculated herein are readily achievable technologically, and could easily be increased to accommodate any likely value of f4.

2. It may prove useful to examine the possibility of utilising electrostatic forces to increase the fraction of disseminated seawater droplets that rise to cloud-base. This could be done,

in principle, by charging the seawater aerosol on production, and harnessing the Earth's electric field to transport them upwards. .

3. If our proposed technique were to be implemented on a global scale, changes in the Earth's temperature distribution would result. The GCM experiments preformed with HadGEM and CAM in this study used prescribed ocean boundary conditions. Further, we have not examined the effects on precipitation or temperature distributions in these simulations, because sea surface temperature is constrained, and this serves as a very strong constraint on the simulations. Consequently it is vital to engage in a prior assessment of associated climatological and meteorological implications, which might involve currently unforeseen feedback processes. For example, GCM studies (Rostayn et al. 2000, Williams et al. 2001) indicate that tropical circulation and rainfall are sensitive to hemispheric contrasts in sea surface temperature induced by the indirect effect of anthropogenic sulphate. Even if it were possible to seed clouds relatively evenly over the Earth's oceans, so that effects of this type could be minimised, they would not be eliminated. Also, the technique would still alter the land-ocean temperature contrast, since the cooling produced would be only over the oceans. In addition, we would be attempting to neutralise the warming effect of vertically distributed greenhouse gases with a surface-based cooling effect, which could have consequences such as changes in static stability which would need careful evaluation. Possible changes in wind and rainfall patterns are among issues that it is crucially important to address. We also need to examine the possibility of significant changes in ocean currents as a consequence of the local cooling produced by our scheme, requiring a coupled ocean atmosphere climate model. Since suitable clouds cover about 1/6 of the Earth's surface then if all were seeded (f3 = 1) the average negative forcing below them will be about (6 x -3.7 W m^{-2}) = -22 W m^{-2} if the globally averaged negative forcing is -3.7 W m^{-2}. If f3 = 0.3 the average local cooling would be about -74 W m^{-2}. It is important to establish the level of local cooling which would have significant effects on ocean currents, on local meteorology and ecosystems (through for example, photosynthesis). This work will require a fully coupled ocean/atmosphere climate system model. We hope to explore some of these issues in the near future.

4. The macrophysical properties of clouds may also respond to changes in aerosol concentrations in ways not foreseen at the time of formulation of the Albrecht (1979) hypothesis. For example, Wood (private communication) has pointed out that the most important recently identified aspect of the aerosol-cloud-climate problem for low clouds is that the macrophysical properties of the clouds respond to changes in aerosol concentration in ways not foreseen at the time of formulation of the Albrecht (1989) hypothesis (i.e. that reduction in warm rain production – resulting from increasing cloud droplet concentration and reduced droplet size - leads to thicker clouds). For marine stratocumulus clouds, recent studies with a Large Eddy Simulation (LES) model (Ackerman et al. 2004), and a simple mixed layer model (Wood 2007) show that the response of the cloud liquid-water-path on relatively short timescales (< 1 day) is a balance between moistening of the marine boundary layer (MBL) due to precipitation suppression, which tends to thicken the cloud, and drying by the increased entrainment associated with the extra vigour that a reduction in precipitation content brings to the MBL. Under some conditions the clouds thicken, and under

others the clouds thin. Thus it is unjustifiably simplistic to assume that adding CCN to the clouds will always brighten them according to the Twomey equation (4). Also, even without precipitation, LES studies (e.g. Wang, Wang and Feingold 2003, Xue and Feingold 2006) show that the enhanced water vapour transfer rates associated with smaller, more numerous droplets can lead to feedbacks on the dynamics that tend to offset, to some extent, the enhanced reflectivity due to the Twomey effect. The effects are either not treated, or are poorly treated by GCM parameterizations of clouds and boundary layer processes. It is clearly critical to an authoritative assessment of our scheme to acquire a full quantitative understanding of the issues raised in this section. Unfortunately, the accurate characterization of aerosol/cloud interactions while critical to our methodology, and critical to understanding of the climate system as a whole, is extremely difficult, and uncertain, as highlighted in the recent Intergovernmental Panel on Climate Change Assessment Report (IPCC2007). The execution of more work on these effects is a high priority.

7. Discussion

It follows from the discussion in Section 6 – particularly item 4 – that although separate computations agree in concluding that this cloud seeding scheme is in principle powerful enough to be important in global temperature stabilisation, there are important clearly-defined gaps in our knowledge which force us to conclude that we cannot state categorically at this stage whether the technique is in fact capable of producing significant negative forcing. Perhaps the most urgent requirement, in attempting to clarify this situation, is the performance of computations with a state-of-the-art LES model. It is also necessary to establish whether outstanding technological issues can be satisfactorily resolved.

If it is found that the unresolved issues defined in Section 6 (especially item 4) do not yield the conclusion that the cloud-albedo seeding technique is much weaker than is estimated from the GCM computations, we may conclude that it could stabilize the Earth's average temperature T_{AV} beyond the point at which the atmospheric CO_2 concentration reached 550 ppm but probably not up to the 1000 ppm value. The corresponding amount of time for which the Earth's average temperature could be stabilised depends, of course, on the rate at which the CO_2 concentration increases. Simple calculations show that if it continued to increase at the current level, and if the maximum amount of negative forcing that the scheme could produce is –3.7 W m^{-2}, T_{AV} could be held constant for about a century. At the beginning of this period the required global seawater dissemination rate dV/dt (if f_3=1) would be about 0.14 m^3 s^{-1} initially, increasing each year to a final value of approximately 23 m^3 s^{-1}.

Our view regarding priorities for work in the near future is that we should focus attention on outstanding meteorological issues outlined earlier in this paper, particularly in Section 6, as well as technological ones described in our companion paper. At the same time we should develop plans for executing a limited-area field experiment in which selected clouds are inoculated with seawater aerosol, and airborne, ship-borne and satellite measurements are made to establish, quantitatively, the concomitant microphysical and radiative differences between seeded and unseeded adjacent clouds: thus, hopefully, to determine whether or not this temperature-stabilization scheme is viable. Such further field observational assessment of our technique is of major importance.

Advantages of this scheme, if deployed, are that: (1) the amount of cooling could be controlled – by measuring cloud albedo from satellites and turning disseminators on or off (or up and down) remotely as required: (2) if any unforeseen adverse effect occurred, the entire system could be switched off instantaneously, with cloud properties returning to normal within a few days: (3) it is relatively benign ecologically, the only raw materials required being wind and seawater: (4) there exists flexibility to choose where local cooling occurs, since not all suitable clouds need be seeded.

A further positive feature of the technique is revealed by comparing the power required to produce and disseminate the seawater CCN with that associated with the additional reflection of incoming sunlight. As determined in the companion paper, about 1500 spray-vessels would be required to produce a negative forcing of –3.7 W m^{-2}. Each vessel would require about 150 kW of electrical energy to atomise and disseminate seawater at the necessary continuous rate (as well as to support navigation, controls, communications etc.), so the global power requirement is about 2.3×10^8 Watts. Ideally, this energy would be derived from the wind. The additional rate of loss of planetary energy, resulting from cloud seeding, required to balance the warming caused by CO_2-doubling would be $\Delta F.A_E = -1.9 \times 10^{15}$ W. Thus the ratio of reflected power to required dissemination power is about 8×10^6. This extremely high "efficiency" is largely a consequence of the fact that the energy required to increase the seawater droplet surface area by four or five orders of magnitude – from that existing on entry to the clouds to the surface area achieved when reflecting sunlight from cloud-top – is provided by nature.

BIBLIOGRAPHY

Abdul-Razzak, H. and S.J. Ghan 2005: Influence of slightly soluble organics on aerosol activation. J. Geophys. Res. 110:D06206-1-6. doi:10.1029/2004JD005324.

Ackerman, A.S., O.B.Toon, and P.V.Hobbs, 1993: Dissipation of marine stratiform clouds and collapse of the marine boundary layer due to the depletion of cloud condensation nuclei by clouds. Science. 262, 226-229.

Ackerman, A. S., 2004: The impact of humidity above stratiform clouds on indirect aerosol climate forcing. Nature, 432, 1014–1017.

Albrecht, B.A., 1989: Aerosols, cloud microphysics and fractional cloudiness. Science. 245, 1227-1230.

Andreas, E.L., J.B.Edson, E.C.Monahan, M.P.Rouault, and S.D.Smith 1995: The spray contribution to net evaporation from the sea: a review of recent progress. Boundary Layer.Met.,72, 3-52.

Blanchard, D.C., 1969: The oceanic production rate of cloud nuclei. J.Rech.Atmos. 4, 1-11.

Blanchard, D.C. and A.U.Woodcock, 1957: Bubble formation and modification in the sea and its meteorological significance. Tellus. 9, 145-147.

Blyth, A.M. and J.Latham, 1990: Airborne studies of the altitudinal variability of the microphysical structure of small, ice-free, Montanan cumulus clouds. Q.J.R.Met.Soc. 116, 1405-1423.

Bower, K.N., Jones, A. and Choularton, T.W. 1999. A modeling study of aerosol processing by stratocumulus clouds and its impact on GCM parameterisations of cloud and aerosol. Atmospheric Research, Vol. 50, Nos. 3-4, The Great Dun Fell Experiment, 1995 - special issue, 317-344.

Bower, K.N., Choularton, T.W., Gallagher, M.W., Beswick, K.M., Flynn, M.J., Allen, A.G., Davison, B.M., James, J.D., Robertson, L., Harrison, R.M., Hewitt, C.N., Cape,J.N., McFadyen, G.G., Milford, C., Sutton, M.A., Martinsson, B.G., Frank, G.,Swietlicki, E., Zhou, J., Berg, O.H., Mentes, B., Papaspiropoulos, G., Hansson, H-C.,Leck, C., Kulmala, M., Aalto, P., Väkevä, M., Berner, A., Bizjak, M., Fuzzi, S., Laj, P.,Facchini, M-C., Orsi, G., Ricci, L., Nielsen, M., Allan, B.J., Coe, H., McFiggans, G.,Plane, J.M.C., Collett, J.L.Jr., Moore, K.F. and Sherman, D.E., 2000 ACE-2 Hillcloud: An Overview of the ACE-2 Ground Based Cloud Experiment. Tellus, 52B, No.2, (The ACE-2 Experiment - special issue), 750-778. (ISSN0280-6509)

Bower, K.N., Choularton, T.W., Latham, J., Sahraei, J. & Salter, S.H., 2006. Computational assessment of a proposed technique for Global warming Mitigation via albedo-enhancement of marine stratocumulus clouds. Atmos. Res. 82, 328-336.

Brenguier, J-L, H. Pablowska, L. Schuller, R. Pruesker, J. Fischer & Y. Fouquart, 2000: Radiative Properties of Boundary Layer Clouds: Droplet effective radius versus number concentration. J. Atmos. Sci., 57, 803-821.

Charlson, R.J., J.E. Lovelock, M.O. Andreae, and S.G. Warren, 1987: Oceanic phytoplankton, atmospheric sulphur, cloud albedo and climate. Nature, 326, 655-661.

Cooper, W.A., R.T.Bruintjes, and G.K.Mather, 1997: Calculations pertaining to hygroscopic seeding with flares. J.Appl.Met. 36, 1449-1469.

Davies T, Cullen M, Malcolm A, Mawson M, Staniforth A, White A, Wood N., 2005. A new dynamical core for the Met Office's global and regional modelling of the Atmosphere, *Quart. Jou. Roy. Met Soc,* **131,** 1759-1782

Day, J.A., 1964: Production of droplets and salt nuclei by the bursting of air-bubble films. Q.J.R.Met.Soc. 90, 72-85.

De Leeuw,G., 1986: Vertical profiles of giant particles close above the sea surface. Tellus. 38, 51-61.

Edwards J.M. & Slingo A. 1996 Studies with a flexible new radiation code I: choosing a configuration for a large-scale model Q.J.R. Met. Soc., **122**, 689-719

Exton, H.J., J.Latham, P.M.Park, S.J.Perry, M.H.Smith, and R.R.Allan, 1985: The production and dispersal of marine aerosol. Q.J.R.Met.Soc. 111, 817-837.

Fairall, C.W., K.L.Davidson, and G.E.Schacher,1983: An analysis of the surface production of sea-salt aerosols. Tellus. 35, 31-39.

Gettelman, A., H. Morrison, and S.J. Ghan, 2008: A new two-moment bulk stratiform cloud microphysics scheme in the NCAR Community Atmosphere Model (CAM3), Part II: Single-column and global results. submitted to J. Climate.

Ghan, S.J., G.Guzman and H.Abdul-Razzak, 1998: Competition between sea salt and sulfate particles as cloud condensation nuclei. J. Atmos. Sci., 55, 3340-3347.

Gregory, D. and Rowntree P. R., 1990. A mass flux convection scheme with representation of cloud ensemble characteristics and stability dependent closure. Mon. Weather. Rev., 118, 1483-1506.

Illingworth, A.J., 1988: The formation of rain in convective clouds. Nature. 336, 754-756.

IPCC, 2007: Climate Change 2007: The Physical Science Basis. Contribution of Working Group I to the Fourth Assessment Report of the Intergovernmental Panel on Climate Change [Solomon, S., D. Qin, M. Manning, Z. Chen, M. Marquis, K.B. Averyt, M. Tignor and H.L. Miller (eds.)]. Cambridge University Press, Cambridge, United Kingdom and New York, NY, USA, 996 pp.

Johns T, Durman C, Banks H, Robesrtrs M McLaren A, Ridley J, Senior C, Williams K, Jones A, Keen A, Rikard G, Cusack S, Joshi M. Ringer M, Doug B, Spencer H. Hill R, Gregory J, Pardaens A, Lowe J, Bodas-Saldeco A, Stark S, Searl Y. 2004 HadGEM1 – Model description and analysis of preliminary experiments for the IPCC Fourth Assessment Report. Hadley Centre Technical Note No. 55, Met Office Exeter http://www.hadleycentre.com/research/hadleycentre/pubs/HCTN/index.html

Johnson, D.B., 1982: The role of giant and ultragiant aerosol particles in warm rain initiation. J.Atmos.Sci. 39, 448-460.

Latham,J., 1990: Control of global warming? Nature 347. 339-340.

Latham,J. and M.H.Smith, 1990: Effect on global warming of wind-dependent aerosol generation at the ocean surface. Nature. 347, 372-373.

Latham, J., 2002: Amelioration of global warming by controlled enhancement of the albedo and longevity of low-level maritime clouds. Atmos. Sci. Letters. (doi:10.1006/Asle.2002.0048)

Latham, J., 2007: Cooling may be possible, but we need safety Data. Nature, 447, 908.

Martin G, Dearden C, Greeves C, Hinton T, Inness P, James P, Pope V, Ringer M, Slingo J, Stratton R, Yang G-Y 2004. Evaluation of the atmospherice performance of HadGAM/GEM1 Hadlecy Centre Technical Note No. 54. Met Office: Exeter http://www.hadleycentre.com/research/hadleycentre/pubs/HCTN/index.html

Moore,D.J. and B.J.Mason, 1954: The concentration, size distribution and production rate of large salt nuclei over the oceans. Q.J.R.Met.Soc. 80, 583-595.

Morrison, H. and A. Gettelman, 2008: A new two-moment bulk stratiform cloud microphysics scheme in the NCAR Community Atmosphere Model (CAM3), Part I: Description and numerical tests. submitted to J. Climate.

O'Dowd, C.D, J.A.Lowe, and M.H.Smith, 1999a: Coupling of sea-salt and sulphate interactions and its impact on cloud droplet concentration predictions. Geophys.Res.Lett., 26, 1311-1314.

O'Dowd, C.D, J.A.Lowe, and M.H.Smith, 1999b: Observations and modelling of aerosol growth in marine stratocumulus. Atmos.Env. 33, 3053-3062.

O'Dowd, C.D, J.A.Lowe, M.H.Smith, and A.D.Kaye, 1999c: The relative importance of non-sea-salt sulphate and sea-salt aerosol to the marine cloud condensation nuclei population: An improved multi-component aerosol-cloud droplet parametrization. Q.J.R.Met.Soc. 125, 1295-1313.

Pattison, M.J. and S.E.Belcher,1999: Production rates of sea-spray droplets. J.Geophys.Res. 104, 18,397-18,407.

Penner, J.E., M.Andreae, H.Annegarn, L.Barrie, J.Feichter, D.Hegg, A.Jayaraman, R.Leaitch, D.Murphy, J.Nganga, and G.Pitari, 2001: Aerosols, and their direct and indirect effects. Climate Change 2001: The Scientific Basis, J.T.Houghton, Y.Ding, D.J.Griggs, M.Noguer, P.J. van der Linden, X.Dai, K.Maskell, and C.A.Johnson, Eds., Cambridge Univ. Press, United Kingdom and New York, NY. 881pp.

PengY., Lohmann, U., Leaitch, R., Banic, C. & Coutoure, M., 2002: The cloud-albedo / cloud droplet effective radius relationship for clean and polluted clouds from RACE and FIRE.ACE. J. Geophys. Res. 107, D11, 4106, 1-6.

Pincus, R and Baker, M.B., 1994: Effect of precipitation on the albedo susceptibility of clouds in the marine boundary layer. Nature, 372, 250-252.

Ramanathan, V., Cess, R., Harrison, E., Minnis, P., Barkstrom, B., Ahmad, E. and Hartmann, D., 1989: Cloud-radiative forcing and climate: Results from the Earth Radiation Budget Experiment, Science, 243, 57-63.

Ramaswamy, V., et al., 2001: Radiative forcing of climate change. In: Climate Change 2001: The Scientific Basis. Contribution of Working Group I to the Third Assessment Report of the Intergovernmental Panel on Climate Change [Houghton, J.T., et al. (eds.)]. Cambridge University Press, Cambridge, United Kingdom and New York, NY, USA, pp. 349-416.

Rosenfeld, D, 2000: Suppression of rain and snow by urban and industrial air pollution. Science 287, 1793-1796.

Rotstayn, L.D., B.F.Ryan and J.E.Penner, 2000: Precipitation changes in a GCM resulting from the indirect effects of anthropogenic aerosols. Geophys. Res. Lett., 27, 3045-3048.

Schwartz, S. E. & Slingo, A., 1996: Clouds, Chemistry and Climate: Proceedings of NATO Advanced Research Workshop. Ed. P. Crutzen.

Seufert, W & U. Seufert, 1983. Critics in a spin over Flettner's ships. New Scientist, 656-659.

Slingo,A., 1990: Sensitivity of the Earth's radiation budget to changes in low clouds. Nature 343, 49-51.

Smith, M.H., P.M.Park,P.M and I.E.Consterdine, 1993: Marine aerosol concentrations and estimated fluxes over the sea. Q.J.R.Met.Soc. 119, 809-824.

Smith, R. N. B., 1990. A scheme for predicting layer clouds and their water content in a general circulation model. Q. J. R. Meteorol. Soc., 116, 435-460.

Stevens, B., W.R.Cotton, G.Feingold, and Moeng, Chin-hoh., 1998: Large-eddy simulations of strongly precipitating, shallow, stratocumulus-topped boundary layers. J.Atmos.Sci, 55, 3616-3638.

Stevens, B., G. Vali, K. Comstock, R. Wood, M. VanZanten, P.H. Austin, C.S. Bretherton & D.H. Lenschow, 2005: Pockets of open cells and drizzle in marine stratocumulus. Bull. Am. Meteorol. Soc., 86, 51-57.

Twomey, S., 1971: The composition of cloud nuclei. J. Atmos. Sci., 28, 377- 381.

Twomey, S., 1977: Influence of pollution on the short-wave albedo of clouds. J. Atmos. Sci., 34, 1149-1152.

Twomey, S., 1991: Aerosols, Clouds and Radiation, Atmos Env. 25A, 2435-2442.

Wang Shouping, Wang Qing and G. Feingold, 2003: Turbulence, Condensation, and Liquid Water Transport in Numerically Simulated Nonprecipitating Stratocumulus Clouds. J. Atmos. Sci. 60, 262-278.

Wigley, T.M.L., 1989: Possible climate change due to SO2-derived cloud condensation nuclei. Nature, 339, 365-367.

Williams,K.D., A.Jones, D.L.Roberts, C.A.Senior, and M.J.Woodage, 2001: The response of the climate system to the indirect effects of anthropogenic sulfate aerosol. Climate Dyn., 17, 845-856.

Wood, R., 2007: Cancellation of aerosol indirect effects in marine stratocumulus through cloud thinning. J. Atmos. Sci., 64, 2657-2669.

Woodcock,A.H., 1953: Salt nuclei in maritime air as a function of altitude and wind force. J.Meteorol. 10, 362-371.

Xue, Hiuwen and G. Feingold, 2006: Large-Eddy Simulations of Trade Wind Cumuli: Investigation of Aerosol Indirect Effects. J. Atmos. Sci. 63, 1605-1622.

Acknowledgments:
We gratefully acknowledge NCAS for the use of HPCx computing resources, the UK Met Office for use of the HADGAM numerical model, and EPSRC for providing funding for Laura Kettles. Mary Barth, Steve Ghan, Brian Hoskins, Don Lenschow, James Lovelock, Mike Smith, Tom Wigley, Lowell Wood and Rob Wood provided very helpful advice and comments during the course of this work.

EFFECTS OF CLOUD NUCLEATION SCHEMES ON CLOUD PROPERTIES, PRECIPITATION AND CLIMATE

Surabi Menon[1], Susanne Bauer[2], Dorothy Koch[2], Robert McGraw[3] and Igor Sednev[1]
[1]Lawrence Berkeley National Laboratory, Berkeley, CA, USA
[2]Columbia University/NASA Goddard Institute for Space Studies, New York, NY, USA
[3]Brookhaven National Laboratory, Upton, NY, CA

1. **Introduction**: For climate change predictions, radiative forcings from aerosols and aerosol-cloud interactions continue to be quite uncertain due in part to the complexity in treating and quantifying aerosol effects on clouds and precipitation. Part of the complexity arises from cloud droplet nucleation and the autoconversion schemes used in large-scale models. Radiative forcings from aerosol-cloud interactions are estimated to be between -0.2 to -2 W m^{-2} (IPCC, 2007). Constraining these forcings and their resulting climate effects are important for future climate predictions, especially for predicting future precipitation changes. In this paper, we examine nucleation schemes used in a climate model and the resulting impacts on precipitation and radiation.

2. **Methodology**: We investigate changes to radiation and precipitation due to aerosol-cloud interactions with the NASA Goddard Institute for Space Studies (GISS) Climate model that is coupled to the aerosol chemistry and transport model of Koch et al. (2006) as well as to an aerosol microphysical model (Bauer et al. 2008). Our focus is the evaluation of the treatment of anthropogenic aerosols and their effects on clouds and precipitation. We examine both liquid-phase and mixed-phase clouds. We first evaluate our standard aerosol-cloud nucleation scheme in the coupled aerosol-climate model that predicts aerosol mass alone for externally mixed aerosols. Our standard semi-prognostic cloud droplet nucleation scheme for the aerosol mass-based model is based on empirical relationships between cloud droplet number versus aerosol concentrations obtained from various field campaigns given in Gultepe and Isaac (1999). We have updated this scheme and the newer nucleation scheme is based on Lohmann et al. (2007). Both schemes include some dependence on cloud cover changes and in-cloud turbulence as given in Menon and Del Genio (2007). For the Lohmann et al. scheme the cloud droplet nucleated, Q_{nucl}, is given as a function of aerosol concentration (Na) and cloud updraft velocity (ω) obtained by taking into account grid-mean velocity and sub-grid turbulence, and α = 0.023 cm^4 s^{-1} is a constant obtained from aircraft measurements.

$$Q_{\text{nucl}} = \max\left[\frac{1}{\Delta t}\left(0.1\left(\frac{N_a\omega}{\omega + \alpha \mathrm{N}_a}\right)^{1.27} - N_{old}\right), 0\right]$$

The coupled aerosol microphysical-climate model predicts aerosol size distributions in addition to mass for internally-mixed aerosols using the quadrature method of moments as described in Bauer et al. (2008). Here, we use a physically-based cloud nucleation scheme, that accounts for solubility, size, supersaturation changes, etc., based on Abdul-Razak and Ghan (2000). Both versions of the model use similar ice nucleation schemes, which allow for aerosol effects on ice nuclei for heterogeneous freezing processes, in addition to freezing of warm cloud droplets, as given in Morrison et al. (2005).

3. **Results**: Sensitivity studies for simulations that include present-day aerosol concentrations allow us to examine features of the nucleation scheme that are critical for simulating realistic clouds and precipitation. As an example we show differences in

cloud droplet number concentration (CDNC) using the Gultepe and Isaac scheme versus that obtained using the Lohmann et al. scheme in Fig.1. As can be seen CDNC values increase significantly over the oceans, especially the southern oceans with an overall average CDNC increase of 40%.

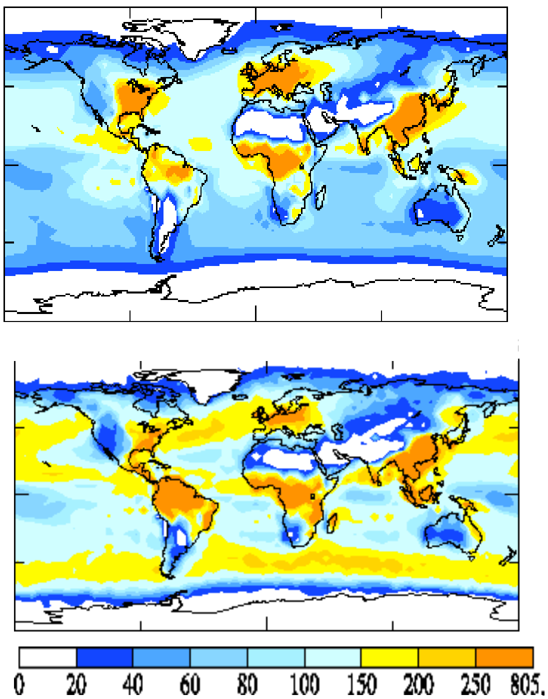

Figure 1: Annual values of cloud droplet number (cm^{-3}) for present-day aerosol distributions from the Gultepe and Isaac scheme (top panel) and the Lohmann et al. scheme (bottom panel).

Prior evaluation of CDNC values with an enhanced satellite-retrieved data set from Bennartz (2006) indicates that CDNC values may be under-predicted over the oceans, as shown in Fig. 2, but are within measurement uncertainties (Menon et al. 2008). These were based on comparison of CDNC values for June to August for the Atlantic Ocean region for present-day aerosol distributions. Thus, the higher values over the ocean obtained with the Lohmann et al. scheme may be comparable to observed values.

With the newer aerosol microphysical scheme, values obtained are comparable to those shown in the bottom panel of Fig.1 except for smaller values found near the southern mid-latitude ocean regions. Further evaluation for differences between CDNC produced using the mass-based scheme versus the aerosol microphysical scheme for similar aerosol distributions are ongoing and sensitivity to updraft velocity, mixing state and supersaturation will be presented. Although not shown, ice crystal concentrations for both schemes are similar since these are based on freezing of cloud droplets and depend on supersaturation and temperature.

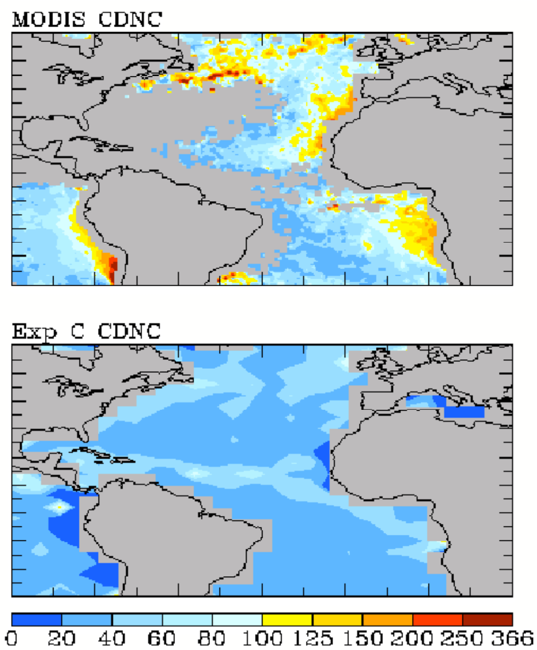

Figure 2: June-July-August values of cloud droplet number (cm-3) for present-day aerosol distributions from MODIS (top panel) and the Gultepe and Isaac scheme (bottom panel). (From Menon et al. 2008)

The indirect effect, obtained from differences in net cloud radiative forcing (both shortwave and longwave) between present-day and pre-industrial aerosol distributions using the Lohmann et al. nucleation scheme is -0.4 Wm^{-2}. Prior values of the indirect effect using the Gultepe and Isaac scheme (Menon and Del Genio, 2007) was about -0.65 Wm^{-2}, although these included different aerosol emissions. However, we note that smaller values for the indirect effect obtained for the Lohmann et al. scheme, are mainly due to smaller differences in CDNC between present-day and pre-industrial aerosol distributions and thus lower liquid water path and cloud optical depth differences. For similar aerosol burdens, differences in CDNC based on particular schemes used needs to be evaluated to understand how this may impact precipitation and radiation.

4. **Conclusion**: Although we find differences in CDNC and thus the indirect effect due to the choice of a particular cloud droplet nucleation scheme used, we need to fully evaluate our aerosol-cloud process treatment with satellite-based observations of cloud properties and precipitation to constrain our simulations of aerosol-cloud interactions and to determine which nucleation scheme performs best. Resulting radiation and precipitation characteristics can then be evaluated more meaningfully. This work is ongoing and will be presented at the conference.

5. Acknowledgement: We acknowledge funding support from the NSA Modeling Analysis and Prediction Program and the DOE Atmospheric Radiation Measurement Program.

6. References

Abdul-Razak, H. and S. Ghan, 2000: A parameterization of aerosol activation 2. Multiple aerosol types. J. Geophys. Res., 105, 6837-6844.

Bauer,S., D. Wright, E. Lewis, L_S. Chang, R. McGraw, S. Schwartz, R. Ruedy and D. Koch, 2008: The multiconfiguration aerosol tracker of mixing state MATRIX, an aerosol microphysical module for global atmospheric models. Atmos. Phys. Chem. Disc., In Review.

Bennartz, R. 2007: Global assessment of marine boundary layer cloud droplet number concentration from satellite. J. Geophys. Res., 112, doi:10.1029/2006JD007547

Cloud microphysics and aerosol indirect effects in the global climate model ECHAM5-HAM. Atmos. Chem. Phys. ; 7 ; 3425-3446

Gultepe, I. and G.A. Isaac, 1999: Scale effects on averaging of cloud droplet and aerosol number concentrations: Observations and models. J. Clim., 12, 1268-1279.

IPCC 2007: Climate Change 2007: The Physical Science Basis, edited by S. Solomon et al., Cambridge Univ. Press, New York.

Koch,D. G. Schmidt, and C. Field (2006): Sulfur, sea-salt and radionuclide aerosols in GISS ModelE, J. Geophys. Res., 111, doi:10.1029/2005JD007024.

Lohmann, U., P. Stier, C. Hoose, S. Ferrachat, E Roeckner and J. Zhang, 2007:

Menon, S, A.D. Del Genio, Y. Kaufman, R. Bennartz, D Koch, N. Loeb, and D. Orlikowski, 2008: Analyzing signatures of aerosol-cloud interactions from satellite retrievals and the GISS GCM to constrain the aerosol indirect effect. J. Geophys. Res., 113, doi:10.1029/2007JD009442.

Menon, S. and A. D. Del Genio, 2007: Evaluating the impact of carbonaceous aerosols on clouds and climate in Human Induced Climate Change: An Interdisciplinary Assessment, edited by Schlesinger et al., pp.34-48, Cambridge Univ. Press, New York.

Morrison, H., J.A. Curry, V. Khvorostyanov, 2005: A New Double-Moment Microphysics Parameterization for Application in Cloud and Climate Models. Part I: Description, J. Atmos. Sc., 62, 1665-1677.

Characteristics of the Boundary-Layer Clouds in a Global 14km-mesh Experiment by NICAM

*A. T. Noda[1)], K. Oouchi[1)], M. Satoh[1),2)], H. Tomita[1)],
T. Nasuno[1)], S. Iga[1)], H. Miura[3)]

1)Frontier Research Center for Global Change, Japan Agency for Marine-Earth Science and Technology, Japan
2)Center for Climate System Research, The University of Tokyo, Japan, 3) The Colorado State University, U.S.A.

Introduction

We have shown NICAM's high capability as a global cloud-resolving model through series of high-resolution experiments (*e.g.*, Miura *et al.*, 2007, *Science*, **318**, 1763-1765). As a next step, we are conducting a several month-long experiment targeted at boreal summer season of the year 2004 in order to assess NICAM's climatology under a specified period, and to understand an inclusive behavior of precipitation systems associated with large-scale circulations. As a part of the model verification, we shall focus on the behavior of the low-level clouds, and argue their characteristics.

Model setup

The horizontal resolution is nearly uniform, and is 14 km. We use a parameterization of explicit cloud microphysics by Grabowski (1998). The improved version of the Mellor-Yamada Level 2 model (*e.g.*, Nakanishi and Niino, 2004) is used for the turbulent closure scheme. The NCEP global analysis data at 00UTC on Jun 1, 2004 and Reynolds SST are given for the model initialization and the bottom boundary condition, respectively. The model integration is performed for more than 3 months.

Spatial structure and statistical behavior

It is well known that the low clouds favors to develop over regions off the west coast of continents such as California, Namibia and Peru. NICAM well-reproduces the spatial distribution of such persistent low-level clouds (Fig. 1). Figure 2 shows a spatial structure of the Peruvian marine stratocumulus appeared in this experiment. The cloud water content increases due to moisture supply from the ocean surface as apart from the coastal region ($\sim$ 80°W). The cloud layer evolves gradually higher and higher according to the growth of the mixed layer, and then turns to decrease at around 105°W. Such overall characteristics of the cloud environment agree with past numerical studies for the Peruvian low-level cloud in summer season. The boundary-layer air starts to interact actively with the free atmosphere according to the decrease of thermal stability between them.

The low-level cloud changes according to the interaction through radiation and turbulent processes, which often make the regional differences of cloud behaviors. Thus, we will report more detailed behavior of the low-level clouds appeared in NICAM with paying attention to the spatial change of stratification as well their statistical features against environmental change.

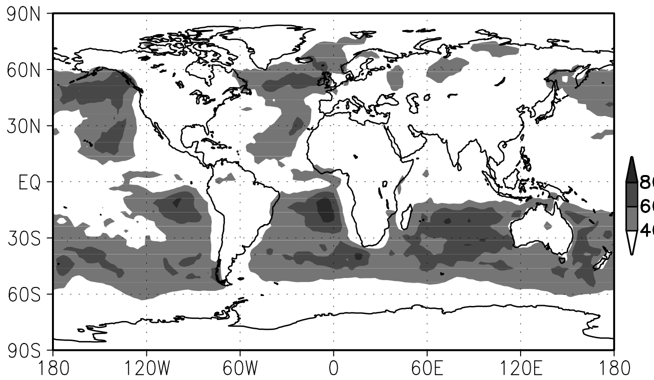

Figure 1: Low-level cloud in 14km-mesh NICAM. Sum of cloud water and cloud ice contents (g/m^2) accumulated up to 2km altitude averaged over June $\sim$ August 2004.

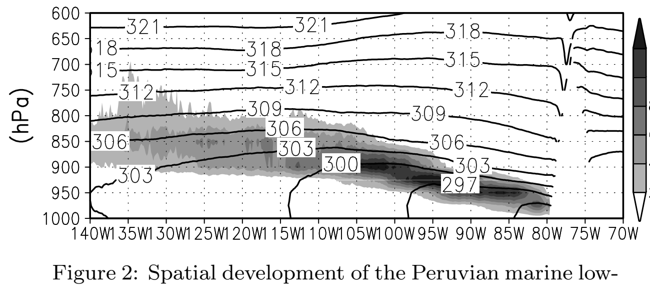

Figure 2: Spatial development of the Peruvian marine low-level cloud. Cloud water mixing ratio (shade; 10^{-2} g/kg) and virtual potential temperature (contour; K) along 10°S averaged over June $\sim$ August 2004.

AEROSOL EFFECTS ON CLOUDS IN EC-EARTH

Trude Storelvmo and Ulrike Lohmann

Institute for Atmospheric and Climate Science, ETH Zurich, 8092 Zurich, Switzerland

1 INTRODUCTION

More than three decades ago, Twomey (1974) stated the first hypothesis on how anthropogenic aerosols may influence climate through their impact on clouds. According to this hypothesis, often termed the *first aerosol indirect effect*, an increase in atmospheric pollution will lead to an increase in cloud albedo, all else being equal.

More than three decades and hundreds of publications later, aerosol indirect effects on climate are still a puzzle to the scientifc community ((Baker and Peter, 2008)), adding uncertainty to future climate projections. While the number of hypotheses on how aerosols may affect clouds, and thereby climate, has increased over this time period, the first aerosol indirect effect (AIE) is the only effect which can be calculated as a pure forcing directly comparable to other natural and anthropogenic forcing agents. In the Intergovernmental Panel on Climate Change (IPCC) fourth asessment report (AR4), the first aerosol indirect effect (AIE) was singled out as the most uncertain contributor to the net anthropogenic forcing of climate (Forster et al., 2007). Despite the fact that this effect, also named the cloud albedo effect, has been studied extensively in recent decades, our level of understanding of this effect was in IPCC AR4 still characterized as very low, radiative forcing estimates varying between -0.22 and -1.85 W/m^2. Hence, the highest estimates predict the AIE forcing to be comparable to that of greenhouse gases, but of opposite sign. Nevertheless, out of the coupled model simulations presented in IPCC AR4 predicting climate change over the next century, only about 1/3 included aerosol indirect effects. To predict aerosol indirect effects in numerical models requires a method for calculations of cloud droplet number concentration in the model based on aerosol mass or number concentration. In this paper, we investigate different methods applied to predict cloud droplet number concentration (CDNC) in the the coupled model simulations that included the AIE, 4 methods in total. We carry out this CDNC scheme intercomparison in the Integrated Forecasting Sytem (IFS) modelling framework, developed at the European Centre for Medium-Range Weather Forecast (ECMWF). The purpose is to provide an estimate of the spread in anthropogenic forcings caused by the prediction of CDNC alone, by performing a series of model experiments varying the CDNC scheme while all other aspects of the modelling framework are kept unchanged. The uncertainty range for the shortwave radiative forcing (SWCF) of the coupled model simulations in IPCC AR4 (Meehl et al., 2007) spans from -1.7 W/m^2 to 0.4 W/m^2. A major contributor to this wide range of SWCFs is the variety of parameterization of the aerosol indirect effect among the models.

2 MODEL DESCRIPTION AND SETUP

2.1 The Integrated Forecasting System

The global atmospheric tool in this study is the Integrated Forecasting System (IFS), which is the operational forecast model from ECMWF. An extended version of the IFS is also the atmospheric component of an earth system model currently under developement, namely the EC-earth model.

All simulations were carried out using a semi-lagrangian dynamical core at T95 spectral truncation, 40 levels in the vertical and a dynamical timestep of one hour. The physical schemes in the model most relevant for this study are the warm cloud microphysics scheme and the radiation scheme. The treatment of warm stratiform cloud microphysics follows Tiedke (1993). Cloud condensate and cloud cover are prognostic variables, while precipitation release is diagnosed. Warm-phase clouds form in a model grid box when the relative humidity exceeds a critical height-dependent threshold, and dissipate as a result of evaporation and/or precipitation processes. The cloud droplet effective radius (r_e) is calculated based on cloud droplet number concentration and liquid water content, following the formulation of Martin et al. (1994):

$$r_e = (\frac{3LWC}{4\pi\rho_w k N_l})^{1/3} \quad (1)$$

where LWC is the liquid water content, ρ_w is the density of water, N_l is the cloud droplet number concentration and k is a constant (k equals 0.67 over continents, and 0.80 in maritime air masses). Shortwave radiative properties of liquid clouds as a function of cloud droplet effective radius are calculated following Fouquart (1987).

2.2 Description of the aerosol treatment

As the focus of this study is to assess the forcing uncertainty introduced by applying various CDNC schemes, we prescribed the monthly average aerosol mass concentrations. The aerosol fields were the same as in e.g. Chen and Penner (2005) and Penner et al. (2006), and included total and natural sulfate, black carbon, organic carbon, and mineral dust and seasalt aerosols divided into two size categories.

2.3 Description of the cloud droplet schemes

Below follows a short presentation of the 4 methods applied to calculate cloud droplet number concentration (N_l) in this sensitivity study. In all cases N_l is given in cm^{-3}.

1. *Boucher and Lohmann (1995), hereafter BL95*

   The representations of N_l as a function of sulfate mass presented in BL95 have been used extensively in model studies of the aerosol indirect effects over the last decade. The empirical relationships in this paper are based on measurements from aircraft campaign carried out over North-America and the North and North-East Atlantic over different seasons and conditions. Based on these measurements, the following two relationships were obtained, for maritime and continental conditions, respectively:

   $$N_l = 10^{2.24+0.257\log(M_{SO_4})} \quad (2)$$

   $$N_l = 10^{2.06+0.48\log(M_{SO_4})} \quad (3)$$

   where M_{SO_4} is the sulfate mass concentration in $\mu g/m^3$.

2. *Jones et al. (2001), hereafter J01*

   The CDNC parameterization presented in J01 was originally in Jones et al. (1994), but was extended in J01 by taking not only sulfate but also seasalt aerosol concentrations into account. Based on simultaneous aircraft measurements of N_l and N_a from four regions (Pacific ocean, Summer 1987; South Atlantic, Winter 1991, British Isles, Winter 1990 and 1992; Azores, Summer 1992), the following relationship was presented:

   $$N_l = max\{3.75{\cdot}10^2(1-e^{-2.5{\cdot}10^{-9}N_a}, N_{min})\} \quad (4)$$

Here, N_a represents all sulfate and sea salt aerosols, and N_{min} = $5 cm^{-3}$. It is assumed that seasalt and sulfate are externally mixed. While the number of sulfate aeroosols are prediced from sulfate mass, the number of seasalt aerosols is a function of windspeed.

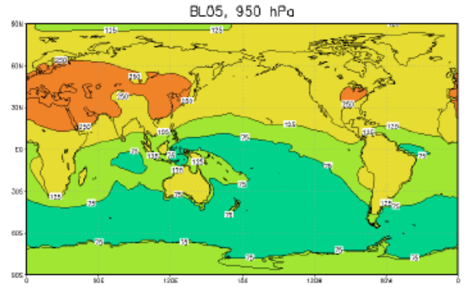

Fig. 1: Cloud Droplet Number Concentration (cm^{-3}) at 950 hPa as predicted folowing the method of Boucher and Lohmann (1995).

3. *Menon et al. (2002), hereafter M02*

The relationships between N_l and aerosol mass concentrations presented in M02 were based on partly the same field campaigns as those presented in BL05. However, they extended the BL05 approach by taking into account not only sulfate mass, but also seasalt and organic mass concentrations, obtaining the following relationships:

$$N_l = 10^{\{2.41+\log(M_{SO_4}{}^{0.50} M_{OM}^{0.13})\}} \quad (5)$$

$$N_l = 10^{\{2.41+\log(M_{SO_4}{}^{0.50} M_{OM}{}^{0.13} M_{SS}{}^{0.05})\}} \quad (6)$$

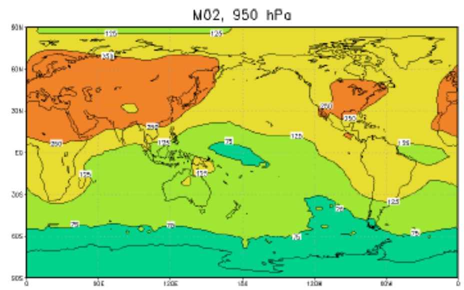

Fig. 2: Cloud Droplet Number Concentration (cm^{-3}) at 950 hPa as predicted folowing the method of Menon et al. (2002)

where M_{SO_4}, M_{OM} and M_{SS} are the mass concentrations in $\mu g/m^3$, of sulfate, organic matter and seasalt respectively.

4. *Dufresne et al. (2005), hereafter D05* presented modified versions of the relationships presented in BL95. By fiting (2) and (3) to satellite data from the POLDER instruments, they obtained the following relationship:

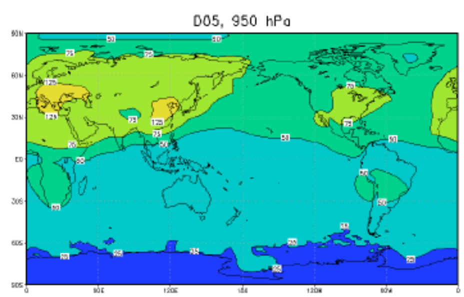

Fig. 3: Cloud Droplet Number Concentration (cm^{-3}) at 950 hPa as predicted folowing the method of Dufresne et al. (2005)

$$N_l = 10(1.7+0.2\log(M_{SO_4})) \quad (7)$$

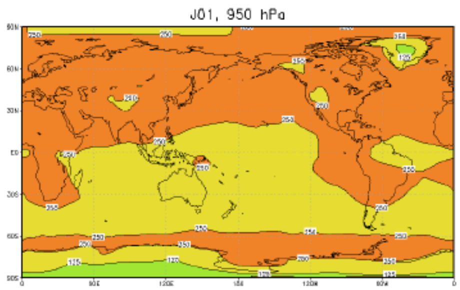

Fig. 4: Cloud Droplet Number Concentration (cm^{-3}) at 950 hPa as predicted folowing the method of Dufresne et al. (2005)

3 RESULTS AND DISCUSSION

As evident from Figure 1-4, the four different CDNC schemes lead to significant differences in the CDNC values at 950 hPa. The highest CDNCs are produced by J01, while the D05 CDNC parameterization resulted in the lowest CDNCs. Similarly, as seen from Table 1, the anthropogenic changes in CDNC values at 950 hPa differ by one order of magnitude, leading to anthropogenic changes in the shortwave radiative flux at the top of the atmosphere (a surrogate for AIE, as changes in longwave radiation due to anthropogenic aerosols are typically small) ranging from -0.53 W/m^2 to -1.91 W/m^2. Generally, large anthropogenic changes in CDNC are expected to yield large AIEs. However, the AIE is not only dependent on the anthropogenic CDNC perturbation, but also on the optical thickness of the unperturbed clouds.

4 CONCLUSION

In this study, we have demonstrated that the various CDNC schemes applied in the coupled model simulations pesented in IPCC AR4 yield aerosol indirect effects that range from -0.53 W/m^2 to -1.91 W/m^2, in simulations where aerosol fields and all other aspects of the model remained unchanged. This result indicates that most of the spread in the anthropogenic shortwave forcings from coupled simulations in IPCC AR4 could possibly be explained simply by the different treatments of the AIE in the models. However, as all results presented are based on relatively short model simulations (1 year), they must be considered as preliminary. Additionally, the aerosol indirect effect is strongly dependent on the model state (e.g. the amount of low vs. high clouds) and preindustrial vs. present-day aerosol fields. Hence, the same study carried out in a different model and/or with different aerosol fiels could result in different results. Nevertheless, the spread in AIEs obtained in this study is significant, suggesting that the AIE is the primary contributor to the spread in shortwave anthropogenic forcing estimates, adding uncertainty to predictions of future climate.

References

Baker, M. B. and T. Peter, 2008: Small-scale cloud processes and climate. *Nature, 451, 299-300*.

Boucher, O. and U. Lohmann, 1995: The sulfate-ccn-cloud albedo effect - a sensitivity study with two general circulation models. *Tellus, 47B, 281-300*.

Chen, Y. and J. Penner, 2005: Uncertainty analysis for estimates of the first indirect effect. *Atmos. Chem. Phys.,5,2935-2948*.

Dufresne, J. L., J. Quaas, O. Boucher, S. Denvil, and L. Fairhead, 2005: Contrasts in the effects on climate of anthropogenic sulfate aerosols between the 20th and the 21st century. *Geophys. Res. Lett.,32,doi:10.1029/2005GL023619*.

Forster, P., V. Ramaswamy, P. Artaxo, T. Berntsen, R. Betts, D. W. Fahey, J. Haywood, J. Lean, D. C. Lowe, G. Myhre, J. Nganga, R. Prinn, G. Raga, M. Schulz, and R. V. Dorland, 2007: Changes in atmospheric constituents and in radiative forcing. *In: Climate Change 2007:The Physical Science Basis. Contribution of Working Group I to the Fourth Assessment Report of the Intergovernmental Panel on Climate Change,*

Tab. 1:

CDNC scheme	Aerosol indirect effect (W/m^2)	ΔCDNC at 950 hPa (cm^{-3})
Boucher and Lohmann (1995)	-0.53	22.3
Jones et al. (2001)	-1.91	42.5
Menon et al. (2002)	-1.49	113.6
Dufresne et al. (2005)	-0.62	10.6

Cambridge University Press, Cambridge, United Kingdom and New York, NY, USA.

Fouquart, Y., 1987: Radiative transfer in climate modeling. *In: M. E. Schlesiger (Ed.) Nato Advanced Study Institute on Physically-based Modeling and Simulation of Climate and Climate Changes, pp 223-283*.

Jones, A., D. L. Roberts, and A. Slingo, 1994: A climate model study of indirect radiative forcing by anthropogenic sulphate aerosols. *Nature, 370, 450-453*.

Jones, A., D. L. Roberts, M. J. Woodage, and C. E. Johnson, 2001: *Indirect sulphate aerosol forcing in a climate model with an interactive sulphur cycle*. J. Geophys. Res., 106, 20293-20310.

Martin, G. M., D. W. Johnson, and A. Spice, 1994: The measurement and parameterization of effective radius of droplets in warm stratocumulus clouds. *J. Atmos. Sci., 51, 1823-1842*.

Meehl, G., T. F. Stocker, W. D. Collins, P. Friedlingstein, A. T. Gaye, A. M. Gregory, A. Kitoh, R. Knutti, J. M. Murphy, A. Noda, S. C. B. Raper, I. G. Watterson, A. J. Weaver, and Z.-C. Zhao, 2007: Global climate projections. *In: Climate Change 2007: The Physical Science Basis. Contribution of Working Group I to the Fourth Assessment Report of the Intergovernmental Panel on Climate Change, Cambridge University Press, Cambridge, United Kingdom and New York, NY, USA*.

Menon, S., A. D. D. Genio, D. Koch, and G. Tselioudis, 2002: Gcm simulations of the aerosol indirect effect: Sensitivity to cloud parameterization and aerosol burden. *J. Atmos. Sci, 59, 692-713*.

Penner, J. E., J. Quaas, T. Storelvmo, T. Takemura, O. Boucher, H. Guo, A. Kirkevag, J. Kristjansson, and O. Seland, 2006: Model intercomparison of indirect aerosol effects. *Atmos. Chem. Phys.,6,3391-3405*.

Twomey, S., 1974: Pollution and the planetary albedo. *Atmos. Environ., 8, 1251-1256*.

9.3 SCAVENGING OF LIGHT ABSORBING CARBON PARTICLES BY ICE CRYSTALS

D. Baumgardner[1], R. Subramanian[2], G. Kok[2] and C. Twohy[3]
[1]Centro de Ciencias de la Atmósfera, Universidad Nacional Autonoma de México
[2]*Droplet Measurement Technologies*
[3]*Oregon State University*

BACKGROUND

Black carbon particles, hereafter referred to as light absorbing particles (LAC)[1], are some of the most ubiquitous and radiatively active of all aerosol particle found in the atmosphere. In the boundary layer they serve to absorb solar radiation and cool the earth's surface but in the upper troposphere, they augment climate warming from greenhouse gases. In a recent review, Ramanathan and Carmichael (2008) estimate that the emissions of LAC are the second strongest contributor to current global warming after carbon dioxide emissions. These LAC emissions lead to the 'dimming' at the earth's surface with subsequent implications for hydrological processes. There are major uncertainties, however, in the estimates of the environmental impact of LAC. Although there are good estimates of the emission strength of LAC (Bond et al., 2004), the efficiency of the removal mechanisms remain largely unknown. For example, in an evaluation of 16 global aerosol models, Textor et al. (2006) found that the atmospheric residence time of LAC assumed in these models varied from 5 to 10 days with a standard deviation of ±30%. The parameterizations varied from constant removal rates by dry and wet deposition to more elaborate schemes that used varying schemes of aging that changed LAC particles from hydrophobic to hydrophilic.

Wet deposition by precipitation has been assumed to be the primary mechanism for removing LAC from the atmosphere but there are very few measurements that can validate this assumption. Freshly emitted LAC is highly hydrophobic and laboratory research and some field studies show that these particles become more water soluble as they age and are coated with hygroscopic material. LAC particles have also been found in water droplets (Twohy et al., 1989) and ice crystals (Ström and Ohlsson, 1998; Twohy and Poellot, 2005) suggesting that some fraction of these particles are removed by cloud particles.

Measurements of LAC in cirrus crystals have recently been made in the upper troposphere over the Pacific in outflow of pollution from Asia. The remainder of this presentation describes a new technology for measuring LAC mass and evaluates the properties of the LAC particles in the ice crystals compared to those in the cloud-free environment

METHODOLOGY

The instrument used for measuring the mass concentration of individual LAC particles is the Single Particle Soot Photometer (SP2). Particles enter a focused, 1.064 µm wavelength laser beam and will be heated to the point of incandescence if they contain LAC. The light emitted during incandescence is measured with a photomultiplier and the relationship between peak intensity and carbon mass is established through calibration. A separate detector measures the peak scattering intensity from which an optical diameter is derived using Mie theory.

---

[1] Suggested by Bond and Bergstrom (2006) who recommended this nomenclature for research related to the radiative impact of these types of particles.

An indication of the amount of non-LAC that is mixed with the LAC is derived by comparing the optical diameter with the mass equivalent diameter of the LAC. This latter dimension is calculated from the measured mass, assuming a density of 1.9 g cm^{-3} as recommended by Bond and Bergstrom (2006). The difference between the optical diameter and the mass equivalent diameter will be referred to here as an “equivalent coating thickness” under the assumption that the LAC can be collapsed into an equivalent sphere covered with the non-light absorbing material. Details of the SP2 technique and uncertainties can be found in Schwarz et al. (2006) and references therein. The derivation of equivalent coating thickness is discussed by Baumgardner et al. (2007).

The SP2, as operated during the project described below, measured LAC with mass equivalent diameter that varied from approximately 70 to 187 nm (± 20 nm), and optical diameters from 120 to 360 nm (± 30 nm). Particles containing LAC larger than 187 nm are counted but since they saturated the detector, their actual mass and diameter can not be determined.

The SP2 was mounted on the NCAR HIAPER aircraft and sampled from either an inlet that brought in environmental air or from a counterflow virtual impactor inlet (CVI) that separated cloud particles from gases and interstitial aerosols and evaporated them using dry, heated nitrogen (Twohy et al., 1997). The water vapor was measured with a tunable diode laser to derive the total water content and the residuals of the ice particles were sampled with the SP2 and ice nuclei (IN) counter. Some of the residuals were also captured on electron microscope grids for subsequent analysis after the flights. Only the water content and LAC measurements from the SP2 will be discussed here.

RESULTS AND DISCUSSION

A pilot project, the Pacific Dust Experiment (PacDEx), was conducted from April 29 to May 24, 2007 to evaluate the properties of aerosols in air masses that originated in Asian and to study the transformation of these particles as they aged and interacted with clouds. It has been well documented through satellite measurements (Yu et al., 2008) that dust and pollution that originates in Asia is carried across the Pacific as a result of vertical transport via the warm conveyer belt mechanism (Stohl et al., 2002) that is strongest in the springtime.

The flights were designed to follow air masses originating over China during major dust outbreaks and to track them eastward. There were 15 flights that originated either from Alaska or Japan. The flights of May 2, 5 and 17th are evaluated here to compare measurements made in the Western Pacific (134º to 145º E) to those made in the Central Pacific (160º to 180º E) and in conditions in and out of cloud.

Figure 1 illustrates the differences in the vertical structure of the number concentration of LAC (solid lines) and the number fraction of LAC, where the number fraction is the ratio of the LAC concentration divided by all particles detected by the SP2 (LAC plus those that didn’t incandesce). The black lines are measurements made in the western Pacific, close to the source of the anthropogenic aerosols and the red lines are the measurements from the central Pacific. These profiles show the maximum LAC concentration near the surface for the most western measurements and an enhanced concentration in a layer centered at four kilometers in the central Pacific, a distance approximately 8000 km downwind of the source.The western and central Pacific profiles of the number fraction are similar and indicate that almost 15-20% of the particles detected by the SP2 include LAC in the upper troposphere.

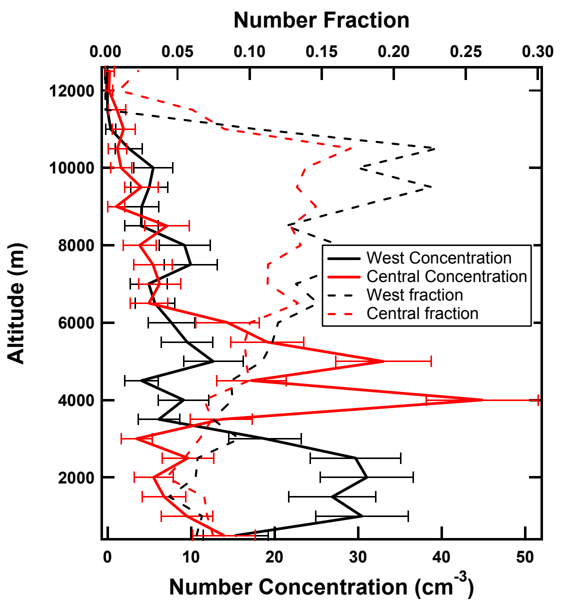

Figure 1

The measurements from the three days were averaged for those periods when the aircraft was above 8000 m to evaluate the LAC properties in these regions of enhanced LAC number fraction, stratifying by region over the Pacific and whether the LAC particles were in the residual of ice crystals or in the ambient air. The periods in cloud were elected by the value of ice water content derived from the CVI (> 0.01 g m^{-3}) and when the SP2 from sampling from the CVI.

Figure 2 shows the size distributions of the LAC mass as a function of the optical diameter derived from the light scattering signal. The LAC mass reaches a maximum at approximately 160 nm and is about four times larger in the West Pacific. In the west and Central Pacific, the mass of LAC in the ice crystals is about half the ambient LAC. The primary difference between the in and out of cloud mass concentrations is that the in cloud mass is larger than the ambient when the optical diameter exceeds 300 nm and 320 nm, respectively, for the central and west Pacific as shown by the red curves that are the ratios of in-cloud to no-cloud mass.

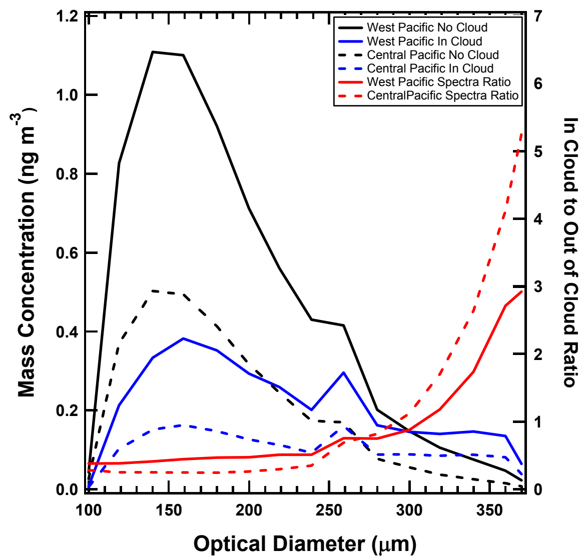

Figure 2

The differences in the properties of the LAC particles can be seen more distinctly when we compare the frequency distributions of the mass equivalent diameters for the in and out of cloud measurements in the west and central Pacific as seen in Figs 3a and b. The mass equivalent diameters are broadly distributed from 60 to 180 nm in the out of cloud LAC but are much more narrowly distributed with a peak at 160 nm for the in cloud particles.

The equivalent coating thickness is also quite different between the crystal residuals and the ambient LAC (Fig. 4a and b). Although the frequency distributions are broad, the ambient coatings are a maximum around 20 nm whereas the crystal residuals coatings peak at 60 nm.

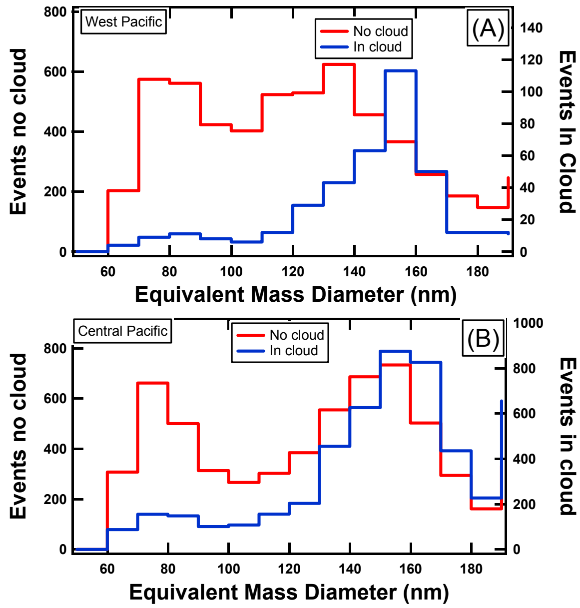

Figure 3

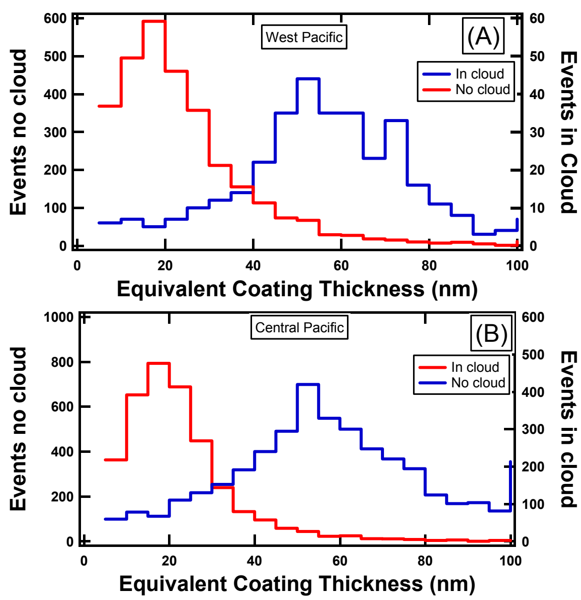

Figure 4

A comparison of the fraction of particles that contained LAC, as illustrated in Figs. 5a and b, show that the crystal residuals have twice as many LAC particles per total number of particles detected as found outside the clouds in the west Pacific but in the central Pacific, the out of cloud fractions were twice those found in cloud. In addition, those clouds nearer the pollution source have a larger number fraction than those 8000 km further downwind. There were also almost 40% of the cloud samples in the central Pacific that had a very small fraction of LAC. Analysis of these clouds is currently in progress to determine if they were in air masses whose origins were different than those with higher concentration fractions.

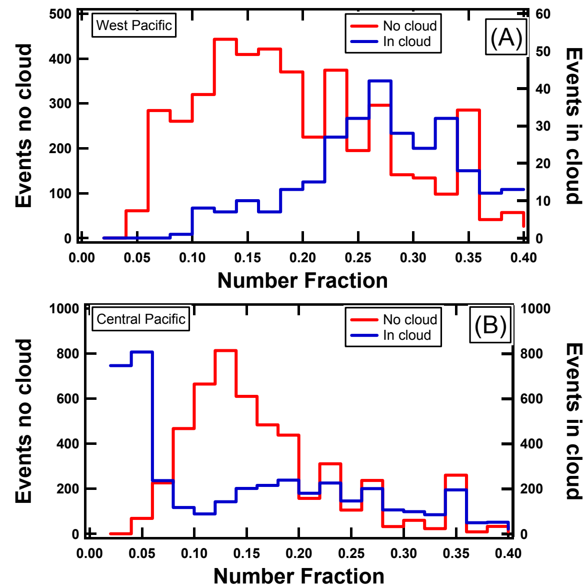

Figure 5

Discussion

The prevalence in cloud of more LAC particles, larger mass equivalent diameters and thicker equivalent coatings than measured in the surrounding cloud-free environment suggests that the scavenged LAC aerosols have possibly undergone some type of cloud processing but there are a number of possible processes that could explain the in and out of cloud differences. If we assume that a large proportion of the LAC is transported from the polluted boundary layer by way of deep convection, then there are several mechanisms by which these particles arrive in the ice crystals or on their surfaces: 1) the LAC, coated with hygroscopic material can activate as water droplets that become ice crystals via homogeneous freezing during their ascent through the cloud, 2) the LAC might be an ice nuclei (IN) that becomes an ice crystal during its ascent through the convective cloud or 3) the LAC may be an IN that doesn't become an ice crystal until some later time after being transported out the top of a convective cloud.

If larger LAC particles or LAC with thicker coatings of soluble material are better IN this is one explanation for the differences between the in and out of cloud LAC aerosol seen in Figs. 3 and 4. An alternative explanation is that ice crystals are collecting LAC particles on their surfaces by inertial scavenging and when they are evaporated in the CVI, multiple LAC particles on a crystal coagulate and are measured as a single particle. This would not only appear as a larger equivalent diameter but would also lead to thicker equivalent coating. Inertial scavenging would also explain the higher number fraction of LAC in clouds compared to the ambient environment.

In order to incorporate these results into global aerosol models, it is useful to express the scavenging efficiency of the ice clouds as a mass of LAC with respect to mass of water. Figure 6 is a frequency distribution of the second by second ratios of LAC mass to ice water content measured with the CVI.

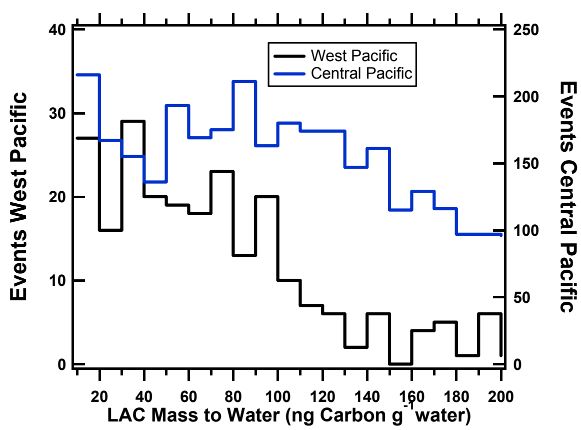

Figure 6

Fifty percent of the measurements show that 10-100 ng of carbon are scavenged per gram of water in clouds near the source of the LAC; however, the remaining 50% varies from 100 to 200 ng. In the clouds much farther downwind more than 50% of the measurements show scavenging efficiencies of larger than 100 ng g^{-1} of water. These derived efficiencies are the first that have been made whereby the LAC mass was measured directly. Previous estimates were made using a light absorption technique then converting to LAC with a scale factor. Table I shows a comparison with scavenging efficiencies reported by other investigators for other types of clouds.

Table I

Water Type/ Location	Soot/LWC Ng g^{-1}	Reference
Rainwater/Sweden	20-600	Ogren et al., 1983,1984
Rainwater/Seattle	30-400	Ogren et al., 1983,1984
Cloud water/ Eastern Pacific	23-79	Twohy et al., 1989
Cirrus crystals/ west and central Pacific	10-200	This study

Summary

Measurements of the mass of light absorbing carbon have been made for the first time in cirrus ice crystals in the upper troposphere. Comparison of LAC properties over the western and central Pacific, in cirrus clouds and the ambient environment, show that the equivalent coating thickness and mass equivalent diameters of the LAC found in ice crystal residuals are on average more than twice the thickness and diameter found in the ambient LAC aerosols. These differences are possibly a result of inertial scavenging by ice crystals of LAC aerosols that have been transported by deep convection to the upper troposphere; however, given that there are multiple pathways by which LAC can be incorporated by ice crystals, a more detailed investigation is necessary to study these processes.

Acknowledgements

The authors would like to thank the National Science Foundation for supporting their participation in PacDex, Jeff Stith and the flight crew of the Research Aviation Facility, National Center for Atmospheric Research, for their support of the aircraft and instrumentation, and to V. Ramanathan for his continuing inspiration and guidance.

References

Baumgardner, D., G.L. Kok and G.B. Raga 2007: On the Diurnal Variability of Particle Properties related to Light Absorbing Carbon in Mexico City, *Atmos. Chem. Phys.*, 7, 2517-2526.

Bond, T. C., and Bergstrom, R. W.: Light absorption by carbonaceous particles: An investigative review, *Aerosol Sci. and Tech.*, 40, 27-67, 2006.

Bond T C, Streets D G, Yarber K F, Nelson S M, Woo J-H and Klimont Z, 2004: A technology-based global inventory of black and organic carbon emissions from combustion *J. Geophys. Res.* 109 D14203

Eckhardt, S., A. Stohl, H. Wernli, P. James, C. Forster, and N. Spichtinger, 2004: A 15-Year Climatology of Warm Conveyor Belts, *J. of Climate,*17, 218–237.

Moteki, N, Y. Kondo 2006 Effects of mixing state on black carbon measurement by Laser-Induced Incandescence *Aerosol Science and Technology*, 41:398–417, 2007

Ogren, J.A. et al., 1983: Determination of elemental carbon in rainwater, *Anal. Chem.*, 55, 1569-1572.

Ogren, J.A. et al., 1984: Measurement of the removal rate of elemental carbon from the atmosphere, *Sci. Tot. Env.,* 36, 329-338.

Ramanathan, V. and G. Carmichael, 2008: Global and regional climate changes due to black carbon, *Nature Geoscience*, 1, 221-227.

Schwarz, J.P et al. 2006: Single-particle measurements of mid latitude black carbon and light-scattering aerosols from the boundary layer to the lower stratosphere, *J. Geophys. Res.* 111, D16207, doi:10.1029/2006JD007076.

Slowik, J. G., Cross, E., Han, J., Davidovits, P., Onasch, T. B., Jayne, J. T., Williams, L. R., Canagaratna, M. R., Worsnop, D. R., Chakrabarty, R. K., Arnott, W. P., Schwarz, J. P., Gao, R. S., Fahey, D. W., and Kok, G. L. 2007 Intercomparison of instruments measuring black carbon content and optical properties of soot particles, *Aerosol. Sci. Technol.*, 41:295–314

Stohl, A., S. Eckhardt, C. Forster, P. James, and N. Spichtinger 2002: On the pathways and timescales of intercontinental air pollution transport, J. Geophys. Res., 107(D23), 4684, doi:10.1029/2001JD001396.

Ström, J. and S. Ohlsson, 1998: In-situ measurements of enhanced crystal number densities in cirrus clouds caused by aircraft exhaust, J.Geophys. Res., 103, 11 355–11 361.

Textor, C. et al., 2007: Analysis and quantification of the diversities of aerosol life cycles within AeroCom, Atmos. Chem. Phys., 6, 1777–1813.

Twohy, C.H. et al., 1989: Light-absorbing material extracted from cloud droplets and its effect on cloud albedo, *J. Geophys. Res.*, 94, 8623-8631.

Twohy, C. H., Schanot, A. J., and Cooper, W. A.: 1997: Measurement of condensed water content in liquid and ice clouds using an airborne counterflow virtual impactor, J. Atmos. Oceanic Technol., 14, 197–202, 1997.

Twohy, C.H. and Poellot, 2005: Chemical characteristics of ice residual nuclei in anvil cirrus clouds: evidence for homogeneous and heterogeneous ice formation, *Atmos. Chem. Phys. Discuss.,* 5, 2289-2297

Yu,H., L. A. Remer,M. Chin, H. Bian,R. G. Kleidman,and T. Diehl, 2008: A satellite-based assessment of transpacific transport of pollution aerosol, *J. Geophys. Res.*, 113, D14S12, doi:10.1029/2007JD009349

Rain Intensity Spectral Shift: An Aerosol Effect?

Jen-Ping Chen[1], Shaw-Cheng Liu[1,2], Chien-Jung Hsu[1,2]
Anupam Hazra[1] and Pei-Yun Tang[1]

[1] Department of Atmospheric Sciences, National Taiwan University
[2] Research Center for Environment Change, Academia Sinica

1. INTRODUCTION

Under increasing awareness of human influence on the environment, growing attention is paid to the possible effect of anthropogenic aerosols on cloud properties and precipitation formation. As pointed out by Twomey in 1974, increasing anthropogenic pollution would result in more numerous cloud condensation nuclei (CCN) and cloud drops, as well s narrower drop size spectrum. These effects not only cause an increase in the reflectance of cloud on incident sunlight but may also retard the formation of raindrops. Under constrained supply of moisture, increasing cloud drop number should result in smaller cloud droplets, such that the chances for them to collide and coagulate, by which raindrops may formation, are reduced.

Evidences seem to be mounting on the impact of anthropogenic aerosols on cloud drop number concentration, such as the study of smoke from sugarcane fire (Warner and Twomey 1967), from paper mills (Hobbs et al. 1970; Mather 1991), from urban activities (Squires 1966; Braham 1974), and from ship effluent (Coakley et al. 1987; Radke et al. 1989; Albrecht 1989; Ferek et al. 2000). Yet, for precipitation suppression by aerosols, the observational evidences seem to be conflicting and inconclusive. Warner and Twomey (1967) used aircraft observation to verify the above normal cloud drop number concentration found previously in Australia could be a result of sugarcane fires. But more extensive statistical analysis of the long-term ground measurement data showed no evidence of subsequent changes in surface precipitation (Warner 1971). This viewpoint was shared by Woodcock and Jones (1970) who studied similar circumstances over Hawaii. Using advance satellite measurements, Rosenfeld (2000) contended that industrial and urban pollutions suppressed rainfall in some areas of Australia, but his stance was disputed by Ayers (2005) who analyzed precipitation measured on the ground for the relevant event. Givati and Rosenfeld (2004, 2005) analyzed long-term ground data and reported a reduction of orographic rainfall in downwind of polluted regions in central and northern Israel over past several decades. But Alpert et al. (2008) re-analyzed the rainfall data in Israel and revealed no systematic reductions in mountain rainfall, and there were even increases in some regions.

Evidences of aerosol effect on precipitation appear not only inconclusive but also in disagreement. For instance, Rosenfeld (1999) found rain suppression by forest fire in Indonesia, whereas Lin et al. (2006) found increasing rainfall associated with elevated aerosol loading during the biomass burning seasons over the Amazon region (both using satellite-based measurements). Increasing rainfall due to aerosols influence was also pointed out by Hobbs (1970) and Hindman et al. (1977) who suggested that giant CCN from paper mills exhaust may actually enhanced precipitation. Such a mechanism was also applied to explain the increase of precipitation downwind of major urban areas (Chagnon et al., 1976; Braham 1981), although other mechanisms such as the heat island effect were also proposed (Rozoff et al. 2003). Bewilderingly, Jirak and Cotton (2006) found decreasing precipitation over the past half-

Corresponding author:
Dr. Jen-Ping Chen
Department of Atmospheric Sciences
National Taiwan University
jpchen@as.ntu.edu.tw

century at downwind directions of Denver and Colorado Springs, Colorado, a result in accordance with Rosenfeld's rain suppression argument.

Some of the above studies suffer from either inadequate statistical procedure, as cautioned by Gatz (1979) and Dabberdt et al. (2000), or failing to verify with true ground measurements, while others seem to be in disagreement. Lacking of concrete observational confirmation, the issue of aerosol effect on precipitation remains a hypothesis to this date, even though some theoretical studies have successfully demonstrated such influences (e.g. Levin et al 2005, Teller and Levin, 2006). But it does not mean that we should ignore these findings. On the contrary, these seemly contradicting results hinted us that the effect of aerosol on precipitation is not a simple matter. Like a quixotic cat stepping out the room to see where the bouncing ball came from, one might need to look at the data from a different perspective.

In this study we look beyond the total precipitation change and examine the spectral distribution of rainfall intensity as an effective means to decipher the aerosol effects. A numerical model with the capability of simulating aerosol effect on precipitation is applied to simulate the observed spectral change and provide a direct link to the physical mechanisms behind it. We also take note of other possible causes of changes in rainfall intensity.

2. OBSERVED SPECTRAL SHIFT

The fast economic development and worsen air pollution condition during the past decades makes East Asia an ideal area to exemplify aerosol effect on hydrological cycle. Taiwan not only has strong local production of air pollutants but also receives them by long-range transport from the neighboring countries with escalating economic activities. So, conceivably one should be able to find in here signs of aerosol influences, if they indeed exist. However, after analyzed hourly precipitation data measured at 21 ground stations at Taiwan over the past half a century, we found no long term trend in total precipitation (Fig. 1A) comparable to the pollution situation. This seems to be a disappointing result. But a few other signatures lead us to look into deeper. First, the total rain hours decreased significantly (Fig. 1B). To maintain the same amount of rainfall accumulation, this decrease in frequency must be accompanied by an increase in average rainfall intensity (Fig. 1C). How was this peculiar "rain less (frequently) but also rain more (strongly)" situation formed? Could it be due to more frequent strong rain, or perhaps just the light rain (which does not contribute much to the total rainfall) was disappearing? The answer to it has strong implication to the physical mechanisms behind, and we suggest aerosols may be playing a crucial role here.

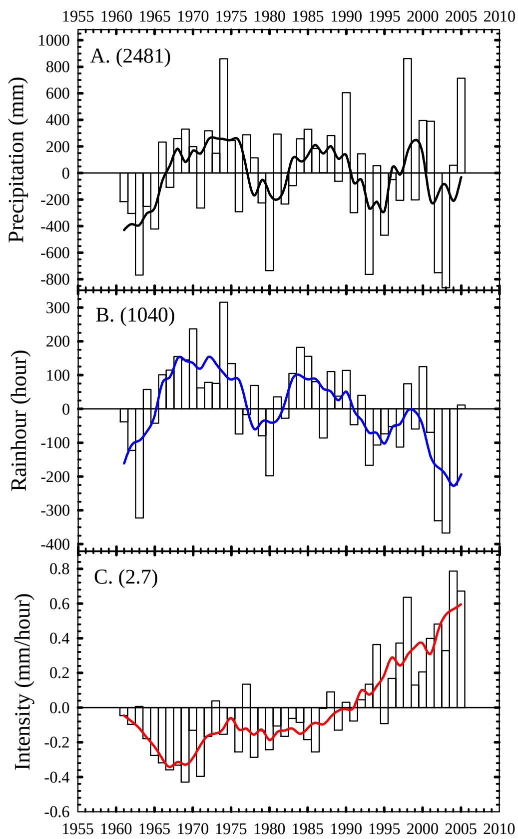

Figure 1: Rainfall characteristics observed over Taiwan during the past five decades. Values are deviations from the 50-year averages (number in the brackets) of all hourly observations from 21 ground stations.

Figure 2 shows the rainfall intensity spectrum (RIS) in Taiwan over the past 5 decades. One can see a significant decrease in light rain frequency accompanied by more frequent heavier rain occurred in the last three decades, during which Taiwan and the surrounding regions experienced explosive industrialization and economic development. It is not just a simple shift of the probability function toward heaver precipitation because there is a net reduction of total frequency. The change in RIS is like tipping a balance beam: decrease in lighter rain and increase in heavier rain occurred simultaneously.

By ignoring precipitation intensity greater than 30 mm hr^{-1}, which usually resulted from rare and sporadic events of storms, we categorize rainfall less than or equal to 5 mm hr^{-1} as lighter rain while the rest as heavier rain. The long-term records clearly show a significant decrease in lighter rain and increase in heavier rain. Incidentally, these two trends nearly compensated each other. So it is likely that, for the situation in Taiwan, the positive and negative aerosol effects canceled out each other. In some other areas one might significantly outweigh the other.

Before getting into the detailed mechanisms, one needs to ask: why bother with it if the net effect is negligible? It is important to realize that the ecosystem and the climate system are sensitive to not only the averages or extremes but also the whole spectrum of rain intensity. For example, soil moisture is not only important to weather and short-term climate (Namias, 1952; Karl, 1986; Hung et al. 1996) but also essential to sustain many microbes, insects and plant lives, as well as to seed germination and growth of the seedlings (Tan and Tu, 2003; Wagenvoort 1981; Oberbauer and Miller, 1982). Light rain is important because it usually has the highest frequency (accumulated rain time) and tends to be absorbed completely by surface soil. If the duration between precipitation events is too long, soil water may drop below the permanent wilting point, and the rainfall after will not be able to revive the plants. Longer draught may lead to soil degradation and even desertification. In this regard, timely rainfall by even a small amount could be vital to the ecosystem. On the other hand, it takes strong or long enough rainfall to supply water into the deep soil, by tapping into which forest and pastures may adapt to large fluctuations in rainfall. Strong rain is also important to water discharge into ground water table, as well as to rivers and lakes for the downstream areas. (If rainfall intensity exceeds soil infiltration capacity, surface runoff occurs.) Yet, excessive (too strong or too long) rainfall may result in root rot, flood, soil erosion and even landslides and debris flows (Starkel 1976; Alva et al. 1985; Watson and Laflen 1986; Fraser et al. 1999). Therefore, it is important to understand the changes in the whole range of RIS.

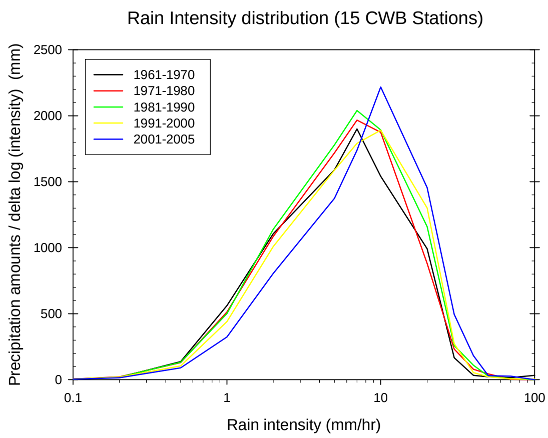

Figure 2: Rainfall intensity spectrum observed over Taiwan. The ordinate is the accumulated frequency (in terms of days) during the indicated time period, and the abscissa is the rainfall intensity category.

3. AEROSOL EFFECT SIMULATIONS

The effect of aerosol on precipitation formation involves many microphysical processes. Processes involving ice nuclei are highly complicated and uncertain in many ways. So we focus on the role of hygroscopic aerosols which act as condensation nuclei. Condensation nuclei affects activation, condensation growth, coalescence. They even affect the ice phase processes, such as accretion, Bergeron-

Findeisen, and homogeneous freezing (not the solute effect but via the number effect. There have been numerous numerical studies on the effect of aerosols on precipitation, and most of them showed rain suppression by hygroscopic aerosols in shallow clouds, but for convective clouds the results are somewhat ambiguous (e.g. Teller and Levin 2006; Tao et al. 2007). Here we will not get into the details of various model and their outcomes. Instead, we focus on the model produced RIS which is seldom analyzed in previous studies.

We apply the modified MM5 of Cheng et al (2007) who adopted the two-moment warm cloud scheme of Chen and Liu (2004) to include aerosol effects on cloud drop and raindrop formation. For this study, the Chen and Liu (2004) warm cloud scheme is also coupled with the Resiner scheme for ice-phase processes in order to show the effect of aerosols on cold-rain (via ice processes) formation. With this model, we simulated a few cases of rain-producing cloud systems that are common over the Taiwan area. Two of them are summertime thermal convections and the others are cold fronts occurred in late winter and spring. Three types of typical aerosol size distributions from Whitby (1978) were applied to initialize cloud formation: (1) clean continental, (2) average continental background, and (3) urban aerosols. Without going into the details of microphysical processes, we only look at the statistics of hourly surface rainfall intensity from all grid points in the inner-most domain which has a horizontal resolution of 3 km by 3 km.

Figure 3 shows the simulated RIS. The two summertime convective clouds show similar responses of RIS to aerosol types,

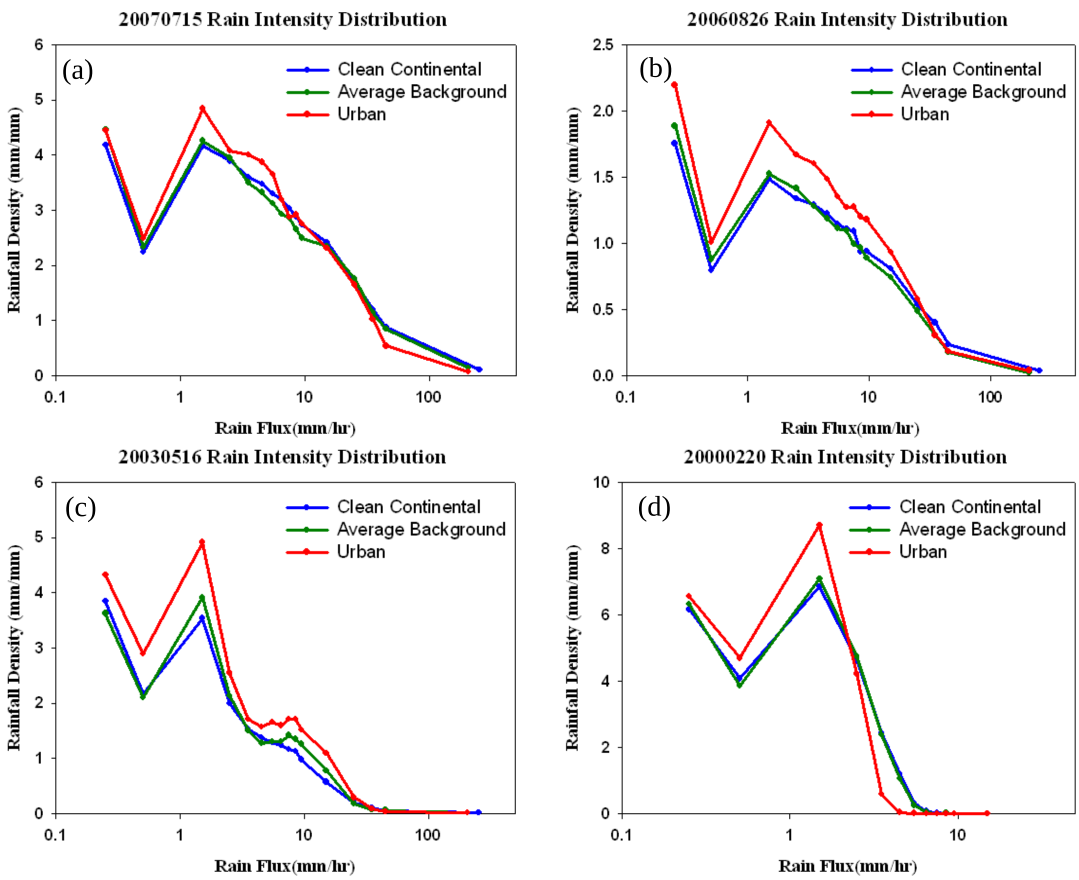

Figure 3: Simulated rainfall intensity spectrum under different aerosol conditions. The abscissa is the rainfall intensity, and the ordinate is the rainfall "density" (total rainfall within a certain range of intensity divided by the range) but normalized against the total rainfall of each

with more frequent occurrence between 0.5 and 10 mm/hr, and somewhat less frequent for > 30 mm/hr rain intensities. The differences between the average background and clean continental aerosol types are less significant, but the pattern is similar. Note that, for the 2006/06/26 case, the mean total rainfall increases from 30 mm for the clean continental aerosols to 37 mm for the urban aerosols, whereas for the 2007/07/15 case, it decreases from 115 mm to 100 mm. For the cold front clouds occurred in 2003/05/16, the frequency increased over the whole RSI for unban aerosols comparing to that for the other two aerosols types. When comparing the average background with clean continental aerosol types, the pattern is similar except for a slight decrease in the lightest rain of < 0.5 mm/hr. Overall rainfall for this case ranges from 29 mm to 41 mm, being higher for more polluted aerosol types,. The 2000/02/20 case generated much less rain, so the RIS shifted toward the light rain end. The responses to aerosol types seem to behave similar to that for the summertime clouds, except that the crossover point is at about 2 mm/hr. The overall rainfall is about the same for all three aerosol types.

In general, the RIS responds significantly to the change of aerosol types. However, with the assumption that aerosol pollution increases with time, such responses seem to be different from the observed RIS changes (Fig. 2), which show less frequent light rain and more frequent heavier rain as time progress Note that Fig. 2 is normalized against the total rainfall for each spectrum. So it is only fair to normalize the RIS in Fig. 3 because the total rainfall varies between different simulations. The modified RIS is given in Fig. 4. One can see that two of the cases now look different. For the 2006 case, the RIS is similar between the urban and average background types, while both show more light rain than the clean continental situation. In the 2003 case it becomes less

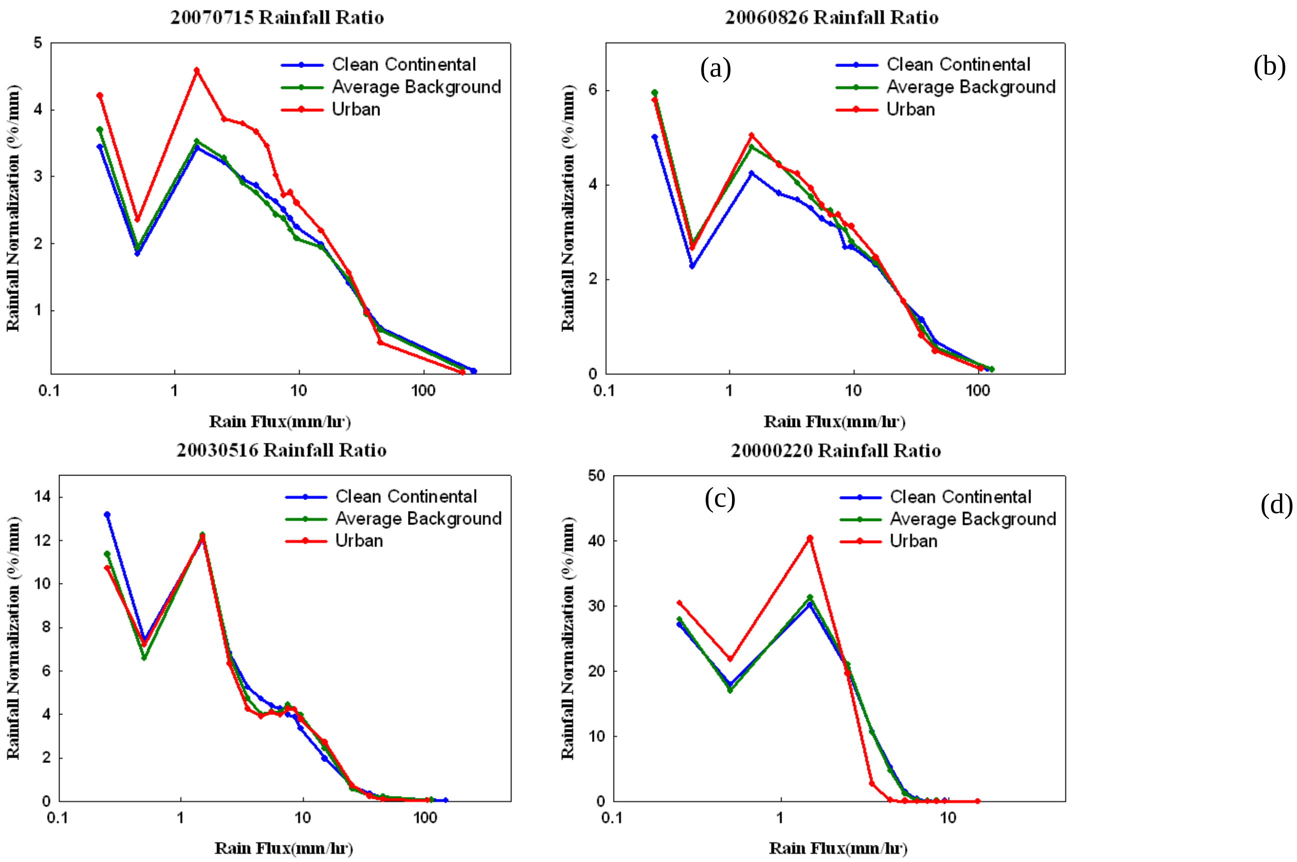

Figure 4: Same as Fig. 3 except they are normalized against total rainfall of each simulation.

frequent for rain intensity lower than 1 mm/hr and between 3 and 8 mm/hr for the urban and average background situations. Although getting closer, the simulation still cannot reproduce the observed spectral shift.

4. DISCUSSION

Reductions in light precipitation may be a regional scale rather than a local scale process, as substantiated by the recent reports of reduction in light precipitation over most of Mainland China by Qian et al. (2006). Persistent and chronic decrease of light precipitation may pose a serious threat to the drought problem because light precipitation is a critical source of water in the replenishment and retention of soil moisture. So the spectral shift in rain intensity may have important consequences in the problem of desertification and impacting the ecosystem and regional climate.

The simulations above showed that aerosols do affect precipitation, in both total quantity and the intensity spectrum. These changes are associated with responses from the warm-cloud and mixed-phase cloud microphysical processes, and perhaps the dynamics, which are too complicated to be elaborated here. But the resulting RIS changes are in disagreement with the observed trend under the assumption that aerosol concentration increases with time. If the model is performing correctly, then there must be some other mechanisms that caused the observed RIS change. More likely, it is a combination of different factors.

One of the possible mechanisms is associated with the phenomenon of regional warming. By analyzing space-based and ground-based global rainfall data, Lau and Wu (2007) also found a significant shift in the intensity spectrum of tropical rainfall during the period 1979–2003, with less light rain and more heavy rain (> about 15 mm/hr), except for the lightest (trace) rain for which the frequency increased. They attributed it to the changes in the relative proportion of warm rain versus cold (mixed phase) rain, and changes in convection intensity and location, as a consequence of warmer surface and greater moisture supply to the atmosphere. Taiwan also experienced significant warming that is about twice of the global average, but the absolute humidity remains about the same. Although the environment setting is not exactly the same, Taiwan may conceivably under a similar influence from regional warming.

A different effect of the regional warming is to cause an increase of cloud base height. During the past century, the lifting condensation level In Taiwan has increased from about 550 m to 650 m. This would allow more time for raindrops to evaporate. Figure 5 shows a simple calculation of the reduction of rain as a function of cloud base height by assuming well-mixed air below the cloud base. One can see that smaller raindrops evaporate much faster during falling, while larger raindrop do not change much in size unless the cloud base is high. If we may assume that lighter rain usually associate with smaller raindrops, then the elevation of cloud base would significantly reduce the occurrence of light rain but not for heavier rain. If one impose such a effect to the simulations presented above, the results would be much like the observed RIS.

Another potential mechanism is the change of weather systems. It is possible that the shift of RIS did not occur in each individual event, but rather as a composite of more strong rain events and less light rain events. Hsu and Chen (2002) suggested that during the past few centuries, there were

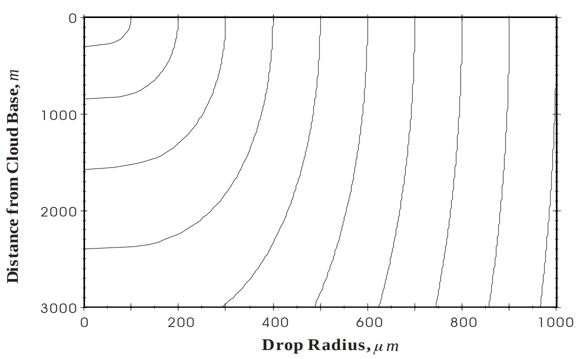

Figure 5: Change of drop size with distance from the cloud base due to evaporation, assuming well-mixed air blow cloud.

significant fluctuations in large-scale circulation, and this might lead to changes in the precipitation systems over Taiwan. Other likely candidates include the change of land use that altered the cloud formation, or even the change in surface emission of ice nuclei which have strong effect on cloud microphysics.

4. SUMMARY

In this study we investigated the phenomenon of rainfall intensity spectral shift that occurred in Taiwan and possibly other areas in the world. A regional cloud model is used to examine the possible cause due to increasing aerosols in this region. The results showed that in many cases increasing aerosols not only enhanced the moderate rain but also the light rain, a pattern dissimilar to the observation which shows decrease in light rain and increases in moderate rain. This indicates that other mechanisms may be responsible for the observed spectral shift. More likely, it is a combined effect of different mechanisms. For instance, the elevation of cloud base height (due to regional warming) may cause the lighter rain to diminish but not significantly alter the heavier rain. Other possible causes include the regional warming effect on cloud's thermodynamic structure or the dynamic of regional to synoptic scale circulation. We did not obtain conclusive results in this study, as many other mechanisms may be in play at the same time. So, besides looking into more cases of for the aerosol effect on RIS, we will need to examine further the factors of regional warming and other mechanisms mentioned above.

ACKNOWLEDGEMENTS

This study is supported partially by the National Science Council of the Republic of China under Grant NSC 94-2752-M-002-012-PAE.

REFERENCE

Albrecht, B. A., 1989. Aerosols, cloud microphysics, and fractional cloudiness. Science, 262, 226-229.

Alpert, P., N. Halfon, and Z. Levin, 2008: Does air pollution really suppress precipitation in Israel? Submitted to J. Appl. Meteorol.

Alva, A. K., L. E. Lanyon, and K. T. Leath, 1985: Influence of fungal-soil water interactions on phytophthora root rot of alfalfa. Biology and Fertility of Soils, 1, 91-96. DOI 10.1007/BF00255135.

Ayers G.P. 2005. Air pollution and climate change: Has air pollution suppressed rainfall over Australia? Clean Air & Environmental Quality, 39, 51-57.

Braham, R. R., 1974: Cloud physics of urban weather modification: a preliminary report. Bull. Amer. Meteor., 55, 100-106.

——. 1981: Urban precipitation processes. In Changnon, S. A., editor, METROMEX: a review and summary. Meteorological Monograph 18, Boston, MA: American Meteorological Society, 75-116.

Changnon, S. A., Jr., R.G. Semonin, and F. A. Huff, 1976: A hypothesis for urban rainfall anomalies. J. Appl. Meteorol., 15, 544-560.

Chen, J.-P., and S.-T. Liu, 2004: Physically-based two-moment bulk-water parameterization for warm cloud microphysics. Q. J. Royal Meteor. Soc., 130, Part A, 51-78.

Cheng, C.-T., W.-C. Wang, and J.-P. Chen, 2007: A modeling study of aerosol impacts on cloud radiative properties and precipitation. Q. J. R. Meteorol. Soc., 133, Part B, 283–297.

Coakley, J. A., Jr., R. L. Bernstein, and P. A. Durkee. 1987. Effect of ship-stack effluents on cloud reflectivity. Science, 237, 1020-1022.

Dabberdt, W. F., et al., 2000: Forecast issues in the urban zone: Report of the 10th prospectus development team of the U.S. Weather Research Program. Bull. Am. Meteorol. Soc., 81, 2047–2064.

Ferek, R.J., et al., 2000: Drizzle suppression in ship tracks. J. Atmos. Sci., 57, 2707–2728..

Fraser, A.I., T.R. Harrod, and P.M. Haygarth, 1999: The effect of rainfall intensity on soil erosion and particulate phosphorus transfer from arable soils. Water Science and Technology, 39, 41-45.

Gatz, D. F., 1979: Investigation of pollutant source strength rainfall relationships at St. Louis. J. Appl. Meteorol., 18, 1245–1251.

Givati, A., and D. Rosenfeld, 2004: Quantifying precipitation suppression due to air pollution. J. Appl. Meteor., 43, 1038–1056.
Hindman, E.E. II, P.V. Hobbs and L.F. Radke, 1977: Cloud condensation nuclei from a Paper Mill. Part I: Measured effects on clouds. J. Appl. Meteor., 16, 745-752.
Hobbs, I.V., L.F. Radke, and S.E. Shumway, 1970: Cloud condensation nuclei from industrial sources and their apparent influence on precipitation in Washington State. J. Atmos. Sci., 27, 81-89.
Hsu, H.-H., and C.-T. Chen, 2002: Observed and projected climate change in Taiwan. Meteorol. Atmos. Phys., 79, 87-104.
Huang, J., H. M. van den Dool, and K. P. Georgakakos, 1996: Analysis of model-calculated soil moisture over the United States (1931–1993) and applications to long-range temperature forecasts, J. Clim., 9, 1350–1362.
Jirak, I. L. and W. R. Cotton, 2006: Effect of Air Pollution on Precipitation along the Front Range of the Rocky Mountains. J. Appl. Meteor., 45, 236-245.
Karl, T. R., 1986: The relationship of soil moisture parameterizations to subsequent seasonal and monthly mean temperature in the United States. Mon. Weather Rev., 114, 75–686.
Lau, K.-M., and H.-T. Wu, 2007: Detecting trends in tropical rainfall characteristics, 1979–2003. Int. J. Climatol., 27, 979–988.
Lin, J.C., T. Matsui, R.A. Pielke, Sr., C. Kummerow. Effects of biomass burning-derived aerosols on precipitation and clouds in the Amazon Basin: A satellite-based empirical study, In Press, J. Geophys. Res., 2006.
Mather, G. K. 1991 Coalescence enhancement in large multicell storms caused by the emissions from a Kraft paper mill. J. Appl. Meteorol. , 30, 1134-1146.
Namias, J., 1952: The annual course of month-to-month persistence in climatic anomalies. Bull. Am. Meteorol. Soc., 33, 279–285.
Oberbauer, S., and P. C. Miller, 1982: Effect of water potential on seed germination. Ecography, 5 (2), 218–220.
Qian, Y., D. Gong, R. Leung, W. Wang, D. P. Kaiser, 2006: Potential Effects of Increasing Aerosols on Solar Radiation, Atmospheric Stability and Precipitation in China. AGU Fall Meeting, A11D-05.
Radke, L.F., J.A. Coakley, Jr., and M.D. Ring, 1989: Direct and remote sensing observations of the effects of ships on clouds. Science, 246, 1146-1149.
Rosenfeld, D. 1999. TRMM observed first direct evidence of smoke from forest fires inhibiting rainfall. Geophys. Res. Lett., 26, 3105–3108.
——, 2000: Suppression of rain and snow by urban air pollution. Science, 287, 1793–1796.
Rozoff, C. M., W. R. Cotton, and J. O. Adegoke, 2003: Simulation of St. Louis, Missouri, land use impacts on thunderstorms. J. Appl. Meteor., 42, 716-738.
Squires, P., 1966: An estimate of the anthropogenic production of cloud nuclei. J. Rech. Atmos., 2, 297-308.
Starkel, L., 1976: The role of extreme (catastrophic) meteorological events in contemporary evolution of slopes. In: Geomorphology and Climate (E. Derbyshire, ed.), John Wiley, London, 203-246.
Tan, C. S., and J. C. Tu, 2003: Effect of soil moisture on seed germination, plant growth and root rot severity of navy bean in Fusarium solani infested soil. Commun. Agric. Appl. Biol. Sci., 68, 609-612.
Tao, W.-K., X. Li, A. Khain, T. Matsui, S. Lang, and J. Simpson, 2007: Role of atmospheric aerosol concentration on deep convective precipitation: Cloud-resolving model simulations, J. Geophys. Res., 112, D24S18, doi:10.1029/2007JD008728.
Teller, A., and Z. Levin, 2006: The effects of aerosols on precipitation and dimensions of subtropical clouds: a sensitivity study using a numerical cloud model. Atmos. Chem. Phys., 6, 67–80.
Twomey, S., 1974: Pollution and the plantary albedo. Atmos. Environ., 8, 1251-1256.
Whitby, K.T., 1978. The physical characteristics of sulfur aerosols. Atmos. Environ., 12, 135-159.
Wagenvoort, W.A. 1981. Seed germination as affected by soil type and soil moisture. Acta Hort. (ISHS), 119, 293-298.
Warner, J., 1968: A reduction in rainfall associated with smoke from sugar-cane fires -- An inadvertent weather modification? J. Appl. Meteor., 7, 247-251.
Warner, J., and S. Twomey, 1967: The Production of Cloud Nuclei by Cane Fires and the Effect on Cloud Droplet Concentration. J. Atmos. Sci., 24, 704–706
Watson, D.A.; J.M. Laflen, 1986: Soil strength, slope, and rainfall intensity effects on interrill erosion. Transactions of the ASAE TAAEAJ, 29, 98-102.
Woodcock, A.H., and R. H. Jones, 1970: Rainfall Trends in Hawaii. J. Appl. Meteor., 9, 690-696.

INFLUENCE OF URBAN PLUMES ON MICROPHYSICS OF PRECIPITATING STRATOCUMULUS

T.W.Choularton[1], K.N. Bower[1], P.Connolly[1], H.Coe[1], J.Crosier[1], M.W.Gallagher[1], D.Topping[1], S. Romakkaniemi[1*],
Phil Brown[2]
[1] Centre for Atmospheric Science, SEAES, University of Manchester, Simon Building, Brunswick Street, Manchester M13 9PL. UK
[2] The MetOffice,

INTRODUCTION

This paper presents results obtained from a flying programme conducted to investigate the interaction of urban aerosol with stratocumulus clouds downwind of the UK. The objectives of the study were:

1. To investigate the evolution of an urban plume as it is advected to the northeast over East Anglia and the North Sea in cloudy conditions. Changes in chemical speciation and the partitioning of species between the gas and particulate phases will be investigated.
2. To measure the changes in the size distribution and Cloud Condensation Nucleus (CCN) activity spectrum of the aerosol.
3. To measure changes in cloud microphysics as the aerosol properties in the plume change, particularly those of the sub-set of aerosol acting as CCN.
4. To investigate the differences in the composition of aerosol that form cloud droplets and those that remain unactivated and interstitial to the cloud, and to observe how this changes as the plume ages.
5. To investigate the role of vertical exchange between the boundary layer and the free troposphere to understand its effect on the transport of aerosols and trace gases on the cloudy plume.
6. To model the evolution of the boundary layer, the particles and the cloud microphysics using LES modelling and an explicit model of cloud-aerosol interactions

THE MEASUREMENT PROGRAMME

The interaction of ageing aerosol emitted from urban areas of the UK was investigated as the plumes advected away from the area over the sea in a stratocumulus capped boundary layer. Detailed measurements of the size distribution and chemical composition of the aerosol were made on the UK community's new research aircraft a BAE 146. These measurements were complimented by detailed measurements of the liquid water content and cloud microphysics. Detailed measurements of precursor trace gases were also made.

The aircraft made a series of horizontal passes perpendicular to the line of the plume below cloud, within the cloud deck and above the cloud top. This series of passes was repeated at 50 km intervals moving downwind from the source. Within cloud an airborne CVI was used to measure the droplet residual aerosol components to investigate the nucleation scavenging of the particulate.

A key measurement of the aerosol size resolved composition was made using an Aerodyne Aerosol Mass Spectrometer. This instrument is able to provide size resolved information of the semi volatile components of the aerosol including major ions and organic material. Some information is available on the main functional groups in the organic material and the state of oxidation.
Several sorties took place during the summer of 2005, studying the plumes of

several eastern UK cities as they evolved, as they were transported east. The changes in the chemical composition, size distribution and nucleation properties of the aerosol will be presented as a function of plume age for the different case studies.

The compositions of cloud drop residuals were successfully measured with the AMS and shown to be composed mainly of a mixture of sulphate, organics and nitrate. Changes as a function of age were noted, including the relative mass concentrations of inorganics to organics and the amount of oxidation in the organic fraction. The overall level of organic oxidation was higher than is typically seen in urban environments, A total of 12 case studies were flown around the UK.

THE RESULTS OBTAINED

In this paper we will concentrate on the results of 1 case study flown on 14 September 2005 over Kent and the Thames Estuary. The results in figure 1 show a transect through stratocumulus cloud about 100 km from London. The results presented are droplet residuals sampled through a CVI mounted on the aircraft and fed to an aerodyne AMS it can be seen that one plume contained predominantly sulphate

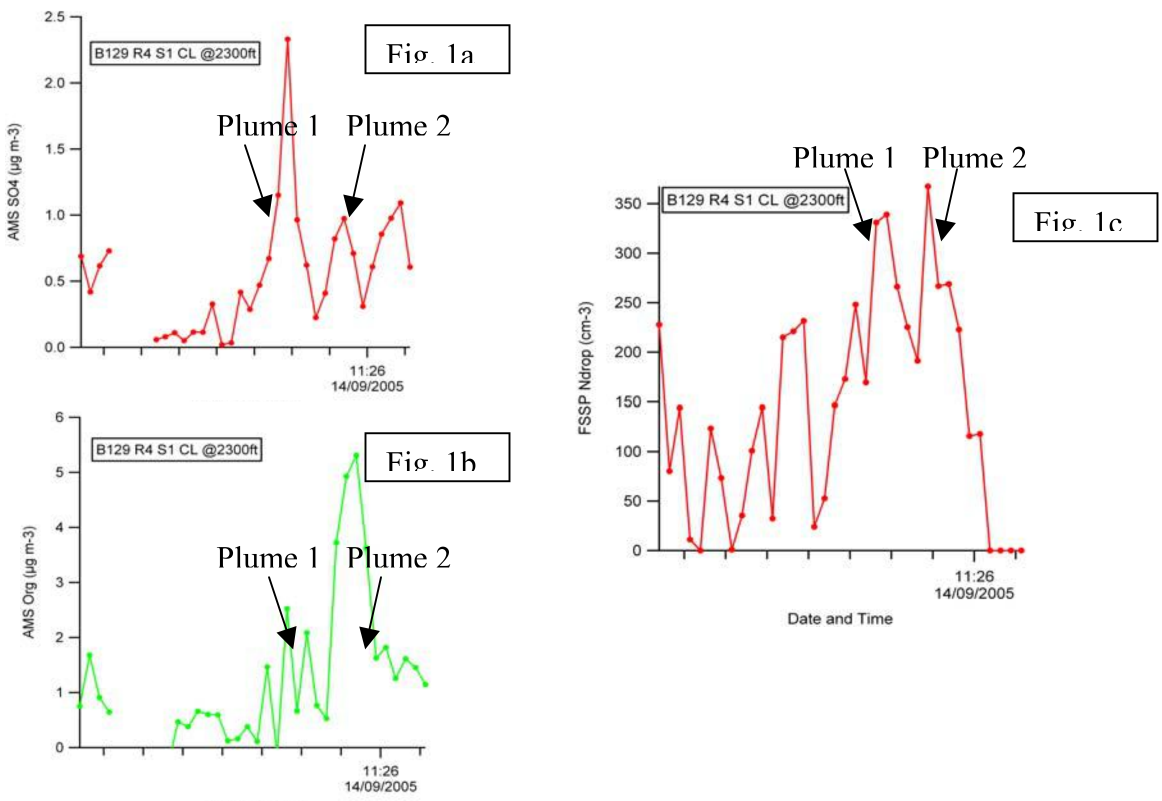

Figure 1: CLOPAP case study from flight B129. Plume 1 contains predominantly sulphate aerosol internally mixed with some organic material, whereas plume 2 contains predominantly organic aerosol internally mixed with some sulphate (parts a and b). Part c shows that both aerosol plumes are effective as CCN increasing the droplet number in the cloud.

aerosol internally mixed with a small amount of organic material whilst a neighbouring plume consisted of predominantly organic material internally mixed with sulphate. The organic material sampled shows evidence of being highly oxidised with 10% mass 44 fragments. Both plumes resulted in increased droplet number in the cloud to roughly the same degree. This suggests that aged organic aerosol acting as an excellent CCN when internally mixed with inorganic ions close to the source. The likely scenario for the two plumes is that they had rather different sources. The following process probably formed plume 1, organic seeds of hydrophilic hydrocarbons produced from engine exhausts in the urban environment with a size of about 30 nm. Such particles are widely observed on urban areas. These would grow as additional oxidised secondary organic material was added. This would cause the particles to be weakly hydrophilic. At this point nitric acid and then sulphuric acid would be deposited to the particles. The sulphuric acid tending to displaced the nitric acid. Plume 2 probably formed in a similar way but evolved in a much more organic rich environment, hence deposition of secondary organic material dominated. In this case the atmospheric boundary layer was stratocumulus capped throughout and hence it is no clear how much of a role cloud processing played in the evolution of the plume. Other flights in cloud free conditions did show plumes of similar composition at a similar distance for urban sources.

THE CLOUD MODEL

In order to test quantitatively whether the properties of the plumes could be reproduced a parcel model was used. This model is based on the ADDEM model of Topping and McFiggans

In order to infer CCN measurements from the AMS data and the aerosol size distribution measured on board the aircraft we adopted the approach of using detailed parcel model simulations with bin-microphysics.

The equilibrium vapour pressure of the aerosol particles was calculated using Kohler theory.

$RH_{eq} = 100 \times \exp\left(\frac{4\sigma M_w}{RTD}\right) \times a_w$, where σ is the surface tension, M_w is the molecular weight of water, D is the diameter of the aerosol particle and is calculated using fits to density-mass fraction from a thermodynamic model, R is the gas constant, T the temperature and a_w is the activity of water.

For a single component aerosol, the activity is inferred from a polynomial fit to activity-mass fraction data from a thermodynamic model.

$a_{w,i}(x_s) = \sum_{j=0}^{N-1} A_j x_s^j$, here, x_s is defined as the mass-fraction of the aerosol particle (aerosol mass divided by total mass):

$$x_s = \frac{m_s}{m_s + m_{H2O}}.$$

Rearranging this, the mass of water is given by:

$$m_{H2O} = \frac{m_s(1 - x_s)}{x_s}$$

For an internal mixture of aerosol, we use the ZSR theory for calculating the water content. That is, the activity of water of the different component i are equal and the water content inferred from all sub components must equal the total water content. That is we solve the equation:

$W - \sum_{i=1}^{M}\left(\frac{m_{s,i}\left[1 - x_{s,i}\{a_w\}\right]}{x_{s,i}\{a_w\}}\right) = 0$, where, W is the water content of the aerosol, $m_{s,I}$ is the mass of the i^{th} aerosol component and the functions $x_{s,i}\{a_w\}$ are the inverse of the polynomial fits described above. This equation is solved by numerical optimisation for the system in question.

These equations are solved in bins in the framework of a Lagrangian parcel model for the aerosol size distributions and compositions observed. The vertical winds were obtained from direct observations from the aircraft and also from the results of large Eddy simulation of the stratocumulus capped boundary layer. The organic fraction of the aerosol was assumed to be fulvic acid for the case under consideration

RESULTS OF THE MODELLING

Figure 2 shows the results obtained for the number of droplets above 5 um diameter produced by each of the plumes as a function of the proportion of ammonium sulphate for internally mixed aerosol of ammonium sulphate and fulvic acid for each plume. The observations are indicated on the diagrams. It can be seen that for internally mixed aerosol the results are insensitive to the proportion of ammonium sulphate in the mixture over a wide range of conditions. This can be contrasted with figure 3, which shows results for externally mixed ammonium sulphate and fulvic acid. It can be seen that good agreement can be achieved between the observed and modelled droplet number in both plumes and that the number of droplets above 5 um is rather insensitive to the proportions of ammonium sulphate and fulvic acid over a wide range of the ratios of the two compounds. On the other hand if the fulvic acid and ammonium sulphate are externally mixed then the number of cloud droplet sis much more sensitive to the relative contributions of the two compounds.

This result may readily be explained by reference to figure 4, which shows the Kohler curves for particles of dry mass 10 – 17 Kg. This figure shows that the pure fulvic acid particle, representing an external mixture is only weakly hygroscopic and requires a high supersaturation to activate the particles, whilst the mixtures of ammonium sulphate and fulvic acid over a wide range of compositions require similar but much lower super saturations to activate.

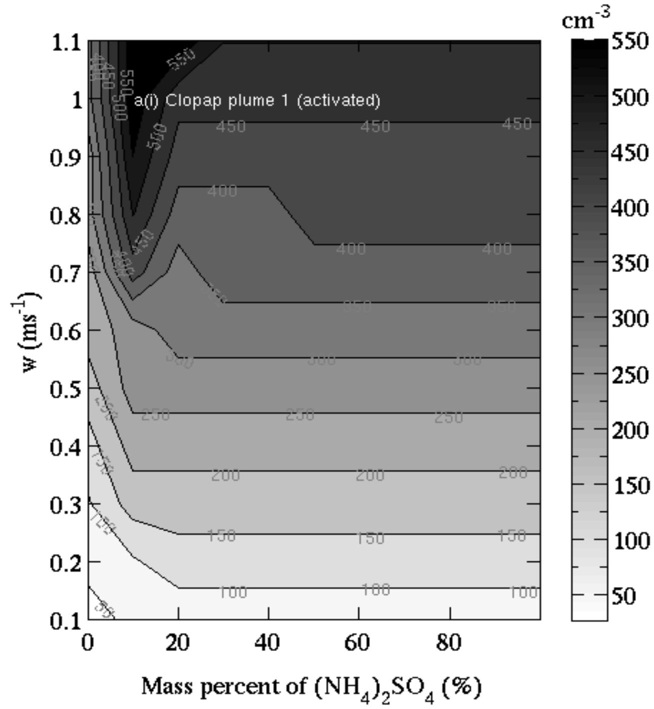

Figure 2a Modelled droplet number concentrations as a function of vertical wind and aerosol composition for plume 1

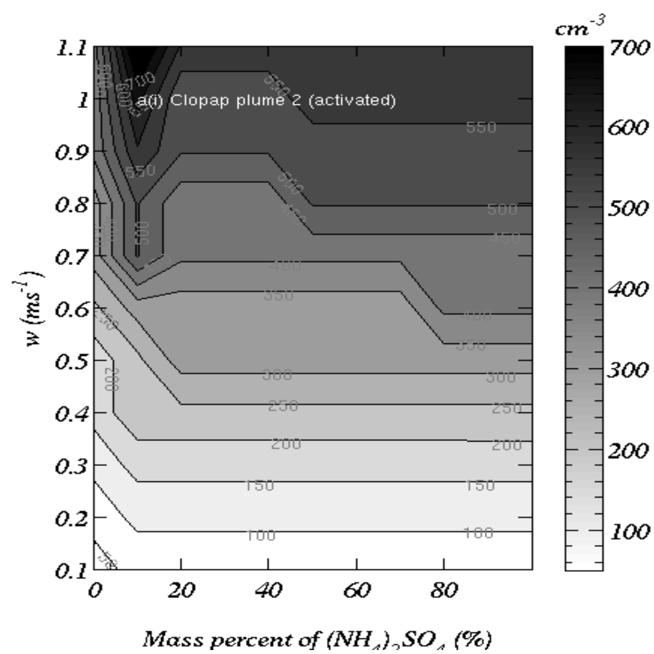

Figure 2b Modelled droplet number concentrations as a function of vertical wind and aerosol composition for plume 2

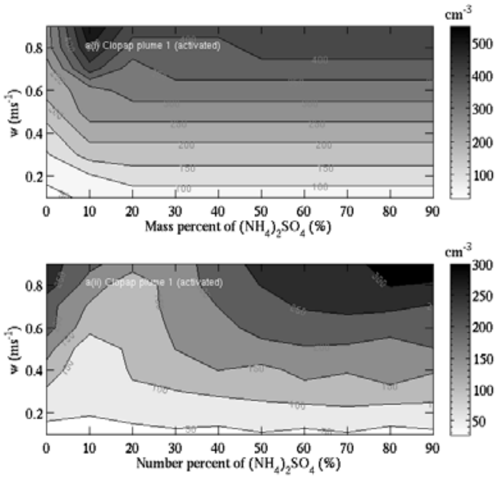

Figure 3 Modelled droplet number concentrations as a function of vertical wind and aerosol composition comparison between internally and externally mixed aerosol

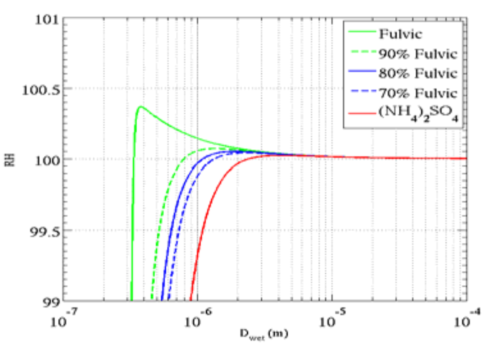

Figure 4 Kohler curves for fulvic acid and ammonium sulphate aerosol and internal mixtures of the two

DISCUSSION

It has been shown that aged pollution aerosol consists of an internal mixture of organics, sulphate, nitrate ammonium; the organic component is dominated by highly oxidized secondary material. The relative contributions and absolute loadings of the components vary with location and season. During the CLOPAP experiments the observations were made much closer to sources and hence the plumes had marked structure with very different aerosol composition in different parts of the plume. It was found, however, that most of the aerosols act as cloud condensation nuclei, irrespective of their composition and the ratio of the species found in the cloud droplets were every similar to those found in the total aerosol confirming that the particles were internally mixed. Hence much of the organic material along with the other species is incorporated into cloud droplets. It was observed, in CLOPAP, that by 100 km down wind of London the urban aerosol produced from that area has this characteristic internally mixed structure and was a good CCN. This is an important result, as the lifetime of organic aerosol will be limited as by being incorporated into cloud droplets it will be readily removed by rainout and wet deposition. Further, however, it means that urban produced aerosol will modify cloud structure only a short distance downwind of the urban environment. Further decline in sulphate loadings will have only a minor effect on the aerosol indirect effect if the lost sulphate is replaced by organic matter.

ACKNOWLEDGMENT

This work was supported by the Polluted Troposphere Programme of the Natural Environment Research Council

A STUDY INTO THE EFFECTS OF AEROSOLS ON INTENSE HECTOR THUNDERSTORMS IN 2005/2006

Paul Connolly[1], Geraint Vaughan[1], Peter May[2], Patrick Minnis[3], Kirk Ayers[4], Grant Allen[1], Min Zhu[1], Tom Choularton[1]

1. University of Manchester

2. Bureau of Meteorology, Melbourne

3. NASA Langley Research Center, Hampton, Virginia

4. SSAI, Hampton, Virginia

INTRODUCTION

The Hector thunderstorm is studied with an emphasis on what determines the properties (e.g. amount of condensate, ice particle concentration) of the high anvil clouds. Hector occurs over the Tiwi Islands (see Figure 1) during the monsoon build up and during break periods from the monsoon.

Generally, there is a transition season from October to December where thunderstorms (Hectors) are observed over the Tiwi Islands with high regularity. During late December the convective activity tends to be embedded within Oceanic Monsoon systems.

During the transition period there is a trend for a high frequency of storm days. Storm-free days during this period are generally correlated with the presence of very dry middle level air and enhanced 700 mbar southerly flow. Similar convection over the Tiwis can be observed during well defined `break' periods from the Oceanic Monsoon.

During Austral summer 2005/2006 two joint projects studied the development and evolution of Hector; these projects were ACTIVE and TWP-ICE.

The ACTIVE project was a NERC funded consortium project to study the role that deep convection in the tropics plays in transporting aerosol and chemical species from the planetary boundary layer to the upper troposphere. The rationale for ACTIVE in addition to the measurements is explained in Vaughan *et al.* (2008).

Previous studies of Hector have established that convection over the islands commences with a few isolated cells that form randomly over the islands. These cells generally `aggregate' to form a continuous line E-W in the middle of the islands. After an initial quiescent period, the cells develop rapidly and are vertically erect with cloud-tops around 17-18 km. The ascent of the tops of the cells to this altitude occurs in about 30 minutes.

A finding from ACTIVE was that aerosol properties and concentrations changed markedly throughout the season changing from polluted biomass burning to more clean aged organic and ammonium sulphate internal mixtures (Allen *et al.* 2008). Hector storms were observed throughout this regime, so a question that arises is: "*can we observe an aerosol effect on Hector?*"

FACTORS AFFECTING HECTOR

There are many factors that may affect the strength/intensity of multi-cell thunderstorms; many of these are inter-related. Convective activity over the Maritime Continent of Indonesia and tropical northern Australia is dominated by interactions between the diurnal heating cycle, the local topography of the many islands and the prevailing large scale circulation (Ramage 1968). Crook (2001) showed the importance of low level wind direction and speed in Hector development. The findings suggested the strongest Hectors were the result of low wind speeds, when the wind was orientated in a W-E direction. The reason for this is that it results in longer residence times of air over the islands (see Figure 1), increasing the heating of the air and increasing convective instability.

However, aerosols may also play an important role in modifying this convective activity, primarily by altering the microphysical processes that occur within the storms. Previous studies have shown that it has been very difficult to quantify the impact of aerosols on such storms.

The strong convection that occurs over the Maritime Continent extends through a large enough depth in the earth's atmosphere, such that the highest proportion is mixed-phase cloud.

Lohmann *et al.* (2005) identified some possible indirect effects that aerosols may have on certain cloud types. As well as the well known 1st and 2nd indirect effects in stratocumulus there are other indirect effects that concern mixed phase clouds such as Hector. An important indirect effect for mixed phase clouds was termed the "thermodynamic" indirect effect. This has been observed in thunderstorms over Texas (Rosenfeld *et al.* 2000) and modelled successfully in an number of studies (Khain *et al.* 2001).

In this scenario, it is said that increased aerosol loadings result in smaller droplets which in turn implies that the population of a subset of aerosols known as ice nuclei will be shared amongst a smaller fraction of the cloud/rain drops. The result of this is hypothesized to suppress the glaciation of the cloud (implying a possible reduction in precipitation for comparatively small aerosol loadings).

Also of importance is the "riming" indirect effect where it has been hypothesized that smaller cloud droplets reduce the effectiveness of riming.

Lohmann *et al.* (2003) found that this effect is not so clear in Arctic clouds; while Connolly *et al.* (2007) found that riming actually increased with increased aerosols in deep tropical storms – leading to increased precipitation. In their model simulations this led to more precipitation being released in more polluted conditions – which was due to riming. This apparently suppresses the thermodynamic indirect effect.

Connolly *et al.* (2007) also simulated Hectors. They predicted an optimal value for the droplet number concentration in Hector for intermediate values of around 400 cm^{-3}. Lower values resulted in removal of precipitation by warm rain and the thermodynamic indirect effect, while higher values had increased precipitation due to increased riming. The optimal value of 400 cm^{-3} was due to a balance between these two effects.

OBSERVATIONS

The observations for this data set are taken from the joint ACTIVE/TWP-ICE campaigns which took place in Austral summer 2005/2006.

For this study we have focussed solely on the Hector thunderstorm as it is a natural laboratory for answering many scientific questions about intense convection.

Radar and satellite (Minnis et al 2007) measurements of Hector and its cirrus outflow region were averaged over the domain shown in Figure 1.

The radar serves as a quantitative measure of anvil area in the domain, whereas the satellite data gives us a quantitative measure of brightness temperature. Hence we can investigate whether shielding of the surface by high cirrus has an effect of the development of Hector.

In addition to the remotely sensed measurements and the radiosondes a Dornier Do-228 aircraft flew in the boundary layer and free troposphere to sample the aerosol physical and chemical characteristics (Allen *et al.* 2008). The aerosol chemical characteristics for several different periods are shown in Figure 2.

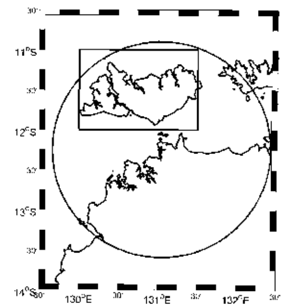

Figure 1. The averaging domain for the radar and satellite generated statistics

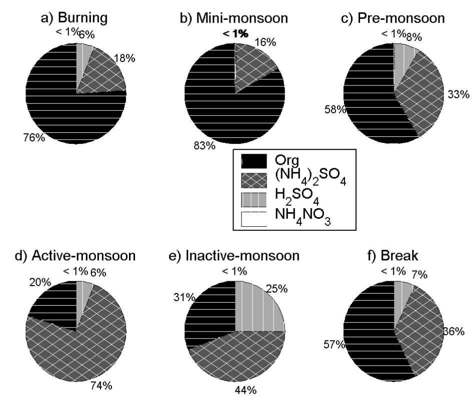

Figure 2. Aerosol composition inferred from an aerodyne Aerosol Mass Spectrometer (AMS). For each of the periods described in Allen et al (2008).

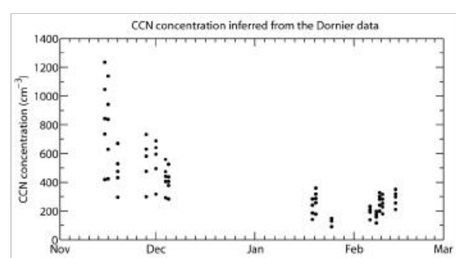

Figure 3. Droplet number concentrations calculated using a thermodynamic aerosol model

embedded with a cloud parcel model, showing the variation with time throughout the period.

MODELLING

CCN were not measured directly from the Do-228. In any case reliable CCN measurements including the spectrum of CCN as a function of supersaturation are difficult to make from an aircraft. Instead we adopted the approach of using the available measurements to model the dependence of the CCN spectrum on the updraught speed. This was done by synthesizing the aerosol size distribution and chemical composition information from the Dornier (see Figure 2) using a state of the science aerosol model (Topping *et al.* 2005).

In addition, simulations of Hector were performed with the WRF model at 1km resolution. The simulations will not be described in detail here but will be published in a forthcoming paper.

Generally the simulated storm intensity was lower than observed, with rainfall being typically lower (half as much) as the radar predicted rainfall accumulation. However, storm tops and anvil area were in accord with the radar measurements.

Figure 4 shows the results from WRF runs for 4 different values of assumed droplet number. It can be seen that the value of 300 cm-3 gives the larges anvil area of each of the four cases. This supports the findings from (Connolly *et al.* 2007).

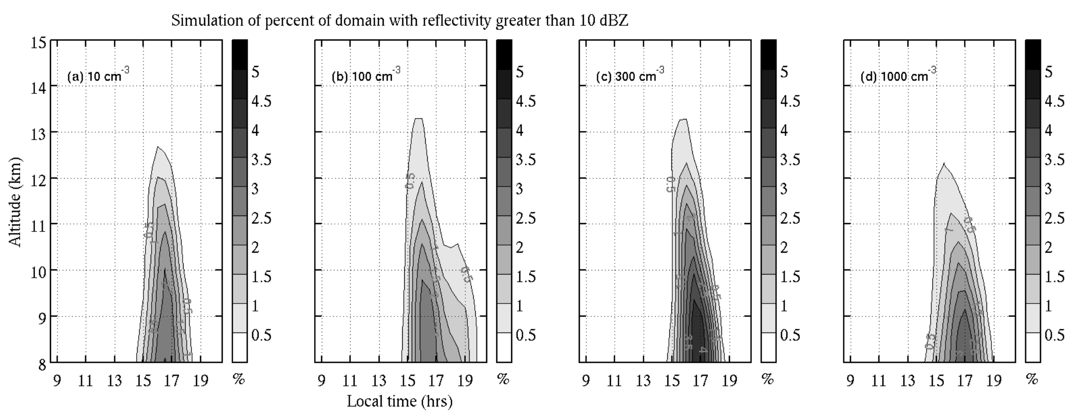

Figure 4. Simulated radar reflectivity from the WRF model showing an optimal value of droplet number (plot c) for the fraction of the domain that has reflectivity values above 10 dBZ at upper levels in the cloud.

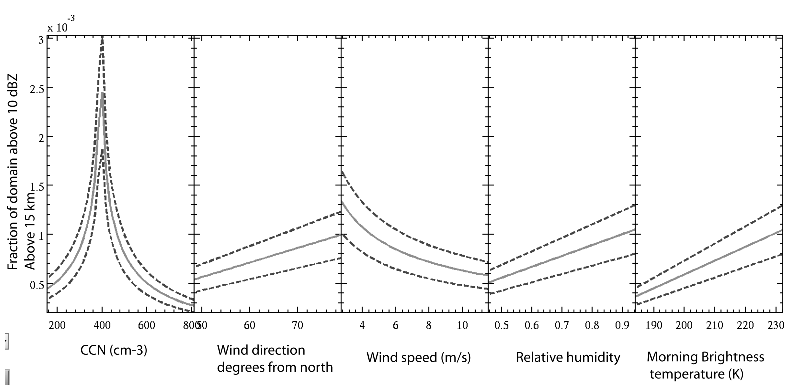

Figure 5. Graphical representation of a multiple non-linear regression to the dataset. Solid lines are regression parameters and the dashed lines show the inter-quartile range. The graph shows the observed

optimal value of droplet number at 400 cm^{-3} and how this affects the reflectivity fraction (left most plot). The wind direction and wind speed show the same sensitivities expected from the study of Crook 2001 with low wind speeds favouring more intense storms (middle two plots); there are linear dependencies of relative humidity and brightness temperature on the intensity of the storm with high humidity's and low brightness temperatures favouring more intense storms. This latter point supports the case for shielding by morning cirrus having an effect on the storm intensity.

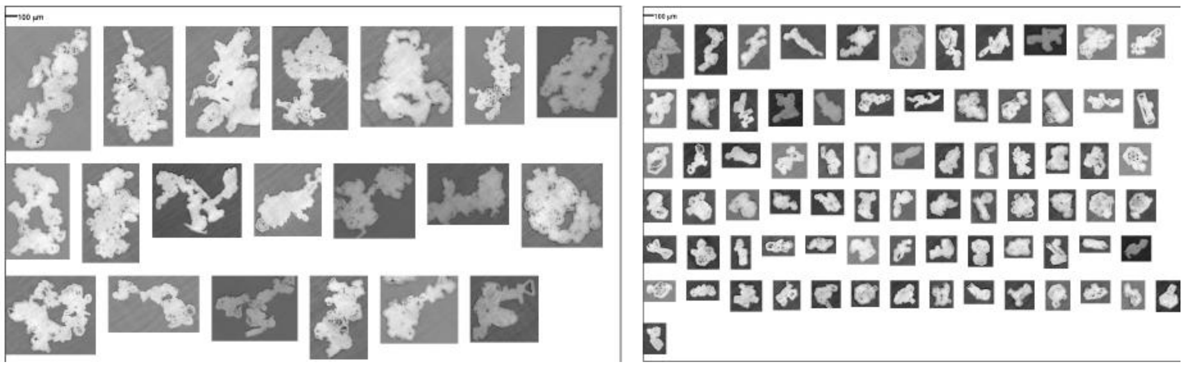

Figure 6. Left CPI images of chain aggregates imaged in an intense thunderstorm during the biomass burning period. Right CPI images of smaller aggregates in a weaker thunderstorm during `clean' conditions.

ICE MICROPHYSICS

In addition to the observed aerosol impacts on the anvil water contents aircraft measurements with the Cloud Particle Imager probed the intricate shapes of ice crystals in the anvils. We noted that the stronger Hector clouds observed in the pre-Christmas transition period were comprised of large chain-like aggregates (see Figure 6 left panel).

Further analysis of the anvil of a relatively weak Hector observed in the post Christmas break period showed crystals that we much smaller and crystal aggregates that were comprised of fewer individual crystals (see Figure 6 right panel). Hence not only is anvil thickness sensitive to the strength of Hector, but the microphysical properties if the anvils also show important variations due to different met and aerosol conditions.

SUMMARY

This paper is an attempt to quantify the effects of cloud condensation nuclei on the evolution of an intense tropical convective system known as Hector. The data is taken from the ACTIVE and TWP-ICE field campaigns. A relatively large dataset is synthesized including radar reflectivity measurements; aircraft measurements of aerosol size distributions and composition; radiosonde measurements of atmospheric humidity and winds and cloud particle images and size distribution measurements within the anvil region of the storm.

A principal components analysis was performed (not shown here) to infer the important variables in describing the variation; it reveals that no one parameter dominates the characteristics of the anvil cloud, but three points can be extracted from the analysis: (1)

low level wind speed over the Tiwi Islands is inversely related to the amount of high anvil cloud, since this affects the residence time of air over the islands, and hence the time air can be warmed by conduction; (2) low level humidity is directly related to the amount of high cloud over the Tiwi Islands detraining from the convection, this might be expected from simple thermodynamic calculations; (3) CCN are related to the amount of anvil cloud in a non-linear way, the amount of high anvil cloud was a maximum when boundary layer CCN concentrations were approximately 400 cm-3.

The principal components analysis highlighted that the inter-connection between CCN and high anvil was responsible for 15% of the total variation in the data set.

This data will be presented in more detail at the conference including details of the impact of aerosols on anvil microphysics.

BIBLIOGRAPHY

Allen, G., G. Vaughan, et al. (2008). "Aerosol and trace-gas measurements in the Darwin area during the wet season." JGR **113** (D06306).

Connolly, P. J., T. W. Choularton, et al. (2007). "Cloud resolving simulations of intense tropical, Hector thunderstorms: Implications for aerosol cloud interactions." QJRMS **132**: 3079--3106.

Connolly, P. J., A. J. Heymsfield, et al. (2007). "Modelling the influence of rimer surface temperature on the glaciation of intense thunderstorms: The rime-splinter mechanism of ice multiplication." QJRMS **132**: 3059--3077.

Crook, A. (2001). "Understanding Hector: The Dynamics of Island Thunderstorms." MWR **129**: 1550--1563.

Khain, A., D. Rosenfeld, et al. (2001). "Simulating convective clouds with sustained supercooled liquid water down to -37.5°C using a spectral microphysics model." GRL **28**: 3887-3890.

Lohmann, U. and J. Feichter (2005). "Global indirect aerosol effects: A review." ACP **5**: 715-737.

Lohmann, U., J. Zhang, et al. (2003). "Sensitivity studies of the effect of increased aerosol concentrations and snow crystal shape on the snowfall rate in the Arctic." JGR **108**: 4341--4357.

Minnis, P., and Co-authors, (2006) “Large-scale cloud properties and radiative fluxes over Darwin during TWP-ICE.” *Proc. 16th ARM Sci. Team Mtg.*, Albuquerque, NM, March 27-31.

Ramage, C. S. (1968). "Role of a tropical ``maritime continent'' in the atmospheric circulation." MWR **96**: 365-370.

Rosenfeld, D. and W. L. Woodley (2000). "Deep convective clouds with sustained supercooled liquid water down to -37.5° C." Nature **405**: 440--442.

Topping, D. O., G. B. McFiggans, et al. (2005). "A curved multi-component aerosol hygroscopicity model framework: Part 2 - Including organic compounds." ACP **5**: 1223--1242.

Vaughan, G., G. Schiller, et al. (2008). "SCOUT-O3/ACTIVE." BAMS, in press.

ACKNOWLEDGEMENTS

ACTIVE was funded by the UK NERC under grant no. NE/C512688/1.

AEROSOL-CLOUD INTERACTIONS IN DEEP CONVECTIVE CLOUDS OVER THE AMAZON BASIN

A. M. L. Ekman[1], R. Krejci[1], A. Engström[1], J. Ström[2], M. de Reus[3]
[1]Department of Meteorology, Stockholm University, Stockholm, Sweden
[2]Department of Applied Environmental Science, Stockholm University, Stockholm, Sweden
[3]Institut für Physik der Atmosphäre, Universität Mainz, Mainz, Germany

1 INTRODUCTION

Deep convective clouds are known to be important mechanisms for redistributing atmospheric pollutants and aerosols from the boundary layer to the upper troposphere [*Wang and Crutzen*, 1995]. The outflow regions of deep convective clouds are also favourable environments for new particle formation due to the low temperatures, high water vapour content, low condensational sink and relatively high H_2SO_4 concentrations. For polluted environments (SO_2 concentrations exceeding approx. 1 ppb), it has been shown that binary H_2SO_4-H_2O nucleation theory can reproduce the high concentrations of nucleation mode aerosols ($d < 18nm$) observed (e.g. *Engström et al.* [2008]). *Krejci et al.* [2003] conducted flight measurements over the wet season Amazon Basin during the LBA-CLAIRE 1998 campaign and observed high concentrations ($>$ 1e3 cm^{-3}) of nucleation mode aerosols at $\sim$ 12 km altitude. This concentration is remarkably high as SO_2 concentrations over the Amazon Basin generally are very low during this time of the year.

In the present study, we use a 3D interactive aerosol-cloud-resolving model to show that the high nucleation mode number concentrations observed over the rain forest can not be reproduced assuming realistic conditions regarding the chemistry, aerosol population, aerosol solubility and scavenging properties of the hydrometeors. As a consequence of the underestimate, the modeled formation of aerosols in the larger modes is also too low. We examine if activation nucleation theory can explain the discrepancy between observed and modeled aerosol nucleation and if isoprene has the potential of increasing the formation of new aerosols and subsequent aerosol growth.

2 INTERACTIVE AEROSOL-CLOUD-RESOLVING MODEL AND SIMULATED CASE

A three-dimensional, mesoscale, non-hydrostatic cloud-resolving model (CRM) is used to simulate the deep convective cloud development. The model was originally developed by *Wang and Chang* [1993] and *Wang and Crutzen* [1995], with aerosol physics and chemistry included according to *Ekman et al.* [2004]. It consists of four main modules; a cloud dynamics module, a chemistry module, a microphysical module, and an aerosol module. In each model grid, predictions are made for mixing ratios and number concentrations of four hydrometeors (cloud droplets, rain droplets, ice crystals and graupel). The chemistry module predicts the concentrations of 25 gaseous and 8 aqueous chemical species. The model domain area is 400x400 km^2 and the model top is at 24 km. The spatial resolution of the model represents a horizontal grid interval of 2 km and a vertical grid interval of 0.4 km.

The number of aerosols available as cloud condensation nuclei (CCN) at a certain supersaturation is calculated using the Köhler equation. Four modes are used to describe the aerosol population (nucleation mode, Aitken mode, accumulation mode and coarse mode). Each aerosol mode is represented by a lognormal size distribution. This allows for the population to be described by four parameters; the prognostic variables number concentration (N), mass (M) and median diameter (Dp), and a predefined geometric standard deviation (σ_g). 5% of the total aerosol population larger than 0.1 μm are assumed to act as potential ice nuclei (IN) through heterogeneous freezing of cloud droplets. The aerosol number concentration and mass are affected by transport, mixing, condensation, coagulation, dry deposition and impact scavenging by falling raindrops, graupel and ice crystals. New aerosols are formed through binary H_2O-H_2SO_4 nucleation [*Vehkamäki et al.*, 2002].

Two days with weather conditions typical for the Amazonian wet season and when the highest nucleation mode aerosol concentrations were measured were chosen for simulation. In both cases the air mass had passed regions of intense convective activity 2-3 days prior to measurements. The aerosol number concentration was measured by two condensation particle counters (CPC1-2), One Differential Mobility Particle Sizer (DMPS) and an Optical Particle Counter (OPC). Measured properties of the boundary layer (BL) size distributions are used to initialize the model (Table 1). All aerosols are by default assumed to be 30% soluble [$(NH_4)_2SO_4$)]. Measured average vertical profiles [cf. *Krejci et al.*, 2003] are used to describe the vertical distribution for each aerosol category. A constant initial SO_2 concentration of 220 ppt is applied horizontally and vertically. This SO_2 concentration is to be regarded as an upper limit for the Amazon Basin at this time of the year. For other modeled chemical compounds, we assume typical BL/UT background values. Data from the European Centre for Medium-Range Weather Forecast is used for initializing the meteorological fields.

Table 1: Model parameters used to describe initial boundary layer aerosol distribution.

Aerosol mode	Number $[cm^{-3}]$	Median diameter $[nm]$	σ_g
	28th of March		
Nucleation	5	6.5	1.50
Aitken	280	22.0	1.55
Accumulation	160	70.6	1.50
Coarse	2	325.7	1.50
	29th of March		
Nucleation	20	6.5	1.50
Aitken	215	22.0	1.57
Accumulation	240	70.6	1.65
Coarse	3	325.7	1.50

3 RESULTS

As seen from Figure 1, the model underestimates the number concentration at 12 km for all observed aerosol modes, or is within the lower end of the confidence interval. Observed number concentrations for the nucleation mode are remarkably high, up to $2.5 \cdot 10^4\ cm^{-3}$, and with a rather large measured variability. This indicates that the air mass was not well mixed or aged, and that the particles have been formed recently, most likely in conjunction with a deep convective outflow region. We first examine the sensitivity of the modeled aerosol size distribution to various conditions regarding the aerosol composition, droplet growth conditions and ice scavenging efficiency. The default binary $H_2SO_4 - H_2O$ nucleation is used. The following simulations are performed:

1. 10% soluble aerosol mass (*eps01*).
2. 100% soluble aerosol mass fraction (*eps10*).
3. 30% of initial aitken mode assumed externally mixed hydrophobic (*bc03*).
4. Mass accommodation coefficient decreased (1.0 to 0.04, *acc004*).
5. Ice impact scavenging reduced by 90% (*iceim01*)

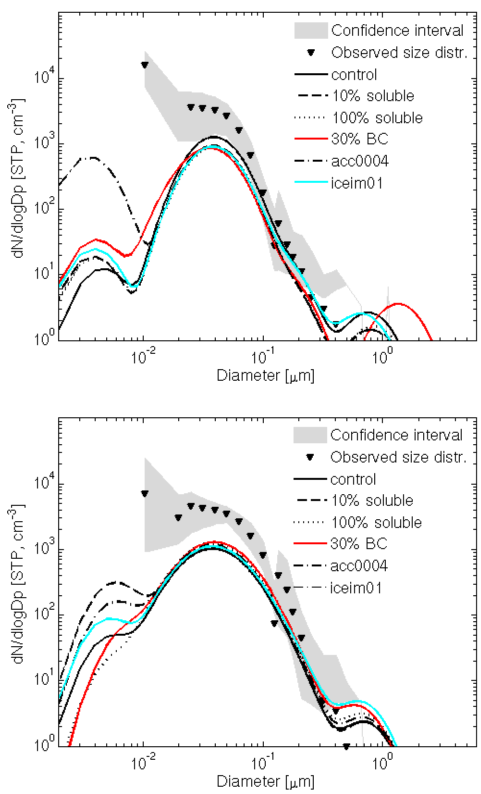

Figure 1: Observed and simulated (control and sensitivity) aerosol size distribution at 12 km after 5h of simulation, **(upper)** 28th of March and **(lower)** 29th of March.

As shown in Figure 1, changing the aerosol solubility and aerosol surface characteristics within reasonable limits is not sufficient to obtain the observed number of nucleation mode aerosols. The Aitken and accumulation mode aerosol concentration is also underestimated in all simulations. We have tested the sensitivity of the model to constraining the supersaturation to 0.8% but found no significant change in the resulting UT aerosol size distribution. Interestingly, a decreased aerosol solubility does not necessarily result in higher aerosol concentrations compared to the control. The change in available CCN and IN affects the latent heat release at different stages of cloud development which in turn affects the entire cloud dynamics and thereby the nucleation and impact scavenging of aerosols (cf. *Ekman et al.* [2007]).

Krejci et al. [2003] showed that a 2-3 day growth of aerosols from the nucleation mode to the Aitken mode could explain the high Aitken mode number concentrations observed. An initial nucleation mode number concentration of approximately $1 - 2{\cdot}10^4\ cm^{-3}$ was used in their calculations. Using the CRM we estimate that a BL SO_2 concentration of approximately 5 ppb would be needed to form this amount of nucleation mode aerosols at the top of the deep convective cloud. This SO_2 concentration is remarkably high and it is not likely that something similar would occur within or close to the LBA-CLAIRE region (cf. *Andreae et al.* [1990]).

Kulmala et al. [2006a] showed that cluster activation theory quantitatively can explain observed BL nucleation events at several global locations. The theory cluster activation suggests that the formation rate of nano-meter sized clusters (J_1) can be described by:

$$J_1 = A \cdot [H_2SO_4], \tag{1}$$

where A is a rate constant containing details of the cluster activation process. In absence of a mechanistic understanding of A, an empirically derived value of $2 \cdot 10^{-6}\ s^{-1}$ has been recommended. However, observations show large variations, and values of A as high as $3.5 \cdot 10^{-4}$ s^{-1} can be found in the literature. No estimates of A are available for tropical regions or from the free troposphere. *Kerminen and Kulmala* [2002] showed that the formation rate of particles with diameter 3 nm (J_3) can be approximated by:

$$J_3 = J_1 \exp\Big\{ - 0.153 \frac{CS'}{GR} \Big\}, \tag{2}$$

where CS' is the reduced condensation sink and GR is the growth rate due to available condensable vapours. *Claeys et al.* [2004a,b] showed that isoprene oxidation products, e.g. 2-methyltetrol, formed either through gas-phase photo-oxidation of isoprene or through aqueous phase acid-calalyzed reaction with hydrogen peroxide may contribute to secondary organic aerosol (SOA) formation. They estimated the yield of 2-methyltetrol from isoprene to be on average 0.2%.

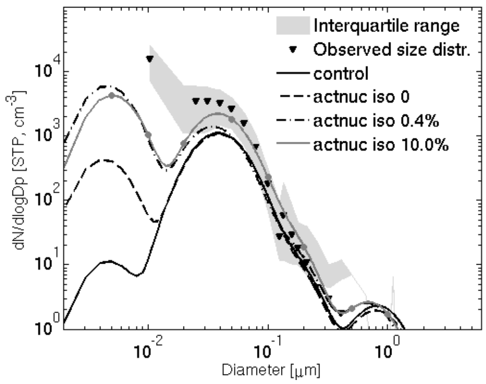

Figure 2: Observed and simulated aerosol size distribution (28th of March) at 12 km after 5h of simulation using activation nucleation for 0% SOA yield, 0.4% SOA yield and 10% SOA yield.

An additional set of sensitivity simulations is conducted where isoprene is included as a prognostic variable in the model in a similar manner as other chemical compounds. A BL isoprene concentration of 5 ppb is assumed based on observations [*Warneke et al.*, 2001]. In the model, isoprene can be depleted by OH-oxidation and also through a prescribed SOA-mass yield, which as a reference is assumed to be 0.4% throughout the model atmosphere. Figure 2 shows that using activation nucleation, together with no other condensable vapours but H_2SO_4, the model still underestimates the observed UT nucleation mode number concentration by several orders of magnitude, even if the higher end value of A found in the literature is applied ($A = 3.5 \cdot 10^{-4}\ s^{-1}$). However, by adding a 0.4% SOA yield from isoprene, the number of nucleation mode particles increases substantially. If the SOA mass yield from isoprene is increased to 10%, the simulated nucleation mode aerosol concentration decreases to 1.2e3 cm^{-3} as the small aerosols grow faster and are transferred into the Aitken mode. These sensitivity simulations illustrate that a small yield of condensable vapours derived from isoprene has the potential of a) increasing the number of small particles formed in the outflow b) reducing the underestimate in Aitken and accumulation mode number through condensational (and coagulational) growth. However, even when an SOA yield from isoprene is included and the higher end value of A form the literature is applied, the nucleation mode number concentration is still underestimated by 79% compared to observations.

4 CONCLUDING REMARKS

The simulations using cluster activation theory should only be regarded as a first indication of the potential of organic compounds (such as isoprene) to contribute to new particle formation in the UT, as no explicit parameterization of the cluster nucleation activation mechanisms is available. In the present study, isoprene is used as a contributor of SOA, but we do not exclude that other volatile organic vapours may contribute in the formation of new aerosols over the Amazon (e.g. mono- and sesqui- terpenes). In addition, *Kulmala et al.* [2006b] showed that homogeneous nucleation of organic vapours may occur within convective clouds due to higher organic vapour saturation ratios found for low UT temperatures. In general, we encourage more laboratory and field studies of the potential of organic compounds to participate in new particle and SOA formation at low temperatures.

References

Andreae, M. O., and T. W. Andreae (1988), The cycle of biogenic sulfur compounds over the Amazon Basin .1. Dry season, *Journal of Geophysical Research-Atmospheres*, *93*(D2), 1487–1497.

Andreae, M. O., H. Berresheim, H. Bingemer, D. J. Jacob, B. L. Lewis, S. M. Li, and R. W. Talbot (1990), The atmospheric sulfur cycle over the Amazon Basin .2. Wet season, *Journal of Geophysical Research-Atmospheres*, *95*(D10), 16,813–16,824.

Claeys, M., B. Graham, G. Vas, W. Wang,

R. Vermeylen, V. Pashynska, J. Cafmeyer, P. Guyon, M. O. Andreae, P. Artaxo, and W. Maenhaut (2004a), Formation of secondary organic aerosols through photooxidation of isoprene, *Science*, *303*(5661), 1173–1176.

Claeys, M., W. Wang, A. C. Ion, I. Kourtchev, A. Gelencser, and W. Maenhaut (2004b), Formation of secondary organic aerosols from isoprene and its gas-phase oxidation products through reaction with hydrogen peroxide, *Atmospheric Environment*, *38*(25), 4093–4098.

Ekman, A. M. L., C. Wang, J. Wilson, and J. Strom (2004), Explicit simulations of aerosol physics in a cloud-resolving model: a sensitivity study based on an observed convective cloud, *Atmospheric Chemistry and Physics*, *4*, 773–791.

Ekman, A. M. L., A. Engström, and C. Wang (2007), The effect of aerosol composition and concentration on the development and anvil properties of a continental deep convective cloud, *Quarterly Journal of the Royal Meteorological Society*, *133*, 1439–1452.

Engström, A., A. M. L. Ekman, R. Krejci, J. Ström, M. de Reus, and C. Wang (2008), Observational and modelling evidence of tropical deep convective clouds as a source of mid-tropospheric accumulation mode aerosols, *Geophysical Research Letters*, *submitted*.

Kerminen, V. M., and M. Kulmala (2002), Analytical formulae connecting the "real" and the "apparent" nucleation rate and the nuclei number concentration for atmospheric nucleation events, *Journal of Aerosol Science*, *33*(4), 609–622.

Krejci, R., J. Ström, M. de Reus, P. Hoor, J. Williams, H. Fischer, and H. C. Hansson (2003), Evolution of aerosol properties over the rain forest in Surinam, South America, observed from aircraft during the LBA-CLAIRE 98 experiment, *Journal of Geophysical Research-Atmospheres*, *108*(D18), 4561.

Kulmala, M., K. E. J. Lehtinen, and A. Laaksonen (2006a), Cluster activation theory as an explanation of the linear dependence between formation rate of 3nm particles and sulphuric acid concentration, *Atmospheric Chemistry and Physics*, *6*, 787–793.

Kulmala, M., A. Reissell, M. Sipila, B. Bonn, T. M. Ruuskanen, K. E. J. Lehtinen, V. M. Kerminen, and J. Ström (2006b), Deep convective clouds as aerosol production engines: Role of insoluble organics, *Journal of Geophysical Research-Atmospheres*, *111*(D17), D17,202.

Vehkamäki, H., M. Kulmala, I. Napari, K. E. J. Lehtinen, C. Timmreck, M. Noppel, and A. Laaksonen (2002), An improved parameterization for sulfuric acid-water nucleation rates for tropospheric and stratospheric conditions, *Journal of Geophysical Research-Atmospheres*, *107*(D22), 4622.

Wang, C., and J. S. Chang (1993), A 3-dimensional numberical-model of cloud dynamics, microphysics, and chemistry .1. Concepts and formulation, *Journal of Geophysical Research-Atmospheres*, *98*(D8), 14,827–14,844.

Wang, C., and P. J. Crutzen (1995), Impact of a simulated severe local storm on the redistribution of sulfur-dioxide, *Journal of Geophysical Research-Atmospheres*, *100*(D6), 11,357–11,367.

Warneke, C., R. Holzinger, A. Hansel, A. Jordan, W. Lindinger, U. Poschl, J. Williams, P. Hoor, H. Fischer, P. J. Crutzen, H. A. Scheeren, and J. Lelieveld (2001), Isoprene and its oxidation products methyl vinyl ketone, methacrolein, and isoprene related peroxides measured online over the tropical rain forest of surinam in march 1998, *Journal of Atmospheric Chemistry*, *38*(2), 167–185.

A CASE STUDY ANALYSIS OF THE IMPACT OF AEROSOL PARTICLES ON OROGRAPHIC SNOWPACK USING DETAILED MICROPHYSICAL MODEL

I. Geresdi[1], R. M. Rasmussen[2], K. Ikeda[2] and G. Thompson[2]
[1]University of Pecs, Hungary
[2]NCAR, Boulder, Colorado, USA

1. INTRODUCTION

The impact of elevated concentrations of aerosol particles due to pollution and other natural and anthropogenic sources on clouds and precipitation is recognized as one of most important scientific issues in cloud physics. This is especially important in the case of orographic precipitation associated with snowfall, since a large fraction of water used by society is derived from snowmelt in the spring, especially in regions with limited summer precipitation. The Western U.S. derives a significant fraction (over 70%) of its water from snowmelt, and thus any impacts on the snowpack can be of critical importance.

This study will present results of a model simulation of orographic precipitation from the 13-14 Dec 2001 winter storm that was extensively sampled during the IMPROVE-2 field project.

2. MODEL DESCRIPTION

A detailed microphysical scheme is used to simulate the formation of water drops and various ice species (Rasmussen et al, 2002). The model simulates four different types of hydrometeors: water drops, pristine ice crystals, furthermore snow and graupel particles. Thirty six size bins are used to describe the evolution of the size distribution for each of these four hydrometeor types. Cloud droplets are initialized based on specified equations for CCN concentration as a function of the supersaturation (Rasmussen et al, 2002). In this paper the results for the extra clean air mass is presented. The domain size in vertical and horizontal direction was about 16 km and 344 km, respectively. The horizontal grid spacing was 1km.

3. RESULTS

The observation shows that the cloud formation in the investigated case occurred in extreme clean maritime air mass (Ikeda et al, 2007). The Fig 1. shows the simulated cloud water and drizzle mixing ratio. Due to the low CCN concentration the formation of the drizzle size water drops is very efficient. Freezing drizzle drops appear well above the -10 °C isoterma. The presence of the large water drops also promotes the formation of the graupel particles by heterogeneous freezing of supercooled water drops or by riming of the snow particles. Due to the melting only a few solid precipitation elements (mostly graupel particles) reached the surface. The aircraft observation (Ikeda et al, 2007) allows us verification of the simulation results. Data and simulated results at the column where the updraft velocity reached its maximum values were used for the comparison. Fig 2. depicts the simulated water drop size distribution and some calculated concentration data which allow us the comparison with the FSSP and 2DP observation. At the elevation of the Conver's fly the local maximum of cloud water mixing ratio changed between 0.15 and 0.30 g/cm^3. This agrees well with the observed range of 0.1 – 0.25 g/cm^3. Both the observation and the simulation show low cloud drop concentration (about 10 cm^{-3}). Because the CCN concentration was about 2 – 3 times larger, the low cloud droplet concentration may be the consequence of the efficient drizzle formation due to the collision-coalescence process. The observed local maximum of the concentration of the particles in the size range of 100 – 300 μm was between 40 and 60 L^{-1}. The Fig 2. shows the typical simulated value of 50 L^{-1}. There is also good agreement in the case of the larger particles. The simulation shows that while in the size range of 100 – 300 μm most of the particles are supercooled drizzle, in the case of the larger particles the concentration of the snow particles is about one order larger than that of liquid particles.

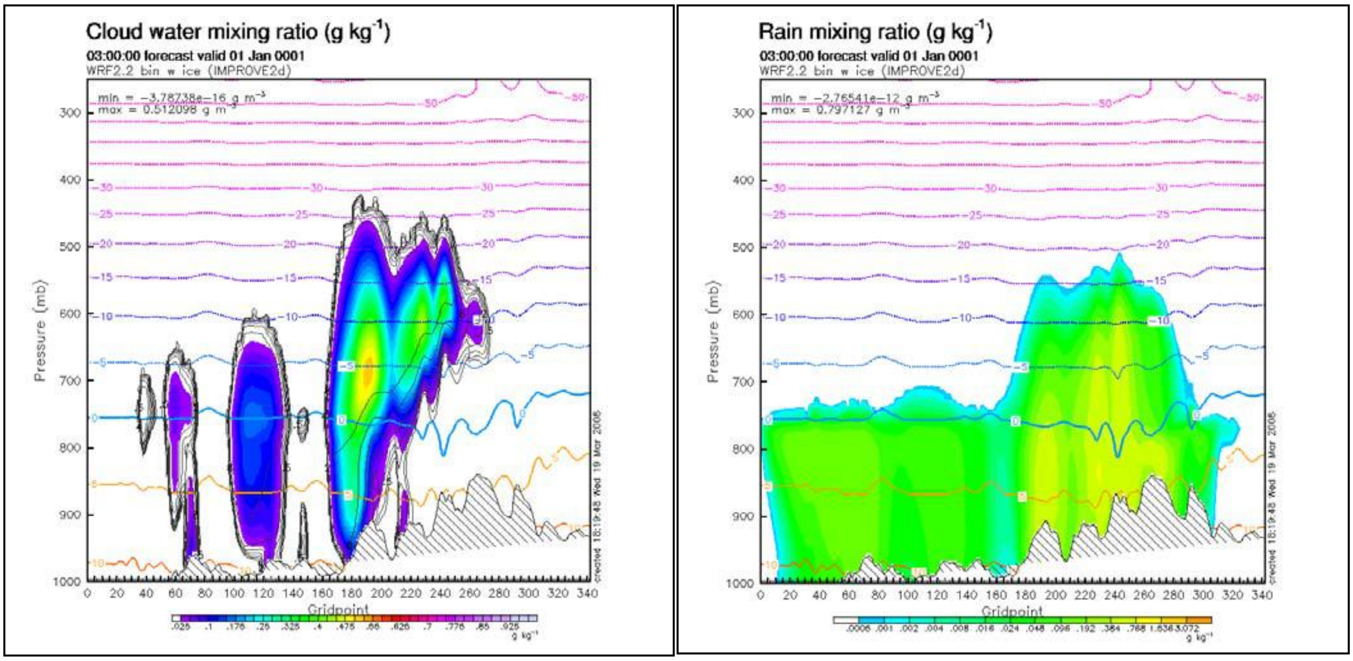

Fig. 1. Simulated cloud water and rain water conten when the CCN concentration is low.

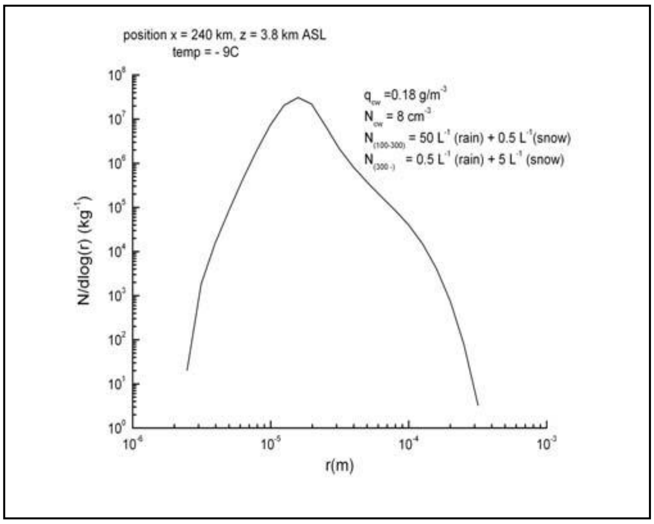

Fig. 2. Simulated size distribution of the water drops. The q_{cw} and N_{cw} show the cloud drop mixing ratio and concentration, respectively. $N_{(100\text{-}300)}$ shows the simulated particle concentration in the size interval of 100 and 300 μm. $N_{(300\text{-})}$ shows the number concentration of the particles larger than 300 μm.

Acknowledgement

The research was supported by the National Program for Research and Development (NKFP; project number 3/022/2005).

References

Ikeda, K, Rasmussen, R. M., Hall, W. D. and Thompson, G., 2007: Observation of freezing drizzle in extratropical cyclonic storms during IMPROVE-2, **J. Amt. Sci., 64, 3016- 3042**

Rasmussen, R., Geresdi, I., Thompson, G., Manning, K., and Karplus, E., 2002: Freezing drizzle formation in stably stratified layer clouds: Part I. The role of radiative cooling of cloud droplets, cloud condensation nuclei, and ice initiation **J. Atmos. Sci., 59, 837-860**

AN AEROSOL-DROPLET CLOSURE STUDY BASED ON RECENT AIRBORNE MEASUREMENTS

Wanmin Gong[1], W. Richard Leaitch[2], J. Walter Strapp[3], Anne Marie Macdonald[1], Katherine L. Hayden[1], Desiree Toom-Sauntry[2], Kurt G. Anlauf[1], Amy Leithead[1], Shao-Meng Li[1], Nicole Shantz[1], and Mark D. Couture[3]

[1]Air Quality Research Division, Environment Canada, Toronto, Ontario, M3H 5T4, Canada
[2]Climate Research Division, Environment Canada, Toronto, Ontario, M3H 5T4, Canada
[3]Meteorological Research Division, Environment Canada, Toronto, Ontario, M3H 5T4, Canada

1. INTRODUCTION

Aerosol activation is fundamental to cloud formation. It controls the cloud droplet number concentration, which has direct implication on cloud optical properties and precipitation formation. It also determines where the aerosol mass addition due to in-cloud production (e.g., of sulfate) will reside after cloud evaporation and, hence, the cloud processed aerosol size spectrum, which will affect aerosol activation in subsequent cloud cycles [Feingold and Kreidenweis, 2000]. A number of factors (dynamical, microphysical, and chemical) affect how the aerosols to take up water and act as cloud condensation nuclei. There have been numerous studies devoted to the effect of aerosol physical and chemical properties on droplet activation (see McFiggans et al., 2005 for an in-depth review).

Aircraft measurements of trace gases, aerosol particle physics and chemistry, and cloud microphysics and dynamics were made (below and in clouds) during two recent field campaigns: ICARTT 2004 (over southwestern Ontario, northern Ohio, and eastern Michigan) and Canadian SOLAS 2003 (over the western North Atlantic Ocean). In this study, the observed cloud droplet number concentrations in non-precipitating towering cumulus and stratocumulus are compared with the predictions from a detailed aerosol parcel model, which solves the diffusional growth equation for condensation of water on aerosol particles following an air parcel during its adiabatic ascent. Effects of updraft velocity, below-cloud aerosol properties (number concentration, size distribution, and composition), and uptake of nitric acid on predicted cloud droplet number concentrations are assessed for these cases.

Corresponding author's address: Wanmin Gong, AQRD, Environment Canada, Toronto, Ontario, M3H 5T4, Canada;
E-Mail: wanmin.gong@ec.gc.ca.

2. EXPERIMENTAL

ICARTT-CTC 2004

During the summer of 2004, several coordinated field campaigns were conducted over North America, the North Atlantic, and western Europe as part of the International Consortium for Atmospheric Research on Transport and Transformation (ICARTT). These field programs were intended to study the emissions of aerosol and ozone precursors, their chemical transformations and removal during transport to and over the North Atlantic, and their impact downwind on the European continent (Fehsenfeld et al., 2006). One of the campaigns, an airborne study conducted by the Environment Canada scientists using the National Research Council of Canada (NRCC) Convair 580, based at Cleveland, Ohio, focused on Chemical transformation and Transport by Clouds (CTC). Measurements focused on trace gases (CO, O_3, NO_x, SO_2, HNO_3, HCHO, H_2O_2), aerosol particle size distribution and chemistry, and cloud microphysics and chemistry. A total of 23 flights were conducted, and clouds (stratocumulus, cumulus and towering cumulus) were sampled downwind of emission regions near Lake Erie and Lake Michigan.

The aerosol was sampled inboard through a shrouded isokinetic inlet with a diffuser. Inboard, the particle size distributions from 0.01 μm to about 17 μm were measured with a TSI Scanning Mobility Particle Sizer (SMPS) and a TSI Aerodynamic Particle Sizer (APS). Outboard, size distributions from 0.14-20 μm diameter were measured with a PMS PCASP-100X and a PMS FSSP300, suspended from pylons under the wings of the aircraft. Aerosol composition was characterized by an Aerodyne Quadrapole Aerosol Mass Spectrometer (Q-AMS) and a Particle-In-Liquid Sampler (PILS). The Q-AMS and PILS measurements are discussed by Hayden et al. (2008). The cloud droplet size distributions were measured with two PMS FSSP100 probes and an FSSP300.

Canadian SOLAS 2003

During one week in October 2003 measurements were made from the NRCC Convair 580 as part of flights for the Canadian Surface Ocean and Lower Atmosphere Study (C-SOLAS). Flights were conducted over the Atlantic Ocean within a few hundred kilometers of Nova Scotia, Canada. Two of six project flights (Oct. 13 and Oct. 14) are discussed here. The aerosol and cloud sampling was conducted near 42^{o} 48'N, 62^{o}W and near 44^{o}50' N, 57^{o}20'W on Oct. 13 and Oct. 14, respectively.

The aerosol and cloud instrumentation used in C-SOLAS were the same as described above for the ICARTT study. No trace gases were sampled except for ozone.

3. AEROSOL-CLOUD DROPLET CLOUSRE

3.1 Parcel model

A kinetic adiabatic parcel model, described by Shantz et al. [2003] and Lohmann et al. [2004], is used for this study. The model solves the diffusional growth equation for condensation of water on aerosol particles based on Pruppacher and Klett [1997], following an air parcel during its adiabatic ascent. The model has been coupled with a size-resolved aqueous-phase chemistry module [Gong, 2002; Kreidenweis et al., 2003] to investigate the interaction between aerosol activation, mass transfer, and aqueous-phase oxidation. This model has also been used to examine the re-distribution of particle nitrate from absorption of HNO_3 by the cloud droplets (Hayden et al., 2008). In the present application, the chemistry module is used to calculate the kinetic uptake of HNO_3 from the gas phase by the growing solution/cloud droplets. The addition of the HNO_3 is fed back to the water activity of the droplet through the change in solute mass due to dissolution and dissociation of the HNO_3. A moving-bin or Lagrangian approach is used, i.e., each of the discrete size bins (or size classes) is allowed to grow or shrink responding to mass transfer and aqueous-phase oxidation.

The parcel model is initialized with the observed aerosol size distributions, particle compositions, trace gas concentrations, state parameters and updraft velocities near the cloud base. The observed aerosol size distribution is fitted with a bi-modal lognormal distribution, one corresponding to the Aitken mode (with a geometric diameter between 0.01 and 0.1 μm) and the other to the accumulation mode (with a geometric diameter between 0.1 and 1 μm). Each mode of the initial aerosol size distribution is represented by 20 to 60 size bins (or classes), uniformly spaced on a logarithmic scale, that provides good resolution around the critical activation diameter in each case.

The aerosol chemistry is represented in the model by two broad components: sulfate (modelled as ammonium-sulfate) and organic (modelled as adipic acid). The present measurements with the AMS and the PILS made from the Convair indicate the clear-air fine particle aerosol was dominated by sulfate and organic material with little nitrate. In the case of the ICARTT measurements, the measured ammonium-to-sulphate molar ratio indicates predominantly ammonium sulphate, while in the C-SOLAS study the sulfate was more acidic. For organics with relatively low solubility, the model allows them to dissolve according to aerosol water mass and compound solubility during growth [Shantz et al., 2003]. Surface tension depression by

Table 1. Observed droplet number concentration, cloud base updraft, and below-cloud aerosol properties for the selected ICARTT-CTC flights.

FLT #	Mean N_d (cm^{-3})	N_d range (cm^{-3})	Mean updraft ($m\ s^{-1}$)	Updraft range ($m\ s^{-1}$)	Cloud-base N_a (>100nm) (cm^{-3})	Range of N_a (>100nm) (cm^{-3})	F_{org} (bulk) (%)	F_{org} (< 100nm) (%)	F_{org} (> 100nm) (%)
12	1340	1180-1500	2.3	1.5 – 3.1	1830	1400-2360	31	70	51
14	1420	1320-1520	3.3	2.0 – 4.6	640	640-780	84	71	77
19	1300	1000-1500	1.8	1.2 – 2.4	1440	1210-1440	40	47	42
20	1325	1200-1550	2	1.0 – 3.0	870	580-1050	45	38	56
21	1100 (1200)	1000-1200 (1100-1300)	2.75 (2.0)	2.0 – 3.5 (1.2 - 2.8)	1560 (2005)	1300-2200	28 (21)	9 (75)	14 (18)

organic compounds (adipic acid here) is modelled following Ervens et al. [2004].

3.2 ICARTT Continental Towering Cu

Towering cumuli were sampled on six out of the 23 flights conducted by Convair 580 during ICARTT. Five of those six flights were selected for the present analysis based on the availability of data and an identifiable connection between cloud base and the sampling points in cloud.

Table 1 summarizes the estimated adiabatic cloud droplet number concentrations (N_d) for the 5 flights from the measurements on the lowest cloud passes, based on the maximum N_d and the N_d coinciding with the maximum liquid water content (LWC) (Leaitch et al., 1986). The N_d range included in Table 1 reflects the uncertainty stemming from different algorithms for correcting dead time and coincidence for the FSSP100 probes (e.g., Baumgartner et al., 1985; Brenguier et al., 1994). Also included in Table 1 are the estimated cloud-base mean and the range of the peak gust velocities in the updraft cores. The below-cloud aerosol compositions for the selected flights are shown in terms of organic mass fraction (%) based on the AMS measurements for both bulk and size-segregated (i.e. smaller and larger than 100 nm) from the AMS operating in the “time-of-flight” (TOF) mode (Hayden et al., 2008).

Figure 1 shows the cloud-base aerosol number-size distribution for the 5 flights. Both Table 1 and Figure 1 have two entries for FLT 21, one based on the near cloud-base measurements towards the beginning of the cloud sampling and the other based the cloud-base measurements near the end of the sampling of the same towering cumulus field. The below-cloud aerosol number concentration, size distribution and composition differ significantly between the two entries. Flights 12, 19, and 21 have relatively higher number of aerosols in the greater-than-100-nm range as indicated in Table 1.

Model calculated N_d based on the cloud-base updraft, aerosol size distribution and composition are compared with the N_d from the observations in Figure 2. The base-case refers to the model calculation using the estimated mean updraft velocity in the adiabatic core (4th column in Table 1) and the separate aerosol compositions for the smaller (Aitken) and the larger (accumulation) modes as given in the last two columns in Table 1.

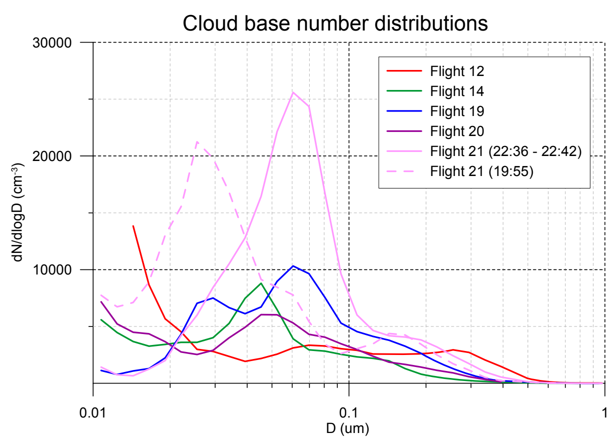

Figure 1. Cloud-base aerosol size distribution from SMPS and APS measurement for the 5 selected flights during the ICARTT-CTC 2004 field campaign.

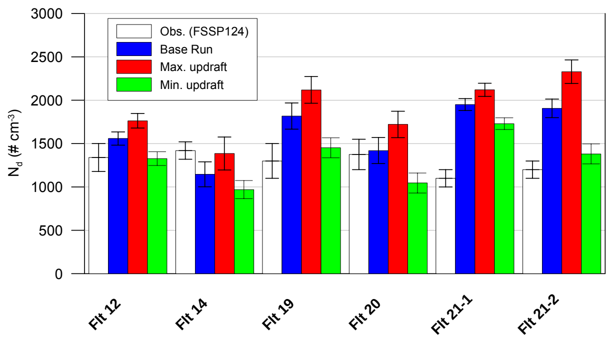

Figure 2. Model calculated N_d compared to observations. The error bars on modelled N_d represent the uncertainties given the size resolution used in the model calculation.

The aerosol-droplet closure is achieved well for two flights, FLT 12 and 20, i.e., the modelled and observed droplet concentrations agree within the uncertainty bounds. The model underestimated N_d for FLT 14, a case with lowest number concentration for below-cloud particles greater than 100 nm (see Table 1), and the model overestimated N_d for FLT 19 and 21, both cases with relatively abundant large (> 100nm) particles below cloud.

A number of things could impact the model-calculated droplet number concentrations, e.g., updraft velocity and below-cloud aerosol (physical and chemical) properties. Also shown in Figure 2 are modelled N_d using the upper and lower bounds of updraft core velocities (see Table 1, 5th column). The updraft is one of the more important factors controlling aerosol activation in clouds [e.g., Peng et al., 2005; Fountoukis et al, 2006]. As seen, using the lower bound of the updraft velocity improved the modelled N_d in comparison to the observations for FLT 12, 19, and 21, those flights with overestimation previously. On the other hand, the modelled N_d was improved by using the upper bound updraft velocity for FLT 14. Note that other closure studies dealing with cumulus have used probability weighted updraft velocities (Conant et al., 2004; Snider et al., 2003) and average updraft velocities (Fountoukis et al, 2007), which tend to be smaller than the updraft velocity used in this study. Statistical analysis was carried out for the updraft velocities at various sampling levels, and it was found that the mean updraft estimated for the adiabatic core corresponds to roughly the 95th percentile of the probability distribution of updraft velocities at cloud-base level for the present study.

There are several issues/uncertainties related to the determination and representation of chemical composition of below-cloud aerosols which may impact the model calculation of N_d. Concerning the organic component of the below-cloud aerosols, its hygroscopic property is not well characterized by the current measurement techniques. For the current model calculation, the organic component is modelled as adipic acid which is slightly soluble (25 g L^{-1}). Many of the existing aerosol-droplet closure studies have treated the aerosol organic component either as being completely insoluble (e.g., Snider and Brenguier, 2000; Fountoukis et al., 2007) or the same as ammonium sulphate (e.g., Conant et al., 2003, Peng et al., 2005). Another issue is that, while the AMS TOF measurement is able to provide information on size-resolved composition, the sensitivity of the Q-AMS used during these flights limits the ability to measure small mass concentrations with high temporal resolution which introduce uncertainties in the size-resolved composition information, particularly for smaller particles. The AMS was also operated in 'mass spec' (MS) mode (Hayden et al., 2008) to provide information on aerosol bulk mass composition with a better temporal resolution. It would be of interest to see the impact of assuming a homogeneous composition based on the AMS MS measurements on model calculated N_d.

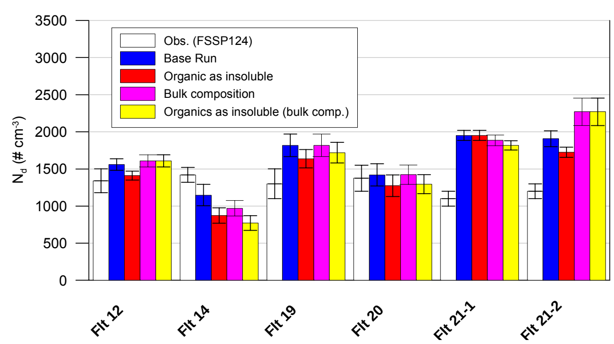

Figure 3. Sensitivity of model calculated N_d in response to the different assumptions in terms of below-cloud aerosol composition.

Figure 3 includes three sets of sensitivity tests: 1) composition as in the base case but organic component modelled as “insoluble” (with solubility of 0.1 g L^{-1}); 2) homogeneous composition with size-independent organic mass fractions as given in Table 1 (column 8), as adipic acid; and, 3) using the size-independent organic mass fractions but modelled as insoluble.

The sensitivities vary from flight to flight for the different cases:

(1). In general, the model-calculated droplet numbers are reduced when the organic component is treated as insoluble. The only exception is for “FLT 21-1” where organic fractions for the two modes are small (9 and 14 %) to start with, and the solubility of the small fraction of organic component does not make much difference in aerosol activation particularly when an internally mixed aerosol is assumed in the current calculation. For FLT 12, 19 and 21-2, treating the organic component as insoluble helps the aerosol-droplet closure. FLT 14 was conducted near the Conesville power plant and FLT 20 was conducted just outside Toledo. In both cases the aircraft encountered significant sulfur plumes, and it may be reasonable to expect that the particles may be more hygroscopic because of condensation of SO_2.

(2). The impact of using the size-independent composition based on the AMS MS measurement made a difference for FLT 14 and 21 but hardly any for FLT 12, 19, and 20. For FLT 14 and 21, there is a significant change in the overall organic fraction between the estimates based on the AMS MS and TOF measurements. For FLT 19, there is no significant difference in organic fractions between the two modes based on the AMS TOF measurements and also no real difference between the bulk and the size-resolved organic fractions. For FLT 12 and 20, there is a significant difference between the AMS MS- and TOF-based organic fractions. Particularly for FLT 12, the bulk organic fraction is considerably smaller than the organic fractions for both modes based on the AMS TOF measurements. The fact that the change in aerosol composition between the two cases did not result in noticeable changes in modelled N_d is a result of competing factors compensating each other: the smaller organic fraction lowers the critical activation diameter for aerosols but, at the same time, also enhances the water uptake on aerosols and therefore lowers the maximum supersaturation reached in the updraft.

3.3 C-SOLAS Marine stratocumulus

Marine stratocumuli were sampled on six flights during C-SOLAS. Two of those cases are discussed. These two cases were chosen because of the similarities of the shapes of the particle size distributions, but contrasting total number concentrations and particle chemistry.

Table 2 summarizes the mean and range of N_d for the two flights based on the profiles through the clouds. For these stratocumuli, we use one standard deviation of the gust velocity (based on Peng et al., 2006) as well as the maximum measured gust. The below-cloud aerosol number concentrations are given for N_a>0.1 μm, and the aerosol compositions for the selected flights are shown in terms of organic mass fraction (%) based on the AMS and PILS measurements.

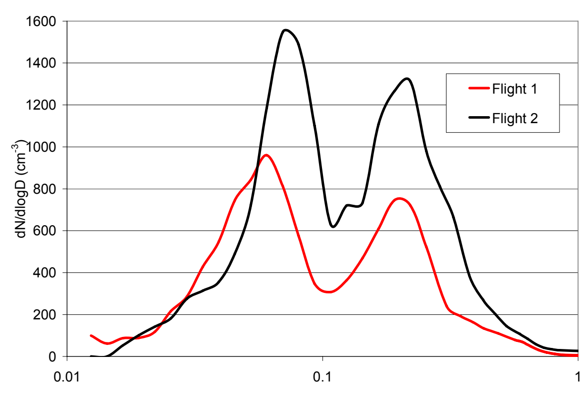

Figure 4. Cloud-base aerosol size distribution from SMPS and APS measurement for the two C-SOLAS cases of marine stratocumulus.

Figure 4 shows the cloud base number size distributions for the two flights. There is a strong similarity between the shapes of the

Table 2. Observed droplet number concentration, cloud base updraft, and below-cloud aerosol properties for the two selected flights from C-SOLAS.

FLT	Mean N_d (cm^{-3})	N_d range (cm^{-3})	One Std Dev of Gusts ($m\ s^{-1}$)	Maximum Gust ($m\ s^{-1}$)	Cloud-base N_a (>0.1 μm) (cm^{-3})	Range of N_a (>100nm) (cm^{-3})	F_{org} (bulk) (%)	F_{org} (< 100nm) (%)	F_{org} (> 100nm) (%)
Oct 13	220	200-300	0.14	0.20	261	223-299	25	0-100	25
Oct 14	660	510-760	0.50	1.0	522	480-564	53	0-100	53

Table 3. Model calculated droplet concentrations.

Updraft (cm/s)	Flight 1 – organic solubility of modes 2 & 3			All H_2SO_4		Flight 2 – organic solubility of modes 2 & 3			All H_2SO_4
	0.01g/l	5g/l	200g/l			0.01g/l	5g/l	200g/l	
	Internal mixture					Internal mixture			
14	195	225	225	225		215	215	215	256
20	253	253	253	249					
50	330	330	330	308		538	531	531	533
100	401	401	401	401		771	771	771	681

two distributions. The primary difference is that the distribution from the Oct. 14 flight or FLT 2 is about twice the total number concentration of particles >0.05 μm diameter compared with Oct. 13 (FLT 1). In terms of mass, the difference between the two distributions is that for Oct. 13 the organic material comprises about 25% of the total, whereas on Oct. 14 the organic mass was more than 50% of the total, and for particles below 400 nm diameter the organic represented approximately 75% of total mass. Thus, the difference in the distributions from Oct. 13 to Oct. 14 is made up mostly of an increase in organic mass.

Table 3 shows the results of the basic simulations of the N_d for various updrafts and the assumptions about the solubility of the organic material. In addition, the simulated N_d are given for the assumption that the entire aerosol is assumed to be sulfuric acid. Note that sulfate component in all simulations is to be sulfuric acid, and within each mode of the modelled size distribution the organic and sulfate are assumed to be internally mixed..

Reasonable agreement between the simulated N_d and the range of observed N_d (Table 2) is obtained for the appropriate updraft speed and regardless of the assumption about the organic solubility.

Higher updrafts that corresponding to the Oct. 14 case when applied to the Oct .13 case yield values of N_d that are significantly lower than the observed N_d for Oct. 14. This indicates that the addition of the organic to the below-cloud aerosol had an impact on the N_d. We note that in the reverse case, where the lower updrafts corresponding to the Oct. 13 case are applied to the Oct. 14 case that there is mostly a reduction in the simulated N_d relative to the Oct. 13 results. Thus, there are interactions between changes in the aerosol chemistry and the updraft that can produce subtle and not so obvious differences in the N_d. Further, assuming that the organic has the same properties as sulfuric acid can have somewhat unexpected results. Because of the high solubility and easy dissociation of sulfuric acid in solution, particles composed of sulfuric acid are good CCN. However, as we see from Table 3, when the assumption that the particles are composed of purely sulfuric acid, as opposed to organic materials, is applied there is a significant reduction in the N_d for the Oct. 14 case. This results from the competition for water vapour at cloud base. It should be clear that simply identifying the CCN activity of compounds does not equate to an understanding of the N_d.

4. DISCUSSION

The N_d, N_a and updrafts are all much higher in these continental cumuli as compared with the marine stratocumulus cases here. That we obtain reasonable closure of the aerosol particles and cloud droplets in both environments means that we are approaching a level at which we can start to become confident in the application of aerosol activation in models of larger scale. However, uncertainties remain, not the least of which are the accommodation coefficient and the specification of the updraft.

For the continental towering cumulus cases, aerosol-droplet closure is achieved for 4 out of 5 flights investigated given the known uncertainties in updraft and below-cloud aerosol properties. The issue of aerosol mixing state in activation is only partially and indirectly addressed in this study when there is a significant overlapping between the two modes with different compositions (e.g., FLT 12). For FLT 21, particularly, where an aerosol-droplet closure is not achieved satisfactorily from the present study, there is evidence from the measurements with the PCASP to suggest that the below-cloud aerosol particles were not entirely internally mixed. This would impact the aerosol-droplet closure.

REFERENCES

Baumgardner, D., W. Strapp, and J.E. Dye, (1985): Evaluation of the Forward Scattering Spectrometer Probe. Part II: Corrections for Coincidence and Dead-Time Losses. *J. Atmos. Oceanic Technol*., 2, 626–632.

Brenguier, J., D. Baumgardner, and B. Baker, (1994): A Review and Discussion of Processing Algorithms for FSSP Concentration Measurements. *J. Atmos. Oceanic Technol*., 11, 1409–1414.

Conant, W. C., et al. (2004), Aerosol–cloud drop concentration closure in warm cumulus, *J. Geophys. Res.*, *109*, D13204, doi:10.1029/2003JD004324.

Ervens, B., G. Feingold, S. L. Clegg, and S. M. Kreidenweis (2004), A modeling study of aqueous production of dicarboxylic acids: 2. Implications for cloud microphysics, *J. Geophys. Res.*, 109, D15206, doi:10.1029/2004JD004575.

Fehsenfeld, F. C. et al., (2006), International Consortium for Atmospheric Research on Transport and Transformation (ICARTT): North America to Europe - Overview of the 2004 summer field study, *J. Geophys. Res*., 111, D23S01, doi:10.1029/2006JD007829

Fountoukis, C. et al., (2007), Aerosol-cloud drop concentration closure for clouds sampled during the International Consortium for Atmospheric Research on Transport and Transformation 2004 campaign, *J. Geophys. Res*., 112, D10S30, doi:10.1029/2006JD007272.

Feingold, G., and S. Kreidenweis (2000), Does cloud processing of aerosol enhance droplet concentrations?, *J. Geophys. Res.*, *105*(D19), 24,351–24,361.

Gong, W. (2002), Modelling cloud chemistry in a regional aerosol model: Bulk vs. size resolved representation, *Air Pollution Modeling and Its Applications*, 15, edited by C. Borrego and G. Schayes, pp. 285-293, Plenum, New York.

Hayden K.L., A.M. Macdonald, W. Gong, D. Toom-Sauntry, K.G. Anlauf, A. Leithead, S.-M. Li, W.R. Leaitch, and K. Noone, 2008: Cloud processing of nitrate, *J. Geophys. Res.*, submitted.

Kreidenweis S. M. et al, (2003), Modification of aerosol mass and size distribution due to aqueous-phase SO2 oxidation in clouds: Comparisons of several models, *J. Geophys. Res*., 108 (D7), 4213, doi:10.1029/2002JD002697.

Leaitch, W.R., Strapp, J.W., Isaac, G.A., Hudson, J.G. (1986), Cloud droplet nucleation and cloud scavenging of aerosol, *TELLUS*, 38 B (5), pp. 328-344.

Lohmann, U., Broekhuizen, K., Leaitch, R., Shantz, N., Abbatt, J. (2004), How efficient is cloud droplet formation of organic aerosols?, *Geophysical Research Letters*, 31 (5), pp. L05108 1-4.

McFiggans et al., (2006), The effect of physical and chemical aerosol properties on warm cloud droplet activation, *Atmos. Chem. Phys*., 6, 2593-2649

Peng, Y., U. Lohmann, and W.R. Leaitch, 2005: Importance of vertical velocity variations in the cloud droplet nucleation process of marine stratus clouds. *Journal of Geophysical Research*, 110, D21213, doi. 1029/2004JD004922.

Shantz, N. C., Leaitch, W. R., and Caffrey, P. F. (2003), Effect of organics of low solubility on the growth rate of cloud droplets, *J. Geophys. Res.-Atmos.*, 108, 4168, doi:10.1029/2002JD002540.

Snider J. R., S. Guibert, J.-L. Brenguier, J.-P. Putaud, (2003), Aerosol activation in marine stratocumulus clouds: 2. Köhler and parcel theory closure studies, *J. Geophys. Res*., 108 (D15), 8629, doi:10.1029/2002JD002692.

MYSTERIOUS SMALL AEROSOLS OR WHY LIGHTNING MAY TAKE PLACE IN THE EYEWALLS OF HURRICANES

A. P. Khain, N. Cohen, N. Benmoshe and A. Pokrovsky
Department of Atmospheric Sciences, The Hebrew University of Jerusalem, Israel
khain@vms.huji.ac.il

ABSTRACT

Lightning is much spread phenomena over the land than over the sea. According to the state-of-the art concept, the charge separation takes place within cloud zones where graupel and ice crystals collide in the presence of a significant amount of supercooled water. In maritime clouds most of droplets formed at the cloud base fall out not reaching the freezing level. Nevertheless, lightning takes place sometimes in eye walls of hurricanes, where clouds are, supposedly, the most maritime in the word. In this study we address the following question: "Why can lightning take place in deep maritime convective clouds over ocean and, in particular, in the hurricane eyewalls at all?"

Numerical simulations using the spectral microphysics Hebrew University cloud model show that the formation of lightning requires two conditions: a) significant vertical velocities ($W_{\max} >\sim 13 m/s$), which take place only in small fraction of the deepest maritime clouds, and b) the existence of small aerosols with the radii of about 0.01 μm in the CCN size spectra.

1. INTRODUCTION

Observations indicate that the concentration of maritime cloud condensational nuclei (CCN) (at 1% supersaturation) is about 60-100 cm^{-3} (Pruppacher and Keltt 1997; Levin and Cotton 2007). It is widely accepted that aerosol size distributions over the sea contain higher number of larger CCN than those over the land because of the sea spray production. At the same time there is no agreement as regards the concentration and even the existence of small aerosol particles (AP) with radii below, say, 0.01-0.02 μm in the maritime atmosphere.

According to Twomey and Wojciehowsky (1969), Hegg and Hobbs (1992), Hegg et al (1993); Pruppacher and Keltt (1997); Levin and Cotton (2007) the concentration of activated CCN in maritime atmosphere increases monotonically with the increase in supersaturation up to the values as high as 8-10% (**Figure 1**). It is a general practice to describe the dependence of cloud nucleation nuclei (CCN) concentration using a semi empiric formula

$$N_{ccn} = N_o S^k , \qquad (1)$$

where N_{ccn} is the concentration of activated AP at supersaturation S (in %) with respect to water, N_o and k are the measured parameters. Parameter k is known as the slope parameter. According to many studies (see Pruppacher and Keltt 1997) the values of k vary from 0.3 to 1.3 within a wide range of supersaturations in different zones of the ocean, and even within different air masses in the same geographical location (Hudson and Li

1995). The large values of k within the whole range of supersaturation variation indicate the existence of a significant amount of small aerosols in the maritime atmosphere.

At the same time, in some observational (e.g., Hudson 1984; Hudson and Frisbie 1991; Hudson and Li 1995; Hudson and Yum, 1997; 2002) and laboratory (Jiusto and Lala 1981) studies a decrease in the value of k with the increase in the supersaturation was reported. According to these results _no_ new CCN can be activated at supersaturations exceeding some threshold S_{thr} which varies from ~0.1 % (Cohard et al, 1998; Emde and Wacker 1993) to ~ 0.6% (Hudson and Li 1995). The $k(S)$ dependence with the condition $k \approx 0$ at $S > S_{thr}$ is used in several studies (e.g., Cohard et al 1998; Abdul-Razzak et al. 1998) for parameterization of aerosol activation in cloud and mesoscale models. Khain et al (2004 and 2005) assumed no drop nucleation at S>1.1% while simulating deep maritime clouds.

Figure 1 depicts the variability of $N_{ccn}(S)$ dependencies reported for maritime aerosols in different studies. The existence/absence of S_{thr} of about 0.6% indicates the lack/presence of aerosols (CCN) with the radii below ~0.01 μm in the maritime atmosphere.

According to Hudson (2005) (personal communication) the amount of small aerosols in his measurements had been somehow underestimated because of the experimental difficulties. At the same time, Hobbs (personal communication 2005) expressed his doubts concerning the results indicating the lack of small aerosols in the maritime atmosphere. A discussion during a meeting dedicated to the WMO/IUGG scientific review processing (France, Toulouse, October 2006) showed that the question concerning the existence of small condensational nuclei in the maritime atmosphere remains open.

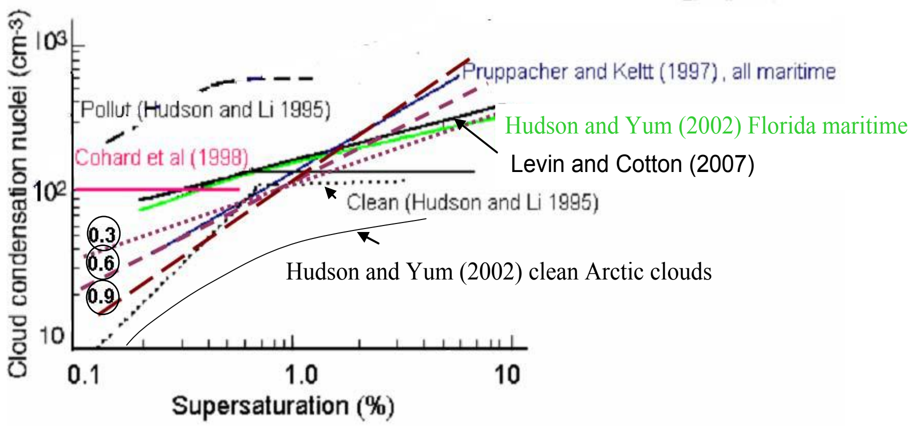

Figure 1 *Dependencies of the activated CCN concentration on supersaturation over the sea reported by different authors. Lines denoted 0.3, 0.6 and 0.9 correspond to dependencies (1) with corresponding values of slope parameter k. One can see that the dependence presented by Pruppacher and Klett (1997) for "all maritime" cases is close to the case k=0.9, while Levin and Cotton (2007) characterize the mean maritime CCN by the slope parameter close to 0.3.*

Many numerical simulations of aerosol effects on cloud microphysics, dynamics and precipitation (e.g., Khain 2004, 2005, 2008; van der Heeven et al 2006, Wang et al 2005, Tao et al 2007) have been carried out under different AP concentrations typical of maritime and continental conditions. In most studies parameter N_o is usually varied within a wide range from a few tens to several thousand AP per cm^3. The role of the slope parameter is usually not discussed, and implicitly its role is assumed not to be decisive. However, it is not the case because the values of supersaturation in deep maritime clouds can be very high and small aerosol particles (if they do exist) may be activated into droplets.

There are some observations which can be interpreted as evidences of the existence of the small aerosols in the maritime atmosphere. The first evidence is the formation of bimodal droplet size distributions in maritime clouds a few km above the cloud base (e.g. Warner 1969a,b; Pinsky and Khain 2002; Segal et al, 2003). The appearance of small cloud droplets at so high distances above cloud base near the cloud axes can be attributed to in-cloud droplet nucleation, when super saturation in ascending cloud parcels exceeds the local maximum at the cloud base. As a result, small APs which remained haze particles at the cloud base are activated within the clouds several km above the cloud base.

Second evidence of the existence of small AP follows from the AP budget. According to results of many studies (Twomey, 1968, 1971; Radke and Hobbs, 1969; Dinger et al., 1970; Hobbs, 1971; Levin and Cotton 2007) sea spray contributes mainly to the large size AP tail of the AP size distribution, but most CCN in the accumulation mode are formed by collisions of smaller aerosols having another source different from the sea spray. The small AP can be of continental nature (like Saharan dust, which is often was found in convective storms near the Eastern African coast and in storms and hurricanes reaching the American coast) or can form via different chemical reactions over the sea (Pruppacher and Klett 1997).

Another phenomenon which allows us to suspect an important effect of small aerosols on the microstructure of maritime clouds is the lightning in TC eyewalls and in maritime deep clouds in the ITCZ. According to a widely accepted concept the charge separation in clouds takes place in the zones of low temperatures (about -15 ^oC to -20 ^oC), where collisions between low and high density ice take place in the presence of a significant amount of supercooled water (Black and Hallet 1999; Takahashi, 1978; Saunders 1993, Cecil et al 2002a,b; Sherwood et al 2006).

The significant difference in the lightning density over the land and the sea is well known (e.g., Williams and Satori, 2004; Williams et al 2004) (**Figure 2**). The lower lightning density over the sea is usually attributed to low vertical velocities in maritime convection (Black et al 1996; Szoke et al 1986; Jorgensen et al 1985; Williams et al 2004, 2005) as well as to low aerosol concentration. Both factors must lead to the formation of raindrops below freezing level collecting most small droplets nucleated near the cloud base. This effect should dramatically decrease the amount supercooled water droplets aloft and prevent the charge separation process. At the same time Figure 2 and **Figure 3** show that quite intense lightning may exist in maritime clouds (including extremely maritime clouds within the TC eyewalls) forming over open sea.

Khain et al (2008a) have shown that lightning at the periphery of landfalling TC can be caused by synergetic effects of higher instability at the TC periphery (producing vertical velocities of 18-20 m/s, which are unusually high for maritime clouds) and continental aerosols involved into the TC circulation. However, this explanation cannot be extended to the TC eyewall clouds, which hardly contain continental aerosols (with sizes larger ~0.02 μm) penetrating to the TC center from the periphery. The continental aerosols penetrating the TC circulation from the nearest continent should be eliminated from the atmosphere either via the nucleation scavenging or via washout

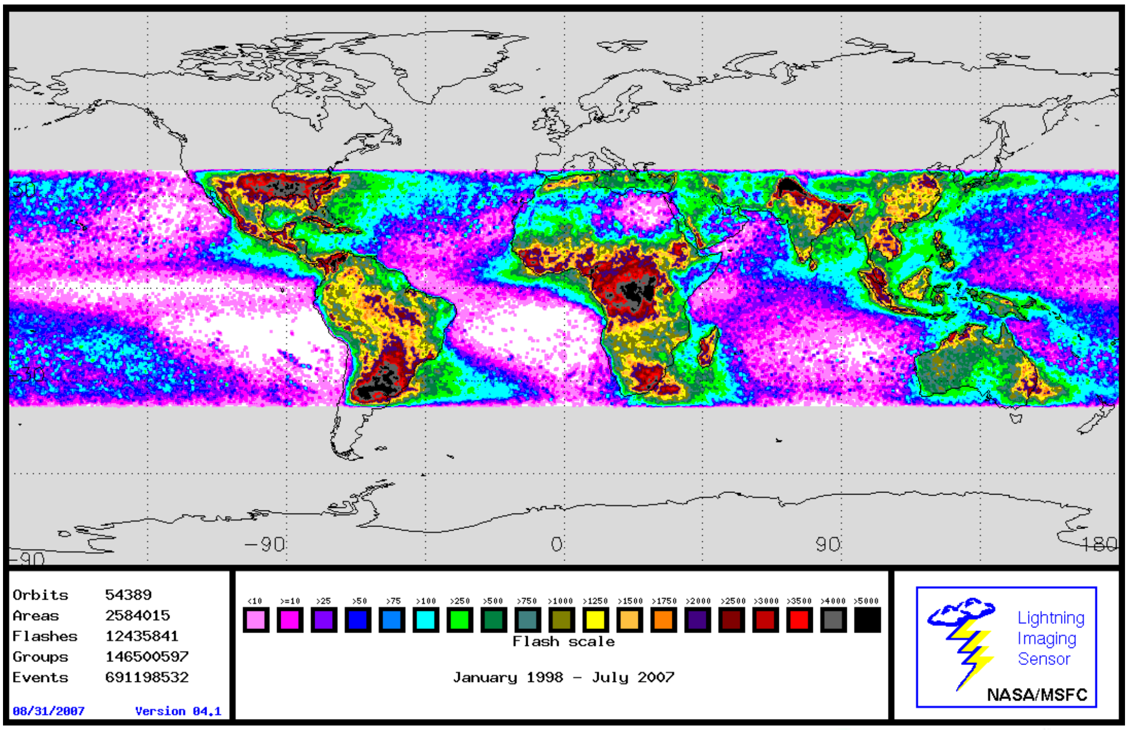

Figure 2. LIS Global Lightning [*Distribution*](http://thunder.msfc.nasa.gov/data/query/distributions.html) *since launch, January 1998 - July 2007. It is possible to see the ITCZ lightning belts just above and below the equator.http://thunder.msfc.nasa.gov/data/query/distributions.html*

processes. Besides, the clouds in the eyewall supposedly contain a huge amount of giant CCN (or even droplets) at the cloud base because of sea spray formation under strong winds. These large CCN and droplets should create extremely maritime clouds with the intense formation of warm rain at the low height levels. Hence, in this study we address a question, which is just opposite to that usually asked, namely: "If warm rain processes in maritime clouds are so efficient why lightning can form in deep maritime convective clouds and, in particular, in the hurricane eyewalls at all?" We hypothesize that the formation of supercooled water in deep maritime convective clouds needed for lightning

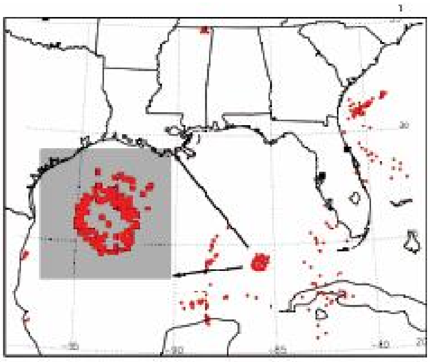

Figure 3. Eye-wall lightning density in in hurricane Rita during its intensification from Cat 3 to 5 (14–15 UTC, 21 Sep 2005) (right) (after Shao et al., EOS, 86, 42, 18 Oct. 2005)

formation is caused by in-cloud nucleation of AP with radii smaller than about 0.01 μm. These AP hardly can be activated at the cloud base of maritime clouds because of a relatively low supersaturation there. Besides, these AP hardly can be scavenged by precipitation because of their small sizes and very low scavenging rate. We also suppose that the lightning takes place only in a small fraction of clouds, in which the vertical velocity is comparatively high (according to Jorgensen and LeMone 1989; Jorgensen et al 1985 the fraction of deep convective cores with the maximum vertical velocities exceeding 10 m/s is about 5%).

The hypothesis will be tested using a spectral bin-microphysics of the Hebrew University cloud model (HUCM).

2. MODEL DESCRIPTION

The HUCM is a 2-D mixed-phase model (Khain and Sednev 1996; Khain et al 2004, 2005, 2008b) with spectral bin microphysics (SBM) based on solving the system of kinetic equations for size distribution functions for water drops, ice crystals (plate-, columnar- and branch types), aggregates, graupel and hail/frozen drops, as well as atmospheric aerosol particles (AP). Each size distribution is described using 43 doubling mass bins, allowing simulation of graupel and hail with the sizes up to 5 cm in diameter. The model is specially designed to take into account the AP effects on the cloud microphysics, dynamics, and precipitation. *The initial* (at t=0) CCN size distribution is calculated using the empirical dependence **(1)** and applying the procedure described by Khain et al (2000). At t>0 the prognostic equation for the size distribution of non-activated AP is solved. Using the supersaturation values, the critical AP radius is calculated according to the Kohler theory. The APs with the radii exceeding the critical value are activated and new droplets are nucleated. The corresponding bins of the CCN size distributions become empty.

Primary nucleation of each type of ice crystals is performed within its own temperature range following Takahashi et al (1991). The dependence of the ice nuclei concentration on supersaturation with respect to ice is described using an empirical expression suggested by Meyers et al. (1992) and applied using a semi-lagrangian approach (Khain et al 2000) allowing the utilization of the diagnostic relationship in the time dependent framework. The secondary ice generation is described according to Hallett and Mossop (1974). The rate of drop freezing is described following the observations of immersion nuclei by Vali (1975, 1994), and homogeneous freezing according to Pruppacher (1995). The homogeneous freezing takes place at temperature about -$38^{o}C$. The diffusion growth/evaporation of droplets and the deposition/sublimation of ice particles are calculated using analytical solutions for supersaturation with respect to water and ice. An efficient and accurate method of solving the stochastic kinetic equation for collisions (Bott, 1998) was extended to a system of stochastic kinetic equations calculating water-ice and ice-ice collisions. The model uses height dependent drop-drop and drop-graupel collision kernels following Khain et al, (2001) and Pinsky et al (2001). Ice-ice collection rates are assumed to be temperature dependent (Pruppacher and Klett, 1997). An increase in the water-water and water-ice collision kernels caused by the turbulent/inertia mechanism was taken into account according to Pinsky and Khain (1998) and Pinsky et al. (1999, 2007). Advection of scalar values is performed using the positively defined conservative scheme proposed by Bott (1989). The computational domain is 178 km x 16 km with the resolution of 350 m and 125 m in the horizontal and vertical directions, respectively.

3 THE EXPERIMENTAL DESIGN AND RESULTS OF SIMULATIONS

To show the potential effect of these "mysterious" small aerosols on cloud microphysics and precipitation, two sets of deep convective clouds simulations have been performed. In the first set, the sounding in the GATE-74 compaign close to that typical of tropical oceans during hurricane season (Jordan 1958) was used. The sounding indicates high about 90 % humidity near the surface. The zero temperature level is at 4.2 km. So, the conditions can be considered as typical of wet tropical oceanic clouds. At the same time the maximum vertical velocities in the simulated clouds ranged from 15 m/s to 18 m/s. It means that these clouds fall into the range of the 5% of the most intense maritime clouds.

Parameter N_o in all simulations was set equal to 100 cm^{-3}. Three values of slope parameter k (0.3; 0.6 and 0.9) were used in simulations. Corresponding runs will be referred to as *M_k03*; *M_k06* and *M_k09*, respectively. Any truncation of small AP was not used in these simulations. The increase in the parameter k indicates the increase in concentration of small aerosols. These values of k cover the range of slope parameters in "all maritime" aerosols reported by Pruppacher and Klett (1997) and Levin and Cotton (2007).

The dependencies $N_{ccn}(S)$ used in

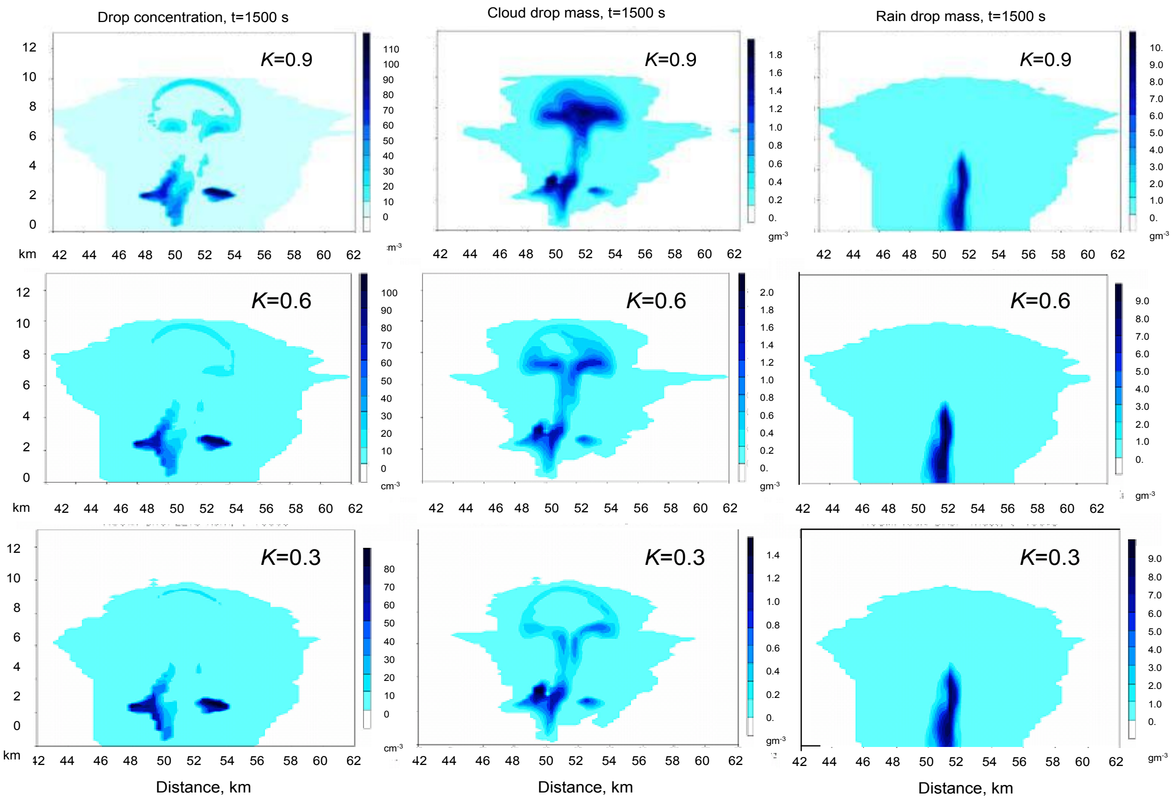

Figure 4*. Fields of the droplet concentration N_d (left), CWC (middle), and RWC (right) for N_0=100 cm^{-3} at different slope parameters.*

the simulations are plotted in Figure 1.

In addition, three supplemental simulations for the same slope parameters have been run in which no small CCN nucleated at S>1.1% were allowed.

Figure 4 shows the fields of the droplet cloud water contents (CWC) and rain water content (RWC), respectively, in the simulations with the GATE-74 sounding and different slope parameters. One can see several typical features common for all maritime clouds: the droplet concentration does not exceed 100 cm^{-3}; warm rain forms fast, mainly below the freezing level. However, there is a dramatic difference in the droplet concentration and the cloud water content above 5 km level. At *k*=0.3 concentration monotonically decreases with height and the CWC above the freezing level is negligible. In the case *k*=0.9 large supercooled LWC forms above 5 km level. The case of *k*=0.6 indicates the intermediate results. The maximum vertical velocities in these simulations are 15-18 m/s.

Figure 5 shows the droplet mass distributions at several height levels along the cloud axes in the *M_k03* and *M_k09* at t=1500 s. One can see that the DSDs are actually similar below 2.5 km. However, a dramatic difference takes place above 5 km. While in the case of *k=0.3* the LWC is negligible at z= 8 km (T=-20^oC), in the *k=0.9* case the LWC is significant, and drop sizes range from 40 to 500 μm at this level. Note that the drop mass spectrum in the *M_k09* at z=7.5 km contains smaller drops (with the diameter of 20μm) than the spectrum at z=5 km. This indicates the nucleation of new droplets (in-cloud nucleation) within the layer from 5 to 7 km. As was shown in detail by Pinsky and Khain (2002), in maritime clouds supersaturation start increasing with height above several hundred meters above the local maximum at the cloud base because increase in the vertical velocity is accompanied by a decrease in the CWC. As soon as the supersaturation exceeds that at the cloud base, new (small) AP are activated (Pinsky and Khain 2002). In Figure 5 (lower panel) the minimum drop size in the droplet spectra monotonically increases with height.

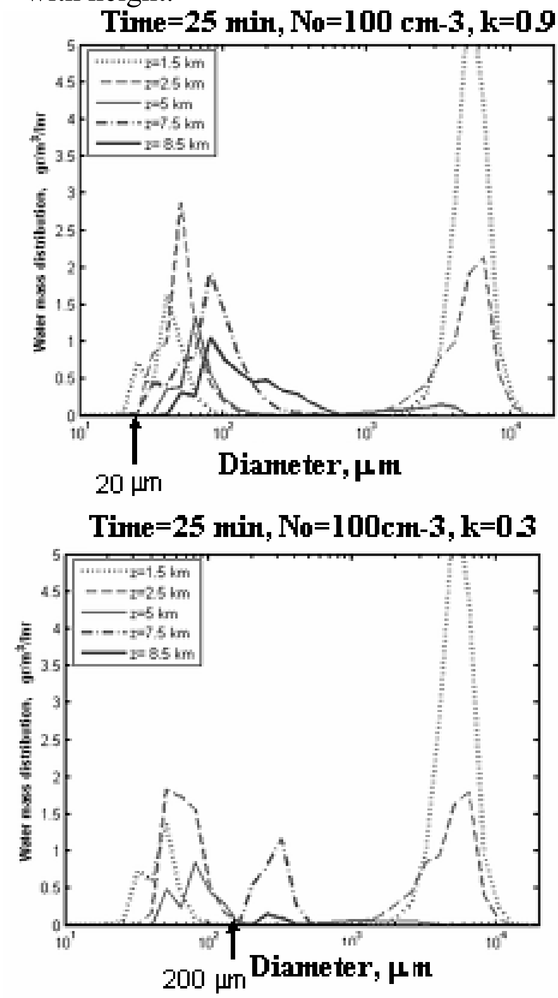

Figure 5*. Droplet mass distribution at several height levels along cloud axes in the cases M_k09 (upper panel) and M_k03 (lower panel) at t=1500s. Numbers 20* μm *and 200* μm *indicate the minimum droplet size in the distributions at z= 7.5 km in the runs.*

The minimum drop diameter at z=7.5 km in this run (*M_k03*) is 200 μm. The latter does not show any in-cloud nucleation in this run.

Figure 6 shows fields of graupel and ice crystal contents in the *M-k09* at t= 1800 s. One can see a large region within the cloud at temperatures below -13 ^oC, where graupel, crystals and supercooled droplets coexist, which is considered as favorable condition for charge separation and lightning formation in the TC eyewall (e.g., Black et al 1996). In the *M-k03* conditions for lightning are unfavorable in spite of high vertical velocities and high supersaturation because the negligible amount of supercooled water.

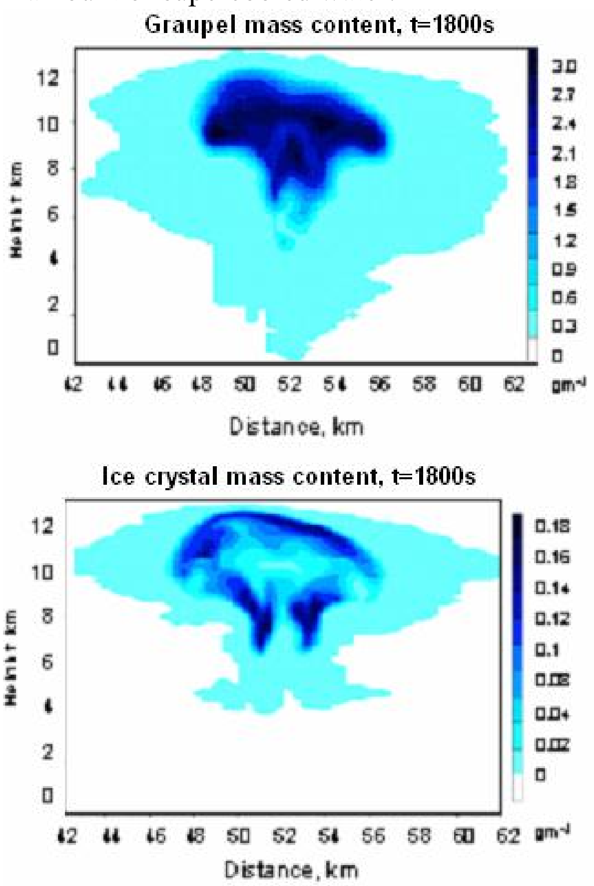

Figure 6. Fields of graupel and ice contents in the simulation M_k09 at t=1800 s.

To investigate the role of the vertical velocity a simulation has been performed which differed from the *M-k09* by more stable sounding under which the maximum vertical velocity reached 7 m/s. Concentrations of ice crystals and graupel within this layer are quite small (not shown). It means that the formation of lightning can hardly be expected. Thus, under small vertical velocities typical of most maritime clouds lightning hardly can be formed even in the presence of small aerosols.

Elimination of small aerosols (which are activated at S>1.1%) in the supplemental simulations decreases significantly both the CWC and droplet concentrations above 4 km level, as well as graupel and ice crystal contents.

4. DISCUSSION AND CONCLUSIONS

This study demonstrates high importance of atmospheric aerosols in the creation of conditions favoring lightning formation over the oceans. Combination of results obtained by Khain et al (2008a) and those in the present study suggests two possible mechanisms by means of which aerosols affect microphysics of the clouds developing over the ocean. First one is the direct penetration of continental aerosols with sizes above ~0.01 μm. These AP nucleate to droplets at the cloud base. In case the concentration of the AP is high, clouds obtain "continental" properties, the production of warm rain decreases and the amount of super cooled water, as well as ice particles increases. The second mechanism considered in this study is based on the fact that the supersaturation in maritime clouds is as a rule significantly higher then in continental clouds. The latter allows activation of small AP with sizes below ~0.01 μm. These AP are not activated at the cloud base (because of a comparably low vertical velocities), but at significant distances above the cloud base, where supersaturation exceeds the local maximum near the cloud base. In this case clouds keep their maritime properties: the droplet concentration maximum does not exceed 100 cm^{-3}, warm rain forms rapidly below the freezing level. At the same time the growth of droplets nucleated well above the cloud base (and even above the freezing level) create a necessary amount of supercooled droplets and foster graupel and ice crystal formation, i.e. create conditions favorable for charge separation and lightning. Thus, the rapid formation of warm rain does not eliminate the possibility of the formation of supercooled droplets at higher levels and lightning.

Note that the existence of corresponding aerosols is not sufficient for lightning formation. In both mechanisms mentioned above, significant vertical velocities ($W_{\max} >\sim 13 m/s$) are required. The lack of high updrafts prevents in-cloud nucleation and the formation of supercooled water at high levels, where co-existence with graupel and crystals is possible. The conclusion concerning the necessity of enhanced vertical velocities agrees well with the observations. According to Molinari at al (1999) and later studies (e.g. Demetriades and Holle, 2006), the lightning in hurricanes takes place when the old eyewall is replaced by a new one, which is, supposedly, accompanied by the formation of clouds with especially high vertical updrafts.

One can assume two main sources of the small CCN over the ocean. One source is related to chemical reactions following by particle collisions to create the accumulated AP mode. We also speculate that small aerosols can be of continental nature and penetrate the ocean with the intrusion of African dust. For instance, Hudson and Yum (2002) show (Figure 1) that the concentration of small aerosols is low under clean Arctic conditions, while it is much higher in the Florida maritime air masses. The latter can explain the existence of intense lightning in the ITCZ near the African coast (Chronis et al 2007). The analysis of the lightning map (Figure 2) indicates a significant lightning downwind of continents. To answer the question as regards the existence of small aerosols in the maritime tropical atmosphere detailed microphysical measurements of deep marine clouds and aerosol spectra in the zones of lightning over the ocean are required. The existence of the bimodal cloud droplet spectra in zones of updrafts a few kilometers above the cloud base would indicate the presence of small aerosols.

The role of small aerosols in the maritime atmosphere is not limited by the influence on lightning. The lightning serves in this case just as an indication of presence of a certain microphysical cloud structure. It is possible that if the role of small aerosols is as important as it is shown here, many concepts concerning the microphysics of deep convective clouds require revision.

Note in conclusion that the effect of in-cloud nucleation discussed in the study can not be found in many numerical models with bulk microphysics because they perform cloud nucleation at the cloud base only. We suppose that the description of in-cloud nucleation has to be included in the meteorological models to represent better the cloud microphysics of maritime clouds and aerosol effects.

Acknowledgements. The authors express deep gratitude to Prof. Hudson and to Prof. Hobbs (Prof. Hobbs passed away in mid 2005) for useful discussions. The study has been performed under the support of the Israel Academy of Science (grant 140/07).

References

Abdul-Razzak H. , S. J. Ghan, and C. Rivera-Carpio, 1998: A parameterization of aerosol activation. 1. Single aerosol type. J. Geophys. Res. 103, D6, 6123-6131.

Black R. A. and Hallett J., 1999: Electrification of the hurricane, J. Atmos. Sci, 56, 2004-2028

Black , M.L , R. W. Burpee, and F.D. Marks, Jr.1996: Vertical motion characteristics of tropical cyclones determined with airborne Doppler radar velocities. *J. Atmos. Sci*. **53**, 1887-1909.

Bott A., 1989: A positive definite advection scheme obtained by nonlinear renormalization of the advective fluxes. *Mon. Wea. Rev*., 117, 1006-1015.

Bott, A., 1998: A flux method for the numerical solution of the stochastic collection equation *J. Atmos. Sci.,* 55, 2284-2293.

Cecil D.J., E.J. Zipser, and S.W. Nebitt 2002a: Reflectivity, ice scattering, and lightning characteristics of hurricane eyewalls and rainbands. Part 1: Quantitative description. Mon Wea. Rev. 130, 769-784.

Cecil D.J., E.J. Zipser, and S.W. Nebitt, 2002a: Reflectivity, ice scattering, and lightning characteristics of hurricane eyewalls and rainbands. Part 2: Intercomparison of observations. *Mon Wea. Rev*., **130**, 785-801

Chronis T, E. Williams, E. Anagnostou, and W. Petersen, 2007: African Lightning: indicator of tropical Atlantic cyclone formation. *EOS*, **88**, 40, 2 October 2007.

Cohard, J-M., J-P. Pinty and C. Bedos, 1998: Extending Twomey's analytical estimate of nucleated cloud droplet concentrations from CCN spectra. *J. Atmos. Sci.,* 55, 3348-3357.

Demetriades N.W.S and R.L Holle, 2006: Long-range lightning nowcasting applications for tropical cyclones. *Preprints, Conf. Meteorology Application of Lightning Data, Atlanta*, AMS, 9 pp.

Dinger, J.E., H.B. Howell, and T.A. Wojciechowski, 1970: On the source and composition of cloud nuclei in a subsident air mass over the North Atlantic, J. Atmos. Sci., 27, 791–797.

Emde, K. and U. Wacker, 1993: Comments on the relationship between aerosol spectra, equilibrium drop size spectra, and CCN spectra. Beitr. Phys. Atmosph., 66, 1-2, 157-162.

Hallett, J. and Mossop, S. C., Production of secondary ice crystals during the riming process. *Natur*e, 249, 26-28, 1974.

Hegg, D. A., R. J. Ferek and P. V. Hobbs 1993: "Cloud Condensation Nuclei Over the Arctic Ocean in Early Spring" *J. Appl. Meteor.*, *34*, 2076-2082.

Hobbs, P. V., 1971: Simultaneous airborne measurements of cloud condensation nuclei and sodium-containing particles over the ocean, Quart. J. Roy. Meteor. Soc., 97, 263-271.

Hudson, J, G., (1984), Cloud Condensation Nuclei measurements within clouds, *J. Clim. and Appl. Meteor.l 23*, 42-51

Hudon J.G., and P.R. Frisbie 1991: Cloud condensation nuclei near marine stratus. *J. Geophys. Res.,* 96, 20795-20808.

Hudson J.G., and H. Li, 1995: Microphysical contrasts in Atlantic stratus. J. Atmos. Sci., 52, 3031-3040.

Hudson, J. G., and S. S. Yum, 1997: Droplet spectral broadening in marine stratus, J. Atmos. Sci., 54, 2642-2654.

Hudson,J.G.,and S.S.Yum,2002:Cloud condensation nuclei spectra and polluted and clean clouds over the Indian Ocean.*J. Geophys.Res*.,**107(D19),8022,** doi:10.1029/2001JD000829.

Jiusto, J. E., Lala, G. G., 1981: CCN-supersaturation spectra slopes (k).*J. Rech. Atmos.*,**15**, 303–311.

Jordan, C.L., Mean soundings for the West Indies area. *J. Meteor.,* 15, 91-97, 1958.

Jorgensen , D. P., E.J. Zipser, and. M.A. LeMone, 1985: Vertical motions in intense hurricanes. *J. Atmos. Sci.,* 42, 839-856.

Jorgensen, D.P., and M.A. LeMone 1989: Vertical velocity characteristics of oceanic convection. *J. Atmos. Sci*., **46**, 621-640.

Khain, A. P., and I. Sednev, 1996: Simulation of precipitation formation in the Eastern Mediterranean coastal zone using a spectral microphysics cloud ensemble model. *Atmos. Res.,* **43**, 77-110

Khain, A. P., M. Ovtchinnikov, M. Pinsky, A. Pokrovsky, and H. Krugliak, 2000: Notes on the state-of-the-art numerical modeling of cloud microphysics. Atmos. Res. 55, 159-224.

Khain A.P., Pinsky, M.B., M. Shapiro and A. Pokrovsky, 2001: Graupel-drop collision efficiencies. *J. Atmos. Sci.,* **58**, 2571-2595.

Khain A., A. Pokrovsky and M. Pinsky, A. Seifert, and V. Phillips, 2004: Effects of atmospheric aerosols on deep convective clouds as seen from simulations using a spectral microphysics mixed-phase cumulus cloud model. Part 1: Model description. J. Atmos. Sci 61, 2963-2982.

Khain, A. D. Rosenfeld and A. Pokrovsky 2005: Aerosol impact on the dynamics and microphysics of convective clouds. Quart. J. Roy. Meteor. Soc. 131, 2639-2663.

Khain, A. P., N. Benmoshe, A. Pokrovsky, 2008a: Aerosol effects on microphysics and precipitation in convective clouds with a warm cloud base: an attempt of classification. *J. Atmos. Sci.* (in press).

Khain, A. N. Cohen, B. Lynn and A. Pokrovsky, 2008b: Possible aerosol effects on lightning activity and structure of hurricanes. *J. Atmos. Sci.* (in press).

Levin Z., and W.R. Cotton, 2007: Aerosol pollution impact on precipitation: A scientific Review, WMO/IUGG report.

Meyers, M. P., W. R. Cotton, 1992: Evaluation of the Potential for Wintertime Quantitative Precipitation Forecasting over Mountainous Terrain with an Explicit Cloud Model. Part I: Two-Dimensional Sensitivity Experiments**.** *J. Appl. Meteor.* **31**, 26–50.

Molinari J., Moore P., and V. Idone, 1999: Convective Structure of hurricanes as revealed by lightning locations, *Mon. Wea. Rev*., 127, 520-534

Pinsky, M., and A. Khain, 1998: Some effects of cloud turbulence on water-ice and ice-ice collisions, *Atmos. Res.,* 47-48, 69-86

Pinsky M. B., A. P. Khain, and M. Shapiro, 2007: Collisions of cloud droplets in a turbulent flow. Part 4: Droplet hydrodynamic interaction. *J. Atmos. Sci , 64, 2462-2482.*

Pinsky, M., A. P. Khain, and M. Shapiro 2001: Collision efficiency of drops in a wide range of Reynolds numbers: Effects of pressure on spectrum evolution. *J. Atmos. Sci.* 58, 742-764.

Pinsky, M. and A. P. Khain, 2002: Effects of in-cloud nucleation and turbulence on droplet spectrum formation in cumulus clouds. *Quart. J. Roy. Meteorol. Soc*., 128, 1–33.

Pruppacher, H. R., A new look at homogeneous ice nucleation in supercooled water drops. *J. Atmos. Sci.,* 52, 1924-1933, 1995.

Pruppacher, H. R., and J. D. Klett, 1997: *Microphysics of clouds and precipitation.* 2-nd edition, Oxford Press, 1997, 963p.

Radke, L.F., and P.V. Hobbs, An automatic cloud condensation nuclei counter, J. Appl. Meteor., 8, 105–109, 1969.

Radke, L.F., and P.V. Hobbs, 1976: Cloud condensation nuclei on the Atlantic seaboard of the United States, Science, 193, 999–1002.

Saunders, C.P.R.1993: A review of thunderstorm electrification processes, J. Appl. Meteor., 32, 642-655.

Segal, Y., A. Khain, and M. Pinsky, 2003: Theromodynamic factors influencing the bimodal spectra formation in cumulus clouds. *Atmos. Res.* 66, 43-64.

Sherwood S.C., V. Phillips and J. S. Wettlaufer (2006). Small ice crystals and the climatology of lightning. *Geophys. Res. Letters*, 33, L058804, doi. 10.1029/2005GL.

Shao X.M., Harlin J., Stock M., Stanley M., Regan A., Wiens K., Hamlin T., Pongratz M., Suszcynsky D. and Light T., Los Alamos National Laboratory, Los Alamos, N.M, 18 October 2005, Katrina and Rita were lit up with lightning, *EOS*, Vol. 86, No.42, page 398-399.

Szoke, E.J., E.J. Zipser, and D.P. Jorgensen, 1986: A radar study of convective cells in mesoscale systems in GATE. Part 1: Vertical profile statistics and comparision with hurricanes. *J. Atmos. Sci*., **43**, 182-197.

Tao W-K., X. Li, A. Khain, T. Matsui, S. Lang, and J. Simpson· The role of atmospheric aerosol concentration on deep convective precipitation: Cloud-resolving model simulations. J. Geophys. Res. VOL. 112, D24S18, doi:10.1029/2007JD008728, 2007

Takahashi, T., 1978: Riming electrification as a charge generation mechanism in thunderstorms. *J. Atmos. Sci*., **35**, 1536-1548.

Takahashi, T., Endoh, T., and G. Wakahama, 1991: Vapor diffusional growth of free-falling snow crystals between –3 and -23 C. *J. Meteor. Soc. Japan*, **69**, 15-30.

Twomey, S., On the composition of cloud nuclei in the northeastern United States, *J. de Rech. Atmos.,* **3**, 281-285, 1968.

Twomey, S., The composition of cloud nuclei, *J. Atmos. Sci.*: **28**, 377–381, 1971.

Twomey S. and T.A. Wojciechowski, Observations of the geographical variation of cloud nuclei. J. *Atmos. Sci.*, **26**, 648-651, 1969.

Vali, G., Remarks on the mechanism of atmospheric ice nucleation. Proc. 8th Int. Conf. on Nucleation, Leningrad, 23-29 Sept., Gidrometeoizdat, 265-269, 1975.

Vali, G., Freezing rate due to heterogeneous nucleation. *J. Atmos. Sci.,* 51, 1843-1856, 1994.

Van den Heever, S. C.; G.G. Carrió, W.R. Cotton, P. J. Demott, A. J Prenni, 2006: Impacts of Nucleating Aerosol on Florida Storms. Part I: Mesoscale Simulations. J. Atmos. Sci., 63, Issue 7, 1752-1775

Wang C. 2005: A modelling study of the response of tropical deep convection to the increase of cloud condensational nuclei concentration: 1. Dynamics and microphysics. *J. Geophys. Res.,* v. 110; D21211, doi:10.1029/2004JD005720.

Warner, J., 1969a: The microstructure of cumulus cloud. Part 1. General features of the droplet spectrum, *J. Atmos. Sci.,* 26, 1049-1059.

Warner, J., 1969 b: The microstructure of cumulus cloud. Part 2. The effect of droplet size distribution of the cloud nucleus spectrum and updraft velocity. *J. Atmos. Sci.,* 26, 1272-1282.

Williams E, G., Satori, 2004: Lightning, thermodynamic and hydrological comparison of the two tropical continental chimneys. *J. Atmos. and Solar-terristical Phys*. 66, 1213-1231.

Williams E., T. Chan and D. Boccippio, 2004: Islands as miniature continents: Another look at the land-ocean lightning contrast. J. Geophys. Res., v.109, D16206, doi:10.1029/2003JD003833

Williams E., V. Mushtak, D. Rosenfeld, S. Goodman and D. Boccippio, 2005: Thermodynamic conditions favorable to superlative thunderstorm updraft, mixed phase microphysics and lightning flash rate. *Atmos. Res.*, **76**, 288-306**.**

THE ROLE OF BOUNDARY LAYER AEROSOL PARTICLES FOR THE DEVELOPMENT OF DEEP CONVECTIVE CLOUDS: A HIGH-RESOLUTION 3D MODEL WITH DETAILED (BIN) MICROPHYSICS APPLIED TO CRYSTAL-FACE

Delphine Leroy, Wolfram Wobrock and Andrea I. Flossmann

Laboratoire de Météorologie Physique, Université Blaise Pascal-CNRS-OPGC,
24, avenue des Landais, F-63177 Aubière Cedex, France
E-mail : A.Flossmann@opgc.univ-bpclermont.fr

1. ABSTRACT

The presented study reproduces aircraft microphysical measurements using a three-dimensional (3D) model with detailed microphysics and is then used to analyze in particular the role of boundary layer aerosol particles on the anvil and the ice phase. The simulated case is a convective cloud which develops a large anvil around 10 km height and which was sampled during the Cirrus Regional Study of Tropical Anvils and Cirrus Layers – Florida Area Cirrus Experiment (CRYSTAL-FACE). The model couples the 3D dynamics of a cloud scale model with a detailed mixed phase microphysical code. The microphysical package considers the evolution of the wet aerosol particles, drop and ice crystals spectra on size grids with 39 bins. With this model hereafter called DESCAM 3D, we are able to simulate the cloud with features close to the observed and to provide explanations of the observed phenomena concerning cloud microphysics as well as cloud dynamics.

The same CRYSTAL-FACE cloud has already been simulated by other groups also with a 3D model with detailed microphysics. They investigated the role of mid-tropospheric aerosol particles versus boundary layer aerosol on the microphysical properties of the anvil. Similar simulations with our DESCAM 3D lead to quite different results. Reducing the number of mid-tropospheric aerosol particles causes only minor changes in the cloud anvil. However, changing the aerosol particle spectrum in the boundary layer from clean to polluted modifies strongly the dynamical evolution of the convective clouds and thus impacts stronger on the microphysical properties of the anvil. The presented results are under publication (Leroy et al, 2008).

2. MODEL DESCRIPTION AND SETUP

The 3D model with detailed (bin) microphysics used herein couples the 3D non-hydrostatic model of Clark and Hall (1991) with the Detailed Scavenging Model DESCAM (Flossmann et al., 1985) A detailed description of the microphysical package, including sensitivity studies of DESCAM under mixed phase conditions can be found in Leroy et al. (2007).

Below only a brief summary of the essential features is given. The microphysical model employs five distribution functions: three number density distributions functions respectively for the wet aerosol particles (AP), the drops and the ice crystals and two mass density distribution of aerosol particles inside drops and ice particles. The five functions are discretized over 39 bins that cover a range of radius from 1 nm to 6 µm for the wet AP and from 1 µm to 6 mm for the liquid or solid hydrometeors. All together, the detailed microphysics introduces 195 supplementary prognostic variables to the initial code.

The microphysical processes that are considered in the model are: condensational growth and activation/deactivation of AP, condensation and evaporation of droplets, coalescence, homogeneous and heterogeneous nucleation, vapour deposition on ice crystals and riming. Droplet nucleation relies on the calculation of the activation radius derived from the Koehler equation (Pruppacher and Klett, 1997), but is also dependent on temperature as described in Leroy et al. (2007). Growth rate of drops and ice crystals are given by Pruppacher and Klett (1997). Homogeneous and heterogeneous nucleation follows respectively the works of Koop et al. (2000) and Meyers et al. (1992). Ice crystals are assumed to be spherical and the density of ice is 0.9 g m^{-3}. Coalescence and riming are treated with the numerical scheme of Bott (1998). The collection kernels for coalescence of drops are calculated with the collection efficiencies of Hall (1980) and the terminal velocities of Pruppacher and Klett (1997). Riming description includes collection of droplets by large ice crystals as well as collection of small ice particles by large drops. The collection kernels for riming are set to be the same as those for coalescence of drops, i.e. we assume that the collection efficiency of a spherical ice crystal is equal to the one of a water drop of the same mass.

Aggregation and secondary production of ice particles during riming is also neglected in the model for the moment.

To initialize the microphysics, aerosol particle spectra as a function of altitude are needed. In the first simulation aerosol particle spectra are almost identical to those used by Fridlind et al. (2004) in their case called "baseline" which combines aerosol measurements from the Twin Otter and Citation aircrafts on July the 18th and from the WB-57 on July the 19th. Aerosol particle spectra follow log-normal distributions. The total number of aerosol particles in the boundary layer is 1800 cm^{-3}. Aerosol particles are assumed to be ammonium sulphate, entirely soluble and with a molecular weight of 132 g mol^{-1}.

For the simulations presented in this paper, the model domain is 32 km x 32 km in the horizontal and 15 km in the vertical. The resolution is 250 m for both the horizontal and the vertical coordinates. The dynamical time step is 1 second. The thermodynamical conditions are given by the sounding from Miami airport at 15 UTC. To initialize convection, a perturbation (8 km wide and 2 km deep) is imposed in the north east part of the model domain and is maintained during the first ten minutes of integration in order to represent a localized sensible and latent heat flux. In the center of the perturbation the temperature is 1.5 °C higher and the relative humidity is 2 % higher than in the environment.

3. SIMULATION AND OBSERVATION

According to Heymsfield et al. (2005), the cloud reached the tropopause near 14 km altitude by the time of the aircraft penetration. The length of the in-cloud flight path can be estimated to 20 km with the knowledge of the aircraft speed (roughly 120 m s^{-1}) and the duration of the measurements (170 s).

In the simulations, a vigorous convective cell develops and exceeds rapidly 10 km height.

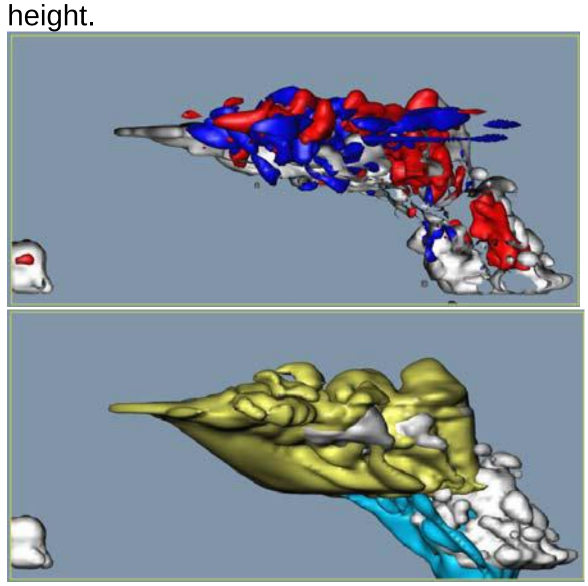

Fig.1: contours of the cloud after 42 min of integration; upper figure: the regions with updrafts larger than 8m/s in red and the downdrafts larger than 8m/s in blue; lower figure: the regions with cloud drops (grey), rain drops (blue) and ice crystals (yellow) larger than 0.01 g/m^3.

After 38 min of integration, cloud top is already above 12 km height. Through the strong north-easterly wind in the high altitudes, the hydrometeors spread and an anvil forms.

Thus, after 42 minutes of integration (Fig.1), the anvil is roughly 20 km wide and the top of the cloud reaches in the simulation an altitude of 13 km. Therefore, the model results between 38 and 42 minutes of integration will be used to compare with the available airborne observations.

The principal measurements from the airplane are summarized in Table 1. Heymsfield et al. (2005) divided the flight track into four areas named A, B C and D. Letter A is attributed to the measurements in the anvil and is not discussed here. Regions B and C consider the updraft core of the cloud. Region B is entirely glaciated, vertical velocities reach 23 m s^{-1} and temperature increases to -33°C while the environment is about -35°C. On the contrary, vertical velocity stays below 13 m s^{-1} in region C. Liquid water is also detected in region C although temperature is 3°C lower than in region B (compare Fig. 4 in Heymsfield et al, 2005). Finally, region D refers to a downdraft area upwind of the core, with low water and ice content. In the following, we will keep this nomenclature.

Table 1 gives the observed and modeled values of the vertical velocity encountered along the simulated flight track from A to A'.

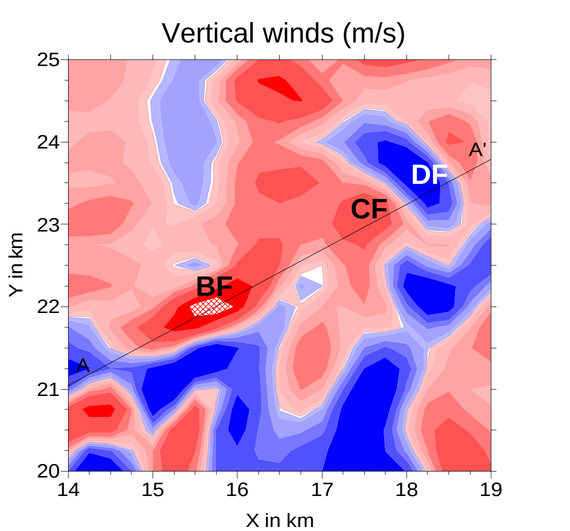

Fig.2: Simulated aircraft trajectory at z = 10.250 km at t = 41 min 40 s

The maximum vertical velocities are 25.5 m s^{-1} and 14 m s^{-1} respectively for regions B_F and C_F, and are in agreement with the corresponding measurements (23 m s^{-1} and 13 m s^{-1}). In the downdraft region, a value of -8 m s^{-1} was observed. In the model, the descent is slightly stronger with vertical velocities up to -13 m s^{-1}.

Heymsfield et al. (2005) presented size distributions measured with a FSSP probe for particles between 5 and 56 µm in diameter, and with a PMS 2D-C probe as well as a high volume particle spectrometer (HVPS) imaging probe for size ranges from about 60 µm to 6 cm. The IWC is then recalculated from those measurements. For the analysis of the FSSP probe, all particles were assumed to be solid spheres. For the presentation of the model results (cf. Table 1), the contribution of the small (r_i<40 µm) and the large ice particles (r_i>40 µm) to the IWC are also separated.

The measured IWC reaches 1 g m^{-3} in region B as well as in region C for both ice crystal categories. In our simulations, the IWC for precipitating ice is always larger than the IWC for cloud ice. In region B_F, the simulated values of IWC are clearly underestimated compared to the observations (respectively 0.2 and 0.7 g m^{-3} for cloud and precipitating ice). Agreement is much better in simulated region C_F with values of 0.75 and 1.2 g m^{-3} for cloud and precipitating ice. At least, the values of the IWC are low in both simulated and observed regions D. Upwind of downdraft region D cloud free conditions prevailed. In the model for this transition range some cloudy air still persist (IWC = 0.3 g m^{-3} ; LWC=0.2 g m^{-3}).

Liquid water was only observed in region C and the corresponding LWC was near 0.3 g m^{-3} which is well reproduced by DESCAM 3D: the LWC is negligible in region B_F and only reaches values of 0.3 g m^{-3} in region C_F (Tab.1).

According to Heymsfield et al. (2005), the measured number of particles along the flight path is 88 cm^{-3} in the glaciated region B but increases up to 221 cm^{-3} particles in region C where liquid water is present (Tab 1). However, it should be kept in mind that reliable measurements of small ice crystals are difficult to obtain using FSSP devices (Gardiner and Hallett, 1985 ; Twohy et al., 1997).

At 10 km altitude, the maximum simulated numbers are close to 200 cm^{-3} for the drops and 5 cm^{-3} for the ice crystals in region C_F which is in agreement with the observations of Heymsfield et al. (2005). In region B_F, the simulated number of drops and ice crystals are both around 10 cm^{-3}. The total number of particles is thus underestimated compared to the observation of 88 cm^{-3} (Tab.1)

We can conclude that overall, the simulated parameters show quite good agreement with the observations. However, in region B, the simulated number of crystals is too low compared to the observations and this lack of ice particles leads to an underestimation of the IWC of both cloud and precipitating particles. The temperature variation along the AA' line differs from the observations but it is possible to improve the model results when shifting the flight path.

It has to be pointed out that the flight track is arbitrary in our simulation as the direction of the simulated anvil is different to the observed one at 10 km (compare satellite image in Heymsfield et al., 2005). This is due to a change in upper tropospheric wind direction between Miami and the measurement site. Thus, the flight track should have a different orientation with respect to the modeled cloud. As the regions B and C seem to correspond to different ascending areas, in the following, updrafts were identified where simulated vertical winds, temperature and microphysical parameters are all coherent with the observations, but the condition that these regions must be oriented along the prescribed south western flight track given in Heymsfield et al. (2005) will be disregarded. This will be called in the following 'virtual flight track'.

Table 2 shows the values of vertical velocity w, temperature T, LWC and IWC for two different regions along the virtual flight track.

Region	Parameter	Observed	Simulated
B	Maximum vertical velocity (m s^{-1})	23	25.5
	Maximum IWC for cloud ice (g m^{-3})	1.1	0.2
	Maximum IWC for precipitating ice (g m^{-3})	1.1	0.7
	Maximum number of hydrometeors (cm^{-3})	88	20
C	Maximum vertical velocity (m s^{-1})	13	14
	Maximum IWC for cloud ice (g m^{-3})	1	0.75
	Maximum IWC for precipitating ice (g m^{-3})	1.1	1.2
	Maximum LWC (g m^{-3})	0.3	0.3
	Maximum number of hydrometeors (cm^{-3})	221	205
D	Minimum vertical velocity (m s^{-1})	-8	-13
	Maximum IWC for cloud ice (g m^{-3})	0.4	0.2
	Maximum IWC for precipitating ice (g m^{-3})	0.4	0.45
	Maximum number of hydrometeors (cm^{-3})	20	10

Table 1 : Observed (taken from Heymsfield et al, 2005) and simulated values of vertical velocity, liquid and ice water content along the flight track AA'.

region	**Position**		**Vertical wind** (m s^{-1})	**Temperature** (°C)	**LWC** (g m^{-3})	**IWC** (g m^{-3})
	X (km)	Y (km)				
B_v	20.75	24.25	16.2	-34.5	0.1	1.7
C_v	19	26	9.6	-36.8	0.5	1.0

Table 2 : Vertical velocity, temperature, LWC and IWC for two regions along the virtual flight track in the model domain after 38 min 20 s of integration corresponding to the observational feature of regions B and C presented in Table 1.

The altitude of 10.125 km is the same for the two regions: The initial sounding gives a temperature of -36 °C for this altitude. The parameters at B_v (*v* for virtual) are close to the observations in region B: the vertical wind is 16.2 m s^{-1}, temperature is 1.5 °C higher than the environmental value, and liquid water is almost negligible. At position C_v the vertical winds are around 10 m s^{-1}, the temperature of -36.8 °C is lower than the environment, and liquid water and ice are both present. In fact, between 35 and 41 minutes of integration, it is possible to find several regions that are close to 10 km in altitude and that match the observations either for the region B or C. Here we focused on these two points because they appeared at the same time: 38 min 20 s. Regarding the position of the two regions in the model domain, our region C_v is north-west from region B_v, 2.6 km apart, which is coherent with the observations.

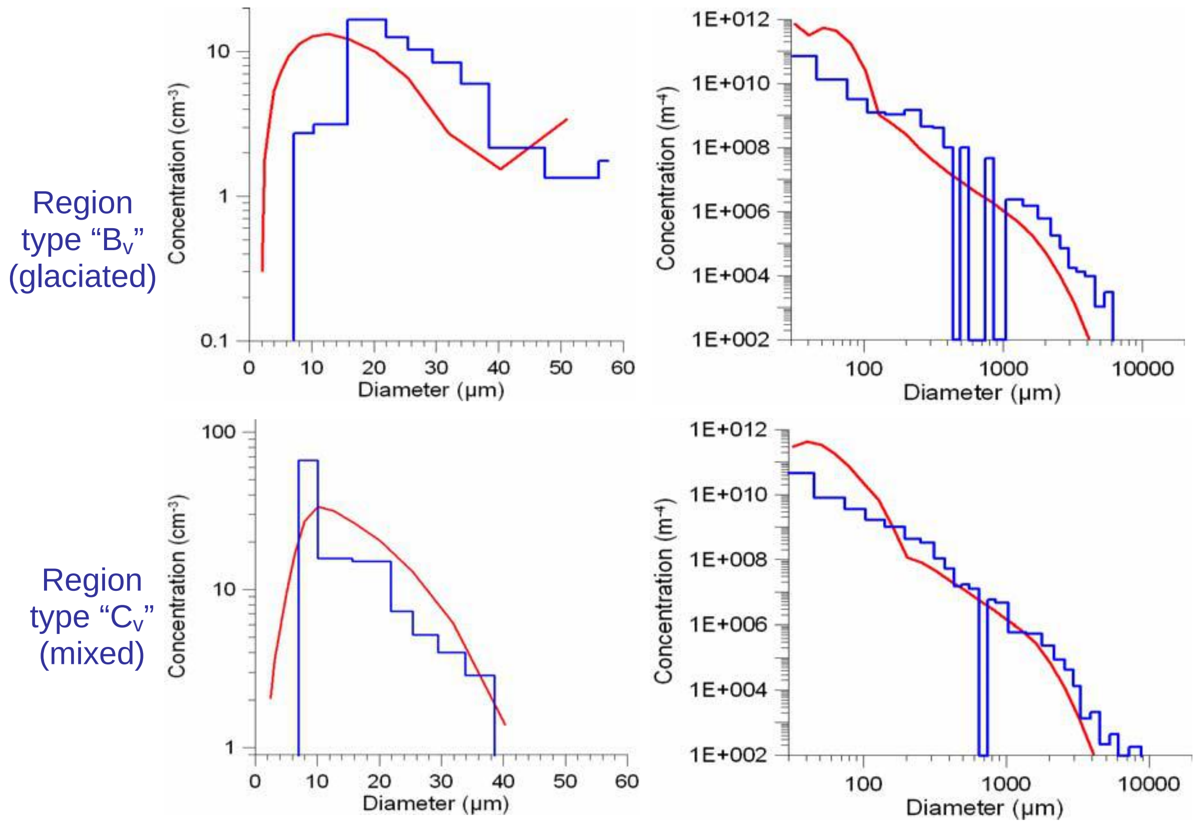

Fig.3: Modelled particle spectra in red for position B_V and C_V (Tab 2) compared to the observed histograms by Heymsfield et al. (2005) in blue.

Fig. 3 compares simulated and observed particle spectra in region B (position [6] in Heymsfield et al., 2005) and C (position [8]). Model results agree quite well with observations in region B and C (Figs. 3). Simulated particle spectra and integrated values are consistent with measurements for both small and large sizes.

Thus, we can conclude that generally the model succeeds in reproducing the observations.

4 IMPACT OF BOUNDARY LAYER AEROSOL PARTICLES

Following Fridlind et al. (2004), we then investigated the role of the aerosol particles above 6 km height on the development of the cloud (anvil). In a numerical experiment,

the number of aerosol particles was reduced to only 5% of the number in the reference case for all layers above 6 km. We did not follow Fridlind et al. (2004) who reduced the AP number concentration to 0 as our model does not allow droplet formation by homogeneous nucleation. The total number of aerosol particles is now 150 cm^{-3} instead of 3000 cm^{-3} for the reference case between 6 and 10 km, and 5 cm^{-3} instead of 100 cm^{-3} above 10 km. This second calculation will be referred to as case "5%AP6".
In the model, the aerosol particles serve both as cloud condensation nuclei and ice nuclei. Thus, changes in the aerosol particles concentration are potentially able to impact on droplet activation as well as homogeneous and heterogeneous nucleation. However, as mentioned before, heterogeneous nucleation is described by the Meyers et al. (1992) formula which relates the number of ice nuclei only to supersaturation. Thus, changes in the aerosol concentration can only have an indirect impact on heterogeneous nucleation by changing the supersaturation.

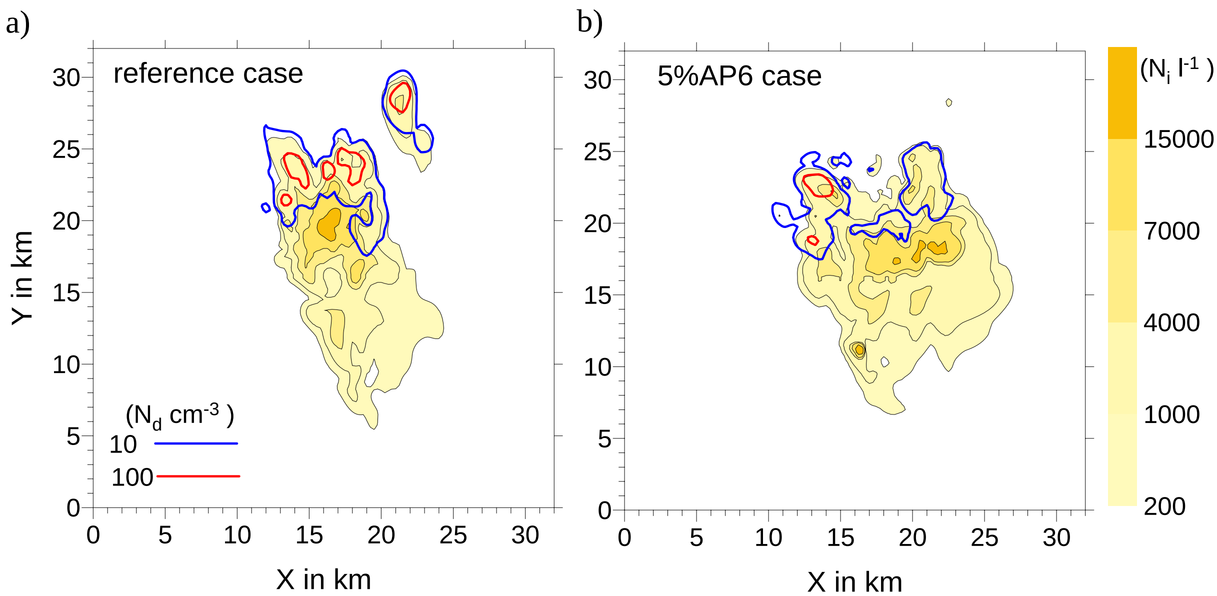

Figure 4 : Number concentration of ice crystals (l^{-1}) in yellow and droplets (cm^{-3}, blue and red lines) at 10 km and after 42 minutes of integration for the reference (Fig. 3a) and the 5%AP6 (Fig. 3b) cases.

Figs. 4a and b display the horizontal extension of these simulated clouds in 10 km altitude after 42 minutes of integration. Fig. 4a depicts the results for the reference case, Fig. 4b the results for the 5%AP6 case. Both figures display the number concentrations of ice crystals and cloud droplets and both cases show numerous similarities: the number concentrations for the ice crystals cover the same order of magnitude between 200 to 15000 particles /l, the number of cloud droplet is significantly larger but their presence is restricted to small regions located at the upwind edge of the cloud field associated to the updraft core. Furthermore the maxima in crystal numbers are located downwind from those of the drop numbers in both cases.
Although the size of the horizontal areas of both the droplet field and the crystal field do not differ significantly between the reference and the 5%AP6 case, the shape shows several differences. In the reference case the ice crystal field is mainly oriented from north to south while the horizontal distribution of the crystals in the 5%AP6

case indicates no privileged direction but extends also to the east and the west. The main surface area occupied by the droplets in the reference case appears in a connected and almost closed field, the droplet field for the 5%AP6 case, however, is divided in several smaller patches.
Considering also the evolution of the other cloud properties not shown here this last finding suggests that in the case with negligible AP concentration above 6 km the cloud is more advanced in its time evolution and the central convective core starts to decay. We can conclude from this comparison that both cases have experienced different dynamical evolutions.
However, our modeling results cannot confirm the hypothesis of Fridlind et al. (2004) that mid-tropospheric AP are regulating the ice crystal concentration in the studied sub-tropical anvil. The dominating hydrometeors in the anvil are ice crystals and their number does not show an important variation when the AP number concentrations are modified between 6-10 km. As we cannot confirm the role of the mid-tropospheric aerosol, we will study in the following the role of the boundary layer aerosol.

5 IMPACT OF BOUNDARY LAYER AEROSOL PARTICLES

As already shown by Yin et al. (2005), aerosol particles from the boundary layer can be transported up to the high levels, detrained and then re-entrained at mid-cloud levels. Moreover, Heymsfield et al. (2005) used a Paluch diagram (Paluch, 1979) to analyze the role of entrainment for their observations and found that the air they sampled at 10 km height seems to be a mixture of cloud base air and air that originated about 2 km above aircraft level. Thus, it seems highly possible that aerosol particles from the boundary layer impact on the anvil properties.
For this study we use again the same aerosol spectra as Fridlind et al. (2004). In the so-called *clean* case, the number of aerosol particles below 1 km is reduced to 400 cm^{-3} instead of 1800 cm^{-3} in the reference case. In addition, for the *polluted* boundary layer, this number is increased up to 6500 cm^{-3}. Above 1 km, the aerosol particle spectra remain identical to the reference case.

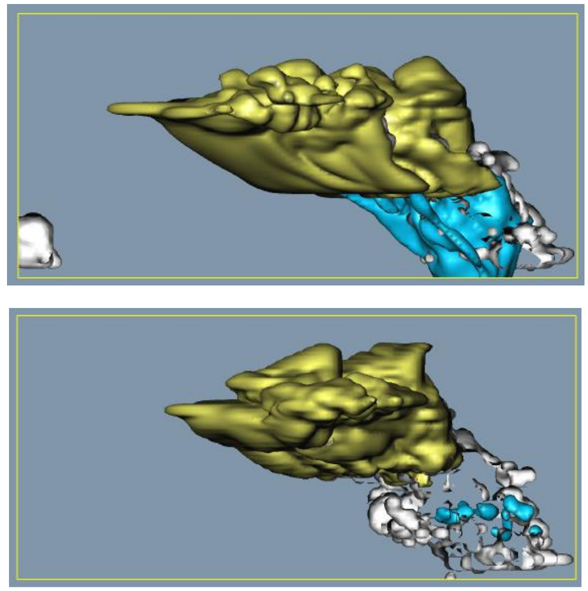

Fig. 5: contours of the cloud after 42 min of integration; upper figure (a): clean case; lower figure (b): polluted case; with cloud drops (grey), rain drops (blue) and ice crystals (yellow) larger than 0.01 g/m^3.

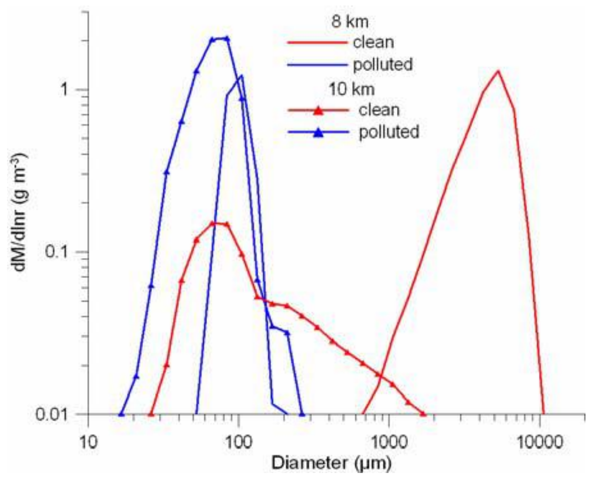

Fig.6: Modelled mean mass spectra of ice crystals at 8 and 10 km height and after 38 min of integration for both polluted and clean cases.

The horizontal and vertical distribution of cloud ice and precipitating ice water content is shown in Fig 5. Fig. 5 demonstrates that the larger anvil for the clean cloud in 10 km is composed of ice crystals. The horizontal extension of cloud top and anvil in the polluted case (Fig. 5b) is significantly smaller, but the cloud ice content is higher and thus indicates a stronger number concentration of small ice crystals. The content of precipitating ice covers the same order of magnitude with maximum values of more than 1 g/m^3 in both cases. The numerical results for the precipitating ice (not shown here) are strongly determined by the cut-off radius chosen to split the ice crystal spectrum in cloud and precipitating particles. In our calculation a cut-off radius of 40 µm was used. Fig. 6 presents the mean mass distribution function of the ice crystals at 8 and 10 km altitude. We can detect from this illustration that the small mode of the ice spectra also counts for the precipitating ice as its diameter exceeds 80 µm. Thus the high content of precipitating ice for the polluted case is caused by these medium sizes of the ice crystals in the upper tropospheric levels.

In the polluted case, the size of the ice crystals never exceeds 300 µm in diameter at 8 as well as at 10 km height. In the clean case, the IWC is low at 10 km at 38 min with only very few ice crystals with diameters above 300 µm. On the contrary, at 8 km, the ice spectrum in the clean case covers now precipitating diameters from 1 mm to 1 cm (Fig.6).

From this numerical analysis, it is evident that the aerosol loading in the boundary layer has important consequences on the microphysical properties of deep convective clouds even at altitudes as high as 10 km. The number of aerosol particles determines primarily the mass of precipitating hydrometeors and therefore, impacts on the dynamics and thus on cloud development. As the dynamical evolution of the cloud is strongly influenced by the number of AP originating from the boundary layer, changes in the lowest layers of the cloud can easily propagate to the highest altitude. These findings are e.g. in agreement with those of Carrió et al. (2007) who extended the work of van den Heever et al. (2006) to the anvil properties and showed that the enhancement of CCN effects on ice crystals spectra in the anvil-cirrus cloud.

6 CONCLUSIONS

In this study a high resolved 3D cloud model with detailed microphysics called DESCAM 3D is used to simulate a deep convective cloud with anvil. The studied cloud was observed during the CRYSTAL-FACE campaign and is described in Heymsfield et al (2005). Measurements of vertical velocity and temperature as well as microphysical parameters (LWC, IWC, hydrometeors spectra) are available for both the anvil and the updraft core of the cloud at 10 km height. The updraft core is divided into two regions: one is entirely glaciated, vertical winds are up to 20 m s^{-1} but the temperature of -33°C is about 1.5°C higher than the environment, the other region is colder than the environment, vertical velocity is around 10 m s^{-1} and high numbers of small water droplets are present.

The model is able to simulate realistically the cloud with a top up to 14 km and a large anvil. Simulated flight trajectories at 10 km show good agreement with the observations for the vertical winds and the microphysical parameters. In particular, the simulated spectra are generally consistent with those measured, although improvements in the results may be obtained from further model improvements. This concerns e.g. a decreasing value of the ice density with increasing ice crystal size as well as a consideration of ice habits. Furthermore, a higher vertical and horizontal resolution down to a few meters would be desirable to resolve small scale supersaturation peaks.

Following the work of Fridlind et al (2004), we then investigated the respective role of mid-tropospheric and boundary layer aerosol particles on cloud properties. Our findings significantly differ from those of Fridlind et al (2004) who concluded from their modeling studies that aerosol entrained between 6 and 10 km account for about two-thirds of the anvil nuclei. We found that aerosol particles above 6 km have only a limited impact on the number of small cloud droplets prevailing in or next to

the updraft cores at 10 km but do not change the number of ice crystals in the dominating anvil regions. On the other hand we could identify changes in the dynamical evolution of the cloud which are caused by changes in thermodynamic properties (especially supersaturation). Theses dynamical and thermodynamical differences suggest that a comparison between simulations under low number concentrations and regular conditions do not allow to correctly quantify the role of mid-tropospheric aerosols on cloud formation in upper tropospheric levels.
Modifications in the dynamical and microphysical evolution of the cloud are even more pronounced when changing from a clean to a polluted boundary layer. In clean air masses, rain drops formed in large quantities early in cloud development. Those big drops fall through the cloud updraft and hamper cloud development. On the contrary, clouds forming in a polluted environment are characterized by a huge number of small cloud droplets and rain formation is suppressed. Updrafts in the polluted cloud extend rapidly to high altitudes and thus, the polluted cloud reaches higher levels. Our results agree with those of Khain et al. (2005) who investigated the aerosol impact on the dynamics of deep convective clouds with a 2D model with spectral microphysics. However, concerning the case studied it is evident that a 3D dynamical model is mandatory in order to reproduce the complex dynamics.

7 ACKNOWLEDGEMENTS

The calculations for this paper have been done on computer facilities of the “Institut du Développement et des Ressources en Informatique Scientifique” (IDRIS, CNRS) in Orsay (France) and the “Centre Informatique National de l’Enseignement Supérieur” (CINES) in Montpellier (France), under project no.940180. The authors acknowledge with gratitude the hours of computer time and the support provided.

8 REFERENCES

Bott A., 1998 : A flux method for the numerical solution of the stochastic collection equation. *J. Atmos. Sci.*, **55**, 2284-2293.

Carrió, G. G., S. C. van den Heever and W. R. Cotton, 2007 : Impacts of nucleating aerosol on anvil-cirrus clouds : A modeling study. *Atmos. Res.*, **84**, 111-131.

Clark T. L., and W. D. Hall, 1991 : Multi-domain simulations of the time dependent Navier-Stokes equations : benchmark error analysis of some nesting procedure, *J. Comp. Phys.*, **92**, 456-481.

Flossmann A. I., W. D. Hall and H. R. Pruppacher, 1985 : A theoretical study of the wet removal of atmospheric pollutants. Part I : The redistribution of aerosol particles captured through nucleation and impaction scavenging by growing cloud drops. *J. Atmos. Sci.*, **42**, 583-606.

Fridlind A. M., A. S. Ackerman, E. J. Jensen, A. J. Heymsfield, M. R. Poellot, D. E. Stevens, D. Wang, L. M. Miloshevich, D. Baumgardner, R. P. Lawson, J. C. Wilson, R. C. Flagan, J. H. Seinfeld, H. H. Jonsson, T. M. VanReken, V. Varutbangkul and T. A. Rissman, 2004 : Evidence for the predominance of mid-tropospheric aerosols as subtropical anvil cloud nuclei. *Science*, **304**, 718-721.

Gardiner B. A. and J. Hallett, 1985 : Degradation of in-cloud forward scattering spectrometer probe measurements in the presence of ice particles. *J. Atmos. Oceanic. Technol.*, **2**, 171-180.

Hall W. D., 1980 : A detailed microphysical model within a two-dimensional dynamic framework : Model description and preliminary results. *J. Atmos. Sci.*, **37**, 2486-2506.

Heymsfield A. J., L. M. Miloshevich, C. Schmitt, a. Bansemer, C. Twohy, M. R. Poellot, A. Fridlind and H. Gerber, 2005 : Homogeneous ice nucleation in subtropical and tropical convection and its influence on cirrus anvil microphysics. *J. Atmos. Sci.*, **62**, 41-64.

Khain A. P., D. Rosenfeld and A. Pokrovsky, 2005 : Aerosol impact on the dynamics and microphysics of deep convective clouds. *Q. J. R.*

Meteorol. Soc., **131**, 2639-2663. DOI:10.1256/qj.04.62

Koop T., H. P. Ng, B. Luo, A. Tsias and T. Peter, 2000 : Water activity as the determinant for homogeneous ice nucleation in aqueous solutions. *Nature*, **406**, 611-615.

Leroy D., W. Wobrock, A. I. Flossmann, 2008: The role of boundary layer aerosol particles for the development of deep convective clouds: a high-resolution 3D model with detailed (bin) microphysics applied to CRYSTAL-FACE *Atmos. Res.*, under revision.

Leroy D., W. Wobrock, and A. I. Flossmann, 2007 : On the influence of the treatment of aerosol particles in different bin microphysical models : a comparison between two different schemes. *Atmos. Res.*, **85**, 269-287. doi : 10.1016/j.atmosres.2007.01.003

Meyers M. P., P. J. Demott and W. R. Cotton, 1992 : New primary ice nucleation parameterizations in an explicit cloud model. *J. Appl. Met.*, **31**, 708-721.

Paluch I. R., 1979 : The entrainment mechanism in Colorado cumuli. *J. Atmos. Sci.*, **36**, 2467-2478.

Pruppacher H. R. and J.D. Klett, 1997 : *Microphysics of clouds and precipitation*. 2nd ed. Kluwer Academic, 954p.

Twohy C. H., A. J. Schanot and W. A. Cooper, 1997 : Measurements of condensed water content in liquid and ice clouds using an airborne counterflow virtual impactor. *J. Atmos. Oceanic. Technol.*, **14**, 197-202.

van den Heever S. C., G. G. Carrió, W. R. Cotton, P. J. DeMott and A. J. Prenni, 2006 : Impacts of nucleating aerosol on Florida storms. Part I : Mesoscale simulations. *J. Atmos. Sci.*, **63**, 1752-1775.

Yin Y., K. S. Carslaw and G. Feingold, 2005 : Vertical transport ad processing of aerosols in a mixed-phase convective cloud and the feedback on cloud development. *Q. J. R. Meteorol. Soc.*, **131**, 221-245.

SUMMARY OF THE WMO/IUGG ASSESSMENT ON THE EFFECTS OF AEROSOL POLLUTION ON PRECIPITATION.

Zev Levin[1] and William Cotton[2]
[1] Department of Geophysics and Planetary Science, Tel Aviv University, Israel
[2] Department of Atmospheric Science, Colorado State University, Ft. Collins, Colorado, USA

1. INTRODUCTION

Changes in precipitation regimes and the frequency of extreme weather events are of great importance to life on the planet. Thus, a plausible hypothesis is that by influencing the amounts, chemical composition and distribution of natural and anthropogenic aerosols, changes in precipitation of significance to local communities may possibly occur. However, quantitative testing of that hypothesis has proved difficult.

Much of the work that was carried out over the years addressed the issues of the effects of aerosols on clouds. The fundamental scientific understanding of cloud microphysical processes achieved in those years was summarised in many textbooks (e.g. Mason, 1971; Pruppacher and Klett, 1978). Based on many measurements and models the consensus emerged that, everything else being equal, the addition of more cloud condensation nuclei (CCN) to a cloud, leads to the formation of smaller and more numerous cloud drops. It has also been observed that the addition of giant CCN (GCCN) to clouds can lead to the formation of larger cloud drops (e.g. Mather, 1991). Furthermore, recent work in shallow orographic clouds, show that riming efficiency in polluted clouds is smaller, leading to smaller snow crystals (Borys et al., 2000; 2003). All these observations and related modelling studies suggest as a sound physical hypothesis that, other things being the same, the consequence of pollution on clouds should be a reduction in precipitation.

Unfortunately, the connection between aerosol loading and the amount of precipitation on the ground is not yet clear. This is partly because feedbacks between the microphysical and dynamical processes exist and can sometimes lead to enhancement or to suppression of precipitation via atmospheric dynamical rather than cloud microphysical effects of aerosol. Recent examples in support of this proposition may be found in the work of Rotstayn and Lohmann (2002), Rotstayn (2007) and Rotstayn et al. (2007). Over the years, there have been a number of attempts to shed light on this connection but the results vary widely between increases in rainfall, decreases rain amounts and no connection at all.

The World Meteorological Organization (WMO) and International Union of Geodesy and Geophysics (IUGG) recognised the importance of this issue and formed a group to assess the knowledge and suggest directions for future research. The final report from this group was unable to reach an unambiguous conclusion that a systematic reduction in precipitation is the demonstrated result of particle pollution that enhances CCN levels (Levin and Cotton, 2007).

2. THE EFFECTS OF AEROSOLS ON CLOUDS

Warm clouds are those that contain no ice. Measurements have shown that increase in CCN from natural or anthropogenic sources increases cloud drop concentrations and reduces cloud drop size (the First Indirect effect or the 'Twomey' effect). These ideas have been confirmed by many in situ measurements (e.g. Warner and Twomey, 1967), and by analysis of ship tracks using satellite images (Coakley et al. 1987, Durkee et al. 2000, 2001).

Using satellite images to determine the effective radius of cloud particles near cloud tops, Rosenfeld (2000) suggested that an increase in aerosol optical depth corresponds to slower growth of the cloud drops due to the increase in their concentrations and the decrease in their effective radius. Slow growth in the warm clouds may lead to the suppression of precipitation development. Radar echoes from the TRMM satellite were interpreted as showing that the development of precipitation in these clouds diminishes, although the number of such documented cases has been small and is controversial (Ayers, 2005; Rosenfeld et al. 2006).

Airborne and ground measurements of clouds and precipitation in the Amazon region (Andreae et al., 2004) showed that clean continental clouds with relatively low concentrations of aerosols, behaved similarly to marine clouds, namely, growth by coalescence occurs early and rapidly as the cloud develops. On the other hand, clouds that developed in the smoky atmospheres grew deeper with precipitation particles growing higher up in the clouds. Andreae et al. (2004) argued that the slow growth of the drops, led to ice formation higher up in the clouds and to enhanced updrafts due to the increased release of latent heat. Such clouds sometimes led to hail and lightning formation.

3. AEROSOL POLLUTION IMPACT ON RAINFALL ON THE GROUND

3.1 Convective Clouds

Warner and Twomey (1967) and Warner (1968) summarised the potential effects of sugarcane smoke on rainfall, by looking at multi-decadal rainfall records from stations upwind and downwind of these prolific anthropogenic aerosol sources. In spite of expectation that there would be direct correlation between increased pollution and rain suppression, they could not conclusively see any such correlation (Warner, 1971).

Rain enhancement of up to 30% from warm clouds downwind of paper mills in Washington State were reported by Hobbs et al. (1970). Hindman et al. (1977) analysed the same case using a one-dimensional numerical model. He concluded that the emitted GCCN from the paper mill could not by themselves account for the observed large increase in rainfall and that the combined effects of heat, water vapour and CCN from the paper mill in combination may be responsible for the increased precipitation.

Using MODIS and TRMM satellite data, Lin et al. (2006) analysed the effects of forest fires on precipitation in the dry season in the Amazon region. They report on increases in cloud heights and in precipitation with increases in aerosol optical depth. The increase cloud height led to enhanced growth of ice crystals, which culminated in heavier precipitation. However, in spite of the good correlation between these variables, the authors could not clearly establish causal links between aerosols and the observed changes in cloud height or with precipitation increases. The role of enhanced convection due to the heat from the fires and/ or from heat due to absorption of solar radiation by the smoke itself could not be ruled out.

3.2 Effects of Urban Pollution on Rainfall

Extensive studies were conducted to explain the anomalous behaviour of the precipitation around La Porte, downwind of Chicago. In that case, local records suggested an upward shift in warm season rainfall, thunderstorms and hail from the late 1930s to about 1965. The puzzling thing about this case is the fact that the anomaly appeared and then disappeared. Changnon (1980) reviewed the observations and concluded that the microphysical effects must have played a role, but without a dynamical or meteorological context, this effect would not have occurred.

A large field experiment (METROMEX) was carried out around St Louis Missouri, motivated by the examination of historical data that revealed summer increases in the immediate downwind area of the city (Figure 1). The records show increases in: (1) rainfall (10–17%); (2) moderate rain days (11–23%); (3) heavy rainstorms (80%); (4) thunderstorms (21%); and (5) hailstorms (30%) (Changnon et al, 1971). In his summary of METROMEX, Braham (1974) reported that the CCN production from the city was about 10^4 $cm^{-2}s^{-1}$, much higher than the surrounding rural areas, accompanied by an increase in cloud drop concentrations and a decrease in drop size. However, the radar

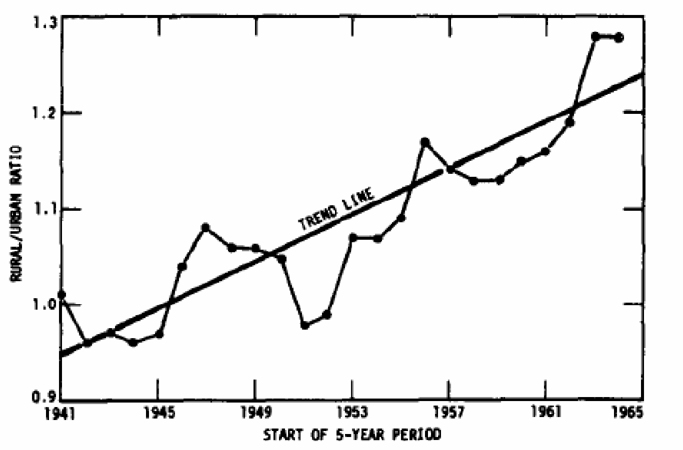

Figure 1. Five-year moving averages and time trend of Centerville (downwind of St. Louis) summer rainfall, 1941-1968. (From Changnon et al, 1971).

echoes from these clouds usually occurred lower in the atmosphere than their counterparts in the rural surroundings. This seems to contradict our physical understanding of cloud growth, but it was concluded that one way to explain the observations is to assume that the urban area also emitted GCCN, which were not detected by the CCN sampling methods in use, but could be responsible for the increased precipitation.

More recently, Van der Heever and Cotton, (2007) simulated the effects of pollution on precipitation during the passage of a storm in the St. Louis area. The data used was of a specific day. The simulation was carried out using two main cases; one with the city of St Louis without pollution and the second with the pollution containing both small CCN and GCCN. The results show that the temporal and spatial distribution of the rain changes due to the effects of pollution (see Figure 2 which shows the difference in rain amount and distribution between a simulation run without pollution and with pollution). At the beginning of the storm, polluted clouds produced much heavier precipitation; however, as the storm progressed, the difference between the integrated amounts of rain from the beginning of the storm of the polluted minus the clean case diminished. After 1.5 hour, the integrated rain amount over the whole area was higher in the clean case. This work demonstrates the complexity of the interaction of aerosols and precipitation. Part of the complexity appears because the initial rain cleans the atmosphere from pollution, thus reducing the effects of pollution on further rainfall. In addition, downdrafts produced by the precipitation enhance the development of neighbouring clouds, thus increasing the integrated rain amounts over the whole area. Van der Heever and Cotton, (2007) concluded that the effect of pollution on precipitation in an urban setting strongly depends on the background aerosol loading. Adding more pollution to an already polluted atmosphere has very little effect on precipitation amounts. They further indicated that effects of land-use play a dominant role in those precipitation anomalies.

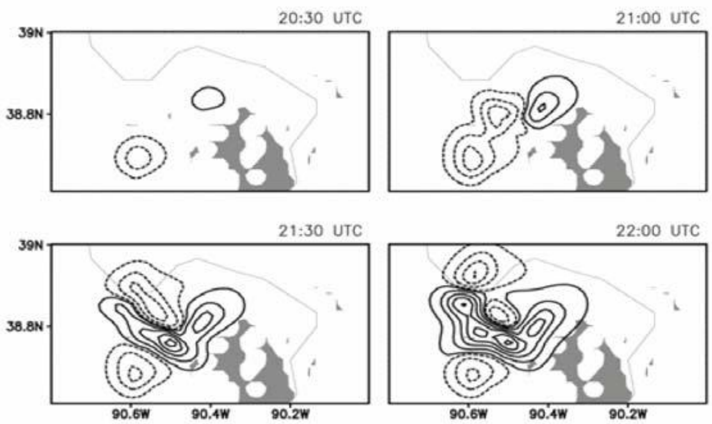

Figure 2. Model results showing accumulated surface precipitation from clean-polluted clouds around the city of St Louis. Solid lines represent pollution suppressing precipitation; Dash lines represent the opposite. Contour interval is 5 mm starting from 1 mm. Note the changes in spatial and temporal distribution of rain. (From Van Den Heever and Cotton, 2007).

Jin et al. (2005) analysed diurnal, weekly, seasonal, and interannual variations of urban aerosols with an emphasis on summer months using 4-years of the NASA-MODIS observations, in situ AERONET observations, and in situ EPA PM2.5 data for one mid-latitude city (New York) and one sub-tropical city (Houston). Analysis of monthly mean aerosol optical thickness and rainfall did not show strong relationships between aerosol and rainfall in a climatological sense.

The lack of direct relationship between rainfall and urban aerosol optical thickness implies that urban rainfall anomalies are not fully related to changes in aerosol. This observation is consistent with the earlier conclusions from METROMEX (Ackerman et al., 1978).

It is therefore clear that, in spite of many measurements, there is no conclusive evidence that aerosol pollution from urban regions affects precipitation in a consistent, systematic or repeatable manner.

3.3 Rain from Orographic Clouds

Orographic clouds are expected to exhibit the most consistent microphysical response to microphysical changes primarily because the dynamical responses are thought to be minimal and where natural variability is smaller. Borys et al. (2000) and Borys et al. (2003) provided some evidence that pollution can delay precipitation in winter orographic clouds in the Rocky Mountains. Clouds growing in a polluted environment had more numerous and smaller drops. The reduced drop size leads to less efficient riming and therefore to smaller ice crystals (Figure 3), smaller fall velocities, and less snowfall.

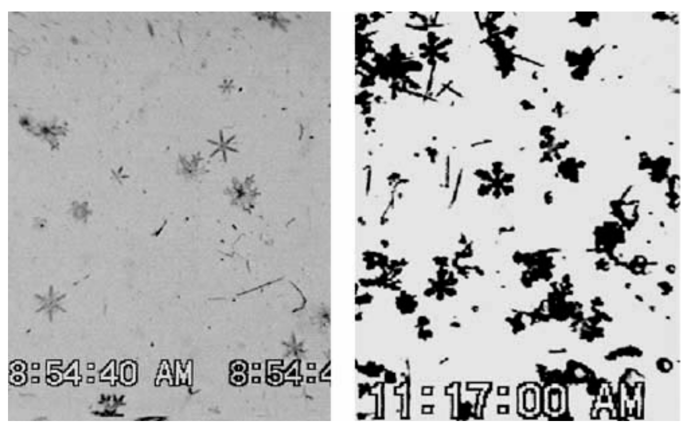

Figure 3. Light riming of ice crystals in clouds affected by pollution (left) compared to heavier riming in non-polluted clouds (right). (From Borys et al., 2003).

Givati and Rosenfeld (2004) analysed about 100 years of orographic precipitation records in regions downwind of pollution sources and compared them to precipitation in regions upwind of the mountain. In their study, they documented the precipitation trends in the orographic enhancement factor, R_o, which is defined as the ratio between precipitation over the hill with respect to the upwind lowland precipitation amount. Two geographical areas were chosen for this study: California and Israel. The topography in both regions is similar, although the mountains in Israel are much lower than the Sierra Nevada. Their statistical results for both locations show that downwind of prevailing winds of pollution sources, on the upslope of mountains and mountain tops, orographic precipitation is reduced by ~20% and ~7%, respectively. It was hypothesized that this decrease is due to an increase in droplet concentrations and a decrease in droplet size. Farther downwind on the lee side of mountains, the amount of precipitation is increased by ~14%. The authors postulate that this increase is due to smaller cloud particles taking longer time to grow, allowing the winds aloft to carry them over the mountaintop (see earlier study of similar effects, produced by deliberate over-seeding with ice-producing particles, by Hobbs, 1975a and 1975b). However, they hypothesized that the integrated rainfall amount over the whole mountain range was reduced by the progressively increased pollution over the years. Subsequent studies show similar decreasing trends in R_o (ratio of precipitation at high altitude sites to that at upstream low altitude sites) over a few western States in the US (Rosenfeld and Givati, 2006; Griffith et al, 2005) and the east slopes of the Colorado Rockies during upslope flow (Jirak and Cotton, 2006). They argue that although absolute precipitation amounts and R_o are affected by fluctuations in the atmospheric circulation patterns, such as those associated with the Pacific Decadal Oscillation and the Southern Oscillation Index, these cannot explain the observed trends in R_o.

Recently, Alpert et al. (2008) re-analysed the data from Israel using the orographic ratio method, taking the ratio between the stations on the Samaria Mountain and the stations located upwind along the seashore, as well as stations on the mountains in the western Galilee and the seashore near the city of Haifa. Their results show the opposite effects from those reported by Givati and Rosenfeld (2004; 2005), namely, the orographic ratio actually increased (see Figure 4) over the years. They concluded that at least in Israel, other factors beside aerosol pollution dominate the precipitation amount in orographic clouds. They showed that by calculating R_o for all the stations on the mountain against the all the stations along the coast there are more cases in which R_o

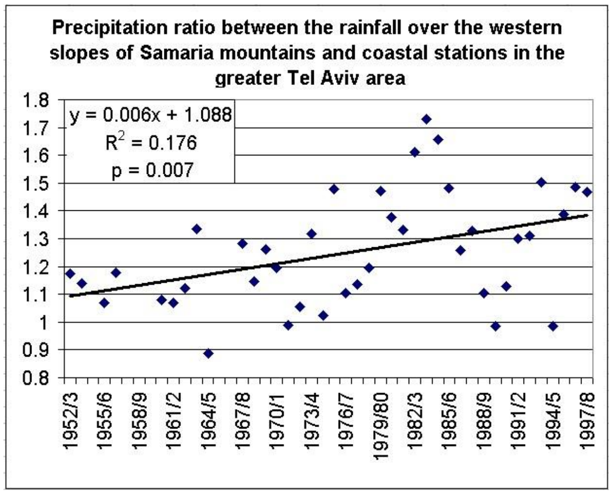

Figure 4: The annual precipitation ratios between the Samaria hills and the central coast clusters for the period 1952-1998, are plotted along with the best-fit line. The dates on the abscissa represent the winter season (November – April) which is the rainy period in Israel. Note the significant increasing trend of the orographic ratio (r=0.42, p=0.007) in contrast to the results of Givati and Rosenfeld (2004), (from Alpert et al, 2008).

increased rather than decreased over the years (see Figure 5). Alpert et al (2008) and Paldor (2008) further argued that the orographic ratio is not an appropriate method to estimate the effect of pollution on rainfall. This is because the data are very noisy and because Ro can decrease not only by decreasing the numerator but also by increasing the denominator. To make things worse, many of the stations upwind of the mountains used by Givati and Rosenfeld (2004 and 2005) were located in or downwind of urban pollution sources, where the rain actually increased over the years. Thus, these stations were affected not only by pollution but also by other probably much more important factors such as urban land-use effects (e.g. urban heat island, changes in frictional velocity). Such urban effects on increased downwind precipitation have been found by many others investigators in many other locations (e.g. Braham, 1974; Landsberg, 1981: Goldreich, 2003: Goldreich and Manes, 1979).

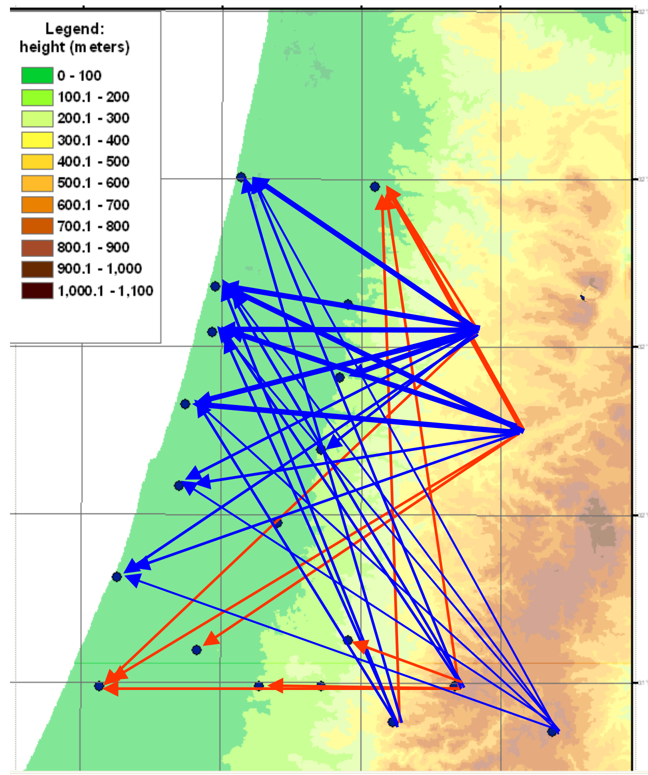

Figure 5. The orographic ratio in central Israel between mountain stations and stations along the shore and inland stations. Blue lines indicate an increase in R_o over the past 50 years and red lines indicate the opposite. The thicker the line the larger is R_o. Note that most R_o indicate an increase over the years, in contrast to the report by Givati and Rosenfeld (2004). (Based on the paper by Alpert et al, 2008).

In summary, it is clear that, although pollution does affect clouds, the hypothesised effects on precipitation are still not clearly understood. It seems quite probable that other factors such as synoptic scale processes, urban effects and dynamical factors on a mesoscale dominate the precipitation amounts over the microphysical processes, while long-term trends cannot be divorced from changing weather patterns driven by global warming.

4. SUMMARY

The following key conclusions can be drawn:

1) It has been demonstrated beyond doubt that anthropogenic emissions of CN and CCN in populated areas dominate over natural emissions.

2) It has been demonstrated equally unequivocally that clouds growing in more polluted air contain near higher cloud base concentrations of smaller droplets than clouds growing in less polluted air.

3) Where temporal and spatial trends in precipitation have been analysed, changes in atmospheric dynamical processes have offered the best explanations, rather than changed cloud microphysics, with all other things being equal.

4) We must acknowledge that the work done to date is incapable of definitively ruling out microphysical forcing on precipitation efficiency as a part of the story in some circumstances. Although the observations suggest that the effect on total precipitation on the ground due to modification in cloud microphysics is relatively small.

5) In our view there have been no experiments yet designed and carried out anywhere that consider and link in an integrated way all or most, of the processes involved simultaneously. Such experiments are needed in order to demonstrate causality, with time-series studies to define precipitation trends, while covering at the same time both microphysical and dynamical forcing on precipitation processes (i.e. all confounders at once) and their interactions.

6) It is possible that comprehensive studies of orographic precipitation would lead to much clearer picture about the microphysical effects of pollution on precipitation under different types of synoptic conditions.

REFERENCES

Ackerman, B., S.A. Changnon, and others. 1978. Summary of METROMEX, Volume 2: Causes of Precipitation Anomalies, Illinois State Water Survey, Champaign, IL, pp. 395.

Alpert, P., N. Halfon, and Z. Levin. 2008. Does pollution really suppress precipitation in Israel? *J. Appl. Meteor. and Climatology*. In Press.

Andreae, M. O., D. Rosenfeld, P. Artaxo, A.A. Costa, G. P. Frank, K. M. Longo, and M. A. F. Silva-Dias. 2004. Smoking rain clouds over the Amazon, *Science*, **303**: 1337-1342.

Ayers G.P. 2005. Air pollution and climate change: Has air pollution suppressed rainfall over Australia? *Clean Air & Environmental Quality*, **39**, 51-57.

Borys, R.D., D.H. Lowenthal, and D.L. Mitchel. 2000. The relationship among cloud physics, chemistry and precipitation rate in cold mountain clouds, *Atmos. Environ*., **34**, 2593–2602, 2000.

Borys, R.D., D.H. Lowenthal, S.A. Cohn, and W.O.J. Brown. 2003. Mountaintop and radar measurements of anthropogenic aerosol effects on snow growth and snow rate, *Geophys. Res. Lett*., **30(10)**, 1538, doi:10.1029/2002GL016855, 2003.

Braham, Jr., R.R. (1974). Cloud Physics of urban weather modification – A preliminary report, *Bull. Amer. Meteor. Soc*., **55**, 100-106.

Changnon Jr., S.A., F.A. Huff and R.G. Semonin. 1971. METROMEX: an investigation of inadvertent weather modification. *Bull. Amer. Meteor. Soc*., **52**, 958-968.

Changnon, Jr., S.A.. 1980. More on the LaPorte anomaly: A review. *Bull. Amer. Meteor. Soc*., **61**, 702.

Coakley, J.A. Jr., R.L. Bernstein, and P.A. Durkee. 1987. Effects of ship-track effluents on cloud reflectivity, *Science*, **255**, 423–430.

Durkee, P. A., R. E. Chartier, A. Brown, E. J. Trehubenko, S. D. Rogerson, C. Skupniewicz, and K. E. Nielsen, S. Platnick and M.D. King. 2000. Composite Ship Track Characteristics. *J. Atmos. Sci*., **57**, 2542-2553.

Durkee, P. A., K. J. Noone, R. J. Ferek, and others. 2001. The Impact of Ship-Produced Aerosols on the Microstructure and Albedo of Warm Marine Stratocumulus Clouds: A Test of MAST Hypotheses 1i and 1ii. *J. Atmos. Sci*., **57**, 2554–2569.

Givati, A., and D. Rosenfeld. 2004. Quantifying precipitation suppression due to air pollution, J*. Appl. Meteor*., **43**, 1038–1056.

Givati, A. and D. Rosenfeld. 2005. Separation between Cloud-Seeding and Air-Pollution Effects. *J. Appl. Meteor*., **44**, 1298- 1315.

Goldreich, Y. (2003). The Climate of Israel, Observations, Research and Applications, Cluwer Academic press, N.Y..

Goldreich, Y. and A. Manes. 1979. Urban effects on precipitation patterns in the greater Tel-Aviv area, *Arch. Meteor. Geophys. Biokl*., **27B**, 213-224

Griffith, D. A., M. E. Solak, and D. P. Yorty. 2005. Is air pollution impacting winter orographic precipitation in Utah? Weather modification association. *J. Weather Modif*., **37**, 14–20, 2005.

Hindman, E.E., II, P.V. Hobbs, and L.F. Radke. 1977. Cloud condensation nucleus size distributions and their effects on cloud droplet size distributions, *J. Atmos. Sci*., **34**, 951-955.

Hobbs, P.V., L.F. Radke and E. Shumway. 1970. Cloud condensation nuclei from industrial sources and their apparent effect on precipitation in Washington State. *J. Atmos. Sci*., **27**, 81-89.

Hobbs, P.V. 1975a. The nature of winter clouds and precipitation in the Cascade Mountains and their modification by artificial seeding. Part I: Natural conditions, *J. Appl. Meteor*., **14**, 783–804.

Hobbs, P.V. 1975b. The nature of winter clouds and precipitation in the Cascade Mountains and their modification by artificial seeding. Part III: Case studies of the effects of seeding, *J. Appl. Meteor.*, **14**, 819–858.

Jin, M., J.M. Shepherd, and M.D. King. 2005. Urban aerosols and their variations with clouds and rainfall: A case study for New York and Houston, *J. Geophys. Res*., 110, D10S20, 10.1029/2004JD005081.

Jirak, I.L., W.R. Cotton. 2006. Effect of Air Pollution on Precipitation along the Front Range of the Rocky Mountains, *J. Appl. Meteor. Climate*., **45**, 236-246.

Landsberg, H. H. 1981. The Urban Climate, Academic Press, N.Y

Levin, Z. and W.R. Cotton. 2007. Aerosol Pollution Impact on Precipitation: A Scientific Review, Report of the International Aerosol Science Assessment Group to the WMO and the IUGG, 482pp.

Lin, J. C., T. Matsui, R. A. Pielke Sr. and C. Kummerow. 2006. Effects of biomass-burning-derived aerosols on precipitation and clouds in the Amazon Basin: a satellite-based empirical study. *J. Geophys. Res*., **111**, D19204, doi:10.1029/2005JD006884.

Mason B.J. 1971. The Physics of Clouds, Oxford University Press. Publishing, Dordrecht, Holland.

Mather, G.K. 1991. Coalescence enhancement in large multicell storms caused by the emissions from a Kraft paper mill, *J. Appl. Meteor*., **30**, 1134–1146, 1991.

Paldor, N., 2008: A note on the estimation of trends in annual rainfall using paired gage observations, *Journal of Applied Meteorology and Climatology*, In press.

Pruppacher, H. R., and J. D. Klett. 1978. Microphysics of Clouds and Precipitation. Reidel Publishing, Dordrecht, Holland.

Rosenfeld D. 2000. 'Suppression of rain and snow by urban and industrial air pollution', *Science*, **287**: 1793–1796.

Rosenfeld D., and A. Givati. 2006. Evidence of orographic precipitation suppression by air pollution induced aerosols in the western U.S. *J. Appl. Meteor. and Climat*., **45**, 893-911.

Rosenfeld D., I.M. Lensky, J. Peterson and A. Gingis. 2006. Potential impacts of air pollution aerosols on precipitation in Australia. *Clean Air and Environmental Quality*, **40**, 43-49.

Rotstayn, L. D., and U. Lohmann. 2002. Tropical rainfall trends and the indirect aerosol effect. *J. Climate*, **15**: 2103-2116.

Rotstayn L.D. 2007. Possible impacts of pollution aerosols on Australian Climate and weather: A short review. *Clean Air and Environmental Quality*, **41**, 26-32.

Rotstayn, L. D., W. J. Cai, M. R. Dix, and others. 2007. Have Australian rainfall and cloudiness increased due to the remote effects of Asian anthropogenic aerosols? *J. Geophys. Res*., **112** (D9, D09202): doi:10.1029/2006JD007712.

Twomey, S., K. A. Davidson, and K. J. Seton. 1978. Results of five years' observations of cloud nucleus concentration at Robertson, New South Wales. *J. Atmos. Sci*., **35**: 650-656.

van den Heever, S., and W. R. Cotton. 2007. Urban aerosol impacts on downwind convective storms, *J. Appl. Meteorol*. **46**, 828-850.

Warner J. 1968. A reduction in rainfall associated with smoke from sugar-cane fires: an inadvertent weather modification, *J. Appl. Meteorol*. **7**: 247–251.

Warner, J., and S. Twomey. 1967. The production of cloud nuclei by cane fires and the effect on cloud droplet concentration. *J.Atmos. Sci*., **24**: 704-706.

Warner J. 1971. Smoke from sugar-cane fires and rainfal' In: Proceedings, International Conference on Weather Modification, Canberra, American Meteorological Society. p. 191–192.

DOES THE POLLUTION AFFECT THE DEVELOPMENT OF THE THUNDERSTORMS OVER THE CITY OF SÃO PAULO, BRAZIL?

Carlos Augusto Morales and Rosmeri Porfirio da Rocha
University of São Paulo
Institute of Astronomy, Geophysics and Atmospheric Science
Departament Atmospheric Science
morales@model.iag.usp.br and rosmerir@model.iag.usp.br

ABSTRACT

This study presents the main meteorological components associated with the development of thunderstorms over the city of São Paulo during the summers of 2000 through 2004. The main work is based on hourly measurements of air-temperature (T), web-bulb temperature (Tw), pressure (P), wind velocity and direction, rainfall and thunder and lightning observations collected at the Meteorological Station of the University of São Paulo located in the southern region of the city. The analysis consists in diagnosing the mean diurnal cycle of these meteorological variables as a function of days with and without-thunderstorm. The wind diurnal cycle shows that for the days with thunderstorms the morning flow is from northwest rotating to southeast after 16:00 local time and it remains from east until the night. For the days without thunderstorms, the wind is well characterized by the sea-breeze circulation that in the morning has the wind flowing from northeast and in the afternoon from southeast. In terms of air temperature, the thunderstorms days show that the air temperature diurnal cycle presents higher amplitude and the maximum temperature of the day is 3.2^{o}C higher than in days without thunderstorms. Another important factor found is the difference between moisture that is higher during thunderstorm days. In terms of precipitation, the thunderstorm days are responsible for more than 60% of the total rain accumulation during the summer, which characterizes the convective development of such clouds. Moreover, the rainfall distribution shows that thunderstorm days have higher rainfall rate intensities and an afternoon precipitation maximum; while in the days without thunderstorms there isn't a defined precipitation diurnal cycle. Later, pollution parameters like optical thickness and aerossol concentrations during the days of thunderstorm development are used to investigate if the severity of these storms are affect, i.e., number of lightning flashes and rainfall amount.

1. INTRODUCTION

The city of São Paulo, the biggest in South America with more than 18 million people, is located in the sub-tropics. The summer precipitation is responsible for almost 60% of the annual rainfall. As a consequence, extreme events of precipitation and severe thunderstorms cause unprecedented damages for the population like flash floods, traffic jam, deaths and etc. (Pereira Filho et al. 2004). Moreover, there is a heat island effect that might contribute to the development of the thunderstorms (Pereira Filho et al. 2000, 2003, 2004 and 2006). Gin et al. (2005) found that most of the flash floods in the city of São Paulo and surrounding cities were associated with high rainfall rates and lightning flash rates.

This study intends to characterize then mean meteorological conditions associated with the days with and without the presence thunderstorms. This work relies on meteorological observations during the months of December through March between the summers of 1999-2000 and 2003-2004.

2. DATA AND METHODOLOGY

2.1 Weather station

The climatological weather station of the Institute of Astronomy, Geophysics and Atmospherics Sciences (IAG) of the University of São Paulo (USP) is found in the “Parque Estadual das Fontes do Ipiranga” (latitude of 23°39'S and longitude of 46°37'W). This weather station gathers the most important observational data base of the city of São Paulo since 1932. This historical data is almost digitalized, and in general, passed a preeliminary quality-control and has very few data gaps.

In order to investigate the main meteorological conditions contribution to the development of thunders, this work uses hourly time series between 7 and 24 local time (LT) of: a) air-temperatue; b) wet-bulb temperature; c) atmospheric pressure at the weather station level; d) relative humidity; wind velocity and direction at 10 meters height. Additionally, we use reports of the occurrance of thunderstorms that were obtained by visual inspection of the meteorological operators (observation of lightning bolts or thunder).

2.2 Methodology

The IAG-USP weather station makes hourly observation from 7 in the morning until midnight and the thunderstorms are visually identified or by listening the thunder. Therefore, it is possible to identify and separate the days with thunderstorms (CT) and without (ST). Based on these days categories we compute the mean diurnal cicle of the meteorological variables. The period of this study corresponds only to the summer months, i.e., December, January, February and March (DJFM) from 1999-2000 and 2003-2004, and it corresponds a total of 605 days.

3. RESULTS

3.1 Diurnal Cycle

During the summers of 2000-2004, 605 days, 241 thunderstorm days were reported by the IAG/USP weather station, i.e., 40% of the summer days in the city of São Paulo had the presence of lightning or thunder. Therefore it characterizes the convective activity of the summer precipitation in São Paulo area.

Figure 1 presents mean diurnal cycle for the days with and without thunderstorms in São Paulo city while table 1 shows the mean, maximum and minimum values found during the day for air temperature, atmospheric pressure, wet-bulb temperature and mixing ratio (r).

Figure 1a shows that in both days (CT and ST) the barometric tide imposes a pressure difference between the afternoon minimum (16 LT) and night maximum (22 LT) and early morning (10 LT) of 1.8 and 1.5 hPa (Table 1) for the days of CT and ST respectively.

The CT days are also characterized by a higher amplitude of the air temperature as observed in Figure 1b and Table 1. This higher amplitude is caused mainly by the maximum temperature that in the CT days is in average 3.2^{o}C higher than in the ST days, while the differences of the minimum temperature is lower, only 1.3^{o}C. Table 1 shows that the CT days are in average 2.1 ^{o}C warmer than in the ST days and with a temperature amplitude considerably higher (7.5 ^{o}C) than in the ST days (5.7 ^{o}C).

Table 1 – Minimum, Maximum, Mean and amplitude for Thunderstorm days (CT) and non-thunderstorm days (ST) in the city of São Paulo for Atmospheric Pressure (P), Air Temperatue (Ta), Wet-bulb temperature (Tw), and mixing ratio (r).

	P (mm Hg)		Ta (^oC)		Tw (^oC)		r (g/kg)	
	CT	ST	CT	ST	CT	ST	ST	CT
Min	696.0	696.4	20.7	19.4	19.7	18.2	20.4	18.5
Max	697.7	697.9	28.2	25.0	21.5	20.1	21.5	19.7
Mean	697.0	697.2	24.2	22.1	20.7	19.2	20.7	18.9
Ampl	1.8	1.5	7.5	5.7	1.8	1.9	1.1	1.2

The wet-bulb temperature (Tw) (Fig. 2a) shows a similar diurnal cycle for the CT and ST days with diurnal amplitude of 1.8 and 1.9 ^oC (Table 1) respectively. The major difference found is that in the CT days the Tw is always higher, but the diurnal difference is very low and practically constant (~ 1.5 ^oC). The higher values of Tw in CT days imply in a more humidity environment than in the ST days, which is also reinforced in the diurnal cycle of the mixing ratio of Figure 2b and Table 1. Along the day, the air is wetter in the CT days. Besides that, the ST days show a maximum around 15 LT while at the CT days is after 17 LT. Moreover the CT days show a little reduction in the mixing ratio during 9 and 14 LT that can be associated to the predominance of the northwestern flow as will be discussed next.

From a climatic point of view, the city of São Paulo is greatly affect by the South Atlantic sub-tropical anti-cyclone that imposes a mean northeast wind in most of the year, except in the spring where the mean wind is from the southeast (Dametto and Rocha, 2005). A major difference between the CT and ST days is found in the temporal evolution of the mean flow as shown in Figure 3. The zonal wind component (Fig. 3a) between the morning and afternoon period is from the west and intense and only in the later afternoon, after 16 LT, the intensity decreases after it rotates to east. The ST days present a distinct evolution, i.e., the zonal wind is very weak in the morning and increases the intensity of the eastern wind (ocean to continent) in the afternoon.

(a)

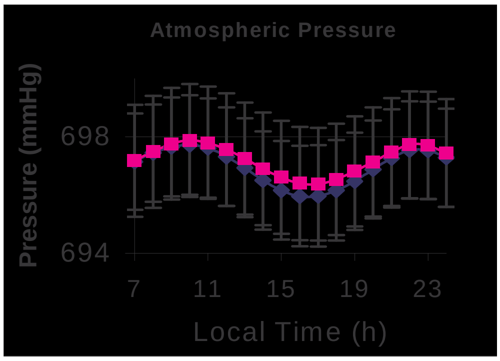

(b)

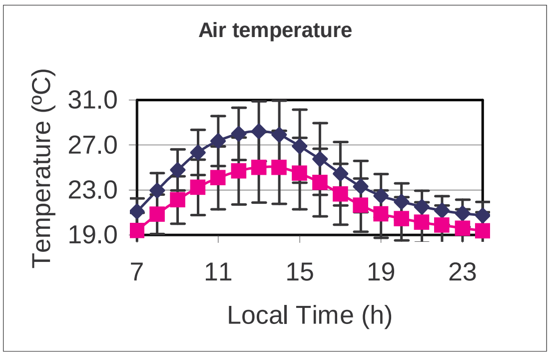

Figure 1 – Mean diurnal cycle for the CT (blue) and ST (purple) days: (a) atmospheric pressure at the weather station level (mmHg); (b) air temperature (^oC). The vertical error bars are the standard deviation.

The meridional wind also presents a different diurnal cycle between the CT and ST days, both in the intensity and in the north to south direction change time, as presented in Figure 3b. In the CT days, the northern wind is more intense in the morning and it changes to south 2 hours later, 14 LT, of the ST days (12 LT). This meridional component rotation from north to south around mid-day (12 LT) is very characteristic of the entrance of the sea breeze in the city of São Paulo (Oliveira et al., 2003).

(a)

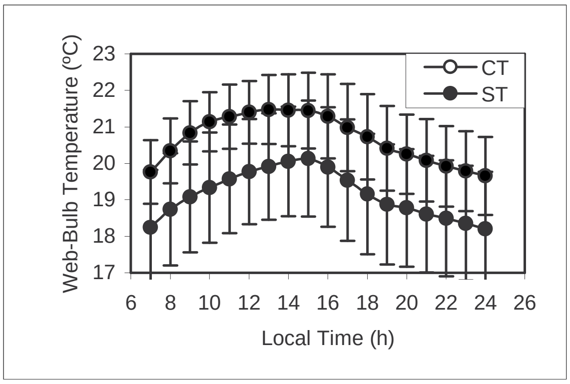

(b)

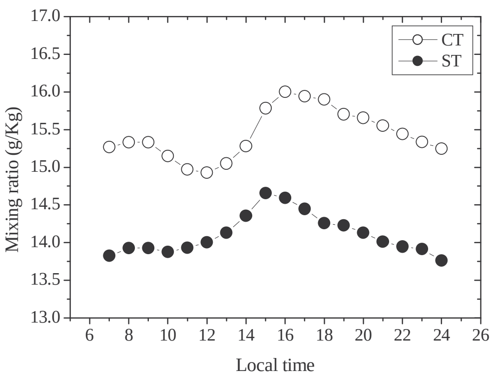

Figure 2 – Mean diurnal cicle for the CT (open circle) and ST (closed circle) days: (a) web bulb temperature (^{o}C), vertical bars represent the standard deviation; (b) mixing ratio (g/kg).

Figure 4 shows that in the CT days the wind is more intense in the morning and it gets weaker in the afternoon. In another hand the ST days present strong winds in the afternoon. Considering Figures 3a, 3b and 4, it can be noted that in the CT days the wind in the morning is from northwest rotating to southeast after 16 LT, and it remains from east with low intensity until the beginning of the night. For the ST days, the diurnal wind pattern is more characteristic of the sea-breeze penetration as investigated by Oliveira and Silva Dias (1986), i.e., in the morning the predominant wind is from northeast and in the afternoon is from southeast and as shown in Figure 4, the maximum intensity is found in the afternoon period. As discussed by Oliveira et al. (2003), this diurnal cycle of the wind intensity differs from the expected pure process of the planetary boundary layer (PBL) evolution, where it is expected higher velocities in the nocturnal period associated with PBL decoupled. They suggest this behavior to the sea-breeze penetration, with the decrease of the velocity in the beginning of the afternoon (~12 LT, Fig. 4), when the mean wind from northeast is rotating to southeast, and just after the establishment of the southeastern wind it intensifies and it presents a maximum at the end of the afternoon (16-18 LT), after the passage of the sea-breeze. Contrarily, in the CT days the wind is more intense in the morning (Fig. 4) when the wind blows from northwest (Fig. 3a and 3b) and during the evening after it changes to southeast decreases significantly the intensity, differentiating the classical pattern of the sea breeze in the city of São Paulo as presented by Oliveira et al. (2003).

The predominance of the northwestern flow during extreme events of precipitation over the state of São Paulo was also obtained by Carvalho et al. (2002) by analyzing the synoptic scale patterns. Their results indicate that the anomalous northwestern flow in low levels is found in period where the South Atlantic Convergence Zone (SACZ) is low and intense. At local scale, CT and ST days composites present that during day the northwestern flow predominance imposed by the synoptic system as presented by Carvalho et al. (2002) delays and weakness the intensity of the southeastern wind in the afternoon period associated with the penetration of the sea-breeze in the city.

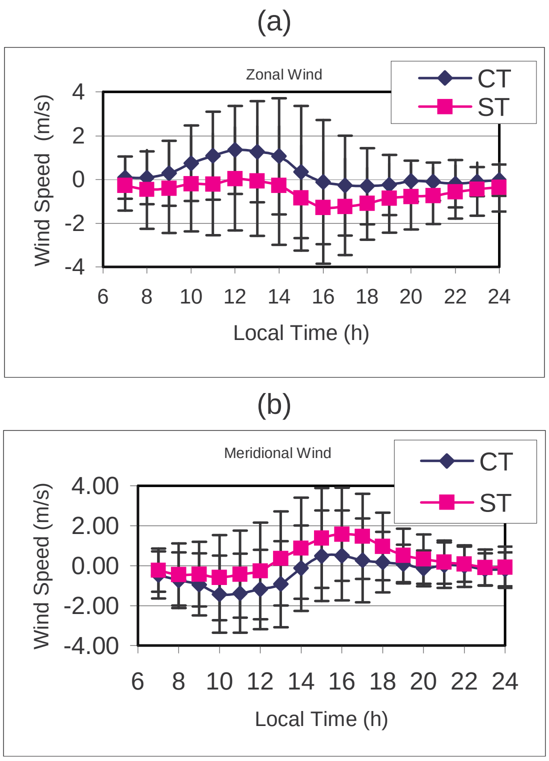

Figure 3 – Mean diurnal wind cycle for the CT and ST days: (a) zonal wind (m/s); (b) meridional wind (m/s). The vertical bars represent the standard deviation.

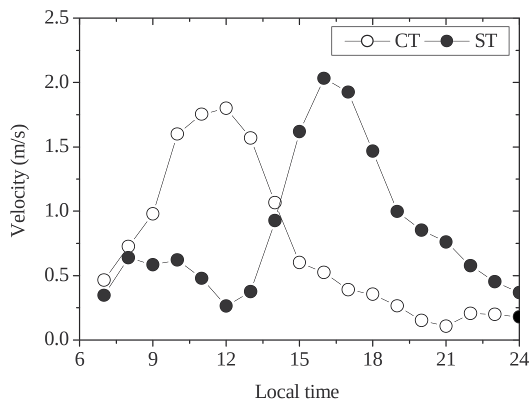

Figure 4 – Mean diurnal cycle of the wind intensity (m/s) for the CT and ST days.

Although the criteria applied to identify thunderstorm days does not necessarily imply that the precipitation falling at the IAG/USP weather station is from thunder clouds, once the identification is made visually, the contribution of CT days to the total seasonal precipitation is expressively as presented in the rainfall rate diurnal cycle of Figure 5.

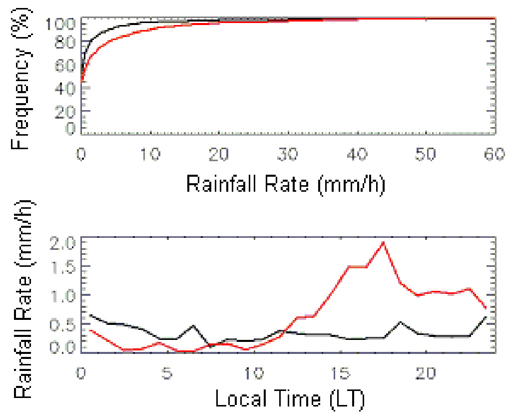

Figure 5 – Mean rainfall rate diurnal cycle for the CT and ST days. (a) Cumulative probability distribution (top); (b) Hourly precipitation rate (mm/h).

The ST days present weak precipitation (< 1 mm/h) and homogeneous distribution along the day. In the CT days, the precipitation is weak in the morning and there is a maximum in the afternoon period (17 LT). The cumulative probability distribution shows that in the CT days there are more intense rainfall rates than in the ST days. As presented in Table 2, the daily precipitation for CT days (9.4 mm/day) is double of the ST days (4.7 mm/h) and even superior than the mean climatology of the DJFM that is 7.3 ± 13.5 mm/day. Although it was only observed 40% of the days with thunderstorms, these days represent 61% of the total precipitation observed in the summers of 2000-2004 in the city of São Paulo (Table 2).

Table 2 – Mean and standard deviation of the daily precipitation and percentage of the total precipitation for CT and ST days.

	Mean Precipitation (mm/day) $\pm\sigma$	% of the Total precipitation
CT	9.5 ± 14.6	61%
ST	4.7 ± 11.5	39%

4. CONCLUSIONS

The diurnal evolution of the air temperature, web-bulb temperature and atmospheric pressure is similar for the CT and ST days, although the CT days present higher amplitude for all variables. For example, the mean daily air temperature is around 2.1 ^{o}C warmer in CT days than in ST with thermal mean amplitude of 7.5 ^{o}C and 5.7 ^{o}C respectively. The CT days are also characterized by lower pressure in the afternoon when compared to ST days.

The mixing ratio, the surface wind and the precipitation present distinct diurnal evolution for CT and ST days:

The precipitation shows a noticeable diurnal cycle with strong rain events occurring in the afternoon for the CT days. For the ST days, the precipitation is weaker and almost distributed along the day. Therefore, it means that the thunderstorms that represent 40% of the summer days contribute to 60% of the total precipitation observed in the summer time;

In the CT days the city of São Paulo has a predominance of northwestern flow in the morning period and from east in the afternoon, which is very different from the ST days where in the morning the wind is northeastern, following the summer climatology, and in the afternoon it flows from southeastern and it is more intense than in CT days. The changes in wind direction and in the wind intensity in the ST days are more similar to the penetration of the sea breeze in the city of São Paulo as documented by Oliveira et al. (2003). In the other hand, for the CT days the highest wind intensity is observed in the morning period and in the early afternoon when there is northwestern flow. Apparently, the presence of the northwestern flow delays the entrance of the sea breeze (southeast wind) and weakens the southeast wind in the afternoon that is associated to the sea breeze. Comparing the diurnal cycle obtained with the large-scale re-analyses of extreme events of precipitation in the State of São Paulo (Carvalho et al. 2002) is possible to characterize that the ST days are associated to the weaker and intense continental SACZ patterns, which shows an anomalous northwest circulation. This aspect will be addressed in the future by the large-scale re-analyzes composites of the NCEP and ECMWF;

The CT days are in average wetter than the ST days. The daily maximum of mixing ratio for CT days is observed at 16 LT, which is one hour later than the ST days, and this could be the effect of the main circulation of the region. The sea breeze enters in the city earlier in the ST days and therefore it increases the mixing ratio before. Moreover, another important difference is that in the morning period there is a strong reduction in the mixing ratio during the CT days, which is not observed for the ST days.

5. REFERENCES

CARVALHO, L.M., JONES, C., LIEBMANN, B. Extreme precipitation events in southeastern South America and lage-scale convective patterns in the South Atlantic Convergence Zone, J. Clim., vol. 15, pp. 2377-2394, 2002.

GIN, R.B.B, WILLIAMS, E., BENETI, C.A., PEREIRA FILHO, A., JUSEVIVIUS, M., KAWANO, M., BIANCHI, R., AND BELLODI. The electrical and meteorological conditions in thunderstorms in the vicinity of São Bernardo do Campo, São Paulo. VIII Int. Symp. on Lightning Protection, pp. 137-142, 2005.

OLIVEIRA, A.P. BONSTEIN, R.D., AND SOARES K. Annual and diurnal wind patterns in the city of São Paulo. Water, Air and Soil Pollution: Focus 3: 3-15, 2003.

PEREIRA FILHO, A. J. . Chuvas de verão e as enchentes na Grande São Paulo: El Niño, brisa marítima e ilha de calor. In: II Seminário Brasileiro de Hidrometeorologia, 2000, Rio de Janeiro. XI Congresso Brasileiro de Meteorologia. Rio de Janeiro : Sociedade Brasileira de Meteorologia, 2000.

PEREIRA FILHO, A. J. ; HAAS, R. . Hydrometeorological analysis of flash floods in tropical urban environments and their societal impacts. In: 7th International Conference on Southern Hemisphere Meteorology and Oceanography, 2003, Wellington. 7th International Conference on Southern Hemisphere Meteorology and Oceanography. Boston : AMS, 2003.

PEREIRA FILHO, A. J. ; BARROS, Mário Thadeu Leme de ; HALLAK, Ricardo ; GANDU, Adilson Wagner . ENCHENTES NA REGIÃO METROPOLITANA DE SÃO PAULO: ASPECTOS DE MESOESCALA E AVALIAÇÃO DE IMPACTOS . In: XIII Congresso Brasileiro de Meteorologia, 2004, Fortaleza. PUDN2 - Planejamento Urbano e Desastres Naturais. Brasília : Sociedade Brasileira de Meteorologia, 2004.

PEREIRA FILHO, A. J. ; Silva, F. D. S . Características estatísticas espaço-temporais de sistemas precipitantes no Leste de São Paulo. In: XVI Congresso Brasileira de Meteorologia, 2006, Florianópolis. XVI Congresso Brasileira de Meteorologia, 2006.

INTERACTION OF MICROPHYSICAL AND DYNAMICAL TIMESCALES IN OROGRAPHIC PRECIPITATION

A. Muhlbauer,* P. Spichtinger and U. Lohmann
Institute for Atmospheric and Climate Science, ETH Zurich, Switzerland

1. INTRODUCTION

The development of orographic precipitation depends on the interaction of processes which operate on different timescales (Smith 1979; Jiang and Smith 2003; Smith and Barstad 2004; Kirshbaum and Durran 2004; Roe and Baker 2006). Dynamical timescales are inherent to the flow dynamics (e.g. advection timescale, timescale of instability growth) and can be distinguished from timescales governed by microphysical processes (e.g hydrometeor conversion timescale, timescale of hydrometer fallout). The interaction between these different timescales controls the development of orographic clouds and determines the orographic precipitation distribution. So far, the relevance of dynamical and microphysical timescales for orographic precipitation has only been analyzed within the framework of linear models (Smith 1979; Smith and Barstad 2004) or with numerical models and simplified microphysics (Jiang and Smith 2003; Kirshbaum and Durran 2004). Recent studies indicate that the interaction of these timescales may also be relevant for aerosol-cloud-precipitation interactions in orographic clouds (Muhlbauer and Lohmann 2008). Here, aerosol particles act as cloud condensation nuclei (CCN) and influence microphysical properties of clouds by shifting the cloud droplet size spectrum towards smaller radii. Due to the smaller collision efficiencies of the smaller cloud droplets the development of precipitation is retarded which presumably leads to a reduction in warm-phase orographic precipitation through the aerosol indirect effect. Simulations by Muhlbauer and Lohmann (2008) indicate that in the case of orographic clouds the magnitude of the indirect aerosol effect on precipitation depends strongly on the flow dynamics and on geometrical aspects of the terrain. The question arising in this context is, if it is possible to understand the magnitude (and maybe also the sign) of aerosol effects on orographic precipitation qualitatively by considering the interaction of the timescales most important for orographic precipitation (e.g. timescale of advection, microphysical timescales).

The main goal of this study is to identify the important and dominant timescales for the orographic precipitation development in a state-of-the-art numerical model and to quantify their role in different dynamical and thermodynamical regimes. A further goal of this work is to investigate the effect of aerosols on the microphysical timescales and the feedbacks on the orographic precipitation distribution in warm-phase orographic clouds.

* *Corresponding author address:* Andreas Muhlbauer, Institute for Atmospheric and Climate Science, ETH Zurich, Universitaetsstrasse 16, 8092 Zurich, Switzerland.
E-mail: andreas.muehlbauer@env.ethz.ch

The paper is structured as follows: In section 2 we briefly introduce the modeling approach focusing on the numerical model and the parameterizations which are employed. In section 3 we discuss the model setup, the initial conditions and the experimental design. In section 4 we present the model simulation and discuss our results in section 5.

2. NUMERICAL MODEL

The model simulations are performed with the nonhydrostatic, fully compressible limited-area mesoscale weather prediction model COSMO[1] (Doms and Schättler 2002; Steppeler et al. 2003). The elastic equations are solved in a split-explicit time-splitting approach (Wicker and Skamarock 2002) with a two time-level total variation diminishing (TVD) 3rd order Runge-Kutta scheme in combination with a 5th order horizontal advection scheme. All prognostic moisture and aerosol variables are advected by a 2nd order positive-definite advection scheme after Bott (1989).

Since the main focus of this study is given to aerosol-cloud-precipitation interactions via the aerosol indirect effect all radiative effects such as the change in cloud albedo are neglected. Thus, no radiation parameterization is considered here.

For the vertically turbulent diffusive processes, a 2.5 level Mellor-Yamada scheme with a prognostic TKE (turbulent kinetic energy) equation is used (Herzog et al. 2002).

The coupled cloud-microphysical and aerosol-microphysical processes are treated in a two-moment bulk approach. The aerosol-microphysical processes which are considered in the model are the nucleation of gas-phase sulfuric acid, the condensation of sulfuric acid on pre-existing aerosol particles, coating of insoluble aerosols by sulfuric acid, inter- and intramodal coagulation and the uptake of water vapor. The cloud-microphysics parameterization accounts for the activation of aerosols to cloud droplets, condensation/evaporation of cloud droplets, autoconversion of cloud droplets to rain, accretion of cloud droplets by rain, self-collection of cloud droplets by rain, evaporation of rain and the break-up of large rain drops. For a more in detail explanation of the processes and the underlying model equations we refer to Seifert and Beheng (2006) and Muhlbauer and Lohmann (2008).

[1] COnsortium for Small-scale MOdeling, http://www.cosmo-model.org

3. MODEL SETUP

3a. *COMPUTATIONAL DOMAIN*

The 3D computational domain is composed of 200 times 100 gridpoints in the horizontal with a grid spacing of 2 km which yields a domain of –200 km $\leq$ x $\leq$ 200 km along the x-axis and –100 km $\leq$ y $\leq$ 100 km along the y-axis. At the lateral model boundaries an open relaxation boundary condition (Davies 1976) is introduced in the x-direction whereas periodic boundaries are prescribed in the y-direction. At the model bottom a free-slip boundary condition is used. A Rayleigh damping sponge layer is introduced at the upper rigid boundary to damp reflections of vertically propagating gravity waves. The damping layer starts at 10 km height and covers approximately one half of the vertical model domain. A terrain following SLEVE coordinate system (Schär et al. 2002) is introduced in the vertical with 60 layers and a vertical grid spacing varying between 10 m in the lowermost and approximately 1400 m in the uppermost layer. The model top is located at roughly 23 km height and the timestep of the model is 10 s.

3b. *IDEALIZED TOPOGRAPHY*

The idealized topography has the form of a 3D finite mountain ridge (Kirshbaum and Durran 2005) such that

$$h(x,y) = \begin{cases} \frac{h_0}{16}\left[1+\cos(\pi r)\right]^4 & , \ r \le 1 \\ 0 & , \ r > 1 \ , \end{cases} \tag{1}$$

and

$$r^2 = \begin{cases} \left(\frac{x-x_0}{4a}\right)^2 + \left(\frac{|y-y_0|-B}{4b}\right)^2 & , \ |y-y_0| > B \\ \left(\frac{x-x_0}{4a}\right)^2 & , \ |y-y_0| \le B \end{cases} \tag{2}$$

Here, h_0 is the peak height of the mountain ridge, a is the mountain half-width in x-direction, b is the mountain half-width in y-direction and the parameter B controls the width of the mountain ridge line. The mountain range is centered in the computational domain at $x_0 = 100$ and $y_0 = 50$ in gridpoint space. Unless otherwise stated we use the idealized topography with the parameters $h_0 = 1000$ m, $a = 20$ km, $b = 10$ km and $B = 30$ km.

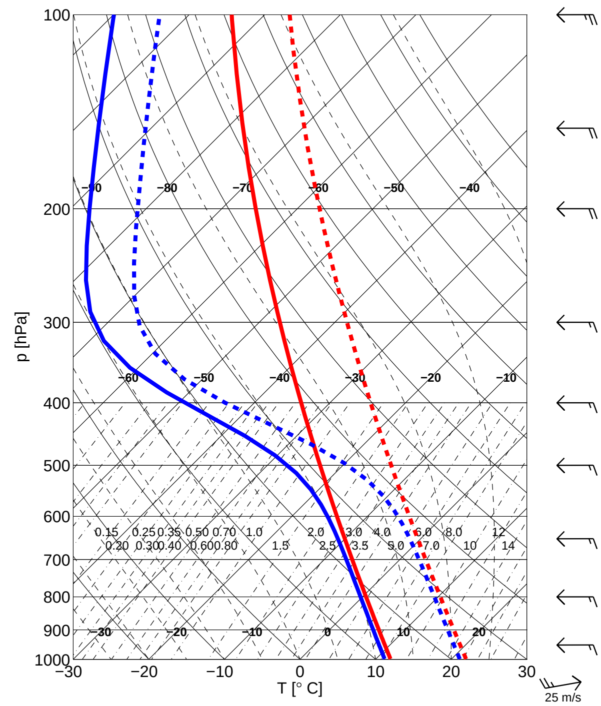

Figure 1: Atmospheric soundings for the idealized simulations showing the temperature (red) and dewpoint temperature (blue) in a skewT-logp diagram. The soundings are given analytically with the surface temperatures $T_{sl} = 285$ K (solid) and $T_{sl} = 295$ K (dashed). The dry Brunt-Väisälä frequency is $N_d = 0.011$ s^{-1} and the surface pressure is $p_{sl} = 1000$ hPa. The windspeed is $U = 15$ m s^{-1} and is prescribed constant with height within the first 10 km and increases linearly above.

3c. *DYNAMICAL INITIAL CONDITION*

The model is initialized with a horizontally homogeneous basic state which is given by a dry atmosphere at rest with surface pressure $\bar{p}_{SL}$ and surface temperature $\bar{T}_{SL}$. The basic state is hydrostatically balanced and the temperature increases with the logarithm of pressure such that $\partial\bar{T}/\partial\ln\bar{p} = 42$ K. The initial horizontally homogeneous profiles of pressure $p(z)$ and temperature $T(z)$ are calculated analytically as a function of surface pressure p_{SL}, surface temperature T_{SL} and the dry Brunt-Väisälä frequency N_d by following Clark and Farley (1984).

The model basic state is made similar to the actual state by setting $\bar{p}_{SL} = p_{SL}$ and $\bar{T}_{SL} = T_{SL}$ so that the difference between the two states arises solely from the vertical temperature gradient. In our simulations, the surface pressure is $p_{SL} = 1000$ hPa and the surface temperature is prescribed by the set of temperatures $T_{SL} = 285$ K and $T_{SL} = 295$ K, re-

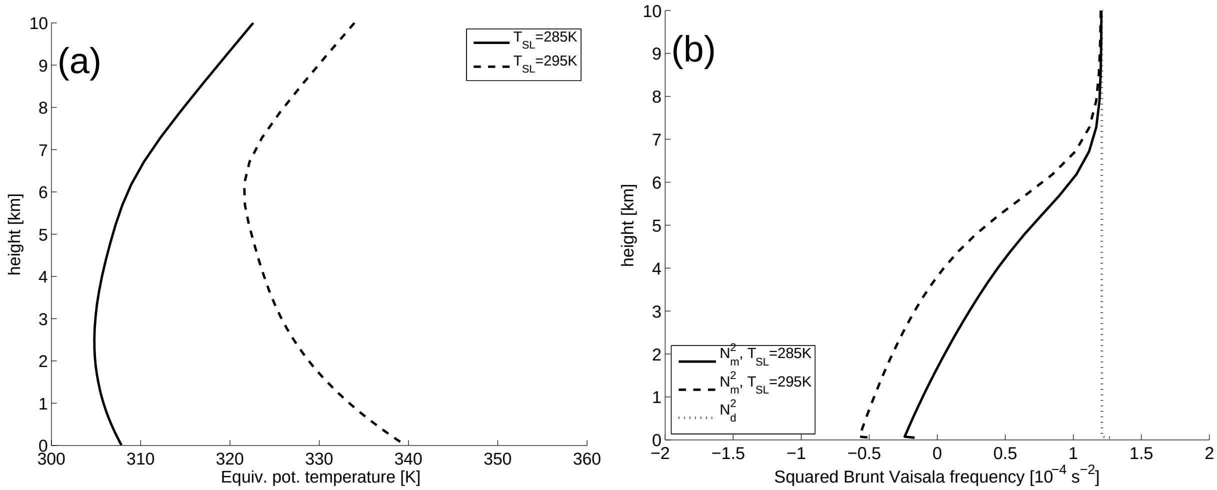

Figure 2: Vertical profiles of equivalent potential temperature (a) and squared Brunt Väisäla frequency (b) for the sounding with $T_{SL} = 285$ K (solid) and $T_{SL} = 295$ K (dashed), respectively. The dry squared Brunt-Väisäla frequency (dotted) is shown for comparison.

spectively. The dry Brunt-Väisälä frequency is chosen to be constant with height with $N_d = 0.011$ s^{-1}. The vertical profile of the relative humidity is prescribed by a modified Fermi function (Spichtinger 2004) of the type

$$RH(z) = a + \frac{b-a}{1+\exp\left[-c\left(z-z_0\right)\right]} \tag{3}$$

with the parameters $a = 0.95$, $b = 0.03$, $c = 0.0015$ m^{-1}, $z_0 = 6000$ m and $0 \leq RH \leq 1$. The vertical decay of the relative humidity profile is controlled with the parameters c and z_0. The modified Fermi function gives a vertical profile of relative humidity which starts with the value $RH = 0.95$ at the surface and decays smoothly with height towards the value $RH = 0.03$. Figure 1 shows the resulting vertical profiles of temperature and dewpoint temperature in a skew T-log P chart. The horizontal wind profile U is prescribed unidirectionally and the windspeed is vertically constant with $U = 15$ m s^{-1} up to 10 km and increases linearly above to 40 m s^{-1}. Both soundings are potentially and statically unstable as shown by the vertical profiles of the equivalent potential temperature θ_e and the squared Brunt-Väisala frequency N_m^2 (see figure 2). The lifting condensation level (LCL) is comparable in both soundings and is located at approximately $z_{LCL} \approx 100$ m altitude. The depth of the unstable layer varies in both soundings and is roughly 1500 m in the cold sounding ($T_{SL} = 285$ K) and approximately 3600 m in the warm sounding ($T_{SL} = 295$ K).

Thus, we may expect pre-existing thermal perturbations to grow in the unstable environment and to initiate convective motions in the orographic cloud. To initiate convective motions in the statically unstable regions, small-amplitude perturbations are generated and are added to the temperature stratification at the lowermost model level. The small-amplitude perturbations are drawn from a Gaussian distribution with zero mean and scaled to a root-mean-

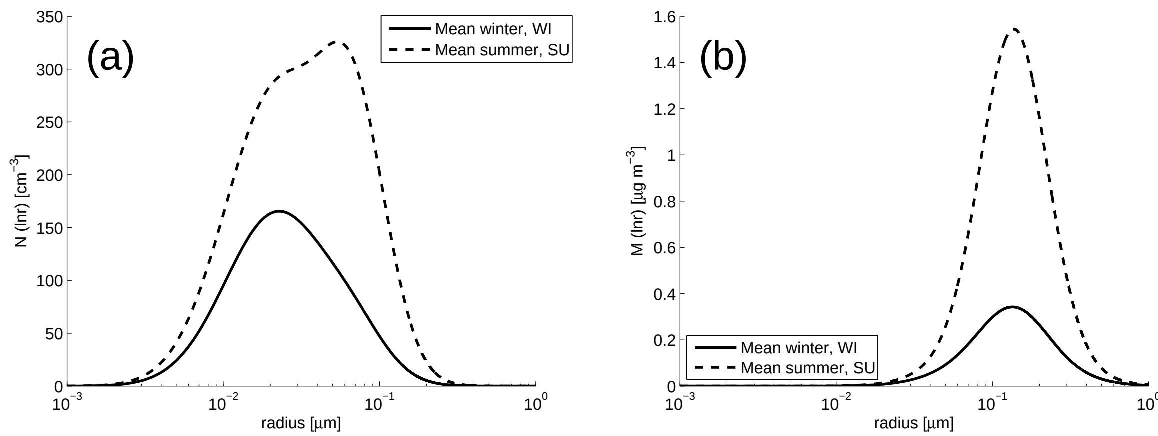

Figure 3: Aerosol initial condition for the idealized simulations. Panel (a) shows the aerosol number distribution for wintertime conditions (solid) and for summertime conditions (dashed). The aerosol spectra are seasonal means over wintertime and summertime conditions at the JFJ in Switzerland. The mass distribution is calculated analytically from the number distribution by assuming a mean density of $\rho = 1.5$ g cm^{-3} which was determined by an AMS mass closure in Cozic et al. (2007).

squared (rms) amplitude of 0.1 K (not shown). In order to remove all 2Δ structures the Gaussian perturbation field is filtered twenty times with a simple Laplacian filter operator. Since the Rossby number $Ro = U/fL$ is usually much greater than unity for the characteristic scales which are considered here ($U = 15$ m s^{-1}, $f \approx 10^{-4}$ s^{-1} at midlatitudes and $L = 20$ km), the effect of the Coriolis force is neglected in this study. Moreover, model simulations by Colle (2004) showed that the inclusion of rotation has little impact on the orographic precipitation sensitivity.

3d. *MICROPHYSICAL INITIAL CONDITION*

The initial aerosol spectra shown in figure 3 are seasonal means of wintertime (WI) and summertime (SU) aerosol size distribution measurements taken with a scanning mobility particle sizer (SMPS) at the Jungfraujoch (JFJ) in central Switzerland (Weingartner et al. 1999). The high-altitude research station at the JFJ is a free-tropospheric site during wintertime where aerosol number concentrations are generally low.

	Mode	N [cm^{-3}]	r [μm]	σ	M [μg m^{-3}]
Winter	AIT	310	0.022	2.13	0.07
	ACC	40	0.070	1.61	0.44
Summer	AIT	530	0.022	2.13	0.26
	ACC	260	0.070	1.61	1.74

Table 1: Parameters of the aerosol size distribution. The mass density M in each mode is computed from the aerosol size distribution by assuming a mean aerosol density of $\rho = 1.5$ cm^{-3} (Cozic et al. 2007). The total aerosol mass densities are $M_{WI} = 0.51$ μg m^{-3} for the winter aerosol spectrum and $M_{SU} = 2.0$ μg m^{-3} for the summer aerosol spectrum. The abbreviations AIT and ACC denote the Aitken mode and accumulation mode, respectively.

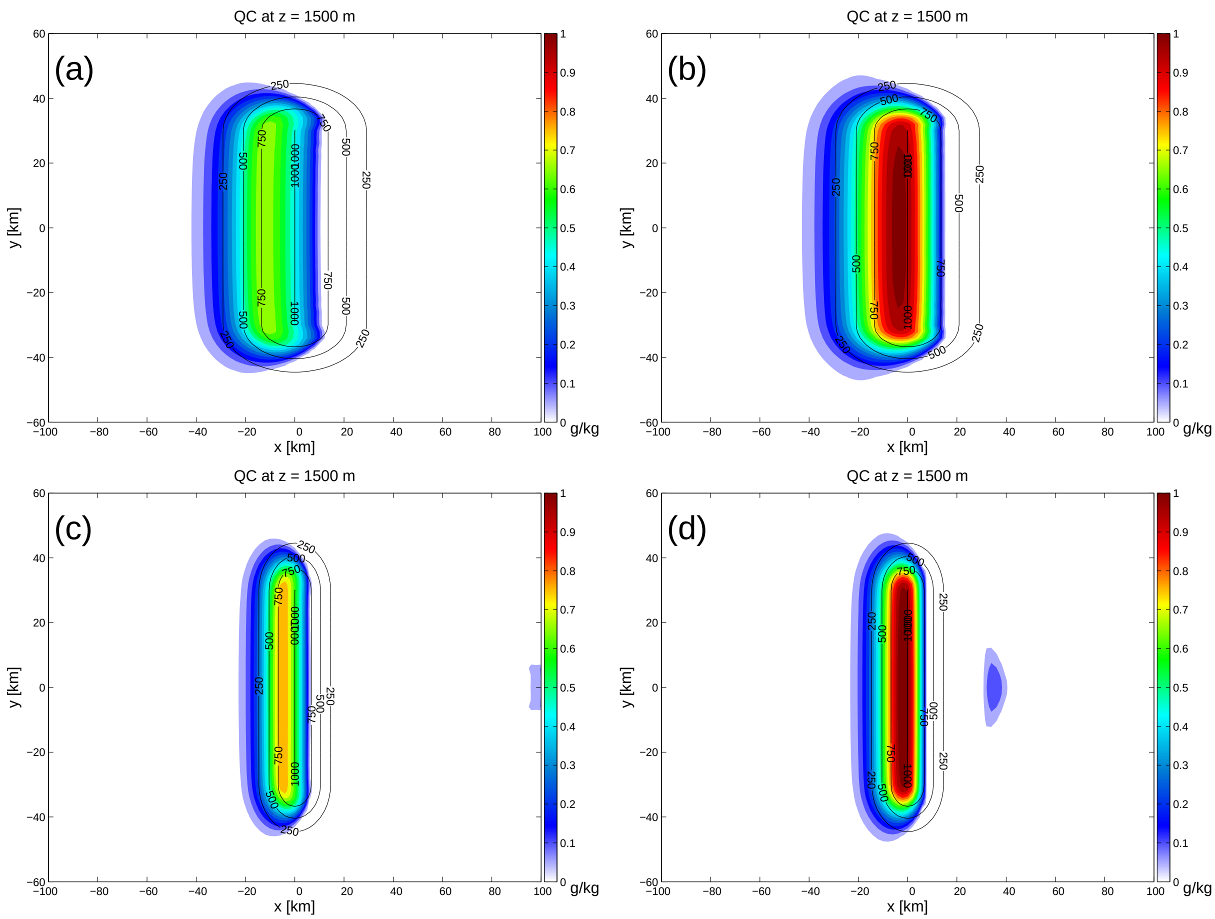

Figure 4: Cloud liquid water mixing ratio QC at $z = 1500$ m height and contours of the underlying topography. The simulation with wintertime (WI) aerosol conditions are shown in the left panels (a) and (c) whereas the simulations with the summertime (SU) aerosol conditions are shown in the right panels (b) and (d). The half-width of the finite mountain ridge is $a = 20$ km in the upper panels (a) and (b) whereas it is $a = 10$ km in the lower panels (c) and (d). Only parts of the computational domain are plotted.

During summertime the air at the JFJ is no longer decoupled from the Alpine boundary layer and convective processes as well as slope wind circulations transport boundary layer air to the JFJ which leads to a general increase in aerosol number concentrations during the summer (Weingartner et al. 1999; Choularton et al. 2008). The aerosol spectra satisfy a lognormal size distribution of the form

$$N(\ln r) = \sum_{i=1}^{2} \frac{N_i}{\sqrt{2\pi}\ln\sigma_i} \exp\left[-\left(\frac{\ln r - \ln\tilde{r}_i}{\sqrt{2}\ln\sigma_i}\right)^2\right] \tag{4}$$

with the three free parameters being the aerosol

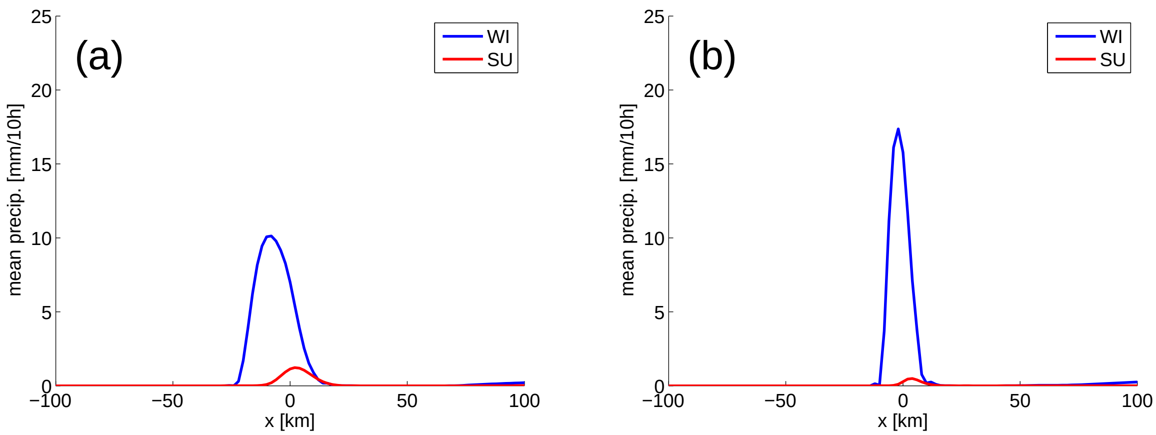

Figure 5: Precipitation distribution along the topography for the simulation with wintertime (WI) aerosol (blue) and summertime (SU) aerosol (red), respectively. The half-width of the idealized topography is $a = 20$ km in panel (a) and $a = 10$ km in panel (b).

number densities N_i, the count median radii $\tilde{r}_i$ and the geometric standard deviations σ_i. The specific parameters of the lognormal aerosol size distribution are summarized in table 1. The aerosol initial condition is prescribed vertically constant. Assuming a mean density of the aerosol of $\rho = 1.5$ g cm^{-3} the mass distribution of the aerosols can be calculated directly from the number distribution. The mean aerosol density of $\rho = 1.5$ g cm^{-3} was obtained by an aerosol mass spectrometry (AMS) mass closure in Cozic et al. (2007). Integration over the mass distributions yields the aerosol mass densities (in this case $\approx$ PM1) which are $M_{SU} = 2.0$ μg m^3 and $M_{WI} = 0.51$ μg m^3.

4. MODEL SIMULATIONS

In the following section we consider 3D simulations of moist flows past topography for the two thermodynamically distinct initial conditions ($T_{SL} = 285$ K and $T_{SL} = 295$ K) discussed in section 3. The aerosol initial conditions are initialized with the observed aersol size distributions. Since the mean summertime aerosol size spectrum exhibits considerably larger aerosol number concentrations than the mean wintertime aerosol spectrum we consider simulations with the summertime aerosol spectrum as polluted (in the following denoted with SU) and the simulations with the wintertime aerosol spectrum as clean (in the following denoted with WI). However, since the aerosol measurements were obtained at a high-altitude research station the aerosol concentrations are typical for remote-continental conditions in central Switzerland.

Since the characteristic nondimensional mountain height $\hat{h} = N_d h/U$ is approximately $\hat{h} = 0.73$ for our setup, we expect the orographic flow to develop structures of a linear hydrostatic mountain wave.

4a. *Stratiform orographic precipitation*

At first we consider the flow over a mountain range with a characteristic mountain half-width of $a =$

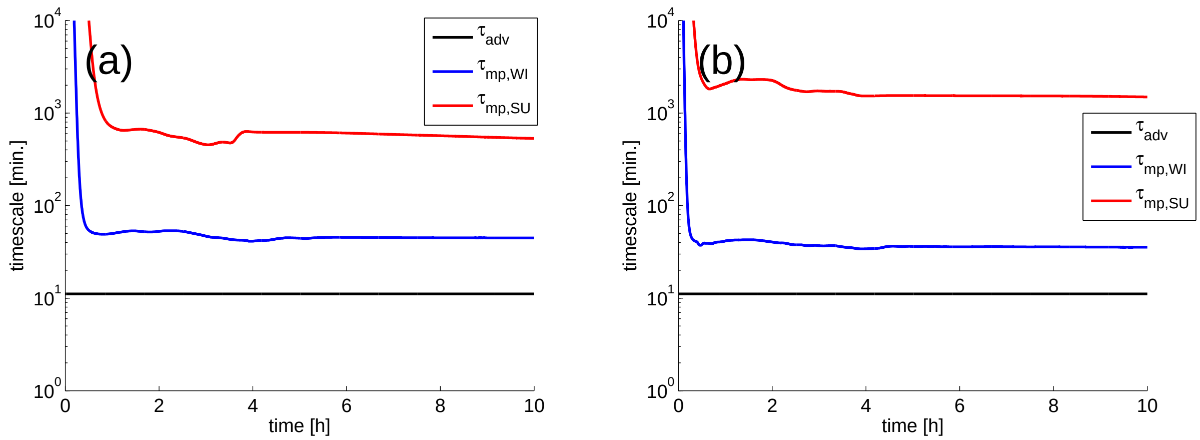

Figure 6: Dynamical and microphysical timescales. The dynamical timescale for advection τ_{adv} (black) is shown together with the microphysical timescale τ_{mp} for the simulation with wintertime aerosol spectrum (WI) and the simulation with summertime aerosol spectrum (SU). The simulation with wide mountain ($a = 20$ km) is shown in panel (a) whereas the simulation with narrow mountain ($a = 10$ km) is shown in panel (b).

20 km. The resulting field of cloud liquid water after 10 h simulation time is shown in figure 4. A stable orographic cloud forms on the upslope side of the mountain as a result of the forced upslope ascent with maximum cloud liquid water mixing ratios on the order of 0.7 g kg. The simulations SU with increased aerosol number concentrations show considerably higher values of cloud liquid water of up to 1.0 g kg. Similar results are obtained if the mountain half-width is reduced to $a = 10$ km although the lifting imposed by the mountain wave is stronger in this case. Again, cloud liquid water increases in the simulations with higher aerosol number concentrations.

Figure 5 shows the averaged precipitation distribution along the topography after 10 h of simulation. The simulation with increased aerosol number concentrations depict a clear downstream shift of the orographic precipitation regardless of the width of the mountain. However, the upslope component of the orographic precipitation is lower in the case of the narrow mountain ($a = 10$ km) than in case of the wide mountain ($a = 20$ km). The loss in orographic precipitation at the divide is as much as 90 $\%$ in the case of the wide mountain whereas the loss is almost 97 $\%$ in the case of the narrow mountain. Similar to the results by Muhlbauer and Lohmann (2008), the magnitude of the indirect aerosol effect on precipitation depends also on geometrical aspects of the mountain range. This effect can qualitatively be understood by comparing the timescales of advection as well as the microphysical timescale to develop precipitation in both simulations as shown in figure 6.

Therefore, we approximate the advective timescale (i.e. the time it takes an airparcel to travel over the mountain) with

$$\tau_{adv} = a/U \tag{5}$$

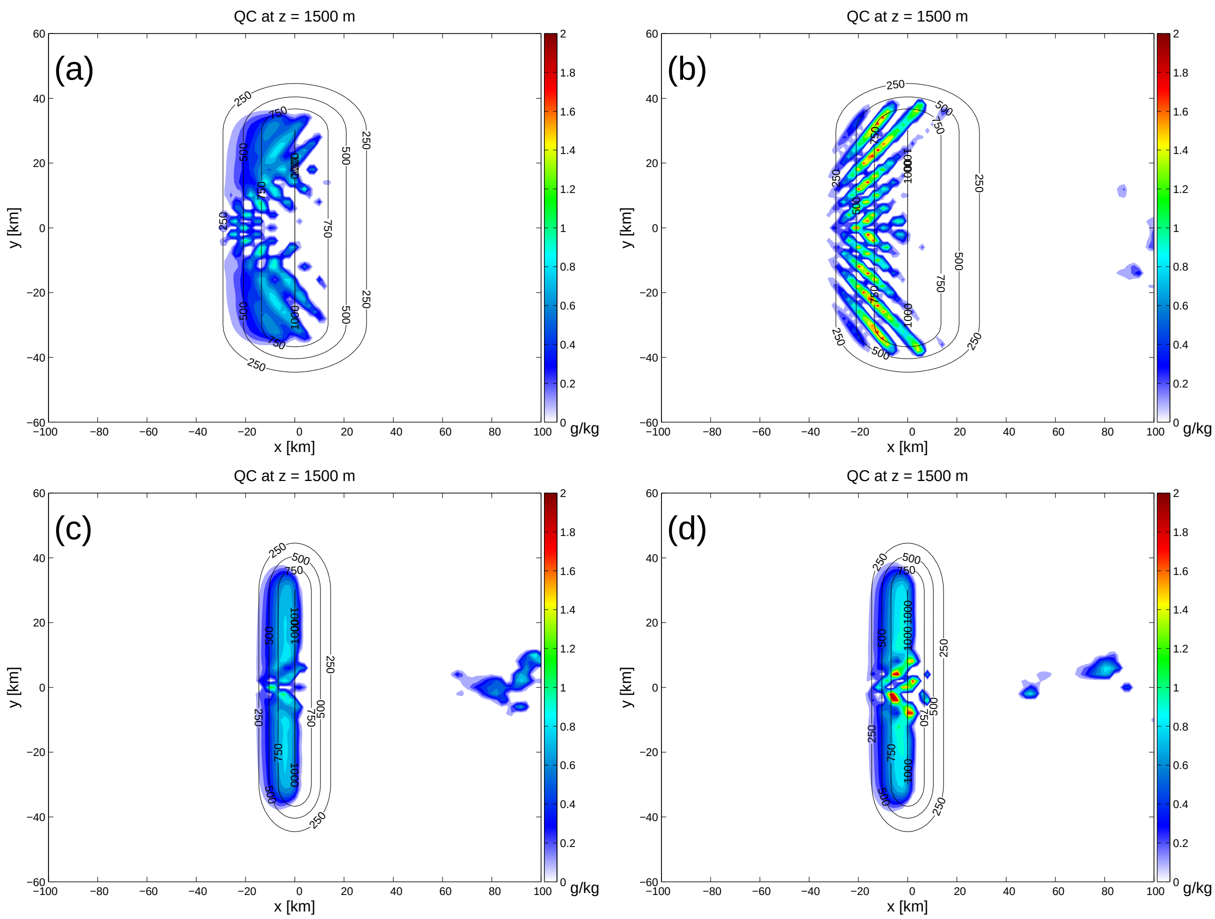

Figure 7: Same as figure 4 but for the simulations with $T_{SL} = 295$ K.

as the ratio of the mountain half-width a to the mean incoming windspeed U which yields $\tau_{adv} = 11$ min. for the narrow mountain range and $\tau_{adv} = 22$ min. for the wide mountain range. The microphysical timescales τ_{mp} (i.e. the time to convert water vapor to precipitation) is determined directly from the model simulations from the timescales of autoconversion and accretion such that

$$\tau_{mp} = \frac{L_c}{\left(\frac{\partial L_c}{\partial t}\right)_{AU} + \left(\frac{\partial L_c}{\partial t}\right)_{AC}} \qquad (6)$$

with L_c the cloud liquid water content. The conversion rates for the cloud water mass are $\left(\frac{\partial L_c}{\partial t}\right)_{AU}$ for autoconversion and $\left(\frac{\partial L_c}{\partial t}\right)_{AC}$ for accretion.

For a detailed discussion on the parameterization of autoconversion and accretion we refer to Seifert and Beheng (2006). The conversion rates of e.g. condensation and nucleation are assumed to be small and, thus, are neglected. Comparing the timescales for the simulation WI and SU in figure 6 reveals that the microphysical timescale τ_{mp} is much larger in the simulation SU than in the simulation WI and also

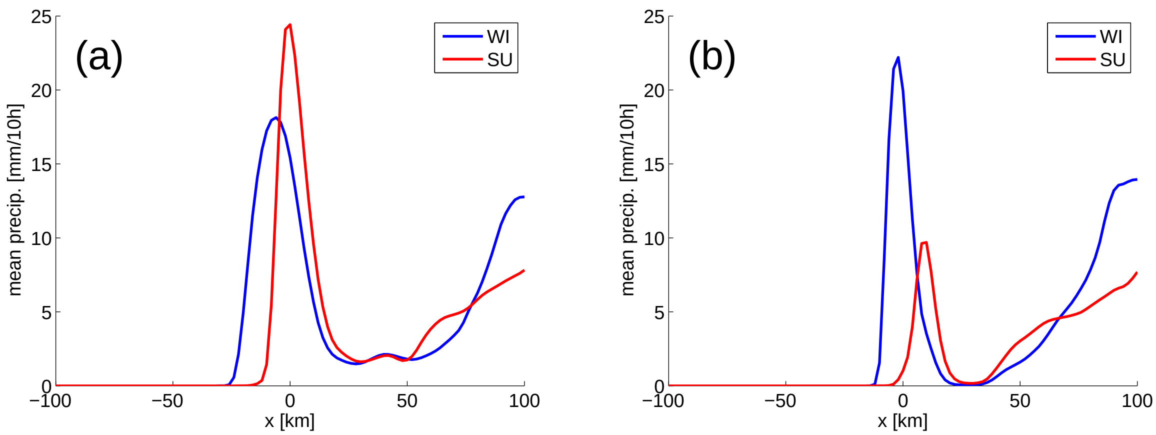

Figure 8: Same as figure 5 but for the simulations with $T_{SL} = 295$ K. The half-width of the idealized topography is $a = 20$ km in panel (a) and $a = 10$ km in panel (b).

much larger than the advective timescale. This may be interpreted such that the advection time of an air-parcel in the updraft region of the mountain wave is to short to yield a conversion of the cloud water to rain by autoconversion and accretion. Because the advection time is a function of the mountain width explains qualitatively why the aerosol indirect effect on precipitation is larger for the narrow mountain than for the wide mountain.

4b. *Convective orographic precipitation*

In the second example we repeat our simulations with the unstable sounding with $T_{SL} = 295$ K discussed in section 3. The fields of cloud liquid water are shown in figure 7 after 10 h of simulation. In contrast to the previous simulations which developed a single contiguous orographic clouds the orographic cloud breaks up into multiple small convective cells on the upslope side of the mountain embedded in the mean cross barrier flow. At the centerline the cells develop small cellular convective structures whereas at the flanks of the mountain the convective cells organize themselves into elongated rainbands. Similar to the previous simulations the cloud liquid water is increased with increasing aerosol number concentrations. Increasing the aerosol number concentrations lead also to an interesting dynamical feedback on the convective clouds which is exhibited in a higher degree of organization of the elongated rainbands.

Similar features in the cloud development are evident in the simulation with the narrow mountain. In both cases (WI and SU) reducing the mountain width does not allow the convective clouds to break up and to organize themselves into rainbands. However, small convective cells develop on the upslope side of the mountain close to the centerline which are advected to the leeward side by the cross-barrier flow and contribute to the leeward precipitation pattern. The convective cells are more strongly developed if the aerosol number concentrations are increased and exhibit higher liquid water contents. The precipitation distribution for the convective orographic precipitation case is shown in figure 8. In the case of the wide mountain ($a = 20$ km) the

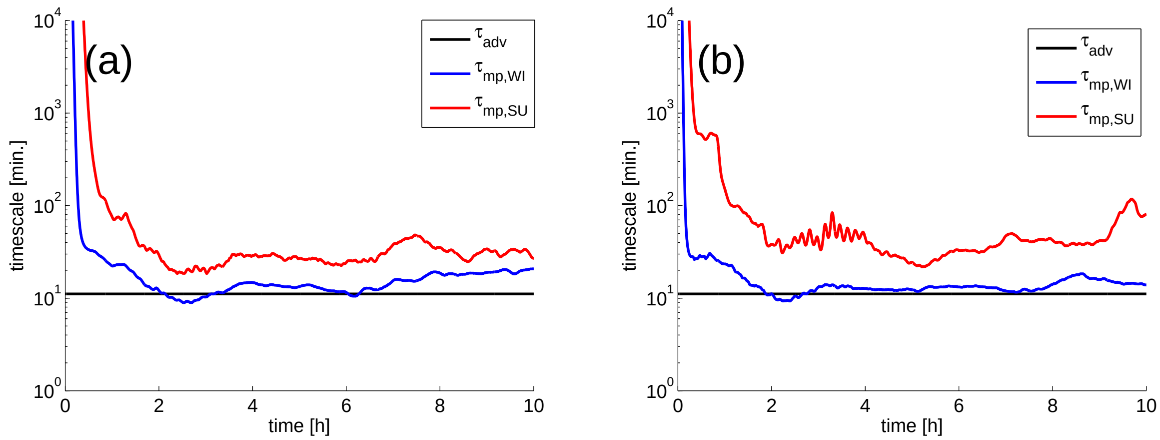

Figure 9: Same as figure 6 but for the simulations with $T_{SL} = 295$ K. The simulation with wide mountain ($a = 20$ km) is shown in panel (a) whereas the simulation with narrow mountain ($a = 10$ km) is shown in panel (b).

precipitation is reduced on the upslope side of the mountain but increased close to the mountain top and on the leeward side of the mountain. In the simulation with narrow mountain a similar orographic precipitation pattern can be found but, again, the precipitation distribution is shifted towards the leeward side of the mountain. In both simulation an increase in the aerosol number concentrations leads to a decrease in the upslope component of the orographic precipitation but also to a reduction of the total orographic precipitation. Similar to the previous simulations the overall precipitation loss is smaller in the simulation with wide mountain (13 %) than in the simulation with narrow mountain (41 %). The timescales for the convective orographic precipitation case are shown in figure 9. In the wide mountain case the microphysical timescales are on the same order of magnitude and are comparable to timescale of advection leading to a relatively small indirect aerosol effect. In contrast, the microphysical timescale is larger in the simulation with increased aerosol load and is considerably larger than the advective timescale if the mountain width is decreased which leads to a larger indirect aerosol effect on orographic precipitation for narrow mountain ranges. However, the differences between the microphysical timescales induced by the aerosol concentrations are much lower in the convective orographic precipitation case than in the stratiform suggesting that other dynamical timescales besides the advection timescale are important in this case.

5. DISCUSSION AND OUTLOOK

In this paper timescales relevant for the orographic precipitation development are analyzed in view of the indirect aerosol effect. It turns out, that for stratiform as well as convective orographic precipitation a qualitative understanding on the magnitude of the indirect effect on orographic precipitation can be established by comparing the advective timescale (i.e. the timescale of airparcels in the updraft region of a mountain wave) to the microphysical timescale (i.e. the time required to transform water vapor into precipitation). However, the advection timescale alone is not able to explain why the indirect aerosol effect is much lower for convective orographic precipitation than for stratiform orographic precipitation and why the formation of elongated rainbands is enforced if the aerosol number is increased. This suggest that additional relevant timescales exist (e.g. timescale for convective growth) which are important for the development of orographic precipitation and for magnitude of the indirect aerosol effect on orographic precipitation. Investigating these timescales and their role in explaining aerosol-cloud-precipitation interactions in warm-phase and mixed-phase orographic clouds is subject to further research.

Acknowledgments

We thank Axel Seifert from the German Weather Service (DWD) and Oliver Fuhrer from the Swiss National Weather Service (MeteoSwiss). We acknowledge the European Centre for Medium-range Weather Forecasts (ECMWF) for providing computing time within the special project Cloud-Aerosol Interactions (SPCHCLAI) and the financial support provided by the International Conference on Clouds and Precipitation (ICCP).

References

Bott, A., 1989: A positive definite advection scheme obtained by nonlinear renormalization of the advective fluxes. *Mon. Weather Rev.*, **117**, 1006–1015.

Choularton, T., K. Bower, E. Weingartner, I. Crawford, H. Coe, M. Gallagher, M. Flynn, J. Crosier, P. Connolly, A. Targino, M. Alfarra, U. Baltensperger, S. Sjogren, B. Verheggen, J. Cozic, and M. Gysel, 2008: The influence of small aerosol particles on the properties of water and ice clouds. *Faraday Discuss.*, **137**, 205–222.

Clark, T. L. and R. Farley, 1984: Severe downslope windstorm calculations in two and three spatial dimensions using anelastic interactive grid nesting: A possible mechanism for gustiness. *J. Atmos. Sci.*, **41**, 329–350.

Colle, B. A., 2004: Sensitivity of orographic precipitation to changing ambient conditions and terrain geometries: An idealized modeling perspective. *J. Atmos. Sci.*, **61**, 588–606.

Cozic, J., B. Verheggen, E. Weingartner, J. Crosier, K. Bower, M. Flynn, H. Coe, S. Henning, M. Steinbacher, M. C. Coen, A. Petzold, and U. Baltensperger, 2007: Chemical composition of free tropospheric aerosol for PM1 and coarse mode at the high alpine site Jungfraujoch. *Atmos. Chem. Phys. Dis.*, **7**, 12145–12184.

Davies, H., 1976: A lateral boundary formulation for multi-level prediction models. *Q. J. R. Meteorol. Soc.*, **102**, 405–418.

Doms, G. and U. Schättler, 2002: A description of the nonhydrostatic regional model LM. Part I: Dynamics and numerics. Technical report, Deutscher Wetterdienst, Offenbach, Germany.

Herzog, H.-J., G. Vogel, and U. Schubert, 2002: LLM - a nonhydrostatic model applied to high-resolving simulations of turbulent fluxes over heterogeneous terrain. *Theor. and Appl. Climatol.*, **73**, 67–86.

Jiang, Q. and R. Smith, 2003: Cloud timescales and orographic precipitation. *J. Atmos. Sci.*, **60**, 1543–1559.

Kirshbaum, D. J. and D. R. Durran, 2004: Factors governing cellular convection in orographic precipitation. *J. Atmos. Sci.*, **61**, 682–698.

— 2005: Observations and modeling of banded orographic convection. *J. Atmos. Sci.*, **62**, 1463–1479.

Muhlbauer, A. and U. Lohmann, 2008: Sensitivity studies of the role of aerosols in warm-phase orographic precipitation in different dynamical flow regimes. *J. Atmos. Sci.*, in press.

Roe, G. H. and M. Baker, 2006: Microphysical and geometrical controls on the pattern of orographic precipitation. *J. Atmos. Sci.*, **63**, 861–880.

Schär, C., D. Leuenberger, O. Fuhrer, D. Lüthi, and C. Girard, 2002: A new terrain-following vertical coordinate formulation for atmospheric prediction models. *Mon. Weather Rev.*, **130**, 2459–2480.

Seifert, A. and K. D. Beheng, 2006: A two-moment cloud microphysics parameterization for mixed-phase clouds. Part I: Model description. *Meteorol. Atmos. Phys.*, **92**, 45–66.

Smith, R., 1979: The influence of mountains on the atmosphere. *Adv. Geophys.*, **21**, 87–230.

Smith, R. and I. Barstad, 2004: A Linear Theory of Orographic Precipitation. *J. Atmos. Sci.*, **61**, 1377–1391.

Spichtinger, P., 2004: *Eisübersättigte Regionen*. Ph.D. thesis, Deutsches Zentrum für Luft- und Raumfahrt, 208 pp.

Steppeler, J., G. Doms, U. Schättler, H. Bitzer, A. Gassmann, U. Damrath, and G. Gregoric, 2003: Meso-gamma scale forecasts using the nonhydrostatic model LM. *Meteorol. Atmos. Phys.*, **82**, 75–96.

Weingartner, E., S. Nyeki, and U. Baltensperger, 1999: Seasonal and diurnal variation of aerosol size distributions ($10 < d < 750$ nm) at a high-alpine site (Jungfraujoch 3580 m asl). *J. Geophys. Res.*, **104**, 26809–26820.

Wicker, L. J. and W. C. Skamarock, 2002: Time-splitting methods for elastic models using forward time schemes. *Mon. Weather Rev.*, **130**, 2088–2097.

INTERACTIONS OF ASIAN EMISSIONS WITH STORMS IN THE PACIFIC OCEAN: EARLY RESULTS FROM THE PACIFIC DUST EXPERIMENT (PACDEX)

J. Stith[1], W. A. Cooper[1], V. Ramanathan[2], D. C. Rogers[1], P. J. DeMott[3], T. Campos[1], B. Adhikary[4]
[1]National Center for Atmospheric Research
[2]Scripps Institute of Oceanography
[3]Colorado State University
[4]University of Iowa

1. INTRODUCTION.

The long-range transport of dust and anthropogenic aerosols and pollution from Asia across the Pacific Ocean into North America is one of the most widespread and major pollution events on the planet. This plume passes through Pacific Ocean extra tropical cyclonic storms, which are important climate regulators. The effect of this mixed dust-pollution plume on the Pacific cloud systems and the associated radiative forcing is an outstanding problem for understanding climate change and has not been adequately explored.

PACDEX was a pilot study using quasi-Lagrangian sampling of this Asian-Pacific dust and pollution plume with the NSF/NCAR G-V research aircraft to follow the plume as it interacted with maritime Pacific storms. The aircraft was instrumented for measuring cloud active aerosols, selected trace gases, upward and downward spectral irradiance, actinic flux, and several instruments for measuring size-resolved cloud microphysics. Detailed information on the instrumentation is provided at http://www.eol.ucar.edu/projects/pacdex/science/instrumentation.html. Source-specific chemical transport modeling was also used to guide the research flights, which took place in April and May of 2007.

The concentrations of ice forming nuclei (IN) were measured by the Colorado Statue University Continuous Flow Diffusion Chamber. Comparisons between IN measurements from this instrument and particle size distributions in many different locations reveal a significant correlation between the concentrations of particles greater than 0.5 microns and IN (DeMott et al, this conference and private communication). This may be due to the presence of mineral dusts in the large particle mode acting as IN. Particle concentrations between 0.1 and 1.0 microns were measured in situ by an Ultra-High Sensitivity Aerosol Spectrometer (UHSAS, manufactured by DMT). Here, we report on this large particle mode using measurements from the UHSAS between 0.5 and 1.0 microns. (Further comparisons between IN and this large particle mode are in progress.) Bulk samples for chemical analysis and electron microscopy were taken in many of these regions and are currently undergoing analysis. Preliminary results confirm the presence of mineral aerosol in the large particle regions that have been examined, to-date.

Fast-response CCN measurements were made with a double-column Continuous-Flow Streamwise Thermal Gradient CCN Chamber. The continuous-flow thermal gradient diffusion chamber (Roberts and Nenes, 2005) was developed for autonomous operation in airborne studies employing a novel technique of generating a supersaturation along the streamwise axis of the instrument. CCN data presented here were provided courtesy of Greg Roberts, Scripps Institute of Oceanography.

Several Pacific storms were sampled extensively during PACDEX, including measurements in warm cloud regions, cold regions (ice only) and mixed phase regions. This paper will present early results from sampling of these Pacific Maritime storms and will compare some of the microphysical characteristics of a near-source (Western Pacific) storms, with a mid-Pacific storm, with emphasis on possible effects due to Asian dust and pollution.

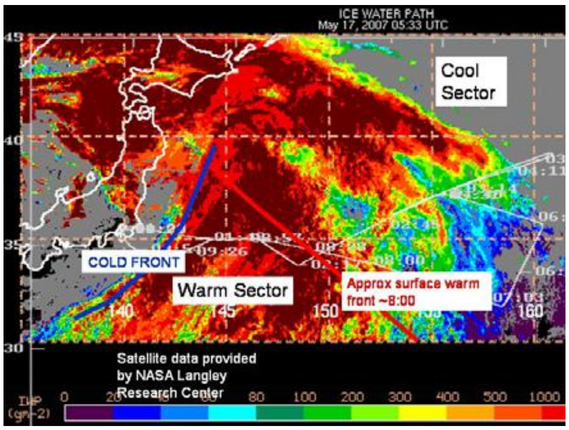

Figure 1. Ice water path observations of the storm on 17 May 2007 at 05:33 (UTC), midway through the aircraft sampling. The flight track of the G-V is plotted, as are the approximate location of the surface cold and warm front.

2. Results

On 17 May 2007 an extratropical cyclonic storm was sampled just East of Japan (Fig. 1). The G-V made several passes through the warm front horizontally and also did several vertical profiles through the frontal surface. An example of one of these profiles is given in Fig. 2. The location of the frontal surface was identified by reference to wind shifts and temperature changes and is shown by the arrow in the figure. Three distinct regions are also evident in the figure in the chemical measurements of CO, O_3, and aerosols. The top region (above the warm front, i.e. in warm sector air) contained relatively high levels of CO, but surprisingly low concentrations of aerosol. The region immediately below the warm front (i.e. cool sector air) contained less CO, but higher concentrations of aerosols. The lowest layer, which was in the boundary layer in

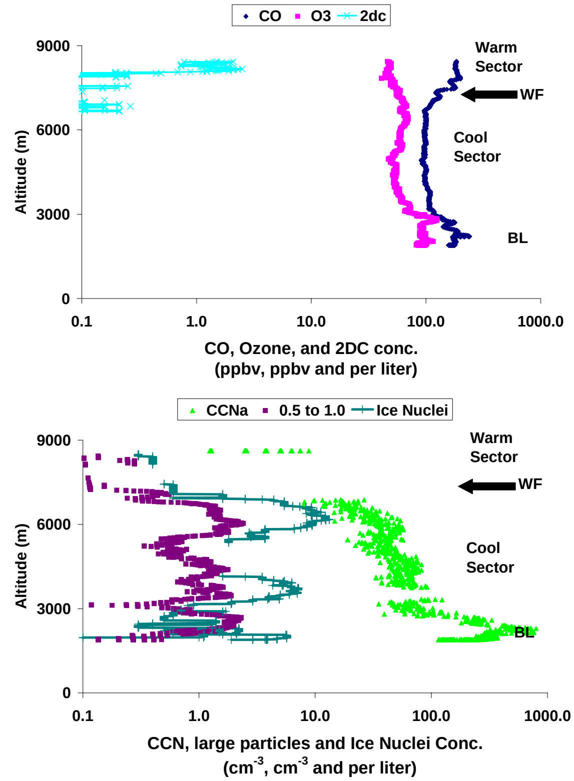

Figure 2. Vertical (descent) profile through the warm front near the southern part of the track in Fig. 1. The location of the warm front on the ascent is indicated by the arrow. Ozone data courtesy of Ru-shan Gao, NOAA. CCN supersaturation was ~ 0.2%. IN were measured at ~-17C and 102% RH.

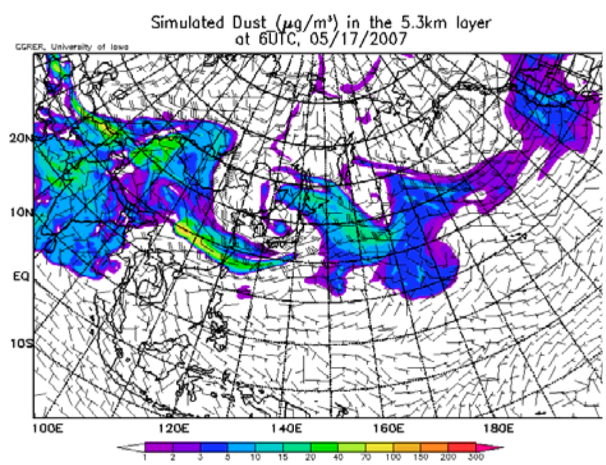

Figure 3. STEM simulation of the location of dust on 17 May 2007. Note the high dust levels near 160 E in the cool sector of the storm in Fig. 1

Carmichael et al., 2003) chemical modeling system indicated dust (and other aerosols, not shown) located primarily in the cool sector region, northeast of the warm frontal region (Fig. 3). This is consistent with our observations of the large particles, IN and CCN in the cool sector (Fig. 2).

The trajectories of air in the warm sector and cool sector regions are given in Fig. 4. These suggest that both trajectories were from anthropogenic source regions in Asia. The cool sector air passed near dust source regions. HYSPLIT precipitation history is given in Fig. 5

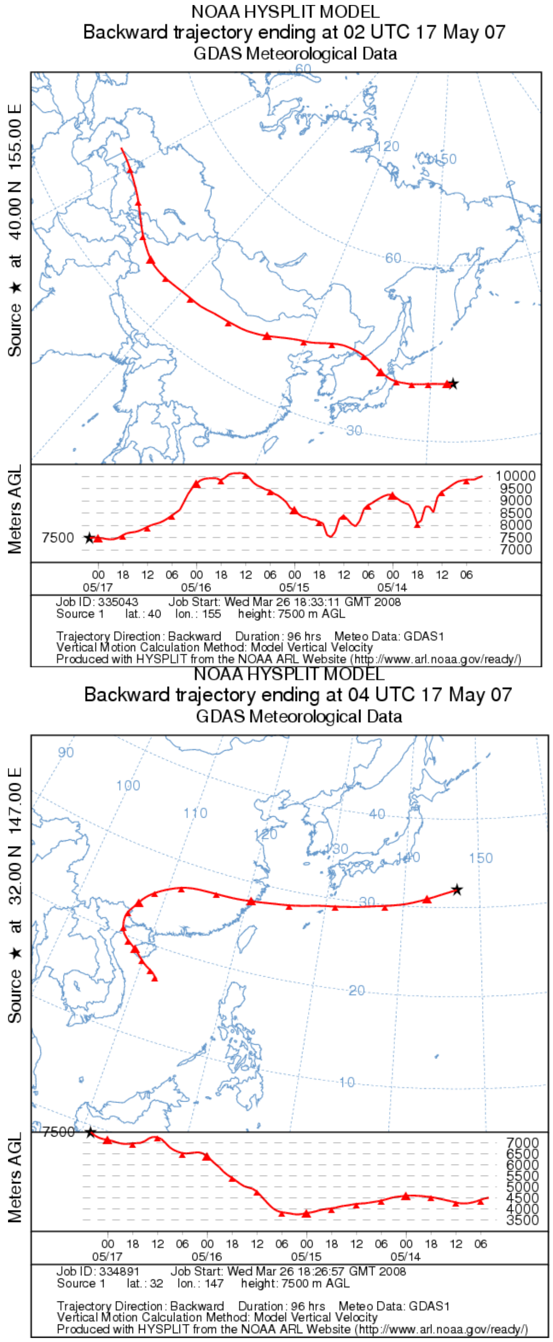

Figure 4. 96 hour HYSPLIT (Draxler and Rolph, 2003) back trajectories for air near the sampling location for the cool sector air (top) and warm sector air (bottom).

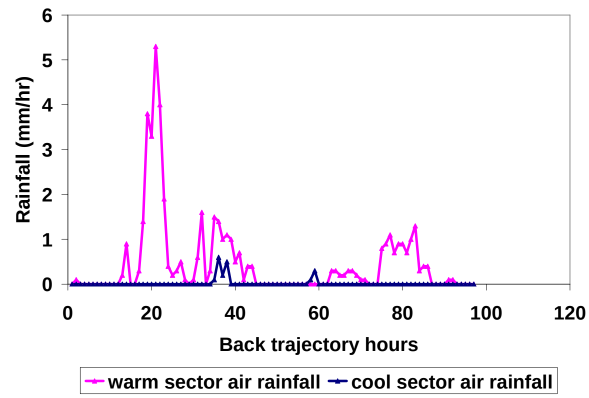

Figure 5. HYSPLIT back trajectory rainfall rate for the two airmass regions.

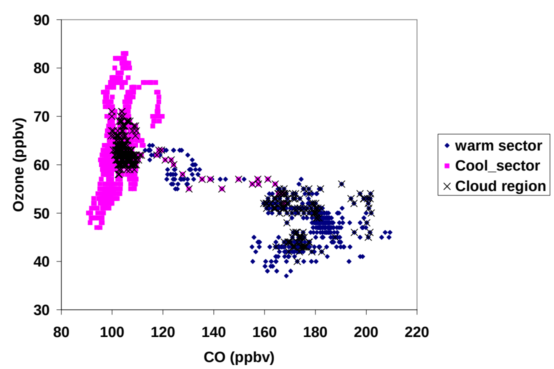

Figure 6. Mixing analysis of the warm and cool sector air (excluding the boundary layer) for the vertical profile in Fig. 2 and a second nearby profile (ascent).

cool sector air contained the highest levels of CO and aerosols. Forecasts of dust concentrations made with the Sulfur Transport and Deposition Model (STEM,

Figs. 4 and 5 offer a possible explanation

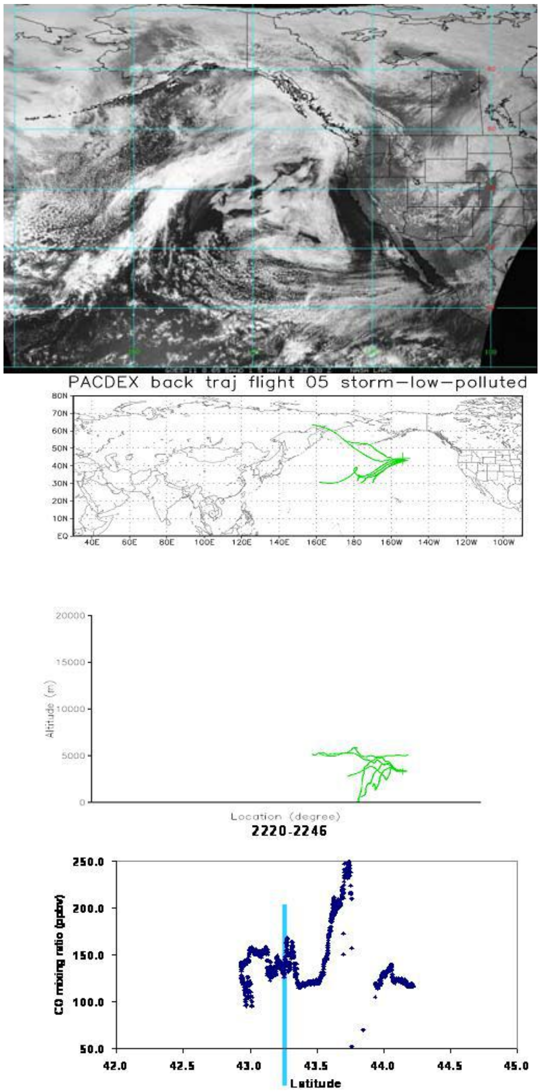

Figure 7. The storm on 5 May 2007 (top), the results of the STEM model trajectory, in horizontal and vertical coordinates (middle) and in situ sampling of CO through the front (bottom). The position of the front is indicated by the light blue line.

for the differences in chemical characteristics between the warm and cool sectors. The warm sector air originated from source regions of anthropogenic pollution (i.e. high levels of CO), but encountered many hours of precipitation in cloud before we sampled the air, which may have removed most of the aerosols and left the CO.

A mixing diagram, using ozone and CO is given in Fig. 6. Only a small portion of the air (about 400 m) near the frontal surface was a mixture of the two airmasses. Therefore, only the lower portion of the clouds in the warm sector would have encountered the higher concentrations of dust and other aerosols in the cool sector.

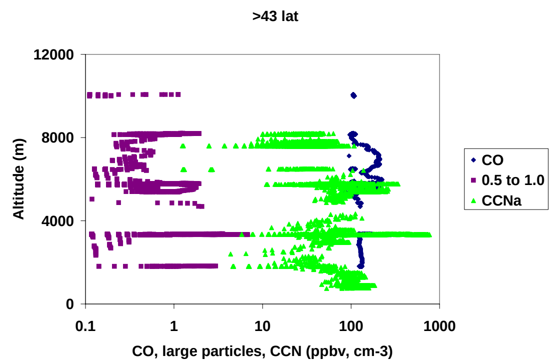

Figure 8. Vertical profile of CO, CCN (at approximately 0.1 % supersaturation), and large particles in the airmass north of the front in Fig. 7.

A second storm was sampled in the mid-Eastern Pacific on 5 May 2007. This storm was much weaker than the 17 May storm and consisted of a nearly stationary front, located approximately midway between Alaska and Hawaii (Fig. 7). Trajectory analysis of the STEM model through the frontal region showed a clear bifurcation of the trajectories north and south of the front. The (cold) airmass on the north side of the front came from Russia and relatively high altitudes, while the southern side of the front was from lower altitudes in the central North Pacific. Preliminary chemical analysis of this case suggest a major component of the aerosol contained organic and black carbon (Jim Anderson, Arizona State University, Private communication), which may be due to biomass burning in Russia that was transported across the Pacific; however, this hypothesis is currently being investigated.

Comparison of the CO and CCN concentrations in Figs 2 and 8, suggest that similar levels of each are found in the more polluted sides of the frontal regions of these storms, even though they occur in different regions of the Pacific. However, the concentrations of CCN are not particularly high, even in the more polluted airmasses associated with these storms. Comparison of vertical profiles of droplet concentrations in these two storms confirms that similar

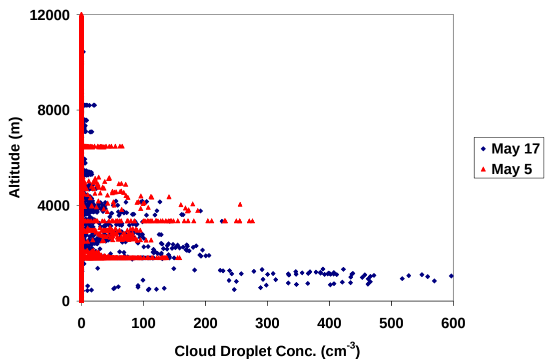

Figure 9. Vertical profile of droplet concentrations for the storms on May 5 and May 17 1007.

concentrations of droplets are found in each (Figure 9).

These early results from PACDEX suggest roughly similar levels of pollutants and CCN in Western and mid-Eastern Pacific storms. These aerosol observations are corroborated by measurements confirming similar vertical profiles of cloud droplet concentrations in both of the storms that were sampled. Future analysis will examine additional storms and will also focus on studying the interactions of the dust regions with cold portions of these storms.

REFERENCES

Carmichael, G. R., Y. Tang, G. Kurata, I. Uno, D.G. Streets, J.-H. Woo, H. Huang, J. Yienger, B. Lefer, R.E. Shetter, D.R. Blake, A. Fried, E. Apel, F. Eisele, C. Cantrell, M.A. Avery, J.D. Barrick, G.W. Sachse, W.L. Brune, S.T. Sandholm, Y. Kondo, H.B. Singh, R.W. Talbot, A. Bandy, A.D. Clarke, and B.G. Heikes, Regional-Scale chemical transport modeling in support of intensive field experiments: overview and analysis of the TRACE-P observations, Journal of Geophysical Research, 108(D21), 8823, doi:10.1029/2002JD003117, 2003.

Draxler, R.R. and Rolph, G.D., 2003. HYSPLIT (HYbrid Single-Particle Lagrangian Integrated Trajectory) Model access via NOAA ARL READY Website (http://www.arl.noaa.gov/ready/hysplit4.html). NOAA Air Resources Laboratory, Silver Spring, MD.

Roberts, G., and A. Nenes, A continuous-flow streamwise thermal-gradient CCN chamber for airborne measurements, Aero Sci Tech (39), 206-221, 2005.

Acknowledgments.

The support of the US National Science foundation for PACDEX and many of the PACDEX investigators is gratefully acknowledged. The National Center for Atmospheric Research is supported by the National Science Foundation. P. DeMott is supported by NSF grant ATM0611936. The authors also acknowledge the NOAA Air Resources Laboratory (ARL) for the provision of the HYSPLIT transport and dispersion model and/or READY website (http://www.arl.noaa.gov/ready.html).

ON THE RELATIVE EFFECTS OF MODIFYING AEROSOL LOADINGS AND THERMODYNAMIC CONDITIONS TO PRECIPITATION FROM MIXED-PHASE CONVECTIVE CLOUDS

A. Teller[1], Z. Levin[2]

[1] Research Applications Laboratory, National Center for Atmospheric Research, Boulder, CO, USA
[2] Department of Geophysics and Planetary Sciences, Tel Aviv University, Tel Aviv, Israel

1. INTRODUCTION

Recent numerical modeling studies and observations show that an increase of aerosol loading due to air pollution can either increase or decrease precipitation from convective clouds depending on the environmental conditions. Currently, none of these studies provide a quantitative evaluation of the relative contribution of these factors to precipitation suppression or enhancement. It is essential to study these relative contributions in order, for example, to learn about the effects of air pollution on precipitation amount in different regions.
The **Factorial Method** (FM) used in this study is a statistical tool that can be used to design and to analyze experiments in which the interaction of the various parameters affect the final product. In the present study this method is used in numerical simulations aimed at evaluating the sensitivity of precipitation to changes in various parameters, including aerosol loading and atmospheric sounding.
The Tel Aviv University 2D (TAU 2D) cloud model was used to determine the relative sensitivity of precipitation from Eastern Mediterranean winter mixed-phase convective clouds, to changes in the concentration of Cloud Condensation Nuclei (CCN), and initial atmospheric thermodynamic conditions.

2. THE METHOD

2.1 <u>THE FACTORIAL METHOD</u>

The experimental setup in this study is based on the unreplicated 2^k factorial design of experiments discussed in many statistical textbooks. Here we use the method and the notation of Montgomery (2001).
In this study the relative contributions of two factors to changes in surface precipitation from a single cloud are tested. The factors chosen for this study include the initial atmospheric sounding (affecting the bulk physical properties of the cloud e.g. liquid water content, vertical velocity and cloud top height) and initial CCN concentration. A more in depth study on the contribution of different mechanism of ice formation (nucleation by deposition and immersion freezing) is discussed in Teller and Levin (2008).
The method of calculation is illustrated for a case in which the sensitivity of precipitation to three parameters (e.g. CCN concentration, atmospheric thermodynamic profile, and initial ice concentration) is evaluated. The factors are denoted by A, B and C, respectively. It is also assumed that each of these factors can be set to only two different values (high and low) where the high value (a strong effect) denotes a condition in which precipitation is expected to be suppressed.
In this study it is assumed that the response of the surface precipitation to the different factors is a monotonic function containing no singular points.
Each run of the simulation is labeled according to the value of the factors used such that a high value of any factor A, B or C is denoted by a lowercase letter a, b, c and the low value of each factor is denoted by the absence of the corresponding letter. Therefore in an example of three factors we have 8 simulation runs (2^3) labeled by (1), a, b, c, ab, ac, bc and abc (the label (1)

represents a reference i.e. a run where all factors are set to their lower values.
Figure 1 shows a graphical illustration of the experimental design with three factors where the eight experiments can be presented on a cube with each experiment occupying one of the corners.

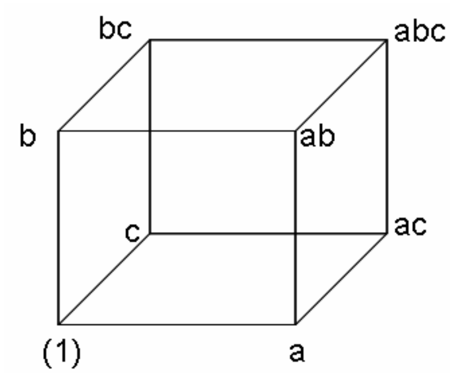

Figure 1 *- Graphical illustration of an experimental setup containing 3 factors with 2 values each (a 2^3 experimental design). The 8 experiments are placed at the corners of a cube where each dimension represents a single main effect (A, B, C)*

The term "effect" shows the average sensitivity of the result to a change in one factor and it is calculated by subtracting the average of the results when the factor is set to its low value from the average of the results when the factor is set to its high value. The “interaction” effect is the contribution of the combined changes by more than one factor within the experimental design.
The difference between the averages of the simulations with A set high and low is calculated by:

$$\mathrm{Eff_A} = \frac{1}{4}\cdot(\mathrm{a + ab + ac + abc}) - \frac{1}{4}\cdot(\mathrm{b + c + bc + (1)}) \qquad \mathrm{Eq.\,1}$$

Similarly, the difference between the averages of the factors B and C are calculated by:

$$\mathrm{Eff_B} = \frac{1}{4}\cdot(\mathrm{b + ab + bc + abc}) - \frac{1}{4}\cdot(\mathrm{a + c + ac + (1)}) \qquad \mathrm{Eq.\,2}$$

$$\mathrm{Eff_C} = \frac{1}{4}\cdot(\mathrm{c + ac + bc + abc}) - \frac{1}{4}\cdot(\mathrm{a + b + ab + (1)}) \qquad \mathrm{Eq.\,3}$$

The effect of the interactions between two factors is defined as half of the difference between the average effects of one factor when the second one is set to its high value to the average effects of the second factor when the first is set to its lower value.
For example, the effect of the interaction AB in the above design is calculated by:

$$\mathrm{Eff_{A\,(B=high)}} = \frac{1}{2}\cdot(\mathrm{abc - bc}) + \frac{1}{2}\cdot(\mathrm{ab - b}) \qquad \mathrm{Eq.\,4}$$

$$\mathrm{Eff_{A\,(B=low)}} = \frac{1}{2}\cdot(\mathrm{ac - c}) - \frac{1}{2}\cdot(\mathrm{a - (1)}) \qquad \mathrm{Eq.\,5}$$

And the difference between these terms is the interaction:

$$\begin{aligned}\mathrm{Eff_{AB}} &= \frac{1}{2}\left(\mathrm{Eff_{A\,(B=high)}} - \mathrm{Eff_{A\,(B=low)}}\right) = \\ &= \frac{1}{4}[\mathrm{abc + ab - bc - b - (ac + a - c - (1))}] = \\ &= \frac{1}{4}(\mathrm{abc + ab + c + (1) - bc - b - ac - a}) \qquad \mathrm{Eq.\,6}\end{aligned}$$

The effect of the interaction AB can be seen as the difference between two diagonal planes in the cube of Figure 1.
To evaluate the relative contribution of each effect to the total variability (which is the most significant advantage of the FM), one needs to calculate the sum of squares of each effect and compare it to the total sum of squares (i.e. the total variance of the data).
The sum of squares of the effect A is calculated by:

$$SS_{\mathrm{A}} = \frac{1}{2^3}\cdot(\mathrm{a + ab + ac + abc - b - c - bc - (1)})^2 \qquad \mathrm{Eq.\,7}$$

The calculations of the sum of squares of the effects B, C and the interactions between the effects are performed in the same way.

2.2 <u>THE CLOUD MODEL AND THE EXPERIMENTAL SET UP</u>

We use the TAU 2D numerical cloud model (Yin et al., 2000) to calculate the relative contribution of thermodynamic conditions and aerosol loading on changes in precipitation. This is a detailed microphysical model that uses the Spectral Method of Moments (Tzivion et al., 1987) for calculating the growth of water drops and ice particles. The model is used with 300 m height resolution and 300 m lateral resolution.

The initial thermodynamic profile is taken from Levin et al. (2005) and Teller and Levin (2006) and represents somewhat typical winter-like conditions in the eastern Mediterranean with ground temperature 19 ºC. It is a theoretical profile that enables the development of a mixed-phase convective cloud. The sensitivity of the precipitation to a change in the atmospheric thermodynamic conditions is tested by shifting the entire thermodynamic sounding to colder temperatures (without changing the relative humidity).

The initial conditions of the CCN vertical size distribution profiles and their chemical compositions for the Mediterranean clouds are set according to the airborne physical and chemical measurements reported by Levin et al. (2005).

The simulations are run with initial surface CCN concentrations that vary between 225 cm^{-3} ("clean cloud") 600, 900 and 1530 cm^{-3} ("polluted cloud"). The shape of the size distribution profile is identical in all the cases.

3. RESULTS

3.1 THE EFFECTS OF AEROSOLS AND THERMODYNAMIC CONDITIONS ON PRECIPITATION

Figure 2 shows the total accumulated precipitation on the ground as a function of the initial CCN concentration for the cases analyzed. This figure shows the suppression effects of colder atmospheric thermodynamic condition and increased CCN on precipitation.

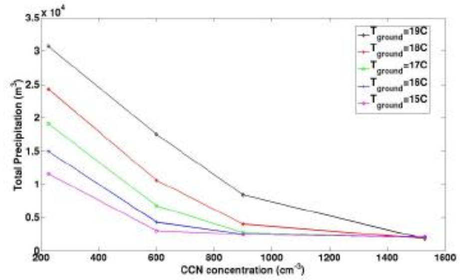

Figure 2 *- Total ground precipitation as a function of initial CCN concentration.*

Figure 3 shows for the case with Tg=19 ℃ the average Liquid Water Content (LWC), graupel content and ice crystals (in g m^{-3}) as a function of time and height in the clean and polluted clouds; 225 and 1530 cm^{-3}, respectively. It shows that in the clean cloud (Figure 3a) at a height of 4000 to 5500 m the LWC and the graupel content are about equal; 1 g m^{-3}. Later on graupel particles descend and slowly melt. Below 2000 m (~0 ℃) a large fraction of the graupel particles melt, thus contributing to the rainfall on the ground. The graupel particles contribute about 65% of the total accumulated precipitable content. At lower altitudes the LWC increases due to the melting of the graupel particles.

Figure 3b shows that the graupel content reaches a lower maximum value and at a later stage as compared to the clean case. The graupel particles begin to melt after falling below about 2000 m but their contribution to the total precipitation is only about 30%. As was pointed out by Teller and Levin (2006) the content of ice crystals in the polluted case is greater because a larger fraction of the ice crystals remaining aloft.

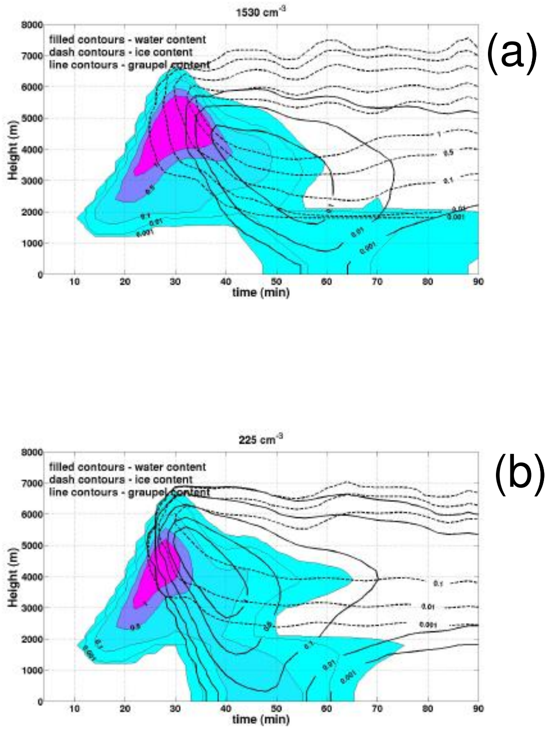

Figure 3 *- The horizontal averaged Liquid Water Content (LWC), graupel content and ice crystals content (in g m^{-3}) as a function of time and height in the (a) clean (225 cm^{-3}) and (b) polluted (1530 cm^{-3}) clouds at Tg=19 ℃.*

3.2 <u>THE RELATIVE CONTRIBUTION OF ATMOSPHERIC SOUNDING AND CLOUD MICROPHYSICS TO PRECIPITATION</u>

Figure 4 shows the relative contribution of the atmospheric sounding, the initial CCN concentration and their interactions when the effect of these two factors is analyzed. Figure 5 shows a graphical illustration of how to interpret the results shown on Figure 4. The gray rectangles in Figure 5 mark the experimental design while each corner in a rectangle marks a single experiment. The figures show the relative contribution of CCN and atmospheric sounding to the suppression of precipitation in each experimental design.

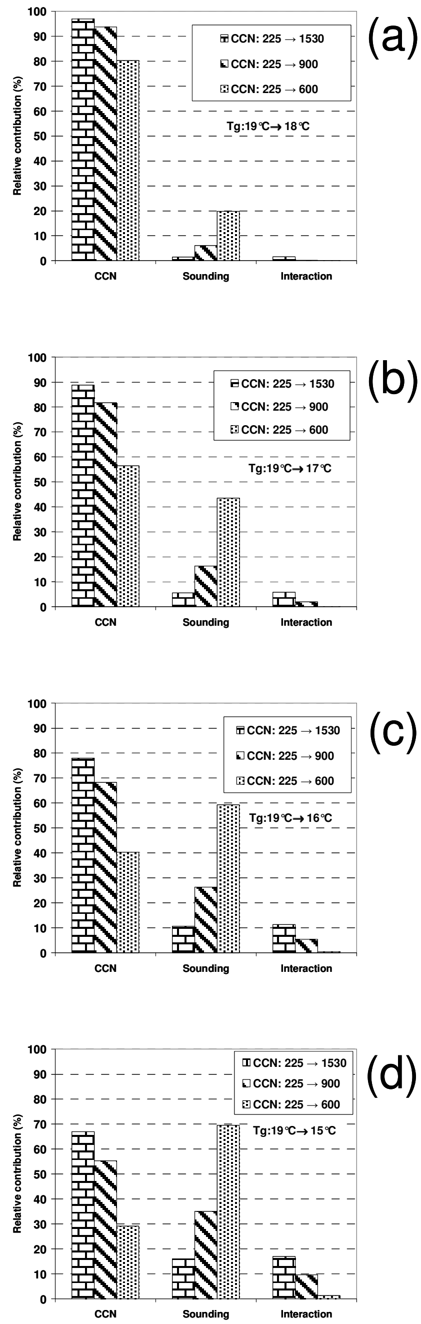

Figure 4 *- The relative contributions to precipitation suppression due to changing of CCN concentrations and atmospheric soundings.*

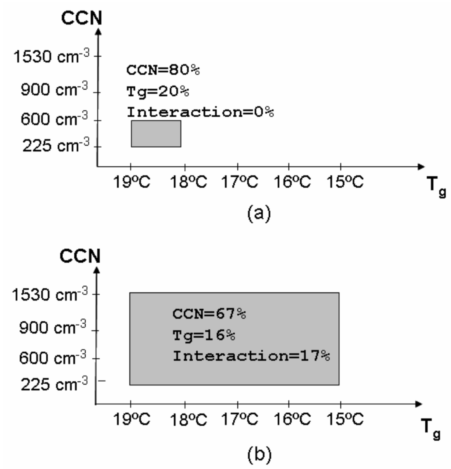

Figure 5 *- Graphical illustration of the experimental design for calculation the relative contributions to precipitation suppression due to changing of CCN concentrations and atmospheric soundings*

The relative quantitative effects of increased CCN and decreased Tg to the suppression of precipitation can be seen by the relative contribution of each when the Tg is first changed from 19 °C to 17 °C, the CCN from 225 cm^{-3} to 600 cm^{-3} and then Tg is changed from 19 °C to 15 °C and CCN from 225 cm^{-3} to 900 cm^{-3}. From Figure 4 it becomes clear that the increase in CCN by 375 cm^{-3} when the temperature is lowered from 19 °C to 17 °C contributes 56% to the suppression of precipitation, while the change in Tg only contributes 43%. However, further lowering Tg to 15 °C and increasing CCN in the same amount as in the previous experiment, namely to 600 cm^{-3}, reduces the effects of CCN to 29%, while increasing the effects of the lower temperature to 69%. Further increase of the CCN to 900 cm^{-3} with Tg lowered from 19 °C to 15 °C, again increases the relative contribution of the CCN to 55%. This illustrates that similar contribution to suppression of precipitation is obtained by either changing Tg by 2 °C or increasing CCN by about 400 cm^{-3}.

4. SUMMARY

We find that a decrease of about 2 °C in the entire profile of the ambient temperature while keeping the relative humidity constant has the same contribution to precipitation suppression as an increase of about 400 cm^{-3} in the CCN concentration.
Other conclusions from similar experiments, which include the ice nucleation process as a factor affecting precipitation, are that the suppression of precipitation is affected more by the increased CCN than by the ice generation processes. However, in colder atmospheric conditions the reverse is true, namely increased ice formation more strongly affects precipitation than increases in CCN.

5. FUTURE WORK

The current study was carried out using the TAU-2D cloud model which is able to simulate only single clouds on a 2 dimensional domain. The proposed Factorial Method will be used for studying the interactions of aerosol-cloud-precipitation in a 3D framework through the use of the Weather Research and Forecast (WRF) simulation coupled with a new bin-microphysics scheme described by Geresdi and Rasmussen (2002) and Rasmussen et al. (2002), which is based on the multi moment method (Tzivion et al. 1987).
One important feature of the above mentioned microphysical scheme is the ability to track the aerosol masses in the droplets and in the ice particles during the cloud development.
With the new FM scheme we will be able to simulate complicated scenarios using the WRF dynamics in 3D.

6. REFERENCES

Geresdi, I., and R. Rasmussen (2005), J. Atmos. Sci., 62(7), 2037.

Levin, Z., et al. (2005), JGR, 110, D20202, doi:10.1029/2005JD005810.

Montgomery, D., C. (2005), Design and Analysis of Experiments, 5th edition, 684 pp. J. Wiley & Sons Inc, New York.

Rasmussen, R.M. et al. (2002), J. Atmos. Sci., 59, 837–860.

Teller, A., and Z. Levin (2006), Atmos. Chem. Phys, 6, 67–80.

Teller, A., and Z. Levin (2008), JGR, doi:10.1029/2007JD008960, 2008.

Tzivion, S. et al. (1987), J. Atmos. Sci., 44, 3139–3149.

Yin Y. et al. (2000), Atmos. Res., 53, 91–116.

INFLUENCE OF ICE CRYSTAL SHAPE ON RETRIEVAL OF CIRRUS OPTICAL THICKNESS AND EFFECTIVE RADIUS

H. Eichler[1], A. Ehrlich[1], M. Wendisch[1], M. Wirth[2], G. Mioche[3], J.-F. Gayet[3]

[1] Institute for Atmospheric Physics, Johannes Gutenberg University Mainz, Germany
[2] Deutsches Zentrum für Luft- und Raumfahrt (DLR), Oberpfaffenhofen, Germany
[3] Laboratoire de Météorologie Physique, Université Blaise Pascal, Clermont Ferrand, France

1. INTRODUCTION

Spectral upwelling radiances above cirrus were measured with the SMART-Albedometer (Spectral Modular Airborne Radiation measurement sysTem) during the field campaign CIRCLE-2 (CIRrus CLoud Experiment-2) in May 2007.

The objective of the campaign was to characterize radiative and microphysical properties of cirrus for improving their representation in mesoscale and global climate models. The campaign also dealt with the validation of satellite observations.

In particular, airborne measurements were made with two research aircraft which were equipped with lidars in nadir looking configuration. In addition, in situ measurements of cloud and aerosol properties as well as upwelling spectral radiances were obtained with the German Falcon aircraft. 15 flights were made over continental Europe, the North Sea and the Atlantic Ocean. A lookup table algorithm as described in Platnick et al. (2001) was used to derive effective radii of the ice particles (R_{eff}) and cirrus optical thickness (τ) from a wavelength pair of spectral cloud reflectances. The cirrus retrieval algorithm was performed for different shape assumptions and thus the influence of ice particle habit on the retrieved properties was quantified. The retrieved R_{eff} were compared with the microphysical measurements, while the retrieved τ were compared with the lidar-derived values.

2. INSTRUMENTATION

The SMART-Albedometer (cf. Wendisch et al. (2001)) measured spectral upwelling radiances in the wavelength range 350-2200 nm. The viewing angle of the optical inlet is 1.5°. Two plain-grated spectrometers operating in the wavelength ranges 350-1050 nm and 900-2200 nm with spectral resolutions (FWHM) of, 2-3 nm and 9-16 nm, respectively, were used. The temporal resolution of the radiance measurement is about 0.5 s which leads to an averaging of 100 m at an aircraft velocity of 200 ms^{-1}.

Backscatter ratios were measured at 1064 nm with the lidar operated by DLR (Deutsches Zentrum für Luft- und Raumfahrt). An extinction correction was made assuming a backscatter-to-extinction-ratio of 20. The *Klett*-inversion method was used to determine the cloud optical thickness.

An FSSP-300 (Foward Scattering Spectrometer Probe, measureing the size distribution and concentration of particles between 3.0-20 μm) and a CPI (Cloud Particle Imager, measureing shapes, concentrations and size distributions of particles from 20 μm to 2.3 mm) operated by LaMP (Laboratoire de Météorologie Physique, Université Blaise Pascal, Clermont Ferrand, France) were used to calculate R_{eff}.

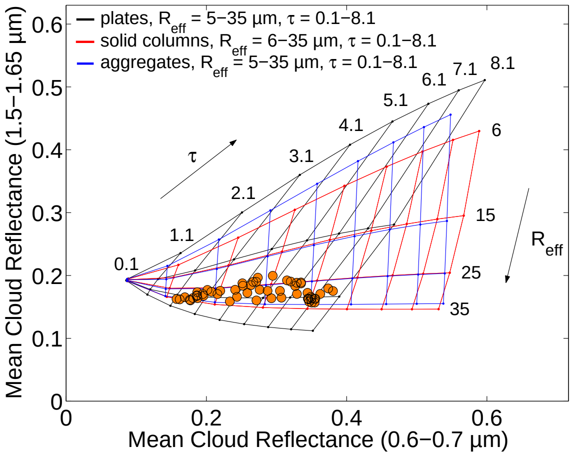

Fig. 1: Cloud retrieval solution space for three particle habits. Observed cloud reflectances of the flight on 22 May, 2007 (period 1, 43146-43220 s, UTC) over land are represented by dots.

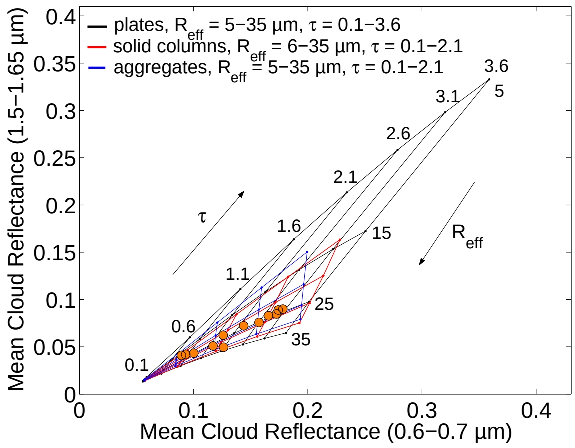

Fig. 2: Cloud retrieval solution space for three particle habits. Observed cloud reflectances of flight on 22 May, 2007 (period 2, 43419-43435 s, UTC) above the North Sea are represented by dots.

3. METHODOLOGY

By performing 1D-radiative transfer modeling with *libRadtran* (the *lib*rary of *Rad*iative *tran*sfer, cf. Mayer and Kylling (2005)) downwelling irradiances at flight height were calculated and combined with the *measured* radiances in order to derive time series of cirrus cloud-top reflectances. Using the ice cloud parametrization by Key et al. (2002) as input to the radiative transfer model, a lookup table of modeled cloud reflectances was generated for a range of optical thicknesses and effective radii (τ = 0.1-8.1, $\Delta\tau$ = 0.5, R_{eff} = 5-35 μm, ΔR_{eff} = 5 μm, cf. Figure 1). In the Key-parametrization optical properties (volume extinction coefficient, asymmetry parameter, and single scattering albedo) for different particle habits (used here: plates, rough aggregates, solid columns) are parameterized as function of ice water content and R_{eff} of 30 in situ particle size distributions. Optical properties are integrated over 56 spectral bands ranging from 0.2-5.0 μm, the wavelength ranges for the cloud retrieval are 0.6-0.7 μm and 1.5-1.65 μm. In the first band, ice is almost non-absorbing and the reflectance largely dependends on cirrus optical thickness (τ). The second band is absorbing for ice particles and provides particle size information. It is used to derive the effective radius (R_{eff}). In order to compare modeled and measured cloud reflectances, measured values were also averaged over the two spectral bands.

The surface albedo is a crucial input to the cloud retrieval algorithm especially for thin cirrus. An algorithm for nonlinear extrapolation of the surface albedo from clear-sky radiance measurements at flight altitude similar to Wendisch et al. (2004) was applied.

4. RESULTS

Results of the cloud retrieval are presented for the flight performed on 22 May, 2007 over two different surfaces - open water (North Sea) and land with green vegetation. Only one aircraft was operated during that day. The flight track led along the West Coast of Jutland, Denmark, were an inhomogeneous thin and narrow cirrus band advected from the Northwest was present in 7-10.4 km altitude. A flight leg above the cloud in nearly 11 km height over both surface types was followed by in-cloud legs at several levels.

Radiative transfer calculations were made for three different ice-crystal habits and the observed solar zenith angle of 37°. The cirrus lookup tables calculated for land and water surfaces along with the measured reflectances are shown in Figures 1 and 2. The cloud retrieval solution space shows contours of constant

Table 1: Statistics of retrieved τ and R_{eff} for flight 22 May, 2007 (period 1, 43146-43220 s) over land (SD, standard deviation).

	Mean	SD	Min	Max
	optical thickness τ			
plate	4.9	1.7	2.2	7.6
solid column	3.0	1.0	1.3	4.6
rough aggregate	3.0	1.0	1.3	4.6
lidar	1.9	0.4	1.0	3.0
	effective radius R_{eff} [μm]			
plate	24.5	1.8	21.0	28.6
solid column	29.2	3.4	22.4	35.6
rough aggregate	29.6	4.0	22.0	36.7

Table 2: Statistics of retrieved τ and R_{eff} for flight 22 May, 2007 (period 2, 43419-43435 s) above North Sea (SD, standard deviation).

	Mean	SD	Min	Max
	optical thickness τ			
plate	2.1	0.8	0.9	3.0
solid column	1.2	0.4	0.5	1.8
rough aggregate	1.3	0.4	0.7	1.9
lidar	1.7	0.6	0.8	2.6
	effective radius R_{eff} [μm]			
plate	24.6	3.2	19.3	32.5
solid column	20.6	6.1	8.8	33.2
rough aggregate	22.6	5.7	12.9	36.2

optical thickness (rather horizontal lines) and particle effective radius (almost vertical lines). Increasing the cloud optical thickness (e.g., 0.1-8.1 in Figure 1 and 0.1-3.6 in Figure 2) results in increasing reflectances in the non-absorbing wavelength range 0.6-0.7 μm, while increasing the effective radius (e.g., 5-35 μm in Figures 1 and 2) leads to decreasing reflectances at the absorbing wavelength range 1.5-1.65 μm. Each pair of measured cloud reflectances corresponds to a pair of τ and R_{eff}. Via interpolation of modeled cloud reflectances to the observed reflectance values, time series of τ and R_{eff} for the observed cirrus were derived (cf. Figure 3 and Figure 4). In these plots the cirrus inhomogeneity is obvious, retrieved τ of one particle habit vary by a factor of about 3, retrieved R_{eff} show a variation by a factor of 0.3-2.5. The observed cloud had higher reflectances at 43146-43220 s (period 1, flight track over Jutland) than at 43419-43435 s (period 2, flight track above the North Sea). Statistics of the retrieved values are shown in Table 1 and Table 2 in which lidar-derived τ are also presented.

Due to the limited dynamical range of the lidar, it is hard to invert reliably for $\tau > 2$. For that reason it is difficult to compare with lidar-derived values during period 1, where optical thicknesses derived from reflectances are higher than 2. Modeled reflectances of solid columns and rough-aggregates are very similar, so that retrieved τ are nearly identical ranging from 1.3-4.6 for period 1 (mean = 3), and 0.5-1.9 for period 2 (mean = 1.3)(cf. Tables 1 and 2). Assuming plates, retrieved τ amount to 2.2-7.6 over Jutland (mean = 4.9) and 0.9-3 above the North Sea (mean = 2.1), respectively. Obviously, the reflectance of plates is very dissimilar to the one of solid-columns and rough-aggregates resulting in 60 % higher retrieved τ. As mentioned before, the optical thickness of the cloud in period 1 is probably too high to determine reliable values with a lidar. The lidar-derived τ of 1.7 $\pm$ 0.6 during the second part of interest though agrees well with the values derived from reflectance measurements.

For solid-columns, effective radii retrieved for period 1 are about 30 % higher than for period 2 with means of about 29.2 μm and 20.6 μm, respectively. Similar values were derived for rough-aggregates (cf. Table 1 and 2). For plates, retrieved effective radii were about 15 % smaller in the first time span and 20 % larger in the second time span. It can be concluded that the influence of particle shape on the retrieved τ is larger than on retrieved R_{eff}.

Effective radii were also determined from in situ measurements made directly after the above-cloud flight legs. R_{eff} were obtained from the ratio of ice water content (IWC) to volume extinction coefficient σ_{ext} (R_{eff} = 3000*IWC/σ_{ext}) which were calcu-

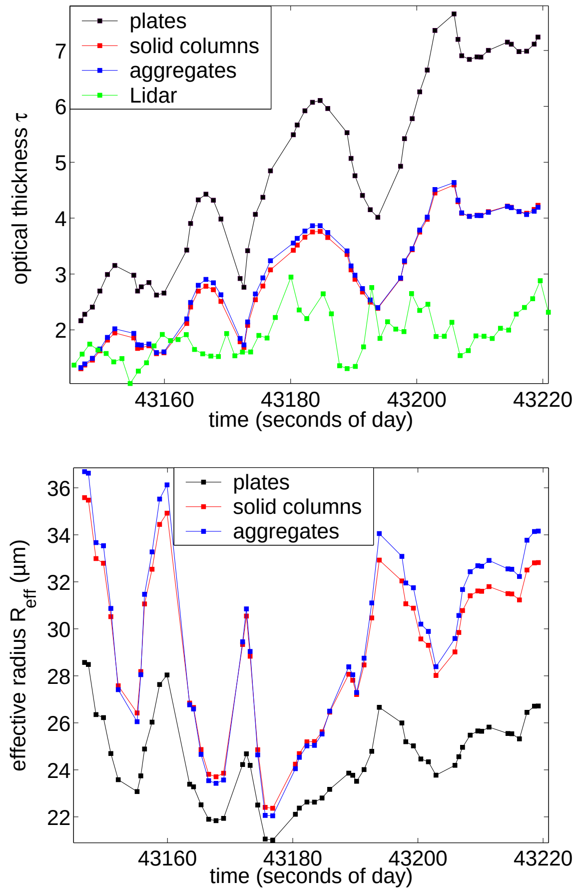

Fig. 3: Time series of retrieved optical thickness τ (upper figure) and effective radius R_{eff} (lower figure) for flight 22 May, 2007 (period 1, 43146-43220 s) over land. Lidar-derived τ are also shown.

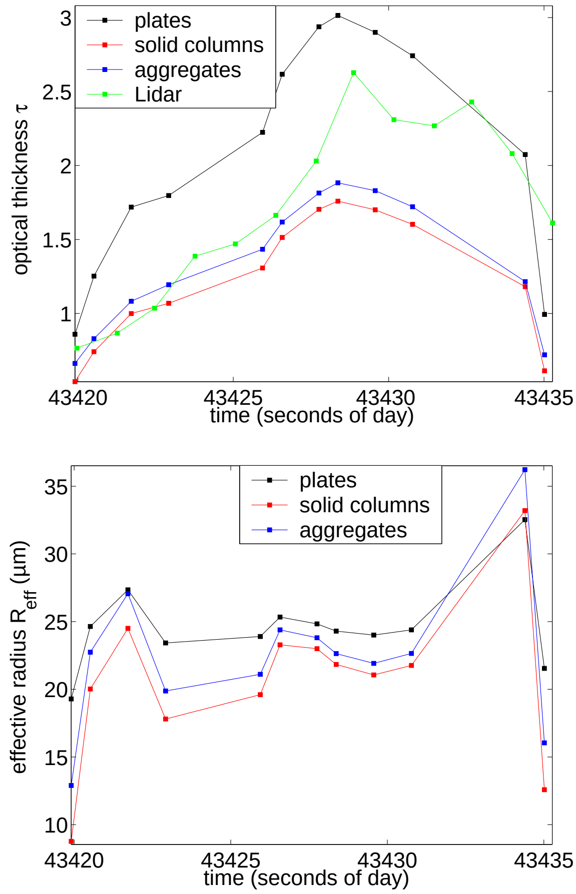

Fig. 4: Time series of retrieved optical thickness τ (upper figure) and effective radius R_{eff} (lower figure) for flight 22 May, 2007 (period 2, 43419-43435 s) above North Sea. Lidar-derived τ are also shown.

lated from the whole size distribution (Gayet et al., 2002). R_{eff} determined from microphysical measurements were dependent on flight height within the cirrus. The lower the flight altitude, the bigger the R_{eff}. For the two uppermost in-cloud legs at 9.5 km and 8.8 km, mean R_{eff} amounted to 26.8 μm and 31.3 μm, respectively. Within the range of the measurement variations (means$\pm$ standard variations) caused by the inhomogeneity of the cirrus, this value calculated for the uppermost leg was also derived from reflectance measurements.

5. SUMMARY

A cloud retrieval assuming different particle habits (plates, solid columns, rough aggregates) was made for measurements of upwelling radiances performed during the CIRCLE-2 campaign. Retrieved optical thicknesses were found to be strongly dependent on particle shape, with largest differences between solid columns (or aggregates) and plates of more than 50 %. Retrieved effective radii were less dependent on assumed particle habit. The retrieved cloud properties were found to be in good agreement with lidar-derived τ and R_{eff} from microphysical in situ measurements.

6. BIBLIOGRAPHY

Gayet, J.-F., Asano, S., Yamazaki, A., Uchiyama, A., Sinyuk, A., Jourdan, O., and Auriol, F.: Two case studies of winter continental-type water and mixed-phase stratocumuli over the sea. 1. Microphysical and optical properties, J. Geophys. Res., 107, doi:10.1029/2001JD001106, 2002.

Key, J. R., Yang, P., Baum, B. A., and Nasiri, S. L.: Parameterization of shortwave ice cloud optical properties for various particle habits, J. Geophys. Res-Atmos., 107, Art. No. 4181, 2002.

Mayer, B. and Kylling, A.: Technical note: The libRadtran software package for radiative transfer calculations - description and examples of use, Atmos. Chem. Phys., 5, 1.855–1.877, 2005.

Platnick, S., Li, J., King, M., Gerber, H., and Hobbs, P.: A solar reflectance method for retrieving the optical thickness and droplet size of liquid water clouds over snow and ice surfaces, J. Geophys. Res., 106, 15 185–15 199, 2001.

Wendisch, M., Müller, D., Schell, D., and Heintzenberg, J.: An airborne spectral albedometer with active horizontal stabilization, J. Atmos. Oceanic Technol., 18, 1856–1866, 2001.

Wendisch, M., Pilewskie, P., Jäkel, E., Schmidt, S., Pommier, J., Howard, S., Jonsson, H. H., Guan, H., Schroder, M., and Mayer, B.: Airborne measurements of areal spectral surface albedo over different sea and land surfaces, J. Geophys. Res-Atmos., 109, Art. No. D08 203, 2004.

ACKNOWLEDGEMENTS

The authors greatfully acknowledge the financial support from WMO, IUGG, IAMAS and ICCP that enabled the first author to attend the conference. Thanks go to Claudia Emde, Ulrich Hamann, and Bernhard Mayer for their helpful tips on using *libRadtran*, the *lib*rary of *Rad*iative *tran*sfer, which was used for 1D-radiative transfer modeling.

THE INFLUENCE OF ENTRAINMENT ON AEROSOL-CLOUD INTERACTIONS IN MARINE STRATOCUMULUS

Adrian Hill[1*], Graham Feingold[1], Hongli Jiang [2]

[1]NOAA Earth System Research Laboratory, 325 Broadway, Boulder, CO
[2]NOAA Earth System Research Laboratory/CIRA, 325 Broadway, Boulder, CO

1. INTRODUCTION

While there is little doubt that increasing aerosol concentrations in marine stratocumulus enhances cloud drop number concentrations (N_d) (IPCC, 2007), the occurrence of dynamic feedbacks and the influence of entrainment and mixing mean that the cloud albedo response is still very uncertain. Recent modeling studies have highlighted three mechanisms by which entrainment can play a role in aerosol-cloud interactions in marine stratocumulus (Sc):

1) Increasing aerosol concentrations, which results in increased N_d and reduced cloud drop size, can cause an evaporation-entrainment feedback that reduces the liquid water content of polluted cloud through a more efficient evaporation process (e.g. Wang et al., 2003).
2) The nature of the entrainment and subsequent mixing between the entrained clear air and the cloudy air can influence the evolution of the cloud drop size distribution and hence the effective radius (r_e) (e.g. Grabowski, 2006). Although many mixing scenarios can be envisaged two bounding mixing types have been proposed (e.g. Baker and Latham, 1979; Jensen et al., 1985). First, homogeneous mixing in which, upon entrainment, the cloudy air homogenizes rapidly, before any evaporation occurs and all drops are exposed to the same subsaturation. This causes all drops to evaporate as a group, leading to a reduction in cloud drop effective radius (r_e). The alternative mixing type is extreme inhomogeneous mixing, in which evaporation occurs in small regions that are first exposed to entrained air, leading to a region of droplet-free, yet saturated air, which is then mixed through the cloudy volume. Such mixing results in a reduction in N_d, while r_e remains unaffected.
3) Changes in cloud drop size with increasing aerosol can modify the precipitation and sedimentation rates of a cloud, which in turn can alter the cloud top entrainment, leading to a response in cloud liquid water content (e.g. Ackerman et al., 2004; Bretherton et al., 2007).

In the following we present a summary of modeling results that investigate the first two mechanisms within the framework of a non-precipitating cloud. These results are taken from a paper that is in review at present, i.e. Hill et al., 2008.

2. MODEL AND CASE DESCRIPTION

The model used in this work is the BR-LEM, which is the UK Met. Office Large Eddy Simulation Model (LEM) (Gray et al., 2001) with a fully integrated, size-resolved, cloud microphysical scheme (Tzivion et al., 1987, 1989). In the BR-LEM, the cloud drop size distribution is divided into 25 size bins with a range of 1.56 to 504 µm (radii) and mass doubling from one bin to the next. The method of moments is used to solve for both mass and number concentration in each size bin that results from non-precipitating processes (condensation/evaporation) and

* Corresponding author address: Adrian Hill, Earth System Research Laboratory, Boulder, CO 80305, email: adrian.hill@noaa.gov

precipitating processes (collision-coalescence and collisional breakup).

This version of the BR-LEM employs a simple aerosol activation scheme in which a single prognostic variable is used to represent total aerosol concentration (N_a) and aerosol activation. The aerosol is assumed to be fully soluble ammonium sulphate with a log-normal distribution (mean radius = 0.1 µm, geometric standard deviation = 1.5). Aerosol activation is based on the ambient supersaturation, and the local, predicted N_a. Upon activation, aerosols are removed from the distribution and upon complete evaporation of droplets, an equal number of aerosols are returned to the distribution. In the absence of non-conservative processes (collision-coalescence, breakup and sedimentation), this scheme guarantees domain-wide conservation of total number, i.e., $N_d + N_a$.

While bin-microphysics is a very useful tool for studying aerosol-cloud interactions, its use does not alleviate the assumption of homogeneous mixing because all drops are assumed to be exposed to the same fields. Thus, in this work we apply a methodology for simulating extreme inhomogeneous mixing in the bin microphysical framework. In this application, the fractional change in total mass due evaporation is used to scale both the mass and number mixing ratios in each bin, i.e.:

$$n_{kf} = n_{k0} \frac{M_f}{M_0}$$

$$m_{kf} = m_{k0} \frac{M_f}{M_0}$$

where M_0 is total, local liquid water mass mixing ratio before evaporation, i.e. the sum of all mass bins, M_f is the total, local liquid water mass after evaporation, n_{k0} and m_{k0} are the drop number concentration and mass mixing ratio in a bin (k) before evaporation.

To investigate the roles of increasing aerosol and mixing assumption, we used the BR-LEM to perform 8 3-D simulations of an idealised non-precipitating nocturnal marine Sc. The initial thermodynamic and dynamic profiles for all simulations were based on Duynkerke et al. (2004) with the exception that at all heights θ_l was increased by 0.25 K and q_t was decreased by 0.5 g kg^{-1}. All simulations used a 4 X 4 km horizontal domain with a dx and dy = 40 m. Vertical resolution was set to 20 m for “low” resolution and 5 m for “high” resolution. At each vertical resolution we performed a homogeneous and extreme inhomogeneous simulation of a clean cloud (N_a = 100 cm^{-3}) and a polluted cloud (N_a = 1000 cm^{-3}). In all simulations cloud top longwave radiation was simulated using the Edward-Slingo radiative transfer scheme. The duration of all simulations was 5 hours, with a typical timestep of 0.15 seconds (high resolution) and 0.5 seconds (low resolution). Typical values are stated here because the BR-LEM employs a variable timestep.

3. SIMULATION RESULTS

A brief summary of results is given here; details and figures will be furnished at the conference.

We find that irrespective of resolution or mixing assumption increasing aerosol from 100 to 1000 cm^{-3} results in a reduction in LWP of between 7.0 and 7.9% for 20 m resolution, and between 5.3 and 5.7% for 5 m resolution (Figure 1a and b respectively). Such a change in LWP with increasing aerosol is a manifestation of an evaporation-entrainment feedback (Wang et al., 2003), in which more efficient evaporation of smaller detrained drops from the polluted cloud enhances the cloud top cooling rate, leading to stronger cloud dynamics and an increase in cloud top entrainment. This leads to an increase in entrainment warming of the boundary layer, which in turn reduces the LWP of the polluted cloud relative to the clean cloud. Figure 1 shows that within the non-precipitating framework the response of LWP to increasing N_a is relatively insensitive to mixing assumption. However, increasing vertical resolution from 20 to 5 m results in a reduction in the LWP response.

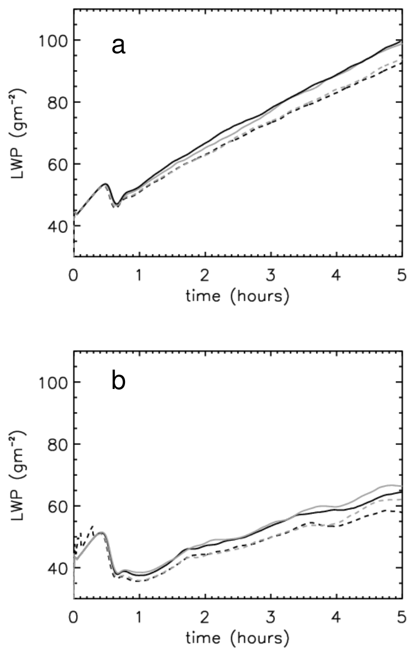

Figure 1: Liquid water path (g m^{-2}) from (a) simulations with 5 m vertical resolution and (b) simulations with 20 m vertical resolution. The solid lines show the clean simulations while the dashed lines show the polluted simulations. Black lines represent simulations that assume homogeneous mixing and the grey lines represent the inhomogeneous mixing assumption

As expected, increasing aerosol from 100 to 1000 cm^{-3} results in an increase in N_d and assuming inhomogeneous mixing tends to reduce N_d, relative to homogeneous (Figure 2). Figure 2 shows that at both resolutions, assuming inhomogeneous mixing in the polluted cloud leads to a larger response in N_d than that shown by the clean cloud. For example, relative to the standard homogeneous case, assuming inhomogeneous mixing in the low (high) resolution clean simulation leads to a 7.0% (3.1%) decrease in cloud averaged N_d (shown in Figure 2) for the last 3 hours of simulation, while assuming inhomogeneous mixing in the polluted simulation leads to 16.4% (12.8%) decrease in N_d. Similar trends are also obvious in the cloud averaged drop effective radius (Figure 3). The greater response of the polluted cloud to mixing assumption results from its greater evaporation rate relative to the clean cloud. As the inhomogeneous mixing scheme used in this work requires that all mass lost through evaporation is lost through complete evaporation of drops, the greater evaporation rate in the polluted case results in the largest change in N_d. However, although the polluted cloud is more sensitive to mixing assumption, it is clear from Figures 2 and 3 that increasing resolution tends to reduce the impact of mixing assumption on both the clean and polluted cloud.

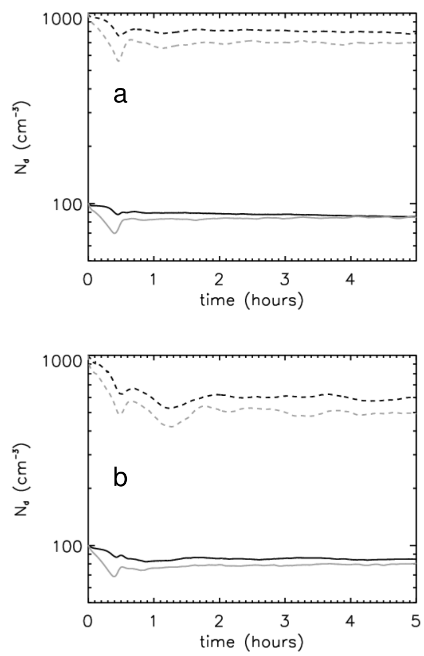

Figure 2: Cloud averaged drop number concentration (cm^{-3}) from (a) simulations with 5 m vertical resolution and (b) simulations with 20 m vertical resolution. The solid lines show the clean simulations while the dashed lines show the polluted simulations. Black lines represent simulations that assume homogeneous mixing and the grey lines represent the inhomogeneous mixing assumption

4. SUMMARY

Based on simulations of idealized non-precipitating marine Sc, which have been undertaken with 3-D LES with fully integrated bin microphysics, we show that increasing aerosol results in an evaporation entrainment feedback which tends to reduce LWP. The simulations presented show that this is a robust feature for the two vertical resolutions tested, and is relatively insensitive to mixing assumption. When the role of mixing assumption is considered we find that, as expected assuming extreme inhomogeneous mixing causes a reduction the cloud averaged N_d and an increase in the r_e. We show that the polluted cloud is more sensitive to mixing assumption and we propose that this is due to the stronger evaporation rate associated with the smaller drops of the polluted cloud. Finally we show that increasing vertical resolution results in a reduction of the influence of the both the evaporation-entrainment feedback and the mixing assumption.

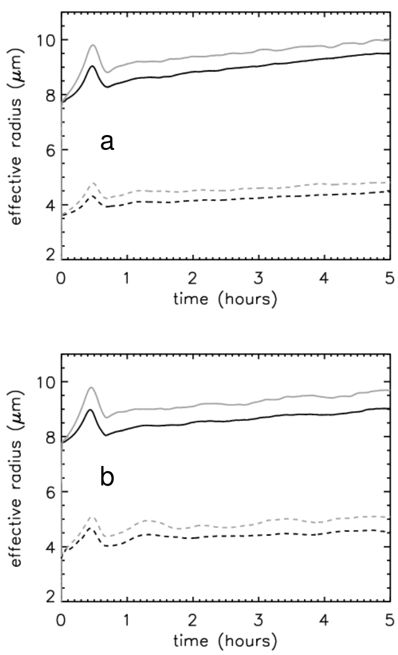

Figure 3: Cloud averaged effective radius (μm) from (a) simulations with 5 m vertical resolution and (b) simulations with 20 m vertical resolution. The solid lines show the clean simulations while the dashed lines show the polluted simulations. Black lines represent simulations that assume homogeneous mixing and the grey lines represent the inhomogeneous mixing assumption

ACKNOWLEGEMENTS: We acknowledge support from NOAA's Climate Goal. Adrian Hill is supported by the National research council (NRC) post-doctoral research associateship program. We thank the NOAA ESRL High Performance Computing Systems for computational and technical support.

REFERENCES

Ackerman, A. S., M. P. Kirkpatrick, D. E. Stevens, and O. B. Toon, 2004: The impact of humidity above stratiform clouds on indirect aerosol climate forcing. *Nature*, **432**, 1014-1017.

Baker, M. B. and J. Latham, 1979: The evolution of droplet spectra and the rate of production of embryonic raindrops in small cumulus clouds. *J. Atmos. Sci.*, **36**, 1612 - 1615

Bretherton, C. S., P. N. Blossey, J. Uchida: Cloud droplet sedimentation, entrainment efficiency, and subtropical stratocumulus albedo. *Geophys. Res. Letters*,**34**, doi:10.1029/2006GL027648

Duynkerke, G. P., and co-authours, 2004: Observations and numerical simulations of the diurnal cycle of the EUROCS stratocumulus case, *Quart. J. Roy. Meteor. Soc.*, **130**, 3369-3296

Grabowski, W. W., 2006: Indirect impact of atmospheric aerosols in idealized simulations of convective-radiative quasi equilibrium. *J. Climate*, **19**, 4664-4682

Gray, M. E. B., J. Petch, S. H. Derbyshire, A. R. Brown, A. P. Lock, H. A. Swann, P. R. A. Brown, 2001: Version 2.3 of the Met. Office Large Eddy Model: Part II. Scientific documentation. Met O (APR) Turbulence and Diffusion Note, No 276

Hill, A. A., G. Feingold and H. Jiang, The influence of mixing on the climate forcing of non-precipitating marine stratocumulus, *J. Atmos. Sci.*, **in review**

Jensen, J. B., P. H. Austin, M. B. Baker, and A. M. Blyth, 1985: Turbulent Mixing, Spectral Evolution and Dynamics in a Warm Cumulus Cloud. *J. Atmos. Sci.*, **42**, 173-192

Tzivion, S., G. Feingold, and Z. Levin, 1987: An efficient numerical solution to the stochastic collection equation. *J. Atmos. Sci.*, **44**, 3139-3149.

Tzivion, S., G. Feingold, and Z. Levin, 1989: The evolution of raindrop spectra. Part II: Collisional/Breaup and evaporation in a rainshaft. *J. Atmos. Sci.*, **46**, 3312-3328.

Wang, S., Q. Wang, and G. Feingold, 2003: Turbulence, condensation and liquid water transport in numerically simulated nonprecipitating stratocumulus clouds. *J. Atmos. Sci.,* **60**, 262-278.

ON THE CONTRIBUTION OF HESITANT AND SMALL CLOUDS TO THE TWILIGHT ZONE IN A SPARSE CUMULUS FIELD

Ilan Koren[1], Orit Altaratz[1], Graham Feingold[2], Lorraine A. Remer[3] Tamir G. Reisin[4] and Lazaros Oreopoulos[3,5]

[1]Department of Environmental Sciences, Weizmann Institute, Rehovot, Israel
[2]NOAA Earth System Research Laboratory, Boulder, Colorado, USA
[3]Laboratory for Atmospheres, NASA Goddard Space Flight Center, Greenbelt, Maryland, USA
[4]Soreq Nuclear Research Center, Yavne, Israel
[5]Joint Center for Earth Systems Technology, University of Maryland, Baltimore County, Baltimore, Maryland, USA

1. INTRODUCTION

Cloud aerosol interactions pose the largest source of uncertainty in climate change estimations. The common notion is that clouds must be first separated from aerosols to retrieve their properties from measurements. Only later are the cloud properties merged with the aerosol ones in order to study the interactions and to estimate forcing. However, it has been shown that the assumed-to-be cloud free area within a cloud field is filled with forming and evaporating clouds, undetectable small clouds and hydrated aerosols. This area, defined as the twilight zone, has unique optical properties (Koren et al, 2007).

The twilight ingredients, when averaged over the pixel size of the satellite remote sensor, create an apparent gradual transition from cloudy to cloud-free atmosphere. However, when zooming-in, the zone emerges as non uniform, and affected by many separated processes. Here we describe two of the twilight components: small and hesitant clouds.

2. THE TWILIGHT INGREDIENTS

The range between detectable clouds and dry aerosol contains several subsets that can be classified according to the Kohler theory or their optical properties. We will use both to define a few of the components. Cloud droplets (on the right-hand side of the Kohler curves) can be either too small in size to be detected or may have a weak signature below the instrument sensitivity (thin clouds). Weak- signature clouds can be forming or dissipating detectable clouds, or what we define here as hesitant clouds.

Aerosols (on the left-hand side of the Kohler curves) can change their microphysical and optical properties as a function of their hygroscopicity properties and the environmental relative humidity.

The cloud halo is a relatively short transition zone where some of the ingredients can be found in the form of small cloud fragments, the thinning of the detectable cloud, and humidified aerosols.

3. HESITANT CLOUDS

Within the twilight zone there are pockets of high humidity that are close to the critical supersaturation (defined by the Kohler equation; Pruppacher and Klett, 1997). Such pockets are sensitive to small perturbations in the local thermodynamic properties and can oscillate between growing droplets that form a clear visible cloud to humidified aerosols (between the left and the right side of the Kohler curve). We define such pockets as hesitant clouds (fig 1).

These pockets can be in a state of low supersaturation, not enough to activate the aerosols. Small changes, in the environmental conditions (temperature or specific humidity), can increase the supersaturation to an activation mode and create growing droplets (Reisin et al, 2008). If the perturbation is small, such a cloud is not likely to develop strong enough internal dynamics. Therefore, it will likely evaporate again and continue to oscillate between the two modes.

Although hesitant clouds are common in many cloud fields, there are cases when it is particularly easy to see them. Frequently hesitant clouds are distributed like any other detectable cloud, namely each cloud sits in a pocket of high humidity. Some of these clouds form as detectable clouds and some are hesitant. Since the hesitant cloud's optical signature is relatively weak, the best geometry to see them is near the forward scattering angle from the sun (fig. 1).

The distribution and optical forcing of hesitant clouds as well as their interactions with anthropogenic aerosols is now being analyzed in LES models and observations.

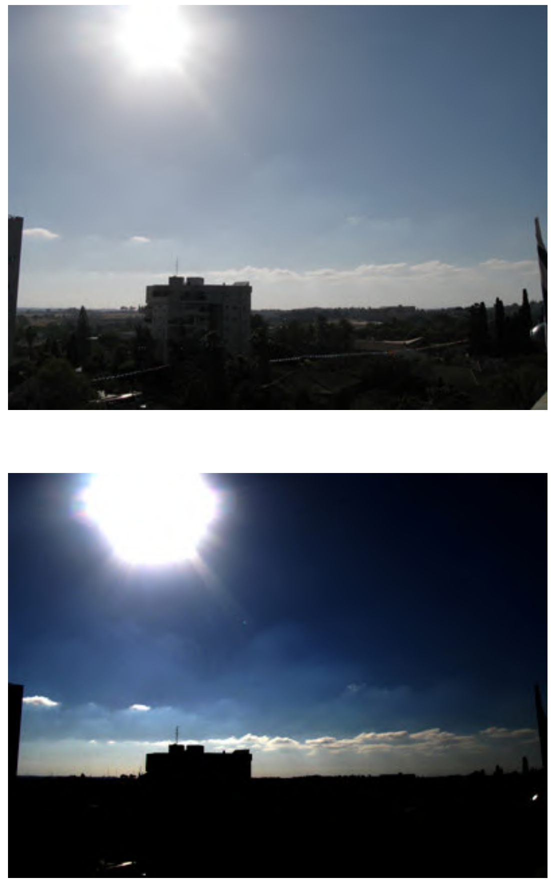

Figure 1.Upper - Forward scattering view of a scattered cumulus cloud field. Lower – enhanced contrast reveals the presence of many high humidity pockets with hesitant clouds within the cloud field. Some of these pockets were shown to oscillate between weak and distinct clouds.

4. SMALL CLOUDS

Small clouds below the detector spatial resolution may also have an important contribution to the twilight radiative forcing.

Figure 2 shows (upper panel) that in a scattered cumulus cloud field the clouds exhibit a power-law size distribution ($n(a) = b/a^m$) where 'a' is the cloud size in area units (Koren et al, 2008). This suggests that at any sensor spatial resolution, a significant fraction of the clouds will be less than the pixel size and missed in the analysis. The slope, m, of the distribution is larger than 1 ($1<m<2$) and therefore the contribution of the smallest clouds to the total cloud area ($A(a) = b/a^{m-1}$) is significant.

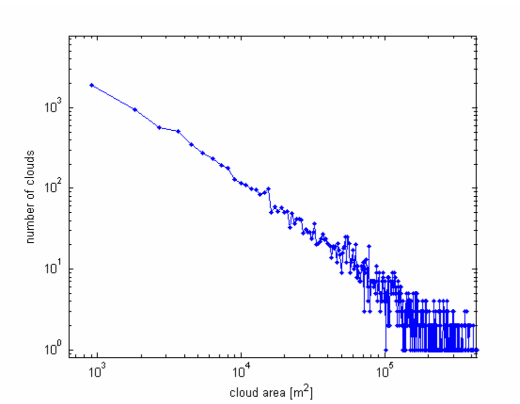

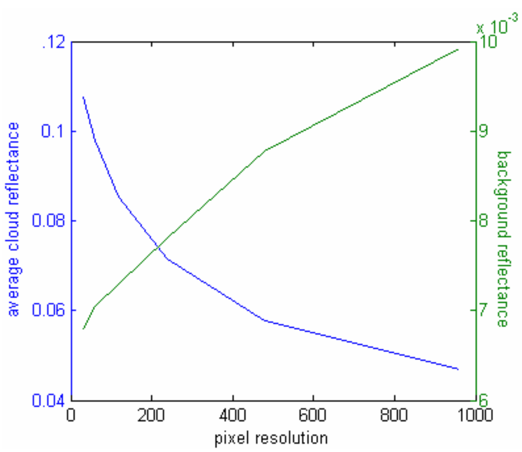

Figure 2.Upper – Size distribution of scattered cumulus cloud over the Bahamas from Landsat (The source for this dataset was the Global Land Cover Facility, http://www.landcover.org). Lower – The effect of the detector resolution on the cloud and background reflectance (1.65 µm).

It has also been shown that the reflectance per cloud size increases more slowly than the rate at which the cloud area per cloud size decreases (Koren et al., 2008). Therefore, small clouds contribute significantly to the total cloud reflectance.

Subpixel clouds far from larger clouds may be classified as non-cloudy and contribute significantly to the apparent aerosol properties, while small clouds near other (larger) clouds are merged together with the surrounding background pixels resulting in an apparent larger cloud with weaker reflectance. (Fig 2, lower).

5. BIBLIOGRAPHY

Koren, I., L. A. Remer, Y. J. Kaufman, Y. Rudich, and Martins J. V.: On the twilight zone between clouds and aerosols, *Geophys. Res. Lett., 34, L08805, doi:10.1029/2007GL029253, 2007.*

Koren, I., Oreopoulos, L., Feingold, G., Remer, L. A., and Altaratz, O.: How small is a small cloud?, *Atmos. Chem. Phys. Discuss., 8, 6379-6407, 2008.*

Pruppacher, H.R., and J.D. Klett, 1997: Microphysics of Clouds and Precipitation. *Kluwer Acad.*, Norwell, Mass, 1954pp.

Tamir G. Reisin, Ilan Koren, Orit Altaratz and Sabine Wurzler, numerical simulations of hesitant clouds in the twilight zone, *Proceedings of the 15th Int. Conf. on Clouds and Precip., Cancun, Mexico, ICCP2008*

Acknowledgments

This paper is dedicated to the memory of Yoram J Kaufman, a dear friend and a brilliant scientist. This research was supported in part by the Israel Science Foundation (grant 1355/06) and NASA's Radiation Sciences Program and Interdisciplinary Studies. GF was supported by NOAA's Climate Goal. The source for this dataset was the Global Land Cover Facility, http://www.landcover.org

THE DIFFERENCE OF RADIATIVE SIGNALS BETWEEN PRECIPITATING CLOUDS AND NON-PRECIPITATING CLOUDS DERIVED FROM TRMM PR AND VIRS MEASUREMENTS

Qi Liu, Yunfei Fu, Liang Sun and Yu Wang

School of Earth and Space Sciences, University of Science and Technology of China, Hefei 230026, China

1. INTRODUCTION

Satellite-based rainfall remote sensing has been an active research field for over three decades, which currently focuses on the improvement of precipitation retrieval techniques through (VIR) and microwave (MW) measurements. Precipitation detection that discriminate precipitating clouds (PCs) from non-precipitating clouds (N-PCs) is essential for the performance of rainfall retrieval algorithm, especially for those based on VIR measurements. Mistakes in the identification of PCs undoubtedly lead to significant bias in retrieved surface rainfall. A variety of studies have been dedicated to the exploration of efficient precipitation detection schemes relying on VIR measurements (Inoue 2000; Inoue and Aonashi 2000; Liu et al. 2007).

Thermal infrared signals that are well correlated with cloud top temperature of dense clouds are preferred indices for differentiating PCs and N-PCs, which are generally applied in terms of threshold. Depending on geographic locations and precipitation types, the selection of threshold to identify precipitation is somewhat arbitrary and highly diverse, such as 210K for convective clouds in Bay of Bengal (Zuidema 2003), 230K for active convective systems in tropics (Tian et al. 2004), and so on. Furthermore, GPI (GOES Precipitation Index, Arkin and Meisner 1987) and AGPI (Adjusted GOES Precipitation Index, Adler et al. 1993) both simply employ the 235K to classify cloudy pixels into the PCs and N-PCs on a globe scale and then assign a rainrate of 3mm/h to the acquired PCs, upon which daily and monthly mean surface rainfall could be sequentially estimated.

Reflected visible signals are not affected by low cloud top temperature and are also commonly used indices for detecting PCs during daytime. By analyzing satellite and surface measurements from the First Algorithm Intercomparison Project of Global Precipitation Climatic Program (AIP-1, Lee et al. 1991, Arkin and Xie 1994), King et al. (1995) suggested that the visible index is a little better than infrared counterpart in representing the precipitation area, especially for denoting those orographic and shallow precipitation systems. However, above results is still highly uncertain since the two kinds of datasets are badly matched and $2.5^{o}\times2.5^{o}$ is too coarse to define exact PCs or N-PCs. Consequently, there is large ambiguity in acquired PCs and resultant surface rainfall.

The Tropical Rainfall Measuring Mission (TRMM) conducting associated observations of Precipitation Radar (PR) and Visible and Infrared Scanner (VIRS) provides synchronous measurements of precipitation profiles and multichannel cloud top radiances (Simpson et al. 1988; Kummerow et al. 1998), which presents an opportunity to examine the relationship between radiative properties of cloud top and low-layer hydrometeors/precipitation. Especially, according to the decision of PCs and N-PCs offered by PR, the difference of VIR signals between these two categories of clouds could be achieved.

2. DATA

Jointly conducted by National Aeronautics and Space Administration (NASA) and Japan Aerospace Exploration Agency (JAXA), the TRMM satellite was launched in November 1997 and supplies valid measurements up to the present. The TRMM satellite has a unique sun-asynchronous orbit and operates at an altitude of 400km (350km before August 2001). Similar to the Advanced Very High Resolution Radiometer (AVHRR), VIRS receives upward radiances at five channels, i.e., 0.63, 1.6, 3.7, 10.8 and 12.0um, across 720km swath with a horizontal resolution of about 2.1km. PR, the first spaceborne meteorological radar, works at Ku band (13.8GHz) and scanned a swath of 220km with a horizontal resolution of 4.3km and a vertical resolution of 250m. The sensitivity of PR is 17dBz equivalent to a rainrate of about 0.5mm/h. The similar cross-track scanning mode of VIRS and PR ensures a little lag in observing the same target, which makes it feasible to jointly use these two sets of measurements with high reliability.

TRMM 1B01 and 2A25 products derived from VIRS and PR, respectively, were collocated to establish the merged dataset, from which 12 front and 11 typhoon snapshots occurring in East Asia and western Pacific in summer 2005 were particularly selected. In order to ensure enough volumes both for visible and infrared measurements, samples herein are all in daytime. The clear sky composites from D1 dataset of International Satellite Cloud Climatology Project (ISCCP, Schiffer and Rossow 1983; Rossow and Schiffer 1991) were employed to perform cloud test and then PCs and N-PCs were further classified according to PR precipitation decision. Preliminary statistics show that the total pixels are 78708 (76388), where there are

41122 (41656) PCs pixels and 36211 (34597) N-PCs pixels in front (typhoon). Besides, the averaged percentage of clear sky pixels is less than 2% in the each definite $5^{o}\times 5^{o}$ domain.

3. Result

The frequency distribution of RF1 for PCs and N-PCs is shown in Fig.1. For a convenient comparison, gaussian fitting was implemented and the key parameters in the acquired probability distribution function (PDF) are summarized in Table 1. The RF1 distributions of PCs are approximately symmetric while the frequency of N-PCs is a bit higher on the low-value side of RF1 relative to the gaussian fitting, indicating a rapid decrease of N-PCs with increasing RF1. It's apparent that the RF1 of PCs and N-PCs in typhoons is systematically higher than those in fronts. The distribution width of PCs in typhoon is the most narrow and the mode of RF1 is 0.95, while the mode for PCs in front is only about 0.8 approaching that of N-PCs in typhoon. Since RF1 is well sensitive to the cloud optical thickness that is mostly determined by the upper-layer cloud water content, the difference of RF1 frequency distribution between PCs and N-PCs illustrates that cloud water/ice content in PCs is much higher than those in N-PCs within the same precipitation system, i.e., front or typhoon. In addition, it cloud be deduced that there is more intense ascending and subsequently more upper-level water/ice content generated in typhoons than in fronts.

The reflectance of 1.6um (RF2) that is an important water-absorptive band in shortwave has been well applied in cloud parameter retrieval due to the close relationship between RF2 and effective radius or thermodynamic phase of cloud droplet. As shown in Fig.2, the RF2 frequency distributions of PCs and N-PCs largely overlap where modes and peak widths are similar, which is true for clouds both in fonts and in typhoons, implying that there is not conspicuous discrepancy of cloud droplet size/phase between PCs and N-PCs in these typical mesoscale precipitation systems. It seems that as the clouds develops from N-PCs to PCs in fronts and typhoons, the density of cloud droplet increases markedly which results in the evident cumulation of cloud water/ice content, but the cloud droplet size distribution hardly varies in this process. Therefore, it is hard to differentiate PCs and N-PCs by only using RF2.

The brightness temperature of 3.7um (TB3) is also sensitive to upper-layer cloud droplet size and phase, which is particularly used in cloud parameter retrieval for nocturnal cases. Because the selected samples are all during daytime, TB3 herein is actually the equivalent brightness temperature arising from both emission and reflected radiances. As shown in Fig.3, the frequency distributions of PCs and N-PCs are quite similar in typhoons but present evident differences in fronts where TB3 of PCs is much lower than those of N-PCs. Noting that the frequency of PCs is about two times that of N-PCs in the range from 250K to 260K while the frequency of N-PCs increases markedly when TB3 exceeds 270K. Quantitatively, the gaussian fitting parameters indicate that TB3 distributions are basically identical for PCs and N-PCs regardless of the precipitation system type. Information on TB3 is consequently also not well adequate in differentiating PCs and N-PCs in these mesoscale precipitation systems.

Thermal channel of 10.8um, suffering little impact of water vapor and other absorptive gas, is the most common observational band. The brightness temperature of 10.8um (TB4) represents the surface temperature of the object in substance if the target could be considered as black or gray body. As shown in Fig.4, PCs and N-PCs in typhoon have similar pattern of frequency distribution on TB4 and both peak near 220K, with the implication that PCs and N-PCs are both associated with high cloud top within typhoon domain, while the frequency distribution on TB4 of PCs and N-PCs in fronts are distinct. In addition, it was revealed to some extent that ascending draft is much stronger in typhoons than those in fronts when taking into account the evident differences of N-PCs mode between in fronts and in typhoons (refer to Table 1). High and cold clouds in fronts are probably PCs while low and warm clouds hardly generate precipitation, which provide feasibility to effectively differentiate PCs and N-PCs. However, the conclusion is not the same in typhoons where most clouds could rise to a quite high altitude due to the intense upward airflow, and consequently it is hard to identify PCs only via the cloud top temperature. The frequency distribution of PCs and N-PCs on 12.um brightness temperature (TB5) displayed in Fig.5 is alike the distribution of TB4.

In addition, the ratio of 0.6um reflectance to 1.6um reflectance (RF1/RF2) and the brightness temperature difference between 10.8um and 3.7um or 12.0um (BTD_{34} or BTD_{45}) are also exploringly examined and the results are shown in Fig.6, Fig.7 and Fig.8, where the frequency is plotted in two-dimensional space of TB4 and RF1/RF2 (BTD_{34} or BTD_{45}). As a whole, the index composed of multichannel radiances is a bit more efficient than single channel measurement, especially when employing both reflectance ratio and thermal infrared brightness temperature. Statistical results show that dual-channel indices, RF1/RF2 as well as RF1&TB4, show much higher performance than single-channel ones, implying potential in routinely identifying PCs through visible and infrared observations. For instance, a combined threshold of 230K&3.0 (TB4&RF1/RF2) has a probability of detection (POD) higher than 77% with the false alarm ratio (FAR) less than 30% for identifying PCs in fronts. As a comparison, when the GPI (235K threshold of TB4) scheme is applied, it is found that the FAR approached 50% though POD is approximately the same. Furthermore, GPI algorithm is proved to be absolutely not practicable in identifying PCs within typhoons.

4. SUMMARY

The associated observations of PR and VIRS aboard TRMM satellite made it feasible to obtain precipitation decision and cloud top radiances for the same cloud target simultaneously. By using combined datasets from PR and VIRS, narrowband signals were analyzed to clarify the radiative difference between PCs and N-PCs. PCs and N-PCs were determined by PR within a set of typical mesoscale precipitation systems, i.e., fronts and typhoons occurred during boreal summer in East Asia and western Pacific. PDF method was used and various shortwave, longwave, multichannel indices for PCs detection were evaluated based upon the statistical results. It was found that radiative signals at the horizontal resolution of PR (~4.3km) from PCs and N-PCs are generally similar in both front and typhoon situations. Among the five channels of VIRS (0.63μm, 1.6μm, 3.7μm, 10.8μm, 12.0μm), only 0.63μm reflectance (RF1) and 10.8μm Brightness Temperature (TB4) shows acceptable discriminability from PCs to N-PCs, respectively. Two dual-channel indices, RF1/RF2 and RF1&TB4, show much higher performance than single channel ones, implying potential in operationally identifying PCs for visible and infrared observations. The combined use of RF1 and TB4 were proved to be the optimal strategy for detecting PCs. Likewise, the GOES precipitation index (GPI) was examined, which revealed that GPI is effective for differentiating PCs from N-PCs in front but cannot be relied on in typhoon cloud clusters.

5. BIBLIOGRAPH

Adler, R. F., A. J. Negri, P. R. Keehn, et al. (1993). "Estimation of monthly rainfall over Japan and surrounding waters from a combination of low-orbit microwave and geosynchronous IR data." J. Appl. Meteor. 32: 335-356.

Arkin, P. A. and B. N. Meisner (1987). "The relationship between large-scale convective rainfall and cold cloud over the Western Hemisphere during 1982-1984." Mon. Wea. Rev. 115: 51-74.

Arkin, P. A. and P. Xie (1994). "The global precipitation climatology project: First Algorithm intercomparison project." Bull. Amer. Meteor. Soc. 75: 401-419.

Inoue, T. (2000). "Early results on comparison between cloud information by VIRS and rain information by PR/TMI." REMOTE SENSING AND APPLICATIONS: EARTH, ATMOSPHERE AND OCEANS 25(5): 977-980.

Inoue, T. and K. Aonashi (2000). "A comparison of cloud and rainfall information from instantaneous visible and infrared scanner and precipitation radar observations over a frontal zone in east Asia during June 1998." JOURNAL OF APPLIED METEOROLOGY 39(12): 2292-2301.

King, P. W. S., W. D. Hogg and P. A. Arkin (1995). "The role of visible data in improving satellite rain-rate estimates." J. Appl. Meteor. 34: 1608-1621.

Kummerow, C., W. Barnes, T. Kozu, et al. (1998). "The Tropical Rainfall Measuring Mission (TRMM) sensor package." Journal Of Atmospheric And Oceanic Technology 15(3): 809-817.

Liu, C. T., E. J. Zipser and S. W. Nesbitt (2007). "Global distribution of tropical deep convection: Different perspectives from TRMM infrared and radar data." J. Climate 20: 489-503.

Rossow, W. B. and R. A. Schiffer (1991). "Isccp Cloud Data Products." Bulletin Of The American Meteorological Society 72(1): 2-20.

Schiffer, R. A. and W. B. Rossow (1983). "The international Satellite Cloud Climatology Project(ISCCP): The first project of the World Climate Research Program." Bull. Amer. Meteor. Soc. 64: 779-784.

Simpson, J., R. F. Adler and G. R. North (1988). "A proposed Tropical Rainfall Measuring Mission (TRMM) satellite." Bull. Amer. Meteor. Soc. 69: 278-295.

Tian, B. J., B. J. Soden and X. Wu (2004). "Diurnal cycle of convection, clouds and water vapor in the tropical upper troposphere: Satellites versus a general circulation model." J. Geoph. Res 109: D10101, doi:10.1029/20003JD004117.

Zuidema, P. (2003). "Convective clouds over the Bay of Bengal." Mon. Wea. Rev. 131: 780-798.

Acknowledgments. TRMM products were provided by TRMM Science Data and Information System. ISCCP D1 datasets were obtained online from http://isccp.giss.nasa.gov.

Table 1. The fitting PDF of VIRS five channels for PCs and N-PCS within fronts and typhoons*

Channel	Parameter	Front		Typhoon	
		PCs	N-PCs	PCs	N-PCs
0.6μm	a	5.42	3.39	8.35	5.39
	b	0.14	0.24	0.09	0.13
	x_0	0.85	0.63	0.93	0.81
	R	0.98	0.96	0.99	0.96
1.6μm	a	15.32	10.72	18.3	15.4
	b	0.05	0.07	0.04	0.05
	x_0	0.20	0.22	0.19	0.19
	R	0.99	0.98	0.99	0.99
3.7μm	a	12.39	6.05	14.05	12.43
	b	5.91	10.21	5.36	5.24
	x_0	256.8	260.3	259.4	260.7
	R	0.99	0.91	0.99	0.97
10.8μm	a	4.84	2.71	5.68	4.91
	b	16.13	31.67	13.50	15.07
	x_0	218.5	241.9	213.9	219.0
	R	0.98	0.87	0.95	0.95
12.0μm	a	4.64	2.71	5.56	4.90
	b	17.04	31.77	13.84	15.22
	x_0	216.3	239.5	211.0	216.1
	R	0.98	0.86	0.96	0.95

*Gaussian function is expressed as following.

$$f(x) = a \cdot \exp[-\frac{(x - x_0)^2}{2b^2}]$$

a, *b* and x_0 are all parameters, denoting the peak altitude, standard deviation and mode, respectively. *R* is the correlation coefficient between fitting curve and measurements.

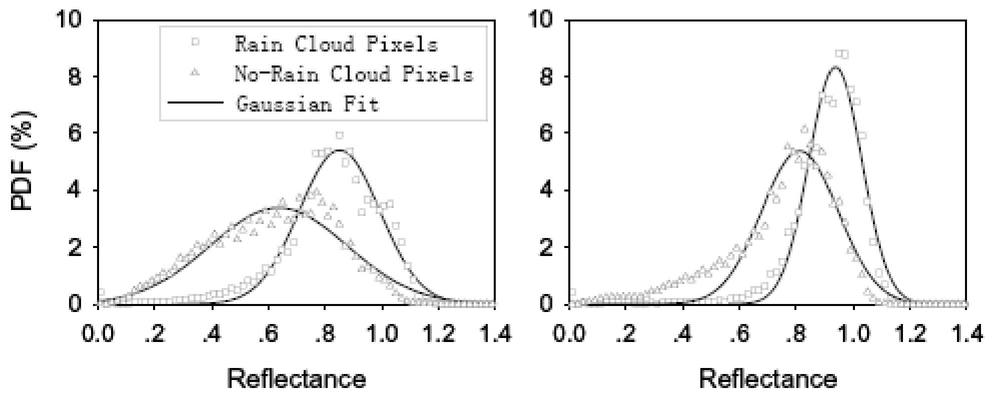

Figure 1. 0.6um reflectance of precipitating clouds and non-precipitating clouds within fronts (left) and typhoons (right)

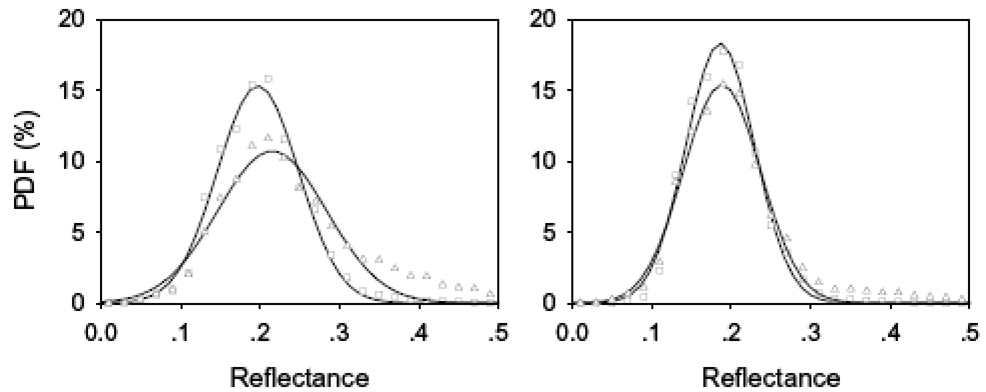

Figure 2. Same as Figure 1 but for 1.6um reflectance

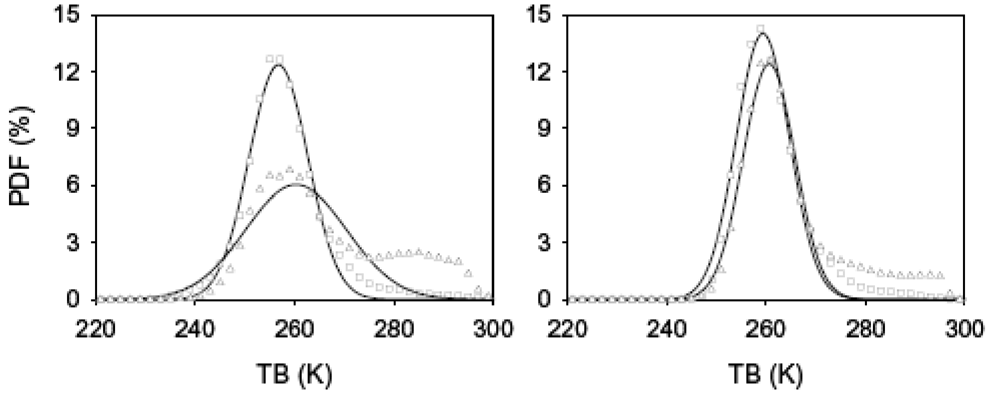

Figure 3. Same as Figure 1 but for 3.7um brightness temperature

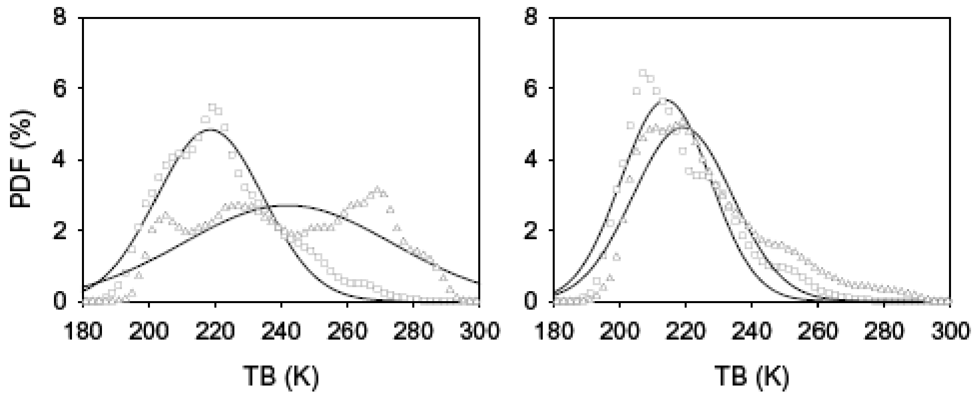

Figure 4. Same as Figure 1 but for 10.8um brightness temperature

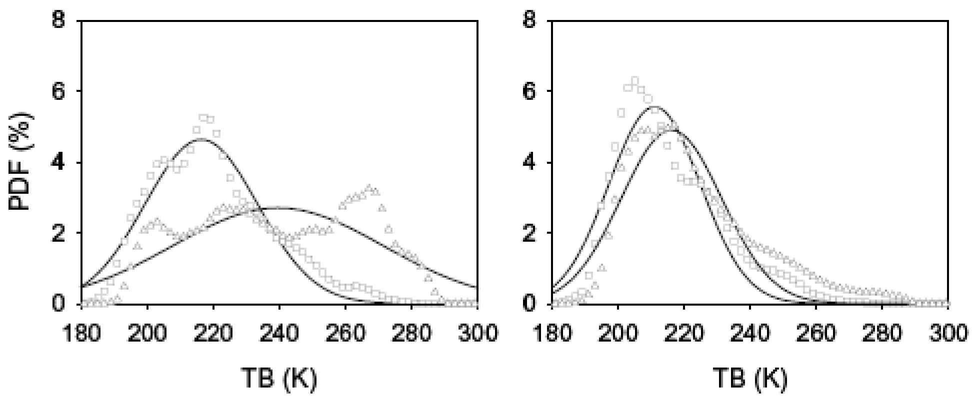

Figure 5. Same as Figure 1 but for 12.0um brightness temperature

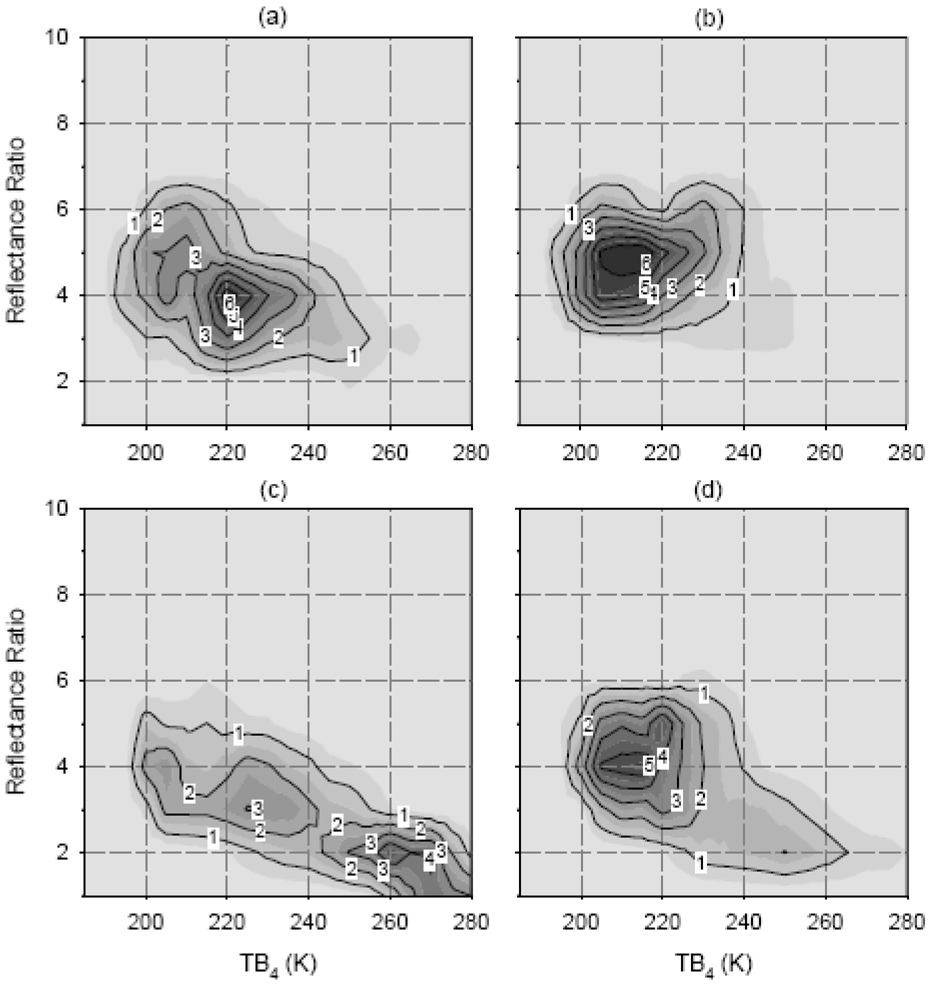

Figure 6. Frequency pattern of precipitating clouds (a,b) and non-precipitating clouds (c,d) in two-dimensional space composed of TB_4 and RF1/RF2 within fronts (left) and typhoons (right)

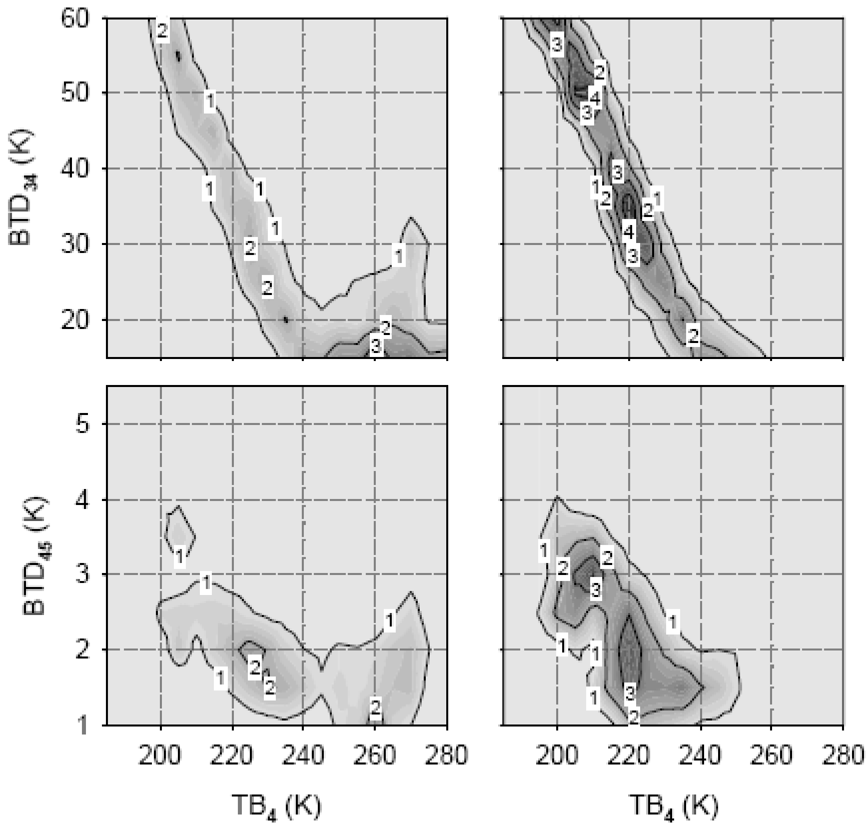

Figure 7. Frequency pattern of precipitating clouds (left) and non-precipitating clouds (right) in two-dimensional space composed of BTD_{34} (upper) or BTD_{45} (lower) and TB_4 within fronts

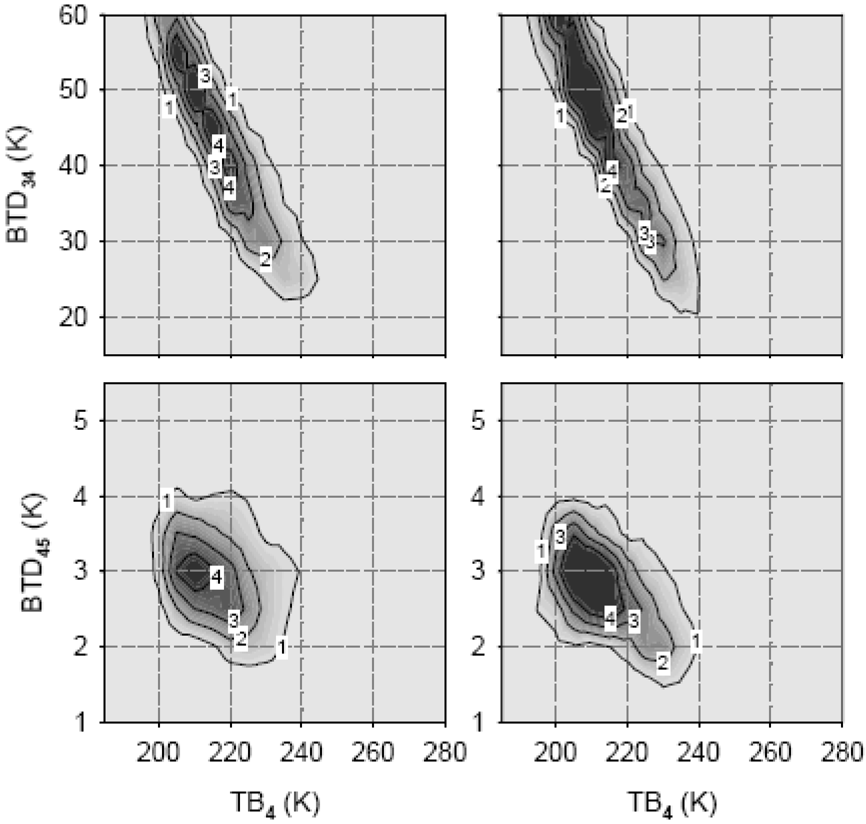

Figure 8. Same as Figure 7 but for clouds within typhoons

DYNAMICAL, MICROPHYSICAL, AND RADIATIVE INTERACTIONS BETWEEN AEROSOLS AND CUMULUS CLOUDS

Mikhail Ovtchinnikov, Larry Berg, and Evgueni Kassianov
Mikhail.Ovtchinnikov@pnl.gov

Pacific Northwest National Laboratory, P.O Box 999, MSIN: K9-24, Richland, WA 99354, USA

1. INTRODUCTION

Narrowing down uncertainties in aerosol indirect effect estimates requires improvements in understanding of cloud-aerosol interactions, which involve many different processes. Cloud related vertical motions can transport aerosols from the boundary layer to higher altitudes. Microphysical interactions involve processes that change physical and chemical properties of aerosol particles and cloud droplets, including nucleation scavenging, collision-coalescence, and aqueous chemistry. Evaluating relative contributions of these processes using in-situ measurements is difficult because of sampling issues. Remote sensing can provide a more representative sampling and a number of recent studies reported positive correlations between retrieved cloud fraction and aerosol optical depth (AOD) in neighboring cloud-free regions. Possible physical mechanisms that might lead to higher AOD in the vicinity of clouds include growth of aerosol particle size due to water uptake in near cloud regions of enhanced humidity (or cloud halos) and increase in aerosol concentration due to either cloud-driven transport of particles from other layers or production of new particles in cloud outflows. Alternatively, these findings could be largely a result of cloud-aerosol radiative interactions when areas around clouds are brightened by the sunlight scattered by cloud particles. This cloud-induced enhancement of reflectance then leads to a high bias in the AOD retrieved using a plane-parallel approximation. This study is aimed at unraveling roles of various processes in these complex interactions through closer integration of modeling and observational approaches.

2. APPROACH

We use large-eddy simulations coupled with size resolved aerosol and cloud particle distributions (Ovtchinnikov and Marchand, 2007) to model cloud aerosol interactions in a field of cumulus clouds. The simulated cloud and aerosol fields are analyzed for evidence of cloud processing of aerosols that could be detected by in-situ and remote observations. This is done by sampling the model fields along simulated flight paths to mimic aircraft measurements and by using a 3D radiative transfer model to compute radiances to serve as proxies for remote sensing observations. The presented model results are also compared against real measurements, including those from the recent Cumulus Humilis Aerosol Processing Study (CHAPS) conducted in the vicinity of Oklahoma City, OK, June 4-25, 2007.

3. OBSERVATIONS AND PRELIMINARY MODELING RESULTS

The principal objective of CHAPS was to examine the influence of anthropogenic aerosols from a mid-size urban area on the microphysics of cumuliform clouds, and the effects of these clouds on urban aerosols that pass through fields of fair weather cumulus. During the campaign, the DOE Gulfstream-1 (G-1) Research Aircraft made in-situ measurements of aerosol and cloud microphysics, including size distributions and composition from a time-of-flight aerosol mass spectrometer (AMS) and proton transfer mass spectrometer. A counterflow virtual impactor (CVI) allowed sampling of cloud droplets and examination of the composition of the residual dried particles.

Figure 1 shows a field of cumulus cloud sampled on June 23, 2007 as seen from the MODIS Airborne Simulator (MAS) and form a ground-based total sky imager (TSI). Most of the clouds are around one kilometer in diameter.

The G-1 flight pattern (fig. 2) was designed to sample below, within, and above the cloud layer, both inside and outside the pollution plume from Oklahoma City.

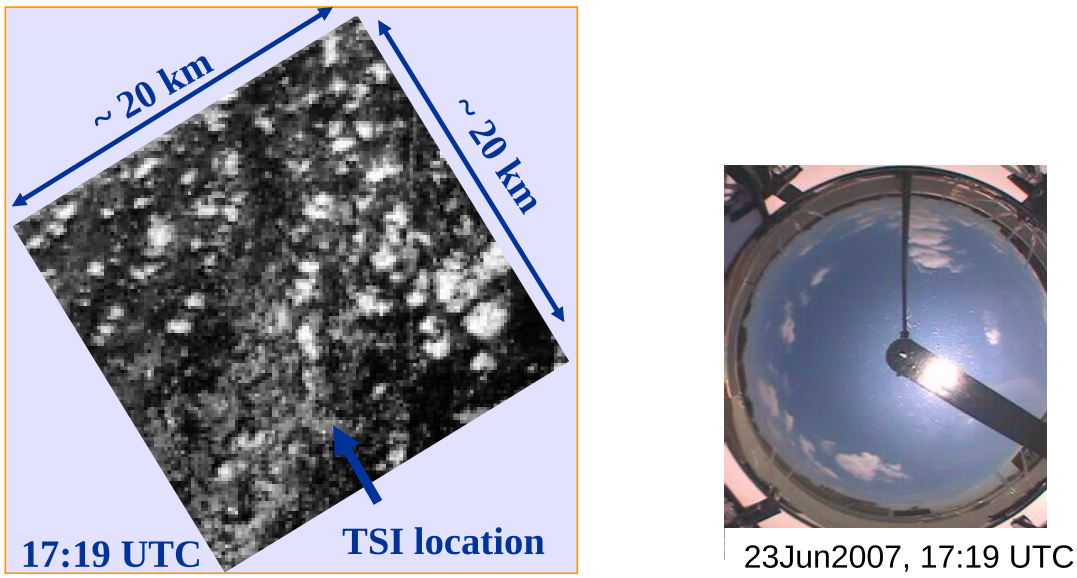

Figure 1. *A top-down (left) and bottom-up (right) views of the same field of cumulus clouds obtained form the MAS and TSI, respectively. The MAS flown on the NASA ER-2 provides a ground resolution of 50 meters. The TSI provides a hemispheric sky image.*

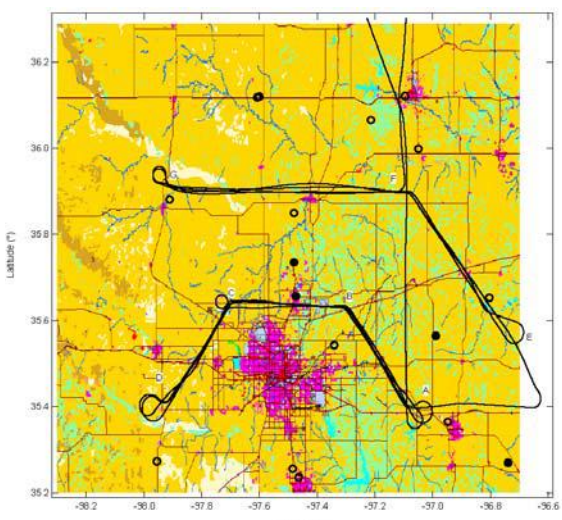

Figure 2. *A map of the Oklahoma City area with superimposed ground track of G-1 research flight on June 23, 2007. Small circles indicate locations of surface cites providing auxiliary measurements.*

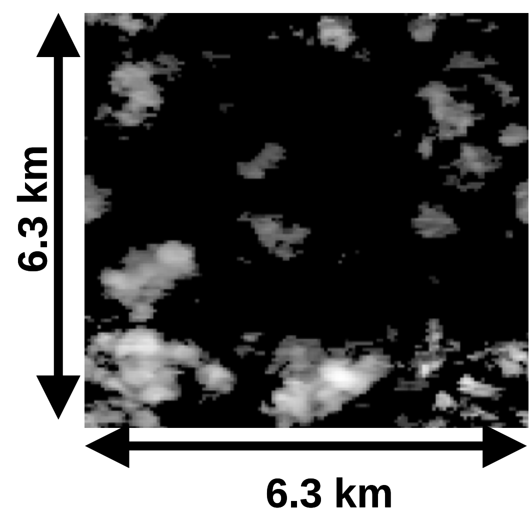

Figure 3. *Model simulated liquid water path for the June 23, 2007 case. Horizontal resolution is 50 meters, comparable to the MAS image on Figure 1.*

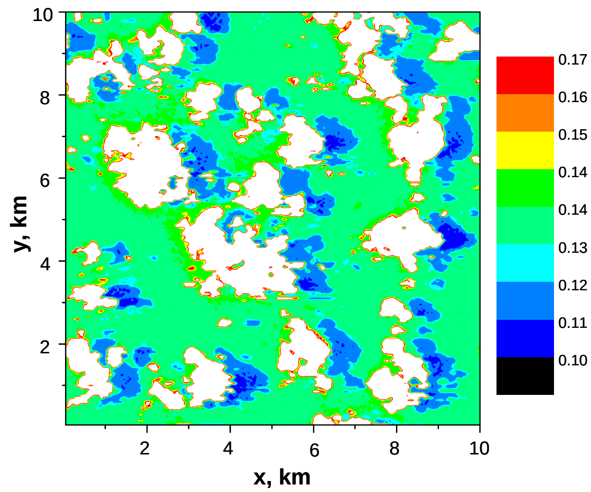

Figure 4. *Horizontal distribution of nadir reflectance at 0.47 μm wavelength computed using a 3D Monte Carlo radiative transfer algorithm from the model-generated cloud and aerosol properties. On this image clouds appear white and cloud shadows are blue.Pixel size is 50 x 50 m^2.*

The model initialized using the atmospheric profiles from soundings taken just north of Oklahoma City and driven by measured surface fluxes produce a cloud field similar to the observed one (fig. 3). To compare with G-1 observations of CO concentrations in this study, a passive tracer transport is implemented in the model. Tracking the CO concentrations allows one to quantify and separate transport effects from other aspects of cloud processing. CO can also serve as a marker for the city plume.

Model-generated cloud properties provide input to a 3D Monte Carlo radiative transfer algorithm that computes radiances that would be observed by satellite or suborbital instruments (fig. 4). These calculations are then used to study which aspects of the cloud aerosol interaction can and cannot be diagnosed from present remote sensing techniques. Results of this analysis will be presented at the conference. The synthetic radiances are also used to test and improve aerosol optical depth retrieval algorithms (Kassianov and Ovtchinnikov, 2008).

4. REFERENCES

Kassianov, E., and M. Ovtchinnikov, 2008: On reflectance ratios and aerosol optical depth retrieval in the presence of cumulus clouds, *Geophys. Res. Lett.* (in press).

Ovtchinnikov M, and R.T. Marchand, 2007: Cloud model evaluation using radiometric measurements from the Airborne Multiangle Imaging Spectroradiometer (AirMISR).*Rem*. *Sens*. *Envir*. **107,**185-193.. doi:10.1016/j.rse.2006.05.024.

ACKNOWLEDGEMENTS

The Pacific Northwest National Laboratory is operated for the DOE by Battelle Memorial Institute under contract DE-AC06-76RLO 1830. This research was supported in part by the DOE Atmospheric Science Program and by the NASA Radiation Sciences Program. The data were provided by the DOE Atmospheric Radiation Measurement (ARM) Program Climate Research Facility and the NASA Langley Research Center.

ROLE OF CLOUD RADIATION INTERACTION IN THE DIURNAL VARIATION OF PRECIPITATION

SETHU RAMAN AND ADRIENNE WOOTTEN
DEPARTMENT OF MARINE, EARTH AND ATMOSPHERIC SCIENCES
NORTH CAROLINA STATE UNIVERSITY, RALEIGH, NC 27695-8208

1. Introduction

Forecasting convection in the summer is a challenge for meteorologists due to the meso scale and local scale effects. These effects are enhanced and many times are caused by horizontal gradients in surface heat fluxes caused by the presence of different soils with different heat capacities or by land use. Parameterizations in most of the weather forecast models experience problems in accounting for variations of such heat flux gradients that cause low level convergence and convection initiation. Another problem the models face is the convection caused by cloud radiation interaction. This process is dominant during nights. In the Sandhills region of North Carolina, a strong gradient in soil type is present with soil changing from clay in the Sandhills to sand in the coastal regions.

In this paper, a case study is presented to illustrate the diurnal variation of convection and precipitation and the processes involved. We then discuss the diurnal variation of convection over the Sandhills region using observations for six years. Cloud radiation interaction processes that may be responsible for the diurnal variation are discussed. Performance of a weather forecasting model in predicting diurnal variation of convection is presented.

2. A Case Study of Nocturnal Convection

This section describes briefly the diurnal convection pattern over the Sandhils region during a typical summer day, 10 August 2001. Location of the stations used in this analysis are shown

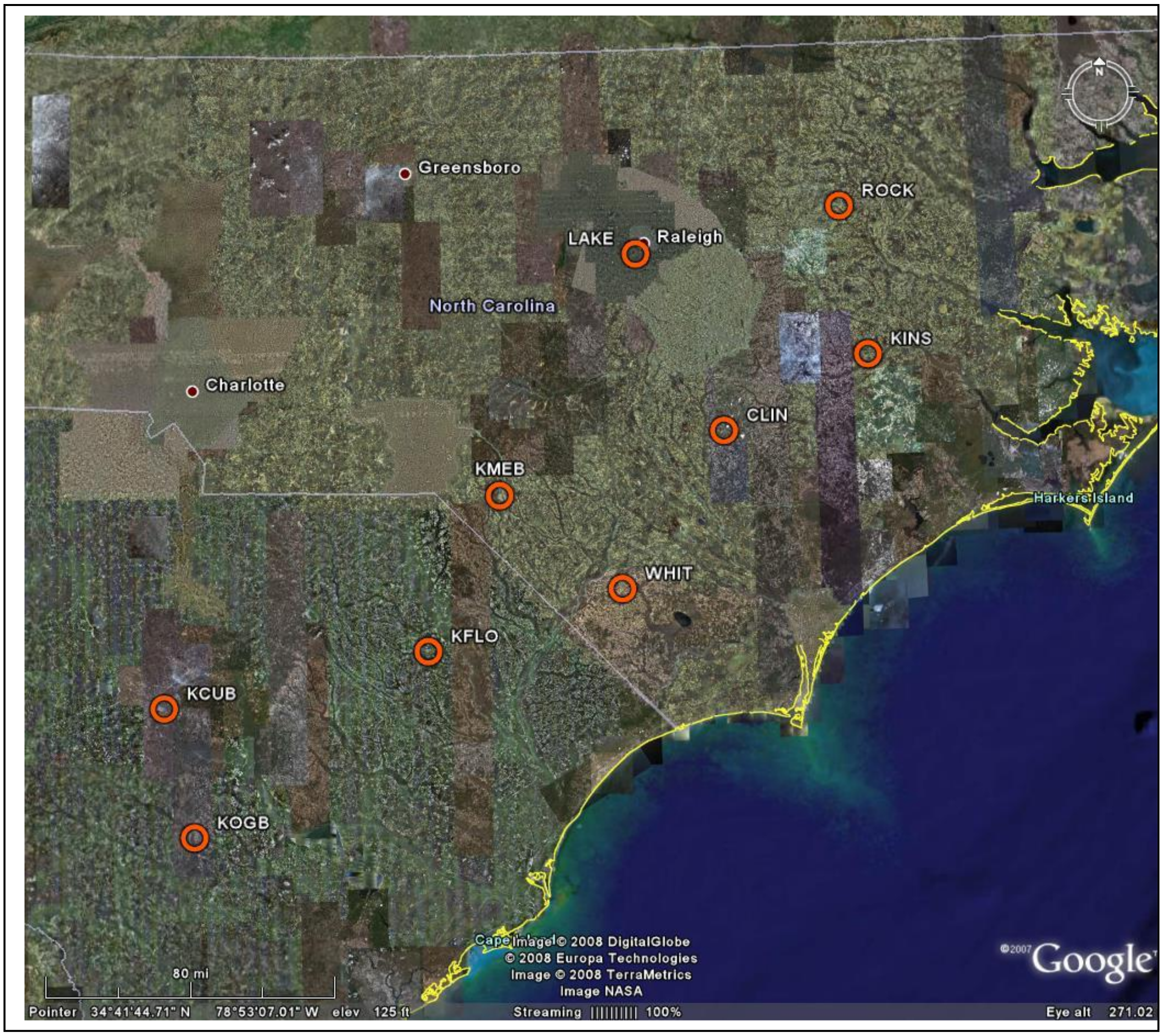

Figure 1. Regional map showing Sandhills and coastal surface weather stations

in Figure 1. Radar reflectivity from the Doppler radar located at Columbia, SC radar shows apparent lack of convection during day time with the exception of those storms along the sea breeze front close to the coast in the afternoon (Fig. 2 a-c). This convection is also visible through the GOES-8 IR imagery at 1900 GMT 1400 LT as shown in Figure 2. However, just before the sunset in the Carolinas, a line of storms begins to form along the southern edge of the Sandhills (Fig 3 a-d). As the night progresses strong convection is present along the Sandhills region while convection elsewhere has disappeared. Around 2300 LT (Fig 3c), a group of storms advances northward along the Sandhills, becoming more intense along the way. This group of storms proceeded further up the Sandhills into North Carolina by 0200 on 11 August (Fig 3d), the next day. Precipitation amounts by this night time convection were significant (1.35 in or 34 mm) at the Colombia automated weather station (KCUB). This convection was highly localized over the Sandhills as can be seen from the regional distribution of the nocturnal precipitation shown in Figure 4 a-d. The precipitation distribution is mapped from 1700 LT on August 10 to 0200 on August 11, 2001 in Figures 4 a-d to investigate how local the convection was. Precipitation was not observed at other weather stations through the night, and Columbia (KCUB) recorded the maximum precipitation as the storms reached maturity.

3. Clmatological Analysis of Diurnal Precipitation

In this study, observations for the summer, May through September, from 2001 to 2006 was used for the stations shown in Figure 1. The stations used were NC ECONet (North Carolina Environmental and Climate observing Network) and the National Weather Service ASOS (Automated Surface

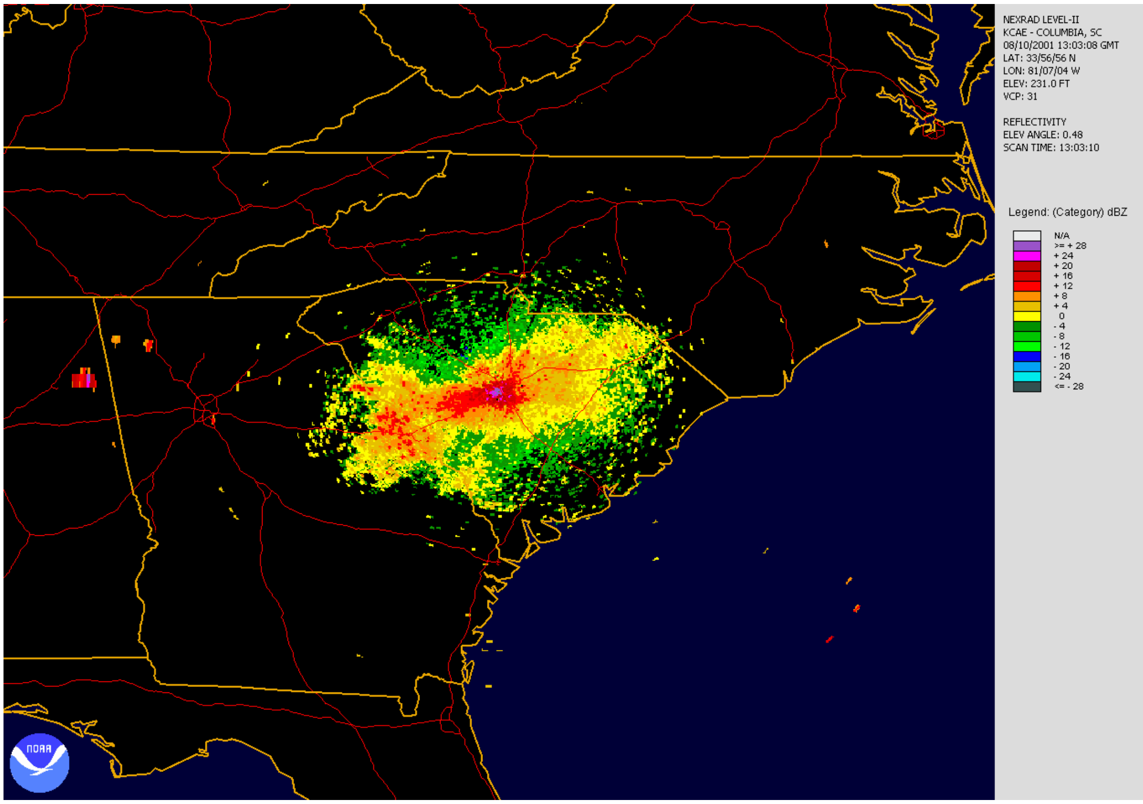

Figure 2a. Radar image from Columbia, SC 1300 GMT (8EST) 8/10/2001

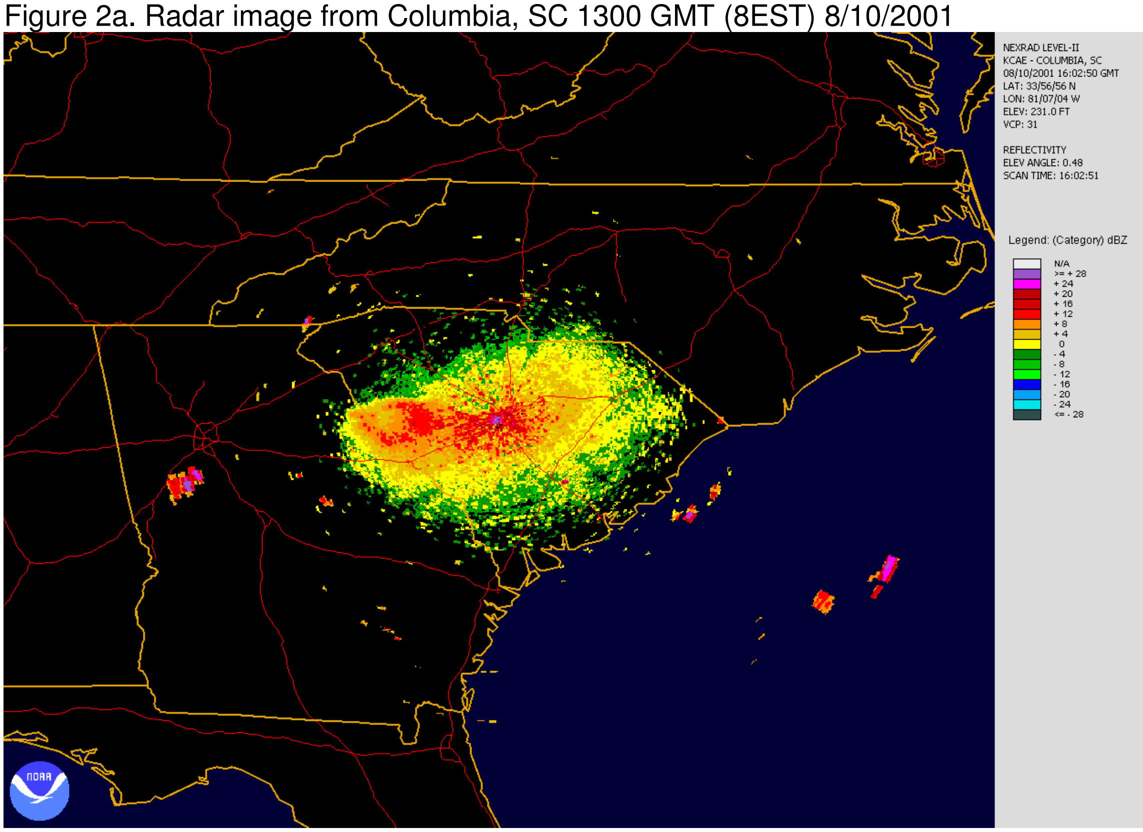

Figure 2b. Radar image from Columbia, SC 1600 GMT (1100 LT) 8/10/2001

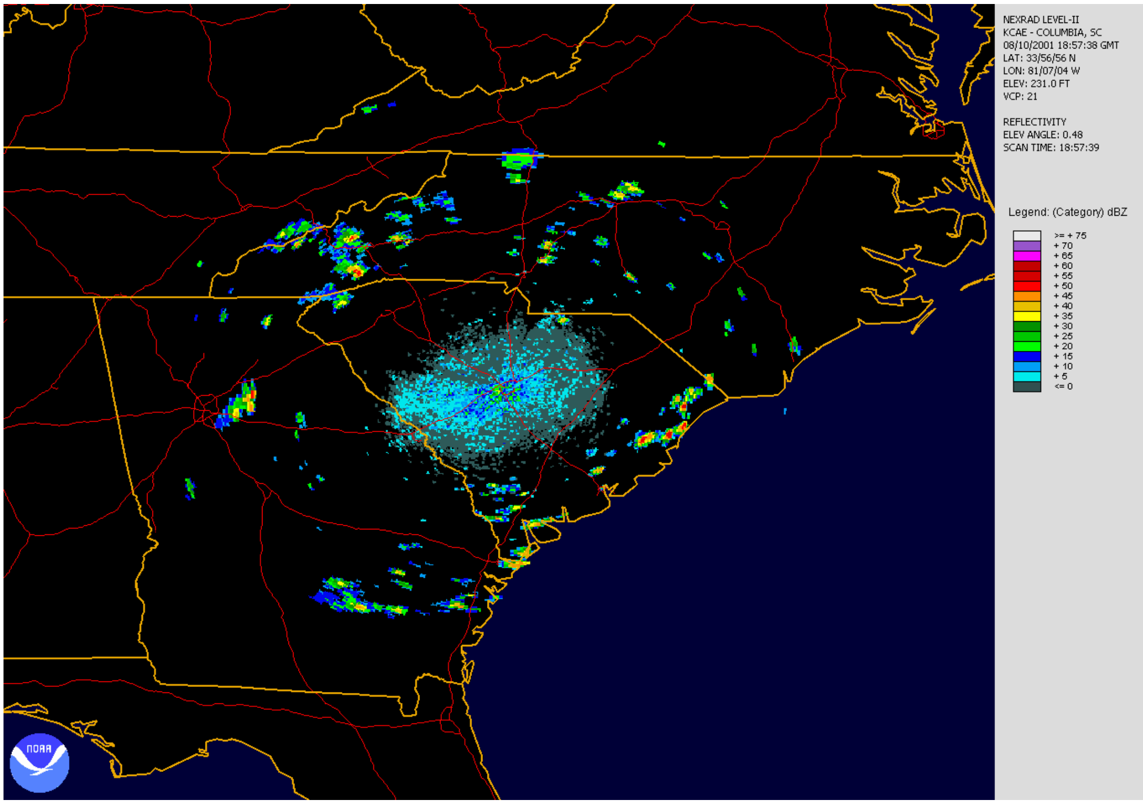

Figure 2c. Radar image from Columbia, SC 1900 GMT (1400 LT) 8/10/2001

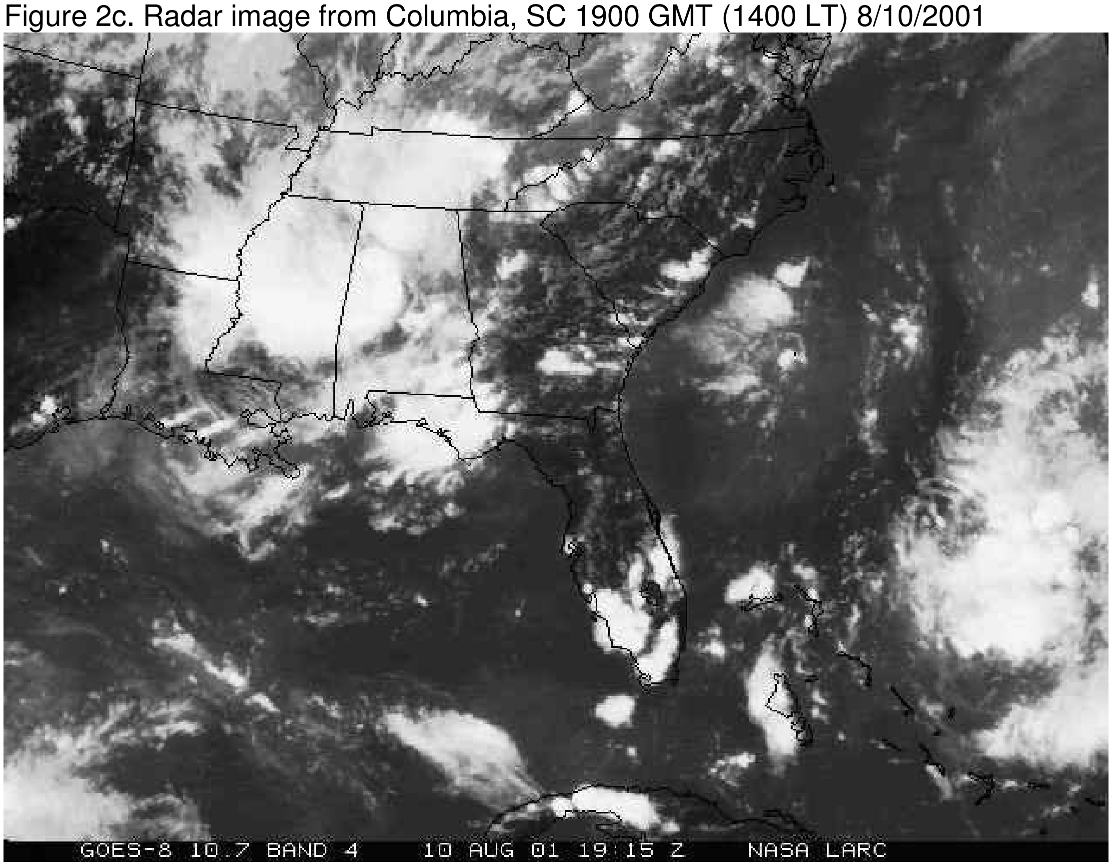

Figure 2d. GOES-8 IR image, 19GMT (1400 LT) 8/10/2001

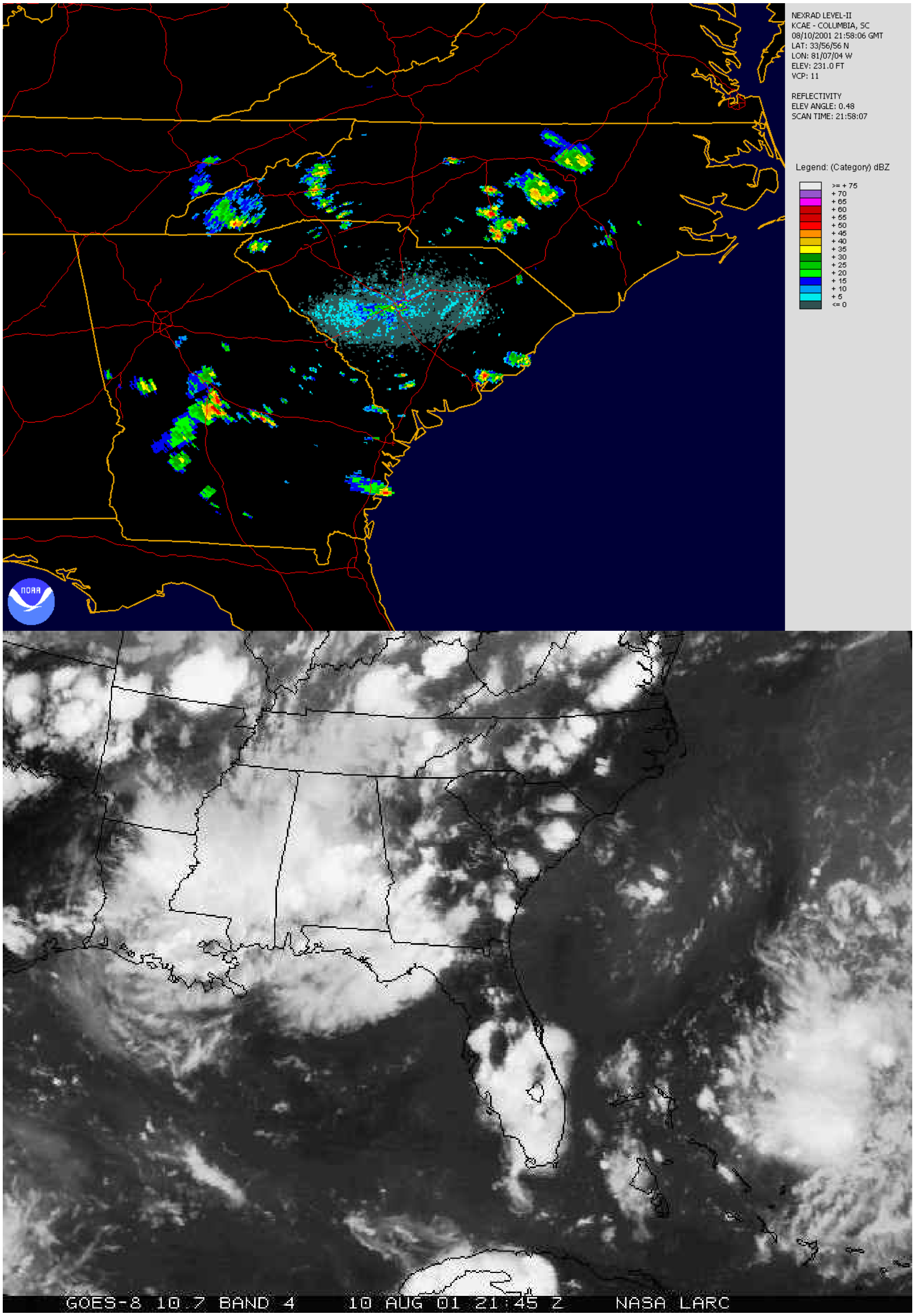

Figure 3a. Radar and Satellite from 8/10/2001 2200 GMT (1700 LT)

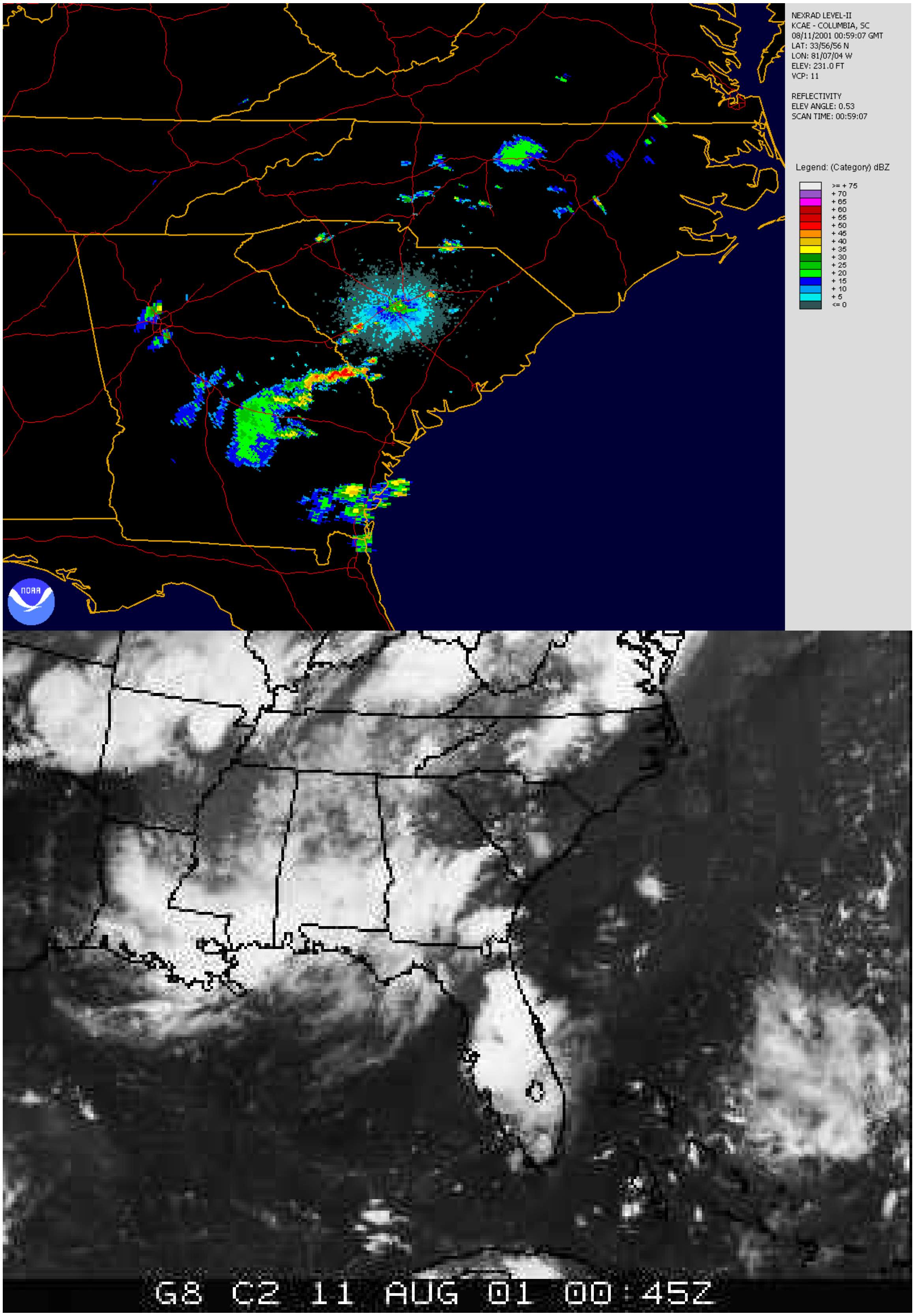

Figure 3b. Radar and Satellite from 8/11/2001 0100 GMT (8/10/2001 2000 LT)

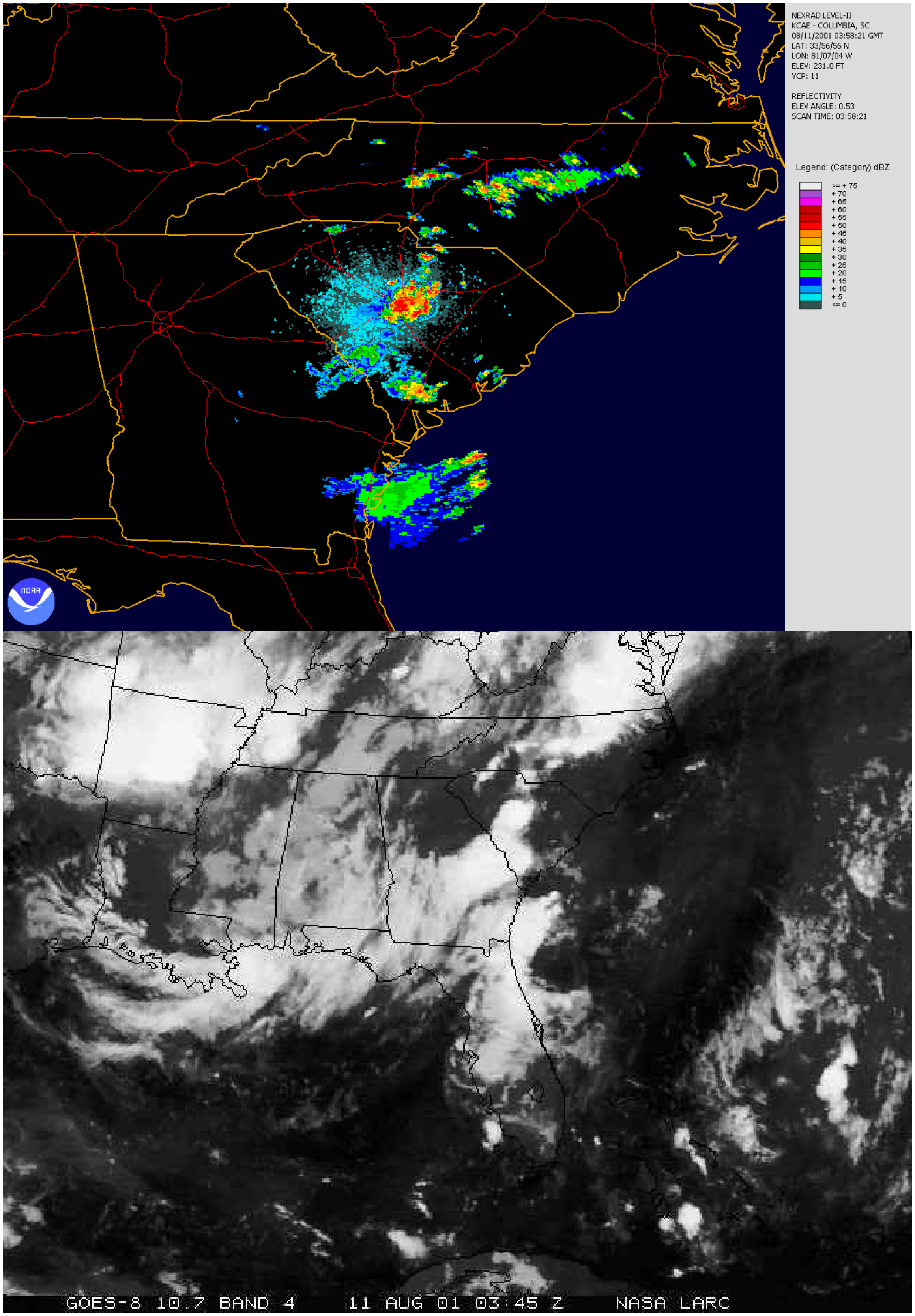

Figure 3c. Radar and Satellite from 8/11/2001 0400GMT (8/10/2001 2300 LT)

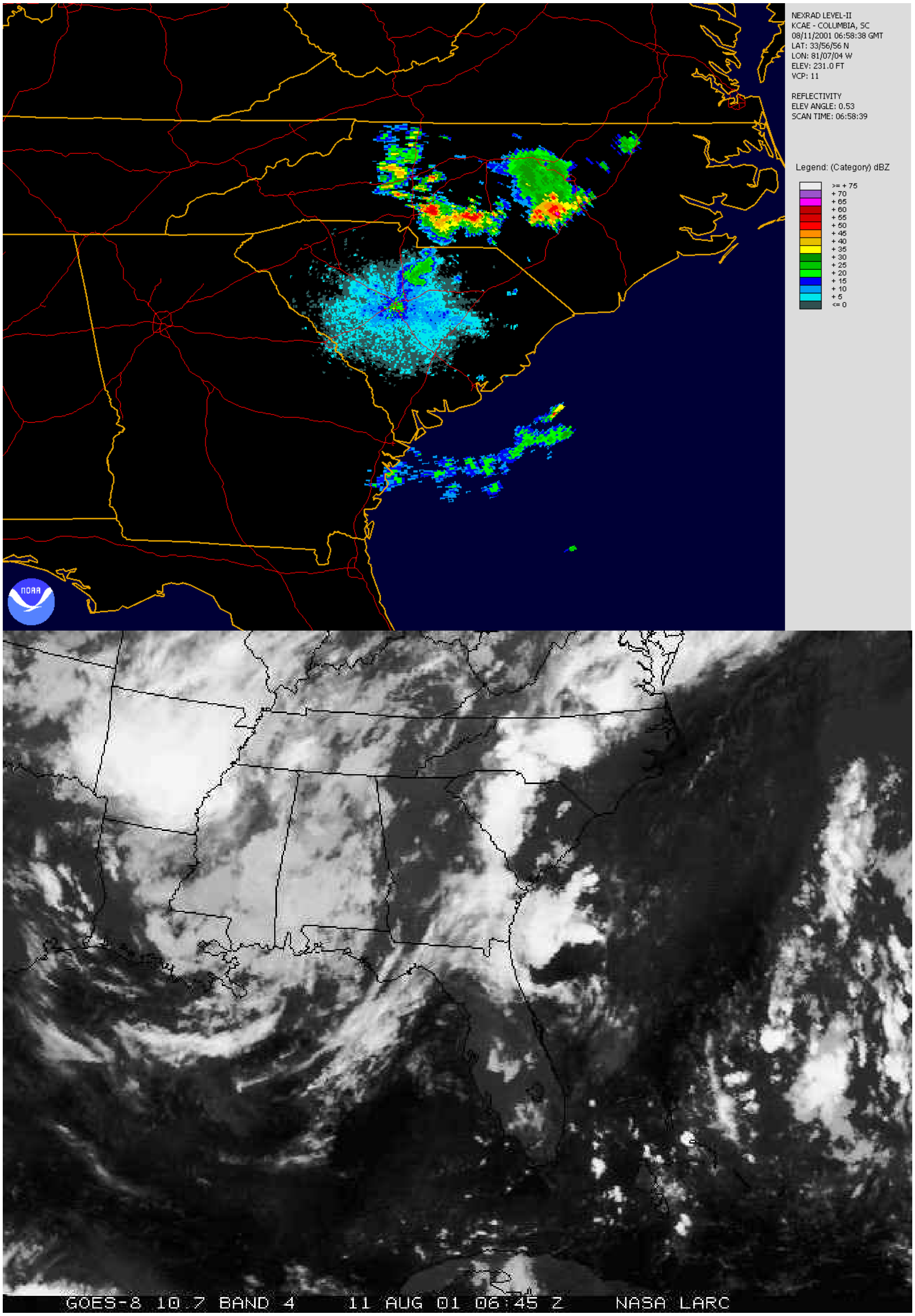

Figure 3d. Radar and Satellite from 8/11/2001 0700 GMT (0200 LT)

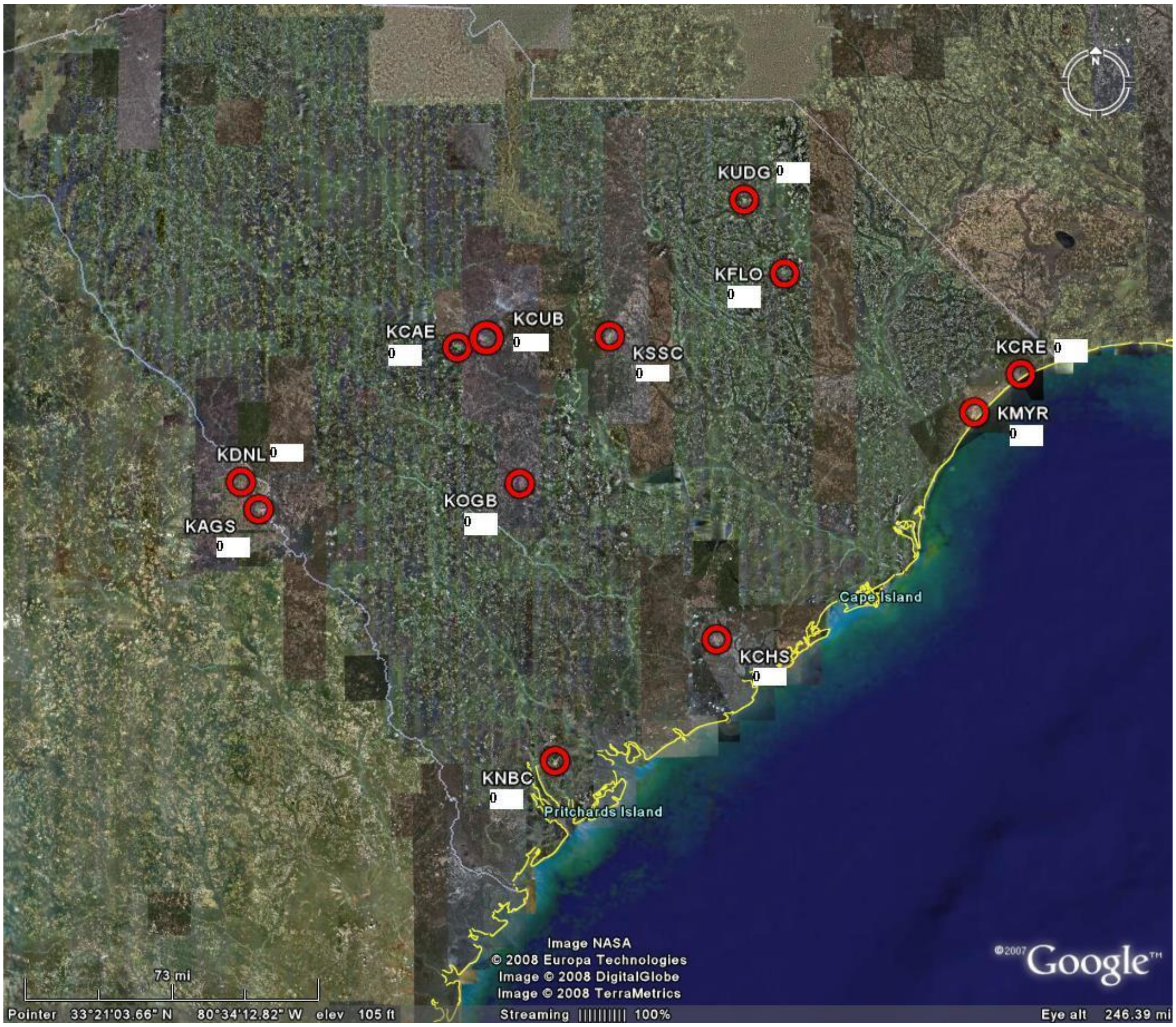

Figure 4a. Precipitation map for 2200 GMT (1700 LT) 8/10/2001. Values inside the white rectangles show the precipitation in inches for the previous hour.

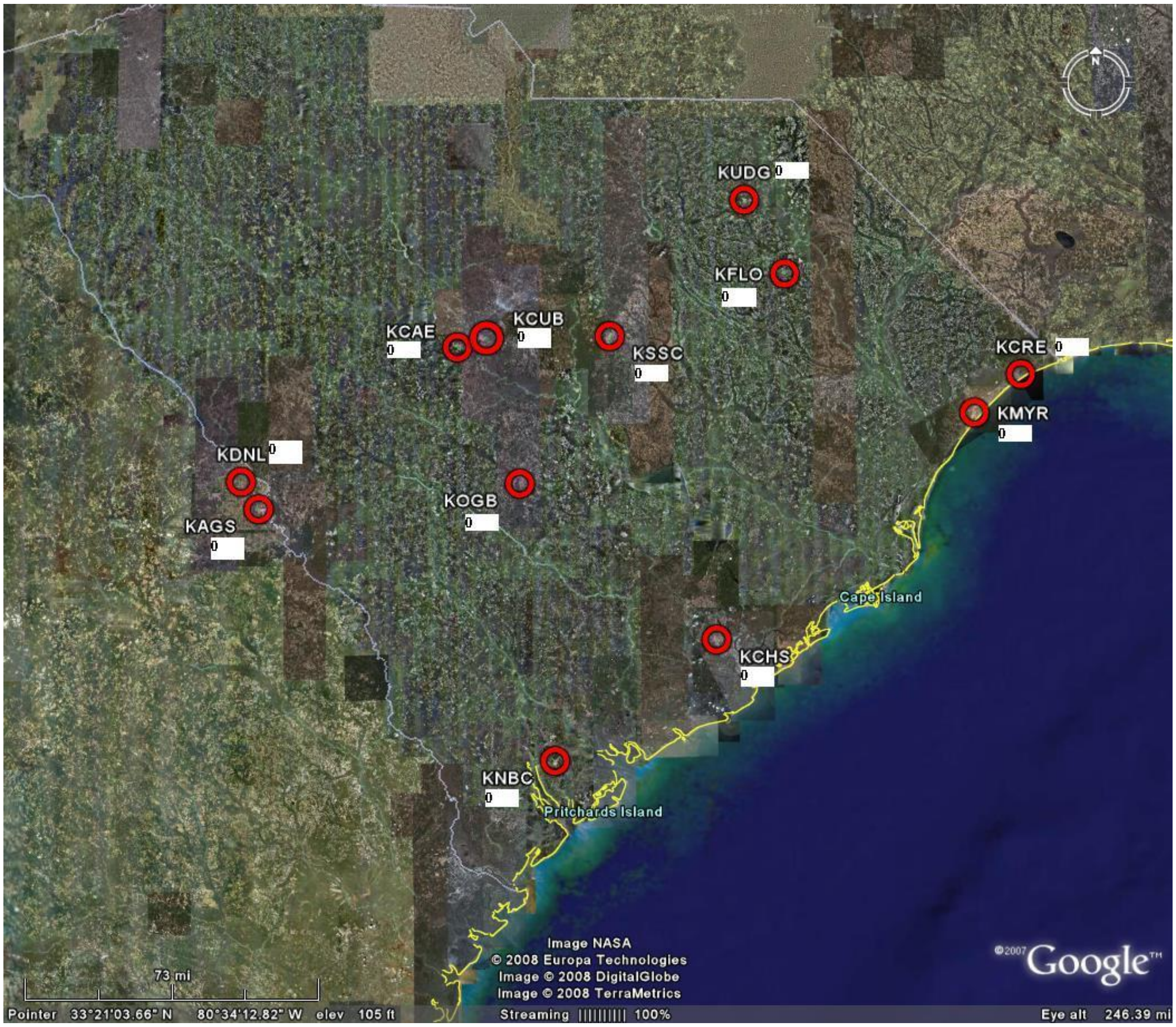

Figure 4b. Precipitation map for 8/11/2001 0100 GMT (8/10/2001 2000 LT)

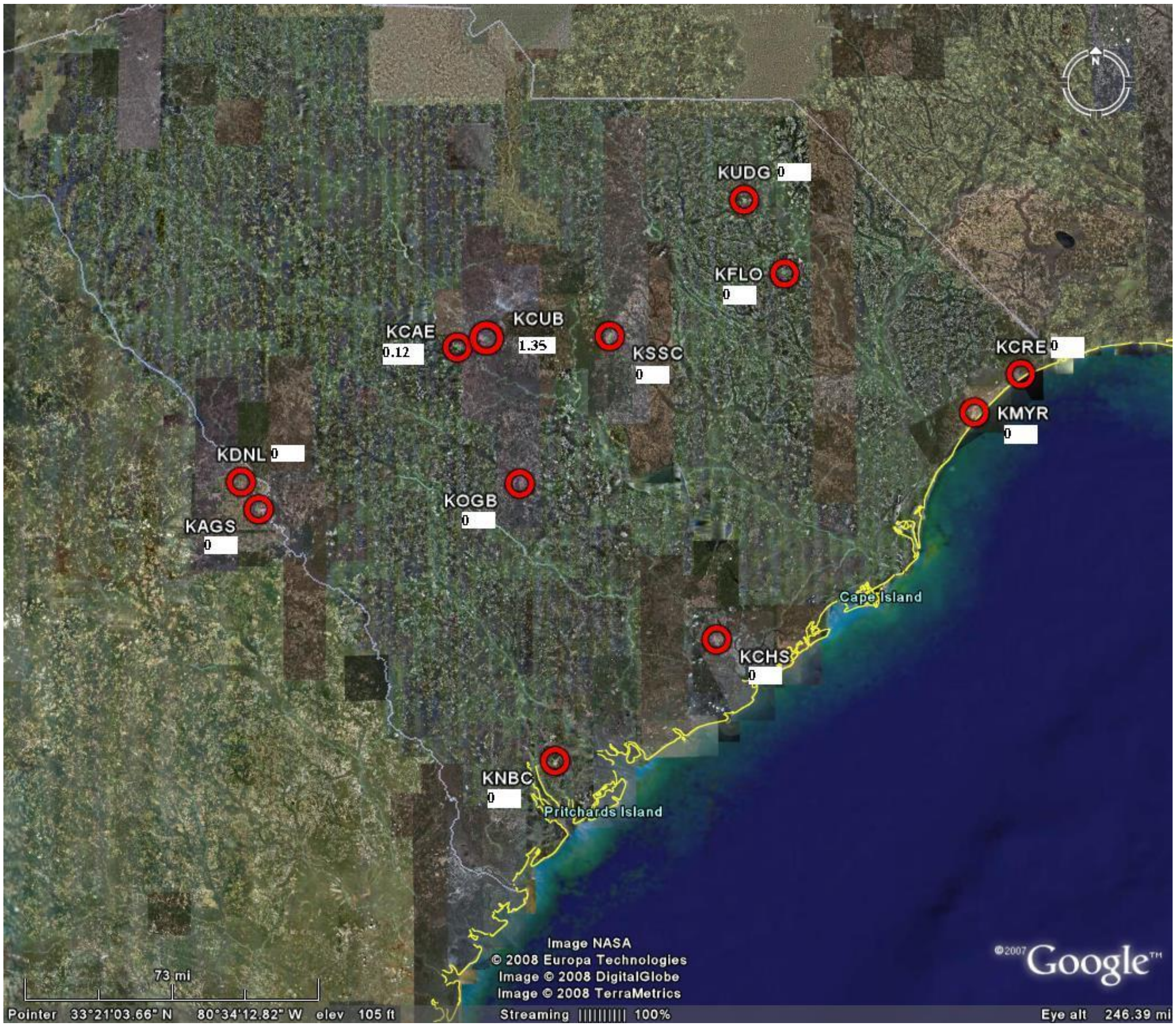

Figure 4c. Precipitation map for 8/11/2001 0400 GMT (8/10/2001 2300 LT). Precipitation over the previous hour at KCUB (Columbia) was 1.35 inches or 34 mm.

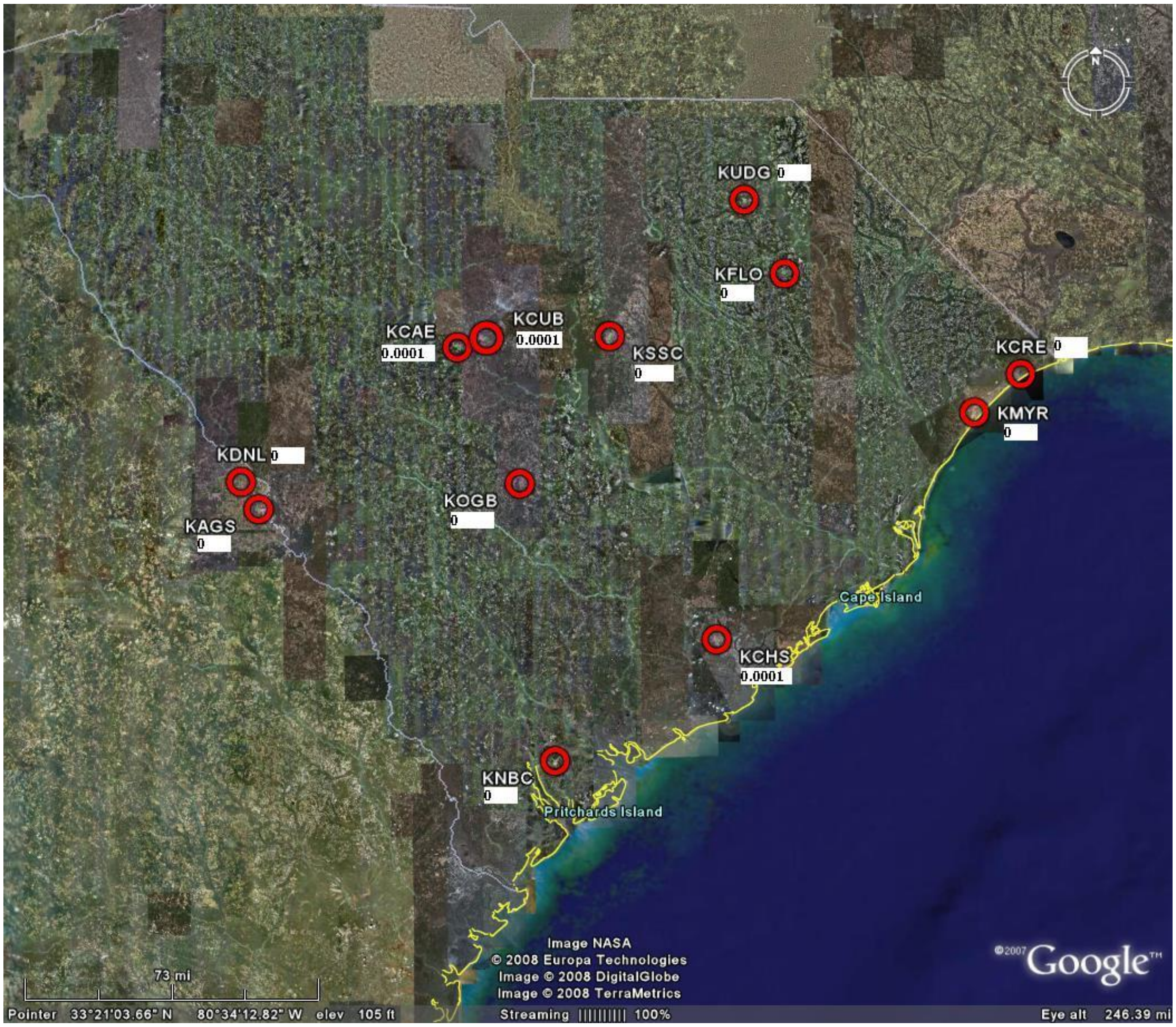

Figure 4d. Precipitation map for 8/11/2001 0700 GMT (0200 LT)

Observing Stations used in this study are distributed between the Sandhills region and the coastal region of North Carolina and South Carolina. Locations of these stations were shown in Figure 1 and the names and locations of all these stations are provided in Table 1. Rainfall data recorded from a tropical cyclone was removed as it is not considered a mesoscale convection. The data was checked for quality, and any observations that were flagged by the State Climate Office of North Carolina as poor quality were not used in this study. Also any of the hourly observations not recording rainfall were discarded since we focus on the actual convection, there was no need to keep observations with no recorded rainfall. The rainfall data was then separated into day and night, assuming day to be 6 a.m. EST to 6 p.m. EST and night to be 6 p.m. to 6 a.m. EST. At this point the data was also tested for autocorrelation, which is the preceding observation effecting the current observation, using the Durbin-Watson Test. There was a minor amount of autocorrelation in the data, which has a negligible effect on the results.

3.1 Statistical Analysis of the Observations

With all of the data from 14 stations separated into day and night amounts for each month, and overall, we performed several Welch's t-tests on the data It tests for the difference between the true mean of two stations or two times, but unlike other t-tests it assumes that the two groups being tested have unequal variances, but like the other t-tests an approximately normal population distribution. This t statistic also assumes the original hypothesized difference to be 0, and tests for the difference having significant difference from 0:

Station ID	Station name	Latitude	Longitude
ROCK (Rockymount, NC)	Upper Coastal Plain Res. Stn.	35.89295	-79.72389
LAKE (Raleigh, NC)	Lake Wheeler Rd Field Lab	35.72816	-78.67981
KFLO (Florence, SC)	Florence Airport	34.18536	-79.72389
KCUB (Columbia, SC)	Owens Downtown Airport	33.97047	-80.99525
WHIT (Whiteville, NC)	Border Belt Tobacco Res. Stn.	34.41347	-78.7923
KMEB (Maxton, NC)	Laurinburg-Maxton Airport	34.79194	-79.36585
KOGB (Orangeburg, SC)	Orangeburg Municipal Airport	33.4568	-80.8595
KINS (Kinston, NC)	Cunningham Research Station	35.30288	-77.57306
CLIN (Clinton, NC)	Horticultural Crops Research Stn.	35.02218	-78.28195

Table 1. Listing of Weather Stations and their Locations

$$t = \frac{\overline{X}_1 - \overline{X}_2}{\sqrt{\frac{s_1^2}{N_1} + \frac{s_2^2}{N_2}}} \qquad (1)$$

where $\overline{X}_i$, s_i^2 and N_i are the i^{th} sample mean, sample variance, and sample size, respectively. There are also degrees of freedom associated with this test.

$$v = \frac{\left(\frac{s_1^2}{N_1} + \frac{s_2^2}{N_2}\right)^2}{\frac{s_1^4}{N_1^2 * v_1} + \frac{s_2^4}{N_2^2 * v_2}}$$

$$v_1 = N_1 - 1$$

$$v_2 = N_2 - 1$$

(2 - 4)

However, $t_{critical}$ is also dependent on the test in question. If it is hypothesized that $\mu_1 < \mu_2$ then the value used as $t_{critical}$ will be the opposite sign of the value given in the table. If it is hypothesized that $\mu_1 > \mu_2$ then the value used as $t_{critical}$ is the same as in the original alpha table, where μ_i is the i^{th} unknown true population mean. $t_{critical}$ is determined by the degree of freedom of each variable (v), and the probability that serves as the level of significance for the test (α). The α value in all tests was 0.05. The Welch's t-test was performed on the different times (day vs. night)

3.2 Comparison of Model Forecasts with Observations

The 6 hr archived forecast precipitation data from the North American Mesoscale (NAM) Model was retrieved for the last phase of the project. This data was for the months of June, July and August 2006, with four 6 hr model runs in each day at 12 km resolution. For this portion of the analysis only two of the original nine stations were used. These stations were KCUB (Columbia) and LAKE (Lake Wheeler). To make the forecast validation easier, the observed precipitation data for each day in the same time period was separated into 6 hr. groups which matched the 6 hr forecast runs. For example all the observations from 0600 Z to 1200 Z (0100 LT to 0700 LT) were grouped together to match the 0600 Z model run which forecasts total surface precipitation from 0600 Z to 1200 Z. Welch's T-test was then performed for the difference between observed and forecast precipitation, along with a calculation for percent forecast error as follows:

$$PercentError = \left(\frac{\sum Obs. - \sum FX}{\sum Obs.} \right) * 100 \quad (5)$$

Where $\sum Obs.$ is the sum of all the observed precipitation in a given model run, and $\sum FX$ is the sum of all the forecast precipitation in a given model run. The model runs are 0600 GMT, 1200 GMT, 1800 GMT and 0000 GMT (0100 LT, 0700 LT, 1300 LT, and 1900 LT). Local time (LT) is the Eastern Standard Time (EST). The statistical analysis described above was performed for all these model runs.

4. Discussion of Results

4.1 Statistical Results

As expected from the initial analysis there is significant difference between day and night precipitation in the Sandhills region. However, the diurnal variation in this precipitation also seems to change with each month as shown in Figure 5 for the Sandhills region. While there is a difference between night and day precipitation in the region, the greatest difference shown by ANOVA and Welch's T-tests were in July and May in the Sandhills. Figure 5 showed the difference between the summed day precipitation and summed night precipitation for each month and over all the different months in the Sandhills. The difference between the summed day precipitation and summed night precipitation for each

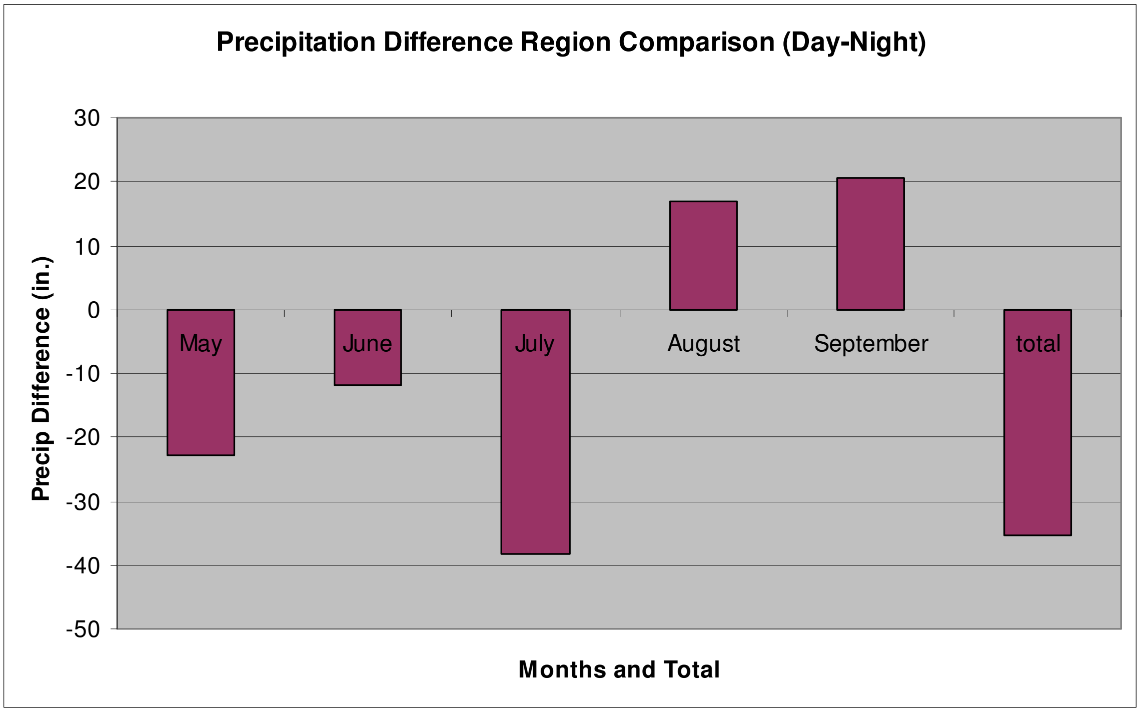

Figure 5. Precipitation differences - Night precipitation total for each month and overall subtracted from Day precipitation total for each month and overall.

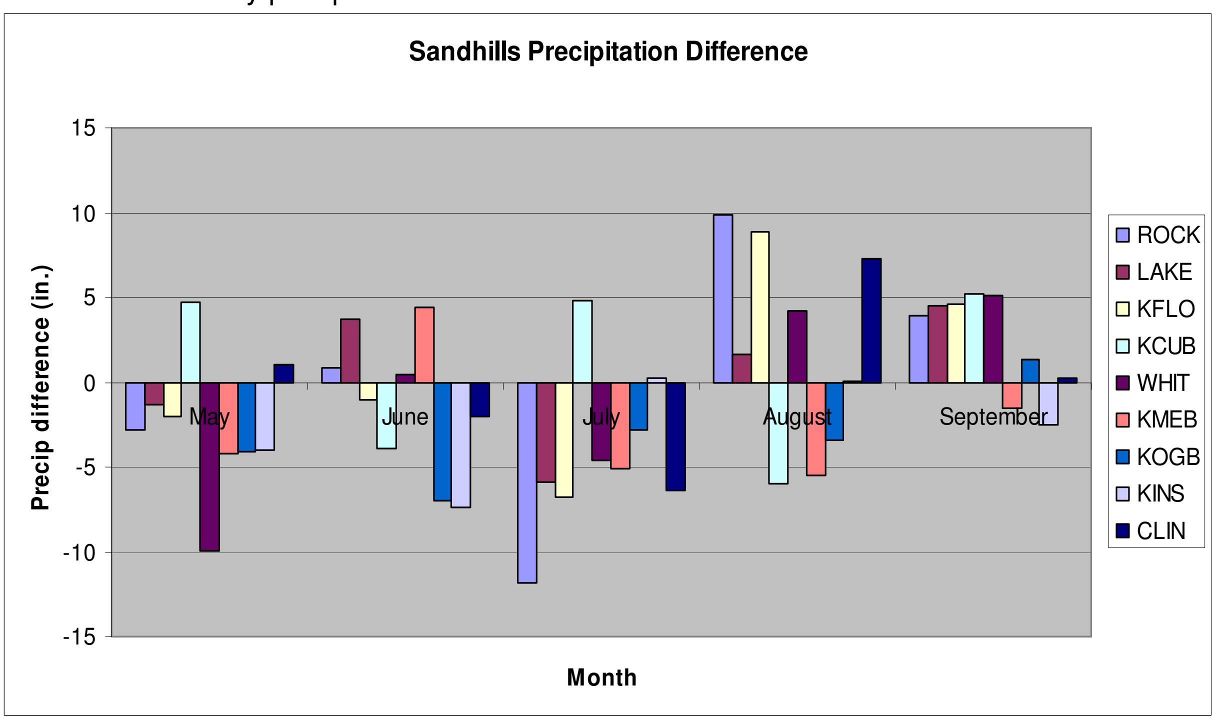

Figure 6. Sandhills inter-station comparison of precipitation difference: Night precipitation total for each month subtracted from Day precipitation total for each month

month for all the sites in the Sandhills is shown in Figure 6. The p-values for each T-test performed for both regions together and both regions individually over all the months in the time period is given in Table 2.

4.2 Forecast Validation

The 12 km resolution NAM (North American Mesoscale) model used to test for the difference between observed and forecast precipitation did show a strong difference between the two. The p-values from the T-test indicate this especially well with the 19 EST (0Z) model run (Table 3). Specifically for Columbia (KCUB) which lies in the heart of Sandhills, there was a strongly significant difference between observed and forecast precipitation. The T-test showed that the NAM model was under-predicting the observed precipitation at KCUB (Sandhills). However, at LAKE, located at the northern end of the Sandhills region, there was no significant difference between observed and forecast precipitation in any of the model runs. Figure 7 shows the percent error of the NAM model at both the sites, and while the error at LAKE appear significant, in terms of T statistic used, it is not significant. Figure 8 shows the sum difference between observed and forecast precipitation, that is:

$$AmountDifference = \sum Obs. - \sum FX \quad (14)$$

Where $\sum Obs.$ and $\sum FX$ are same as what is described for them previously. Of particular interest is the (statistically significant) percent error in the 1900 LT model run for KCUB, and the (not statistically significant) percent error in the 0100 LT model run for the same station. Both of these are model runs forecasting night precipitation, yet the 1900 LT run showed significant difference for KCUB, while the 0100 LT model run did not show any difference for this site. Also at KCUB (Columbia), the model significantly under-predicted

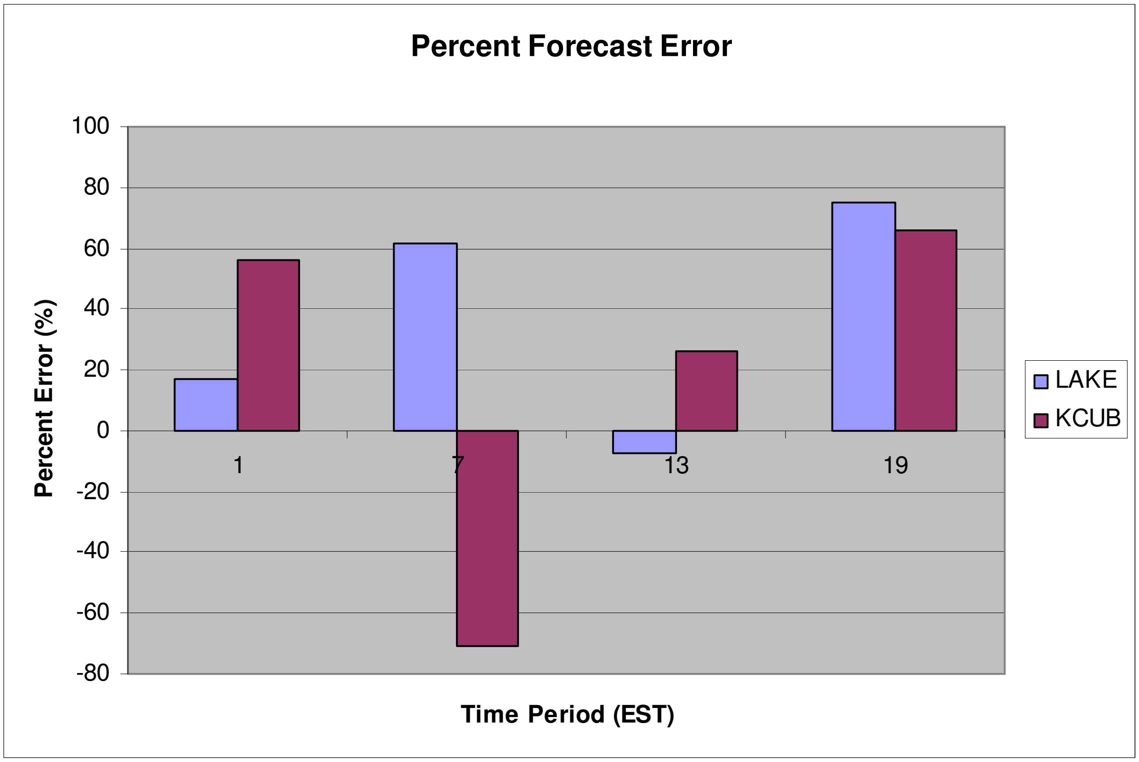

Figure 7. NAM Percent Error for each model run: a negative bar represents the model over-predicting and a positive bar represents the model under-predicting

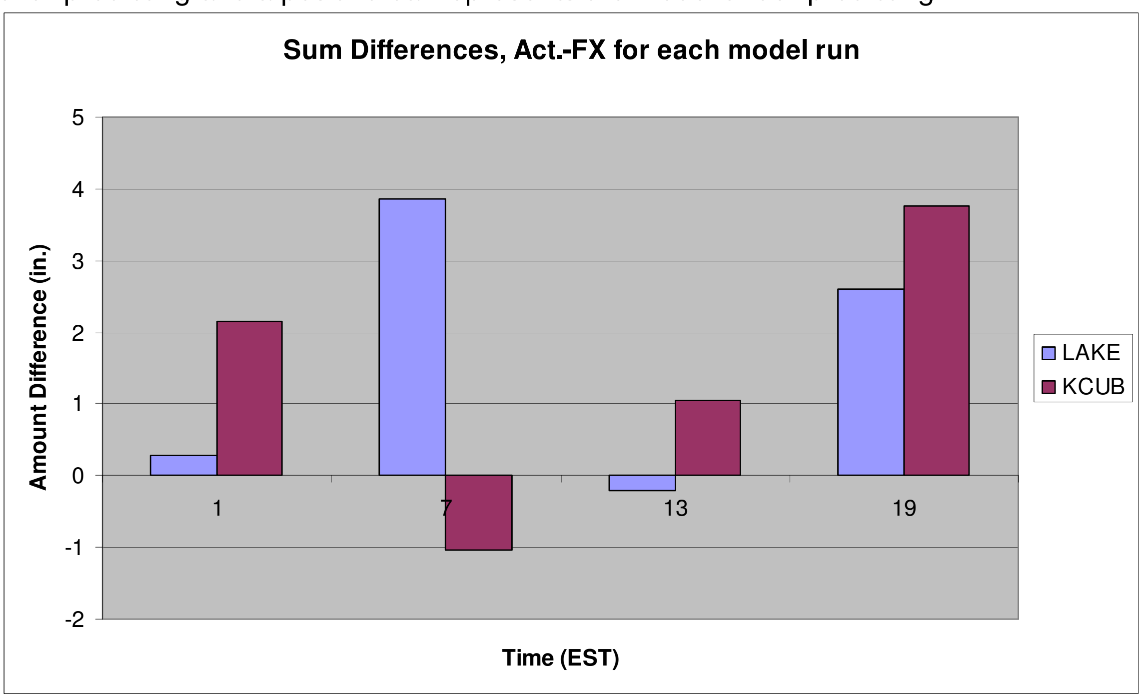

Figure 8. Sum Differences between observed and forecast precipitation.

Month	p-value
May	0.0958
June	0.3767
July	0.0265
August	0.3778
September	0.0514

Table 2. The p-values for Day vs. Night precipitation in the Sandhills region for each month

Sum Differences Difference (Obs-FX) FX-Forecast Data
Significant Difference when p-value<0.05 Obs.-Observed Data

LAKE

Run	Observed	FX	Obs.-FX	Percent Error	p-values
1	1.64	1.3623	0.277	16.932	0.366
7	6.29	2.4355	3.854	61.278	0.217
13	2.77	2.9753	-0.205	-7.411	0.427
19	3.47	0.8745	2.595	74.796	0.059

KCUB

Run	Observed	FX	Obs.-FX	Percent Error	p-values
1	3.7608	1.6191	2.141	56.945	0.212
7	1.4509	2.4877	-1.036	-71.461	0.18
13	3.9931	2.9510	1.042	26.096	0.23
19	5.6813	1.9237	3.757	66.138	0.042

Table 3. Percent Error and p-values

the precipitation. We believe that the reason for this under prediction in the Sandhills region could be the inability of the model land use physics to properly represent horizontal gradients in surface turbulent heat fluxes caused by gradients in soil type, between sand and clay in this case. This process essentially initiates convection during the day time in the absence of any frontal dynamics and forms clouds. After sun sets, cloud – radiation interaction essentially appears to be the main process in causing deep convection and the current numerical models are not able to simulate this deep convection well.

Acknowledgements

Funding for this research was provided by the Division of Atmospheric Sciences, National Science Foundation under the Grants ATM – 0233780 and ATM-342691. We thank Ryan Boyles, Aaron Sims, and Mark Brooks of the State Climate Office of North Carolina for providing technical assistance
.

SENSITIVITY OF THE MARINE STRATOCUMULUS DIURNAL CYCLE TO THE AEROSOL LOADING

I. Sandu[1], J.L. Brenguier[1], O. Geoffroy[1], O. Thouron[1], V. Masson[1]

[1] GAME/CNRM, METEO-FRANCE - CNRS, FRANCE

1 INTRODUCTION

Anthropogenic aerosols may have a noticeable impact on cloud radiative properties and on precipitation efficiency. They are therefore likely to also significantly affect the life cycle of boundary layer clouds and hence impact the earth radiation budget. It is however difficult to document such impacts from observations. Indeed, different aerosol types generally correspond to different air masses, hence to different vertical profiles of moisture and stability. Yet, the accuracy of temperature and humidity measurements is not sufficient to distinguish cloud albedo variations caused by aerosol changes from those caused by the thermodynamics forcing fluctuations.

These interactions between aerosols and the dynamics of boundary layer cloud systems (typically marine stratocumulus) have therefore been explored with high resolution numerical models (LES), that now include detailed parameterizations of turbulence, radiative transfer, surface fluxes, droplet activation, condensational growth, collection and sedimentation and drizzle precipitation. The results of such recent LES studies (Ackerman et al., 2004; Lu and Seinfeld, 2005) are however contrasting. Thus, it appears that, depending on the large scale forcings, an aerosol induced increase of the droplet concentration can lead to either an increase or a decrease of the liquid water path (LWP), hence contrasting with the cloud thickening that is expected from a reduction of the precipitation efficiency.

These previous studies were however mainly focused on rather short periods, corresponding to either nocturnal or diurnal situations. In this study, we focus on the coupling between aerosol impacts on cloud microphysics and the diurnal cycle, using 36 hours LES simulations of pristine and polluted marine stratocumulus clouds (characterized by low and respectively high droplet concentrations).

2 DESCRIPTION OF THE LES MODEL

The non-hydrostatic model Méso-NH (Lafore et al., 1998) is used for LES modeling of marine stratocumulus. The Meso-NH configuration chosen here uses an anelastic system of equations and a 3D turbulence scheme (Cuxart et al., 2000). The conservative variables, liquid water potential temperature θ_l and total water mixing ratio q_t, are advected with a positive definite second order centered scheme. The surface sensible and latent heat fluxes are proportional to the difference in temperature and specific humidity between the ocean and the air just above the surface.

The model includes a two-moment bulk microphysical scheme based on the parameterization of Khairoutdinov and Kogan (2000), which was specifically designed for LES studies of warm stratocumulus clouds. The radiative transfer is computed using the ECMWF operational model radiation code. Savijarvi and Raisanen (1998) parameterization is used for the cloud longwave optical properties, while the cloud optical thickness and the asymmetry factors are computed following Fouquart (1987). The single scattering albedo corresponds to cloud droplets formed on sulfates, which have a low absorption coefficient, similar to that of pure water. Concomitant impacts due to aerosol absorbing properties (the semi-direct effect) are thus neglected.

3 SIMULATIONS OF A DIURNAL CYCLE FOR VARIOUS AEROSOL CONCENTRATIONS

The LES simulations carried out here correspond to a typical summer situation over the NE Pacific, the initial conditions being similar to those of the FIRE I case (Duynkerke et al., 2004). The subsidence rate is computed from a constant divergence rate D of 6×10^{-6} s^{-1}. No large scale advection was considered in the reference case (W6 case hereafter).

To simulate aerosol impacts on the cloud droplet number concentration (CDNC), we simulated first a quasi-periodic diurnal cycle for pristine conditions (cloud condensation nuclei (CCN) concentration of 50 cm^{-3}). The simulation is then repeated for polluted conditions, that is for higher CCN concentrations (200 and 600 cm^{-3}). The pristine simulation (N^{50}_{CCN}) starts at 21 LT and lasts for 39 hours. Polluted simulations (N^{200}_{CCN} and N^{600}_{CCN}) start at 0 LT with the same field as the pristine one and are run for 36 hours. This set-up allows to analyze the coupling between the diurnal cycle and the response of the stratocumulus topped boundary layer (STBL) to the CDNC increase.

The sudden change of the CCN concentration, at 0 LT, produces a rapid increase of the CDNC (from 40 cm^{-3} for N^{50}_{CCN} to 120 cm^{-3} and 220 cm^{-3} for N^{200}_{CCN} and N^{600}_{CCN}, respectively) and a decrease of the domain averaged droplet effective radius at cloud top. Precipitation is consequently inhibited in the polluted cases, while the pristine cloud is continuously drizzling.

Fig. 1 reveals that the diurnal cycle is significantly affected by CDNC changes. The system response however is non-trivial: during the first night of simulation, the LWP increases with increased CCN loading as expected, but this tendency is reversed after 10 LT. Indeed, the two polluted clouds are getting constantly thinner than the pristine one during the last 26 hours of the simulation.

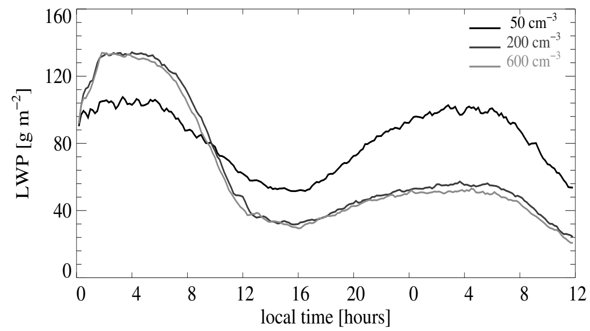

Figure 1: Time evolution of the horizontal mean LWP (g m^{-2}) for the N^{50}_{CCN} (black), N^{200}_{CCN} (grey) and N^{600}_{CCN} (light grey) simulations.

4 CLOUD DROPLET SEDIMENTATION AND ENTRAINMENT AT CLOUD TOP

The cloud droplet radius being smaller, the droplet sedimentation velocity is reduced in the polluted clouds. The inhibition of drizzle and the weaker cloud droplet sedimentation further result in higher liquid water contents (LWC) at cloud top (Fig. 2a), especially during the first 11 hours when the polluted clouds LWP is larger. The polluted clouds behave thus like adiabatically stratified cloud layers almost up to their tops: the LWC increases linearly with height from the base to the top, and the LWP is proportional to the LWC at cloud top. In constrast, the divergent flux of liquid water substantially reduces the water content in the upper 60 meters of the pristine cloud.
Our results are in accord with the earlier findings of Stevens et al. (1998); Ackerman et al. (2004); Bretherton et al. (2007), namely that entrainment tends to be reduced in the presence of a divergent liquid water flux, caused both by drizzle and cloud droplets sedimentation. Thus, the entrainment velocities appear to be larger for the polluted (non-precipitating) clouds (Fig. 2b). This is especially noticed during the first 12 hours of simulation when the pristine case liquid water flux is maximum, and therefore acts the most efficiently to reduce entrainment.
Comparisons of the vertical velocity variance (Fig. 3 of Sandu et al. (2008)) indicate that the polluted case maintains more vigorous vertical overturning during the first night and the

early morning, which is consistent with the development of a more well mixed vertical structure (i.e. positive bouyancy flux in the entire boundary layer, Fig. 3), more entrainment (Fig. 2b), and the development of a deeper PBL (Fig. 3). Moreover, despite its lower intensity during the last 24 hours of simulation (Fig. 1b of Sandu et al. (2008)), the drizzle flux, as well as the flux of cloud water, act to stabilize, and therefore weaken, the vertical motions within the cloud layer as suggested by Stevens et al. (1998). As a result, the cloud top entrainment is slightly damped compared to the polluted case during this period (Fig. 2b).

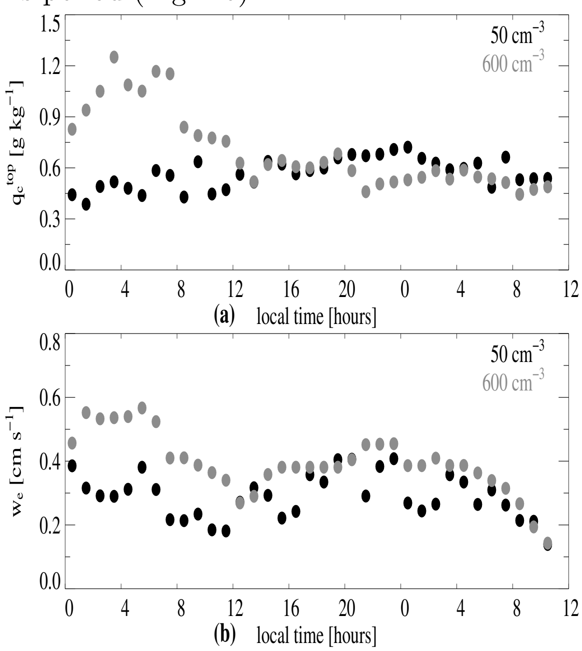

Figure 2: Time evolution of the hourly averaged (a) horizontal mean cloud water mixing ratio (g kg^{-1}), integrated over the upper 30 meters of the cloud layer, (b) entrainment velocity (m s^{-1}) for the N^{50}_{CCN} (black) and N^{600}_{CCN} (light grey) simulations.

5 THE COUPLING WITH THE DIURNAL CYCLE

The simulations reveal that by inhibiting the sedimentation of liquid water, the CDNC increase leads to an intensified cloud top entrainment, but also to a more efficient mixing of the STBL (Fig. 3), hence a stronger transport of water vapor towards the cloud during the first night. So the initial response of the STBL to a CDNC increase is an increase of the LWP.

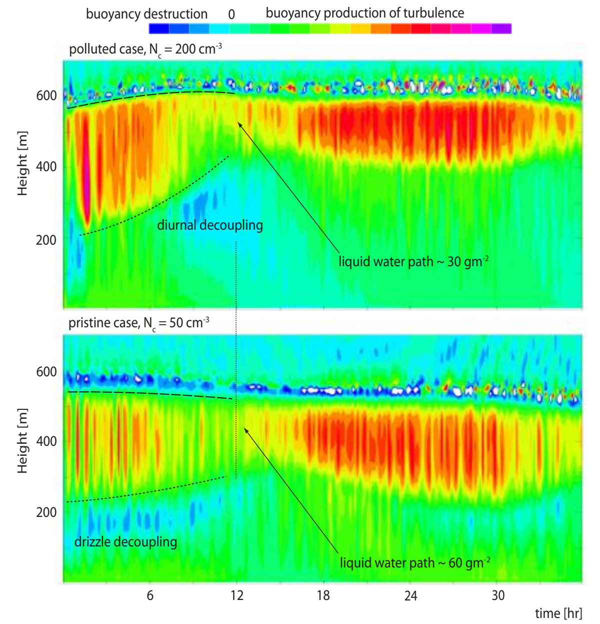

Figure 3: Time evolution of the horizontal mean bouyancy flux for the N^{50}_{CCN} (lower panel) and N^{600}_{CCN} (upper panel) simulations.

When the sun rises however, the response is reversed and the LWP of the polluted clouds decreases more than its pristine counterpart (Fig. 1). This evolution is mainly due to the enhanced entrainment rate at cloud top, but it is significantly reinforced by a decoupling of the STBL (see the negative values of the bouyancy flux under the cloud base in the upper panel of Fig. 3) that results from absorption of solar radiation in the cloud layer (which is proportional to cloud water) and a reduction of the sensible heat flux from the surface. The pristine case is less affected because drizzle evaporative cooling in the upper part of the subcloud layer counteracts the heating by SW absorption and advection of warm air from the surface, hence damping the diurnal cycle. During the day, the pristine case is less decoupled (Fig. 3) and its LWP decreases less than the one of the polluted cases (Fig. 1). During the following night, both the pristine and the polluted STBL become well mixed again (Fig. 3) and the LWP increases (Fig. 1). The polluted case which because of intensified entrainment warming and drying has a much higher cloud base, never reaches the same

LWP values as during the first night (Fig. 1). On the opposite, its LWP remains much smaller than the one of the pristine cloud.

6 SENSITIVITY TO LARGE SCALE CONDITIONS

To test the sensitivity of the pristine and polluted simulations to the large scale forcings the same exercise was repeated with different conditions. For the first case (1K case), the same subsidence as for the W6 case is used, but a continuous cooling of 1 K day^{-1}, accounting for horizontal advection of a colder air mass in the simulated domain, is applied. The second case (MST case) is similar to W6 except for the humidity jump at the inversion level, that is reduced from -3 g kg^{-1} to -1 g kg^{-1}. Finally, in the third case (W4 case), the divergence used to compute the subsidence rate is reduced to 4×10^{-6} s^{-1}, the other conditions being similar to W6.

It appears that drizzle is inhibited in all polluted cases, while all the pristine clouds are precipitating. Even if the moister inversion leads to less entrainment (MST), the STBL is maintained cooler in the 1K case and the weaker subsidence favors a more pronounced raise of the cloud top (W4), all pristine clouds show similar evolutions (not shown). In fact, if the LWP increases due to the imposed forcings, the rain rate, and hence the amount of drizzle evaporating under the cloud, are equally increasing. The transport of water vapor is more efficiently embedded and this prevents the LWP from increasing. The diurnal cycles are periodic in all pristine cases.

In the lack of drizzle, polluted clouds are more sensitive to large scale conditions during night-time, as illustrated in figure 4 by the relative LWP difference between the polluted and the pristine cloud. However, they tend toward the same minimum LWP around 15 LT, becoming always thinner than the pristine ones during daytime. The processes responsible for the LWP reduction (enhanced entrainment, SW absorption heating and reduced sensible heat flux) appear to scale with the LWP maximum at 6 LT. In the end, the heating and drying of the polluted STBL leads in all cases to a non-reversible evolution, that is the clouds never restore during the second night the same LWP as during the first one.

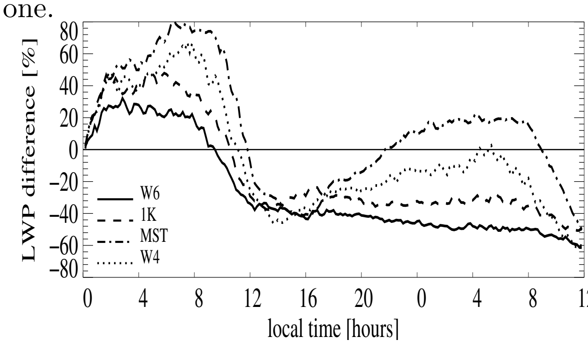

Figure 4: Time evolution of the relative difference in horizontal mean LWP (%) between the polluted cloud N_{CCN}^{600} and the pristine cloud N_{CCN}^{50}, for the 4 cases: W6 (full), 1K (dashed), MST (dash-dotted) and W4 (dotted). This difference was computed as the LWP difference between the two clouds, normalized by the LWP of the pristine cloud.

7 WHAT HAVE WE LEARNED FROM THESE SIMULATIONS ?

These simulations emphasized the mechanisms through which aerosol impacts the diurnal cycle of marine stratocumulus. Thus, it appeared that by inhibiting drizzle and by weakening the cloud droplet sedimentation, the increase of the CDNC, associated to an increase of the aerosol loading, not only enhances the cloud top entrainment, but also affects the interactions between the diabatique transport of condensed water (through sedimentation) and the radiative transfer. The aerosol modifies thus the (de-)coupling of the STBL, and hence the evolution of its thermodynamical state. The energy fluxes at boundaries of the system are therefore modified, and the polluted (non-precipitating) and the pristine (precipitating) simulations diverge quite rapidly. Moreover, it was shown that once the threshold necessary for the inhibition of drizzle is being crossed, the supplementary increase of the CDNC does no longer affect the evolution of the cloud.

Our simulations corroborate previous findings that during night-time aerosol induced LWP changes are sensitive to the large scale forcings, via enhancement of cloud top entrainment, so that ultimately the LWP may be reduced when the free troposphere entrained air is sufficiently dry. During the day however, enhanced entrainment, inhibition of drizzle evaporation below cloud base and reduced sensible heat flux lead to a more pronounced decoupling of the boundary layer, that significantly amplifies the LWP reduction of the polluted clouds. While at night, the sign of the LWP difference between pristine and polluted clouds depends upon large scale forcings, during the day, the LWP of polluted clouds is always smaller than the one of the pristine clouds (for the range of conditions tested).

So, our results suggest that, during daytime when the albedo of boundary layer stratocumulus significantly affects the Earth radiative budget, polluted clouds should exhibit a lower LWP. Such a reduction of the LWP can be sufficient to counteract the increase of the optical thickness due to more numerous smaller droplets (Twomey effect), hence leading to an albedo comparable to that of pristine clouds growing in a similar (thermo-) dynamical environment. This is the opposite of what was parameterized in climate models for the IPCC (2007). It is thus crucial to corroborate such findings with observational studies of the second indirect effect.

These LES simulations suggest in the same time some interesting insights and new approaches for validating their results. Indeed, even if the mechanisms through which aerosol impacts on the cloud layer are not directly measurable, the simulations allow to identify several observable signatures of these mechanisms. The most obvious one is the impact of the CDNC on the vertical profile of the LWC. The simulations showed that the LWC profiles of polluted clouds are close to adiabatically stratified profiles, while in pristine clouds, the LWC profiles are noticeably sub-adiabatic in the upper 50 meters below cloud top. The sub-adiabaticity is due to sedimentation of the cloud droplets and precipitation of drizzle drops. We therefore suggest that previous experiment data sets (ACE-2, EPIC, DYCOMS-II) might be reanalyzed, with a focus on the vertical profiles of LWC below cloud top. The simulations equally emphasized the enhanced variance of vertical velocity at cloud top in polluted clouds, the different morphologies of the upper cloud layer (closed versus open cells) and the damping of the diurnal cycle in precipitating cases. Forthcoming field experiments should hence first focus on such features, like the LWC vertical profile at cloud top and some specific signatures in the turbulence field. The transition period between night and day, which is critical for the STBL evolution, should also be carefully documented.

Acknowledgments

One of the authors, Irina Sandu acknowledges Meteo-France support for her Ph.D in the GMEI group of CNRM. We are also grateful to Bjorn Stevens for his thorough advices during the analysis of the simulations.

BIBLIOGRAPHY

Ackerman, A. S., Kirkpatrick, M. P., Stevens, D. E., and Toon, O. B. (2004). The impact of humidity above stratiform clouds on indirect aerosol climate forcing. *Nature*, 432:1014–1017.

Bretherton, C. S., Blossey, P. N., and Uchida, J. (2007). Cloud droplet sedimentation, entrainment efficiency, and subtropical stratocumulus albedo. *Geophys. Res. Lett*, 34:doi:10.1029/2006GL027648.

Cuxart, J., Bougeault, P., and Redelsperger, J. (2000). A turbulence scheme allowing for mesoscale and large-eddy simulations. *Quart. J. Roy. Meteor. Soc.*, 126:1–30.

Duynkerke, P. G., de Roode, S. R., van Zanten, M. C., Calvo, J., Cuxart, J., Cheinet, S., Chlond, A., Grenier, H., Jonker, P. J., Kohler, M., Lenderink, G., Lewellen, D., Lappen, C.-L., Lock, A. P., Moeng, C.-H., Muller, F., Olmeda, D., Piriou, J.-M., Sanchez, E., and Sednev, I. (2004). Observations and numerical simulations of the diurnal cycle of the eurocs stratocumulus case. *Quart. J. Roy. Meteor. Soc.*, 604.

Fouquart, Y. (1987). *Radiative transfer in climate modeling, in Physically-Based Modeling and Simulation of Climate and Climatic Changes.* M.E. Schlesinger, NATO Advanced Study Institute, Erice, Sicily.

Khairoutdinov, M. and Kogan, Y. (2000). A new cloud physics parameterization in a large-eddy simulation model of marine stratocumulus. *Mon. Wea. Rev.*, 128:229–243.

Lafore, J., Stein, J., Asencio, N., Bougeault, P., Ducrocq, V., Duron, J., Fischer, C., Hereil, P., Mascart, P., Pinty, V. M. J., Redelsperger, J., Richard, E., and de Arellano, J. V.-G. (1998). The meso-nh atmospheric simulation system. part i: adiabatic formulation and control simulations. *Ann. Geophys.*, 16:90–109.

Lu, M. L. and Seinfeld, J. H. (2005). Study of the aerosol indirect effect by large-eddy simulation of marine stratocumulus. *J. Atmos. Sci*, 62:3909–3932.

Morcrette, J. (1991). Radiation and cloud radiative properties in the ecmwf operational weather forecast model. *J. Geophys. Res.*, 96:9121–9132.

Savic-Jovcic, V. and Stevens, B. (2007). The structure and mesoscale organization of precipitating stratocumulus. *J. Atmos. Sci.*

Savijarvi, H. and Raisanen, P. (1998). Long-wave optical properties of water clouds and rain. *Tellus*, 50A:1–11.

Sandu, I.,J. L. Brenguier, O. Geoffroy , O. Thouron, V. Masson (2008). Aerosol impacts on the diurnal cycle of marine stratocumulus clouds. *J. Atmos. Sci*, in press.

Stevens, B., Cotton, W. C., Feingold, G., and Moeng, C.-H. (1998). Large-eddy simulations strongly precipitating, shallow, stratocumulus-topped boundary layers. *J. Atmos. Sci*, 55:3616–3638.

Shortwave radiative impacts from aerosol effects on marine shallow cumuli

Paquita Zuidema[1], Huiwen Xue[2], and Graham Feingold[3]

[1] *U of Miami (RSMAS) Miami, FL*
[2] *Peking U., Beijing, China*
[3] *NOAA/ESRL, Boulder, CO*

The net shortwave radiative impact of aerosol on simulations of two shallow marine cloud cases is investigated using a Monte Carlo radiative transfer model. For the first broken shallow cumulus case, increased aerosol concentrations are associated not only with smaller droplet sizes but also reduced cloud fractions and cloud dimensions, a result of evaporation-induced mixing and lack of precipitation. Three-dimensional radiative transfer (3DRT) effects alter the fluxes by 10% to 20% from values calculated using the independent column approximation for these simulations. The first (Twomey) aerosol indirect effect is dominant but the decreased cloud fraction reduces the magnitude of the shortwave cloud forcing substantially. 3DRT effects slightly decrease the sensitivity of the cloud albedo to changes in droplet size under an overhead Sun for the two ranges of cloud liquid water paths examined, but not strongly so. A popular two-stream radiative transfer approximation to the cloud susceptibility overestimates the more directly-calculated values for the low liquid-water-path clouds within pristine aerosol conditions by a factor of two despite performing well otherwise, suggesting caution in its application to the cloud albedos within broken cloud fields. An evaluation of the influence of cloud susceptibility and cloud fraction changes to a ``domain'' area-weighted cloud susceptibility found that the domain cloud albedo is more likely to increase under aerosol loading at intermediate aerosol concentrations rather than under the most pristine conditions, contrary to traditional expectations.

The second simulation (cumulus penetrating into stratus) is characterized by higher cloud fractions and more precipitation. This case has two regimes: a clean, precipitating regime where cloud fraction increases with increasing aerosol and a more polluted regime where cloud fraction decreases with increasing aerosol. For this case the domain-mean cloud albedo increases steadily with aerosol loading under clean conditions, but increases only slightly after the cloud coverage decreases. Three-dimensional radiative transfer effects are mostly negligible for this case. Both sets of simulations suggest that aerosol-induced cloud fraction changes must be considered in tandem with the Twomey effect for clouds of small dimensions when assessing the net radiative impact, because both effects are drop-size dependent and radiatively significant.

A paper based on this work is in press with the Journal of Atmospheric Sciences. The accepted manuscript is available through http;//www.rsmas.miami.edu/users/pzuidema/publications.html.

INVESTIGATIONS INTO THE ICE NUCLEATING ABILITY OF PROPANE FLAME SOOT

I. Crawford[1], P. Connolly[1], D. Liu[1], O. Möhler[2], M. Gallagher[1]
(1) Centre for Atmospheric Science, University of Manchester, Manchester, UK
(2) Institute for Meteorology and Climate Research (IMK-AAF), Forschungszentrum Karlsruhe, Germany.

1. MOTIVATION

Much controversy surrounds soot's potential behaviour as Ice Nuclei (IN). Many laboratory and field studies have shown that soot particles may act as efficient IN with the potential to impact on climate by the modification of the occurrence, lifecycle and optical properties of mixed phase and glaciated clouds given its ubiquity in the atmosphere. Many studies of cirrus and orographic cloud ice formation have centralised around the homogeneous freezing of supercooled sulphuric acid droplets as being the major mechanism. Numerical parameterisations have been developed to estimate the ice crystal number concentration and size for given conditions and solutes which can be used to determine cloud radiative properties. However heterogeneous nucleation has been given relatively little mention. An aerosol substrate such as soot may act as efficient ice nuclei by requiring significantly less extreme conditions to bring about the onset of freezing then are offered by homogeneous freezing.

If soot does behave as efficient ice nuclei (IN) then it has significant potential to impact on climate by the modification of the lifecycle and optical properties of mixed phase and glaciated clouds given its ubiquity in the atmosphere. Soot may offer significant concentrations of active IN in the lower troposphere where an increase in ice crystal number concentration may result in more rapid and frequent glaciation of mixed phase clouds by such mechanisms as the Bergeron-Findeisen process. This would likely act to reduce cloud top albedo and increase ice phase precipitation, reducing cloud lifetime. However these effects are highly uncertain and no estimates of the forcings associated with these processes have been put forward.

2. AIDA CHAMBER

The AIDA cloud chamber is a large ($84 m^3$) chamber capable of simulating cloud formation by controlling the pressure within the chamber (Figure 1). It has been used to simulate ice cloud formation over the whole temperature range of interest for tropospheric clouds.

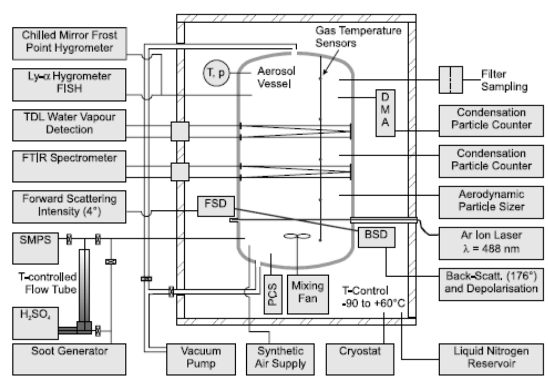

Figure 1 The AIDA chamber

During 2006, a series of experiments were conducted at 244K & 228K to investigate the ice nucleating efficiency of Combustion Aerosol Standard (CAST, Jing-CAST Technologies) generator propane flame soot as a function of organic carbon content – so called `flame soot'.

3. METHOD

The amount of organic carbon present on this flame generated soot is characterised by the richness of the fuel to air mix during the combustion. This was confirmed by online measurements from the chamber of the `flame soot' and other aerosol with the new Single Particle Soot Photometer (SP-2) and a Time of Flight Aerosol Mass Spectrometer (ToF-AMS). The occurrence of these aerosols in the cloud phase was also measured by use of linking these instruments to a Pumped Counterflow Virtual Impactor (PCVI.) This enabled us to design several experiments to investigate the influence of OC coating on soot on the IN efficiency. Varying the fuel air mixture we looked at 3 different tests: (1) `low coating thickness'; (2) `medium coating thickness'; and (3) `high coating thickness'. Experiments were also performed with an external mixture of sulphuric acid particles and `flame soot'. A suite of cloud microphysics probes was also deployed. Measurement of ice crystal size, habit and ice water content were made using a Cloud Particle Imager (CPI). A Cloud Droplet Probe (CDP) and WELAS OPC measured droplet size and liquid water content.

4. RESULTS

An in-depth analysis of the data shows that only the `low coating thickness' displays any significant ice nucleating ability. Figure 2 demonstrates the range of temperatures and ice saturations required for the tested soot to activate. It can be seen that the medium and high coating thickness soot require significantly higher ice saturation and colder temperatures to activate than the low coating thickness soot. Also the activated fraction is only of the order of 1% for the medium and high coating thickness soot in contrast 30-35% activation for the low coating thickness soot.

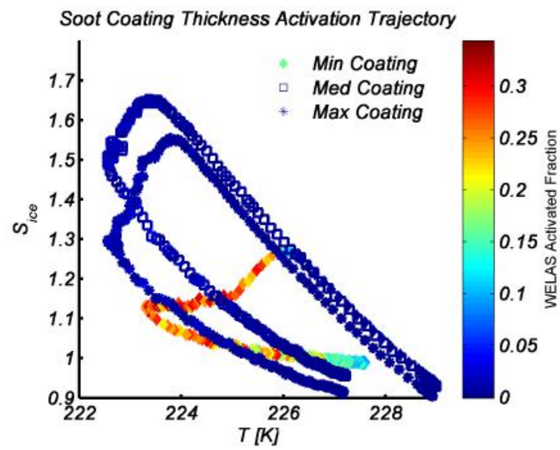

Figure 2 Soot Coating Thickness Activation Trajectories

When the `low coating thickness' soot is externally mixed with sulphuric acid little difference is observed in ice nucleating efficiency at 228K however the heterogeneous freezing mode of the `medium coating thickness' soot was suppressed as it was observed that droplets formed on sulphuric acid aerosol homogeneously froze in preference to the heterogeneous soot pathway (Figure 3). This shows that the organic material acts to suppress the uptake of water to the particles and that they are effectively interstitial for a range of conditions relevant to cirrus clouds.

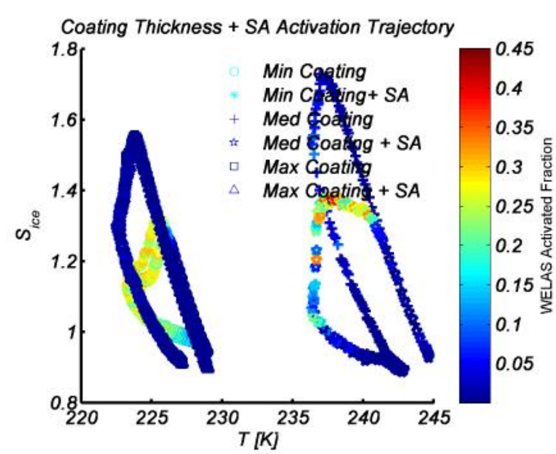

Figure 3 Soot Coating Thickness + SA Activation Trajectories

5. ACKNOWLEDGEMENTS

This research was funded by the ACCENT Access to Infrastructures programme.

THE FOURTH INTERNATIONAL ICE NUCLEATION WORKSHOP (ICIS-2007): OBJECTIVES AND PRELIMINARY RESULTS

Paul J. DeMott[1], Ottmar Möhler[2], Olaf Stetzer[3], Masataka Murakami[4], Ulrich Bundke[5], Holger Klein[5], Zamin Kanji[6], Richard Cotton[7], Hazel Jones[8], Thomas Leisner[2], Daniel Cziczo[3,12], Markus Petters[1], Anthony Prenni[1], Sonia Kreidenweis[1], Stefan Benz[2], Maren Brinkmann[2], Daniel Rzesanke[2], Martin Schnaiter[2], Roland Schön[2], Harald Saathoff[2], Robert Wagner[2], Berko Sierau[3], Mathieu Nicolet[3], Ulrike Lohmann[3], Stephané Gallavardin[3], Atsushi Saito[4], Bjorn Nillius[5], Heinz Bingemer[5], Jonathan Abbatt[6], James Bowels[7], Admir Targino[8], James Dorsey[8], Karin Ardon[9], Zev Levin[9], Eli Ganor[9], Dimitrios G. Georgakopoulos[10], and Gabor Vali[11]

[1]Department of Atmospheric Science, Colorado State University, Fort Collins, CO, USA
[2]Institute for Meteorology and Climate Research, Forschungszentrum Karlsruhe, Germany
[3]Institute for Atmospheric and Climate Science, ETH Zürich, Zürich, Switzerland
[4]Meteorological Research Institute of Japan, Tsukuba City, Japan
[5]Universität Frankfurt, Frankfurt, Germany
[6]Department of Chemistry, University of Toronto, Toronto, Canada
[7]Meteorological Office, Exeter, United Kingdom
[8]Centre for Atmospheric Science, University of Manchester, Manchester, United Kingdom
[9]Department of Geophysics and Planetary Sciences, Tel Aviv University, Tel Aviv, Israel
[10]Department of Agricultural Biotechnology, Agricultural University of Athens, Athens, Greece
[11]Department of Atmospheric Sciences, University of Wyoming, Laramie, Wyoming, USA
[12]Atmos. Sci. & Global Change Div., Pacific Northwest National Laboratory, Richland, WA, USA

1. INTRODUCTION

The International Workshop on Comparing Ice Nucleation Measuring Systems (ICIS-2007) was held at the AIDA (Aerosol Interaction and Dynamics in the Atmosphere) facility of the Institute for Meteorology and Climate Research (IMK-AAF) at Forschungszentrum Karlsruhe, Germany during 10 to 28 September 2007. This workshop was coordinated by a group of scientists in recognition of renewed interest in ice nucleation research and the need to understand the technically-challenging measurements of ice nuclei made using different techniques. Funding was coordinated via multiple agencies, as acknowledged in Section 5. This research is largely motivated by the fact that full understanding of ice formation in clouds and its relation to atmospheric ice nucleating aerosols remains elusive and presents an impediment to quantifying aerosol indirect effects on climate via impacts on ice-containing clouds. The meeting was the first of its kind in more than 30 years and fourth of its type ever; therefore it is also dubbed the Fourth International Ice Nucleation Workshop. Primarily, this paper discusses objectives and results. Other aspects of the workshop design and experimental plan including the coordinated "ground-truth" cloud simulations performed in the large AIDA expansion chamber are discussed in the separate contribution of Möhler et al. (2008) to this conference.

The key objective of the workshop was to compare and contrast methods for ice nuclei measurement by a variety (nine) of existing and new instruments intended for laboratory and/or field use, with the purpose of assessing the range and consistency of present measurement capabilities. Secondarily, the workshop offered the opportunity for specialized experiments to validate present understanding of ice nucleation by different aerosol types and testing of the ability of ice nuclei measurements to predict ice formation in clouds.

2. EXPERIMENTAL SETUP

There were 10 instrumental systems participating in this workshop representing five different basic methodologies for ice nucleation measurements. This contrasts with seven techniques used at the 3rd Workshop in 1975 (Vali, 1975; 1976). However, present at the 4th Workshop were three different versions of continuous flow diffusion chambers (CFDC) and one continuous flow mixing chamber. These devices did not exist in 1975 and all are being used or planned for use as aircraft-capable instruments. The instrument list is shown in Table 1. All except the static chambers were operated on-site.

Table 1. Participating Instruments

Instrument	Orientation	Ice detection
CSU CFDC-1H	Vertical, cylindrical	OPC/active evaporation
ZINC	Vertical, parallel plate CFDC	OPC/active evaporation, depolarization
FINCH	Vertical continuous mixing chamber	Depolarization
MRI CFDC	Vertical cylindrical	OPC/passive evaporation
MINC CFDC	Vertical, cylindrical	OPC/passive evaporation
UKMO CFDC	Vertical, cylindrical	OPC/passive evaporation
UTOR CFDC	Horizontal parallel plate	OPC
UF-FRIDGE	Horizontal static diffusion chamber	CCD microscope
TAU-FRIDGE	Same as above	CCD microscope
AIDA	N/A	OPC/FTIR/CPI
IMK EDB	N/A	Drop freezing

ZINC: Zürich Ice Nucleus Chamber
FINCH: Frankfurt Ice Nucleus Chamber
CSU CFDC-1H: Colorado State University Continuous Flow Diffusion Chamber – HIAPER version 1
MINC: University of Manchester CFDC
UKMO CFDC: United Kingdom Meteorological Office CFDC
MRI CFDC: Meteorological Research Institute of Japan CFDC
UTOR CFDC: University of Toronto CFDC
UF-FRIDGE: University of Frankfurt Freezing Ice Deposition Growth Experiment
TAU-FRIDGE: Tel Aviv University FRIDGE
FZK-EDB: Forschungzentrum Karlsruhe Electro-dynamic Balance
AIDA: Aerosol Interactions and Dynamics in the Atmosphere chamber.

Continuous flow diffusion chambers. Four similar CFDC instruments employing cylindrical geometry in a vertical orientation were used. These follow the fundamental design of Rogers (1988). The Colorado State University (CSU) CFDC was most similar to the design of Rogers et al. (2001), but employed separate refrigeration compressors for each wall and an actively-controlled (both walls ice coated and held to the same temperature) ice saturation region in the lower 1/3 of the chamber to evaporate liquid particles and retain nucleated ice particles for enhanced detection. The version used was one recently certified for use on the U.S. National Science Foundation G-V (also referred to as HIAPER) aircraft. The other CFDC ice nucleus counters were from the University of Manchester (MINC), the UK Meteorological Office (UKMO), and the Meteorological Society of Japan (MRI). These three CFDC instruments utilize a passive evaporation region (hydrophobic but not cooled outer, warm wall) to aid phase separation of liquid and ice particles by size. Two other continuous flow chambers were of a parallel plate design. The University of Toronto (UTOR) CFDC was a horizontally-oriented (warm plate above a cold plate) device operated without an evaporation section. Consequently, detection of activation conditions much above 100% was limited for this workshop. The Zürich Ice Nucleus Counter (ZINC) of ETH-Zürich is a vertically-oriented parallel plate chamber utilizing an active evaporation region (Stetzer et al., 2008). All of the CFDC instruments utilize an optical particle counter (OPC) to discriminate ice crystals from water droplets and haze particles based on their grown size. These OPC devices varied in the number of size channels used from 2 to 255. The lower size used for ice discrimination was 2 μm for CSU and UKMO, 3 μm for MINC and MRI, and 5 μm for UTOR, The ZINC instrument also employs a linear depolarization detector for phase discrimination.

Other aspects varied amongst the CFDC type instruments. For example, the CSU CFDC used an additional set of impactors on inlet air to better assure removal of supermicron particles during sampling and it also used diffusion dryers on this air to remove excess moisture to assure that no spurious supersaturations occur as sample enters the cold region of the instrument.

Mixing chamber. The Fast Ice Nucleus Chamber (FINCH) constructed at Frankfurt University is a mixing type ice nucleus instrument, described by Bundke et al. (2008). Sample air is mixed in a turbulent region with separate major streams of humidified and dry air to create a steady state supersaturation and temperature condition flowing vertically downward within a laminar flow region encased in sheath flow. Sample flow rates up to 10 vlpm are possible. Ice crystals formed are separated from the flow by a virtual impactor and detected by a circular depolarization detector.

Static diffusion chambers. The static diffusion chambers are of the same design, termed the FRankfurt Ice nuclei Deposition freezinG Experiment (FRIDGE) and also briefly described by Bundke et al. (2008). One device was operated by the University of Frankfurt (UF-FRIDGE) and one by Tel Aviv University (TAU-FRIDGE). Ice nuclei were collected on filters during ICIS and brought to the instrument sites for processing at controlled temperature and relative humidity conditions. The filters are placed in Vaseline on a hydrophobic cooled plate. The FRIDGE instruments operate at low pressure and then meter water vapor to control the relative humidity over the particles.

Electrodynamic levitator. An electrodynamic balance, similar to that described by Duft and Leisner (2004) was operated to freeze droplets embedded with the aerosol particles examined during the workshop.

AIDA. The AIDA cloud chamber facility has been described previously (Möhler et al. 2006; references therein) and for this workshop by Möhler et al. (2008). The 84 m^3 chamber is precooled to a set temperature within a surrounding volume and then the chamber is evacuated to produce cooling and cloud formation within the inner volume.

Instrumentation for this workshop included optical particle detectors, an FTIR detector for the ice phase, Lyman-α and tunable diode laser hygrometers, a pumped counter flow virtual impactor for capturing cloud particles and forwarding the residual nuclei to the single particle analyzing Particle Ablation Laser Mass Spectrometer (PALMS) single particle mass spectrometer (Cziczo et al. 2006), a Cloud Particle Imager (CPI) and Cloud Droplet Probe (CDP) (see paper by Targino et al. at this conference), assorted condensation particle counters (CPC), differential mobility analyzers (DMA), and Aerodynamic Particle Sizer (APS) instruments to characterize particles generated first into the 4 m^3 aerosol chamber (NAUA) before drawing them into AIDA.

Description of AIDA experiments and methods are detailed by Möhler et al. (2008).

Structure of workshop. To encourage participation in this workshop after so many years of inactivity, an informal structure was used. This means that investigators were free to choose to participate and report on any particular set of experiments. This recognized the fact that some of the instrument systems were in their first year of operations. Further, it was decided to focus measurements on calibration ice nuclei measurements versus validating capabilities for measuring natural ambient number concentrations of ice nuclei.

Experimental configuration. Ice nucleation instruments were set up on two levels between the AIDA and NAUA chambers so that sampling could be directed from either chamber, as described by Möhler et al. (2008). Aerosols were generated into the NAUA chamber at the beginning of an experimental day, then a portion of these particles were transferred to AIDA prior to the first cloud expansion experiment in later morning. Groups sampling aerosol particles in real time were free to measure from the NAUA chamber at any time and from AIDA before and sometimes after expansion. Some specialized sampling was done by a few groups to obtain particles from AIDA without warming, to sample during AIDA expansion, and to sample cloud particle residual nuclei from the PCVI for IN reprocessing.

Aerosol types. As stated, sampling used known IN types that could be generated in the laboratory. Four mineral dust aerosol populations were examined. These included a milled product representative of the composition of a Southwestern U.S. desert dust (Arizona Test Dust – "ATD") that has been commonly used in ice nucleation studies, a surface dust sample collected from the Sahara near Cairo ("SD4"), a surface dust sample from a site subjected to strong Saharan dust transport events for many millennia (Canary Islands dust – "CID"), and a dust collected as settled particles from a dust storm in Israel during April 2007 ("ID1"). A single black carbon soot particle type produced by a graphite spark generator was also examined for ice nucleation activity. Finally, both manufactured (Snomax®, York Snow, Inc.) and live bacterial cells of pseudomonas syringae were tested.

Aerosol particle generation of dusts used a brush generator for dry suspension of particles. A cyclone impactor was used on the generator flow to reduce the number of aerosol particles above 1 micron because the high concentrations of such particles produced for this study, mostly unrealistic for the atmosphere, limit the ability to resolve ice formation by OPC-sizing methods. The CSU CFDC employed an additional two-stage impactor for further limiting the entry of particles larger than a 50% cut-size of 1.2 microns. A typical dust size distribution is shown in Figure 1. Chemical composition measurements will not be discussed here.

Other workshop activities. In addition to the daily experimental activities, a series of participant seminars were given to describe the instruments in detail. Additionally, select invited seminars were given to provide context to the goal of atmospheric ice nuclei measurement. Seminars also provided an educational aspect for the attending and participating graduate students.

To encourage completion of analyses and comparison, a data workshop was scheduled prior to the end of the experimental workshop. This data workshop was held in Pontresina, Switzerland in February 2008. Major results were presented by each group, a matrix of comparative experimental data was assembled, and a deadline of April 2008 was set for completion of a data archive.

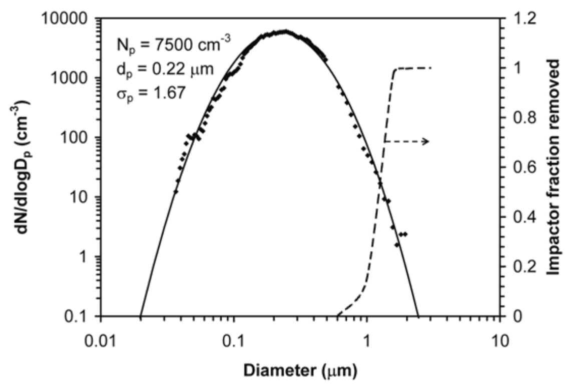

Figure 1. NAUA chamber size distribution (and lognormal fit) at 7736 s after generation of ATD particles during experiment NAUA_6. The CFDC-1H inlet impactor efficiency curve is also shown to indicate the part of the distribution not sampled.

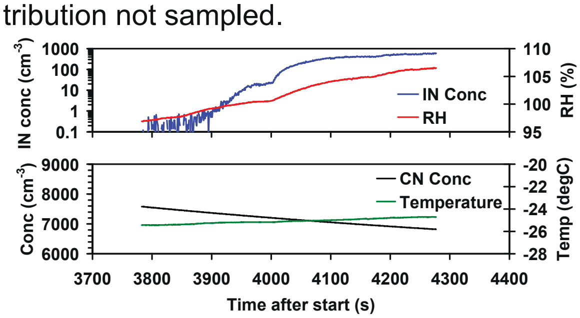

Figure 2. CSU CFDC-1H data time series for sampling ATD from the NAUA chamber showing the increase in IN number concentration as relative humidity (RH) was raised at near -25ºC. The total aerosol number concentration larger than 12 nm (CN concentration) is also shown, decaying as aerosols are sampled by the IN counters.

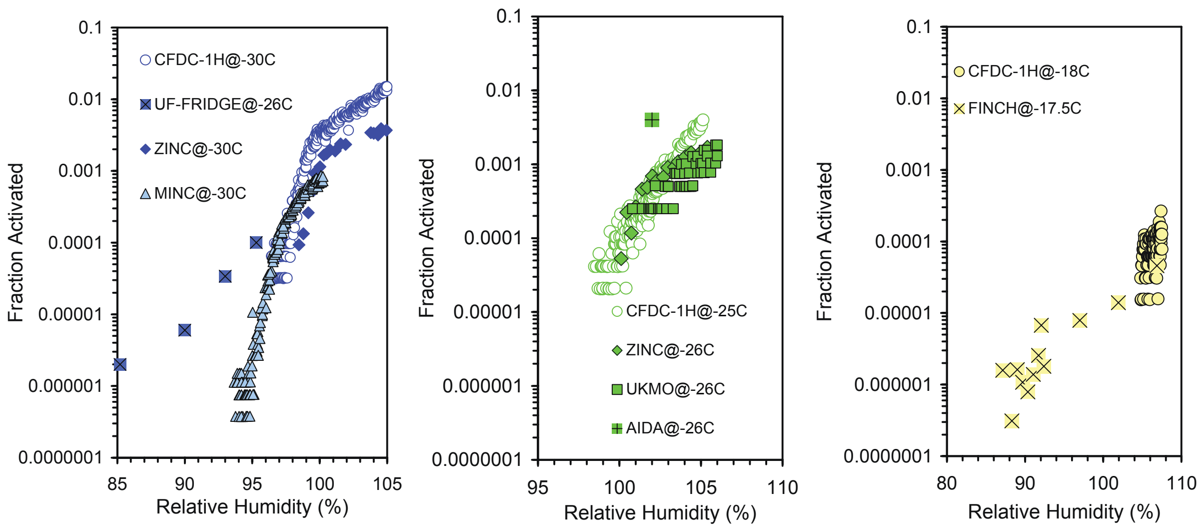

Figure 3. Ice nuclei active fraction (IN number concentration/total number concentration) in RH scans by several devices for the Saharan dust particles. Four narrow temperature regimes are represented: -18ºC in yellow, -25ºC in green, -30ºC in blue. Fraction activated in an AIDA expansion at -25ºC is arbitrarily placed at 102% RH (see text).

3. PRELIMINARY RESULTS

A typical procedure for many of the continuous flow instruments during NAUA sampling is shown in Figure 2. This involved ramping relative humidity (RH) in time while modestly changing temperature in order to obtain an "RH scan" of activation conditions.

The result of RH scans of SD4 particles at selected temperatures for some other instruments are shown in Figure 3. This shows the good agreement between the different ice nuclei measuring devices that existed in many cases over multiple orders of magnitude of IN number concentrations. These results also demonstrate that there is little apparent limitation on measured number concentrations in most of the flowing systems. An exception to this case, still under analysis, is the mixing chamber device (FINCH). Results indicate that the mixing chamber method is capable of detecting ice nuclei concentrations under a few hundred per liter, but that vapor competition effects may limit detection of higher ice nuclei concentrations. Thus, FINCH and the CFDC-1H agreed on the total number of ice nuclei from SD particles at -18ºC, where small numbers concentrations (<1 cm^{-3}) were active. Nevertheless, both FINCH and the filter processing device (UF-FRIDGE) appear for this aerosol to express shallower ice nucleation curves, suggesting ice nucleation at lower relative humidity at the respective temperatures indicated, not consistent with the flow diffusion chamber measurements.

Also shown in Figure 3 is the total IN fraction activated in an AIDA expansion experiment. Direct comparison between the AIDA simulation and the IN instruments is complicated by differences in the thermodynamics that particles are exposed to. Data from the AIDA expansion demonstrate that virtually all of the dust particles activated first as liquid droplets at the peak cloud supersaturation, while only a minor fraction froze. Direct comparison between AIDA and the IN instruments is only valid for the supersaturation at which all particles activate as cloud droplets. This was not independently estimated, for example via CCN measurements, so the AIDA data point is arbitrarily placed at 102% RH. IN instrument data only agree with AIDA for a higher RH, the largest discrepancy obtained in such comparisons for dust particles.

Instrument comparisons are shown for sampling bacterial ice nuclei in Figure 4. These ice nucleating aerosols show "plateau-like" profiles of ice nuclei activation versus RH in most of the IN measuring systems, with only modest temperature dependence of maximum active fraction. Activation was measured as warm at -5.5ºC in the CFDC-1H. We suggest that the maximum fraction activated in Figure 4 is simply the total number of bacterial cells from atomized and dried solutions. That 99% of the particles emitted during generation are much smaller particles coming from the matrix material used to encase the bacteria pellet form during commercial production is supported by size distribution data and AIDA cloud droplet data (not shown). It is seen in Figure 4 that the magnitude of the activated fraction "plateau" value varied amongst the instruments, possibly due to differing efficiencies for transmitting the large (~0.8 μm aerodynamic diameter) cells. The AIDA experiment supports a maximum activated fraction of 0.01. Modest variability in onset RH conditions for ice formation at different temperatures is also noted amongst the measuring systems. The apparent lower active fractions in FINCH results may again reflect an upper IN concentration limit in the 100 per liter range for the present configuration. This is consistent with the fact that about 10 cm^{-3} were found to activate in the CFDC-1H. 0.1% of the aerosol distribution, typically representing several hundred per liter nucleated,

The largest amount of comparative data was obtained for ATD particles over three days of experiments. Conditions for freezing 0.1% of the aerosol distribution, typically representing several hundred per liter nucleated are compared in Figure 5 as a function of water relative humidity and temperature. The results show instances of both agreement and discrepancies in different instances. A band of very good overall agreement within the few % RH instrumental uncertainties encompasses more than 60% of the test results and the part of the parameter space in Figure 5 that also includes the AIDA expansion experiment data. Note that relatively few instruments were capable of measurement below -40ºC and that the scatter in the UTOR CFDC data there is likely due to the present limitations of a two-channel optical particle counter system for detecting smaller ice crystals under these conditions. Also encouraging is the fact that the filter processing measurement, while never activating equivalent high numbers of ice nuclei, did agree with the flowing systems for the conditions required to nucleate the first few tens per liter at below water saturation.

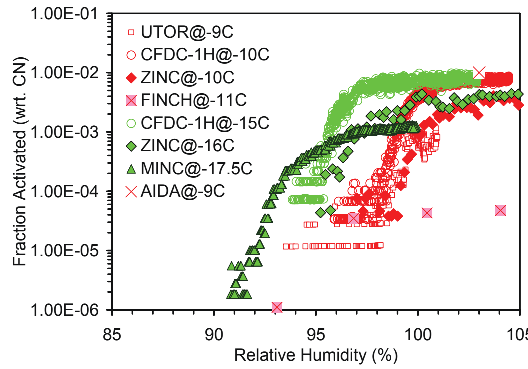

Figure 4. As in Figure 3, but for bacterial ice nuclei from Snomax®.

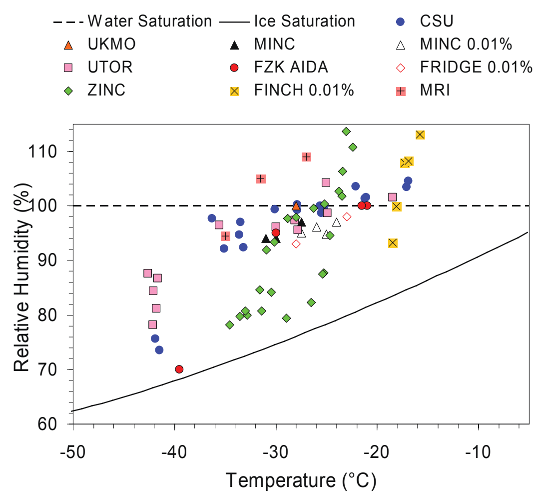

Figure 5. Comparison of activation conditions of ATD particles in various instruments. Conditions are for freezing of 0.1% activation of particles except as noted.

Investigators are working to understand other possible discrepancies in Figure 5. The spread of onset RH conditions for activation is larger at more modest supercooling in ZINC and FINCH. Fluid dynamics model simulations after the workshop suggested that variable humidity in the FINCH sample air lead to RH values on mixing that were spuriously higher than the steady state value measured. Corrections were established, but have already been applied in Figures 3 and 5. It is hypothesized that the bifurcation in different onset ice formation conditions in the ZINC instrument may relate in some way to two sampling factors which differed from most other investigators. These were the absence of an inlet pre-impactor to remove larger aerosol particles and the absence of an inlet dryer to reduce RH in the sample stream. The first factor means that ZINC might have been sensitive to ice formation on the small fraction of particles above 1 μm. Higher inlet RH can lead to spurious supersaturations exceeding the steady state RH in CFDC instruments, although the RH was expected to be low in the NAUA chamber due to backfill with synthetic dry air. The source for why the MRI CFDC required higher RH than any of the diffusion chambers for ice activation is still being investigated.

4. CONCLUSIONS AND PLANS

The Fourth International Workshop on Ice Nucleation (ICIS 2007) was an ambitious undertaking on the part of investigators. We judge it also to have been highly successful based on the good agreement in many experiments and the ongoing lessons being learned from issues identified in other experiments that should lead to improved understanding of measurements, and improved accuracy and consistency within the expanding research community now becoming involved in making ice nucleation measurements.

Analyses and comparisons from ICIS 2007 are continuing at the time of this writing, but some findings from the workshop bear special note here due to their implications for the present state of ice nuclei measurement systems and for atmospheric ice nucleation. A major question from the broader cloud and aerosol indirect effects community regards how representative are ice nuclei measurements of expected primary ice formation in clouds. In this paper, we show a sampling of comparisons between ice nuclei measuring systems and the results of cloud expansions performed in the AIDA chamber. While we have not attempted a mechanistic investigation of how ice forms in the IN counting devices versus the AIDA cloud expansion, it is encouraging to note the good quantitative comparisons obtained for similar sets of processing conditions in the majority of cases. This likely occurs due to the deterministic aspects of ice nucleation.

A related finding is that continuous flow diffusion chambers of any particular configuration are capable of detecting virtually any concentration of ice nuclei (or homogeneously freezing aerosols) that may be present at any moment in the atmosphere. While this capability was inherent in the design of such instruments, confirmation of the lack of sensitivity to the number concentrations of atmospheric surrogate ice nuclei gives additional confidence to atmospheric measurements indicating that relatively low number concentrations of IN are often the normal situation (e.g., Möhler et al. 2007). Thus, it should be assumed that such instruments would not miss detecting high numbers of ice nuclei as an explanation for large ice enhancements (ice crystal concentrations far exceeding expected ice nuclei concentrations) noted in some cloud types.

The workshop results also raise the issue of what particles are ice nuclei in warmer supercooled clouds. The mineral dusts studies showed a strong decrease in ice forming activity by deposition, condensation and immersion freezing warmer than about -17 to --20ºC, as well as a requirement of water saturation for ice nucleation at temperatures warmer than about -25ºC. It is possible, if not likely, that warmer temperature ice nucleation is due to larger dust particles. Sizes were limited to below about 2 microns in these studies. The potential role of biological particles as important atmospheric IN is reemphasized by the results. The high efficiency of bacterial ice nuclei at very modest supercooling was readily detected by all instruments, so it seems feasible to combine IN instruments with biological methods to determine the atmospheric concentrations of biological ice nuclei.

A summary of the workshop is planned for separate publication in the near future. A special journal issue is also being coordinated to include detailed results from all investigators and more extensive intercomparison than is presented here. A future workshop is under discussion to include measurements in both indoor and outdoor laboratory environments using both surrogate and real atmospheric ice nuclei.

5. ACKNOWLEDGMENTS

We gratefully acknowledge numerous and skilful support from the AIDA team for organization issues, instrument setup, and AIDA chamber operation during the experiments. We also thank Thomas Schwartz from the Institut für Technische Chemie of Forschungszentrum Karlsruhe for support in preparing the bacterial cultures. A variety of grants and organizations supported the group and investigators individually to participate in the experimental and data workshops. Forschungszentrum Karlsruhe provided funding for the facility infrastructure within the Helmholtz Research Programme "Atmosphere and Climate". The European Network of Excellence ACCENT financially supported Eli Ganor, Masataka Murakami, Atsushi Saito, Hazel Jones, and Admir Targino for attendance. The U.S. National Science Foundation (Grant ATM-0611936) supported P. DeMott's group for this project. The European Science Foundation's INTROP program supported the data workshop in Pontresina.

6. REFERENCES

Bundke,, U., B. Nillius, R. Jaenicke, T. Wetter, H. Klein, H. Bingemer, 2008: The Fast Ice Nucleus Chamber FINCH, *Atmospheric Research*, doi:10.1016/j.atmosres.2008.02.008

Cziczo, D. J., D. S. Thomson, T. L. Thompson, P. J. DeMott, and D. M. Murphy, 2006: Particle analysis by laser mass spectrometry (PALMS) studies of ice nuclei and other low number density particles. *Intnl. Journal Mass Spec.*, **258**, 21-29.

Duft and Leisner, T., 2004: Laboratory evidence for volume-dominated nucleation of ice in supercooled water microdroplets. *Atmos. Chem. Phys.*, **4**, 1997–2000.

Möhler, O. P. J. DeMott, and O. Stetzer, 2008: The fourth international ice nucleation workshop ICIS-2007: Methods and instruments. 15th International Conference on Clouds and Precipitation, July 7-11, Cancun, Mexico (in this Proceedings).

Möhler, O., P.J. DeMott, G. Vali, and Z. Levin, 2007: Microbiology and atmospheric processes: The role of biological particles in cloud physics, *Biogeosciences*, **4**, 1059–1071.

Möhler, O., P. R. Field, P. Connolly, S. Benz, H. Saathoff, M. Schnaiter, R.Wagner, R. Cotton, M. Krämer, A. Mangold, and A. J. Heymsfield, 2006: Efficiency of the deposition mode ice nucleation on mineral dust particles. *Atmos. Chem. Phys.*, **6**, 3007–3021.

Rogers, D. C., 1988: Development of a Continuous Flow Thermal Gradient Diffusion Chamber for Ice Nucleation Studies. *Atmospheric Research*, **22**, 149-181.

Rogers, D. C., P. J. DeMott, S. M. Kreidenweis and Y. Chen, 2001: A continuous flow diffusion chamber for airborne measurements of ice nuclei, *J. Atmos. Oceanic Technol.*, **18**, 725-741.

Stetzer, O., B. Baschek, F. Lüönd, U. Lohmann, 2008: The Zurich Ice Nucleation Chamber (ZINC)-A New Instrument to Investigate Atmospheric Ice Formation, *Aerosol Science and Technology*, **42**:1, 64 - 74

Vali, G., 1976: The Third International Workshop on Ice Nucleus Measurements. Proceedings. University of Wyoming. 187 pp.

Vali, G., 1975: Workshop Summary: Ice Nucleation Workshop 1975, Laramie, Wyoming, 19 May – 6 June, 1975. *Bull. Amer. Meteor. Soc.*, **11**, 1180-1184.

FREEZING OF CLOUD BY MINERAL PARTICLES IN THE AIDA CHAMBER

Martin Gallagher[1],Paul Connolly[1], Ottmar Möhler[2], Paul Field[3], Rachel Burgess[1], Tom Choularton[1],

1. University of Manchester

2. Forschungzentrum Karlsruhe

3. Met Office, UK,

INTRODUCTION

Ice formation in the atmosphere remains an uncertainty. There are two primary ways by which it forms: homogeneously, by `spontaneous' freezing of solutions at temperatures colder than -35C or heterogeneously, meaning with the presence of an ice nucleus.

Modelling the formation of ice in atmospheric models presents a difficult challenge. Not least since the theoretical framework required explaining the differences between difference nucleants has not been reached.

The heterogeneous nucleation of ice can occur at temperatures below 0C by modes of direct vapour deposition; condensation or immersion-freezing and contact-freezing which all have differing efficiencies over a range of atmospheric conditions. Added to this is the complexity of secondary ice formation processes (Hallett *et al.* 1974); however, these secondary processes are not the focus of this paper.

In this paper we will build on the results of Möhler *et al.* (2006) who presented a framework for parameterising heterogeneous ice deposition at cold temperatures (T<-40C) by three different dust samples: Arizona Test Dust (ATD); Saharan Dust (SD2) and Asian Dust (AD1).

Here we will present the necessary framework for dealing with parameterisation of the condensation or immersion freezing modes at temperatures warmer than -35C. This is distinct from the paper by Möhler *et al.* (2006), which dealt with the ice deposition mode.

MOTIVATION FOR THIS STUDY

Measurements from CRYSTAL-FACE demonstrated an important link between the concentration of desert dust, advected across the Atlantic Ocean and the glaciation of layer clouds DeMott *et al.* (2003), Sassen *et al.* (2003) and Cziczo *et al.* (2004). The mineral particles were observed to glaciate cloud at temperatures of -5.2 to -8.8 C.

Möhler *et al.* (2006) Studied and describe ice nucleation on three different dusts by deposition at cirrus cloud temperatures. They were able to describe the fraction of dust particles acting as deposition nuclei using an exponential function that was dependent on the ice supersaturation. Their parameterisation only dealt with deposition nucleation.

It is difficult to quantify the relative importance of the different heterogeneous ice nucleation modes in the atmosphere (Cantrell *et al.* 2005). Indeed Field *et al.* (2006) found that in some situations even the same dust sample may act in different modes at similar temperatures. At temperatures colder than -40C they observed a dual nucleation event happening first at ice saturation ratios of 1.1 to 1.3 and then secondly at ratios of 1.35 to 1.5.

In this paper we will use results from three campaigns at the AIDA facility to attempt to quantify nucleation behaviour on the three different types dust particles in the temperature range appropriate for heterogeneous freezing.

Better quantification of the different modes and sources of heterogeneous ice nucleation will ultimately enhance our skill in weather forecasting.

OBSERVATIONS

Cloud formation and evolution was simulated in the laboratory at the large AIDA expansion chamber; the experiments aimed to form cloud under natural and controlled conditions.

The AIDA consists of a cylindrical, 7 m by 4m, 84 m3 vessel encased in a large cold box. The vessel itself is connected to a vacuum and air supply system and can be evacuated to a pressure below 0.1 hPa and filled with particle free synthetic air. This ensured that background particle concentrations measured with a CPC were less than 0.1 cm^{-3}.

Experiments were prepared by injecting humid air into the chamber and then slowly cooling throughout the night to the required temperature for the experiment.

The reason for the slow cooling of the cold box to the required temperature is twofold: firstly it means that the air can saturate (eventually resulting in frost forming on the interior of the aerosol vessel); and secondly it ensures that the difference between the temperature of the metal aerosol vessel and the air inside is not so large to prevent frost formation on the interior. The frost coating on the chamber wall results in conditions close to ice saturation at the start of the experiment.

Dust aerosol samples (AD1, SD2 and ATD) were prepared in the way described by , Möhler *et al.* (2006) - page 1545 - and were introduced into the chamber with a PALAS brush generator; a mechanical fan mixed the air in the chamber at the start of the experiment giving homogeneous conditions within the chamber.

The aerosol size distribution (0.5µm <Dp< 40µm) is sampled using the WELAS optical particle counter from PALAS, which is situated at the bottom of the AIDA vessel; total number concentrations of particles (0.01µm <Dp <3µm) are measured with a modified CNC 3010, able to sample at reduced pressures.

To simulate cloud formation, the chamber volume is expanded using a mixture of Vacuum pumps and the expansion volume. The point at which the pumps start to expand the volume is set to t=0s and typically the experiments last ~600s. Combinations of these pumps to expand the volume are able to yield cooling rates in the chamber (by quasi adiabatic expansion) of up to 4 K min^{-1}. As cooling proceeds, conditions of saturation are reached and cloud is formed on the aerosol particles within the chamber.

Cloud particles (10µm <Dp <2000µm) were imaged with the SPEC Cloud Particle Imager[1] (CPI), which is situated at the bottom

---

[1] Many instruments were available for sampling cloud during the experiments.

of the AIDA vessel. This instrument was chosen due to its availability throughout the three separate AIDA campaigns – inter comparisons with the other probes show that use of this probe is justified for these (`warmer than cirrus') experiments.

MODELLING

The Aerosol-Cloud and Precipitation Model (ACPIM), developed at the University of Manchester was applied to the chamber for studying the heterogeneous nucleation rates.

This enabled the nucleation rates to be extracted by a reverse modelling technique and also checked for consistency using a forward modelling technique.

The full details of this method shall be explained in more detail at the conference.

RESULTS

The CPI data produced images of crystals which were then be processed using the method described in Connolly *et al.* (2007) to yield the ice particle concentration. The geometric properties of the images are the main criteria for distinction between ice and liquid. Examples of ice images from experiment using AD1 at -20C are shown in Figure 1.

More generally we find that all three dusts we efficient freezing nuclei at temperatures colder than -25C (see Figure 2) and that the data supports the singular freezing hypothesis. That is during all experiments the freezing process had no explicit time-dependence over the range of temperatures studied.

These results will be discussed in more detail at the conference.

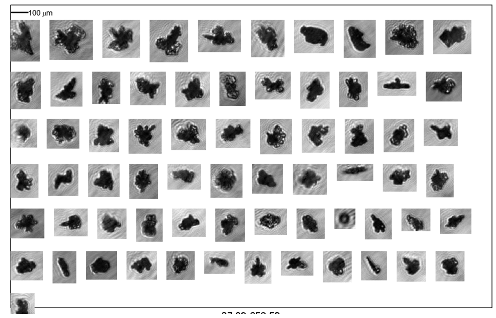

Figure 1. Examples of ice crystals formed on AD1 during an experiment at -20C.

SUMMARY

We have presented results of experiments at the AIDA chamber facility for freezing of three different types of mineral particles at temperatures between -15C and -33C. The three different dusts are AD1, SD2 and ATD.

The dust samples used had particle sizes that were log-normally distributed with mode diameters between 0.3 and 0.5 µm and standard deviations of 1.6-1.9.

The results from the freezing experiments can be made to fit a model of a singular freezing process. An important parameter in this model is the number of germs per unit area of the aerosol sample that are active on the sample at a given temperature.

However, in the temperature range of these experiments the CPI was the most suitable

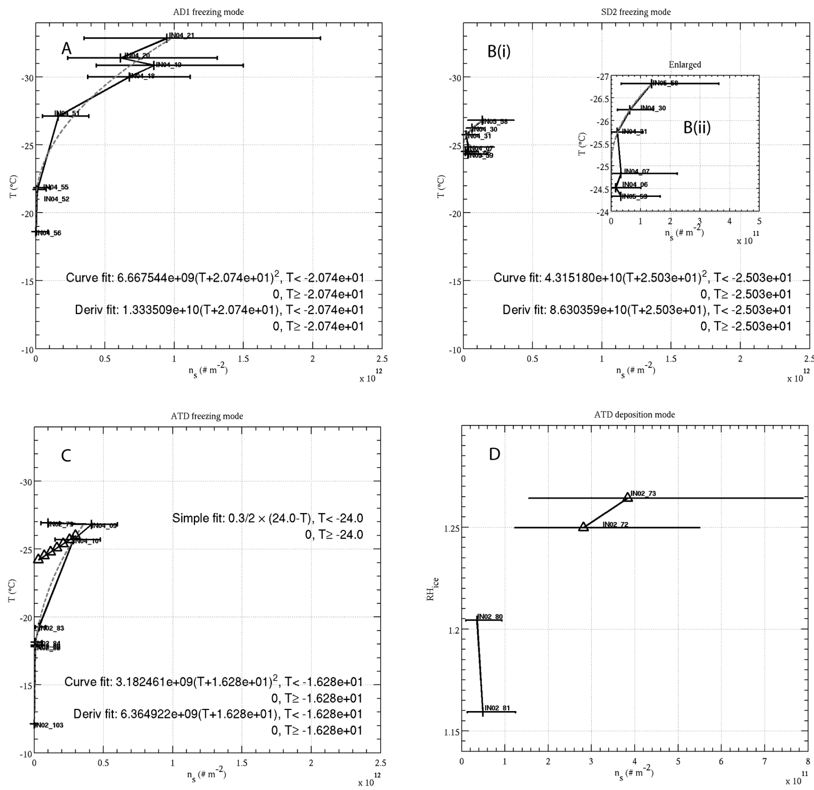

Figure 2. (A) shows the curve of number of germs active between 0C and the temperature on the y-axis for AD1; in all graphs, error bars assume 5 and 95 confidence intervals of the Poisson distribution. The gray dashed line shows a robust fit to the data and equations for the curves and their derivatives are shown for the freezing experiments. B(i) shows the same for number of germs active between 0C and the temperature on the y-axis for SD2, while B(ii) is an enlargement of this. (C) shows the same for number of germs active between 0C and the temperature on the y-axis for ATD. A simple visual fit (shown by the triangles) yielded a good comparison with the experiments. (D) shows the number of germs active between 0 and RHice on the y-axis for ATD in experiments below water saturated conditions (i.e. nucleation due to deposition).

The different dusts showed different nucleation abilities, with ATD showing a rather sharp increase in active germ density at temperatures less than -24 C. AD1 was the next most efficient freezing nuclei and showed a more gradual increase in activity than the ATD sample. SD2 was the least active freezing nuclei.

A process model (ACPIM) was used to derive the germ density as a function of temperature for each of the three samples. This method enables better quantification of the nucleation rates and the germ density than by using the data alone. Quadratic curves are then fitted to the dependence of germ density on temperature.

The quadratic curve fits were then used independently within the process model to simulate the ice formation rates from the experiments in order to test the validity of this theory.

Good agreement is found for the germ density vs temperature curves for AD1 and SD2; however, the curve for ATD does not yield results that agree well with the observations. The reason for this is that we need more experiments between -20 and -24C to quantify the rather sharp increase in active germ density on ATD.

The curves presented can be used as a parameterisation in atmospheric cloud models to predict the concentration of ice crystals by the freezing mode of ice nucleation and examples of this will be presented at the conference.

BIBLIOGRAPHY

Cantrell, W. and A. J. Heymsfield (2005). "Production of ice in tropospheric clouds." bams **86**: 795--807.

Connolly, P. J., M. J. Flynn, et al. (2007). "Evaluation of Cloud Particle Imager Probes using Ice Crystal Analogues: The depth-of-field." JAOT.

Cziczo, D. J., D. M. Murphy, et al. (2004). "Single particle measurements of the chemical composition of cirrus ice residue during CRYSTAL-FACE." GRL **109**(D04201): 1-13.

DeMott, P. J., K. Sassen, et al. (2003). "African dust aerosols as atmospheric ice nuclei." GRL **30**(14): 1732-1735.

Field, P. R., O. Möhler, et al. (2006). "Some ice nucleation characteristics of Asian and Saharan desert dust." ACPD **6**: 1509-1537.

Hallett, J. and S. C. Mossop (1974). "Production of secondary ice particles during the riming process." Nature **249**: 26-28.

Möhler, O., P. R. Field, et al. (2006). "Efficiency of the deposition mode ice nucleation on mineral dust particles." ACPD **6**: 1539-1577.

Sassen, K., P. J. DeMott, et al. (2003). "Saharan dust storms and indirect aerosol effects on clouds: CRYSTAL-FACE results." grl **30**(12): 1633-1636.

ACKNOWLEDGEMENTS

We would like to acknowledge funding from ACCENT and NERC for monies for numerous trips to the AIDA facility.

HETEROGENEOUS IMMERSION FREEZING EFFICIENCIES OF ICE ON MINERAL DUST AND BIOGENIC PARTICLES

Daniel Rzesanke[1], Maren Brinkmann[2] and Thomas Leisner[1,2]

[1] Institut für Umweltphysik, Universität Heidelberg, Germany
[2] Forschungszentrum Karlsruhe, Germany.

1. INTRODUCTION

Heterogeneous immersion freezing of cloud droplets is a key process in the formation of cirrus clouds as well as for the initiation of precipitation from tropospheric clouds.

We investigate and compare the ice nucleating abilities of various naturally occurring heterogeneous nuclei like mineral dust particles and bacteria suspended in levitated water droplets inside an electrodynamic balance.

2. EXPERIMENTAL

Suspensions of various heterogeneous ice nuclei were filtered to remove particles larger than 2µm. After characterizing the number and size distribution of suspended particles with a Coulter counter, the suspensions were diluted to render on the average only one particle per droplet of 100µm diameter.

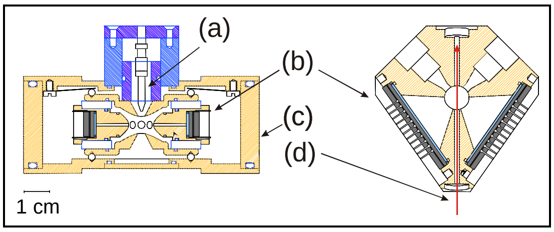

Figure 1: Scheme of the experimental setup. (a) Droplet injector, (b) levitator with light scattering detectors, (c) climate chamber, (d) HeNe laser beam

Droplets of that size were generated from the suspensions using a piezo- driven droplet dispenser and injected into an electrodynamic balance which was kept on a temperature of interest well below the freezing point of water. The balance forms a small climate chamber and the electrodes are of classical hyperboloidal design (cf. Figure 1). Details of the setup are given in Stöckel 2005. Once injected, the droplets are rapidly quenched (t_q~100ms) to the trap temperature. At that temperature, the droplets stay liquid for a certain amount of time t_l and then eventually freeze completely. Freezing is a two step process. In the first step it takes only a few µs to heat the droplet to the freezing temperature (0°C) via the latent heat release from ice formation. Further freezing is limited by the rate by which heat is transferred to the cold atmosphere surrounding the droplet. For droplets of our size, this process takes roughly 10ms.

In our experiments, the temperature of the trap is adjusted to yield a liquid time t_l, which is long compared to both t_q and t_f. Freezing is detected by monitoring the depolarization of the scattered light from a HeNe laser beam directed onto the droplet.

Size, charge and index of refraction of the liquid droplets are determined from light scattering analysis, electrostatic balance voltage and still image microscopy.

3. DATA ANALYSIS

In contrast to temperature ramp experiments, we repeat this experiment several thousand times (N_0) at a fixed temperature with fresh droplets from the same sample, recording t_l for every freezing event. These data are used to analyze the freezing dynamics by plotting the logarithm of the fraction of droplets not frozen up to a certain time t as a function of t ($\ln(N_u(t)/N_0)$). In classical homogeneous nu-

Corresponding author's address:
Thomas Leisner, IMK-AAF, Forschungszentrum Karlsruhe, Postfach 3640, 76021 Karlsruhe, Germany; Thomas Leisner@imk.fzk.de

cleation theory this should yield a straight line the slope of which is the negative product of the homogeneous nucleation rate J_{hom} and the droplet volume V_{hom}.

$$\frac{d}{dt}[\ln(N_u(t)/N_0)] = - J_{hom} \cdot V_{hom} \qquad \text{Eq.1}$$

J_{hom} is a very steep function of T, effectively preventing macroscopic samples of water from being supercooled below about -40°C. We assume that in hypothetical heterogeneous freezing experiments with an idealized suspension of identical nuclei, the above analysis can be applied but V_{hom} has to be replace by V_{het}, the volume of liquid that is in contact with the surface of the heterogeneous germ, and J_{hom} is replaced by the much larger heterogeneous freezing rate J_{het}. Alternatively to J_{het}, one can report the temperature at which homogeneous freezing would lead to the same homogeneous freezing rate (T_{hom}). The difference between the actual temperature and T_{hom} is a convenient measure for the ice nucleating power of specific heterogeneous germs. In reality, suspensions of realistic heterogeneous nuclei contain particles of various sizes and nucleating abilities, so that a distribution of J_{het} and T_{hom} has to be expected. This is reflected in our experiment by a deviation from the straight line behaviour in Eq. 1 and a model curve can be fit to the experimental data in order to extract the distribution of J_{het} or T_{hom} respectively. We analyze our data assuming Gaussian distributions of T_{hom}.

4. RESULTS AND DISCUSSION

We have used suspensions from Arizona Test Dust (ATD) particles, Saharan Dust samples and suspensions of Pseudomonas syringae bacteria for our experiments.

In the case of ATD, we observe freezing on a 30 seconds timescale around a temperature of -26°C. Typical integral freezing time distributions are given in Fig. 2a (symbols) for two different temperatures. The rapid increase in nucleation rate within a temperature range of only 1°C is clearly visible. It can be seen that the curves do not exhibit a constant slope but display a steep initial decrease which is followed by a much shallower slope at later times.

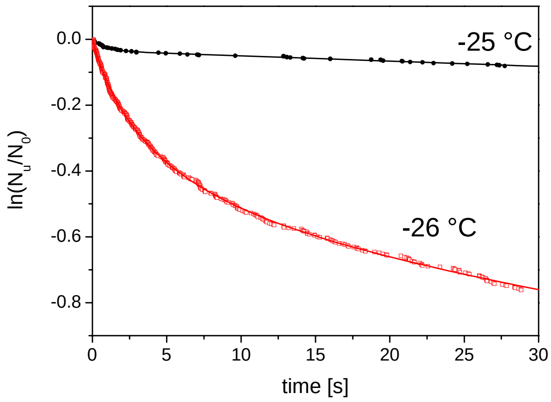

Figure 2 Arizona test dust suspensions: Logarithm of the fraction of unfrozen droplets as a function of time for two different temperatures (symbols) and results from a model assuming bimodal distributions of T_{hom} (solid lines), details cf. text.

This is indicative for a broad range of "freezing abilities" encountered with this type of particles. A more careful analysis reveals that the behaviour of the ATD particles can be described well by assuming a bimodal distribution of T_{hom}, consisting of a more ice active fraction and a narrower but less ice active fraction. This distribution yields the lines in Fig. 2. More analysis of the particles under investigation is needed to relate these findings to the structural properties of the ATD particles.

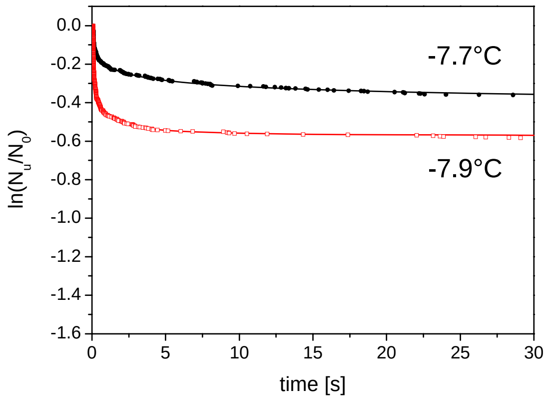

Fig. 3 Pseudomonas Syringae suspension: Logarithm of the fraction of unfrozen droplets as a function of time for two different temperatures (symbols) and results from a model assuming bimodal distributions of T_{hom} (solid lines), details cf. text.

Pseudomonas syringae suspensions are much more ice active, yielding nucleation rates comparable to ATD at temperatures around -8°C. As for ATD, the freezing rate is a strong function of temperature, as shown in Figure 3 (symbols). In this case, we are able to fit the observed distribution of freezing times with a single broad mode of nucleation ability T_{hom} (Fig. 3, solid line).

For bacteria suspensions we find that the ice nucleation ability degrades as the sample ages, reflecting the degeneration of the bacteria in a solution without nutrients. This effect has to be taken into account when assessing the ice nucleating abilities of bacteria in cloud water.

BIBLIOGRAPHY

P. Stöckel, I. M. Weidinger, H. Baumgärtel and T. Leisner: Rates of homogeneous ice nucleation in levitated H_2O and D_2O droplets, Journal of Physical Chemistry A 109, 2540-2546, (2005)

EXPERIMENTAL STUDY ON IMMERSION FREEZING UNDER MIXED PHASE CLOUD CONDITIONS

Felix Lüönd[1], Olaf Stetzer[1] and Ulrike Lohmann[1]
[1]Institute for Atmospheric and Climate Science, ETH Zurich, Switzerland

1. INTRODUCTION

Knowledge about heterogeneous ice nucleation in the atmosphere is important for the understanding of the formation of precipitation and of cloud radiative properties. In mixed-phase clouds, heterogeneous ice nucleation is the dominant process in the formation of ice crystals. Once nucleated, crystals can grow rapidly to precipitation size via the Bergeron-Findeisen process. Vali (1999) has classified four different mechanisms of heterogeneous ice nucleation: Deposition nucleation, condensation freezing, immersion freezing and contact freezing. This work focuses on the ice nucleation ability of various insoluble aerosol species in the immersion mode. In this mechanism, an ice nucleus (IN) is immersed in a cloud droplet and initiates freezing at some supercooling of the droplet.

2. OVERVIEW OF THE EXPERIMENT

The present experiment aims at investigating the freezing of cloud droplets with single immersed ice nuclei. Other than in experiments with droplets produced from suspensions (e.g. Vali, 2008), the content of each droplet is known. An overview sketch of the experimental setup is shown in Fig. 1. Aerosol particles (e.g. mineral dust, such as Kaolinite, Montmorillonite, Illite or Arizona Test Dust) are immersed in water droplets by activation in a water-based condensation particle counter (W-CPC). Droplets exiting the W-CPC typically have a temperature of 40°C to 50°C, depending on the W-CPC settings. The standard temperature is 44°C. Depending on this temperature, average droplet sizes cover a range between 3 μm and 4 μm in diameter. Droplets are passed to the newly developed IMCA chamber (Immersion Mode Cooling ChAmber, details are given in the following) through a heated tube. The IMCA chamber continuously cools the droplets to the

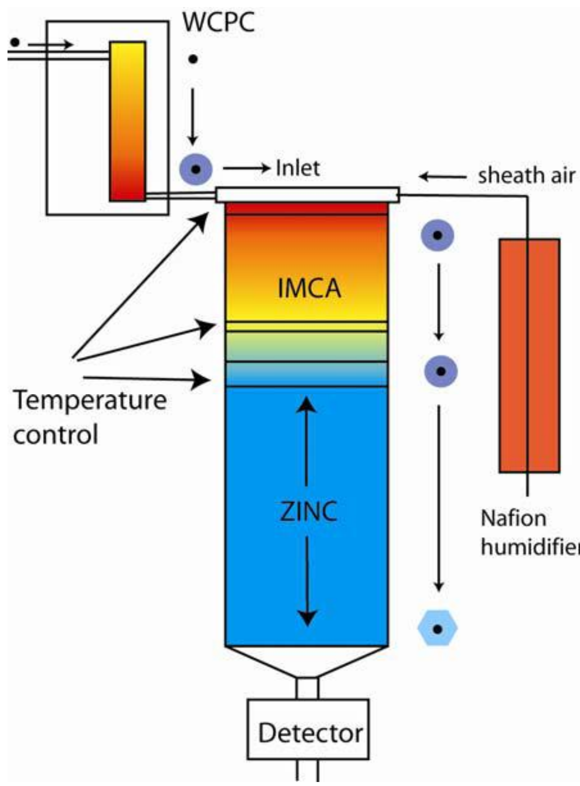

Figure 1: Experimental setup. Colours qualitatively indicate temperature from below 0°C (blue) to typically 44°C (red).

experimental temperature which is held constant in the ZINC chamber (Zurich Ice Nucleation Chamber, described in detail by Stetzer et al., 2008). Subsequent to the ZINC chamber, a depolarization detector (Nicolet, 2008) is used to determine the fraction of frozen droplets, from which the median freezing temperature can be derived. This experimental setup simulates the pathway an IN can make in the atmosphere from the dry aerosol particle via activation and cooling to freezing, although the short time scale of the cooling process as well as the high supersaturation in the W-CPC may not be realistic in the atmosphere. Median freezing temperatures are determined for various aerosol species. In the future, an additional window port at the lower end of the IMCA chamber will also allow to retrieve information about the time dependence of the frozen fraction of the droplets.

3. THE ZINC CHAMBER

The Zurich Ice Nucleation Chamber has been built as a parallel-plate continuous flow diffusion chamber (CFDC). This system allows to maintain a wide range of supersaturations with respect to ice via applying different temperatures to the ice coated walls. In the present experiment, the ZINC chamber is used to maintain the experimental temperature at saturation with respect to water in order not to evaporate the unfrozen droplets. Experimental temperatures reach down to around -30°C in the present setup.

4. THE IMCA CHAMBER

Between the W-CPC and the ZINC chamber, the droplets have to be cooled by up to 80°C roughly. To achieve this cooling in a controlled manner, the IMCA chamber implements a 74 cm long, vertical extension of the ZINC chamber with a streamwise temperature gradient along its walls. A schematic picture of the IMCA chamber is given in Fig. 2. The chamber is divided into two parts: The upper (above 0°C) and the lower (below 0°C) section. The temperature gradient along the aluminum walls is established by three temperature control stages. The heating elements keep the top of IMCA at the temperature at which the droplets leave the W-CPC. The low temperature coolers keep the lowermost part of the chamber at the experimental temperature. The third cooling unit in between defines the transition between above and below 0°C. All coolers consist of copper blocks with embedded copper tubes carrying cooling liquid from the cryostats. The heating elements are copper blocks with embedded electrical heaters manufactured by Probag.

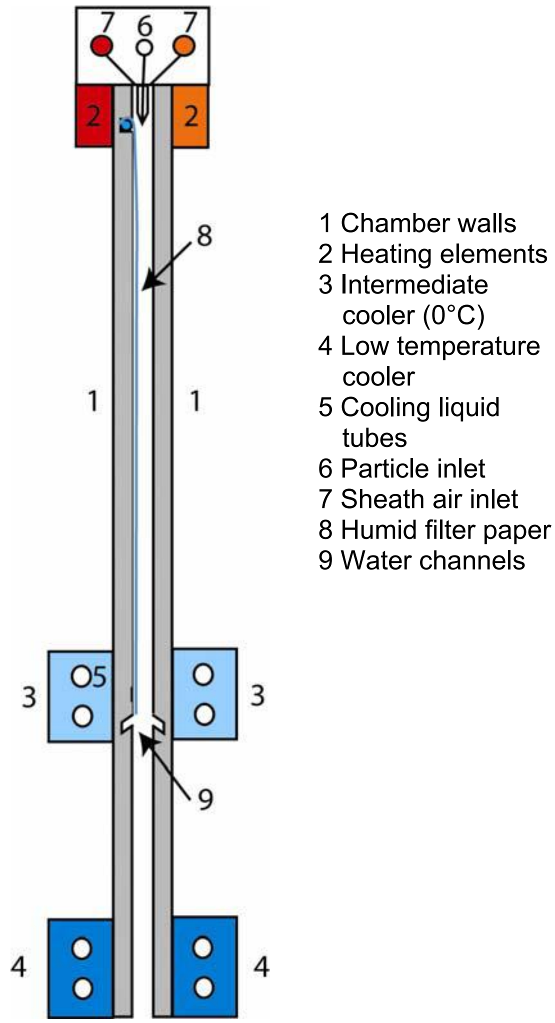

Figure 2: Sketch of IMCA chamber (not to scale).

The chamber has been designed to fulfill the main requirement of continuously cooling the droplets without losing them due to evaporation. The width of the chamber (i.e. the distance between the walls) is 0.5 cm, which leads to an acceptable adaptation of the sample air temperature to the wall temperature. FLUENT simulations have shown that for flow rates around 5 lpm, the horizontal temperature difference between the air and the walls does not exceed 3°C in the lower section (with the steeper temperature gradient). This difference reduces to below 1°C between the cooling blocks. The sample air carrying the aerosol particles needs to be merged with humidified sheath air on both walls in order to channel the sample flow in the central part of the chamber. A Nafion humidifier tube manufactured by Permapure is used to humidify the sheath air flows. The total flow rate is 5 liters per minute. Lower flow rates would allow for even better temperature adaptation. However, the laminar flow pattern in the ZINC chamber is increasingly disturbed by a buoyant upstream on the warm wall with decreasing total flow rate.

As the sample air cools down along the chamber, excess water vapour condenses on the walls. This leads to a water layer in the first section above 0°C, and an ice layer below 0°C. As the walls are heated to different temperatures $T_{top,w}$ and $T_{top,c}$ at the top of the chamber, additional humidification of the warmer wall is required to prevent the warm wall from drying out: The rate of water vapour diffusion from the warmer to the cooler wall due to a gradient in vapour pressure is larger than the rate of water vapour being deposited on the warmer wall due to cooling of the sample air. Thus, a humidified filter paper is attached to the warm wall (8 in Fig. 2). The supply water is pumped into a channel at the top of the chamber, and excess water running down the wall is collected in a channel at the position of the intermediate cooling unit. The position of this channel, which is implemented on the cooler wall as well, is also important to make sure that no water from the first section runs down to the second section below 0°C. This would lead to freezing up of the chamber.

5. SIMULATION RESULTS

Evaporation is one of the main challenges in this experiment since water droplets with a diameter around 3 μm are extremely sensitive to conditions below 100% relative humidity with respect to water. FLUENT simulations were performed to design the chamber in a way that the droplets do not evaporate during the cooling process. The relative humidity in the chamber is defined by the vapour pressures above the walls, the humidity of the entering air and the air flow rate. For the situation with equal wall temperatures at the top of the chamber, i.e. $T_{top,w} = T_{top,c}$, FLUENT simulations yield values between 99% and 100% in the first section, and values down to around 70% in the second section, depending on the experimental temperature. This drop is due to the difference in vapour pressure over water and ice. Profiles of temperature, saturation and flow velocity from the simulation were used to calculate droplet evaporation according to Pruppacher and Klett (1997). For $T_{top,w} = T_{top,c}$, it turns out that the droplets would already evaporate completely in the first section. $T_{top,w} > T_{top,c}$ leads to a supersaturation with respect to water in the upper part of the chamber, similar to the situation in the ZINC chamber. A temperature difference of 14°C leads to a maximum saturation around 104% which can be seen in Fig. 3.

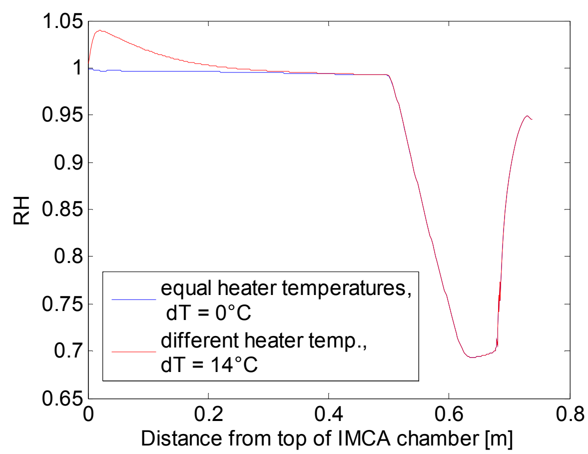

Figure 3: Relative humidity with respect to water in the IMCA chamber at the droplet position. The steep increase in RH at the lower end is caused by the saturation in the ZINC chamber.

With the first section of the IMCA chamber having a length of 35 cm, the droplets have time enough to grow to around 8 μm in diameter before the saturation drops below 100%. As the second section is only one third of the first section in length, the droplets are exposed to a low RH for a relatively short time only. Thus, they are able to leave the chamber and enter the ZINC chamber with a diameter around 3 µm. The evolution of droplet size down the IMCA chamber is shown in Fig. 4.

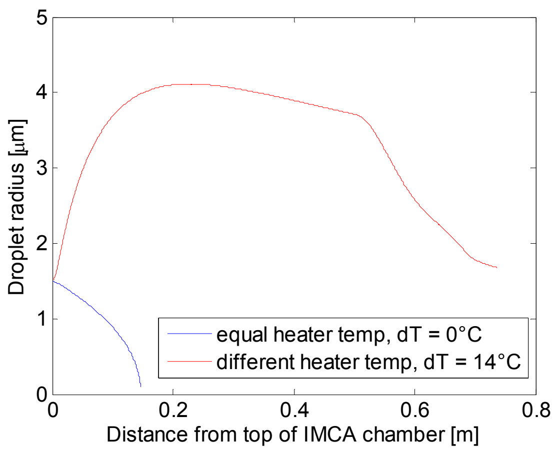

Figure 4: Droplet radius as a function of position in IMCA chamber for the case of no supersaturation (blue curve) and supersaturation at the top of IMCA (red curve)

Figures 3 and 4 have been obtained assuming an experimental temperature of -32°C.

Correct humidification of the sheath air is of crucial importance. Merging the sheath air with the incoming sample air leads to a subsaturated region at the injection point of the droplets. If the saturation at this point is too low, the droplets evaporate shortly after injection in the chamber. A FLUENT simulation of the saturation conditions in this region is visualized in Fig. 5: The air in both sheath air channels is saturated to 64% at the warmer temperature (51°C). The resulting relative humidity at the injection point of the droplets is sufficient to not evaporate the droplets. On the cooler wall, the sheath air is considerably supersaturated locally. Condensing water runs down the wall and is removed by the water channel at the intermediate cooling unit.

6. SUMMARY

The IMCA chamber has been developed to study heterogeneous ice nucleation in the immersion mode. Droplets with single immersed ice nuclei are obtained by W-CPC activation. Continuous cooling of the droplets is achieved by a streamwise temperature gradient in the IMCA chamber.

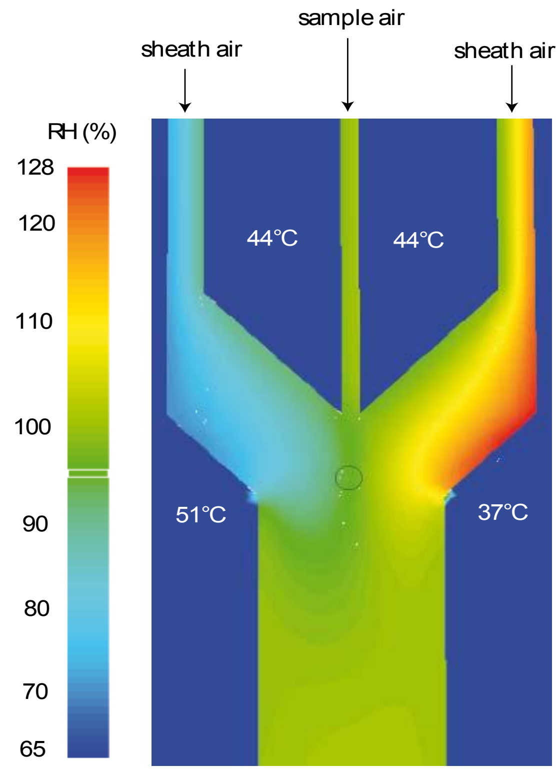

Figure 5: Combination of humidified sheath air and sample air containing W-CPC droplets (FLUENT simulation). Both sheath air flows are saturated to 64% at 51°C.

Sheath air is merged with the sample air and is previously humidified sufficiently to make droplets evaporate only to a minor degree at the injection point. Loss of droplets by evaporation during the cooling process is avoided by establishing a supersaturation in the upper part of the IMCA chamber.

7. BIBLIOGRAPHY

Nicolet, M.: Characterization of ice crystals and water droplets with the ice optical detector device (IODE) using depolarization measurements. PhD thesis at the Institute for Atmospheric and Climate Science, ETH Zurich, 2008

Pruppacher, H. R., Klett J. D. (1997).

Microphysics of Clouds and Precipitation. Second edition. Kluwer Academic Publisher, Dordrecht NL (ISBN 0–7923–4211–9)

Stetzer, O., B. Baschek, F. Lüönd and U. Lohmann: The Zurich Ice Nucleation Chamber (ZINC) – A New Instrument to Investigate Atmospheric Ice Formation. Aerosol Science and Technology, 42: 64 – 74, 2008

Vali, G.: Ice nucleation theory – A tutorial for presentation at the NCAR/ASP 1999 summer colloquium, 1999

Vali, G.: Repeatability and randomness in heterogeneous freezing nucleation. Atmos. Chem. Phys. Discuss, 8: 4059 – 4097, 2008

THE FOURTH INTERNATIONAL ICE NUCLEATION WORKSHOP ICIS-2007

O. Möhler[1], P. J. DeMott[2], O. Stetzer[3], and the ICIS-2007 team

[1] Forschungszentrum Karlsruhe, Germany.
[2] Colorado State University; Fort Collins, CO, USA.
[3] ETH Zurich, Switzerland.

1. INTRODUCTION

The Fourth International Workshop on Comparing Ice Nucleation Measuring Systems (ICIS-2007) was hosted at the AIDA (Aerosol Interaction and Dynamics in the Atmosphere) facility of the Institute for Meteorology and Climate Research (IMK-AAF) at Forschungszentrum Karlsruhe, Germany (see also contribution by DeMott et al. in the same volume). Since 2002, numerous experimental series were conducted at the AIDA facility to investigate processes of aerosol-cloud interaction, in particular homogeneous and heterogeneous ice nucleation. More recently, the AIDA facility was also offered and intensively used as a platform for testing and intercomparing water, aerosol and cloud particle instruments, which are normally used in field experiments or employed on balloon platforms and research aircrafts.

The ICIS-2007 was held during September 2007 in recognition of renewed interest in ice nucleation research and the development of new instruments. It was the first since 1975 (Vali, 1975) for the purpose of comparing ice nucleation measuring systems. These included existing and new designs of continuous flow diffusion chambers, new designs of IN mixing and static diffusion chambers, and the AIDA cloud expansion chamber. Instruments were also available to analyse the clouds formed during the AIDA experiments as well as ice residual particles.

Corresponding author's address:
Ottmar Möhler, IMK-AAF, Forschungszentrum Karlsruhe, Postfach 3640, 76021 Karlsruhe, Germany; Ottmar.Moehler@imk.fzk.de

2. ICIS-2007 PARTICIPANTS

The participants of the ICIS-2007 workshop are named in Table 1 together with their instruments. Four ice nucleation instruments with the cylindrical Continuous Flow Diffusion Chamber (CFDC) design of Rogers (1988) were operated by the Colorado State University (CSU CFDC-1H; Rogers et al., 2001), the Meteorological Research Institute Tsukuba, Japan (MRI CFDC), the UK Met Office (UKMO CFDC) and the University of Manchester, UK (MINC). New designs and experimental methods were employed by the ETH Zurich, Switzerland (vertical parallel-plate design Zurich Ice Nucleus Chamber ZINC; Stetzer et al., 2008), the University of Toronto, Canada (horizontal parallel-plate design UTOR CFDC), the University of Frankfurt, Germany (dynamic mixing IN chamber FINCH and static diffusion chamber FRIDGE; Bundke et al., 2008), the Tel Aviv University, Israel (static diffusion chamber TAU-FRIDGE), and the Institute for Meteorology and Climate Research (IMK-AAF) of Forschungszentrum Karlsuhe, Germany (single particle electrodynamic balance trap experiment IMK EDB; Duft and Leisner, 2004).

The single particle mass spectrometer PALMS from the ETH Zurich analysed the chemical nature and composition of aerosol particles as well as ice residual particles selected from AIDA ice clouds with a Pumped Counterflow Virtual Impactor (PCVI). The mixed-phase and ice clouds formed in the AIDA chamber were analysed with a Cloud Particle Imager (CPI) and a Cloud Droplet Probe (CDP) from the University of Manchester, UK (see paper by Targino et al. at this conference).

Table 1: List of participants and instruments employed during ICIS-2007. The workshop was organised by Paul DeMott, Ottmar Möhler and Olaf Stetzer. The names in bold characters are the principle investigators or contact persons for the respective instruments and facilities.

Name	Institute	Instrument
Ottmar Möhler, Stefan Benz, Harald Saathoff, Martin Schnaiter, Roland Schön, Robert Wagner	IMK-AAF, Forschungszentrum Karlsruhe, Germany	AIDA (host)
Continuous Flow Diffusion Chambers with cylindrical design (Rogers 1988):		
Paul DeMott, Markus Petters	Colorado State University, Fort Collins, CO, USA	CSU CFDC-1H
Masataka Murakami, Atsushi Saito, Takuya Tajiri	MRI, Tsukuba, Japan	MRI CFDC
Richard Cotton, James Bowels	UK Met Office	UKMO CFDC
Hazel Jones	University of Manchester, UK	MINC
New designs and instruments:		
Olaf Stetzer, Mathieu Nicolet, Berko Sierau, Ulrike Lohmann	ETH Zurich, Switzerland	ZINC
Zamin Kanji, Jon Abbatt	University of Toronto, Canada	UTOR CFDC
Ulrich Bundke, Björn Nillius	University of Frankfurt, Germany	FINCH
Heinz Bingemer, Werner Haunold, Holger Klein, Thomas Wetter	University of Frankfurt, Germany	FRIDGE
Zev Levin, Eli Ganor, Karin Ardon	Tel Aviv University, Israel	TAU-FRIDGE
Thomas Leisner, Daniel Rzesanke	MK-AAF, Forschungszentrum Karlsruhe, Germany	IMK EDB
Supporting ice nuclei and cloud particle instruments		
Dan Cziczo, Stéphane Gallavardin	ETH Zurich, Switzerland	PALMS single particle MS
Admir Tagino, James Dorsey	University of Manchester	CPI, CDP
Dimitri Georgakopoulos	Agricultural University of Athens, Greece	Bacteria preparation

3. EXPERIMENTAL SETUP

The ice nucleation instruments were located on two platforms around the aerosol preparation and characterisation (APC) chamber (Figure 1). The stainless steel APC chamber with a volume of 3.7 m^3 was used as an aerosol reservoir for continuous sampling with the ice nucleation instruments.

After the dust or soot aerosol was added to the APC chamber a minor fraction was transferred to the larger AIDA chamber for cloud simulation runs. The ice nucleation instruments were connected to both chambers, but sampled most often from the APC chamber and measured the ice nucleation efficiency of the aerosol as a function of humidity and temperature. Only the CSU-CFDC instrument more frequently sampled the aerosol from the AIDA chamber, for instance to investigate the effect of cloud activation on the heterogeneous ice nucleation potential of dust and soot particles.

Filter samples were taken from the aerosol in both the APC and the AIDA chamber for ice nucleation experiments in the static diffusion chamber FRIDGE. The single particle mass spectrometer PALMS sampled and analysed the aerosol also from both chambers.

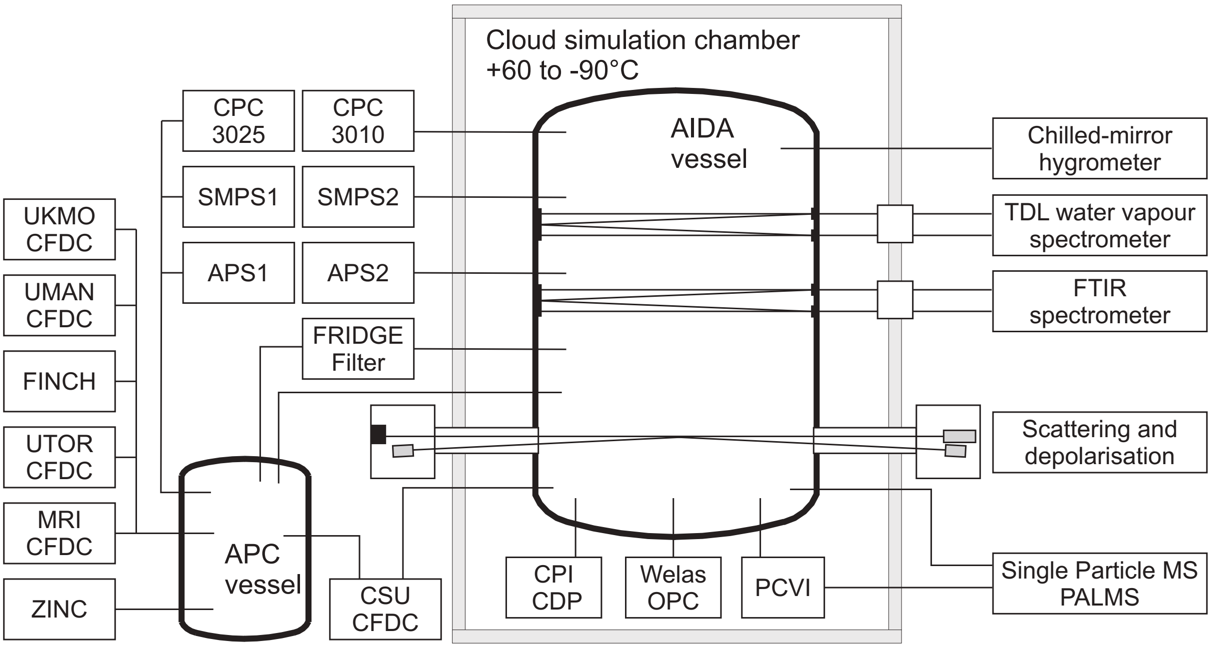

Figure 1: Schematic of the AIDA facility with instruments provided by ICIS participants.

More details about the different ice nucleation instruments are given in a paper by DeMott et al. in this volume. During AIDA cloud expansion runs, droplets and ice crystals larger than about 5 µm in diameter were selectively sampled from the AIDA chamber with a Pumped Counterflow Virtual Impactor (PCVI). The non-volatile residual particles of the ice crystals heated to +30°C were also analysed with the PALMS instrument. The optical cloud imaging and scattering probes CPI, CDP and Welas optical particle counter were mounted on vertical sampling tubes directly below the AIDA vessel.

4. EXPERIMENTAL PROGRAM

During the ICIS-2007 workshop, the response of the different instruments for heterogeneous ice nucleation in the temperature range between 0 and -45°C was investigated for three different dust samples (ATD, SD4, ID1, CI1), one soot sample (GSG), and two different bacteria samples (Snomax^{TM}, *P. Syringae* cells).

Table 2: List of experiments with different types of aerosols added to the APC chamber.

Date	NoE	Aerosol
Sep 11	1	Arizona Test Dust ATD
Sep 12	2	Arizona Test Dust ATD
Sep 13	3	Saharan Dust SD4
Sep 14	4	Sulphuric Acid, Ammonium Sulphate
Sep 17	5	Arizona Test Dust ATD
Sep 17	6	Arizona Test Dust ATD
Sep 18	7	Arizona Test Dust ATD
Sep 19	8	Arizona Test Dust ATD
Sep 20	9	GSG Spark Generator Soot
Sep 21	10	GSG Spark Generator Soot
Sep 22	11	Israelian Dust ID1
Sep 22	12	Israelian Dust ID1
Sep 24	13	Israelian Dust ID1
Sep 25	14	Saharan Dust SD4
Sep 26	15	Canary Island Dust CI1
Sep 27	16	Snomax^{TM} Bacerial Cells
Sep 28	17	*P. Syringae* Bacteria

5. AIDA CLOUD SIMULATION

A fraction of the aerosol from the APC chamber was transferred to the larger AIDA chamber which was then operated as an expansion cloud chamber (Möhler et al., 2006) to investigate the heterogeneous ice nucleation efficiency of the aerosol under simulated cloud conditions. The AIDA cloud simulation results are compared to the ice nucleation measurements with the flow diffusion, mixing, and static diffusion instruments.

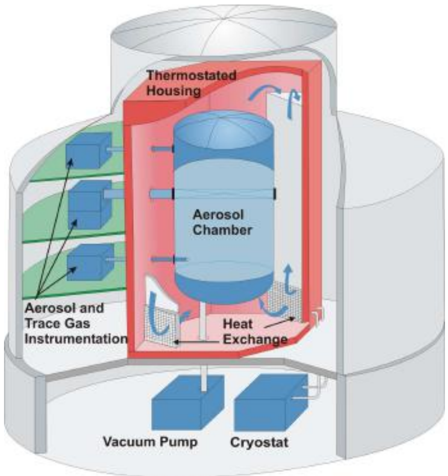

Fig. 2: Schematic of the AIDA facility

During static and homogeneous temperature and pressure control, a thin ice layer on the aerosol chamber walls maintains almost ice saturated conditions at lower temperatures. Ice supersaturated conditions are achieved by controlled pumping, typically from 1000 to 800 hPa. The corresponding expansion causes a cooling of the stirred chamber volume and thereby an increase of the relative humidity. With the highest pumping speed, maximum cooling rates of about $4\ \mathrm{K\ min^{-1}}$ can be achieved in the AIDA chamber. This corresponds to the cooling rate of an adiabatically expanding air parcel ascending in the upper troposphere at an updraft speed of about $6\ \mathrm{m\ s^{-1}}$. During the simulation runs, the ice saturation ratio typically increases at a rate of about 0.1 to $0.5\ \mathrm{min^{-1}}$.

5. AEROSOL CHARACTERISATION

Figure 3 shows as a typical example the time series of pressure, temperature, aerosol number concentration, and aerosol mass concentration measured in the APC chamber during experiment number 6 with ATD aerosol.

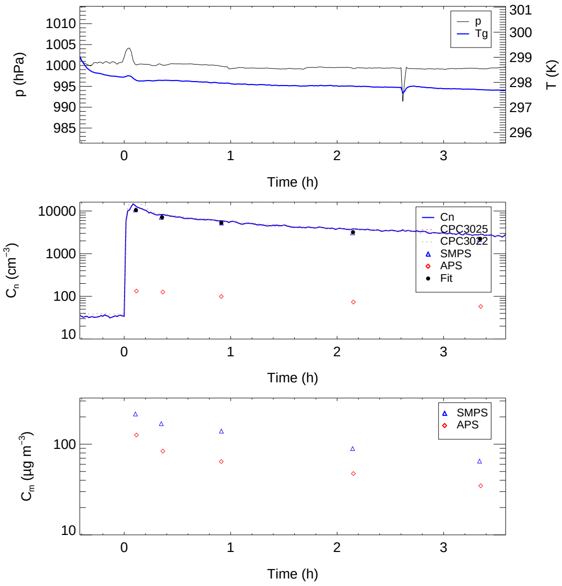

Fig. 3: APC chamber time series of temperature and pressure (panel 1), aerosol number concentration (panel 2) and aerosol mass concentration (panel 3) during experiment 6.

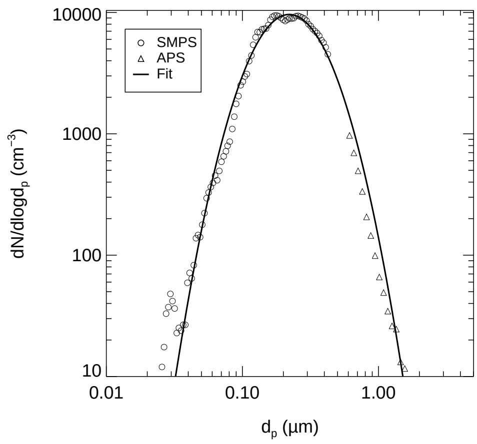

Fig. 4: Size distribution of the ATD aerosol in the APC chamber during experiment 6.

Within a few hours the dust aerosol concentration decreased from about 15000 cm^{-3} to about 3000 cm^{-3}, mainly due to coagulation processes, settling losses and sampling dilution. The dust particle sizes typically ranged from about 0.5 to 1.5 µm in diameter.

This contribution to the ICCP conference in Cancun will introduce the objectives, methodologies and some comparison results from the ICIS-2007 workshop. More results will be presented in further contributions to the same session.

ACKNOWLEDGEMENTS

We gratefully acknowledge numerous and skilful support from the AIDA team for organisation issues, instrument setup, and AIDA chamber operation during the experiments. We also thank Thomas Schwartz from the Institut für Technische Chemie of Forschungszentrum Karlsruhe for support in preparing the bacterial cultures. A variety of grants and organizations supported the group and investigators individually to participate in the experimental and data workshops. Forschungszentrum Karlsruhe provided funding for the facility infrastructure within the Helmholtz Research Programme "Atmosphere and Climate". The European Network of Excellence ACCENT financially supported five participants for attendance. The U.S. National Science Foundation (Grant ATM-0611936) supported P. DeMott's group for this project. The European Science Foundation's INTROP program supported the data workshop in Pontresina.

BIBLIOGRAPHY

Bundke,, U., B. Nillius, R. Jaenicke, T. Wetter, H. Klein, H. Bingemer (2008), The Fast Ice Nucleus Chamber FINCH, *Atmos. Res.,* doi:10.1016/j.atmosres.2008.02.008

Duft and T. Leisner (2004), Laboratory evidence for volume-dominated nucleation of ice in supercooled water microdroplets. *Atmos. Chem. Phys.*, 4, 1997–2000.

DeMott, P. J. et al. (2008), The Fourth International Ice Nucleation Workshop (ICIS-2007): Objectives and preliminary results, Proceedings of the 15th International Conference on Clouds and Precipitation, July 7-11, Cancun, Mexico (in this volume).

Möhler, O., P. R. Field, P. Connolly, S. Benz, H. Saathoff, M. Schnaiter, R. Wagner, R. Cotton, M. Krämer, A. Mangold, and A. J. Heymsfield (2006), Efficiency of the deposition mode ice nucleation on mineral dust particles, *Atmos. Chem. Phys.*, *6*, 3007-3021.

Rogers, D. C. (1988), Development of a continuous flow thermal gradient diffusion chamber for ice nucleation studies, *Atmos. Res.*, *22*, 149–181.

Rogers, D. C., P. J. DeMott, S. M. Kreidenweis and Y. Chen (2001), A continuous flow diffusion chamber for airborne measurements of ice nuclei, *J. Atmos. Oceanic Technol.*, 18, 725-741.

Stetzer, O., B. Baschek, F. Lüönd, U. Lohmann (2008), The Zurich Ice Nucleation Chamber (ZINC) - A New Instrument to Investigate Atmospheric Ice Formation, *Aerosol Sci. Technol.,* 42, 64 – 74.

Vali, G. (1975), Workshop Summary: Ice Nucleation Workshop 1975, Laramie, Wyoming, 19 May – 6 June, *Bull. Amer. Meteor. Soc.*, *11*, 1180-1184.

CHARACTERISATION OF ICE NUCLEATION ABILITY OF MINERAL DUST IN THE AIDA CHAMBER

Admir C. Targino[1], Hugh Coe[1], Ottmar Möhler[2]

[1] Centre for Atmospheric Science, University of Manchester, Manchester, UK
[2]IMK-AAF, Forschungszentrum Karlsruhe, Germany

1. INTRODUCTION

The role of airborne desert dust in ice nucleation has been described in various studies [e.g., *Twohy and Poellot*, 2005; *DeMott et al.*, 2003]. Analysis of ice crystal residuals in clouds showed that metals and crustal material are found in considerable amounts in cold clouds [*Targino et al.*, 2006; *Cziczo et al.*, 2004].

Understanding of ice crystal nucleation and subsequent growth is of utmost importance to yield prognostic cloud parameterisation schemes which can be incorporated, for example, in general circulation models. Of highest importance for an accurate parameterisation of the optical properties of cold clouds are their microphysical parameters, such as the morphology of the hydrometeors and the partitioning of the cloud elements between solid and liquid phase. Ice formation via heterogeneous pathways is rather difficult to describe, not only due to the various freezing modes, but also because ice nuclei (IN) consist of a variety of insoluble particles, such as mineral dusts, soot as well as some biological material. This broad range of IN candidates introduces complexity to the parameterisation and incorporation of ice forming processes in atmospheric models. Ice crystal habit will be a determinant in the estimate of cloud optical properties, as the different heterogeneous freezing mechanisms tend to yield different ice crystal habits, and the scattering properties of spherical and non-spherical elements differ considerably.

In September 2007 ice nucleation studies were conducted by the University of Manchester (UoM) at the AIDA (Aerosol Interaction and Dynamics in the Atmosphere) facility at the *Forschungszentrum Karlsruhe*, Germany, to look at nucleation and growth of ice crystals on a variety of IN.

In this contribution we will present results from cloud chamber expansions using mineral dust as ice nucleators.

2. EXPERIMENTS

The study presented here was carried out between 12 - 28 September, 2007 within the framework of the International Workshop on Comparing Ice Nucleation Measuring Systems (ICIS 2007). The UoM contributed with a suite of instruments which provided on-line measurements of size and shapes of ice crystals, namely a standard Cloud Particle Particle Imager (CPI Model 230X), for real-time CCD images of ice crystals in the size range 10-2000 μm, and a Cloud Droplet Probe (CDP-100), which measured number and size of hydrometeors in the size range 2-47 μm.

A range of particles were used as IN, including: Arizona test Dust (ATD), supplied by PTI (Powder Technology Inc., USA), Israel dust (ID), collected *in situ*, Sahara Dust (SD), collected outside Cairo, and Canary Island dust (CID), collected on the Canary Island of Lanzarote. The studies focused on the ice nucleation efficiency of these aerosols as IN and the dependence of ice activity on temperature (T) and saturation with respect to ice (S_{ice}).

The AIDA facility consists of a cylindrical aluminium aerosol vessel, with wall thickness of 20 mm, 7 m high and 4 m in inner diameter (84 m^3 volume), encased in a large thermally insulated box whose temperature can reach down to -90 °C, by using either a refrigerant from a chiller or liquid nitrogen, depending on the temperature required [*Möhler et al.*, 2006]. After conditions of uniform temperature and relative humidity inside the aerosol chamber

Corresponding author's address:
Dr A Targino, SEAES, University of Manchester, Oxford Road, M13 9PL, Manchester, United Kingdom
Email: ad.targino@manchester.ac.uk

are reached, the aerosol to be studied is added. The pressure, T and S_{ice} in the chamber are controlled by a pumping system. After pumping starts, T drops due to volume expansion and S_{ice} increases. Ice nucleation is usually observed shortly after the ice saturation ratio is exceeded. The expansions started at a pressure close to 1000 hPa, S_{ice} of about 0.8, and the initial T ranged from -17 to -40°C. Typically, two or three consecutive experiments were carried out during the day, starting at the same gas (air) temperature, each using the same aerosol sample.

3. RESULTS

3.1 Elemental Composition

For each dust sample, individual particles were analysed by Scanning Electron Microscopy (SEM) equipped with Energy-Dispersive X-ray analysis (EDX). Thereafter a hierarchical cluster analysis was performed on the X-ray signal detected by the SEM-EDX in order to identify the major particle classes and their abundances.

Aluminium (Al), Chlorine (Cl), Silicon (Si), Calcium (Ca) and Iron (Fe) were the major elements found across the analysed particles (Table 1), appearing in different amounts and combinations. CID particles contained large amounts of Ca, followed by Al and Si. SD particles were made up of Ca and Si, and, interestingly, about 6% of the particles analysed contained Na and Cl, suggesting the presence of sea salt. ATD and ID particles were characterised by clusters of alumino-silicates. *Vlasenko et al.* [2005] found comparable results when analysing ATD samples with similar EDX technique. In their study, Ca was also found in minor proportions in ATD samples. About 54% of the ATD particles and 65% of ID showed little trace of crustal material (sub-groups **G4**, Table 1). In these sub-groups, C and O accounted for over 85% of the characteristic X-ray signal detected. Due to the polycarbonate membrane used on the EDX analysis, it is not possible to separate the Carbon (C) and Oxygen (O) contributions from the particles and the substrate. However, the results are an indication that a fraction of the ID and ATD particles are made up of low-Z material.

Canary Island dust	
G1 (21.0%)	C(19) O(18) Mg(3) Al(4) Si(10) Ca(39)
G2 (40.9%)	C(35) O(19) Al(3) Si(9) Ca(27)
G3 (16.0%)	C(64) O(12) Si(5) Ca(11)
G4 (22.1%)	C(18) O(25) Al(6) Si(34) Ca(7) Fe(4)
Sahara dust	
G1 (6.10%)	C(15) O(9) Na(18) Si(4) Cl(38) Ca(10)
G2 (16.6%)	C(18) O(27) Al(6) Si(23) Ca(12) Fe(3)
G3 (46.6%)	C(20) O(17) Si(7) S(4) Ca(39)
G4 (30.7%)	C(54) O(14) Si(4) Ca(20)
ATD	
G1 (15.4%)	C(28) O(23) Al(4) Si(40)
G2 (26.0%)	C(52) O(16) Al(4) Si(17) Ca(4)
G3 (4.5%)	C(15) Al(66) S(3) Cl(5) K(3) Ca(4)
G4 (54.1%)	C(89) O(4) Si(3)
Israel dust	
G1 (10.2%)	C(31) O(19) Mg(3) Al(3) Si(8) Ca(29)
G2 (16.8%)	C(38) O(23) Al(8) Si(18) Ca(3) Fe(4)
G3 (8.0%)	C(13) O(28) Al(9) Si(38) Fe(3)
G4 (65.0%)	C(74) O(11) Si(6) Ca(3)

Table 1: Average relative abundance (%) and composition of particle groups (G) of dust used during ICIS 2007. The numbers in parenthesis are mean percent of X-ray counts. Only elements with X-ray counts larger than 3% are displayed.

3.2 Cloud expansions

Fig. 1 shows surface plots of the dependence of ice concentration on both T and S_{ice} for a cloud expansion using ATD as IN at a starting T of -27°C and S_{ice}~ 0.8. Note that ice crystals can grow through either increase in S_{ice} or decrease in T. Fig. 2 illustrates the habit-segregated concentration for the same expansion as well as some examples of ice crystals captured by the CPI. Initial ice formation occurred when S_{ice} reached about 1.3, and the first crystal habit observed was spheroids followed by more irregular habits (small irregular and stellar types), as S_{ice} increased. Saturation with respect to water (S_{water}) never reached one, suggesting that deposition nucleation was the main ice formation pathway in this experiment.

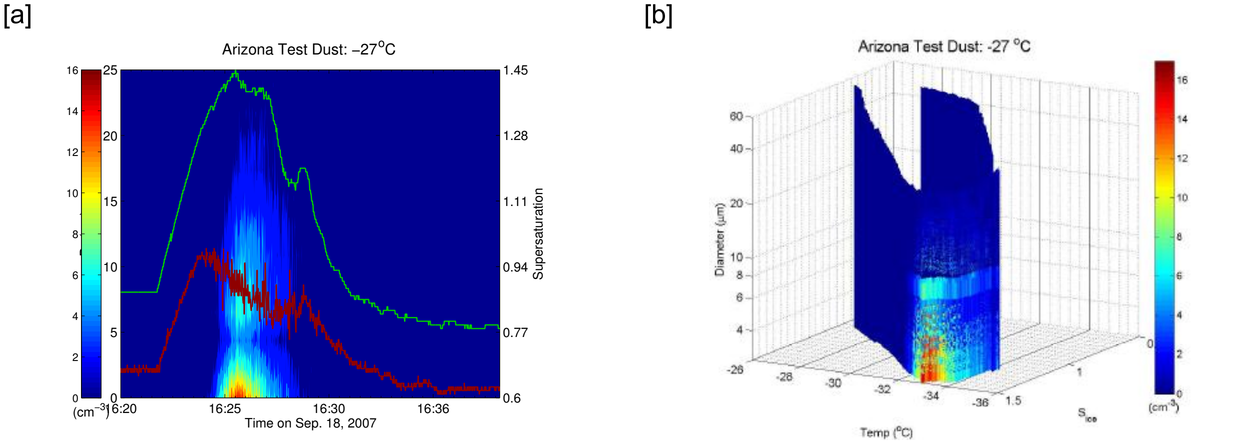

Fig. 1: [a] Time series of S_{ice} (green line), S_{water} (brown line), and ice element concentration (coloured surface) obtained by the CDP (2-47 μm)during a cloud expansion using ATD as IN. [b] 3-D evolution of T, S_{ice} and ice element concentration for the same cloud expansion as Fig. 1a.

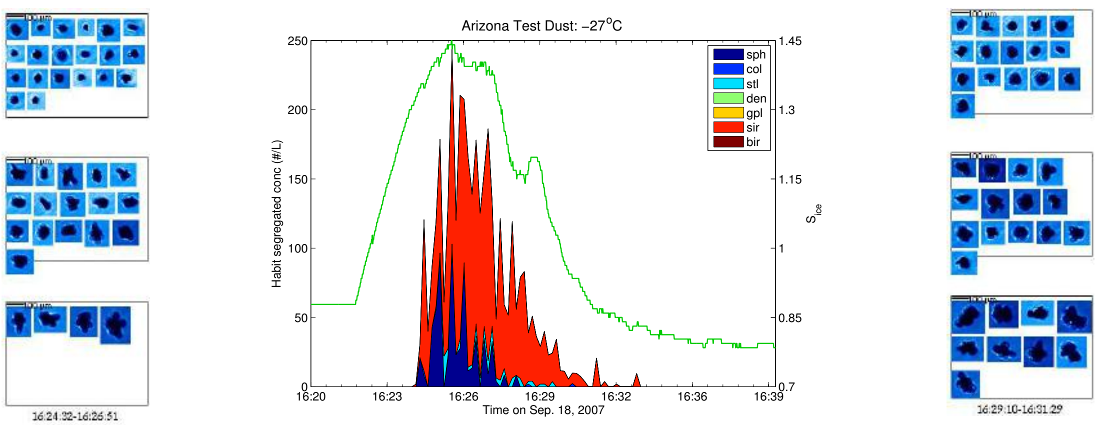

Fig. 2: [central panel] Habit-segregated concentration of hydrometeors obtained by the CPI (10-2000 μm)during the cloud expansion depicted in Fig. 1. Also shown are S_{ice} (solid green line). [left panel] Images of ice crystals captured by the CPI at the beginning of the expansion (~ 16:24 – 16:26 hrs). [righ panel] Images of ice crystals captured by the CPI at the end of the expansion (~ 16:29 – 16:31 hrs). Key: *sph*: spheroidal; *col*: columns; *stl*: stellar; *den*: dendrites; *gpl*: graupel; *sir*: small irregular; *bir*: big irregulars.

All dust samples used during ICIS 2007 were active as ice nuclei, showing strong dependence on both S_{ice} and T. We have chosen three expansions with similar T ranges and cooling rates to illustrate the ice activation dependence on T and S_{ice} (experiments IN-18, IN-22 and IN-24). In all cases displayed in Fig. 3 the nucleation onset occurs as soon as S_{ice} exceeds 1.0. About 250s into the experiment, ice crystal nucleated on ID reached larger concentrations (about 30 cm^{-3}) compared to other samples, even though S_{ice} was lower or comparable to experiments with CID and SD, and T the highest. ID also appears to have a second nucleation event growing at T of approximately -24°C and S_{ice} ~ 1.4, as shown in Fig. 4. Since the ID sample contained different mineralogical groups, it is hypothized that particles of different chemical composition are activated at different temperature ranges within the same sample, giving rise to the observed dual nucleation modes. CID dust was efficient ice nucleator, however it seems to require higher values of S_{ice} and lower temperatures to reach ice concentrations comparable to ID and SD. Fig. 5 shows the fraction of particles activated (*fi*) as a function of *T* and S_{ice} for these expansions.

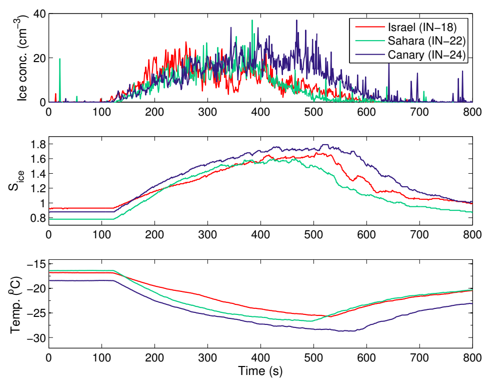

Fig. 3: Time series of ice crystal concentration, *T* and S_{ice} during three expansions using ID, SD and CI dust as ice nucleators.

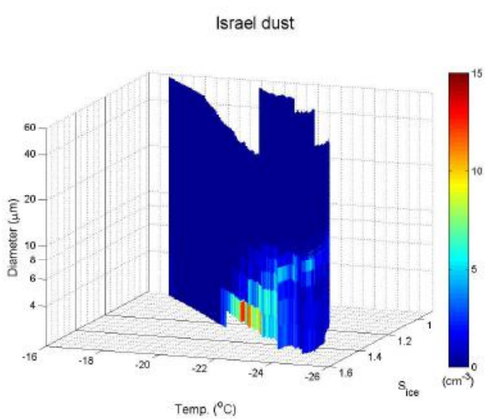

Fig. 4: 3-D evolution of *T*, S_{ice} and ice crystal concentration for a cloud expansion using ID as ice nucleators.

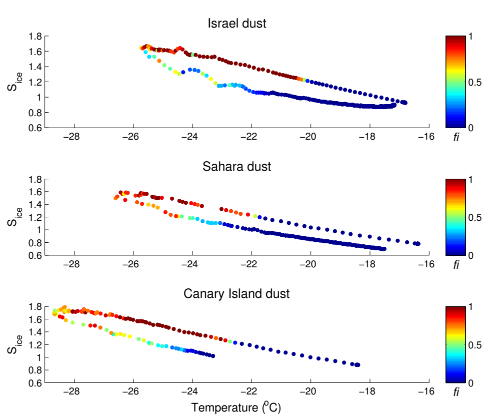

Fig. 5: Activation curve as function of *T* and S_{ice} for expansions shown in Fig. 3.

4. CONCLUSIONS

ICIS 2007 provided a unique opportunity to study the ice nucleation activity of various dust aerosols, combining a range of representative dust samples with advanced measurement techniques. The onset of ice nucleation occurred at S_{ice} between 1.0 and 1.2 for ID, CID and SD for experiments with initial T ~ -17°C, however, higher ice concentrations were observed on ID experiments even when values of S_{ice} were lower (about 1.3) than those for experiments with CID and SD. The fraction of particles activated in CID experiments was comparable to that yield when using ID and SD as nucleating dust, however higher values of S_{ice} were required (about 1.7) to yield similar ice concentrations.

EDX analysis applied on the various dust samples showed that there is heterogeneity in their elemental composition, which might have impacts on the efficiency of nucleation and growth of ice crystals. Differences in mineralogical composition found within the ID samples are suggested to be responsible for the dual nucleation modes observed.

5. REFERENCES

DeMott, P. J. et al. *Geophys. Res. Lett.*, 30, 1732, doi:10.1029/2003GL017410, 2003.

Cziczo, D. J. et al. *Geophys. Res. Lett.*, 31, L12116, doi:10.1029/2004GL01982, 2004.

Möhler, O. et al. *Atmos. Chem. Phys.*, 6, 3007–3021, 2006.

Targino, A. C. et al. *Atmos. Chem. Phys.*, 6, 1977–1990, 2006.

Twohy, C. H. and Poellot, M. R. *Atmos. Chem. Phys.*, 5, 2289-2297, 2005.

Vlasenko, A. et al. *Aerosol Sci. Tech.*, 39, 452–460, 2005.

Acknowledgments

Financial support for this work was given by ACCENT and NERC (UK). Thanks to the AIDA team for their assistance and cooperation during ICIS 2007. The first author would like to thank ICCP for providing financial support which made it possible to attend the conference.

CARBONACEOUS AEROSOL PROCESSING BY CLOUDS AND FOGS

Jeffrey L. Collett, Jr[1], Lynn Mazzoleni[1,2], Xinhua Shen[1], Pierre Herckes[1,3], Taehyoung Lee[1], Suresh Raja[1,4], Kalliat T. Valsaraj[5]
[1]Atmospheric Science Department, Colorado State University,Fort Collins, CO USA
[2]currently at Los Alamos National Laboratory, Los Alamos, NM, USA
[3]currently at Arizona State University, Tempe, AZ USA
[4]currently at Clarkson University, Potsdam, NY USA
[5]Department of Chemical Engineering, Louisiana State University, Baton Rouge, LA USA

1. INTRODUCTION

In many environments, organic compounds account for a significant fraction of fine particle mass. Because the lifetimes of accumulation mode aerosol particles are governed largely by interactions with clouds, it is important to understand how organic aerosol particles are processed by clouds and fogs. Clouds and fogs promote new particle mass formation (e.g., via rapid aqueous oxidation of sulfur dioxide to sulfate) and promote particle removal (e.g., via nucleation scavenging followed by direct drop deposition or drop incorporation into precipitation). Historically, most efforts have been directed toward understanding processing of inorganic species. Thus far we know little about cloud/fog processing of organic aerosol particles and trace gases. While a handful of compounds have received moderate attention (e.g., low molecular weight carboxylic acids), they form only a fraction of the multitude of organic compounds known to be present in the atmosphere.

Recently we have examined the organic composition of fogs and clouds in several environments, including locations in California, along the U.S. Gulf Coast, in Colorado, and in Hawaii. Observations of fog/cloud composition and processing of atmospheric organic matter are highlighted here.

2. EXPERIMENTAL

Clouds and fogs were sampled with active cloudwater collectors at a variety of locations. Most samples were collected with stainless steel versions of the Caltech Active Strand Cloud Collector (ss-CASCC); some were collected with a traditional plastic CASCC (1). Radiation fogs were sampled in the Central Valley of California, in Pittsburgh, and along the U.S. Gulf Coast in Houston and Baton Rouge. Orographic clouds were sampled at most other locations, including Mt. Schmueke (Germany), Costa Rica, Hawaii, and Storm Peak Lab near Steamboat Springs, Colorado. Stratocumulus clouds were sampled by aircraft, using a CSU/NCAR airborne cloudwater collector, over the Eastern Pacific Ocean off the coast of southern California (2).

3. RESULTS AND DISCUSSION

Observations indicate that organic matter is a significant component of the cloud/fog droplets. A summary of the average concentration of total organic carbon (TOC) in clouds and fogs collected at several locations is included in Figure 1. TOC concentrations in individual cloud and fog samples ranged from approximately 1 to 40 ppmC. The highest concentrations were observed in urban areas. The lowest concentrations were observed in remote locations, including the eastern Pacific stratocumulus and orographic clouds sampled on the island of Hawaii. Studies of phase partitioning inside the drops in California radiation fogs reveal that approximately one-fourth of the organic matter in these fog drops is associated with an undissolved phase of suspended particles. Phase partitioning is also observed between dissolved and undissolved phases for individual organic compounds. As compounds become more hydrophobic, they are observed to be increasingly associated with suspended particulate matter (3).

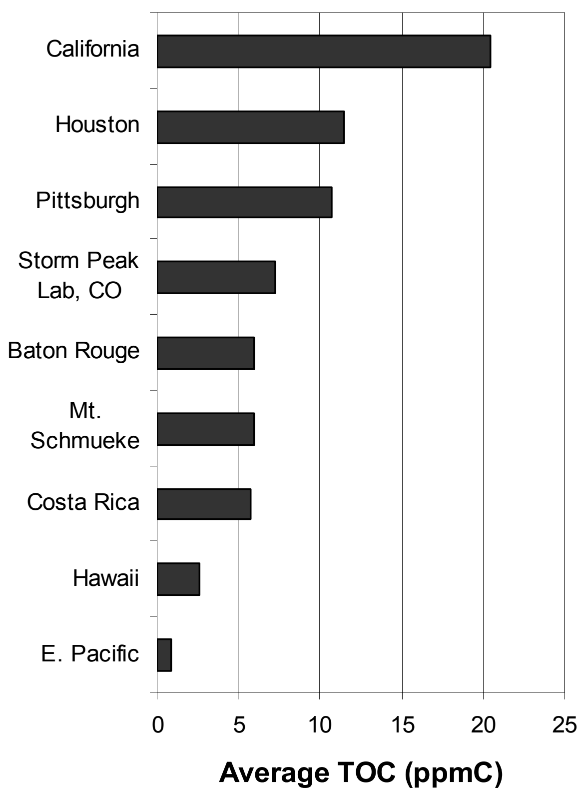

Figure 1. Average total organic carbon concentrations in cloud and fog water collected at several locations.

Studies of organic matter processing by California radiation fogs reveal that the fogs play an important role in removing organic matter from the atmosphere. Eight fog episodes in central California during winter 2000/2001, ranging in duration from 2 to 9 hours, were observed to deposit to the ground between 66 and 952 μg C/m^2. Assuming a typical fog depth of 100 m, this translates into a typical atmospheric "cleansing" rate in the boundary layer of approximately 0.7 μg/m^3. Deposition velocities in these fog systems have typically been observed between 1 and 2 cm/s for fog-borne organic carbon, much higher than dry deposition velocities for accumulation mode aerosol particles.

A variety of efforts have been made to characterize the composition of the fog organic matter, including analyses by GC/MS, HPLC, IC, NMR, IR, and LC/MS. The most abundant species are typically low molecular weight carboxylic acids and small carbonyls and dicarbonyls. These species have been observed collectively to account for roughly 20-30% of the fog dissolved organic carbon (DOC). In California radiation fogs we have also observed significant contributions from hydroxy-carboxylic acids, carbohydrates, biological material, nitrogen and sulfur-containing organics, and a range of high molecular weight components (4). Analyses also reveal the presence of organic molecular markers associated with particles produced by various combustion processes. Comparisons of pre-fog and interstitial aerosol samples reveal differences in the relative particle scavenging efficiencies of the fog drops between organic and elemental carbon and between different types of organic carbon. In one Fresno fog episode, for example, the fog scavenging efficiency for levoglucosan (a residential wood combustion tracer) was in excess of 90%, while the scavenging efficiency for 17α,21β hopane (a vehicle exhaust marker) was only about 33%. These differences likely reflect differences in hygroscopicity between wood smoke particles and vehicle exhaust particles, but may also be influenced by differences in sizes of these particles.

Recent investigations using liquid chromatography coupled with time of flight mass spectrometry (LC/MS) are shedding new light on a variety of interesting compound types present in fog water. These analyses indicate the presence of significant quantities of high molecular weight (greater than 300 Da) organic matter, consistent with earlier

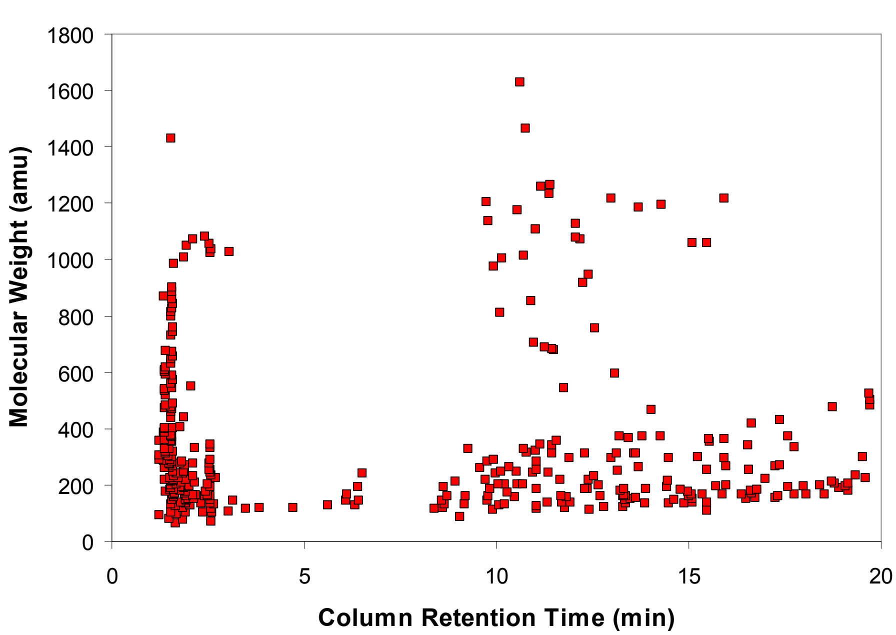

Figure 2. Masses of compounds identified in LC/MS analysis of Fresno fogwater.

measurements we have made using ultrafiltration coupled with TOC analysis (5). Figure 2 provides an overview of some of the mass features seen in LC/MS runs of Fresno fog samples. Data are presented versus chromatographic elution time (Alltech Prevail Organic Acid Column using a water/acetonitrile gradient elution).

Using the accurate mass capabilities of our Agilent TOF-LC/MS system, we are able to begin making some guesses about the molecular formulae and possible structures of fog organics. Some first guesses at molecular structures include nitrophenol (m/z = 139.026), dinitrophenol (184.011), benzoic acid, and malonic acid. Many of the compounds identified appear to be rich in nitrogen. Interestingly, there also appear to be a number of organic compounds containing both nitrogen and sulfur. Possible structures of several key molecular features identified in the fogwater are shown in Figure 3. By alternating the TOF fragmentor voltage between high and low settings we have been able to break off sulfite and sulfate groups (at high voltage), providing further evidence for the inclusion of sulfur within organic structures. Also of interest is the observation that the abundance of some of these sulfur-containing organic compounds appears to increase with time in the fog episode, possibly suggesting formation of these compounds by aqueous phase chemistry.

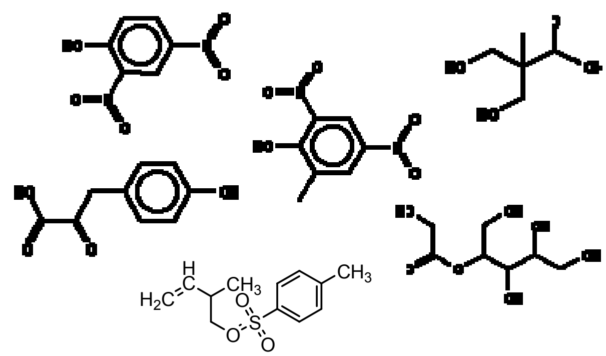

Figure 3. Possible molecular structures of several key components identified by LC/MS in Fresno fogwater.

4. BIBLIOGRAPHY

1. Demoz, B., Collett, Jr., J. L. and Daube, Jr., B. C. (1996) On the Caltech Active Strand Cloudwater Collectors. *Atmos. Res.*, **41**, 47-62.
2. Straub, D. J., Lee, T., and Collett, Jr., J. L. (2007) The chemical composition of marine stratocumulus clouds over the

eastern Pacific Ocean. *J. Geophys. Res.*, in press.
3. Herckes, P., Hannigan, M. P., Trenary, L., Lee, T. and Collett, Jr., J. L. (2002) The organic composition of radiation fogs in Davis (California). *Atmos. Res.*, **64**, 99-108.
4. Herckes, P., Leenheer, J. A., and Collett, Jr., J. L. (2007) Comprehensive characterization of atmospheric organic matter in Fresno, California fog water. *Environ. Sci. Technol.,* 41, 393-399.
5. Herckes, P., Lee, T., Trenary, L., Kang, G. U., Chang, H. and Collett, Jr., J. L. (2002) Organic matter in central California radiation fogs. *Environ. Sci. Technol.*, **36**, 4777-4782.

Acknowledgements

This work was supported by the U.S. National Science Foundation (ATM-9980540, ATM-0222607, ATM-0355291, ATM-0521643). We are grateful to several collaborators who assisted in various field experiments mentioned here including D. Straub, H. Herrmann, W. Jaeschke, B. Huebert, S. Pandis, K. Moore, H. Chang, J. Reilly, S. Youngster, J. Leenheer, and C. Krauter.

CLOUD CONDENSATION NUCLEI SIZES

James G. Hudson
and
Stephen Noble
Desert Research Institute
Reno, Nevada

1. INTRODUCTION

The physical size of cloud condensation nuclei (CCN) reveals important clues about CCN composition and origins. Among other considerations this can help distinguish natural from anthropogenic particles. The increasing importance of CCN to global climate considerations, the difficulty of making accurate CCN measurements and the sparsity of CCN measurements led Dusek et al. (2006) to investigate the possibility of deducing CCN concentrations and spectra from particle size measurements. These are much easier to obtain and are more readily available than CCN measurements.

Dusek et al. (2006) found a rather limited range of CCN sizes that suggested that indeed it may be possible to use particle size distribution measurements to estimate CCN spectra. However, Hudson (2007) pointed out that all of the measurements considered by Dusek et al. (2006) had apparently been made in rather polluted air masses. Hudson (2007) presented measurements in a variety of different air masses that showed so much variability in the sizes of CCN that it would be extremely difficult to deduce accurate CCN concentrations from particle size distribution measurements alone.

On the other hand Dusek et al. (2006) also considered the possibility that the relationship between particle size and CCN critical supersaturation (S_c) may depend on air mass. They suggested that the range of CCN sizes may still be sufficiently limited within each air mass so that CCN spectra can be accurately determined from particle size measurements. This assumes that an accurate relationship between particle size and CCN S_c can be determined in each air mass and that the air mass of the measurements can be correctly ascertained. Here we present further measurements of CCN sizes that address this controversy.

2. MEASUREMENTS

Size-S_c measurements are more easily done with the DRI instruments because they simultaneously provide the entire CCN spectrum. The mean S_c obtained from these instruments of measurements of narrow size slices from a differential mobility analyzer (DMA) produces the size-S_c data. The latest data are surface measurements in Reno, Nevada and Seoul, Korea and aircraft measurements in the 2007 PASE and ICE-L projects.

The Pacific Aerosol Sulfate Experiment (PASE) was conducted over the central Pacific near the equator directly south of Hawaii. This is as far as possible from continental or anthropogenic sources. The ICE-L project was conducted over Colorado and Wyoming. Hudson (2007) and Hudson and Da (1996) showed that maritime CCN tend to be smaller than continental or especially polluted CCN (i.e., Figs. 1 and 2). Figure 1 shows that the CCN sizes in maritime air tended to be like soluble salts such as NaCl or ammonium sulfate. On the other hand Figure 2 in continental air masses showed larger CCN sizes for the same S_c values.

3. RESULTS

Figures 3 and 4 show measurements from PASE that are largely consistent with previous marine measurements—relatively small CCN similar to Fig. 1. However at the largest sizes (above 150 μm) the S_c values tend to be higher than those of ammonium sulfate; i.e., more like the continental/polluted measurements. To compare different sizes or S_c Fitzgerald et al. (1982) introduced the hygroscopicity or solubility parameter, B, which is non-dimensional. For NaCl this is 1.23 and for ammonium sulfate it is 0.70. B is lower for less hygroscopic substances, which have to be larger to produce the same S_c values as more hygroscopic substances. B tends to be higher in maritime air masses and lower in more polluted air masses.

Figure 5 shows B for the data in Fig. 3. For most of the PASE measurements B, displayed this same inverse function of particle size. Volatility measurements during PASE indicated that the vast majority of CCN behaved like ammonium sulfate. The volatility measurements showed that very few CCN could be NaCl. The B values of the larger CCN suggested that they may have been internal mixtures of ammonium sulfate and insoluble or less soluble materials such as organics. Reanalysis of Hudson (2007) often showed somewhat the same tendency in other maritime air (Fig. 6). Figure 7 shows that B often tends oppositely in continental air where B often increased with CCN size. Figures 8-15 show further examples from PASE of the tendency for B to decrease with particle size. However, the relationship of B with particle size showed considerable variability; i.e., different slopes.

Figures 16 and 17 display one of the data points displayed in Figs. 4 and 10 respectively. Figures 16 and 17 display both the spectra that produced one of the data points in Figs. 4 and 10 and one of the calibration points used to produce the calibration curve that relates the raw data channels to S_c. The ambient spectra is plotted in green and the calibration spectra is plotted in red. Since these are for the same DMA sizes they clearly show the differences in behavior within the cloud chamber between the ammonium sulfate particles used for the calibrations and ambient particles. The ambient particles grew smaller droplets that were detected in lower voltage (droplet size) channels. This shows specifically how these ambient particles were not the same as ammonium sulfate particles; they have lower B values.

Figure 18 shows a further complication for CCN size-S_c measurements that can only be revealed with spectral instruments such as the DRI CCN spectrometers. This is a bimodal spectrum that was produced here by the exhaust from a diesel generator superimposed upon the ambient aerosol. The right hand mode is the ambient maritime distribution similar to Figs. 16 and 17 whereas the left hand mode was caused by particles from the diesel generator. Although this was a somewhat contrived situation it probably represents a naturally mixed air mass that could occur when polluted air advects over the ocean. This shows the inadequacy of using only the mean S_c of a measurement. Figures 19 and 20 display the differences between the single mode and the bimodal distribution.

Figure 21 exhibits the complication of the width of the spectra. Panel A displays broad spectra that are typically observed in polluted air compared with the narrower spectra often observed in maritime air masses. This also shows the inadequacy of mean S_c alone to describe the relationship of size with S_c.

Figure 22 shows that B is not always related to the total particle concentration (CN), which is often used to characterize whether an air mass is clean (maritime) or polluted. This makes it more difficult to know which size-S_c relationship to use in order to deduce CCN from particle size measurements.

4. CONCLUSIONS

The results presented exhibit some of the difficulties associated with efforts to deduce CCN concentrations from particle size measurements.

Acknowledgements. This work was supported by NSF grants ATM-0342618, ATM-0313899, and NSF subaward 235435 from Drexel CCN in PASE.

References:

Dusek, U., G.P. Frank, L. Hildebrandt, J. Curtius, J. Schneider, S. Walter, D. Chand, F. Drewnick, S. Hings, D. Jung, S. Borrmann, M.O. Andreae (2006), Size matters more than chemistry for cloud-nucleating ability of aerosol particles, *Science, 312*, 1375-1378.

Fitzgerald, J.W., W.A. Hoppel, and M.A. Vietti (1982), The size and scattering coefficient of urban aerosol particles at Washington, DC as a function of relative humidity, *J. Atmos. Sci.*, *39,* 1838-1852.

Hudson, J.G., 2007: Variability of the relationship between particle size and cloud-nucleating ability. *Geophys. Res. Let*., **34**, L08801, doi:10.1029/2006GL028850.

Hudson, J.G. and X. Da, 1996: Volatility and size of cloud condensation nuclei. *J. Geophys. Res.,* ***101***, 4435-4442.

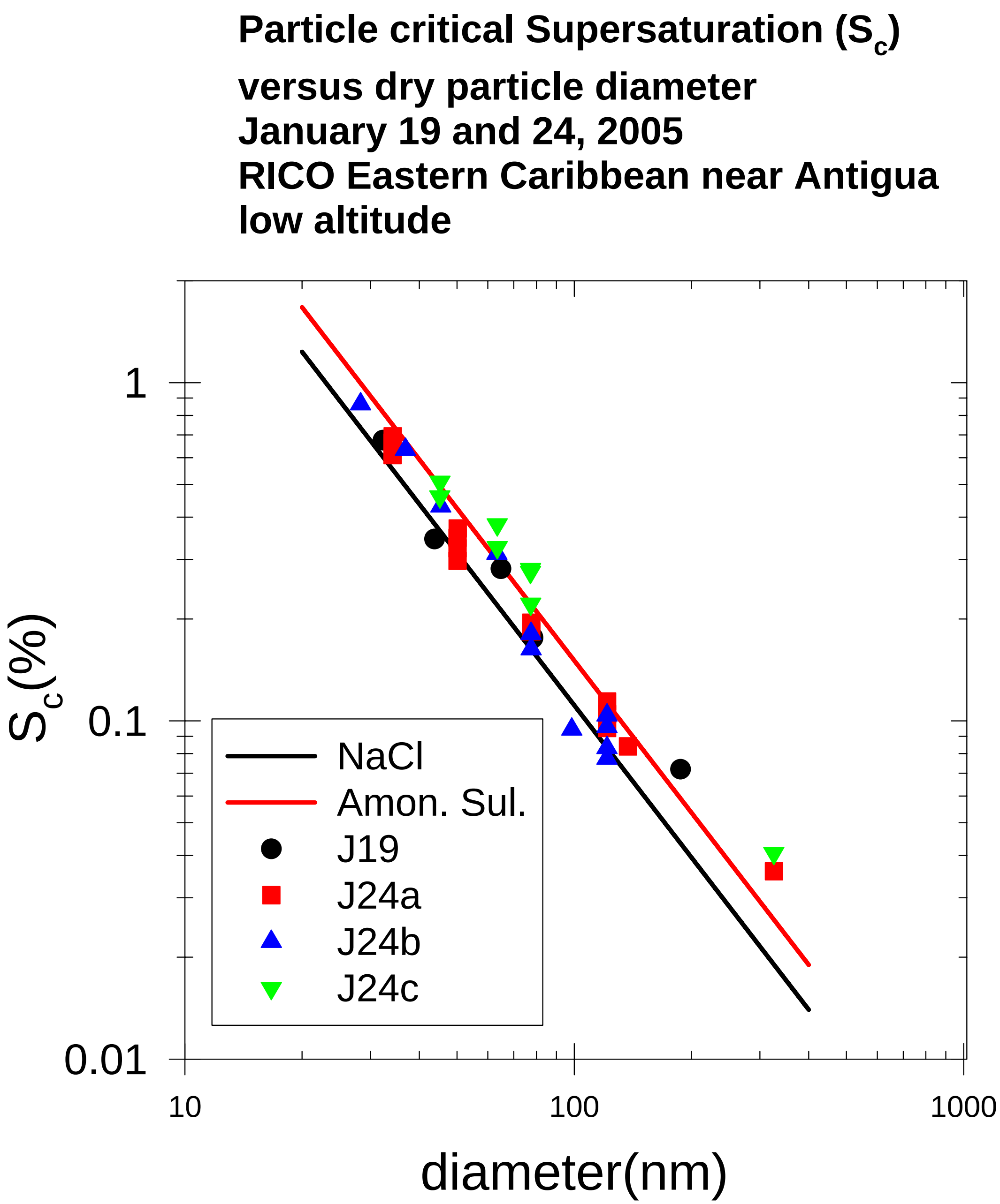

Figure 1. Critical supersaturaiton (S_c) versus dry particle size for Several measurements in clean maritime air masses (from Hudson [2007]).

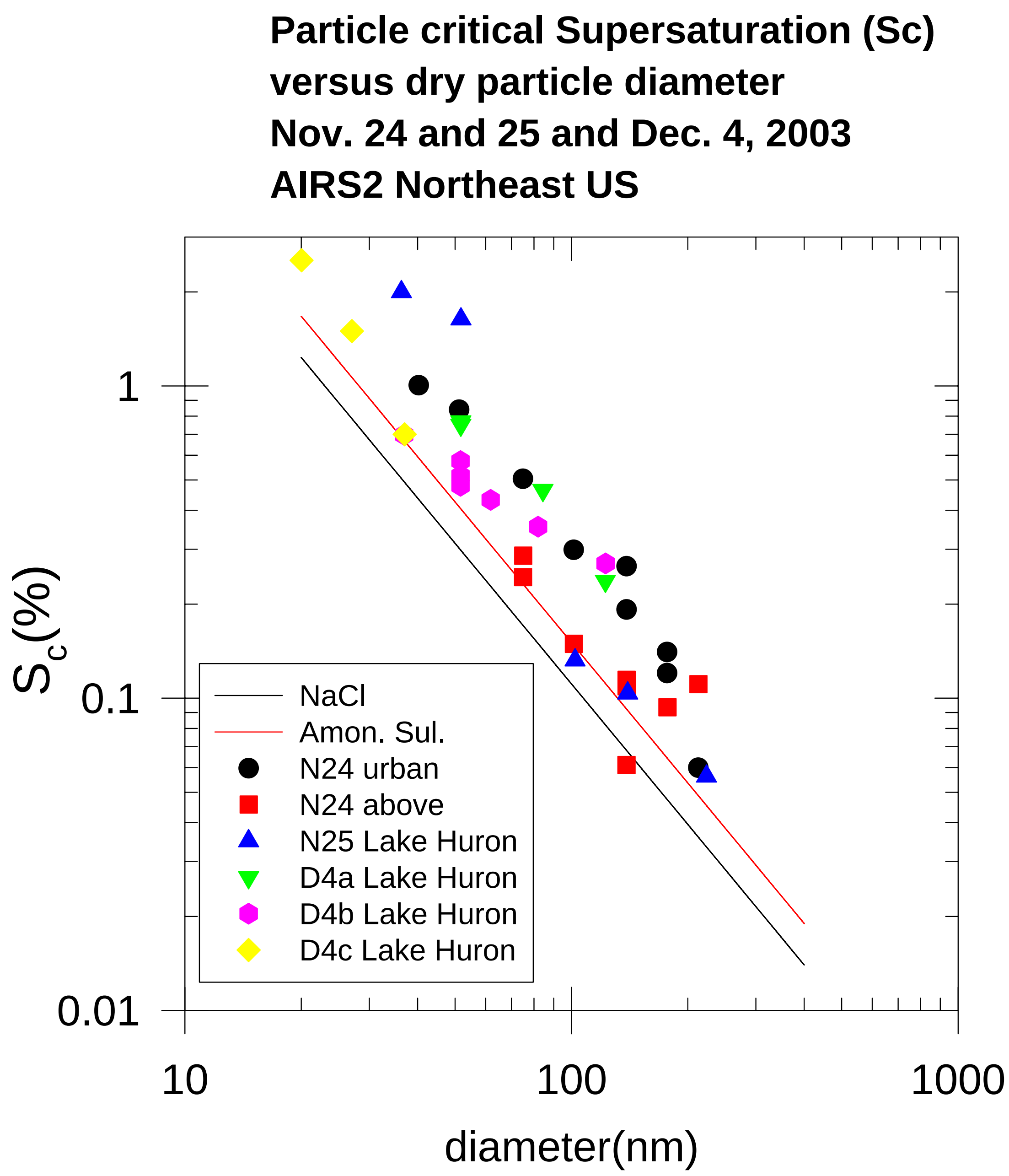

Figure 2. As Fig. 1 but for continental air masses (from Hudson [2007]).

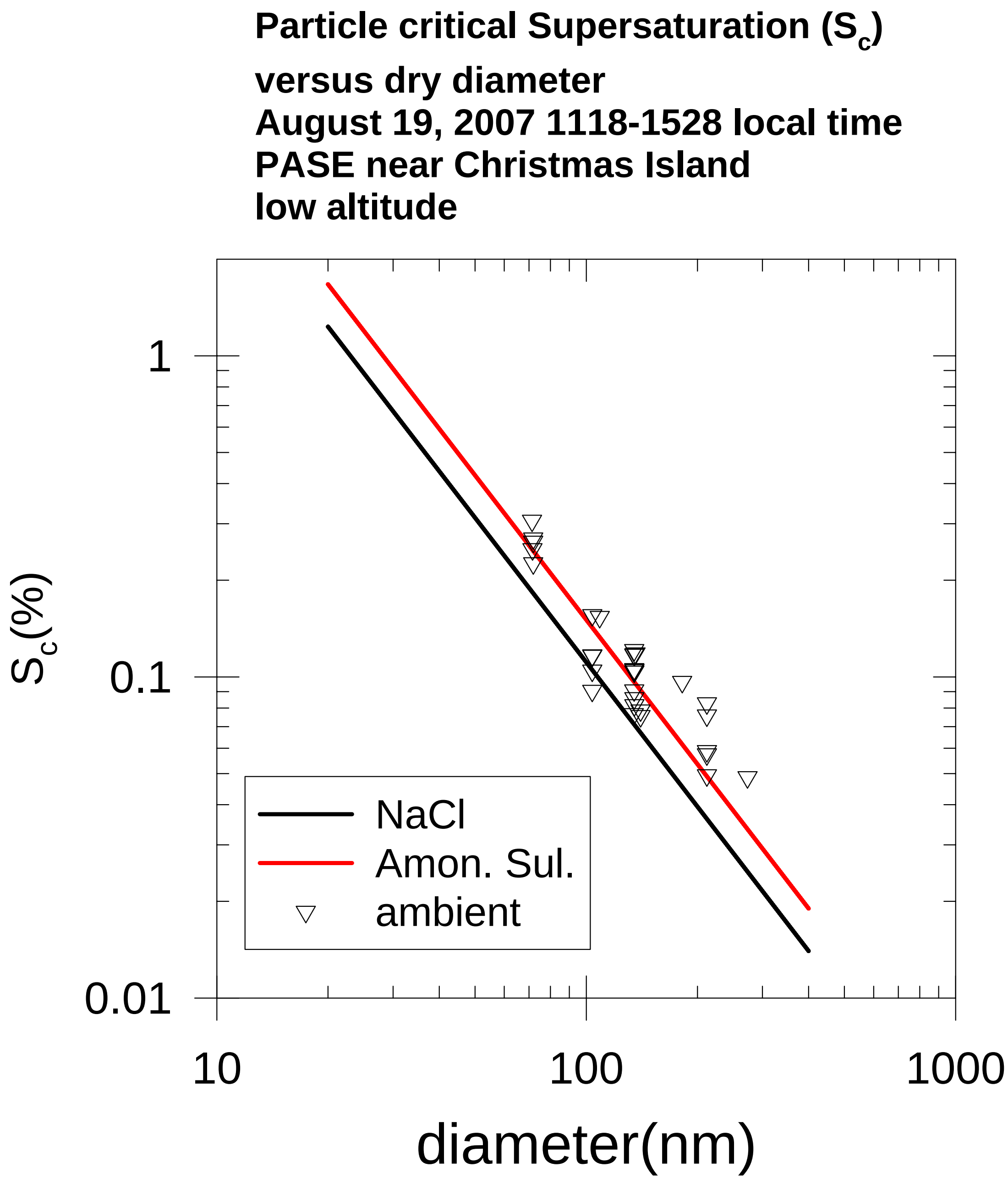

Figure 3. As Fig. 1 but for the recent PASE project.

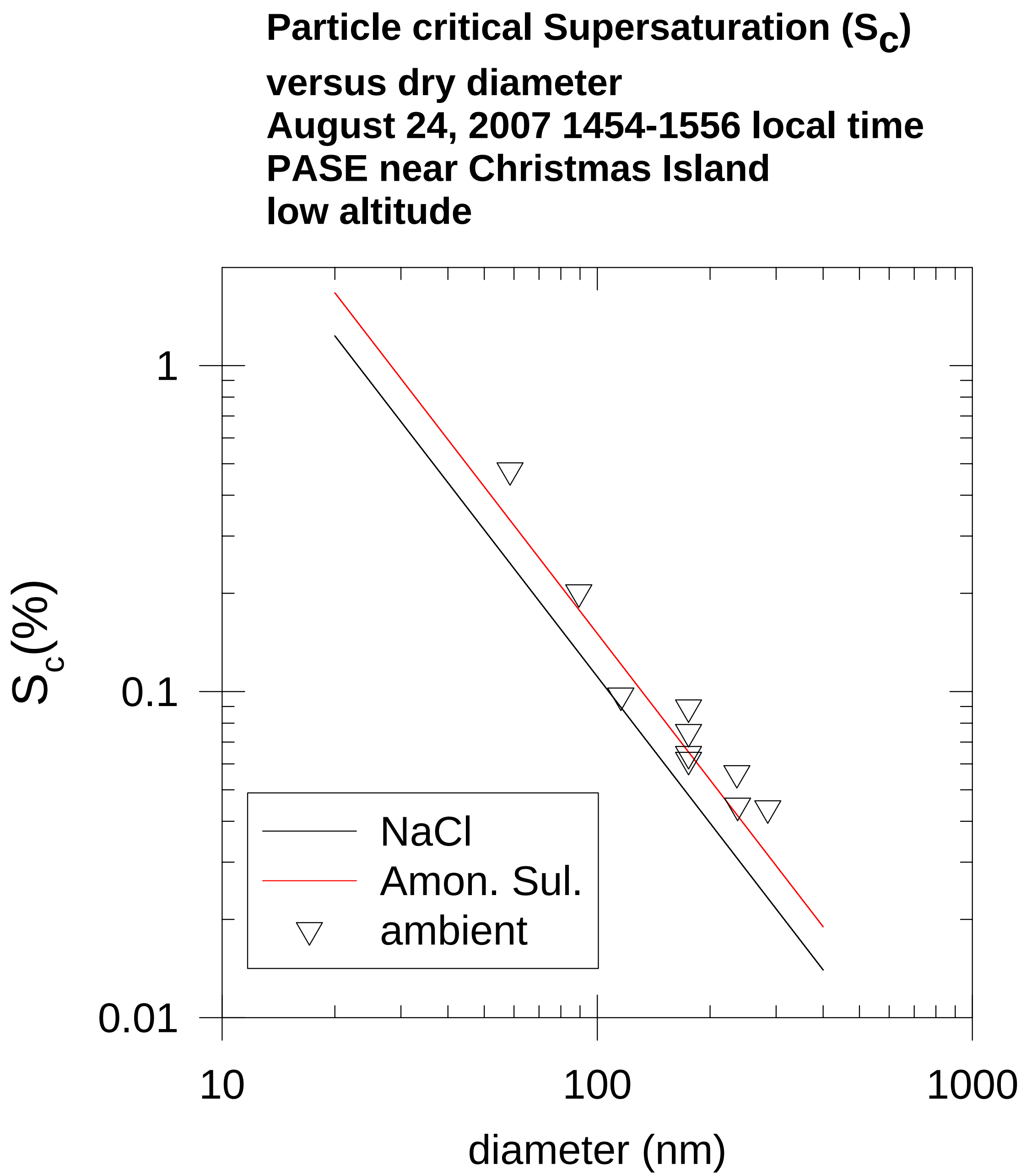

Figure 4. As Fig. 3 for a different flight.

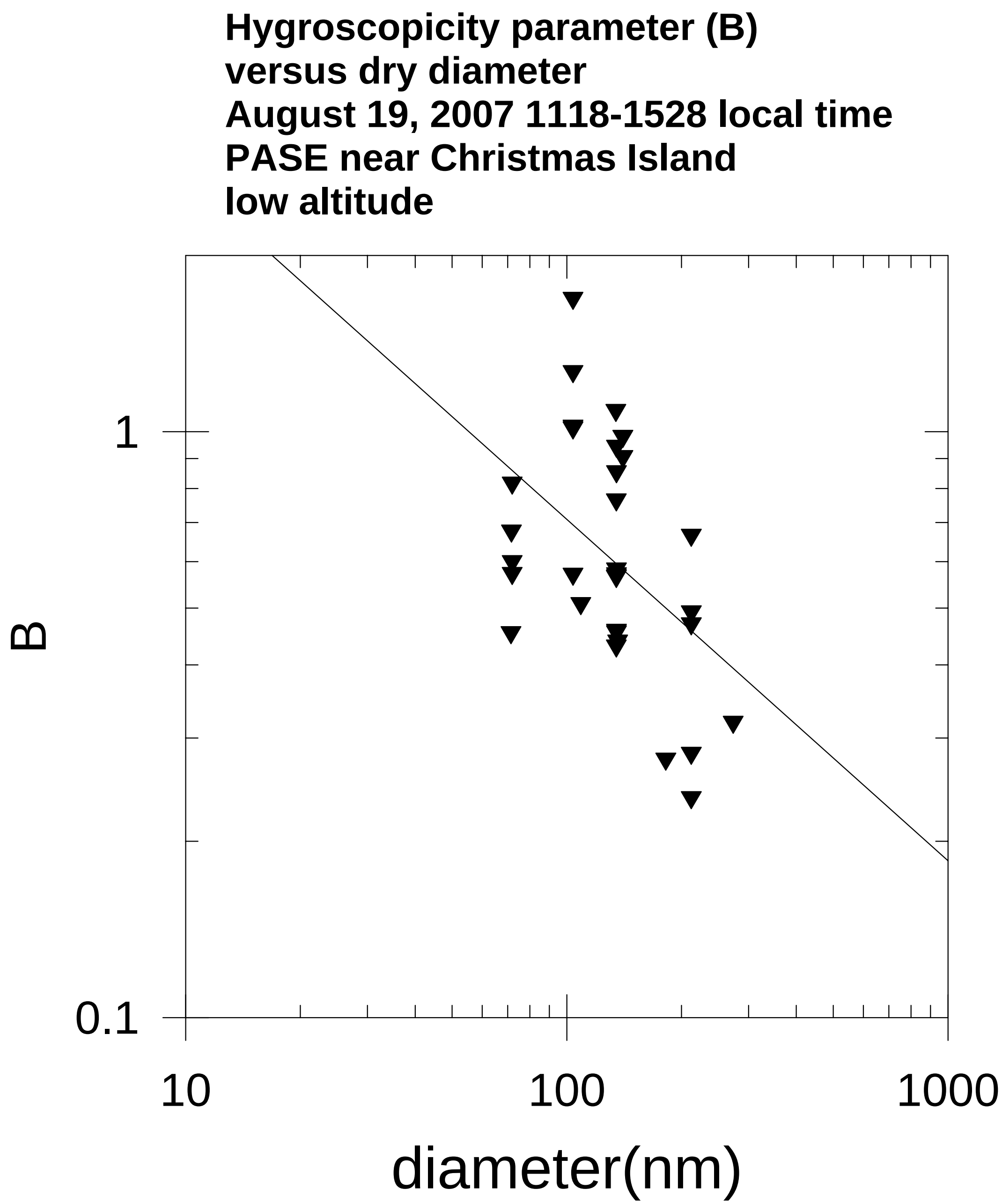

Figure 5. Hygroscopicity parameter (B) versus dry particle size for the data displayed in Fig. 3.

Solubility parameter (B)
versus dry particle diameter
January 19 and 24, 2005
RICO Eastern Caribbean near Antigua
low altitude

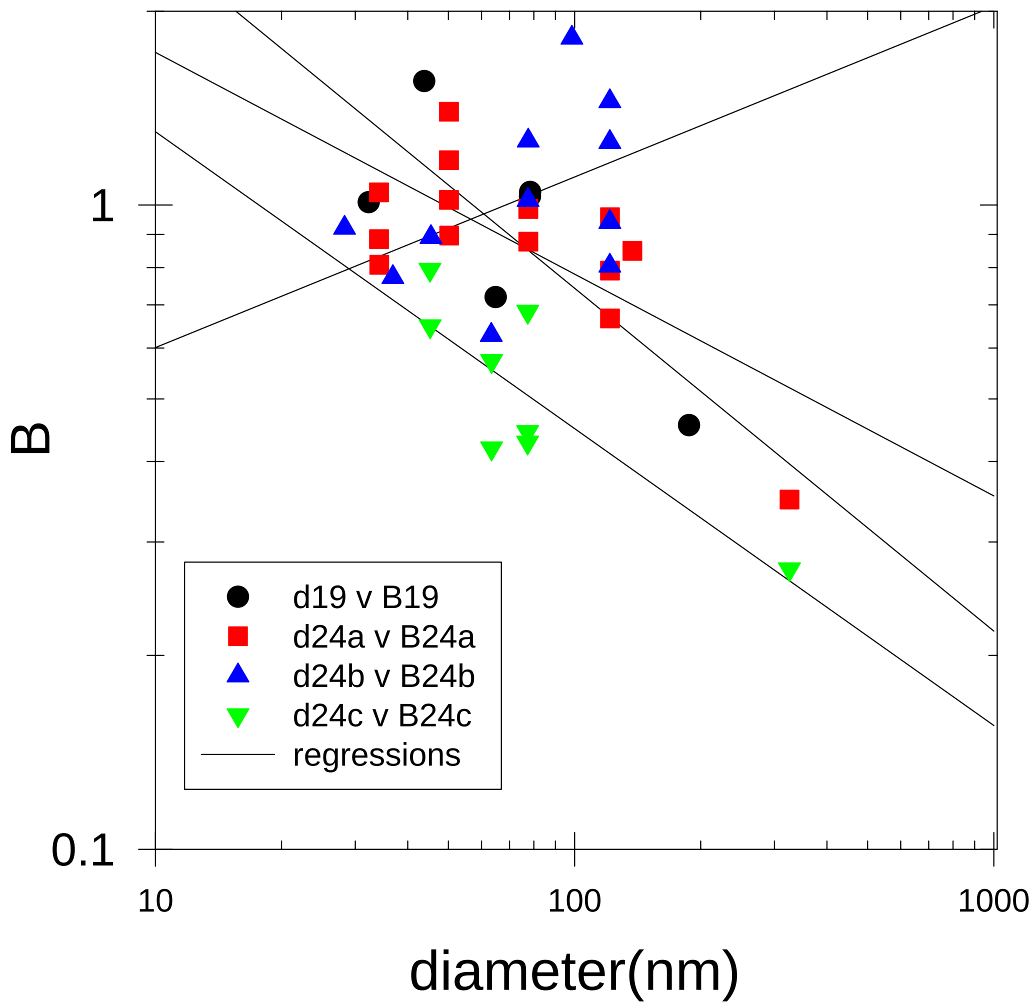

D19
$y = 0.94 - 0.53x$
$r^2 = 0.59$

D24a
$y = 0.58 - 0.34x$
$r^2 = 0.51$

D24b
$y = -0.49 + 0.26x$
$r^2 = 0.20$

D24c
$y = 0.57 - 0.46x$
$r^2 = 0.69$

Figure 6. As Fig. 5 but for the data displayed in Fig. 1. Also shown are the linear regressions.

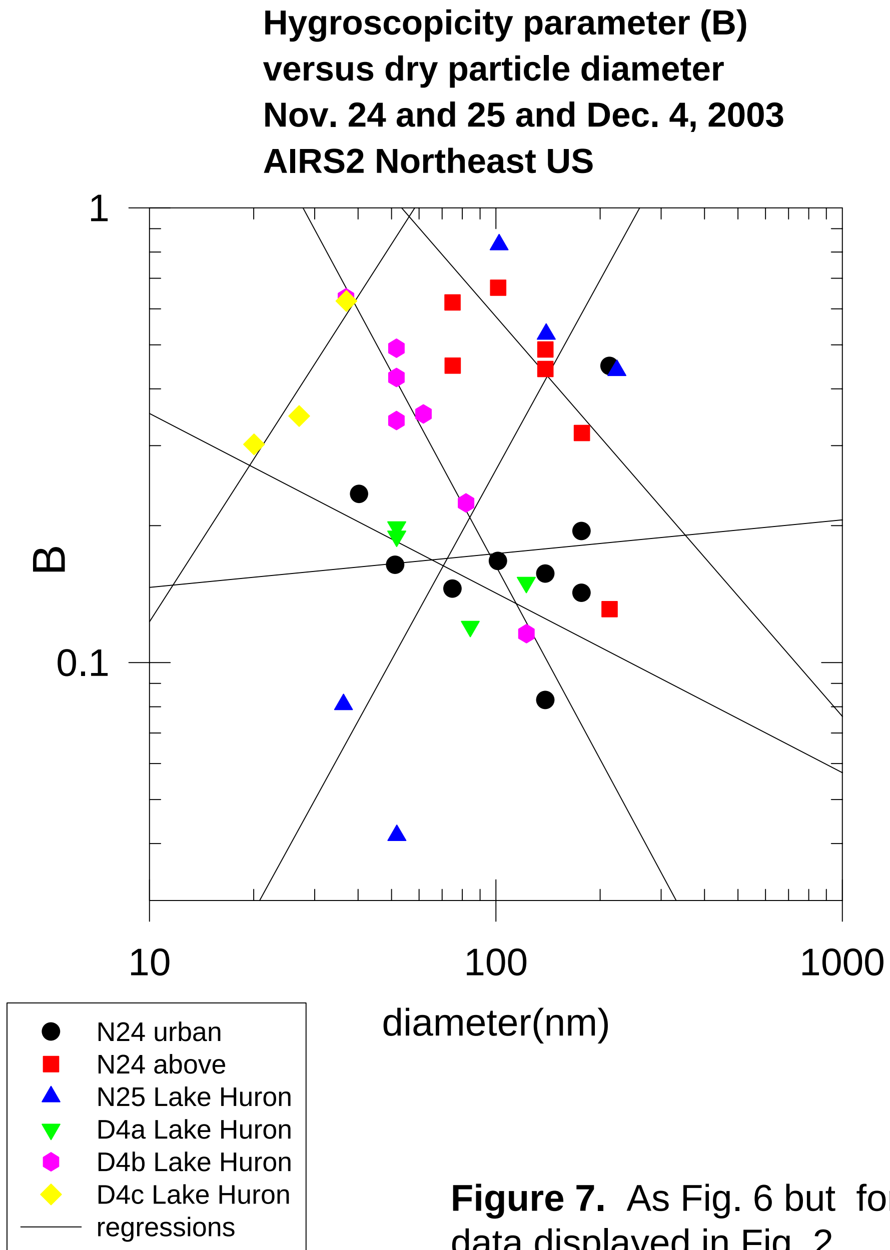

N24 urban
$y = -0.91 + 0.07x$
$r^2 = 0.009$

N24 above
$y = 1.52 - 0.88x$
$r^2 = 0.23$

N25 Lake Huron
$y = -3.35 + 1.39x$
$r^2 = 0.62$

D4a Lake Huron
$y = -0.057 - 0.40x$
$r^2 = 0.51$

D4b Lake Huron
$y = 2.04 - 1.41x$
$r^2 = 0.96$

D4c Lake Huron
$y = -2.10 + 1.19x$
$r^2 = 0.90$

Figure 7. As Fig. 6 but for the data displayed in Fig. 2.

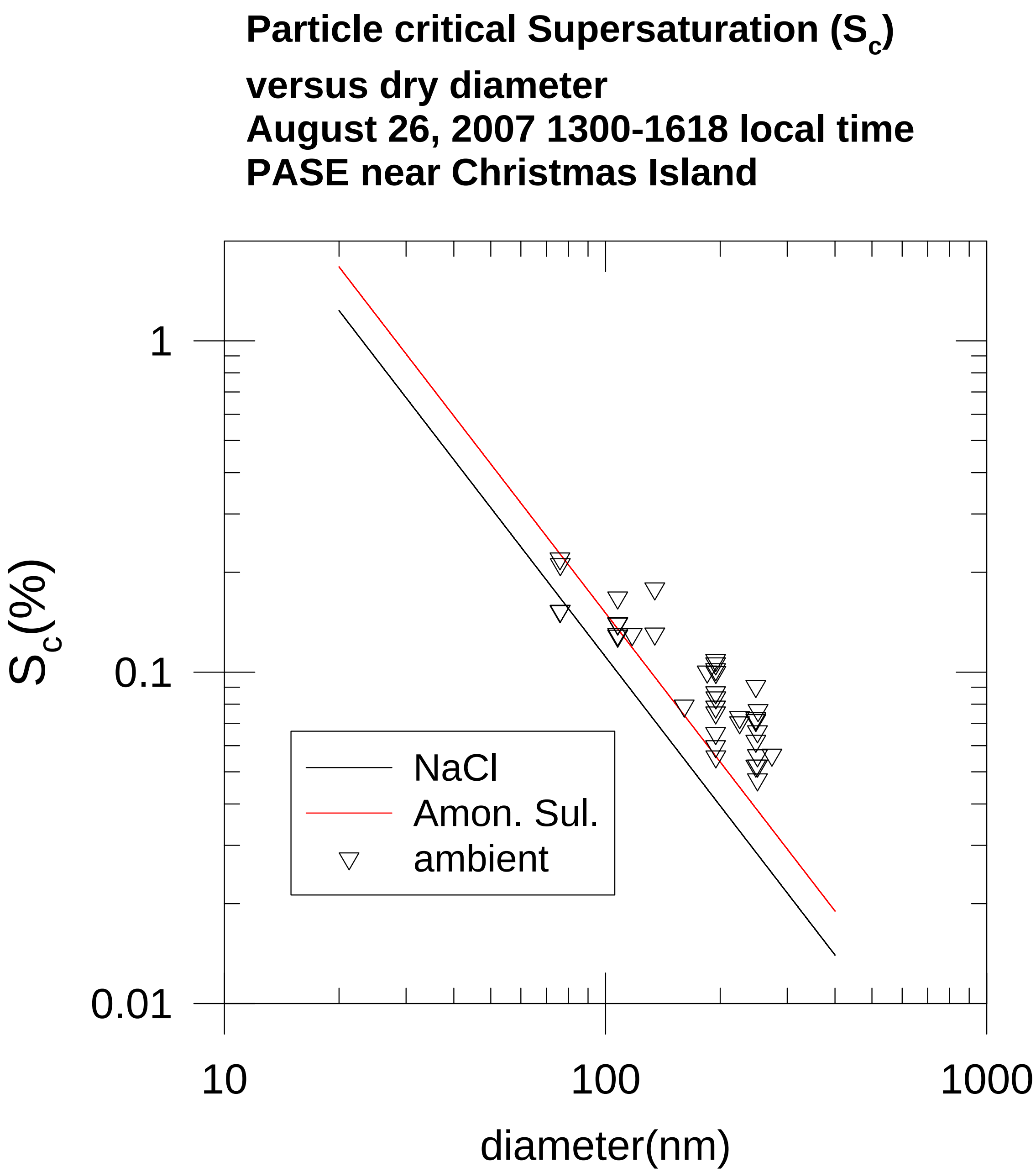

Figure 8. As Fig. 3 for a different flight.

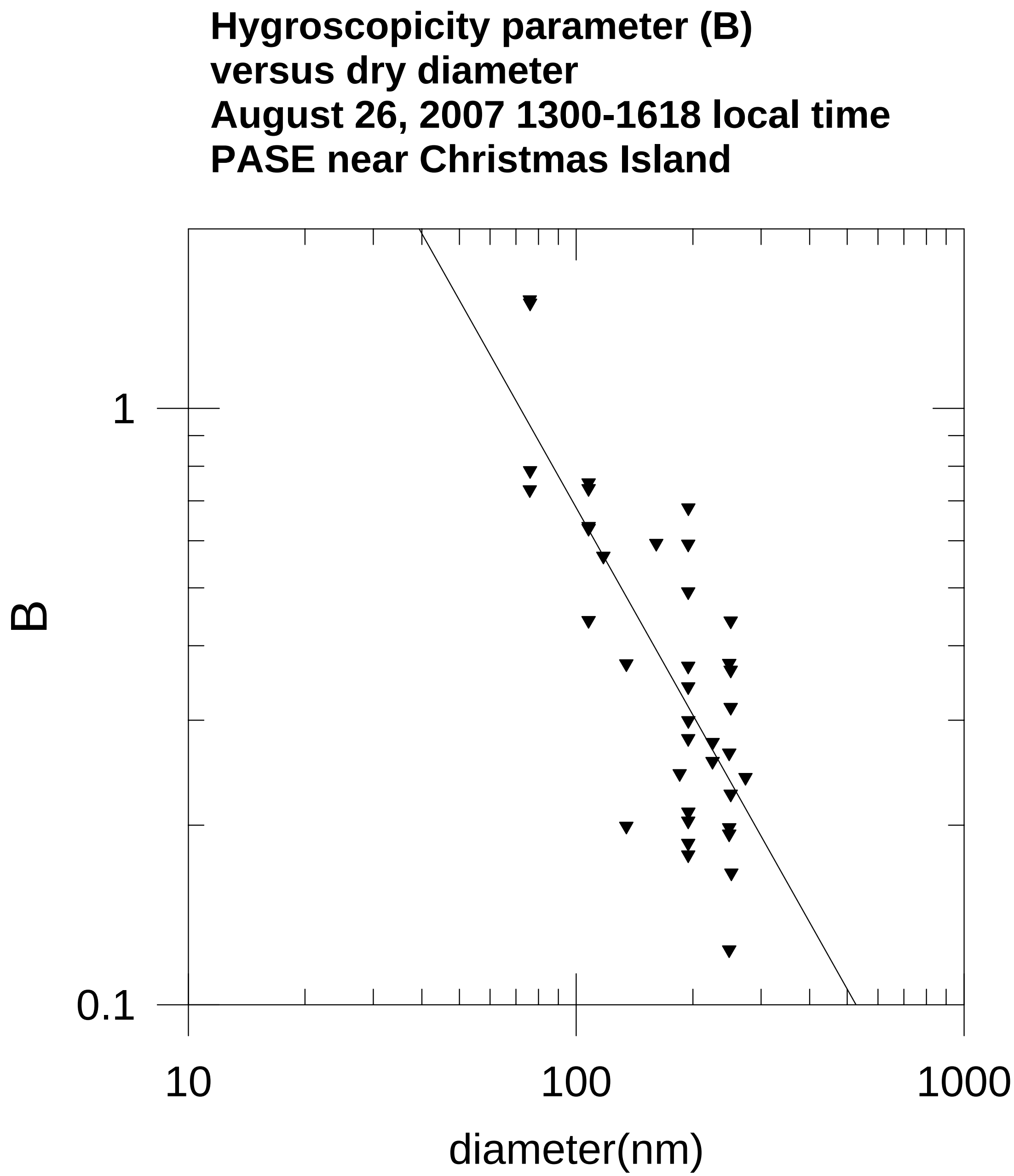

Figure 9. As Fig. 5 but for data displayed in Fig. 8.

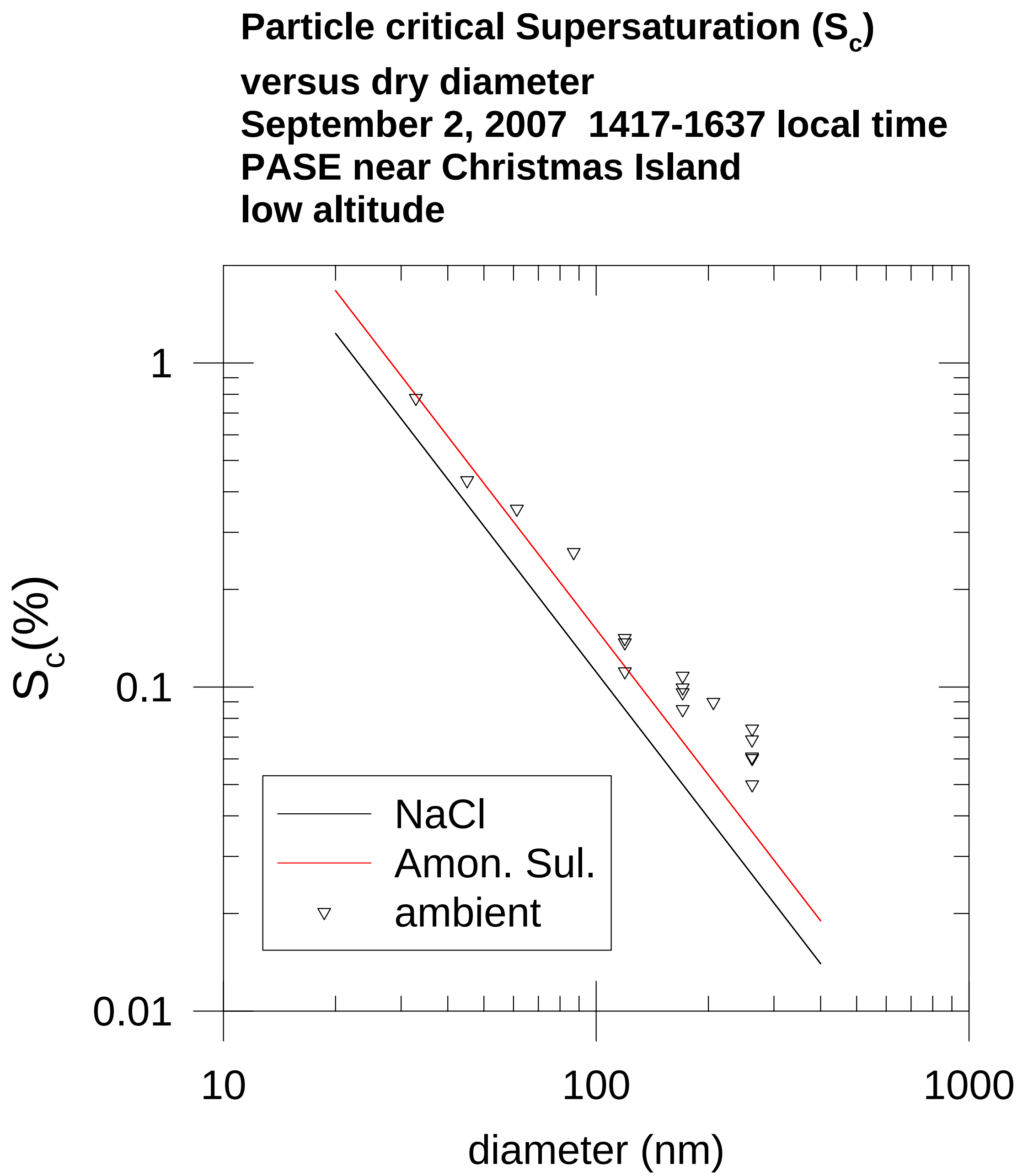

Figure 10. As Fig. 3 for a different flight.

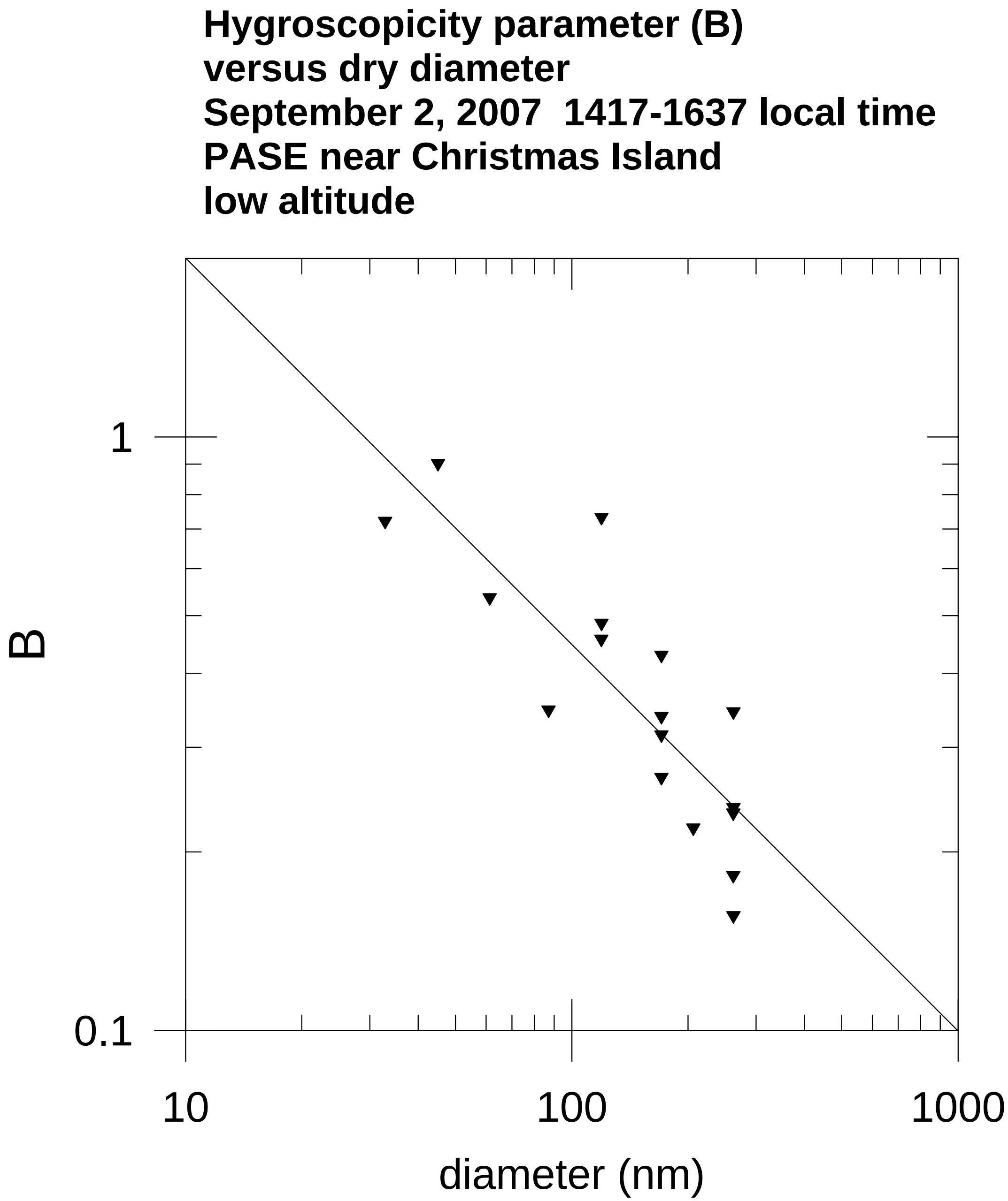

Figure 11. As Fig. 5 but for data displayed in Fig. 10.

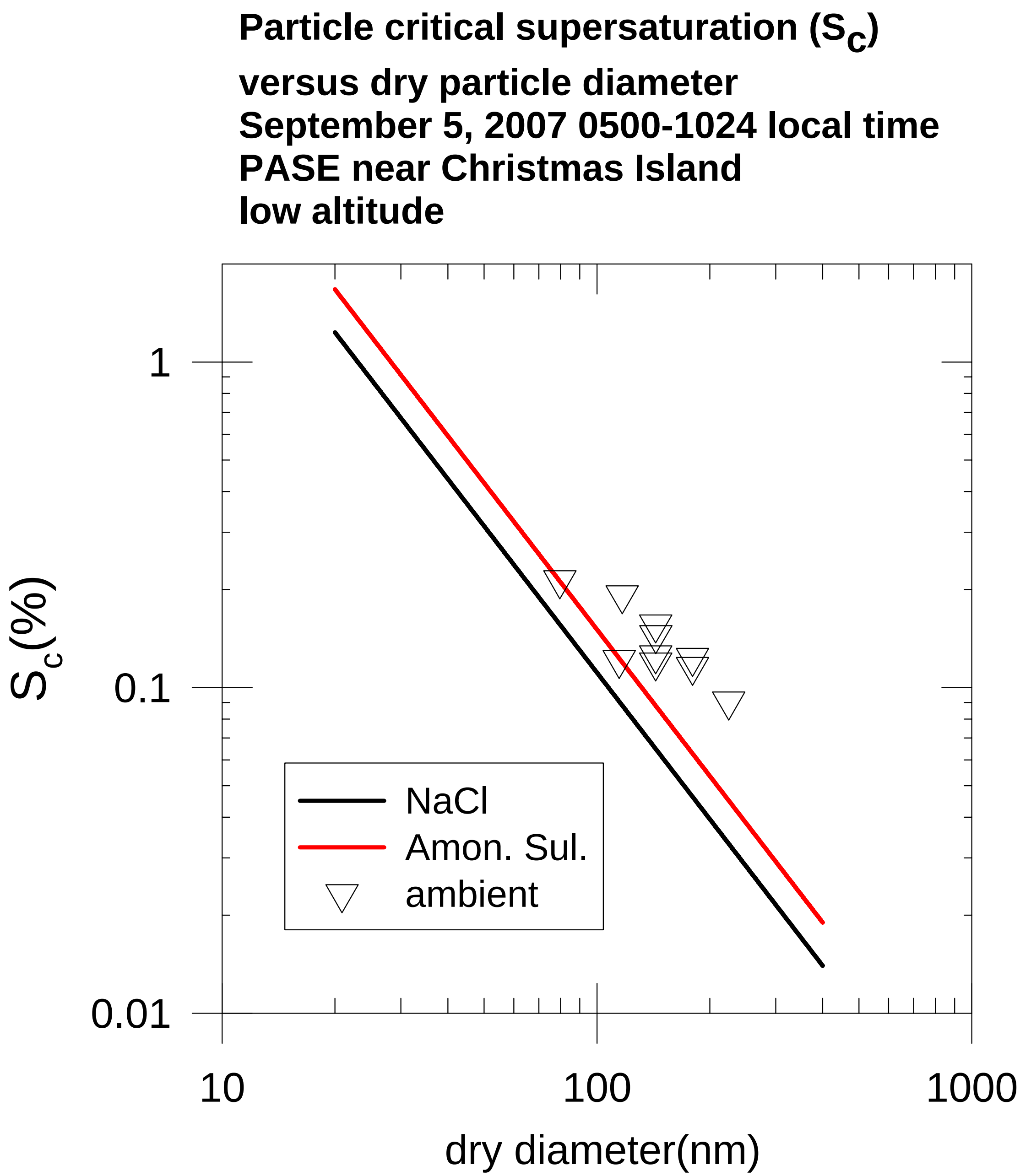

Figure 12. As Fig. 3 for a different flight.

Solubility parameter (B)
versus dry particle diameter
September 5, 2007 0500-1024 local time
PASE near Christmas Island
low altitude

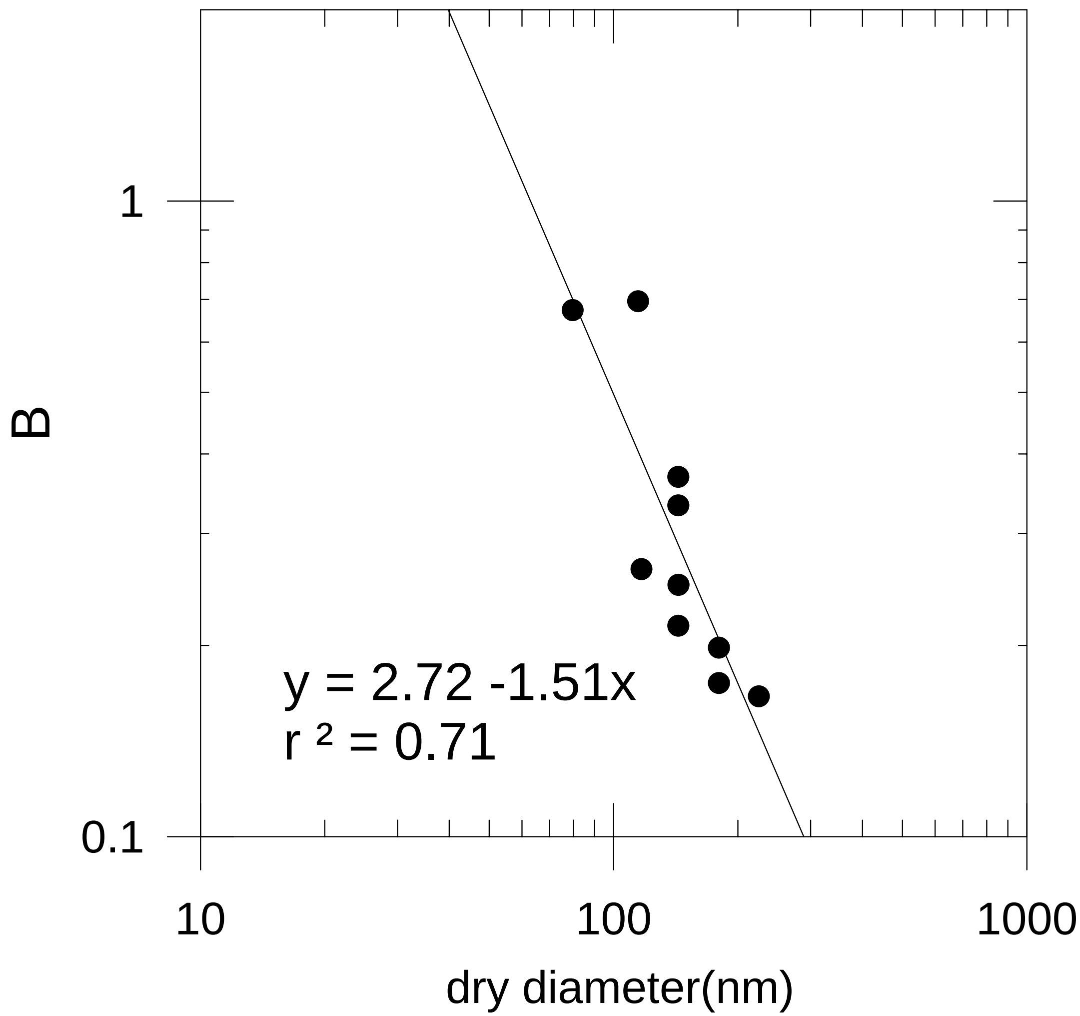

Figure 13. As Fig. 5 but for data displayed in Fig. 12.

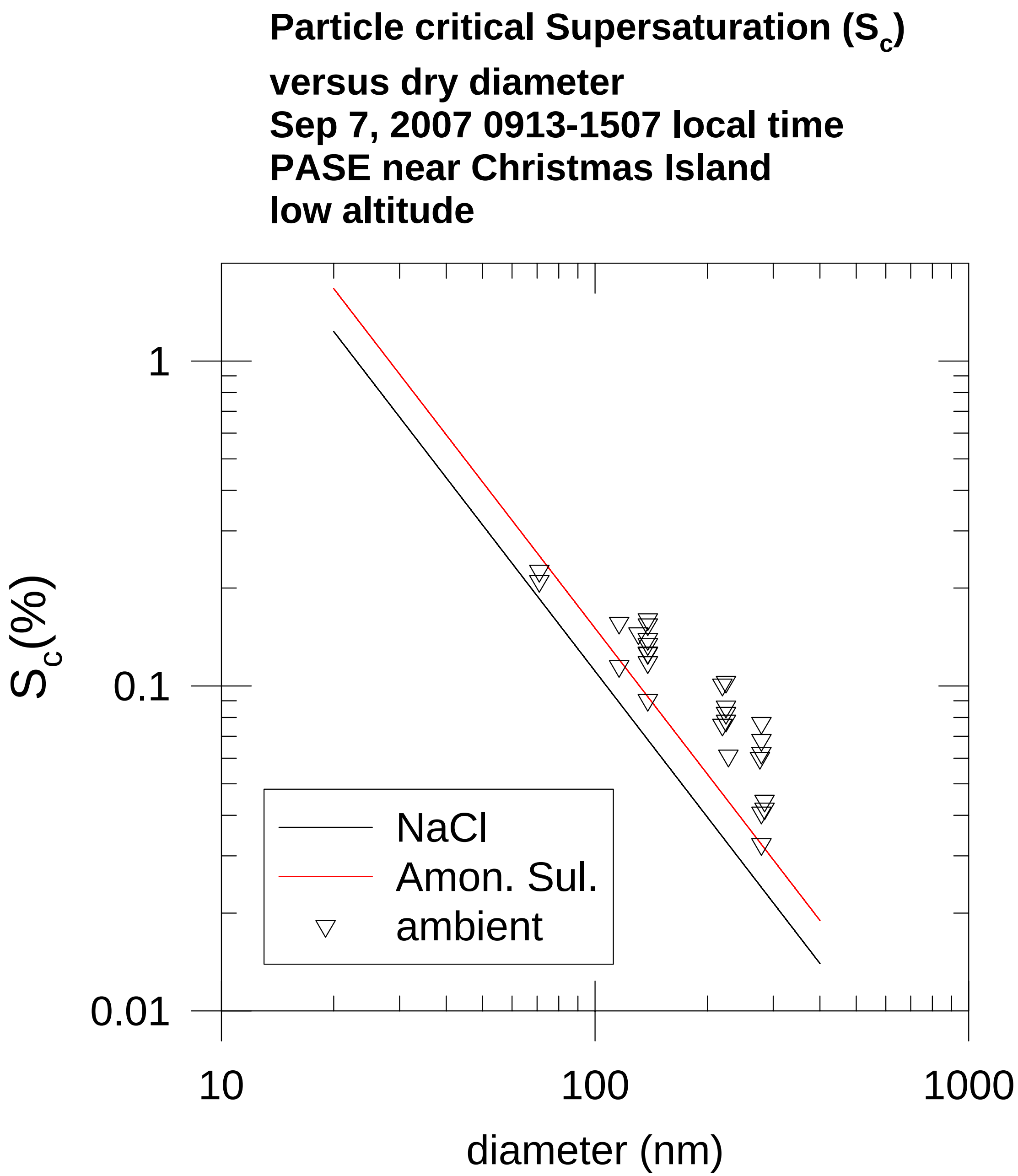

Figure 14. As Fig. 3 for a different flight.

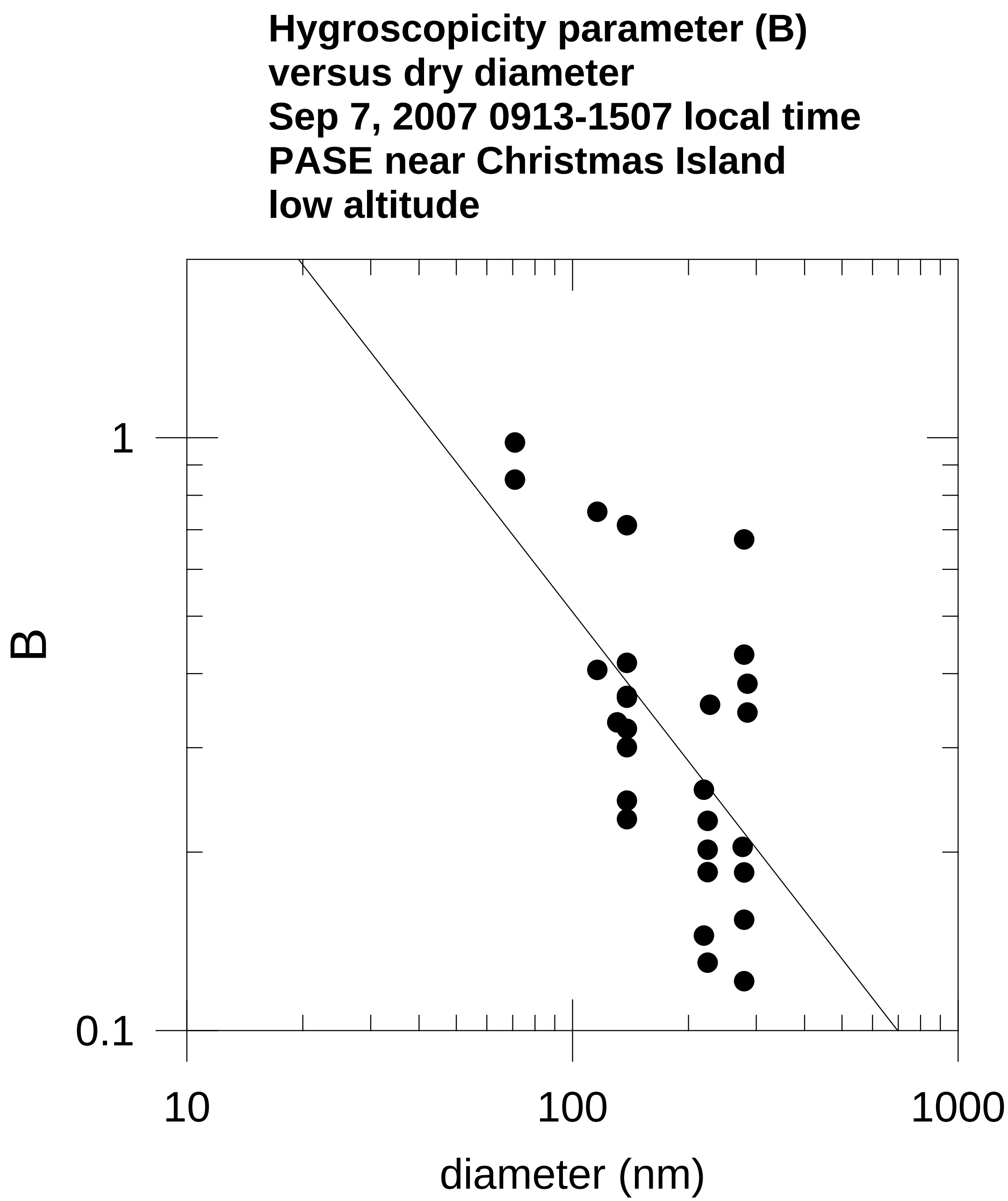

Figure 15. As Fig. 5 but for data displayed in Fig. 14.

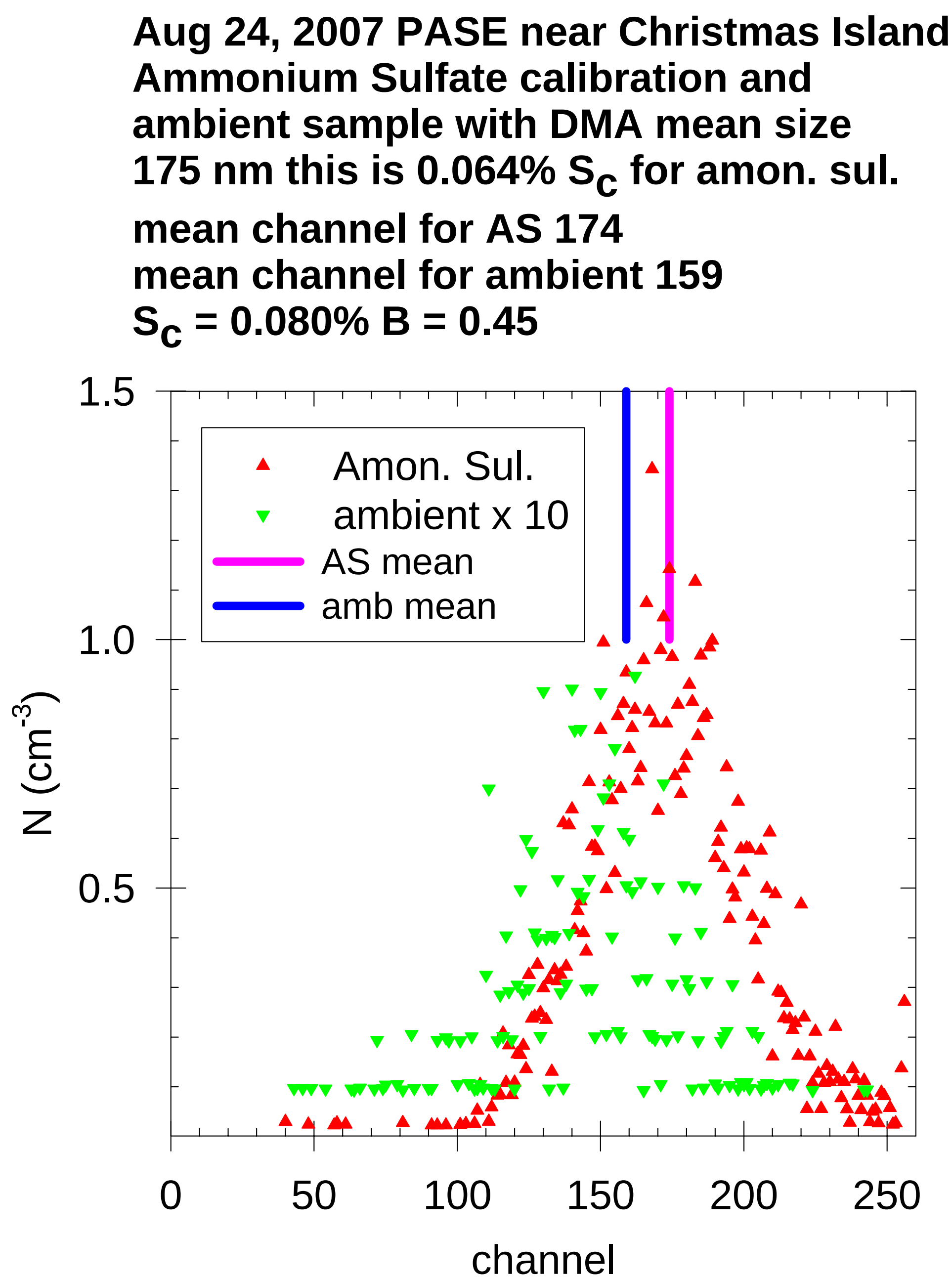

Figure 16. Plots of cloud chamber number concentrations versus channel number, which is related to droplet size, for ambient aerosol and ammonium sulfate calibration particles of the same sizes from the DMA.

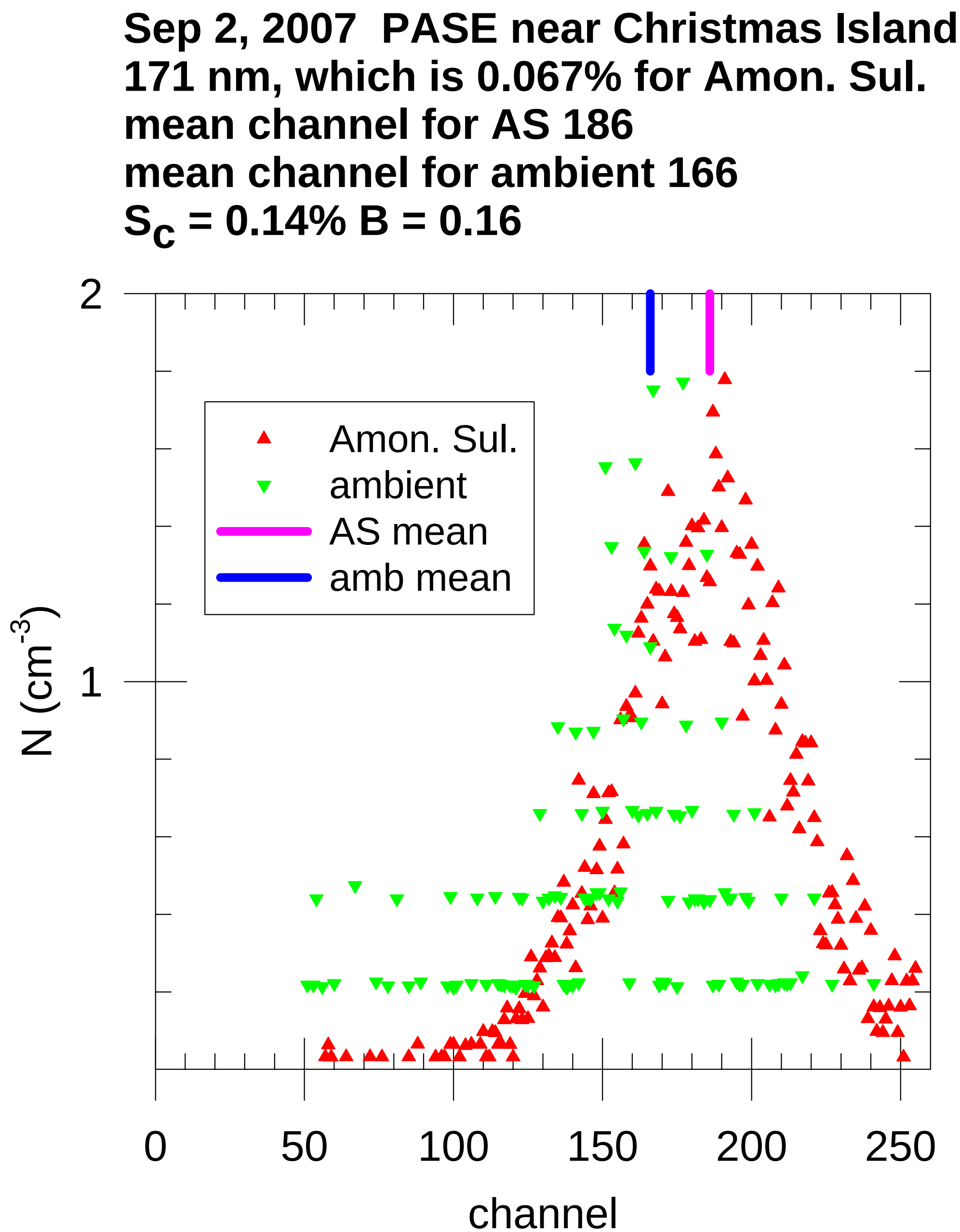

Figure 17. As Fig. 16 but for a different flight.

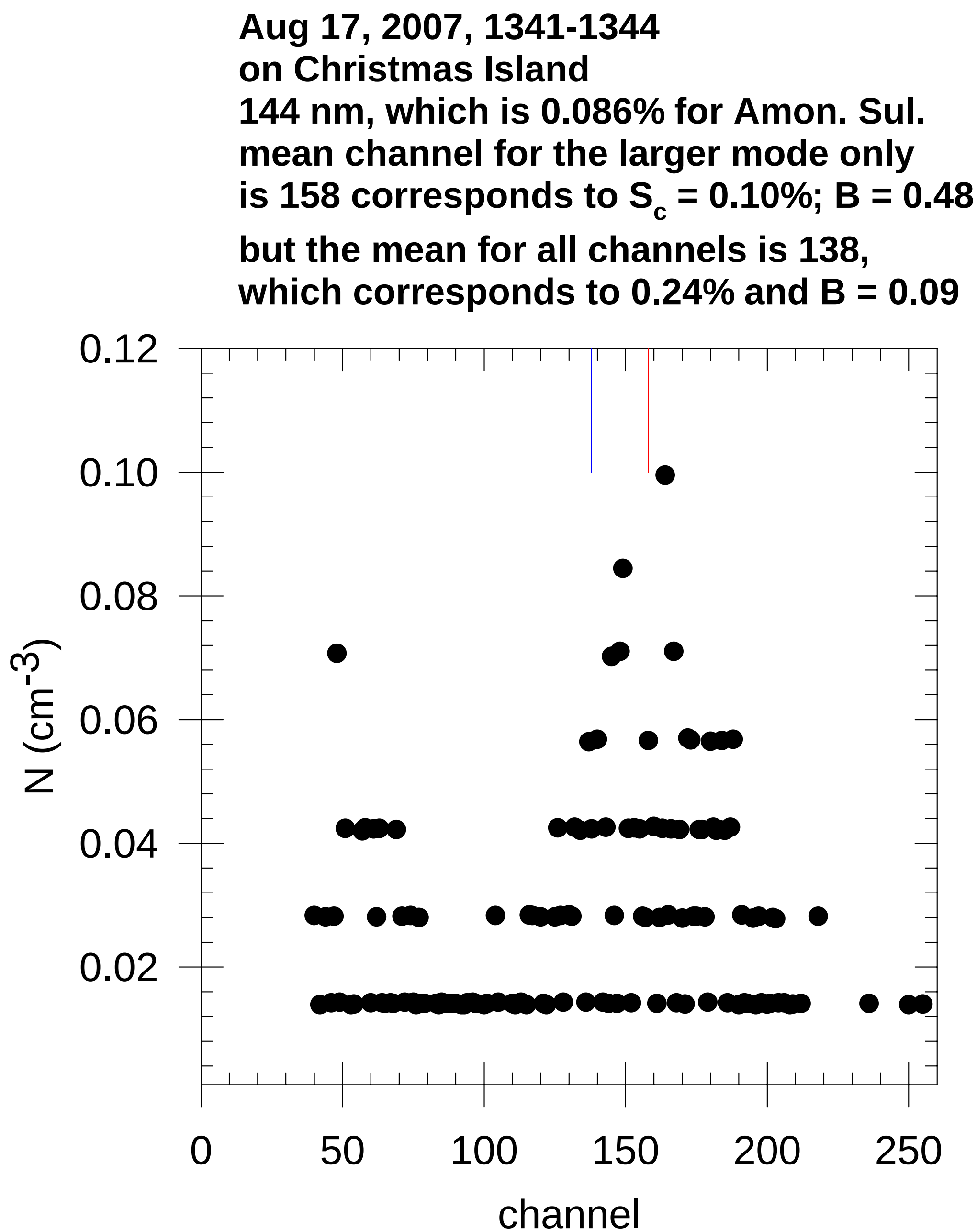

Figure 18. As Fig. 16 but for surface measurerments of a diesel plume and ambient aerosol showing a bimodal distribution.

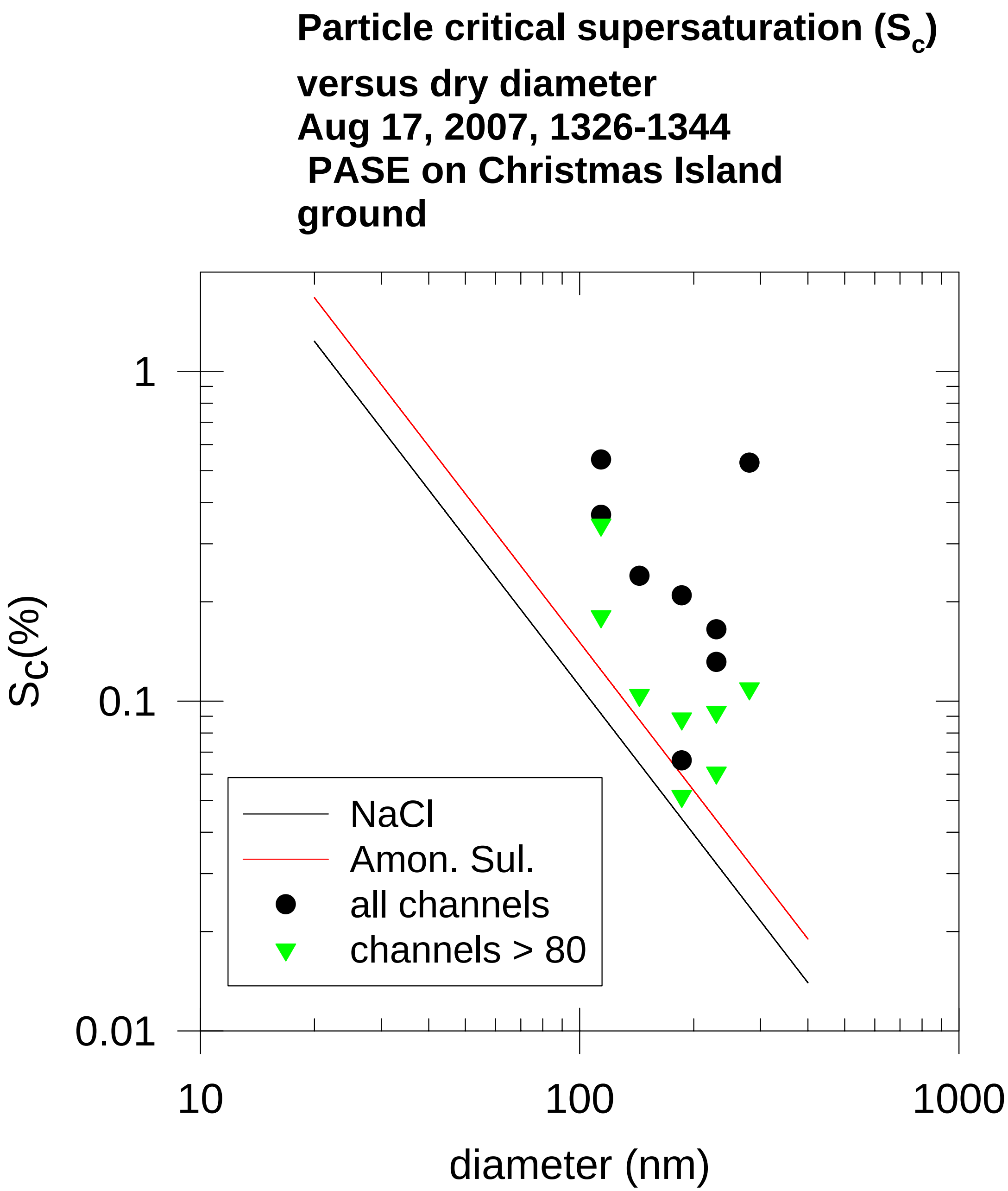

Figure 19. As Fig. 3 for the situation noted in Fig. 18. Considering different concentrations for different threshold channels, which result in different S_c.

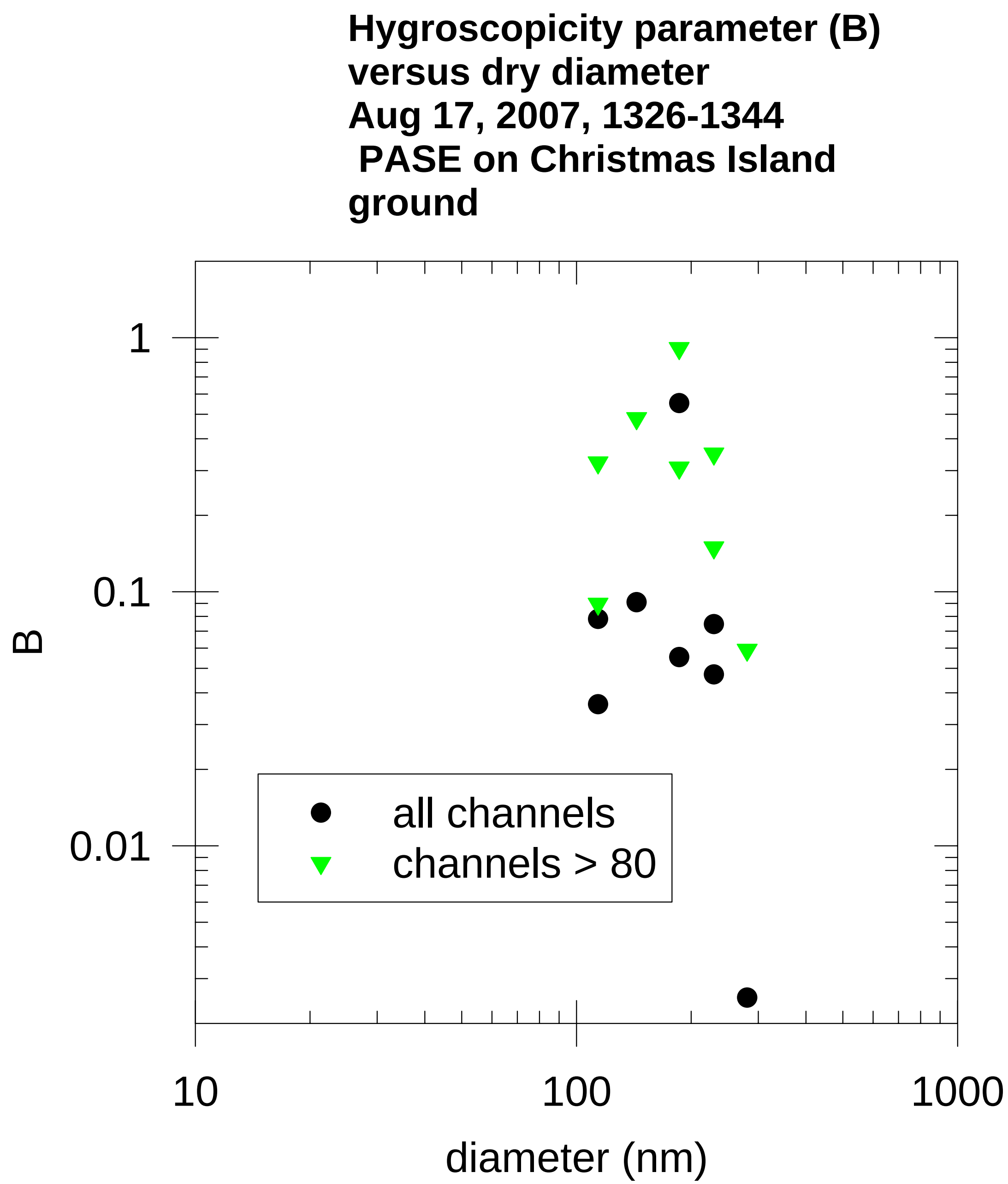

Figure 20. As Fig. 5 but for data displayed in Fig. 19.

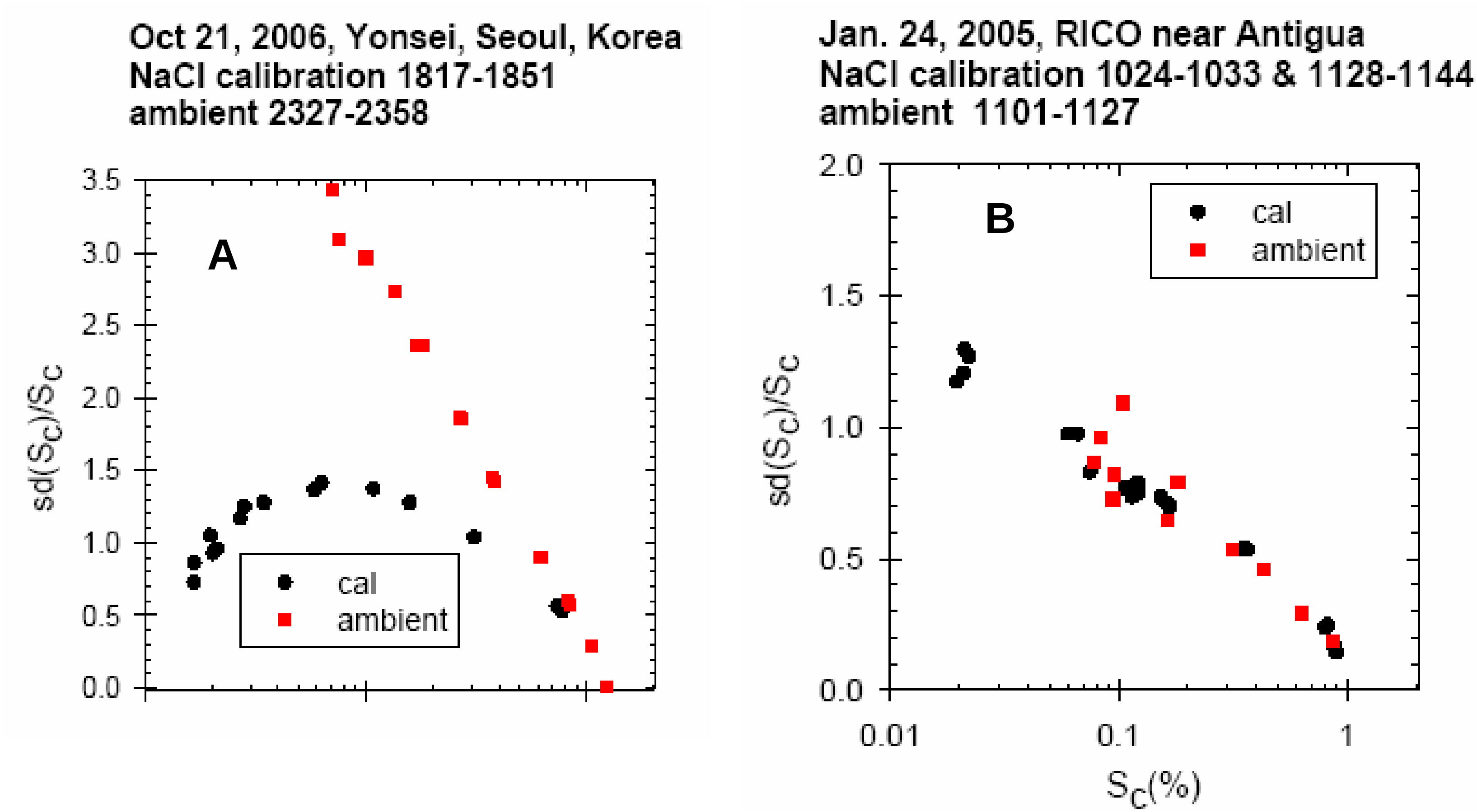

Figure 21. Relative variability (standard deviation; sd) of S_c for dirty air (panel A) and clean air (panel B). The ambient is much wider than the calibration in panel A and similar to the narrow calibration aerosol in panel B. This suggests the inadequacy of only using the mean values of S_c to express solubility (B).

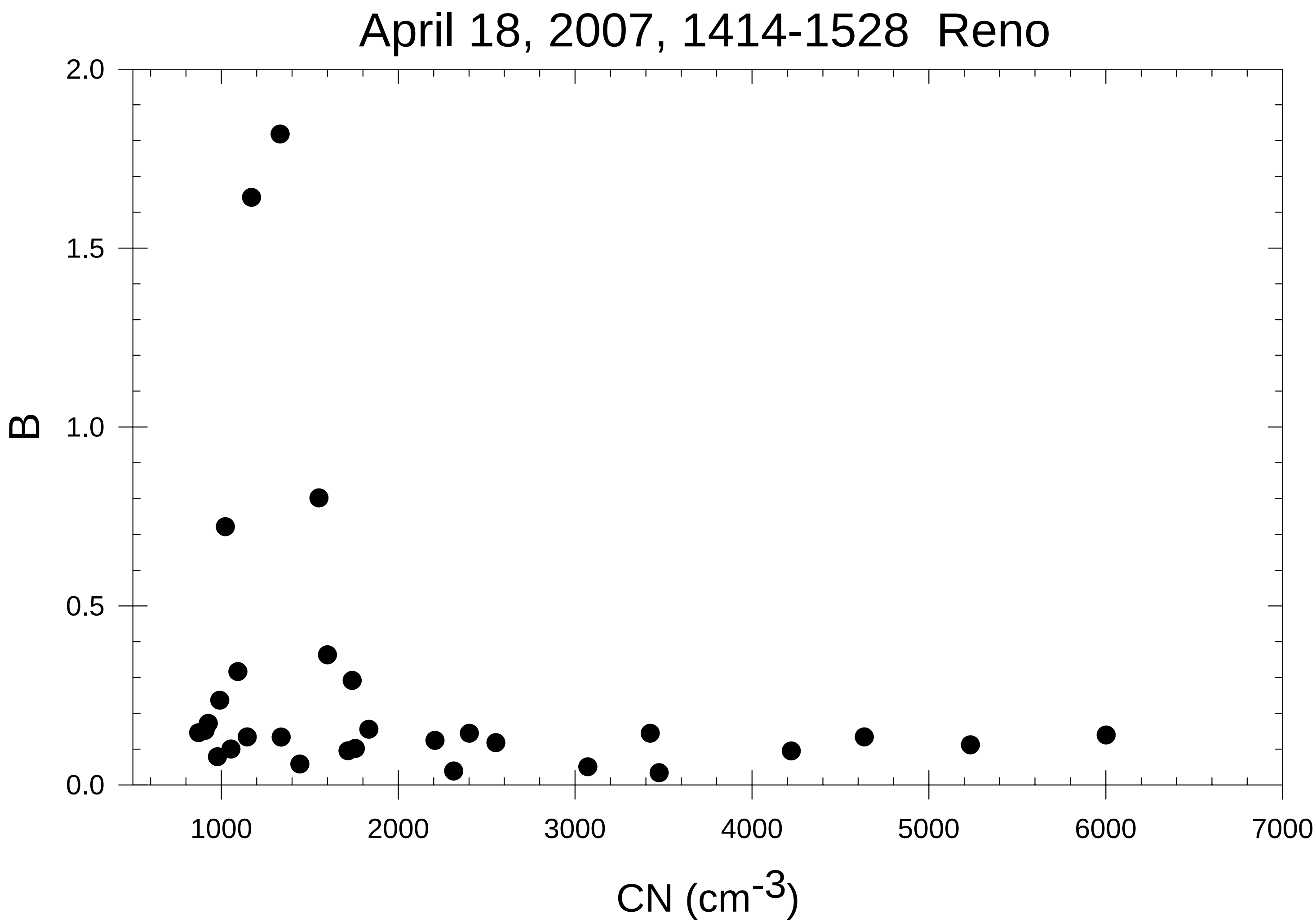

Figure 22. Particle solubility (B) from size versus Sc measurements lotted against total particle concentrations (CN). Notable is the great deal of variability of B for the same CN concentrations between 1000 and 1500 cm-3.

Invited talk

MASS SPECTROMETRIC ANALYSIS OF SMALL ICE CRYSTAL RESIDUALS IN MIXED PHASE CLOUDS DURING THE CLACE PROJECTS

M. Kamphus[1], S. Borrmann[1, 2], S. Walter[2], J. Curtius[3], J. Schneider[2], S. Mertes[4] and E. Weingartner[5]

[1]Institute for Atmospheric Physics, Johannes Gutenberg-University, Mainz, D-55099, Germany
[2]Particle Chemistry Department, Max Planck Institute for Chemistry, Mainz, D-55020, Germany
[3]Institute for Atmospheric und Environmental Sciences, Johann Wolfgang Goethe-University, Frankfurt, D-60438, Germany
[4]Leibniz Institute for Tropospheric Research, Leipzig, D-04318, Germany
[5]Laboratory of Atmospheric Chemistry, Paul Scherrer Institute, Villigen, 5232, Switzerland

1. INTRODUCTION

Heterogeneous nucleation is the main initiation process of precipitation in mid latitudes. However, the relationship between the ability to act as ice nuclei (IN) and the chemical composition of aerosol particles is not yet fully understood. First ambient measurements in pure ice clouds, e.g. cirrus clouds, are described in the literature but these measurements are restricted to aircraft based equipment. Ground based measurements can only be conducted on mountain sites in mixed phase clouds, but separation of ice nuclei from cloud condensation nuclei (CCN), which outnumber the IN by a factor of ~ 100 is necessary. A series of intensive ground based field experiments was carried out from 2001 to 2007 at the Jungfraujoch station in the Swiss Alps under the name CLACE (Cloud and Aerosol Characterization Experiment). During CLACE a newly designed Ice-CVI (counter-flow virtual impactor) was combined with different aerosol mass spectrometers in order to investigate the chemical composition of ice nuclei in mixed phase clouds.

Corresponding author's address: Stephan Borrmann, Johannes Gutenberg-University, Institute for Atmospheric Physics, D-55099 Mainz, Germany; E-Mail: borrmann@uni-mainz.de.

2. MEASUREMENTS

The Sphinx laboratory at the Jungfraujoch is situated at 3580 meters above sea level in the Swiss Alps at 7° 59' 2" E, 46° 32' 53" N. During the winter months it is mostly located in the free troposphere and frequently surrounded by mixed phase clouds. The CLACE campaigns were conducted from February to mid of March. Here, results from CLACE 3 to 6 (2004 – 2007) are presented.

2.1. Inlet systems

Three different inlet systems were available during the CLACE campaigns, sampling the entire background aerosol, the interstitial (not activated) aerosol particles, and residuals from small ice crystals and supercooled droplets.

The "total" inlet is heated, thereby evaporating cloud water and ice and thus sampling interstitial and activated aerosol particles. It is part of the GAW (Global Atmospheric Watch) project, permanently installed at the Jungfraujoch and operated by the Paul Scherrer Institute (PSI).

The interstitial inlet samples the not activated aerosol with a cut off at 2.5 µm. It

is installed by the Paul Scherrer Institute especially for the CLACE campaigns.
To separate the ice residuals from the cloud condensation nuclei and the not activated aerosol, an Ice-CVI was operated by the IfT Leipzig during the CLACE campaigns. It consists of four main parts, an omni-directional, exponentially-tapered, upward looking horn to aspirate the cloud air. In the virtual impactor (VI) particles larger than 20 µm ($D_{50\%}$ cut size diameter) are virtually impacted, whereas smaller particles remain in the sample flow. Downstream of the VI a pre-impactor (PI) is installed which separates the small ice particles from supercooled droplets by freezing the latter upon contact with impaction plates colder than 0°C. The CVI itself is located downstream of the PI to reject the interstitial particles. The CVI inlet is installed inside a wind tunnel to accelerate the incoming air up to 120 m s^{-1}, which is needed to reach a $D_{50\%}$ cut size of about 5 µm. A controlled counterflow is blown out of the inlet tip, which allows only hydrometeors of sufficient inertia to enter the system. The supercooled drops and larger ice crystals have already been removed by the PI and VI, respectively, thus only the small ice particles (5 µm < D_{ice} < 20 µm) are sampled. Inside the CVI the small ice particles are injected into a particle-free and dry carrier air for complete sublimation. A more detailed description of the Ice-CVI can be found in Mertes et al. (2007).

2.2. Aerosol mass spectrometer

During the CLACE campaigns online mass spectrometry was applied to investigate the chemical composition of ambient aerosol particles. There are two different techniques to perform aerosol mass spectrometry, thermal vaporization of aerosol particles with subsequent electron impact (EI) ionization as used by the Aerodyne AMS instruments and a combined vaporization and ionization with intense laser pulses as used by single particle instruments. Both techniques were deployed during the CLACE campaigns.

Aerosol mass spectrometer (AMS):
The particles enter the instrument through an aerodynamic lens. Particles in the size diameter range from 60 nm to 600 nm are focused into a narrow particle beam. The vacuum-aerodynamic particle diameter can be derived by measuring the particle flight time between a chopper wheel and the mass spectrometric detection. The particles are evaporated with an electric heater at 600°C. The resulting vapor is ionized with EI ionization at 70 eV. The resulting ions are analyzed with different mass filters. During CLACE 3 and 4, a quadrupole mass spectrometer was used. A disadvantage of this mass filter is the low mass scanning velocity and resolution of the mass spectra. Experimental details for the Q-AMS can be found in Jayne et al. (2000). During CLACE 5 and 6 the new generation of the AMS instrument with a time-of-flight (TOF) mass filter (Drewnick et al. (2005)) was deployed at the Jungfraujoch. These instruments combine fast sampling rates with high spectral resolution. Both instruments have in common that only material which is vaporized at temperatures of 600°C can be analyzed. The vaporization and the theoretical well understood EI ionization can be calibrated and quantitative results on sulfate, nitrate, ammonium and organics can be given.

Single particle mass spectrometer:
Refractory material can be analyzed in single particle mass spectrometer with laser ablation on the expense of not being quantitative. The particles enter the instrument through an aerodynamic lens. Particles with a diameter between 300 nm and 3000 nm are focused into a particle beam. At two positions in the particle beam light scattering experiments are performed with two 532 nm cw laser beams. From the time between the two light scattering signals the flight time and hence the diameter of the particles can be derived. The particle velocity is used to trigger the third laser which is a pulsed excimer laser working at 193 nm. Single particles are vaporized and the resulting vapor is ionized within one

laser pulse. The ions are analyzed in a bipolar time-of-flight mass spectrometer. A detailed description of the single particle mass spectrometer deployed at the Jungfraujoch can be found in Kamphus et al. (2008).

3. RESULTS

3.1. Q-AMS mass closure

During the CLACE 3 and 4 campaigns mass spectrometric measurements were conducted with the Q-AMS. Concentrations of sulfate, nitrate, ammonium and organics were measured for the background aerosol, the interstitial aerosol and ice nuclei. Comparison of different sizing techniques (AMS and scanning mobile particle sizer, SMPS) allows the measurement of the mean density for the aerosol population at the Jungfraujoch. Thus, it is possible to derive mass concentrations from the number concentrations measured with a SMPS. A comparison of the mass concentrations measured with the Q-AMS with the SMPS data is shown in Figure 1 for the background aerosol, the interstitial aerosol and the ice nuclei.

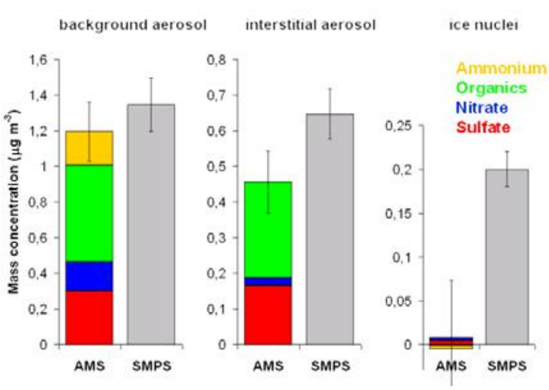

Figure 1: Comparison of Q-AMS and SMPS results at different inlets.

For the background and interstitial aerosol ammonium, nitrate, sulfate and organics account for most of the aerosol mass. But for the ice nuclei a large portion of the aerosol mass detected by the SMPS cannot be detected by the Q-AMS. The aerosol components which are not detected by the Q-AMS are likely composed of refractory materials like carbon black and mineral dust. Single particle analysis with laser ablation is a suitable technique to detect these refractory materials, so during CLACE 5 and 6 our Single Particle Laser Ablation Time-of-flight mass spectrometer (SPLAT) was deployed at the Jungfraujoch.

3.2. SPLAT background, IN, CCN

During the CLACE 5 and 6 campaigns our single particle laser ablation instrument was applied to especially investigate the refractory components of the ambient aerosol and its role in ice nucleation. In contrast to the Q- and TOF-AMS measurements, the SPLAT instrument can only detect particles larger than 300 nm. In addition to this, only qualitative results can be drawn from the measurements due to the complex theoretically not well understood ablation process, which arranges for slightly different mass spectra even for the same component.

Measurements were conducted at the total inlet and, whenever clouds were present and the Ice-CVI was operational, at the Ice-CVI to sample ice nuclei. In order to measure CCN, the pre-impactor of the CVI was removed during one day. The spectra for the background aerosol, the ice nuclei and cloud condensation nuclei were classified with a k-means algorithm which results in different chemical classes and number of particles belonging to these classes. Figure 2 shows the classification results for the background aerosol particles, ice nuclei and cloud condensation nuclei.

It can clearly be seen that the IN are dominated by the two classes with strong signals from mineral dust (class 1 and 6). They account for 57% of the particles. For the background aerosol and the CCN this value decreases to 8% and 12% respectively. Another component which shows strong variation is sulfate. In the IN it can be found in 44% of the particles (class 4 and 6), whereas sulfate is dominating in 73% of the spectra for background aerosol (class 2, 4 and 5). Finally, in the CCN sulfate can be found in 92% of the spectra (class 2, 4 and 6).

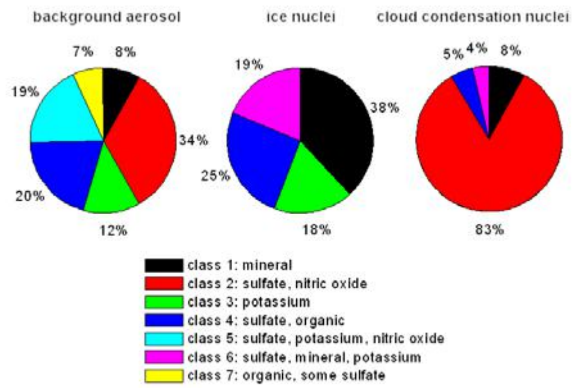

Figure 2: Results from the classification of the particles analyzed with the SPLAT instrument.

All spectra for the IN, CCN and the background aerosol show a high degree of internal mixing. There is hardly any class described by mass signals which cannot be found in one of the other classes. The relation of the intensity of different mass signals is the most important criterion for defining the different particle classes.
A comparison with other studies can be drawn from the CRYSTAL-FACE data presented by Cziczo et al. (2004). With a single particle mass spectrometer they analyzed cirrus IN behind a CVI onboard an aircraft. Their instrument (PALMS) also utilizes 193 nm for the ablation laser. For mineral dust/fly ash an increase from 1% of outside cloud particles to 44% for ice nuclei was found. This value increased further to 64% during a dust event. In the CRYSTAL-FACE data a particle class containing sulfate, potassium, organics and nitric oxide (termed as SKON group) was very dominant. 95% of the outside cloud particles belonged to this group. For the IN there was a decrease to 28% and 8% during a dust event. In our single particle spectra the SKON group is comparable to class 2, 4 and 5. So, for the background aerosol and the CCN 72% and 88% of the particles belong to the SKON corresponding classes. For the IN there is a strong decrease to 25%. In summary, there is a very nice agreement between the CRYSTAL-FACE data from cirrus measurement and our measurements in mixed phase clouds for the mineral dust/fly ash as well as the SKON group.

3.3. TOF-AMS (HOA/OOA)

With the W-TOF-AMS it is possible to separate ions with an identical integer mass, for example $C_2H_3O^+$ (m/z 43.0184) and $C_3H_7^+$ (m/z 43.0551). $C_2H_3O^+$ can be considered as a marker for oxygenated organic aerosol (OOA), whereas $C_3H_7^+$ is related to hydrogenated organic aerosol (HOA). Figure 3 shows the ratio between the two m/z 43 signals at the different inlets during the CLACE 6 campaign. While the background aerosol and the cloud condensation nuclei are mainly composed of oxidized organic components, in the ice residuals predominantly un-oxidized organics (HOA) were found. These results are in agreement with Cozic et al. (2008) who found during CLACE 3 and 4 that

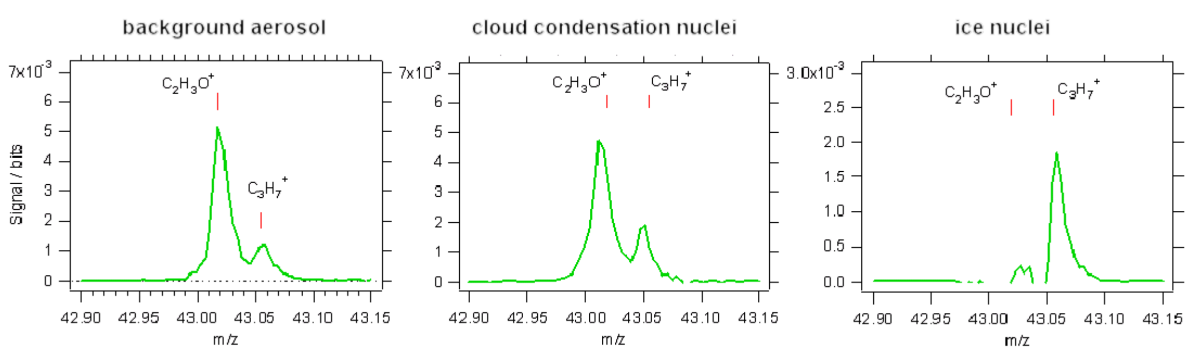

Figure 3: W-TOF-AMS high resolution mass spectra for m/z 43. $C_2H_3O^+$ is a marker for OOA, $C_3H_7^+$ for HOA.

carbonaceous aerosols are enriched in ice residuals.

3.4. Lead in single particles

With the single particle instrument (SPLAT) we were able to detect lead in single aerosol particles at the Jungfraujoch during CLACE 5 and 6. Figure 4 shows the distribution of the lead isotopes for a background aerosol particle. Lead is identified clearly by the isotopic pattern which is close to the natural occurrence of the isotopes (^{204}Pb 1.4%, ^{206}Pb 24.1%, ^{207}Pb 22.1%, ^{208}Pb 52.4%). Approximately 9% of the detected background aerosol particles contained lead. For the cloud condensation nuclei this value decreased to

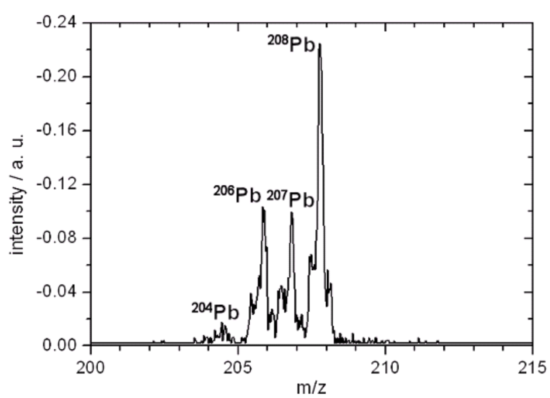

Figure 4: Single particle spectrum showing lead isotopic pattern

4%, while for the ice residuals there was a strong increase to 42%. The reason for the enrichment is not clear. We think that the main source for lead is aviation fuel which contains lead with concentrations up to 0.56 g/l.

4. CONCLUSION

As shown in the previous sections the combination of different mass spectrometric techniques with special inlet systems is an ideal tool to investigate the role of chemistry in heterogeneous ice nucleation in mixed phase clouds. AMS instruments are able to measure the non-refractory part of the aerosol quantitatively and give a detailed view into the ratio of oxygenated/ hydrogenated organic aerosol. With the single particle instrument with laser ablation further information about the refractory aerosol can be obtained. Thus, both instruments complement each other. A large data set on mixed phase clouds was generated during the CLACE campaigns, but for the ice nuclei, where concentrations are lower as 1 cm^{-3}, only general conclusion could be drawn. With further improvements on the efficiency especially of our single particle instrument, we want to perform time resolved measurements and correlate these to meteorological data. Further CLACE campaigns are planned to achieve this goal.

5. BIBLIOGRAPHY

Cozic, J., Mertes, S., Verheggen, B., Cziczo, D. J., Gallavardin, S. J., Walter, S., Baltensperger, U., and Weingartner, E.: Black carbon enrichment in atmospheric ice particle residuals observed in lower tropospheric mixed-phase clouds, J. Geophys. Res., in press, 2008.

Cziczo, D. J., Murphy, D. M., Hudson, P. K., and Thomson, D. S.: Single particle measurement of the chemical composition of cirrus ice residue during CRYSTAL-FACE, J. Geophys. Res., 109, D04201, doi: 10.1029/2003JD004032, 2004.

Drewnick, D., Hings, S., DeCarlo, P., Jayne, J. T., Gonin, M., Fuhrer, K., Weimer, S.,. Jimenez, J. L., Demerjian, K. L., Borrmann, S., and Worsnop, D. R.: A new Time-of-Flight Aerosol Mass Spectrometer (TOF-AMS) - Instrument Description and First Field Deployment, Aerosol Sci. Technol., 39, 637-658, 2005.

Jayne, J. T., Leard, D. C., Zhang, X., Davidovits, P., Smith, K. A., Kolb, C. E., and Worsnop, D. R.: Development of an Aerosol Mass Spectrometer for Size and Composition Analysis of Submicron

Particles, Aerosol Sci. Technol., 33, 49-70, 2000.

Kamphus, M., Ettner-Mahl, M., Brands, M., Curtius, J., Drewnick, F., and Borrmann, S.: Comparison of two aerodynamic lenses as an inlet for a single particle laser ablation mass spectrometer, submitted to Aerosol Sci. Technol., 2008.

Mertes, S., Verheggen, B., Walter, S., Connolly, P., Ebert, M., Schneider, J., Bower, K.N., Cozic, J., Weinbruch, S., Baltensperger, U., and Weingartner, E.: Counterflow virtual impactor based collection of small ice particles in mixed-phase clouds for the physico-chemical characterization of tropospheric ice nuclei: sampler description and first case study. Aerosol Sci. Technol., 41, 848-864, 2007.

Acknowledgements

Financial support by the German Research Foundation DFG within SFB 641 and grant HE 939/8 is gratefully acknowledged. The authors would like to thank the International Foundation High Altitude Research Stations Jungfraujoch and Gornergrat (HFSJG) for providing the excellent infrastructure at the Jungfraujoch. Support by the project European Supersites for Atmospheric Aerosol Research (EUSAAR) and the European network of excellence ACCENT (access to infrastructures, field stations) is acknowledged.

CLOUD-PROCESSING AND AEROSOL OPTICAL PROPERTIES AT A POLLUTED CONTINENTAL SITE

J.A. Ogren[1], E. Andrews[1,2], J. Allan[3], K. Bower[3], H. Coe[3], B.Corris[3], M. Flynn[3], D. Liu[3], W. Morgan[3], and P. Williams[3]

[1]Earth System Research Laboratory, NOAA, Boulder, CO 80305, USA
[2]Cooperative Institute for Research in Environmental Sciences, University of Colorado, Boulder, CO 80305, USA
[3]SEAES, University of Manchester, Manchester, M13 9PL, UK

1. INTRODUCTION

The magnitude, and even the sign, of the climate forcing by aerosol particles is strongly dependent upon both the aerosol single-scattering albedo (SSA), which is the fraction of the aerosol light extinction that is due to scattering, and the angular dependence of light scattering, which can be parameterized by aerosol properties such as the asymmetry parameter or the backscattering fraction (BFR). Long-term monitoring at a variety of surface sites reveals a systematic decrease in aerosol SSA as the aerosol loading decreases, i.e., aerosols are "blacker" in the cleanest air and an increase in BFR, i.e., aerosols are smaller in the cleanest air (Delene and Ogren, 2002).

One hypothesis for this behavior is that clouds preferentially scavenge large and primarily scattering aerosols more effectively than small and/or absorbing aerosols, which is what would be expected if the absorbing component of the aerosol is dominated by hydrophobic black carbon and the scattering component is dominated by hygroscopic species like sulfates. If the clouds precipitate, the aerosol that remains after the cloud dissipates will be smaller and enriched in black carbon relative to the water-soluble species that often dominate aerosol light scattering.

To address this hypothesis, we have been conducting a series of field campaigns in a variety of locations, with a focus on scattering and absorption of aerosol particles in cloud-free air, in interstitial air inside of clouds, and in the evaporated residuals of cloud droplets. The current work emphasizes an experiment in November-December, 2006 at Holme Moss, a field site on the moors about 30 km northeast of Manchester, UK that has been used as a research site by the University of Manchester (UM) for more than a decade for both field campaigns and long term climatological measurements (e.g., Beswick et al., 2003; http://cloudbase.phy.umist.ac.uk/field/).

Long-term climatology suggested that the site, at 525 m asl, would frequently be in cloud (150-200 hrs/month in autumn), and the site was indeed in fog ~22% of the sampling period (fog defined here for simplicity as visibility < 5 km). While the site had potential to receive fresh pollution from Manchester and Leeds, during the campaign the wind was primarily from the southwest meaning Manchester was the main source of aerosol sampled.

2. EXPERIMENTAL APPROACH

Identical instruments for measuring aerosol light scattering and light absorption were operated downstream of two complementary inlets. A counterflow virtual impactor (CVI) provided samples of cloud droplet residuals, i.e., the aerosol particles that remain when a cloud droplet

---

Corresponding author's address: John A. Ogren, NOAA R/GMD1, 325 Broadway, Boulder, CO 80305, USA; E-Mail: John.A.Ogren@noaa.gov

evaporates, and a radial impactor provided a sample of the interstitial particles smaller than the cloud droplets sampled by the CVI. The interstitial inlet was also used to sample ambient aerosols during cloud-free periods.

The radial impactor size cut was set to 5 μm diameter, i.e., all particles larger than 5 μm were assumed to be cloud droplets and all smaller particles were called interstitial. Based on calculations, the size cut of the CVI was approximately 8 μm, so there was a 3 μm gap in measurements between interstitial and cloud aerosol measurements – likely the particles in this size range were small cloud drops. Measurements of particles from both inlets were made at low relative humidity so that they could be directly compared. Aerosol light scattering coefficient was measured with an integrating nephelometer (Model 3563, TSI, Inc., St. Paul, USA) and light absorption coefficient was measured with a filter-based light photometer (Model PSAP, Radiance Research, Seattle, USA). All the measurements reported here are at a wavelength of 550 nm. Nephelometer data were corrected for truncation errors following the procedures recommended by Anderson and Ogren (1998) and the PSAP data were adjusted using the procedures recommended by Bond et al. (1999). Aerosol light extinction coefficient, σ_{ep}, was calculated as the sum of the corrected scattering and absorption coefficients. Cloud liquid water content (LWC) was measured with tunable diode laser hygrometer (MayComm, Wilmington, USA) downstream of the CVI.

3. RESULTS

The Holme Moss site was a very interesting location to sample aerosol. While observed aerosol extinction was fairly typical for a semi-remote location (median extinction ~20 Mm^{-1}), the aerosol single scattering albedo was consistently significantly lower than most sites at which NOAA had previously made measurements (Holme Moss median SSA ~0. 84). In other words, Holme Moss was an ideal location for measuring absorbing aerosol. The source of the absorbing aerosol is likely the diesel exhaust from vehicular traffic transported to the site from Manchester as well as nearer rural activities (peat burning and residential coal fires).

During cloudy periods at the site, the interstitial aerosol tended to be smaller and more absorbing than the ambient aerosol observed during clear conditions. There was also a decrease in aerosol extinction during cloud events compared to clear conditions, e.g., $\sigma_{ep,interstit} < \sigma_{ep,clear}$. These results are consistent with the systematic variation reported by Delene and Ogren (2002) and with observations made at other sites (Figure 1) where the aerosol properties could be segregated by the presence or absence of cloud (e.g., Ogren et al., 2004). These data suggest that clouds are preferentially scavenging the larger, more scattering aerosol leaving small absorbing aerosol in the interstitial air. Interestingly, cloud water collected at the Holme Moss site showed a distinct grayish tinge suggesting that at least some of the absorbing aerosol was incorporated into the cloud droplets and the single particle soot photometer (SP2, DMT, Boulder, USA) showed that the cloud drop residuals did contain some black carbon.

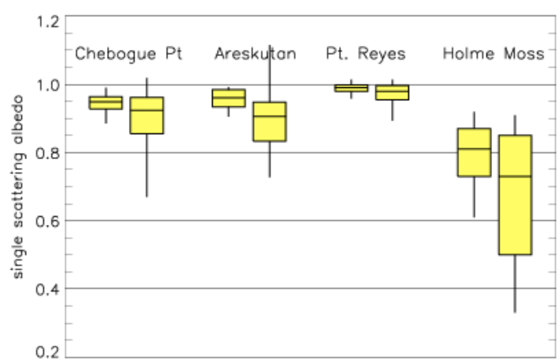

Figure 1: Single scattering albedo measured through inlet with 5 μm radial impactor; clear is SSA when no cloud is present, cloud is SSA for interstitial aerosol.

The extremely windy conditions at the site (wind speeds typically > 10 m/s) resulted in the CVI sampling non-ideally. Based on wind tunnel studies by Noone et al., (1992) sampling efficiencies for winds > 10 m/s are 45% for 8 um droplets and decrease precipitously for larger drops, e.g. ~20% sampling efficiency for 10 um droplets at 10 m/s wind speed. Based on the poor CVI sampling conditions and the detection limits of the optical instruments, the aerosol optical data needs much more analysis before any cloud drop residual optical properties can be produced. Two more sensitive chemical instruments did show differences in the cloud drop residuals compared to interstitial air. The cloud drop residuals from the CVI tended to have a higher fraction of sulfate (based on aerosol mass spectrometer, AMS, measurements) and lower soot content (based on SP2 measurements).

The suite of instruments deployed at Holme Moss provided some indication of how aerosol particles might interact with water vapor in the atmosphere. Measured aerosol hygroscopicity was surprisingly high (median f(RH)~2.0, where f(RH) is the ratio of light scattering at 85% to the value at 40%) considering the polluted influence suggested by the low values of SSA. For comparison, Sheridan et al., (2001) showed that smoke aerosol from local field fires at a rural continental site in the US was significantly less hygroscopic than the background aerosol at the site. However, when put in the context of AMS measurements, the measured f(RH) at Holme Moss was consistent with the composition dependence of f(RH) described by Quinn et al (2005) (Figure 2).

A cloud condensation nuclei counter (CCN, DMT, Boulder, USA) was used to measure CCN concentrations as a function of supersaturation. The CCN activated fraction (ratio of CCN concentration to total aerosol concentration (CN)) was highly variable, and complete activation was not observed even at the highest supersaturations studied (1.5 percent). The CCN activated fraction appeared to increase with increasing SSA (Figure 3) and decrease with increasing organic contribution to the aerosol.

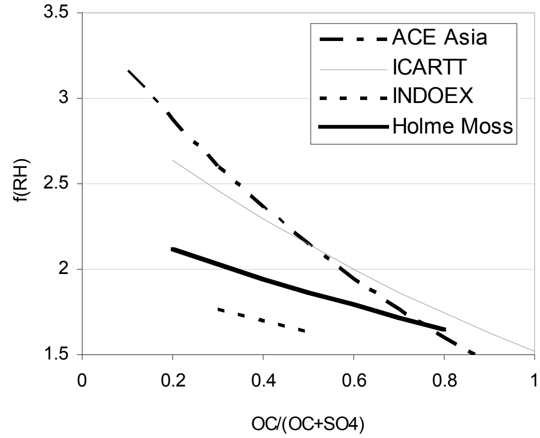

Figure 2: f(RH) as a function of aerosol composition (based on figure from Quinn et al., (2005)); Holme Moss line added for this report.

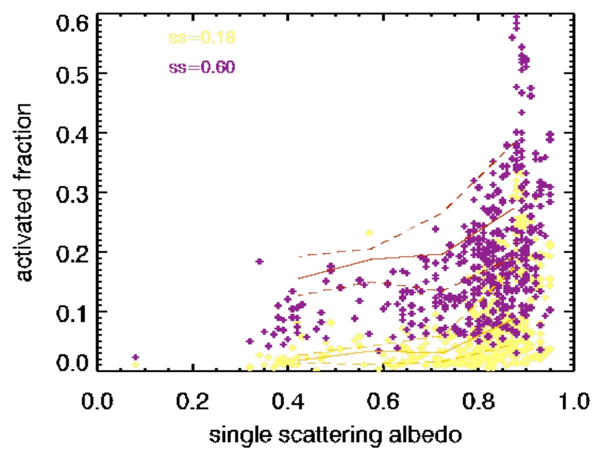

Figure 3: CCN activated fraction (CCN/CN) for two supersaturations (given in percent) as a function of single scattering albedo

4. CONCLUSIONS

Based on the results from Holme Moss and several other field campaigns, we have found that clouds tend to scavenge larger, less scattering aerosol leaving the darker, smaller aerosol in the interstitial air. In terms of intrinsic aerosol properties, this means that BFR increases and SSA decreases in cloud scavenged air and interstitial aerosol. As BFR and SSA are both important factors in aerosol radiative forcing, it follows that the radiative properties of the cloud-processed aerosol are quite different than the pre-cloud aerosol.

Aerosol composition (as indicated by SSA and aerosol mass spectrometry chemical measurements) allows us to explore how particle composition influences the interactions between water and aerosol particles which has implications for both direct (aerosol hygroscopicity) and indirect (CCN activity) forcing.

Future plans include evaluating the Holme Moss data set in conjunction with several other similar data sets to develop

1) improved parameterization of elemental carbon (EC) processing by clouds

2) better understanding of size and composition dependent aerosol processing by clouds

3) reduced uncertainty in EC cycle and lifetime in atmosphere

4) better understanding of the cloud processing mechanisms affecting aerosol properties

Incorporation of findings from these planned explorations into climate models will reduce the uncertainty in predictive modeling capabilities and improve our ability to identify the amount of aerosol radiative forcing versus other forcing factors such as greenhouse gases.

5. ACKNOWLEDGEMENTS

This US part of this work was supported by the U.S. Department of Energy Atmospheric Science Program and the NOAA Climate Forcing Program. The UK participation in this project was supported by the NERC APPRAISE Programme, grant number NE/E011187/1. Corris is supported through NERC studentship number NER/S/A/2004/12356.

6. REFERENCES

Anderson, T. L., and J. A. Ogren, 1998: Determining aerosol radiative properties using the TSI 3563 integrating nephelometer. *Aerosol. Sci. Tech.,* **29**, 57-69.

Beswick, K., T.W. Choularton, D.W.F. Inglis, A.J. Dore, D. Fowler, 2003: Influences on long-term trends in ion concentration and deposition at Holme Moss. *Atmos. Environ*., **37**, 1927-1940.

Bond, T. C., T. L. Anderson, and D. Campbell, 1999: Calibration and intercomparison of filter-based measurements of visible light absorption by aerosols. *Aerosol Sci. Tech.,* **30**, 582-600.

Delene, D. J., and J. A. Ogren, 2002: Variability of aerosol optical properties at four North American surface monitoring sites. *J. Atmos. Sci.,* **59**, 1135-1150.

Noone, K.J., H-C Hansson, R.K.A. Mallant, 1992: Droplet sampling efficiency from crosswinds:an inlet efficiency calibration," *J. Aerosol Sci.,* **23**, 153-164.

Ogren, J.A., E. Andrews, D. Covert, K. Noone, 2004: Effects of cloud scavenging on aerosol single scattering albedo. *Proceedings of the 14th International Conference on Clouds and Precipitation*, Bologna, Italy, July 2004.

Quinn, P. K., T.S. Bates, A.D. Clarke, W. Wang, M. Rood, E. Andrews, J. Allan, C.M. Carrico, D. Coffman, 2005: Impact of particulate organic matter on the relative humidity dependence of light scattering: A simplified parameterization," *Geophys. Res. Lett*., **32**, L22809, doi:101029/2005GL024322.

Sheridan, P.J., D.J. Delene, J.A. Ogren, 2001: Four years of continuous surface aerosol measurements from the Department of Energy's Atmospheric Radiation Measurement Program Southern Great Plains Cloud and Radiation Testbed site. *J. Geophys. Res.*, **106**, 20735-20747.

ICE NUCLEI MEASUREMENTS IN THE AMAZON BASIN

Anthony J. Prenni[1], Markus D. Petters[1], Paul J. DeMott[1], Sonia M. Kreidenweis[1], and Traci Lersch[2]
[1]Colorado State University, Department of Atmospheric Science, Fort Collins, Colorado, USA
[2] RJ Lee Group, Monroeville, PA, USA

1. INTRODUCTION

The Brazilian Amazon Basin is the largest intact tropical forest in the world, covering four million square kilometers [*Skole et al.*, 1994]. With large emissions of gases and particulate matter, this ecosystem plays an important role in the global atmosphere. Tropical forests emit large numbers of aerosols directly to the atmosphere, including bacteria, pollen, spores, algae, protozoa, fungi, and leaf fragments. Secondary organic aerosol (SOA) also forms from emissions and subsequent oxidation of biogenic gases. In addition to surface sources, large quantities of wind-blown dust from North Africa reach the Amazon Basin during the wet season [*Artaxo and Hansson*, 1995; *Formenti et al.*, 2001]. Assessing gaseous and particulate emissions from the Amazon Basin and the climatic effects of these emissions has been the focus of several major field campaigns. However, until recently there have been no measurements aimed at characterizing ice nuclei (IN) in this region. Such measurements are critical for understanding cloud and precipitation processes. Ice phase processes also influence cloud lifetime, cloud scale dynamics, lightning and radiative forcing [*Harrington and Olsson*, 2001; *Vavrus*, 2004]. Interestingly, precipitation in the Amazon Basin exceeds that of its African counterpart, the Congo Basin, by roughly a factor of two, and this difference is thought to be due to differences in the aerosols on which the clouds form [*Rosenfeld and Woodley*, 2001].

The ability of dust particles to initiate ice nucleation has been well documented [*Archuleta et al.*, 2005; *DeMott et al.*, 2003; *Hung et al.*, 2003; *Koehler et al.*, 2007]. However, less is known about the role of organic and biological particles as IN. In this paper, we present recent IN measurements from the AMazonian Aerosol characteriZation Experiment 2008 (AMAZE-08). These measurements are focused on ice formation at cumulus cloud temperatures.

2. EXPERIMENTAL

Ice nuclei measurements were conducted from February 9 – March 9, 2008 as part of AMAZE-08 field campaign using a recently developed version of the Colorado State University Continuous Flow ice thermal Diffusion Chamber (CFDC) [*Rogers et al.*, 2001]. Measurements were made at Tower TT34 (02° 35.675´S, 060° 12.557´W) in the Reserva Biologica do Cuieiras in Brazil. The site, 60 km NNW of Manaus, is located within a pristine rainforest. This time period is during the wet season, when winds come predominantly from the ENE across 1600 km of untouched forest. For IN measurements, aerosol particles were sampled through a PM-10 inlet from the top of TT34 through a ¾"-stainless steel laminar aerosol sampling line. The instrument was situated inside an air conditioned container where temperatures varied from 20-26 °C. A self-regenerating dryer designed by the Institute for Tropospheric Research (IfT, Leipzig, Germany) maintained the relative humidity in the sampling line between 15 and 40%. Additional diffusion driers were employed to further dry the aerosol before it entered the CFDC. The inlet was at 38.75 m, and the canopy near the tower varied between 30 and 35 m. Boundary layer height typically varied from 100-200 m at night to 1500-1800 m during the day.

The CFDC permits observation of freezing at controlled temperatures, pressures, and humidities [*Rogers et al.*, 2001]. The processing section of the CFDC consists of an annular gap between two vertical, ice-coated cylinders. A laminar flow of aerosol passes through this annular space between two flows of dry, particle-free sheath air for a period of ~10 seconds. The sheath flow (85% of total) constrains the aerosol to a region of well-defined temperature and humidity, which is determined by the temperatures of the ice-covered walls and the location of the aerosol sample. Particles which form ice grow preferentially, due to the high supersaturations experienced by ice crystals compared to liquid particles. Discrimination of nucleated ice crystals from liquid particles is done by measuring particle size distributions at the outlet of the CFDC using an optical particle counter (OPC). Amplification of the size difference between ice crystals and solution/cloud droplets is achieved due to the existence of an ice-saturated region in the lower third of the chamber. This method allows for operation of the CFDC above water saturation, in that activated water droplets evaporate prior to reaching the OPC [*Rogers*, 1994]. An inlet impactor upstream of the CFDC removes particles larger than ~1.5 μm (Rogers et al., 2001b), so that large aerosol particles are not erroneously identified as ice. The sample location, thermodynamic conditions, and airflow residence time are calculated in real-time by the instrument data system [*Rogers*, 1988]. An inertial impactor immediately downstream of the CFDC is used to capture ice crystals on Transmission Electron Microscope (TEM) grids, allowing for subsequent identification of the elemental composition of the particles on which ice forms [*Kreidenweis et al.*, 1998]. The CFDC is sensitive in real time to all nucleation modes, except contact freezing, since the residence time is fairly short.

3. RESULTS AND DISCUSSION

Data collected throughout the study period are shown in Figure 1. IN concentrations are given as 3-5 minute averages. Data collection was not continuous, but rather was limited due to frost accumulation in the chamber, which resulted from the high absolute humidity of the sample aerosol. For each sampling period, data were collected for 1-7 hours, after which time the chamber was warmed to room temperature and subsequently dried using compressed air. IN concentrations show some temporal variablity, with maximum concentrations of ~50 L^{-1} near -30 °C and minimum concentrations below the CFDC detection limit at temperatures of -20 °C and warmer. Despite this variability, measurements revealed no clear diurnal cycle, which we might expect if there were a local source. However, we note that our inlet impactor removes particles larger than ~1.5 μm, a size range which may include many biological particles, and so we may not have been able to observe a local source if the particles were larger than ~1.5 μm. Future work is planned to correlate IN concentration with biological particle concentrations, which were measured using a TSI UV-APS.

As noted earlier, another possible source of IN to this region is long range transport of desert dust. We have begun TEM analysis of the IN to determine if the particle composition is consistent with such a source, but at the time of this writing, TEM grids from only two days of the project have been analyzed. These samples were collected on March 6, 2008, when IN concentrations were ~4 L^{-1} at -30 °C, and on

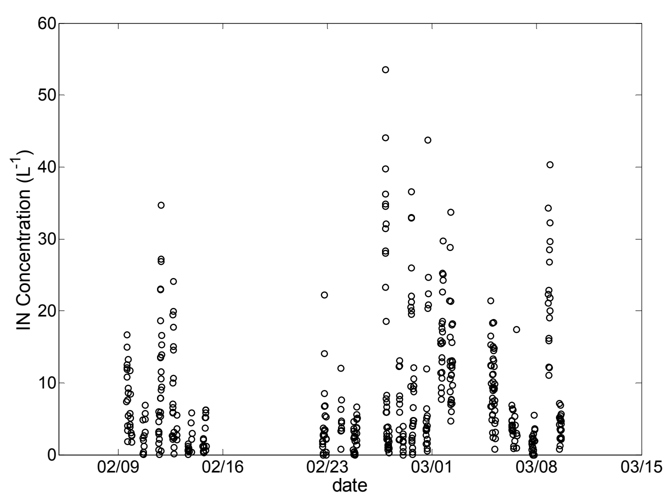

Figure 1. Measured IN concentrations throughout AMAZE-08.

March 8, 2008, when IN concentrations were ~25 L^{-1} at -30 °C. On both of these days dust particles comprise a major fraction of the measured IN, supporting the notion that long range transport of dust may play an important role in ice nucleation in this region during the wet season. Carbonaceous particles also are present on both days, both internally and externally mixed with the dust, suggesting a potential role for primary biological and/or secondary organic aerosol particles. Sample TEM images for two particles are shown in Figure 2. More extensive analysis is currently in progress, and a more complete data set is expected to provide insight into sources of IN to the Amazon Basin.

Average IN concentrations are shown as a function of temperature in Figure 3. A clear temperature dependence is apparent from the data, with average IN concentrations of ~1 L^{-1} at -20 °C and ~10 L^{-1} at -30 °C. For comparison, the Fletcher parameterization [*Fletcher*, 1962] for IN concentration is shown as a solid line for $A = 1\times10^{-5}\ L^{-1}$ and $\beta = 0.6\ (°C)^{-1}$. Although the data are comparable in magnitude at -20 °C, our measurements do not exhibit as strong of a temperature dependence as predicted by the Fletcher curve, but the slope is consistent with previous CFDC measurements [*Richardson et al.*, 2007]. Also apparent from the figure is the rather broad range of measured concentrations for similar temperature conditions. For example, average IN concentrations at -30 °C covered a range of <1 L^{-1} to > 20 L^{-1}. In general, our measurements appear to fall into two regimes: high IN and low IN groups. To understand the cause for these two regimes, work is in progress comparing IN concentrations and compositions with concurrent measurements of ambient aerosol composition and airmass back trajectories, as determined from HYSPLIT. Preliminary analysis of back trajectory data suggests that these groups may result from differences in dust transport to this region during different times of the study. However, we reiterate that these analyses are preliminary, and further work is needed.

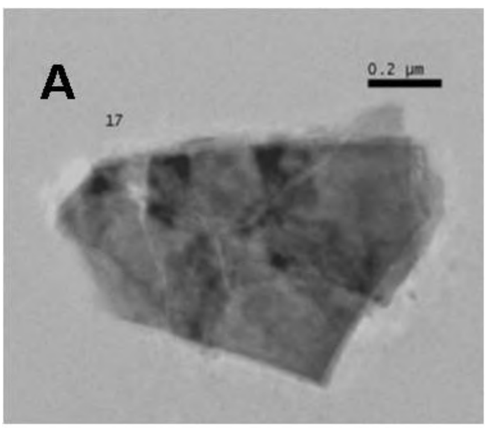

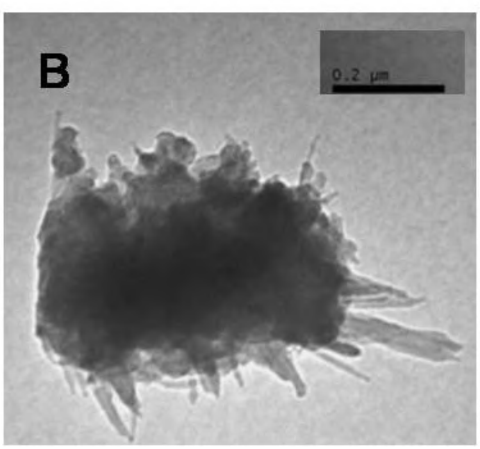

Figure 2. TEM images of residual IN particles composed primarily of (A) silicon and aluminum, and (B) silicon with carbonaceous content.

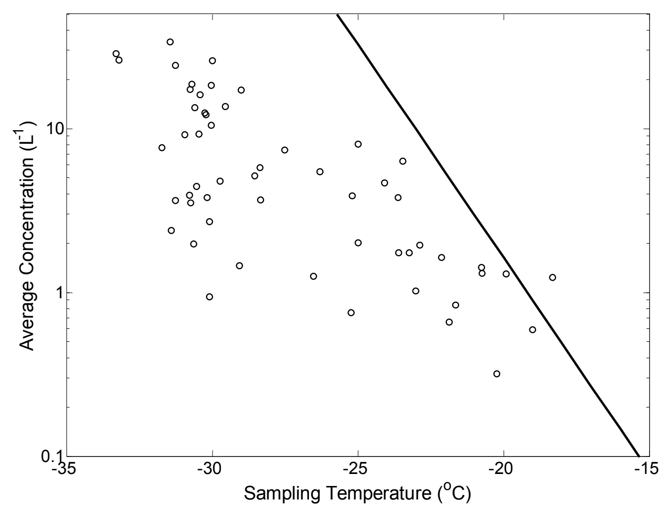

Figure 3. Average IN concentration as a function of sampling temperature.

4. ACKNOWLEDGMENTS

This work is supported by the NASA New Investigator Program, grant NNG04GR44G. The authors also wish to acknowledge Scot Martin, Paulo Artaxo, and the entire AMAZE-08 Team.

5. REFERENCES

Archuleta, C. M., et al. (2005), Ice nucleation by surrogates for atmospheric mineral dust and mineral dust/sulfate particles at cirrus temperatures, *Atmospheric Chemistry and Physics*, *5*, 2617-2634.

Artaxo, P., and H.-C. Hansson (1995), Size distribution of biogenic aerosol particles from the Amazon Basin, *Atmospheric Environment*, *29*(3), 393-402.

DeMott, P. J., et al. (2003), African dust aerosols as atmospheric ice nuclei, *Geophysical Research Letters*, *30*(14), Art. No. 1732.

Fletcher, N. H. (1962), *Physics of Rain Clouds*, 386 pp., Cambridge University Press.

Formenti, P., et al. (2001), Saharan dust in Brazil and Suriname during the Large-Scale Biosphere-Atmosphere Experiment in Amazonia (LBA) - Cooperative LBA Regional Experiment (CLAIRE) in March 1998, *Journal of Geophysical Research*, *106*(D14), 14919-14934.

Harrington, J. Y., and P. Q. Olsson (2001), On the potential influence of ice nuclei on surface-forced marine stratocumulus cloud dynamics, *Journal of Geophysical Research-Atmospheres*, *106*(D21), 27473-27484.

Hung, H. M., et al. (2003), Kinetics of heterogeneous ice nucleation on the surfaces of mineral dust cores inserted into aqueous ammonium sulfate particles, *Journal of Physical Chemistry A*, *107*(9), 1296-1306.

Koehler, K. A., et al. (2007), Potential impact of Owens (dry) Lake dust on warm and cold cloud formation, *Journal of Geophysical Research-Atmospheres*, *112*(D12).

Kreidenweis, S. M., et al. (1998), Isolating and identifying atmospheric ice-nucleating aerosols: A new technique, *Atmospheric Research*, *46*(3-4), 263-278.

Richardson, M. S., et al. (2007), Measurements of heterogeneous ice nuclei in the western United States in springtime and their relation to aerosol characteristics, *Journal Of Geophysical Research-Atmospheres*, *112*(D2).

Rogers, D. C. (1988), Development of a continuous flow thermal gradient diffusion chamber for ice nucleation studies, *Atmospheric Research*, *22*, 149-181.

Rogers, D. C. (1994), Detecting ice nuclei with a continuous-flow diffusion chamber - Some exploratory tests of instrument response, *Journal of Atmospheric and Oceanic Technology*, *11*(4), 1042-1047.

Rogers, D. C., et al. (2001), A continuous-flow diffusion chamber for airborne measurements of ice nuclei, *Journal of Atmospheric and Oceanic Technology*, *18*, 725-741.

Rosenfeld, D., and W. Woodley (2001), Pollution and clouds, *Physics World*, *14*(2), 33-37.

Skole, D. L., et al. (1994), Physical and human dimensions of deforestation in Amazonia, *Bioscience*, *44*(5), 314-322.

Vavrus, S. (2004), The impact of cloud feedbacks on Arctic climate under greenhouse forcing, *Journal of Climate*, *17*(3), 603-615.

SENSITIVITIES OF MODELLED HYGROSCOPIC GROWTH AND ACTIVATION ON SURFACE TENSION AND THE AMOUNT OF SOLUBLE SUBSTANCE IN AEROSOL PARTICLES

F. Stratmann[1], H. Wex[1], D. Topping[2], and G. McFiggans[2]

[1]Leibniz-Institute for Tropospheric Research, Leipzig, Germany
[2]Centre for Atmospheric Sciences, University of Manchester, Sackville Street, Manchester, UK

1. INTRODUCTION

The Köhler-equation is widely used to model hygroscopic growth and activation of aerosol particles. In the Köhler equation, the Kelvin term accounts for the effect of the curvature of the droplet surface while the Raoult term (or water activity) describes the influences of soluble material dissolved in the droplet. All together, the important parameters for the prediction of the hygroscopic growth and activation are the number of ions or molecules that are dissolved in the droplet (N_{ion}) and the surface tension (σ).

Here a study regarding the sensitivity of hygroscopic growth and activation on N_{ion} and σ will be presented. We will show that N_{ion} is the relevant parameter when determining the hygroscopic growth and σ has only negligible influence at relative humidities below 95%. However, when modelling the critical super-saturation needed for activation, both parameters, i.e., N_{ion} and σ need to be considered. Interestingly, the sensitivity of the critical super-saturation with respect to σ may be a factor of three larger than that regarding N_{ion}.

The insensitivity of hygroscopic growth below 95 % relative humidity and the high sensitivity of activation on σ control the possibility of achieving closure between hygroscopic growth and activation properties. Furthermore, the strong influence of surface tension needs to be kept in mind when modelling the effect of partitioning on droplet activation (*Sorjamaa and Laaksonen* [2003], *Sorjamaa et al.*, [2004], *Kokkola et al.*, [2006]).

2. MODELLING

The Köhler equation can be written as:

$$S_d = \exp\left(\frac{4M_w\sigma}{RT\rho_w d_d}\right)\cdot\exp\left(-\frac{N_{ion}}{n_w}\right)$$

with

$$N_{ion} = \frac{\phi\nu\rho_s V_s}{M_s} = \phi\nu n_s$$

(N_{ion} being the number of ions dissolved in the droplet, for the other symbols see nomenclature at the end of this abstract). Two different base cases were examined, one using a value of N_{ion} resulting in a high hygroscopicity (ammonium sulphate), and the other one simulating a less hygroscopic substance (HULIS, HUmic LIke Substance).

While N_{ion} for a particle of a known dry size can be calculated from literature data for ammonium sulphate, N_{ion} for HULIS varies, depending on the HULIS sample. Values for the different parameters were used following those determined in *Wex et al.* [2007].

To obtain accurate values regarding the sensitivity of S_d and d_d on σ and N_{ion}, calculations were performed for varying values of σ and N_{ion} for the two base cases. For a comprehensive description of the derivation of the sensitivities, the readier is referred to *Wex et al.* [2008]. Here, in Figure 1, we directly show the resulting sensitivities for a 1% variation of either σ or N_{ion} for the two different substances and for dry particle sizes of 50 and 100nm.

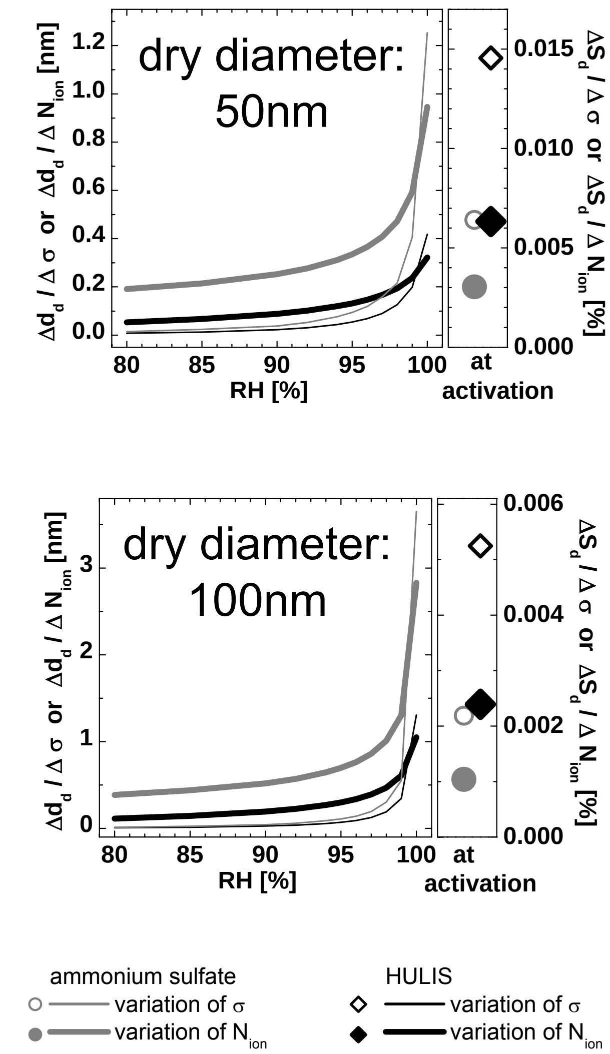

Fig. 1: *Sensitivities of d_d (left parts of each panel) and S_d (right part of each panel) to a 1% variation in N_{ion} (thick lines / filled symbol) or in σ (thin lines / open symbol). Two different dry diameters (50 nm (upper panel) and 100 nm (lower panel)) were examined, for a more and a less hygroscopic substance, i.e. for ammonium sulphate and for HULIS, respectively.*

3. RESULTS AND DISCUSSION

3.1. Sensitivities. The following important conclusions can be drawn from the sensitivities depicted in Figure 1:

a) The hygroscopic growth regime, i.e., d_d, is more sensitive to a 1% variation of N_{ion} than to a 1% variation in σ.

b) The hygroscopic growth below saturations of 0.95 is almost insensitive to σ, but its sensitivity to σ becomes important at larger saturations above 0.95.

c) S_d is more than twice as sensitive to a variation of σ than to a similar variation of N_{ion}.

d) In the hygroscopic growth regime the more hygroscopic substance is more sensitive towards changes in both, N_{ion} and σ, than the less hygroscopic one, with an increasing sensitivity towards larger dry diameters.

e) S_d of the less hygroscopic substance is more sensitive towards changes in both, N_{ion} and σ, than that of the more hygroscopic substance, with an increasing sensitivity towards lower dry diameters.

The sensitivities shown in Figure 1 can be used to estimate deviations in S_d or d_d due to uncertainties in N_{ion} and σ assuming

$$\Delta f = \frac{\partial f}{\partial x} \cdot \Delta x \approx \frac{\Delta f}{\Delta x_{1\%}} \cdot \Delta x$$

with $f = S_d \text{ or } d_d$ and $x = N_{ion} \text{ or } \sigma$. For a 50nm HULIS particle

$$\frac{\partial f}{\partial x_{1\%}} \approx \frac{\Delta S_d}{\Delta \sigma} = 0.0145$$

and a $\Delta\sigma$ =72.8–50=22.8 mN/m, i.e., a 31% change in surface tension, $\Delta S_d = 0.0145 \cdot 31\% = 0.45\%$ (absolute) can be observed.

The above example was given for an error in σ on purpose, as this value is largely uncertain for atmospheric particles. It can be directly measured only for bulk solutions (or for droplets much larger than freshly activated cloud droplets), and during these measurements, different concentrations and time scales prevail than during activation.

As mentioned among the important implications that can be deduced from Figure 1, the hygroscopic growth regime is insensitive to σ up to high RHs (relative humidities), i.e. information on σ simply can not be drawn from measurements of the hygroscopic growth for RHs below 95%. On the other hand, σ strongly influences the activation. Therefore, deriving S_d from measurements of the hygroscopic growth is only possible, if the examined substance has no influence on σ, i.e. if σ has the value of water, or if the right value of σ can be estimated.

3.2. Variable surface tension and influence of partitioning. To complicate the matter further, it has been shown for HULIS, that a concentration dependent σ should be used when describing the activation behaviour [*Ziese et al.*, 2008]. In this context, also partitioning of surface active substances to the droplet surface may play a role. Figure 2 shows Köhler curves for a fulvic acid particle (similar to HULIS, values taken from *Topping et al.* [2007]) with an initial radius of 100 nm, for the partitioning and the non-partitioning case (thick and thin lines, respectively). Also shown, in grey, are the corresponding surface tensions.

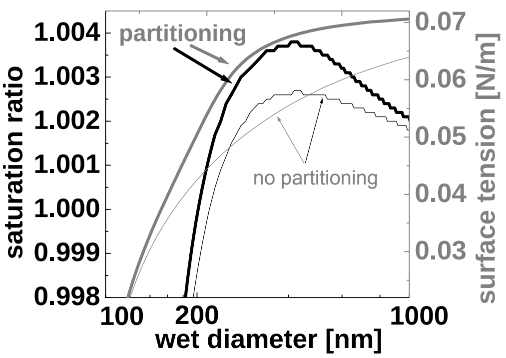

Fig. 2: Köhler curves for a fulvic acid particle (similar to HULIS, values taken from Topping et al. [2007]) with an initial radius of 100 nm, for a partitioning and a non-partitioning case (thick and thin lines, respectively). Also shown, in grey, are the corresponding surface tensions.

Figure 2 clearly shows, that consideration of bulk to surface partitioning increases the critical saturation ratio, i.e. S_d. This increase in S_d between the partitioning and the non-partitioning case is larger than one that would only originate in a change of σ, because it has to be attributed to both, the increase in σ and, additionally, the change in the amount of soluble substance in solution (+0.11% instead of 0.08% if only σ changed).

Overall, it becomes obvious that the value of σ depends on several factors, as there are the presence of surface active substances, their concentration in the droplet solution that changes during droplet growth, and possible partitioning or additional salting out effects of the surface active material between droplet bulk and surface. These effects aggravate the prediction of the value of σ that is effective during the activation process.

3.3. Influence on droplet number. We examine the effect of an erroneous value of σ on the prediction of the droplet number. For this, the change in the number of activated droplets for a 10% change in σ from 72.8 mN/m to 65.5 mN/m is derived. The estimates are based on a measured atmospheric aerosol number size distribution taken from data presented in *Wex et al.*, [2002] and represent an averaged number size distribution measured at an urban location in Germany on August 01, 2002.

For a fixed super-saturation, the critical diameter for the activation was determined, once using σ = 72.8 mN/m and again using σ = 65.5 mN/m. The number of activated droplets was determined as the integral of the measured number size distribution above that diameter. The number of activated droplets was determined, and the relative difference between the cases with different σ was derived. Figure 3 shows the measured particle number concentration and the fraction of the particles that would be activated for the two different values of σ und similar atmospheric super-saturation conditions.

Here S_d was chosen such, that for σ = 72.8 mN/m the dry particle size for activation was 125 nm. Lowering σ (for a constant S_d) caused a lowering of the dry size from 125 nm to 112.5 nm for both ammonium sulphate and HULIS.

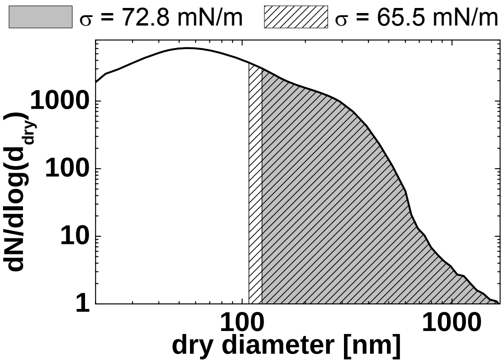

***Fig. 3:** Critical diameters and activated particles (highlighted areas) for a constant S_d and two different values of σ, differing by 10%.*

The number of activated droplets associated with the different dry sizes was found to be increased by 20% due to the use of the lower σ. This implies that surface tension effects may have to be accounted for when deriving the correct number of particles activated to become cloud droplets.

Nomenclature:

d_d	droplet diameter
M_s	molecular weight of the solute
M_w	molecular weight of water
n_s	number of moles of the solute
n_w	number of moles of water
N_{ion}	number of ions or molecules in the droplet
R	ideal gas constant
S_d	water vapor saturation at the droplet surface
T	temperature
V_s	Volume of the dry particle
Φ	osmotic coefficient
ν	number of ions or molecules per molecule in solution
ρ_s	density of the solute
ρ_w	density of water
σ	surface tension

BIBLIOGRAPHY

Kokkola, H., et al. (2006), Cloud formation of particles containing humic-like substances, *Geophys. Res. Lett.*, *33*, L10816, doi:10810.11029/12006GL026107.

Sorjamaa, R., and A. Laaksonen (2003), Surfactant partitioning and the Raoult effect in Köhler theory, *J. Aerosol Sci.*, *34*, 145-146.

Sorjamaa, R., et al. (2004), The role of surfactants in Köhler theory reconsidered, *Atmos. Chem. Phys.*, *4*, 2107-2117.

Topping, D. O., G. B. McFiggans, G. Kiss, Z. Varga, M. C. Facchini, S. Decesari, and M. Mircea (2007), Surface tension of multi-component mixed inorganic/organic aqueous systems of atmospheric significance: measurements, model predictions and importance for cloud activation predictions, *Atmos. Chem. Phys.*, *7*, 2371-2398.

Wex, H., C. Neusüß, M. Wendisch, F. Stratmann, C. Koziar, A. Keil, A. Wiedensohler, and M. Ebert (2002), Particle scattering, back-scattering, and absorption coefficients: an in-situ closure and sensitivity study, *J. Geophys. Res.*, *107*, doi:10.1029/2000JD000234.

Wex, H., T. Hennig, I. Salma, R. Ocskay, A. Kiselev, S. Henning, A. Massling, A. Wiedensohler, and F. Stratmann (2007), Hygroscopic growth and measured and modeled critical super-saturations of an atmospheric HULIS sample, *Geophys. Res. Lett.*, *34*, doi:10.1029/2006GL028260.

Wex, H., Stratmann, F., D. Topping, and G. McFiggans (2008) The Kelvin versus the Raoult term in the Köhler equation, submitted to J. Atmos. Sci..

Ziese, M., H. Wex, E. Nilsson, I. Salma, R. Ocskay, T. Hennig, A. Massling, and F. Stratmann (2008), Hygroscopic growth and activation of HULIS particles: experimental data and a new iterative parameterization scheme for complex aerosol particles, *Atmos. Chem. Phys.*, *8*, 1855-1866

INTERACTION OF SAHARAN DUST WITH LIQUID AND ICE CLOUDS

Cynthia Twohy[1], Susan Van den Heever[2], Sonia Kreidenweis[2], Trude Eidhammer[2], Paul DeMott[2], Andrew Heymsfield[3], Aaron Bansemer[3], Bruce Anderson[4], Gao Chen[4], and Edward Browell[4]

[1] Oregon State University, Corvallis, OR USA
[2] Colorado State University, Fort Collins, CO USA
[3] National Center for Atmospheric Research, Boulder, CO USA
[4] NASA Langley Research Center, Hampton, VA USA

1. INTRODUCTION

Crustal dust originates from Africa in the summer months. Dust liberation is anti-correlated with precipitation frequency in the Sahel region, and has increased in magnitude over the past few decades (Prospero, 1996). The impact of this dust on tropical convection is potentially large. If it contains soluble material, dust may act as a cloud condensation nucleus (CCN), decreasing mean droplet size and inhibiting precipitation (Rosenfeld et al., 2001; Mahowald and Kiehl, 2003; Koehler et al., 2007). Dust is also known to be an effective ice nucleus (DeMott et al, 2003; Twohy and Poellot, 2005; Field et al. 2006, etc). Dunion and Velden (2004) showed that the Saharan Air Layer (SAL) seemed to inhibit the development of hurricanes in the Atlantic, and Evan et al. (2006) demonstrated that dust is anticorrelated with tropical cyclone activity. They proposed that this effect is caused by dynamical and radiative effects related to the SAL. However, dust nucleation impacts on microphysics, latent heat release and vertical transport (e.g., Khain et al., 2005; Van Den Heever et al. 2006) could also impact convection development in complex ways.

Analysis of microphysical properties of small cumulus clouds over the ocean reveal that in most cases, number concentrations were higher than expected for clean marine clouds, despite low liquid water contents. This suggests that a substantial fraction of dust and other non-marine particles may be acting as cloud condensation nuclei (CCN) in the region. Here, the chemical properties of dust and actual cloud residual nuclei in the tropical Eastern Atlantic, where few measurements exist, are presented. Modeling simulations are used to further study activation of dust as cloud condensation nuclei and its possible role in affecting microphysical properties and precipitation in deep convection.

2. OBSERVATIONS

In the NASA African Monsoon Multidisciplinary Activities (NAMMA) experiment, aerosol particle physiochemical characteristics and cloud size distributions were measured aboard the NASA/University of North Dakota DC-8 aircraft in summer of 2006. Both low-level small cumulus clouds, deep convection, and anvil cirrus outflow from mesoscale systems impacted by various amounts of dust were sampled.

Ambient aerosol and cloud residual particles were collected with a counterflow virtual impactor (CVI, Noone et al., 1988) to assess the percentage and size of dust particles actually incorporated into these clouds. The CVI removes interstitial aerosol and collects and evaporates droplets or ice crystals, while retaining their individual residual nuclei. It can also be used as an ambient aerosol inlet outside of cloud, by turning off the counterflow out the tip. Once collected by the CVI, residual particles were captured by a two-stage jet impactor. The small particle stage collected 0.17 to

0.65 μm diameter unit-density spherical particles, corresponding to 0.11 to 0.48 μm diameter for 1.7 g cm^{-3} density particles. The large particle stage collected larger particles up to several microns in size. For simplicity of display, percentages from both stages have been averaged, but when there are substantial differences as a function of size those differences are noted.

Particulate samples were analyzed by transmission electron microscopy and energy dispersive X-ray spectrometry to detect chemical elements. Individual particles were identified as crustal dust, salts, industrial metals, sulfate, carbonaceous, or mixtures of these types as in Twohy and Poellot (2005). While sulfate aerosols can be routinely detected, volatile material like HNO_3 and volatile organics will be underrepresented by this technique.

3. RESULTS

3.1 Dust Near the Source

On 5 Sept 2006, a mission was flown directly over the Sahara Desert, and air was sampled at several altitudes near and downwind of the dust source.

The first ambient sample was collected at 2.1 km directly over Mauritania in Northwestern Africa. The top of the dust layer was at about 6 km. These particles from near the dust source were primarily unmixed crustal dust, with aluminosilicates being the most common type (Fig. 1). About 20% of the particles (by number) were dust mixed w/ soluble material like sulfur or chlorine, and a few particles were metals without significant silicon which could be different types of mineral dust. The HYSPLIT back trajectory may help explain the mixed particle types, as it showed some interaction of the air with the Atlantic and Mediterranean oceans four to seven days prior to sampling.

A typical X-ray spectrum (Fig. 2) reveals clay-like particles that contain not only insoluble elements like aluminum, silicon, and iron, but also soluble or slightly soluble elements like potassium, calcium and magnesium. As opposed to kaolinite which is more common closer to the equator (Prospero 1981), these smectitic clays are expected to adsorb water and other polar substances (organics, sulfuric and nitric acid).

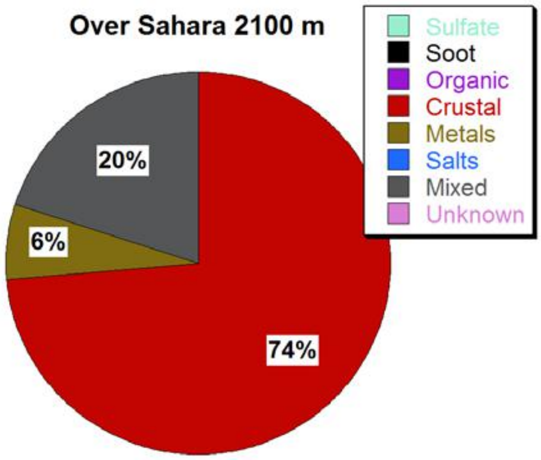

Fig. 1. Percentage of different particle types by number from a NAMMA aerosol sample over Mauritania (100 particles total on 2 size stages analyzed). About 20% of the dust particles were mixed with soluble material. Note that the "metals" category could include iron-containing crustal material with little or no silicon.

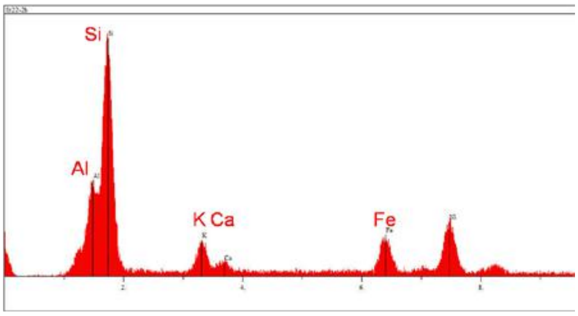

Fig. 2. X-ray spectrum of typical Saharan dust particle collected near the source. Horizontal axis is electron volts (in thousands) and vertical is intensity or counts. Predominant elements are silicon, aluminum, iron, potassium and calcium. The nickel peak is from the collection grid substrate material.

3.2 Interaction with Marine Air

The second ambient sample presented was collected just off the Mauritanian coast at low level (0.3 km). In contrast to the sample directly over the Sahara, Figs. 3, 4 and 5 show that a large percentage of particles in the marine boundary layer were internally mixed particle types. These were primarily dust with sulfate (in the small particle size range) and dust with sea-salt (in the larger size range.) The source of sulfur could either be pollution from Europe, or the ocean itself. The region just off the coast of northwestern Africa is an area of upwelling and high primary productivity, as evidenced by enhanced levels of chlorophyll, DMS and soluble nitrogen (Robinson et al., 2006). Others (Andreae et al, 1986; Levin et al., 1996) have also noted internally mixed dust particles in the marine atmosphere.

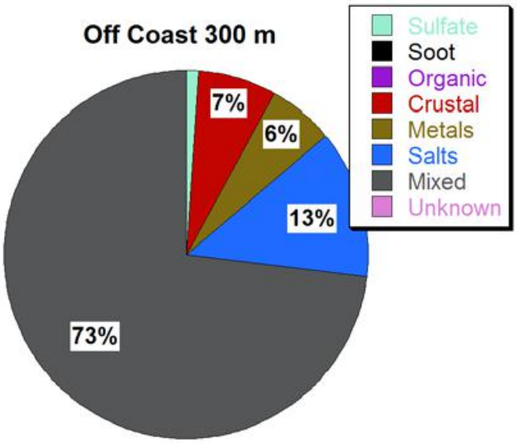

Fig. 3. Composition (% by number) of particles larger than 0.1 µm collected in the marine boundary layer off the coast of western Africa (Mauritania).

Thus small amounts of soluble material are not only naturally present in dust near the source, but increased amounts of soluble material are added through atmospheric processing. This material would make the dust more likely to act as cloud condensation nuclei and be assimilated into the lower and mid-section of convective systems where it may affect the microphysical, radiative and thermodynamic characteristics of these storms. Later, we show that dust and dust/salt/sulfate mixtures comprise a significant fraction of the droplet residual nuclei in small cumulus clouds in this region.

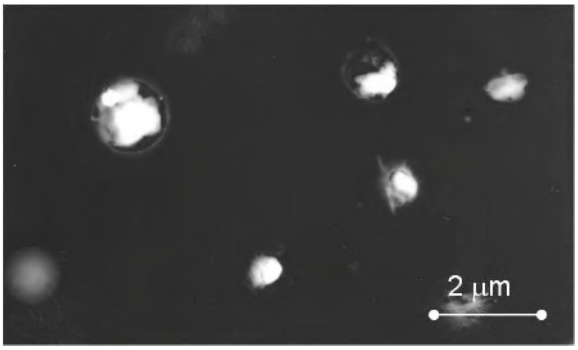

Fig. 4. Aerosol particles collected in the marine boundary layer just off the coast Africa. Particles are mixed with soluble material; an example of elemental analysis given in Fig. 5.

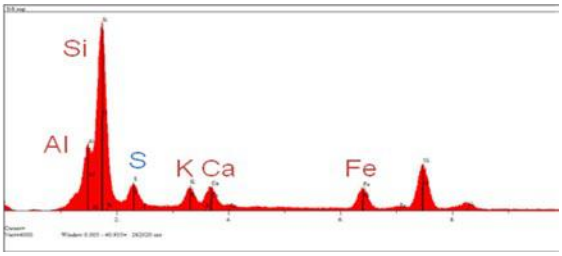

Fig. 5. X-ray spectrum of dust particles in the marine boundary layer mixed with sulfate. Horizontal axis is electron volts (in thousands) and vertical axis is intensity or counts.

3.3 Dust in a MidLevel Cloud

The third sample is representative of dust further offshore, but at higher altitudes with less interaction with marine aerosol. This 3.7 km sample was almost entirely composed of dust aerosol without detectable sulfate or chloride (Fig 6 and 7). A thin water cloud actually embedded in the SAL layer was sampled at 4.3 km. Residual nuclei were also almost entirely dust, with only small amounts of salts and mixed particles present (Fig. 8).

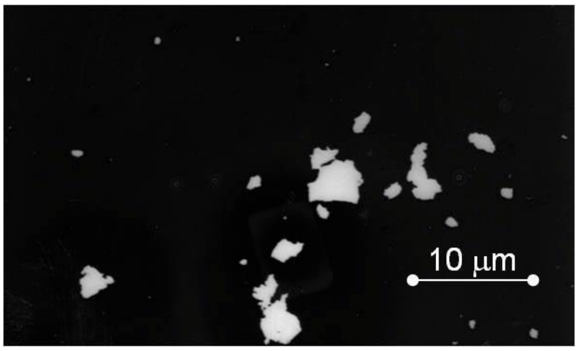

Fig. 6. Aerosol particles collected offshore in the SAL layer at 3.7 km showing dry with little or no non-volatile soluble material.

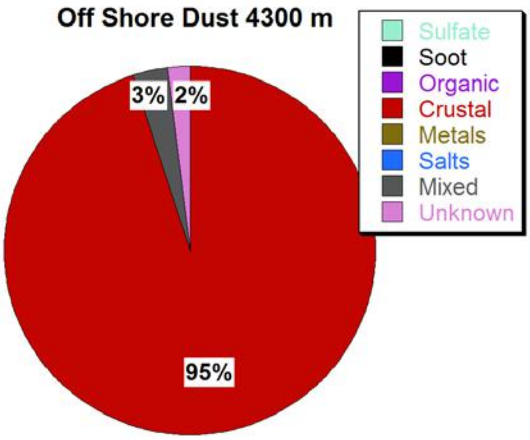

Fig. 7. Composition of aerosol in dust plume at high altitude offshore.

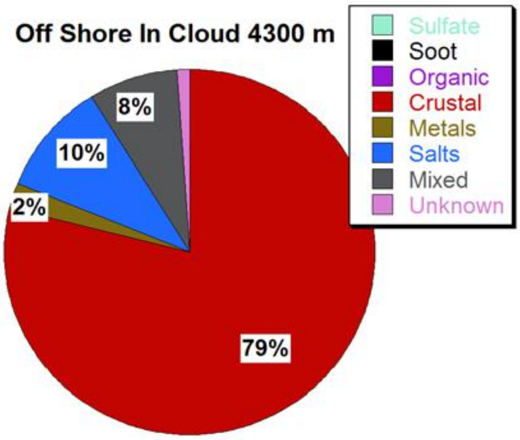

Fig. 8. Composition of residual particles from liquid cloud embedded in dust layer.

3.2 Interaction with Marine Cumulus Clouds

Small cumulus clouds were sampled in the marine boundary layer on several flights. In these cases, the bulk of the dust layer was actually above the low-level clouds, so it was of interest to study if and how the dust interacts with underlying clouds. Samples from three different cloud fields on two days were collected. The first day, shown in Fig. 9 (26 Aug 2006) had back-trajectories from over Africa, while air on the second day (30 Aug 2006) was more from the northeast over the ocean. As expected, high concentrations of salts, most derived from sea-salt and often reacted with sulfate, were observed. But over 40% of the drops sampled contained either solely dust or dust mixed with non-volatile soluble material (Fig. 9). For the three samples (and depending on particle size), the percentage of dust plus internally-mixed cloud residuals ranged from 14% to 54% by number of the total collected.

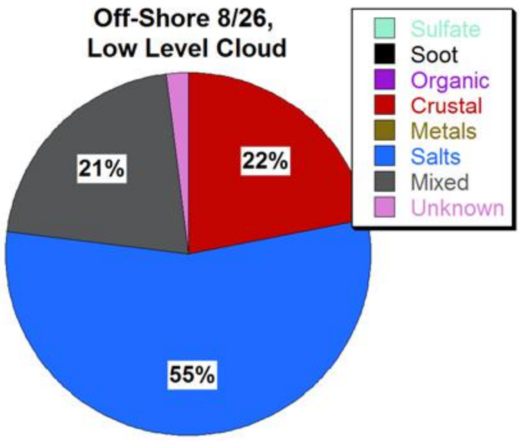

Fig. 9. Percent (by number) of various particles larger than 0.1 μm found in residual nuclei from small cumulus clouds downwind of the Sahara on 8/26/06. Similar results were observed on 8/30/06. "Mixed" particle types were usually crustal dust with soluble material like sulfate or sea-salt.

Average droplet concentrations in these clouds ranged from about 50 to 500 cm^{-3}, with peak concentrations much higher. We estimate, based on residual particle size distributions, that about half or more of the droplet nuclei were measured by this technique. Even if the smaller, unmeasured nuclei contain no dust, this is still a potentially large number of droplets containing dust that may later act as ice nuclei in deep convection.

4. MODELING

A Lagrangian parcel model based on Feingold and Heymsfield (1992) was used to simulate activation of dust as CCN in this environment for a range of different updraft velocities. The original model was modified to parameterize water activity and hygroscopic growth with a single parameter Kappa, κ (Petters and Kreidenweis, 2007). Kappa scales with the fraction of soluble material and is about 1.3 for sodium chloride and about 0.6 for ammonium sulfate. Kappa is 0.00 for a completely insoluble and wettable particle and has been measured to be 0.054 for Saharan dust (Koehler, 2008). This is in general agreement with the typical fraction of soluble and partially soluble material (Ca, K) in fresh Saharan dust as measured in our electron microscope analysis.

The input aerosol distribution was bimodal and based on typical accumulation-mode measurements in the tropical marine boundary layer for the soluble mode (Heintzenberg et al., 2000) and on NAMMA-measured size distributions for the dust mode. Two cases were studied, both with a soluble (sea-salt or sulfate) mode with κ=1.0, N_a=240 cm^{-3}, d_g=0.16, and σ_g=1.5. For the dust mode, N_a=46 cm^{-3}, d_g=0.56, and σ_g=2.0, but with two different Kappa values: κ=0.00 for Case 1, and κ=0.05 for Case 2.

Fig. 10 shows that activation characteristics for the soluble mode are expected to be similar in both Case 1 and 2. For Case 1 with κ=0.00, only a small fraction of dust particles (the largest ones) activate at low updraft velocities. However, the small amount of soluble material present naturally in the dust in Case 2 allows it to be activated with high efficiencies, even at relatively small updraft velocities. In fact, it activates in similar fractions as soluble particles like salt or sulfate.

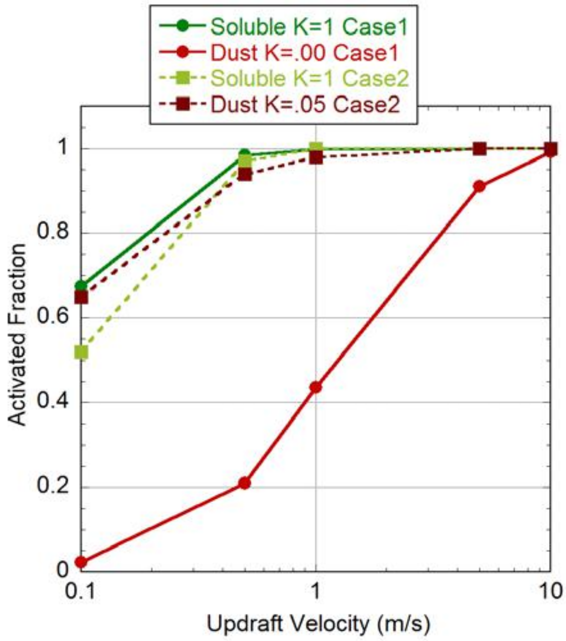

Fig. 10. Fraction of aerosol particles, of each individual mode, activated as a function of modeled updraft velocity. Case 1: Soluble smaller mode with κ =1.0 and larger dust mode with κ =0.00. Case 2: As in Case 1, but with κ =0.05 in the dust mode. Ambient conditions were 900 mb and 292 K. Size distributions described in the text.

Other simulations (not shown) demonstrate that nearly all dust with κ =0.05 would also be activated in the case shown in Fig. 7 and 8, where a cloud formed in an embedded dust layer at mid-levels.

5. DISCUSSION AND CONCLUSIONS

Saharan dust has soluble components that contribute to its ability to act as a cloud condensation nucleus in liquid clouds. This material may be present naturally in the dust at the source, as well as added afterward by interaction with atmospheric gases and particles. Using direct measurements of cloud residual nuclei, we have demonstrated that Saharan dust acts as CCN. In high dust situations such as in the Eastern Atlantic, dust can contribute substantially to the number of droplets in small cumulus clouds.

If even a small fraction of the dust submerged in droplets is lifted to cold temperatures in deep convection, a substantial change in ice concentration is likely. Additional impacts may occur through changes in vertical profiles of latent heat. Interestingly, modeling studies have shown that increased CCN and ice nuclei can increase or decrease precipitation and convective intensity, depending on environmental conditions (Khain et al., 2008). Future modeling work will examine this effect for the Eastern Pacific convective environment.

6. REFERENCES

Andreae, M. O., R. J. Charlson, F. Bruynseels, H. Storms, R. Van Grieken, W. Maenhaut (1986): Internal Mixture of sea salt, silicates, and excess sulfate in marine aerosols, *Science,* 232, 1620–1623.

DeMott, P. J., K. Sassen, M. R. Poellot, D. Baumgardner, D. C. Rogers, S. D. Brooks, A. J. Prenni, and S. M. Kreidenweis (2003): African dust aerosols as atmospheric ice nuclei, *Geophys. Res. Lett., 30*, 1732, doi:10.1029/2003GL017410.

Dunion, J. P. and C. S. Velden (2004): The impact of the Saharan Air Layer on Atlantic tropical cyclone activity, *Bull. Amer. Meteor. Soc*., *85,* 353-365.

Evan, A. T., J. Dunion, J. A. Foley, A. K. Heidinger and C. S. Velden (2006): *Geophys. Res. Lett., 33,* L19813, doi:10.1029/2006GL026408.

Feingold, G. and A.J. Heymsfield (1992): Parameterizations of Condensational Growth of Droplets for Use in General-Circulation Models, *J. Atmos. Sci.*, *49*, 2325-2342.

Field, P. R., O. Mohler, P. Connolly, M. Kramer, R. Cotton, A. J. Heymsfield, H. Saathoff and M. Schnaiter (2006): Some ice nucleation characteristics of Asian and Saharan desert dust, *Atmos. Chem. Phys., 6*, 2991– 3006.

Levin, Z., E. Gaynor and V. Gladstein (1996): The effects of desert particles coated with sulfate on rain formation in the Eastern Mediterranean. *J. Appl. Meteor, 35*, 1511-1523.

Heintzenberg, J., D. C. Covert and R. Van Dingenen (2000): Size distribution and chemical composition of marine aerosols: a compilation and review, *Tellus, 52B*, 1104-1122.

Khain, A., D. Rosenfeld and A. Pokrovsky (2005): *Q. J. R. Meteorol. Soc.*, *131*, 2639–2663.

Khain, A., P. N. BenMoshe and A. Pokrovsky (2008): Factors Determining the Impact of Aerosols on Surface Precipitation from Clouds: Attempt of Classification, *J. Atmos. Sci.*, in press.

Koehler, K. A, S. M. Kreidenweis, P. J. DeMott, A. J. Prenni and M. D. Petters (2007): Potential impact of Owens (dry) Lake dust on warm and cold cloud formation, *J. Geophys. Res. 112,* doi:10.1029/2007JD008413.

Koehler, K.A., 2008: The Impact of Natural Dust Aerosol on Warm and Cold Cloud Formation, Ph.D. Dissertation, Colorado State University, Fort Collins, 207 pp.

Mahowald, N. M. and L. M. Kiehl (2003): *Geophys. Res. Lett*., *30*, 1475, doi:10.1029/2002GL016762.

Noone, K.J., J.A. Ogren, J. Heintzenberg, R.J. Charlson, and D.S. Covert (1988): Design and calibration of a counterflow virtual impactor for sampling of atmospheric fog and cloud droplets, *Aerosol Sci. Technol., 8,* 235-244.

Petters, M.D. and S.M. Kreidenweis (2007): A single parameter representation of hygroscopic growth and cloud condensation nucleus activity, *Atmos. Chem. Phys.*, *7*, 1961-1971.

Prospero, J.M. (1981): Eolian transport to the World Ocean. In The Oceanic Li-

thosphere, The Sea, *Vol. 7*, C. Emiliani, editor, Wiley Interscience, N.Y., *80*, 1-874.
Prospero, J. M. (1996): In *The Impact of Desert Dust from Northern Africa Across the Mediterranean*. Kluwer Academic Publishers, The Netherlands.
Robinson, C. et al. (2006): The Atlantic Meridional Transect (AMT) Programme: A contextual view 1995–2005, *Deep-Sea Research II, 53,* 1485–1515.
Rosenfeld, D., Y. Ridich, and R. Lahav (2001): *Proc. Natl. Acad. Sci*., *98*, 5975-5980.
Twohy, C. H. and M. R. Poellot (2005): Chemical characteristics of ice residual nuclei in anvil cirrus clouds: implications for ice formation processes. *Atmos. Chem. Phys.*, SRef-ID: 1680-7324/acp/2005-5-2289.
Van den Heever, S, G. C. Carrio, W. R. Cotton, P. J. DeMott and A. J. Prenni (2006): Impacts of Nucleating Aerosol on Florida Storms. Part I: Mesoscale Simulations, *J. Atmos. Sci., 63*, 1752-1775.

Acknowledgements

Thanks also due to the crew of the DC-8 aircraft and to Garth Jensen and Julia Sobilik for electron microscopy. Insightful scientific input was provided by Jim Anderson of Arizona State and Joe Prospero of the University of Miami. Finally, we greatly appreciate the leadership of Ed Zipser and his willingness to share flight hours for this work. Twohy, Heymsfield and Bansemer's work was supported by the NASA Radiation Sciences Program under grant #NNX06AC65G. Kreidenweis, Eidhammer and DeMott acknowledge support from NASA's Modeling and Analysis Program (#NNG06GB60G).

CONNECTING HYGROSCOPICITY TO ACTIVATION: HYGROSCOPIC GROWTH AT HIGH RELATIVE HUMIDITIES, SLIGHTLY SOLUBLE SUBSTANCES, AND OTHER EFFECTS

H. Wex[1], T. Hennig[1,6], S. M. Kreidenweis[5], D. Niedermeier[1], E. Nilsson[1,2], R. Ocskay[3], M. D. Petters[5], D. Rose[4], I. Salma[3], M. Ziese[1], and F. Stratmann[1]

[1]Leibniz-Institute for Tropospheric Research, Leipzig, Germany
[2] Lund University, Lund, Sweden
[3]Eötvös University, Institute of Chemistry, Budapest, Hungary
[4]Max Planck Institute for Chemistry, Biogeochemistry Dep., Mainz, Germany
[5]Colorado State University, Fort Collins, Colorado, USA
[6]Stockholm University, Stockholm, Sweden

1. INTRODUCTION

In the past, it often has been tried to connect the hygroscopic growth of aerosol particles with their activation to cloud droplets using the Köhler equation (e.g., *Covert et al.* [1998], *Brechtel and Kreidenweis* [2000], *Svenningsson et al.* [2006]). In these past studies, measurements of the hygroscopic growth were only possible up to 95% relative humidity (RH). In general, connecting the hygroscopic growth of particles to their activation by using the Köhler equation was successful in general when relatively simple substances (e.g., ammonium sulfate) were examined. However, for atmospheric aerosol particles and for mixtures of substances including organic compounds, the number of activated particles predicted from measured hygroscopic growth by the use of a Köhler model often exceeded the measured number (*Broekhuizen et al.*, 2006).

During four measurement campaigns at the ACCENT (Atmospheric Composition Change – the European NeTwork of Excellence) infrastructure site LACIS (Leipzig Aerosol Cloud Interaction Simulator, [*Stratmann et al.*, 2004]), hygroscopic growth up to very high RHs (above 99%) and activation were measured for different types of aerosol particles. This article gives an overview of the results obtained during these campaigns regarding the possibilities to establish connections between hygroscopic growth and activation behavior.

2. MEASUREMENTS

The following substances were used as particle material:
(a) NaCl and three different seawater samples;
(b) soot particles (generated with a spark-generator) that were coated with either ammonium sulfate or levoglucosan (during the ACCENT campaign LExNo (LACIS Experiment in November));
(c) two different atmospheric HULIS (HUmic LIke Substances) samples, collected and prepared in Budapest;
(d) mixtures of succinic acid with ammonium sulfate;
(e) secondary organic aerosol (SOA).

While particles used in (a), (c) and (d) were generated from a solution, using an atomizer, the SOA particles were generated in the gas phase from α-pinene and ozone.

LACIS measured hygroscopic growth and activation for the samples given in (a) and (c) and hygroscopic growth for samples examined in (d) and (e). A HH-TDMA (High Humidity Tandem Differential Mobility Analyzer, [*Hennig et al.*, 2005]) and a continuous-flow streamwise thermal-gradient CCNc (Cloud Condensation Nucleus counter [*Roberts and Nenes*, 2005]) were used to quantify hygroscopic growth and activation during LExNo, i.e. (b), respectively, and a CCNc of the above mentioned type was used to measure the activation for the SOA particles (e). LACIS and the HH-TDMA, measured the hygroscopic growth at high relative humidities (RHs) above 95%, with the HH-TDMA measuring up to 98% and LACIS up to 99.5% RH.

3. MODELING

The modeling was based on the approach described in *Wex et al.* [2007], using a parameter ρ_{ion} defined as: $\boldsymbol{\rho_{ion} = (\Phi \nu \rho_{sol}) / M_{sol}}$ (with the osmotic coefficient Φ, ν being the number of ions the substance dissociates to in solution, the density ρ_{sol}, and the molecular weight M_{sol} of the solute). This parameter ρ_{ion} is included in the water activity term in one of the possible formulations of the Köhler theory. This modeling approach is, in principle, similar to the approach used by Petters and Kreidenweis [2007], in that the hygroscopic growth is described by a single parameter κ in the Raoult (or solubility) term.

The parameter ρ_{ion} combines all parameters of the solute influencing the water activity, for which values are not known a priori. With this approach, the number of unknowns in the Köhler equation is reduced to two: ρ_{ion} in the water activity term and the surface tension σ in the Kelvin term.

In a first step, for the data analysis of the different particle types, ρ_{ion} was derived from measured hygroscopic growth together with using the surface tension of water (σ_w = 72.8mN/m). ρ_{ion} was adjusted such, that the Köhler equation reproduced the measured particle sizes at the respective RHs. Then, the activation was modeled using the values of ρ_{ion} derived at RHs above 95%, together with σ_w. The resulting calculated critical super-saturations needed for activation were compared to the measured ones. In this context, for HULIS particles, a better agreement between measured and modeled activation data was found when a surface tension reduction was considered, using a concentration dependent value for the surface tension (see Section 4.2). For SOA particles, the concept of a constant ρ_{ion} could not be used (Section 4.4).

4. COMPARISON OF MEASURED AND MODELED ACTIVATION BEHAVIOR

4.1. Particles generated from NaCl and seawater and coated soot particles. For these substances, good agreement between measured and modeled activation behavior was obtained when using the surface tension of water. This was found for both, particles from seawater samples (see Figure 1) and coated soot particles (see Figure 2). The slopes of the fits (which were forced through zero) and the correlation coefficients are also given in Figures 1 and 2. Details on the examination of the seawater samples can be found in *Niedermeier et al.* [2008].

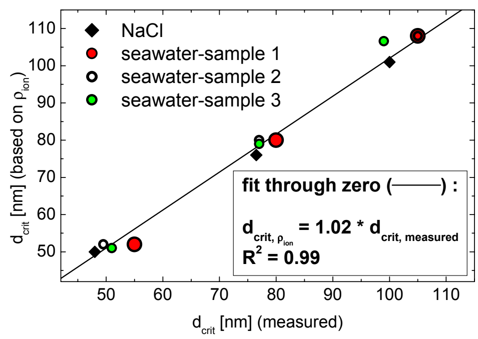

Fig. 1: *Measured and modeled critical diameters for the NaCl particles and for the particles generated from seawater samples.*

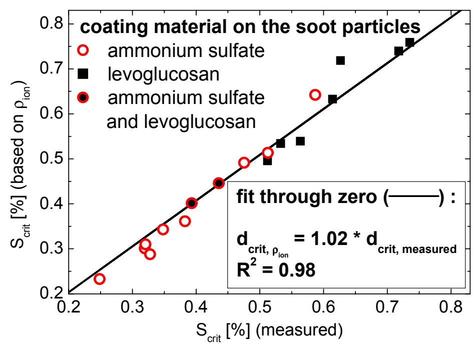

Fig. 2: *Measured and modeled critical super-saturations for the coated soot particles examined during LExNo.*

4.2 HULIS particles. Two HULIS samples were investigated, both extracted from urban aerosol samples from Budapest. Measurements were performed for dry particle sizes in the range from 40 to 160 nm. HULIS has been described as a surface-active substance in the past [*Salma et al.*, 2006]. When using the surface tension of water, the critical super-saturations (S_{crit}) predicted from the hygroscopic growth behavior exceeded the measured values for S_{crit} above 0.6%, which corresponds to dry particle sizes below 70 nm. This can be seen in Figure 3.

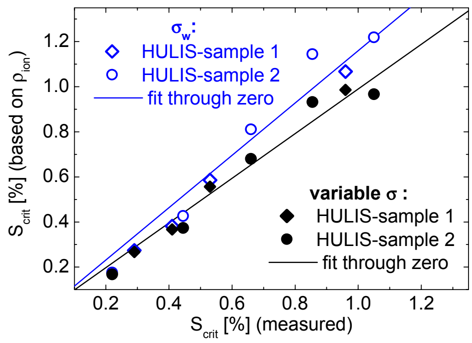

Fig. 3: *Measured and modeled critical super-saturations for the HULIS particles, for the two approaches, one using σ_w and the other one using a variable σ.*

For a fit through zero, a slope of 1.16 is obtained for this dataset. Also shown in Figure 3 are values of S_{crit} that were obtained using a variable, i.e., concentration-dependent surface tension. This variable *σ* was determined following *Szyszkowski* [1908], who suggested a variable *σ* for solution droplets that contain surface-active substances, depending on the concentration of this substance. Particles with smaller dry diameters have a smaller growth factor at the point of activation. Therefore they are more concentrated and can have a smaller *σ*. By using a variable *σ*, the agreement between measured and modeled S_{crit} was improved, compared to using σ_w, as can be seen in Figure 3. The slope of the fit through zero when using a variable *σ* is 0.99. Figure 4 shows the derived variable *σ* for the two HULIS samples and indicates the values for *σ* for the droplets activating on the different dry particle sizes. The above analysis shows the need to account for a concentration dependent *σ* for HULIS particles, and is described in detail in *Ziese et al.* [2008].

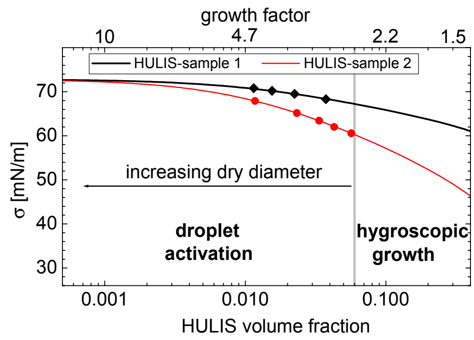

Fig. 4: *Values for σ varying with concentration for the two different HULIS samples. The straight grey line roughly divides the concentration range in a hygroscopic growth and an activation regime. The symbols indicate the values of σ for the droplets activating on the different dry particle sizes in the range from 40 nm to 160 nm.*

4.3. Hygroscopic growth of slightly soluble substances. For particles consisting of a mixture of succinic acid and ammonium sulfate, only hygroscopic growth was measured. This was done for particles with different mass fractions of the two substances, which are indicated in Figure 5. Besides measuring, the hygroscopic growth was also modeled for the mixed particles, following the theory given in *Laaksonen et al.* [1999] and *Henning et al.* [2005]. It can be seen in Figure 5, that measurements and theory are in agreement. Particles on the deliquescence branch (denoted “dry” in Figure 5) differ increasingly from those on the efflorescence branch (denoted “wet”) with an increasing mass fraction of succinic acid. The RH at which deliquescence and efflorescence are in agreement, i.e. at which the particle has fully dissolved, also increases with an increasing mass fraction of succinic acid. It is above 98% RH for a succinic acid mass fraction of 90%, and still at 97% RH for particles with a mixture of 50% succinic acid and ammonium sulfate, each.

This shows clearly, that the

assumption of a constant ρ_{ion} is not necessarily justified, not even within the range of high RHs above 95%. Values derived for ρ_{ion} for slightly soluble substances or for mixtures including such substances at RHs below their full deliquescence would lead to an underestimation of ρ_{ion} and, consequently, an overestimation of S_{crit}.

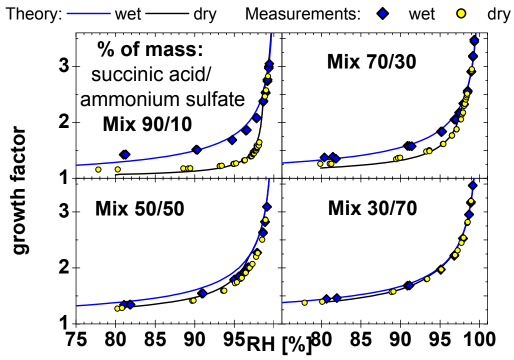

Fig. 5: *Growth factors for particles with a dry diameter of 250 nm, consisting of different mass fractions of succinic acid and ammonium sulfate. Both, deliquescence ("dry") and effloreszence ("wet") was measured.*

4.4. SOA particles. For SOA particles generated from different precursor gases (e.g monoterpenes) and for both, photo-oxidation as well as oxidation by ozone, OH or other oxidizing species, in general a slight hygroscopic growth is observed [e.g. Virkkula et al., 1999; *Varutbangkul et al.*, 2006], while they are commonly found to be more CCN active than their hygroscopic growth factor would suggest [e.g. *VanReken et al.*, 2005, *Prenni et al.*, 2007]. Assuming a constant ρ_{ion} derived from measured hygroscopic growth at RHs below 95% implies, that a very low surface tension of about 30 mN/m is needed to explain the measured CCN activity [e.g. *Prenni et al.*, 2007]. Figure 6 shows values of ρ_{ion} derived from hygroscopic growth and activation measured with LACIS and with the CCNc, respectively. The values were derived assuming different surface tensions, and are given as a function of the SOA volume concentration. Filled symbols originate in measured hygroscopic growth, while open symbols are based on measured activation diameters. Two things can be seen from Figure 6: 1) The hygroscopicity increases as the particles become more dilute. This change in hygroscopicity becomes clearly obvious only at RHs above 98% and thus could not be observed in the past. This explains the low values of σ that had to be assumed in the past, when a constant hygroscopicity was assumed. 2) A value of σ of 30 mN/m is too low to get a consistent transition from hygroscopic growth to activation data, i.e. σ can reasonably be assumed to be not lower than 50mN/m.

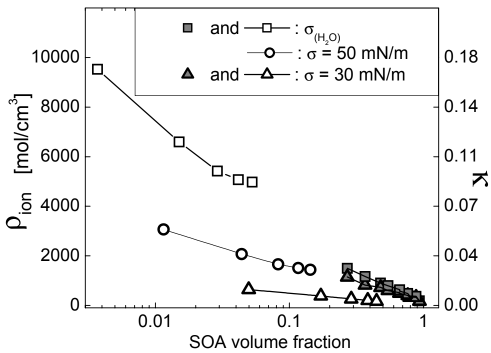

Fig. 6: *Hygroscopicity of SOA particles derived from LACIS (filled symbols) and CCNc (open symbols) measurements assuming different values for σ, expressed as ρ_{ion} (or κ) as a function of the SOA volume fraction.*

5. CONCLUSIONS

The results gained in the course of the experiments described above clearly indicate that a usage of the surface tension of water in the Köhler equation may result an erroneous prediction of the activation behavior, if surface-active substances are present in the droplet. Also, it was shown that substances (or mixtures of substances) exist for which the assumption of a constant hygroscopicity is not valid. Measurements of hygroscopic growth up to very high RHs, together with measurements of the activation behavior are necessary to gain enough insight to be able to consistently describe the water uptake of particles over the whole range from hygroscopic growth up to activation, and therefore to gain an insight on the importance of the different contributing parameters and processes.

BIBLIOGRAPHY

Brechtel, F. J., and S. M. Kreidenweis (2000), Predicting particle critical supersaturation from hygroscopic growth measurements in the humidified TDMA. Part I: theory and sensitivity studies, *J. Atmos. Sci.*, *57*, 1854-1871.

Broekhuizen, K., R. Y.-W. Chang, W. R. Leaitch, S.-M. Li, and J. P. D. Abbatt (2006), Closure between measured and modeled cloud condensation nuclei (CCN) using size-resolved aerosol composition in downtown Toronto, *Atmos. Chem. Phys., 6*, 2513-2524.

Covert, D. S., J. L. Gras, A. Wiedensohler, and F. Stratmann (1998), Comparison of directly measured CCN with CCN modeled from the number-size distribution in the marine boundary layer during ACE1 at Cape Grim, Tasmania, *J. Geophys. Res.*, *103*, 16597-16608.

Hennig, T., A. Massling, F. J. Brechtel, and A. Wiedensohler (2005), A tandem DMA for highly temperature-stabilized hygroscopic particle growth measurements between 90% and 98% relative humidity, *J. Aerosol Sci.*, *36*, 1210-1223.

Henning, S., T. Rosenorn, B. D'Anna, A. A. Gola, B. Svenningsson, and M. Bilde (2005), Cloud droplet activation and surface tension of mixtures of slightly soluble organics and inorganic salt, *Atmos. Chem. Phys.*, *5*, 575-582.

Laaksonen, A., P. Korhonen, M. Kulmala, and R. J. Charlson (1998), Modification of the Köhler equation to include soluble trace gases and slightly soluble substances, *J. Atmos. Sci.*, *55*, 853-862.

Niedermeier, D., H. Wex, J. Voigtländer, F. Stratmann, E. Brüggemann, A. Kiselev, H. Henk, and J. Heintzenberg (2008), LACIS-measurements and parameterization of sea-salt particle hygroscopic growth and activation, *Atmos. Chem. Phys.*, *8*, 579-590.

Petters, M. D., and S. M. Kreidenweis (2007), A single parameter representation of hygroscopic growth and cloud condensation nucleus activity, *Atmos. Chem. Phys.*, 7, 1961-1971.

Prenni, A. J., M. D. Petters, S. M. Kreidenweis, P. DeMott, and P. J. Ziemann (2007), Cloud droplet activation of secondary organic aerosol, *J. Geophys. Res.*, *112*, doi:10.1029/2006JD007963.

Roberts, G., and A. Nenes (2005), A continuous-flow streamwise thermal- gradient CCN chamber for atmospheric measurements, *Aerosol Sci. Technol.*, *39*, 206-221.

Salma, I., R. Ocskay, I. Varga, and W. Maenhaut (2006), Surface tension of atmospheric humic-like substances in connection with relaxation, dilution, and solution pH, *J. Geophys. Res.*, *111*, doi:10.1029/2005JD007015.

Stratmann, F., A. Kiselev, S. Wurzler, M. Wendisch, J. Heintzenberg, R. J. Charlson, K. Diehl, H. Wex, and S. Schmidt (2004), Laboratory studies and numerical simulations of cloud droplet formation under realistic super-saturation conditions, *J. Atmos. Oceanic Technol.*, *21*, 876-887.

Svenningsson, B., et al. (2006), Hygroscopic growth and critical supersaturations for mixed aerosol particles of inorganic and organic compounds of atmospheric relevance, *Atmos. Chem. Phys.*, *6*, 1937-1952.

Szyszkowski, B. (1908), Experimentelle Studien über kapillare Eigenschaften der wässrigen Lösungen von Fettsäuren, *Z. phys. Chem., 64*, 385-414.

VanReken, T. M., N. L. Ng, R. C. Flagan, and J. H. Seinfeld (2005), Cloud condensation nucleus activation properties of biogenic secondary organic aerosol, *J. Geophys. Res.*, *110*, D07206, doi:10.1029/02004JD005465.

Varutbangkul, V., F. J. Brechtel, R. Bahreini, N. L. Ng, M. D. Keywood, J. H. Kroll, R. C. Flagan, J. H. Seinfeld, A. Lee, and A. H. Goldstein (2006), Hygroscopicity of secondary organic aerosols formed by oxidation of cycloalkenes, monoterpenes, sesquiterpenes, and related compounds, *Atmos. Chem. Phys.*, *6*, 2367-2388.

Virkkula, A., R. van Dingenen, F. Raes, and J. Hjorth (1999), Hygroscopic properties of aerosol formed by oxidation of limonene, α-pinene, and β-pinene, *J. Geophys. Res.*, *104*, 3569-3579.

Wex, H., T. Hennig, I. Salma, R. Ocskay, A. Kiselev, S. Henning, A. Massling, A. Wiedensohler, and F. Stratmann (2007), Hygroscopic growth and measured and modeled critical super-saturations of an atmospheric HULIS sample, *Geophys. Res. Lett.*, *34*, doi:10.1029/2006GL028260.

Ziese, M., H. Wex, E. Nilsson, I. Salma, R. Ocskay, T. Hennig, A. Massling, and F. Stratmann (2008), Hygroscopic growth and activation of HULIS particles: experimental data and a new iterative parameterization scheme for complex aerosol particles, *Atmos. Chem. Phys.*, *8*, 1855-1866.

PRECIPITATION TYPE AND RAINFALL INTENSITY FROM THE PLUDIX DISDROMETER DURING THE WASSERKUPPE CAMPAIGN

Clelia Caracciolo[1], Franco Prodi[1,2], Leo Pio D'Adderio[2] and Eckhard Lanzinger[4]

[1]University of Ferrara, Dept. of Physics, Ferrara, Italy, caracciolo@fe.infn.it
[2]Institute of Atmospheric and Climate Sciences (ISAC), Bologna, Italy
[3]Deutscher Wetterdienst (DWD), Hamburg, Germany

1. INTRODUCTION

Pludix is an X-band disdrometer based on the Doppler principle, providing information on the drop size distribution (DSD) and rainfall intensity (R). In the past few years the instrument has been involved in various measuring campaigns (e.g. Caracciolo et. al., 2006), testing its performances in R and DSD measurements, and comparing it with other disdrometers of different operating principles. The instrument has shown good capabilities in both R and DSD estimations. This work describes, for the first time, the research done to determine the capabilities and limitations of Pludix also as a Present Weather Sensor (PWS). Twelve precipitation codes are selected in liquid, mixed and solid precipitation. Pludix is compared with the reference observations of a human observer (hereinafter HO) during a two-year campaign held at the Wasserkuppe weather station – Germany (Bloemink and Lanzinger, 2005). Moreover Pludix is compared with other PW instruments present at the site: the Vaisala FD12P-PWS (V1.83 1999-11-19, SN: 30301) and the optical disdrometer Parsivel M300 (PMTech). The Parsivel M300 used here (Löffler-Mang and Joss, 2000) was produced by PMTech (Germany) and is no longer on the market. The instrument has been completely redesigned in hardware and software and it is now produced by OTT (Germany) under the name "OTT Parsivel". We also test the performance of Pludix in measuring rainfall intensity, comparing it with the other sensors for some significant events. Finally, some drop size spectra analyses for Pludix and the optical disdrometer Parsivel are shown.

2. INSTRUMENTS SET-UP AND METHODOLOGY

Pludix (referred to as Plx in the following tables and figures) is compared with FD12P, Parsivel (referred to as Pars) and human observations during a campaign held at the Wasserkuppe weather station, located in central Germany at an height of 950 m (asl). The instruments are all collocated within a field of about 50 m^2, with Pludix and Parsivel almost neighbours.

Pludix is a rain-gauge/disdrometer based on the analysis of an X-band (9.5 GHz) continuous wave radar signal backscattered by hydrometeors (Prodi et. al., 2000). The shape of the power spectrum in the 0-1024 Hz frequency range has various characteristics, depending on the different precipitation types. Twelve precipitation codes, according to WMO-4680, are considered by analysing the characteristics of the power spectrum in terms of maximum intensity, maximum location in the frequency range and spectrum amplitude. The precipitation types corresponding to the selected codes are: rain (codes 61, 62, 63 – rain not freezing slight, moderate, heavy), snow (codes 71,72,73 – snow slight, moderate, heavy), hail (codes 93, 96 – thunderstorm slight or moderate, heavy with hail), ice crystals (code 78), mixed precipitation (codes 67, 68 - rain and snow slight, moderate or heavy), no significant weather observed (code 00). The Pludix data consist also of number of raindrops n_i of diameter D_i in 21 categories, ranging in size from 0.8 to 7.0 mm, with a constant step of 0.3 mm. The rainfall rate in mm/h is computed from the DSD information. All data are given in 1-minute time intervals.

The reference at Wasserkuppe consists of data from various sources (Bloemink and Lanzinger, 2005). The HO is located about 100 m from the instruments, reporting PW 24 hrs/day with a 1-minute time resolution. A number of instruments report precipitation intensity, 2m temperature, 2m relative humidity, 2m wind speed and dew point temperature.

The FD12P measures the scattering of light of a small volume of the atmosphere. If there are precipitation particles present in this volume, they lead to peaks in the scattered light (FD12P Interface Control Document, 2007). The peaks are related to particle size. Separately, the FD12P has a capacitive sensor (DRD 12) that measures the water content of the precipitation. Combining these two quantities leads to a discrimination between large particles with low water content (i.e. snow) and small particles with high water content (rain). Fine tuning is done by choosing appropriate limits for, for instance, mixed precipitation, hail and freezing rain. In addition, temperature constraints, maximum particle size and a selection algorithm to determine the most significant precipitation type, are used. Every 15 seconds, an “instant” precipitation type is given (among other parameters). Here, the information on the precipitation intensity in mm/h and the fifty-two codes supported by the WMO code table 4680 are used.

Parsivel is a laser-based optical system; a laser sensor produces a horizontal strip of light (Parsivel M300, PMTech Manual, 2002). Precipitation particles passing through the laser beam block off a portion of the beam corresponding to their diameter, thus reducing the output voltage. To determine the particle speed, the duration of the signal is measured. The size range of liquid precipitation particles is 0.2-5mm, the size range of solid precipitation is 0.2-25mm (32 classes), the velocity range is 0.2-20 m/s (32 classes). From particle size and speed, different parameters are derived. We use information on the rain intensity R in mm/h, the DSD in $mm^{-1}m^{-3}$ and the precipitation type (eighteen WMO-4680 precipitation codes). All data are given in 30-seconds time intervals.

Two years of data are analysed (from December 2000 to December 2002); in this period, more than 300 precipitation events were selected, in terms of both liquid and solid precipitation, allowing for a good evaluation of Pludix capabilities. All data are synchronized in 1-minute time intervals, leading to a maximum of 1440 measurements per day. The HO precipitation type, reported in the WMO code 4677, is changed into code 4680 (automatic observation) to match with the output of the other instruments. Differences in Pludix ground noise are observed passing from autumn to summer months, determining the necessity to consider different precipitation type identification criteria for the different seasons.

3. RESULTS AND DISCUSSION

3.1 determination of the capabilities of Pludix as a PWS

Tab. 1 shows the percentage of agreement/disagreement between Pludix and HO (taken as the truth) for the twelve WMO-4680 codes considered by Pludix for the two years of data. The results show that Pludix performs quite well in distinguishing the precipitation type, and is generally in agreement with the HO, especially for the rain codes (codes 61, 62 and 63). The percentage of agreement for codes 62 and 63 grows to 51% and 73%, respectively, during the summer months (June, July and August). Consider now the codes grouped by precipitation type. When HO gives code 61, Pludix gives a rain code in 31.67% of cases. When HO gives code 62, Pludix gives a rain code in 76.69% of cases. When HO gives code 63, Pludix gives a rain code in 81.51% of cases. When HO gives code 67, Pludix gives a mixed code in 12.8% of cases (a rain code in 17.46% of cases, a snow code in 16.99% of cases). When HO gives code 68, Pludix gives a mixed code in 16.11% of cases (a rain code in 43.89% of cases, a snow code in 34.99% of cases). When HO gives code 71, Pludix gives a snow code in 13.85% of cases. When HO gives code 72, Pludix gives a snow code in 42.52% of cases.

Percentage of agreement/disagreement Plx-HO (taken as the truth) – Codes 4680													
	61	**62**	**63**	**67**	**68**	**71**	**72**	**73**	**78**	**93**	**96**	**00**	**other**
61	17.99	13.10	0.58	4.30	0.01	0.29	0.33	0.43	3.45	0.08	0.02	58.61	0.80
62	23.58	48.59	4.52	5.53	0.05	0.20	0.72	0.54	1.05	0.81	0.29	13.01	1.09
63	3.36	30.25	47.90	0.84	0	0	0	0	0	3.36	3.36	10.92	0
67	8.54	6.73	2.19	12.39	0.41	3.83	6.24	6.92	1.44	0	0	48.25	3.05
68	5.56	32.22	6.11	14.44	1.67	1.11	19.44	14.44	0	0.56	0	2.22	2.22
71	5.29	0.19	0.05	5.12	0.02	6.03	4.67	3.15	6.07	0	0	67.64	1.78
72	6.68	0.56	0.24	10.22	0.01	18.03	14.90	9.59	3.26	0	0	33.85	2.66
78	5.63	0.01	0	1.20	0	0.60	0.50	0.11	9.00	0	0	82.50	0.43
00	2.76	0.04	0.02	2.06	0	0.52	0.40	0.47	3.68	0	0	89.17	0.89
other	4.35	1.72	0.20	3.10	0	0.51	0.25	0.30	5.35	0.02	0.03	83.50	0.67
Counts													
HO	55684	10923	119	6390	180	32719	6800	0	7142	0	0	129567	225857
Plx	29140	17170	1536	15934	61	5501	4344	3747	21836	180	105	371605	4222

Tab. 1: Percentage of agreement/disagreement between Pludix and HO (taken as truth) for the 12 WMO-4680 codes considered by Pludix. Two years of data are considered.

Consider now the percentage of agreement/disagreement between Pludix and the other instruments (taken as the truth) for the twelve codes considered by Pludix for the two years of data (Tab. 2).

Agreement/disagreement % Plx-HO (taken as the truth) – Codes 4680					
	liquid	**mixed**	**solid**	**no rain**	**other**
liquid	39.40	4.52	4.17	51.06	0.85
mixed	18.20	12.89	18.89	46.99	3.03
solid	5.82	5.28	22.20	64.99	1.70
no rain	2.82	2.06	5.06	89.17	0.89
Agreement/disagreement % Plx-FD12P (taken as the truth) – Codes 4680					
	liquid	**mixed**	**solid**	**no rain**	**other**
liquid	45.18	5.59	4.50	43.69	1.04
mixed	12.09	9.99	24.08	51.92	1.92
solid	5.33	4.53	22.31	66.31	1.51
no rain	3.27	2.08	5.73	87.90	1.02
Agreement/disagreement % Plx-Pars (taken as the truth) – Codes 4680					
	liquid	**mixed**	**solid**	**no rain**	**other**
liquid	55.37	8.49	2.58	32.23	1.33
mixed	9.61	4.93	17.40	66.79	1.26
solid	5.51	1.90	31.99	58.99	1.61
no rain	3.35	2.26	7.33	86.35	0.70

Tab. 2: Percentage of agreement-disagreement between Pludix and the other sensors taken as the truth for precipitation categories. Two years of data are considered.

Pludix performs quite well in the case of liquid precipitation, and is in good agreement with Parsivel for solid precipitation. The percentage of agreement with HO for the rain, mixed and solid category grows to 47%, 17% and 28%, respectively, during autumn, winter and summer months. Note that the Pludix percentage of agreement in the case of mixed precipitation is low, and in these situations our instrument detects a high percentage of solid precipitation. This is probably due to the fact that in the case of mixed precipitation the refraction index is the one of water (the maximum intensity is high) but the terminal velocity (therefore the frequency) is that of snow; therefore Pludix identifies a snow code instead of a mixed code.

In the following analysis we show that Pludix works better than the others in the case of rain (see also Sect. 3.2). The two years of data are considered. When Pludix gives code 61 consider how many minutes the other three sensors give code 62 or 63 (Fig. 1a). The HO always reports a temperature between 0-15°C during these minutes. Code 63 is probably wrong because R is always below 5 mm/h. When Pludix gives code 63, consider how many minutes the other three sensors give code 61 or 62 (Fig. 1b). The HO always reports a temperature between 0-20°C during these minutes. The rainfall rate is over 10 mm/h for a high percentage of minutes, indicating that the code 63 indicated by Pludix is probably the most reliable.

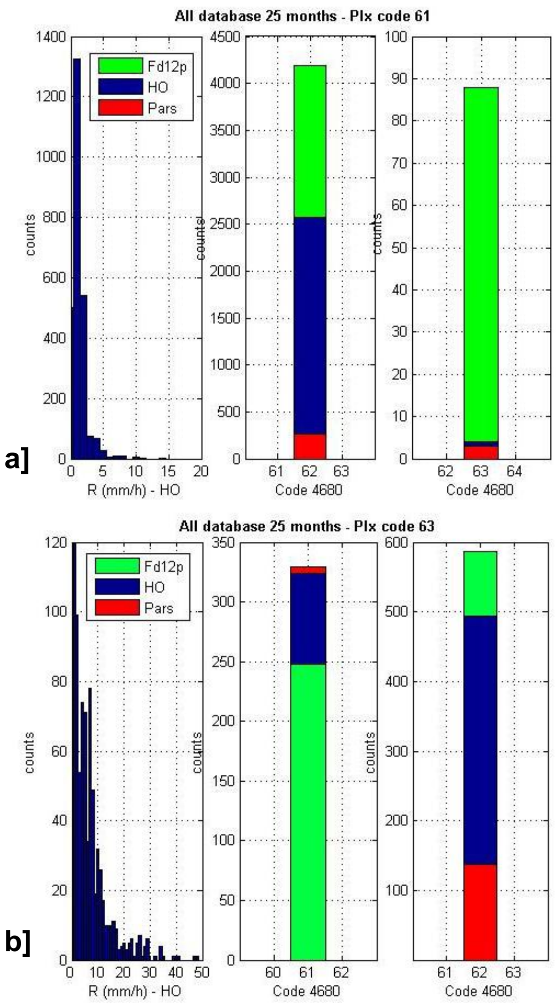

Fig. 1: **a]** HO rainfall rate (mm/h), HO temperature (°C), HO, FD12P and Parsivel WMO-4680 codes 62 and 63 when Pludix gives code 61; **b]** HO rainfall rate (mm/h), HO temperature (°C), HO, FD12P and Parsivel WMO-4680 codes 61 and 62 when Pludix gives code 63. Two years of data are considered.

Fig. 2 shows the 1-minute power spectra of Pludix for some coincident minutes in which Pludix is in agreement with HO for some of the 12 Pludix selected codes (except code 93, not reported by HO). These figures are considered as reference for a subsequent analysis. The frequency interval is divided into three parts: the snow band between 0-200Hz; the rain band between 200-600Hz; the hail band over 600Hz. It is important to point out that these values are indicative. For the rain band (codes 61, 62 and 63), the power spectrum has a characteristic maximum whose frequency is higher as rain intensity grows; the maximum location in the frequency band also usually grows as the rain intensity grows. Moreover the heavy precipitation usually has relatively flattened spectra, with narrow and emphasized maxima at higher frequencies, often with an irregular shape. The presence of heavy rain with hail (codes 93 and 96) is indicated by the high frequency part of the spectrum, with one or more peaks over 550 Hz. The presence of snow (codes 71, 72 and 73) is indicated by a bell-shaped spectra, with a maximum totally in the lower part of the spectrum (below 200 Hz). The bell is usually quite narrow, indicating rather similar terminal snowflake velocities. The maximum is sometimes shifted toward higher or lower frequencies, in the case of higher or lower terminal fall velocities, respectively. The case of rain and snow (codes 67 and 68) is very similar to the rain-snow cases. There is a bell-shaped spectrum of the snow and a hyperbolic extension toward the high frequencies of the rain. More often a single maximum is present, usually at low-medium frequencies, in the transition zone between rain and snow. The presence in the atmosphere of frozen hydrometeors with low terminal velocities gives rise to peaks in the lower part of the spectrum (below 50 Hz). This bristle-like spectrum indicates a superposition of almost monodisperse size distributions of ice crystals (code 78).

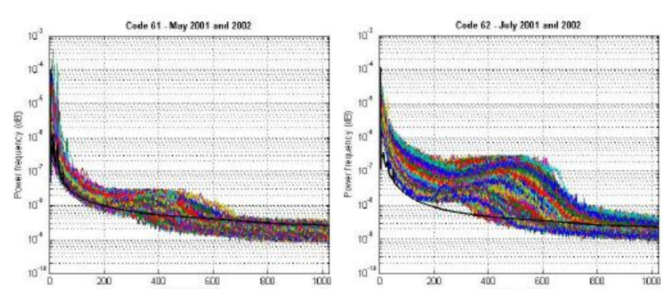

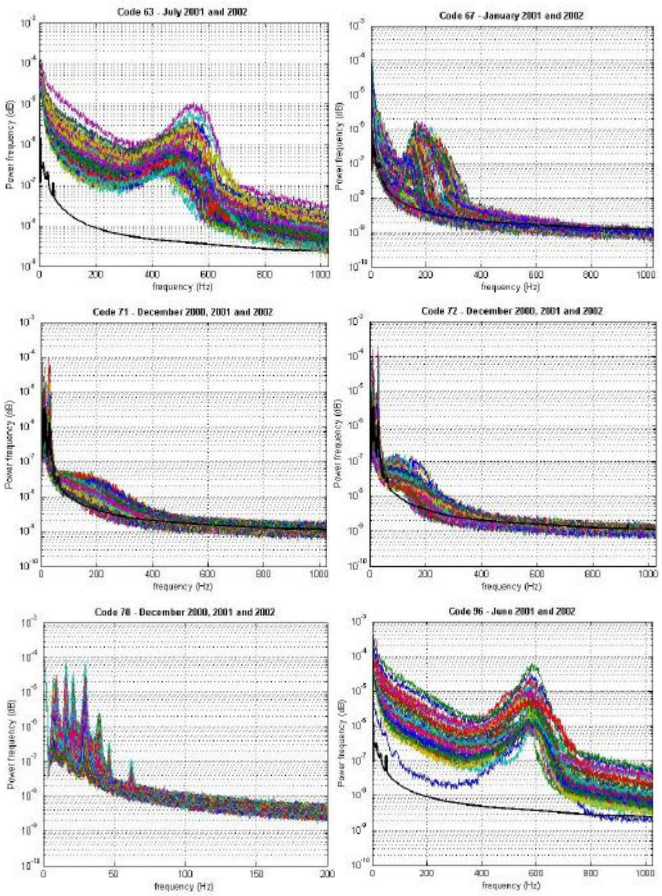

Fig. 2: Typical meteorological situations detected by Pludix in Wasserkuppe from December 2000 to December 2002.

The following analysis shows that Pludix detects some situations (especially rain, rain-shower with hail, ice crystals) that the HO does not detect (Fig. 3). The two years of data are considered. The situations of agreement between HO and Pludix are discarded. When HO gives code 00, Pludix gives rain codes (see, for example, Fig 3a showing the August spectra, where Pludix gives 0.8% of code 61, 0.2% of code 62, 0.1% of code 63). When HO gives code 62, Pludix gives a different rain code. For example in May (Fig. 3b), in 17.9% of cases Pludix gives code 61 and in 8.1% of cases it gives code 63. In December (Fig. 3c), when HO gives code 71, Pludix gives in 8% of cases code 67, in 4% of cases code 72, in 2% of cases code 73 and in 8% of cases code 78. In December (Fig. 3d), when HO gives code 72, Pludix gives in 14.62% of cases code 67 and in 21.82% of cases code 71. It is supposed that Pludix performs better than HO in these cases; in fact it can be seen that the spectra shown in Fig. 3 are similar to the ones shown in Fig. 2, where Pludix is in agreement with the HO for the corresponding codes.

Consider now again Tab. 1. Code 78 is not well detected by Pludix because its spectrum is quite similar to the ground noise (low percentage agreement with HO). Codes 61 and 71 are not well detected because our instrument is less sensitive to these slight precipitations; moreover the HO samples on a large measurement volume, while Pludix samples on a small measurement volume (about 3 m high and 1 m wide above it). When the HO gives codes 61 and 71, Pludix gives code 00 in a high percentage (see Tab. 1).

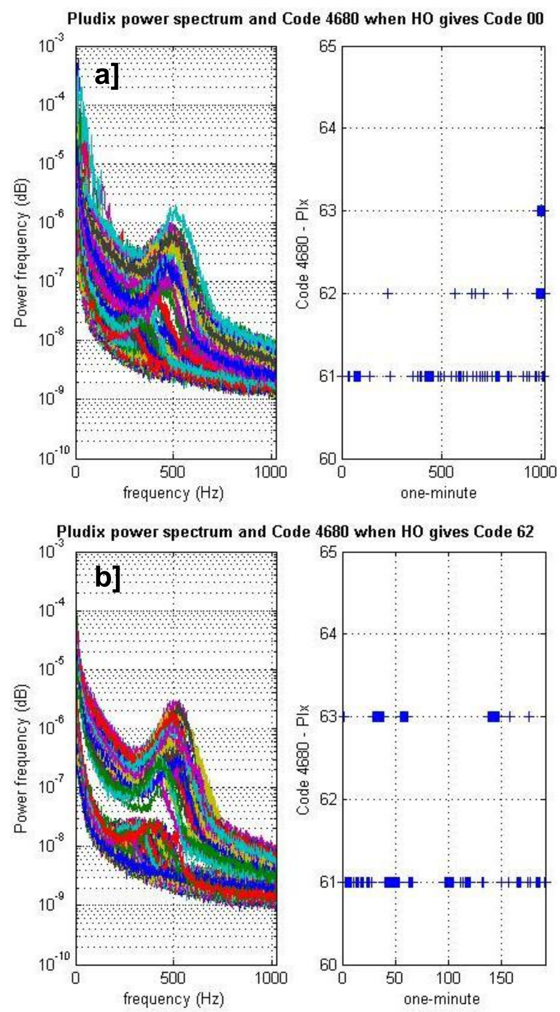

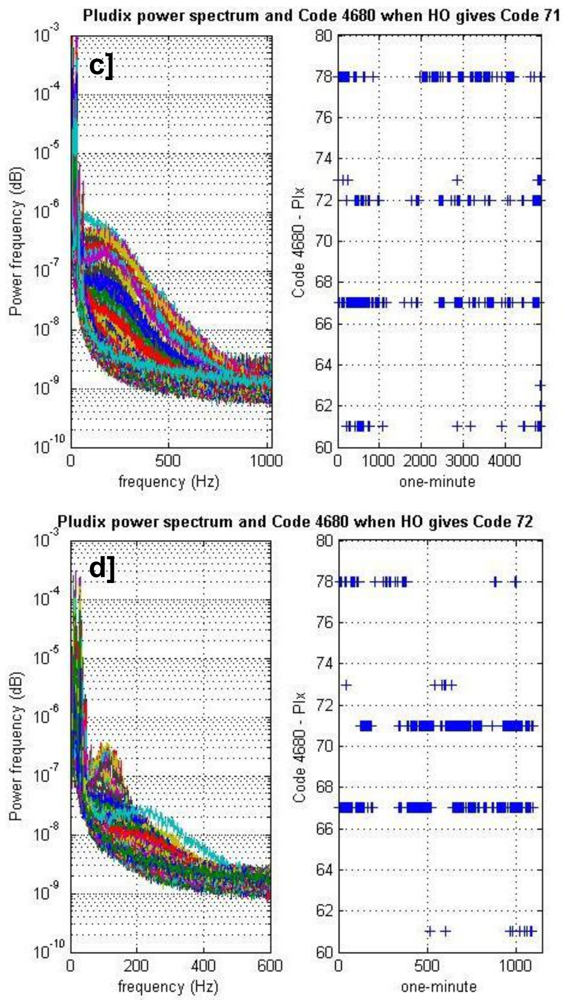

Fig. 3: Pludix power spectrum and WMO-4680 code when HO gives code 00 (August) **a]**; code 62 (May) **b]**; code 71 (December) **c]**; code 72 (December) **d]**.

Consider Fig. 4, in which we analyse the HO rainfall rate (mm/h), temperature (°C) and WMO-4677 codes when Pludix detects no significant weather observed (code 00) for all the two years of data. The HO detects a high percentage of fog/ice fog (codes from 40 to 50) and drizzle (codes from 50 to 60), of difficult identification with Pludix, because of the low terminal velocities. Also FD12P provides an high percentage of fog and drizzle situations (not shown). The agreement is better between Pludix and Parsivel. During the fog/drizzle situations reported by HO, Pludix provides the code 00 in 84.51% of cases.

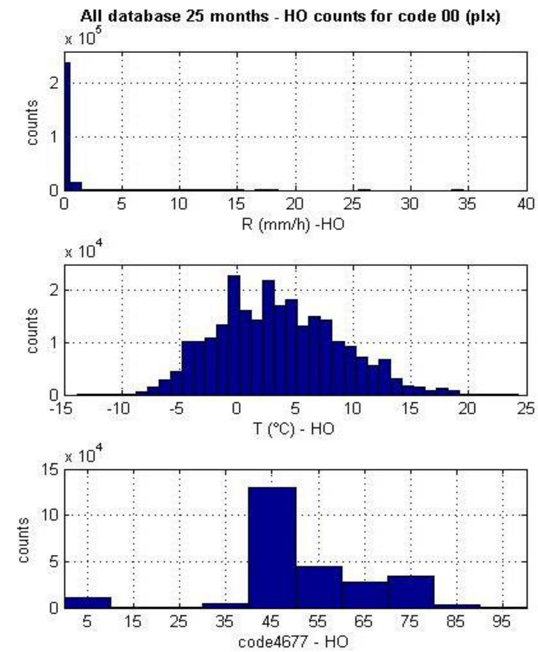

Fig. 4: HO rainfall rate (mm/h), temperature (°C) and WMO-4677 code when Pludix provides code 00. Two years of data are considered.

Consider now only the twelve Pludix selected codes and convert the HO WMO-4677 into 4680. When Pludix gives code 00 observe the percentage of minutes in which the other three sensors give the twelve codes (Tab. 3). The two years of data are taken into account. A good percentage of agreement is seen in the case of code 00 between Pludix and the other three sensors (especially Parsivel). There is a percentage of cases in which the other sensors (especially HO and FD12P) detect codes 61 and 71.

Percentage of frequency of the 12 codes when Plx provides code 00			
WMO4680	**HO**	**FD12P**	**PARS**
61	8.78	8.23	3.49
62	0.38	0.88	0.03
63	0	0.04	0
67	0.83	0.46	3.33
68	0	0.02	0.08
71	5.96	6.55	0.01
72	0.62	1.16	0.31
73	0	2.76	0
78	1.58	0.23	0
93	0	0	0
96	0	0	0
00	31.09	22.69	83.22

Tab. 3: Percentage of frequency of the 12 WMO-4680 codes for HO, FD12P and Parsivel, when Pludix provides code 00. Two years of data are considered.

Therefore, the codes that Pludix recognizes with more difficulty are WMO-4680 61 and 71, corresponding to WMO-4677 60-61 and 70-71 for HO (codes 60 and 70 are intermittent precipitation, codes 61 and 71 are continuous precipitation). The HO is able to detect intermittent precipitation because of its large sample volume, while Pludix, looking over a few cubic meters above it, provides code 00 for these minutes. Tab. 4 shows situations in which Pludix gives code 00 and HO gives different WMO-4677 codes. The two years of data are considered. The HO provides an intermittent rain code 60 in a maximum of 56.6% of cases during winter; the percentages are smaller for the snow situation.

HO WMO-4677 codes when Pludix gives code 00. Total Percentage (two years of data)							
60	**61**	**62**	**63**	**70**	**71**	**72**	**73**
36.4	63.6	10.6	89.4	25.3	74.7	29.2	70.8
Winter							
60	**61**	**62**	**63**	**70**	**71**	**72**	**73**
56.6	43.4	0	100	32.5	67.5	0	100
Spring							
60	**61**	**62**	**63**	**70**	**71**	**72**	**73**
50.1	49.9	0	100	25.8	74.2	0	100
Summer							
60	**61**	**62**	**63**	**70**	**71**	**72**	**73**
48.9	51.1	4.5	95.5	0	100	59.3	40.7
Autumn							
60	**61**	**62**	**63**	**70**	**71**	**72**	**73**
54.2	45.8	0	100	14.9	85.1	0	100

Tab. 4: HO WMO-4677 codes when Pludix gives code 00. Codes 60-61: rain not freezing intermittent or continuous slight; Codes 62-63: rain not freezing intermittent or continuous moderate; Codes 70-71: intermittent or continuous fall of snowflakes slight; Codes 72-73: intermittent or continuous fall of snowflakes moderate. Two years of data are considered.

3.2 comparison between the different instruments in terms of rainfall intensity

Considering all the 1-minute coincident measurements in all the database and only the minutes in which the HO provides rain codes (WMO-4680: 61, 62 and 63), the correlation coefficients between the rainfall rate estimation (mm/h) of HO and the other sensors are: HO-Pludix 0.61, HO-Parsivel 0.46, HO-FD12P 0.59. Thus, Pludix works better in the case of rain. Fig. 5 shows a rain event taken as representative. A good agreement is seen both in rainfall rate values and in WMO-4680 codes among the four instruments.

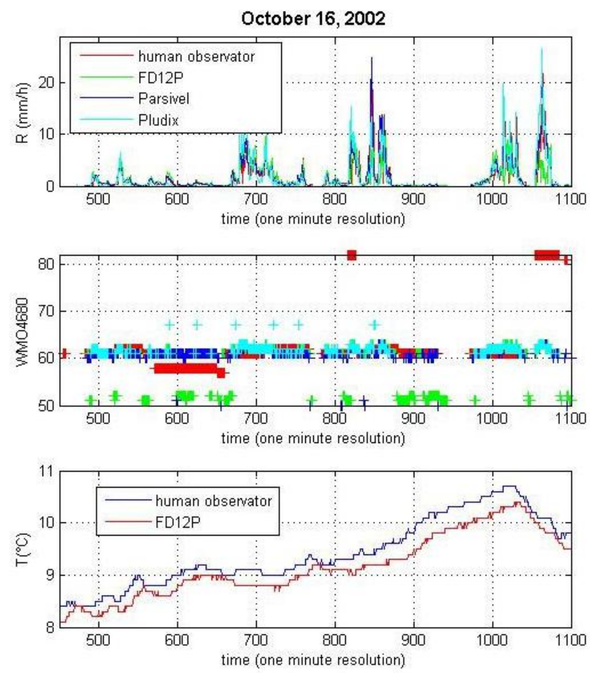

Fig. 5: 1-minute time evolution of R (mm/h), WMO-4680 code and T (°C) for the 16 October, 2002 event in Wasserkuppe.

3.3 comparison between Pludix and Parsivel for different precipitation events

In this section we test the performances of Pludix in PW identification and DSD measurement, comparing it with Parsivel. One rain event, one snow event and one hail event taken as representative are considered.

The rain event of 10 August, 2002

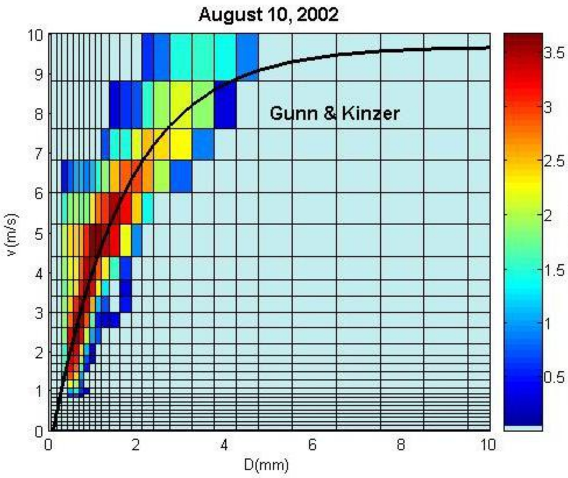

Fig. 6: Parsivel v-D histograms for the 10 August 2002 rain event. The solid line is the Gunn and Kinzer (1949) curve.

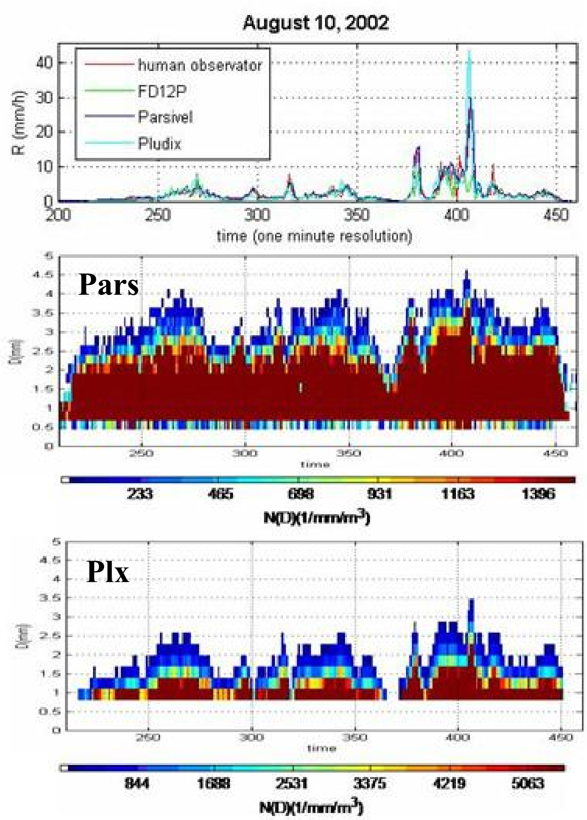

Fig. 7: Rainfall rate time series for the 10 August 2002 rain event for the four instruments; DSDs time series for the 10 August 2002 event for Parsivel and Pludix

Fig. 6 shows the velocity-diameter histogram derived from Parsivel data; N is the number of drops in each 32 velocity and 32 diameter classes. For this event the v-D relationship follows very well the Gunn and Kinzer (1949) relationship for water droplets in stagnant air at sea level: $v(D) = 9.65 - 10.3\exp(-0.6D)$ - D in mm, v in m/s. For this event Pludix shows the characteristic spectra of rain (not shown). Fig. 7 shows the 1-minute rainfall rate evolution for the event for the four instruments and the 1-minute DSD evolution for Parsivel and Pludix. The four instruments are in good agreement in the R estimation. The DSDs derived from Parsivel and Pludix show a good agreement in the mid-diameter range (1<D<3 mm), with a higher concentration of small drops in the first Pludix diameter classes.

The snow event of 24 February, 2001

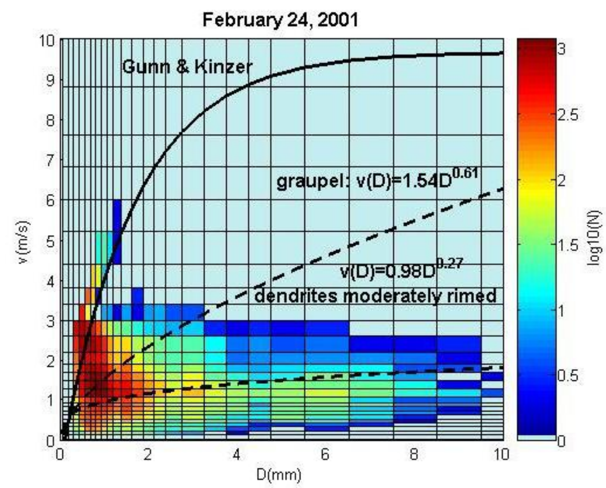

Fig. 8: Parsivel v-D histograms for the 24 February 2001 snow event. The solid line is the Gunn and Kinzer (1949) curve. The dashed lines are two empirical fits for graupel and snowflakes (Pruppacher and Klett, 1998).

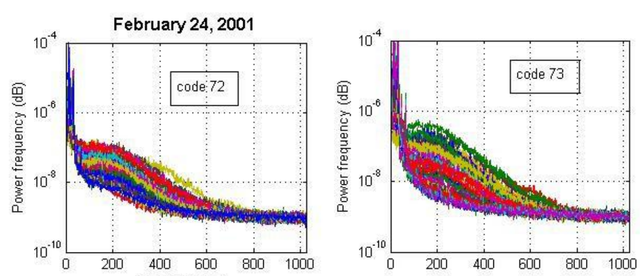

Fig. 9: Pludix power spectra for the 24 February 2001 snow event for the minutes characterized by codes 72 and 73.

Fig. 8 shows the v-D histogram derived from Parsivel data. It can be seen that for this event the v-D relationship is very far from the Gunn and Kinzer (1949) relationship for water droplets, while it follows two of the empirical fits derived for graupel and snow-flakes of different riming degree and consisting of different crystal types (Pruppacher and Klett, 1998). For this event Pludix identifies WMO-4680 snow codes (71, 72 and 73). Fig. 9 shows the Pludix power spectra for the event for the minutes characterized by codes 72 and 73.

The hail event of 05 June, 2002

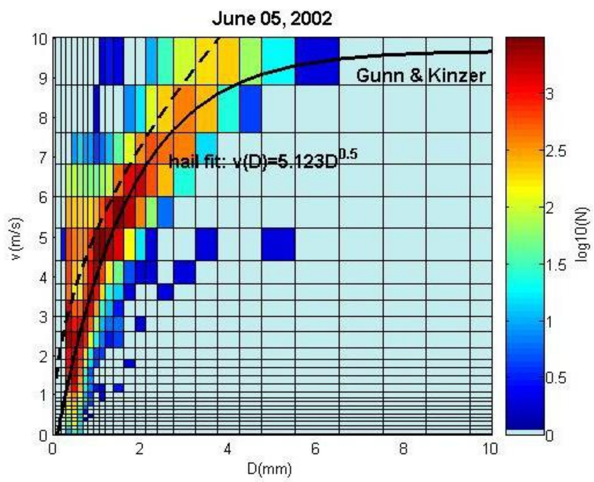

Fig. 10: Parsivel v-D histograms for the 05 June 2002 rain-hail event. The solid line is the Gunn and Kinzer (1949) curve. The dashed line is an empirical fit for hail (Pruppacher and Klett, 1998).

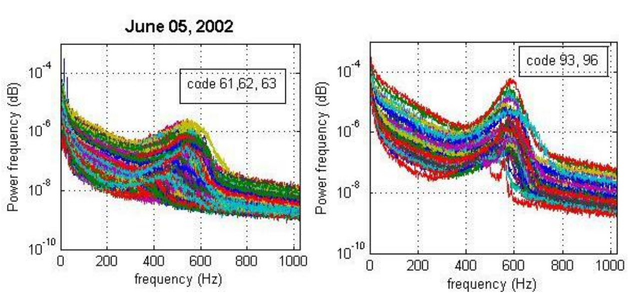

Fig. 11: Pludix power spectra for the 05 June 2002 rain-hail event for the minutes characterized by rain and hail codes.

The 05 June 2002 events is characterized by a rain shower with R>50mm/h (R reported by HO). The v-D relationship derived from Parsivel (Fig. 10) is not far from the Gunn and Kinzer (1949) relationship for water droplets, but it also follows quite well the empirical fit derived for hail (Pruppacher and Klett, 1998). For this event, Pludix identifies WMO-4680 rain codes (61, 62, 63) and for some minutes hail codes (93, 96). Fig. 11 shows the Pludix power spectra for the event for the minutes characterized by the rain and hail codes.

4. CONCLUSIONS

The principle aim of the present work was to determine the capabilities and limitations of Pludix as a PWS. Twelve precipitation codes are selected according to the WMO-4680 table: 3 rain codes, 3 snow codes, 2 hail codes, 1 code for ice crystals, 2 mixed precipitation codes, 1 no significant weather observed code.

The comparison of Pludix with the reference observations of a human observer and with other two PW instruments shows good capabilities of our instrument in detecting the precipitation type, especially the rain. In some situations Pludix works better than the other instruments in the case of rain. Moreover, it detects some situations (especially rain, rain-shower with hail, ice crystals) that the HO does not detect. Codes 61 and 71 are not well detected by Pludix, since it is less sensitive to such slight precipitations; also, the HO samples on a large measurement volume, while Pludix samples on a small measurement volume (about 3 m high and 1 m wide above it). In addition, the HO, due to its large sample volume is able to detect intermittent precipitation.

The test of the performances of Pludix in measuring the rainfall intensity shows that it works better than the other instruments (it has the higher correlation coefficient with HO). Pludix also shows a good agreement with Parsivel in detecting rain, snow and hail situations.

In the future, we are planning to refine the criteria for the PW codes presented here, and eventually introduce new PW codes.

5. REFERENCES

Bloemink, H. I., Lanzinger, E., 2005: *Precipitation type from the Thies disdrometer.* TECO-2005, Bucharest, Romania, 4-7 May 2005, **IOM 82 (TD 1265)**.

Caracciolo C., F. Prodi and R. Uijlenhoet, 2006. *Comparison between Pludix and impact/optical disdrometers during rainfall measurement campaigns.* Atmospheric Research, **82 (1-4), 137-163.**

Gunn, R., Kinzer, G.D., 1949. *The terminal velocity of fall water drops in stagnant air*. J. Met. **6, 243–248**.

Löffler-Mang, M., and J. Joss, 2000: *An optical disdrometer for measuring size and velocity of hydrometeors*. J. Atmos. Ocean. Tech., **17, 130-139**.

Prodi, F., A. Tagliavini and F. Pasqualucci, 2000. *Pludix: an X–band sensor for measuring hydrometeors size distributions and fall rate*. Proc. 13th ICCP, **338-339**

Pruppacher H.R. and J.D. Klett, 1998. *Microphysics of clouds and precipitation*. Kluwer Academic Publishers. **954 pp.**

AIRBORNE PHASE DOPPLER INTERFEROMETRY FOR CLOUD MICROPHYSICAL MEASUREMENTS

P. Y. Chuang[1*], E. W. Saw[2], J. D. Small[1], R. A. Shaw[2], C.M. Sipperley[3], G. A. Payne[3], and W. D. Bachalo[3]

[1]Department of Earth and Planetary Sciences, University of California Santa Cruz, 1156 High Street, Santa Cruz, CA 95064

[2]Department of Physics, Michigan Technological University, 1400 Townsend Drive, Houghton, MI 49931

[3]Artium Technologies Inc., 150 West Iowa Ave, Suite 202, Sunnyvale, CA 94086

1. ABSTRACT

Conducting accurate cloud microphysical measurements from airborne platforms poses a number of challenges. The technique of phase Doppler interferometry (PDI) confers numerous advantages relative to traditional light-scattering techniques for measurement of the cloud drop size distribution, and, in addition, yields drop velocity information. Here, we describe PDI for the purposes of aiding atmospheric scientists in understanding the technique fundamentals, advantages and limitations in measuring cloud microphysical properties. The performance of the Artium Flight PDI (**F/PDI**), an instrument specifically designed for airborne cloud measurements, is studied. Drop size distributions, liquid water content, and velocity distributions are compared with those measured by other airborne instruments.

2. PERFORMANCE

One of the critical instrument parameters that must be determined is the instrument view volume as a function of drop size. We use a new model for determining the view volume. We compare data from a stratocumulus cloud with the model prediction, where the model has two degrees of freedom, one of which can be compared against a known instrument characteristic (laser $1/e^2$ diameter), and the other which is not easily measured (the minimum signal-to-noise ratio for detecting drops), which makes the model essentially a one free-parameter fit. Figure 1 shows a comparison between model and data, showing excellent agreement. This gives us confidence that we know the view volume very well, and thus can infer drop concentrations and other size distribution moments with some accuracy.

3. INTERCOMPARISON

We have performed comparisons with the Gerber PVM-100A as well as a FSSP-100. Figure 2 shows the results from the latter intercomparison, specifically the 10th, 50th (or median) and 90th percentile diameters (hereafter d_{10}, d_{50} and d_{90}) for these distributions, as well as $d_{90} - d_{10}$, which is one measure of the distribution breadth. From these plots, it appears that there is a ~5 μm discrepancy between the measured distributions, which is reasonably consistent among all the distribution parameters, although the discrepancy is greater for d_{10} than it is for d_{90}. The discrepancy in the breadth of the distribution in linear space as measured by $d_{90} - d_{10}$ is ~2 μm (compared to a total width varying from 4 to 10 μm), with the FSSP tending to measure broader distributions by 20 to 50% than the F/PDI.

These parameters, however, do not address the absolute concentrations of the size distribution. An alternate and complementary way of comparing the F/PDI and FSSP is to look at the measured concentration in particular size ranges. Figure 3 shows such a comparison, where the entire FSSP size range (ignoring the first bin, which is generally considered unreliable) has been divided into 6 size bins, and the F/PDI measurements are sampled to match these size bins with a 5 μm shift in size, i.e. a 15 μm drop measured by the F/PDI will be considered a 10 μm drop for this comparison, as suggested by Figure 2. The F/PDI data were shifted to smaller sizes because this was much more convenient than doing the converse for the FSSP sizes, and is not intended to suggest that F/PDI size data are actually biased in this way. The same comparisons performed *without* such a size shift (not shown) yielded comparisons that were generally extremely poor.

For the five largest size bins shown in Fig. 3, there is a good *correlation* between FSSP and F/PDI concentrations. In general, the FSSP infers higher concentrations than the F/PDI, with typical differences on the order of a factor of 2, but as small as ~20%, depending on the size bin. The agreement between FSSP and F/PDI data does not appear to systematically depend on either drop size (e.g. it does not simply improve as drop size increases) or drop concentration (e.g. best agreement is not for the smallest or largest concentrations). For the smallest size bin (2.1 to 7.3 μm), the FSSP predicts drop concentrations about an order of magnitude higher than the PDI. One possible explanation for this discrepancy is that the FSSP was triggering on noise, yielding numerous false drops in the smallest size bin. This is a well-known problem of the FSSP, which is normally dealt with by ignoring the lowest FSSP channel, which we have also done here. This analysis perhaps indicates that the noise problems extend to higher FSSP channels, at least in this data set. Whether this problem can extend to the other size bins and lead to an FSSP overcounting in those comparisons as well is unknown. It is also possible that uncertainties in PDI counting or view volume are partly responsible for these discrepancies.

Overall, we find the correlation in the size-dependent concentration measurements encouraging, but acknowledge that the differences in performance between these instruments are substantial. Without a controlled experiment with known size distribution, and in the absence of an accepted standard instrument for size distribution measurements, it is not possible to determine which instrument measures more realistic size distributions. The results of this intercomparison clearly indicate that further instrument evaluation under controlled conditions with a known size distribution or an accepted standard is necessary to draw further conclusions.

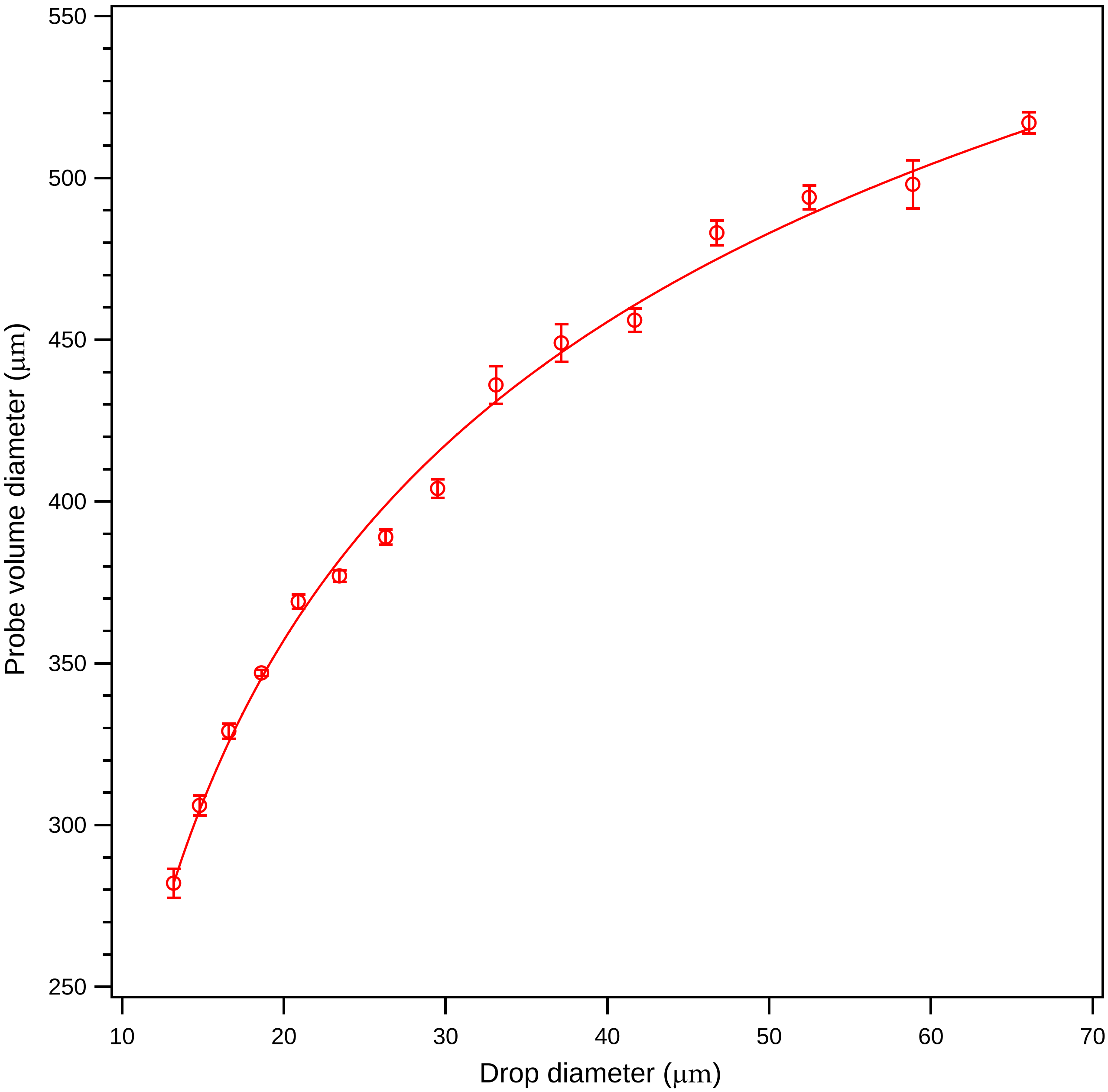

Figure 1: Comparison of modeled probe volume diameter (line) fitted to data (circles) as a function of drop size.

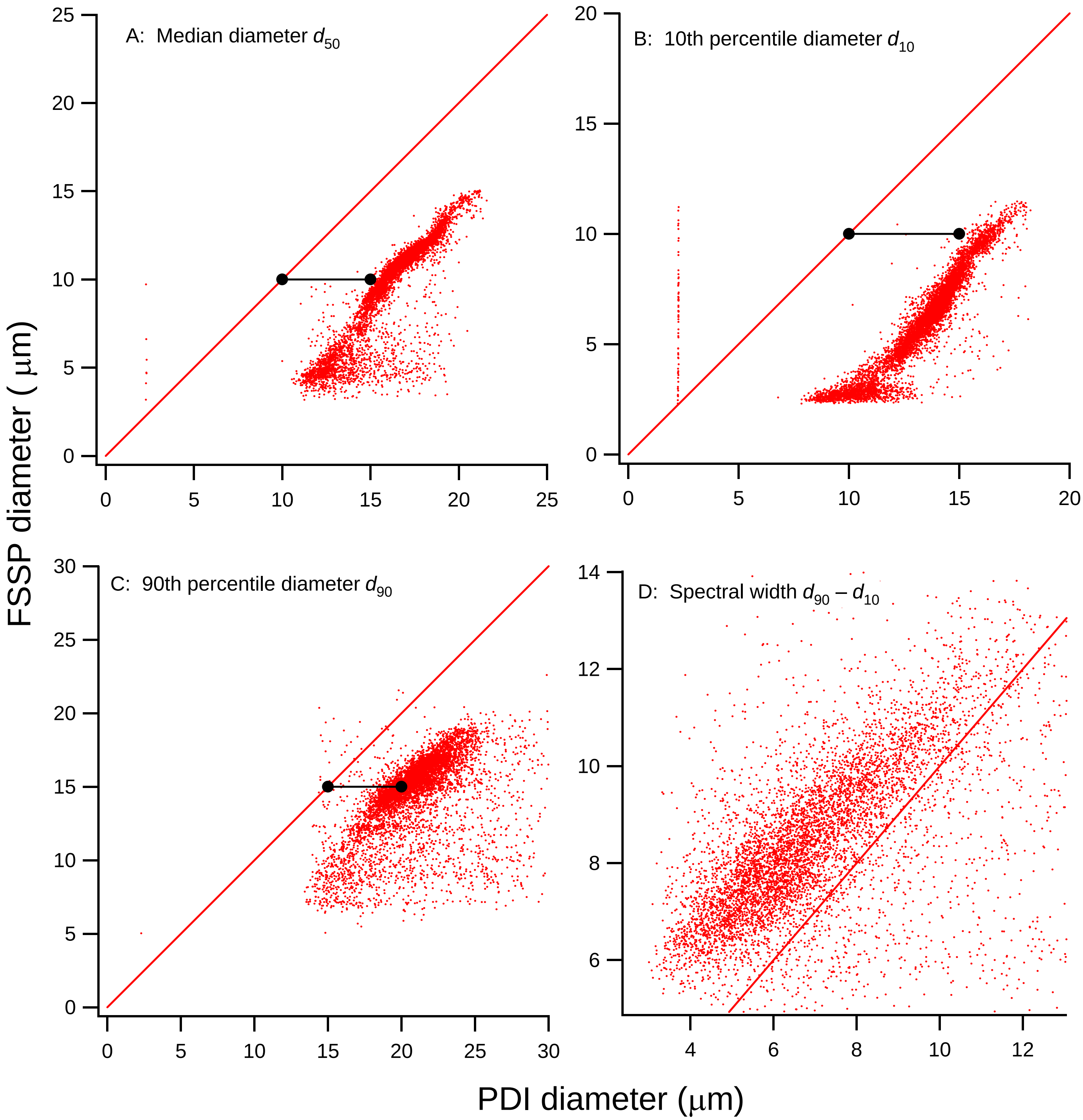

Figure 2: Comparisons of drop size distribution shape as measured by the F/PDI and a FSSP-100. Panels A, B and C represent the d_{50}, d_{10} and d_{90}, respectively for the measured size distributions. In each of these panels, the line terminated by two circles represents 5 µm. Panel D represents $d_{90} - d_{10}$. In all panels, a 1:1 line is drawn. Each dot represents 1 s of data. Approximately 7000 s worth of data is shown.

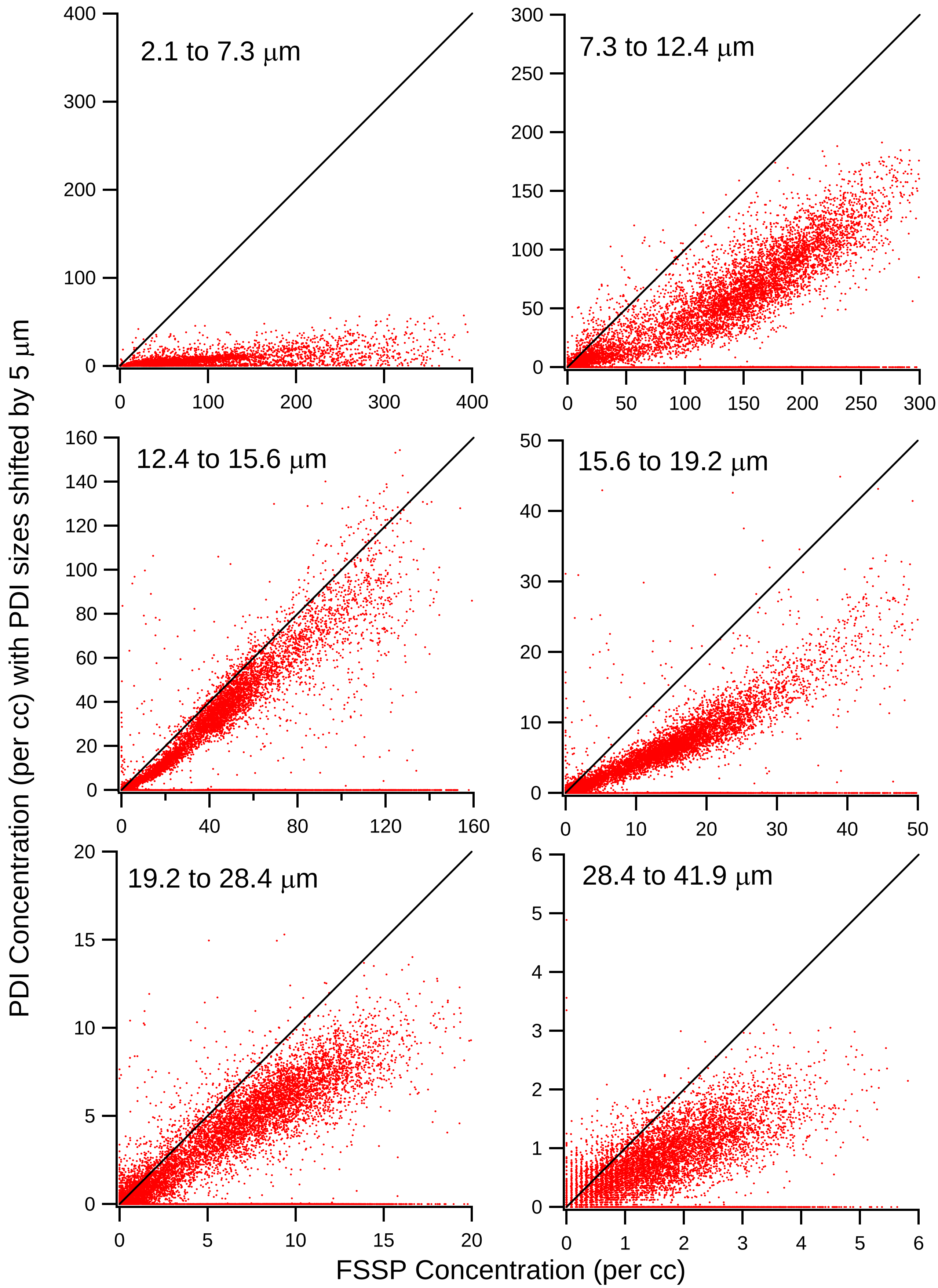

Figure 3: Comparison of the measured drop number concentration by the F/PDI and FSSP in six different nominal size bins. In all cases, the F/PDI distributions have been shifted towards smaller size by 5 μm to account for the sizing discrepancy shown in Fig. 2. This was more convenient than shifting the FSSP distributions upwards by the same amount, and is not meant to imply that these represent the actual drop sizes.

RETRIEVING THREE-DIMENSIONAL CLOUD STRUCTURE USING A TOMOGRAPHY METHOD

Dong Huang[1], Yangang Liu[1], and Warren Wiscombe[1,2]

[1]Brookhaven National Laboratory, Atmospheric Sciences Division, Upton, NY 11973, U.S.A.
[2]NASA Goddard Space Flight Center (code 913), Greenbelt, MD 20771, U.S.A.

1. INTRODUCTION

Three-dimensional distributions of cloud water are needed for studying cloud microphysics and atmospheric radiation, and for validating cloud-resolving and large-eddy-simulation models. In addition to the costly active remote sensing technique like radar, cloud tomography offers the promise of retrieving 3D cloud water distributions using multi-beam microwave emission measurements (Warner et al., 1985&1986). The method was proposed in the 1980s, but neither the technology nor the cloud models were mature enough to make any practical application. Now, the time is ripe for a renewed push. We have created a Tomography Simulator with simulated clouds and simulated microwave radiometers to show the feasibility of the cloud tomography method.

2. MATHEMATIC FORMULATION

The radiative transfer equation relating the microwave radiation intensity to the atmosphere state is:

$$I(\Omega_i) = I_\infty \tau(\Omega_i, 0, \infty) + \int_0^\infty B(T)\alpha(s,\Omega_i)\tau(\Omega_i,0,s)ds, \qquad (1)$$

where $I(\Omega_i)$ is the intensity of radiation reaching a radiometer from direction Ω_i; I_∞ is the intensity of the cosmic background radiation; $B(T)$ is the Planck function at temperature T; α is the absorption coefficient of cloud liquid water determined by the atmosphere state; and $\tau(\Omega_i, s_1, s_2) = \exp[-\int_{s_1}^{s_2} \alpha(s,\Omega_i)ds$ is the transmission between two points s_1 and s_2 along direction Ω_i.

Given a total number of m rays, Eq. (1) can be discretized by dividing a field, which is large enough to contain the cloud, into $n=N^3$ (N^2 for a 2D slice) equal size volume pixels to yield the following matrix equation (Huang et al., 2007):

$$\mathbf{Ax} = \mathbf{b}, \qquad (2)$$

where $\mathbf{x}^T = (\alpha_1, \alpha_2, \cdots, \alpha_n)$ is the vector of absorption coefficients of cloud liquid water; $\mathbf{b}^T = (b_1, b_2, \cdots, b_m)$, is the vector of measurements, b_i equals the right side of Eq.(3); and $\mathbf{A} = (a_{ij})$ is the mxn kernel matrix that representing the radiative transfer operator. When cloud is found in the retrieval to occupy only part of the field or the information of cloud boundary is available from other measurements like Radar, the retrieval process can be refined with a smaller field to get a better spatial resolution.

3. RETRIEVAL ALGORITHM

For a limited-angle tomographic problem like that of the cloud tomography technique, an ideal, unambiguous retrieval would require the data and the kernel matrix **A** to be free of noise and each cloud element to be scanned from all directions (Olson, 1995). Because both conditions are impossible to meet in reality, multiple solutions may satisfy the same radiometric measurements, and special regularization techniques beyond the standard method of least squares are needed to deal with this problem.

Following the Bayesian theorem, we propose an algorithm that can use either the smoothness constraint or the non-negativity constraint, or a double-side constraint defined by an initial estimate of the retrieval, or a combination of any of the above. Essentially, the algorithm solves the following minimization problem (Huang et al., 2008):

$$\min_{x}\left\{\left\|\mathbf{A}'\mathbf{x}-\mathbf{b}'\right\|_2^2\right\} \text{ subject to } \mathbf{x}\geq 0\,, \qquad (3)$$

where $\mathbf{A}'\equiv\mathbf{A}^T\mathbf{A}+\lambda\mathbf{L}^T\mathbf{L}+\tau\mathbf{Q}^{-2}$, $\mathbf{b}'\equiv\mathbf{A}^T\mathbf{b}+\tau\mathbf{Q}^{-2}\mathbf{x}_b$. **L** is the matrix of the two-dimensional first derivative operator; **Q** is the error co-variance matrix of the initial estimate $\mathbf{x}_b$; λ and τ are the regularization parameters determining the amount of the smoothness and double-side constraints imposed on the retrievals. The initial estimate $\mathbf{x}_b$ can be specified by using either a scaled adiabatic profile of cloud liquid water content or another independent observation such as the cloud liquid water field derived from a dual-frequency radar.

4. SIMULATIONS

A two-dimensional 5 Km wide and 1.5 Km high slice of cloudy atmosphere is taken from the simulations of a Large Eddy Simulation (LES) model driven by the data from the Atlantic Stratus Experiment. The original high-resolution LES simulation is degraded to an image of 20 by 20 pixels (250-meter horizontal and 75-meter vertical resolution). Four simulated radiometers of 0.3 K noise level and 2-degree beam width are placed equally on the ground along a line of 10 Km (Figure 1). Each radiometer scans the upper plane within 85° elevation of zenith at a 0.4° increment. This scanning strategy results in a total number of 800 rays hitting the 5 Km by 1.5 Km area.

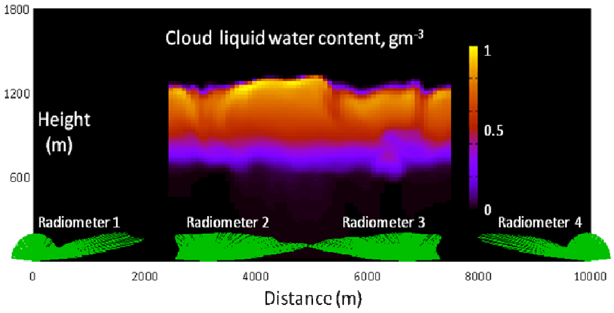

Figure 1. An example of a four-radiometer cloud tomography setup. Each radiometer scans the upper plane to within 5° of the ground; the scans are every 0.4° in angle. The lengths of the green lines from each radiometer are proportional to the simulated brightness temperatures in that direction. The atmospheric background is assumed to be 20 K.

The simulated tomographic data are then inverted using the algorithm described in Section 3. We first examine the effects of adding different constraints on the retrieval of the four-radiometer setup shown in Figure 1 for the stratocumulus cloud. As shown in Figure 2, the retrieved cloud from the standard least squares method shows very unrealistic spatial patterns of the cloud liquid water content. The addition of the non-negativity and smoothness constraints helps to capture the location and spatial extent of the cloud, but gives poor retrievals at cloud edges. The incorporation of a double-side constraint (based on

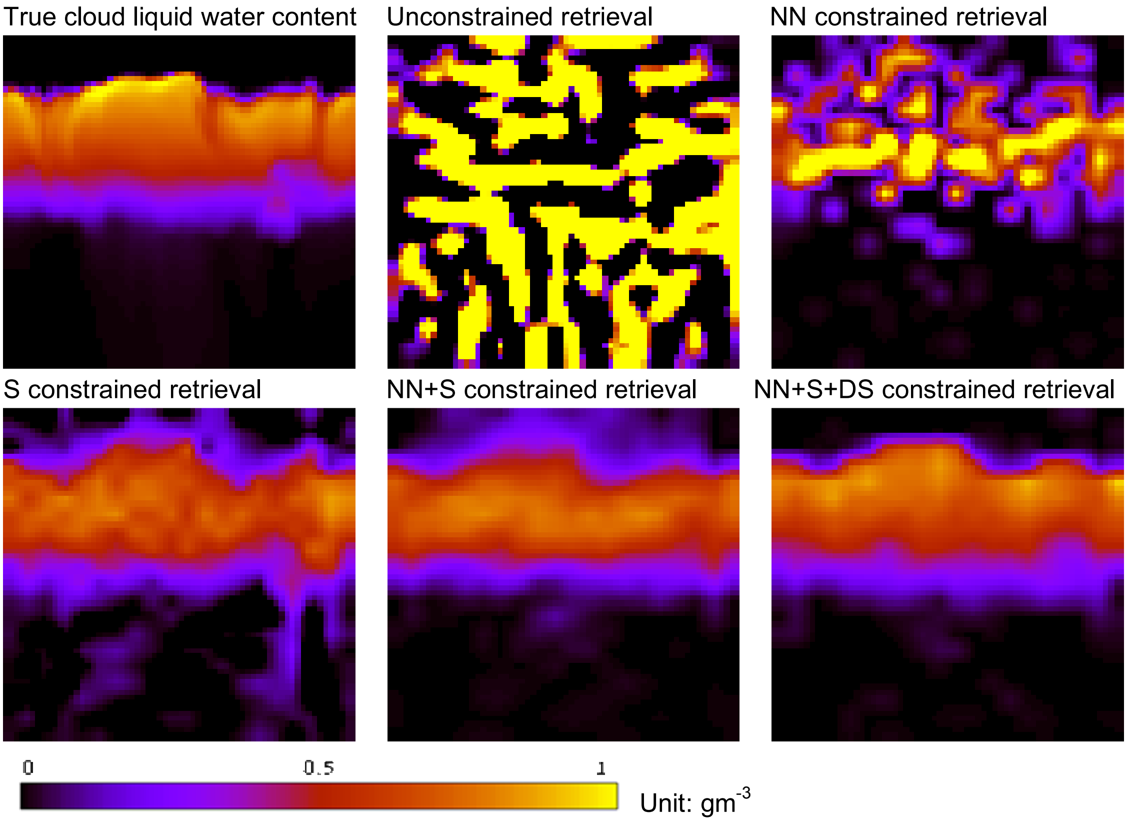

KEY: LS - Least Squares; NN - Non-Negativity; S - Smoothness; DS - Double-Side

Figure 3. The retrieved cloud liquid water content from the cloud tomography simulation shown in Figure 1 using various types of constraints. The true field is also shown as a reference.

scaled adiabatic profiles) produces the best cloud tomography retrieval. It not only accurately captures the location and extent of the stratocumulus cloud, but also accurately reproduces the cloud edges.

We then perform a group of sensitivity studies to identify the key factors that determine the retrieval accuracy of cloud tomography. When more radiometers and/or more scanning angles are used, and/or the radiometer beam width is reduced, and/or when a coarser output resolution is acceptable, a better retrieval can be obtained. The uncertainty in the ancillary data such as environment temperature and water vapor mixing ratio also impacts the retrieval, but the impact is

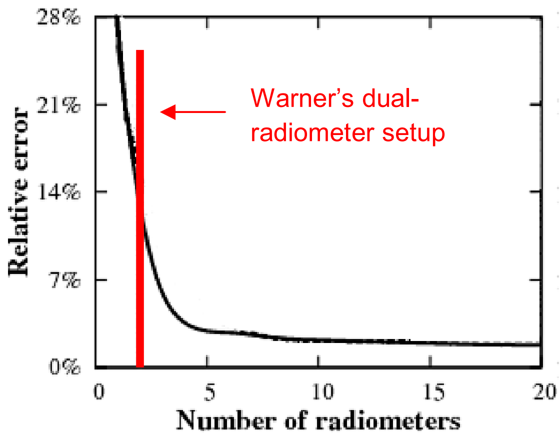

Figure 4. The relative retrieval error decreases when more radiometers are used. Warner's dual-radiometer setup is indicated by a vertical red line. Apparently it is not the optimal choice for this case.

considerably small over the range of uncertainty levels provided by radiosonde or sounding measurements. Among the factors the number of ground radiometers used appears to be the most critical one, as shown in Figure 4. There exists a critical point, say 4, beyond which adding more radiometers doesn't improve the retrieval much. This suggests that in this situation other types of information may be needed to further improve the retrieval, for example range-resolved information from a radar.

Furthermore, we show that the addition of radar data can improve the retrieval even further (Figure 5). The radar data are simulated using a Mie scattering code at the 35G and 94G frequencies and are imposed with a 0.5 dBz Gaussian noise. The difference between the differential attenuation at the two frequencies is converted to cloud liquid water content using the method of Hogan et al. (2005). The derived cloud field is then used as an initial estimate to constrain the retrieval using Eq. (3). The simulations show that the combination of data from two radiometers and one dual-frequency radar obtains the same accuracy as using eight radiometers.

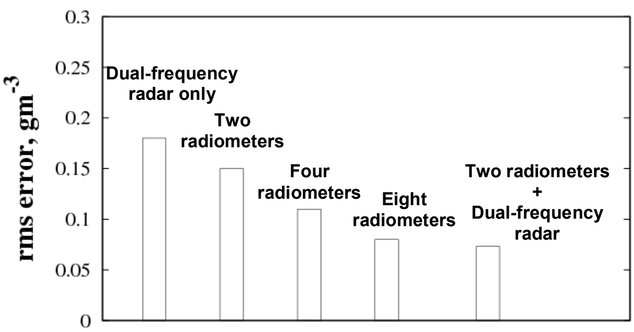

Figure 5. The rms errors for the retrieved cloud liquid water content using different combinations of radiometers and radar.

ACKNOWLEDGEMENTS

This research is supported by the DOE Atmosphere Radiation Measurement program under Contract DE-AC02-98CH10886.

REFERENCES

Hogan, R., N. Gaussiat, and A. Illingworth (2005): Stratocumulus liquid water content from dual-frequency radar. *J. Atmos. Oceanic Technol.*, 22, 1207-1218.

Huang, D., Y. Liu, and W. Wiscombe (2007): Determination of cloud liquid water distribution using 3D cloud tomography. *J. Geophys. Res.*, accepted.

Huang, D., Y. Liu, and W. Wiscombe (2008): Cloud tomography: Role of constraints and a new algorithm. *J. Geophys. Res.*, accepted.

Olson, T. (1995): A stabilized inversion for limited angle tomography. *IEEE Eng. Med. Biol*., 14, 612-620.

Warner, J., J.F. Drake, and P.R. Krehbiel (1985): Determination of cloud liquid water distribution by inversion of radiometric data. *J. Atmos. Sci. Ocean. Tech*., 2, 293-303.

Warner, J., J.F. Drake, and J.B. Snider (1986): Liquid water distribution obtained from coplanar scanning radiometers. *J. Atmos. Sci. Ocean. Tech*., 3, 542-546.

COMPARISON OF MACROSCOPIC CLOUD DATA FROM GROUND-BASED MEASUREMENTS USING VIS/NIR AND IR INSTRUMENTS AT LINDENBERG, GERMANY

Uwe Feister[1], Hans Möller[2], Theo Sattler[3], Janet Shields[4], Ulrich Görsdorf[1], and Jürgen Güldner[1]

1 German Meteorological Service, Meteorological Observatory Lindenberg, Germany[A]
2 IMK, 61118 Bad Vilbel, Germany
3 Sattler-SES, 60596 Frankfurt am Main, Germany
4 Scripps Institution of Oceanography, University of California, San Diego, USA

1. INTRODUCTION

Long-term ground-based observations of macroscopic cloud data such as cloud cover and cloud-base height have been used in studies to derive climate statistics and in attempts to recognize signs of climate change. Ground-based cloud observations have provided valuable macroscopic cloud data over several decades. On the other hand, automation of cloud observations is required worldwide to improve both reliability and - by higher sampling rates – representativeness of cloud data. Automated imagers and sky scanners have the potential to provide not only cloud cover in higher time resolution than conventional cloud observations, but in addition also cloud distribution in the sky.

Different types of instruments and observations have been compared referring to cloud cover over a four-months time period from May 9, 2006 to September 5, 2006 at the Meteorological Observatory Lindenberg. In addition to cloud cover, cloud-base heights derived from signals measured by passive and active sensors were analyzed. A few typical features and capabilities of the individual types of instruments will be discussed. They use different ranges of the radiation spectrum to measure either scattered visible and NIR solar radiation, IR radiation emitted from the atmosphere, or signals that are emitted by the instruments and backscattered from the atmosphere.

2. INSTRUMENTS AND MEASUREMENT CAMPAIGN

In addition to hourly cloud observations of the Lindenberg weather station, measurements from the following instruments were used in the comparison: a Nubiscope (IR scanner), the VIS/NIR Whole Sky Imager (WSI), a Laser ceilograph Tropopauser LD-40, and a Ka-Band cloud radar. The first three instruments were installed on the rooftop of the DWD Radiation Central Station at Lindenberg 52.2086°N, 14.1213°E, 127 m asl), which provides an unobstructed horizon. The Ka band radar was located on the ground close to the radiation platform. The site's weather station, where visual cloud observations were performed, is less than 200 m apart from the sensor on the rooftop.

The *Nubiscope* consists of an infrared sensor (pyrometer) that receives infrared radiation emitted from the atmosphere in the spectral region 8 to14 µm with a full viewing angle of 3°. The pyrometer is sensitive to measured brightness temperatures down to –100 °C. A sky tracker directs the tube containing the pyrometer at 30 different zenith angle steps of 3° between zenith and horizon, and at 36 azimuth steps shifted by 10° each. It takes about 6 minutes to perform one spatial sky scan that consists of 1,080 individual spot measurements. During the campaign, the Nubiscope instrument performed scans every ten minutes for 24 hours. A cloud decision algorithm provides cloud fraction (total and for three height

[A] Corresponding author: uwe.feister@dwd.de

levels), cloud-base heights, and a 'cloud description' parameter (overcast, broken clouds, Cirrus, fog) either in real-time mode or by manual data post-processing.
The *DAY VIS/NIR Whole Sky Imager (WSI)* manufactured at the University of California San Diego (UCSD) has been in operation at DWD since 2000 (Feister and Shields, 2005). Images of the upper hemisphere (180° viewing angle) are acquired every ten or 5 minutes in up to 7 different spectral ranges in the visible and near infrared (NIR) region. Cloud fractions of optically thin and opaque clouds for the upper hemisphere and for selected regions of interest are derived by a cloud decision algorithm from images in two different spectral regions. In this study, images acquired in the blue region (434 – 480 nm) and NIR (845 – 942 nm) were used for cloud post-processing. Time distances between two images of one sequence are less than 30 s for most of the daylight time, but can be longer for very long exposure times with thick clouds and high solar zenith angle.
The *Laser ceilograph Tropopauser LD-40* (Ceilometer, 1995) sends signals at a wavelength of 855 nm in the zenith direction and receives radiation backscattered from a cloud. Cloud-based heights (CBH), which are derived for up to three levels at time steps of 15 s, were averaged for intervals of 6 minutes to be compatible with the time resolution of the Nubiscope.
The *Ka band cloud radar MIRA 36* (Görsdorf and Handwerker, 2006) measures atmospheric backscattered signals of electromagnetic waves sent out by the instrument in the 35.5 GHz (8 mm) band. Parameters such as reflectivity, Doppler velocity and its variation, and linear depolarisation ratios are calculated for the height range of 0.25 to 14 km with 10 s averaging time and 30 m vertical resolution. Cloud-base and cloud-top heights as well as droplet size distribution, liquid and ice water content of the cloud can be derived usually by combination with measurements of other systems. For the time of the campaign, the reflectivity signal averaged for time periods of 10 minutes was used as a parameter that provides information on CBH. Due to interfering effects of aerosol particles and insects in the atmospheric boundary layer and the disproportionate scattering by larger water droplets during precipitation events, CBH values were not derived, but the reflectivities of the lowest three layers were used to derive estimates of the CBH for comparison with Nubiscope values.

3. RESULTS

In this study, we have focussed on the comparison between cloud data of the Nubiscope and the site's macroscopic cloud data that are routinely measured by the Whole Sky imager, the ceilometer and the radar as well as values obtained from conventional cloud observations. Data of each instrument were selected, and if necessary, averaged for the observation times of the Nubiscope to get a consistency in time as close as possible.

3.1 CLOUD COVER FROM NUBISCOPE AND FROM OBSERVATIONS

The Nubiscope cloud fractions (CF in per cent) selected for times of cloud observations, which are performed around minute 40 after the hour, were converted to 8 bins of cloud cover (CC) given in Okta. CF values of less than 1% were defined as 0 Okta (cloudless) and more than 99% as 8 Okta (overcast). The frequency plot of differences between total CC from the Nubiscope and observations is shown in Fig. 1. More than 50% of the differences are within ±1 Okta, which is the estimated uncertainty of CC observations, and about 2/3 of the differences are within ±2 Okta. If only the two types cloudless (CC=0) and cloudy (CC>0) are considered, which evaluates the capabilities of detecting clear sky, the Nubiscope and observer yielded the same decision for those two options in 93.5% of all hourly cases. In 16% of our comparisons, the Nubiscope did not make a decision on CF. The Nubiscope CC also shows a tendency of more frequently underestimating CC compared to observed CC. The results for high-level clouds are shown in Fig. 2. Due to the smaller difference of brightness temperatures between cloudless sky sections and thin clouds, they are more difficult to be detected from measurements in the infrared than low-level thick clouds. Nevertheless, the differences plotted in Fig. 2 between Nubiscope CC and observed CC show a close correspondence in most cases, but also large differences up to -8 Okta in some cases. Similar to total CC, the Nubiscope tends to slightly underestimate high-level clouds. We mention that systematic differences can be reduced by modifying thresholds in cloud decision algorithms.

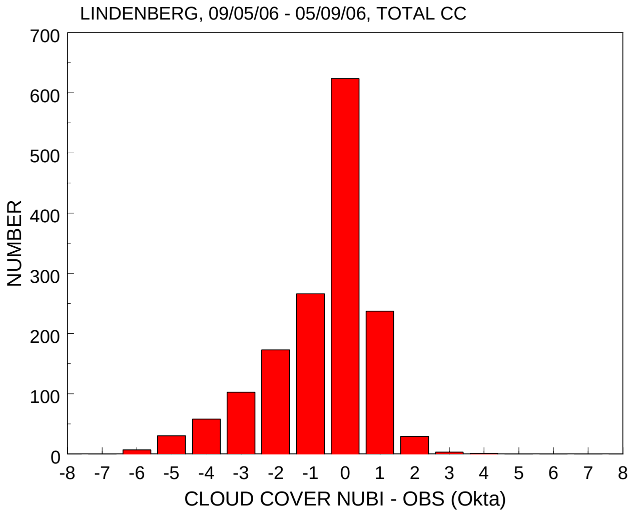

Fig.1 Frequency of differences of total CC from Nubiscope measurements and cloud observations (2,207 day and night values for comparison in the period May to September 2006

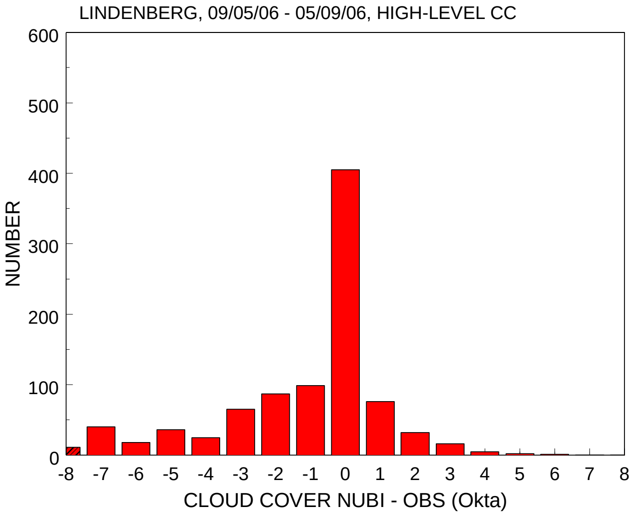

Fig. 2 Frequency of differences of high-level CC from Nubiscope measurements and cloud observations (2,207 day and night values for comparison in the period May to September 2006

3.2 CLOUD COVER FROM NUBISCOPE AND WSI

Due to the small time step of WSI image grabbing of 5 or 10 minutes, the overall number of daylight comparison cases was 7,671. In 991 of them (13%), the Nubiscope did not make a cloud decision. To make a first rough comparison, we defined cloud free as CF < 1%, and cloudy as CF ≥ 1%. We found that 2.6% of cases were defined by both instruments to be cloud free, and 94.8% were found by both instruments to be cloudy. Thus there was agreement between the two instruments in this course comparison, of 97.4%. A more detailed classification of differences in CF is shown in Fig. 3. It can be seen that in more than 50% of cases cloud fractions differ by less than ±5%. More than ¾ of differences of cloud fractions are within ±15%, and about 90% of all cases show CF differences of less than ±25%.

Analogous to the comparison between Nubiscope and observed cloud cover, the number of overestimated cloud fractions from the Nubiscope compared to the Whole Sky Imager is slightly larger than the number of underestimations.
The effect of the limited field of view used by the Nubiscope algorithm (view angles less than 70° corresponding to about 66% of the upper hemisphere) was tested by comparing Nubiscope CF with WSI CF values that were analyzed for this limited view angle. There is still a good correspondence between both CF on the average, though there can be larger differences in individual cases. The individual CC occurrences for each of 8 Okta bins for Nubiscope and WSI are shown in Fig. 4. Differences in frequencies are obvious only for a CC of 1 Okta and for 7 and 8 Okta. Due to the conversion from CF in per cent to CC in Okta, small differences in CF resulted in an apparent larger systematic deviation of CC. In many cases, when the Nubiscope decided on CF=0%, the WSI showed a very small CF of 1% to about 4% that according to our definition of CC was not cloud free any more, i.e. CC=1 Okta. Similarly, due to our definition of CC=8 Okta (overcast, i.e. closed cloud deck without gaps), corresponding to CF = 100%, there were many cases with a WSI decision on CF of 100% (CC = 8 Okta), while the Nubiscope CF of about 98% to 99% resulted in a CC = 7 Okta. It should be noted that threshold settings in both cloud algorithms themselves, and finally the area close to the horizon that is not part of the Nubiscope scan may have also contributed to those differences.

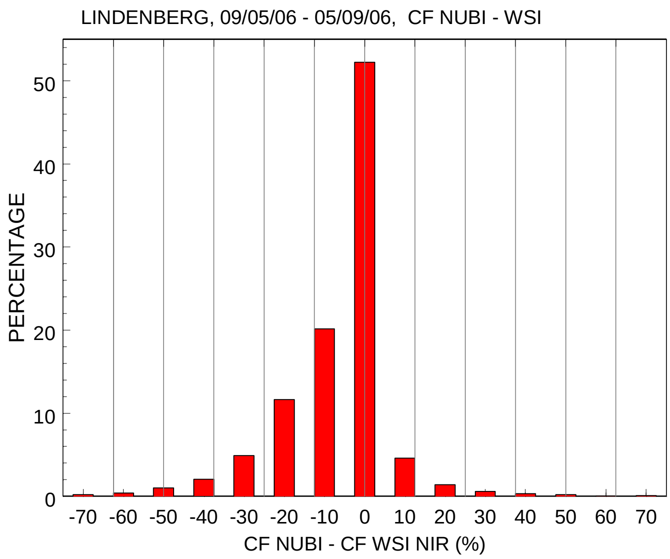

Fig. 3 Frequency of differences of total cloud fraction from Nubiscope and WSI measurements (6,681daylight values for comparison in the period May to September 2006)

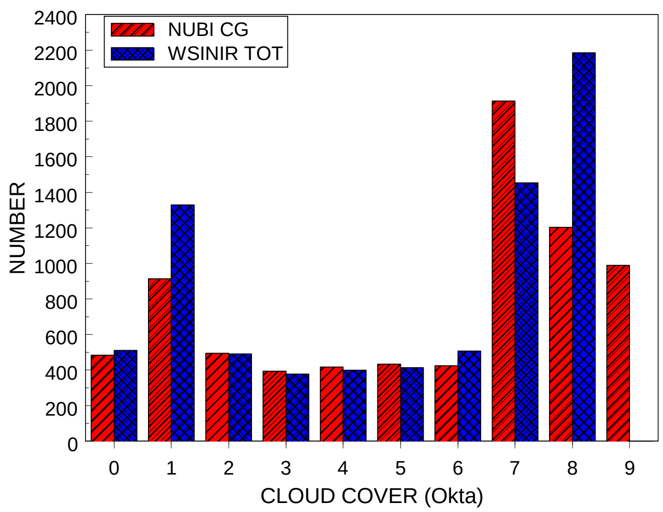

Fig. 4 Number of CC values per Okta from Nubiscope and WSI for the period May to September 2006. CC=9 means no decision by the Nubiscope

3.3 CLOUD-BASE HEIGHTS COMPARISON

The Nubiscope cloud algorithm also derives cloud-base heights (CBH) from IR sky radiances and from measurements of the surrounding surface emission. It does not include external data such as measured vertical temperature profiles and/or air mass characteristics that might be useful to improve the estimated CBH. We have not tried to include CBH estimates from cloud observers, because they may have been affected by the information they take from the ceilometer display.

Day and night CBH values from the Nubiscope and the ceilometer LD-40 are shown in Fig. 5 as differences of CBH between them in dependence of solar zenith angle. In general, CBH from the Nubiscope is somewhat smaller than the ceilometer CBH. A comparison between zenith cloud fraction from WSI and ceilometer performed in another study had shown that the uncertainty of this type of ceilometer becomes larger at higher cloud levels such that high clouds that are recognized in WSI images and are also identified as such by the WSI cloud algorithm, are not detected by the ceilometer or, that the ceilometer detects clouds that are not seen in the WSI image (Feister and Shields, 2005). Therefore, part of the larger CBH differences between Nubiscope and ceilometer especially at higher height levels may be due to erroneous ceilometer signals.

The comparison between nubiscope and radar was performed by using the height of the lowest border of radar reflectivity signals instead, because a radar CBH algorithm working independent of other instruments was not available at the time of the campaign. The radar reflectivities at the lowest height-level are still affected by ground clutter from boundary layer aerosols. Differences between Nubiscope CBH and radar ‘CBH’ in Fig. 5 show more frequently slightly higher Nubiscope CBH values than the corresponding radar reflectivities. A systematic dependence on the time of the day cannot be recognized, but it appears that large differences between Nubiscope and both ceilometer and radar are less frequent during night time. It cannot be decided yet, to what extent this feature is due to atmospheric stability, because during night time, the chance of stable atmospheric conditions is higher than during day time, or if it is an effect of the instruments.

The dependence of CBH from the Nubiscope and from the active sounders at different height levels can be seen in the scatter plot of Fig. 6. Part of the ground clutter of radar signals has been removed for this plot. The correspondence between CBH from Nubiscope and the active sounders shows a closer correspondence with smaller scatter for low-level and mid-level clouds below about 3 km. Systematic differences are more pronounced between Nubiscope CBH and ceilometer CBH up to levels of about 5 km than between Nubiscope and radar. There is still some remaining ground clutter at low height levels in the radar data left. More scatter between CBH from the instruments can be seen at higher levels. It is generally larger between Nubiscope and ceilometer CBH than between Nubiscope and radar CBH. We mention that the definition of cloud-base height is also determined by the type of instrument and observation method as well as the thresholds used in cloud algorithms (Pal et al. 1992, Seiz et al. 2007).

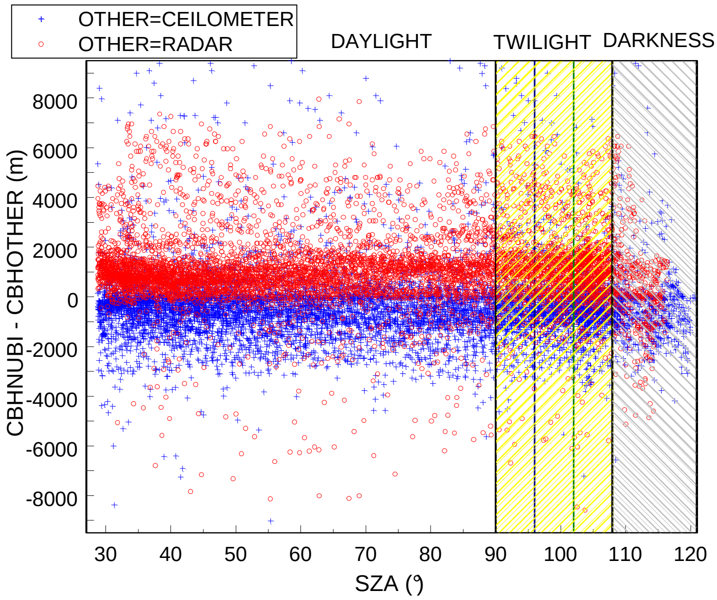

Fig. 5 Differences of cloud-base heights between Nubiscope and ceilometer (plus) or radar (circles) of non-zero signals in dependence of solar zenith angle (SZA) from May to September 2006. Radar is not CBH, but lowest-layer reflectivity signal. Dashed areas mark daylight, twilight (civil, astronomical, nautical), and darkness periods.

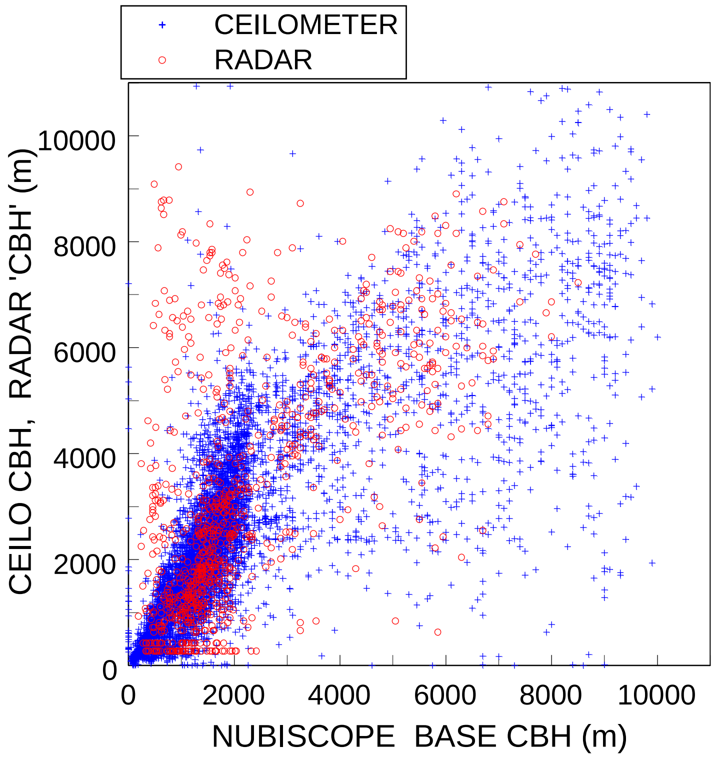

Fig. 6 Cloud-base heights (CBH) from Nubiscope compared to CBH from ceilometer (plus) or lowest-level radar reflectivity (circle) for the period May to September 2006.

4. CONCLUSIONS

A comparison between different types of passive and active sensors that are operated in different spectral ranges in the VIS/NIR (WSI), NIR (ceilometer), infrared (Nubiscope), and mm-wave region (radar) to provide macroscopic cloud parameters was performed in a field campaign. The results are valid mainly for summer conditions at a mid-latitude site, where the upper tropospheric temperatures did not drop below -60 °C, and integrated water path derived from microwave radiometer data ranged between 0.6 and the high value of 4.0 cm with an average of 2.1 cm during the four-months campaign.

For cloud cover, only slight systematic differences have been found between the Nubiscope and WSI as well as between the Nubiscope and cloud observations. In individual cases, cloud detection in the IR is difficult in particular for cold and thin clouds having brightness temperatures close to clear sky temperatures. Their detection requires a high sensitivity of the

receiver. The same decision on cloud or no cloud for the whole sky was taken by both instruments in 95% of cases. In individual cases, larger differences can occur.
The percentage of cases, where the Nubiscope provides no decision on CC would need to be reduced for many applications. Due to the spatial scanning and the smaller time resolution, the Nubiscope cannot provide high resolution cloud structures, as they are provided by the spot measurements of imagers, but it provides data during darkness that are not acquired by the Daylight VIS/NIR WSI. We mention that there is a Day/Night WSI available that provides cloud decisions during day and night (Shields et al. 1998). Referring to cloud-base heights, the comparison shows reasonable agreement between Nubiscope and ceilometer as well as between Nubiscope and cloud radar up to height levels of about 3 km. CBH differences between the instruments in the lower height range are mainly due to the different principles of measurement including the geometries of measurements (zenith looking versus scanning), the assumption on lapse rate used in the Nubiscope cloud algorithm, and the definition of CBH for the respective instrument.

5. BIBLIOGRAPHY

Ceilometer (1995), Gerätehandbuch für Laser Ceilograph LD – WH X 06. Wolkenhöhenmesser nach dem Prinzip der Laufzeitmessung. Jenoptik, Impulsphysik GmbH. Schenefeld, Oktober 1995.

Feister, U., and J. Shields (2005), Cloud and radiance measurements with the VIS/NIR Daylight Whole Sky Imager at Lindenberg (Germany). Meteorol. Z., 14, No.5, 627 – 639.

Görsdorf U., and J. Handwerker (2006), A 36 GHz high sensitivity cloud radar for continuous measurements of cloud parameters - Experiences of 2-years operation and system intercomparison. Proceedings of ISTP, Seventh International Symposium on Tropospheric Profiling; Needs and Technologies, Boulder, 12.-16.06.2006.

Pal, S. R., W. Steinbrecht and A. I. Carswell (1992), Automated method for lidar determination of cloud-base height and vertical extent. Applied Optics, 31, No. 10 / 1, 1488 – 1494.

Seiz, G., J. Shields, U. Feister, E. P. Baltsavias, and A. Gruen (2007). Cloud mapping with ground-based photogrammetric cameras. Intern. J. Remote Sensing, 28, No. 9, 2001- 203.

Shields, J. E., R. W. Johnson, M. E. Karr, and J. L. Wertz (1998), Automated Day/Night Whole Sky Imagers for Field Assessment of Cloud Cover Distributions an Radiance Distributions, Proc. 10th Symposium on Meteorological Observations and Instrumentation, 11 – 16 January 1998, Published by the American Meteorological Society, Boston MA.

ACKNOWLEDGEMENT

We acknowledge the support given by the SCOUT-O3 project for supporting part of this study to improve measurements of radiation and cloud parameters. We also thank staff and data providers at the Lindenberg weather station for their assistance.

Ice Particle Size Distributions Measured with an Airborne Digital In-line Holographic Instrument

Jacob P. Fugal[1]*and Raymond A. Shaw[2]

[1] National Center for Atmospheric Research, Boulder, CO 80027, USA
[2] Department of Physics, Michigan Technological University, Houghton, MI 49931, USA

May 1, 2008

1. ABSTRACT

Holographic data from the prototype airborne digital holographic probe, HOLODEC 1 (Holographic Detector for Clouds), taken during test flights are digitally reconstructed to obtain the size, three-dimensional position, and two-dimensional profile of ice particles and then ice particle size distributions and number densities are calculated using an automated algorithm with minimal user intervention. The holographic method offers the advantages of a well-defined sample volume size that is not dependent on particle size or airspeed, and offers a unique method of detecting shattered particles. The holographic method also allows the volume sample rate to be increased beyond that of the prototype HOLODEC 1 instrument, limited solely by camera technology.

HOLODEC 1 size distributions taken in mixed-phase regions of cloud compare well to size distributions from a PMS FSSP probe also onboard the aircraft during the test flights. In regions of cloud with nearly pure ice, the HOLODEC size distributions compare better to FSSP size distributions corrected for non-spherical ice particles. A straightforward algorithm for detecting shattered particles utilizing the particles' three-dimensional positions eliminates the obvious ice particle shattering events from the data set. Resulting size distributions are reduced by approximately a factor of two for particles 25 to 70 μm in equivalent diameter, compared to size distributions of all particles. The comparison with the FSSP under cloud conditions free of large ice particles provides an estimate of the magnitude of shattering biases in the FSSP and a correction for the FSSP's calibration for particle sizing.

2. HOLOGRAPHY VS. OTHER METHODS TO MEASURE CLOUD ICE PARTICLES

*Corresponding author's address: Jacob P. Fugal; EOL/RAF National Center for Atmospheric Research; PO Box 3000; Boulder, CO 80307; E-Mail: fugal@ucar.edu

Accurate ice particle size distributions and number densities are necessary for understanding and modeling cloud processes such as precipitation formation and radiative transfer, and for validation of remote sensing and satellite measurements. Many methods and instruments have been devised to measure ice particles, yet there is still considerable uncertainty in measuring small (less than about 100 μm) ice particles (Baum et al., 2005; McFarquhar et al., 2007). Beyond the inherent uncertainty in counting statistics, the uncertainty in small ice size distributions results primarily from poorly defined sample volumes, instrument particle-size resolution limits, and instrument-induced ice particle breakup.

Remedies for some of these problems exist: for example, given certain assumptions FSSP size measurements can be corrected for ice, effective instrument resolution can be improved via post-processing (Korolev, 2007), and instrument housings can be modified to reduce shattering (Field et al., 2003b). Furthermore, new instruments are being developed to measure small ice particles without some of these problems, such as the Small Ice Detector (SID) (Field et al., 2003a) and the SPEC 2D-S (Stereo) probe (Lawson et al., 2006). The SID probe measures light scattered by ice particles at many angles, and can yield ice particle size and crystal habit within the size range of approximately 1 to 50 μm. The SPEC 2D-S (Stereo) optical array probe can measure cloud particle size and a two-dimensional (sometimes three-dimensional) profile in the size range of about 10 to 1000 um.

Digital holography is one of several approaches that allows for improvements in the measurement of ice size distributions. In this abstract, we briefly present some results from the Holographic Detector for Clouds (HOLODEC) 1, which is a prototype airborne digital holographic instrument. In relation to the existing uncertainties, holography has the benefit of providing a well-defined sample volume, a uniform and well-defined resolution, and three-dimensional spatial information that can assist in identifying shattered crystals. The difficulty of using digital holography is the added complexity in data processing, which includes digital reconstruction and particle detection.

In the rest of this abstract, we show size distributions taken during the 2003-09-17 Research Flight of the IDEAS 3 field campaign conducted in the Colorado area during August and September 2003 (Fugal et al., 2004). Holograms were reconstructed via commonly used methods (Fugal et al., 2004; Kim and Lee, 2007; Kreis et al., 1997) as further detailed in Fugal et al. (2008). The reconstruction of about 10,000 holograms was done in about 6 days on a 32 processor computer cluster using MATLAB cluster computing software running on a Ubuntu Linux operating system. The next section discusses the cloud environmental conditions in which these holograms were taken using measurements from other instrument aboard the aircraft. The final section shows several results from this single flight.

3. DATA SAMPLE

Here we show the cloud environmental conditions in which the HOLODEC 1 instrument aboard the U.S. National Center for Atmospheric Research C-130 Hercules Q aircraft obtained holograms during Research Flight 2003-09-17. Figure 1 shows the altitude, temperature, and dewpoint during the time period during which we show results from HOLODEC 1 holograms. The bars in the figure (also shown in Figures 2 and 3) show times for which size distributions in Figure 4 are calculated. The black dots in this Figure show times during which we obtained good holograms (also in Figures 2 and 3). Figure 2 shows total and liquid water content as measured by the Nevzorov probe showing when we expect nearly all ice or mixed ice and liquid water cloud particles. While the King probe might be preferable to indicate ice or mixed-phase clouds, it's data quality from this flight was too poor to use in data analysis. Finally, Figure 3 shows 2D-C and FSSP number densities for both data sets as well as times at which HOLODEC 1 recorded good holograms. These time periods are of interest as the low number densities of the 2D-C instrument indicate that there are few large ice particles to shatter on the leading probe parts, and the high number densities of the FSSP indicate we should have measurable number densities of ice particles to compare between the FSSP and HOLODEC probes.

4. RESULTS

After reconstructing the holograms of cloud particles, we have the three-dimensional position of each particle, its two-dimensional profile, and its size. The shattering detection algorithm utilizes the three-dimensional position information of the ice particles to search for extremely localized clusters of ice particles. These clusters are most probably shards of larger particles having impacted on leading probe housing and are swept along an aerodynamic surface that intersects the sample volume. Holograms with these clusters of ice particles are excluded from the size distributions and number densities shown as blue squares in Figures 4 and 5.

Also, we've attempted to correct reported FSSP size distributions which are calibrated for spherical water droplets to randomly oriented droxtal shaped (a type of faceted sphere) ice particles(Yang et al., 2003; Zhang et al., 2004). The correction is only approximate as ice particles appear in many habits and surface conditions. This approximate correction aids in estimating actual size distributions, and, in our case, comparing size distributions of ice particles (Field et al., 2003a).

Figure 4 compares HOLODEC 1 size distributions for all particles, and excluding shattered particles with FSSP size distributions for both uncorrected and ice-corrected size distributions. Note in row (a) that the ice-corrected distribution matches much better than the uncorrected. Row (b) has neither FSSP uncorrected or ice-corrected matching very well, but row (c) has the uncorrected distribution comparing the best. This is consistent with the Nevzorov probe measurements in Figure 2 with nearly pure ice appearing in time period (a) and mixed phase occuring in time periods (b) and (c). The temperatures in Figure 1 also shows time periods (b) and (c) being warmer and at lower altitudes than time period (a). Figure 5 shows the number density of all detected particles as a time series in comparison with the FSSP number densities with the approximate correction for ice particles. The corrected FSSP number densities compare well earlier in the time series where the particles are nearly pure ice, and worse in the time period when the cloud is warmer and mixed phase. Note that the rejected shattered particles (difference of green pentagrams and blue squares) are typically no more than approximately 50 % of all particles in the time series.

Finally, Figure 6 shows some of the reconstructed ice particle images of various sizes as reconstructed by the automated particle finding algorithm. This figure shows the quality of reconstructed

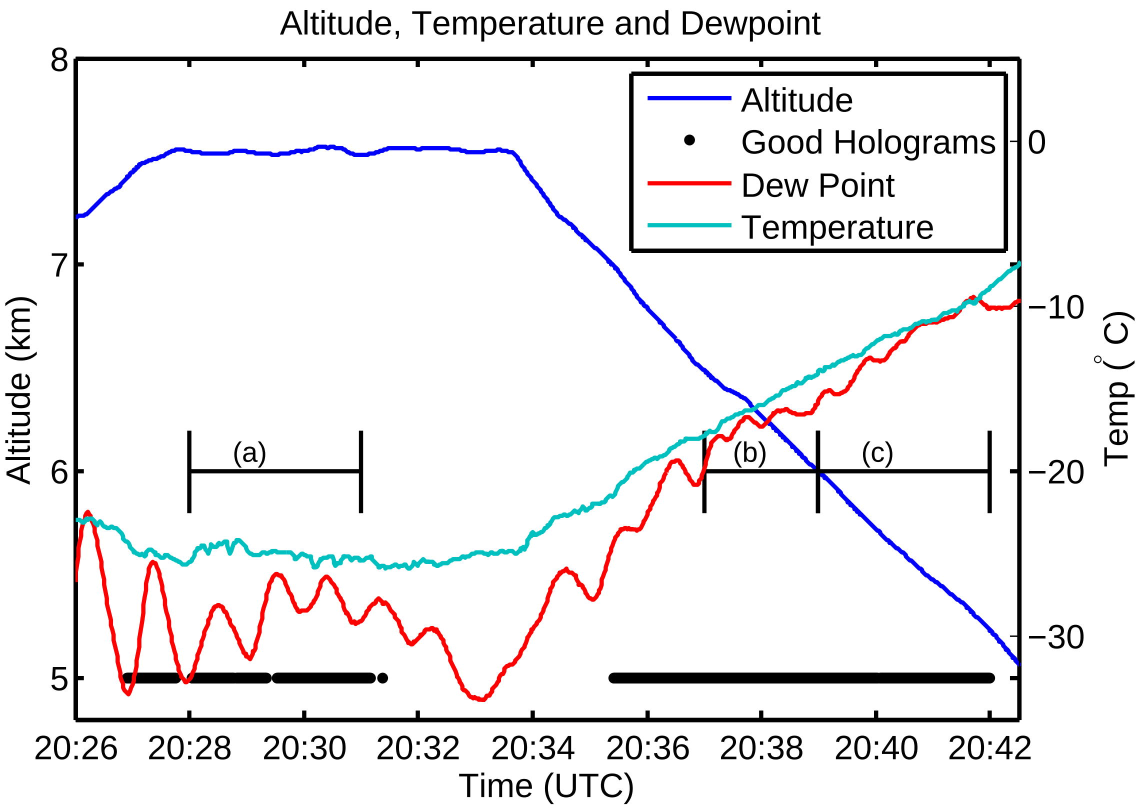

Figure 1: Altitude, temperature and dewpoint during for times of which good holograms were taken and reconstructed for the 2003-09-17 Research Flight. The labels in brackets from (a) to (c) correspond to size distribution panels in Figure 4.

particle images in holograms. It also gives evidence than an automated particle finding algorithm can correctly find the particle position without user intervention even for large complex-shaped particles. This is critical for an instrument such as HOLODEC 1 to be useful for routine cloud particle measurements in the field.

5. CONCLUSION

We have shown that the HOLODEC 1 instrument and its associated automated hologram processing routines can produce size distributions of cloud ice particles in the size range of 25 μm to about 100 μm comparable to that of other commonly used instruments such as the FSSP. It can distinguish ice and water particles when they are large enough ($\sim 100\,\mu$m) to distinguish by shape. It can detect shattered events based on the three-dimensional spatial distributions of cloud ice particles and searching for anomalously high local concentrations of these particles. Finally, we have shown that the automated hologram processing routine can find the position, shape and size of even the larger particles. Future versions of this instrument would be improved by including a camera with a much higher and/or larger image size and therefore have a larger volume sample rate which would yield better statistics in number densities of the larger particles.

ACKNOWLEDGEMENTS

This work is supported by an NSF Graduate Research Fellowship, a NASA Earth System Science Fellowship, a Michigan

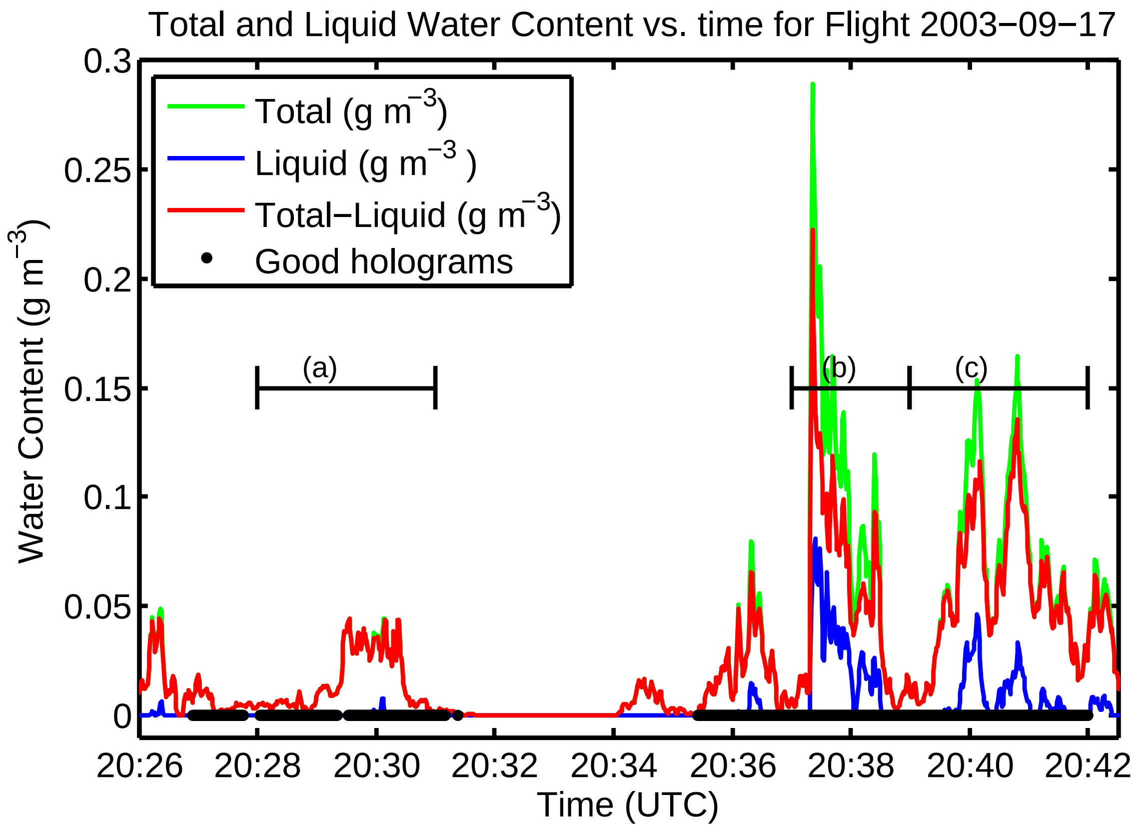

Figure 2: Total, liquid, and ice (total minus liquid) water content for the 2003-09-17 Research Flight. The labels in brackets from (a) to (c) correspond to size distribution panels in Figure 4.

Space Grant Consortium Graduate Fellowship, and NSF Grant ATM-0535488. We thank the staff of NCARs Research Aviation Facility for aiding us in analyzing the data from other aircraft probes taken during the IDEAS 3 campaign. We also thank Ping Yang for providing the library of scattering calculations for droxtals. We thank Paul Field for helpful comments and discussion. The US National Center for Atmospheric Research is under sponsorship of the US National Science Foundation.

References

Baum, A. B., P. Yang, A. J. Heymsfield, S. Platnick, M. D. King, Y.-X. Hu, and S. Bedka, 2005: Bulk scattering properties for the remote sensing of ice clouds. part ii: Narrowband models. *J. Appl. Meteor.*, **44**, 1896–1911.

Field, P. R., A. J. Baran, P. H. Kaye, E. Hirst, and R. Greenaway, 2003a: A test of cirrus ice crystal scattering phase functions. *Geophys. Res. Lett.*, **30**, 1752.

Field, P. R., R. Wood, P. R. A. Brown, P. H. Kaye, E. Hirst, R. Greenway, and J. A. Smith, 2003b: Ice particle interar-

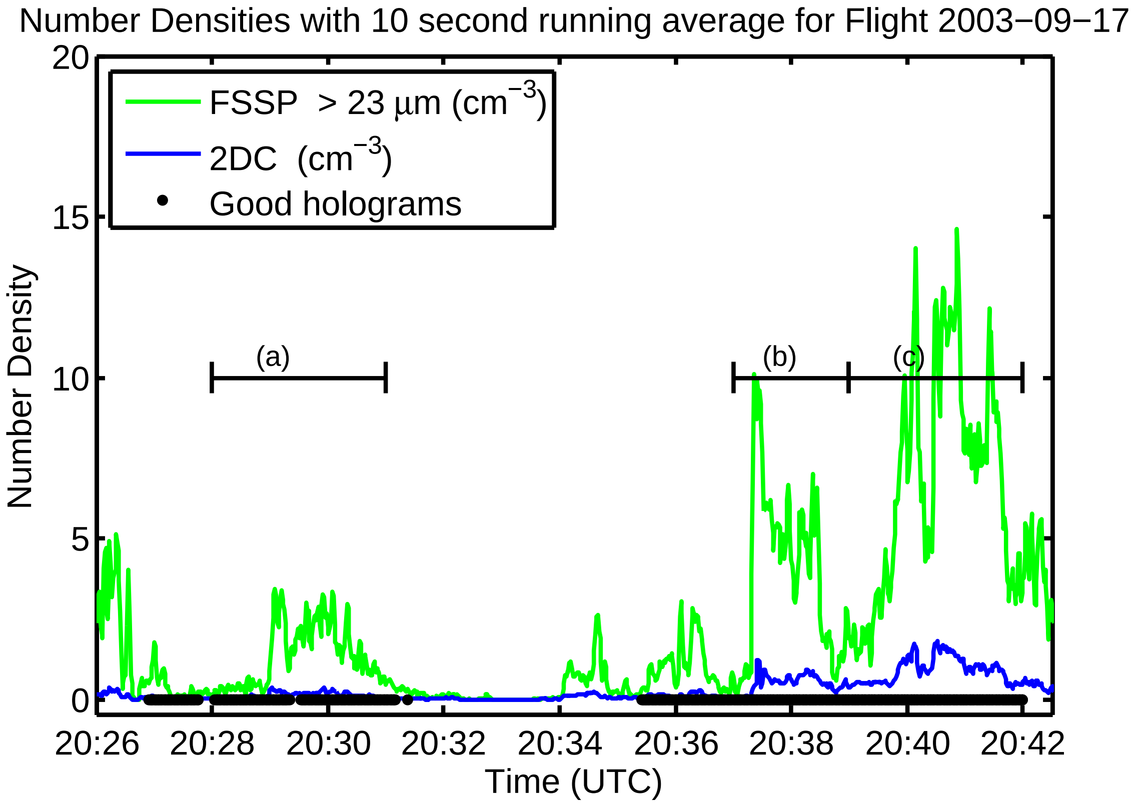

Figure 3: Particle number densities from the FSSP and the 2D-C probes from the 2003-09-17 Research Flight. Also shown are the times where HOLODEC recorded clear holograms. The labels in brackets from (a) to (c) correspond to size distribution panels in Figure 4.

rival times measured with a fast fssp. *J. Atmos. Ocean. Tech.*, **20**, 249–261.

Fugal, J. P., T. J. Schulz, and R. A. Shaw, 2008: Practical methods for reconstruction and characterization of particles in digital inline holograms, to be submitted to Measurement Science and Technology.

Fugal, J. P., R. A. Shaw, E. W. Saw, and A. V. Sergeyev, 2004: Airborne digital holographic system for cloud particle measurements. *Appl. Opt.*, **43**, 5987–5995.

Kim, S. and S. J. Lee, 2007: Measurement of 3d laminar ow inside a micro tube using micro digital holographic particle tracking velocimetry. *J. Micromech. Microeng.*, **17**, 2157–2162.

Korolev, A., 2007: Reconstruction of the sizes of spherical particles from their shadow images. part i: Theoretical considerations. *J. Atmos. Ocean. Tech.*, **24**, 376–389.

Kreis, T. M., M. Adams, and W. P. O. Juptner, 1997: Methods of digital holography: a comparison. *Proc. of SPIE*, **3098**.

Lawson, R. P., D. O'Connor, P. Zmarzly, K. Weaver, B. Baker, Q. Mo, and H. Jonsson, 2006: The 2d-s (stereo) probe: design and preliminary tests of a new airborne, high-speed, high-resolution particle imaging probe. *J. Atmos. Ocean. Tech.*, **23**, 1462–1477.

McFarquhar, G. M., J. Um, M. Freer, D. Baumgardner, G. L. Kok, and G. Mace, 2007: Importance of small ice crystals to cirrus properties: Observations from the tropical warm pool international cloud experiment (twp-ice). *Geophys. Res. Lett.*, **34**, L13803.

Yang, P., B. A. Baum, A. J. Heymsfield, Y.-X. Hu, H.-L. Huang, S.-C. Tsay, and S. A. Ackerman, 2003: Single scattering properties of droxtals. *J. Quant. Spectrosc. Radiat. Transfer*, **79**, 1159–1169.

Zhang, Z. B., P. Yang, G. W. Kattawar, S.-C. Tsay, B. A. Baum, Y. X. Hu, A. J. Heymsfield, and J. Reichardt, 2004: Geometrical-optics solution to light scattering by droxtal ice crystals. *Appl. Opt.*, **43**, 2490–2499.

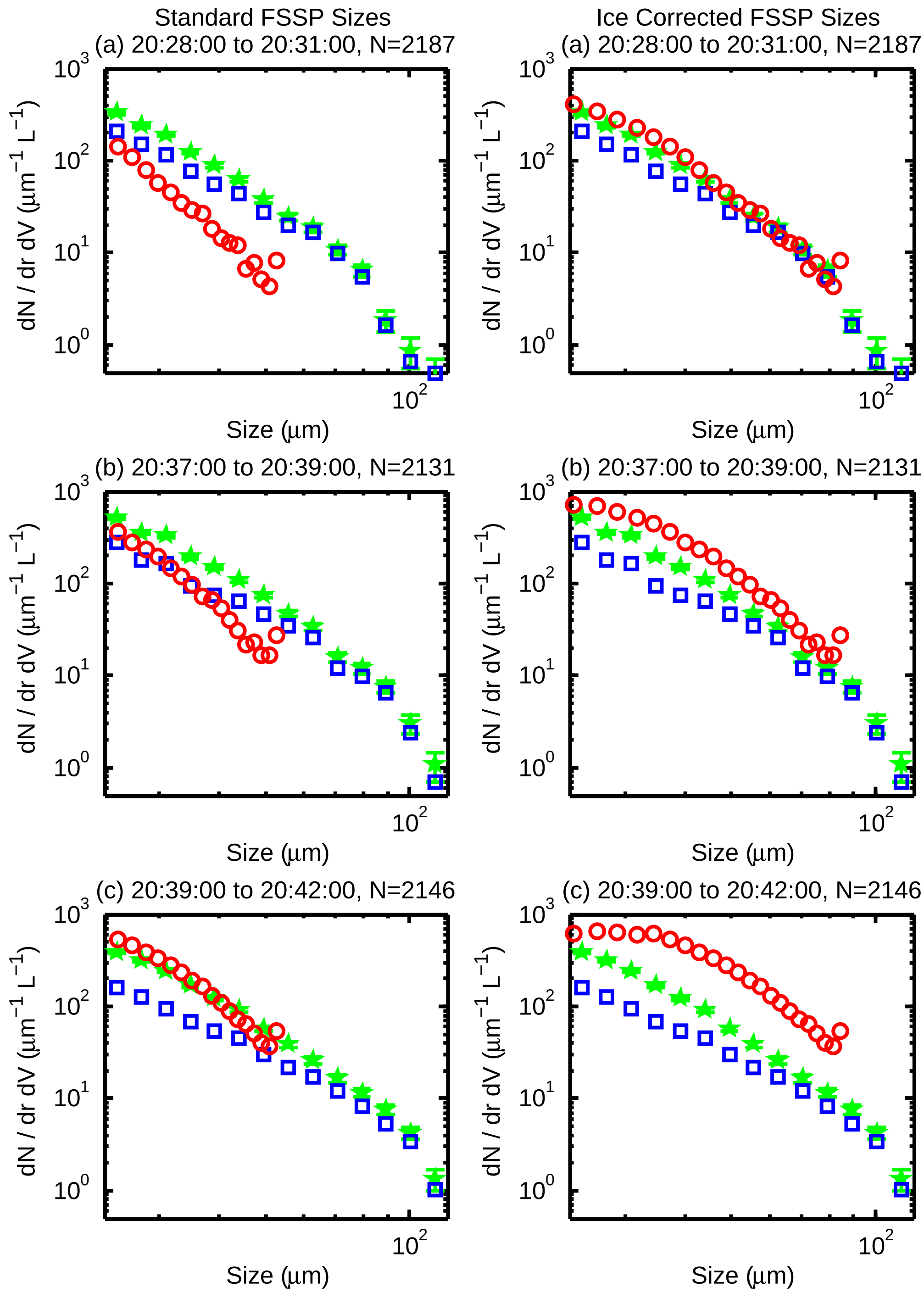

Figure 4: Size distributions for the time shown above each plot as is the number N of particles used to figure the HOLODEC 1 total size distribution. The red circles show the FSSP size distributions, the green pentagrams and error bars show the HOLODEC 1 size distributions, and the blue squares show the HOLODEC 1 size distributions with the holograms with shattered particles excluded. The left column shows FSSP size distributions as calibrated for spherical water droplets. The right column shows FSSP sizes corrected for randomly oriented droxtal (a type of faceted sphere) shaped ice particles.

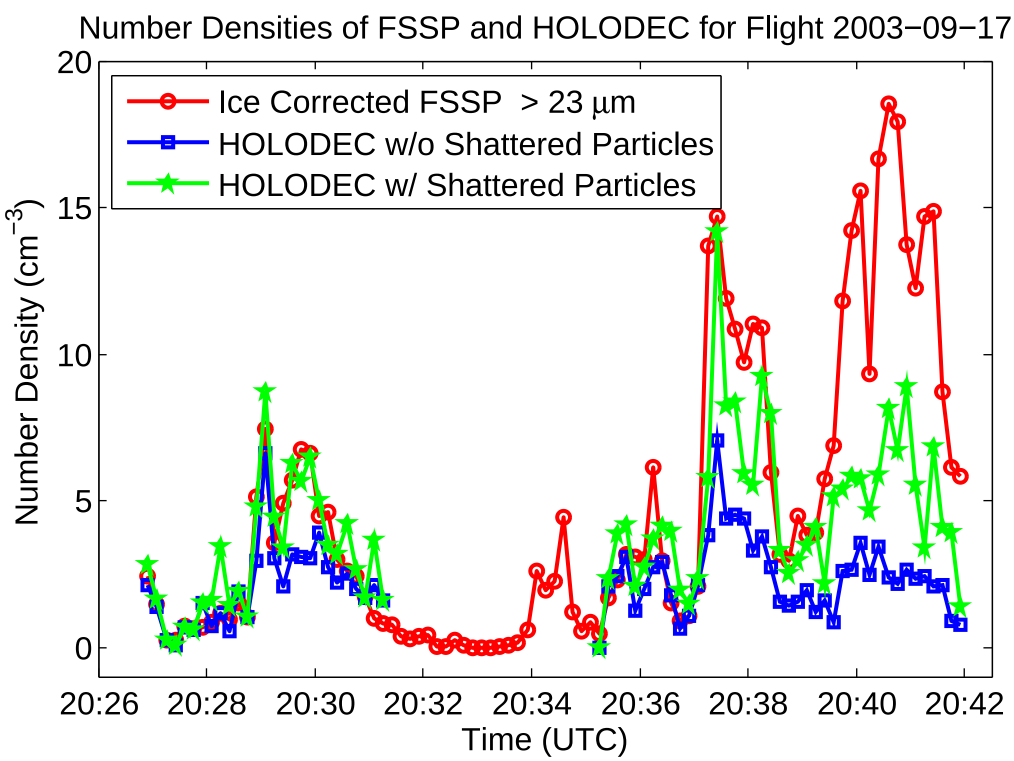

Figure 5: Number densities averaged over 10 second intervals from FSSP (corrected to droxtal-shaped ice particles) and HOLODEC.1

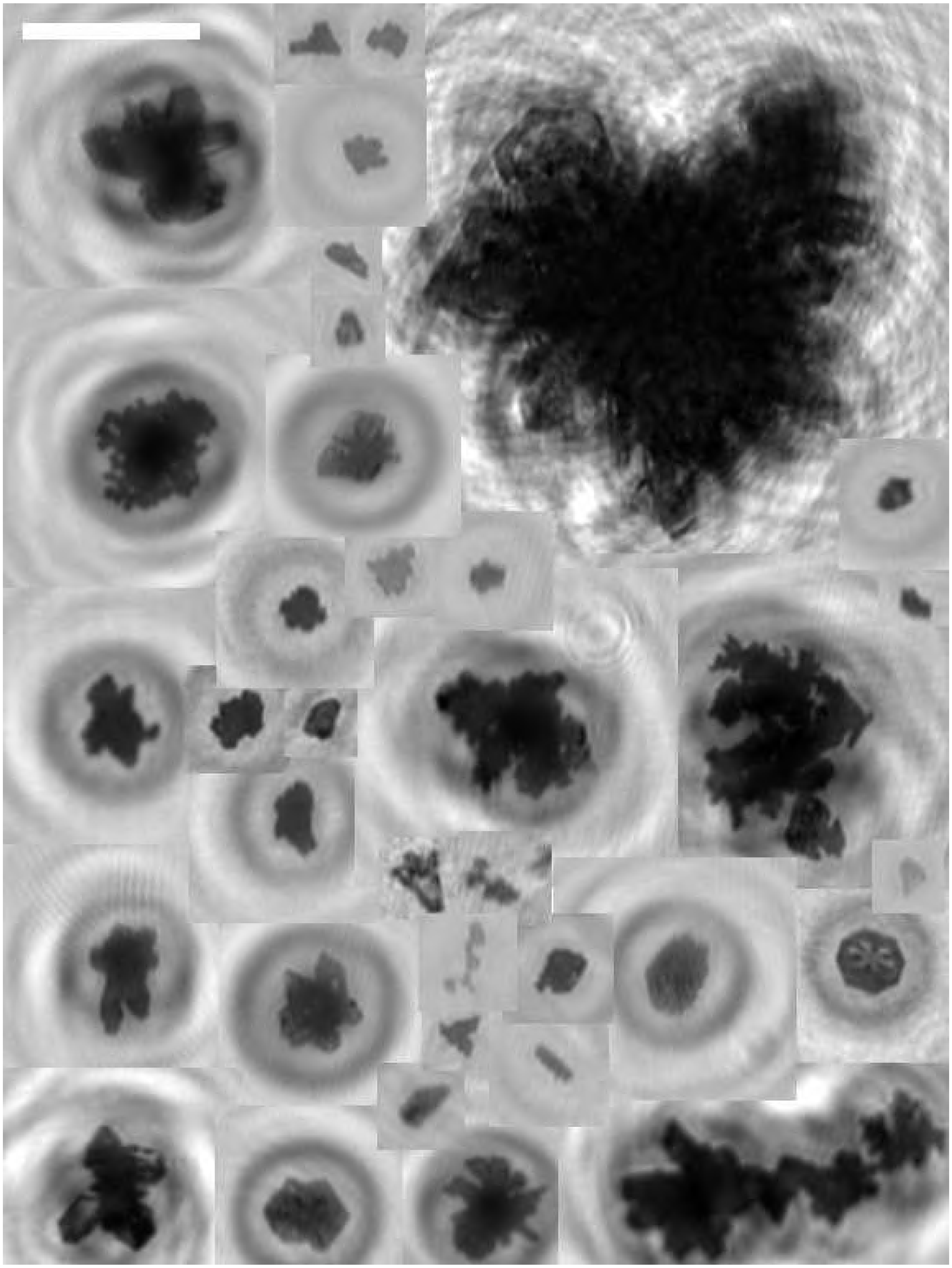

Figure 6: A sample of ice particles taken during Research Flight 2003-09-17. All particles are shown as reconstructed by the automated particle finding algorithm (Fugal et al., 2008) and are only scaled to improve contrast for printing. The white scale bar in the upper left is 0.5 mm in length.

VISIBILITY PARAMETERIZATIONS FOR FORECASTING APPLICATIONS

I.Gultepe[1], J. Milbrandt[2], S. Benjamin[3], G. A. Isaac[1], S. G. Cober[1], and B. Hansen[1]

[1] Cloud Physics and Severe Weather Research Section, Science and Technology Branch, Environment Canada, 4905 Dufferin Street, Downsview, Ontario, Canada, M3H 5T4, Canada.
[2] Numerical Weather Prediction Research Section, Science and Technology Branch, Environment Canada, Dorval, Quebec, Canada
[3] NOAA Earth System Research Laboratory, R/E/GSD, 325 Broadway, Boulder, CO 80305, USA

1. INTRODUCTION

Fog and its effect on visibility (*Vis*) play an important role in our daily life. The total economic loss associated with the impact of fog on aviation, marine and land transportation can be comparable to those of winter storms. For example, in the pre-Christmas period of December 20-23, 2006, the British Airport Authority (BAA) reported that a blanket of fog and freezing fog over the UK forced 175,000 passengers to miss flights from its seven British airports, with Heathrow the worst affected. Early estimates suggested this disruption to air travel cost British Airways at least £25 million (Gadher and Baird, 2007). The costs to stranded passengers in terms of money and inconvenience may be impossible to calculate but it is certainly significant.

In Canada, approximately 50 people per year die due to fog-related motor vehicle accidents (Gultepe et al., 2007). Westcott (2007) stated that approximately 30 deaths occur annually under foggy conditions in Illinois, excluding the city of Chicago. In Europe, a major fog research project called COST-722 (COoperation in Field of Scientific and Technical Research), with objectives of reducing economic and human life losses, was undertaken to develop advanced methods for very short-range forecasts of fog and low clouds (Jacobs et al., 2007). In collaboration with COST-722, Gultepe et al (2008) performed three field projects to study warm fog conditions and developed microphysical parameterization suitable for application to fog and precipitation measurements.

Fog can form over various time and space scales but not all models can resolve small time and space scales e.g. minutes and meters, respectively. Therefore, high-resolution models have been developed to better nowcast fog (Bott et al., 1990). Unfortunately, high-resolution models are not always available; therefore visibility parameterizations have been used in forecasting models.

[1]*Corresponding author email:ismail.gultepe@ec.gc.ca*

There are several *Vis* parameterizations for hydrometeor types e.g. rain and snow (Rasmussen et al., 1999). Fog does not always occur alone but it is associated with other meteorological hydrometers such as rain or snow. Therefore, *Vis* parameterizations should include the visibility from relative humidity with respect to water (RH_w), fog (water or ice), and precipitation-related hydrometeors.

In this work, observations collected during the Fog Remote sensing And Modeling (FRAM) field projects (Gultepe et al., 2008) were analyzed to develop Vis parameterizations. A model simulation was performed using the GEM-REG (Côté et al., 1998) for an "only fog" case (Fig. 1), without rain, which occurred in eastern Canada near Lunenburg Nova Scotia. In this case, the fog occurrence was mainly related to warm air advection from the Atlantic Ocean over the project area. In addition, several parameterizations are suggested for liquid fog, ice fog, *RH*, rain, and snow. Finally their integration together is discussed along with the associated uncertainty.

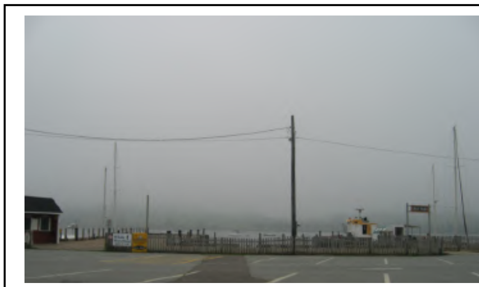

Fig. 1: Marine fog as occurred over Lunenburg port on April 18 2006 during the FRAM field project.

2. VIS DEFINITIONS

a) Daytime definition of Vis

Meteorological Observation Range (MOR) definition by the World Meteorological Organization (WMO) is based on Koschmieder law. Assuming a brightness contrast threshold (ε) as 0.05, daytime visibility (Vis_d) is given as

$$Vis_{d5} = 2.996\beta_{ext}^{-1} \;, \qquad (1)$$

where ln(1/ε)=2.996. β_{ext} is the extinction coefficient given as

$$\beta_{ext} = \sum_{i=1}^{m} \pi Q_{ext}(r) n(r) r^2 dr \;, \qquad (2)$$

where Q_{ext} is the extinction efficiency and equals ~2 for large particles. For ice crystals, it depends on particle shape, particle spectra, and visible light wavelength.

Using ε=0.02 (threshold of luminance contrast or brightness contrast), Eq. 1 is also given as

$$Vis_{d2} = 3.912\beta_{ext}^{-1} \,. \qquad (3)$$

where ε is defined as $(B_r - B_b)/B_b$, B_r is the apparent luminance of the object at range R (known) and B_b is the apparent luminance of the background of the object at range R (known). In the Rapid Update Cycle (RUC) model (Benjamin et al., 2004) *Vis* is obtained by setting ε=0.02 so that Vis_{d5} is based on the WMO MOR definition as

$$Vis_{d2} = 1.3 Vis_{d5} \,. \qquad (4)$$

In general, measurements from *Vis* sensors (e.g. the FD12P and Sentry *Vis*) are given based on the WMO MOR definitions.

b) *Nighttime definition of Vis*

The nighttime *Vis* (Vis_n) is obtained (Rasmussen et al., 1999) using the simplified Allard's law as

$$Vis_n = \frac{I_o}{C_{DB}} \exp(-\beta_{ext} Vis_n) \;, \qquad (5)$$

where C_{DB}=0.084 miles^{-1} and I_o=25 candela. Comparing Vis_d [km] versus Vis_n [km], using the assumed coefficients in Eq. 5, a simplified equation can be obtained as

$$Vis_n = 1.8507 Vis_d^{\;0.814} \,. \qquad (6)$$

For forecasting applications, measurements done with instruments (if they do not perform processing internally) should be converted to nighttime visibilities using Eq. 6.

3. MEASUREMENTS

Surface observations during the FRAM field project were collected at the Center for Atmospheric Research Experiment (CARE) site near Toronto, Ontario during the winter of 2005-2006 and in Lunenburg, Nova Scotia during the summers of 2006 and 2007 (Gultepe et al., 2008). The main observations used in the analysis were fog droplet spectra from a fog measuring device (FMD; DMT Inc.), Vis and precipitation rate (*PR*) from the VAISALA FD12P all-weather sensor and the OTT laser based optical disdrometer called ParSiVel (*Par*ticle *Si*ze and *Vel*ocity), and RH_w together with temperature (*T*) from the Campbell Scientific HMP45 sensor. Liquid water path (*LWP*) and liquid water content (*LWC*) were obtained from a microwave radiometer (MWR). Fog coverage and some microphysical parameters such as droplet size, phase, and LWP were also obtained from satellites (e.g. GOES and MODIS products). Details on some of the instruments can be found in Gultepe and Milbrandt (2007) and are discussed here briefly.

The FD12P Weather Sensor is a multi-variable sensor for automatic weather stations and airport weather observing systems (VAISALA Inc.). The sensor combines the functions of a forward scatter *Vis* meter and a present weather sensor. Fig. 2 shows an example of FD12P measurements for the June 18 2006 case. This sensor also measures the accumulated amount and instantaneous PR for both liquid and solid precipitations, and provides the *Vis* and precipitation type related weather codes given in the World Meteorological Organization (WMO) standard SYNOP and METAR messages.

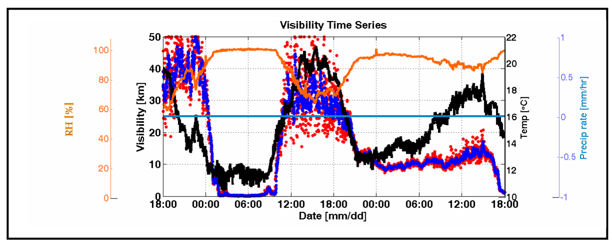

Fig. 2: Time series of FD12P measurements for a fog event occurred during June 18 2006.

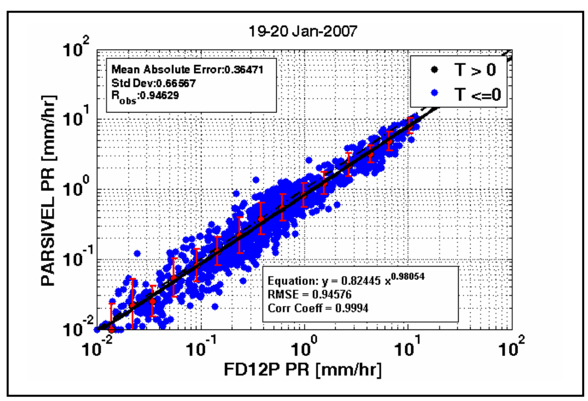

Fig. 3: The OTT Parsivel distrometer *PR* versus FD12P *PR* for a snow event during the winter of 2007.

The FD12P detects precipitation droplets from rapid changes in the scatter signal. The droplet data are then used to estimate precipitation rate and amount. Based on the manufacturer's specifications, the accuracy of the FD12P measurements for *Vis* and *PR* are approximately 10% and 0.05 mm h^{-1} respectively. The PR measurements from both the FD12P and OTT distrometer for a snow event are shown in Fig. 3. This suggests that FD12P *PR* measurements are within acceptable limits and they have been used in the analysis.

The OTT ParSiVel is also designed to operate under all-weather conditions (Löffler-Mang and Joss, 2000; Löffler-Mang and Blahak, 2001). This instrument can provide information on present weather, optical rain gauging, particle spectrum, visibility, and radar reflectivity. It has a built-in heating device to reduce the effects of freezing and frozen precipitation accreting on the critical surfaces on the instrument. The particles are classified into 32 classes of sizes and velocities. The basic measuring range for velocity and size is from 0 to 20 m s^{-1}, and 0.2 mm to 25 mm, respectively. According to the manufacturer, the rain rate error is approximately 5%. The accuracy of the snow precipitation rate is discussed later.

The fog-related microphysics parameters e.g. *LWC*, size, and droplet number concentration (N_d) were calculated from the FMD spectra, and an example of the fog droplet spectra for the fog event on June 18 2006 is given in Fig. 4.

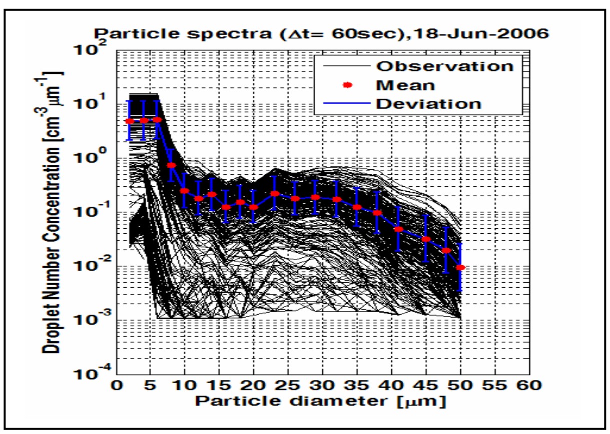

Fig. 4: Fog droplet spectra from the FMD instrument on June 18 2006.

4. GEM-REG PHYSICS AND SIMULATION

The 18 June 2006 case was simulated using the Canadian operational Global Environmental Multiscale (GEM) numerical weather prediction model. The model dynamics are discussed in detail by Côté et al. (1998). GEM has a comprehensive physics package which includes a planetary boundary layer scheme based on turbulent kinetic energy, implicit (explicit) vertical (horizontal) diffusion, and a detailed land-surface scheme. The solar and infrared radiation package is fully interactive with the model clouds. Subgrid-scale convection is treated by the Kain and Fritsch (1993) convective parameterization. The Sundqvist et al. (1989) condensation scheme is used to treat grid-scale clouds. This cloud scheme includes a prognostic equation for a single variable representing non-sedimenting condensed water mass (liquid or frozen). The model uses 58 unevenly spaced terrain-following vertical levels.

5. METHOD AND PREVIOUS STUDIES

In this section, *Vis* parameterizations developed for various hydrometeors and *RH* are given and compared to others that were previously reported.

a) Vis-RH relationships

The *Vis-RH* relationships based on percentiles were obtained using observations from the FD12P Vis and Campbell RH_w measurements. A single fit (applied to means) cannot always be valid for different environments; therefore, the fits for percentiles should be used to more accurately estimate *Vis*. The *Vis* versus RH_w fits from other studies are summarized in Table 1. In general, the *Vis*-RH_w relationship obtained in the present work was significantly different from the one used in the RUC model (Smirnova et al., 2000; Gultepe et al., 2008).

Table 1: *Vis* versus RH_w relationships based on the various field programs and RUC model.

Relationship	Reference
$Vis_{RUC} = 60\exp(-2.5*(RH_w - 15)/80)$	RUC model
$Vis_{FRAM-C} = -41.5\ln(RH_w) + 192.3$	Gultepe et al. (2006a)
$Vis_{AIRS} = -0.018RH_w^{\;2} + 1.46RH_w + 30.8$	Gultepe et al. (2006a)
$Vis_{FRAM-L(95\%)} = -0.00012\mathrm{RH}_w^{2.70} + 27.45$	FRAM
$Vis_{FRAM-L(50\%)} = -5.19*10^{-10}\,\mathrm{RH}_w^{5.44} + 40.10$	FRAM
$Vis_{FRAM-L(5\%)} = -9.68*10^{-14}\,\mathrm{RH}_w^{7.19} + 52.20$	FRAM

b) Vis for fog

i) Liquid fog

Gultepe et al (2006b) developed a parameterization for T>0°C and RH_w~100% that is based on both *LWC* and N_d. The current RUC model uses a *Vis-LWC* relationship for fog visibility (Stoelinga and Warner, 1999). Using information that Vis decreases with increasing N_d and *LWC,* a relationship between Vis_{obs} and $(LWC.N_d)^{-1}$ called the "*fog index*" is determined as

$$Vis_{obs} = \frac{1.002}{(LWC \cdot N_d)^{0.6473}}\,. \qquad (7)$$

This fit suggests that *Vis* is inversely related to both *LWC* and N_d. The maximum limiting *LWC* and N_d

values used in the derivation of Eq. 7 are about 400 cm^{-3} and 0.5 g m^{-3}, respectively. The minimum limiting N_d and *LWC* values are 1 cm^{-3} and 0.005 g m^{-3}, respectively. In Eq. 7, N_d can be fixed as 100 cm^{-3} for marine environments and 200 cm^{-3} for continental fog conditions. These values of N_d are traditionally used in modeling applications which cannot be valid for all environmental conditions.

ii) Ice fog and Vis parameterization

Ice fog forecasting is usually not performed with forecasting models because ice water content (*IWC*) and ice crystal number concentration (N_i) are not accurately obtained from existing microphysics algorithms (Gultepe et al., 2001). If both parameters were available from a high-resolution fog/cloud model, they could be used for ice fog forecasting. Ice fog occurs commonly in northern latitudes when T is below -15°C (based on the first author's observations in Barrow, Alaska). The formation of ice fog usually occurs when the *RH* becomes saturated with respect to ice (RH_i) with no precipitation. Ice fog occurs because of deposition nucleation process that depends on nuclei size and concentration, and temperature. Previous reports suggested that liquid droplets can be found at T down to about -40°C but it is not common to find droplets colder than -20°C. Using aircraft observations collected during the First International Regional Experiment-Arctic Cloud Experiment (FIRE-ACE) Gultepe et al., 2003 found that frost point temperature (T_f) can be related to dew point temperature (T_d) as:

$$T_f = T_d + \Delta f \ , \tag{8}$$

where T_d [°C] and T_f [°C] were obtained using LiCOR instrument humidity measurements (Gultepe et al., 2003) and their difference is parameterized as:

$$\Delta f = p_1 T_d^3 + p_2 T_d^2 + p_3 T_d^1 + p_4 \ , \tag{9}$$

where p_1=0.000006; p_2= -0.0003; p_3=-0.1122; and p_4= 0.1802. If T_d is known, then T_f [°C] is calculated using Eqs. 8 and 9. The following equation is given for saturated vapor pressure by Murray (1967) as

$$e_s = 6.1078 \exp[\frac{a(T - 273.16)}{(T - b)}] , \tag{10}$$

where T [K], e [mb], a=21.8745584 (17.2693882); b=7.66 (35.86) over the ice (water) surface. Then, using T_f and T, relative humidity with respect to ice (RH_i) is obtained from the following equation

$$RH_i = \frac{e_i(T_d + \Delta f)}{e_{si}(T)} \ . \tag{11}$$

If RH_w and T are known, then T_d is calculated using an equation similar to Eq. 11 but for water. Using Eqs. 8-11, RH_i is then calculated. If RH_i is greater than approximately 95%, T<-10°C, and no precipitation occurs, then ice fog regions can be obtained from model simulations. If *IWC* is prognostically obtained, then Vis for ice fog, assuming that N_i and mean equivalent mass diameter (d) are known, can be obtained (Ohtake and Huffman, 1969) as:

$$Vis = \frac{1}{3}\left[3.2\frac{IWC}{N_i}\right]^{1/3} - 1.5\bar{d} \tag{12}$$

Eq. 12 shows how *Vis* changes with *IWC*, N_i, and d. In this work, it is suggested that N_i and d can be taken as 200 cm^{-3} and 7.2 µm (for high IWC e.g.>0.1 g m^{-3}), and as 80 cm^{-3} and 4.5 µm (for low *IWC* e.g.>0.01 g m^{-3}). If ice crystals form due to deposition of vapor directly onto ice nuclei at cold T, N_i can be parameterized as a function of RH_i. A relationship between N_i and RH_i for ice fog does not currently exist. Note that Eq. 12 and its validity will be verified using measurements from the FRAM-ISDAC project which took place over Barrow, Alaska, US, during April of 2008.

c) Vis for rain and snow from previous works

Previously reported *Vis* parameterizations for rain and snow have been used in modeling studies. In Table 2, the subscript *MP* presents the Marshall-Palmer distribution (Marshall and Palmer, 1948). The *SS* signifies the Sekhon and Srivastava (1970 and 1971) works for snow and rain, respectively. The *ST* represents the Stallabrass (1985) study. The *LWC* and *IWC* are in the units of [g m^{-3}] and β in [km^{-1}]. The β_s represents the extinction coefficient given by Seagraves (1984) work that is based on Muench and Brown (1977). Details on this can be found in Gultepe et al (2008). The relationships given in Table 2 are not unique because the *PR* variability with *Vis* is large (Gultepe et al. 2008; Rasmussen et al., 1999).

Table 2: Visibility versus precipitation rates for rain and snow from various studies.

Parameterizations	Notes
RUC model for rain	
$Vis_{MP} = -\log(0.02)/\beta$ $\beta = 2.24 LWC^{0.75}$	$LWC_{MP} = 0.072 PR^{0.88}$ $LWC_{SS} = 0.052 PR^{0.94}$
RUC model for snow	
$Vis_{SS} = -\log(0.02)/\beta_{ST}$ $\beta_{ST} = 10.36 IWC^{0.7776}$	$IWC_{SS} = 0.25 PR^{0.86}$
Seagraves (1984) for snow	
$Vis_S = -\log(0.02)/\beta_S$	$\beta_s = 2.52 PR^{0.77}$

d) Vis for snow and rain using probability curves

The *Vis* for rain and snow cannot be solely obtained from *Vis-PR* mean relationships because of variability in particle spectra. For this reason, percentiles (5%, 95%, 50% values) for *Vis* in rain and snow conditions can be obtained as given in Table 3. If the drizzle phase can be specified from the model, then Eq. 5 in Table 3 can be used for calculating *Vis*. This was summarized in Gultepe et al. (2008).

Table 3: Visibility versus precipitation rates for rain (Vis_R), drizzle (Vis_{DR}), and snow (Vis_S) from the FRAM observations.

Precip type	PR=[mm h^{-1}]; Vis=[km]
Rain (mean)	$Vis_R = -4.116PR^{0.176} + 9.01$
Rain (50%)	$Vis_R = -2.648PR^{0.256} + 7.65$
Rain (95%)	$Vis_R = -0.447PR^{0.394} + 2.28$
Rain (5%)	$Vis_R = -863258PR^{0.003} + 87419$
Drizzle (mean)	$Vis_{DR} = -2.658PR^{-0526} + 6.541$
	PR=[mm h^{-1}]; Vis=[km]
Snow (mean)	$Vis_S = 1.10PR^{-0.701}$
Snow (50%)	$Vis_S = 1.063PR^{-0.682}$
Snow (95%)	$Vis_S = 0.617PR^{-0.591}$
Snow (5%)	$Vis_S = 1.654PR^{-0.795}$

e) New method against Vis-PR relationships

Measurements from the OTT disdrometer were collected during the winter of 2007-2008 and used in the analysis. From the OTT disdrometer measurements, both rain and snow related parameters e.g. *LWC, IWC,* N_d, N_i, particle size, terminal velocities, extinction coefficients, PR_R, and PR_S were obtained for particle sizes>400 microns. Similar to fog *Vis,* Vis_R and Vis_S parameterizations were obtained for a snow/rain event (Fig. 5) which occurred on December 3 2007, respectively, as

$$Vis_R = 1.381\left(\frac{1}{LWC \bullet N_{Rt}}\right)^{0.5633}, \quad (13)$$

and

$$Vis_S = 29.011\left(\frac{1}{IWC \bullet N_{St}}\right)^{0.4433}. \quad (14)$$

While N_{Rt} (total number concentration of rain drops) and N_{St} (total number concentration of snow flakes) are related to various meteorological and thermodynamical parameters, here they are assumed only to be related to *P*R. This is better than using a fixed value as is done in the current forecasting models. Using the OTT disdrometer measurements, N_{Rt} and N_{St} versus *PR* parameterizations (Fig. 6) are obtained, respectively, as

$$N_{Rt} = 3.2PR_R^{0.22} \quad (15)$$

and

$$N_{St} = 8.42PR_S^{0.35}. \quad (16)$$

Note that these relationships can change depending on precipitation process and snow particle shape.

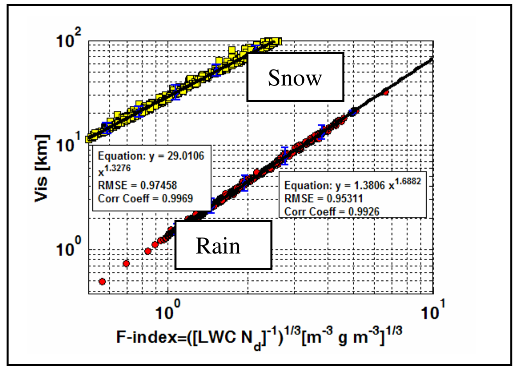

Fig. 5: *Vis* versus fog index for a precipitation event on December 3 2007.

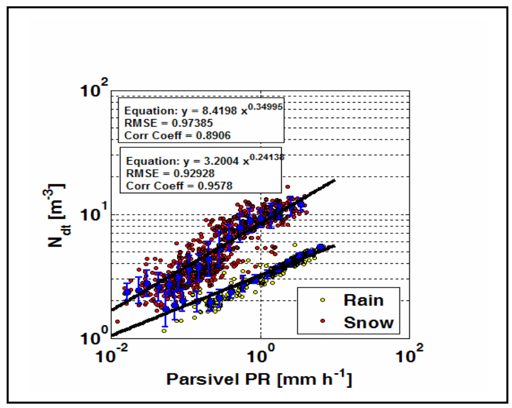

Fig. 6: Rain drop (snow crystal) number concentration versus *PR* for rain (snow) during a precipitation event on December 3 2007.

f) Integration of extinctions coefficients

Equations given for *Vis-f(LWC,*N_d*) (for rain and warm fog), Vis-f(IWC,*N_i*) (for snow and cold fog), and Vis-*RH_w parameterizations can be used to obtain integrated *Vis* values. In the case of both fog and precipitation occurring together, calculated *Vis* values are first converted to extinction coefficients (β_{ext}) using Eq. 1, then, an integrated extinction coefficient is obtained as

$$\beta_{\text{int}} = \beta_{RHw} + \beta_{LWC;IWC} + \beta_{R;S}. \quad (17)$$

The final value of *Vis* is then calculated using Eq. 1 which utilizes β_{int}.

6. RESULTS

In this section, results from the June 18 2006 marine fog case are presented. At the end of the fog episode, around noon local time, some drizzle occurred but it was not considered in the analysis.

a) Synoptic Conditions

The fog event on June 18 lasted approximately 7 h. Several GOES images showed fog areas over the project site (Fig. 7). Fig. 7 shows the foggy areas in green obtained using a technique given by Gultepe et al (2007). Fog coverage was more over land during the early hours of the event. At about 10 AM, the fog moved over the ocean, and then it moved over land again after midnight the following day. A skewT-LogP diagram (Fig. 8) from the NOAA MAPS analysis valid at 9 AM showed that lowest boundary layer was relatively saturated and winds were from southwest, resulting in conditions conducive for fog formation.

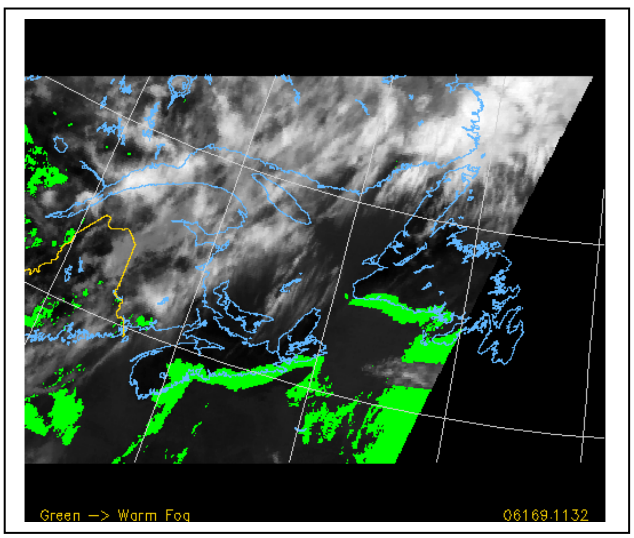

Fig. 7: the GOES fog product (green color) over FRAM project site at 06:32 EST on June 18 2006.

b) Microphysical observations

The fog event on June 18 started to occur at 02:00 AM in the morning (Fig. 2). It lasted about 7 hours and *Vis* was less than 200-300 m. The FMD N_d and *Vis* time series are shown in Fig. 9a and 9b, respectively. The *Vis* versus N_d and *LWC*, representing 1-minute averaging with standard deviation, are shown in Figs. 9c and 9d, respectively. *Vis* nonlinearly decreases with both increasing N_d and *LWC*, suggesting that *Vis* is a function of both parameters. Fog droplet settling rate and *Vis* versus fog index [$1/(LWCN_d)$] are shown in Figs. 9e and 9f, respectively. These plots suggest that droplet settling rate is a function of both *LWC* and N_d. The last two plots show the *Vis* versus reflectivity factor (*Z*) (Fig. 9g) and *Z* versus $LWCR^2_{eff}$ (Fig. 9h). Knowing *Z* for fog droplets and assuming a characteristic particle size (e.g. effective size for fog droplets), fog *LWC* can be obtained from a mm radar.

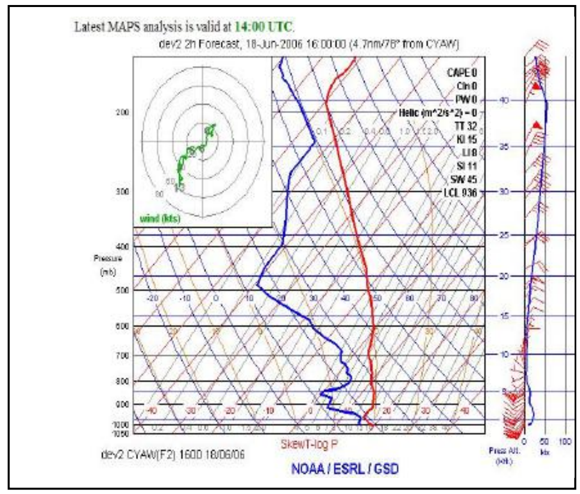

Fig. 8 SkewT-LogP diagram from the MAPS analysis valid at 09:00 AM EST.

c) GEM-REG simulations

Figure 10a depicts the simulated field of liquid water content (*LWC*) at the second lowest model level (approximately 140 m above the surface) at 10:00 UTC on 18 June 2006. Near Lunenburg Bay (the south-west region in Fig. 10a), the simulated *LWC* values are between 0.10–0.20 g m^{-3}. The visibility corresponding to this simulated liquid fog is calculated using Eq. 7. Since the droplet number concentration is not a prognostic variable in the Sundqvist cloud scheme, N_d=80 cm^{-3} is assumed in the simulations, which is typical for a maritime air mass. In fact, this value can change with T (Gultepe and Isaac, 2004). The *Vis* from the simulation is shown in Fig. 10b and it was about 0.20–0.40 km at the Lunenburg Bay area. Fig. 10c shows the RH_w over the projected area. Along the shoreline, RH_w is found to be greater than 95% which corresponds to a saturated layer with respect to water over the 15 km scale. Gultepe et al. (2008) stated that *Vis* can be about 1-2 km if no *LWC* exists which corresponds well with the satellite based fog regions shown in Fig. 7.

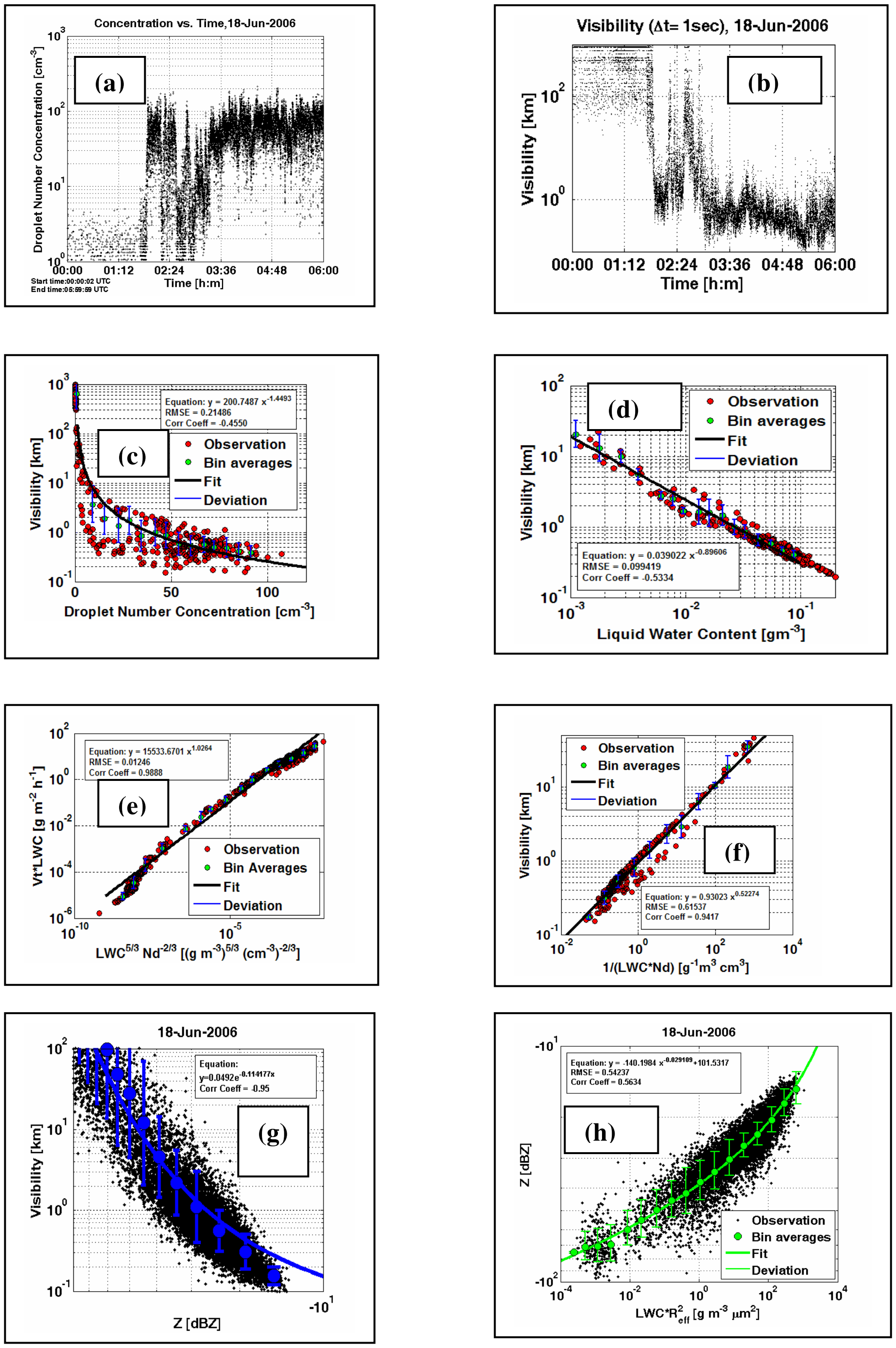

Fig. 9: Microphysical data representing a marine fog case from the FMD instrument collected during June 18 2006.

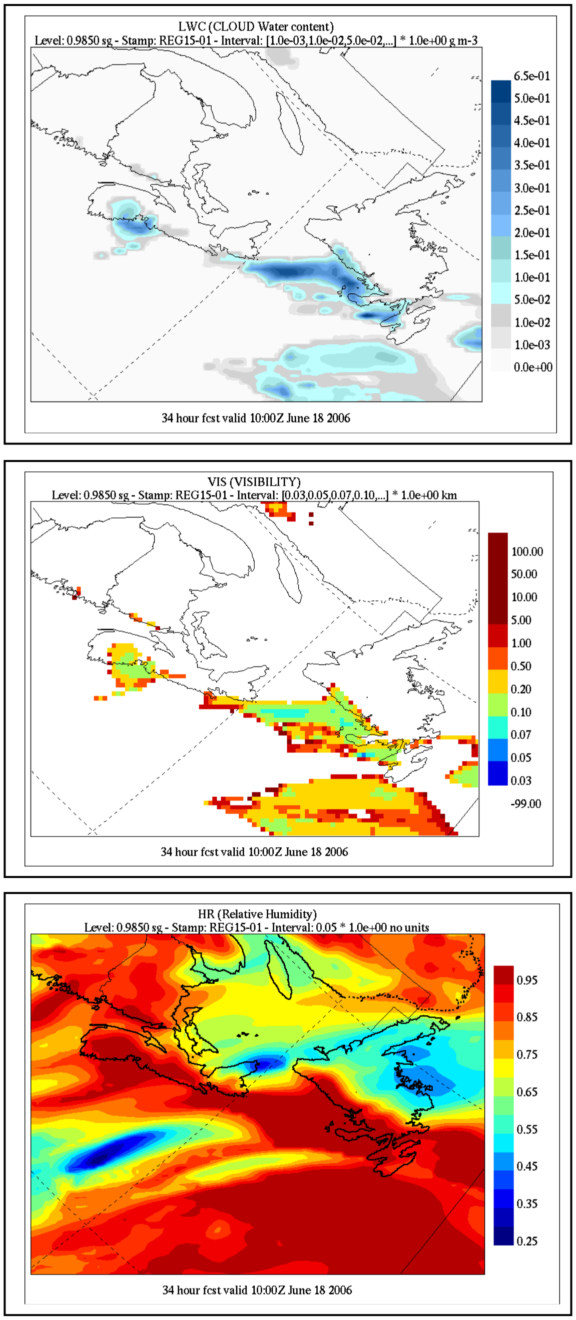

Fig. 10: GEM model simulation of (a) *LWC* [g m^{-3}] and (b) *Vis* [km], and RH_w (c) at the second lowest model level, valid at 10:00 UTC on 18 June 2006.

7. DISCUSSIONS

To accurately forecast/nowcast fog VIS, accurate model output parameters are required e.g. *LWC, N_d, RH*, and *PR*. If model output values for rain, snow, *RH*, and *LWC* are not accurate better than 20-30%, the uncertainty in *Vis* can be as high as 50% (Gultepe et al, 2006b). If fog *LWC* and N_d are not accurately known from a model at the levels closest to the surface, then *Vis* based on other parameters e.g. *PR* or *RH*, or both, cannot be used to obtain accurate *Vis*. Fog *LWC* and N_d are the major factors required for accurate *Vis* calculations and they should be obtained to an accuracy of about 10-20%.

The *Vis* probability curves need to be tested for various geographical regions. The grid-point values of *Vis* obtained from the NWP models do not necessarily correspond directly to point measurements due to issues of model grid-spacing and spatial averaging. Model-based results should also consider subgrid-scale variability of *Vis, PR, RH_w*, and condensed water content. In this work, parameterizations (obtained from *in-situ* measurements) used in the RUC model were applied for comparisons without simulations (Fig. 11). This figure suggests that Vis should also be dependent on some other parameters rather than only PR, as suggested by Eqs. 13 and 14.

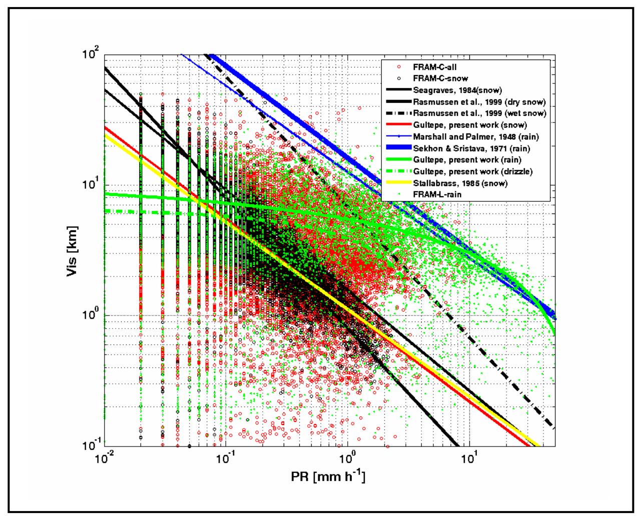

Fig. 11: The *Vis* versus *PR* for rain (green dots and red dots), snow (black dots), drizzle, and for previous studies (Table 3). The results from the present work (Table 2) are also shown. The *Vis* and *PR* are obtained from FD12P measurements.

Marine fog nowcasting/forecasting needs detailed surface fog measurements, high-resolution forecasting model outputs, and satellite observations. Integration of the data from various platforms can be used to obtain accurate fog Vis. Fig. 12 shows intensity of Vis (from July 11 to October 31 2007) related to 24 h back trajectories which ended up at Halifax International Airport, Nova Scotia. It is seen that most of the air parcels coming from the south and southwest sectors result in low *Vis* values. This suggests that analysis of sea surface temperature and back trajectories can help to better nowcast/forecast marine fog conditions.

The simulation results suggest that visibility can be estimated by using parameters produced from the cloud schemes. Applying observation-based parameterizations such as Eq. 7 as an alternative to those based on specific hydrometeor size distribution functions, can be used to compute extinction coefficients directly (as in Eq. 2). Researchers in Environment Canada are currently working on the implementation of a more detailed two-moment version of the cloud microphysics scheme (Milbrandt and Yau, 2005a,b) to treat grid-scale clouds in the high-resolution version (2.5-km grid-spacing) of the GEM model. In this scheme, both *LWC* and N_d are independent prognostic variables. This should allow a more flexible application of the visibility parameterization of Eq. 7, without the restriction of prescribing a value of N_d.

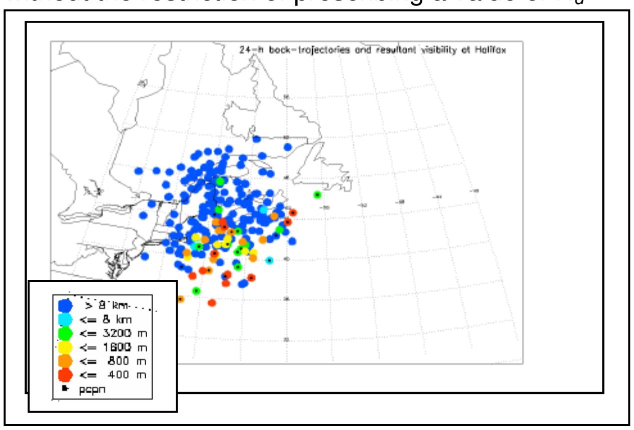

Fig. 12: Visibility intensity at the Halifax International Airport corresponding to source locations of 24-h back trajectories from July 11 to October 31 2007.

8. CONCLUSIONS

Fog *Vis* due to rain/snow is strongly related to their mass content (*MC*) and number concentrations (*N*) rather than *PR*. These two parameters play an important role in parameterizations of Vis. Using a case study, Vis as a function of *MC* and particle number concentration was suggested for both rain (Eq. 13) and snow (Eq. 14) conditions. These equations may represent rain and snow events with different microphysics, however this needs to be validated.

For snow conditions, particle shape and phase (e.g. wet snow) affect *Vis* as much as number concentration. From the definition of extinction, particle surface area is related to snowflake habit, which affects *Vis* significantly. Particle shape effect in Vis calculations can be considered using terminal velocities, particle size, or both. The combination of *IWC* and snowflake size (or N_i) can be used for *Vis* calculations (e.g. Eqs.12 and 14).

The results from the GEM-REG simulation suggest that the microphysics parameterization presented, which includes N_d, can improve *Vis* values from forecasting models. A new microphysical scheme to be used in the GEM limited area model (LAM) (Milbrandt and Yau, 2005a,b) will provide both N_d and *LWC* values in a prognostic way that should lead to more accurate calculations of Vis values.

Finally, back trajectories of air masses together with other data sets e.g. satellite based algorithms, model based products, and ocean surface T data can be integrated to better forecast/nowcast marine fog and its visibility.

An ice fog visibility parameterization as suggested by Ohtake and Huffman (1969) was modified for model simulations and an ice fog area coverage detection based on a new parameterization of RH_i has been suggested. These can be used in nowcasting/forecasting applications. A new equation is given for the frost point *T* calculation that can be used in RH_i calculation over a model grid area. The ice fog Vis parameterization (Ohtake and Huffman, 1969) needs to be verified and this will be done using the new observations obtained during FRAM-ISDAC field project which took place over Barrow, Alaska, US, during April of 2008.

Acknowledgements

Funding for this work was provided by the Canadian National Search and Rescue Secretariat and Environment Canada. Authors are thankful to M. Wasey and R. Reed of Environment Canada for technical support.

References

Benjamin, S.G., D. Devenyi, S.S. Weygandt, K.J. Brundage, J.M. Brown, G.A. Grell, D. Kim, B.E. Schwartz, T.G. Smirnova, T.L. Smith, and G.S. Manikin, 2004: An hourly assimilation/forecast cycle: The RUC. *Mon. Wea. Rev.*, **132**, 495-518.

Bott, A., U. Sievers, and W. Zdunkowski, 1990: A radiation fog model with a detailed treatment of the interaction between radiative transfer and fog microphysics, *J. Atmos. Sci.*, **47**, 2153–2166.

Côté, J., S. Gravel, A. Methot, A. Patoine, M. Roach, and A. Staniforth, 1998: The operational CMC-MRB

Global Environmental Multiscale (GEM) model: Part I - Design considerations and formulation. *Mon. Wea. Rev*., **126**, 1373-1395.

Gadher, D, and Baird, T, cited 2007: Airport dash as the fog lifts, *The Sunday Times*, posted online 24 December 2006. [Available online at http://www.timesonline.co.uk/article/0,,2087-2517675.html.]

Gultepe, I., G. A. Isaac, and S. G. Cober, 2001: Ice crystal number concentration versus temperature for climate studies. *Inter. J. of Climatology*, **21**, 1281-1302.

Gultepe, I., G. Isaac, A. Williams, D. Marcotte, and K. Strawbridge, 2003: Turbulent heat fluxes over leads and polynyas and their effect on Arctic clouds during FIRE-ACE: Aircraft observations for April 1998. *Atmosphere and Ocean,* **41(1)**, 15-34.

Gultepe, I., and G. Isaac, 2004: An analysis of cloud droplet number concentration (N_d) for climate studies: Emphasis on constant N_d*, Quart. J. Roy. Meteor. Soc.,* **130**, Part A, 2377-2390.

Gultepe, I., and G. A. Isaac, 2006 Visibility versus precipitation rate and relative humidity. AMS 12th Cloud Physics Conference, July 9-14, 2006, Madison, Wisconsin, USA, Prints in CD print, p255.

Gultepe, S.G. Cober, P. King., G. Isaac, P. Taylor, and B. Hansen, 2006a: The Fog Remote Sensing and Modeling (FRAM) field project and preliminary results, AMS 12th Cloud Physics Conference, July 9-14, 2006, Madison, Wisconsin, USA, Print in CD, P4.3.

Gultepe, I., M. D. Müller, and Z. Boybeyi' 2006b: A new visibility parameterization for warm fog applications in numerical weather prediction models, *J. Appl. Meteor.* **45**, 1469-1480

Gultepe, I., and J. A. Milbrandt, 2007: Microphysical observations and mesoscale model simulation of a warm fog case during FRAM project, *J. of Pure and Applied Geophy*.**,** **164**, 1161-1178.

Gultepe, I., Pagowski, M., and Reid, J., 2007: Using surface data to validate a satellite based fog detection scheme*, Weather and Forecasting,* **22,** 444-456.

Gultepe, I., S.G. Cober, G. Pearson J. A. Milbrandt B. Hansen, G. A.Isaac, S. Platnick, P. Taylor, M. Gordon, J. P. Oakley, 2008: The fog remote sensing and modeling (FRAM) field project and preliminary results. *Bull. Amer. Meteor. Soc*., Conditionally accepted.

Jacobs, W., Vesa Nietosvaara, Andreas Bott, Jörg Bendix, Jan Cermak, Silas Chr. Michaelides, and Ismail Gultepe, 2007: COST Action 722, Earth System Science and Environmental Management, *Final report on Short Range Forecasting Methods of Fog, Visibility and Low Clouds.* Available from COST-722, European Science Foundation, 500 pp.

Kain, J. S. and J. M. Fritsch, 1993: Convective parameterization for mesoscale models: The Kain-Fritsch scheme. The Representation of Cumulus Convection in Numerical Models, Meteor. Monogr., No. **46**, *Amer. Meteor. Soc*., 165-177.

Löffler-Mang, M., and J. Joss, 2000: An optical disdrometer for measuring size and velocity of hydrometeors. *J. Atmos. Ocean. Tech*., **17**, 130-139.

Löffler-Mang, M., and U. Blahak, 2001: Estimation of the equivalent radar reflectivity factor from measured snow size spectra. *J. Appl. Meteor*., **40**, 843-849.

Marshall, J. S., and W. M. K. Palmer, 1948: The distribution of raindrops with size. *J. Meteor*., **17**, 1054-1061.

Milbrandt, J. A. and M. K. Yau, 2005a: A multi-moment bulk microphysics parameterization. Part I: Analysis of the role of the spectral shape parameter. *J. Atmos. Sci*., **62**, 3051-3064.

Milbrandt, J. A. and M. K. Yau, 2005b: A multimoment bulk microphysics parameterization. Part II: A proposed three-moment closure and scheme description. *J. Atmos. Sci*., **62**, 3065-3081.

Muench, H. S., and H. A. Brown, 1977: Measurements of visibility and radar reflectivity during snowstorms in the AFGL mesonet. Environmental Res. Paper AFGL-TR-77-0148, 36 pp. [Available from the Meteorology Division, Project 8628, Air Force Geophysics Laboratory, Hanscom AFB, MA 01731.].

Murray, F. W., 1967: On the computation of saturation vapor pressure. *J. App. Meteor.,* **6**, 203-204.

Ohtake, T. and P.J. Huffman, 1969: Visual Range in Ice Fog, *J. of App. Meteor*., **8**, 499-501.

Rasmussen, R. M., J. Vivekanandan, J. Cole, B. Myers, and C. Masters, 1999: The estimation of snowfall rate using visibility. *J. Applied. Meteor.,* **38**, 1542-1563.

Seagraves, M.A., 1984: Precipitation Rate and Extinction in Falling Snow, *J. Atmos. Sci.*, **41**, 1827-1835

Sekhon, R. S., and R.C. Srivastava, 1970: Snow size spectra and radar reflectivity. *J. Atmos. Sci.*, **27**, 299–307.

Sekhon, R. S., and R.C. Srivastava, 1971: Doppler radar observations of drop-size distributions in a thunderstorm. *J. Atmos. Sci.*, **28**, 983–994**.**

Stallabrass, J. R., 1985: Measurements of the concentration of falling snow. Tech. Memo., 140, *Snow Property Measurements Workshop.* Lake Louise, AB, Canada, National Research Council Canada. 20 pp.

Smirnova, T.G., S.G. Benjamin, and J.M. Brown, 2000: Case study verification of RUC/MAPS fog and visibility forecasts. Preprints, 9th Conf. on Aviation, Range, and Aerospace Meteorology, AMS, Orlando, 31-36.

Stoelinga, M. T., and T. T. Warner, 1999: Nonhydrostatic, meso-beta scale model simulations of cloud ceiling and visibility for an east coast winter precipitation event. *J. Appl. Meteor.*, **38**, 385-404.

Sundqvist, H., E. Berge, and J. E. Kristjánsson, 1989: Condensation and cloud parameterization studies with a mesoscale numerical weather prediction model. *Mon. Wea. Rev.* **117**, 1641-1657.

Westcott, N. E., 2007: Some aspects of dense fog in the Midwestern United States. *Weather and Forecasting,* **22**, 457-465.

SIMPLE METHOD OF AEROSOL PARTICLE SIZE DISTRIBUTION RETRIEVING FROM MULTIWAVELENGTH LIDAR SIGNALS

A. K. Jagodnicka[1], T. Stacewicz[1], G. Karasiński[1], M. Posyniak[2]

[1]Institute of Experimental Physics, University of Warsaw
ul. Hoża 69, 00-681 Warsaw, Poland

[2]Institute of Geophysics, University of Warsaw
ul. Pasteura 7, 02-093 Warsaw, Poland

ABSTRACT

An improved lidar retrieval of the aerosol particle size distribution (APSD) is presented. A predefined APSD function with few free parameters is directly substituted into the lidar equations. The minimization technique allows to find the parameters which provide the best fit of APSD comparing theoretically generated signals with the experimental ones. The method does not require former knowledge of the lidar ratio. The approach was tested on typical APSD presented by Seinfeld and Pandis (1997). For our purpose these distributions were approximated with two mode combination of lognormal functions. With a lidar working at five wavelengths in UV – near IR spectral range a satisfactory retrieval of synthetic APSD is possible for the particles within the range 100 – 5000 *nm*.

INTRODUCTION

Among many methods of the aerosol investigation the optical remote studies play very important role. Lidars working simultaneously at several wavelengths are often used for these observations. This technique provide opportunity for remote investigation of aerosol particle size distribution (APSD). Such studies are possible due to different properties of the light scattering by particles of different sizes at various wavelengths (λ). A common approach to the retrieving of APSD from the lidar signals consists in determination of total scattering coefficients α_λ and/or the backscattering coefficient β_λ. Both coefficients can be related to APSD function *n(z,r)* by following equations (Seinfeld and Pandis, 1997):

$$\alpha_\lambda(\mathrm{z}) = \int_0^\infty Q_\lambda^E(r)\pi r^2 n(z,r)dr$$

$$\beta_\lambda(\mathrm{z}) = \int_0^\infty Q_\lambda^B(r)\pi r^2 n(z,r)dr \,, \tag{1}$$

where z is a distance from the lidar, r - the particle radius, while Q_λ^E and Q_λ^B denote the efficiencies of total extinction and backscattering, respectively. These efficiencies can be calculated using *e.q.* Mie theory (Bohren and Huffman, 1999), when spherical shape of the particles is assumed.

On the other hand α_λ and β_λ can be found from lidar signals $S_\lambda(z)$ described by lidar equations. For each wavelength:

$$S_\lambda(z) = \frac{A_\lambda}{z^2}\beta_\lambda(z)\exp\left(-2\int_{z_0}^{z}\alpha_\lambda(y)dy\right). \tag{2}$$

where A_λ are the apparatus constants. In each single equation (2) both α_λ and β_λ are unknown, therefore in order to retrieve them an additional information is necessary. The relation - so called *lidar ratio* - is usually used (Klett, 1981). For the white light it takes the form:

$$q_L = \frac{\beta_\lambda}{\alpha_\lambda^k} \,, \tag{3}$$

where k is a number.

Deriving APSD from the scattering coefficients (1) is a classic example of inverse ill-posed problem, typical in earth sciences. Solution of Fredholm integral equations of 1st kind is required. Various inversion techniques have been proposed for this purpose. Successful approach to this problem needs some additional assumptions about the solution, like a smoothness or/and a positivity. This can be obtained with a predefined form of $n(z,r)$ distribution, like histogram or Junge function, log-normal function or linear combination of these functions with different parameters (Seinfeld and Pandis, 1997). In such a case the solution is reduced to finding these parameters.

Such approach was presented by Herman *et al* (1971). They fit Junge distribution to signals from bistatic lidar. Rajeev and Parameswaran (1998) have shown two iterative methods of APSD determination: with assumed Junge distribution or without any assumed shape, taking for calculations an arbitrary lidar ratio. Heitzenberg *et al* (1998) proposed randomized minimization search technique (iterative least square algorithm) to derive an assumed histogram distribution. The research group from ITR applied the inversion with regularization for deriving both APSD and the refractive index using the signals registered with their aerosol and Raman lidar (Müller *et al*, 1999). They developed the technique based on Tichonov regularization (Veselovskii *et al*, 2002, 2004). In recent years the eigenvalue analysis was applied for the lidar data inversion (Veselovskii *et al*, 2005). Detailed review of different approaches to APSD retrieval was done by Böckman (2001). Her hybrid method presented in this paper was later applied for experimental data (Böckmann *et al*, 2005). As the result APSD, the refractive index and single scattering albedo was retrieved.

Another solution to the problem of lidar data analysis was proposed by Kusiel and Zolotov (1997, 2003). They developed mean ordinates method. They assumed APSD function as combination of several log-normal functions. Using these distributions, the optical characteristics (like α_λ and β_λ), were calculated and compared with those measured by lidar technique. Then the mean ordinates over those solutions were calculated and model closest to the mean ordinates was taken as the most probable solution. The mean ordinates method was used for inverting the horizontal lidar data.

A different approach was presented by Ligon *et al* (1996, 2000). In order to shorten the calculation time they used the Monte Carlo method of approximation of APSD.

Certainty of retrieving the APSD was experimentally tested by Joshiyama *et al* (1996). They measured optical parameters of artificial aerosol with bistatic lidar and compared the results with mathematical model.

As mentioned above in all these methods APSD is derived from α_λ and/or β_λ coefficients (1), with the use of lidar ratio (3). The lidar ratio was first suggested by Curcio and Knestrick (1966). They have experimentally evaluated k to be equal to 0.66, while Fenn (1966) reported different values. Then Twomey and Howell (1965) found the linear relation between α_λ and β_λ basing on Mie theory and various size distributions of particles. They also concluded that in general such relation could not be a unique one, and that the linear correlation between the backscattering and the extinction coefficients is evident only for the white light. Good linearity is reported for clouds where a multiple light scattering takes place (O'Connor *et al*, 2004). It is not clear, however, whether the linear lidar ratio can be used for the monochromatic laser radiation. Analysis of large data-set of lidar returns of EARLINET shows about 40 % variability of $\beta_\lambda/\alpha_\lambda$ ratio for aerosols in boundary layer (Pappalardo, 2005). Therefore the value of the lidar ratio is often guessed or assumed (Landulfo *et al*, 2003; Iwasaka *et al*, 2003).

The coefficients α_λ and β_λ that are necessary for APSD inversion can be found using the lidar signal inversion technique by Klett (1981) and Fernald (1984). However in this case the aerosol parameters in the reference point must be known. When the vertical profiling is performed the reference point is usually selected at high altitudes, where the aerosol concentration is negligible and the molecular lidar ratio: $\beta_\lambda/\alpha_\lambda = 3/8\pi$ can be used. Then the backward solving of the lidar equation is applied. In case of clear sky the measurement of total optical thickness by sun-photometers allows to deduce the lidar ratio (G. Karasiński *et al*, 2007), which is usually considered constant with height. Such solutions are not applicable in many experimental situations, *e.q.* for aerosol layer under the cloud cover. Some problems can be also overcame when common measurement by aerosol and Raman lidars is performed, however the Raman signal registration is short-distant and is not well applicable for multiwalelength lidars.

In this paper an approach to the problem of APSD determination is proposed. It does not require the lidar ratio knowledge. Predefined functions $n(z,r)$ are substituted directly to equations describing the lidar signals (2). The experimental estimates of α_λ and/or β_λ values are not needed. Application of the minimization technique allows to derive the best fit of APSD by comparison the artificially generated signals with the lidar returns.

DESCRIPTION OF THE METHOD

In a first step equations (2) representing the registered signals $S_\lambda(z)$, should be converted to so called range corrected form:

$$L_\lambda(z) = S_\lambda(z)\cdot z^2 = A_\lambda \beta_\lambda(z)\exp\left[-2\int_{z_0}^{z}\alpha_\lambda(x)dx\right]\cdot \quad (4)$$

Due to digitization the lidar signals are quantitized *e.q.* in space with the interval of dz. For further analysis the ratio of the signals $L_\lambda(z_l)$ at distance z_l and at its neighbour distance $z_{l+1}=z_l+dz$ is taken:

$$\frac{L_\lambda(z_{l+1})}{L_\lambda(z_l)} = \frac{\beta_\lambda(z_{l+1})}{\beta_\lambda(z_l)}\exp\left[-2\alpha_\lambda(z_{l+1})dz\right]\cdot \quad (5)$$

This form allows to omit the apparatus constants A_λ, which are usually unknown. Left hand side of (5) describe the experimental signals, while the right hand side can be calculated from Mie equations (1) when $n(z,r)$ is assumed. Using a minimization technique with the cost function:

$$\chi^2(z_l) = \sum_\lambda\left\{\frac{L_\lambda(z_{l+1})}{L_\lambda(z_l)} - \frac{\beta_\lambda(z_{l+1})}{\beta_\lambda(z_l)}\exp\left[-2\alpha_\lambda(z_{l+1})dz\right]\right\}^2 \quad (6)$$

allows to find APSD.

In order to fit the size distribution the predefined form is necessary. Sum of modes: $n(r,z) = \sum_{j=1}^{K} n_j(r,z)$ $(K = 1,2)$ is usually used. Each mode is described by the log-normal function:

$$n_j(r,z) = \frac{C_j(z)}{\sqrt{2\pi}\cdot\log\sigma_j(z)}\cdot$$
$$\cdot\frac{1}{r}\cdot\exp\left\{-\frac{\left[\log r - \log R_j(z)\right]^2}{2\cdot\log^2\sigma_j(z)}\right\}, \quad (7)$$

where R_j denotes the modal radius, C_j - concentration of aerosol in a given mode, and σ_j - width.

TEST OF THE METHOD

The approach was tested with the synthetic size distributions after Seinfeld and Pandis (1997). They described several typical APSD with three mode lognormal functions. We assumed a uniform spatial distribution of aerosol. Particles are characterized by the refraction coefficients of water. That allowed to find the scattering coefficients (1). In order to simulate a typical experiment with multiwavelength lidar, the synthetic range corrected lidar signals $L_\lambda(z_l)$ for five wavelengths (1064, 800, 532, 375 and 355 *nm*) were calculated by means of formulas (2). Using these signals the reconstruction of the left hand side of (5) was possible.

Our initial test consisted in approximation of APSD by single lognormal function. Such approach is used by some researchers (Hess *et all*, 1998). A matrix of lognormal functions $n_{RC\sigma}(r,z_0)$ was constructed. Each element of the matrix was expressed by equation (7). In order to cover ranges of parameters predicted by Seinfeld and Pandis (1997), the matrices were generated for the modal radiuses R in the range 5 to 650 *nm*, the particle concentrations C changing from 0.01 to 3500 cm^{-3} and widths σ varying from 1.7 to 7. Using these functions and the equation (1) the matrices of coefficients $\alpha_{RC\sigma\lambda}$ and $\beta_{RC\sigma\lambda}$ were calculated for each wavelength. Integration for particle radiuses from 1 *nm* to 10 *µm* was performed. Then with pairs of elements from $\alpha_{RC\sigma\lambda}$ and $\beta_{RC\sigma\lambda}$ matrices the right hand side of (5) were constructed. For each pair the value of $\chi^2_{RC\sigma}$ was determined by minimization technique. Cost function (6) was applied. The optimal distribution $n(r,z_0)$ was found as the arithmetic mean of all analyzed cases of weights $1/\chi^2_{RC\sigma}$.

Results of these investigation are presented in Fig 1. A good approximation of the assumed APSD by single mode lognormal function was found only for *free troposphere* aerosol (Fig. 1a), due to a specific shape of its distribution. In other cases this approximation was not satisfactory. For some particle radius ranges (like *remote continental*, r≈400-700 *nm*) the discrepancies between the assumed and fited distributions reached two orders of magnitude. For *polar* APSD (Fig. 1c), the approximation is quite good for the particles of radius larger than 300 *nm*, but it is not acceptable for smaller ones. In all cases for r<100 *nm* the approximation is poor.

Much better approximation of APSD can be achieved with two mode lognormal distribution. In such case matrices of $\alpha_{RC\sigma\lambda}$ and $\beta_{RC\sigma\lambda}$ coefficients were prepared for each mode separately: for the accumulation mode modal radiuses R were in a range 5 – 200 *nm* and concentrations C changed from 20 to 3500 cm^{-3}; for the coarse mode R from 200 to 2500 *nm* and C from 0.01 to 20 cm^{-3} were used. For both modes the widths of the functions changed from 1.7 to 7.

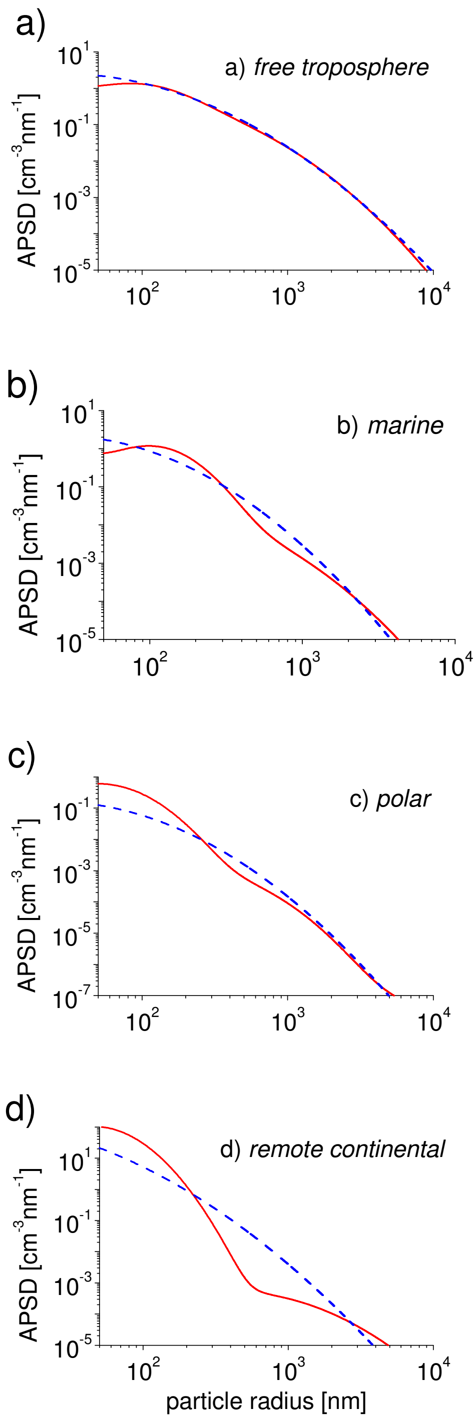

Fig. 1. Reconstruction of APSD with single mode lognormal function. Continuous lines - assumed APSD, dashed lines - their approximation.

When the two mode approximation is applied the systematic search of these matrixes needs the calculation of the cost function (6) for billions of cases. For this reason the Monte Carlo method, probing about 0.1% of all the cases was used.

Similarly to the single mode approximation, the value of $\chi^2_{RC\sigma}$ (6) for each probe was determined and the optimal distribution $n(r,z_0)$ was found as the arithmetic mean of the results with weights $1/\chi^2_{RC\sigma}$.

The fits are presented in Fig 2(a-d). In this case the quite good approximation was received for all considered aerosols. For the particle radiuses beginning from 50 *nm* (i.e. within the range larger than for single mode approximation) the discrepancy between assumed and retrieved distribution is smaller than 20 %. For the particle radiuses smaller than 50 *nm* (except for special cases, like *polar* aerosol – Fig. 2c) the fit is poor. We believe that it is due to a weak contribution of small particles to the light scattering.

EVALUATION OF PARTICLE REFRACTION INDEX

Precise fit of two mode log-normal function to the APSD provides the opportunity to evaluate the refraction index of aerosol particles. In order to verify its value a following numerical experiment was performed. *Marine* aerosol at certain distance z_0 *was* considered. The right hand side of equation (5) was generated for the refraction coefficient of water (Segelstein, 1981) as well as for the refraction coefficient of sea salt (Volz, 1972). Then the matrices of $\alpha_{RC\sigma\lambda}$ and $\beta_{RC\sigma\lambda}$ coefficients were calculated.

The fiting procedure was repeated two times: ones within the broad range of parameters (as described in previous chapter) and then in a narrow range of the parameters, around that determined in the previous step. In this case the matrices of $\alpha_{RC\sigma\lambda}$ and $\beta_{RC\sigma\lambda}$ coefficients were calculated again with high

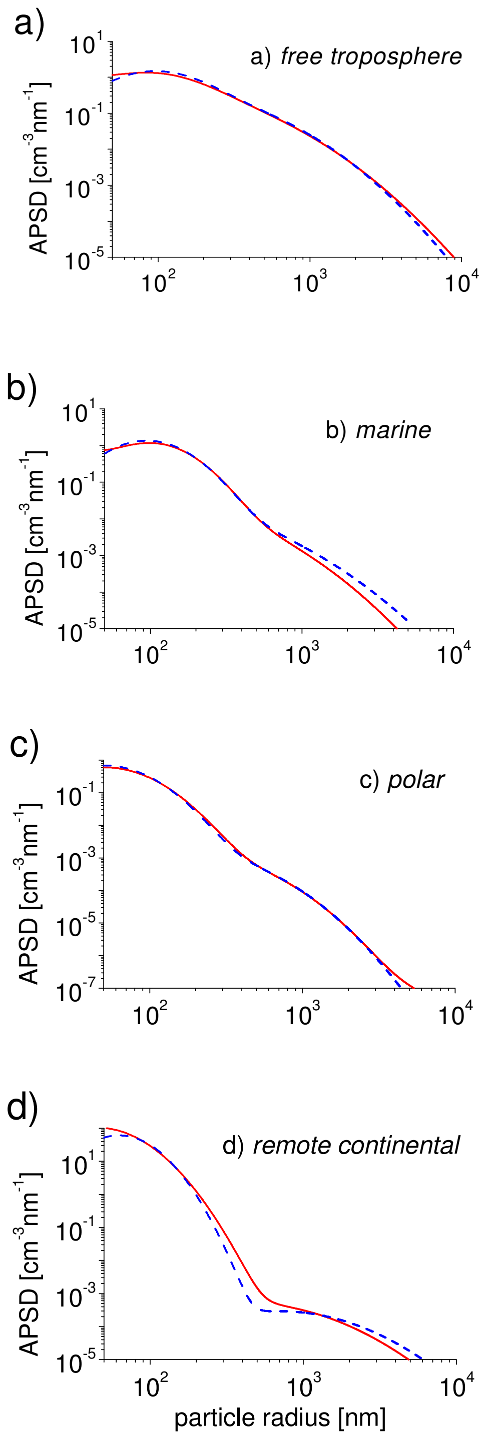

Fig. 2. Reconstruction of APSD with two-mode lognormal function. Continuous lines - assumed APSD, dashed lines - their approximation.

precision for water and for sea salt refraction indexes. Both cases were compared with the lidar signals which also were calculated for the water and for the sea salt. For all considered cases values of the cost function were found. Results of such procedure are shown in Fig. 4(a-d).

The lowest values of χ^2 were obtained for the case when the refractive index assumed for the signal generation coincides with the refractive index that was used in the fit. On the contrary, for the signals with water refractive index and the matrices calculated for the sea salt refractive index the value of χ^2 was about 15 – 20 times larger. This indicates that search for the minimum of χ^2 - parameter versus the refraction index provides the opportunity to determine the optimal refraction index and, in turn, to evaluate the chemical composition of aerosol particles.

EXPERIMET

We applied this method for analysis of measurements performed during the campaign in Warsaw, (Poland) in July 2006. The experiment was done with our multiwavelength lidar (Ernst *et al*, 2003, Chudzyński *et al*, 2006). Its sender generated five wavelength (1064, 782, 532, 391, 355 *nm*).

Example of results, i.e. the effective radius of aerosol particles r_{eff} under the base of cloud as a function of the altitude, is presented in Fig. 4. The registration was done 26th of July 2006 at 11:45 UTC. At this time the sky was covered by sparse cumulus clouds of bases at 1.8 *km* altitude. The effective radius was calculated using the retrieved APSD and the formula:

$$r_{eff}(z) = \frac{\int r^3 n(r,z)dr}{3\int r^2 n(r,z)dr}. \qquad (8)$$

The refraction index of water was assumed. As one can see at low altitudes, up to 1.65 *km*, the effective particle radius r_{eff} is uniform. Its mean value is about 180 *nm*.

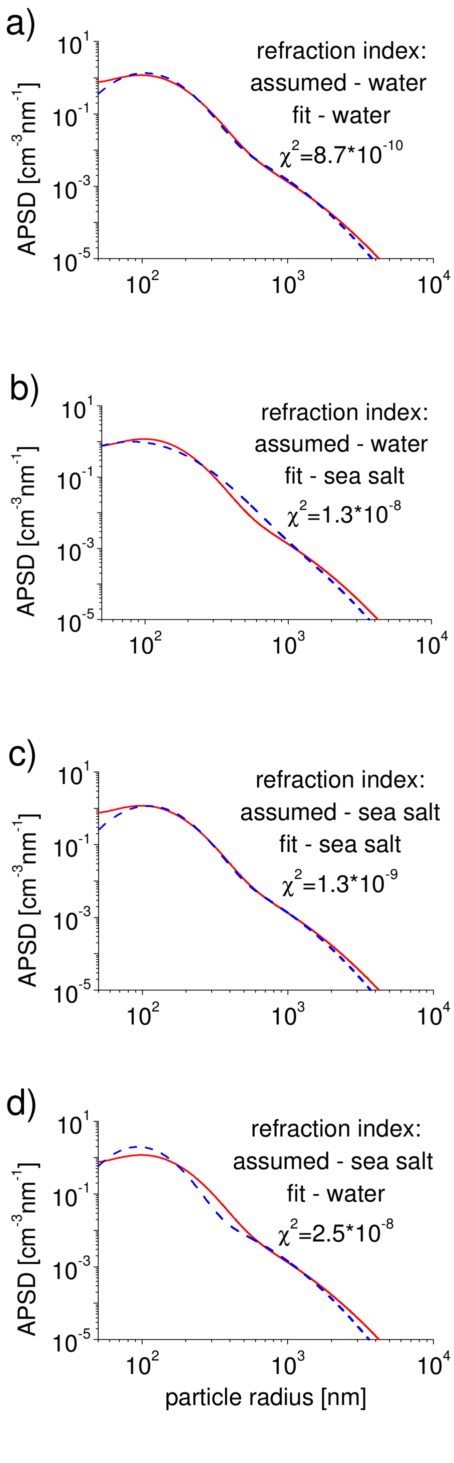

Fig. 3. Illustration of method of the refraction coefficient evaluation (marine aerosol). Continuous lines - assumed APSD, dashed lines - their two - mode approximation.

A fast increase of r_{eff} up to the value of 1200 *nm* is observed starting from about 1.65 *km*, i.e. about 150 *m* below the could base.

More detailed description of investigation of aerosol properties in vicinity of clouds is presented by Jagodnicka *et al* (2008).

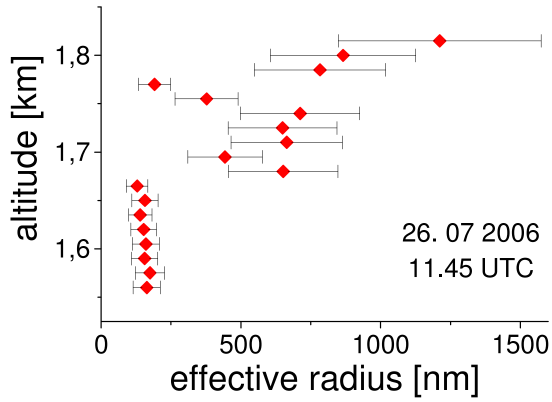

Fig. 4. Effective radius of aerosol particles as a function of the altitude. Measurement done under the base of cumulus (26.06.2006, Warsaw, Poland).

CONCLUSION.

Simple method of aerosol particle size distribution retrieving from lidar signals was presented. Due to application of direct fiting of APSD to the lidar signals this technique does not need knowledge of lidar ratio. Therefore our method can be successfully used when retrieving the aerosol scattering coefficients is difficult, for example under the clouds. To our knowledge this is an unique method providing opportunity to determine the APSD as a function of distance from the lidar.

BIBLIOGRAPHY

Bohren, C.F., D.R. Huffman, 1999: Absorption and Scattering of Light by Small Particles. *John Wiley & Sons*, New York

Böckmann, C., 2001: Hybrid regularization method for the ill-posed inversion of multiwavelength lidar data in the retrieval of aerosol size distribution. *Appl. Opt.*, **40**,1329–1342

Böckmann, C., I. Mironova, D. Müller, L. Schneidenbach, R.Nessler, 2005: Microphysical aerosol parameters from multiwavelength lidar, *J. Opt. Soc. Am.*, **22**, 518-28.

Chudzyński, S., G. Karasiński, W. Skubiszak, T. Stacewicz, 2006: Investigation of atmospheric aerosol with multiwavelenght lidar. *Optica Applicata,* **36**, 621 – 628

Curcio, J.A. , G.L. Knestric, 1958: Correlation of Atmospheric Transmission with Backscattering, *Journal of Optical Society of America*, **48**, 686-689

Ernst, K., S. Chudzyński, G. Karasiński, A. Pietruczuk, T. Stacewicz, 2003: *SPIE Proc.* **5229**, 45 – 50

Fenn, R.W., 1966: Correlation Between Atmospheric Backscattering and Meteorogical Visual Range, Appl. Opt., **5**, 293-295

Fernald, F.G., 1984: Analysis of atmospheric lidar observations: some comments, *Appl. Opt.*, **23**, 652-653.

Heintzenberg, J., H. Müller, H. Quenzel, and E. Thomalla, 1981: Information content of optical data with respect to aerosol properties: numerical studies with a randomized minimizationsearch-technique inversion algorithm*, Appl. Opt.* **20**, 1308–1315

Herman, B.M. ,S.R. Browning, and J.A. Reagan, Determination of Aerosol Size Distributions from Lidar Measurements**.** *J.Atmos.Sci.*, **28,** 763–771

M. Hess, P. Koepke, and I. Schult (1998): Optical Properties of Aerosols and clouds: The software package OPAC, Bull. Am. Met. Soc., **79**, 831-844

Iwasaka, Y., T. Shibata, T. Nagatani, G.-Y. Shi, Y.S. Kim, A. Matsuki, D. Trochkine, D. Zhang, M. Yamada, M. Nagatani, H. Nakata, Z. Shen, G. Li, B. Chen, K. Kawahira, 2003: Large depolarization ratio of free tropospheric aerosols over the Taklamakan Desert revealed by lidar measurements: Possible diffusion and transport of dust particles. *J.Geophys.Res.*, **108**, ACE 20-1-8

Jagodnicka, A.K., T. Stacewicz, M. Posyniak, S. Malinowski, S. Blindheim, M. Gaussa, 2008: Lidar investigation of aerosol particle size distribution in the vicinity of clouds. C*ommunication at 15th International Conference on Clouds and Precipitation ICCP-2008* - Cancun.

Karasiński, G., A.E. Kardaś, K. Markowicz, S.P. Malinowski, T. Stacewicz, K. Stelmaszczyk, S. Chudzyński, W. Skubiszak, M. Posyniak, A.K. Jagodnicka, C. Hochhertz, L. Woeste, 2007: LIDAR investigation of properties of atmospheric aerosol. *Eur. Phys. J.*, **144**, 129 – 140

Klett, J.D., 1981: Stable Analitical Inversion Solution for Processing Lidar Returns. *Appl. Opt.*, **20**, 211-220

Kusiel, S., I. Zolotov, 1997: Determination of the aerosol particle-size distribution from simultaneous data on spectral attenuation and the small-angle phase function. *Appl. Opt.*, **36,** 6047-6056

Kusiel, S., I. Zolotov, 2003: The Use of Direct Observations over the Aerosol Particle Size Distribution for Inverting Lidar Data. *Journal of Atmosheric and Oceanic Technology*, **20**, 1411-1420

Landulfo, E., A. Papayannis, P. Artaxo, A.D.A. Castanho, A.Z. De Freitas, R.F. Souza, N.D. Vieira Junior, M.P. Jorge, O.R. Sanchez-Coyllo, D.S. Moreira, 2003: Synergetic measurements of aerosols over São Paulo, Brazil using LIDAR, sunphotometer and satellite data during the dry season. *Atmos. Chem. Phys.*, **3**, 1523–1539.

Ligon, D. A., J. B. Gillespie and T. W Chen, 1996: Determination of aerosol parameters from light – scattering data using an inverse Monte Carlo technique. *Appl. Opt.*, **35**, 4297 – 4303

Ligon, D.A., J.B. Gillespie and P. Pellegrino, 2000: Aerosol properties from spectral extinction and backscatter estimated by an inverse Monte Carlo method. *Appl. Opt.*, **39**, 4402-4410;

Müller, D., U. Wandinger, and A. Ansmann, 1999: Microphysical particle parameters from extinction and backscatter lidar data by inversion with regularization: Theory. *Appl. Opt.*, ***38,*** 2346–2357

Müller, D., U. Wandinger, and A. Ansmann, 1999: Microphysical particle parameters from extinction and backscatter lidar data by inversion with regularization: Simulation. *Appl. Opt.*, **38,** 2358–2368

O'Connor, E.J., A.J. Illingworth and R.J. Hogan, 2004: A technique for autocalibration of cloud lidar, *J.Atmos. Oceanic Technol.*, **21**, 777-786

Twomey S., H.B. Howell, 1965: The Relative Merit of White and Monochromatic Light for the Determination of Visibility by Backscattering Measurements. *Appl. Opt.*, **4**, 501-506

Pappalardo, G., 2005: Aerosol lidar ratio measurement in the framework of EARLINET, *Geophysical Research Abstracts*, **7**, 08329

Rajeev K and K. Parameswaran, 1998: Iterative method for the inversion of multiwavelength lidar signals to determine aerosol size distribution. *Appl. Opt.* **37**, 4690–4700

Segelstein, D. J., 1981: *Thesis (M.S.).*Department of Physics. University of Missouri-Kansas City

Volz, F. E., 1972: Infrared refractive index of atmospheric aerosol substance, *Appl. Opt.*, **11**, 755-759

Seinfeld J. H., Pandis S.N., 1997*:* Atmospheric Chemistry and Physics, *John Wiley & Sons New York*

Van de Hulst, H. C., 1957: *Light Scattering by Small Particles.* John Wiley & Sons, New York

Veselovskii, I., A. Kolgotin, V. Griaznov, D. Müller, U. Wandinger, D.N. Whiteman, 2002: Inversion with regularization for the retrieval of tropospheric aerosol parameters from multiwavelength lidar sounding, *Appl. Opt.*, **28**, **41**, 3685-3699

Veselovskii, I., A. Kolgotin, V. Griaznov, D. Müller, K. Franke, D.N. Whiteman, 2004: Inversion of Multiwavelength Raman Lidar Data for Retrieval of Bimodal Aerosol Size Distribution. *Appl. Opt.*, **43**, 1180-1195

Veselovskii, I., A. Kolgotin, D. Müller, and D.N. Whiteman, 2005: Information content of multiwavelength lidar data with respect to microphysical particle properties derived from eigenvalue analysis. *Appl.Opt.* **44**, 5292-5303

Yoshiyama H., Ohi A., Kazuyuki Ohta, 1996: Derivation of the aerosol size distribution from a bistatic system of a multiwavelength laser with the singular value decomposition method. *Appl. Opt.,* **35**, 2642-2648

LIDAR INVESTIGATION OF AEROSOL PARTICLE SIZE DISTRIBUTION IN THE VICINITY OF CLOUDS

A. K. Jagodnicka [1], T. Stacewicz [1], M. Posyniak [2], S. Malinowski [2], S. Blindheim [3], M. Gaussa [3]

[1] Institute of Experimental Physics, University of Warsaw, ul. Hoża 69, 00-681 Warsaw, Poland

[2] Institute of Geophysics, University of Warsaw ul. Pasteura 7, 02-093 Warsaw, Poland

[3] Andøya Rocket Range, Andenes, Norway

ABSTRACT

We present Aerosol Particle Size Distribution (APSD) retrieved from multiwavelength lidar profiles in the vicinity of convective clouds. The data were collected in summer 2006 in Warsaw (Poland). For the retrieval of APSD a recent algorithm based on direct fit of this function to the lidar signals was employed.

INTRODUCTION

Remote and nonperturbative investigation with lidars provides information about profiles of atmosphere. In case of muliwavelength lidars aerosol particle size distribution (APSD) can be achieved. In this study we analyzed multiwavelength lidar returns collected in vicinity of boundary layer convective clouds. The data were gathered in July - August 2006 in Warsaw (Poland).

A multiwavelength lidar working at 5 wavelengths described elsewhere (Ernst *et al* 2003a, Chudzyński *et al*, 2006) was used. It consists of the optical sender with pulsed Nd:YAG laser generating at three harmonics (1064, 532 and 355 *nm*) and additional pulsed Ti:Sa laser generating at two harmonics (782 and 391 *nm*). Energies of the light pulses were about 200 *mJ*, while their repetition rate was 10 *Hz*. The laser beams were sent vertically to the atmosphere.

In the optical receiver a Newtonian telescope with the mirror of 40 *cm* in diameter and focal length of 120 *cm* was used. The light, collected by the telescope, was spectrally separated by a polychromator. Acquisition of the lidar echoes was done with a set of photomultipliers and 12 bit 50 *MHz* digitizers. The signals were averaged over 300 pulses.

For retrieval of APSD original method was elaborated (Ernst *et al*, 2003b, Jagodnicka *et al*, 2008). It is based on direct fit of particle size distribution to the lidar signals. APSD was approximated with combination of two lognormal modes with free parameters (Reidmiller *et al*, 2006). Using such function for each lidar wavelength the extinction and backscattering coefficients were calculated and substituted into the lidar equations (Measures, 1992). In this way synthetic lidar signals were achieved. Varying the parameters and using Monte Carlo sampling the best fit of the synthetic signals to experimental ones was found.

In principle, an inversion of the lidar signal is an ill-posed problem and requires many additional assumptions. First, refraction index of the aerosol is taken as this one for water. Second, aerosol particles are assumed spherical. Additionally, activation of CCN and growth of certain classes of particles with height is expected. Signature of this process should be seen in the retrieved particle size spectrum.

AEROSOL AT THE BASE OF CUMULUS

On July 26th at 09:40 UTC scattered *Cumulus* below a weak *Cirrostatus* cover was present. *Cumulus* clouds were developing in a humid marine polar air advecting from north. Noon sounding from Legionowo (~30 *km* north from the measurement site) showed the mixed layer present up to 2000 *m* height. The wind was weak, 3 *m/s* in the boundary layer and 6 *m/s* above. No significant directional shear was observed. The convection period was not long. After some development, the convective clouds disappeared around 14:00 UTC damped by *Cirrostratus*.

In Fig. 1(a - d) determined for single cumulus cloud is shown. Plots were done from below to the base of *Cu* passing through the lidar beam within 2 minutes period. The base (as seen in Figs 1 and 2) oscillated around 1.75 - 1.85 *km* altitude, which is in agreement with the sounding.

The effective radius was calculated according to the formula:

$$r_{eff}(z) = \frac{\int r^3 n(r,z)dr}{3\int r^2 n(r,z)dr}. \qquad (1)$$

Here *n(r,z)* denotes APSD as a function of particle radius *r* and distance from the lidar *z*. The distributions were achieved due to analysis of four consecutive profiles of lidar returns collected every 30 *s*

In all plots of Fig. 1 a rapid increase of effective particle radius is clear. It takes place within a layer of several tens of meters thick. Note that there is no data from the cloud interior. Due to extinction the lidar signals at higher altitudes weaken rapidly and the retrieval of APSD is not possible.

In Fig. 1a a steep increase of r_{eff} from 0.2 up to 1.3 *μm* within 45 *m* deep layer is evident. Vertical resolution of the lidar (~15 *m*) does not allow to see finer details of this layer. Strong gradient corresponds well to the results parcel model of CCN activation (Johnson, 1980).

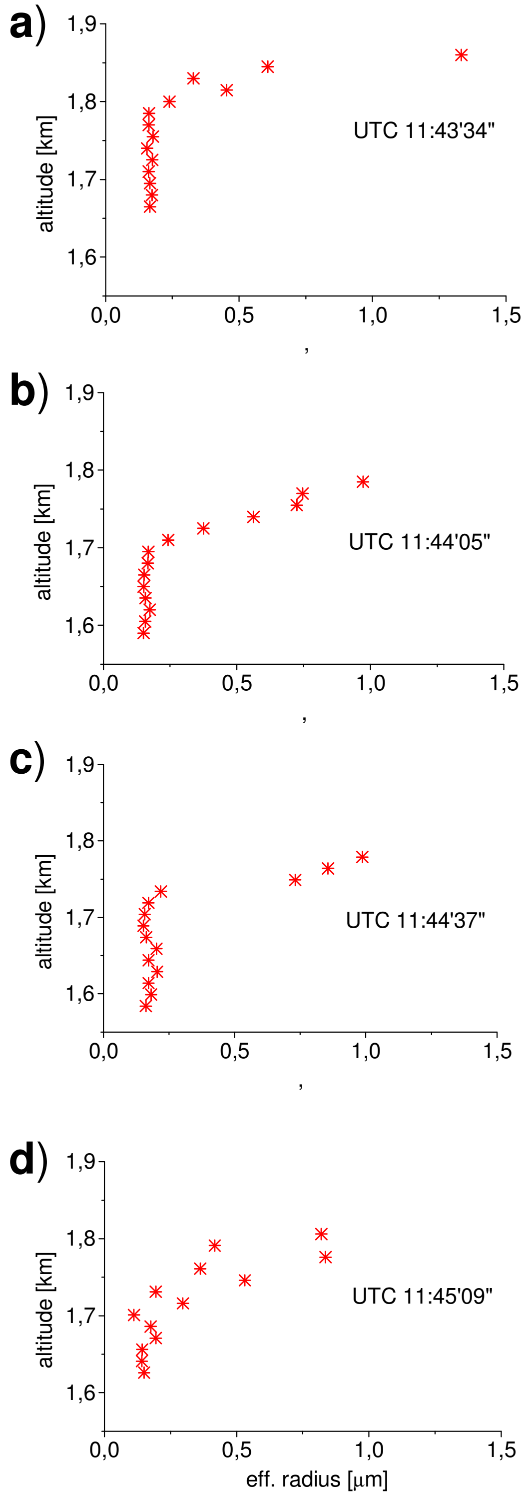

Fig. 1. Effective radius of aerosol particles below the cumulus cloud base (Warsaw, 26.07.2006)

Smaller vertical gradient of r_{eff} (growth from ~0.18 to 1 *µm* within 100 *m* deep layer) can be seen in Fig. 1b. Growth of particles begins at the level of 1.7 *km*, *i.e.* lower than 30 *s* earlier, suggesting spatial inhomogeneity of the updraft. In Fig. 1c, 30 *s* later, the gradient of r_{eff} is also steep what suggests that the growth of particles is similar to this shown in Fig. 1a. In Fig. 1d fluctuations of the effective radius are superimposed on the slower average growth. This may reflect nonuniformity of the APSD below the cloud base within 30 *s* averaging period.

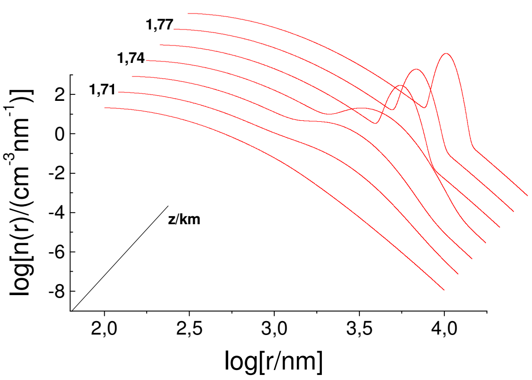

Fig. 2. Aerosol particle size distribution at 11:44'05" UTC (Warsaw, 26. 07. 2006).

In Fig. 2 the APSD taken from lidar profile 11:44'05" UTC (corresponding to r_{eff} in Fig. 1b) is shown. At the 1.7 *km* altitude large particles start to form. The initial modal radius of $r_m = 1$ *µm* grows quickly with height and at 1.8 *km* rises up to 3.2 *µm*. Droplet number concentration in this mode increases through first 50 *m* and then stabilizes. The relative width of the peak decreases with height and at the top of the detection range its value is about 1 *µm*. Such behavior is also consistent with adiabatic model of CCN activation in updraft (Johnson, 1980).

AEROSOL BELOW STRATOCUMULUS BASE

On July 30th, 2006 broken *Cumulus* clouds transformed around 11:00 UTC into stratocumulus. Noon sounding from Legionowo showed mixed layer under capping inversion at 1600 *m* height. Wind was from NW with constant speed of 10 *m/s* in the whole boundary layer and above it. Increased relative humidity in the upper part of the mixed layer corresponds well to the lidar-detected cloud base at the altitudes of 1.2 - 1.3 *km*.

Typical examples of the retrieved effective radius profiles below the cloud base are shown in Fig. 3. In most cases $r_{eff}(z)$ shows some fluctuations and less regular behavior than below *Cu* clouds. There are no evident cases which could be attributed to adiabatic activation of CCN. Note, that at 10 *m/s* wind speed averaging of lidar signal over 30 *s* corresponds to 300 *m* spatial averaging in horizontal. While this value is less than the size of typical convective cell in *Sc*, it is more than the size of large turbulent eddies. It is not surprising, that turbulent mixing, almost certain in stratocumulus topped boundary layer results in the variability of the observed profiles.

SUMMARY AND CONCLUSION

We demonstrated the ability to retrieve effective radius of the aerosol particle size distributions in the vicinity of the clouds from remote sensing with the multivavelength lidar. Presented results seem to confirm presence of process of CCN activation and growth in updraft. First achievements seem encouraging, despite many issues in the measurement technique and retrieval details.

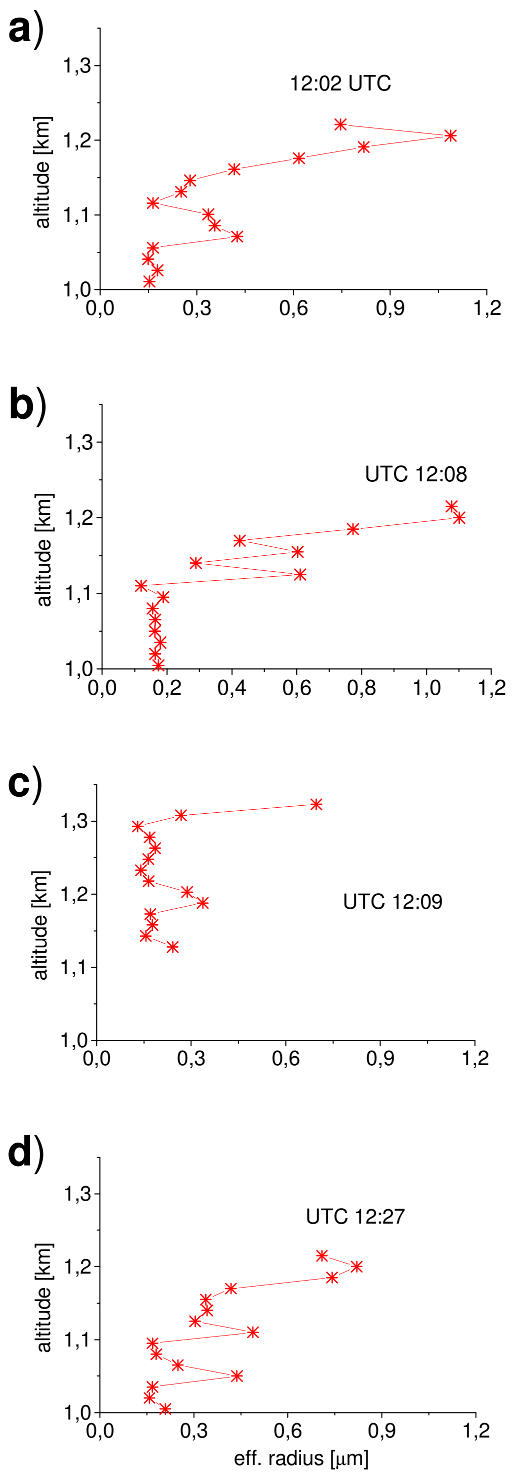

Fig. 3. Profiles of the effective radius of aerosol under stratocumulus deck (Warsaw, 30 of 2006).

For example there are problems with APSD retrieval close to sharp cloud boundaries. In Fig. 4 we present observation of orographic cloud in ALOMAR lidar observatory in northern Norway. Rapid changes in extinction prevent from retrieval of APSD inside the cloud. The model of aerosol below the cloud is also uncertain because an assumption that it consists of water droplets is doubtful.

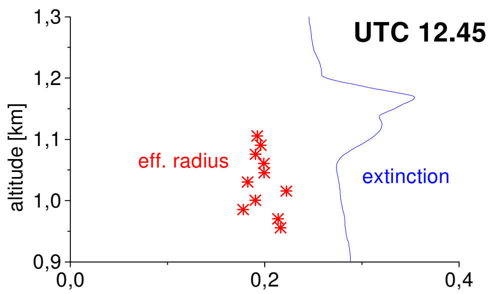

Fig. 4. Effective radius of aerosol particles and the aerosol extinction coefficient in vicinity of thin stratus layer (Andøya, Norway, 3. 07. 2007).

Nevertheless, we believe that further development of presented approach will help to resolve some important problems in cloud physics – e.g. problem of aerosol closure.

BIBLIOGRAPHY

Chudzyński, S., G. Karasiński, W. Skubiszak, T. Stacewicz, 2006: Investigation of atmospheric aerosol with multiwavelength lidar. *Optica Applicata* **36**, 621 – 628

Ernst, K., S. Chudzyński, G. Karasiński, A. Pietruczuk, T. Stacewicz, 2003a: Multiwavelenth lidar for determination of the atmospheric aerosol size distribution. *SPIE Proc.* **5229**, 45 – 50.

Ernst, K., G. Karasiński, A. Pietruczuk, T. Stacewicz, 2003b: Retrieving the atmospheric aerosol size distribution by means of multiwavelength lidar*. SPIE Proc.* **5258**, 156 – 159

Jagodnicka, A.K., T. Stacewicz, G. Karasiński, M. Posyniak, 2008: Simple method of Aerosol Particle Size Distribution retrieving from multiwavelength lidar signals, 15th International Conference on Clouds and Precipitation, Cancun, Mexico

Johnson, D.B., 1980: The influence of cloud base temperature and pressure on droplet concentration. *J. Atmos. Sci.*, **37**, 2079-2085

Measures, R.M., 1992: Laser Remote Sensing: Fundamentals and Applications Malabar, FL: *Krieger Publishing, reprint of 1984 John Wiley ed*.

Reidmiller D.R., Hobbs P.V., Kahn R., 2006: Aerosol Optical Properties and Particle Size Distributions on the East Coast of the United States Derived from Airborne In Situ and Remote Sensing Measurements. *J. Atmos. Sci.*, **63,** 785-814

AN INNOVATIVE EYE SAFE AND COMPACT EZ LIDAR™ FOR POLLUTION AND CLOUD MONITORING

L. Sauvage[1], S. Lolli P. Chazette[2], J. Sanak[2]

[1]*Leosphere, 42 Rue de Clignancourt 75018 Paris, France(lsauvage@leosphere.fr)*

[2] *Laboratoire des Sciences du Climat et de l'Environnement, CEA/CNRS, 91128 Palaiseau Cedex,France*

.

1. Introduction

A compact and rugged eye safe UV lidar, the EZLIDAR™, was developed together by CEA/LMD and LEOSPHERE (France) to study and investigate structural and optical properties of clouds and aerosols.

EZLIDAR™ has been validated by different remote and in-situ instruments as MPL Type-4 Lidar manufactured by NASA at ARM/SGP site or the LNA(Lidar Nuage Aerosol) at the Laboratoire de Metereologie Dynamique LMD (France) and during several intercomparison campaigns. Further the EZLIDAR™ was deployed in different air quality and long distance aerosol transport research campaigns (RATP, LISAIR'05, AMMA Niger campaign in January 2006, ASTAR/IPY in April 2006, TIGERZ'08 together with NASA/AERONET).

Due to its characteristics, EZLIDAR™ is suitable for continuous remote observations of highly resolved structures of tropospheric aerosols and clouds (Fog, low clouds, subvisible cirrus clouds), from 0.1 and up to 20km. The system is a mature meteorological turnkey and unattended remote sensor and then can well serve for operational meteorological networks and pollution agencies as a standardized tool.

2. EZLIDAR™ instrument

EZLIDAR™ Lidar uses a tripled pulse laser source ND:YAG at 355nm wavelength with an energy of 16mJ and pulse repetition frequency of 20 Hz. Both analog and photon counting detection is available. The lidar system provides a real time measurement with scanning capabilities of backscattering and extinction coefficients, Aerosol Optical Depth (AOD), automatic detection of the Planetary Boundary Layer height and clouds base and top from 50m up to 20 km.

In table 1 are schematically reported the instrument characteristics

Range	**50m-20km**	**Environment**	**-20°C../+50°C**
Temporal Res	**1s(PBL)/30s**	**Humidity**	**0-100%**
Spatial Res	**1.5m/15m**	**Waterproofing**	**IP65**
Angular Res	**0.2°**	**Weight**	**~48 kg**
ScanningSpeed	**8°/s**	**Eye Safety**	**IEC60825-1 2001**

Table 1 EZLIDAR technical characteristics

3. Planetary Boundary Layer height determination

Bigger strongly urbanized cities in the world are often exposed to atmospheric pollution events. To understand the chemical and physical processes that are taking place in these areas it is necessary to describe correctly the Planetary Boundary Layer (PBL) dynamics and the PBL height evolution.

EZLIDAR™ algorithm retrieves automatically the PBL height in real-time. The instrument was deployed at LMD in Palaiseau, France to validate the PBL height estimation with those retrieved by the algorithm STRAT [5] from data acquired by the LNA. The 12-days measurement campaign shows (Figure 1) a correlation between the instruments of 95% (for 5 minutes averaging).

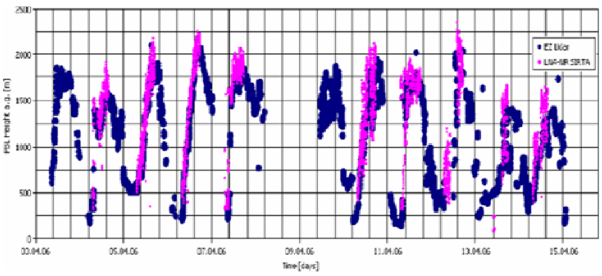

Figure 1 PBL Height retrieval from EZLIDAR (blue) and STRAT (fuchsia)

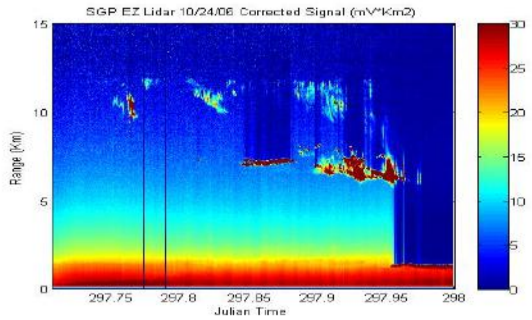

Figure 2 Range corrected signal for EZ lidar at SGP/ARM site, 10/24/06. It is possible to retrieve the height of the cloud layers (cumuli, cirri and altocumuli)

4. Cloud and Aerosol Observations

Knowledge of the vertical structure of cloud and aerosol scattering characteristics or layers from varying climates regimes is fundamental. There are many variables and measurements required to fully understand the radiative impact of cloud and aerosols, but accurate measurements of occurrence, height and thickness are relatively inaccurate and not on large scale. Ongoing research, in order to gather this information needs operational long-term observing sites equipped with diverse arrays of passive and active remote sensing, as well as in situ instrumentation. The direct detection of atmospheric cloud and aerosol generally involves active-based remote sensing techniques such as lidars, that are sensitive to molecular and aerosol particles.

One of the most notable EZ LIDAR™ feature is that its transmitted energy pulses are invisible (UV region) and eye safe, a main requirement for a lidar to be deployed in a continuous running observational site. Data measurements are processed for standard products, including the heights of cloud layers and the vertical distribution of backscattering and extinction coefficients in order to calculate the Aerosol Optical Depth (AOD). In figure 2 is reported the temporal plot of the range normalized measured backscattered signal (NRB)[3] at Southern Great Plain ARM site in Oklahoma, United States, where it can be observed the evolution of some cloud layers.

5. Cloud phase determination

The polarization of the light changes if in the scattering process are involved non-spherical particles as for ice crystals, snow flakes or dust. The particles can be assumed to be spherical in case of wet haze, fog, cloud droplets, and small raindrops. Thus, Lidar measurements of atmospheric depolarization can be used to distinguish between liquid and solid phases of water in the atmosphere and presence of dust. Figures 3 and 4 put in evidence a dust transit from Sahara with relative descent in the Planet Boundary Layer (PBL) over the rural suburbs of Paris.

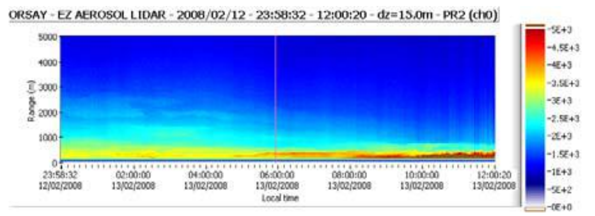

Figure 3 range normalized backscattered signal evidences some aerosols to 3km for a non cloudy sky on the 02/12/08 above Orsay, France

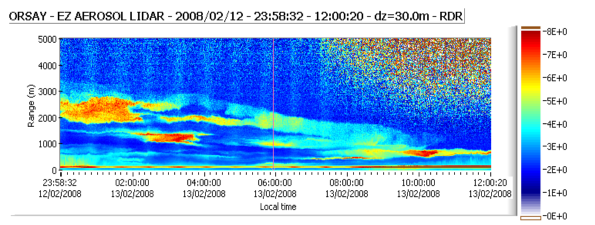

Figure 4 high depolarization ratio (colour map) put in evidence a dust transit from 3km to 1 km (inside the PBL) on the 02/12/08 above Orsay, France

The depolarization ratio, in presence of clouds, put in evidence the presence of ice and super-cooled water, as represented in Figure 6:

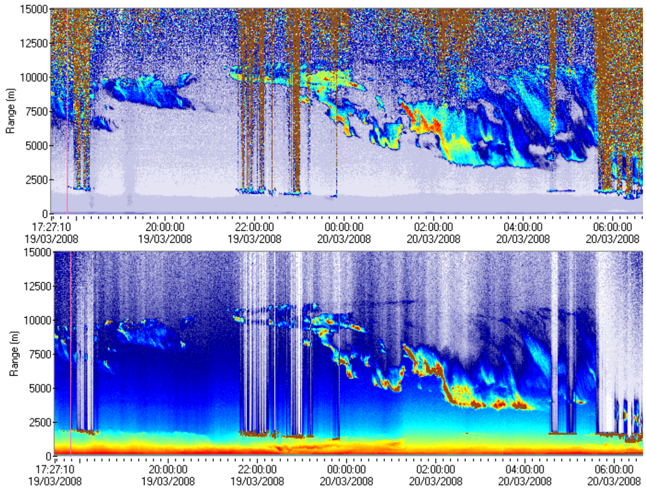

Figure 5 Range normalized measured backscattered signal (upper) evidences the presence of altocumuli and cirri. Depolarization ratio(lower) evidences supercooled water and ice crystals in the clouds (color map) in Chibolton, England, on 03/19/08.

6. Uncertainty analysis

The total and particle backscattering and extinction coefficients are directly retrieved processing the lidar signal returns as described in [3] and plotted in Figure1.. The total backscattering coefficient is given by:

$$\beta_{tot}(z) = \frac{\beta_m \, exp^{(S'(z)-S'_m)}}{1+2\beta_m L_R \int_{z_m}^{z} exp^{(S(z)-S'_m)} dz'} \quad (2)$$

Where z_m is the reference altitude at which the inversion starts, β_m is the known molecular backscattering coefficient at z_m, S' is the normalized range corrected lidar signal return (NRB) plotted in Fig.,2 S'_m is the NRB at the reference altitude z_m and L_R the lidar ratio. The relative uncertainty in retrieving the total backscattering coefficient β_{tot} is given by:

$$\Delta\beta_{tot}(z) = \sqrt{\sum_{j=1}^{3} \left(\frac{\delta\beta_{tot}}{\delta X_j} \Delta X_j \right)^2} \quad (3)$$

with ΔX_j respectively the uncertainty on: lidar ratio L_R, molecular backscattering β_{mol} and NRB. Each source error has been evaluated in a previous study [6], and from (3), it is possible to retrieve the backscattering coefficient with the relative uncertainty as plotted in Figure 6, for a measured profile at SGP at 3.59pm on 10/24/06

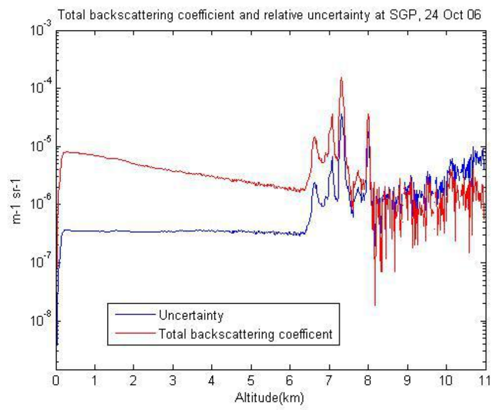

Figure 6 Total backscattering coefficient and relative uncertainty for 3.59pm of 10/24/06 at SGP (NRB plotted in fig.1)

The figure shows that the uncertainty on the backscattering coefficient retrieval is 100% at about 8000m after sounding through the cirrus cloud. This is consistent with the lidar range calculated as described in [7]

7 Conclusions

The EZ LIDAR™ instrument has been validated in several intercomparison campaigns, with different remote and in-situ instruments as sun photometers. PBL height retrieval shows a correlation of 95% with STRAT retrieval algorithm at LMD. [5] Also cloud structure, extinction profile, depolarization ratio and AOD can be retrieved on real-time from validated software.

Outdoor and unattended use capabilities of the EZLIDAR™, already deployed in meteorological observations networks such CLOUDNET, added to its measurements performances define then this instrument as a good candidate for deployment into growing global aerosol and cloud monitoring networks, research measurement campaigns and pollution measurements or future Lidar in Space missions (CALIPSO, EARTHCARE).

8 References

[1] J. R., Campbell, D. L. Hlavka, E. J. Welton, C. J. Flynn, D. D. Turner,J. D. Spinhirne, V. S. Scott, and I. H. Hwang, 2002: Full-time,eye-safe cloud and aerosol lidar observation at Atmospheric Radiation Measurement Program sites: Instrument and data processing. J. Atmos. Oceanic Technol., 19, 431–442.

[2] Ansman, A, M Riebesell, and C Weitkamp. 1990. “Measurements of atmospheric aerosol extinction profiles with Raman lidar.” Optics Letters 15:746-748.

[3] J. D. Klett, "Stable analytical inversion solution for processing lidar returns," Appl. Opt. 20, 211- (1981)

[4]Dave Turner et al. “Raman lidar measurements of the aerosol extinction-to-backscatter ratio over the Southern Great Plains” Journal of geophysical Research, Vol. 106, NO. D17, Pages 20,333–20,347, 2001

[5] Y.Morille, M.Haeffelin, P.Drobinsky, J.Pelon, *STRAT:* an automated algorithm to retrieve the vertical structure of the atmosphere from single channel lidar data, JAOT, Volume 24, Issue 5 (May 2007) pp. 761–775.

[6] S. Lolli EZ“Lidar Uncertainty Analysis in AOD retrievals.” LEOSPHERE internal communications, 2008

[7] S. Lolli L. Sauvage, I. Stachlewska, R. Coulter, R. Newsom “Assessment of EZ LIDAR™ and MPL Lidar Performances for qualitative and quantitative measurements of aerosol and clouds” 24th ILRC Conference, Boulder, USA

A NEW 1M^3 ISOTHERMAL CLOUD CHAMBER FOR THE INVESTIGATION ON CLOUD PHYSICS

Su Zhengjun[(1)(2)], **Zheng** G.G.[(2)], **Guan** L.Y.[(2)], **Huang**geng[(2)], **Zhang** J.H.[(2)]

[(1)]Nanjing University of Information Science & Technology, Nanjing, 210044, P.R. China
[(2)]Chinese Academy of Meteorological Science, Beijing, 100081, P.R. China
Tel：86-10-58995280，Fax：86-10-68406896
e-mail: suzj@cams.cma.gov.cn

1. Introduction

A technical workshop was held to review areas and goals of laboratory research in cloud physics and cloud chemistry, define the basic and practical utility of in terms of past accomplishments and future potential, assess the status and needs for existing and new facilities, and recommend future direction for laboratory research and corresponding facilities development in the disciplines of atmospheric science affected by cloud processes (R. List, 1986). Recently, some new useful facilities have been developed in China. Such as, a device for drop freezing experiment was improved, which consists of the cold-cavity, thermometer, controller of temperature, recorder of signals, cold sink, and environment box. His experimental results show that there is obvious deference in temperature spectra of freezing nuclei for different precipitation samples (Yang, 2005). A 15-liter mixing cloud chamber is developed to improve the creditability of data and test the ice nuclei effectiveness of "the 37 model silver iodide shell" (Yang, 2007a). In order to measuring the relative concentration of freezing nuclei in hydrometeors, based on Vali's even drops freezing experiment methods, a new system of automatically detecting drop frozen signals and processing test data have developed (Yang and Feng, 2007b).

Introducing either artificial ice nuclei (AIN) or cooling materials into super-cooled water cloud to initiate ice formation and Bergeron-Findeison process is now still the basic approach in the experiments and operations of weather modification. Since the first discovery of AgI as an efficient ice nuclei by Vonnegut in 1947, a great deal of theoretic and experimental work on ice nucleation has been conducted around the world. The measurement of ice nuclei can be mainly made with simulating and mechanism methods. Many kinds of instruments and facilities have been used. However, so far, there is none to be able to entirely simulate the conditions occurring in the natural atmosphere and responding to all ice nuclei which nucleate ice through different nucleation modes (mechanisms). The tests of artificial ice nuclei play an important role in weather modification. In China, many such tests have been done in the past 40 years (testing group, 1975; Zhang and Huang, 1979; Shi. et al, 1982; Chen and Feng, 1985; Feng. et al, 1995; Su, 2000), and some guiding results have been obtained for the manufacture of AgI-containing gun shell and small rocket and for the organic ice nuclei. The isothermal cloud chamber at the cloud physics process, cloud simulation and aerosol research is still used as one of very useful equipments. Based on the key techniques of the 2 m^3 and 96 m^3 cloud chambers in CAMS, we originally constructed a new 1m^3 isothermal cloud chamber (ICC).

The new 1m^3 ICC mainly for ice nucleation study is described in this paper. Its structure, attached instruments and experimental procedures are also presented. The experiments of determining the ice nuclei effectiveness for the AgI-containing aerosols produces by 5 kinds formulations have been conducted and the results have been compared with those of two different burning rooms. All experimental results show that the chamber has advantages of stable performance and reproducibility. It would be expected to become a calibration standard for ice nucleation investigation in China.

Due to overcoming the limit of cooling system is not automatically controlled in the chamber, the isothermal state is achieved after we improved the temperature controlling system of the ICC.

2. Facilities and their function

Fig.1. A photograph of $1m^3$ Isothermal cloud chamber (ICC) in CAMS

The equipment for ice nuclei test includes cloud chamber, fog generator, ice nuclei generator, measuring instruments, clean air source, dilution wind tunnel and aerosol sampling syringe.

The main body of the cloud chamber is a cylindric jacket tank with top and bottom and all made from stainless steel, with internal diameter 0.88 m, height 1.76 m and volume $1m^3$(as shown in Fig.1). More than 95% areas of the chamber surface are covered with jacket except the entrances and holes. Its measuring system includes:

- The fog is generated by an ultrasonic nebulizer.
- aerosol dilution and sampling
- temperature measuring system
- counting of ice crystals
- spectrum and concentration of fog droplets
- transparency, and so on.

3. Experiment procedures

General procedures for ice nuclei tests are as follows：Cooling cloud chamber → Sending fog（to clean the background ice nuclei and increase LWC）→generation ice nuclei aerosols diluting aerosols in wind tunnel →sampling（or diluting again）→injecting aerosol sample into cloud chamber→ taking out the slides from chamber and counting ice crystals under microscope →monitoring LWC and chamber temperature during whole test process.

Table1. The results of cooling capability of the new $1m^3$ cloud chamber

	T1 (℃)	T2 (℃)	T3 (℃)	T4 (℃)	Time (hh：mm)	rate (℃/min)	Cooling mode
1	-25.0	29.3	26.60	-24.48	5:37	0.147	double
2	-10.0	29.0	13.05	-9.19	2:23	0.156	double
3	-10.0	31.0	-0.65	-8.47	0:57	0.137	double
4-1	-15.66	31.0	-8.86	-12.73	1:49	0.036	single
4-2		31.0	-12.73	-13.31	0:09	0.076	double
5	-8.68	31.0	-2.47	-7.56	0:49	0.104	double
6-1	-20.69	31.0	-7.58	-12.92	2:29	0.036	single
6-2		31.0	-12.92	-19.13	0:57	0.109	double

From the cumulative number of ice crystals and mass of ice nucleant injected in the chamber the nucleation effectiveness can be calculated

$$N = \sum n \times \frac{V_1}{V_2} \times \frac{S_1}{S_2} \times \frac{1}{m}$$

Where N is active ice nuclei produced by one gram nucleant at temperature t , $\sum n$ the cumulative number of ice crystals in one viewfield of microscope from all sampling slides in a test. Generally, it lasts less than one hour for each test. The rate of ice nucleant can be studied from the cumulative number of ice crystals as a function of time.

4. Some results

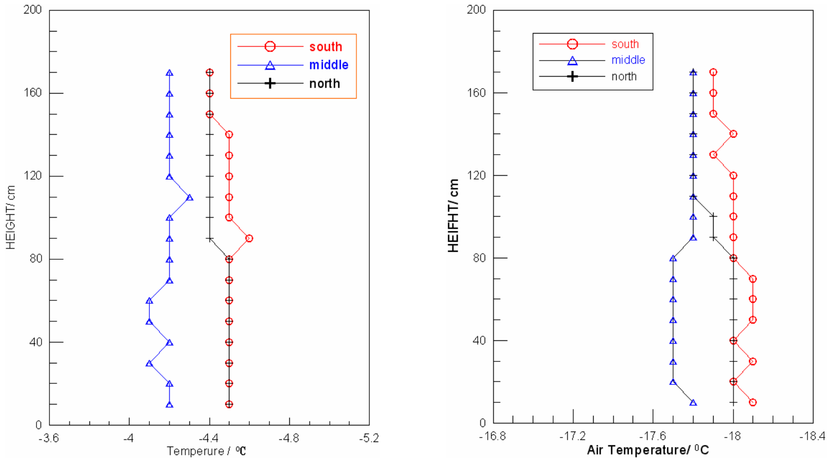

Fig.2. Temperature distribution in the cloud chamber during the investigation (a,-4.4℃; b,-18.0℃)

The best advantage of the cloud chamber is its temperature controlling system. It is entirely automatic, you just set the cloud chamber which you need simulating the fog environment, it will run by its system, and keep it for a long time during the experimental studies. The measurements show that the temperature of the chamber is stable well, its difference inside the chamber is less than 0.3℃.

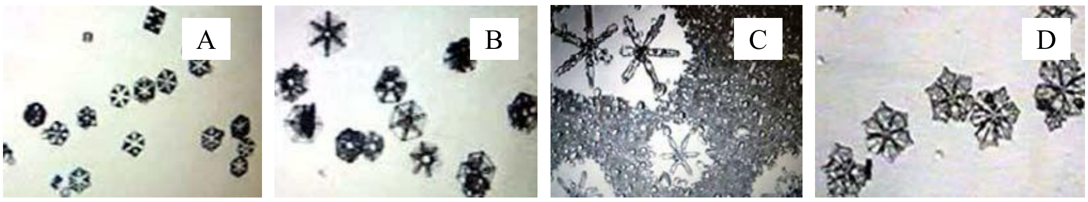

Fig.3. The shape characteristics of ice crystal in the cloud chamber(A-10℃;B-12℃;C-16℃;D-18℃)

5. Discussion

(1) Although the test of AIN is difficult, the comparing experiments and other experiments done in 1m^3 ICC show that the tests have good experimental performances and small data variances. It indicated that the design of cloud chamber structure is rational and the system is highly steady. It gains an advantage over the other cloud chambers ever used in China. The cloud chamber would provide a useful test facility for studying on Cloud Physics process, improving the seeding method, device and formulation of generating ice nuclei and for the research of seeding materials.

(2) The improvement is needed in sending fog unit and sampler diluting unit. The size distribution of fog droplets is great on the small slid for the used nebulizer. And the pre-cooling fog still remains to be solved.

(3) To study the artificial ice nuclei is the main aim of this chamber. The natural ice nuclei, new seeding agents, aerosol and some cloud physical processes cloud also be investigated under the stable environmental temperature, humidity and fog conditions provided.

Key Words: cloud chamber, test, artificial ice nuclei, mechanism investigation

Acknowledgements
This research was conducted under National Nature Science Foundation of China 40205001 and National Key Technology R&D Program 2006BAC12B06.

References

Dennis M. Garvey, 1975: Testing of Cloud Seeding Materials at the Cloud Simulation and Aerosol Laboratory, 1971-1973. *J. App .Meteor.* Vol.14: pp883-890.

Federer B. and Schneider A. 1981: Properties of Pyrotechnic Nucleants Used in Grossversuch IV, *J. Appl. Meteor.,* 20: pp 997- 1005.

Feng D., Wang Yunqing, Chen Ruzhen and Jiang G. 1990: A 2m^3 isothermal cloud chamber for the study of artificial nuclei. *ACTA Meteorologica Sinica*, 4(4): pp494-502.

Nickolay P. Romanov, 2007: Experimental Studies of Poorly Soluble Powder-Like Substances Effect on Modeled Warm Cloud Microstructure//9th WMO Scientific Conference on Weather Modification，Turkey，22-24 Oct., 2007，*WMP-No.44*: pp115-117.

Roland List, John Hallett，Jack Warner, and Roger R. 1986: “The Future of Laboratory Research and Facilities for Cloud Physics and Cloud Chemistry”, *Bulletin of the American Meteoro. Soc.*, Vol.67, No.11: 1389-1397.

Roland List, 1966: A Hail Tunnel with Pressure Control. *Journal of the Atmospheric Sciences*, Vol.23: pp61-66

—,G. B. Lessins, F. Garcia-Garcia, at el, 1987: Pressurized Icing Tunnel for Graupel, Hail and Secondary Raindrop Production. *J. Atmos. and Oceanic Tech.* Vol.4: pp454-463

Sax R. I.,Dennis M. Garvey and Farn P. Parungo. 1979: Characteristics of AgI Pyrotechnic Nucleant Used in NOAA’ Florida Area Cumulus Experiment. *J. Appl. Meteor.*, 18:pp195-202.

SU Zhengjun, J.H. Zhang, L.Y. Guan, *et al.* 2003: Regeneration of the nucleation ability of AgI// 8th WMO scientific conference on weather modification. *Casa.*, *WMO/WMP No.39:* pp433-436.

—, J. H. Zhang, L. Y. Guan, *et.al.* 2003: Analyses and discussion on the standards and methods of the nucleation effectiveness and mechanism, *Journal of Beijing Institute of Meteorology,* No.1:pp6-11, (in Chinese)

Zhang Jihuai, 1989: A medium-size cloud chamber in China, Papers submitted to the *fifth WMO Sci. Conf.* On weather modification and applied cloud physics, Beijing, 1989, pp403-406

Yang Shaozhong, Lou Xiaofeng Huanggeng and Feng Daxiong. 2007a: A 15 L Mixing Cloud Chamber for Testing Ice Nuclei. *Journal of Appl. Meteoro. Sci.,* 18(5): pp716-721 (in Chinese)

— and Feng Daxiong. 2005: An Improved Device for Drop Freezing Experiment Concerning Rain Enhancement. *Meteorological Science and Technology,* 33(5):451-455(in Chinese)

— and —. 2007b: A New apparatus for detecting the concentration of freezing nuclei in water. *ACTA Meteorologica Sinica*, 65(6): 976-982 (in Chinese).

A NEW 1M^3 ISOTHERMAL CLOUD CHAMBER FOR THE INVESTIGATION ON CLOUD PHYSICS

Su Zhengjun(1)(2), **Zheng** G.G.(2), **Guan** L.Y.(2), **Huang**geng(2), **Zhang** J.H.(2)

(1)Nanjing University of Information Science & Technology, Nanjing, 210044, P.R. China
(2)Chinese Academy of Meteorological Science, Beijing, 100081, P.R. China
Tel：86-10-58995280，Fax：86-10-68406896
e-mail: suzj@cams.cma.gov.cn

1. Introduction

A technical workshop was held to review areas and goals of laboratory research in cloud physics and cloud chemistry, define the basic and practical utility of in terms of past accomplishments and future potential, assess the status and needs for existing and new facilities, and recommend future direction for laboratory research and corresponding facilities development in the disciplines of atmospheric science affected by cloud processes (R. List, 1986). Recently, some new useful facilities have been developed in China. Such as, a device for drop freezing experiment was improved, which consists of the cold-cavity, thermometer, controller of temperature, recorder of signals, cold sink, and environment box. His experimental results show that there is obvious deference in temperature spectra of freezing nuclei for different precipitation samples (Yang, 2005). A 15-liter mixing cloud chamber is developed to improve the creditability of data and test the ice nuclei effectiveness of “the 37 model silver iodide shell” (Yang, 2007a). In order to measuring the relative concentration of freezing nuclei in hydrometeors, based on Vali’s even drops freezing experiment methods, a new system of automatically detecting drop frozen signals and processing test data have developed (Yang and Feng, 2007b).

Introducing either artificial ice nuclei (AIN) or cooling materials into super-cooled water cloud to initiate ice formation and Bergeron-Findeison process is now still the basic approach in the experiments and operations of weather modification. Since the first discovery of AgI as an efficient ice nuclei by Vonnegut in 1947, a great deal of theoretic and experimental work on ice nucleation has been conducted around the world. The measurement of ice nuclei can be mainly made with simulating and mechanism methods. Many kinds of instruments and facilities have been used. However, so far, there is none to be able to entirely simulate the conditions occurring in the natural atmosphere and responding to all ice nuclei which nucleate ice through different nucleation modes (mechanisms). The tests of artificial ice nuclei play an important role in weather modification. In China, many such tests have been done in the past 40 years (testing group, 1975; Zhang and Huang, 1979; Shi. et al, 1982; Chen and Feng, 1985; Feng. et al, 1995; Su, 2000), and some guiding results have been obtained for the manufacture of AgI-containing gun shell and small rocket and for the organic ice nuclei. The isothermal cloud chamber at the cloud physics process, cloud simulation and aerosol research is still used as one of very useful equipments. Based on the key techniques of the 2 m^3 and 96 m^3 cloud chambers in CAMS, we originally constructed a new 1m^3 isothermal cloud chamber (ICC).

The new 1m^3 ICC mainly for ice nucleation study is described in this paper. Its structure, attached instruments and experimental procedures are also presented. The experiments of determining the ice nuclei effectiveness for the AgI-containing aerosols produces by 5 kinds formulations have been conducted and the results have been compared with those of two different burning rooms. All experimental results show that the chamber has advantages of stable performance and reproducibility. It would be expected to become a calibration standard for ice nucleation investigation in China.

Due to overcoming the limit of cooling system is not automatically controlled in the chamber, the isothermal state is achieved after we improved the temperature controlling system of the ICC.

2. Facilities and their function

Fig.1. A photograph of $1m^3$ Isothermal cloud chamber (ICC) in CAMS

The equipment for ice nuclei test includes cloud chamber, fog generator, ice nuclei generator, measuring instruments, clean air source, dilution wind tunnel and aerosol sampling syringe.

The main body of the cloud chamber is a cylindric jacket tank with top and bottom and all made from stainless steel, with internal diameter 0.88 m, height 1.76 m and volume $1m^3$(as shown in Fig.1). More than 95% areas of the chamber surface are covered with jacket except the entrances and holes. Its measuring system includes:

- The fog is generated by an ultrasonic nebulizer.
- aerosol dilution and sampling
- temperature measuring system
- counting of ice crystals
- spectrum and concentration of fog droplets
- transparency, and so on.

3. Experiment procedures

General procedures for ice nuclei tests are as follows：Cooling cloud chamber → Sending fog（to clean the background ice nuclei and increase LWC）→generation ice nuclei aerosols diluting aerosols in wind tunnel →sampling（or diluting again）→injecting aerosol sample into cloud chamber→ taking out the slides from chamber and counting ice crystals under microscope →monitoring LWC and chamber temperature during whole test process.

Table1. The results of cooling capability of the new $1m^3$ cloud chamber

	T1 (℃)	T2 (℃)	T3 (℃)	T4 (℃)	Time (hh：mm)	rate (℃/min)	Cooling mode
1	-25.0	29.3	26.60	-24.48	5:37	0.147	double
2	-10.0	29.0	13.05	-9.19	2:23	0.156	double
3	-10.0	31.0	-0.65	-8.47	0:57	0.137	double
4-1	-15.66	31.0	-8.86	-12.73	1:49	0.036	single
4-2		31.0	-12.73	-13.31	0:09	0.076	double
5	-8.68	31.0	-2.47	-7.56	0:49	0.104	double
6-1	-20.69	31.0	-7.58	-12.92	2:29	0.036	single
6-2		31.0	-12.92	-19.13	0:57	0.109	double

From the cumulative number of ice crystals and mass of ice nucleant injected in the chamber the nucleation effectiveness can be calculated

$$N = \sum n \times \frac{V_1}{V_2} \times \frac{S_1}{S_2} \times \frac{1}{m}$$

Where N is active ice nuclei produced by one gram nucleant at temperature t , $\sum n$ the cumulative number of ice crystals in one viewfield of microscope from all sampling slides in a test. Generally, it lasts less than one hour for each test. The rate of ice nucleant can be studied from the cumulative number of ice crystals as a function of time.

4. Some results

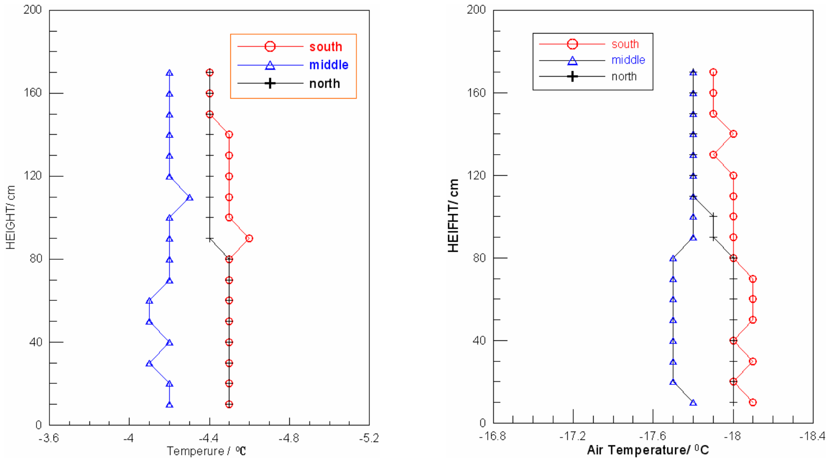

Fig.2. Temperature distribution in the cloud chamber during the investigation (a,-4.4℃; b,-18.0℃)

The best advantage of the cloud chamber is its temperature controlling system. It is entirely automatic, you just set the cloud chamber which you need simulating the fog environment, it will run by its system, and keep it for a long time during the experimental studies. The measurements show that the temperature of the chamber is stable well, its difference inside the chamber is less than 0.3℃.

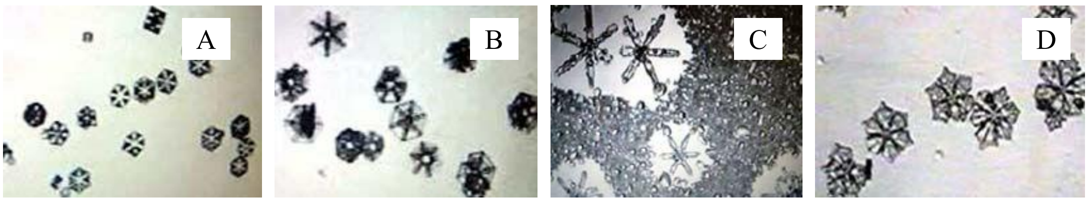

Fig.3. The shape characteristics of ice crystal in the cloud chamber(A-10℃;B-12℃;C-16℃;D-18℃)

5. Discussion

(1) Although the test of AIN is difficult, the comparing experiments and other experiments done in 1m^3 ICC show that the tests have good experimental performances and small data variances. It indicated that the design of cloud chamber structure is rational and the system is highly steady. It gains an advantage over the other cloud chambers ever used in China. The cloud chamber would provide a useful test facility for studying on Cloud Physics process, improving the seeding method, device and formulation of generating ice nuclei and for the research of seeding materials.

(2) The improvement is needed in sending fog unit and sampler diluting unit. The size distribution of fog droplets is great on the small slid for the used nebulizer. And the pre-cooling fog still remains to be solved.

(3) To study the artificial ice nuclei is the main aim of this chamber. The natural ice nuclei, new seeding agents, aerosol and some cloud physical processes cloud also be investigated under the stable environmental temperature, humidity and fog conditions provided.

Key Words: cloud chamber, test, artificial ice nuclei, mechanism investigation

Acknowledgements

This research was conducted under National Nature Science Foundation of China 40205001 and National Key Technology R&D Program 2006BAC12B06.

References

Dennis M. Garvey, 1975: Testing of Cloud Seeding Materials at the Cloud Simulation and Aerosol Laboratory, 1971-1973. *J. App .Meteor.* Vol.14: pp883-890.

Federer B. and Schneider A. 1981: Properties of Pyrotechnic Nucleants Used in Grossversuch IV, *J. Appl. Meteor.,* 20: pp 997- 1005.

Feng D., Wang Yunqing, Chen Ruzhen and Jiang G. 1990: A 2m^3 isothermal cloud chamber for the study of artificial nuclei. *ACTA Meteorologica Sinica*, 4(4): pp494-502.

Nickolay P. Romanov, 2007: Experimental Studies of Poorly Soluble Powder-Like Substances Effect on Modeled Warm Cloud Microstructure//9th WMO Scientific Conference on Weather Modification，Turkey，22-24 Oct., 2007，*WMP-No.44*: pp115-117.

Roland List, John Hallett，Jack Warner, and Roger R. 1986: “The Future of Laboratory Research and Facilities for Cloud Physics and Cloud Chemistry”, *Bulletin of the American Meteoro. Soc.*, Vol.67, No.11: 1389-1397.

Roland List, 1966: A Hail Tunnel with Pressure Control. *Journal of the Atmospheric Sciences*, Vol.23: pp61-66

—,G. B. Lessins, F. Garcia-Garcia, at el, 1987: Pressurized Icing Tunnel for Graupel, Hail and Secondary Raindrop Production. *J. Atmos. and Oceanic Tech.* Vol.4: pp454-463

Sax R. I.,Dennis M. Garvey and Farn P. Parungo. 1979: Characteristics of AgI Pyrotechnic Nucleant Used in NOAA' Florida Area Cumulus Experiment. *J. Appl. Meteor.*, 18:pp195-202.

SU Zhengjun, J.H. Zhang, L.Y. Guan, *et al.* 2003: Regeneration of the nucleation ability of AgI// 8th WMO scientific conference on weather modification. *Casa.*, *WMO/WMP No.39:* pp433-436.

—, J. H. Zhang, L. Y. Guan, *et.al.* 2003: Analyses and discussion on the standards and methods of the nucleation effectiveness and mechanism, *Journal of Beijing Institute of Meteorology,* No.1:pp6-11, (in Chinese)

Zhang Jihuai, 1989: A medium-size cloud chamber in China, Papers submitted to the *fifth WMO Sci. Conf.* On weather modification and applied cloud physics, Beijing, 1989, pp403-406

Yang Shaozhong, Lou Xiaofeng Huanggeng and Feng Daxiong. 2007a: A 15 L Mixing Cloud Chamber for Testing Ice Nuclei. *Journal of Appl. Meteoro. Sci.,* 18(5): pp716-721 (in Chinese)

— and Feng Daxiong. 2005: An Improved Device for Drop Freezing Experiment Concerning Rain Enhancement. *Meteorological Science and Technology,* 33(5):451-455(in Chinese)

— and —. 2007b: A New apparatus for detecting the concentration of freezing nuclei in water. *ACTA Meteorologica Sinica*, 65(6): 976-982 (in Chinese).

DEVELOPMENT OF A TEMPERATURE-DEPENDENT RADAR REFLECTIVITY TO SNOWRATE RELATIONSHIP FOR THE S-BAND

Jonathan P. Wolfe[1], Jefferson R. Snider[2] and Bart Geerts[2]
[1]National Weather Service, Portland, Oregon, USA
[2]*Department of Atmospheric Science, University of Wyoming, Laramie, Wyoming, USA*

ABSTRACT

Weather radar offers a practical way of estimating snowfall rate with high spatial and temporal resolution. Such remotely-sensed snowrates are useful for weather advisory and hydrometeorology. In either application a relationship between equivalent radar reflectivity (Z_e) and water equivalent snowrate (S) is needed. Furthermore, this relationship should be tuned to the location and cloud type of interest. The leading coefficient in the relationship $Z_e = \alpha \cdot S^{\beta}$ can be shown to vary with temperature-dependent properties of the snowflake size distribution. We describe measurements, and a statistical analysis, leading to a value for α which can be applied to wintertime upslope storms occurring in southeastern Wyoming, and report a positive correlation between α and surface temperature. This temperature-dependence is suggestive of a process which produces an inverse relationship between snowflake concentration and temperature, e.g., primary ice nucleation.

1. INTRODUCTION

In western North America snowfall accumulations are measured by a network of surface snowfall gages; including measurements made at weather service offices, snow telemetry pillow sites (SNOTEL), and by Community Collaborative Rain, Hail and Snow (CoCoRaHS) network. In spite of the large number of these precipitation monitoring sites, the network cannot resolve the spatial and temporal variability of precipitation. This challenge is vexing when quantifying either rainfall or snowfall, but in the case of snowfall there is the additional complication of measurement bias (Groisman and Legates, 1994).

Radar is an alternative to a denser network of precipitation gages. Measurements of snowfall rate (S) are derived with high spatial and temporal resolution via radar measurement of the equivalent reflectivity factor (Z_e) and a reflectivity-to-snowrate relationship (Rasmussen et al. 2002; Fujiyoshi et al. 1990; Boucher and Weiler 1985). A disadvantage of this approach, particularly in mountainous regions of the western US, is that terrain limits radar coverage (Pellarin et al. 2002). Because of these limitations a triad of measurement systems – radar, precipitation gages and SNOTEL – is envisioned as components of an improved snowrate and snow accumulation measurement effort (Wetzel et al. 2004).

Radar has been used to derive precipitation rate for over 60 years (Marshall et al., 1947), but variability in the relationship between radar reflectivity and precipitation rate has lead to deemphasis of radar remote sensing, particularly when examining snowfall. In the commonly used parameterization $Z_e = \alpha \cdot S^{\beta}$, where α and β are fitted values, α varies by an order of magnitude and β varies by +/- 15% (Rasmussen et al. 2003; Fujiyoshi et al. 1990). It was shown by Rasmussen et al. (2003) that the theoretical value of β is 1.7, however, the semi-empirical work of Sekhon and Shrivastava (1970) indicates β = 2.2. Here, we attempt to decrease the variability of the Z_e - S relationship by taking one of the fit coefficients to be a function of ambient temperature. Our study is guided by a simple theory which predicts that β is a constant and that α varies positively with temperature.

2. MEASUREMENTS

2a. Measurement Site

Three measurement systems were used in this study. Their focus was a surface site located 25 km northwest of Cheyenne, Wyoming. The surface site is located on the eastern foothills of the Laramie Range at latitude 41° 15' 40" N and longitude 105° 03' 52" W at an elevation of 2092 m. Observations made at the surface site included snowrate, temperature and wind speed from the Hotplate precipitation sensor TPS-3100 (Rasmussen et al. 2002; Yankee Environmental Systems, Inc.) and temperature and wind speed from a Vaisala weather station WXT510 (Vaisala, Inc. 2005). Data from the surface-site sensors were recorded once per second. Four upslope snowstorms were studied during the winter of 2006 (March 8, March 12, March 19 and March 20).

2b. Hotplate Snowrate Sensor

The Hotplate consists of two vertically stacked 13 cm (diameter) circular plates mounted on a pedestal. The Hotplate control circuitry and the plate heating elements are designed to maintain the temperature of the plates at 90 °C, adjusting for convective heat loss which removes heat from both plates, and for the heat demand of the top plate due to snowfall. The power difference between the two plates is used to compute the precipitation rate expressed as a one-minute and five-minute running average. If the value of the 5 minute running average exceeds 0.25 mm hr^{-1}, a provisional precipitation rate is output as a 1 minute running average; otherwise, the provisional precipitation rate is reported as 0 mm hr^{-1}. The provisional rate is divided by a windspeed-dependent catch efficiency and this corrected precipitation rate is output once per second (Rasmussen et al., 2005). Our Hotplate was purchased from Yankee Environmental Systems (Turner Falls, MA) in 2005 and utilized the firmware version 2.6.

We evaluated the accuracy of the Hotplate-derived precipitation rate, and the time-response of the Hotplate, by randomly distributing uniform-sized water drops (2 mm diameter) across the top plate surface. These laboratory-based studies reveal good agreement between our lab-based precipitation rate standard and the values reported by the Hotplate. On average, the absolute departure from the standard was 0.03 mm hr^{-1} for standard values between to 1 and 2.4 mm hr^{-1}. The lab tests also reveal that the Hotplate can respond to the onset of precipitation in 135 s (Wolfe 2007).

During daytime conditions the Hotplate-derived values of air temperature were positively biased by ~2 °C relative to the Vaisala WXT510; consequently, the Vaisala measurements of temperature were used in this analysis. The Vaisala and Hotplate wind speed measurements agreed, on average, within ±20%.

2c. Weather Surveillance Radar

Radar reflectivity measurements made over the surface site were acquired by the Cheyenne (Wyoming) Weather Surveillance Radar-1988 Doppler (Crum and Alberty 1993) hereafter referred to as the WSR. The WSR transmits and receives at a wavelength of 10 cm. The radar range gate, over the location of the surface site (azimuth angle = 299°, range=25 km), can be approximated as a nearly prostrate cylinder with length 1.0 km and diameter 0.40 km. Backscattered radiation detected by the radar is converted to an equivalent radar reflectivity factor, expressed in decibels, and is archived with azimuth angle, elevation angle, data and time. We utilized Level II WSR data obtained from the National Climatic Data Center. The radar scan strategy, which prescribes how the WSR probes the coverage volume, is selected by the radar operator. The two scan strategies used in this study are summarized in Table 1.

Table 1 - WSR scan strategies used in this study.

Volume Coverage Pattern Identifier	Time to complete a volume Scan, s	Elevation Angles, °
21	333	0.50, 1.45, 2.40, 3.35, 4.30, 6.00, 9.90, 14.60, 19.50
32	573	0.50, 1.50, 2.50, 3.50, 4.50

2d. Uncertainties

Here we discuss bias due to the possible misalignment of the Hotplate and WSR time series, plus bias due to our use of radar measurements made at the lowest WSR elevation angle (0.5 °). We synchronized the Hotplate and the surface site data acquisition system clocks to a reference at the beginning of the month of March 2006. Our comparison of these two clocks at the end of the month of March revealed that they had drifted by 300 s. Arbitrarily, the Hotplate clock was chosen for synchronizing the surface measurements (snowrate and temperature) to the Level II WSR data. In addition to the likely drift of the time reference at the surface site, the surface and radar data sets are misaligned because of the time it takes for snowflakes to fall from the elevation of the radar range gate to the surface. Figure 1 shows the cross section along the radial of the WSR that passes over the surface site with the 0.5° and 1.5° beam centers and the 0.5° half power beam width overlaid. It demonstrates that the snowflake fall distances range between 50 and 500 m for these two lowest elevation angles. Assuming a representative snowflake fall speed (1 m/s, Locatelli and Hobbs (1974)), the time mismatch could be as large as 500 s. When we did account for this time mismatch we found no evidence for an improvement in the correlation between the surface and WSR measurements. Hence, for this analysis we did not shift the two time series.

It is evident from Figure 1 that 50% of the 0.5° transmission is blocked by terrain. In contrast, the 1.5° transmission is not affected. This suggests that reflectivities from the 0.5° elevation angle could be negatively biased. This issue is discussed further in Section 4a.

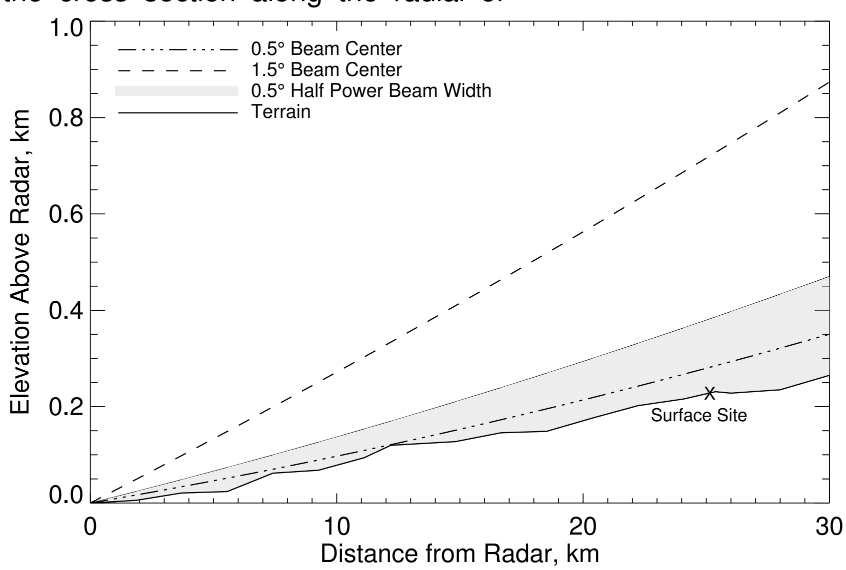

Figure 1 - Cross section of the terrain along the radial of the WSR that passes over the surface site assuming a standard profile of temperature, pressure and humidity.

3. THEORETICAL MOTIVATION

This work correlates measurements of surface snowrate (S), expressed as a water equivalent depth per unit time, with radar-derived values of the equivalent radar reflectivity factor (Z_e). The equation commonly used to describe this correlation is a power law of the form:

$$Z_e = \alpha \cdot S^{\beta} \qquad (\mathrm{mm^6\ m^{-3}}) \qquad (1)$$

The coefficients α and β are often derived by regressing concurrent measurements of Z_e and S. Prior investigators have employed a variety of averaging techniques aimed at of minimizing statistical error due to atmospheric variability and instrument sensitivity issues (Super and Holroyd, 1998; Fujiyoshi et al. 1990; Rasmussen et al. 2003).

Rasmussen et al. (2003) describe how α and β vary with local conditions within the atmospheric volume that is probed by a WSR. For their theoretical analysis they assume that the snowflake size distribution function can be described by the exponential form proposed by Marshall and Palmer (1948) for rain. The function has the form $N(D) = N_o \cdot \exp(-\Lambda D)$, where N_o is the y-intercept of the function, Λ is the slope of the function and D represents the unmelted snowflake diameter. Following Rasmussen et al., we parameterize the snowflake density (ρ_S) in terms of a parameter (Ω) and the unmelted snowflake diameter ($\rho_S = \Omega / D$). In this parameterization ρ_S is the ratio of snowflake mass to its inscribed volume. Both Ω and ρ_S vary with environmental conditions, with the simplest three categorizations being 1) snowflakes with a temperature of 0 °C (wet snow), 2) snowflakes grown by the accretion of supercooled cloud droplets (rimed snow), and 3) snowflakes grown by either vapor diffusion or aggregation in an environment colder than 0 °C (dry snow). For the latter conditions, a representative value of Ω is 0.2 kg m/m^3 (Rasmussen et al., 2003; Liu and Illingworth, 2000). These two relationships (Marshall-Palmer and size-density) allowed Rasmussen et al. to derive a theoretical Z_e-S relationship. Here we restate their result for dry snow conditions

$$Z_e = 2.22 \cdot 10^{19} \cdot \frac{|K_i|^2}{|K_w|^2} \cdot \frac{\rho_w^{5/3}}{\rho_i^2} \frac{\Omega^{1/3}}{V_t^{5/3} \cdot N_o^{2/3}} \cdot S^{5/3} \qquad (\mathrm{mm^6\ m^{-3}}) \qquad (2)$$

In Equation (2), $|K_i|^2$ and $|K_w|^2$ are the moduli of the complex dielectric factors for ice and water, ρ_i and ρ_w are the corresponding bulk densities, and V_t is the snowflake terminal velocity. Moreover, all symbols on the right-side of the Equation 2 are expressed in terms of their meter-kilogram-second equivalent.

We extend Equation 2 by first noting that its derivation starts with separate developments for Z_e and S, leading to relationships which have S proportional to the second moment and Z_e proportional to the sixth moment of the of the Marshall-Palmer size distribution function. Furthermore, we note that these proportionalities require the assumptions that terminal velocity is a constant and that the scattering is described by Rayleigh theory. Finally, we note that the snowflake concentration is the zeroth moment of the Marshall-Palmer function. Using the same assumptions as are implicit in Equation 2 (Rayleigh scattering, Marshall-Palmer size distribution function and size-independent terminal velocity and size independent Ω), we derive an alternate form for the Z_e-S relationship

$$Z_e = 2.19 \cdot 10^{19} \cdot \frac{|K_i|^2}{|K_w|^2} \cdot \frac{\rho_w^2}{\rho_i^2} \cdot \frac{1}{V_t^2 \cdot N} \cdot S^2 \qquad (\mathrm{mm^6\ m^{-3}}) \qquad (3)$$

Here N is the zeroth moment of the size distribution, i.e., the size-integrated concentration of snowflakes. Equation 3 demonstrates that Ω cancels out of the theoretical Z_e-S relationship, that β is a constant, and that α (the group of parameters multiplying S^2 in Equation 3) is a function of the cloud microphysical properties N and V_t. It also shows that α will be larger in cloud volumes containing lower concentrations of snowflakes. In addition, if snowflake concentrations vary inversely with temperature, as is observed in clouds containing ice generated by heterogeneous nucleation (primary ice generation; see, for example, Cooper (1986)) then it follows that α will be larger in cloud volumes observed at warmer temperatures.

The proceeding theoretical analysis of the power-law relationship between radar reflectivity and snowrate leads us to hypothesize that α is temperature dependent. We test that hypothesis.

4. RESULTS

4a. Beam Blockage

Bech et al. (2003) considered situations like that illustrated in Figure 1 and analyzed the effect of the beam blockage on the backscattered signal. We addressed this issue two ways. First, we analyzed the WSR radial velocity data, acquired as the lowest radar tilt angle (0.5°) and found no evidence for beam blockage along the radial between the WSR and the surface site. Second, we regressed the radar reflectivities acquired at the elevation angles 0.5° and 1.5° (over the surface site) and found no evidence for a shift between these when the WSR was operated in scan mode #32 (Table 1). A shift was detected when the WSR was operated in scan mode #31 but interpretation of this shift as beam blockage is complicated by the very weak correlation between the 0.5° and 1.5° reflectivities when operating in this scan mode. These analyses indicated that beam blockage did not significantly bias the reflectivity measurements acquired at 0.5°, at least when the WSR was operated in scan mode #32. In spite of this we remain suspicions about beam blockage at the lowest WSR elevation angle, even though a majority of the WSR measurements were acquired in the #32 scan mode. For this reason we fit the Z_e-S relationship using data collected at elevation angle 0.5°, at elevation angle 1.5°, and by combining data acquired at both elevation angles.

4b. Fitting

Three statistical methods were used to calculate α and each is described in the Appendix. The first minimizes the departure of Z_e from the line $Z_e = \alpha_1 \cdot S^2$, the second minimizes the departure of S^2 from the line $Z_e = \alpha_2 \cdot S^2$, and the third minimizes the departure of $\ln Z_e$ from a line of the form $\ln Z_e = \ln \alpha_3 + \ln S^2$. Also explained in the Appendix is the calculation of the standard errors: $\sigma_{\alpha 1}$, $\sigma_{\alpha 2}$ and $\sigma_{\alpha 3}$.

Figure 2 shows a plot of the Z_e-S pairs binned into three 4 °C temperature intervals starting at -12 °C and ending at 0 °C; colors represent the Coordinated Universal Time (UTC) date of the measurements. Data acquired at both WSR elevation angles (0.5° and 1.5°) is represented here. The figure shows that each temperature interval contains Z_e-S pairs from at least two of the four study days and that a majority of the data was acquired at temperatures warmer than -8 °C. Furthermore, a clear increase in α_3 with increasing temperature is evident. We focus on this particular value of α because the departure of the measured snowrates from the line $Z_e = \alpha_3 \cdot S^2$ is smaller than that for the two other fitting functions. Values of the departure, expressed as a average absolute snowrate error, are equal to 0.2, 0.6 and 0.5 mm/hr for the temperature bins -12/-8, -8/-4 and -4/0, respectively. These departures are noticeably smaller than those obtained for the $Z_e = \alpha_1 \cdot S^2$ parameterization, and insignificantly smaller to that for the $Z_e = \alpha_2 \cdot S^2$ parameterization.

4c. Temperature-dependence of α

Figure 3 presents values for α_1, α_2, and α_3 as a function of temperature for the 0.5° and 1.5° elevation angles (left and middle panel) and for both angles (right panel). Values for α_3 are connected to illustrate the monotonic nature of its increase with temperature. The error bars extend from α minus one standard error to α plus one standard error.

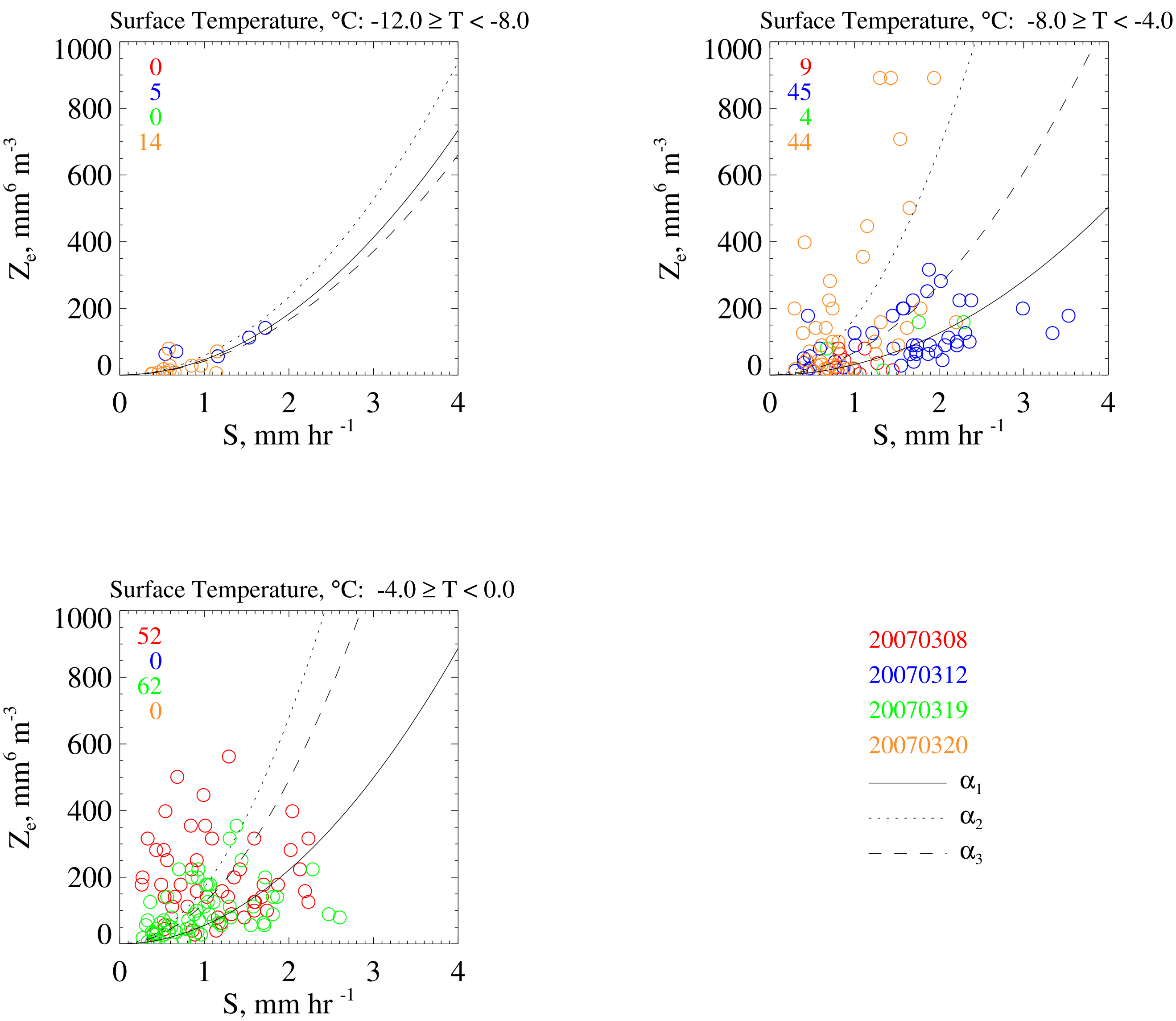

Figure 2 - Plots of Z_e - S pairs for three 4 °C temperature intervals beginning at -12 °C and ending with 0 °C. Data from both radar elevation angles (0.5° and 1.5°) is displayed. Also shown are the best-fit lines corresponding to α_1, α_2 and α_3. The number of data points from each day is shown in the upper-left corner of the panels.

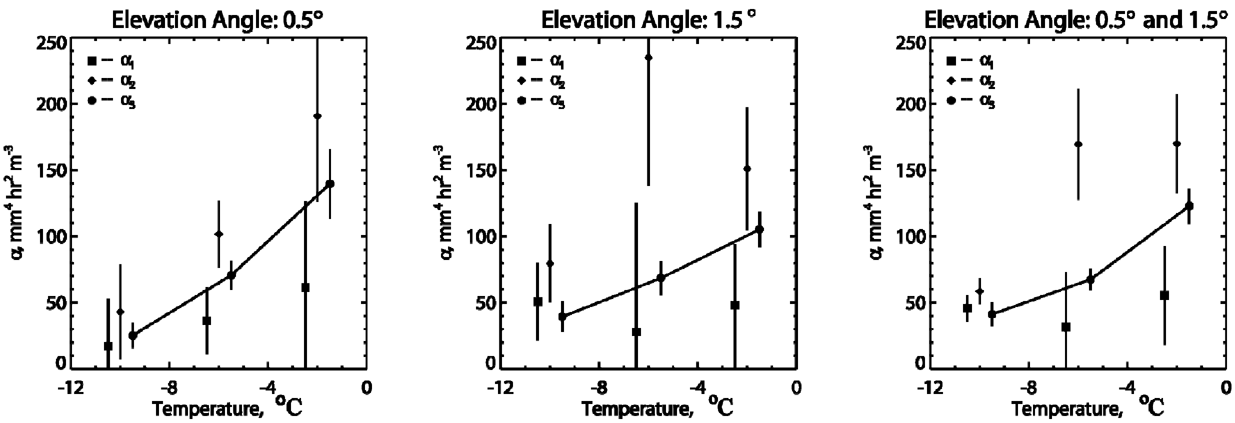

Figure 3 - Values for α_1, α_2, and α_3 versus temperature for the WSR elevation angles 0.5° (left panel) and 1.5° (middle panel). The right panel shows the result obtained by combining data from both elevation angles. Error bars extend from the fitted value minus the standard error to the fitted value plus the standard error. A line connects the temperature-dependent values of α_3.

4d. Validation

Table 2 shows the comparison of radar-derived snowfall accumulation (based on our temperature-dependent α_3 and radar data acquired at 0.5°) versus accumulations from the Community Collaborative Rain, Hail and Snow (CoCoRaHS) network. The CoCoRaHS measurements are reported every 24 hours and correspond to samples accumulated between from 7 am LST (day 1) and 7 am LST (day 2). Results shown in Table 2 are from the four closest CoCoRaHS sites and these are labeled by the distance (km), and by the direction (either to the south or east), from our surface site to the CoCoRaHS. Also compared are accumulations from the Hotplate and a radar-derived accumulation based on the values of α and β recommended by Super and Holroyd (1998) for snow in Denver, Colorado.

Table 2 shows that the best correspondence is between the Hotplate and the radar-derived accumulation based on the α_3 parameterization. This comparison tests our fitting procedure and highlights the point made is Section 4b where we show that α_3 is preferred over either α_2, or α_1, for estimating snowrate from reflectivity (i.e., the mean absolute snowrate departure is smallest for α_3). Also evident from Table 2 is the good agreement between our radar-derived accumulations and those based on Super and Holroyd (1998). There is an important difference between our data set and the data set analyzed by Super and Holroyd. We base our fitting on 235 sample pairs (Figure 2); neither Z_e or S is averaged. In contrast, Super and Holroyd used 458 hourly-averaged snowrate values, acquired over two winter seasons, to build their Z_e - S parameterization for Denver, CO. Our work indicates that parameterizations can be constructed with snowrate measurements from the Hotplate and suggests that improvements may result because of the faster response characteristic of the Hotplate compared to that of conventional snowrate gauges.

The comparison to the CoCoRaHS network shows reasonable agreement on March 8, in particular for the comparison to the 13-E-b site, and on March 19 in the comparison to the 6-S site. On March 12 all of the CoCoRaHS reported substantially larger snorates.

Table 2 - Comparison of 24 hr accumulations expressed in millimeter of water equivalent precipitation

Accumulation Method	7 am (LST) to 7 am (LST) March 8	March 12	March 19	March 20
CoCoRaHS 6-S	NA	6.6	5.6	NA
CoCoRaHS 8-E	2.3	6.9	10.2	0.5
CoCoRaHS 13-E-a	2.8	6.4	6.9	0.5
CoCoRaHS 13-E-b	4.8	7.6	7.4	NA
Hotplate	5.4	4.2	3.2	0.0
Radar-estimated using $Z_e = \alpha_3 \cdot S^2$ (this work)	5.1	3.6	5.0	0.0
Radar-estimated using $Z_e = 130 \cdot S^2$ (Super and Holroyd, 1998)	4.5	3.3	3.6	0.0

NA – not available
LST – local standard time

6. SUMMARY

This study examined the role of temperature in the relationship between snowrate (S) and radar reflectivity (Z_e). In our examination of this temperature-dependence we prescribed the value of the exponent in the fitting equation (Equation 1). It is shown, both theoretically and empirically, that the leading term in the fitting equation (α) increases with temperature. We also show that the radar-derived accumulations agree with the Hotplate accumulations, and that the former agree with subset of the CoCoRaHS measurements made in the vicinity of our surface site. The snowrates reported in this study are relatively small (<4 mm/hr) and are subject to error in both the Hotplate and in the WSR measurements. Both errors are discussed and a formulism is established for estimating the best-fit coefficient and its standard error.

The assertion that α is solely dependent on snowflake number concentration (Equation 3), and that this dependency drives the temperature dependence we report, can be criticized on several fronts. In particular, criticism can be leveled against the assumptions that snowflake terminal velocity is a constant that the vigor of ice nuclei activation is insensitive to either aerosol background or cloud depth (i.e., cloud top temperature). Since the latter of these should vary with cloud top height, something which can be diagnosed using height-resolved WSR measurements, there is some potential for refinement. In this way the technique we propose – using fast response snowrate measurements in combination with the WSR – may help to improve region-wide updates of snowfall.

7. APPENDIX

Described here are the statistical tools we used to derive three estimates of the coefficient in Equation 1. Each approach starts with the paired sets Z_e and S^2. The first takes Z_e to be the dependent variable and employs a least squares procedure called “curvefit” (Integrated Data Language, RSI Inc.) which iteratively minimizes the sum of the square of the departure of the data points from the best-fit line. The calculation proceeds via three steps: 1) A provisional value of α_1 is produced when “curvefit” is initialized with equal weighting applied to all data points, and the resulting α_1 is used to evaluate weights as the either the reciprocal of the actual departure or 0.01 m^3/mm^6. The larger of the two values is chosen as the weight. 2) Curvefit is applied again, with weights set equal to the value chosen in step #1, and the new estimate of α_1 is used to update the weights as in the #1 step. 3) Step #2 is repeated until the absolute relative change of α_1 is less than 0.01. It can be shown that these steps converge to a solution which minimizes the sum of the absolute value of the departures, as opposed to the least squares approach of minimizing the sum of the square of the departures, and is thus preferred in a situation such as this where there are outlier data values (Aster et al., 2005).

The value of α_2 is derived as described for α_1, however S^2 is taken to be the dependent variable and the resulting fit coefficient (γ_2) is converted to an "alpha" (i.e., $\alpha_2 = 1/\gamma_2$). The lower-limit for the weight (steps #1 and #2) is taken to be 1 hr mm^{-1}.

The values of α_1 and γ_2 are used to derive the standard errors as

$$\sigma_{\alpha 1} = \sqrt{\frac{\sum(Z_e - \alpha_1 \cdot S^2)^2}{N \cdot \left(\sum S^4 - \frac{1}{N} \cdot (\sum S^2)^2\right)}} \quad \text{(A1)}$$

$$\sigma_{\gamma 2} = \sqrt{\frac{\sum(S^2 - \gamma_2 \cdot Z_e)^2}{N \cdot \left(\sum Z_e^2 - \frac{1}{N} \cdot (\sum Z_e)^2\right)}} \quad \text{(A2)}$$

$$\sigma_{\alpha 2} = \frac{1}{\gamma_2^2} \cdot \sigma_{\gamma 2} \quad \text{(A3)}$$

Here N is the total number of data points and Equation A3 employs propagation of error (Young, 1962) to derive the α_2 standard error from the values of γ_2 and $\sigma_{\gamma 2}$.

The third approach is based on the principle of maximum likelihood applied to logarithmically transformed sets of Z_e and S^2. From consideration of the principle of maximum likelihood (Young, 1962) it can be shown that the fit coefficient is

$$\alpha_3 = \exp\left(\left\langle \ln Z_e \right\rangle - \left\langle S^2 \right\rangle\right) \quad \text{(A4)}$$

Here $\left\langle \ln Z_e \right\rangle$ and $\left\langle \ln S^2 \right\rangle$ are averages of the log-transformed sets of Z_e and S^2 and the standard error is

$$\sigma_{\alpha 3} = \sqrt{\alpha_3^2 \cdot \frac{\sum(\ln Z_e - \ln \alpha_3 - \ln S^2)^2}{N^2}} \quad \text{(A5)}$$

6. REFERENCES

Aster, R., B. Borchers, and C. Thurber, 2004: *Parameter Estimation and Inverse Problems*, Academic Press.

Bech, J., B. Codina, J. Lorente, and D. Bebbington, 2003: The Sensitivity of Single Polarization Weather Radar Beam Blockage Correction to Variability in the Vertical Refractivity Gradient, *J. Atmos. Oceanic Technol.*, **20**, 845–855.

Cooper, W. A., 1986: Ice initiation in natural clouds. *Precipitation Enhancement—A Scientific Challenge, Meteor. Monogr.,* No. 21, Amer. Meteor. Soc., 29–32.

Crum, T., and R. Alberty, 1993: The WSR-88D and the WSR-88D operational support facility. *Bull. Amer. Meteor. Soc.*, **74**, 1669-1687.

Fujiyoshi, Y., T. Endoh, T. Yamada, K. Tsuboki, Y. Tachibana and G. Wakahama, 1990: Determination of a *Z-R* relationship for snowfall using a radar and high sensitivity snow gauges. *J. Appl. Meteor.*, **29**, 147–152.

Joss J., and A. Waldvogel, 1990: Precipitation measurement and hydrology. Radar in Meteorology: Battan Memorial and 40th Anniversary Radar Meteorology Conference, D. Atlas, Ed., Amer. Meteor. Soc., 577–606.

Groisman, P. Y., and D. R. Legates, 1994: The accuracy of United States precipitation data, *Bull. Am. Meteorol. Soc*., ***75***(2), 215–227.

Locatelli, J.D., and P.V.Hobbs, 1974: Fallspeeds and masses of solid precipitation particles, *J.Geophys.Res.*, 79, 2185-2197

Marshall, J. S., R. C. Langille, and W. M. Palmer, 1947: Measurements of Rainfall by
Radar, *J. Meteor*., **4**, 186-192

Marshall, J.S. and W. M. Palmer, 1948: The distribution of raindrops with size. *J. Atmos. Sci*., **5**, 165-166

Mote, P., A. Hamlet, M. Clark, and D. Lettenmaier, 2005: Declining Mountain Snowpack in Western North America. *Bull. Amer. Meteor. Soc*., **86**, 39-49.

Piechota, T., J. Timilsena, G. Tootle, and H. Hidalgo, 2004: The western U.S. drought:
How bad is it? *Eos, Trans. Amer. Geophys. Union,* **85**, 301-308.

Rasmussen, R. M., J. Hallett, R. Purcell, J. Cole, and M. Tryhane, 2002: The Hotplate
Snowgauge. *11th Conf. on Cloud Physics*, Ogden, UT, Amer. Meteor. Soc., P1.6.

Rasmussen, J. Hallett, M. L. Tryhane, S.D. Landolt, R. Purcell, M.C. Beaubien,
Jeffries, W.Q., F. Hage, and J. Cole, 2005: The hotplate snow gauge, *13th Symposium on Meteorological Observations and Instrumentation*, Savannah, GA, June 20-24, 6.2.

Rasmussen, M. Dixon, S. Vasiloff, F. Hage, S. Knight, J. Vivekanandan, and
Xu, M., 2003: Snow Nowcasting Using a Real-Time Correlation of Radar Reflectivity with Snow Gauge Accumulation. *J. Appl. Meteor*, **42**, 20–36.

Sekhon, R.S and R.C.Shrivastava, 1970: Snow size spectra and radar reflectivity, *J. Atmos. Sci.*, 27, 299-307

Super, A. B., and E. W. Holroyd, 1998: Snow accumulation algorithm for the
WSR-88D radar: Final Report. Bureau of Reclamation Report R-98-05, Denver, CO, July, 75.

Wolfe, J.P., Radar-estimated Upslope Snowfall Rates in Southeastern Wyoming, MS thesis, Dept. of Atmospheric Science, University of Wyoming, May 2007

Young, H.D.,1962: *Statistical Treatment of Experimental Data*, McGraw-Hill, New York, New York.

THE DEVELOPMENT OF AIRBORNE COSSIR FOR ICE CLOUD MEASUREMENTS

Zhaonan Zhang, Bryan Monosmith
Microwave Instruments & Technology Branch
NASA, Goddard Space Flight Center

1. INTRODUCTION

Ice clouds are a key atmospheric entity that couple the global hydrologic and energy cycles and modulate the climate system response to changes in global forcing. Most ice cloud measurements conducted in the past by aircraft or satellite sensors have been limited to the visible and infrared regions of the spectrum. Retrievals of cloud parameters from these sensors are generally limited to regions near the top of the ice clouds. To probe denser ice clouds and study their microphysical properties requires sensors at longer wavelengths. Theoretical analyses have shown that millimeter and sub-millimeter wave radiometric measurements with broad spectral coverage can provide reliable estimations of ice cloud parameters [1], [2]. To realize this potential, an airborne Compact Scanning Sub-millimeter wave Imaging Radiometer, CoSSIR, was developed.

2. NEW FREQUENCY BANDS

The primary version of CoSSIR was composed of six total power sub-millimeter wave radiometers at the frequencies of 183, 220, 380, 487 (V & H), & 640 GHz. The 487 GHz (V & H) channels were dual-polarized and the remaining channels were horizontally polarized. The instrument was first flown on board the NASA ER-2 aircraft during CRYSTAL-FACE in July 2002. After some improvement, the instrument was flown again on board the NASA WB-57 aircraft during the first phase of the CR-AVE in January 2006. During these field campaigns, the instrument could provide water vapor profiling capability up to an altitude of about 15 km.

Studies have shown that water vapor absorption reduces sensitivity to lower clouds for frequencies above 500 GHz. Lower frequencies, 183, 220, & 380 GHz, in sub-millimeter wave range have less water vapor absorption and can thus sense lower altitude ice clouds, which tend to have large particles.

Studies have also shown that two highest water vapor absorption windows with acceptable transmission in sub-millimeter wave range are around 643 GHz and 874 GHz. Simulations demonstrate that the higher frequencies, particularly at 874 GHz, are highly sensitivity to scattering by ice particles. Simulating the polarization ratios of 640 GHz brightness temperature demonstrates greater sensitivity to particle size.

Consequently, multiple sub-millimeter wave frequency, 183 GHz ~ 874 GHz, measurements on water vapor lines provide humidity profile and cloud height information, thereby providing a unique measurement of ice clouds. In order to extend the frequency range from 643 GHz to 874 GHz, a dual-polarization 643 GHz and a single-polarization 874 GHz radiometer were recently developed. The design and development of these radiometers will be described in the next two sections.

The latest version of CoSSIR that measured radiation at the frequencies of 183, 220, 380, 643 (V & H) and 874GHz was flown for the TC4 field campaign in July ~ August, 2007.

3. DESIGN OF RADIOMETERS

The descriptions of the radiometer design are going to focus on the recent developed radiometers, the dual-pol 643 GHz and single-pol 874 GHz radiometers.

The dual 643 GHz radiometers were driven by two independent Gunn oscillators with operating frequencies at 80.375 GHz. Each source signal was fed into a cascade of two varactor doublers and its frequency was multiplied up to 321.5 GHz with a 4 mW power level to provide a LO power for 643 GHz sub-harmonic mixer.

Due to considerations of frequency stability, a DRO, Dielectric Resonator Oscillator, output frequency of 36.417 GHz was selected for the driving source of the 874 GHz receiver. After the source power was amplified by an RF amplifier, the signal frequency was multiplied by 12 with a cascade chain composed of a frequency quadrupler and tripler. Consequently, a signal at frequency of 437 GHz with a 2.5 mW power level was produced to be used for a LO power of 874 GHz sub-harmonic mixer.

The frequency stability of the LO was degraded with the multiplication of the fundamental frequency. For the dual-pol 643 GHz receivers, the frequency stability of Gunn oscillators was typically at 8 MHz/^{0}C. But the stability of the LO was reduced to 32 MHz/^{0}C. In order to keep the down converted IF signal within the IF band a frequency band of 0.1 ~ 6.0 GHz was chosen.

The DRO chosen was of high quality with frequency stability of 3.5 MHz/^{0}C for the 874 GHz LO chain. Since the fundamental frequency was multiplied by 12 and there were other frequency stability issues in the 874 GHz channel, an IF bandwidth of 0.5 ~ 8.0 GHz was selected.

4. DEVELOPMENT OF RADIOMETERS

In the CoSSIR radiometers, stages of multipliers were employed to multiply frequencies up to the LO frequencies. The forwards biases of the multipliers induced by the input RF powers were sensitive to the input power levels and physical temperature. During the development, heat sinking was properly mounted on the multipliers to keep temperatures at a certain range; thermal control chips were attached on the Gunn oscillators to control operating temperatures; and layouts were carefully considered to avoid interference among the channels.

Some innovations were implemented during the development of the 874 GHz radiometer. In the primary version, a DRO was operating at a frequency of 12.140 GHz. A tripler & RF amplifier output frequency of 36.420 GHz was connected to the next stage with a WR-22 flange. In the latest version, a DRO frequency of 36.417 GHz was selected and a K-connector to replace the WR-22 flange in the Trip & RF amplifier. These approaches significantly reduced DC power supply and volume allowing the entire radiometers to be integrated into the original drum.

5. THE COSSIR DRUM

The CoSSIR drum, a cylinder 8.5” diameter and 11” length, with the control unit is shown in Figure 1.

Fig. 1 The CoSSIR drum with the control unit.

The calibration references of the drum were composed of two close coupled external blackbodies at the temperatures of ~250 K and ~300 K. The external blackbody measured to an accuracy of +/- 0.1 K provided a calibration accuracy of about +/- 0.7 K in the brightness temperature range of 200 ~ 300 K.

The scan geometry of CoSSIR was software programmable with versatile scan modes. It can be programmed to perform a conical scan with incidence angles between 0^0 ~ 54^0, or an across track scan, or a combination of both. The details of the scan pattern can be found in Wang et al. [3].

6. LABORATORY CALIBRATION

A few series of laboratory calibration tests of the instrument were conducted with a liquid nitrogen (LN_2) calibration load to verify and enhance radiometry performance. An across track scan mode was programmed in these tests, with the antenna beams pointing at three fixed scenes of cold, hot, and LN_2 loads for one second each in every cycle. The calibration run normally lasted 1~2 hours, after the initial instrument warm up of about 30 minutes. A blower was used to apply cold air at the scan head continually to keep the Gunn oscillators from overheating.

Calibration data was used to adjust bias voltages and video-amps gains to balance the performance of the 643 GHz dual channels. After several testing cycles, the measured brightness temperatures of the 643 GHz dual channels were within 1.0 K during laboratory calibrations.

House keeping data was used to improve the performance of the 874 GHz receiver. The test data showed that the temperature variations of the DRO were less than expected. But the temperature changes of the RF amplifier were still un-controllable, which seriously affected the LO power level and performance sensitivity.

The laboratory calibrations provided unique information about how to adjust bias voltages on each stage and balance the entire operations. The adjustments enhanced performance of radiometers, resulting in a system noise temperature, T_{sys}, of 4000 K for the 643 GHz radiometer and 8000 K for the 874 GHz radiometer.

7. TC4 FIELD CAMPAIGN

The TC4 field campaign was in Costa Rica during July 15 ~ August 10, 2007. CoSSIR was on board the NASA ER-2 aircraft with a cruising altitude of about 20 km. The measurements were therefore above all cloud systems. Previous measurements of ice clouds by CoSSIR (Evans et al., 2005) were limited to the frequency range of 183~640 GHz. The measurements during the TC4 extended the frequency coverage over 183~874 GHz. Additionally, CoSSIR had a dual-polarization measurement capability at 640 GHz during TC4.

A segment of brightness temperature map acquired by the CoSSIR is shown in Figure 2.

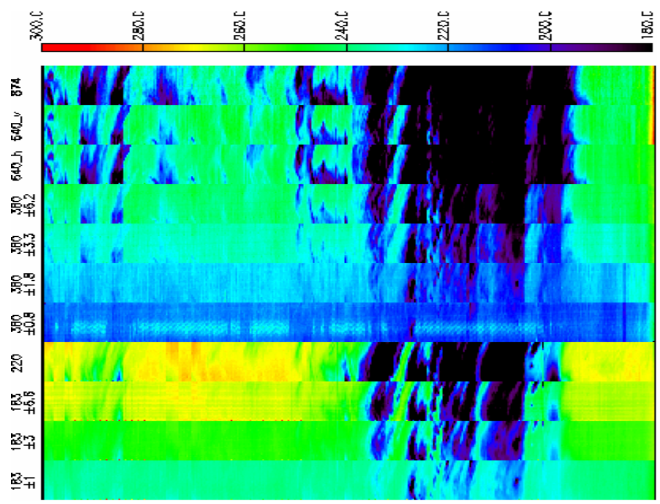

Fig. 2. The brightness temperature maps acquired by the CoSSIR during a flight segment on July 17, 2007 over ocean areas south of San Jose, Costa Rica.

Brightness temperature variations along the flight path obtained at an observation angle of 53.6^0 in the forward direction during a flight on July 17, 2007 over ocean areas south of San Jose, Costa Rica.

The brightness temperature map shows that the regions of low brightness temperatures are a result of millimeter wave and sub-millimeter wave scattering by ice particles in the clouds. The scattering is strongly frequency dependent, the higher the frequency the larger the scattering. The dispersion in the scattering signatures near the water vapor lines of 183 and 380 GHz are caused by water vapor absorption.

For light to moderate ice clouds, the high-frequency channels, particularly at 874 GHz, show a much higher sensitivity to scattering by ice particles. In the cloud-free regions, the polarization ratios of 643 GHz brightness temperature are close to unity as expected; while in the region of ice clouds these ratios are varied from unity, clearly indicating non-spherical features of the ice particles.

8. SCIENTIFIC SIGNIFICANCE

The brightness temperature map presented above clearly demonstrates the recent advance in sub-millimeter wave radiometry for ice cloud sensing. The new 874 GHz radiometer greatly improves the CoSSIR sensitivity to small ice particles. This implies that CoSSIR is able to pick up the measurements of ice clouds where the visible/IR approaches left behind, i.e. saturated. The new polarization measurement capability at 643 GHz can provide information on particle shapes, as well as improve the accuracy of the ice cloud parameter retrievals, e.g., ice water path and particle size.

9. ACKNOWLEDGE

The authors would like to acknowledge Gerald Heymsfield and the Principal Investigator, James Wang for their assistance in preparing and editing this presentation. Ed Means and Eric Simon also contributed to the mechanical, electrical and software modifications to CoSSIR in preparation for the TC4 campaign. Virginia Diodes Inc. is largely responsible for developing sub-millimeter technologies used in CoSSIR, especially the 874 GHz radiometer components.

10. REFERENCES

[1] K.F. Evans, J.R. Wang, P.E. Racette, G. Heymsfield, L. Li, "Ice Cloud Retrievals and Analysis with Data from the Conical Scanning Submillimeter Imaging Radiometer and the Cloud Radar System during CRYSTAL-FACE," J. Appl. Meter., 44, 839-859, June 2005.

[2] J.R. Wang, L.A. Chang, B. Monosmith, Z. Zhang, "Water Vapor Profiling From CoSSIR Radiometric Measurements," IEEE Trans. Geosci. Remote Sens., vol. 46. no. 1. pp. 137-145, Jan. 2008.

[3] J.R. Wang, P.E. Racette, J.E. Piepmeier, B. Monosmith, and W. Manning, "Airborne CoSMIR Observations Between 50 and 183 GHz over Snow-covered Sierra Mountains," IEEE Trans. Geosci. Remote Sens., 45(10), pp. 55-61, 2007.

THE DEVELOPMENT OF AIRBORNE COSSIR FOR ICE CLOUD MEASUREMENTS

Zhaonan Zhang, Bryan Monosmith
Microwave Instruments & Technology Branch
NASA, Goddard Space Flight Center

1. INTRODUCTION

Ice clouds are a key atmospheric entity that couple the global hydrologic and energy cycles and modulate the climate system response to changes in global forcing. Most ice cloud measurements conducted in the past by aircraft or satellite sensors have been limited to the visible and infrared regions of the spectrum. Retrievals of cloud parameters from these sensors are generally limited to regions near the top of the ice clouds. To probe denser ice clouds and study their microphysical properties requires sensors at longer wavelengths. Theoretical analyses have shown that millimeter and sub-millimeter wave radiometric measurements with broad spectral coverage can provide reliable estimations of ice cloud parameters [1], [2]. To realize this potential, an airborne Compact Scanning Sub-millimeter wave Imaging Radiometer, CoSSIR, was developed.

2. NEW FREQUENCY BANDS

The primary version of CoSSIR was composed of six total power sub-millimeter wave radiometers at the frequencies of 183, 220, 380, 487 (V & H), & 640 GHz. The 487 GHz (V & H) channels were dual-polarized and the remaining channels were horizontally polarized. The instrument was first flown on board the NASA ER-2 aircraft during CRYSTAL-FACE in July 2002. After some improvement, the instrument was flown again on board the NASA WB-57 aircraft during the first phase of the CR-AVE in January 2006. During these field campaigns, the instrument could provide water vapor profiling capability up to an altitude of about 15 km.

Studies have shown that water vapor absorption reduces sensitivity to lower clouds for frequencies above 500 GHz. Lower frequencies, 183, 220, & 380 GHz, in sub-millimeter wave range have less water vapor absorption and can thus sense lower altitude ice clouds, which tend to have large particles.

Studies have also shown that two highest water vapor absorption windows with acceptable transmission in sub-millimeter wave range are around 643 GHz and 874 GHz. Simulations demonstrate that the higher frequencies, particularly at 874 GHz, are highly sensitivity to scattering by ice particles. Simulating the polarization ratios of 640 GHz brightness temperature demonstrates greater sensitivity to particle size.

Consequently, multiple sub-millimeter wave frequency, 183 GHz ~ 874 GHz, measurements on water vapor lines provide humidity profile and cloud height information, thereby providing a unique measurement of ice clouds. In order to extend the frequency range from 643 GHz to 874 GHz, a dual-polarization 643 GHz and a single-polarization 874 GHz radiometer were recently developed. The design and development of these radiometers will be described in the next two sections.

The latest version of CoSSIR that measured radiation at the frequencies of 183, 220, 380, 643 (V & H) and 874GHz was flown for the TC4 field campaign in July ~ August, 2007.

3. DESIGN OF RADIOMETERS

The descriptions of the radiometer design are going to focus on the recent developed radiometers, the dual-pol 643 GHz and single-pol 874 GHz radiometers.

The dual 643 GHz radiometers were driven by two independent Gunn oscillators with operating frequencies at 80.375 GHz. Each source signal was fed into a cascade of two varactor doublers and its frequency was multiplied up to 321.5 GHz with a 4 mW power level to provide a LO power for 643 GHz sub-harmonic mixer.

Due to considerations of frequency stability, a DRO, Dielectric Resonator Oscillator, output frequency of 36.417 GHz was selected for the driving source of the 874 GHz receiver. After the source power was amplified by an RF amplifier, the signal frequency was multiplied by 12 with a cascade chain composed of a frequency quadrupler and tripler. Consequently, a signal at frequency of 437 GHz with a 2.5 mW power level was produced to be used for a LO power of 874 GHz sub-harmonic mixer.

The frequency stability of the LO was degraded with the multiplication of the fundamental frequency. For the dual-pol 643 GHz receivers, the frequency stability of Gunn oscillators was typically at 8 MHz/^{0}C. But the stability of the LO was reduced to 32 MHz/^{0}C. In order to keep the down converted IF signal within the IF band a frequency band of 0.1 ~ 6.0 GHz was chosen.

The DRO chosen was of high quality with frequency stability of 3.5 MHz/^{0}C for the 874 GHz LO chain. Since the fundamental frequency was multiplied by 12 and there were other frequency stability issues in the 874 GHz channel, an IF bandwidth of 0.5 ~ 8.0 GHz was selected.

4. DEVELOPMENT OF RADIOMETERS

In the CoSSIR radiometers, stages of multipliers were employed to multiply frequencies up to the LO frequencies. The forwards biases of the multipliers induced by the input RF powers were sensitive to the input power levels and physical temperature. During the development, heat sinking was properly mounted on the multipliers to keep temperatures at a certain range; thermal control chips were attached on the Gunn oscillators to control operating temperatures; and layouts were carefully considered to avoid interference among the channels.

Some innovations were implemented during the development of the 874 GHz radiometer. In the primary version, a DRO was operating at a frequency of 12.140 GHz. A tripler & RF amplifier output frequency of 36.420 GHz was connected to the next stage with a WR-22 flange. In the latest version, a DRO frequency of 36.417 GHz was selected and a K-connector to replace the WR-22 flange in the Trip & RF amplifier. These approaches significantly reduced DC power supply and volume allowing the entire radiometers to be integrated into the original drum.

5. THE COSSIR DRUM

The CoSSIR drum, a cylinder 8.5” diameter and 11” length, with the control unit is shown in Figure 1.

Fig. 1 The CoSSIR drum with the control unit.

The calibration references of the drum were composed of two close coupled external blackbodies at the temperatures of ~250 K and ~300 K. The external blackbody measured to an accuracy of +/- 0.1 K provided a calibration accuracy of about +/- 0.7 K in the brightness temperature range of 200 ~ 300 K.

The scan geometry of CoSSIR was software programmable with versatile scan modes. It can be programmed to perform a conical scan with incidence angles between 0^0 ~ 54^0, or an across track scan, or a combination of both. The details of the scan pattern can be found in Wang et al. [3].

6. LABORATORY CALIBRATION

A few series of laboratory calibration tests of the instrument were conducted with a liquid nitrogen (LN_2) calibration load to verify and enhance radiometry performance. An across track scan mode was programmed in these tests, with the antenna beams pointing at three fixed scenes of cold, hot, and LN_2 loads for one second each in every cycle. The calibration run normally lasted 1~2 hours, after the initial instrument warm up of about 30 minutes. A blower was used to apply cold air at the scan head continually to keep the Gunn oscillators from overheating.

Calibration data was used to adjust bias voltages and video-amps gains to balance the performance of the 643 GHz dual channels. After several testing cycles, the measured brightness temperatures of the 643 GHz dual channels were within 1.0 K during laboratory calibrations.

House keeping data was used to improve the performance of the 874 GHz receiver. The test data showed that the temperature variations of the DRO were less than expected. But the temperature changes of the RF amplifier were still un-controllable, which seriously affected the LO power level and performance sensitivity.

The laboratory calibrations provided unique information about how to adjust bias voltages on each stage and balance the entire operations. The adjustments enhanced performance of radiometers, resulting in a system noise temperature, T_{sys}, of 4000 K for the 643 GHz radiometer and 8000 K for the 874 GHz radiometer.

7. TC4 FIELD CAMPAIGN

The TC4 field campaign was in Costa Rica during July 15 ~ August 10, 2007. CoSSIR was on board the NASA ER-2 aircraft with a cruising altitude of about 20 km. The measurements were therefore above all cloud systems. Previous measurements of ice clouds by CoSSIR (Evans et al., 2005) were limited to the frequency range of 183~640 GHz. The measurements during the TC4 extended the frequency coverage over 183~874 GHz. Additionally, CoSSIR had a dual-polarization measurement capability at 640 GHz during TC4.

A segment of brightness temperature map acquired by the CoSSIR is shown in Figure 2.

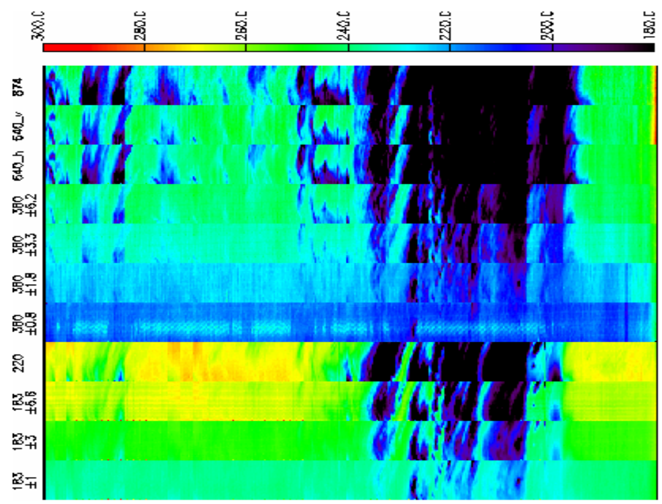

Fig. 2. The brightness temperature maps acquired by the CoSSIR during a flight segment on July 17, 2007 over ocean areas south of San Jose, Costa Rica.

Brightness temperature variations along the flight path obtained at an observation angle of 53.6^0 in the forward direction during a flight on July 17, 2007 over ocean areas south of San Jose, Costa Rica.

The brightness temperature map shows that the regions of low brightness temperatures are a result of millimeter wave and sub-millimeter wave scattering by ice particles in the clouds. The scattering is strongly frequency dependent, the higher the frequency the larger the scattering. The dispersion in the scattering signatures near the water vapor lines of 183 and 380 GHz are caused by water vapor absorption.

For light to moderate ice clouds, the high-frequency channels, particularly at 874 GHz, show a much higher sensitivity to scattering by ice particles. In the cloud-free regions, the polarization ratios of 643 GHz brightness temperature are close to unity as expected; while in the region of ice clouds these ratios are varied from unity, clearly indicating non-spherical features of the ice particles.

8. SCIENTIFIC SIGNIFICANCE

The brightness temperature map presented above clearly demonstrates the recent advance in sub-millimeter wave radiometry for ice cloud sensing. The new 874 GHz radiometer greatly improves the CoSSIR sensitivity to small ice particles. This implies that CoSSIR is able to pick up the measurements of ice clouds where the visible/IR approaches left behind, i.e. saturated. The new polarization measurement capability at 643 GHz can provide information on particle shapes, as well as improve the accuracy of the ice cloud parameter retrievals, e.g., ice water path and particle size.

9. ACKNOWLEDGE

The authors would like to acknowledge Gerald Heymsfield and the Principal Investigator, James Wang for their assistance in preparing and editing this presentation. Ed Means and Eric Simon also contributed to the mechanical, electrical and software modifications to CoSSIR in preparation for the TC4 campaign. Virginia Diodes Inc. is largely responsible for developing sub-millimeter technologies used in CoSSIR, especially the 874 GHz radiometer components.

10. REFERENCES

[1] K.F. Evans, J.R. Wang, P.E. Racette, G. Heymsfield, L. Li, "Ice Cloud Retrievals and Analysis with Data from the Conical Scanning Submillimeter Imaging Radiometer and the Cloud Radar System during CRYSTAL-FACE," J. Appl. Meter., 44, 839-859, June 2005.

[2] J.R. Wang, L.A. Chang, B. Monosmith, Z. Zhang, "Water Vapor Profiling From CoSSIR Radiometric Measurements," IEEE Trans. Geosci. Remote Sens., vol. 46. no. 1. pp. 137-145, Jan. 2008.

[3] J.R. Wang, P.E. Racette, J.E. Piepmeier, B. Monosmith, and W. Manning, "Airborne CoSMIR Observations Between 50 and 183 GHz over Snow-covered Sierra Mountains," IEEE Trans. Geosci. Remote Sens., 45(10), pp. 55-61, 2007.